TAL TECH

DOCTORAL THESIS

Measurement of Higgs Boson Couplings in Final States Featuring Multiple Leptons and Hadronic τ Decay Products

Karl Ehatäht

CERN-THESIS-2023-242
10/11/2023

TALLINNA TEHNIKAÜLIKOOL
TALLINN UNIVERSITY OF TECHNOLOGY
TALLINN 2023

TALLINN UNIVERSITY OF TECHNOLOGY
DOCTORAL THESIS
52/2023

Measurement of Higgs Boson Couplings in Final States Featuring Multiple Leptons and Hadronic τ Decay Products

KARL EHATÄHT

TAL TECH PRESS

TALLINN UNIVERSITY OF TECHNOLOGY
School of Science
Department of Cybernetics

The dissertation was accepted for the defence of the degree of Doctor of Philosophy in Applied Physics on 15 September 2023

Supervisor: PhD Mario Kadastik,
Laboratory of High Energy and Computational Physics,
National Institute of Chemical Physics and Biophysics,
Tallinn, Estonia

Co-supervisor: PhD Christian Veelken,
Laboratory of High Energy and Computational Physics,
National Institute of Chemical Physics and Biophysics,
Tallinn, Estonia

Opponents: PhD Oxana Smirnova,
Lund University,
Lund, Sweden

PhD Thomas Strebler,
Centre de physique des particules de Marseille,
Marseille, France

Defence of the thesis: 10 November 2023, Tallinn

Declaration:
Hereby I declare that this doctoral thesis, my original investigation and achievement, submitted for the doctoral degree at Tallinn University of Technology, has not been submitted for any academic degree elsewhere.

Karl Ehatäht _____
signature

Copyright: Karl Ehatäht, 2023
ISSN 2585-6898 (publication)
ISBN 978-9916-80-057-7 (publication)
ISSN 2585-6901 (PDF)
ISBN 978-9916-80-058-4 (PDF)
Printed by Koopia Niini & Rauam

TALLINNA TEHNIKAÜLIKOOL
DOKTORITÖÖ
52/2023

Higgsi bosoni seoseparameetrite mõõtmine mitmeid leptoneid ja hadronilisi τ laguprodukte sisaldavates lõppolekutes

KARL EHATÄHT

TAL TECH
KIRJASTUS

Contents

Contents i

List of Publications iv

Author's Contributions to the Publications v

Abbreviations vii

1 Introduction 1

2 Theoretical foundations 3
2.1 Overview of modern particle physics 3
2.1.1 Quantum field theory 4
2.1.2 Quantum chromodynamics 8
2.1.3 Electroweak sector 10
2.1.4 Higgs mechanism 12
2.1.5 The standard model of particle physics 15
2.1.6 Effective field theories 17
2.2 LHC phenomenology 19
2.2.1 Event production 19
2.2.2 Particle decays 24
2.3 Higgs boson 29
2.3.1 Decay modes 30
2.3.2 Production mechanisms 32
2.3.3 Measurement frameworks 35
2.4 Associated production of Higgs boson with top quarks 39
2.4.1 Theoretical aspects 39
2.4.2 Experimental characterization 44
2.5 Higgs boson pair production 45
2.5.1 Nonresonant HH production 46
2.5.2 EFT benchmarks and coupling scans 50
2.5.3 Resonant HH production 58
2.5.4 Experimental status 62

3 The LHC and the CMS experiment 66
3.1 The Large Hadron Collider 66
3.2 The CMS detector 70
3.2.1 Tracker 74
3.2.2 Calorimeters 76
3.2.3 Muon detectors 80
3.2.4 Triggers 81

4 Particle- and event-level objects 86
4.1 Object reconstruction and identification 86
4.1.1 Muons 87
4.1.2 Electrons 88
4.1.3 Jets 89
4.1.4 Hadronic τ decay products 94
4.1.5 Missing transverse energy 97

4.2 Object selection criteria 99
4.2.1 Baseline selection for leptons 100
4.2.2 Signal leptons 102
4.2.3 Fakeable leptons 104
4.2.4 τ_{h} candidates 109
4.2.5 Jets 110

5 Signal and background estimation 112
5.1 Monte Carlo simulation 112
5.2 Data-to-Monte Carlo corrections 117
5.3 Fake background estimation 123
5.3.1 Fake factor method 124
5.3.2 Lepton fake rate measurement 126
5.3.3 τ_{h} fake rate measurement 132
5.3.4 Closure uncertainty 137
5.4 Charge flip background estimation 140

6 Signal extraction 143
6.1 Inference 143
6.1.1 Basics 143
6.1.2 Likelihood model 147
6.1.3 Limit setting 153
6.1.4 Unblinding procedure 156
6.2 Shape discriminant 159
6.2.1 Machine learning 159
6.2.2 Boosted decision trees 165
6.2.3 Deep neural networks 169
6.2.4 Matrix element method 173

7 Measurement of $\mathrm{t\bar{t}H}$ production in multilepton final states 182
7.1 Analysis 182
7.2 Results 191

8 Measurement of HH production in multilepton final states 205
8.1 Analysis 205
8.2 Results 214

9 Summary 229

List of Figures 232

List of Tables 245

References 285

Acknowledgements 287

Abstract 288

Kokkuvõte 290

Appendix 1 291
Appendix 2 345
Appendix 3 413
Appendix 4 431
Curriculum Vitae ..... A
Elulookirjeldus C

List of Publications

The present Ph.D. thesis is based on the following publications that are referred to in the text by Arabic numerals.

I CMS Collaboration, "Measurement of the Higgs boson production rate in association with top quarks in final states with electrons, muons, and hadronically decaying tau leptons at $\sqrt{s} = 13$ TeV," *Eur. Phys. J. C*, vol. 81, no. 4, p. 378, 2021. DOI: 10.1140/epjc/s10052-021-09014-x. arXiv: 2011.03652 [hep-ex]

II CMS Collaboration, "Search for Higgs boson pairs decaying to WW^*WW^*, $WW^*\tau\tau$, and $\tau\tau\tau\tau$ in proton-proton collisions at $\sqrt{s} = 13$ TeV," *JHEP*, vol. 07, p. 095, 2023. DOI: 10.1007/JHEP07(2023)095. arXiv: 2206.10268 [hep-ex]

III K. Ehatäht and C. Veelken, "Stitching Monte Carlo samples," *Eur. Phys. J. C*, vol. 82, no. 5, p. 484, 2022. DOI: 10.1140/epjc/s10052-022-10407-9. arXiv: 2106.04360 [physics.data-an]

IV K. Ehatäht and C. Veelken, "Application of the matrix element method to Higgs boson pair production in the channel $HH \to b\bar{b}WW^*$ at the LHC," *Nucl. Instrum. Meth. A*, vol. 1028, p. 166 373, 2022. DOI: 10.1016/j.nima.2022.166373. arXiv: 2108.05267 [hep-ph]

Author's Contributions to the Publications

I I joined the $t\bar{t}H$ multilepton team of the CMS collaboration back in 2017. Since then I worked particularly on those $t\bar{t}H$ multilepton channels that feature at least one τ_h candidate in the final state. My first analysis is based on the CMS data that was recorded in 2017. As a recognition for the work I had done, I was given an opportunity to present the results of these studies in an approval presentation, which is part of a review process internal to the CMS collaboration. The analysis was published as a preliminary result in Ref. [5], but in form of a Public Analysis Summary (PAS) rather than in a scientific journal.

I was among the first adopters of a new data format called NanoAOD, which I extensively tested and contributed to right after its initial prototype was officially commissioned by the CMS collaboration. I had also actively contributed to the NanoAOD companion tool, which augments its contents with data-to-MC SFs and systematic uncertainties. This work earned me a spot in CHEP conference of 2019, where I presented a poster advertising the format [6]. Nowadays, the NanoAOD data format is used by hundreds of collaborators around the world as the default data tier for storing collision and simulation data.

I produced custom NanoAOD samples for the full LHC Run 2 analysis. This was done for three reasons: to ramp up the analysis efforts and bypass the official production schedule, to test the DeepTau ID as early as possible, and to include a custom collection of AK8 jets, which are reconstructed excluding loosely selected leptons from the list of PF candidates that are normally used as input to the jet reconstruction. I processed a total of $2\,500$ MC samples, including hundreds of HH signal and $t\bar{t}$+jets background samples that were needed in the HH multilepton and $b\bar{b}WW^*$ analyses [2, 7].

As for the $t\bar{t}H$ multilepton analysis, I developed and maintained a software framework, which handled the event selection and binning, MC reweighting, application of data-to-MC SFs, propagation of systematic uncertainties, and production of shape templates for final inference, as well as the distribution and monitoring of analysis jobs on the local tier-2 computer cluster in Tallinn and on the WLCG. Throughout the five years that I provided technical support for it, the framework was used by about ten graduate-level students, postdocs and other research staff members on a daily basis. I also coordinated the synchronization efforts to fine-tune the event selection requirements and to iron out bugs, and provided support for the usage of the framework to other members of the analysis group. I also performed a set of auxiliary measurements for the $t\bar{t}H$ multilepton analysis: I developed a framework for measuring lepton FRs, automated and performed the measurement of electron charge misidentification rates, as well as normalization SFs for the DY process, and measured τ_h FRs.

I produced the „datacards" for the final publication. Later on, I modified the datacards according to the binning scheme of STXS stage 1.2 for a followup publication in *Nature*, which combined the results of other CMS analyses to summarize the progress that was made since the discovery of the Higgs boson ten years prior [8].

II My contribution to the HH multilepton analysis is similar to my contribution to the $t\bar{t}H$ multilepton analysis. I continued to provide support for the software framework and updated the framework to match the needs of HH multilepton analysis. In particular, I implemented a reweighting procedure for the HH signal MC samples based on differential cross sections, and updated the data-to-MC SFs, systematic uncertainties, and FRs as necessary. I presented the results of HH multilepton analysis in the 2nd

CERN Baltic Conference in 2022 [9]. The results of HH multilepton analysis presented here are combined with the results of other HH analyses performed by the CMS collaboration, and the outcome of this combination is published in the same *Nature* paper that was mentioned earlier [8].

I would like to point out that I also contributed to the HH $\rightarrow b\bar{b}WW^*$ analysis [7], which is still under collaboration-wide review and has thus not been submitted to a journal at the time of writing. I generated 21 MC samples with full detector simulation for the studies of resonant HH production for this analysis (since they were missing from official production for unknown reasons), ran synchronization exercises with the members of the analysis group from other universities, and documented the methods for fake background estimation and for the stitching of MC samples. The same software framework that was developed for the $t\bar{t}H$ and HH multilepton analyses was also used for producing the datacards of the resonant analysis in the SL channel.

III My contributions are limited to Section 3.1 of the publication, which describes the stitching of MC samples and the validation of the method. For this portion of the work I generated the necessary MC samples from scratch and produced plots for the publication. I implemented the stitching of the DY and W+jets samples in the $t\bar{t}H$ and HH multilepton analyses, as well as in the HH $\rightarrow b\bar{b}WW^*$ analysis [7].

IV I ran DELPHES to produce MC samples for the HH $\rightarrow b\bar{b}WW^*$ signal and for the $t\bar{t} \rightarrow b\bar{b}WW^*$ background with realistic PU conditions, which allowed us to demonstrate the physics performance of the MEM likelihood discriminant. I also explored the possibility of incorporating virtual NLO corrections to MEs and cross-checked the final integrands of both signal and background hypotheses. Inspired by Ref. [10], the MEM LR was regressed with a DNN, the output of which was used as input to an event-level DNN in nonresonant HH $\rightarrow b\bar{b}WW^*$ analysis. The MEM LR was not used in the final version of the analysis [7], however, because of the computing time required to run the MEM on millions of MC and data events, and because the event-level DNN improved only marginally when adding the MEM LR as input.

Abbreviations

2HDM	two-Higgs-doublet model
AK	anti-k_t
AOD	Analysis Object Data
AR	application region
AUC	area under the ROC curve
BDT	boosted decision tree
BM	benchmark
BPIX	barrel pixel detector
BR	branching ratio
BSM	beyond the SM
BX	bunch crossing
C/A	Cambridge/Aachen
CA	control analysis
CHS	charged hadron subtraction
CI	confidence interval
c.o.m	center-of-momentum
CKM	Cabbibo-Kobayashi-Maskawa
CL	confidence level
CMS	Compact Muon Solenoid
CMSSW	CMS software framework
CP	charge conjugation and parity
CPU	central processing unit
CR	control region
CSC	cathode strip chamber
DL	dileptonic
DNN	deep neural network
DPS	double parton scattering
DT	drift tube
DY	Drell-Yan
EA	effective area
EB	ECAL barrel
ECAL	electromagnetic calorimeter
EE	ECAL endcaps
EFT	effective field theory
EM	electromagnetic
ES	ECAL preshower
EW	electroweak
EWSB	electroweak symmetry breaking
FF	fake factor
FH	fully hadronic
FR	fake rate
FPIX	forward pixel detector
FPR	false positive rate
FS	flavor scheme
FSR	final state radiation
ggF	gluon-gluon fusion
GoF	goodness-of-fit
GPU	graphical processing unit
GR	general relativity
GSF	Gaussian sum filter
HB	HCAL barrel
h.c.	Hermitian conjugate
HCAL	hadronic calorimeter
HE	HCAL endcaps
HEFT	Higgs EFT
HEP	high energy physics
HF	HCAL forward
HJT	Higgs-jet tagger
HLT	high-level trigger
HO	HCAL outer
HL-LHC	High Luminosity LHC
HPD	hybrid photodiode
HPS	hadrons-plus-strips
HS	hard scattering
HTT	hadronic top quark tagger
ID	identification
IP	interaction point
ISR	initial state radiation
ITC	inverted top coupling
JEC	jet energy correction
JER	jet energy resolution
JES	jet energy scale
KF	Kalman filter
L1T	Level-1 trigger
LHC	Large Hadron Collider
LIPS	Lorentz-invariant phase space
LO	leading order
LR	likelihood ratio
LV	leading PV
MC	Monte Carlo
ME	matrix element
MEM	matrix element method
MET	missing transverse energy
ML	maximum likelihood
MLE	ML estimate
MPI	multiple-parton interactions
MR	measurement region
MS	minimal subtraction
$\overline{\text{MS}}$	modified MS
MSSM	minimal supersymmetric SM
MVA	multivariate analysis
NMSSM	next-to-MSSM

N^{k}LO (next-to)^k-LO
NP nuisance parameter
NWA narrow-width approximation
OS opposite sign
PAS Public Analysis Summary
PD primary dataset
pdf probability distribution function
PDF parton distribution function
PDG Particle Data Group
PF particle flow
POG physics object group
POI parameter of interest
pQCD perturbative QCD
PS parton shower
PU pileup
PUPPI PU per particle identification
PV primary vertex
QCD quantum chromodynamics
QED quantum electrodynamics
QFT quantum field theory
ReLU rectifier linear unit
RF radiofrequency
ROC receiver operating characteristic
RPC resistive plate chamber
RS Randall-Sundrum
S/B signal over background ratio
SC supercluster
SFOS same flavor opposite sign
SF scale factor
SiPM silicon photomultiplier
SL semileptonic
SM standard model
SR signal region
SS same sign
STXS standard template cross section
SV secondary vertex
TEC tracker endcaps
TF transfer function
TIB tracker inner barrel
TID tracker inner disks
TnP tag & probe
TOB tracker outer barrel
TPR true positive rate
TP trigger primitive
UE underlying event
UV ultraviolet
VBF vector boson fusion
VEV vacuum expectation value
WLCG Worldwide LHC Computing Grid
WP working point

1 Introduction

The standard model (SM) of particle physics offers the most detailed and accurate explanation for the known fundamental constituents of matter and for the forces that act between them — except for gravity, which is instead explained by general relativity (GR). Both theories undoubtedly symbolize the pinnacle of human knowledge, which has accrued over many decades through careful analysis and interpretation of numerous laboratory experiments and astronomical observations. Although both theories are well established in their respective domains, incompatibilities arise in energy regimes where the quantum effects of gravity can no longer be ignored. From this juxtaposition it is already clear that neither the SM nor the GR are complete theories. Not only that, an increasing amount of evidence from studying various astronomical phenomena suggest that most of the matter is in fact made of an unknown substance called dark matter. No direct observation of dark matter has been made yet, however. In order to get closer to solving these problems, both theories must be tested thoroughly to find additional hints, which could point towards a more complete description of the universe. Although the world's largest particle accelerator, the Large Hadron Collider (LHC) [11], fulfilled its primary mission of discovering the Higgs boson in 2012 [12, 13] and thus completing the last missing piece of the SM puzzle, no new discoveries have been made in particle physics since then, despite the incredible efforts made to find evidence for physics beyond the SM (BSM).

One of the main objectives in high energy physics (HEP) research is to detect significant deviations from the SM by measuring the occurrence rates of certain scattering processes and comparing the results to the prediction. A suitable class of processes where such deviations could arise involve the production of one or multiple Higgs bosons. This is inspired by the fact that the Higgs boson is known to interact only with massive particles [14–16]. It is therefore reasonable to assume that any massive particle beyond the SM, if it exists, should also interact with the Higgs field. However, measuring the production rate of processes featuring Higgs bosons is challenging, because of their extremely low rates compared to other SM processes, which act as background to the Higgs boson measurement. Highly specialized analysis techniques are thus needed to separate the rare Higgs boson signal from those backgrounds.

The present thesis details the analysis of the Higgs boson production processes, which are the Higgs boson production in association with a single top quark (tH) or with a pair of top quarks ($\mathrm{t\bar{t}H}$) [1], and the production of Higgs boson pairs (HH) [2]. The former pair of processes is ideal for probing Yukawa-type interactions between Higgs bosons and top quarks, while the latter process provides direct access to the Higgs boson self-coupling. Both are analyzed in multilepton final states, which entail the presence of multiple muons, electrons and hadronically decaying τ leptons. The multilepton channels complement those analysis channels, which look for respective signals in the remaining Higgs boson decay modes that do not result in vector boson pairs or τ lepton pairs. Unlike the HH signal, the $\mathrm{t\bar{t}H}$ process has already been observed [17, 18], but only in a combination of all Higgs boson decay channels. The $\mathrm{t\bar{t}H}$ and HH multilepton analyses are based on proton-proton collision data recorded at $13\,\mathrm{TeV}$ of center-of-momentum (c.o.m) energy by the CMS experiment [19] at the LHC during the Run 2 data-taking period in the years 2016 to 2018.

This document is structured as follows: Section 2 discusses the theory behind $\mathrm{t\bar{t}H}$ and HH production; Section 3 gives a generic overview of the LHC accelerator and the CMS detector; Section 4 explains how the various particles are reconstructed and identified, and how the relevant physics observables are computed; Section 5 covers the estimation of relevant signal and background processes; Section 6 describes the machine learning methods that are utilized in building powerful discriminants to separate the rare $\mathrm{t\bar{t}H}$ and

HH signals from backgrounds, and how their output is used in the statistical analysis to infer new information about the presence or absence of the $\mathrm{t\bar{t}H}$ and HH signals in data. The details that are specific to the $\mathrm{t\bar{t}H}$ and HH multilepton analyses are provided in Sections 7 and 8, respectively.

This thesis uses natural units by setting the speed of light, c, the reduced Planck's constant, $\hbar$, and the gravitational constant, G, all equal to one. Energy, mass and momentum are all expressed in units of electronvolt (eV), which equals to approximately 1.60×10^{-19} J, 1.78×10^{-36} kg and 5.34×10^{-28} kg m s^{-1} in SI units, respectively. Einstein summation convention is implied, but the indices are generally dropped in scalar products and in equations if the contravariant or covariant indices have no particular relevance. Inner products with Dirac matrices are expressed using Feynman slash notation. Minkowski metric with signature $(+, -, -, -)$ is assumed. Quantities in **bold** font refer to a collection of indexable objects such as vectors or lists. The $\mathfrak{fraktur}$ („fraktur") font is used to label Lie algebras, in order to distinguish them from corresponding Lie groups, which are written in the usual math font. SM particles are typed in normal text font, while the corresponding fields are in math font, *e.g.*, Z for the particle and Z for the underlying field. The plus or minus signs that are present in the superscripts of particle names denote the charge of the particle, and are dropped if they do not serve a specific purpose in the discussion and if omitting the superscript does not cause any confusion. The time axis in Feynman diagrams is horizontal and points from left to right.

2 Theoretical foundations

There are four distinct forces that are currently considered as fundamental in the universe: the strong force, the weak force, the electromagnetic force and the gravitational force. The first three forces are described by the standard model (SM) of particle physics, an amalgamation of quantum mechanics and special relativity that provides an explanation for all discovered elementary particles and their interactions. The fourth force, gravity, is best described by the general theory of relativity. It shows how the matter-energy content in the universe affects spacetime and how spacetime in turn dictates the motion of said content.

To date, both theories are remarkably consistent with the experimental data in their respective domains, yet there remain many reasons to believe that the two models are still incomplete. For one, the SM cannot explain 95% of the matter-energy content of the universe, nor as to why there is more matter than anti-matter in the universe. The concept of gravity also breaks down at very high energies or equivalently at very small distances, which are characteristic to the conditions of the early universe. These shortcomings necessitate further scrutiny of these models, with the ultimate goal of finding inconsistencies between the predictions of the theory and the experimental data. Doing so narrows down the class of models that could replace or extend the current framework, or rule out alternative theories that have been put forth.

This chapter is organized into four sections. A concise introduction to the SM and its extensions are first given in Section 2.1. It is followed by Section 2.2, which discusses the phenomenology of particle collisions at the LHC. A more detailed treatment of the topic can be found in standard textbooks and references that the present text is based on Refs. [20–24]. The discussion continues with Section 2.3, which explores the phenomenology of the Higgs boson in more detail. It is followed by Section 2.4, which focuses on associated production of the Higgs boson with a single top or anti-top quark (tH), and with a pair of top quarks ($\mathrm{t\bar{t}H}$). Finally, Section 2.5 goes into the details of Higgs boson pair production (HH), which concludes the discussion. The aforementioned processes are treated as signals in the present work.

2.1 Overview of modern particle physics

Matter particles are described by spin-$\frac{1}{2}$ fermions and the interactions between these particles are mediated by spin-1 vector bosons. In particular, the strong force is carried by gluons (g), the weak force by $\mathrm{W}^{\pm}$ and Z bosons, and the electromagnetic force by photons (γ). Fermions can be arranged into three pairs or „generations" of quarks and leptons, where each such pair of particles share common properties. The first generation of quarks are up (u) and down (d) quarks; the second generation are charm (c) and strange (s) quarks; the third generation are top (t) and bottom (b) quarks. The first generation of leptons are electron (e^{-}) and electron neutrino (ν_{e}); the second generation muon (μ^{-}) and muon neutrino (ν_{μ}); the third generation tau lepton (τ^{-}) and tau lepton neutrino (ν_{τ}). The only spin-0 scalar particle in the SM is the Higgs boson (H) that interacts only with massive particles, including itself.

Each interaction between the particles has to conserve electric charge, color charge and weak isospin. A particle can be subject to a force only if it carries the corresponding charge. For instance, the only particles that carry the color charge and thus interact via the strong force are quarks and gluons, therefore implying that gluons can interact with themselves because they also carry color charge while being the mediators of the force. Neutrinos, photons, gluons, Z and H are all electrically neutral; charged or „down-type"

leptons e^-, μ^- and τ^-, as well as the W^- boson all carry an electric charge of -1; up-type quarks (u, c, t) and down-type quarks (d, s, b) have an electric charge of $+2/3$ and $-1/3$, respectively. Only gluons, photons and Z do not possess the weak isospin. Every particle has an antiparticle that carries the opposite charges. Photons, Z and H are their own antiparticles.

The remainder of this section covers each facet of the SM in more detail. Section 2.1.1 gives a brief overview of quantum field theory (QFT), which is the mathematical foundation that underlies much of the modern particle physics. The discussion continues with Section 2.1.2, which explores the physics of quarks and gluons. In Section 2.1.3 that follows lays out the ingredients that would be needed to describe weak and electromagnetic (EM) interactions. Section 2.1.4 explains how the vector bosons and fermions obtain their masses through the Higgs mechanism. The presented details are summarized in Section 2.1.5, which also highlights some of the shortcomings found in the theory. Finally, Section 2.1.6 introduces a systematic approach for probing theories alternative to the SM.

2.1.1 Quantum field theory

The SM is formulated in terms of quantized fields $\Phi(x)$ that fill all of spacetime. The word „quantized" refers to their operator-like functionality of creating or annihilating individual elementary particles, which is achieved by letting the field operators act on a particular quantum state at a given spacetime position x. More technically, particles are interpreted as superpositions of discrete momentum eigenstates of the Hamiltonian that encodes the motion of the free quantum field. Interaction between the fields in this description is achieved by coupling the free fields at the same spacetime point. The couplings could be written into the theory *ad hoc*, but in the SM they are constructed by imposing that the Lagrangian density $\mathcal{L}[\Phi, \partial\Phi]$, which is equivalent to Hamiltonian, remains extremal under local gauge transformation.

According to Noether's theorem, for every continuous symmetry of a physical system there is a corresponding conserved current [25]. The principle directly emerges from the requirement that the stationary action, which is the Lagrangian density integrated over spacetime, does not change if the fields are deformed in some way, thus leaving the equations of motion intact. A well-known example comes from classical field theory: if the system remains invariant under spacetime translations, then it must conserve 4-momentum. The theorem also applies to global gauge symmetries, which correspond to identical rotations of the fields performed everywhere in spacetime. A more compelling case can be made by imposing invariance under local gauge symmetry, which amounts to specifying a unique gauge transformation at every point across spacetime:

$$\Phi(x) \to \Phi'(x) = \mathcal{U}_{\mathcal{A}}(\boldsymbol{\alpha}(x))\Phi(x) \equiv \exp\left(ig_{\mathcal{A}}\boldsymbol{\alpha}(x)\mathbf{T}_{\mathcal{A}}\right)\Phi(x)\,. \tag{2.1}$$

Local gauge transformation $\mathcal{U}_{\mathcal{A}}$ is an element of some (special) unitary Lie group $G_{\mathcal{A}}$ that acts on the field Φ. The exact form of local gauge transformations depends on the underlying structure of corresponding Lie algebra $\mathfrak{g}_{\mathcal{A}}$ as well as on its representation. The group generators $\mathbf{T}_{\mathcal{A}}$ in this expression correspond to conserved charge operators. Factor i in Eq. (2.1) is there to keep the generators Hermitian, which is equivalent to the requirement that the eigenvalues of charge operators have to be real. The function $\boldsymbol{\alpha}(x)$ is an arbitrary real-valued parametrization that implements the transformation.

Lie groups of unitary kind are preferred in gauge transformations because they preserve normalization of the fields and observables. Unitary group $U(n)$ consists of $n \times n$ unitary matrices, while special unitary group of n, $SU(n)$, imposes an extra condition that their determinant also equals to $+1$. Every possible matrix in these groups can be constructed

from their generators via an exponential map, similarly to how the generators $\mathbf{T}_{\mathcal{A}}$ implement the transformation $\mathcal{U}_{\mathcal{A}}$ in Eq. (2.1). The generators of $U(n)$ and $SU(n)$ groups span vector spaces called Lie algebras, which are labeled as $\mathfrak{u}(n)$ and $\mathfrak{su}(n)$, respectively. Group multiplication rules can be inferred from the commutation relations of its generators: a commutator of two generators can be expressed as a linear combination of all generators of the group. The coefficients in those linear sums correspond to structure constants of the algebra. Lie groups and algebras can be represented by higher-dimensional matrices as long as they replicate the commutation relations exactly. Two common representations exist: fundamental, which consists of $n \times n$ matrices, and adjoint, the elements of which are precisely the structure constants. The representation is said to be irreducible if it cannot be transformed into block-diagonal matrix. The number of generators is determined by the minimum number of parameters needed for specifying a group element. There are n^2 generators in $U(n)$, while in special unitary groups there is one less, $n^2 - 1$, because of the extra condition on their determinant. Of all the conserved charges that are manifested by the group generators, only those that are simultaneously diagonalizable can be reliably measured at a given time. $U(n)$ has n and $SU(n)$ has $n - 1$ such generators that commute with each other.

A way to quantify intrinsic dynamics of a field is to study its rate of change, which is done by computing a derivative. However, local gauge symmetry tells that the field can have a unique phase at every point in spacetime. For a fair comparison of the fields at infinitesimal distances, this change in phase has to be compensated in any sensible definition of a derivative. The solution is to introduce a gauge field $\mathbf{A}_{\mathcal{A}}(x)$ that tells how much the input field should be rotated by group generators $\mathbf{T}_{\mathcal{A}}$ at any given point x in spacetime. The partial derivative ∂ is then promoted to covariant derivative $D_{\mathcal{A}}$ that now varies with the location in spacetime continuum:

$$D_{\mathcal{A}} = \partial + i g_{\mathcal{A}} \mathbf{T}_{\mathcal{A}} \mathbf{A}_{\mathcal{A}} \,. \tag{2.2}$$

When acting on a field, it not only encapsulates the motion of free fields via ∂ operator as before, but it also generates new interactions with gauge fields $\mathbf{A}_{\mathcal{A}}(x)$ at coupling strength $g_{\mathcal{A}}$. Given that the covariant derivative $D_{\mathcal{A}}$ can act on multiple fields, $\mathbf{A}_{\mathcal{A}}(x)$ is identified as a collection of fields that mediate a force. The transformation laws for the gauge fields are derived such that the covariant derivative of a field transforms the same way as the field itself.

Lagrangian density also admits another locally gauge-invariant term, the trace of fully contracted field strength tensor, which is built from the commutator of covariant derivatives defined by Eq. (2.2). In Yang-Mills theories [26], where the generators $\mathbf{T}_{\mathcal{A}}$ do not commute, the resulting field strength tensor explains why the gauge fields interact with themselves. Conceptually, the tensor measures how much the gauge field changes when moving along an infinitesimally small closed loop in spacetime. Similar mathematical structures also appear in general relativity (GR), which postulates that every point in curved spacetime has a unique coordinate system. The analogy for gauge fields in GR are Christoffel symbols, which are coefficients that compensate for the changes between coordinate systems when advancing along the shortest path in spacetime. The curvature of spacetime is encoded in the Riemann curvature tensor that is built from the commutator of covariant derivatives — just like the field strength tensor in gauge theory.

The gauge symmetry group of the SM is $SU(3)_{\mathsf{C}} \times SU(2)_{\mathsf{L}} \times U(1)_{\mathsf{Y}}$. The first term, $SU(3)_{\mathsf{C}}$, gives rise to the quantum chromodynamics (QCD), which is a gauge theory that studies strong interactions. The remaining terms, unified as $SU(2)_{\mathsf{L}} \times U(1)_{\mathsf{Y}}$, implement the electroweak (EW) sector that concerns EM and weak interactions. The gauge transformations of individual fields are determined by the representation of the symmetry group.

It is advantageous to organize multiple fields together into a tuple, also called a multiplet, if they share the same representation of gauge transformations. Multiplets consisting of just one, two or three fields are referred to as singlets, doublets or triplets, respectively.

In addition to gauge transformations, the quantum fields can also be subject to discrete symmetry transformations: charge conjugation (C), parity (P) and time reversal (T). Charge conjugation flips the charges of all fields, while parity transformation and time reversal, respectively, mirror the spatial and temporal components of every field. The exact form of a particular discrete symmetry transformation depends on the type of field it acts on. Intuitively, if the Lagrangian density respects C, P or T symmetry, then the processes that it describes should still be possible when swapping all interacting particles with their anti-particles, reflecting the processes in space, or viewing them to proceed backwards in time. Discrete transformations constrain how different states interact and thereby restrict the variety of processes that can happen. Quantum fields are classified as odd or even, depending on whether their eigenvalue is -1 (for odd) or $+1$ (for even) under the parity transformation. Scalars have intrinsically an even parity, while vectors have an odd parity. Likewise, scalar and vector fields that have the opposite parity, that is odd and even, are respectively referred to as pseudoscalar and pseudovector fields.

In order to ensure relativistic invariance of the quantum fields, they must transform in a certain way under space rotations and Lorentz boosts. Based on how a given field transforms under these operations, it can be either a spin-0 scalar field, a spin-$\frac{1}{2}$ spinor field or a spin-1 vector field. Each of the fields correspond to a certain representation of the Lorentz group that is induced by the Lorentz transformations. Combination of Lorentz transformations with spacetime translation constitutes the Poincaré symmetry group. The structure of the Lorentz group lends itself to the distinction of fields by their intrinsic spin, the states of which can be studied with the help of $SU(2)$ algebra. Excitations of integer-spin fields give rise to bosons, while the excitations of fields with half-integer spin produce fermions. One of the distinguishing factors between the two is that fermions are subject to Pauli exclusion principle, which states that fermions with identical quantum numbers such as spin projections or charges cannot occupy the same energy state, while for bosons there are no such limitations [27]. This property of bosons and fermions results in different collective behavior that is separately studied with Bose-Einstein statistics in case of bosons and with Fermi-Dirac statistics in case of fermions.

A spin-$\frac{1}{2}$ fermion field can be represented by a single 4-component Dirac spinor Ψ, or by a pair of left- and right-handed Weyl spinors Ψ_L and Ψ_R, each of which has two components but behave differently under the Lorentz transformations. The Weyl representation is connected to the Dirac representation through chiral projection:

$$\Psi_L = \frac{1}{2}(1-\gamma^5)\Psi, \qquad \Psi_R = \frac{1}{2}(1+\gamma^5)\Psi, \tag{2.3}$$

where $\gamma^5 \equiv i\gamma^0\gamma^1\gamma^2\gamma^3$ is appropriately in Weyl representation and $\{\gamma^\mu\}_{\mu=0}^3$ stand for 4×4 complex-valued Dirac matrices. They form a basis in Clifford algebra that is defined by anti-commutation relation $\{\gamma^\mu,\gamma^\nu\} = 2\eta^{\mu\nu}$, with $\eta^{\mu\nu}$ being the Minkowski metric. The commutator of Dirac matrices generates Lorentz transformations, which can act on the spinor fields. Certain combinations of the spinor fields called bilinears, such as $\bar{\Psi}(\gamma^5)\Psi$ and $\bar{\Psi}\gamma^\mu(\gamma^5)\Psi$, respectively act as (pseudo)scalars and as (pseudo)vectors under the Lorentz transformations. Parity transformation can be implemented with the application of γ^0 on a Dirac spinor, which swaps its left- and right-handed components. A theory is said to be chiral or parity-violating if it treats left- and right-handed spinor fields differently. This can be achieved by admitting axial terms proportional to $\bar{\Psi}(\gamma^\mu)\gamma^5\Psi$ into the Lagrangian density.

Although chirality is strictly a property of fermion fields, there exists a related notion for particles of any spin called helicity. It is defined as the spin projection on the direction of motion of the moving particle. If the particle travels in the (opposite) direction of its spin, it has positive (negative) or right-handed (left-handed) helicity. Massive vector bosons that are longitudinally polarized have their helicity equal to zero. Unlike chirality, helicity is conserved over time but not a Lorentz-invariant, at least not for massive particles. It is always possible to boost into a frame of reference where the massive particle moves in the opposite direction, thereby flipping its sign of helicity. This is not true for massless particles. In the relativistic limit the helicity eigenstates correspond to Weyl spinors, in which case it is common to use helicity and chirality interchangeably. Thus, helicity provides a handle to study P-symmetry.

It is beneficial to use Weyl spinors when describing the SM because the left-handed spinors and right-handed spinors couple differently to the gauge fields in the EW theory. This is the main reason why it is not possible to simply inject mass terms for the fermions,

$$m\bar{\Psi}\Psi = m(\bar{\Psi}_L\Psi_R + \bar{\Psi}_R\Psi_L)\,, \tag{2.4}$$

into the Lagrangian density as such terms spoil the gauge invariance. Similar reasoning holds when trying to introduce mass terms for the massive vector bosons. Both of these issues are reconciled with the Higgs mechanism.

The SM is a perturbatively calculable theory, which means that the field interactions are considered as perturbations to the free fields. This is realized by first considering the corresponding particles as asymptotically free in the initial and final state of a particular process. Transition between these two states is described by scattering matrix or S-matrix, which is a unitary evolution operator that depends on interaction Hamiltonian. The unitarity condition ensures that the probabilities of all possible transitions add up to one. The evolution operator can be developed into power series in terms of the coupling parameters that are present in the Hamiltonian. Each subsequent term in the series expansion corresponds to an increasingly more sophisticated interaction connecting the initial and final states. It is often convenient to visualize the interactions using Feynman diagrams. The same process can be represented with topologically distinct Feynman diagrams or „channels". The classification is based on Lorentz-invariant Mandelstam variables, labeled as s, t and u, that correspond to the momentum exchanged between incoming and outgoing particles. Trivial contributions to the processes such as particles flying past each other or spontaneous „vacuum bubbles" can be ignored or factorized out in the calculations. The sum of remaining Feynman diagrams in the series constitutes the Lorentz-invariant matrix element (ME) of the process, the square of which is proportional to the probability for the underlying process to occur.

The subleading terms in the series expansion give rise to loop diagrams that create divergences in the prediction. The singularities are caused by allowing intermediate particles, also known as virtual particles, to attain arbitrarily large or small momenta. The apparent dichotomy is understood by first recognizing that the fixed parameters of the theory — such as mass and charge — do not necessarily correspond to the physically measured observables. A well-known phenomenon illustrating this argument is charge screening, where a single electron is surrounded by a spontaneous cloud of virtual electron-positron pairs. Such shielding of the electron modifies its effective charge, depending on how close or far away the electron is probed. At smaller distances, or equivalently at higher energies, more of the bare electron charge would be revealed, whereas at larger distances or lower energies its charge would be dressed by the electron-positron pairs. In similar fashion, self-interaction terms as predicted by the perturbation theory modify its apparent mass.

The mapping of („bare") theory parameters to physical („dressed") observables is carried out with a technique called renormalization. The method splits a Lagrangian density that is written in terms of bare parameters into renormalized and singular parts following some convention or scheme. The Lagrangian density written in terms of renormalized parameters has the same functional form as the initial Lagrangian density written in terms of bare parameters, so that the structure of infinities arising from perturbative calculations in either case stays the same. The divergences are parametrized by some energy scale using a method known as regularization. The renormalized terms also become dependent on this scale in the process, because the bare Lagrangian density has no such dependency. Nevertheless, the divergences from perturbative calculations are automatically canceled by the singular terms, also referred to as counterterms, that are extracted from the bare Lagrangian density. The result becomes finite and can be therefore linked to physical measurements, but the residual dependency of, say, renormalized couplings on the fiducial energy scale still remains. The exact behavior of how the coupling changes with the renormalization scale is governed by the underlying gauge symmetry.

The simplest renormalization scheme is minimal subtraction (MS) scheme, in which the counterterms absorb only the singularities. The most popular way of regularizing divergences is by the means of dimensional regularization, which captures the singular part as an infinitesimal shift with respect to the spacetime dimension. The purely infinite part obtained with this method is usually accompanied by a finite contribution of $\ln(4\pi e^{-\gamma_E})$, where $\gamma_E \approx 0.577$ is Euler's constant. This constant can also be moved into the counterterms. This renormalization scheme is also known as the modified MS ($\overline{\text{MS}}$) scheme.

2.1.2 Quantum chromodynamics

The dynamics of massless quarks and gluons is governed by the QCD Lagrangian density

$$\mathcal{L}_{\text{QCD}} = -\frac{1}{4}\mathbf{G}^2 + i\bar{\Psi}_q \not{D}\Psi_q \,. \tag{2.5}$$

The gluon field strength tensor,

$$\mathbf{G} \equiv G^a_{\mu\nu} t^a = 2\partial_{[\mu} G^a_{\nu]} t^a + g_S f^{abc} G^b_\mu G^c_\nu t^b t^c \,, \tag{2.6}$$

is built from eight gluon fields G^a_μ. It corresponds to the number of generators in the $SU(3)_{\text{C}}$ group that span its algebra $\mathfrak{su}(3)_{\text{C}}$. Factors f^{abc} in Eq. (2.5) are nonvanishing structure constants of $\mathfrak{su}(3)_{\text{C}}$ that give rise to gluon self-interaction terms. The second term in Eq. (2.5) runs over all six quark flavors q. The generators t^a embedded in the covariant derivative are in fundamental representation, thus corresponding to eight 3×3 Gell-Mann matrices, the dimension of which dictates the number of charge eigenstates. Given that there are three such eigenstates, there must also be three distinct eigenvalues or „colors" that can be assigned to the quark fields. As such, there are three independent Dirac spinors, wrapped into a tuple Ψ_q, each corresponding to a different color charge: red, green or blue. While (anti-)quarks carry a single (anti-)color charge at a time, gluons carry both color and anti-color. This property of gluons ensures conservation of color and anti-color charges in strong interactions. Feynman diagrams generated by Eq. (2.5) are shown in Fig. 2.1.

Another feature that stems from the group structure of the theory is that the coupling strength $\alpha_{\text{S}} \equiv \frac{g_S^2}{4\pi}$, renormalized to one loop in perturbation theory, runs with the

renormalization scale μ_R as described by the differential equation

$$\mu_R \frac{\partial \alpha_s}{\partial \mu_R} = -\left(11 - \frac{2}{3} n_f\right) \frac{{\alpha_s}^2}{2\pi}, \tag{2.7}$$

with n_f denoting the number of quark flavors. The exact choice of μ_R can be arbitrary, but it is preferable to select the scale such that the higher-order corrections are as small as possible. Given the wide variety of processes that each can have a unique energy scale, a common scale for reference is needed when combining α_s measurements from multiple experiments. The standard choice for this scale has become the mass of the Z boson m_Z (see Table 2.1 for its value). The current world average of strong coupling at this scale is $\alpha_s(m_Z) = 0.1179$ [24]. Its value at any other scale can be obtained by following the evolution of Eq. (2.7).

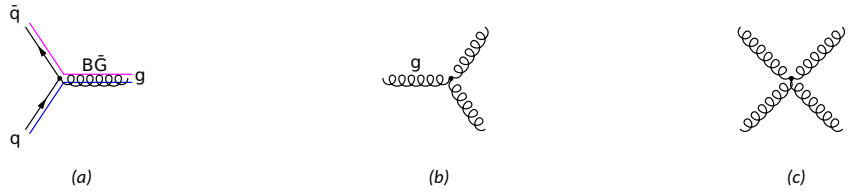


Figure 2.1: Feynman diagrams for QCD interactions: quark-gluon coupling (a), trilinear gluon self-coupling (b) and quartic gluon self-coupling (c). Diagram (a) explicates the color flow from a pair of a quark and its anti-quark $q\bar{q}$ (shown with arrows) in initial state to the gluon g (curly line) with extra lines colored as blue (B) and „anti-green" ($\bar{G}$, i.e., magenta), while in self-interaction diagrams (b)–(c) the color states have already been summed over and the extra colored lines are hence omitted. Probability amplitude of diagrams (a) and (b) scale with g_S, while the amplitude of (c) scales with g_S^2.

The right-hand side of Eq. (2.7) has to be negative because there are no more than six quark flavors discovered thus far. This has a number of consequences: the QCD coupling strength decreases if the energy scale increases or, equivalently, if the corresponding length scale decreases. In other words, quarks behave more as free particles the closer they get, a phenomenon also known as asymptotic freedom. Conversely, at decreasing energy scales the strong force increases, leading to an effect called color confinement. The QCD scale Λ_{QCD} marks the boundary below which the confinement takes over and the theory becomes nonperturbative. The exact value of Λ_{QCD} depends on renormalization and flavor schemes [28]. In three-flavor scheme or higher and in $\overline{\text{MS}}$ renormalization scheme the QCD scale is $\Lambda_{\text{QCD}} \lesssim 0.3\,\text{GeV}$. Quarks that are less massive than the QCD scale are sometimes referred to as light quarks.

Color confinement forbids the existence of isolated colored particles. Instead, the quarks and gluons, commonly referred to as partons, must form a bound state called a hadron that does not possess the color charge. In terms of group theory, such bound states correspond to the singlet states of $SU(3)_C$. The simplest color singlets are mesons, consisting of a quark and an anti-quark that carry opposite color charges, and baryons consisting of three quarks that each carry a different color charge. Baryon number, which is defined as $(n_q - n_{\bar{q}})/3$ with n_q ($n_{\bar{q}}$) denoting the number of (anti-)quarks, is known to be conserved in all SM interactions.

Hadronization is the process where quarks and gluons arrange into hadrons. One of the most successful hadronization models is based on the idea that the confinement force between two quarks increases linearly with distance as they move away from each other [29]. The force field that connects the quarks can be approximated by a massless

string. As the distance between the quarks increases, so does the potential energy stored in the string. It eventually leads to string fragmentation, which creates new quark and anti-quark pairs with appropriate color charges at the points where the string breaks. The break-up process reduces the potential energy of (now multiple) strings in the system, and continues until colorless hadrons remain. Other kinds of phenomenological models that attempt to describe the hadronization process have also been developed, such as cluster-based hadronization [30, 31]. Majority of the particles that are produced during the hadronization move in the direction of the initial partons. The collection of hadrons spread out over time due to randomness of the hadronization process. Charged hadrons diverge from their initial paths even more because of the external magnetic field that is typically applied in particle detectors. The spray of hadrons form a cone-like structure called a hadronic jet. Top quark is the only parton that does not hadronize because it decays via the weak interaction first due to its order of magnitude shorter mean lifetime compared to the hadronization timescale of $\Lambda_{\text{QCD}}^{-1} \approx 2.2 \times 10^{-24}$ s.

2.1.3 Electroweak sector

The electroweak interaction refers to the unified description of EM and weak forces that is modeled with the $SU(2)_{\text{L}} \times U(1)_{\text{Y}}$ Lagrangian density [32–34]

$$\mathcal{L}_{\text{EW}} = -\frac{1}{4}(\mathbf{W}^2 + \mathbf{B}^2) + i\bar{\mathfrak{L}}_L \not{D} \mathfrak{L}_L + i\bar{\ell}_R \not{D} \ell_R + i\bar{Q}_L \not{D} Q_L + i\bar{u}_R \not{D} u_R + i\bar{d}_R \not{D} d_R \,. \tag{2.8}$$

In analogy to the gluon field strength tensor that is given by Eq. (2.6), the field strength tensor $\mathbf{W}$ of $SU(2)_{\text{L}}$ is constructed from three underlying gauge fields W_μ^i that are coupled to $SU(2)_{\text{L}}$ generators in fundamental representation also known as Pauli matrices. The $U(1)_{\text{Y}}$ group has only one generator, thus implying that there is just a single gauge field B_μ and no structure constants whatsoever associated with the group. Particles charged under $SU(2)_{\text{L}}$ carry weak isospin charge that corresponds to the eigenvalue of the diagonalized generator T_3, while the particles charged under $U(1)_{\text{Y}}$ carry weak hypercharge Y. The operator „$\bar{\Psi}_L \gamma^\mu \Psi_L$" appearing in Eq. (2.8) should be interpreted the following way: Ψ_L operator creates a left-handed fermion state and annihilates a right-handed anti-fermion state, while $\bar{\Psi}_L$ annihilates a left-handed fermion state and creates a right-handed anti-fermion state. Similarly to baryon number, the SM interactions conserve lepton number, which is defined as $n_\ell - n_{\bar{\ell}}$ with n_ℓ ($n_{\bar{\ell}}$) denoting the number of (anti-)leptons.

The covariant derivative in Eq. (2.8) acts on different multiplets of left- and right-handed fermions that are grouped together based on how they behave in electroweak interactions. There are two left-handed $SU(2)_{\text{L}}$ doublets $\mathfrak{L}_L = \binom{\nu_\ell}{\ell}_L$ and $Q_L = \binom{u}{d}_L$, constructed from three copies of lepton neutrino and charged lepton pairs, and from complementary up- and down-type quarks pairs with identical color charge, totaling nine left-handed quark doublets. The remaining right-handed fermions form singlets under $SU(2)_{\text{L}}$, except for the right-handed neutrinos, which are completely absent. The omission of right-handed neutrinos reflects the fact that C- and P-symmetry are each maximally violated in weak interactions [35, 36]. In particular, experiments have not found neutrinos that are right-handed, hence not conserving P-symmetry, nor anti-neutrinos that are left-handed, which indicates C-symmetry violation. Fermion fields carry the same weak hypercharge only if they belong to the same multiplet. The fermion multiplets are defined for each generation, and in case of quarks also for each color state. Thus, a total of 45 Weyl fields are needed to describe the fermion content of the SM.

The flavor-changing aspect of the electroweak interactions becomes apparent after

rearranging some of the $SU(2)_{\mathrm{L}}$ gauge fields in covariant derivative Eq. (2.2):

$$W_1 T_1 + W_2 T_2 = (W_1 - iW_2) \cdot \begin{pmatrix} 0 & 1 \\ 0 & 0 \end{pmatrix} + (W_1 + iW_2) \cdot \begin{pmatrix} 0 & 0 \\ 1 & 0 \end{pmatrix} \equiv W^+ T^+ + W^- T^- ,$$

where T_1 and T_2 are proportional to non-diagonal Pauli matrices. The ladder operators $T^{\pm}$ act on the left-handed fermion doublets by projecting out either of the fermion fields in the doublet. Therefore, the Lagrangian density specified by Eq. (2.8) contains terms proportional to $\bar{u}_L \not{W}^+ d_L$, $\bar{d}_L \not{W}^- u_L$, $\bar{\nu}_L \not{W}^+ \ell_L$ and $\bar{\ell}_L \not{W}^- \nu_L$. This means that in weak interactions a down-type quark can turn into an up-type anti-quark, and vice versa, assuming that they belong to the same generation and carry identical color charges. Additionally, leptons and anti-lepton neutrinos, as well as anti-leptons and lepton neutrinos can interact via the weak force, provided that they are from the same generation of leptons. It is important to note that both of these statements are valid for the left-handed fermion fields in interaction eigenstates, since the right-handed fermion fields couple only to the $U(1)_{\mathrm{Y}}$ gauge field.

The excitations of $W^{\pm}$ fields give rise to W^+ and W^- bosons. The remaining gauge fields of the EW symmetry group do not directly correspond to the fields of Z bosons and photons. For the reasons that will be explained later when discussing the Higgs mechanism, the fields W_3 and B need to be rotated by Weinberg angle $\theta_W \approx 29^\circ$ in order to uncover physical field Z and photon field A. After rearranging the gauge couplings of both EW groups, the covariant derivative that applies to left-handed fermion fields in the Lagrangian density Eq. (2.8) can be expressed as

$$D = \partial - \frac{ie}{s_W}(W^+ T^+ + W^- T^-) - \frac{ie}{s_W c_W}(T_3 - s_W^2 Q)Z - ieQA , \tag{2.9}$$

where $s_W \equiv \sin\theta_W$ and $c_W \equiv \cos\theta_W$, e is identified as the electric charge, and Q is the charge operator. The electric charge Q, weak hypercharge Y and weak isospin T_3 operators are all related to one another via the Gell-Mann–Nishijima relation [1]:

$$Q = T_3 + \frac{Y}{2} .$$

Higher order corrections in perturbation theory are typically expressed in terms of fine structure constant $\alpha_{\mathrm{EW}} \equiv \frac{e^2}{4\pi}$, which equals to roughly $1/137$ in the low-energy limit [24] and, in contrast to the behavior of α_{S} in QCD, becomes stronger with increasing energy[2]. For right-handed fermion fields, the terms containing $SU(2)_{\mathrm{L}}$ generators in Eq. (2.9) vanish. It follows that the Z field couples only to the same flavor fields, but with different strengths depending on the chirality, while there is no such discrepancy in EM interactions. By contrast, the left- and right-handed fermions couple to the photon field with equal strength because both fermion fields carry the same electric charge, as determined by the eigenvalue of charge operator Q. Feynman diagrams that result from rearranging gauge fields into physical fields in the EW Lagrangian density given by Eq. (2.8) are shown in Fig. 2.2.

[1] While the expression was first formulated in terms of quantum numbers that are assigned to hadrons [37–39], it was retrofitted in the EW theory by appropriate normalization of the $U(1)_{\mathrm{Y}}$ gauge field.

[2] Similarly to Λ_{QCD}, which demarcates the lowest energy scale where QCD can still be approximated perturbatively, there exists an upper threshold of 10^{286} eV for α_{EW} called the Landau pole, above which the perturbative QED calculations, which are those that involve only charged fermions and photons, eventually break down [40]. However, this scale is never reached in a practical setting because it well exceeds the theoretical energy limit above which gravity takes over.

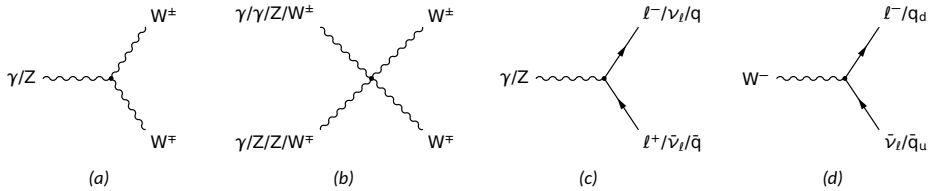


Figure 2.2: Feynman diagrams generated by EW Lagrangian density defined by Eq. (2.8) *after rearrangement of gauge fields into physical fields: three-point (a) and four-point (b) interactions between the EW bosons (shown with wavy lines); decay of electrically neutral γ and Z bosons into a pair of a lepton and its anti-lepton ($\ell^-\ell^+$), into a pair of a quark and its anti-quark ($q\bar{q}$), or into a pair of a neutrino and its anti-neutrino ($\nu_\ell\bar{\nu}_\ell$), all shown with solid arrows (c); decay of W^- boson into a pair of a lepton and an anti-neutrino of the same lepton flavor ($\ell^-\bar{\nu}_\ell$), or into a pair of a down-type quark and an up-type anti-quark ($q_d\bar{q}_u$) (d). The decay of W^+ boson (not shown) would proceed into a pair of an anti-lepton and lepton neutrino of the same lepton flavor ($\ell^-\nu_\ell$), or into a pair of down-type anti-quark and up-type quark ($q_u\bar{q}_d$). Probability amplitudes of all Feynman diagrams scale with e, except for (b), which scales with e^2.*

2.1.4 Higgs mechanism

Neither QCD nor EW Lagrangian densities given by Eqs. (2.5) and (2.8) include fermion mass terms because such terms would violate the local gauge invariance under $SU(2)_\mathrm{L}$ transformations, as demonstrated by Eq. (2.4). For the same reasons it is also not be possible to introduce Proca terms for the massive vector bosons such as $m_i^2 W_i^2$ to the EW theory. Yet, all fermions, as well as W and Z bosons are experimentally found to be massive.

These problems can be cured by first recognizing that the mass terms may arise due to interactions with some yet unknown scalar field. This idea, nowadays most commonly referred to as the Higgs mechanism, postulates a complex-valued Higgs doublet ϕ with EW-invariant Lagrangian density

$$\mathcal{L}_\phi = |D\phi|^2 - V(\phi) \tag{2.10}$$

and scalar potential

$$V(\phi) = \mu^2|\phi|^2 + \lambda(|\phi|^2)^2 \tag{2.11}$$

in the theory [14–16]. The scalar field ϕ has an energy ground state only if the potential $V(\phi)$ is bounded from below, which in turn implies that the parameter λ must be positive. Both μ^2 and λ must also be real, since otherwise the resulting Hamiltonian would be non-Hermitian and therefore would produce probabilities that decay over time. If $\mu^2 > 0$ then the potential acquires minimum at $|\phi|^2 = 0$, whereas $\mu^2 < 0$ produces a minimum at nonzero value of the scalar field. The latter case is more compelling because it describes the field that has a nonzero vacuum expectation value (VEV).

The Higgs doublet ϕ contains four real-valued massless fields, which can be reorganized as fluctuations around electrically neutral VEV like so:

$$\phi(x) = \frac{1}{\sqrt{2}} \begin{pmatrix} g_1(x) + ig_2(x) \\ v + h(x) + ig_3(x) \end{pmatrix}. \tag{2.12}$$

In contact with covariant derivative given by Eq. (2.9), the Goldstone bosons $\{g_i(x)\}_{i=1}^3$ would interact with $W^\pm$ and Z fields such that their propagation amplitude would be

modified. The three Goldstone bosons can be removed by fixing the Higgs doublet in Eq. (2.12) to unitary gauge,

$$\phi(x) = \frac{1}{\sqrt{2}} \begin{pmatrix} 0 \\ v + h(x) \end{pmatrix} . \tag{2.13}$$

This procedure effectively adds longitudinal degrees of freedom or, equivalently, assigns mass to the $SU(2)_{\mathsf{L}}$ gauge bosons. A residual $U(1)_{\mathsf{EM}}$ symmetry still remains but it is not the same unitary group that is present in the original theory. Higgs doublet written in the form given by Eq. (2.13) conserves CP because it is a true scalar, not a pseudoscalar, that remains unchanged under charge conjugation.

This mathematical description provides the basis for electroweak symmetry breaking (EWSB): at high temperatures of the early universe, the fundamental EW forces are described by the corresponding massless gauge fields. After the universe cooled, the Higgs doublet obtained a nonzero VEV and the gauge fields mixed. The resulting physical fields $W^{\pm}$ and Z became massive in the process. Their mass relations $m_{\mathsf{W}} = ev/(2s_W)$ and $m_{\mathsf{Z}} = m_{\mathsf{W}}/c_W$ can be easily derived by inserting the gauge-fixed Higgs doublet given by Eq. (2.13) into the Lagrangian density defined by Eq. (2.10), expanding the covariant derivative in terms of physical fields that are present in Eq. (2.9), and identifying mass terms m_{W}^2 and $m_{\mathsf{Z}}^2/2$. The method also generates additional interaction terms between the Higgs field and the massive boson fields as illustrated by Feynman diagrams shown in Figs. 2.3(a) and 2.3(b). In three-point and four-point diagrams, the Higgs field couples to the physical massive boson fields with strength that is proportional to their squared masses of the fields:

$$g_{\mathsf{V}} = \frac{2m_{\mathsf{V}}^2}{v} \qquad \text{and} \qquad g_{2\mathsf{V}} = \frac{2m_{\mathsf{V}}^2}{v^2} , \tag{2.14}$$

where V stands for either $\mathsf{W}^{\pm}$ or Z. Since the lower component of the Higgs doublet is electrically neutral, the Higgs field does not interact with the photon field. Therefore, the photon field remains massless and acts as the gauge field for the residual $U(1)$ symmetry. The leftover gauge group leads to quantum electrodynamics (QED) that describes interactions between fermions and photons.

The (electrically) charged fermions acquire their masses similarly by coupling to the Higgs doublet and undergoing EWSB. For the charged leptons, this is achieved with the following gauge-invariant Lagrangian density:

$$\mathcal{L}_\ell = -y_{\ell i}(\bar{\ell}^i_R \phi \ell^i_L + \text{h.c.}) \overset{\text{EWSB}}{=} -\frac{y_{\ell i}}{\sqrt{2}}(v+h)\bar{\ell}^i \ell^i , \tag{2.15}$$

where i runs over the three lepton generations and $y_{\ell i}$ stands for real Yukawa coupling between the charged leptons and the Higgs doublet. The lepton masses are directly proportional to the coupling strength, $m_{\ell i} = y_{\ell i} v/\sqrt{2}$.

The gauge-invariant Lagrangian density that produces massive quarks takes the following form:

$$\mathcal{L}_q = -y^u_{ij} \bar{u}^i_R \bar{\phi}^\dagger Q^j_L - y^d_{ij} \bar{d}^i_R \phi^\dagger Q^j_L + \text{h.c.} , \tag{2.16}$$

where indices i and j run over the three generations of quarks. The sum is implicit over the matching pair of color and anti-color charges. The field $\bar{\phi}$ stands for charge-conjugated doublet, $\bar{\phi} = i\sigma_2 \phi^*$, that has its components swapped and is oppositely charged with respect to the original doublet. Interactions between charged leptons and quarks given by Eqs. (2.15) and (2.16), respectively, can be summarized as a single Feynman diagram depicted in Fig. 2.3(c).

Analogously to charged leptons, the up- and down-type quark masses are determined from couplings y^u_{ij} and y^d_{ij}. However, the coupling matrices y^u and y^d include off-diagonal

elements, which makes the interpretability of the resulting mass terms difficult. The workaround is to define physical mass eigenstates from interaction eigenstates using unitary transformation matrices that diagonalize y^u and y^d. This procedure turns the initial Lagrangian density expressed by Eq. (2.16) into

$$\mathcal{L}_q \overset{\text{EWSB}}{=} -\frac{y_{qi}}{\sqrt{2}}(v+h)\bar{q}'_i q'_i\,,$$

where the sum runs over six quark mass eigenstates q'_i that couple to the Higgs field with Yukawa strength y_{qi} that is proportional to their mass: $m_{qi} = y_{qi}v/\sqrt{2}$.

As a result, the weak interactions do not necessarily occur within the same generation of up- and down-type quarks but also between different generations of quarks. In weak interactions of quarks, the mass eigenstates are related to interaction eigenstates by complex-valued Cabbibo-Kobayashi-Maskawa (CKM) matrix [41, 42]:

$$V_{\text{CKM}} = \begin{pmatrix} V_{ud} & V_{us} & V_{ub} \\ V_{cd} & V_{cs} & V_{cb} \\ V_{td} & V_{ts} & V_{tb} \end{pmatrix}.$$

The magnitude of each element in the CKM matrix corresponds to the probability amplitude for an up-type quark transition to a down-type quark in their mass eigenstates. Global fit to all available measurements of the CKM matrix parameters under the unitarity constraint yields the following magnitudes [24]:

$$\begin{pmatrix} |V_{ud}| & |V_{us}| & |V_{ub}| \\ |V_{cd}| & |V_{cs}| & |V_{cb}| \\ |V_{td}| & |V_{ts}| & |V_{tb}| \end{pmatrix} = \begin{pmatrix} 0.97401 & 0.22650 & 0.00361 \\ 0.22636 & 0.97320 & 0.04053 \\ 0.00854 & 0.03978 & 0.99917 \end{pmatrix}.$$

Quarks are therefore most likely to change flavors within the same generation. The interpretation of the CKM matrix elements becomes clear after expressing the weak interaction terms between left-handed quark fields in their mass eigenstates, and reorganizing the resulting up- and down-type fields into triplets U'_L and D'_L in Eq. (2.8):

$$i\bar{Q}_L \not{D} Q_L \supset \frac{e}{s_W\sqrt{2}}(\bar{U}'_L V_{\text{CKM}} \not{W}^+ D'_L + \text{h.c.})\,.$$

This contrasts lepton universality, which tells that the weak interactions do not discriminate leptons based on their flavor. The other terms in the EW Lagrangian density that combine quark fields with corresponding anti-quark fields can be easily rotated into their mass eigenstates because the transformation is unitary. This is to say that the kinetic terms of quarks as well as the interaction terms involving Z and photon fields can be readily expressed in the mass eigenstates, as there is no flavor mixing.

The CKM matrix has 18 real parameters, but its unitary properties bring the number of independent variables down to four: three mixing angles and one complex phase δ_{CP}. Global fits of independent studies that measure the CKM matrix elements indicate that the matrix does adhere to the unitary conditions. The complex phase δ_{CP} is found to be nonzero, which indicates that the combined symmetry of charge conjugation and parity (CP) is not conserved. The CP violation explains why EW interactions with quarks run at different rates compared to identical interactions with anti-quarks. This effect has been observed in experiments such as those involving neutral meson oscillations [43].

Finally, the Higgs field itself is also massive. This can be seen by inserting the gauge-fixed Higgs doublet given by Eq. (2.13) into the scalar potential defined by Eq. (2.11) and ignoring constant terms:

$$V(\phi) \overset{\text{EWSB}}{=} \lambda v^2 h^2 + \lambda v h^3 + \frac{\lambda}{4}h^4\,. \tag{2.17}$$

The first term in Eq. (2.17) corresponds to the mass term of the Higgs boson while the remaining terms describe its self-interaction. Therefore, the Higgs boson H, which is the excitation of the field h, has a mass $m_{\mathrm{H}} = v\sqrt{2\lambda}$. Trilinear and quartic self-interaction terms predicted by the Higgs mechanism depend on coupling parameter λ. The corresponding Feynman diagrams are given in Figs. 2.3(d) and 2.3(e).

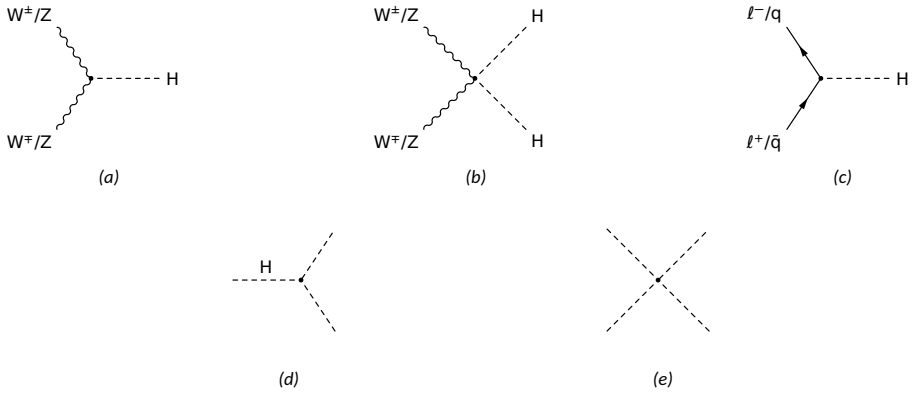


Figure 2.3: Feynman diagrams for processes involving Higgs boson: three-point (a) and four-point (b) interaction of Higgs boson (shown with a dashed line) with vector massive bosons ($W^{\pm}$, Z); Higgs boson interaction with a pair of a charged lepton and its anti-lepton ($\ell^-\ell^+$), or with a pair of a quark and its anti-quark ($q\bar{q}$) (c); trilinear (d) and quartic (e) self-couplings. Probability amplitudes of (a) and (b) are respectively proportional to g_{V} and $g_{2\mathrm{V}}$, which are given by Eq. (2.14)*; the probability amplitude for the fermion vertex (c) is linearly proportional to the corresponding Yukawa coupling or, equivalently, to the mass of the involved fermion; the probability amplitude for self-coupling diagrams (d) and quartic (e) are directly proportional to the self-coupling λ.*

2.1.5 The standard model of particle physics

This concludes the overview of the SM. The full Lagrangian density can be pieced together from individual contributions given by Eqs. (2.5), (2.8), (2.10), (2.15) and (2.16), modulo double application of $\not{\partial}$ on quark fields:

$$\mathcal{L}_{\mathrm{SM}} = \mathcal{L}_{\mathrm{QCD}} + \mathcal{L}_{\mathrm{EW}} + \mathcal{L}_{\phi} + \mathcal{L}_{\ell} + \mathcal{L}_{q}\,. \tag{2.18}$$

Before the EWSB, the fundamental forces are described by massless $SU(3)_{\mathrm{C}} \times SU(2)_{\mathrm{L}} \times U(1)_{\mathrm{Y}}$ gauge fields. After the Higgs doublet acquires nonzero VEV via the Higgs mechanism, all particles that couple to the doublet become massive. The mass of each particle is directly proportional to the coupling strength to the Higgs field, and vice versa. The theory now has $SU(3)_{\mathrm{C}} \times U(1)_{\mathrm{EM}}$ gauge symmetry, because the original EW symmetry was broken in the process. The properties of boson and fermion of the SM are summarized in Tables 2.1 and 2.2, respectively. While neutrinos and photons are theoretically massless in the SM, it is not possible to completely rule out them being massive experimentally, which is why their masses are quoted using upper bounds.

Particle	Spin	T_3	Y	Q	m
H	0	$-1/2$	$+1$	0	$125.10 \pm 0.14\,\text{GeV}$
g	1	0	0	0	0^*
$W^{\pm}$	1	± 1	0	± 1	$80.379 \pm 0.012\,\text{GeV}$
Z	1	0	0	0	$91.1876 \pm 0.0021\,\text{GeV}$
γ	1	0	0	0	$< 10^{-18}\,\text{eV}$

* Theoretical value.

Table 2.1: List of SM bosons, their spin, eigenvalues of weak isospin T_3, weak hypercharge Y and electric charge Q, and mass m with 1σ experimental uncertainty. The masses are taken from Particle Data Group (PDG) [24].

Particle (1st, 2nd, 3rd)	T_3 (L, R)	Y (L, R)	Q	m (1st, 2nd, 3rd)
(ν_e, ν_μ, ν_τ)	$(+1/2, \text{✗})$	$(-1, \text{✗})$	0	$< 1.1\,\text{eV}$
(e^-, μ^-, τ^-)	$(-1/2, 0)$	$(-1, -2)$	-1	(511 keV, 105.6 MeV, 1.777 GeV)
(u, c, t)	$(+1/2, 0)$	$(+1/3, +4/3)$	$+2/3$	(2.16 MeV, 1.27 GeV, 172.76 GeV)
(d, s, b)	$(-1/2, 0)$	$(+1/3, -2/3)$	$-1/3$	(4.67 MeV, 93 MeV, 4.18 GeV)

Table 2.2: List of SM up- and down-type leptons (first two rows) and quarks (last two rows), their eigenvalues of weak isospin T_3, weak hypercharge Y and electric charge Q, and mass m. The weak isospin and hypercharge values are listed for left (L) and right (R) chirality separately. The masses are quoted from Ref. [24] (PDG) for each of the three generations. All quark masses are given in $\overline{MS}$ scheme, except for the top quark mass that is directly measured from data. The cross mark (✗) indicates that the particles (right-handed neutrinos in this case) do not exist in given representation. The signs of all charges are flipped for anti-fermions.

Although the SM explains the interplay between elementary particles and fundamental forces with impressive precision and consistency, it does have a few shortcomings. For example, it fails to address neutrino masses. While theoretically they are considered massless in the SM, various experiments have observed neutrino oscillation [44, 45] in which neutrinos have been found to change flavors as they travel through space. The phenomenon demonstrates that neutrino flavor and mass eigenstates mix, which is similar to quark flavor mixing, thus implying that neutrinos do possess a mass. In analogy to the CKM matrix, the unitary transformation that connects the interaction and mass eigenstates of the neutrinos can be expressed in terms of three mixing angles and a CP-violating phase. The values of these transformation parameters are sensitive to the differences of squared masses between generations, and not to the masses themselves which are currently unknown. The exact mechanism of creating massive neutrinos still remains unresolved, but the most notable candidates for massive neutrinos include Majorana neutrinos and sterile neutrinos.

In addition to neutrino masses, the SM also fails to explain dark matter that is estimated to account for 84% of all matter in the universe [46]. Primary evidence for such a type of matter comes from astrophysical observations. In particular, the rotational velocity is found to not decrease with increasing radial distance, as one would expect from the mass distribution of luminous matter in spiral galaxies. It would either mean that the existing Newtonian dynamics needs to be modified, or that the outskirts of spiral galaxies have more matter that mostly interacts with ordinary matter via gravity. Further evidence, such

as temperature anisotropies in cosmic microwave background, formation of astrophysical structures, or gravitational lensing effects all point to a type of matter that does not couple to the „visible" SM particles, hence the name.

Finally, the unification of the SM with GR proves to be the most ambitious idea in modern particle physics. Merging gravity with the other three fundamental forces implies that gravity must be quantized. The natural choice for a particle that mediates the gravitational force is a massless spin-2 particle called graviton. However, attempts at constructing a quantized theory with gravitons that works at any scale have been unsuccessful because such theory, unlike the SM, is perturbatively nonrenormalizable. As a consequence, the theory breaks down at higher energies than the Planck scale $\Lambda_{\text{Planck}} \simeq 10^{19}\,\text{GeV}$, where the quantum effects of gravity become important. It perhaps hints that the full theory, which unifies all known fundamental forces, may require a more general framework than QFT.

2.1.6 Effective field theories

The shortcomings of the SM have motivated a wide selection of theories that attempt to address the problems of the SM. Theories that go beyond the SM (BSM) oftentimes bring about new phenomena that experimental physicists can put to test. However, it is not very efficient nor practically feasible to consider every exotic BSM model that theorists have proposed. Instead, a coherent framework is needed that quantifies deviations from the SM in a systematic way.

It is not a coincidence that none of the couplings present in the SM Lagrangian density given by Eq. (2.18) have a negative mass dimension. This property stems from the long-believed assumption that any valid theory should be renormalizable for it to have predictive power. The reason being: if the theory includes couplings with negative mass dimension, it would not be possible to find a finite number of counterterms that compensate for the singularities arising from the loop diagrams of these interactions. The SM is perturbatively renormalizable as long as α and α_S remain sufficiently small, but there exists a whole other class of BSM theories, which are nonrenormalizable due to the presence of additional couplings with negative mass dimension. It would seem that these theories cannot make any predictions, since they require an infinite number of parameters to be fixed. However, when assuming that the new interactions become important in the energy scales much higher than currently attainable by the experiments, then additional corrections by those interactions to known physics established at lower scales are suppressed by the scale of new physics.

This is the premise of effective field theories (EFTs), which are applicable or „effective" up to some kinematic limit [47, 48]. The formalism purports an extension to the SM Lagrangian density of the form

$$\mathcal{L}_{\text{EFT}} = \mathcal{L}_{\text{SM}} + \sum_{d>4} \frac{c_i^{(d)}(\Lambda)}{\Lambda^{d-4}} \mathcal{O}_i^{(d)}\,, \tag{2.19}$$

where Λ is sufficiently large energy scale of new physics, $c_i^{(d)}$ are dimensionless complex-valued Wilson coefficients and $\mathcal{O}_i^{(d)}$ the corresponding operators with mass dimension d. The operators $\mathcal{O}_i^{(d)}$ adhere to intended gauge symmetries, and are constructed from the very same fields and derivatives thereof present in the SM. In the standard model EFT (SMEFT), the operators are expected to respect $SU(3)_C \times SU(2)_L \times U(1)_Y$. Odd-dimensional operators are not favored because they violate the conservation of baryon or lepton numbers [49, 50]. This leaves dimension-6 EFT operators as the leading order candidates for new interactions. Higher-order even-dimensional operators are suppressed

by the cutoff scale Λ and are thus typically ignored. Different combinations of higher-order operators can lead to the same S-matrix, which motivates the need for a standard basis for these operators [51]. There are multiple conventions that have resolved the redundancy and identified a finite set of operators, each with a different focus on the physics goals, such as Warsaw [52], SILH [53–56] and Higgs basis [57]. More elaborate schemes than SMEFT have been developed, such as Higgs EFT (HEFT) [58, 59], which exploits the global („custodial") $SU(2)$ symmetry of the Higgs potential by rearranging the Goldstone bosons into an $SU(2)$ matrix and demoting the Higgs field into a singlet of the EW gauge group. This effectively allows the insertion of new Higgs boson interactions into the Lagrangian density via powers of (h/v) terms. The HEFT formalism generally predicts larger deviations from the SM than SMEFT, but is only valid for new physics scales of up to $\mathcal{O}(4\pi v) \simeq 3\,\text{TeV}$ due to unitarity constraints [60, 61]. As a consequence, there is no power counting by the scale parameter Λ in HEFT as in SMEFT. Instead, the different terms in HEFT Lagrangian density are distinguished by their chiral dimension, which equals one for fermion bilinears and for derivative operators.

The current situation is analogous to the early days of particle physics, when the best description of β decays was modeled by a contact interaction between the four fermion fields [62, 63]. As depicted in Fig. 2.4(a), the intermediate W boson that mediates this process was not yet resolvable because the energy scale of the interactions was much lower than the EW scale. Albeit nonrenormalizable, the theory was still successful in explaining the low-energy behavior of the process.

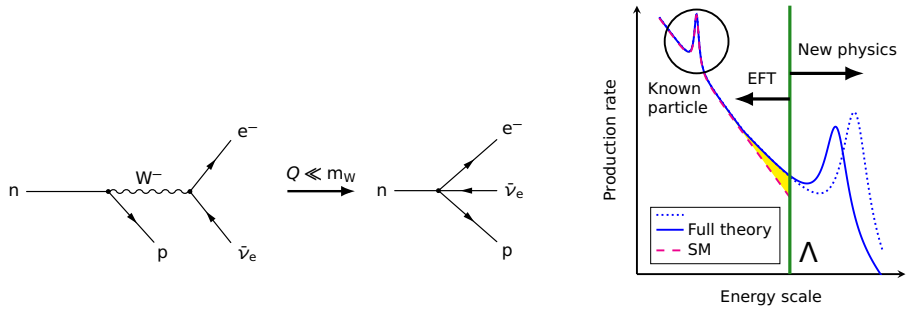


Figure 2.4: (a): Feynman diagrams of β decay for the cases when the W boson could be resolved at high energies Q, as shown on the left-hand side, and when the description becomes effective at significantly lower energies than the mass of the boson m_W, which is depicted on the right-hand side. (b): Illustration of the EFT formalism. Yet unknown UV-completing theories (shown with blue lines) beyond some scale Λ can lead to the same effective description below that scale (demarcated by a green vertical line), thus altering the production rate of known particles with respect to the SM prediction (the latter of which is highlighted with a dashed pink line). Discrepancy between the SM and the effective description (yellow shaded area) can be measured if Λ is reachable by experiments.

The philosophy behind EFTs is that one does not have to know the full theory in order to make consistent predictions about „low-energy" physics that is currently in reach by experiments. This point is also illustrated by Fig. 2.4(b), which demonstrates that different BSM behavior at high energies can lead to the same effective description at low scales. It also explains why it is widely conveyed that signs of new physics should appear in the high-energy tails of kinematic distributions. Deviations from the SM can be quantified in terms of coupling parameters that are associated with nonrenormalizable

higher-dimensional operators. Extracting the corresponding EFT parameters $c_i^{(d)}$ from experimental data helps to place indirect constraints on masses and coupling strengths of the new particles, to restrict viable classes of BSM theories, and to prompt dedicated searches of the corresponding signal models. Thus, the EFT formalism should be viewed as a tool for making incremental progress towards finding a more complete theory.

2.2 LHC phenomenology

Particle colliders function as a testing ground for the SM. Their objective is to accelerate electrically charged particles to a desirable kinetic threshold, collide them and detect the collision byproducts. Depending on the trajectory of accelerated particles, the colliders can be either linear or circular. In circular accelerators, the particles that are being accelerated traverse the circular path numerous times and with every turn receive an energy boost until they reach the desired energy, whereas in linear colliders the particles receive their energy boost only once while they travel along the straight path before colliding. Thus, in general, circular accelerators can reach higher energies compared to linear accelerators, and are therefore ideal for exploring new energy scales.

At relativistic energies, charged particles tend to lose energy in the form of EM radiation by emitting *bremsstrahlung* photons while being accelerated. The effect is more severe for lighter particles, which is why it is more cost-effective to accelerate hadrons than, say, electrons in order to compensate for the radiation loss. The Large Hadron Collider (LHC) does precisely that: it accelerates collection of protons (p) along a circular path and collides them inside the detectors that are located at certain points of the beam line. A more detailed overview of the apparatus is given in Section 3.1. For the purpose of present discussion it is important to recognize that the collision events happening at the LHC are initiated by protons which comes with its own challenges. In the following, Section 2.2.1 gives a brief overview of the phenomenology concerning hadron collision, and Section 2.2.2 describes the theory of particle decays.

2.2.1 Event production

The basis of any physics experiment is the delivery of predictions that can be compared to the measurement. The outcome of collision events is inherently probabilistic, as dictated by underlying Lorentz-invariant matrix elements (MEs) that describe the quantum processes. In case the process of interest happens rarely, lots of data would have to be collected and subsequently filtered. The selection of collision events is based on a series of cuts applied on kinematic observables that are constructed from the detector information, with the aim to maximize the presence of signal events while reducing the amount of background events in the collected data. For a fair comparison to the measurement, these steps need to be repeated in the theoretical prediction as well. However, evaluating these cuts analytically becomes computationally infeasible due to the complicated structure of the resulting phase space [64].

To overcome this problem, the MEs are instead evaluated using Monte Carlo (MC) integration techniques such as importance sampling[3] [65] and multi-channel sampling [66]. These methods allow sampling the underlying phase space more frequently in places where the ME takes the largest values. The task of making theoretical predictions is therefore factorized into several steps, starting with the simulation of relevant processes in identical detector conditions, followed by the analysis of the data and the simulation on equal footing, and finally comparing the results quantitatively. The simulation is produced

[3] The method is briefly discussed in Section 6.2.4.

by first generating a set of events with fixed multiplicities in initial and final states but in random kinematic configurations. A weight is assigned to each event such that distributions of kinematic observables aggregated over all simulated events follow the theoretical prediction. This is facilitated by the MC integration techniques, which help to generate the events more efficiently. For this reason, the simulated events are oftentimes colloquially referred to as MC samples.

This approach is extremely beneficial because the same simulation can be used for different purposes by multiple analysis groups in parallel. MC samples make it also possible to model arbitrary kinematic variables with ease. However, it comes at the cost of statistical and systematical uncertainties on the prediction, in addition to the uncertainties known from theory. The statistical uncertainties can be reduced by generating, as a general rule of thumb, at least an order of magnitude more MC events than expected from the data. The systematic uncertainties originate from discrepancies between data and MC simulation that may occur in some kinematic variables. These differences are corrected with dedicated scale factors (SFs). Overview of such corrections, as well as the extensive list of MC samples used in this thesis are detailed in Section 5. Systematic uncertainties of theoretical origin can be propagated to MC samples by adjusting event weights accordingly. In fact, this brings up another advantage of MC samples: the generated events representing one process can be transformed into a completely different process by appropriately reweighting the events. A comprehensive summary detailing other aspects of MC event generators can be found in Ref. [67].

The main observable of interest in collision experiments is the total scattering cross section. It has dimension of area and is measured in units of barn (b)[4]. In short, the total cross section is defined as the transition rate between initial and final states, normalized to incident flux of particles. If the scattering process with final state $|f\rangle$ is initiated by hadrons A and B at center-of-momentum (c.o.m) energy $\sqrt{s}$, then the expression for its total (hadronic) cross section can be written as:

$$\sigma_{AB\to f} = \sum_{a,b} \int_0^1 dx_a\, f_{a/A}(x_a, \mu_F)\, dx_b\, f_{b/B}(x_b, \mu_F)\, \hat{\sigma}_{ab\to f}(x_a, x_b, \mu_R, \mu_F, \sqrt{s})\,. \quad (2.20)$$

The Bjorken scaling variables x_a and x_b denote the fraction of longitudinal momentum that is transferred from initial hadrons A and B to partons a and b, respectively [68]. The probability for that to happen at some energy scale $\mu_F \gg \Lambda_{\text{QCD}}$ is governed by parton distribution functions (PDFs) $f_{a/A}$ and $f_{b/B}$.

The hard[5] scattering cross section $\hat{\sigma}_{ab\to f}$ in Eq. (2.20) is computed at fixed order in perturbation theory:

$$\hat{\sigma}_{ab\to f} = \frac{(2\pi)^4}{4F} \int d\Pi_n |\mathcal{M}(ab \to f)|^2\,. \quad (2.21)$$

Here F refers to Lorentz-invariant Møller flux factor caused by initial state partons a and b, while $d\Pi_n$ stands for Lorentz-invariant phase space (LIPS) element of the n-particle final state $|f\rangle$. The ME $\mathcal{M}(ab \to f)$ in Eq. (2.21) is expanded in the power series of coupling strength(s) of interest. For example, the perturbation series can be expanded by α_s to include higher order perturbative QCD (pQCD) corrections, or by α_{EW} to include corrections from the EW theory, or both. If no corrections are included, then the ME and therefore

[4] $1\,\text{b} = 10^{-28}\,\text{m}^2$.

[5] A „hard" quantity in particle physics refers to something that has relatively high energy. Conversely, a „soft" observable or process has comparatively low energy.

the cross section itself is said to be at leading order or lowest order (LO), at tree level or at Born level. Complete set of first order corrections brings the calculation to next-to-leading order (NLO). Corrections beyond NLO are possible but become computationally challenging because the number of Feynman diagrams representing each possible subprocess in the ME grows factorially with every order. Ratio of partonic cross sections $\hat{\sigma}'/\hat{\sigma}$ of the same process $ab \to f$, where the numerator is computed to higher perturbative order than the denominator, is referred to as the k-factor. The dependency of the cross section on some kinematic observable x is expressed in terms of differential cross section $d\hat{\sigma}/dx$. Studying the functional form of differential cross section can give a better insight into the underlying theory.

The hard scattering (HS) cross section in Eq. (2.20) depends on the renormalization scale μ_R. The dependency is introduced via coupling strength, with the aim to regularize ultraviolet divergences that occur beyond LO. According to Kinoshita-Lee-Nauenberg theorem, soft and collinear infrared divergences due to higher order corrections cancel each other [69, 70]. However, the theorem does not work with hadronic initial states, where extra partons are radiated that cause collinear infrared divergences. The said infinities are removed by moving the singular behavior from the partonic cross section into PDFs and subsequently regularizing them with factorization scale μ_F that the PDFs hence depend on.

The PDFs are designed to absorb collinear singularities that happen when a parton, after being released from a hadron, goes through successive emissions or „splits" below some scale μ_F. The process continues until the parton enters the HS process as an asymptotically free particle. The evolution of PDFs as a function of scale μ_F is described by DGLAP[6] equations [71–73]. The PDFs can be expanded in power series of α_S, taking into account higher order QCD (as well as QED) corrections to parton splitting. Intuitively, partons in the initial (and final) state are confined to hadrons, while in the HS process they become asymptotically free as implied from the ME formalism. The scale μ_F marks the energy scale that separates soft collinear emissions from the hard process, or equivalently nonperturbative hadron dynamics from perturbatively calculable scattering.

The total cross section should not depend on μ_R and μ_F when including all terms of the perturbation series. In practice, though, the perturbation series is truncated, which means that the theoretical prediction still depends on these scales. While both scales are arbitrary in principle, they are set equal to each other in the computation, in order to avoid residual dependencies that may arise in higher orders of perturbative expansion. Dependencies on these artificial scales can be attenuated by computing the scattering cross section to higher orders. Residual dependencies on these scales due to missing higher orders are taken as a source of systematic uncertainty. This uncertainty is estimated using canonical 7-point method, where both QCD scales are independently varied up and down by a factor of two in the ME, while maintaining the condition that $|\ln(\mu_R/\mu_F)| < 1$ [50, 74, 75]. Optimal choice of the scales is the one that minimizes the uncertainties. A common option is to use constant scales and set them equal to half of the invariant mass of final state particles.

PDFs are determined from global fits to data by dedicated collaborations. The PDF sets used in this thesis are NNPDF3.0 [76] and NNPDF3.1 [77], as recommended by the CMS collaboration [78–80]. They express individual parton content of protons. In the low energy limit, the energy of a proton is dominated by its valence u and d quarks, but when accelerated to higher energies its content turns into a „sea" of virtual quarks and gluons that constantly pop in and out of existence. Figure 2.5 shows the distributions of

[6] The acronym is built from authors' names who derived the equations: Dokshitzer, Gribov, Lipatov, Altarelli and Parisi.

several proton PDFs at a scale that is characteristic to single Higgs boson production. It demonstrates that the gluon PDF becomes dominant at small values of the Bjorken variable. At the c.o.m energy that the LHC collided the protons ($\sqrt{s} = 13$ TeV), any scattering process that requires about a few hundred GeV of energy is most likely initiated by a pair of gluons, followed by a quark-gluon and a quark-quark pair. This is because the resulting Bjorken variable, which is proportional to the fraction of c.o.m energy contributing to the HS process, can take very small values if both incident particles are gluons. Thus, while the colliding protons have a well-defined momentum of $\sqrt{s}/2$ directed along the collision axis, the partons that actually initiate the HS event carry less energy as dictated by the corresponding PDF. At least two sources of PDF uncertainties are distinguished: statistical uncertainties that are related to the way PDFs are extracted from data, and uncertainties due to α_S variation in PDF expressions. Protons can also emit a photon, but the likelihood for that to happen is an order of magnitude smaller compared to sea quarks. The photon structure of the proton is modeled by special „LuxQED" PDFs [81], which are used only to improve the estimated cross sections of a few processes in the present work.

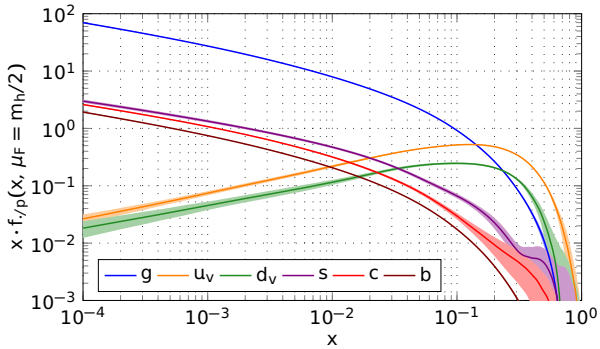


Figure 2.5: Proton PDFs with uncertainty bands from NNPDF 3.1 NNLO set for various partons as a function of the Bjorken scaling variable. Labels u_v and d_v stand for valence u and d quarks. All remaining quarks and gluons are deemed as sea partons. The plot is created with LHAPDF [82].

Two types of flavor schemes exist, depending on how the b quarks are modeled in the initial state [83]. In the four-flavor scheme (4FS), the b quarks do not originate from protons. Instead, the HS event is initiated by four quarks (u, d, c, s) or gluons. In this case, the b quarks are excluded from proton PDFs and can appear only in the final state. They can be produced at the ME level via gluon splitting ($g \to b\bar{b}$) or via top decays. The advantage of this choice is that the b quarks can remain massive in all calculations, thereby yielding an accurate depiction of the kinematics already at LO. While it is natural to exclude b quarks from proton PDFs because b quarks are four times more massive than protons, the resulting fixed order perturbation series may exhibit collinear divergences at energy scales significantly higher than the mass of the b quark. These problems are characteristic to the 4FS but are avoided in the five-flavor scheme (5FS) by letting the PDFs and fragmentation functions to absorb the said divergences. In order to maintain the validity of the factorization procedure in this approach, the b quarks are treated as massless in the initial state. While 5FS simplifies calculations and reduces the final state multiplicity, the differential observables sensitive to the extra b quarks not originating from top decays in this scheme may not be as precisely modeled compared to 4FS. Both descriptions are equivalent when including all orders of perturbation theory. The distinction of flavor schemes becomes relevant in processes that allow b quarks in the initial state, such as

(associated) production of single top events. Example Feynman diagrams comparing both 4FS and 5FS of the same process are shown in Fig. 2.19.

The particles that enter or exit the HS process can radiate additional photons or gluons. Depending on where the extra particles originate, one can distinguish between initial state radiation (ISR) and final state radiation (FSR). The former has the effect of „recoiling" a LO system away from the collision axis, whereas the latter degrades the energy resolution of final state particles at the reconstruction level. Colored particles tend to emit multiple gluons until the radiating particles participate in the scattering process, or until the particles lose energy to the point of reaching the confinement scale followed by hadronization. The cascade of virtual gluon emissions, gluon splitting and subsequent hadronization constitutes parton showering (PS). The hadronization processes as well as PS of simulated events are modeled by Pythia software, which employs the string fragmentation approach [84].

Contributions due to ISR and FSR can be modeled as hard emissions in the ME calculation, or as soft and collinear emissions at the PS level. In both cases, their predictions are sensitive to the value of strong coupling α_S. Uncertainties attributed to the PS are determined by varying the renormalization scale in the strong coupling by a factor of $1/2$ and 2. PS describes soft processes more accurately while ME does a better job at modeling the hard activity. Thus, a matching and merging scheme is required at a certain energy scale in order to avoid double counting the events with the same final state of jets produced by ME and PS. Various procedures exist that resolve the overlap, such as MLM merging at LO [85] and FxFx merging at NLO [86]. These methods are employed by MadGraph5_aMCatNLO event generator [87, 88]. POWHEG, which is another MC generator, resolves the described ambiguities internally when generating the events [89–91].

Other types of hadronic activity may occur in proton-proton collisions, as illustrated by Fig. 2.6. For example, in multiple-parton interactions (MPI) the same protons (depicted as large green blobs) that initiated the HS process (large red circle) may emit secondary partons that interact with each other (purple blob). The proton content that is left over from these scattering processes, gives rise to so-called beam-beam remnants (cyan blobs). The final state particles of the HS process (small red circles) undergo hadronization (small green blobs), thus producing final state hadrons that subsequently decay (dark green blobs). Various color reconnection mechanisms exist that model how color charge is distributed in PS [92]. Figure 2.6 distinguishes between QCD radiation in initial and final states (shown as curly blue and red lines, respectively) from the EW radiation (yellow). The extra activity in collision events that is not described by neither the HS nor the PS is commonly referred to as underlying event (UE). Color reconnection and UE are characterized by a set of parameters called „tunes" implemented in Pythia software [84]. The simulated samples used in this thesis are generated with tunes CP5 [93], CUETP8M1, CUETP8M2 and CUETP8M2T4 [94]. Systematic uncertainties due to different choices of UE parameters or color reconnection models can be estimated by varying the tune parameters.

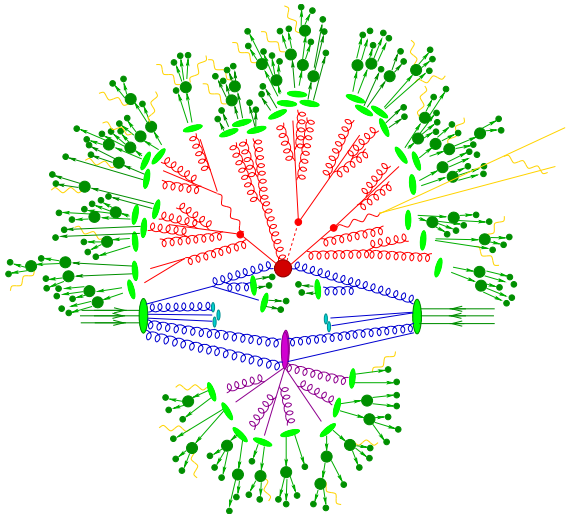


Figure 2.6: Illustration of a proton-proton collision [95].

2.2.2 Particle decays

Particle decay is characterized by its mean lifetime that tells how long, on average, the particle, call it A, can survive at rest before it decays with probability of $1/e$. When moving relativistically, it experiences time dilation that prolongs its decay. Its lifetime is inversely proportional to its total decay width Γ_A, which equals to the sum of partial widths of all unique decay modes: $\Gamma_A = \sum_X \Gamma(A \to X)$. The probability for decay process $A \to X$ to occur is given by the ratio of its partial width to total width, also known as the branching ratio (BR).

A free-field propagator represents the probability amplitude for a particle with 4-momentum p to traverse through spacetime between interactions. The propagator has a singularity at its rest mass m, which tells that the creation and its subsequent annihilation is most effective when the particle adheres to the energy-momentum relation, $p^2 = m^2$. However, this explanation does not account for the radiative corrections that the particle may receive while it travels. The additional corrections can be absorbed into an extra term called self-energy in the propagator, but it has the effect of modifying the particle mass. If the particle is unstable, then the mass shift is going to have an imaginary component. On-shell renormalization conditions can be imposed to make sure that the pole mass m_A, at which the propagator is maximized, remains real. After doing so, the imaginary component of radiative corrections is absorbed into total decay width. In this prescription, the pole mass would then be interpreted as the physical mass of the particle. The whole procedure eventually yields a relativistically invariant Breit-Wigner propagator Δ_{BW} that can be used in ME calculations. Its corresponding probability density has Lorentzian form:

$$|\Delta_{\text{BW}}(p^2)|^2 = \left| \frac{i}{p^2 - m_A^2 + i m_A \Gamma_A} \right|^2 = \frac{1}{(p^2 - m_A^2)^2 + (m_A \Gamma_A)^2} \,. \tag{2.22}$$

In narrow-width approximation (NWA) $\Gamma_A \ll m_A$, which turns Eq. (2.22) into a simple δ-function. It is important to emphasize that the total width is not an artifact of the theory nor is it in any way related to measurement precision, but it is in fact a real physical parameter that dictates the width of the resonant mass peak. This is also the reason why Γ_A is sometimes referred to as mass width. An illustrating plot for Lorentzian mass

peaks can be found in Fig. 2.4(b), which shows the mass resonances on a linearly falling background.

The probability density defined by Eq. (2.22) reaches its maximum when the particle goes „on-shell" or, equivalently, has a mass equal to its physical mass. Otherwise, the particle is deemed as „off-shell" or virtual (as opposed to real), and is usually denoted with an asterisk in decay chains and Feynman diagrams. An off-shell particle can decay into real particles and an on-shell resonance into virtual particles, but these processes become more suppressed as the virtual particles move further away from their mass shell.

In analogy to the partonic cross section defined by Eq. (2.21), which describes „two-to-many" process, the partial decay width can be viewed as „one-to-many" process:

$$\Gamma(A \to X) = \frac{(2\pi)^4}{2m_A} \int d\Pi_n |\mathcal{M}(A \to X)|^2 , \tag{2.23}$$

where $d\Pi_n$ stands for LIPS element of n-particle final state X. The expression Eq. (2.23) is valid only in the rest frame of the particle. Massless particles cannot decay into massive particles unless they go off-shell. The decay widths and thereby BRs directly depend on the relative coupling strength between the mother particle and its descendants. It is important to recognize that the mass and charge of a particle are not observables. Instead, they are parameters of the theory that describe statistical properties of the particle: its decay width given by Eq. (2.23) and scattering cross section given by Eq. (2.21).

Particle detectors cannot detect unstable particles directly if they decay before interacting with the detector material. The detectors can register those decay products that are not only sufficiently stable to reach the detector, but also energetic enough to exceed the detection thresholds. Particles seen by the detector may result from a series of intermediate resonances. The resonances can be inferred from their decay products if they leave an imprint to the detector material or get absorbed by the material. It is therefore important to understand the properties of decay products, such as lifetimes, masses and charges, as well as their abundance in typical hadron collisions, in order to make informed decisions when designing a detector.

None of the massive elementary particles in the SM are directly observable, with the exception of electrons and muons, because the unstable particles either decay into lighter ones or, in case of quarks, also hadronize. The latter does not apply to top quarks, since their experimentally measured mass width of $\Gamma_\mathrm{t} = 1.42\,\mathrm{GeV}$ exceeds the QCD scale. Instead, they decay into pairs of a W boson and a bottom quark almost always before the hadronization can even occur. It should be noted that top quark is never a decay product itself because it is the most massive particle of the SM.

Barring the top quark, massive vector bosons decay unequivocally into fermions, because these are the only lighter particles that couple to the bosons. At surface level, decays into lepton and corresponding anti-neutrino pairs contribute about 33% to the decay width of W, and decays into quarks contribute to the rest of its width. This is understood in the following way: W fields couple to the first and second generation of quarks in three copies of color, totaling six quark doublets, and to three generations of leptons. Since there is no preference between quarks and leptons, the branching ratio of leptonic decays can be simply approximated by the number of lepton fields to the total number of fields that the W fields are coupled to. In practice, the BR of leptonic decays is reduced slightly after accounting for the higher order perturbative effects. Decays into any flavor of lepton and corresponding neutrino pair still remain equally probable, as expected from lepton universality. The total width of W amounts to $\Gamma_\mathrm{W} = 2.085\,\mathrm{GeV}$ [24].

The same simple arguments do not work when attempting to ballpark the BRs of the Z boson, because left-handed and right-handed fermions couple to the boson with

different strengths. Some manipulation of the EW Lagrangian density defined by Eq. (2.8) is required: moving out the chiral projections with Eq. (2.3), and grouping the operators that are associated with the Z field into vectorial and axial terms c_V and c_A yields:

$$\bar{\Psi}_L(T_3 - s_W^2 Q)\not{Z}\Psi_L - \bar{\Psi}_R s_W^2 Q \not{Z}\Psi_R = \bar{\Psi}\not{Z}(c_V + c_A\gamma^5)\Psi\,,$$

where $c_V = T_3 - 2s_W^2 Q$ and $c_A = T_3$, and Ψ represents spinor field of some fermion f. Considering that the vectorial and axial amplitudes do not interfere with each other, it follows that

$$\Gamma(Z \to f\bar{f}) \propto (c_A^2 + c_V^2) = T_3^2 - 2s_W^2 T_3 Q + 2s_W^4 Q^2\,.$$

Plugging in the operator eigenvalues from Table 2.2 and factoring in the number of color charges assigned to the five quarks that the boson can decay into tells that Z boson decays hadronically with about 69% probability, followed by „invisible" decays into neutrinos in 20% of the cases, and thus leaving 10% of the total decay width to the charged leptons. Lepton universality still holds, as the decays into different flavors are evenly split between the three generations. On the other hand, Z decays into down-type quarks are preferred over up-type quarks.

Despite the low BR for Z to decay into directly observable electrons or muons, these decay modes have been instrumental in precision measurements of the resonance. This is made possible thanks to the large cross section of the Drell-Yan (DY) process that produces the boson by annihilating a quark with its anti-quark. The quarks can also annihilate into a virtual photon γ^* that decays into the same particles as Z. Interferences between the production of either boson cannot be disentangled. Nevertheless, the Z peak in dilepton mass distribution can be easily distinguished at Z boson mass of around $91\,\text{GeV}$ from the sharply falling spectrum created by the virtual photons. As showcased in Fig. 2.7, at low dilepton mass of about $\lesssim 10\,\text{GeV}$, resonances from heavy meson decays take over, such as J/ψ at $3\,\text{GeV}$ that is made up of charm quarks, or Υ at $9.5\,\text{GeV}$ that consists of bottom quarks. Since the Z peak in DY events has a clear signature in leptonic channels and a sufficiently wide peak of $\Gamma_Z = 2.495\,\text{GeV}$ [24] with respect to the experimental resolution, it is often used as standard candle for developing and assessing selection criteria for leptons in analyses that are performed on data collected from high energy collisions.

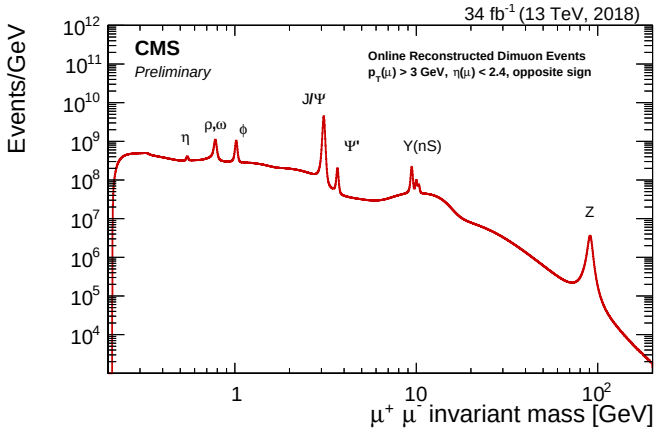


Figure 2.7: Dimuon invariant mass spectrum reconstructed from CMS data collected in 2018 [96].

τ lepton has an extremely narrow width of $\Gamma_\tau \approx 2.2 \times 10^{-9}$ MeV compared to its mass, which corresponds to a mean lifetime of 2.90×10^{-13} s. To put it in perspective, a τ moving at energy $E = 100$ GeV would travel approximately $Ec \ln 2/(m_\tau \Gamma_\tau) \approx 3.4$ mm before its survival probability halves. Its decay vertex would be displaced from the point of the HS event that created it, but the decay process would still remain well within the cavity of the CMS detector. τ decays always proceed through an off-shell W boson, which continues to decay into lighter particles than the τ lepton. As shown in Fig. 2.8, these particles can be electrons and muons with complementary neutrinos, or light quarks (u, d and s). The quarks subsequently form hadrons, which are collectively labeled by symbol τ_h. Considering that the quark fields are coupled to the W field in threefold, and that $|V_{ud}|^2 + |V_{us}|^2 \approx 1$, then one would crudely estimate 40% for the BR of leptonic τ decays, evenly split between electrons and muons, and 60% for the BR of hadronic τ decays. More accurate predictions are closer to 35% and 65%, respectively, after accounting for the properties of hadrons that the τ leptons decay into, as well as higher order perturbative effects [97]. Latest measurements of W, Z and τ BRs obtained from fit to data are compatible with the SM and are presented in Table 2.3.

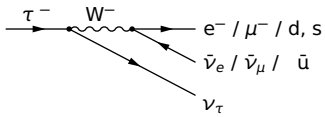


Figure 2.8: Feynman diagram illustrating a τ lepton decay.

	Electrons	Muons	τ leptons	Leptonic		Hadronic
				Average	Total	
W	10.71%	10.63%	11.38%	10.86%	32.72%	67.41%
Z	3.363%	3.366%	3.370%	3.366%	10.01%	69.91%
τ	17.82%	17.39%	✗	17.61%	35.21%	64.79%

Table 2.3: Measured leptonic and hadronic branching ratios (BRs) of W, Z and τ lepton [24].

The simplest charged mesons that the quarks from hadronic τ decays can bound to are rho mesons $\rho^\pm(770)$, pions $\pi^\pm$, or kaons $\mathrm{K}^\pm$ and $\mathrm{K}^{*\pm}$. The number between parentheses in the rho meson name denotes its approximate mass in MeV, to distinguish it from its excited resonant states [98]. Pions and rho mesons are the bound states of $\mathrm{u}\bar{\mathrm{d}}$ or $\bar{\mathrm{u}}\mathrm{d}$, depending on their total electric charge, but with different spins: pions are (pseudo)scalar, while the more massive rho mesons are vectors. This is explained by $SU(2)$ representation that the quark spin states belong to: two spin-$\frac{1}{2}$ particles combine either into a spin-0 or a spin-1 bound state. The situation is analogous for kaons, as both the (pseudo)scalar meson $\mathrm{K}^\pm$ and the more massive vector meson $\mathrm{K}^{*\pm}$ are bound states of $\mathrm{u}\bar{\mathrm{s}}$ or $\bar{\mathrm{u}}\mathrm{s}$, depending on their total electric charge.

Each of the mesons have neutral counterparts with similar masses: $\rho^0(770)$, π^0, K^0 and K^{*0}. Neutral kaons correspond to various bound states consisting of d and $\bar{\mathrm{s}}$ quarks. This statement stems from an observation that the light quarks have rather small masses relative to Λ_QCD that they can be treated as massless or, at the very least, with equal masses in pQCD calculations. If assuming the latter, then the QCD Lagrangian density would admit

global $SU(3)$ transformations that rotate the u, d and s fields in flavor space. Even though the flavor symmetry is spoiled by the mass differences of light quarks, it is a good enough approximation that allows to organize light hadrons in a mathematically consistent way. This is done by expressing the direct product of $SU(3)$ irreducible representation, which stands for quark states, or its complex conjugate representation, which stands for anti-quark states, as a direct sum of irreducible representations. It successfully explains how there can be multiple neutral mesons besides π^0 that have effectively the same quark content. The organizational scheme, named „Eightfold Way", was formally developed by Gell-Mann and Ne'eman during the 1950s [99, 100].

Due to its short mean lifetime of 4.5×10^{-24} s, $\rho^{\pm}(770)$ decays resonantly into $\pi^{\pm}\pi^0$ before it can interact with any of the detector material. Neutral pion has a longer mean lifetime of 8.5×10^{-17} s, but it is still not long enough for it to be directly seen by the detector before it decays into two photons. This is not the case for charged pions or kaons, since their mean lifetime of about 10^{-8} s, equivalent to proper lifetime of a few meters, is sufficient that either of the mesons can be observed directly. However, kaons rarely occur in hadronic τ lepton decays, as only 1% of the hadronic decays end up in the $\mathrm{K}^{\pm}\nu_{\tau}$ final state. In fact, it is more likely to see multiple pions produced by intermediate resonances such as $a_1^{\pm}(1260)$ or $\rho^{\pm}(1450)$ [101, 102] than kaons in hadronic τ decays. The point is illustrated by Table 2.4 that lists the BRs of dominant τ_{h} decay modes. The hadronic final state must have an odd number of charged mesons, as otherwise it would violate charge conservation. Decay modes that produce one, three or five charged mesons $h^{\pm}$ with any number of neutral mesons are called „1-prong", „3-prong" or „5-prong", respectively. The latter is an extremely rare decay channel, accounting for just a mere 0.15% of τ_{h} width.

	Decay mode	Primary meson resonance	BR
„1-prong"	$h^{\pm}$		17.77%
	$\pi^{\pm}$		16.70%
	$h^{\pm}+\pi^0$		41.21%
	$\pi^{\pm}+\pi^0$	$\rho^{\pm}(770)$	39.34%
	$h^{\pm}+2\pi^0$		14.62%
	$\pi^{\pm}+2\pi^0$	$a_1^{\pm}(1260)$	14.29%
„3-prong"	$h^{\pm}h^{\pm}h^{\mp}$		15.13%
	$\pi^{\pm}\pi^{\pm}\pi^{\mp}$	$a_1^{\pm}(1260)$	14.37%
	$h^{\pm}h^{\pm}h^{\mp}+\pi^0$		7.84%
	$\pi^{\pm}\pi^{\pm}\pi^{\mp}+\pi^0$	$\rho^{\pm}(1450)$	7.13%
	Other modes		3.44%

Table 2.4: Common τ_{h} decay modes and corresponding BRs [24]. The BRs are quoted with respect to the decay width of τ_{h}. Dominant final state of each exclusive decay mode, primary resonance and the full BR of the final state are shown separately on indented lines.

Other hadrons, too, undergo a series of decays into more stable hadrons or leptons. The most notable hadrons are those formed from b quarks such as B mesons that are paired with a light quark. The mean lifetime of B mesons, about 1.5×10^{-12} s, is just long enough that they travel a significant distance before typically decaying into lighter D mesons that contain a c quark (because $|V_{cb}| \gg |V_{ub}|$), but sufficiently short that the decay processes

would still occur within the bounds of a detector. At the LHC, the distances that the b hadrons traverse are slightly longer than that of τ lepton, usually in the order of a cm. Not only are b hadrons more massive than other hadrons, they also tend to keep most of the energy from its parent b quark as well [103]. In addition, the jets that enclose the b hadron activity feature a higher number of charged constituents, including electrons and muons, compared to the jets that are produced from the hadronization of lighter quarks, simply because the decay chain of b hadrons is longer. Figure 2.9 depicts a possible composition of a b jet, where its constituent B meson decays semileptonically into D meson. Because of its comparable lifetime to B mesons, the D meson would be displaced before further decaying. All of these properties, and many more, can be measured and are thus taken advantage of by dedicated „b tagging" algorithms that attempt to distinguish b jets from lighter jets [104].

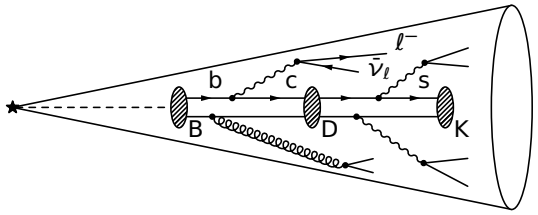


Figure 2.9: Anatomy of a b jet. The B *meson is significantly displaced from the HS collision point (★) before it decays weakly into a* D *meson. The* D *meson itself may convert into a kaon* K *through weak interaction. A charged lepton (ℓ^-) may be created as a byproduct of weak decays. Hadron constituents may emit extra QCD or EM radiation. Other hadrons produced in the b quark hadronization may enter the b jet cone, but they are not displayed here.*

Muon always decays through an off-shell W into an electron plus complementary neutrinos. This is expected, because electrons are the only charged particles that are also less massive than muons. Mean lifetime of a muon is an enormous $2.2\,\mu s$, only second to a free neutron that undergoes β-decay with a half-life of little over $10\,\mathrm{min}$. In comparison to τ lepton made earlier, a $100\,\mathrm{GeV}$ muon would have a half-life survival distance of $450\,\mathrm{km}$. Electrons and protons are the only known massive particles that do not decay. After all, they form bound states with neutrons, which are ultimately the building blocks of stable matter.

2.3 Higgs boson

The seminal papers on EWSB were published by three independent groups of researchers in 1964: Brout and Englert [14], Higgs [15], and Guralnik, Hagen and Kibble [16]. By 1967 these ideas were incorporated into the EW theory developed by Glashow [32], Salam [33] and Weinberg [34], and its renormalizability was finally demonstrated in 1971 by 't Hooft and Veltman [105]. In the following couple of years, Lee [106–109] popularized the work on EWSB in a series of four papers [110]. Progress on the theoretical front of particle physics was well ahead of its experimental counterpart at the time, but the tides started to turn right around then.

Processes involving neutrinos like β decays were hitherto described by $V-A$ theory as 4-point interactions between nucleons, charged leptons and neutrinos. It even accounted for the parity violation [62, 63] and agreed well with experimental data, but did so only

in the low-energy limit. The EW theory amended this problem by postulating W bosons as the mediators of β decays, but it additionally claimed the existence of Z boson, which was yet to be confirmed. The first hints of the proposed bosons were detected in 1973, when a bubble chamber named Gargamelle managed to capture processes such as elastic $e^- \nu_\mu$ scattering that were consistent with the EW theory [111, 112]. This further propelled dedicated searches of W and Z bosons. Both were eventually discovered in 1983 [113–116], which earned EW gauge theory and symmetry breaking a permanent spot in the SM.

The remaining puzzle pieces of the SM started to fall into place, culminating with the discovery of the top quark in 1995 [117, 118] and ν_τ in 2000 [119]. The last free parameter of the SM, mass of the Higgs boson, remained elusive until 2012 when both ATLAS [12] and CMS [13] collaborations confirmed the observation of a particle that very much resembles the sought-after Higgs boson. The combination of LHC Run 1 measurements by the two experiments reported a Higgs boson mass of $m_{\mathrm{H}}^{\mathrm{CMS+ATLAS}} = 125.09 \pm 0.21\,(\mathrm{stat}) \pm 0.11\,(\mathrm{syst})\,\mathrm{GeV}$ [120]. However, this was later updated after the inclusion of results on LHC Run 2 data recorded by the CMS detector in 2016 [121], raising the global estimate to $m_{\mathrm{H}}^{\mathrm{PDG}} = 125.10 \pm 0.14\,\mathrm{GeV}$ [24]. Its discovery has since finalized the SM, thus marking the end of an era, but it has also launched the particle physics community to a new era of research that is still continuing to this day: precision measurements in the Higgs sector. These searches include measurement of production and decay rates of the Higgs boson, its quantum numbers and differential observables, which all serve to better understand the EWSB and the SM in general.

The rest of this section explores the properties of the Higgs boson and explains how to measure them in more detail. Section 2.3.1 covers known Higgs boson decay modes and Section 2.3.2 its main production mechanisms. The discussion concludes with Section 2.3.3, which gives an overview of frameworks that facilitate the measurement of Higgs boson properties.

2.3.1 Decay modes

The Higgs boson is a short-lived particle with a theoretical decay width of $\Gamma_{\mathrm{H}} = 4.10\,\mathrm{MeV}$ at $m_{\mathrm{H}} = 125.09\,\mathrm{GeV}$ [50], which corresponds to a proper lifetime of $1.56 \times 10^{-22}\,\mathrm{s}$. This is a relatively narrow width when compared to massive vector bosons. Direct access to the width of the on-shell resonant peak of the Higgs boson is unfeasible due to large experimental resolution of about $1\,\mathrm{GeV}$ [122], which exceeds the desired resolution by at least two orders of magnitude. Higgs boson width can be indirectly inferred from relative rates of its off-shell and on-shell production [123]. The method relies on the knowledge of SM couplings to the Higgs boson, but the model-dependency can be mitigated with the consideration of anomalous BSM couplings. This method has provided the most stringent constraints on Higgs boson width to date, which amount to $3.2^{+2.4}_{-1.7}\,\mathrm{MeV}$ [124].

Matrix element of any process is proportional to the product of coupling strengths between interacting particles. Higgs boson couples to fermions with a probability amplitude that is linearly proportional to fermion mass, and to gauge bosons with a probability amplitude that is proportional to their mass squared. Thus, the basic assumption is that the Higgs boson is more likely to decay into a pair of massive particles than into lighter particles. However, there are some caveats to this claim. Higgs boson decaying into a pair of top quarks is kinematically forbidden because $m_{\mathrm{H}} \ll m_{\mathrm{t}}$. It can decay into a pair of massive vector bosons, but does so as long as at least one of the vector bosons goes off-shell since $m_{\mathrm{H}} < 2m_{\mathrm{W,Z}}$. Such decays are suppressed by the virtuality of one of the bosons [125]. A decay process does not necessarily have to occur at the tree level but may also proceed via loops, although the corresponding decay widths are scaled down by the extra couplings.

Loop-induced Higgs boson decays are primarily mediated by virtual top quarks for which Higgs boson has the strongest affinity, but other decay mechanisms involving W loops are also possible, as illustrated by Feynman diagrams in Fig. 2.10. The loop processes enable Higgs boson decay modes into massless bosons that are not otherwise possible at the tree level: $H \to gg$, $H \to \gamma\gamma$ and $H \to Z\gamma$. Higgs boson branching ratios and the corresponding uncertainties as predicted by the SM are provided in Table 2.5.

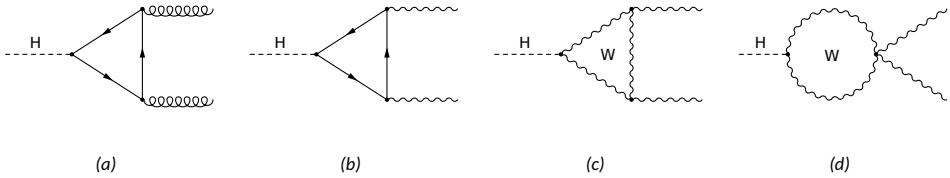


Figure 2.10: Loop-induced Higgs boson decays: into a pair of gluons via fermion loop dominated by top quarks (a); into $\gamma\gamma$ or $Z\gamma$ via the same fermion loop (b), or via cubic (c) or quartic (d) W fusion.

$H \to$	$b\bar{b}$	WW^*	gg	$\tau^-\tau^+$	$c\bar{c}$
BR	0.5824	0.2137	8.187×10^{-2}	6.272×10^{-2}	2.891×10^{-2}
Uncertainty	$^{+1.24\%}_{-1.27\%}$	$^{+1.55\%}_{-1.53\%}$	$^{+5.14\%}_{-5.09\%}$	$\pm 1.65\%$	$^{+5.54\%}_{-1.99\%}$

$H \to$	ZZ^*	$\gamma\gamma$	$Z\gamma$	$\mu^-\mu^+$
BR	2.619×10^{-2}	2.270×10^{-3}	1.533×10^{-3}	2.176×10^{-4}
Uncertainty	$^{+1.55\%}_{-1.53\%}$	$^{+2.06\%}_{-2.08\%}$	$^{+5.82\%}_{-5.83\%}$	$^{+1.67\%}_{-1.70\%}$

Table 2.5: Branching ratios of the Higgs boson at mass $m_H = 125\,\text{GeV}$ as predicted by the SM [50]. Uncertainties on the BRs are obtained by adding theoretical uncertainties and parametric uncertainties resulting from heavy quark masses and strong coupling α_S in quadrature. Theoretical uncertainties reflect the omission of higher order corrections in the corresponding MEs.

Technically, the uncertainties on Higgs boson BRs should be propagated to the simulation such that the sum of all Higgs boson BRs remains equal to unity [50]. This in turn implies that changing a BR in one direction would induce changes to all other BRs in the opposite direction. The size of these secondary shifts can be estimated as follows: Let BR_i denote the branching ratio of a particular Higgs boson decay, *e.g.*, $H \to WW^*$. It is assumed that a change in the nominal BR is solely caused by the increase or decrease of the corresponding partial width Γ_i:

$$BR_i \to BR_i' = BR_i + \Delta BR_i = \frac{\Gamma_i + \Delta\Gamma_i}{\Gamma_H + \Delta\Gamma_i}\,.$$

From this conjecture one can work out that all other BRs would need to be uniformly scaled by a factor of

$$\frac{BR_j'}{BR_j} = 1 - \frac{\Delta BR_i}{1 - BR_i} \qquad (i \neq j)\,.$$

This effect is most pronounced when varying the BR of $H \to b\bar{b}$ decays, which causes a 1.7% shift in all other Higgs boson BRs. However, the effect is much milder when varying

the BR of any other Higgs boson decay mode: 0.4% for $H \to WW^*$ decays and per mille for $H \to \tau^-\tau^+$ decays. Given that the $H \to b\bar{b}$ decays are not actually featured in any of the signals studied in this work, the described anti-correlation effects are in fact ignored.

Only a subset of Higgs boson decay modes have been detected with varying degrees of sensitivity. The discoverability of a decay mode not only depends on its BR, which regulates the occurrence probability of the decay process, but also on type of the resulting decay products. For instance, the detection of $H \to b\bar{b}$ decays relies heavily on accurate identification of b jets to distinguish them from lighter jets. This is needed to overcome the enormous multijet background, which arises solely from QCD interactions between the partons that are expelled from the initial state protons. The detection of hadronic decay modes of the Higgs boson is further complicated by the fact that the energy resolution of hadronic jets is intrinsically inferior to that of electrons and muons. The presence of extra jets produced from any quark or gluon that pass the identification criteria increases the number of combinations that would need to be considered in order to reconstruct a viable candidate of the Higgs boson.

For these reasons, the searches of Higgs boson decays encompass multiple Higgs boson production processes, which are discussed in the next section. It suffices to say that the alternative, so-called associated production modes of the Higgs boson imply the presence of extra particles in the final state, which provide an additional handle for detecting the decay processes. Higgs boson itself was discovered in $H \to \gamma\gamma$ and in $H \to ZZ^* \to 4\ell$ decay modes [12, 13] also known as „golden channels", where the symbol ℓ collectively stands for an electron or a muon from this point onward. The former decay mode was instrumental in confirming the scalar nature of the Higgs boson, since Landau-Yang theorem forbids any massive vector boson to decay into two photons [126, 127]. Subsequent studies of spin and parity properties of the new resonance in the same golden channels, but on more data and with refined analysis techniques, solidified its compatibility with the SM prediction [128, 129]. Higgs boson has also been observed in $H \to b\bar{b}$ [130, 131], $H \to WW^*$ [132–134] and $H \to \tau^-\tau^+$ [135, 136] decay modes. There is also evidence for $H \to \mu^-\mu^+$ [137, 138] and $H \to Z\gamma$ [139] decays, but more data is needed before any claims about their observation can be made. The $H \to c\bar{c}$ process, which is the only Higgs boson decay process that captures its interactions with up-type fermions, has remained elusive to this day [140, 141].

2.3.2 Production mechanisms

Higgs boson production modes can be inferred from the decay processes by reversing those that have gluons or quarks in the final state because these are the particles that initiate the HS processes in hadron colliders. At surface level, it only leaves Higgs boson production via gluon-gluon fusion (ggF), shown in Fig. 2.11(a), which corresponds to the inverted Feynman diagram in Fig. 2.10(a), and Higgs boson production from the annihilation of quark and anti-quark pair, as depicted in Fig. 2.3(c). However, the latter is suppressed for a multitude of reasons. First, the probability for a proton to emit a gluon is about an order of magnitude higher compared to the case where the proton emits a quark. Additionally, the initial quarks need to enter narrow kinematic configuration that is able to generate an on-shell Higgs boson. The quarks must also have the correct quantum numbers: opposite color and anti-color charges, same quark flavors and matching helicities. The latter is understood in the following way: in order to create a spin-0 particle such as Higgs boson, the initial state fermions must have opposite spin projections: $\pm\frac{1}{2}$ and $\mp\frac{1}{2}$. The 3-momenta of the quarks similarly point in the opposite direction in the rest frame of the Higgs boson. Therefore, both relativistic fermions must possess either left-handed or right-handed helicities. Finally, Higgs bosons have much stronger coupling to top quarks

than to any other quark. The only such production mechanism that has comparable cross section to that of other mechanisms is $b\bar{b} \to H$. Given how much lighter first and second generation quarks are with respect to the b quark, the production rates from lighter quarks must be at least an order of magnitude smaller.

As such, the most viable mechanisms, aside from the dominating ggF, are the associated production modes, where the Higgs boson is accompanied by extra particles in the final state. In decreasing order of cross section, these processes are: vector boson fusion (VBF), where a Higgs boson is produced in association with the pair of quarks that initiated the process ($qq \to Hqq$) as shown in Fig. 2.11(b); the so-called Higgs-*strahlung*, or simply VH, where the Higgs boson is radiated off of a massive W or Z vector boson, collectively denoted by V, as depicted in Fig. 2.11(c); associated production with a pair of top quarks, or $t\bar{t}H$ in short, where the Higgs boson is emitted from a top quark line as illustrated by Feynman diagrams in Fig. 2.11(d)–(f); associated production with a pair of bottom quarks ($b\bar{b}H$) that is identical to $t\bar{t}H$ when swapping top quarks with bottom quarks, but 5FS processes such as $b\bar{b} \to H$ and $bg \to bH$ are included here as well; associated production with a single top or anti-top quark (tH), which, alongside with $t\bar{t}H$, will be covered in more detail in Section 2.4; associated production with a pair of top quarks and a massive vector boson, or $t\bar{t}VH$ in short, shown in Fig. 2.12(c). Figure 2.13 displays cross sections per production mode as function of c.o.m energy at the LHC. The increase in production cross section with the c.o.m energy is driven by PDFs. Total cross sections and corresponding uncertainties of each production mode are given in Table 2.6.

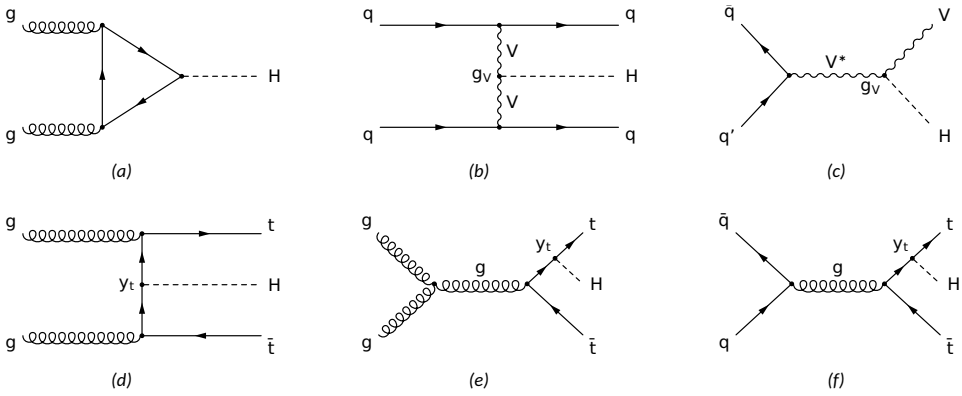


Figure 2.11: LO Feynman diagrams for the dominant production modes of a single Higgs boson: ggF dominated by virtual top quarks (a), VBF (b), VH initiated by quarks (c), and associated production with a pair of top quarks initiated by gluons (d)–(e) and by light quarks (f).

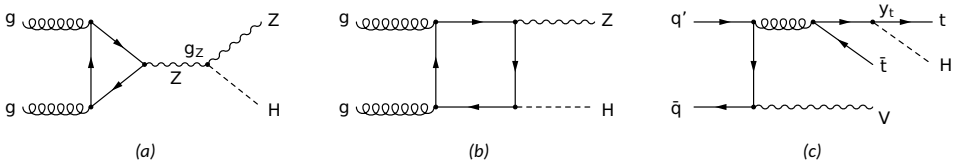


Figure 2.12: LO Feynman diagrams for the subdominant production modes of a single Higgs boson: gluon-induced ZH via triangle (a) and box (b) loop dominated by top quarks, and one of the many possibilities for $t\bar{t}VH$ production (c). In the latter case, the Higgs boson may be radiated from the V leg also.

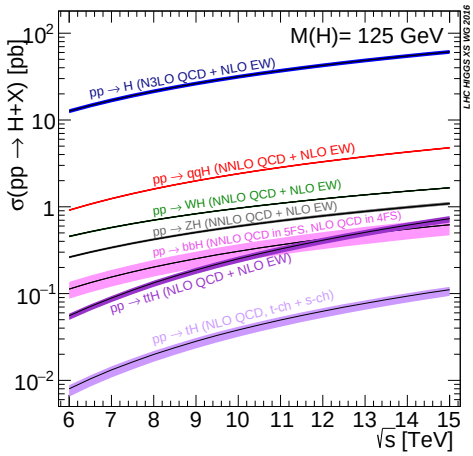


Figure 2.13: Cross sections for various Higgs boson production mechanisms parametrized by c.o.m energy at the LHC [50].

Process		Cross section [pb]	Uncertainty [%]		
			PDF	α_S	QCD scale
ggF		48.58	±1.9	±2.6	±3.9
VBF		3.782	±2.1	±0.5	$^{+0.4}_{-0.3}$
WH		1.373	±1.7	±0.9	$^{+0.5}_{-0.7}$
ZH		0.8839	±1.3	±0.9	$^{+3.8}_{-3.1}$
$\xrightarrow{\text{including}}$ gg $\to$ ZH		0.1227	±1.8	±1.6	$^{+25.1}_{-18.9}$
$t\bar{t}H$		0.5071	±3.0	±2.0	$^{+5.8}_{-9.2}$
$b\bar{b}H$		0.4880	[	$^{+20.2}_{-23.9}$	]
tH	t-channel	7.425×10^{-2}	±3.5	±1.2	$^{+6.5}_{-14.9}$
	W-channel	1.517×10^{-2}	±6.1	±1.5	$^{+4.9}_{-6.7}$
	s-channel	2.879×10^{-3}	±2.2	±0.2	$^{+2.4}_{-1.8}$
$t\bar{t}WH$		1.582×10^{-3}	±4.3	✗	$^{+3.2}_{-8.7}$
$t\bar{t}ZH$		1.535×10^{-3}	±3.0	✗	$^{+1.9}_{-6.8}$

Table 2.6: Cross sections of processes that produce a single Higgs boson with mass $m_H = 125\,\text{GeV}$ at c.o.m energy of $13\,\text{TeV}$ at the LHC [50, 142]. The PDF and α_S uncertainties are computed as recommended by the PDF4LHC working group [79]. The QCD scale uncertainties are due to missing higher orders in perturbation theory. All cross sections are computed in 5FS, except for the cross section of $b\bar{b}H$ that is obtained from matching 4FS (NLO in pQCD) and 5FS (NNLO in pQCD) calculations. Cross sections of $t\bar{t}H$, tH and $t\bar{t}VH$ are computed to NLO in pQCD; VBF and VH to NNLO in pQCD; ggF to N^{3}LO in pQCD. Cross sections of all processes but tH and $b\bar{b}H$ include additional NLO EW corrections. The uncertainties on $b\bar{b}H$ cross section are added in quadrature. Symbol ✗ means that the uncertainty is not available.

The ggF production mode has the largest cross section and the simplest final state. These properties are ideal for studying the golden decay channels. The VBF production mode, on the other hand, offers a rather distinct jet topology compared to the ggF Higgs production mechanisms. In particular, it is characterized by two „forward" jets, which are separated by a wide angle and have large invariant dijet mass. The jets are created by initial state quarks that continue their hadronization process roughly in the same direction after they have exchanged a vector boson. The vector boson then radiates a Higgs boson that tends to decay such that its decay products fly in the direction perpendicular to the collision axis. These features provide a unique handle for detecting the VBF production process. Associated productions of the Higgs boson with a vector boson are typically searched in subchannels, where the vector boson decays leptonically ($\mathrm{Z} \to \ell\ell$ and $\mathrm{W} \to \ell\nu$) or invisibly ($\mathrm{Z} \to \nu\nu$). The VH production mode has been essential for the discovery of $\mathrm{H} \to \mathrm{b\bar{b}}$ decays [130, 131]. Of the two possible production modes, WH is clearly the dominating one, contributing to roughly 60% of the inclusive VH cross section. The corresponding cross section is about six times smaller compared to the equivalent process induced by quarks, but the Z boson has harder transverse momentum, which significantly improves its acceptance.

2.3.3 Measurement frameworks

Couplings of Higgs boson to vector bosons, g_{V}, can be inferred from VBF and VH production, or by searching for $\mathrm{H} \to \mathrm{VV}^*$ decays. From this example it is evident that the searches of production and decay modes go hand-in-hand, since the information about Higgs boson couplings is present in both. In order to exploit the variations in signal and background composition that occur in different regions of the phase space, the analyses are often divided into independent subcategories. The categorization is based on the properties of reconstructed objects in signal events that pass the selection cuts, such as their multiplicity or flavor. It generally enhances sensitivity of the analysis, provided that there is sufficient event statistics in each event category.

In a similar vein, multiple analysis results that address the same physics can be combined to yield even more precise physics results. The combination efforts require coordination to ensure mutual exclusivity of the phase space covered by each analysis if they are performed on the same data, *i.e.*, collected by the same detector. The level of agreement between the analysis results and the SM can be studied with two separate but related methods: with μ-framework or with κ-framework.

The former quantifies compatibility of the measurement with the SM in terms of signal strength parameter μ. It is a number that scales the simulated signal contribution such that it gives the best match between observed yields in data and expected yields in the simulation[7]. If the goal is to compare the measurement of some Higgs boson production mechanism $\mathcal{G}$ to the SM expectation, then the ratio would be defined as $\mu_{\mathcal{G}} = \sigma_{\mathcal{G}}/\sigma_{\mathcal{G}}^{\mathrm{SM}}$, where the cross section in the numerator is obtained from the measurement and the denominator corresponds to the SM prediction. Similarly, signal strength $\mu^{\mathcal{F}}$ of some Higgs boson decay mode $\mathcal{F}$ would be defined as the ratio of measured to expected BRs of that decay mode. The measurements of production or decay modes are said to be compatible with the SM if $\mu = 1$ within the uncertainties. Signal strength parameters have been extracted separately for production and decay modes from CMS data collected during LHC Run 2 operations. The results confirm the observation of five major production modes ggF, VBF, WH, ZH and $\mathrm{t\bar{t}H}$, and five decay modes $\gamma\gamma$, ZZ^*, WW^*, $\tau\tau$ and $\mathrm{b\bar{b}}$ of the Higgs boson.

[7] More formal definition of the signal strength parameter will be given in Section 6.1.

Deviations from the SM are systematically scrutinized in the κ-framework [143]. It capitalizes on the idea discussed earlier that Higgs boson couplings affect both production and decay modes simultaneously. The framework assumes that the functional structure of the SM remains the same and only the values of individual Higgs boson couplings that are otherwise fully specified in the SM may deviate from their predicted values in the presence of BSM physics. Any such deviation can be absorbed into dimensionless coupling modifiers $\kappa_{\mathscr{P}}$ that are associated with particles $\mathscr{P}$. This formalism is unable to explain any BSM physics that otherwise implies new Lorentz-invariant structures in the Lagrangian density. For example, the only way to realize CP-odd fermion interactions with Higgs boson is to include terms that feature the γ^5 operator. Such „anomalous couplings" are introduced to the theory with more general approaches like EFT.

According to the κ-framework, the cross section measurement that corresponds to certain Higgs boson production mode $\mathscr{I}$ and decay channel $\mathscr{F}$ can be decomposed in the following way:

$$\sigma(\mathscr{I} \to \mathrm{H} \to \mathscr{F}) = \sigma(\mathscr{I} \to \mathrm{H})\mathrm{BR}(\mathrm{H} \to \mathscr{F}) = \sigma_{\mathscr{I}}^{\mathrm{SM}}\mathrm{BR}_{\mathscr{F}}^{\mathrm{SM}} f_{\mathscr{I}}(\boldsymbol{\kappa}) f_{\mathscr{F}}(\boldsymbol{\kappa}), \tag{2.24}$$

where $f_{\mathscr{I}}$ and $f_{\mathscr{F}}$, respectively, refer to the normalization functions of production and decay processes that depend on a set of coupling modifiers $\boldsymbol{\kappa}$. Although not explicated, the former also depends on c.o.m energy at which the process is created. The SM cross section and branching ratio are fully restored by setting all coupling modifiers equal to unity, which effectively means that the normalization functions in Eq. (2.24) drop out. The normalization functions are second-degree or higher order polynomials of the coupling modifiers, but their exact form generally depends on the perturbative corrections that the cross sections and BRs receive. Nevertheless, the coupling modifiers still factorize out the same way after accounting for dominant higher order pQCD corrections, thus making it possible to derive the scaling behavior at just LO in EW.

At basic level, there is one coupling modifier per interaction to the Higgs boson: two for the couplings to the massive bosons, nine for the fermions, and one for the self-coupling. Depending on the analysis, the scaling behavior of mechanisms that feature a quantum loop, such as ggF production or $\mathrm{H} \to \gamma\gamma$ decay, can be expressed in terms of basic coupling modifiers, or by a single effective coupling modifier. In practical applications, however, the coupling modifiers that have no discernible impact to production or decay processes can be safely ignored. For instance, it is sufficient to consider just the coupling modifiers to top and bottom quark interactions, κ_{t} and κ_{b}, when expressing the scaling behavior of ggF production, because contributions to the fermion loop from fermions lighter than the bottom quark are negligible. In case there are multiple competing mechanisms contributing to the same process, such as fermion loop and W loop in $\mathrm{H} \to \gamma\gamma$ decays, the scaling behavior must include interference terms, which are sensitive to the relative sign of coupling modifiers.

Connection to signal strength parameters can be made by noticing that the normalization functions $f_{\mathscr{I}}$ and $f_{\mathscr{F}}$ in Eq. (2.24) precisely correspond to $\mu_{\mathscr{I}}$ and $\mu^{\mathscr{F}}$ given earlier. Therefore, by varying the coupling modifiers in some range it is possible to evaluate the level of compatibility between data and simulation. Best fit of fundamental coupling modifiers extracted from CMS data collected during LHC Run 2 is presented in Fig. 2.14. It demonstrates incredible agreement with the linear proportionality of Higgs boson coupling strength with the mass of particles it interacts with, as predicted by the Higgs mechanism, over three orders of magnitude in mass scale.

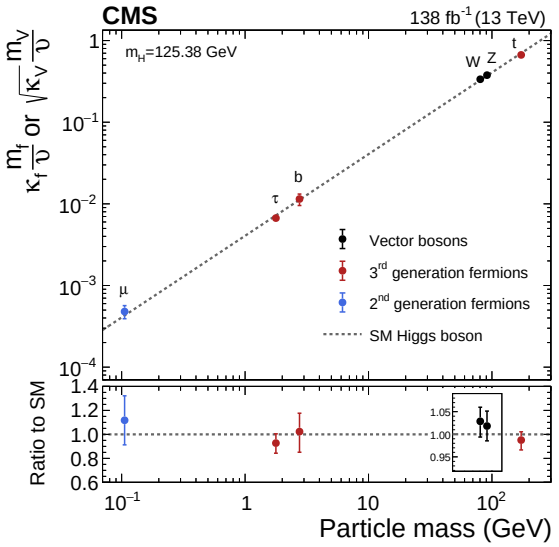


Figure 2.14: Coupling modifiers of Higgs boson to fermions and massive vector bosons as function of their mass measured in CMS data recorded in LHC Run 2 [8]. The results published in Ref. [1] are included in this measurement. Higgs boson mass is quoted from dedicated measurement performed by the CMS collaboration on data collected in 2016 [121].

While the κ-framework maximizes the sensitivity of a coupling measurement, it is not flexible in accommodating changes in signal hypothesis after the measurement has concluded. In particular, if the theory inputs are updated, the measurement would have to be repeated. A complementary approach would be to measure fiducial differential cross sections of a process, which minimizes the model-dependency. In fiducial cross section measurement, the phase space of interest is limited only to the kinematic region that is visible to the detector or where the detector performs at maximum efficiency. The fiducial volume is further restricted by analysis cuts that are applied at the reconstruction level. Such an approach would avoid theory assumptions that are associated with the extrapolation to the phase space that is not accessible by the detector. However, it also means that the sensitivity of the analysis deteriorates significantly due to simpler cuts, since it is not feasible to implement complicated selection strategies in MC event generators.

Standard template cross section (STXS) framework makes a compromise between theory dependency and re-interpretability [50, 144]. This is achieved by splitting the expected signal events into mutually exclusive fiducial-like regions by Higgs boson production modes. The fiducial volumes are then further divided into bins based on kinematic variables that are available at the MC generator level post-showering. The binning is designed to increase the chances of observing possible BSM effects and to make connection to EFT parameters, while retaining maximum sensitivity of the analysis and keeping the number of bins as small as possible in order to avoid prohibitively large statistical uncertainties in each bin. From power expansion of the EFT Lagrangian density given by Eq. (2.19) it is evident that the BSM effects become stronger with the energy of interactions. As explained earlier, signs of new physics are expected to appear in the high-energy tails rather than in the bulk of kinematic distributions. In principle, it is possible to infer constraints on Wilson coefficients from fit to STXS bins, but it is not the most accurate method as it relies on assumptions that the EFT effects on acceptance and on backgrounds are negligible or at the very least covered by the uncertainties on the SM prediction [145].

There are multiple versions or „stages” of the framework, with each subsequent version having finer granularity of the binning scheme than the previous one, in order to accommodate the increasing amount of available data. For example, the latest iteration of the framework, STXS stage 1.2, recommends a scheme where the $t\bar{t}H$ events are binned by transverse momentum of the Higgs boson, p_T^H, while the earlier versions of the framework do not recommend to partition the $t\bar{t}H$ events at all. Variable p_T^H is particularly sensitive to potential CP-violating effects of the top Yukawa coupling, but also to Higgs boson self-coupling [146]. The STXS stage 1.2 binning scheme of other single Higgs boson production modes are shown in Fig. 2.15.

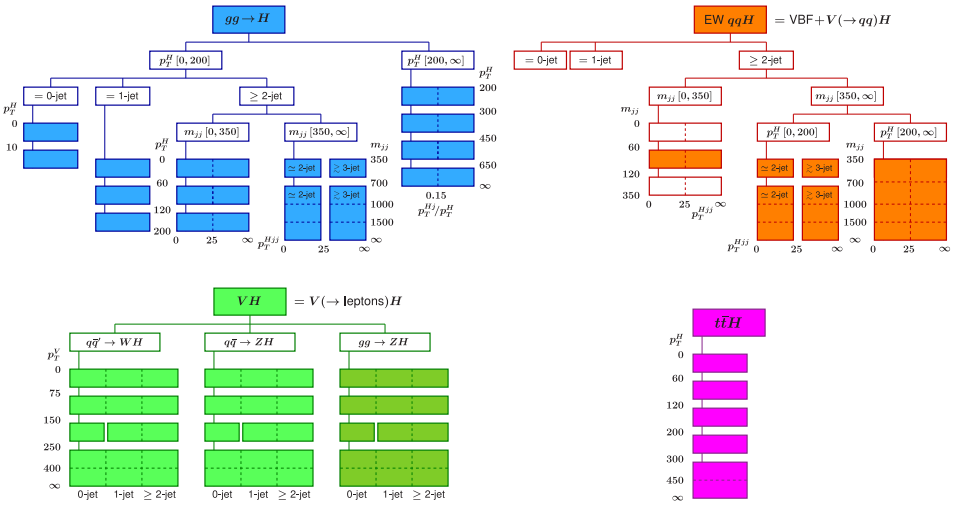


Figure 2.15: STXS stage 1.2 binning of the following Higgs boson production modes: ggF (blue, 16 bins); VBF and VH with hadronically decaying vector boson (orange, 10 bins); VH with leptonically decaying vector boson (green, 15 bins) and $t\bar{t}H$ (purple, 5 bins). The variables featured in the binning scheme are: multiplicity of jets; transverse momentum of the Higgs boson (p_T^H) and massive vector boson (p_T^V); dijet mass (m_{jj}); magnitude of the transverse momentum sum of the Higgs boson and a single jet (p_T^{Hj}), or Higgs boson and two jets (p_T^{Hjj}). Only those signal events are considered for the binning, where absolute pseudorapidity of the Higgs boson is less than 2.5. All thresholds on momentum and mass variables are given in units of GeV. *The plots are created by the LHC Higgs Working Group [50].*

Unlike fiducial cross section measurements, this prescription makes it possible to later combine multiple analyses that target different Higgs boson decay modes, thereby improving statistical uncertainties of the signal in each bin. When it comes to the STXS measurement, all STXS bins enter simultaneous fit to data, where each bin has been assigned its own signal strength parameter. The inclusive cross section measurement of a Higgs boson production mode can be reproduced if the same signal strength parameter is assigned to all STXS bins of that production mode. However, one needs to also account for anti-correlated uncertainties that are associated with the migration of events between the bins [147].

2.4 Associated production of Higgs boson with top quarks

This section is dedicated to the phenomenology of associated Higgs boson production with a pair of top quarks ($t\bar{t}H$) and associated Higgs boson production with a single top or anti-top quark (tH). The eventual goal of studying these processes is to probe top Yukawa coupling y_t. Section 2.4.1 provides arguments as to why this might be interesting, and highlights some of the intricacies concerning $t\bar{t}H$ and tH production from theoretical perspective. Section 2.4.2 describes the current status of experimental searches of these processes.

2.4.1 Theoretical aspects

Top quark plays a prominent role in EW symmetry breaking due to its large mass. In particular, the Higgs boson self-coupling λ evolves with the energy scale, the same way how α_S changes with the energy scale as described by its renormalization group equation given by Eq. (2.7). It is possible to gauge the vacuum structure of the early universe by rolling the self-coupling back to the Planck scale in present day vacuum potential modeled by Eq. (2.11). It turns out that the top Yukawa coupling y_t contributes to the evolution of λ and thereby to the effective vacuum potential in a major way that renders the present day vacuum meta-stable, meaning that the vacuum potential possesses an additional, even deeper minimum at larger values of the Higgs field [148]. Since the true vacuum was not realized in the early universe by this argument, it may suggest that there exists another BSM mechanism below the Planck scale that prevented this from happening [149]. If the current vacuum is truly meta-stable or if there is new physics at play here, the outcome is particularly sensitive to the precise value of y_t (as well as self-coupling λ) either way. The situation is illustrated by Fig. 2.16, which shows a phase diagram for SM vacuum that is parametrized by the masses of the Higgs boson and the top quark. Moreover, any deviation of y_t from its predicted SM value may jeopardize the unitarity and renormalizability of the SM altogether [150, 151]. Therefore, it is important to measure not only the Higgs boson self-coupling λ, but also the top Yukawa coupling to the highest possible accuracy.

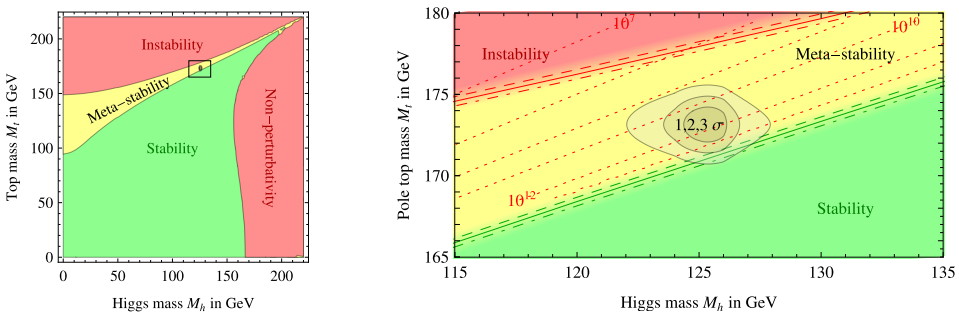


Figure 2.16: Stability regions of SM vacuum as a function of Higgs boson and top quark masses spanning over a wide range of values (a) and zoomed into experimentally relevant range (b) [148]. In unstable regions, the effective vacuum potential $V(\phi)$ becomes unbounded from below; in meta-stable regions, the current minimum of $V(\phi)$ is not global; in stable regions, the current minimum of $V(\phi)$ coincides with the global minimum. The red dotted lines correspond to the energy scale given in GeV*, at which the vacuum becomes unstable. The shaded contour regions that are centered around Higgs boson and top quark mass indicate the associated uncertainties.*

Anomalous Yukawa couplings are predicted in several types of two-Higgs-doublet models (2HDM) [152], such as in minimal supersymmetric SM (MSSM) theories [153], in twin Higgs models [154], and in composite Higgs models [155, 156], to name a few. Such theories postulate additional Higgs boson-like particles that modify the effective coupling to the existing SM particles. While SM Higgs boson itself has been confirmed to be CP-even in $H \to VV^*$ and $H \to \gamma\gamma$ channels, the CP-violating nature of its fermionic couplings still remains to be determined. The most generic way to parametrize CP-violating top Yukawa interactions is to consider the following Lagrangian density [157, 158]:

$$\mathcal{L}_{t\bar{t}H} = -\frac{y_t}{\sqrt{2}}\,\bar{t}\,(c_\alpha \kappa_t + i s_\alpha \tilde{\kappa}_t \gamma^5)\,t h\,,$$

where $c_\alpha \equiv \cos\alpha$ and $s_\alpha \equiv \sin\alpha$, and $\alpha \in [0, 2\pi)$ corresponds to CP-mixing phase. Scalar coupling modifier κ_t and pseudoscalar coupling modifier $\tilde{\kappa}_t$ can in principle take any real values. However, such parametrization affects other SM processes like ggF production and $H \to \gamma\gamma$ decays. Setting $\kappa_t = 1$ and $\tilde{\kappa}_t = 2/3$ reproduces the SM rates of both processes for every value of α, but such coupling configuration does modify the production cross section of $t\bar{t}H$ and tH processes. Assuming nonzero coupling modifiers, the interaction remains CP-even when $\alpha = 0$ or $\alpha = \pi$, but becomes CP-odd with $\alpha = \pi/2$. The SM scenario is restored when $\tilde{\kappa}_t = 0$ and $c_\alpha \kappa_t = 1$. In SMEFT, the couplings may receive the following tree-level contributions from dimension-6 operators $\mathcal{O}_{t\phi}$:

$$\kappa_t = 1 - \frac{3}{2\sqrt{2}} c_{t\phi} \frac{m_t v}{\Lambda^2}\,, \qquad \tilde{\kappa}_t = -\frac{3}{2\sqrt{2}} c_{t\phi} \frac{m_t v}{\Lambda^2}\,,$$

where $c_{t\phi} e^{i\alpha}$ would be the Wilson coefficient that is associated with $\mathcal{O}_{t\phi}$ and Λ is the scale of new physics [159]. Another interesting special case is the inverted top coupling (ITC) scenario where $\tilde{\kappa}_t = 0$ and $c_\alpha \kappa_t = -1$. The CP-violating nature of top Yukawa coupling has been studied by ATLAS and CMS collaborations [160, 161], but the work that will be presented later in Section 7 does not consider CP-violation in top Yukawa interactions. For this reason, the CP-mixing angle α is taken to be zero without any loss of generality. In the following, the interaction between top quark and Higgs boson is parametrized only by the scalar coupling modifier κ_t, which is defined as the ratio of measured top Yukawa coupling y_t to its SM expectation $y_t^{SM} \simeq 1$.

The top Yukawa coupling can be determined indirectly by measuring ggF or gluon-induced ZH production cross sections, or $H \to \gamma\gamma$ and $H \to Z\gamma$ decay rates. Even probing the sign of y_t is possible with these processes, since the Feynman diagrams that are sensitive to y_t interfere with the other diagrams that also contribute to a given process [150, 162]. However, these mechanisms proceed through quantum loops. Some yet unknown BSM mechanism may affect the loops and compensate for the deviations in y_t such that it still reproduces the expected SM rates. This motivates accessing y_t directly from $t\bar{t}H$ and tH production side, where the coupling appears already at the tree level.

At the LHC, the $t\bar{t}H$ process can be initiated by a pair of gluons through dominant t-channel or s-channel diagrams, as shown in Figs. 2.11(d) and 2.11(e), respectively, or by a pair of quarks as illustrated by the Feynman diagram in Fig. 2.11(f). At LO in EW, its production cross section scales trivially with κ_t^2, and is therefore not sensitive to the sign of the coupling but only to its magnitude. The simulated $t\bar{t}H$ events used in this thesis are generated at NLO in pQCD, but it is normalized to cross section of $\sigma_{t\bar{t}H}^{SM} = 507.1$ fb, which features additional NLO EW corrections.

The Higgs boson and top quark in the final state of tH are always accompanied by an extra b quark, light quark, or W boson. Based on this, the tH production is accordingly

separated into the following channels: s-channel tH production, W-channel or simply tHW, and t-channel or tHq. As illustrated by the Feynman diagrams in Fig. 2.17, the s-channel process is initiated by a pair of quarks that annihilate into a virtual W boson, which then proceeds to decay into a b quark and a top quark. Since its cross section adds just 3% to the inclusive cross section of the tH process, the s-channel signal is omitted from the discussion of the analysis that is presented in Section 7. The second largest tH production channel in terms of cross section is tHW, the Feynman diagrams of which are shown in Fig. 2.18. The process is realized in 5FS, where the initial state b quark produces an on-shell W and a top quark in the final state. The dominant production mode that contributes to the inclusive tH cross section the most is tHq, where a W boson is exchanged between a light quark q and heavier top or b quarks. The corresponding LO Feynman diagrams are displayed in Figure 2.19 for 5FS where the initial state features a b quark, and for 4FS where the b quark appears only in the final state.

In all three tH production modes, the Higgs boson may couple to the top quark with strength y_t, or to the W boson with strength g_W that is defined by Eq. (2.14). Under the assumptions of the SM, the diagrams where the Higgs boson is radiated by a W interfere destructively with the diagrams where the Higgs boson is emitted from a top quark line. It can be also viewed as a consequence of unitarity in weak interactions [158, 163]. On a process level, both tHq and tHW experience interferences between diagrams where the Higgs boson is emitted either from a top quark or from a W boson. This becomes evident when expressing the scaling of their cross sections in terms of the relevant coupling modifiers $\kappa_\mathrm{t} = y_\mathrm{t}/y_\mathrm{t}^\mathrm{SM}$ and $\kappa_\mathrm{W} = g_\mathrm{W}/g_\mathrm{W}^\mathrm{SM}$ as follows [164]:

$$\sigma_{\mathrm{tH}q}(\kappa_\mathrm{t}, \kappa_\mathrm{W}) = (2.63\kappa_\mathrm{t}^2 - 5.21\kappa_\mathrm{t}\kappa_\mathrm{W} + 3.58\kappa_\mathrm{W}^2)\sigma_{\mathrm{tH}q}^\mathrm{SM}\,, \tag{2.25}$$

$$\sigma_{\mathrm{tHW}}(\kappa_\mathrm{t}, \kappa_\mathrm{W}) = (2.91\kappa_\mathrm{t}^2 - 4.22\kappa_\mathrm{t}\kappa_\mathrm{W} + 2.31\kappa_\mathrm{W}^2)\sigma_{\mathrm{tHW}}^\mathrm{SM}\,. \tag{2.26}$$

The corresponding scaling behavior of the expected cross section as a function of coupling modifiers is depicted in Fig. 2.20. These relations tell that the cross section of tHq shrinks most drastically when $\kappa_\mathrm{t}/\kappa_\mathrm{W}$ equals to 1, or to 1.38 in case of tHW cross section. Furthermore, the Higgs bosons that are produced in tH processes for the case of maximum destructive interference between κ_t and κ_W tend to have a lot softer p_T than the other scenarios. The effect is a lot more pronounced in tHW than it is in tHq, however. On the other hand, the production cross section of tH processes is enhanced by about an order of magnitude with respect to the SM scenario if $\kappa_\mathrm{t}/\kappa_\mathrm{W} = -1$. The extreme sensitivity of tH interactions on the relative sign of y_t and g_W couplings is particularly useful when studying alternative hypotheses like the ITC scenario. It is worth noting that the coupling modifiers κ_t and κ_W influence other processes besides t$\bar{\mathrm{t}}$H and tH. For example, ggF production rate of a single Higgs boson grows with κ_t^2, while κ_W^2 is featured in WH production rate and H $\rightarrow$ WW* decay rate. Therefore, when searching for BSM signal as a function of those coupling modifiers, the event yields from processes that depend on κ_t or κ_W must be scaled accordingly if the analysis is sensitive enough to those processes[8].

[8] This is also the main reason why the HH process was eventually ignored in t$\bar{\mathrm{t}}$H multilepton analysis. Despite its rather steep scaling behavior in terms of κ_t, the SM HH process has simply too small cross section times branching ratio that effectively no events passed the analysis cuts even when normalizing the final yields to a BSM scenario.

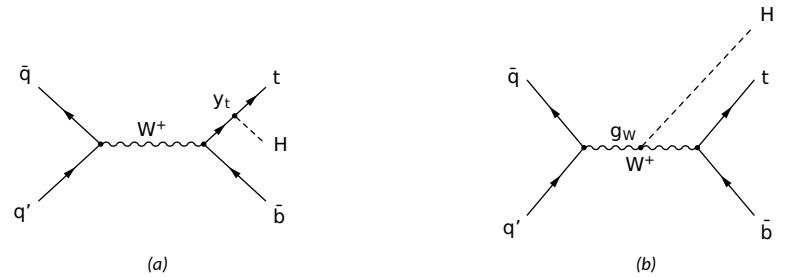


Figure 2.17: Feynman diagrams at LO for the production of a Higgs boson in association with a single top quark in the s-channel.

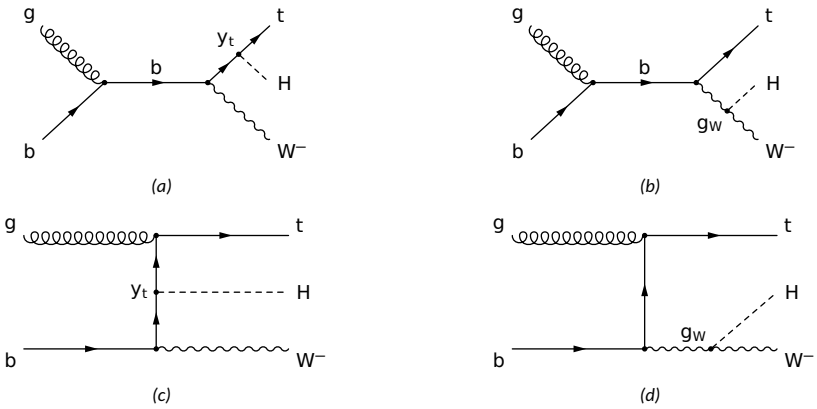


Figure 2.18: Feynman diagrams at LO for the production of a Higgs boson in association with a single top quark and a W boson in the s-channel (a)–(b) and t-channel (c)–(d), all in 5FS.

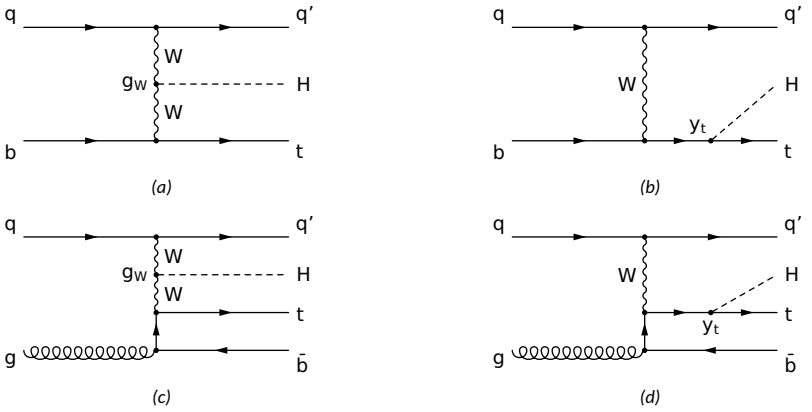


Figure 2.19: Feynman diagrams at LO for the production of a Higgs boson in association with a single top quark in the t-channel in 5FS (a)–(b) and in 4FS (c)–(d).

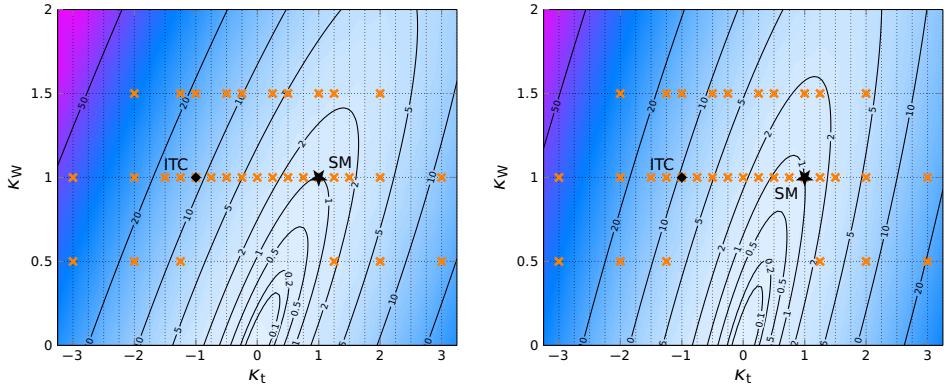


Figure 2.20: Contour plots showing expected BSM cross section in units of SM cross section as a function of κ_t and κ_W values for the tHq process (a) and for the tHW process (b), computed at $\sqrt{s} = 13$ TeV in 5FS. Only the pairs of κ_t and κ_W coupling modifiers that are marked with orange crosses in the plot are considered in the BSM coupling scan. Each of these points define a unique ratio of κ_t/κ_W. The SM and ITC scenarios are marked with a star (★) and a diamond (♦) symbol, respectively.

In 5FS, all three tH production modes are well-defined up to NLO in pQCD, but the processes start to interfere with each other at higher orders in a way that they cannot be uniquely separated [158]. The tHW process interferes with $t\bar{t}H$ at NLO in pQCD when defined in 5FS, and already at LO when specified in 4FS. Therefore, the simulated tHW events are produced at LO in 5FS, the Feynman diagrams of which are depicted in Fig. 2.18, to avoid rather sizable interference effects with the $t\bar{t}H$ process. The tHq process is generated at LO in 4FS, as shown in Figs. 2.19(c) and 2.19(d), because the extra b quarks that result from gluon splitting are modeled more accurately in 4FS than in 5FS. The corresponding NLO process mildly interferes with the s-channel at NNLO. The tHq and tHW samples were initially generated for the ITC scenario. However, since the event kinematics varies depending on the coupling scenario, it would not be possible to just transform the generated events from ITC to any other scenario based on inclusive observables. Instead, the event samples for the remaining SM and BSM scenarios are obtained through reweighting. This is accomplished by evaluating MEs for every coupling scenario under consideration in a given event. The event-level weight is then derived from the ratio of MEs, in which the numerator corresponds to the coupling scenario of interest and the denominator to the ITC scenario. The BSM coupling scenarios are studied in Section 7, where the coupling modifier κ_t is varied between -3 and $+3$ with a step size of 0.25, while κ_W spans values $\{0.5, 1, 1.5\}$. These particular ranges were motivated by Run 1 analysis results, which provided the strongest constraints on κ_t and κ_W that were known at the time of MC sample production. These results are summarized in Table 2.7, which also quotes even more stringent constraints on those coupling modifiers from superseding analyses. The particular values of couplings that were ultimately chosen for the coupling scans are highlighted with orange crosses in Fig. 2.20.

Experiment	Data	κ_t	κ_W
ATLAS and CMS	Run 1 [134]	$1.40^{+0.24}_{-0.21}$	$0.87^{+0.13}_{-0.09}$
ATLAS	Run 2 (2016–2017) [165]	$1.09^{+0.15}_{-0.14}$	1.05 ± 0.09
	Run 2 (2016–2018) [166]	0.94 ± 0.11	1.05 ± 0.06
CMS	Run 2 (2016) [164]	$1.11^{+0.12}_{-0.10}$	$1.10^{+0.12}_{-0.17}$
	Run 2 (2016–2018) [8]	$1.01^{+0.11}_{-0.10}$	1.02 ± 0.08

Table 2.7: Observed 1σ constraints on κ_t and κ_W coupling modifiers, while assuming no BSM interactions with the Higgs boson.

2.4.2 Experimental characterization

Dedicated measurements of the $t\bar{t}H$ process are performed in three separate channels based on the decay modes of the Higgs boson: $H \to b\bar{b}$, $H \to \gamma\gamma$, and the so-called multilepton channels, where the Higgs boson decays into a pair of vector bosons or τ leptons, which then subsequently decay into electrons, muons and τ_h. Other Higgs boson decay modes have either too small BR ($H \to \mu\mu$) or are difficult to resolve ($H \to c\bar{c}$). The first one in the list, $H \to b\bar{b}$, has the largest BR and is therefore a good candidate for such searches. However, the signal is dwarfed by huge QCD background, by the production of top quark pair with extra jets ($t\bar{t}$+jets), or by the production of single (anti-)top quarks. The background composition varies with the phase space region that is usually defined in terms of signal. In $t\bar{t}H(\to b\bar{b})$ events, the phase space of the signal region is divided into three categories, depending on the decay mode of the top quark pair: in fully hadronic (FH) case both top quarks decay hadronically with 45% probability; in semileptonic (SL) case just one of the top quark decays hadronically, while the other decays leptonically with 44% probability; in dileptonic (DL) events both top quarks decay leptonically with 11% probability. The analyses rely heavily on accurate identification of b jets [167, 168] as well as on the correct association of the jets with the Higgs boson and top quark candidates. This is achieved with modern multivariate analysis (MVA) techniques such as boosted decision trees (BDTs) and matrix element method (MEM), which will be formally introduced in Section 6. The latest searches of $t\bar{t}H$ in $H \to b\bar{b}$ channel published by the ATLAS and CMS collaborations show strong evidence of $t\bar{t}H$ production that is compatible with the SM expectation [169, 170]. Statistical uncertainties on the results are small compared to systematic uncertainties, which reflects the fact that the number of selected events in those analyses is huge. The systematic uncertainties can be suppressed with more accurate modeling of the input processes.

Although $H \to \gamma\gamma$ has one of the smallest BRs, it features a clean diphoton signal that helps to resolve the Higgs boson. The backgrounds that dominated the $H \to b\bar{b}$ channel are suppressed significantly in the $H \to \gamma\gamma$ channel, leaving only $t\bar{t}$+$\gamma\gamma$ and light jets+$\gamma\gamma$ as the main processes that obscure the signal. Analyses performed in this channel on full LHC Run 2 data claimed observation of the $t\bar{t}H$ production [160, 161]. The CP-structure of top Yukawa couplings was also probed, ruling out pure CP-odd interactions. The analysis done by the ATLAS collaboration also considered tH as part of the signal, but no observation of the process was made. The statistical component of total uncertainty on the results dominates here due to low number of selected events in this channel.

The analysis presented in Section 7 and published in Ref. [1] was performed on LHC Run 2 data collected by the CMS detector. It targeted $t\bar{t}H$ multilepton final states, which implies the presence of multiple electrons, muons and τ_h. The final states that feature electrons and muons but not τ_h are sometimes referred to as pure multilepton final states.

The leptons and τ_{h} are expected to originate from the top quark pair, and from $\mathrm{H} \to \mathrm{VV}^*$ or $\mathrm{H} \to \tau\tau$ decays, except for $\mathrm{H} \to \mathrm{ZZ}^* \to 4\ell$ events, which are vetoed in order to avoid overlap with dedicated measurements of this particular decay mode. The latest analysis done by the ATLAS collaboration was based on the data collected in 2016, which was sufficient for claiming evidence on SM-like $\mathrm{t\bar{t}H}$ signal [171]. The main backgrounds in this channel are $\mathrm{t\bar{t}}$+jets and associated production of massive vector bosons V with a pair of top and anti-top quarks, or $\mathrm{t\bar{t}V}$ in short, but also backgrounds that arise from misidentification of jets as leptons or τ_{h}. Statistical and systematical uncertainty have similar magnitude in this analysis.

Dedicated searches of tH signal have been performed only on LHC Run 2 data collected by the CMS detector in 2016, yielding slight preference towards positive y_{t}, while assuming that $\kappa_{\mathrm{V}} = 1$ [172]. Given that tH process is sensitive to y_{t} at LO just like $\mathrm{t\bar{t}H}$, the process is considered as an additional source of signal in the $\mathrm{t\bar{t}H}$ multilepton analysis presented here. The $\mathrm{t\bar{t}H}$ process itself is commonly included as part of signal in dedicated searches of Higgs boson decay modes. The observation of $\mathrm{t\bar{t}H}$ was announced in late LHC Run 2 data-taking period independently by ATLAS and CMS collaborations [17, 18]. The results by the CMS collaboration were based on data collected up to 2016 data-taking period, while the ATLAS collaboration additionally included the data collected in the following year. The latest results of dedicated $\mathrm{t\bar{t}H}$ and tH analyses done by the ATLAS and CMS collaborations on data collected in LHC Run 2 are summarized in Table 2.8.

H decay mode	ATLAS	CMS
$\mathrm{b\bar{b}}$	$\mu = 0.35 \pm 0.20(\mathrm{stat})^{+0.30}_{-0.28}(\mathrm{syst})$ at $1.0(2.7)\sigma$ on $139\,\mathrm{fb}^{-1}$ of data [169]*§	$\mu = 1.15 \pm 0.15(\mathrm{stat})^{+0.28}_{-0.25}(\mathrm{syst})$ at $3.9(3.5)\sigma$ on $77.4\,\mathrm{fb}^{-1}$ of data [170]‡
$\gamma\gamma$	$\mu = 1.43^{+0.33}_{-0.31}(\mathrm{stat})^{+0.21}_{-0.15}(\mathrm{syst})$ at $5.2(4.4)\sigma$ on $139\,\mathrm{fb}^{-1}$ of data [160]†‡	$\mu = 1.38^{+0.29}_{-0.27}(\mathrm{stat})^{+0.21}_{-0.11}(\mathrm{syst})$ at $6.6(4.7)\sigma$ on $137\,\mathrm{fb}^{-1}$ of data [161]†‡
Multilepton	$\mu = 1.6 \pm 0.3(\mathrm{stat})^{+0.4}_{-0.3}(\mathrm{syst})$ at $4.1(2.8)\sigma$ on $36.1\,\mathrm{fb}^{-1}$ of data [171]	$\mu = 0.92 \pm 0.19(\mathrm{stat})^{+0.17}_{-0.13}(\mathrm{syst})$ at $4.7(5.2)\sigma$ on $137\,\mathrm{fb}^{-1}$ of data [1]†
Combination (first observation)	$\mu = 1.32 \pm 0.18(\mathrm{stat})^{+0.21}_{-0.19}(\mathrm{syst})$ at $5.8(4.9)\sigma$ [17]	$\mu = 1.14^{+0.17}_{-0.16}(\mathrm{stat})^{+0.26}_{-0.22}(\mathrm{syst})$ at $4.5(4.1)\sigma$ [18]
(the latest fit)	$\mu = 0.74 \pm 0.17(\mathrm{stat})^{+0.17}_{-0.16}(\mathrm{syst})$ [166]	$\mu = 0.94 \pm 0.15(\mathrm{stat})^{+0.13}_{-0.12}(\mathrm{syst})$ [8]

* Does not consider FH decays of the top quark pair in the signal process.
† Also measures tH production rate.
‡ Also measures the CP-mixing angle.
§ Also measures in STXS bins.

Table 2.8: Summary of the latest dedicated $t\dot{t}H$ analyses performed by the ATLAS and CMS collaborations on LHC Run 2 data. Signal strength μ of $t\dot{t}H$ production rate is quoted with the corresponding observed (expected) significance.

2.5 Higgs boson pair production

This section presents the essential ingredients of the theory behind Higgs boson pair production (HH). Measuring the production rate of HH events gives direct access to Higgs boson self-coupling λ, which is known to dictate the vacuum structure. This section is partitioned in the following way: Section 2.5.1 discusses HH production mechanisms that are predicted by the SM, as well as the scaling behavior of the relevant SM coupling parameters in various production and decay processes; Section 2.5.2 looks at the HH

production through the lens of a more general EFT formalism; Section 2.5.3 describes the possibility of HH production through some yet unknown resonance; Section 2.5.4 concludes the section by summarizing the status of experimental HH searches in various Higgs boson decay modes.

2.5.1 Nonresonant HH production

Following the discovery of the Higgs boson with mass m_{H} it is possible to indirectly deduce its self-coupling parameter using the familiar SM relation $\lambda = m_{\mathrm{H}}^2/(2v^2)$. However, the validity of this correspondence still has yet to be tested. Deviations of λ from its designated SM value can have profound implications for EW phase transition, during which the Higgs field acquired a nonzero VEV [51]. If the transition was not smooth, it could have led to an excess of matter over anti-matter [173], which may happen for large deformations of λ. Such deviations can arise explicitly from a variety of BSM models that typically introduce new Higgs boson-like scalars to the theory [174].

Modifications of Higgs boson self-coupling can be studied within the EFT framework. In SMEFT, for instance, the Wilson coefficients c_6 and c_H that are associated with dimension-6 operators $\mathcal{O}_6 \sim (|\phi|^2)^3$ and $\mathcal{O}_H \sim (\partial|\phi|^2)^2$ give different contributions to the cubic and quartic Higgs boson self-interaction terms in Higgs potential [51]:

$$\frac{\delta\lambda^3}{\lambda^3} \sim \left(\frac{2v^2}{m_{\mathrm{H}}^2}c_6 - 3c_H\right), \qquad \frac{\delta\lambda^4}{\lambda^4} \sim \left(\frac{12v^2}{m_{\mathrm{H}}^2}c_6 - \frac{50}{3}c_H\right).$$

This has motivated the distinction of trilinear (λ_{HHH}) and quartic (λ_{HHHH}) self-interaction terms in the Higgs potential given by Eq. (2.17):

$$V(h) = \frac{m_{\mathrm{H}}^2}{2}h^2 + \lambda_{\mathrm{HHH}}vh^3 + \frac{\lambda_{\mathrm{HHHH}}}{4}h^4.$$

The trilinear coupling is associated with Higgs boson pair production, as depicted in Fig. 2.3(d), while the quartic coupling corresponds to the production of three Higgs bosons, as shown in Fig. 2.3(e). The SM cross section of triple Higgs boson production, which is known up to NNLO accuracy in pQCD, is by a factor of ~ 300 smaller than that of double Higgs boson production [175, 176]. Unfortunately, it is too small for probing the quartic coupling experimentally at the LHC, even when accounting for the planned upgrades of the accelerator [177], which are expected to increase the amount of delivered data by an order of magnitude. However, accessing the trilinear coupling is certainly viable, as the future upgrades of the LHC are projected to increase the experimental sensitivity to a level that is sufficient for establishing the existence of SM HH production [8]. For these reasons, the quartic coupling will not be considered and λ will refer only to the trilinear coupling in the following.

The trilinear coupling λ has been commonly studied within the κ-framework, where any deviation of λ from its expected SM value $\lambda_{\mathrm{SM}} \simeq 0.13$ is expressed through multiplicative coupling modifier $\kappa_\lambda = \lambda/\lambda_{\mathrm{SM}}$. Limits on κ_λ can be inferred from single Higgs boson production and decay processes where the trilinear coupling appears at the loop level. Feynman diagrams of a few such examples are shown in Fig. 2.21. The constraints on κ_λ can be extracted from the rates of these single Higgs boson processes, or by studying the influence of λ on the shape of differential distributions of kinematic variables such as transverse momentum of the Higgs boson, p_T^{H}, or invariant mass of final state particles [146, 178]. At LO, cross sections and branching ratios vary trivially according to some quadratic form of κ_{t} and κ_{V}, but the scaling behavior becomes more intricate when accounting for

NLO EW contributions from κ_λ, as illustrated by Fig. 2.22. The effects of κ_λ on p_T^{H} distribution are the most pronounced in $\mathrm{t\bar{t}H}$ and tH production mode but barely noticeable in VBF events. In particular, the extra contributions from Higgs boson self-coupling interactions to $\mathrm{t\bar{t}H}$ and tH processes tend to cause the p_T of the Higgs boson to be softer compared to LO [146]. Global fits of single Higgs boson processes to 2016 and 2017 data collected by the ATLAS detector placed bounds of $-3.2 < \kappa_\lambda < 11.9$, while assuming that the SM holds for all other couplings [179]. The same fits on full LHC Run 2 data collected by the CMS detector yielded slightly more stringent limits of $0.1 < \kappa_\lambda < 11.3$ [180]. Relaxing the SM assumption degrades the constraining power considerably due to additional degrees of freedom in the fit. Extraction of κ_λ from differential information of single Higgs boson processes provided in the form of STXS bins does not improve the limits, either [179].

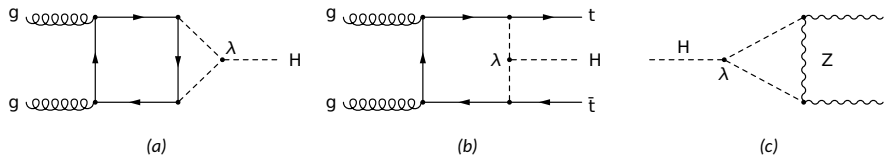


Figure 2.21: Feynman diagrams of some single Higgs boson processes that are sensitive to Higgs boson self-coupling λ at the loop level: ggF (a) and $\mathrm{t\bar{t}H}$ (b) production, and $H \to ZZ^*$ decay (c).

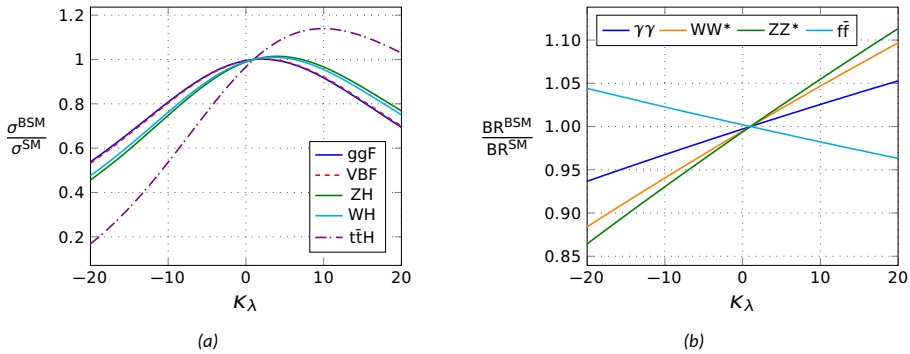


Figure 2.22: Approximate scaling of production cross section of single Higgs boson processes at $\sqrt{s} = 13\,\mathrm{TeV}$ (a) and branching ratios of Higgs boson decay modes (b) as a function of trilinear self-coupling modifier κ_λ computed to NLO in EW. The scaling behavior in both cases is perturbatively valid only for $|\kappa_\lambda| \lesssim 20$. Symbol $\mathrm{f\bar{f}}$ in (b) stands for any pair of massive fermions. The plots are recreated from the information available in Refs. [146, 178].

Higgs boson self-coupling λ can be directly probed by studying the production of HH events, where the coupling appears at the tree level. In decreasing order of cross section as predicted by the SM, the mechanisms that produce two on-shell Higgs bosons are ggF HH, VBF HH, VHH and $\mathrm{t\bar{t}HH}$. Feynman diagrams of these processes can be constructed by starting with the diagrams of corresponding single Higgs boson processes shown in Fig. 2.11, and either splitting the single Higgs boson line into two, or by attaching a second Higgs boson to a top quark line or to a vector boson line. The resulting diagrams of the dominant ggF and VBF mechanisms are presented in Fig. 2.23. The corresponding cross sections are detailed in Table 2.9. Subdominant VHH and $\mathrm{t\bar{t}HH}$ processes are omitted here and not simulated in this work due to ~ 2.5 times smaller cross section compared to the VBF HH process [50].

It follows that the ggF HH production mode contains destructive interferences between the triangle diagram shown in Fig. 2.23(a), which is sensitive to λ and y_t, and the box diagram depicted in Fig. 2.23(b), which is sensitive only to y_t^2. Cross section of the ggF HH process is dominated by the box diagram, but reduced by up to 50% due to interference between the triangle and box amplitudes [51]. The interplay between the box and triangle diagrams does not only influence the HH production cross section but also its event kinematics. In particular, the kinematic observable that is most sensitive to Higgs boson self-coupling is the invariant mass of the HH system, m_{HH}. The triangle diagram contributes mostly to the soft m_{HH} spectrum near the kinematic threshold of $2m_H$. The box diagram as well as the negative interference term, on the other hand, start peaking at the shoulder that roughly corresponds to the $t\bar{t}$ production threshold of $2m_t$. In order to create two on-shell Higgs bosons via self-interaction, the virtual Higgs boson that mediates the process needs to just barely exceed the kinematic threshold of creating the two bosons, whereas in the box diagram the two Higgs bosons are created independently from each other. It explains why the triangle amplitude contributes mostly to the low m_{HH} region, while events from the box diagram populate the medium m_{HH} spectrum.

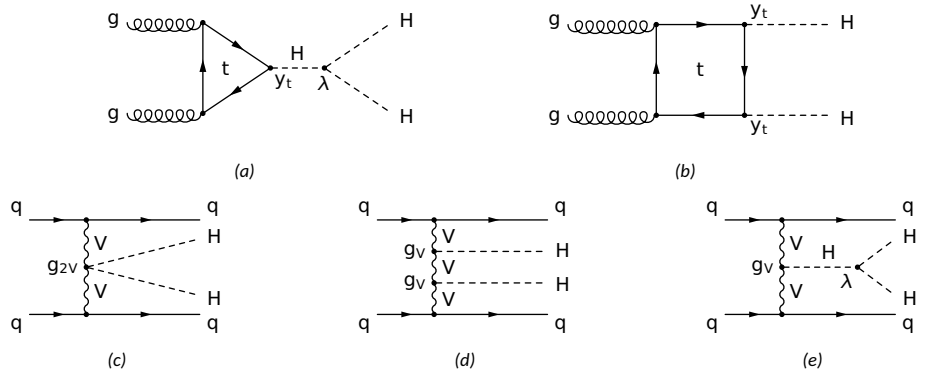


Figure 2.23: Feynman diagrams at LO for the SM production of two Higgs bosons via ggF (a)–(b) and via VBF (c)–(e).

Process	Cross section [fb]	Uncertainty [%]		
		PDF+α_S	QCD scale	m_t
ggF HH	31.05	± 3.0	$^{+2.2}_{-5.0}$	$^{+4}_{-18}$
VBF HH	1.730	± 2.1	$^{+0.03}_{-0.04}$	✗

Table 2.9: Cross section of dominant processes that produce two on-shell Higgs bosons with mass $m_H = 125\,\text{GeV}$ at $\sqrt{s} = 13\,\text{TeV}$ at the LHC. Cross section of the ggF process is computed to NNLO in pQCD using heavy top limit approximation [175]. The last column indicates the uncertainty that captures the effects of the top mass scheme, which is the leading source of uncertainty in this estimate. Cross section of the VBF HH process is calculated to the full N^{3}LO accuracy in pQCD and hence does not feature the uncertainty that is associated with the top mass approximation [181].

A higher value of $|\kappa_\lambda|$ relative to the SM expectation would increase the fraction of events at the kinematic threshold of the m_{HH} distribution. A negative κ_λ would also flip the sign of the interference term, thereby enhancing the peak at medium m_{HH} values even more. As a result, negative values of κ_λ produce a harder m_{HH} spectrum compared to

positive values of the coupling modifier. This also affects the acceptance of HH events, because harder Higgs boson pairs produce more energetic decay products, which in turn are more likely to pass the analysis requirements. Maximum destructive interference is achieved at $\kappa_\lambda \simeq 2.45$ [182], although the precise location of the minimum varies in the literature depending on the perturbative order of the cross section. Figure 2.24(a) explicitly demonstrates the rich variety of kinematics that are induced by different values of κ_λ.

Cross section of the ggF HH process that is used in the current work is estimated at NNLO in pQCD using the so-called full theory approximation [175]. In this procedure, the top quark mass m_t is preserved in all calculations of real QCD emissions at NNLO, but the virtual contributions are computed in the heavy top limit where $m_t \to \infty$ is assumed. In this approximation, the triangle and box loops between gluons and Higgs bosons reduce to effective single-point couplings like depicted in Figs. 2.25(b) and 2.25(c). The virtual contributions that are computed in the heavy top limit are then rescaled to the full theory with a factor that is determined in finite top mass limit at LO. The method comes with 2.6% uncertainty, which is far below the uncertainties that arise due to different choices of renormalization schemes and scales of m_t [183], as evidenced by Table 2.9. The resulting cross section scales with κ_λ quadratically,

$$\frac{\sigma_{\text{ggF}}(\kappa_\lambda)}{\sigma_{\text{ggF}}^{\text{SM}}} = 0.356\kappa_\lambda^2 - 1.624\kappa_\lambda + 2.267\,, \tag{2.27}$$

while the size of its uncertainties due to the choice of QCD scale and top mass scheme varies with κ_λ according to

$$\frac{\delta\sigma_{\text{ggF}}(\kappa_\lambda)}{\sigma_{\text{ggF}}^{\text{SM}}} = \begin{cases} \max\left(0.407\kappa_\lambda^2 - 1.819\kappa_\lambda + 2.467\,,\quad 0.409\kappa_\lambda^2 - 1.814\kappa_\lambda + 2.430\right) \\ \min\left(0.309\kappa_\lambda^2 - 1.385\kappa_\lambda + 1.858\,,\quad 0.318\kappa_\lambda^2 - 1.416\kappa_\lambda + 1.880\right) \end{cases},$$

where the uncertainties from both sources are combined linearly [183]. PDF uncertainties, which are typically added in quadrature, remain fairly flat at $\pm 3\%$ across all values of κ_λ. The same uncertainties are attributed to other BSM scenarios where other couplings besides κ_λ are shifted away from their SM value. The scaling behavior of inclusive ggF HH cross section and corresponding uncertainty with κ_λ is also displayed in Fig. 2.24(b).

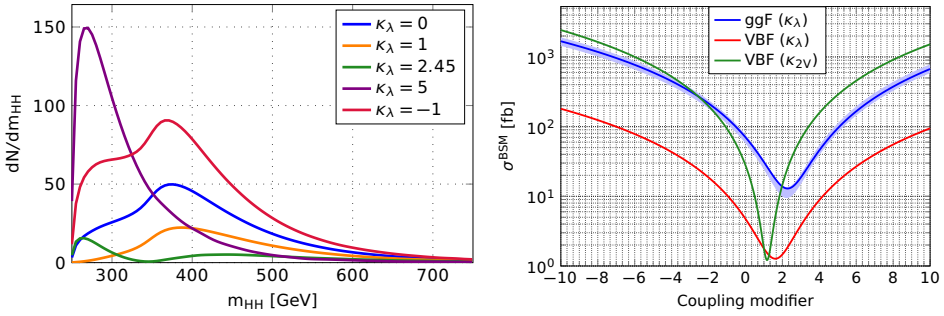


Figure 2.24: (a): density plot for invariant mass of the Higgs boson pair, m_{HH}, for selected values of κ_λ in ggF HH production process. The distributions are scaled to match the expected signal yield N delivered by the LHC in Run 2 data-taking period. The plot is obtained from MC samples simulated at NLO in pQCD; (b): cross sections of ggF (blue) and VBF (red) HH production as a function of κ_λ, and VBF HH production as a function of κ_{2V} (green). The uncertainty band covers the effects of choosing QCD scale and top mass scheme in ggF HH cross section estimate.

VBF HH production receives interfering contributions from the self-coupling vertex, and three-point and four-point coupling vertices g_{V} and $g_{2\mathrm{V}}$, which are defined by Eq. (2.14). The latter cannot be probed directly in single Higgs processes, nor in ggF HH production processes. Deviations of these couplings from the SM expectation are quantified in terms of coupling modifiers $\kappa_{\mathrm{V}} = g_{\mathrm{V}}/g_{\mathrm{V}}^{\mathrm{SM}}$ and $\kappa_{2\mathrm{V}} = g_{2\mathrm{V}}/g_{2\mathrm{V}}^{\mathrm{SM}}$, where it is understood that the changes in coupling strength are fully correlated between W and Z bosons. The VBF HH cross section is known up to N^{3}LO in pQCD [181]. Contributions from the scattering of longitudinal vector bosons to the cross section drops out at $\kappa_{2\mathrm{V}} = |\kappa_{\mathrm{V}}|^2$, thus resulting in maximum destructive interference [184].

2.5.2 EFT benchmarks and coupling scans

The SM can be augmented by a HEFT Lagrangian density, which introduces new nonrenormalizable Higgs field operators to the theory. The Higgs field itself appears as a singlet under the EW symmetry. Assuming no new particles besides the SM ones, nor any new CP-violating interactions in the Higgs sector, the terms in SM Lagrangian density $\mathcal{L}_{\mathrm{SM}}$ that are relevant to HH production via ggF can be improved in the following way [182]:

$$-\lambda_{\mathrm{SM}} v h^3 - \frac{y_{\mathrm{t}}^{\mathrm{SM}}}{\sqrt{2}}(v+h)\bar{t}t \subset \mathcal{L}_{\mathrm{SM}} \rightarrow$$
$$\rightarrow \mathcal{L}_{\mathrm{EFT}} \supset -\kappa_\lambda \lambda_{\mathrm{SM}} v h^3 - \frac{y_{\mathrm{t}}^{\mathrm{SM}}}{\sqrt{2}}\left(v + \kappa_{\mathrm{t}} h + \frac{c_2}{v}h^2\right)\bar{t}t + \frac{\alpha_{\mathrm{S}}}{12\pi v}\left(c_g h - \frac{c_{2g}}{2v}h^2\right)\mathbf{G}^2,$$

where the first line brings out the operators from $\mathcal{L}_{\mathrm{SM}}$ that are generalized by the EFT formalism in the next line. Three new effective couplings are introduced: interaction between two Higgs bosons and top quarks with strength c_2; interaction between one Higgs boson and two gluons with strength c_g; interaction between two Higgs bosons and two gluons with strength c_{2g}. The last two also arise from heavy top limit approximation, with c_g and c_{2g} representing the effective couplings of triangle and box loops in ggF HH production that are reduced to contact interactions between Higgs bosons and gluons. In SMEFT, the two couplings are fully (anti-)correlated: $c_{2g} = -c_g$. Couplings c_2 and c_{2g} can be directly probed in HH production but not in single Higgs boson production. SM is restored by setting $\kappa_\lambda = \kappa_{\mathrm{t}} = 1$ and $c_2 = c_g = c_{2g} = 0$. The Feynman diagrams of additional processes that contribute to ggF HH production in this EFT prescription are shown in Fig. 2.25. More detailed comparison of HEFT and SMEFT models can be found in Ref. [61]. Explicit correlations between κ_λ, κ_{t} and c_2 in various BSM models can be found in Ref. [185].

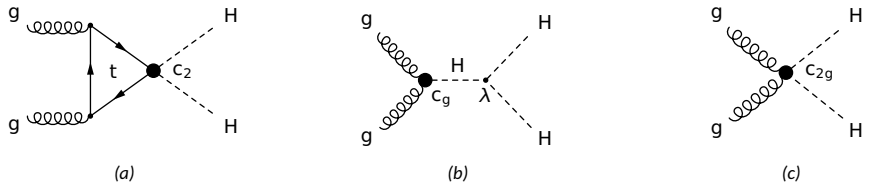


Figure 2.25: Feynman diagrams at LO for the ggF production of two Higgs bosons with effective BSM couplings.

All five couplings and coupling modifiers $\{\kappa_\lambda, \kappa_{\mathrm{t}}, c_2, c_g, c_{2g}\}$ influence the inclusive ggF HH production rate as well as HH signal topology. The squared MEs feature pure SM terms,

interference terms between the SM and dimension-6 EFT operators and pure EFT terms. Interferences between the SM and dimension-8 EFT operators as well as contributions from terms suppressed by $\mathcal{O}(\Lambda^{-6})$ where Λ denotes the cutoff scale at 3 TeV are ignored. At LO, the inclusive cross section of ggF HH process can be parametrized by fifteen linearly independent combinations of the five couplings as follows [182]:

$$\begin{aligned}\frac{\sigma^{\text{BSM}}_{\text{ggF}}}{\sigma^{\text{SM}}_{\text{ggF}}} \cong\ & A_1^{\text{LO}}\kappa_t^4 + A_2^{\text{LO}}c_2^2 + A_3^{\text{LO}}\kappa_t^2\kappa_\lambda^2 + A_4^{\text{LO}}c_g^2\kappa_\lambda^2 + A_5^{\text{LO}}c_{2g}^2 + A_6^{\text{LO}}c_2\kappa_t^2 + \\ & + A_7^{\text{LO}}\kappa_t^3\kappa_\lambda + A_8^{\text{LO}}\kappa_t\kappa_\lambda c_2 + A_9^{\text{LO}}c_g\kappa_\lambda c_2 + A_{10}^{\text{LO}}c_2c_{2g} + A_{11}^{\text{LO}}c_g\kappa_\lambda\kappa_t^2 + \\ & + A_{12}^{\text{LO}}c_{2g}\kappa_t^2 + A_{13}^{\text{LO}}\kappa_\lambda^2 c_g\kappa_t + A_{14}^{\text{LO}}c_{2g}\kappa_t\kappa_\lambda + A_{15}^{\text{LO}}c_g c_{2g}\kappa_\lambda\,.\end{aligned} \tag{2.28}$$

The coefficients $\mathbf{A}^{\text{LO}} = \{A_i^{\text{LO}}\}_{i=1}^{15}$ can be extracted from simultaneous fit to inclusive cross sections that each corresponds to a different coupling scenario [186]. The cross sections can be computed with MC generators. Uncertainties on the coefficients are driven by a limited number of generated events, but also by the choices of QCD scale and PDF sets. NLO corrections in pQCD improves the parametrization with eight additional terms [187]:

$$\begin{aligned}\frac{\sigma^{\text{BSM}}_{\text{ggF}}}{\sigma^{\text{SM}}_{\text{ggF}}} &\cong \text{Poly}_{23}^{T}(\kappa_\lambda,\kappa_t,c_2,c_g,c_{2g})\cdot\mathbf{A}^{\text{NLO}} = \\ &= \ldots + A_{16}^{\text{NLO}}\kappa_t^3 c_g + A_{17}^{\text{NLO}}\kappa_t c_2 c_g + A_{18}^{\text{NLO}}\kappa_t c_g^2\kappa_\lambda + A_{19}^{\text{NLO}}\kappa_t c_g c_{2g} + \\ &\quad + A_{20}^{\text{NLO}}\kappa_t^2 c_g^2 + A_{21}^{\text{NLO}}c_2 c_g^2 + A_{22}^{\text{NLO}}c_g^3\kappa_\lambda + A_{23}^{\text{NLO}}c_g^2 c_{2g}\,.\end{aligned} \tag{2.29}$$

In the above, $\text{Poly}_k(\mathbf{c})$ is shorthand for a function of N couplings (or coupling modifiers) $\mathbf{c} = \{c_i\}_{i=1}^{N}$ that is wrapped into a k-dimensional vector. Each component of the vector is a product of the couplings, $\prod_{i=1}^{N} c_i^{p_i}$, with a unique combination of exponents p_i such that every component is linearly independent from other components in the vector. When setting $c_2 = c_g = c_{2g} = 0$ and $\kappa_t = 1$, then Eq. (2.28) reduces to a quadratic function of κ_λ, like the one given by Eq. (2.27). Parametrization at NNLO in pQCD adds two more terms to Eq. (2.29), which are proportional to c_g^4 and $c_g^3\kappa_t$ [188].

Small changes in any of the five couplings can drastically alter the ggF HH production rate as well as the event-level kinematics. Testing all possible combinations of the couplings in five-dimensional parameter space is simply not feasible, since it would require a prohibitive amount of computing time to generate the MC samples with full detector simulation for all possible coupling scenarios. However, the problem can be simplified if the couplings give rise to a finite number of possible configurations of the HH system. A viable strategy can be devised with this premise by first identifying a manageable number of coupling scenarios or benchmarks (BMs) that uniquely modulate the distributions of selected observables, and search for BSM signals in those BMs. At LO, invariant mass of the Higgs boson pair, m_{HH}, and polar angle θ^* between collision axis and either of the Higgs bosons in the rest frame of HH system, also known as the helicity angle, unambiguously describe the full kinematics of HH production via ggF. Azimuthal angle of either Higgs boson has no relevance here because the HH system is rotationally invariant about the collision axis. Similarly, the redundancy in θ^* can be resolved by considering $|\cos\theta^*|$ instead when attempting to uniquely describe the topology of a HH system.

The idea of finding a finite number of representative BMs was initially proposed and demonstrated in Ref. [182]. A large number of MC samples were generated at LO, each for a different coupling scenario. Only those coupling combinations were considered in the MC simulation that were not yet excluded experimentally. For example, there is no point in

identifying unique features in m_{HH} for a κ_{t} value of $\mathcal{O}(10)$ if it has been already established that such value is excluded by experiments. Searches of other unconstrained parameters such as c_g and c_{2g} can be confined to a narrow region around the SM point, especially given that the SM kinematics of a HH system changes rapidly in response to small variations of the couplings. The coupling scenarios were iteratively grouped together if they shared similar features in m_{HH} distributions until the designated number of clusters was reached. As it turned out, alternative variables such as $|\cos\theta^*|$ or transverse momentum of either Higgs boson, p_T^{H}, are not as sensitive to coupling variations as m_{HH}. The combination of couplings that produced kinematic distributions most similar to other distributions within the cluster was chosen as the BM. It was found that one needs twelve BMs to cover all possible, yet distinct enough features that may occur in m_{HH} distribution in response to different coupling values. The precise coupling values of the twelve shape BMs are listed in Table 2.10, and the corresponding distributions of m_{HH} are shown in Fig. 2.26.

Benchmark	κ_λ	κ_{t}	c_2	c_g	c_{2g}	$\sigma^{\mathrm{BSM}}_{\mathrm{ggF}}/\sigma^{\mathrm{SM}}_{\mathrm{ggF}}$	k
SM	1	1	0	0	0	1	1.40
JHEP04BM1	7.5	1	−1	0	0	5.83	1.59
JHEP04BM2	1	1	0.5	−0.8	0.6	0.426	1.70
JHEP04BM3	1	1	−1.5	0	−0.8	31.6	1.67
JHEP04BM4	−3.5	1.5	−3	0	0	271	1.67
JHEP04BM5	1	1	0	0.8	−1	1.75	1.59
JHEP04BM6	2.4	1	0	0.2	−0.2	0.748	1.67
JHEP04BM7	5	1	0	0.2	−0.2	5.21	1.85
JHEP04BM8	15	1	0	−1	1	4.66	1.37
JHEP04BM8a	1	1	0.5	0.4	0	1.17	2.05
JHEP04BM9	1	1	1	−0.6	0.6	4.38	1.93
JHEP04BM10	10	1.5	−1	0	0	17.6	1.69
JHEP04BM11	2.4	1	0	1	−1	5.30	1.82
JHEP04BM12	15	1	1	0	0	111	1.75
JHEP03BM1	3.94	0.94	$-1/3$	$3/4$	−1	6.76	1.83
JHEP03BM2	6.84	0.61	$1/3$	0	1	5.11	1.80
JHEP03BM3	2.21	1.05	$-1/3$	$3/4$	$-3/2$	4.49	1.63
JHEP03BM4	2.79	0.61	$1/3$	$-3/4$	$-1/2$	1.92	1.63
JHEP03BM5	3.95	1.17	$-1/3$	$1/4$	$3/2$	4.60	1.36
JHEP03BM6	5.68	0.83	$1/3$	$-3/4$	−1	5.50	1.57
JHEP03BM7	−0.10	0.94	1	$1/4$	$1/2$	3.90	1.93

Table 2.10: EFT shape BMs in terms of five couplings (κ_λ, κ_{t}, c_2, c_g, c_{2g}) that were developed to study BSM effects in ggF HH signal. Second middle horizontal line separates older BMs derived in LO theory, which were subsequently published in JHEP 04 journal [182], from those later found in NLO pQCD theory and then released in JHEP 03 publication [189]. The only exception is JHEP04BM8a, which was proposed in Ref. [187]. The second-to-last column quotes the ratio of the corresponding cross section to the SM cross section, both computed at NLO in pQCD. The last column lists NLO-to-LO k-factors computed with Eqs. (2.28) *and* (2.29)*, where the LO cross section coefficients are taken from [182] and the NLO coefficients from Table 2.11, while assuming* $\sigma^{SM,LO}_{ggF} = 19.85\,\mathrm{fb}$ *[187].*

The distributions of m_{HH} determined at NLO in pQCD remain by and large the same compared to the shapes obtained from LO simulation, except for the eighth BM point for which its characteristic dip at around $350\,\mathrm{GeV}$ in m_{HH} disappeared after including the

NLO corrections [187]. A different coupling configuration was proposed that restored the feature in m_{HH}, and was thus named BM point 8a. The NLO corrections not only increase the total cross section by a factor of 1.5–2, depending on the BM, but the shapes of kinematic distributions are also slightly modulated, as illustrated by Fig. 2.26. They also push the m_{HH} distribution of the SM signal towards a softer spectrum than what is found in LO production. Additionally, at the ME level, ISR from gluons causes the HH system to recoil away from the collision axis, which in turn modifies p_T^{H}.

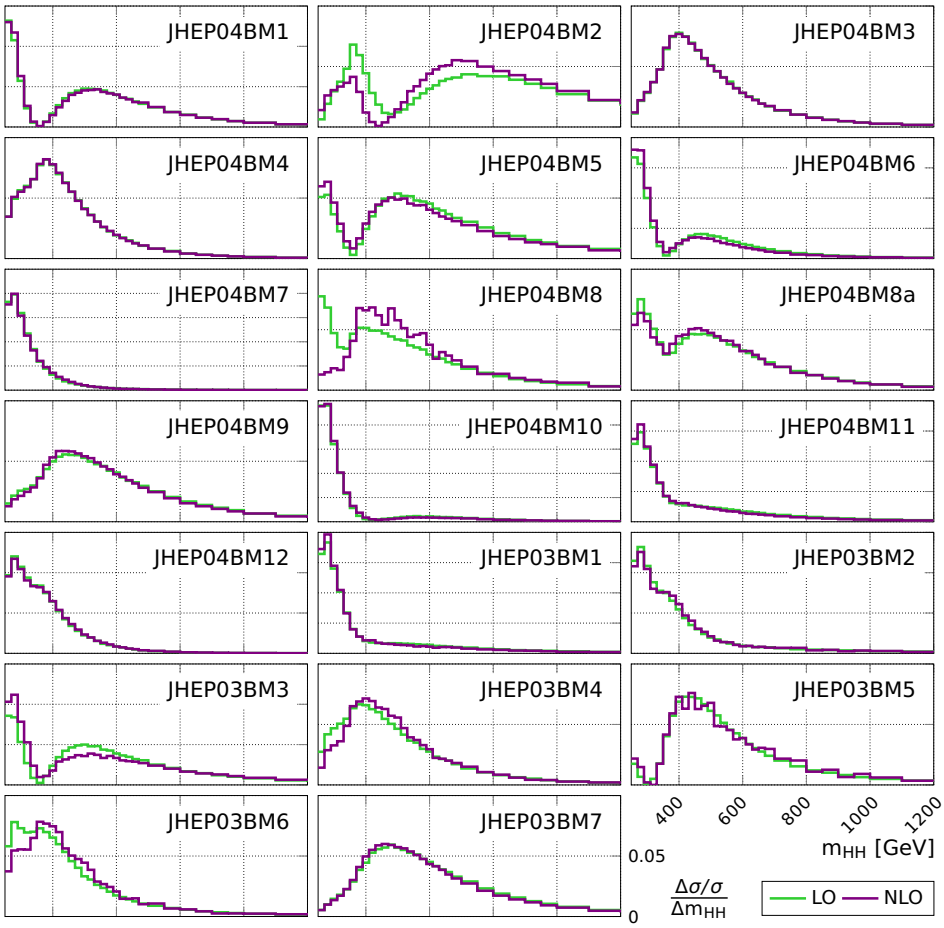


Figure 2.26: Density plots of m_{HH} for all EFT BM scenarios that are listed in Table 2.10. The distributions are obtained by reweighting MC samples that are simulated at LO or at NLO in pQCD. No NLO corrections are applied to distributions extracted from the LO samples. Grid lines are spaced by the same amount in all plots.

The exploration of EFT shape BMs was reconsidered in Ref. [189], which took advantage of previously unavailable simulation of the ggF HH production at NLO in pQCD, but also replaced the custom clustering algorithm with an autoencoder, which is a type of neural network suitable for detecting unique features [190]. The features are represented in lower-dimensional latent space of the autoencoder, where they are subsequently grouped into k clusters using the k-means clustering algorithm [191, 192]. The procedure yielded a total of seven alternative shape BMs that each displayed distinct features in m_{HH} distribution. The

resulting coupling values are documented in Table 2.10 and corresponding plots of m_{HH} shown in Fig. 2.26.

In this work, both sets of EFT shape BMs are considered in searches of ggF HH signal. The two sets are distinguished from each other by attaching a prefix to the BM name, which corresponds to the journal where the BM was initially published. For example, JHEP04BM2 refers to the second BM extracted from LO MC simulation [182], while JHEP03BM2 is the second BM that is defined in the more recent publication [189].

Complementary alternative to EFT BM scans is to directly perform linear scans of single or multiple couplings while fixing all other parameters to their SM values, which brings in the assumption that the BSM effects arise only from those couplings that are scanned. Instead of generating a MC sample for every possible coupling scenario of interest, inspired by Ref. [193], a more efficient approach can be devised by first recognizing that the number of events N_O found in bin ΔO of some observable O is proportional to the squared sum of all MEs of the process:

$$N_O \sim \Delta\sigma \sim \int_{\Delta O} dO \frac{d\sigma}{dO} \sim \int_{\Delta O} dO \frac{d}{dO} \left| \sum_{i=1}^{p} \mathcal{M}_i \right|^2 .$$

Since each amplitude $\mathcal{M}_i$ depends on a product of real couplings $\mathbf{c}$, the above expression can be organized into the following quadratic form:

$$N_O(\mathbf{c}) = \text{Poly}_p^T(\mathbf{c})\, M_O\, \text{Poly}_p(\mathbf{c}) , \tag{2.30}$$

where M_O is a real $p \times p$ matrix. Given that $N_O \geqslant 0$, the matrix M_O must also be positive semidefinite and hence symmetric [194]. In principle, the matrix M_O can be determined in each bin ΔO independently by a simultaneous fit to the expected event yields, which are obtained after the event selection cuts for $p(p+1)/2$ chosen coupling scenarios.

However, in analogy to Eqs. (2.28) and (2.29), Eq. (2.30) can be arranged into a linear sum of k unique coupling products, with $p \leqslant k \leqslant p(p+1)/2$:

$$N_O(\mathbf{c}) = \text{Poly}_k^T(\mathbf{c}) \cdot \mathbf{A}_O . \tag{2.31}$$

It is possible to eliminate $\mathbf{A}_O$ from Eq. (2.31) completely by carefully choosing $n \geqslant k$ coupling scenarios $C^{\text{fix}} = \{\mathbf{c}_i^{\text{fix}}\}_{i=1}^n$ to write the following linear expression:

$$\underbrace{\begin{pmatrix} N_O(\mathbf{c}_1^{\text{fix}}) \\ \vdots \\ N_O(\mathbf{c}_n^{\text{fix}}) \end{pmatrix}}_{\equiv \mathbf{N}_O^{\text{fix}}} = \underbrace{\begin{pmatrix} \text{Poly}_k^T(\mathbf{c}_1^{\text{fix}}) \\ \vdots \\ \text{Poly}_k^T(\mathbf{c}_n^{\text{fix}}) \end{pmatrix}}_{\equiv C^{\text{fix}}} \cdot \mathbf{A}_O .$$

The $n \times k$ matrix C^{fix} can be inverted with Moore-Penrose method [195, 196], thus allowing to rewrite Eq. (2.31) as:

$$N_O(\mathbf{c}) = \text{Poly}_k^T(\mathbf{c}) \cdot (C^{\text{fix}})^{-1} \cdot \mathbf{N}_O^{\text{fix}} . \tag{2.32}$$

The above relation transforms a collection of n known yields $\mathbf{N}_O^{\text{fix}}$ into number of events that is expected from coupling scenario $\mathbf{c}$ in the same bin ΔO. The transformation is applied on per-bin basis, thus ensuring the correct normalization as well as the shape of the resulting distribution in observable O. The optimal choice of C^{fix} depends on a number of factors: on the available MC samples that have already been produced, on the variety of kinematics

that is covered by the choice of couplings, and on numerical stability of the resulting matrix C^{fix}. The latter can be quantified in terms of condition number of the matrix, which tells how many times relative uncertainties in the input yields $\mathbf{N}_O^{\text{fix}}$ could possibly be amplified in the output distribution [194].

It is not necessary or even reasonable (from the point of numerical stability) to use all couplings in the parametrization of observables, since the physics model given by Eq. (2.29) works with single coupling dependencies as well. For example, it is clear that when parametrizing ggF HH cross section in terms of just κ_λ, then one needs to specify just $\text{Poly}_3^T(\kappa_\lambda) = (1, \kappa_\lambda, \kappa_\lambda^2)$ for three different values of κ_λ when constructing C^{fix} in Eq. (2.29). The values chosen in the present work are: the SM scenario ($\kappa_\lambda = 1$), maximum interference case ($\kappa_\lambda = 2.45$) and high κ_λ regime ($\kappa_\lambda = 5$). For these reasons, the ggF HH MC samples employed in this thesis are generated for $\kappa_\lambda \in \{0, 1, 2.45, 5\}$ at NLO in pQCD using POWHEG event generator [197–199]. The box-only scenario ($\kappa_\lambda = 0$) was included for validation purposes. The distribution of m_{HH} shown in Fig. 2.24(a) for $\kappa_\lambda = -1$ is obtained with the matrix-based reweighting method.

In the present work, the existing MC samples that were produced with the intention to provide limits for EFT BMs were simulated just for the twelve JHEP04 BMs at LO using the MadGraph5_aMCatNLO event generator [87]. The LO MC samples could be reweighted to other BM points using Eq. (2.28), if the cross section coefficients $\mathbf{A}^{\text{LO}}$ are parametrized by variables that describe the HH kinematics. Such parametrization was performed in Ref. [185], where the authors measured the cross section coefficients in bins of m_{HH} and $|\cos\theta^*|$. reweighting to any other BM scenario can be factorized into two steps: first, the shape profile that spans m_{HH} and $|\cos\theta^*|$ is flattened by multiplying the weight of each event that belongs to the i-th bin in the two-dimensional plane with $(\sigma_i/\sigma)^{-1}$, where σ_i refers to the exclusive cross section of that bin and σ is the total cross section. The cross sections can be replaced with respective event counts N_i and N, which are extracted from the input MC sample prior to any event selection. The second step is to multiply the weight of each event in the i-th bin with (σ_i'/σ'), where both cross sections now correspond to the target BM scenario. The exactness of the reweighting procedure is dictated by the width and range of the bins, wherein the cross section coefficients are determined. The flattening step is universal enough that it enables to combine multiple MC samples that each are produced with identical generator and showering settings but with different coupling scenarios into one sample. In fact, this is the preferred mode of operation, since it enhances the event statistics of the resulting distribution that represents a BM scenario, thereby reducing statistical uncertainties assigned to the BSM signal process. The method also combats pathological cases, in which a distribution that features a valley is reweighted to another distribution that now has a peak in the same bin of the distribution. Such cases can be mitigated by not using just one but all available MC samples in the reweighting procedure.

However, one would also need to incorporate NLO corrections to the existing LO MC samples. The extra step can be avoided if the LO samples are ignored altogether and NLO samples are used instead, even though they were initially produced for κ_λ scan. The corresponding cross section coefficients $\mathbf{A}^{\text{NLO}}$ are available in Ref. [187] that allow reweighting the samples to any coupling scenario. Unfortunately, the measurement was parametrized only by m_{HH} and restricted to $250\,\text{GeV} < m_{\text{HH}} < 1040\,\text{GeV}$. Since some analysts in CMS collaboration target boosted HH signal for which $m_{\text{HH}} \gtrsim 1\,\text{TeV}$, it was decided to measure the NLO cross section coefficients again, which would be then utilized by all HH analyses performed by CMS collaborators. By following the procedure detailed in Ref. [187], the coefficients were measured in 36 bins of m_{HH} up to $5\,\text{TeV}$ and in four

bins of $|\cos\theta^*|$, using dedicated MC samples produced with POWHEG [197–199] as input. The MC samples were generated without detector simulation and are therefore not used anywhere else in this work, except for extracting the cross section coefficients. In order to avoid unexpected inconsistencies between the measurements, constant cross section coefficients were also determined from the same set of samples. The resulting coefficients that implement inclusive ggF HH cross section given by Eq. (2.29) are listed in Table 2.11. The inclusive ggF HH cross section of any coupling scenario is improved to NNLO precision in pQCD by applying a flat k-factor of ~ 1.11 that is calculated for the SM case.

By combining the matrix-based reweighting procedure with the method that reweighs NLO MC samples to different BM points, it is possible to perform scans of other parameters besides κ_λ or EFT BMs. One can first reweigh the samples with parametrized cross section coefficients $\mathbf{A}^{\text{NLO}}(m_{\text{HH}}, |\cos\theta^*|)$ to produce a few kinematic distributions that are then utilized in the matrix-based reweighting procedure implemented by Eq. (2.32). The advantage of this approach is threefold: it maximizes the available statistics of NLO MC samples, it minimizes the number of distributions needed for the scan, and it allows to later adjust the scan range and step size without having to explicitly run the analysis again in order to create the missing distributions.

A_1^{NLO}	2.244	A_7^{NLO}	−1.590	A_{13}^{NLO}	0.439	A_{19}^{NLO}	−0.001
A_2^{NLO}	12.409	A_8^{NLO}	3.467	A_{14}^{NLO}	−0.965	A_{20}^{NLO}	−0.022
A_3^{NLO}	0.346	A_9^{NLO}	1.921	A_{15}^{NLO}	−0.696	A_{21}^{NLO}	0.046
A_4^{NLO}	0.156	A_{10}^{NLO}	−5.594	A_{16}^{NLO}	−0.003	A_{22}^{NLO}	0.013
A_5^{NLO}	1.401	A_{11}^{NLO}	−0.850	A_{17}^{NLO}	0.012	A_{23}^{NLO}	−0.018
A_6^{NLO}	−9.646	A_{12}^{NLO}	1.959	A_{18}^{NLO}	0.016		

Table 2.11: Cross section coefficients in Eq. (2.29) *that parametrize inclusive ggF HH cross section at NLO in pQCD.*

For instance, the initial plan of performing a c_2 scan envisaged the production of 56 individual distributions for dedicated values of c_2 between -2 and 3, in steps of 0.1 for $|c_2| > 1$ and in steps of 0.05 for $|c_2| \leqslant 1$. This assortment of distributions would have to be obtained for each analysis channel, its subcategories and decay modes of the Higgs bosons, which severely increases the computation resources needed to create these distributions. Furthermore, extending the grid to higher dimensions becomes computationally prohibitive and would jeopardize further combination efforts with other HH analyses down the line. A more efficient approach is to produce two other of distributions for selected values of c_2 besides the SM scenario that represent kinematic extremes in the scan region [200]. This is because the NLO polynomial in Eq. (2.29) contains constant, linear and quadratic terms in c_2, which means that one needs at least three coupling scenarios with different values of c_2, while keeping all other couplings at their SM values, in order to specify the transformation matrix C^{fix} in Eq. (2.32). As illustrated by Fig. 2.27, good candidates would be $c_2 = 3$, which approximates the asymptotic shape of m_{HH} at large c_2 values quite well, and $c_2 = 0.35$, which corresponds to the case of maximum destructive interference and give rise to m_{HH} distribution that presents a shallow dip at around $m_{\text{HH}} = 380\,\text{GeV}$. In more general three-dimensional scan over κ_λ, κ_t and c_2, the same polynomial expression that implements the matrix-based reweighting given by Eq. (2.32) has the form

$$\text{Poly}_6^T(\kappa_\lambda, \kappa_t, c_2) = (\kappa_t^4, c_2^2, \kappa_t^2\kappa_\lambda^2, c_2\kappa_t^2, \kappa_t^3\kappa_\lambda, \kappa_t\kappa_\lambda c_2)\,. \tag{2.33}$$

The same three coupling scenarios that were chosen for the one-dimensional c_2 scan are

also used for the general three-dimensional case to keep the computational efforts minimal but to also make the task of finding the remaining coupling scenarios tractable. In order to define C^{fix} for the reweighting procedure, three additional coupling scenarios are needed. These are the box-only scenario ($\kappa_\lambda = c_2 = 0$, $\kappa_t = 1$), the case of maximum interference between the box and triangle diagrams ($\kappa_\lambda = 2.45$, $\kappa_t = 1$, $c_2 = 0$), and the scenario where $\kappa_t = c_2 = 1$ but $\kappa_\lambda = 0$. The latter is also displayed in Fig. 2.27. The above relation can be utilized in two-dimensional κ_t–c_2 scan, for which $\kappa_\lambda = 1$ is used as argument to Eq. (2.33), and one-dimensional c_2 scan, where $\kappa_\lambda = \kappa_t = 1$ is assumed. Similarly, c_2 is set to zero in κ_λ–κ_t scans, which brings Eq. (2.33) to a simple quadratic form in terms of the scanned couplings.

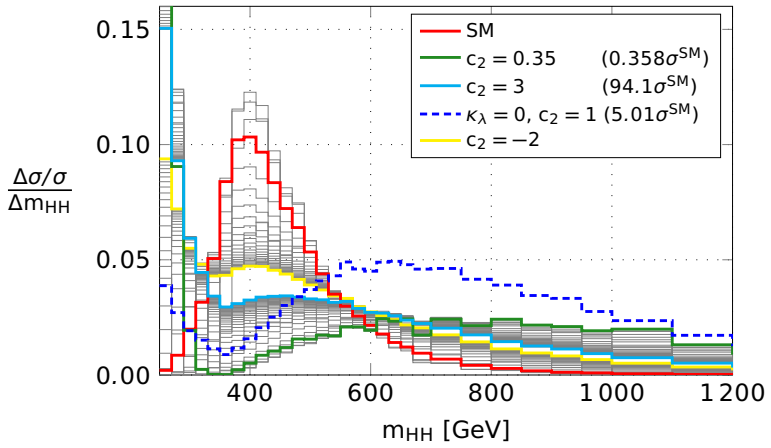


Figure 2.27: Density plots of m_{HH} for the intended 56 scan points of c_2 (solid lines) between -2 (yellow, for reference) and $+3$, plus another scenario for κ_t–c_2 scan (dashed line). All other couplings not explicated in the legend are set to their SM values. Colored lines highlight the chosen points used in the c_2 scan. The corresponding BSM cross sections are quoted in parentheses as multiple of the SM cross section, both computed at NLO accuracy in pQCD using Eq. (2.29). The distributions are obtained by reweighting SM MC samples that are simulated at NLO in pQCD.

The matrix-based reweighting is not extended to c_g nor c_{2g} couplings for several reasons. First, according to Eq. (2.29) the ggF HH cross section is parametrized by 23 independent coupling terms, which implies that C^{fix} in Eq. (2.32) would have to be at least a 23×23 matrix. Inverting such a large matrix is prone to numerical instabilities, not to mention that the whole reweighting procedure becomes very cumbersome to validate. Second, c_g and c_{2g} appear uncorrelated in HEFT, so there is no good motivation for studying them separately, either. Third, subtle variations of the c_2 coupling have been shown to drastically modify the event kinematics and production cross section of the ggF HH process [187]. The effects of varying c_g or c_{2g} couplings are not as pronounced, however. To summarize, constraining the c_2 coupling helps to narrow down the parameter space of various BSM models where the c_2 coupling is uniquely connected to the κ_λ and κ_t modifiers [185].

The matrix-based reweighting method is completely universal, since it makes no assumptions about the underlying processes that induce the coupling parametrization in the final observables. Thus, it can be also employed in scanning of SM couplings that the VBF HH production is sensitive to: κ_λ, κ_V and κ_{2V}. The square sum of the Feynman diagrams shown in Figure 2.23 results in the following parametrization:

$$\text{Poly}_6^T(\kappa_\lambda, \kappa_V, \kappa_{2V}) = (\kappa_{2V}^2, \kappa_V^4, \kappa_V^2\kappa_\lambda^2, \kappa_{2V}\kappa_V^2, \kappa_{2V}\kappa_V\kappa_\lambda, \kappa_V^2\kappa_\lambda)\,.$$

The above relation reduces to a simple quadratic function in one-dimensional κ_λ or κ_{2V} scan. As evidenced by Fig. 2.24(b), the VBF HH process is much more sensitive to κ_{2V} compared to κ_λ. At anomalous values, the former not only enhances VBF HH production cross section but also the falling tail in m_{HH} distribution. On the other hand, the gain in sensitivity on κ_V from VBF HH processes is not great compared to single Higgs processes. Combination studies of the latter have already demonstrated a good compatibility of κ_V with the SM expectation, at the level of $\lesssim 10\%$ [8]. Some BSM theories that propose alternative gauge groups do accommodate small modifications in all three couplings [184]. The size of these deviations help to also understand whether the Higgs boson really belongs to $SU(2)_L$ doublet, as currently established by the SM.

The six coupling scenarios that implement the transformation matrix C^{fix} in Eq. (2.32) are the SM coupling scenario, the cases where either κ_λ or κ_{2V} is turned off or doubled, and the case where $\kappa_V = 1.5$ [201]. Only one coupling is varied at a time, while the remaining couplings maintain their SM values. The VBF HH production process is simulated at LO for each coupling scenario. The cross sections are extracted from the corresponding MC samples and scaled to N^{3}LO accuracy in pQCD using a k-factor of ~ 1.03 that is derived for the SM case. Distributions of m_{HH} and $|\cos\theta^*|$ extracted from these MC samples are shown in Fig. 2.28. As $|\kappa_{2V}|$ approaches to large values, the m_{HH} spectrum asymptotically follows arithmetic averages of $\kappa_{2V} = 0$ and $\kappa_{2V} = 2$ distributions.

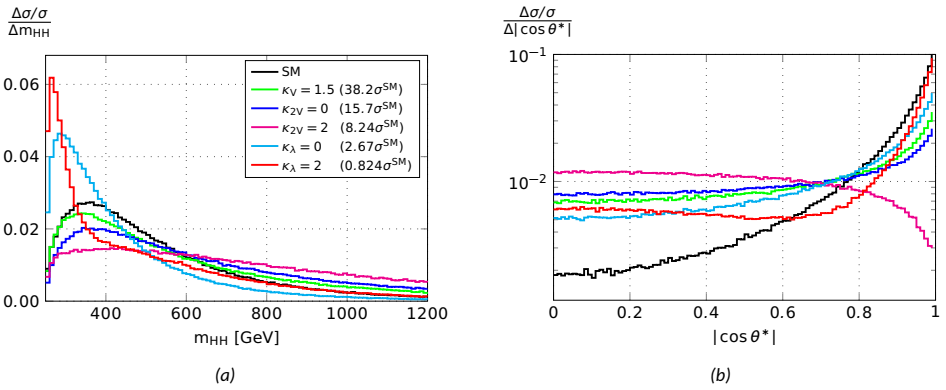


Figure 2.28: Density plots of m_{HH} (a) and $|\cos\theta^*|$ (b) for various coupling values in VBF HH production. SM values are assumed for all couplings not explicitly shown in the legend. The distributions are extracted from corresponding MC samples that are simulated at LO. The corresponding BSM cross sections are quoted in parentheses as multiple of the SM cross section, both estimated from the MC samples.

2.5.3 Resonant HH production

Many BSM models consider the possibility that the on-shell Higgs boson pair may be produced by some yet unknown heavy resonance X. A Feynman diagram for generic resonant HH production is depicted in Fig. 2.29, where the intermediate resonance is induced via ggF. Instead of modulating the m_{HH} spectrum as described in the previous section, the invariant mass of the Higgs boson pair that results from X decay would be localized at mass $m_X (\geqslant 2m_H)$ of the resonance. This signature is universal among many resonant HH production mechanisms, but the details differ in how such resonances arise, and what problems the alternative phenomenological models attempt to address.

In Higgs singlet models, for instance, a new scalar field is introduced to the theory such that it couples only to the Higgs doublet [202, 203]. After EWSB, the two fields

acquire different VEVs and the physical fields would result from mixing the singlet field with the neutral component of the doublet, analogously to how Z boson and photon fields arise from the mixing of $SU(2)_L \times U(1)_Y$ gauge fields. Excitations of the lighter field would be identified as the Higgs bosons, while excitation of the heavier field would correspond to some unknown particle. Such models are sometimes referred to as Higgs portals, since they promote the idea of a hidden sector of particles that only the Higgs is able to interact with [204, 205]. The new particle could also function as a viable dark matter candidate [206].

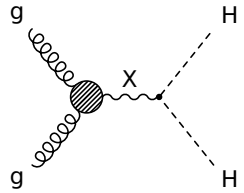


Figure 2.29: Feynman diagram for ggF production of an intermediate resonance X and its subsequent decay into two SM-like Higgs bosons.

Other models that feature resonant HH production try to address the EW hierarchy problem, which is concerned about the large discrepancy of the EW scale v and the Planck scale Λ_{Planck}. The premise here is that the SM itself should be considered as an EFT, a low-energy manifestation of more complete theory. The simplest yet most convincing argument for this claim would be that there is no valid description of gravity beyond Λ_{Planck}. Although the BSM interactions to the Higgs boson are suppressed by the new scale $\Lambda > v$, as indicated by Eq. (2.19), the Higgs boson mass, on the contrary, should receive corrections that are proportional to Λ^2 [207]. The conundrum can be resolved by either adding new particles that cancel the large increase in Higgs boson mass, or create some other mechanism that circumvents this problem.

In 2HDM, which is typically seen in the context of MSSM, new scalar particles arise with the addition of a second $SU(2)_L$ Higgs doublet [208, 209]. Different types of models are generated, depending on how the two Higgs doublets interact with fermions. For example, in type I 2HDM, the extra doublet couples to all charged fermions, while in type II one of the doublets couples to up-type quarks and the other doublet couples to the remaining charged fermions. The prescription produces one CP-odd and two mixed CP-even fields, plus two additional charged scalar fields. The CP-even fields would yield the familiar Higgs boson and a new heavier scalar particle that would be responsible for resonant HH production. Some extensions to the framework introduce a CP-violating phase to the theory [210], while others incorporate an extra singlet [211] or two [212]. The field content of MSSM is extended by a CP-even scalar and a CP-odd pseudoscalar field in next-to-minimal supersymmetric SM, thus predicting yet another Higgs-like scalar Y, which has motivated dedicated searches of asymmetric X$\rightarrow$YH decays [213]. A comprehensive overview of other resonant HH production mechanisms can be found in Ref. [51].

Another way to get around the hierarchy problem is to add one or more dimensions to four-dimensional spacetime. The extra dimensions would have to be incredibly microscopic that it would not be possible to observe them directly. One can think of the following analogy: a long line drawn on a piece of paper has a certain width to it, which becomes significant when looked at up close, but imperceivable from a distance. The concept is almost as old as GR itself, dating back to the 1920s when Kaluza and Klein attempted to unify GR with EM by adding a fifth dimension to spacetime [214, 215]. Although the theory

did not turn out to be the correct one, the idea of compactified extra dimensions persisted and inspired many models like string theory in the coming years.

One of such models was developed by Randall and Sundrum (RS) in late 1990s, which explicitly tackled the hierarchy problem [216]. The authors proposed a five-dimensional metric that yields a line element of the form

$$ds^2 = e^{-2ky}\eta_{\mu\nu}dx^\mu dx^\nu + dy^2\,,$$

which was shown to respect Poincaré symmetries and field equations of GR. The familiar spacetime coordinates x are now accompanied by a fifth dimension, which is parametrized by variable y. The extra dimension spans the interval between 0 and πr_c with periodicity condition $(x,y) = (x,-y)$. The symbol r_c corresponds to the radius of extra dimension, while factor k tells how much the four-dimensional spacetime is warped when moving along the fifth dimension. Slices of this five-dimensional hyperspace at particular values of y are referred to as „branes", while the hyperspace volume that is enclosed by branes is called „bulk". It can be shown that the ultraviolet mass scale Λ_{UV} at $y = 0$ is related to the infrared scale Λ_{IR} at $y > 0$ via the following relation:

$$\Lambda_{\text{IR}} = e^{-ky}\Lambda_{\text{UV}}\,.$$

The scale Λ_{UV} could be identified as the Planck scale and Λ_{IR} as the EW TeV scale in the above expression if $kr_c\pi \simeq 35$. It follows that there is no hierarchy of different scales, but one fundamental scale that is exponentially suppressed by the geometry of five-dimensional spacetime. A lower-dimensional analogue of the classic RS model is shown in Fig. 2.30.

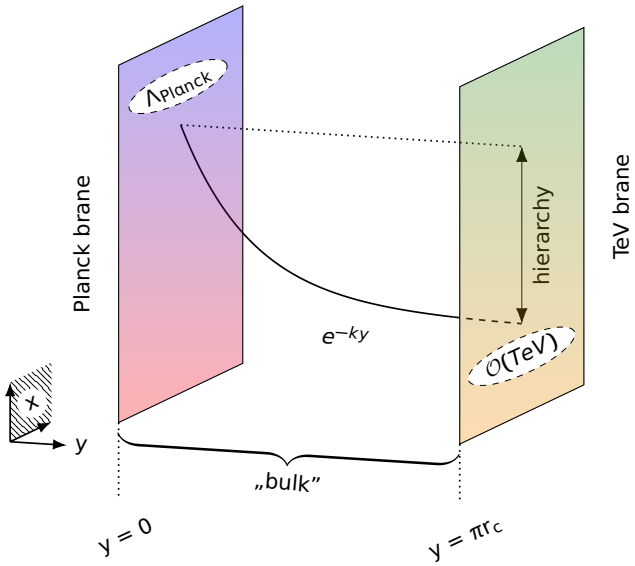


Figure 2.30: Schematic of the original RS model.

The original RS model confined the SM particles exclusively to the TeV brane, but subsequent iterations of the model considered the possibility by which the matter and gauge fields were allowed to wander into the bulk region [217]. Perturbations in the tensor component of the metric result in gravity-mediating spin-2 graviton, while fluctuations

in the scalar term of the metric yield a spin-0 particle called radion, which is needed to stabilize the size of extra dimensions [218]. Both radions and gravitons dynamically acquire their masses, which can be specified explicitly in the theory. The new particles are expected to interact with the SM content, including the Higgs boson [219, 220].

The study on HH production in multilepton channel, which is presented in Section 8, specifically looks for the resonant signal in the decays of radions and gravitons as they appear in the bulk RS scenario, although the resulting phenomenology of radions is very similar to the original RS model [221]. The corresponding MC samples are generated at LO for the following range of invariant masses, totaling 19 mass points: from 250 GeV to 270 GeV in steps of 10 GeV; from 280 GeV to 320 GeV in steps of 20 GeV; from 350 GeV to 900 GeV in steps of 50 GeV; and final mass point at 1 TeV. Searches of resonant HH production in the boosted region would require different analysis techniques not employed here and are hence omitted from the current discussion. Decay widths of the new resonances are assumed to be negligible in the simulation, which is in line with conclusions of phenomenological studies on the bulk RS model [221]. The only production mode considered here is ggF, because other production mechanisms are suppressed by quark PDFs at the LHC. The cross sections of Higgs boson pair production via bulk RS radions and gravitons are shown in Fig. 2.31. The precise figures depend on the choice of free parameters in the model.

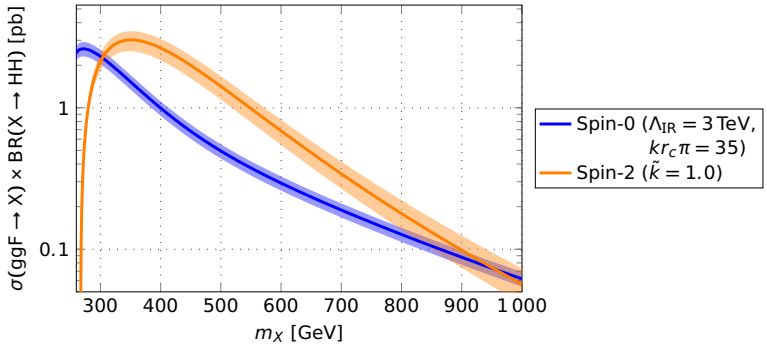


Figure 2.31: Theoretical HH production cross section at 13 TeV via radions (blue line) and gravitons (orange line) as a function of mass m_X of the resonance as they appear in the bulk RS model [221]. Symbol $\tilde{k}$ stands for $k/\overline{\Lambda}_{Planck}$, where $\overline{\Lambda}_{Planck} = \Lambda_{Planck}/\sqrt{8\pi} \approx 2.4 \times 10^{18}$ GeV denotes the reduced Planck scale. The shaded bands cover QCD scale and PDF uncertainties, which are added in quadrature. HH production cross section increases with $1/\Lambda_{IR}^2$ in case of radions and with $\tilde{k}^2$ in case of gravitons.

Unlike in nonresonant production, where p_T^H of either Higgs boson is theoretically limited only by the c.o.m energy, the distribution of p_T^H of the Higgs bosons produced in resonant decays at LO has a sharply falling peak at upper kinematic threshold of $\sqrt{m_X^2/4 - m_H^2}$. The tail of p_T^H distribution is more pronounced for radion decays compared to graviton decays, which develops due to wider angular distribution of the Higgs boson pair that are produced in these decays. As demonstrated by Fig. 2.32, the Higgs bosons tend to fly into the transverse plane where $\theta^* \sim \pi/2$ more often in graviton decays than in radion decays. The plot is in agreement with the theory prediction, according to which the differential cross section with respect to Jacobian term $\sin\theta^* d\theta^*$ in the rest frame of the graviton follows $\sin^4\theta^*$ [222] but stays constant for radions, since there are no products of spin vectors present in the MEs that model a scalar particle decaying into other scalars.

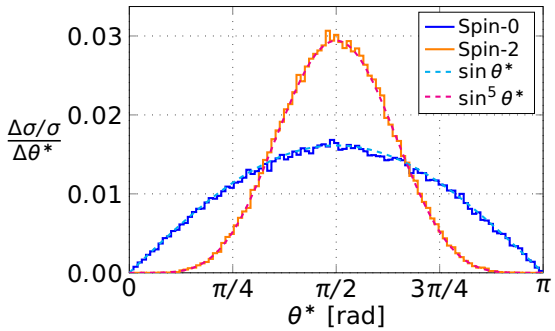


Figure 2.32: Angular distribution of spin-0 (blue) and spin-2 (orange) resonances produced via ggF that subsequently decay into a pair of Higgs bosons at polar angle θ^* in the rest frame of the resonance. The distributions extracted from LO MC samples (solid histogram) are compared to shapes as predicted by theory (dashed curve).

2.5.4 Experimental status

Experimental searches of HH production started in late LHC Run 1 data-taking period [223, 224] and are still ongoing today but at considerably higher intensity and wider range of analysis channels. A total of ~ 4300 pairs of Higgs bosons are expected in the SM out of tens of billions of events that were recorded by the CMS detector during LHC Run 2 data-taking period. Similarly to single Higgs boson studies, the Higgs boson pairs are searched in mutually exclusive phase space regions defined by HH decay modes. As shown in Fig. 2.33, by considering only those single Higgs boson decay modes for which there is direct experimental evidence available today, one might consider up to 28 unique ways the Higgs boson pair might decay into. However, only a fraction of those decay modes are experimentally viable for probing the HH production. In order to gain sensitivity to the HH signal, some phase space regions with high event statistics may be further divided by HH production modes into ggF and VBF categories, or by the kinematic regime into resolved (or low m_{HH}) and boosted (or high m_{HH}) regions. Analyses that target the VBF category require the presence of additional two jets that are separated by a wide angle and have a large invariant mass. Higgs boson decay products are much more collimated in boosted HH events, which makes it more difficult to resolve them with the same analysis techniques utilized in the low m_{HH} regime. For this reason, the hadronic decay products of a boosted Higgs boson are clustered into a single jet with larger cone radius instead of two distinct jets with smaller cone radius as commonly employed in the resolved analyses. The background composition also changes with increasing m_{HH}, further motivating the distinction of resolved and boosted regimes.

Each individual analysis targets a particular experimental signature, but there is no single „golden channel" that alone is simultaneously sensitive enough for probing the SM hypothesis and the various EFT shape BMs. This very much applies to the HH multilepton analysis presented here, as it provides excellent sensitivity to kinematic scenarios that exhibit soft m_{HH} spectrum. Compared to other HH analyses, in particular those targeting $\mathrm{H} \to \mathrm{b\bar{b}}$ decays, the multilepton channels excel in the low m_{HH} regime because of relatively low energy thresholds that the selected electrons, muons and τ_{h} are required to satisfy. On the contrary, the multilepton channels are not as sensitive to the kinematic scenarios that display very energetic m_{HH} spectrum compared to the channels that involve more probable $\mathrm{H} \to \mathrm{b\bar{b}}$ decays because the selection thresholds play less of an important role in signal acceptance.

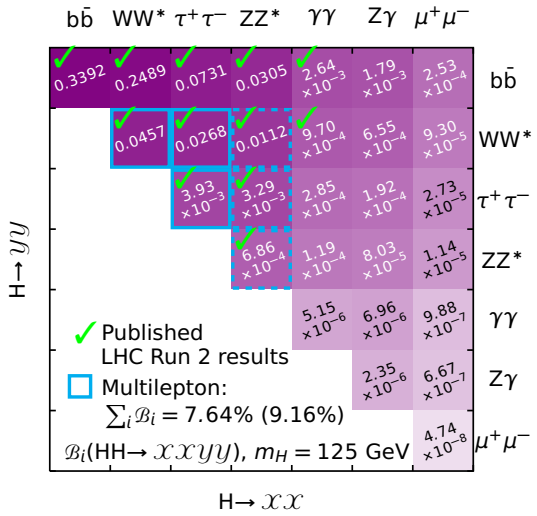


Figure 2.33: Branching ratios of Higgs boson pair decays. Inputs are taken from [50]. Cells marked with a green tick symbol (✓) indicate the decay modes for which there are published analysis results based on LHC Run 2 data. Multilepton decay modes are highlighted with blue cell borders. Dashed cell borders indicate that the decay mode is technically included in the signal hypothesis but the analysis was not optimized for those events.

The same challenges that are prevalent in single Higgs boson searches are now amplified in HH searches: the decay modes with clean final state have way too small BR, while the decay modes with larger BR show poor signal over background ratio (S/B). Therefore, the results of multiple HH analyses need to be combined in order to reach maximum possible sensitivity, which in turn implies that the analyses have a common set of deliverables. Analyses that target nonresonant HH production typically quantify upper limits on HH production cross section, constraints on κ_λ and on κ_{2V}, multidimensional limits involving SM and EFT parameters, and limits on EFT shape BMs. This is different from resonant HH searches, where a radion or a bulk RS graviton with unknown mass m_X is presumed to decay into a pair of SM Higgs bosons. Although the signal hypothesis is fixed to a specific scenario, the resulting peak in m_{HH} that is located at m_X is representative of all mechanisms that feature a heavy narrow-width resonance decaying into a pair of Higgs bosons. Limits in resonant HH analyses are quoted for spin-0 and spin-2 hypothesis separately for selected values of m_X.

The HH searches have been performed by the ATLAS and CMS collaborations on data collected in LHC Run 2 in seven decay modes. The most sensitive analyses cover HH $\to$ b$\bar{\text{b}}$b$\bar{\text{b}}$ [225–230], HH $\to$ b$\bar{\text{b}}\tau\tau$ [231–233] and HH $\to$ b$\bar{\text{b}}\gamma\gamma$ [234, 235] decay modes. These are followed by multilepton analysis, which captures HH $\to$ VV*V$'$V$'^*$, HH $\to \tau\tau$VV* and HH $\to \tau\tau\tau\tau$ signal, and HH $\to$ b$\bar{\text{b}}$WW* [7, 236, 237] analysis, which is sometimes combined with HH $\to$ b$\bar{\text{b}}\tau\tau$ and HH $\to$ b$\bar{\text{b}}$ZZ* decay modes to target DL final states [238]. Finally, there are analyses targeting HH $\to$ b$\bar{\text{b}}$ZZ* $\to$ b$\bar{\text{b}}4\ell$ [239] and HH $\to$ WW$^*\gamma\gamma$ [240, 241] decay modes. The decay modes have been analyzed thus far are marked with a green tick symbol as a visual aid in the BR matrix that is depicted in Fig. 2.33. All aforementioned HH analyses have only studied the dominant ggF and VBF production modes. The CMS collaboration has very recently published preliminary results on subdominant VHH production by exploiting those unique final states, which arise from both Higgs bosons decaying into a pair of b quarks [242].

In FH channels, such as $HH \to b\bar{b}b\bar{b}$ and $HH \to b\bar{b}\tau\tau$ with both τ decaying hadronically, the overwhelming majority of background events that pass the analysis selection cuts are coming from QCD multijet processes. Although their contribution to the signal region (SR) diminishes in the boosted regime, the same goes for the efficiencies of state-of-the-art b jet identification algorithms [167, 168] that the present channels heavily profit from. Since it is not computationally feasible to model the QCD background with MC simulation without inflating the statistical uncertainties on the estimation, especially in the tails of distributions where BSM signal is expected to surface, data-driven techniques are oftentimes employed to model the multijet background in the SR. Channels like $HH \to b\bar{b}\tau\tau$ and $HH \to b\bar{b}VV^*$, where one or two leptons are required in the final state, have to discriminate against massive $t\bar{t}$+jets, DY and W+jets backgrounds, which can produce the same experimental signature. In multilepton and $HH \to b\bar{b}ZZ^* \to b\bar{b}4\ell$ channels, where the multiplicity of final state electrons, muons and τ_h is higher, the dominant backgrounds come from WZ and ZZ production processes, followed by associated production of a single boson with a pair of top quarks. Although the QCD background is less of an issue in those channels, it can still seep into the SR if hadronic jets are misidentified as leptons or τ_h. Such „fake background" is generally modeled with data-driven approaches, which will be discussed in more detail in Section 5.3. Finally, $HH \to b\bar{b}\gamma\gamma$ channel has two types of backgrounds: nonresonant $\gamma\gamma$+jets, which has continuously falling energy spectrum, and single Higgs boson production processes, where the Higgs boson decays into two photons. Limits on more generic production of $X \to YH$ process, where X and Y represent distinct species of hypothetical particles, can be converted into limits on HH production if the Y particle has the same mass as the Higgs boson. Limits on resonant HH production in $b\bar{b}b\bar{b}$ [243], $b\bar{b}\tau\tau$ [244] and $b\bar{b}\gamma\gamma$ [245] decay modes set by the CMS collaboration are indeed deduced from the limits of $X \to YH$ production.

The analyses that require the presence of multiple leptons, τ_h or photons in the final state have generally fewer background events, but also much smaller signal rate because of low BRs of the involved decay processes. Thus, $HH \to b\bar{b}\gamma\gamma$, $HH \to WW^*\gamma\gamma$, $HH \to b\bar{b}ZZ^* \to b\bar{b}4\ell$ and multilepton channels are generally limited by the available data, which is also reflected by the enlarged statistical uncertainties in the corresponding results. This is not a problem in the remaining channels, however, any systematic biases that may arise in the modeling of signal and background processes become pronounced. It may create tensions in the signal extraction, which can be relieved by improving the uncertainty model, but at the expense of increasing systematic uncertainties. Results of the latest HH analyses are summarized in Table 2.12, demonstrating good compatibility with the SM expectation.

HH decay mode	Mass range of X in resonant $X \to HH$	ATLAS	CMS
$b\bar{b}b\bar{b}$ (▲, ●)	ATLAS: $[251, 5000]$ ([226]^{G}); $[260, 1000]$ ([225]^{V}); CMS: $[1000, 3000]$ ([230]^{G}); $[1000, 4000]$ ([243]$^{\ddagger G}$)	$-3.5(-5.4) < \kappa_\lambda < 11.3(11.4)$, $0(-0.1) < \kappa_{2V} < 2.1(2.1)$, $5.4(8.1)\sigma_{SM}$, $130(130)\sigma_{SM}^{\text{VBF-only}}$ [227]$^{\dagger GV}$; $-0.8(-0.9) < \kappa_{2V} < 2.9(3.1)$, $840(550)\sigma_{SM}$ [225]^{V}	Resolved: $-2.3(-5.0) < \kappa_\lambda < 9.4(12.0)$, $-0.1(-0.4) < \kappa_{2V} < 2.2(2.5)$, $3.9(7.8)\sigma_{SM}$ [228]^{GV} Boosted: $-9.9(-5.1) < \kappa_\lambda < 16.9(12.2)$, $0.6(0.7) < \kappa_{2V} < 1.4(1.4)$, $9.9(5.1)\sigma_{SM}$ [229]^{GV} VHH: $-38(-30) < \kappa_\lambda < 37(29)$, $-12(-7.6) < \kappa_{2V} < 14(8.9)$ [242]
$b\bar{b}\tau\tau$ (▲, ●)	ATLAS:		
(FH)	$[1200, 3000]$ ([231]^{G});	✗	✗
(FH, SL)	$[251, 1600]$ ([232]^{G})	$4.7(3.9)\sigma_{SM}$ [232]^{GV}	$-1.7(-2.9) < \kappa_\lambda < 8.7(9.8)$, $-0.4(-0.6) < \kappa_{2V} < 2.6(2.8)$, $3.3(5.2)\sigma_{SM}$, $124(154)\sigma_{SM}^{\text{VBF-only}}$ [233]^{GV}
	CMS: $[280, 3000]$ ([244]$^{\ddagger G}$)		
$b\bar{b}\gamma\gamma$ (▲, ●)	ATLAS: $[251, 1000]$ ([234]^{G})	$-1.5(-2.4) < \kappa_\lambda < 6.7(7.7)$, $4.2(5.7)\sigma_{SM}$ [234]^{GV}	$-3.3(-2.5) < \kappa_\lambda < 8.5(8.2)$, $-1.3(0.9) < \kappa_{2V} < 3.5(3.1)$, $-0.6(-0.4) < c_2 < 1.1(0.9)$, $7.7(5.2)\sigma_{SM}$ [235]$^{\dagger GV}$
	CMS $[260, 1000]$ ([245]$^{\ddagger G}$)		
Multilepton (●)			
(4W)	$[250, 500]$ ([246]^{*G});	$160(120)\sigma_{SM}$ [246]^{*G}	✗
(4V, 2V2τ, 4τ)	$[250, 1000]$ ([2]^{G})	✗	$-6.9(-6.9) < \kappa_\lambda < 11.1(11.7)$, $-1.0(-1.0) < c_2 < 1.5(1.4)$, $21.3(19.4)\sigma_{SM}$ [2]$^{\dagger GV}$
$b\bar{b}WW^*$	ATLAS:		
(SL)	$[500, 3000]$ ([236]^{*G})	$300(300)\sigma_{SM}$ [236]^{*G}	✗
(DL)	✗	$40(29)\sigma_{SM}$ [238]^{G}	✗
(SL, DL)	CMS: $[250, 900]$ ([7]^{G}); $[800, 3500]$ ([247]^{*G}) $[800, 4500]$ ([237]^{G})	✗	$-7.2(-8.7) < \kappa_\lambda < 13.8(15.2)$, $-1.1(-1.4) < \kappa_{2V} < 3.2(3.5)$, $14(18)\sigma_{SM}$ [7]$^{\dagger GV}$
$b\bar{b}ZZ^* \to b\bar{b}4\ell$ (●)	✗	✗	$-9(-10) < \kappa_\lambda < 13(15)$, $32(40)\sigma_{SM}$ [239]^{G}
$WW^*\gamma\gamma$	$[260, 500]$ ([240]^{*G})	$230(160)\sigma_{SM}$ [240]^{*G}	$97(53)\sigma_{SM}$ [241]$^{\dagger GV}$
Combination	ATLAS: $[260, 3000]$ ([248]^{*G})	$-0.4(-1.9) < \kappa_\lambda < 6.3(7.6)$, $0.1(0.0) < \kappa_{2V} < 2.0(2.1)$, $2.4(2.9)\sigma_{SM}$ [249]	$-1.2(-1.0) < \kappa_\lambda < 6.5(6.3)$, $0.7(0.7) < \kappa_{2V} < 1.4(1.4)$ (obs. at 6.6σ), $3.4(2.5)\sigma_{SM}$ [8]
	CMS: $[250, 3000]$ ([250]^{*G})		

* Performed on 2016 data only.
† Provides limits for EFT BMs.
‡ Scalar $X \to YH$ search with $m_Y \in 125\,\text{GeV}$.
^{G} Considers ggF HH signal hypothesis.
^{V} Considers VBF HH signal hypothesis.

Table 2.12: Summary of the latest HH analyses performed by the ATLAS and CMS collaborations on LHC Run 2 data. Mass ranges of the unknown resonance are given in the units of GeV*. Last two columns quote observed and expected upper limits on HH production cross section in the units of SM cross section and constraints on various couplings based upper limits at 95% CL. Expected limits are given in parentheses. The combination of ATLAS results considers single Higgs boson channels plus three HH channels (which are marked with a black triangle, ▲), while the combination of CMS results includes only five HH channels (which are marked with a black bullet, ●).*

3 The LHC and the CMS experiment

The European Organization for Nuclear Research, commonly referred to by its French abbreviation „CERN", is the largest international organization that conducts cutting-edge research in high energy physics (HEP). The organization has grown in size from a just dozen states since its inception in 1954 to more than 70 states today, including 23 member states, ten associated member states (including Estonia that intends to become a full member by 2023 at the latest), three observer states and 41 other countries contributing to CERN research program on a regular basis. CERN has more than $11\,000$ active users from 700 institutes working in scientific, technical and administrative fields as part of more than 30 accelerator experiments [251].

The largest and most powerful particle accelerator in the world is currently the CERN Large Hadron Collider (LHC) [11]. The accelerator supports eight independent experiments that each have their own instruments for collecting the collision data. Behind every experiment is a highly skilled team who develops and maintains the hardware and software, performs the data analysis, and publishes the results. One of the two general-purpose detectors that is located on the $27\,\mathrm{km}$ long circular path of the LHC is the Compact Muon Solenoid (CMS) detector [19]. Since the analyzed data in this work is collected by the said detector, the remainder of this section is precisely dedicated to the description of the LHC in Section 3.1, followed by Section 3.2, where a brief overview of the CMS apparatus is given.

3.1 The Large Hadron Collider

Plans for the LHC already started right after the discovery of Z boson [252], with the primary physics goal of improving the SM of particle physics even further. Its construction began in 1998 and concluded ten years later, which was then followed by a 14 month long testing period. The hadron collider is installed in the tunnel of the now defunct Large Electron-Positron Collider, which resides about $100\,\mathrm{m}$ below the ground surface of the Geneva region that is shared between Switzerland and France. It accelerates and collides mostly protons (pp), but it can and has been used for colliding lead ions with protons (p-Pb) or colliding just the lead ions (Pb-Pb). These heavy ion collisions create conditions for nuclear matter to transition into an exotic form of plasma that consists of asymptotically free quarks and gluons. Month-long experiments with the heavy ions are typically scheduled at the end of a data-taking year, leaving the rest of the year for pp collisions. The remainder of this section focuses exclusively on pp collisions at the LHC.

Protons are accelerated through a chain of linear and circular pre-accelerators before they enter the LHC ring, as illustrated in Fig. 3.1. The whole process starts with a vessel of hydrogen gas, from which hydrogen atoms are pulled. The hydrogen atoms are stripped from electrons and the residual protons are injected into LINAC2[9], which accelerates them to $50\,\mathrm{GeV}$. The protons are subsequently transferred to Proton Synchrotron Booster, where they are accelerated to $1.4\,\mathrm{GeV}$. Next, the protons are passed to Proton Synchrotron, where they are lumped into bunches that each contain about 100 billion protons. Once the bunches are boosted to $26\,\mathrm{GeV}$ in the ring, they are then passed to the Super Proton Synchrotron, which raises their energy to $450\,\mathrm{GeV}$. The resulting stream of protons is split into two and directed into the LHC ring at two separate interaction points (IPs). One beam („Beam 1") enters the LHC cavity at IP2 and runs clockwise, while the other beam („Beam 2") enters the LHC ring at IP8 and travels anti-clockwise (from ground-level perspective).

The LHC ring has eight IPs in total. Two general-purpose detectors, ATLAS and CMS, are

[9] LINAC stands for linear accelerator. LINAC2 was replaced by LINAC4 after LHC Run 2 concluded.

respectively located at IPs 1 and 5. The proton beams also cross at IPs 2 and 8, where ALICE and LHCb detectors are situated. The former is designed to collect and study the data from Pb-Pb collisions, while the latter is specialized in b quark physics and CP-violation. Smaller complementary experiments (LHCf, MilliQan, MoEDAL, and TOTEM) occupy the aforementioned IPs (1, 5, 8, and 5). They tackle specific questions of particle physics, such as the existence of magnetic monopoles (MoEDAL) or millicharged particles (MilliQan), or determine the characteristics of pp collisions (TOTEM) and cosmic ray phenomena (LHCf). The remaining IPs are equipped with instruments that facilitate the LHC operations, like beam collimation at IPs 3 and 7, two independent radiofrequency (RF) systems that are responsible for accelerating the protons at IP4, and beam dumping at IP6.

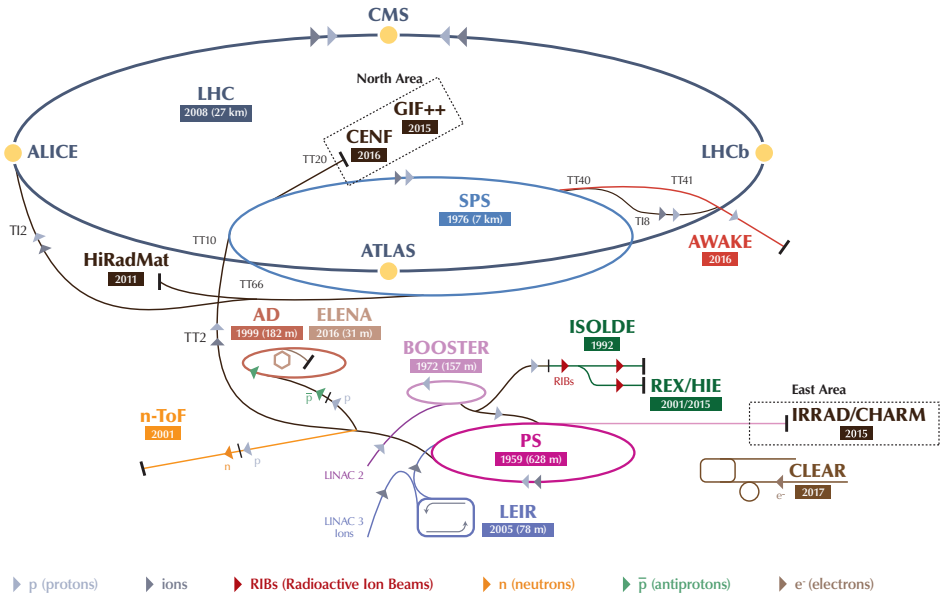


Figure 3.1: Schematic of the CERN accelerator complex at the tail end of the LHC Run 2 operations in 2018 [253]. Each accelerator system in the plot is labeled by its name, date of commission and, in case circular accelerators, its circumference. Injection paths from one system to another are shown with arrows, the color of which tells the type of particle that is transferred, as indicated by the legend.

At every lap in the LHC, the protons receive energy by electric potential difference that is present only in RF cavities. The ratio between voltage oscillation frequency in the RF cavities, f_{RF}, and the revolution frequency of proton bunches, f_{rev}, determines the total number of vacant segments or „buckets" of the circular path that could be populated by proton bunches. Since the proton bunches are separated by an interval Δt of 25 ns, only a small fraction of buckets are actually populated with the protons. The precise number of proton bunches in a train, N_b, depends on the choice of filling scheme at the beam injection time.

The protons are guided by 1232 superconducting dipole magnets along the circular path of the LHC. The magnetic coils sustain a field strength of up to 8.3 T. Such strong magnetic fields are necessary to provide sufficient centripetal force that is able to bend the trajectory of protons. Various multipole magnets are placed between the dipole magnets in succession to prevent the proton bunches from dispersing in the transverse plane while they travel inside the vacuum cavities of the LHC. Right before the proton bunches reach

the detector, they are squeezed together by a series of quadrupole magnets. The beams cross each other at a subtle angle θ_c inside the detectors.

Proton trajectories are continually corrected by multipole magnets, which causes the protons to oscillate about the longitudinal axis. The collective motion of protons is generally described by two phase space parameters: amplitude modulation $\beta(l)$ and transverse emittance ε. As the name already implies, the former quantifies oscillation amplitude, which varies with longitudinal position l in the accelerator, while transverse emittance tells how much phase space is covered by these oscillations. Amplitude modulation at the collision point is commonly denoted by β^*.

Instantaneous luminosity is a parameter of the accelerator that quantifies the collision rate of a scattering process. Assuming that the colliding proton bunches contain the same number of protons, N_p, and that the proton density in both bunches follows a Gaussian distribution with variance σ_T^2 in transverse direction, then instantaneous luminosity at the LHC can be approximated by

$$\mathcal{L}_{\text{inst}} = \frac{f N_b N_p^2}{4\pi\sigma_T^2} \mathcal{R}(\sigma_T, \sigma_L, \theta_c, d)\,, \tag{3.1}$$

with $\sigma_T = \sqrt{\beta^* \varepsilon / \gamma_L}$ and σ_L standing for the bunch width and length, respectively, and γ_L referring to the Lorentz factor of the accelerated protons [254]. Reduction factor $\mathcal{R}$ in Eq. (3.1) captures the degradation of instantaneous luminosity that is caused by colliding proton bunches at angle θ_c or at some unknown offset d, but also includes the effects of bunch size variation at low values of β^*. It is worth noting that shorter than $25\,\text{ns}$ bunch spacing would lower the instantaneous luminosity due to parasitic beam-beam effects [255].

Integrated luminosity L over some time period T is obtained from:

$$L = \int_0^T \mathcal{L}_{\text{inst}}(t)\mathcal{F}(t)dt\,,$$

where $\mathcal{F}(t)$ accounts for luminosity decay, which is caused mainly by collisions. The proton beam circulates in the accelerator anywhere between a few hours up to a day and a half, but it usually averages to $T \approx 10\,\text{h}$. Once the beam has been exhausted, it is extracted from the storage ring, diluted, and dumped into a graphite block. Every new injection of the beam starts a new „fill" recording, which contains multiple discrete data-taking intervals or „runs", during which the detector conditions do not change. Collision events collected after 2^{18} revolutions of the beam in a $23\,\text{s}$ long interval comprise a luminosity „block" or „section" of a run. Each fill, run, luminosity block and recorded event is assigned a unique number that is sequentially incremented.

Integrated luminosity can be thought of as a measure of collected data, because the product of integrated luminosity and the cross section of some process, which is usually known or at the very least hypothesized, yields the total number of events that is expected from the proton collisions. About 70% of total pp interactions are inelastic and hence contribute to the production of new particles. The corresponding cross section is sometimes called minimum bias cross section and amounts to $\sigma_{\text{MB}} = 69.2(\pm 4.6\%)\text{mb}$ at $\sqrt{s} = 13\,\text{TeV}$ [256]. As detailed in Table 3.1, peak instantaneous luminosity ranged from 14 to $21\,\text{Hz/nb}$ during LHC Run 2, which means that pp interactions were produced at a rate of up to $\mathcal{L}_{\text{inst}}\sigma_{\text{MB}} = 970\,\text{MHz}–1.45\,\text{GHz}$. However, given that bunch crossings (BXs) are happening at a rate of $N_b f_{\text{rev}} = 25–28.8\,\text{MHz}$, then one would expect

$$\langle \mu_{\text{PU}} \rangle = \frac{\mathcal{L}_{\text{inst}}\sigma_{\text{MB}}}{N_b f_{\text{rev}}} \approx 40–50 \tag{3.2}$$

pp interactions per BX on average. This average turned out to be smaller, between 23 and 32, for the full data-taking period because the LHC machine was not constantly operating at its peak instantaneous luminosity.

Each pp interaction from a BX produces particles that leave tracks inside the detector volume. The tracks can be traced back to common points. Only one of those points called the primary vertex is considered as the HS event, while all other pp interactions in the event are deemed as pileup (PU). One can distinguish between in-time PU if the extra pp interactions are happening in the same BX as the HS event, and out-of-time PU, in which case the detector does not have enough time to clear up the information from previous BX or receives new information from the next BX too early. The average number of PU vertices per BX follows Poisson distribution with mean $\langle \mu_{\text{PU}} \rangle$, which increases linearly with instantaneous luminosity as evidenced by Eq. (3.2). Figure 3.2 shows the distribution of $\langle \mu_{\text{PU}} \rangle$ for each data-taking year and for their aggregation.

$\sqrt{s}$ [TeV]	Δt [ns]	f_{RF} [MHz]	f_{rev} [kHz]	$N_b{}^{\dagger}$	N_p	$\lvert\theta_c\rvert$ [µrad]
13	25	400	11.245	2220–2556	$\sim 10^{11}$	145–185
β^* [cm]	ε [µm]	σ_L [cm]	$\mathcal{L}_{\text{inst}}{}^{\dagger}$ [Hz/nb]	$\langle \mu_{\text{PU}} \rangle$		
25–40	1.9–2.2	6.4–9.4	14–21	23–32		

Table 3.1: A selection of parameters characterizing the LHC machine during its Run 2 operations. Parameters marked with a dagger (†) indicate their peak values. If the parameter changed between the data-taking years, a range is shown instead.

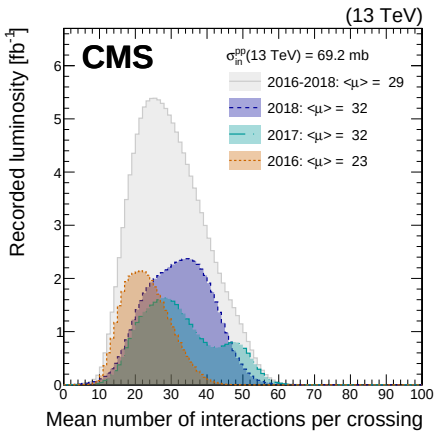


Figure 3.2: PU profile in LHC Run 2 data broken down by data-taking years [256].

The LHC program is scheduled into multiple „Phases" and „Runs" based on the c.o.m energy of pp collisions and instantaneous luminosity supplied by the machine, as depicted in Fig. 3.3. The LHC Runs span multiple years of data-taking operations, which also include shorter breaks (Technical Stops) that are reserved for minor upgrades, tuning and maintenance work. There are Long Shutdowns between each LHC Run, during which the whole accelerator complex is turned offline for major upgrades. Even though the year 2015 is part of LHC Run 2, the amount of data recorded in that year was too low and detector conditions too different compared to the following years. Therefore, it was not practically feasible to include this data in LHC Run 2 analyzes. Just like most CMS analyses, the work

presented here considers only the data that was recorded over the next three years, from 2016 to 2018. The data is acquired in multiple chunks or „eras", which refer to periods of time when the collected data was acquired with consistent detector and trigger settings. Acquisition eras are denoted by uppercase letters and enumerated in alphabetical order. There are seven acquisition eras in 2016 (labeled as B-H), five in 2017 (B-F) and four in 2018 (B-D).

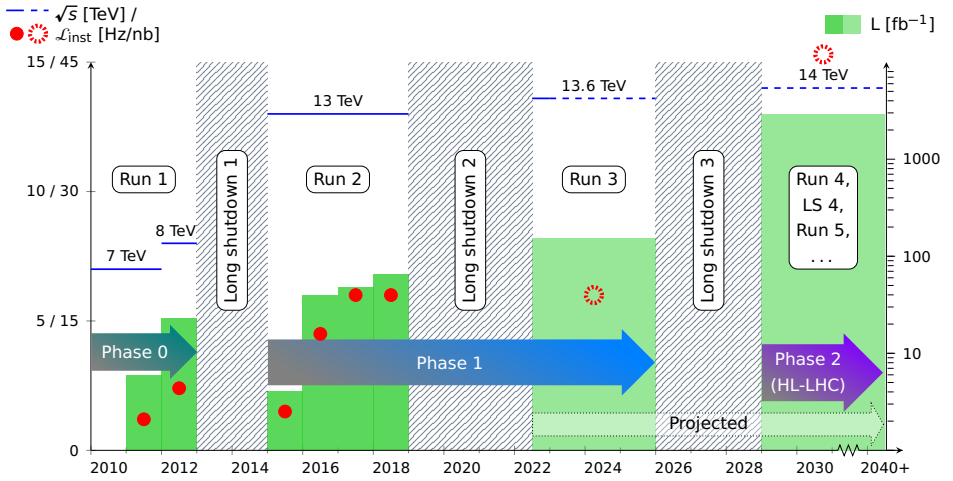


Figure 3.3: Long-term schedule of the LHC program. The plot shows c.o.m energy $\sqrt{s}$ (blue line), peak instantaneous luminosity $\mathcal{L}_{inst}$ (red circles) and accumulated integrated luminosity L (solid green areas) of pp collisions delivered by the LHC in each data-taking year or projected period. The projections are based on Refs. [177, 257].

The LHC will be upgraded to High Luminosity LHC (HL-LHC) after Run 3 [177]. The new machine is expected to produce proton-proton collisions at c.o.m energy of $\sqrt{s} = 14\,\text{TeV}$ at an instantaneous luminosity of $\mathcal{L}_{\text{inst}} = 50\,\text{Hz/nb}$. This comes at the cost of increased PU activity, as 200 parasitic proton-proton collisions are foreseen to occur per BX on average. The HL-LHC is projected to deliver about $250\,\text{fb}^{-1}$ of data per year over the span of at least twelve years, with the ultimate goal of accumulating at least $3\,\text{ab}^{-1}$ of data by the end of its operations. This is more than 20 times the amount of data collected during LHC Run 2 data-taking period. Such significant boost in the amount of recorded data will greatly benefit the analyses that suffer from limited event statistics.

3.2 The CMS detector

The CMS detector consists of various subdetectors that are placed around the beam line in concentric layers. The detector is centered precisely around the collision point where proton bunches cross each other. Despite having „compact" in the name, the whole apparatus is still impressively large: it stands at $21.6\,\text{m}$ long, has a radius of $7.3\,\text{m}$ and weighs about $12\,500\,\text{t}$ in total. Layout of the CMS detector with a couple of people for scale can be found in Fig. 3.4.

Each subdetector measures either energy or momentum of particles that are produced from the proton collisions. In the innermost layer is the tracker that determines the position of charged particles as a function of time. The second layer consists of electromagnetic calorimeter (ECAL) and hadronic calorimeter (HCAL), which absorb particles with electro-

magnetic and hadronic origin, and measure their deposited energy. Muon detectors are placed to the outermost layer because muons have particularly long proper lifetime compared to other collision products. Each of these subdetectors are explored in more detail in Sections 3.2.1 to 3.2.3. The discussion concludes with Section 3.2.4, which describes how the CMS detector handles the unprecedented rates of collision data.

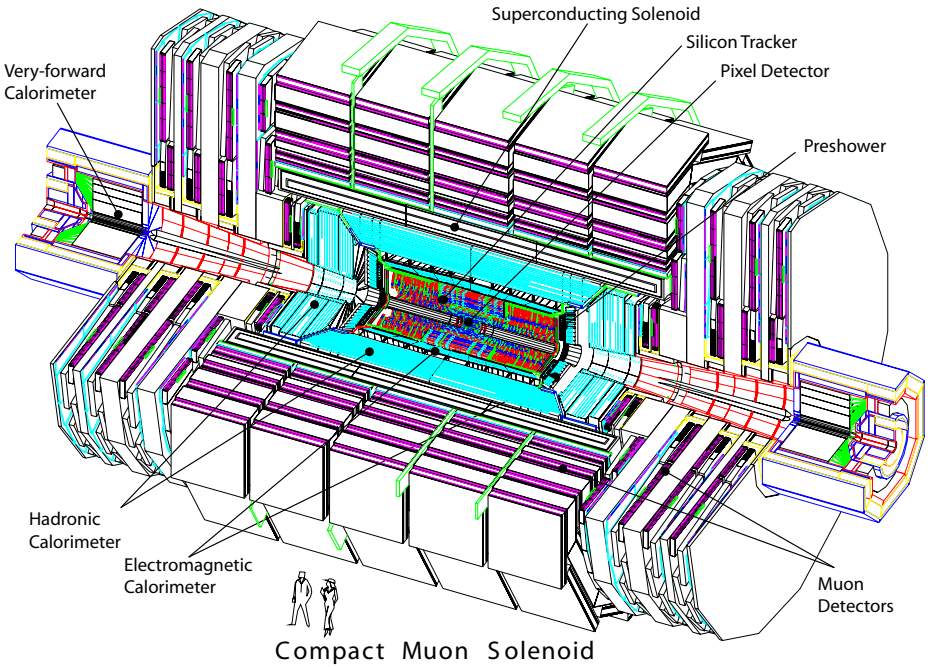


Figure 3.4: Cutaway view of the CMS detector [19].

One of the defining features of the CMS detector is its $12.5\,\mathrm{m}$ long and $6\,\mathrm{m}$ wide solenoid magnet, which is placed between the HCAL and muon detection system. The solenoid is able to generate field strength of $|\mathbf{B}| = 3.8\,\mathrm{T}$, which is directed along Beam 1 inside the coil. The purpose of such a strong magnetic field is to detect electrically charged particles when they pass through the detector material. In particular, an electrically charged particle with mass m and charge q would be subject to Lorentz force $\mathbf{F} = (q/m)\,\mathbf{p} \times \mathbf{B}$ when it travels through the magnetic field with momentum $\mathbf{p}$. Since the acting force is always perpendicular to its direction of motion, the trajectory of the charged particle curls into a helix, the axis of which coincides with the direction of the magnetic field. It follows that the track bending happens on a plane that is perpendicular to the beam line. Radius of this curved path provides an estimate for the mass of the particle, while the sign of the curvature tells whether the particle is positively or negatively charged. The equation of motion of a charged particle can be fully specified by its 3-momentum components at a closest approach to a reference point and by another two parameters quantifying the distance of its track to that reference point [258].

The tracker, calorimeters and the solenoid are all housed inside a steel yoke, which provides structural support for the whole detector. It additionally guides and homogenizes some of the magnetic field outside of the solenoid. The magnetic field present outside of the coil can only influence the trajectory of muons. The 12-sided steel structure consists

of three radial layers with varying thickness that interleave with the muon detectors. Figure 3.5 illustrates how different types of particles interact with the detector material in the presence of the magnetic field.

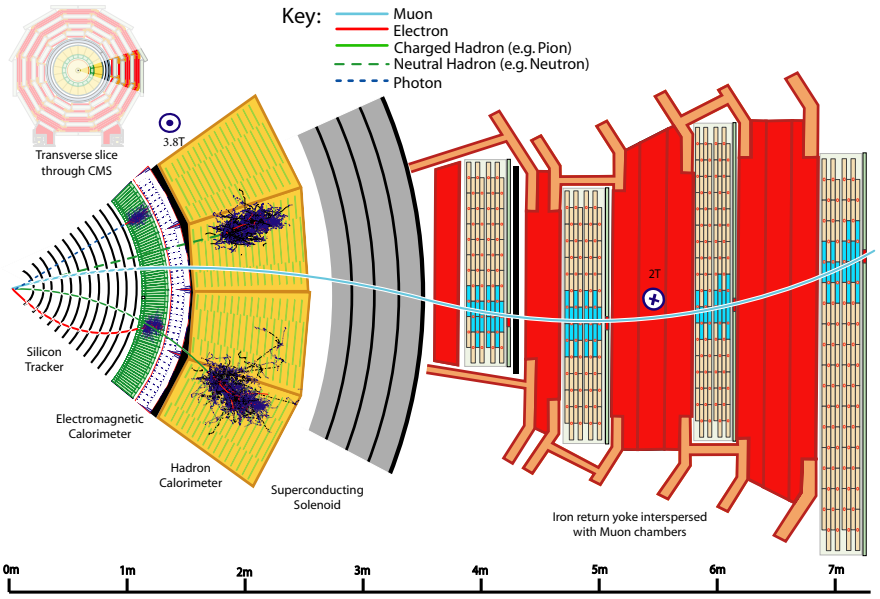


Figure 3.5: Transverse view of one of the twelve azimuthal sectors of the CMS detector at its center point facing in the direction of Beam 2. The sketch demonstrates how different particles interact with various parts of the detector [259].

The instruments that are facing parallel to the beam line constitute the central „barrel" region of the CMS detector, while the subsystems that are placed perpendicular to the collision axis at the both ends of the barrel make up the „endcaps" of the detector. As seen from Fig. 3.4, for instance, the barrel portion of the return yoke has five segments, which are surrounded or „capped" by three layers of steel plates from both ends, hence the name „endcaps".

Given the distinct cylindrical shape of the barrel region, it is more convenient to parametrize the three-momentum of particles using modified cylindrical coordinates (p_T, θ, ϕ) than Cartesian coordinates (p_x, p_y, p_z). The two coordinate systems are related to each other in the following way:

$$p_T = \sqrt{p_x^2 + p_y^2}\,, \qquad \theta = \arccos\frac{p_z}{|\mathbf{p}|}\,, \qquad \phi = \arctan\frac{p_y}{p_x}\,, \tag{3.3}$$

with $|\mathbf{p}| = \sqrt{p_x^2 + p_y^2 + p_z^2}$. The origin of the coordinate system is set at the center of the CMS detector. The x-coordinate points to the center of the LHC ring, the y-coordinate points to the ground surface and the z-coordinate points in the direction of Beam 2. The definition of the y-coordinate coincides with the radial distance r from the beam line. Transverse momentum p_T refers to the projection of three-momentum onto the transverse plane spanned by x- and y-coordinates. Azimuthal angle ϕ quantifies the position of this projection on the transverse plane, whereas polar angle θ tells how far away from the

beam line a given particle travels. Both coordinate systems are depicted in Fig. 3.6(a). All kinematic variables are defined in the laboratory frame of reference where they are measured.

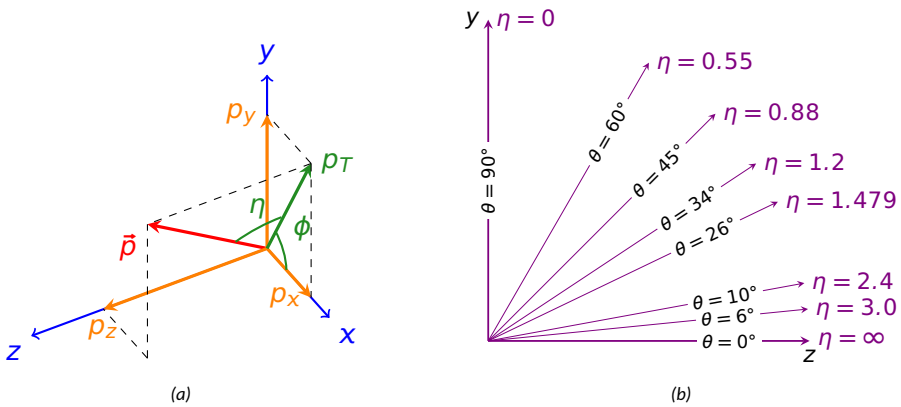


Figure 3.6: (a): Coordinate systems parametrizing three-momentum (shown in red), viewed from the ground surface inside the LHC ring. The Cartesian projections are shown in orange, while the default CMS coordinates are shown in green. (b): A selection of values for pseudorapidity η and corresponding polar angle θ.

It is fairly common to use pseudorapidity, defined as $\eta = -\ln\tan(\theta/2)$, instead of polar angle. If a particle flies perpendicular to the beam line, that is at an angle $\theta = \pi/2$, then its pseudorapidity is equal to zero. The advantage of using pseudorapidity over the polar angle is that differences in the former remain invariant under Lorentz boosts along the collision axis, which helps to construct an invariant measure for the angular separation between two particles i and j under such boosts using

$$\Delta R_{ij} = \sqrt{(\eta_i - \eta_j)^2 + \underbrace{(\phi_i - \phi_j)^2}_{\in[-\pi,\pi]}}. \tag{3.4}$$

Some example pseudorapidity values and corresponding polar angles are listed in Fig. 3.6(b). Longitudinal view of the CMS detector in Fig. 3.7 shows the coverage of individual subdetectors in terms of pseudorapidity. A related quantity is rapidity, which is defined as

$$y = \frac{1}{2}\ln\left(\frac{E - p_z}{E + p_z}\right),$$

where E refers to particle energy. Similarly to pseudorapidity, it remains invariant under Lorentz boosts in the direction of the z-axis. At energy scales much higher than the particle mass, rapidity becomes approximately equal to pseudorapidity. Spatial distances ΔR^y_{ij} in y–ϕ plane are computed analogously to Eq. (3.4), but with pseudorapidity coordinates swapped for rapidity coordinates.

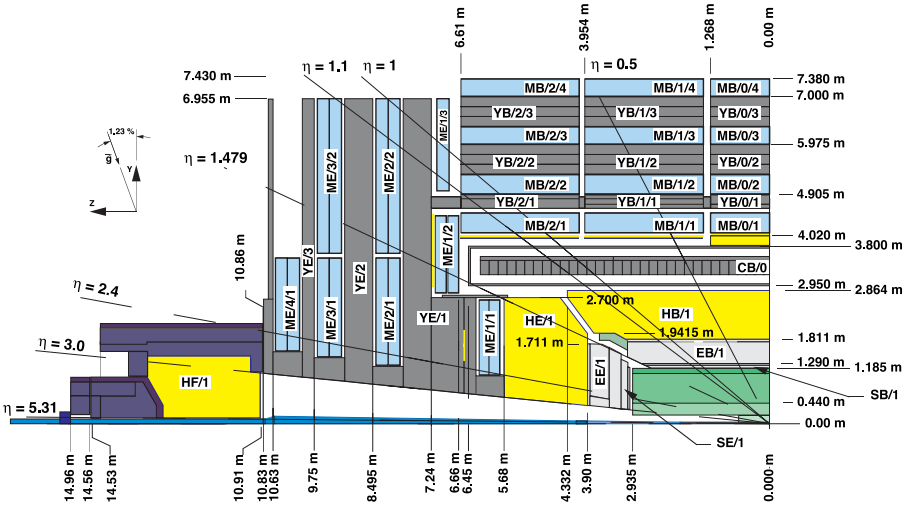


Figure 3.7: Longitudinal view of a quadrant of the CMS detector that highlights the following subdetectors and structural elements [260]: tracker (green); ECAL (white) split between barrel (EB) and endcap (EE) regions; HCAL (yellow) in barrel (HB), endcap (HE) and forward (HE) regions; muon detectors (blue) in barrel (MB) and endcap (ME) regions, interleaved with the steel yoke (YB and YE, in gray). Muon detectors are segmented into five „wheels" in the barrel region or into two „rings" in the endcap region (both enumerated by the first number), and into four „stations" in both MB and ME (indicated by the second number). Magnetic field generated by the solenoid (CB) points from left to right.

In addition to the transverse momentum defined in Eq. (3.3), it is sometimes advantageous to employ transverse momentum in an analysis. The observable is expressed as

$$m_T = \sqrt{E^2 - p_z^2} = \sqrt{p_T^2 + m^2}\,, \tag{3.5}$$

where m denotes particle mass. As explained in Section 4.1.5, it provides a viable handle for estimating the mass of particles or energy scale of processes that feature a mixture of visible (leptons, jets) and invisible (neutrinos) decay products. The observable remains invariant under Lorentz boosts along the collision axis.

3.2.1 Tracker

Particles produced from pp collisions first encounter silicon material of the tracker [261]. The particles would ionize the silicon atoms while passing through the substance, leaving behind charges that are collected by electrodes under some bias voltage at different points in the detector. The position and time of these charges is then registered, which enables the tracking of particles that interacted with the silicon material. Spatial resolution of the tracker is therefore dictated by the spacing of the electrodes in a silicon module and alignment of the modules around the beam line. The found tracks are fed into various algorithms that aim to reconstruct and identify these particles. The ionized paths can be traced down to a common point where the HS collision took place, or to secondary vertices that resulted from decay processes of particles with distinct lifetimes such as b hadrons. Because the particle tracks are very close to each other at the collision point but then spread out over some distance, the spatial resolution of the tracker is understandably highest near the collision point. The whole tracker is cooled down to temperatures below $-10\,^{\circ}$C, which prevents the on-site electronics from entering a positive feedback loop of

self-heating and increasing leakage current that eventually damages the instruments.

At the core of the tracker is the pixel detector, which is surrounded by a collection of silicon strip detectors. From its initial construction until the end of 2016 data-taking period, the barrel portion of the pixel detector (BPIX) consisted of three $54\,\text{cm}$ long layers of silicon sensors, which were installed 4.4, 7.3 and $10.2\,\text{cm}$ away from the beam line. The barrel region was complemented by two endcap disks in the forward region (FPIX) from both ends. The disks were placed perpendicularly around the collision axis at 34.5 and $46.5\,\text{cm}$ from the IP. The last BPIX layer covered pseudorapidity range of $|\eta| < 1.3$, while the FPIX extended the coverage to $|\eta| < 2.5$. Each silicon sensor with its supporting structure, readout electronics and cooling were engineered to minimize the material budget, which was necessary to avoid disturbing the particles that penetrate the tracker as much as possible. The small area of $100 \times 150\,\mu\text{m}^2$ of each silicon pixel resulted in a high spatial resolution of 10–$25\,\mu\text{m}$.

The pixel detector was completely swapped out for a new one after the 2016 data-taking period concluded [262]. The Phase 1 upgrade was necessary to counter increasingly intense luminosity conditions in the following years. The new BPIX now had four layers of pixels, which were moved to radii of 2.9, 6.8, 10.9 and $16\,\text{cm}$. The FPIX also received an additional disk, however, all three disks were separated into mechanically independent half-rings, which eased the installation process. In addition, the on-site readout chips and cooling system were also renewed during the upgrade. Comparison of the pixel detector alignment before and after the upgrade is available in Fig. 3.8.

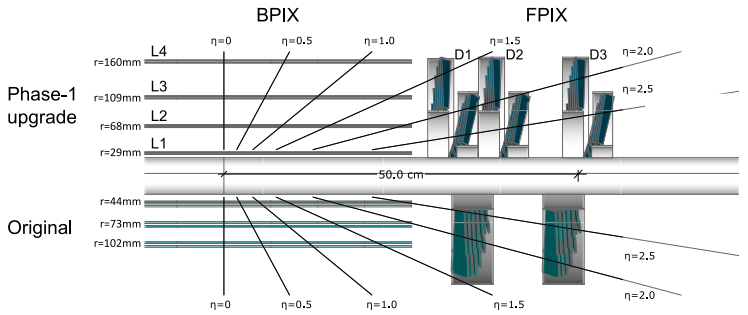


Figure 3.8: Layout of one quadrant of the pixel detector before the Phase 1 upgrade (below) and after the upgrade (above) in longitudinal view [262].

As shown in Fig. 3.9, the surrounding silicon strip detector is divided into multiple regions based on the position and alignment of its layers: tracker inner barrel (TIB), tracker inner disks (TID), tracker outer barrel (TOB) and tracker endcaps (TEC). The silicon strip detector is installed around the beam line, occupying a region of 22.5–$113.5\,\text{cm}$ in radial direction and 248–$564\,\text{cm}$ in longitudinal direction. Due to lower particle flux in the outer layers of the tracker, radial strips instead of close-to-square pixels are used in the strip detector as a cost-saving measure. The average size of silicon strips varies from $10\,\text{cm} \times 80\,\mu\text{m}$ in the innermost layers of TIB to $25\,\text{cm} \times 180\,\mu\text{m}$ in the outermost disks of TEC, which lowered the spatial resolution by an order of magnitude compared to the pixel detector. However, thanks to the higher number of layers and disks, the strip detector is able to provide many more measurement points than the pixel detector.

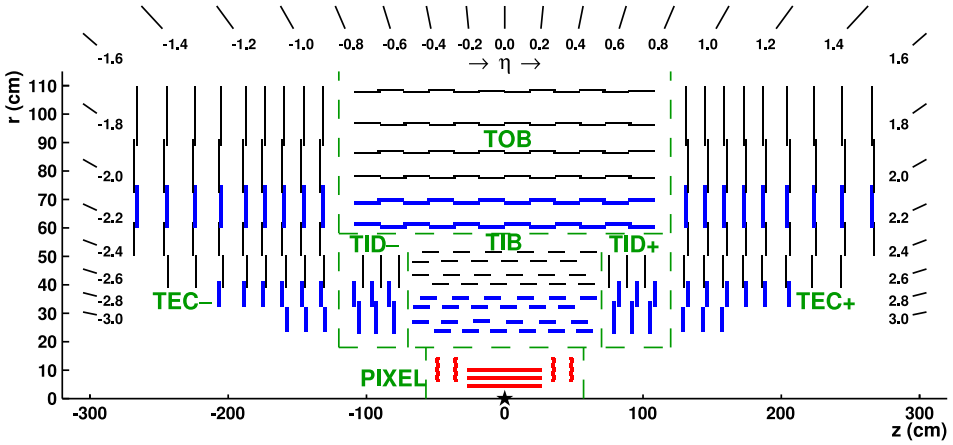


Figure 3.9: Longitudinal view of the CMS tracker, including its pixel detector before the Phase 1 upgrade [263]. Silicon strips shown by thin black (thick blue) lines provide measurement in two (three) coordinates, which is achieved with a single (double) layer of silicon strip modules. The pixel detector, which is indicated by thick red lines, also measures coordinates in three dimensions in each layer.

3.2.2 Calorimeters

The next detector subsystem that the particles meet is the ECAL, which is followed by the HCAL. Both units intend to quantify the absorbed energy of all particles but the muons. Electrons and photons are stopped in the ECAL, while hadrons pass through the ECAL but are eventually absorbed into the HCAL material.

When an electron enters the ECAL volume and interacts with the calorimeter material, it may prompt the electron to emit a *bremsstrahlung* photon. Photons, on the other hand, convert into electron-positron pairs while traversing through the calorimeter. The cascade of *bremsstrahlung* emissions ($\mathrm{e} \to \mathrm{e}\gamma$) and photon conversions ($\gamma \to \mathrm{e}^+\mathrm{e}^-$) continues until the remaining particles lose their last bit of energy through ionization. An incident electron or photon that enters the ECAL would lose a fraction of $(1 - e^{-X/X_0})$ of its energy after passing through the detector material of thickness X and radiation length of X_0. It follows that a small radiation length of the absorption material allows for more compact calorimeters. Lateral spread of the EM showers is characterized by Molière radius R_M, which is equal to the width of the shower that contains 90% of its energy on average. Smaller R_M is preferred because it would result in more localized showers.

The working principle of HCAL is very similar: once a hadron enters the calorimeter bounds, it splits into lighter hadrons such as pions. The avalanche of light hadrons proceeds until the energy for the inelastic collisions to continue has been exhausted. In analogy to radiation length that characterizes the ECAL material, the longitudinal development of hadron showers is described by nuclear interaction length of the HCAL material, λ_I. Hadron showers are typically more diffuse and longer compared to EM showers.

The ECAL is constructed from $61\,200$ lead tungstate ($PbWO_4$) crystals, which are mounted at $r = 1.29\,\mathrm{m}$ from the beam line in the barrel part (EB). It is complemented by 7324 crystals on either side at $|z| = 315.4\,\mathrm{cm}$, which constitute the endcaps of the ECAL (EE). The EB covers a fiducial volume of up to $|\eta| < 1.479$, which is extended to $|\eta| < 3$ by the EE. Preshower detectors (ES) are placed in front of the EE crystals in regions $1.653 < |\eta| < 2.6$. Geometrical arrangement of the ECAL modules is depicted in Fig. 3.10.

The scintillating lead tungstate material has a small radiation length of $X_0 = 0.89\,\mathrm{cm}$ and a narrow Molière radius of $R_M = 2.2\,\mathrm{cm}$. The ECAL crystals have a tapered shape, with front-

facing area of R_M^2 ($1.3 \times 1.3 R_M^2$) and rear-facing area of $1.18 \times 1.18\, R_M^2$ ($1.36 \times 1.36 R_M^2$) in the EB (EE). A single crystal in the EB covers a solid angle of 0.0174×0.0174 in the η-ϕ plane and has a length that corresponds to $25.8 X_0$. The crystals in the EE are slightly shorter, measuring at $24.7 X_0$, and vary from 0.0175×0.0175 to 0.05×0.05 in η–ϕ dimension. A mechanical arrangement of 5×5 crystals forms a tower in the EB and a supercrystal in the EE.

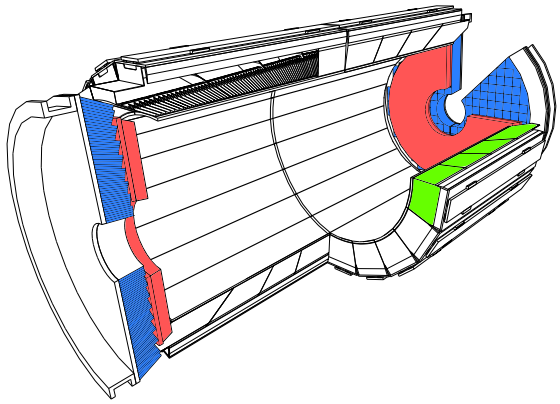


Figure 3.10: Layout of the CMS ECAL [19]: the EB (green) consisting of two sets of 18 supermodules, two „Dees" on either side of the EE (blue) and the ES (red) in front of them.

The scintillating medium is optically transparent: a charged particle that strikes the material would produce light that peaks broadly near the UV spectrum. The intensity of the generated light scales proportionally with the kinetic energy of the charged particle. The light is collected and subsequently converted into an electric signal by photodetectors, which are installed at the back of each crystal. The optical transparency of crystals is continuously monitored with lasers in order to derive corrections that compensate for fluctuations in the transparency due to irradiation and temperature. The calorimeter has to operate at a temperature of $18\,^\circ$C within $0.05\,^\circ$C margin.

Unlike the rest of the ECAL, ES is built from two layers of lead radiators that are interleaved with silicon strip sensors. The purpose of the ES is to identify neutral pions as well as to improve the positioning of electrons and photons outside the EB. With a thickness of $20\,\text{cm}$, the effective radiation length of the ES with its on-site electronics amounts to about $3 X_0$. This translates to 95% showering probability before the EM particles break out the sampling detector and reach the EE crystals.

A particle shower would extend over a cluster of ECAL crystals or „cells" in the calorimeter. An array of 3×3 cells is enough to capture approximately 94% of the energy from incident electrons or photons. Magnetic field that is generated by the surrounding solenoid causes the ECAL deposits to spread along the ϕ direction. The total energy that is associated with an electron or a photon is obtained by summing the energy deposits of adjacent cells that make up a cluster, which is then corrected according to calibration data, position, energy scale, temperature and transparency of the crystals. The energy resolution of a 3×3 cell configuration can be approximated by

$$\frac{\Delta E}{E} = \frac{2.8\,\text{GeV}^{\frac{1}{2}}}{\sqrt{E}} \oplus \frac{0.12\,\text{GeV}}{E} \oplus 0.3\%\,, \tag{3.6}$$

where the first term on the right-hand-side stands for the stochastic fluctuations in the response of photodetectors, the second term models noise from electronics, digitization

and PU, and the last (constant) term captures nonuniformities of the crystals, calibration errors and energy leakage. Electron and photon clusters can be discerned from each other by looking for tracker tracks that are aligned with the cluster: electron clusters have a track pointing towards them, while photons do not leave any tracks in the tracker.

The HCAL consists of four subdetectors: barrel (HB) and endcap (HE) calorimeters, which are installed inside the solenoid, plus forward (HF) and outer (HO) calorimeters, which are placed outside of the solenoid. The arrangement of each subsystem can be found in Fig. 3.11. Unlike the ECAL, which is a homogeneous calorimeter, the HCAL is a typical sampling calorimeter: it is built from alternating layers of a passive absorber and an active medium. The purpose of the absorber is to initiate particle showers, while the active sensors measure the energy that is deposited into them. Since only a fraction of total energy is actually detected in the active layers of HCAL, the total energy of a hadronic jet must be inferred from the calibration. In addition, about two thirds of hadron energy would already be lost to tracker and ECAL regardless. Considering that the material budget of the tracker amounts to just $0.02\lambda_I$ in central rapidities [262], most of the lost energy would be deposited to $PbWO_4$ crystals of the ECAL, which account for $1.1\lambda_I$ [24]. Because of these reasons the energy resolution of the HCAL is much lower compared to the ECAL. Experiments prior to the LHC Run 1 data-taking period with a test beam comprising mostly electrons and pions revealed that the combined energy resolution of EB and HB amounts to [264]:

$$\frac{\Delta E}{E} = \frac{84.7\%}{\sqrt{E}} \oplus 7.4\%\,,$$

thus demonstrating that the uncertainties on the deposited energy are dominated by random fluctuations of the sampling. This is also consistent with the jet energy measurement studies performed in LHC Run 1, where it was found that the uncertainty on the jet energy in central rapidities varies between 15 and 20% for jets with $p_T < 30\,\text{GeV}$, and can go as low as 5% for jets with $p_T > 1\,\text{TeV}$ [265]. The uncertainties increase with $|\eta|$.

Both halves of the HB are built from 18 tapered brass wedges, each of which is sandwiched between steel plates for keeping them in place. The wedges are installed $1.77\,\text{m}$ from the beam line, thus covering a fiducial region of $|\eta| < 1.392$. Each wedge is $313\,\text{cm}$ long when measured from the beam-facing side, $96\,\text{cm}$ thick and weighs about $26\,\text{t}$ [266]. The wedges are segmented into 16 „towers" in $|\eta|$ and into four azimuthal sectors in ϕ, such that each tower covers a solid angle of 0.087×0.087 in the η-ϕ plane. One such segment of the brass absorber has 16 trays for plastic scintillators, which are evenly spaced throughout the wedge. At $\eta = 0$, the effective thickness of the HB with its supporting steel plates amounts to $5.8\lambda_I$, which increases with decreasing θ as a function of $1/\sin\theta$.

The 36 wedges of the HE are constructed from the same very same active and passive materials. The wedges are positioned around the beam line $4\,\text{m}$ from the collision point on either side of it. Each wedge is divided into another 14 towers in $|\eta|$ and embeds 17 layers of plastic scintillators. Since the HE occupies a volume that spans $1.3 < |\eta| < 3$, its first tower overlaps with the last tower of the HB. At $|\eta| > 1.6$, the granularity of the HE amounts to 0.17×0.17 in η-ϕ. Its angular resolution improves to the level of HB at $|\eta| < 1.6$ because the number of scintillators doubles in more central towers.

The scintillators in both HB and HE emit UV light when encountering a hadron. The light is then shifted to green spectrum by fiber optics and transferred to hybrid photodiodes (HPDs), which convert the light to electric signal and amplify it before sending the signal to the front-end electronics system for further processing. Some HPDs in the HE were replaced with silicon photomultipliers (SiPMs) during Phase 1 upgrade of the CMS detector, in order to improve the detection efficiency and resilience against radiation damage [267].

After a successful testing period, the remaining HPD in the HE were also swapped out for SiPMs during the technical stop between 2017 and 2018 data-taking years.

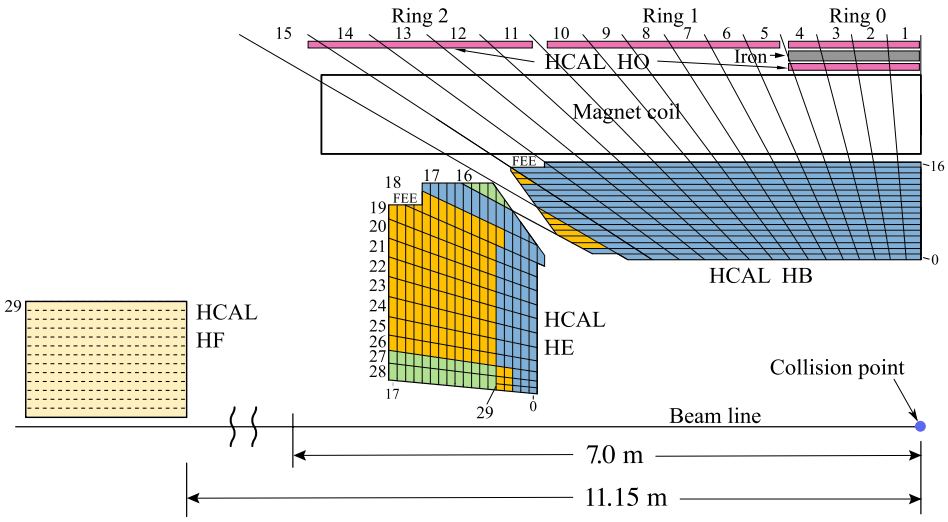


Figure 3.11: Segmentation of the CMS HCAL [19]. The outer numbers (1–29) enumerate the η towers, while the inner numbers (0–16 in HB, 0–17 in HE) count the layers in a calorimeter tower. The different colors represent a group of scintillator units that can be read out and calibrated separately (before the Phase 1 upgrade).

Moving further up in $|\eta|$, the next HCAL subdetectors the particles encounter are the two steel cylinders of HF, which are located $11.2\,\mathrm{m}$ from the collision point and cover a pseudorapidity region of $2.85 < |\eta| < 5.2$. Both of those units have a thickness equivalent to $10\lambda_I$, an outer radius of $130\,\mathrm{cm}$ and a $25\,\mathrm{cm}$ wide hole at the center for the beam to pass through. The steel blocks are split into 13 rings radially and 18 sectors laterally. The resulting calorimeter towers span an angular section of $\Delta\eta \times \Delta\phi \simeq 0.17 \times 0.17$ each. The HF measures Cherenkov radiation, which is emitted by charged particles when they travel at speeds exceeding that of light in the medium. The Cherenkov light that is produced by particle showers inside the steel absorber is registered by quartz optics. The optical lines that are installed into the grooves of both steel blocks guide the light signal out of the absorber to readout electronics. In order to protect the on-site electronics from intense radiation damage, the HF is housed in a compact radiation shield made of concrete and steel.

The purpose of the HO is to catch remaining hadrons that punch through the EB, HB and the magnetic solenoid, and thereby to further improve the estimate of total transverse momentum of all reconstructed particles. The barrel region of $|\eta| < 1.3$ spanned by the HO is split into five radial rings in η and twelve sectors in ϕ. The segmentation in ϕ follows closely the barrel structure of the muon system. In order to increase the effective thickness of the calorimeter where the absorption depth is minimal, a $19.5\,\mathrm{cm}$ thick steel slab is squeezed between two scintillator tiles of the central ring. The remaining rings have just one layer of scintillators, since the particles that enter the outer rings would have to pierce through more material and hence do not require extra medium to stop the particles. The scintillation light is read out by SiPMs, which have been employed in the HO since the very beginning of LHC Run 2 data-taking period [268].

3.2.3 Muon detectors

Muons typically fly through the tracker and calorimeters, but may lose a little bit of energy while doing so. However, hadrons are much less likely to punch through the same amount of material, since the effective absorption depth of the calorimeters alone already amounts to no less than $11.8\lambda_I$. In order to identify muons, measure their 3-momentum, and trigger the on-site instruments to select the collision event, four layers of muon detectors called „stations" are installed between iron yoke plates outside of the magnetic solenoid in both the barrel and endcaps, as indicated in Fig. 3.7. The muon barrel system employs drift tubes (DTs), which extend to $|\eta| < 1.2$, while muon endcaps rely on cathode strip chambers (CSCs), which cover pseudorapidity region of $0.9 < |\eta| < 2.4$ and thus slightly overlap with the barrel region. Resistive plate chambers (RPCs) are present in both barrel and endcaps to provide fast signals for triggering purposes. Following closely the structure of iron return yoke, the muon system is azimuthally divided into 12 separate sectors. An optical alignment system is used to monitor the relative position of the muon chambers with respect to the rest of the CMS detector, which can change over time in response to construction tolerances, mechanical and thermal stress, and intense magnetic fields.

The three types of gaseous detectors utilized in the muon stations are all based on the same design principle: one or several cathode and anode terminals are placed into a tightly sealed gas volume. The electrodes shape the electric field that charged particles follow. When a muon travels through the gas chambers, it ionizes the gas atoms by knocking some electrons off them. The positively charged ions and negatively charged electrons that are left behind flock towards cathode and anode, respectively. The muon track is reconstructed from the position of electrodes that collected the induced charges. Various factors are considered when designing a gaseous detector, such as acceptable spatial resolution, triggering times, cost, effectiveness and durability of materials in an extremely irradiated environment.

Muon stations in the barrel region consist of either two or three so-called superlayers that each have four staggered layers of rectangular $13 \times 42\,\mathrm{mm}^2$ DT cells. The described configuration is also shown in Fig. 3.12(a). A DT cell holds a mixture of 85% Ar and 15% CO_2 gases at standard atmospheric pressure. Like depicted in Fig. 3.12(b), it comes with five individual electrodes: one $2.4\,\mathrm{m}$ long anode wire ($+3600\,\mathrm{V}$) suspended in the middle of the cell, two anode strips ($+1800\,\mathrm{V}$) on the innermost sides of the cell and another two cathode strips ($-1200\,\mathrm{V}$) on the outermost walls of the cell. It could take at most $380\,\mu\mathrm{s}$ for an electron to reach from a cathode strip to the anode wire. The DT cells are oriented such that the outer superlayers, SL1 and SL3, measure muon coordinates in the transversal r-ϕ plane, while the middle superlayer provides the measurement in the longitudinal r-z plane. The only exceptions are the outermost muon stations, which are missing the middle layer. The intentional gap between SL1 and SL3 provides optimal resolution for measuring muon transverse momentum. The DT chambers achieve a spatial resolution down to $100\,\mu\mathrm{m}$ in the transversal plane.

As shown in Fig. 3.12(c), a CSC consists of seven trapezoidal planes that each cover either a 10° or 20° degree sector in ϕ. The six gaps between the planes are filled with a mix of 40% Ar, 50% CO_2 and 10% CF_4 gases. Copper strips are placed on both sides of odd panels and run radially outwards at constant ϕ, thus defining the azimuthal coordinate. Anode wires run along the azimuth on both sides of even panels and therefore define the radial coordinate. CSCs were better suited for endcaps because they are more robust in terms of temperature, irradiation and nonuniformity of the magnetic field. In addition, they have faster response time but a coarse $2\,\mathrm{mm}$ spatial resolution at the first trigger level.

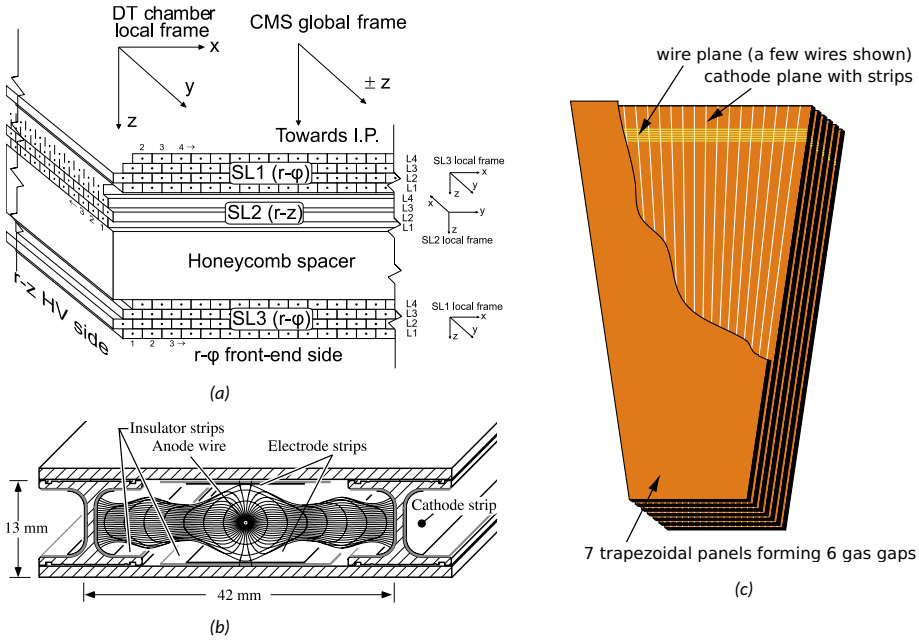


Figure 3.12: Elements of the muon system. (a): Layout of DT chambers in the muon barrel system. (b): A DT cell with its anode wire and surrounding electrode strips on each side of the cell that shape the electric field inside of it. (c): Cutaway sketch of a CSC sector. Figures (a) and (b) were taken from Ref. [260], while (c) was obtained from Ref. [19].

The RPC elements are built from two $2\,\mathrm{mm}$ thick plates of bakelite, which is a type of synthetic plastic that does not conduct electricity nor heat. The plates are separated by $2\,\mathrm{mm}$ from each other and a $9\,\mathrm{kV}$ potential is applied between them. The gap between the anode and cathode plates is mostly filled with $C_2H_2F_4$ gas. A pair of single-gap RPC elements are stacked on top of each other, with metallic readout strips between them, to form a double-gap RPC unit. The RPC units are mounted on either side of DT chambers in the first two muon stations and in front of the DT chambers in the outermost two muon stations. The RPCs are also installed in the three innermost stations in the endcap region up to $|\eta| < 1.6$. Their spatial resolution is in the order of $1\,\mathrm{cm}$, which is much worse compared to other muon detectors [269]. However, the main advantage of RPCs is their fast response time that remains well below the bunch spacing, which is ideal for triggering purposes.

3.2.4 Triggers

Not all collision events can be recorded by the CMS instruments for long-term storage because of unprecedented data rates: one BX alone would generate 1–$3\,\mathrm{MB}$ of raw data. Recording every such collision, which occurs at the rate of $40\,\mathrm{MHz}$, would fill up all known storage devices in just a few months. Besides, only a minuscule fraction of pp collisions produce the HS events that are relevant for searches of new physics. In order to filter out these „interesting" events and thereby reduce the data rates to manageable levels, advanced systems called triggers have been implemented, which decide whether or not to keep the data from a given BX. The triggering system has two tiers: a hardware-based Level-1 trigger (L1T), and a software-based high-level trigger (HLT) [270]. The event selection at the trigger level is usually referred to as „online" selection, whereas the analysis cuts that are applied on the recorded data are commonly referred to as „offline" selection.

The preliminary decision is first carried out by the L1T, which reduces the data rates from $40\,\text{MHz}$ down to about $100\,\text{kHz}$. This is achieved by fast electronic systems that are installed on-site. These devices generate a set of trigger primitives (TPs) from the deposits in the ECAL and HCAL, and from the hits in the muon chambers. The basic trigger objects go through multiple processing and evaluation steps before a global decision of approving the event is made. If that is the case, then the full detector information is read out from the buffer pipelines and passed on to the HLT.

The HLT makes the final decision of keeping the event based on global event information. It runs very simplified but fast algorithms on commodity computers that aim to reconstruct and identify various particle candidates and event-level observables, and impose cuts on them. These trigger conditions can be updated during the data-taking because the whole decision process is implemented in software. HLT reduces the data rates considerably down to about $1\,\text{kHz}$, therefore making long-term storage for offline analysis possible [271]. The offline reconstruction is run promptly after the HLT decision. This complements other data-taking paradigms, where the events are selected with special HLT requirements targeting a distinct kinematic signature, such as dimuon events in DY or dijet events in VBF production, but the event reconstruction is either significantly simplified (like in data scouting) or delayed (as in data parking) to maintain as low data rates as possible [272].

In the context of triggers, a sequence of selection criteria constitutes a trigger „path". There are hundreds of trigger paths that each probe a different aspect in physics. For instance, there are HLT paths for selecting electron candidates that each pass certain quality cuts, such as on the later spread of 5×5 ECAL cluster in η direction[10] ($\sigma^{5\times5}_{i\eta i\eta}$), on the ratio of deposited energy in the HCAL to the ECAL in η–ϕ cone of size 0.15 (H/E), or on the difference in the reciprocals of SC energy and track momentum ($1/E_{\text{SC}} - 1/p$) [273]. However, the most common way of classifying the HLT paths is by the requested number of electron, muon, and τ_{h} candidates, and the corresponding p_T thresholds that each candidate must exceed. The set of conditions that concern one particular object in the HLT path is referred to as „leg". For instance, electron-plus-muon cross triggers consist of an electron leg and a muon leg, while a triple muon trigger has three legs, one for each requested muon. If all selection conditions imposed by the trigger path are satisfied, then it said that the trigger path is „fired".

A collection of HLT paths comprise data streams, which are bundled into primary datasets (PDs) based on the HLT type. The HLT paths used in this work are listed in Table 3.2 and contribute to the following PDs: `SingleMuon` PD recorded by single muon triggers and muon-plus-τ_{h} cross-triggers; `SingelElectron` PD by single electron triggers and electron-plus-τ_{h} cross-triggers; `DoubleMuon` PD by double and triple muon triggers; `DoubleEG` PD by double and triple electron triggers; `MuonEG` PD by electron-plus-muon cross-triggers ($1\text{e} + 1\mu$, $1\text{e} + 2\mu$, $2\text{e} + 1\mu$); and `Tau` PD by double-τ_{h} triggers. In the 2018 data-taking

[10] The variable is formally defined as

$$\sigma^{5\times5}_{i\eta i\eta} = \sqrt{\frac{\sum_i^{5\times5} w_i \cdot (\eta_i - \overline{\eta}_{5\times5})^2}{\sum_i^{5\times5} w_i}},$$

where η_i refers to the pseudorapidity coordinate of the i-th crystal in a 5×5 array that is centered around the most energetic crystal at position $\overline{\eta}_{5\times5}$. The logarithmic weights are calculated as $w_i = \max\{0, 4.7 + \ln(E_i/E_{5\times5})\}$, where the ratio of deposited energies is taken between the i-th crystal and the whole cluster. It follows that crystals storing less than 0.9% of total energy are excluded from the sum. The spread in η is generally more pronounced in EE than in EB due to physically larger crystal dimensions in the former.

period, the SingleElectron and DoubleEG PDs were merged into one EGamma PD. A binary data unit called „trigger bit" is used to indicate whether or not the trigger was fired in the event. Each PD stores the status of only those HLTs that contribute to its data streams. There is no such distinction needed for MC datasets, because each simulated event contains the trigger bits of every trigger that was enabled during the data-taking.

Trigger type	HLT paths		
1e	2016: $p_T(\mathrm{e}) > 25/27^{\dagger}$	2017: $p_T(\mathrm{e}) > 32^{\dagger}/35$	2018: $p_T(\mathrm{e}) > 32$
1μ	2016: $p_T(\mu) > 22^{\dagger}/24$	2017: $p_T(\mu) > 24^{\dagger}/27$	2018: $p_T(\mu) > 24$
$1\mathrm{e} + 1\mu$	2016: $p_T(\mathrm{e}) > 23$, $p_T(\mu) > 8$	2017, 2018: $p_T(\mathrm{e}) > 23$, $p_T(\mu) > 8/12$	
	2016: $p_T(\mathrm{e}) > 8$, $p_T(\mu) > 23$	2017, 2018: $p_T(\mathrm{e}) > 12$, $p_T(\mu) > 23$	
$1\mathrm{e} + 1\tau_{\mathrm{h}}$	2016: $p_T(\mathrm{e}) > 24$, $p_T(\tau_{\mathrm{h}}) > 20/30$	2017, 2018: $p_T(\mathrm{e}) > 24$, $p_T(\tau_{\mathrm{h}}) > 30$	
$1\mu + 1\tau_{\mathrm{h}}$	2016: $p_T(\mu) > 19$, $p_T(\tau_{\mathrm{h}}) > 20$	2017, 2018: $p_T(\mu) > 20$, $p_T(\tau_{\mathrm{h}}) > 27$	
$2\tau_{\mathrm{h}}$	2016: $p_T(\tau_{\mathrm{h}}) > 35$	2017, 2018: $p_T(\tau_{\mathrm{h}}) > 35/40$	
2e	2016–2018: $p_T(\mathrm{e}) > 23, 12$		
2μ	2016–2018: $p_T(\mu) > 17, 8$		
3e	2016–2018: $p_T(\mathrm{e}) > 16, 12, 8$		
3μ	2016–2018: $p_T(\mu) > 12, 10, 5$		
$2\mathrm{e} + 1\mu$	2016–2018: $p_T(\mathrm{e}) > 12$, $p_T(\mu) > 8$		
$1\mathrm{e} + 2\mu$	2016–2018: $p_T(\mathrm{e})$, $p_T(\mu) > 9$		

Table 3.2: List of the HLT paths used in the current work. Only the p_T thresholds applied to the trigger objects are shown (in units of GeV). A combination of multiple HLT paths with different p_T thresholds was employed, either to combat higher instantaneous luminosity conditions or to take advantage of other looser selection criteria of the trigger (not shown in the table). These are also the main reasons for prescaling the triggers, since the trigger rates would otherwise be too high for data recording. Prescaled triggers are marked with a dagger (†) in the table. Different p_T thresholds on the leading, subleading and third objects are delimited by a comma. This nomenclature refers to the ranking of objects after they have been sorted by their p_T in descending order.

Offline analysis is performed on events that feature a fixed number of leptons and τ_{h} candidates in the final state. Those leptons and τ_{h} candidates that are selected to represent a particular final state of the signal must adhere to a certain quality criteria, which are detailed in Section 4.2. The requirement on the multiplicity of final state objects is further complemented by trigger cuts, whereby events are selected only if they have fired the appropriate HLT paths. In particular, if the analysis requires the presence of one, two or three leptons and any number of τ_{h} candidates in final state, then the selected events must have fired at least one single lepton trigger, a combination of single and double lepton triggers, or a combination of single, double and triple lepton triggers, respectively. Events are accepted if any of the triggers considered in the combination have fired, which effectively comes down to checking the logical OR of the corresponding trigger bits. Mixing low lepton multiplicity triggers with high lepton multiplicity triggers this way helps to boost the number of accepted events in analyses that suffer from low signal yields. If the goal is to select at least two τ_{h} candidates and no leptons, or at least three τ_{h} candidates and one lepton in final state, then a double-τ_{h} trigger is expected to be fired. Similarly, a lepton-plus-τ_{h} cross-trigger is expected to be fired in those events, where exactly one lepton and at least one τ_{h} candidate is requested in the final state. Double-τ_{h} and lepton-plus-τ_{h} cross-triggers are generally not combined with double or triple lepton triggers because higher p_T thresholds in the former do not increase the selection efficiency, but

would otherwise complicate the procedure of correcting MC yields to match data. The compatibility of final state objects with the corresponding HLT paths is improved by raising the p_T cuts on selected objects in the event selection to match the highest thresholds of the requested triggers, whereby the p_T cuts are progressively lowered in accordance with the thresholds imposed in subleading trigger legs. Based on the triggers paths that are listed for 2016 data-taking period in Table 3.2, the minimum p_T thresholds should be about $25\,\text{GeV}$ for the leading lepton, $12\,\text{GeV}$ ($10\,\text{GeV}$) for the subleading lepton (muon) and $9\,\text{GeV}$ for the third lepton. Likewise, a selected lepton is required to pass more stringent cut of $|\eta| < 2.1$ to match the maximum pseudorapidity threshold of the lepton leg in lepton-plus-τ_h cross-triggers. The same principle of imposing more stringent thresholds to match those of the triggers apply to selected τ_h candidates that are expected to trigger lepton-plus-τ_h cross-triggers or double-τ_h triggers: the p_T threshold that is applied to the leading τ_h candidates must be increased to at least $30\,\text{GeV}$ and the cut on maximum $|\eta|$ should be decreased down to 2.1 when selecting the events with the cross-trigger, or to a minimum of $35\,\text{GeV}$ on both τ_h candidates when selecting events with the double-τ_h trigger. In practice, the thresholds might be raised to account for the turn-on effect, by which the trigger becomes fully saturated or efficient if the triggering objects attain slightly higher p_T than what is already imposed by the trigger. The correspondence is further refined by requiring that the flavor of selected leptons matches with the HLT paths that fired in the event: if the selected event features n electrons and m muons, then at least one of the HLT paths with up to n electron or up to m muon legs must have fired.

If a collision event fires any of the HLT paths in a data stream, then the event is saved to the corresponding PDs. It follows that the same collision event can simultaneously trigger multiple HLT paths and therefore end up in different PDs. For this reason, a logic for selecting the data events had to be devised such that no data event was selected twice at the analysis level. This was achieved by attributing a priority to each PD that could potentially overlap with other PDs. Higher priority is assigned to those PDs that were collected using HLT paths with higher object multiplicity. For the same multiplicity of objects, a higher priority is given to those PDs that feature a higher number of muon legs in the corresponding HLT paths, because reconstruction and identification are higher for muons than for electrons. These guiding principles produce the following ranking of PDs, starting from the highest: `DoubleMuon`, `MuonEG`, `DoubleEG`, `SingleMuon` and `SingleElectron`.

For example, if an event fired single and double muon triggers and an electron-plus-muon cross-trigger, it would be saved to `SingleMuon`, `DoubleMuon` and `MuonEG` PDs. When those PDs are later analyzed, then the same event would be selected from the `DoubleMuon` PD but not from the other two PD. Special measures are implemented to avoid biases with respect to MC simulation that arise from flavor matching the selected leptons to HLT legs. The reasons can be understood by continuing the above example, where it is now assumed that the selection requirements succeeded in picking an electron-muon pair in final state, but failed to identify the second muon that together with the first muon caused the double muon trigger to fire in the first place. Such an event would still be selected from `DoubleMuon` PD but then rejected by the flavor matching condition, because the test is performed against trigger bits that are not present in this PD. This eventually leads to a subtle data loss compared to MC simulation. The complication is resolved by creating a separate ranking of PDs for each flavor combination of final state leptons. In the current example where two leptons are requested in final state, the ranking proceeds as follows, starting from a PD with the highest priority: `DoubleEG` and `SingleElectron` for dielectron final states; `MuonEG`, `SingleMuon` and `SingleElectron` for final states

with an electron-muon pair; `DoubleMuon` and `SingleMuon` for dimuon final states. When processing PDs not included in the ranking, then events would be selected from those PDs but they would eventually fail the flavor matching cut. To conclude the example, the data event from `DoubleMuon` PD would be rejected by the flavor matching cut just like before, but the event would ultimately be selected from `MuonEG` PD, thus closing the gap with the MC simulation.

The firing rates of some triggers can be very high if they employ too relaxed selection criteria on the trigger objects, or because the instantaneous luminosity has reached peak levels, which has the effect of producing more events per collision that fire these triggers than expected. In order to maintain reasonable data rates, the effectiveness of such triggers would have to be reduced by „prescaling" them. A trigger that is prescaled by factor f^{pre} would randomly keep only one event out of f^{pre} events that fired the trigger. Prescaled triggers are suitable for auxiliary measurements that require a lower threshold than those implemented in unprescaled triggers. The analyses presented in this work utilize a combination of primarily unprescaled triggers. Prescaled triggers are used in a few cases for maximum selection efficiency if they are temporarily prescaled at high instantaneous luminosity, or if the quality cuts on the trigger objects are slightly looser. In such instances, the prescaled triggers are always paired with unprescaled triggers, so that their combined selection efficiency remains unaffected.

Although not every event is recorded for long-term storage, it is imperative to know total integrated luminosity that was seen by the CMS instruments while it was fully operational, in order to correctly normalize the simulated MC samples. This is accomplished with the van der Meer scanning method, which infers the effective beam size from various physical observables that change in response to how the proton beams are displaced. The physical observables are measured with dedicated luminometers, which are installed in several places of the CMS detector, or directly modeled from the standard detector readouts. The integrated luminosity is estimated from the beam parameters for a given luminosity block. Total integrated luminosity over some extended period is obtained from the sum over all luminosity blocks in that period. The luminosity measurements are later overlayed with the periods of time when the detector was fully operational and the data delivered by the CMS detector in those periods passed certain quality criteria. After Following these steps, the total integrated luminosity that was initially delivered by the LHC during its Run 2 operations was reduced by 15%. The data that was analyzed in the present work is certified based on these very quality conditions. The corresponding integrated luminosities and uncertainties for each data-taking year of the LHC Run 2 period are shown in Table 3.3.

	2016	2017	2018	2016–2018
Integrated luminosity [fb^{-1}]	(35.9) 36.3	41.5	59.7	(137) 138
Uncertainty [%]				
Uncorrelated per year	(2.2) 1.0	2.0	1.5	
Total	(2.5) 1.2	2.3	2.5	(1.8) 1.6

Table 3.3: Amount of pp collision data recorded by the CMS detector in 2016 [274], 2017 [275] and 2018 [276] data-taking years when the detector was fully operational. Integrated luminosities and corresponding uncertainties that are given in parentheses refer to a preliminary recommendation that was based on the initial luminosity measurement on data collected in 2016 [277] and was later revised in Ref. [274]. Breakdown of correlated uncertainties between individual years and by systematic sources is not shown.

4 Particle- and event-level objects

Signals from the CMS detector, such as calorimeter deposits or hits in the pixel detector, need to be organized in such a way that they can be attributed to individual particles. Abstraction of raw detector data as simple particle- and event-level objects is necessary because it allows the development of common analysis methods that can easily manipulate the said objects. However, the translation of detector signals to standard particle objects is a monumentally difficult task since it requires intricate knowledge of how the particles interact with the detector, and deep understanding of cutting edge machine learning techniques in order to achieve the best possible performance. For this reason, the CMS collaboration has physics object groups (POGs), which are teams of experts who specialize in the reconstruction, identification and calibration of particle objects or event-level observables. Section 4.1 is dedicated to offline algorithms that reconstruct and identify electrons, muons, τ_{h} and hadronic jets, and event-level quantities like missing transverse energy. Section 4.2 details the selection requirements that are employed in $\mathrm{t\bar{t}H}$ and HH analyses presented in this work.

4.1 Object reconstruction and identification

Particle flow (PF) algorithm was developed by the CMS collaboration to reconstruct preliminary candidates for final state particles [259]. The algorithm links together geometrically close signals in each layer of the CMS detector. These signals can be tracks in the tracker, energy clusters in the calorimeters or hits in the muon system. A link between the different subsystems is established by extending the tracks outwards to calorimeter deposits, while taking into account the effects of the magnetic field on charged particles.

The tracks are also extrapolated towards the IP, clustered to appear from a common origin and fitted to locate the position of each vertex [263]. If a vertex is reconstructed within the luminous region where protons collide, which is also known as the beam spot, then it would be classified as primary vertex (PV). It is also beneficial to reconstruct the so-called secondary vertices (SVs) outside the luminous region, since they typically represent points where heavy hadrons decayed. The PV with the highest sum of p_T^2 of all its associated tracks is chosen as the leading PV (LV), while all other PVs would be considered as PU vertices. The degree of compatibility between the LV and one of its tracks is quantified in terms of three-dimensional impact parameter d^{LV}, which corresponds to the distance between the LV and the track at its closest approach. The corresponding line between them could be projected onto the transverse plane, which yields (signed) transversal impact parameter d_{xy}^{LV}, or onto the collision axis defining (signed) longitudinal impact parameter d_z^{LV}. Ratio between the measured impact parameter and its corresponding uncertainty, $d^{\mathrm{LV}}/\sigma_d^{\mathrm{LV}}$, defines the significance of the impact parameter. Placing upper cuts on the impact parameters and their significances helps to improve the integrity of the tracks that are associated with the LV by excluding tracks that are produced by cosmic rays or PU, which typically have large impact parameter values.

The tracks are found by joining together nearby hits in the tracker that have not already been associated with a track. The quality cuts that each hit or track has to satisfy are iteratively relaxed in order to maximize the reconstruction efficiency. The calorimeter clusters, on the other hand, are determined by first identifying a seed, which is a calorimeter cell with the highest energy. A cluster is formed around the seed by grouping together its nearby cells that contain energy above the noise level. The clustering is performed in the EB, EE, ES, HB and HE separately. Due to collimated nature of the particles in the forward region, the energy deposits in the HF are not clustered.

As already illustrated by Fig. 3.5, the modular structure of the CMS detector is based around the idea that each particle species leaves a distinct imprint in the detector. In particular, muons produce hits in the tracker and in the muon system, whereas electrons leave hits only in the tracker and end up depositing all of their energy to adjacent ECAL crystals. Photons also leave deposits to the ECAL but there are no tracks pointing towards them. Charged hadrons are found by associating tracks with HCAL clusters, however, all HCAL clusters that are not connected to a track would be interpreted as deposits by neutral hadrons.

Following these principles, in decreasing order of detection accuracy, the PF algorithm first reconstructs muons, followed electrons and isolated photons, hadrons and nonisolated photons. Once a PF candidate is reconstructed, its linked elements are excluded from the global event before the reconstruction of a new candidate is attempted. The definition of particle candidates is further refined with dedicated identification algorithms and to mitigate the effects from PU. The specifics of muon and electron reconstruction, identification and selection are detailed in Sections 4.1.1 and 4.1.2, respectively. The eventual PF candidates also enter the τ_{h} and jet reconstruction algorithms, as explained in Section 4.1.4 and Section 4.1.3. The discussion concludes with Section 4.1.5, where MET is formally defined.

4.1.1 Muons

Muon candidates that are reconstructed from tracker hits are referred to as „tracker tracks", while the candidates that are built by clustering hits in the DTs and CSCs to form segments or short track stubs, which can be stringed together by a fitting algorithm, are called „standalone tracks" [278]. In the „inside-out" approach, the tracker tracks with $p_T > 0.5\,\mathrm{GeV}$ and a total momentum $p > 2.5\,\mathrm{GeV}$ are extrapolated from the inner detector to the muon system. In case a tracker track can be successfully matched to a muon segment, then the corresponding pair would constitute a „tracker muon". In the complementary „outside-in" approach, a compatible tracker track is found for a given standalone track, both of which can be combined into a „global muon" if possible. Tracker and global muon candidates that share the same tracker track are merged into a single candidate. Muon PF candidates are derived from the properties of global and tracker muon candidates that pass certain quality criteria. The PF algorithm also takes into account the deposited energy of calorimeter clusters that appears along the path of a muon candidate. Muon energy corrections are extracted from comparing data to simulated Z boson decays and to low-mass meson resonances. The measured scale corrections are in the order of 0.2–0.3% and come with negligible uncertainties.

The CMS Muon POG has developed a list of identification (ID) criteria for muon candidates with varying degree of selection efficiency and misidentification rates [278]. As detailed in Table 4.2, the muon candidates used in the current work are required to pass either loose or medium ID definition, depending on the context. In the former case, the muon candidate must be reconstructed by the PF algorithm, and must be associated with a global muon candidate, a tracker muon candidate, or both. These conditions are sufficient for identifying „prompt" muons that originate from H, W, Z or τ decays at the LV, as well as muons from hadron decays with nearly 100% efficiency, while also suppressing the rate at which charged hadrons could be misidentified as muons. The medium ID working point (WP) for muons is designed to reject muons from in-flight decays of hadrons while keeping the efficiency for prompt muons at near maximum. A muon candidate passing the medium ID definition must satisfy the loose ID conditions and a variety of track quality requirements, which include cuts on the fraction of hits in the inner tracking system, on the degree of

compatibility between muon segments and inner tracks, and on the goodness-of-fit test statistic of globally fitted tracks.

A charge is assigned to a muon based on the curvature of its refitted („best") track. A „tight charge" condition can be imposed in some analysis channels in order to improve the quality status of the estimated muon charge. The requirement accepts the muon candidate if the relative uncertainty on the p_T of its best track is less than 20%, which corresponds to a 5σ significance for measuring the charge correctly, or equivalently to about one-in-a-million chance for assigning an incorrect charge to the muon.

In comparison to the data that was collected in LHC Run 1, a decrease in signal-to-noise ratio and a loss of tracker hits associated with a track was observed in the data that was recorded in 2015 and in most of the 2016 data-taking year (acquisition periods B–F) [279]. The problem becomes more pronounced with increased instantaneous luminosity, leading to an overall track inefficiency of about 5%. It was initially speculated that the problem was caused by an unprecedentedly higher rate of highly ionizing particles from the PU. However, the root cause was later found to be in the APV25 chip, which is responsible for reading and amplifying the signal that is detected by the silicon strips. In particular, the amplifier circuit of the chip took too much time to discharge, leaving it saturated (and effectively „blind") for the next BX. The problem was fixed at the hardware level by adjusting a parameter called feedback voltage bias before the acquisition period F in 2016 concluded. Mitigation strategies were implemented in track reconstruction and identification algorithms of muons, electrons and b jets, which improved their robustness against high instantaneous luminosity conditions.

4.1.2 Electrons

PF algorithm uses tracks that are found in the inner tracker and combines them with the calorimetry information to reconstruct electron candidates [280]. In order to capture more of the ECAL energy that is smeared by the magnetic field, the cluster area is stretched in the azimuthal direction, leading to the formation of a supercluster (SC). The reconstruction algorithm can be seeded by tracker hits, provided that there are at least two or three of those, or by ECAL SCs that store at least $4\,\text{GeV}$ of energy. The tracks are extrapolated to the ECAL in the former „tracker-driven" case or to the outermost pixel layers in the latter „ECAL-driven" approach. The tracker-based seeding method is more effective at recovering electrons that are not isolated or have a low p_T. Generic tracks are constructed by Kalman filter (KF) algorithm, which iteratively updates the extrapolated track to the next layer of the tracker, given the previous state of the track, assumptions about the particle charge, and measurements in the current layer. Both positive and negative charge hypotheses are considered in the track finding algorithm.

Electrons can already shower inside the tracker and emit bremsstrahlung photons in the process because the effective radiation length of the tracker material amounts to $0.5X_0$ at $\eta = 0$. In practice it can lead to fewer hits in the tracker layers, sudden changes or kinks in the electron trajectory, and energy losses. The energy that is lost to *bremsstrahlung* photons can be recovered by Gaussian sum filter (GSF) algorithm, which is a substantially slower version of the KF algorithm. The GSF algorithm searches for ECAL deposits in directions tangent to the track at every tracker layer crossed by the track. It is seeded by KF tracks with $p_T > 2\,\text{GeV}$ that also have a compatible energy cluster. All electron candidates are required to have a GSF track. The reconstruction efficiency exceeds 98% over the tracker acceptance, except for the narrow transition between EB and EE ($1.44 < |\eta| < 1.57$), where it can drop to as low as 80% for electrons with $p_T < 45\,\text{GeV}$. Some 1–2% of electron energy that would otherwise be lost in the tracker or due to shower leakage in the ECAL is

recovered with dedicated scale corrections. Additional smearing corrections are applied to simulated electrons in order to match the energy resolution of data[11]. Total uncertainties on these corrections are estimated to be at around per mille level of the corrected energy.

The CMS e/γ POG has trained two BDTs in order to distinguish reconstructed prompt electrons from all other electron candidates, with one training considering lepton isolation variables, like those shown in the right-hand side of Eq. (4.4), and the other training excluding them [280]. The latter version of the discriminant is used throughout this work, as it allows a more explicit control over the isolation status of selected electrons and avoids spurious correlations that typically spoil nonprompt background estimation. Both discriminants exploit a variety of shower-shape and tracker-related variables, including those implemented at the trigger level. In order to manage differences in the kinematics between soft and hard electrons and in the material budget of the tracker, the training phase space was binned by transverse energy of the lepton, $E_T = \sqrt{p_T^2 + m_\ell^2}$, and by absolute pseudorapidity. Two bins in the former (5–10 GeV and > 10 GeV) and another three bins in the latter ($|\eta| < 0.8$, $|\eta| > 0.8$ in EB, and EE) yields a total of six independent training models for each of the two discriminants. Both of them have two WPs with 80 and 90% selection efficiency, and a „loose" WP delivering close to 98% selection efficiency for prompt electrons.

A special criterion was developed to eliminate electron candidates that originate from photon conversions [281]. The so-called conversion veto rejects the electron candidate if any of its track candidates converge to a SV that is shared with the tracks of another electron candidate with opposite charge. The electron candidate is also rejected by the veto if its GSF track has missing hits in the innermost layer of the pixel detector. The electron charge is determined by at least two of the three independent measurements with a common outcome [273]: the curvature of the GSF track, the curvature of the KF track that is matched to a GSF track, and azimuthal angle between the associated ECAL SC and innermost hit of the GSF track with respect to the beam spot. In some analysis channels that are particularly sensitive to the charge of the selected leptons, a tight charge condition is applied to electrons, which requires all three charge estimates to agree with each other.

4.1.3 Jets

Products of parton hadronization form naturally a cone-like structure around the parton direction. It typically includes charged and neutral hadrons like pions and protons, but there can also be photons from neutral pion decays and leptons from weak hadron decays in the cone. Thus, a computationally efficient recipe is needed that is able to group together $\mathcal{O}(1000)$ PF candidates and produce tens of jets that may occur in a single pp collision event. Observables derived from the resulting hadronic jets should also remain stable when adding infinitesimally soft partons to the jet, or when allowing any of their constituents to split collinearly.

There are two mainstream algorithms that respect these fundamental requirements: seedless infrared-safe cone or SIScone [282], and sequential recombination clustering [283]. However, with all things equal, the former runs about two orders of magnitude slower compared to the latter, while not providing much gain in terms of quality of physics results [284]. The sequential recombination algorithm is a generalization of the classic k_t jet clustering algorithm. It is based on two distance measures, with one referring to the

[11] The concepts of energy scale and resolution are explored in more detail in the next section.

distance between two „protojets"[12] i and j, $d_{ij} = \min\{k_{Ti}^{2p}, k_{Tj}^{2p}\}\Delta R_{ij}^{y}/R_0$, and the other quantifying the distance between protojet i and the beam axis as $d_{iB} = k_{Ti}^{2p}$. Symbol k_T was conventionally used to label transverse momentum of the (proto)jet. Angular distance ΔR_{ij}^{y} between the protojets is computed according to Eq. (3.4), but with rapidity instead of pseudorapidity. The size parameter R_0 regulates the geometric size of the resulting jet in y-ϕ plane, whereas the power factor p steers the balance between geometric proximity and energy scale of its constituents. The algorithm first considers all input particles as protojets, and computes distance measures d_{iB} and d_{ij} for every single input and their pairwise combinations. If the smallest distance happens to be between two protojets, then their 4-momenta are summed to obtain a new protojet that replaces the former two protojets. However, if the smallest distance happens to be between a protojet and the beam axis, then the protojet is promoted to a jet candidate and excluded from the algorithm. These steps are repeated until there are only jet candidates left.

There are three popular implementations of the sequential recombination method: (inclusive) k_t algorithm, which is recovered by setting $p = 1$ [285]; Cambridge/Aachen (C/A), which is restored by choosing $p = 0$ [286, 287]; and anti-k_t (AK), which is realized by fixing $p = -1$ [283]. The k_t algorithm tends to cluster together soft particles first, while the AK algorithm does the opposite. The C/A algorithm makes a compromise between the two implementations, since it ignores the energy information completely and relies solely on the spatial distances. The AK algorithm has at least two favorable characteristics over the alternatives: it is guaranteed to produce circular jets with constant radius R, and the resulting jets have a stable catchment area, which quantifies contamination from PU and UE to the jet cone. The last feature plays a crucial role in the evaluation of jet energy corrections (JECs), as it allows to efficiently subtract the excess energy that enters the (active) jet area from the energy sum of its PF constituents [288–290].

All jets in this work are reconstructed with the AK algorithm. Size parameter value of 0.4 is suitable for approximating jets that result from the hadronization of single partons, while the value of 0.8 is more appropriate for capturing hadronization products from collinear pairs of quarks that are otherwise difficult to resolve, such as those resulting from hadronic decays of boosted W, Z or Higgs bosons. The corresponding jet collections are henceforth referred to as AK4 jets and AK8 jets, respectively.

This is a standard practice in CMS analyses, however, a slight modification of the AK8 algorithm was needed in order to resolve final state leptons and hadronic jets from SL $\mathrm{H} \to \mathrm{WW}^*$ decays. The issue is that a signal lepton from one W boson may be lost if it is merged with an AK8 jet from the other W boson by the reconstruction algorithm, which in turn reduces the efficiency of selecting signal events. The chances of losing final state leptons this way increase with the energy of the Higgs boson, which is especially relevant for heavy unknown resonances that decay into a pair of highly boosted Higgs bosons. One viable solution is to remove all potential signal lepton candidates from the inputs to the AK8 reconstruction algorithm. This approach was inspired by the earliest searches of resonant SL $\mathrm{HH} \to \mathrm{b\bar{b}WW}^*$ signal by CMS collaborators who tackled the very same problem [247]. Following this recipe, the AK8 jets used in $\mathrm{HH} \to$ multilepton analysis are all reconstructed without PF lepton candidates that pass the „loose" selection criteria, which are detailed in Section 4.2.1. An alternative approach that does not require a complete rerun of the jet clustering algorithm could be based on lepton subjet fractions [291], but this was never tested in the context of current work.

Several strategies are available for mitigating PU contamination in the reconstructed jets. The standard approach of suppressing the PU effects in jet reconstruction has been

[12] They are also sometimes called „pseudojets" to distinguish them from the final jet candidates.

the charged hadron subtraction (CHS) method, which excludes charged hadrons from the jet clustering algorithm if they are associated with a PU vertex [259]. The method does not account for neutral particles that can also arise from PU, however. This aspect is addressed in the PU per particle identification (PUPPI) method, which assigns a weight to every jet constituent based on the momentum collinearity of its surrounding particles [292]. Charged particles that are associated with the LV are given a weight of 1, while all other charged particles receive a weight of 0 [256]. Neutral particles are given a weight between 0 and 1 depending on their p_T and distance to other constituents. The final jet 4-momentum is obtained from the weighted vectorial sum of its constituents. The CHS and PUPPI methods perform similarly with AK4 jets, but PUPPI is more effective at suppressing the PU content in AK8 jets because of explicit handling of neutral particles that are more likely to enter the wider cone. Thus, the AK4 jets are reconstructed with the CHS method, while the AK8 jets are built with the PUPPI method.

A simulated jet is considered to arise from PU or UE activity, or from calorimeter noise if it does not have any generator-level jets within its radius. Generator-level jets are constructed from all Pythia generator-level particles, excluding neutrinos, with the same algorithm as the corresponding reconstruction-level jets, but without any PU mitigation techniques. Reconstructed jets from electronic noise are identified with the PF jet ID, which requires a certain fraction of jet energy to originate from electrons, photons, and charged and neutral hadrons, as well as asking a minimum number of neutral and charged constituents from the jet. Specific conditions can be found in Ref. [293] for the 2016 data-taking year, and in Ref. [256] for 2017 and 2018 data-taking years. Loosest possible selection WP of the PF jet ID is employed, which keeps about 99% of genuine jets and rejects 99% of „fake" jets in the central region ($|\eta| < 2.4$). The rejection rate of fake jets abruptly drops to 35% for AK4 jets and to 15% for AK8 jets in the forward region ($|\eta| > 2.4$).

Various discriminating variables and kinematic observables have been developed to facilitate the precision measurements in Higgs and EW sectors. For example, a likelihood discriminant can be applied to AK4 jets to separate quark-induced jets from jets that arise from the hadronization of gluons [293]. The quark-gluon discriminant benefits from lower constituent multiplicity, narrower momentum spread and stronger hardness of quark jets compared to gluon jets. It is not explicitly used in the jet selection, but the likelihood score does enter as input to a dedicated jet tagging algorithm that attempts to identify hadronic jets from SL $\mathrm{H} \to \mathrm{WW}^*$ decays in the $\mathrm{t\bar{t}H}$ analysis.

The multi-pronged nature of wide jets, like those reconstructed with the AK8 algorithm, can be characterized with the N-subjettiness variable τ_N [294]. It is defined as p_T-weighted average angular distance between AK8 jet constituents and closest N subjet axes that are determined with k_t clustering algorithm. A low value of τ_N tells that most of the radiation is aligned with the subjet axes, while the opposite hints that a significant fraction of the energy is further away from designated subjets and the wide jet itself may have more than just N subjets. Upper cut on the ratio $\tau_{21} \equiv \tau_2/\tau_1$ has been found to provide good discriminating power in identifying jets with double-pronged topology [256].

As detailed in Section 2.2.2, b jets share numerous detectable and unique features, which has inspired many b tagging algorithms designed to recognize them from lighter jets. Over the years, the b jet identification algorithms have evolved from a likelihood-based approach that combines secondary vertex information with track variables[13] [104] to DeepCSV classification algorithm [295], which uses a deep neural network (DNN) to distinguish b jets, c jets and light jets using high-level track and vertex features as input. DNNs have also been used to improve the energy resolution of b jets [296], which specifically improve

[13] Hence the acronym „CSV" in the following.

the sensitivity of those analyses that target $H \to b\bar{b}$ decays. Latest advancements in b jet tagging algorithms[14] have culminated with a multiclass tagger called DeepJet [168], which is a multi-tiered neural network algorithm that aims to identify jets containing one and two b hadrons, jets with leptonic b hadron decays, c jets, light quark jets and gluon jets based on low-level features. The DeepCSV algorithm can be used to tag AK4 jets as well as AK8 subjets, but the DeepJet classifier is applicable only to AK4 jets. There exists a dedicated algorithm for tagging AK8 jets, however [299].

The DeepJet architecture consists of convolutional, recurrent and dense network layers, in that order. Each of these network layers serve a certain purpose in the identification algorithm. Convolutional layers take low-level track and energy variables of individual jet constituents as input to transform and compress them to high-level features. This kind of feature engineering has its roots in kernel-based image processing, where a predefined kernel is convolved with an input image to enhance certain features (like edges) or to apply effects (like blurring) to the image. Convolutional neural networks aim to accomplish the opposite by promoting the elements of a convolutional kernel to learnable weights, thus resulting in a convolutional filter that encapsulates common features found from a series of input images. The „image" in the present context of b tagging algorithms refers to a jet, pixels in the image to its charged and neutral constituents as well as its associated SVs, and color channels of the image to the properties of each jet constituent and SV parameters. The convolutional layers are connected to long short-term memory cells in the recurrent layers, which are able to learn sequential dependencies in an unbiased way from arbitrarily-sized input data and produce fixed-length collection of features in return. Charged constituents are ordered by their impact parameter significance, neutral constituents by their shortest angular distance to a SV, and SVs by flight distance significance. Finally, the output of recurrent layers is combined with global jet information and passed to a DNN, which makes the final decision of figuring out the jet flavor. Mathematical formulation of DNNs is given in Section 6.2.3. The model was trained, validated and tested on simulated QCD multijet and FH $t\bar{t}$ events, and the jets were labeled by their generator-level hadron content.

Multiple WPs can be devised by cutting on the b tagging score to achieve a certain target identification efficiency or misidentification rate. The DeepJet b tagger comes with loose, medium and tight WPs, which correspond to probabilities of 10, 1 and 0.1% for light jets to be misidentified as b jets. The respective b jet identification efficiencies are about 94, 83 and 66%. The precise numbers fluctuate depending on the jet and event kinematics, as they tend to peak out for jets with p_T between 100 and $300\,\text{GeV}$, and for events with a low number of reconstructed PVs, for example.

The energy of reconstructed jets has to be calibrated in data and simulated MC events separately. This is achieved with dedicated JECs, which are factorized into multiple levels as shown in Fig. 4.1 [265, 290]. At the first level are the PU offset corrections, which intend to eliminate the excess energy from PU particles that might enter a given jet catchment area. These corrections are determined from simulated QCD dijet events with and without the PU-induced background. They depend on p_T, η and catchment area of the jet, and on ρ_{PU}, which is the median p_T density of soft radiation in the event [284]. Additional η-dependent corrections are applied in order to account for residual differences in UE activity when compared to the detector simulation. After the application of PU offset corrections, the jets undergo a second level of corrections to account for jet energy response $\mathcal{R}$, which refers to the ratio between reconstructed and generator-level jet p_T. The corrections are derived

[14] Algorithms based on graph neural net [297] and transformers [298] have shown to significantly improve the accuracy of jet tagging with respect to the algorithms that have been commissioned by the CMS collaboration thus far.

from simulated QCD dijet events and parametrized by jet p_T and η. Few-percent residual differences are found between data and MC simulation when considering alternative definitions of jet energy response. These are compensated with additional corrections to data that are extracted from dedicated CRs enriched with DY, γ+jets or QCD multijet events.

The final product of JECs typically amount to $\lesssim 10\%$ for jets with $|\eta| < 2.4$, but can jump up to 50% for jets entering the EE region that is not covered by the tracker. The total JEC uncertainties increase substantially from 2–4% for jets within the tracker acceptance up to 5–10% outside of it. The uncertainties more than double for AK4 jets with $p_T < 20\,\text{GeV}$ compared to AK4 jets with $p_T > 50\,\text{GeV}$ due to PU. There are eleven sources of JEC uncertainties, six of which are correlated between every data-taking year, while the other five remain uncorrelated. They account for dependencies of JECs on jet flavor composition, differences in alternative formulations of jet energy response, systematical and statistical uncertainties that arise from the JEC measurements at every level, and changing detector conditions between the barrel, endcap and forward regions. While the JECs are different between the AK4 and AK8 jets, the corresponding uncertainties are identical and fully correlated between the jet collections.

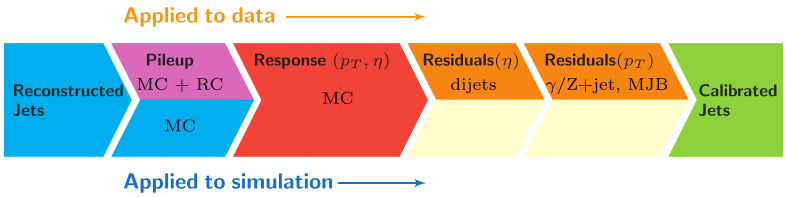


Figure 4.1: Schematic for factorized application of JECs to jets that are reconstructed in data and simulated MC events. RC (random cone) and MJB (multijet balance) refer to specific jet energy calibration methods. Image is adapted from Ref. [265].

The same JEC uncertainty scheme is used across all data-taking years. The only exception applies to the 2018 data-taking year, during the last two thirds of which the 15th and 16th HE sectors in the negative η side did not work due to a failure in their power supply unit. The effects of the so-called HEM („HE-minus") issue had to be assessed by each CMS analysis group independently. This was accomplished with a dedicated JEC uncertainty that explicitly mimicked relative energy loss in the affected areas of the detector. More specifically, a one-sided JEC uncertainty was proposed such that its down-variation corresponds to a 20% (35%) decrease in jet energy only for jets that passed the tight WP of PF jet ID, entered azimuthal slice between -1.57 and -0.87, and pseudorapidity region between -2.5 and -1.3 (-3.0 and -2.5). This uncertainty turned out to have very low impact in the analyses presented here. Additionally, no excess of data events was observed in the affected geometrical regions compared to the MC simulation after all analysis cuts had been applied. It indicates that prompt lepton selection criteria (presented in Section 4.2) remained resilient towards jets faking prompt leptons despite the ineffectiveness of the two HE sectors.

At first order, the distribution of $\mathcal{R}$ can be approximated with a simple normal distribution, the mean of which is dictated by jet energy scale (JES) and variance by jet energy resolution (JER). The purpose of JECs is to then adjust the JES such that $\mathcal{R}$ matches to unity in both data and MC simulation. This is also illustrated by Fig. 4.2, which depicts $\mathcal{R}$ for jets that have already been calibrated. The plot also shows the effects of shifting JES and JER within their uncertainties.

It turns out that the JER is higher for simulated jets compared to jets reconstructed from data. In order to mitigate this discrepancy, a special jet smearing procedure is performed on simulated AK4 and AK8 jets after they have been calibrated. The method works by scaling the 4-momentum of simulated jets by a factor that depends on relative p_T difference between reconstructed and matching generator-level jet (δp_T), and on resolution SF between the data and MC simulation ($s_{\text{JER}} \gtrsim 1$). If no matching jets are found at generator level for a given reconstructed jet, then a stochastic approach is followed instead. The fallback treatment replaces δp_T with a random sample from normal distribution that has a zero mean and a standard deviation equal to intrinsic jet p_T resolution, σ_{JER}. Typical values of σ_{JER} are $> 20\%$ and 5–10% for central AK4 jets with $p_T < 20$ and $> 100\,\text{GeV}$, respectively. Just like the JECs, jet smearing parameters s_{JER} and σ_{JER} were extracted for each individual data-taking year as piecewise-smooth functions of jet p_T and η from the same CRs where the JECs were measured [265].

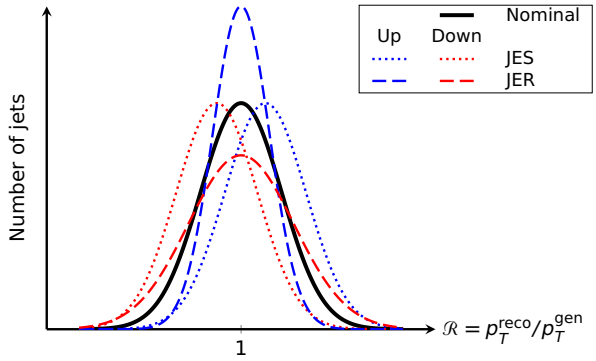


Figure 4.2: Illustrative density plot for jet energy response $\mathcal{R}$, which is defined as a ratio of reconstructed jet p_T over generator-level jet p_T. JES (dotted lines) determines the mean response, whereas JER (dashed lines) tells how the responses are spread around the mean. Either of those can be shifted up (blue lines) or down (red lines) within their designated uncertainties. Black line shows the nominal jet energy response after all JECs and smearing steps have been applied.

Total uncertainties on JER are propagated from systematic variations of s_{JER} to calibrated jets in the smearing procedure. The uncertainties can be split into multiple fully decorrelated components depending on p_T and η of the jets. This is achieved by smearing only those jets that end up in barrel, endcap or forward regions. In that case the split JER uncertainties are estimated for low-p_T ($< 50\,\text{GeV}$) and high-p_T ($> 50\,\text{GeV}$) jets separately if they are reconstructed outside of tracker acceptance.

4.1.4 Hadronic τ decay products

In about 35% of the cases a τ decays into an electron or a muon with equal probability, plus a neutrino of respective flavor. The charged leptons are detected through the usual reconstruction and identification methods presented in previous sections, while the neutrinos remain invisible to the detector. The remaining 65% of hadronic τ decay products, τ_{h}, are recovered with custom techniques as discussed below.

According to Table 2.4, about 96% of τ_{h} end up in 1-prong or 3-prong final states with up to two extra π^0. A neutral pion from a τ_{h} promptly decays into a pair of photons inside the tracker. Photons themselves may further convert to electron-positron pairs while passing through the tracker material. The collection of electrons and photons (e/γ) produced by a τ_{h} are eventually absorbed into the ECAL crystals. The corresponding calorimeter clusters

form a rectangular strip that is stretched along the ϕ coordinate by the magnetic field. The exact dimensions of the strip scale inversely with the energy of e$/\gamma$ candidates associated with the strip, because charged tracks bend less in the magnetic field if they are more energetic.

These characteristics establish the main premise of hadrons-plus-strips (HPS) algorithm, which reconstructs a τ_{h} candidate from PF candidates that are enclosed by an η–ϕ cone with radius of 0.5 around the axis of an AK4 jet seeding the algorithm [300]. Only the leading τ_{h} candidate is kept, which means that there can be up to one τ_{h} candidate per single AK4 jet. The algorithm filters out eligible charged hadron PF candidates by requiring them to have a p_T of at least $0.5\,\mathrm{GeV}$, to produce sufficient number of hits in the tracker, and to originate from the LV by requiring $|d_{xy}^{\mathrm{LV}}|$ to be less than $1\,\mathrm{mm}$. The selected tracks represent individual charged hadrons of a τ_{h} candidate.

Neutral pions associated with the τ_{h} candidate are reconstructed from e$/\gamma$ PF candidates that are confined to a rectangular strip in the η–ϕ plane not larger than 0.15×0.3 and not smaller than 0.05×0.05 in size. The strip is iteratively assembled from leading e$/\gamma$ candidates that are located within the strip boundaries but have not yet been formally included to the strip. With every additional e$/\gamma$ candidate, the position of the strip is recomputed from p_T-weighted average of its e$/\gamma$ constituents and the strip size is dynamically adjusted according to function $f(p_T^{\mathrm{e}/\gamma}) + f(p_T^{\mathrm{strip}})$, where $p_T^{\mathrm{e}/\gamma}$ refers to the transverse momentum of the new e$/\gamma$ candidate and p_T^{strip} corresponds to the vectorial p_T sum of e$/\gamma$ constituents already merged with the strip. The parametrization $f(p_T)$ follows analytic form a/p_T^b, where the input transverse momentum p_T is given in units of GeV. The parameters responsible for resizing the strip in η (ϕ) direction are given the values of $a = 0.20$ and $b = 0.66$ ($a = 0.35$ and $b = 0.71$), which ensures a 95% efficiency for selecting the correct e$/\gamma$ candidates from hadronic τ decays. The HPS algorithm proceeds to produce multiple strips that each represent a neutral pion until there are no e$/\gamma$ candidates left to consider.

Reconstructed τ_{h} decay modes are determined from the number of charged PF hadrons associated with the τ_{h} candidate and from the multiplicity of HPS strips. Only those 1-prong and 3-prong τ_{h} candidates compatible with the decay modes listed in Table 2.4 are kept for further analysis. The τ_{h} reconstruction algorithm also addresses the case where one of the charged pions in a 3-prong τ_{h} candidate fails to be reconstructed. This typically happens when the τ_{h} candidate becomes highly boosted to the point that it is not possible to resolve all of its tracks. Given that the presented analyses do not probe such high energies where this can be an issue, the alternative 2-prong decay modes will not be considered here. Correspondence to a specific meson resonance is made with the intent to maximize τ_{h} reconstruction efficiency over misreconstruction rate of jets as τ_{h} by requiring the reconstructed τ_{h} to have its mass close to primary meson resonances. The τ_{h} candidate is rejected if any of its charged constituents or strips are outside of signal cone radius defined by $\min\{\max\{3\,\mathrm{GeV}/p_T, 0.05\}, 0.1\}$.

The 4-momentum of a τ_{h} candidate is obtained from vectorial 4-momentum sum of its charged hadron and e$/\gamma$ constituents, while its impact parameters are directly copied from its leading track. The energy of a genuine τ_{h} candidate that includes up to one π^0 is corrected based on the differences between data and MC simulation in a CR enriched with DY events in $\mu\tau_{\mathrm{h}}$ final state. A reconstructed τ_{h} candidate is deemed as genuine if it is matched to a generator-level τ_{h} that is closer than angular distance of 0.3 to the reconstructed τ_{h} and has a p_T less than twice the reconstructed p_T. A generator-level τ_{h} is constructed from visible descendants of a hadronically decaying τ at the generator-level. The corrections to τ_{h} energy scale are extracted by matching the Z peak found

in visible invariant mass of the $\mu\tau_h$ system with between the data and MC simulation. The measurement was performed in bins of reconstructed τ_h decay mode for each data-taking year separately. The resulting nominal corrections range from -1.6 to 0.4%, with uncertainties fluctuating between 0.6 and 1.4%. Separate energy corrections were derived for τ_h with $p_T > 100\,\text{GeV}$ in a CR dominated by highly boosted $W \to \tau\nu_\tau$ events. The measurement was based on the reconstructed τ_h mass and yielded nominal corrections ranging from -5.6 to 4.2% with uncertainties between 1.2 and 4%.

The distinction of τ_h candidates from other reconstructed objects is improved even further with DeepTau ID algorithm, which is a multiclassifier based on neural networks that is able to simultaneously separate genuine τ_h candidates from jets, electrons and muons [301]. Similarly to the DeepJet architecture, the DeepTau network consists of convolutional layers that process low-level PF particle information to generate novel features, followed by fully connected hidden layers that combine the output of convolutional layers and high-level τ_h inputs to perform the final classification step. The low-level information is extracted from τ_h isolation cone, which corresponds to a circular region that has a radius of 0.5 from the τ_h axis in η–ϕ plane. The isolation region is divided into a grid, where each grid cell contains various attributes of the leading PF particles, such as track and vertex quality variables, PUPPI probabilities, and calorimeter information. The high-level inputs include general τ_h properties like 4-momentum and charge, multiplicity of neutral and charged constituents, isolation and vertex variables, and observables quantifying spatial energy distribution in HPS strips. The training and validation of the τ_h identification algorithm was performed on simulated DY, W+jets, $t\bar{t}$ and QCD multijet events.

The final output scores of the network are transformed into probabilities for the reconstructed τ_h candidate to originate from a genuine τ_h, a jet, an electron or a muon. Final discriminants against jets ($D_{\text{jet}}^{\tau_h}$), electrons ($D_{e}^{\tau_h}$) and muons ($D_{\mu}^{\tau_h}$) are expressed as likelihood ratios of respective probabilities. A discriminant score of 1 tells that the τ_h candidate is likely a genuine τ_h, while a score of 0 indicates that the τ_h candidate probably belongs to the alternative class of particles. A set of WPs are devised for each discriminant by cutting on the discriminant score in order to attain certain efficiency levels for identifying genuine τ_h. The resulting WPs of each discriminant are summarized in Table 4.1.

		VVTight	VTight	Tight	Medium	Loose	VLoose	VVLoose	VVVLoose
$D_{\text{jet}}^{\tau_h}$	efficiency	40	50	60	70	80	90	95	98
	misidentification rate	0.2–0.5	0.4–0.8	0.6–1	1–2	2–4	4–9	7–10	10–20
$D_{e}^{\tau_h}$	efficiency	60	70	80	90	95	98	99	99.5
	misidentification rate	0.01	0.03	0.07	0.2	0.5	1	3	7
$D_{\mu}^{\tau_h}$	efficiency	✗	✗	99.5	99.8	99.9	99.95	✗	✗
	misidentification rate			0.03	0.04	0.06	0.2		

Table 4.1: WPs of the DeepTau ID discriminant, corresponding τ_h identification efficiencies and approximate misidentification rates for low-p_T τ_h candidates, both expressed in terms of percentages [301]. Identification efficiencies are extracted from simulated $H \to \tau\tau$ events. The misidentification rates for $D_{\text{jet}}^{\tau_h}$ are obtained from simulated W+jets and $t\bar{t}$ events, and from simulated DY events for $D_{e}^{\tau_h}$ and $D_{\mu}^{\tau_h}$. Jets from W+jets sample tend to pass as genuine τ_h more frequently than jets from $t\bar{t}$ sample for the same WP. The WPs are referred to by labels given in columns. The letter „V" in WP names stands for „very", e.g., VVLoose reads as „very very loose". A cross mark (✗) means that the WP is not defined for a given label.

4.1.5 Missing transverse energy

Although neutrinos are not directly measured by the CMS detector, their integral contribution to the final state can still be inferred from momentum imbalance in the transverse plane. In particular, considering that partons initiating a HS process have no transverse momentum component, it follows from conservation of momentum that the total transverse momentum estimated from all final state particles should also equal to zero. This assumption leads to the idea of missing transverse energy (MET)[15], $\mathbf{E}_T^{\text{miss}}$, which is defined as the negative vectorial transverse momentum sum of all PF particles reconstructed in the event. The observable can be fully described by its magnitude, E_T^{miss}, and azimuthal angle, ϕ_T^{miss}.

The MET estimation includes type-1 corrections, which are obtained by propagating JECs from fully calibrated (and, in case of MC simulation, also smeared) AK4 jets with $p_T > 15\,\text{GeV}$ to the MET [302]. In order to exclude jets that overlap with electrons or photons from type-1 corrections, only those jets are considered that have an EM energy fraction smaller than 90%. For similar reasons, the energy contribution from overlapping muons is subtracted from uncorrected jet momentum in the procedure. Uncertainties due to JES and JER are propagated to the MET in a consistent way by recomputing it for every systematic variation of the jet energies.

There are three types of PF particles contributing to the MET: particles that are clustered into jets for the purpose of applying type-1 corrections, particles reconstructed as muons, electrons, photons or τ_{h} candidates, and unclustered particles that are not associated with any of the aforementioned physics objects. The energy contribution from the latter class of particles is referred to as unclustered energy [302]. Uncertainties on unclustered energy are estimated from intrinsic momentum resolution of unclustered PF candidates as a function of their p_T, η and flavor, which are then propagated to the MET.

Given that MET not only receives contributions from particles that belong to the HS event, but also particles from PU and UE activity, it may not always be the most optimal observable for gauging the total energy from final state neutrinos. A viable alternative would be to use H_T^{miss} instead, which is constructed the same way as E_T^{miss}, but only using AK4 jets with $p_T > 25\,\text{GeV}$ and $|\eta| < 2.4$, and electrons, muons and τ_{h} passing „fakeable" ID criteria as detailed in the next section. Although H_T^{miss} is more resilient against soft activity, the variable has worse energy resolution than E_T^{miss}. Both variables are strongly correlated for typical signal events that feature genuine energy loss due to neutrinos, but not so much for backgrounds such as DY, where the apparent energy loss has purely instrumental origins [303]. A compromise can be made with a linear discriminant that takes the form of $E_T^{\text{miss}}\text{LD} = 0.6E_T^{\text{miss}} + 0.4H_T^{\text{miss}}$. The discriminant was specifically designed to reject events with „fake" MET in the context of $\text{t}\bar{\text{t}}\text{H} \rightarrow$ multilepton analysis based on LHC Run 1 data. Subsequent optimization of linear coefficients and WPs of the discriminant for LHC Run 2 conditions did not result in significantly different parametrization. However, the effectiveness of the discriminant suffered, probably due to increased PU activity compared to LHC Run 1, since for the same signal efficiency of 95% at $E_T^{\text{miss}}\text{LD} > 30\,\text{GeV}$ the background rejection rate dropped by a factor of 2 to about 40%. Minimum threshold on $E_T^{\text{miss}}\text{LD}$ is imposed in the event selection of analysis channels, where the anticipated signal process is expected to produce at least two leptons plus some neutrinos, with the primary goal to reject background events that feature one or multiple Z bosons. The conditions are tightened if the final state feature leptons that have the same flavor and/or same charge, and relaxed if there are sufficient number of jets in the event as expected

[15] The acronym likely comes from pronouncing it as „missing E-T".

from signal process.

MET can be useful in gauging the mass scale of a particle or the energy scale of a whole process when combined into a transverse mass like quantity with other visible particles. For example, in single W boson production events, the transverse mass of a W boson can take the following form:

$$m_T(\ell, \mathbf{E}_T^{\text{miss}}) = \sqrt{2 p_T^{\ell} E_T^{\text{miss}} (1 - \cos\Delta\phi)}\,, \tag{4.1}$$

where $\Delta\phi$ refers to the azimuthal difference between MET and its descendant lepton ℓ, and p_T^{ℓ} stands for the reconstructed transverse momentum of the lepton. This expression follows directly from Eq. (3.5) after replacing neutrino momentum with MET, and assuming that the lepton has negligible mass compared to its energy [24]. Its value peaks around m_{W}, but is smeared by longitudinal momentum imbalance, which randomly boosts the W boson to positive or negative direction in z coordinate. A similarly defined observable is

$$\sqrt{s}_{\text{min}}(\text{vis}) = \sqrt{m_{\text{vis}}^2 + 2(m_T^{\text{vis}} E_T^{\text{miss}} - \mathbf{p}_T^{\text{vis}} \cdot \mathbf{E}_T^{\text{miss}})}\,, \tag{4.2}$$

which provides an estimate for the minimum energy scale necessary for producing visible particles („vis") with combined 3-momentum $\mathbf{p}_{\text{vis}}$ and mass m_{vis} [304, 305]. The observable proves to be especially useful in searches of a resonant HH signal, because the resonant mass directly dictates the overall energy scale of the process.

One could also use MET as a constraint when quantifying kinematic compatibility between reconstructed events and some signal topology. In particular, a possible decay chain of a signal process may feature mother particles p_i whose masses $m(p_i)$ are known with an experimental uncertainty $\sigma(p_i)$. Every mother particle eventually decays into daughter particles d_{ij} in the final state, which features fully reconstructed leptons and jets, but also undetected neutrinos ν_k. To ascertain neutrino momenta, one can evaluate how much off-shell each intermediate particle goes relative to its uncertainty under the additional constraint that the transverse momentum of neutrinos always remains consistent with the MET:

$$\chi^2 = \min_{\sum_k \mathbf{p}_T(\nu_k) = \mathbf{E}_T^{\text{miss}}} \sum_i \frac{(m^2(p_i) - m^2(\sum_j d_{ij}))^2}{\sigma^4(p_i)}\,. \tag{4.3}$$

By randomly sampling over the neutrino angles and transverse momenta, one can evaluate Eq. (4.3) to find the best configuration of neutrinos that is compatible with the expected topology. Determining the neutrino momenta is not important here; instead it is the fact that one can evaluate Eq. (4.3) for a range of topologies to obtain the most compatible one. This is the premise behind Higgsness and topness variables, which quantify Eq. (4.3) for DL HH $\to \text{b}\bar{\text{b}}\text{WW}^*$ signal and for DL $\text{t}\bar{\text{t}}$ background events [305, 306]. The topness score alone can be exploited to detect and reject $\text{t}\bar{\text{t}}$ background in analyses where this process is expected to surface. One can similarly determine the so-called m_{T2} variable, which is the transverse mass of the whole decay chain that is most compatible with the reconstructed final state [307, 308].

The activity of an event can be generally characterized by the H_T variable, which corresponds to the scalar p_T sum of all selected leptons, τ_{h} and jets in the event. Adding it to E_T^{miss} defines another useful quantity called S_T^{MET} [309], which bears similarities with the standard transverse mass observable, since both peak broadly at around the invariant mass of some resonant particle. Both H_T and S_T^{MET} also tend to have quite pronounced tails in their respective distributions of HH signal events compared to backgrounds, which make them good candidates for signal extraction.

Data events with abnormally high MET can occur for a variety of reasons. Spurious MET may arise from noise caused by the sensors and readout electronics of calorimeters, from beam halos induced by proton interactions with its surrounding pipe instrumentation or with residual gas molecules left in the vacuumed tunnel, and from reconstruction errors. For each of those cases, a set of algorithms or „filters" have been developed that clean or reject events with anomalously high MET, which can otherwise lead to more pronounced tails beyond the TeV scale in its respective distribution [302]. The filters are able to catch about 85–90% of anomalies with a false positive rate of just less than 0.1%.

All analyzed data and simulated MC events are required to pass a total of seven different MET filters in order to eliminate events with anomalous MET. First, there are filters that locate noisy HPDs in the HCAL by analyzing the geometrical distribution, shape and timing of signal pulses. A complementary filter is employed to find isolated instances of noise in the HCAL by comparing deposition patterns to those found in the ECAL. The total accumulated energy of every ECAL tower can be accessed through corresponding L1T ECAL TP. However, in a limited number of ECAL towers, the energy registered by individual crystals cannot be retrieved due to lack of appropriate data links. If those towers hold more energy than what would be possible to encode in a single TP, then it would cause the measured energy to be underestimated. In addition, some 3–5 supercrystals of the EE were known to create random high-amplitude noise pulses. These rare issues with the ECAL are addressed with another pair of dedicated filters. Beam halo interactions may produce muons of several hundred GeV that can occasionally reach the detector. Such muons generally leave identifiable traces to calorimeters and CSCs along a line of constant azimuth. Likewise, high-p_T muon tracks with poor momentum resolution can also cause anomalies in the MET estimates. Both of these pathological cases are handled by separate MET filters. Finally, there is a filter that requires the presence of at least one high-quality PV in the event, which helps to mitigate effects from PU interactions. A PV is deemed high-quality if it is reconstructed within BPIX boundaries with a sufficient number of compatible tracks.

Despite the described efforts to reduce massive tails in MET, the excess was still observed in 2017 data. The root cause for this was found to be a regression in the ECAL readout algorithm, which had the effect of amplifying electronic noise in the EE. The recommended short-term solution was to exclude all jets with $p_T < 50\,\text{GeV}$ in region of $2.65 < |\eta| < 3.139$ from MET calculations as well as from analysis phase space. Both proposals are followed here.

4.2 Object selection criteria

An analysis channel is defined based on the multiplicity of selected physics objects, which are supposed to represent final state particles of a particular signal process. These objects should adhere to certain quality criteria that exploit the difference in kinematic properties between signal and common background processes, but also take into account the effectiveness of the detector and triggers. However, reconstructed objects are generic by default and do not adhere to all of the requirements that are specific to a given analysis. Additional ID requirements are thus imposed on the reconstructed objects in order to improve their level of correspondence with particular analysis channels.

The present section gives a detailed overview of the object-level cuts that are applied to reconstructed leptons, τ_h and jets in $\text{t}\bar{\text{t}}\text{H}$ and HH multilepton analyses. Section 4.2.1 describes the baseline ID criteria for selecting electrons and muons. This is followed by Section 4.2.2, which documents the selection requirements for final state electrons and muons. The next section after that, Section 4.2.3, defines fakeable leptons, which are

needed for estimating nonprompt background in the SR. The discussion concludes with Sections 4.2.4 and 4.2.5, which detail the selection of final state τ_h and jets, respectively.

4.2.1 Baseline selection for leptons

A common baseline or „loose" lepton selection is defined for the purpose of performing certain standard procedures. In particular, loose leptons are used for the „cleaning", which entails the removal of reconstruction duplicates based on their proximity to other objects in the η–ϕ plane. A reconstructed electron is rejected if it happens to be closer than R_ℓ to a loose muon, where the symbol R_ℓ refers to intrinsic lepton cone size of 0.3. Similarly, a reconstructed τ_h is exempt from further analysis if it overlaps with a loose muon or a loose electron within R_ℓ. Reconstructed muons are never cleaned, however. This order of priority between the different physics objects is based on the effectiveness of corresponding reconstruction algorithms. The cleaning step therefore resolves ambiguities that arise from geometrical overlapping of reconstructed objects.

Loose leptons are also used to formulate event selection criteria for rejecting events that feature a Z boson, which is commonly found in background events, or resonances from low-mass mesons like J/Ψ or Υ, since this particular phase space region is not well modeled with the present MC simulation nor relevant in the current work. The decision of rejecting a given event is based on the invariant mass of the presumed resonance, which can be approximated by the invariant mass of its decay products. Since those resonances can produce a pair of leptons that have the same flavor but oppositely-signed charges (SFOS), a cut on the invariant mass of the lepton pair, $m_{\ell\ell}$, is utilized to reject such events. In case of meson resonances, the angular separation between the leptons also tends to be much smaller than R_ℓ, however. This presents a problem if a low-mass meson decays into a pair of muons, but one of the muons leaves significant energy deposits to the ECAL through FSR photons. This muon could be incorrectly reconstructed as an electron and thus immediately removed from the event after the cleaning step because of its close vicinity to the second muon from the meson decay. Therefore, events with a genuine low-mass meson resonance could still evade the veto if only cleaned loose leptons are considered. For these reasons, events with low-mass meson resonances are rejected if there exists a pair of loose uncleaned leptons with an invariant mass of less than $12\,\text{GeV}$. Events featuring a Z boson are suppressed by requiring that the event contains no pair of SFOS loose cleaned leptons with an invariant mass closer than $10\,\text{GeV}$ to the Z boson mass. The Z boson veto is always applied in channels that require at least two leptons in the final state.

The SRs of CMS analyses that search for $\text{H} \to \text{ZZ}^* \to 4\ell$ events in single Higgs boson production [122] or in $\text{HH} \to \text{b}\bar{\text{b}}\text{ZZ}^*$ production [239] may potentially overlap with the SRs of $\text{t}\bar{\text{t}}\text{H}$ and HH analyses presented here. The overlap would induce spurious correlations that are difficult to model when eventually combining the results of single Higgs boson analyses with those of HH searches. This is also the reason why single Higgs boson processes are considered as background in HH analyses. A veto is designed to minimize this overlap by requiring that there are no two pairs of SFOS loose leptons with a combined invariant mass of less than $140\,\text{GeV}$ in the event. The condition is always imposed in channels that require four leptons in the final state.

The selection criteria for loose leptons is intended to maximize the signal efficiency by retaining as many prompt leptons as possible. The specific cuts were formulated based on the guidelines from the CMS Muon and e/γ POGs. These recommendations are combined with the lowest thresholds of the HLT paths listed in Table 3.2, in order to make sure that none of the leptons that fired the trigger during the data-taking are

rejected by the offline cuts. Following these principles, a loose muon is expected to have a p_T of at least $5\,\text{GeV}$, which is raised to a threshold of $7\,\text{GeV}$ for loose electrons. Maximum reconstruction and triggering efficiency is maintained if the loose muons are reconstructed inside the muon system and loose electrons within the tracker acceptance. Thus, a centrality requirement is imposed with a cut of $|\eta| < 2.4$ on loose muons and $|\eta| < 2.5$ on loose electrons. Additionally, loose leptons must be associated with the LV by satisfying the requirements of $|d_{xy}^{\text{LV}}| < 0.5\,\text{mm}$, $|d_z^{\text{LV}}| < 1\,\text{mm}$ and $d^{\text{LV}}/\sigma_d^{\text{LV}} < 8$. These conditions have the effect of dismissing leptons that originate from PU interactions and also those with poorly reconstructed tracks. Loose leptons are also required to pass the loosest WPs of their respective POG ID criteria, which are designed to identify prompt leptons as opposed to nonprompt leptons or jets misreconstructed as leptons. Throughout this work, only the CMS e$/\gamma$ POG ID that was trained without the isolation variables is used, in order to avoid complication that may arise from estimating nonprompt background with data-driven techniques. A loose electron track is expected to leave a hit in each layer of the pixel detector, except for at most one layer that is allowed to not have any hits associated with the track.

After applying all of these requirements in the loose lepton selection, weak hadron decays still remain as major source of nonprompt leptons, since nonprompt leptons arising from PU activity or reconstruction errors are already suppressed with cuts on impact parameter and CMS POG ID variables. Unlike prompt leptons, a nonprompt lepton that comes from a hadron decay is typically surrounded by other decay products of the same hadron. The additional hadronic activity accompanying the lepton could be inferred from an excess of energy localized around the lepton. This argument has lead to the notion of lepton isolation, which quantifies the extra energy caused by additional particles in the lepton cone. There are many ways to express the variable, but the standard one for leptons is the (absolute) PF isolation, which takes the following form:

$$I_\ell^{\text{PF}} = I_\ell^{\text{CH}} + \max\left\{0,\, I_\ell^{\text{NH}} + I_\ell^{\gamma} - \rho_{\text{PU}}\mathcal{A}\right\}, \tag{4.4}$$

where I_ℓ^{CH}, I_ℓ^{NH} and I_ℓ^{γ} are the scalar p_T sum of charged hadrons, neutral hadrons and photons, all contained in a cone of fixed radius R_ℓ around the lepton, but excluding the lepton itself. Dependency on PU is suppressed by requiring the charged hadrons to originate from the LV and by subtracting median neutral contributions due to PU. The latter is estimated similarly to how the additive PU offset corrections are derived in jet energy calibration, but using effective areas (EAs) of the lepton, $\mathcal{A}$, instead of jet catchment areas. The EAs are extracted from simulation in bins of $|\eta|$, lepton flavor and data-taking year, while assuming a fixed cone size of R_ℓ. A lepton selection criterion can be devised based on lepton isolation by requiring its value to be less than certain fraction of lepton p_T.

The decay products of a mother particle become more collimated with its increasing energy and the designated cone that is supposed to confine the daughter particles should shrink accordingly. However, this subtlety is not accounted for in standard PF isolation, as it can lead to a loss in identification efficiency of boosted prompt leptons when selecting them based on this isolation variable. For example, in SL decays of $\text{H} \to \text{WW}^*$ in $\text{t}\bar{\text{t}}\text{H}$ events, the lepton from one W boson would be rejected 10% of the time because it happens to be closer than R_ℓ to one of the quarks from the other W boson. Furthermore, a larger isolation cone picks up more energy from PU, which can cause genuine prompt leptons to be vetoed if the contamination from PU in a given event happens to be larger than expected. The efficiency loss can be easily recovered by replacing the static lepton isolation cone of size R_ℓ with a dynamically changing cone of size $R(\ell)$ in the definition of standard

PF isolation. The dynamically changing cone shrinks with increasing lepton p_T as follows:

$$R(\ell) = \min\{\max\{10\,\text{GeV}/p_T(\ell), 0.05\}, 0.2\}\,.$$

The EAs in Eq. (4.4) should also be multiplied by a factor of $(R(\ell)/R_\ell)^2$, since they were originally measured for the fixed cone size. The resulting PF „mini-isolation" variable, I_ℓ^{mini}, was first proposed in Ref. [310] and is also exploited in loose lepton selection. In particular, PF mini-isolation of a loose lepton is required to be less than 40% of its p_T. The cut is intentionally a bit conservative because a tighter cut would introduce a bias in nonprompt background estimation as explained in Section 4.2.3. A lepton is considered to be more isolated if its isolation variable has a small value.

4.2.2 Signal leptons

The identification of prompt leptons is further improved with a dedicated MVA [311, 312]. The BDT-based algorithm was trained on a variety of lepton variables exploiting their kinematics (p_T, $|\eta|$), isolation (charged and neutral components of I_ℓ^{mini}) and impact parameters ($|d_{xy}^{\text{LV}}|$, $|d_z^{\text{LV}}|$, $d^{\text{LV}}/\sigma_d^{\text{LV}}$), while also taking into account their basic ID criteria (segment compatibility for muons, CMS e/γ POG ID for electrons) as well as the properties of nearby jets that are associated with the leptons. Jets with $p_T > 15\,\text{GeV}$ are matched to leptons based on the condition that the lepton must be a constituent of the jet.

A total of four training variables are extracted from the jets that are associated with each lepton. First is the number of charged jet constituents that originate from the LV. In principle, there should be no tracks from the LV nearing a prompt lepton, while there can be multiple such tracks in the vicinity of a nonprompt lepton if the lepton comes from a hadron decay. The second variable is the DeepJet b tagging score, which tends to be higher for nonprompt leptons that originate from b hadron decays compared to other leptons. The third training variable is lepton-to-jet p_T ratio, $p_T^{\text{ratio}} = p_T^\ell/p_T^j$, which should be close to unity for prompt leptons and less than one for nonprompt leptons that originate from hadron decays. If the lepton has no jets associated with it, then the jet p_T in the denominator is replaced by the sum of lepton p_T and its standard PF isolation that was computed for an enlarged lepton cone size of 0.4 to match the cone size of AK4 jets. The fourth and final training variable is the relative jet-to-lepton p_T, which corresponds to the magnitude of the lepton momentum projection onto a plane that is aligned perpendicular to lepton-subtracted jet momentum:

$$\mathbf{p}_T^{\text{rel}} = \mathbf{p}_\ell - \frac{\mathbf{p}_\ell \cdot (\mathbf{p}_j - \mathbf{p}_\ell)}{|\mathbf{p}_j - \mathbf{p}_\ell|} \cdot (\mathbf{p}_j - \mathbf{p}_\ell)\,.$$

Figure 4.3 specifically illustrates how $\mathbf{p}_T^{\text{rel}}$ is constructed. Its magnitude, p_T^{rel}, can be expressed more concisely as $|\mathbf{p}_j \times \mathbf{p}_\ell|/|\mathbf{p}_j - \mathbf{p}_\ell|$. The observable helps to separate prompt leptons that are accidentally clustered into jets and thus take a random orientation within the jet from nonprompt leptons that typically fly in the same direction as the hadronic jet itself. For this reason, p_T^{rel} should, on average, be smaller for nonprompt leptons than for prompt leptons. A value of zero is used for the track multiplicity, p_T^ℓ/p_T^j and p_T^{rel} variables in the prompt lepton MVA if no matching jets are found to the lepton.

The prompt lepton MVA was trained on electrons and muons separately. The training was further split by detector conditions, with one training assuming the detector conditions before the Phase 1 upgrade and another training after the upgrade. As expected, the latter outperforms the former because of the pixel detector that was swapped out for a better one during the upgrade. Prompt (signal) leptons were sourced from a simulated $\text{t}\bar{\text{t}}\text{H}$ sample

and nonprompt (background) leptons from a SL $\mathrm{t\bar{t}}$+jets sample. The background sample provides a mixture of light and heavy flavored jets similar to the nonprompt background composition of $\mathrm{t\bar{t}H}$ multilepton analysis. The trained model is more successful at identifying prompt muons and rejecting nonprompt electrons than rejecting nonprompt muons or identifying prompt electrons. A DNN-based approach was attempted to replace the BDTs, but it did not lead to any significant gains in performance.

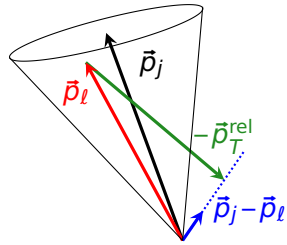


Figure 4.3: Visualization of lepton (red) and its associated jet (black) momenta. The relative lepton-to-jet p_T variable (green) is constructed by projecting lepton momentum onto a plane that is perpendicular to the lepton-subtracted jet momentum (blue).

The output of prompt lepton MVA is a floating point number between -1 and $+1$, with the former labeling nonprompt leptons and the latter prompt leptons in the training. A high prompt lepton MVA score hence indicates that a given input lepton is more compatible with prompt leptons than it is with nonprompt leptons. Independent cuts on prompt muon and electron MVA scores were first developed for the $\mathrm{t\bar{t}H}$ analysis with the purpose of selecting final state (signal) leptons in the SR. The optimization was based on expected upper limits in the 2ℓSS channel, which drives the overall performance of the analysis due to its superior event statistics compared to other channels, since it requires the presence of just two leptons with same sign (SS) charges in the final state. Assuming baseline lepton selection, the extracted WPs enable to correctly identify about 90% of prompt muons and 60% of prompt electrons at a misidentification rate of roughly 3% per nonprompt lepton. The optimization was repeated for the HH analysis, which is more limited by signal statistics than the $\mathrm{t\bar{t}H}$ analysis. The resulting looser WPs provide a relative 15–60% increase in ID efficiency of prompt leptons. Most of these gains can be attributed to low-p_T electrons, which are recovered by the relaxed cuts on prompt lepton MVA score. The prompt lepton MVA has been extensively utilized by other CMS analyses, including the searches for $\mathrm{t\bar{t}t\bar{t}}$ [313], $\mathrm{t\bar{t}W}$ [314], $\mathrm{H} \to \mathrm{WW}^*$ [315], WW double parton scattering (DPS) [316], supersymmetric signals [317] and $\mathrm{HH} \to \mathrm{b\bar{b}WW}^*$ [7], but also in a separate followup study of CP phase effects in top Yukawa interactions in $\mathrm{t\bar{t}H}$ multilepton channels [318] and in top quark EFT studies [319].

Leptons that are selected in the final state of some SR must satisfy the tight lepton selection criteria. This entails picking only those loose leptons that pass the appropriate prompt lepton MVA WP. The requirement is complemented by other quality cuts of tight lepton selection, which further increase the chances of choosing genuine prompt leptons. The extra conditions require the DeepJet score of the jet that is associated with a tight lepton to not exceed the medium b tagging WP, which helps to suppress nonprompt leptons that come from b hadron decays. The CMS Muon POG ID threshold is raised from loose to medium WP specifically for tight muons. Tight electrons, on the other hand, are required to not originate from a photon conversion nor have missing hits in any of the pixel layers. In 2ℓSS channels with up to one extra τ_h in the final state, the tight leptons must also pass the tight charge condition, which has the effect of reducing prompt lepton

ID efficiency by a few percent. The tight charge condition helps to especially suppress processes like DL $t\bar{t}$+jets, which is the main source of backgrounds where the charge of one of the leptons is incorrectly measured. There are two additional requirements imposed on tight leptons, with one concerning the so-called cone-p_T variable and the other HLT emulation cuts on electrons, both of which are explained in the next section.

4.2.3 Fakeable leptons

No matter how effective the tight lepton selection requirements are at filtering out prompt leptons, some nonprompt leptons or jets might still „fake" as prompt leptons and pass the tight cuts due to random fluctuations in the hadronization and decay processes. The probability for nonprompt leptons or jets to contaminate the SR increases with the cross section of the process that produced them in the first place. Common processes that fit this description are QCD multijet, $t\bar{t}$+jets and DY, since they generally do not feature the required number of prompt leptons in final state but have many orders of magnitude higher production cross section than the signal process. However, in order to maintain sufficiently low statistical uncertainties on the predicted yields in the SR, one would need to generate at least ten times as many MC events than what would be expected from the data for the same process. It follows that modeling the „fake" contributions due to nonprompt leptons or jets in the SR with MC simulation is either computationally prohibitive or does not yield reliable results. Fake backgrounds are for this reason estimated with data-driven techniques like the ABCD method or the fake factor (FF) method, which extract the fake background directly from the data.

The strategy that is chosen for modeling fake backgrounds in the current work is based on the FF method. It is formally introduced in Section 5.3.1, but for the present discussion it is sufficient to acknowledge that much of the efforts in making this method viable concern the probabilities, also known as fake rates (FRs), for nonprompt leptons to pass the tight selection criteria. This definition implies that the FRs are estimated from a more inclusive class of leptons than the tight lepton collection. This wider class of leptons cannot consist of just loose leptons for reasons that are explained shortly. Thus, yet another set of requirements is needed in order to specify the inclusive lepton collection, hereby referred to as „fakeable" leptons.

In a nutshell, the FF method works by collecting data events to a fake application region (AR), from which the events are extrapolated to the SR as fake background by appropriately reweighting them using fake factors — hence the name of the method. The fake AR is constructed the same way as the SR, but demanding all final state leptons to pass looser fakeable selection instead of the tight cuts. Orthogonality between the SR and fake AR is achieved by requiring that at least one lepton in the fake AR fails the tight cuts. A FF of the form

$$F_i = \frac{f_i}{1 - f_i} \tag{4.5}$$

is attributed to each selected lepton i based on its properties, but only in case it fails the tight cuts in the fake AR. The numerator of Eq. (4.5) refers to the probability for a fakeable lepton to pass the tight cuts, from which it follows that the denominator corresponds to the probability for a fakeable lepton to fail the tight cuts. Fake background estimate in the SR is eventually obtained by assigning a product of FFs to each data event in the fake AR. Conceptual illustration of the procedure is shown in Fig. 4.4.

There are four main principles that one should follow when deciding on the choice of cuts in fakeable lepton selection. First, none of the leptons that pass the tight criteria should fail the fakeable selection requirements. This condition ensures that the FRs remain

well-defined.

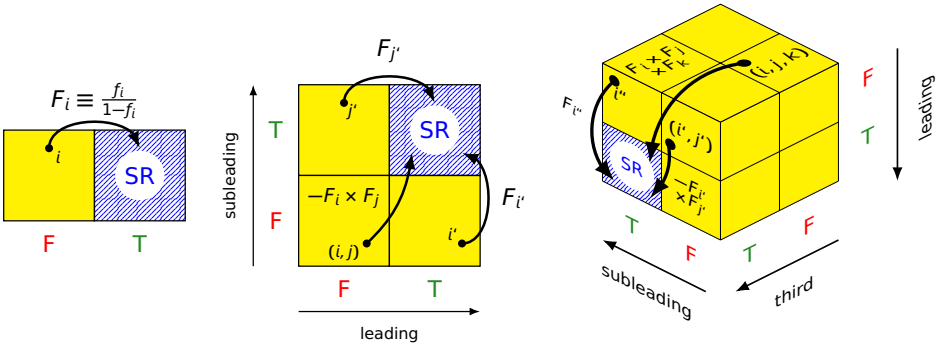


Figure 4.4: Mechanics of the FF method demonstrated on single lepton (left), dilepton (middle) and triple lepton (right) final states. All fakeable leptons that pass the tight cuts („T") contribute to the SR (highlighted with a blue hatched pattern). However, if any of the fakeable leptons fail the tight cuts („F"), then they enter the fake AR (shaded in solid yellow) instead. Extrapolation of an event from the fake AR to the SR is indicated with a curved arrow, which is accompanied by a corresponding FF of the form $F_i \equiv f_i/(1-f_i)$, where f_i refers to the FR of some lepton i that failed the tight cuts. If more than one lepton fails the tight cuts, then the final event weight is given by the product of the corresponding FFs. An extra minus sign is assigned to the event weight if an even number of fakeable leptons fail the tight cuts, which prevents the fake background to be overestimated in the SR.

Second, in order for the FF method to work, the resulting FRs need to be lower than the efficiency for fakeable prompt leptons to pass the tight cuts. In addition, the fake AR should feature a higher number of events with nonprompt leptons than with prompt leptons. This requirement alone can be easily fulfilled by taking the tight criteria as baseline for the fakeable selection and removing the cut on prompt lepton MVA score. Figure 4.5 demonstrates how prompt ID efficiencies and FRs can be deduced from the cross-contamination of events with prompt and nonprompt leptons in the fake AR and the SR. The phase space spanned by the fake AR can be easily expanded by relaxing other cuts in tight lepton selection.

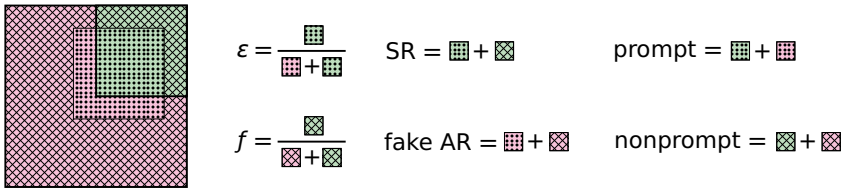


Figure 4.5: Venn diagram showing how events with prompt (dots) and nonprompt (hatched area) in single lepton final states could populate the fake AR (pink) and the SR (green), and how the corresponding prompt ID efficiencies (ε) and FRs (f) are inferred from those event counts.

Third, the fakeable cuts need to be loose enough such that the unweighted number of events in the fake AR would be higher than the effective number of fake background events in the SR, in order to avoid inflating statistical uncertainties on the fake background when extrapolating to the SR. It implies that the weights assigned to data events in the fake AR should average to less than 1, from which, in light of Eq. (4.5), it follows that the FRs should not be higher than 50%.

The fourth and final condition to follow when developing the fakeable criteria is the universality of FRs, which postulates that the FF method should produce an unbiased

estimate of the fake background regardless of the origin of nonprompt leptons. The requirement would allow the use of the same FRs in every analysis channel, as long as the fakeable and tight lepton definitions do not change throughout the analysis. This is accomplished by fine-tuning the fakeable selection such that the FRs extracted for processes dominated by heavy quarks like $\mathrm{t\bar{t}}$+jets are similar to FRs measured for backgrounds that feature a higher fraction of light quarks and gluons such as QCD multijet.

Natural contenders for variables that could parametrize the FRs would be the flavor, reconstructed p_T and $|\eta|$ of nonprompt leptons. However, studies on simulated MC events leading up to the publication of Ref. [320] revealed that FRs of muons from b hadron decays can be many factors higher in QCD events than in $\mathrm{t\bar{t}}$+jets events when measuring them in bins of reconstructed lepton p_T. The reason being that leptons from QCD multijet events tend to be more isolated and hence pass the tight cuts more frequently than leptons found in $\mathrm{t\bar{t}}$+jets events within the same p_T range. More isolated leptons are more likely to pass the prompt MVA WP because the discriminant has been trained on isolation variables. This discrepancy in FRs is closed significantly at the MC generator level when parametrizing them by the p_T of the mother parton that produced the nonprompt lepton. Measuring the FRs as a function of mother parton p_T mitigates background-specific biases and suppresses random fluctuations that are associated with the hadronization and decay processes, which in turn brings nonprompt leptons of different origin to a similar footing. Given that partons are obviously not available at the reconstruction level, jets that are associated with nonprompt leptons are then used as a proxy to mother partons. In case a lepton has no jets associated with it, its mother parton p_T is instead approximated by the sum of reconstructed lepton p_T and standard PF isolation. The isolation variable is computed for an enlarged cone size of 0.4, which intends to mimic the cone size of AK4 jets.

It is important to recognize that these biases would not only affect the FR measurement, but also the discrimination of fake background in the SR. This has motivated the notion of „cone-corrected" lepton p_T, or cone-p_T in short, which is defined in the following way:

$$\text{cone-}p_T = p_T^{\ell} \times \begin{cases} 1 & \text{if the lepton passes prompt lepton MVA WP}, \\ 0.9/p_T^{\text{ratio}} & \text{otherwise}. \end{cases} \tag{4.6}$$

Cone-p_T always resolves to reconstructed p_T for tight leptons as expected from prompt leptons, whereas for fake and nonprompt leptons the cone-p_T variable typically exceeds the reconstructed p_T because the former carries extra hadronic energy from its mother parton. The purpose of factor 0.9 in Eq. (4.6) is to make the transition in average cone-p_T distribution as a function of prompt lepton MVA score smooth at around the WP. All observables that are utilized in signal extraction should be derived from cone-p_T instead of p_T^{ℓ}, to avoid biases that are associated with the discrimination of nonprompt leptons and fakes against prompt leptons in the SR, which in turn has demonstrably known to cause tension between data and prediction. Likewise, all fakeable leptons are assumed to be ordered by their cone-p_T, unless indicated otherwise, to prevent biases that arise from selecting final state leptons based on their p_T^{ℓ}. Leading, subleading, third and fourth leptons are hereby referred to as such based on their ranking in cone-p_T.

Residual flavor dependencies in FRs would still remain even when parametrizing them by cone-p_T. These effects can be reduced by adjusting other cuts with respect to tight leptons in the fakeable lepton definition. The relative abundance of light and heavy flavor fakes can be modulated by tightening or loosening the cuts on the DeepJet score of the jet that is associated with the fakeable lepton, which primarily affects leptons coming from a heavy quark decays but not so much the prompt leptons or those nonprompt leptons that

originate from light jets. Another powerful variable for regulating the light and heavy flavor content in fakes is the CMS e/γ POG ID, which is more successful at discarding light jets that fake as electrons than it is at rejecting genuine nonprompt electrons from b hadron decays in favor of prompt electrons.

Cone-p_T of fakeable and tight leptons has to exceed $10\,\text{GeV}$, which is chosen to be at least 50% higher than the equivalent threshold on reconstructed p_T of loose leptons. The issue is that the FR measurement is performed in bins of cone-p_T rather than in bins of reconstructed p_T of the lepton, whereas the cut imposed on reconstructed p_T ensures that the lepton has the full potential to fire the trigger. From the definition of cone-p_T given by Eq. (4.6), a too low cut on cone-p_T would place an implicit condition on the isolation of nonprompt leptons for them to pass the p_T threshold of the trigger. This would give nonprompt leptons from QCD multijet events a higher chance to pass the tight selection and therefore artificially increase the fake background yields in the SR by inflating the FRs. The complication is avoided by raising the cuts on cone-p_T to a level where the implicit requirements on lepton isolation are no longer relevant. A related cut is imposed on p_T^{ratio} of fakeable leptons that do not pass the prompt lepton MVA WP. The selection criteria helps to improve the balance between light and heavy flavor fakes but at the same time creates implicit conditions on the isolation of nonprompt leptons. Assuming an isolation cut of the form $1/p_T^{\text{ratio}} - 1 < C$ where C refers to some constant, it follows that a nonprompt lepton passes the p_T threshold of the trigger if its cone-p_T exceeds $0.9 \cdot (C+1)$ times the reconstructed p_T, as otherwise it would be implicitly affected by the isolation cut.

Extra care is needed to make sure that the measurement region (MR)[16] where the FRs are extracted does not introduce any additional biases. This entails setting the thresholds in fakeable lepton selection such that the nonprompt lepton content and the kinematic profile in the MR would resemble the composition of the fake AR as much as possible. To this end, fakeable and tight electrons are required to satisfy at least as tight cuts on $\sigma_{i\eta i\eta}^{5\times5}$, H/E and $1/E_{\text{SC}} - 1/p$ observables as implemented in single electron HLT. Those particular variables are used in the training of CMS e/γ POG ID, which itself is used as input to the prompt lepton MVA. It follows that the probability for electrons to pass the prompt lepton MVA WP correlates strongly with the probability for them to satisfy the trigger cuts. However, FRs should not depend on whether leptons pass or fail the trigger requirements. This is because the leptons that are selected in the MR must fire the trigger, whereas events selected in the fake AR may include multiple leptons, but only one of those leptons needs to fire the trigger. This sort of bias is avoided by mimicking the trigger-level cuts in fakeable and tight electron selection.

Fakeable selection criteria was devised for $\text{t}\bar{\text{t}}\text{H}$ and HH multilepton analyses by following the aforementioned guidelines and principles. As later presented in Section 5.3.2, sufficiently low FRs of less than 30% were achieved for the electrons and muons across all measurement bins. This was complemented by a good compatibility in the extracted FRs between $\text{t}\bar{\text{t}}$+jets and QCD multijet backgrounds. The resulting muon and electron selection requirements, including those of loose and tight leptons, are all summarized in Table 4.2. The fakeable selection was fine-tuned separately for the HH analysis because prompt lepton MVA WP was relaxed there with respect to the $\text{t}\bar{\text{t}}\text{H}$ analysis. On top of that, the HH multilepton signal does not feature any b quarks in the final state, which is why a b jet veto is employed when selecting HH multilepton events. As a result, the fake background composition is skewed more towards light flavors in the HH multilepton

[16] Object and even selection requirements of the MR are elaborated in Section 5.3.2. In literature, such as in Ref. [321], it is sometimes referred to as „determination region".

analysis compared to the $t\bar{t}H$ multilepton analysis.

	Observable	Loose	Fakeable	Tight
Muons	p_T	$> 5\,\text{GeV}$	$> 10\,\text{GeV}^{*}$	$\leftarrow$
	$\lvert\eta\rvert$	< 2.4	$\leftarrow$	$\leftarrow$
	$\lvert d_{xy}^{\text{LV}}\rvert$	$< 0.5\,\text{mm}$	$\leftarrow$	$\leftarrow$
	$\lvert d_{z}^{\text{LV}}\rvert$	$< 1\,\text{mm}$	$\leftarrow$	$\leftarrow$
	$d^{\text{LV}}/\sigma_d^{\text{LV}}$	< 8	$\leftarrow$	$\leftarrow$
	$I_{\mu}^{\text{mini}}/p_T$	< 0.4	$\leftarrow$	$\leftarrow$
	CMS Muon POG ID	$\geqslant$ loose WP	$\leftarrow$	$\geqslant$ medium WP
	DeepJet score of nearby jet	✗	$<$ interpolated WP†	$<$ medium WP
	$1/p_T^{\text{ratio}} - 1$	✗	$< 0.5^{\dagger\ddagger}$ or $0.8^{\dagger\S}$	✗
	Prompt lepton MVA score	✗	$\leftarrow$	$> 0.85^{\ddagger}$ or $0.5^{\S}$
Electrons	p_T	$> 7\,\text{GeV}$	$> 10\,\text{GeV}^{*}$	$\leftarrow$
	$\lvert\eta\rvert$	< 2.5	$\leftarrow$	$\leftarrow$
	$\lvert d_{xy}^{\text{LV}}\rvert$	$< 0.5\,\text{mm}$	$\leftarrow$	$\leftarrow$
	$\lvert d_{z}^{\text{LV}}\rvert$	$< 1\,\text{mm}$	$\leftarrow$	$\leftarrow$
	$d^{\text{LV}}/\sigma_d^{\text{LV}}$	< 8	$\leftarrow$	$\leftarrow$
	$I_{\text{e}}^{\text{mini}}/p_T$	< 0.4	$\leftarrow$	$\leftarrow$
	$\sigma_{i\eta i\eta}^{5\times5}$	✗	$< 0.011/0.030$ in EB / EE	$\leftarrow$
	H/E	✗	< 0.1	$\leftarrow$
	$1/E_{\text{SC}} - 1/p$	✗	> -0.04	$\leftarrow$
	Conversion rejection	✗	✓	$\leftarrow$
	# missing hits in tracker	$\leqslant 1$	0	$\leftarrow$
	CMS e/γ POG ID	$\geqslant$ loose WP	$\geqslant$ WP-80†‡ or WP-90†§	$\geqslant$ loose WP
	DeepJet score of nearby jet	✗	$<$ medium‡ or tight†§ WP	$<$ medium WP
	$1/p_T^{\text{ratio}} - 1$	✗	$< 0.7^{\dagger}$	✗
	Prompt lepton MVA score	✗	$\leftarrow$	$> 0.8^{\ddagger}$ or $0.3^{\S}$

* Applied to cone-p_T.
† Required only if it does not pass the prompt lepton MVA WP, otherwise the corresponding criterion from tight lepton selection is imposed.
‡ Employed in the $t\bar{t}H$ analysis.
§ Employed in the HH analysis.

Table 4.2: Tiered selection criteria for muons (top section) and electrons (bottom section). Tick (cross) mark indicates that the cut is (not) applied. Left arrow (←) means that the cut from the previous tier is imposed. The sliding cut on DeepJet *score of the nearby jet that is associated with a fakeable muon is defined as linear interpolation from medium WP at cone-p_T of $20\,\text{GeV}$ to loose WP at cone-p_T of $45\,\text{GeV}$.*

Tight selection criteria without the prompt lepton MVA cut serves as a good starting point for defining the fakeable selection criteria. The extra requirement that was relaxed for fakeable muons with respect to tight selection was the cut on CMS Muon POG ID, which was loosened from medium to loose WP. As for electrons, the only condition that was relaxed with respect to tight selection, besides the prompt lepton MVA requirement, was the upper cut on the DeepJet score in the HH analysis. The cut was loosened from medium to tight WP for jets that are associated with electrons. Some cuts can be tightened in fakeable selection to have a better control over the closure between light and heavy flavors in the MR, as long as they do not cause tight leptons to fail the fakeable selection. This condition is respected if more restrictive cuts are applied only to those fakeable leptons

that do not pass the prompt lepton MVA WP. As detailed in Table 4.2, this tactic is employed to impose tighter cuts on p_T^{ratio} of both electrons and muons, on CMS e/γ POG ID for electrons, and on DeepJet score of jets that are associated with muons.

When implementing a SR, it is important to remember that SRs of different channels as well as the fake AR and SR of the same channel need to be kept separate. Overlap between the fake AR of one channel and analysis regions of some other channels is allowed, because unweighted data events from a fake AR do not directly enter the signal extraction. Besides, extrapolation of the same event from separate fake ARs to their respective SRs uses different FFs, which has the effect of decorrelating the fake background estimate between the SRs.

The approach that is chosen to define the analysis regions here starts by requesting at least N fakeable leptons from an event, where N defines the lepton multiplicity of the channel. If all leptons in this collection pass the tight cuts, then the event belongs to the SR, otherwise the event contributes to the fake AR of the same channel. Obviously, if the event does not have enough fakeable leptons, then it does not contribute to the channel at all. In case there are more than N fakeable leptons in the event, then only the leading N are kept and the rest discarded. Overlap with another SR is resolved by vetoing those events that feature more than N tight leptons. In contrast to the counting method, whereby the designated channel is determined by the multiplicity of fakeable and tight leptons, the presented approach maximizes the utilization of available data. For example, if an event has three fakeable leptons but only the subleading lepton passes the tight cuts, then it would contribute to the fake ARs of dilepton and trilepton channels. The leading N fakeable leptons are also flavor-matched to trigger legs, as described in Section 3.2.4.

4.2.4 τ_{h} candidates

At the baseline level, τ_{h} are required to satisfy $p_T > 20\,\text{GeV}$, which corresponds to the lowest p_T threshold of the triggers listed in Table 3.2. In order to attain maximum identification efficiency, loose τ_{h} are additionally expected to remain well within the geometric acceptance of the tracker by demanding that $|\eta| < 2.3$. Contamination from PU is suppressed with condition $|d_z^{\text{lV}}| < 2\,\text{mm}$. The only decay modes accepted here are 1-prong with up to two neutral pions and 3-prong with up to one neutral pion. A τ_{h} is disregarded if it happens to be closer than $\Delta R = 0.3$ to a loose lepton. All selected τ_{h} must pass the loosest WPs of every DeepTau ID discriminant.

Final state τ_{h} in the SRs are required to pass a tighter WP of $D_{\text{jet}}^{\tau_{\mathrm{h}}}$, which ranges from VLoose to VTight depending on the channel. In case of HH multilepton analysis, Medium WP is used across all channels for selecting a tight τ_{h}. Optimal WPs were obtained for each channel separately based on whichever produced the lowest upper limits in a given channel. Just like leptons, not every τ_{h} that is selected in the SR actually corresponds to the genuine particle that it is assumed as. As evidenced by Table 4.1, τ_{h} could be faked by jets or, to a lesser extent, by electrons. However, most leptons that could be misidentified as τ_{h} are already eliminated in the cleaning step, which leaves jets as the major source of τ_{h} fakes. This is also the reason why only $D_{\text{jet}}^{\tau_{\mathrm{h}}}$ was leveraged to refine τ_{h} definition for the SRs.

A strategy is needed for estimating the additional background that is induced by fake τ_{h} in the SR. Fortunately, the FF method can be easily extended such that τ_{h} would be handled on the same footing as leptons. This motivates the introduction of fakeable τ_{h} collection, which is defined by selecting those loose τ_{h} that pass VVLoose WP of $D_{\text{jet}}^{\tau_{\mathrm{h}}}$, thus ensuring that fakeable τ_{h} form a superset of tight τ_{h} in every analysis channel. Only the leading τ_{h} are kept to fulfill the multiplicity requirement of a given channel. Events

featuring a sufficient number of fakeable τ_{h} would contribute to the SR in case all those τ_{h} also satisfy the channel-specific tight cuts. Otherwise, the event is added to the fake AR of the channel.

Separate FRs are needed to quantify the probability for jets that fake as loose τ_{h} and pass the VVLoose WP of $D_{\mathrm{jet}}^{\tau_{\mathrm{h}}}$ to pass tighter WPs of the discriminant. The jet-to-τ_{h} FRs are parametrized by the p_T, $|\eta|$ and decay mode of the reconstructed τ_{h}. Flavor dependency of the FRs, which was extensively studied in Ref. [321], as well as different trigger conditions of the SR inflating the fake background yields are addressed by measuring dedicated FRs for each individual case. In particular, the FRs for the $\mathrm{t\bar{t}H}$ analysis are extracted from a $\mathrm{t\bar{t}}$ CR dominated by heavy flavor fakes, whereas the FRs for the HH analysis are obtained from a DY CR, which is mostly populated by light flavor fakes. Residual biases in the origin of fakes are taken as a source of systematic uncertainties. As for the triggers, the FRs are measured for jets passing or failing the double-τ_{h} trigger or the τ_{h} leg of lepton-plus-τ_{h} cross-trigger, as well as for the case where no trigger conditions are applied. Further details of the FR measurement procedure are provided in Section 5.3.3.

4.2.5 Jets

AK4 jets are selected by requiring that their $p_T > 25\,\mathrm{GeV}$ and that they satisfy the loosest WP of PF jet ID. Jets are considered as „central" if they are confined to the acceptance region of $|\eta| < 2.4$, or as „forward" in case they are reconstructed in the outer region spanning $2.4 < |\eta| < 5$. Forward jets are characteristic not only to VBF production but also to the topology of tH signal via the t-channel. Those jets that have a fakeable lepton as its constituent are discarded, as well as jets that overlap with a fakeable τ_{h} within $\Delta R = 0.4$. The jets are cleaned against all leptons and τ_{h} that pass the fakeable cuts, and not against the leading leptons and τ_{h} that are picked to fulfill the multiplicity requirement of a given channel. Fakeable leptons are used because cleaning against loose leptons would remove too many genuine jets that fake as leptons, and cleaning against tight leptons would lead to different jet multiplicity distributions between fake AR and SR. Noisy jets that create a massive tail in MET as described in Section 4.1.5 are also removed.

Events containing a pair of resolved b jets are identified with the requirement that the events have at least two central jets, both of which are required to pass the loose WP or at least one of which is required to pass the medium WP of DeepJet discriminant. The reason for accepting events with just one b jet passing the medium WP is to account for the possibility that one b jet from the pair might fall outside of geometrical acceptance, may be cleaned with respect to leptons or τ_{h} candidates, merged with another jets by the reconstruction algorithm, or just fail the loose WP of the b tagging algorithm. To recover such events, one less b jet is requested, but the second jet now has to pass a tighter (medium) WP to reject backgrounds with light quark or gluon jets that fake as b jets. This criterion is employed in the $\mathrm{t\bar{t}H}$ analysis but inverted into a b jet veto in HH multilepton analysis, because no b quarks are expected from the signal. The b jet veto entails rejecting those events that feature more than one b jet satisfying the loose WP or any b jets passing the medium WP. Probability for two light quark or gluon jets to pass the loose WP is about the same as the probability for just one light quark or gluon jets to satisfy the medium WP, Central jets failing the loose WP of DeepJet b tagging discriminant together with forward jets form a light jet collection, which is particularly useful in distinguishing tH events from $\mathrm{t\bar{t}H}$ events.

AK8 jets that are reconstructed without loose leptons are employed only in HH $\rightarrow$ multilepton analysis for the purpose of capturing boosted SL H $\rightarrow$ WW^* decays. It allows the recovery of a signal that would otherwise be lost through the cleaning against fakeable

leptons. This scenario becomes especially relevant in resonant searches where both Higgs bosons gain high momentum from an unknown particle, which in turn boost the W bosons. AK8 jets are selected by imposing that their p_T exceeds at least $100\,\text{GeV}$ and that they pass the loosest WP of PF jet ID. The selected AK8 jets are expected to be more compatible with double-prong substructure than with single-prong substructure, which is realized by asserting that their corresponding N-subjettiness ratio, τ_{21}, does not surpass a value of 0.75 [293]. Only those central AK8 jets are considered that have two subjets each with $p_T > 20\,\text{GeV}$. The leading AK8 jets that happen to be closer than $\Delta R = 1.2$ to a fakeable or tight lepton, depending on the analysis region, are chosen to represent hadronic decay products of a boosted W boson. Up to two such candidates are accepted. The rest are discarded in case there are more.

5 Signal and background estimation

The signal processes are always modeled with MC simulation. Background processes, on the other hand, can be estimated with MC samples or extracted directly from the data by appropriately reweighting the recorded events. One needs to account for potential shape mismodeling in the simulated samples and also correct for the differences in selection efficiency between the data and MC simulation by applying appropriate scale factors (SFs) to the selected MC events. Section 5.1 gives a complete overview of the MC samples used in this work. This is followed by Section 5.2, which describes the corrections that are applied to the simulation in order to improve its agreement with data prior to the signal extraction. The discussion continues with Section 5.3, which explains the data-driven techniques for estimating backgrounds that arise from misidentifying jets as prompt leptons or τ_{h}. Finally, Section 5.4 gives an overview of the methods that are employed in determining backgrounds that are caused by incorrectly measuring the electron charge.

5.1 Monte Carlo simulation

The production of MC samples in the CMS collaboration consists of several steps. First, MC generators produce a set of HS events in a given production and decay channel of the process. The parton-level objects that are returned by the MC generators are deemed unphysical because they have not undergone the showering step, yet. The MC samples used in this thesis are generated at LO and at NLO in pQCD with MadGraph5_aMCatNLO [87, 88], and at NLO in pQCD with POWHEG [89–91]. A handful of samples are generated with MCFM at LO [322–324]. Heavy resonances generated with MadGraph5_aMCatNLO at NLO are subsequently decayed with MadSpin [325]. The simulated decays of the Higgs boson into a pair of vector bosons are delegated to the JHU generator in single Higgs production events [326–329]. In other processes, the decays of the Higgs boson as well as the decays of τ lepton into hadrons via W boson are modeled by Pythia [84].

The second step of MC sample production is the modeling of PS and UE, which is also executed by Pythia. The resulting particles returned by Pythia are commonly referred to as generator-level particles and the higher-level information deduced from them as „MC truth". Their interactions with the CMS detector material and trigger response are simulated using Geant4 [330] in the third step. At this stage, minimum bias events are randomly mixed into the simulation such that the resulting number of PU interactions of the whole MC sample follows the profile inferred from data [331]. The minimum bias overlay samples are generated with Pythia to contain pure PU events, which are common to every MC production campaign. Just like the data, the resulting simulated events undergo digitization, reconstruction and identification stages in the final step. Separate MC samples are produced for each of the three data-taking years, in order to account for the changing detector and trigger conditions between the years.

The results are bundled into ROOT-based [332] Analysis Object Data (AOD) format, which is oftentimes downsized into MiniAOD format by reducing and compressing its event and particle content by a factor of 10 [333]. However, it would still require CMSSW for reading, which puts unnecessary constraints in developing the analysis software. For these reasons, many analysis groups converted the MiniAOD files into a much simpler columnar storage that can be processed with just plain ROOT software. In order to reduce redundant expenditure of the computing resources and human time on creating and maintaining such data formats, which in practice had very similar content regardless, a general yet refined lightweight NanoAOD tier was developed [6, 334]. It would satisfy the needs of a typical physics analysis and, as a bonus, increase the consistency of analysis results, which further

simplifies combinations thereof. Packaging hundreds of billions of data and simulated MC events into these formats requires millions of CPU-hours of computing and petabytes of disk space for storing them. Running such intense computing tasks is only feasible thanks to the Worldwide LHC Computing Grid (WLCG), which is a network of hundreds of computing centers that facilitate these operations [335]. The data and MC simulation utilized in this work are based on the NanoAOD data tier with slight modifications to accommodate lepton-subtracted AK8 jets, which are not present in the official version of the format. The NanoAOD files are produced on the grid, which is accessed through CRAB interface [336].

The MC samples that span the full kinematic range of the process (up to fiducial cuts) are commonly referred to as inclusive samples. If the simulated process has a huge cross section, like it is the case with single W+jets production, it is sometimes desirable to enhance the statistics of the process and thereby reduce its statistical uncertainties in the phase space region that is more relevant to the analysis. For this reason, exclusive MC samples are produced in mutually disjoint slices of the inclusive phase space. Multiple MC samples covering the same phase space can be merged or „stitched" together in an unbiased way, provided that the input samples are produced with consistent generator settings [3].

The full list of MC simulations employed in this work are shown in Tables 5.1 and 5.2, the first of which details single or double Higgs boson production processes, while the second lists the background processes. Most of the MC samples were provided centrally by the relevant subject experts in the CMS collaboration, but a handful of MC samples were produced privately following the same setup as the central production. Special attention was given in ensuring that the generated events as well as the mixed minimum bias events remain statistically independent across the whole MC sample.

Process	Decay modes	Generator, order in pQCD
ggF H	$H \to \tau\tau, \mu\mu, ZZ(\to 4\ell, 2\ell 2q), WW(\to \ell\nu 2q, 2\ell 2\nu)$	POWHEG, NLO [337]
VBF H	$H \to \tau\tau, \mu\mu, ZZ \to 4\ell, WW(\to \ell\nu 2q, 2\ell 2\nu)$	POWHEG, NLO [338]
VH	$H \not\to b\bar{b}$	MG5@NLO, NLO
ZH	$H \to b\bar{b}, Z \to 2\ell$; $H \to \tau\tau, WW$	POWHEG, NLO [339]
WH	$H \to b\bar{b}, W \to \ell\nu$	POWHEG, NLO [339]
$t\bar{t}H$	All	MG5@NLO, NLO
tHq+j	All	MG5@NLO, LO[§]
tHW	All	MG5@NLO, LO
$t\bar{t}VH$	All	MG5@NLO, LO
ggF HH	$HH \to 4V, 2V2\tau, 4\tau, 2b2\tau$	POWHEG, NLO [197–199][*]; MG5@NLO, LO[†§]
VBF HH	$HH \to 4V, 2V2\tau, 4\tau, 2b2\tau$	MG5@NLO LO[‡§]

[*] Nonresonant HH production for $\kappa_\lambda \in \{0, 1, 2.45, 5\}$.

[†] Resonant and nonresonant HH production for JHEP04 EFT BMs.

[‡] Nonresonant HH production for the coupling scenarios listed in Fig. 2.28.

Table 5.1: List of MC samples for single and double Higgs boson production processes that are generated for estimating signal and background contributions. The corresponding cross sections with appropriate uncertainties are detailed in Tables 2.6 and 2.9 and relevant BRs in Tables 2.3 and 2.5. The abbreviation „MG5@NLO" stands for MadGraph5_aMCatNLO. Processes that have (not) been marked with the „§" sign are produced in 4FS (5FS). Suffix „+j" in the names of LO processes indicates that the extra light quark and gluon jets are included in the ME.

	Process [production details]	Decay modes / final states	Generator, order in pQCD (EW)	σ [pb]; order in pQCD(+EW)
DY	W+j	$\ell\nu$	MG5@NLO, LO	61500; NNLO[(F)]
DY	Z/γ^*+j $[10 < m_{\ell\ell} < 50\,\text{GeV}]$	$\ell\ell$	MG5@NLO, LO	18600; NLO[(S)]
DY	$[m_{\ell\ell} > 50\,\text{GeV}]$	$\ell\ell$	MG5@NLO, LO or NLO	6080, NNLO (NLO)[(F)]
	$t\bar{t}$	All	POWHEG, NLO [340]	832; NNLO[(T)]
Single top production	t or $\bar{t}$ [tW]	All	POWHEG, NLO [341]	71.7; NLO[(H)]
Single top production	$[t]$	All	POWHEG, NLO [342][§]	136 or 81; NLO[(H)]
Single top production	$[s]$	$b\bar{b}\ell\nu$	MG5@NLO, NLO[§]	6.35 or 3.97; NLO[(H)*]
Single top production	$[tW\ell\ell]$	All	MG5@NLO, LO	1.1×10^{-2}; LO[(S)]
$t\bar{t}V$	$t\bar{t}W$, $t\bar{t}WW$ $\equiv t\bar{t}W(W)$	$W \to \ell\nu$	MG5@NLO, NLO (NLO)	0.650; NLO (NLO) [50, 343]*
$t\bar{t}V$	$t\bar{t}WW \equiv t\bar{t}W(W)$	All	MG5@NLO, LO	6.98×10^{-3}; LO[(S)]
$t\bar{t}V$	$t\bar{t}(Z/\gamma^*) \equiv t\bar{t}Z$	$Z/\gamma^* \to \ell\ell, \nu\nu$	MG5@NLO, NLO	0.273; NLO (NLO) [50][(S)]
VV or diboson	WW [DPS]	$2\ell 2\nu$	Pythia, LO	0.223; LO[(S)]
VV or diboson	$[W^\pm W^\pm$+j$]$	$2\ell 2\nu$	MG5@NLO, LO	4.93×10^{-2}; LO[(S)]
VV or diboson	$[W^\pm W^\mp]$	$2\ell 2\nu$, $\ell\nu 2q$	POWHEG, NLO [344, 345]	119; NNLO [346]*
VV or diboson	$W(Z/\gamma^*) \equiv WZ$	$3\ell\nu$,	MG5@NLO, NLO	4.92; NNLO [347]
VV or diboson		$2\ell 2q$, $\ell\nu 2q$	MG5@NLO, NLO	5.60, 10.7; NLO[(S)]
VV or diboson	$\underbrace{(Z/\gamma^*)(Z/\gamma^*)}$ $[q\bar{q}]$	4ℓ, $2\ell 2\nu$,	POWHEG, NLO [344, 345]	1.38, 0.620; NNLO [348][(S)]
VV or diboson	$\equiv ZZ$	$2\ell 2q$	MG5@NLO, NLO	6.07; NNLO [348][(S)]
VV or diboson	[gg]	4ℓ,	MCFM, LO [349]	2.70×10^{-3}; NLO [350][(S)]
VV or diboson		$2\ell 2\ell'$	MCFM, LO [349]	5.40×10^{-3}; NLO [350][(S)]
VVV or triboson	WWW	All	MG5@NLO, NLO[§]	0.209, NLO[(S)]
VVV or triboson	WWZ	All	MG5@NLO, NLO[§]	0.168, NLO[(S)]
VVV or triboson	WZZ	All	MG5@NLO, NLO	5.70×10^{-2}, NLO[(S)]
VVV or triboson	ZZZ	All	MG5@NLO, NLO	1.47×10^{-2}, NLO[(S)]
X+γ	Wγ	$W \to \ell\nu$	MG5@NLO, NLO[§]	192, NLO[(S)]
X+γ	$(Z/\gamma^*)\gamma$	$Z/\gamma^* \to \ell\ell$	MG5@NLO, NLO	55.6, NLO[(S)]
X+γ	(t or $\bar{t}$)γ	All	MG5@NLO, NLO[§]	1.02, NLO[(S)]
X+γ	$t\bar{t}\gamma$	All	MG5@NLO, NLO	4.22, NLO[(S)]
X+γ	WZγ	$W \to \ell\nu$, $Z \to q\bar{q}$	MG5@NLO, NLO[§]	4.34×10^{-2}, NLO[(S)]
Other rare backgrounds	(t or $\bar{t}$)b(Z/γ^*)	$Z/\gamma^* \to \ell\ell$	MG5@NLO, NLO[§]	7.36×10^{-2}, NLO[(S)]
Other rare backgrounds	$t\bar{t}t\bar{t}$	All	MG5@NLO, NLO	8.21×10^{-3}, NLO[(S)]
Other rare backgrounds	(t or $\bar{t}$)$t\bar{t}$W	All	MG5@NLO, LO	7.32×10^{-3}, LO[(S)]
Other rare backgrounds	$t\bar{t}$WZ	All	MG5@NLO, LO	3.89×10^{-3}, LO[(S)]
Other rare backgrounds	$t\bar{t}$ZZ	All	MG5@NLO, LO	1.98×10^{-3}, LO[(S)]

[(F)] Computed with FEWZ program [351]. [(H)] Computed with HatHor program [353, 354].
[(T)] Computed with Top++ program [352]. [(S)] Estimated directly from simulated MC samples.

Table 5.2: List of MC samples that are generated for the purpose of estimating contributions from background processes and for developing systematic uncertainties on data-driven background yields. Cross sections σ correspond to $\sqrt{s} = 13\,\text{TeV}$ at the LHC. If the cross section value is accompanied by asterisk (*), then the inclusive production cross section is quoted instead. The symbol ℓ stands for e, μ or τ in the above. MC generator MadGraph5_aMCatNLO is abbreviated as „MG5@NLO" in the table. Processes that have (not) been marked with the „§" sign are produced in 4FS (5FS). The cross section of processes with single top quark or anti-quark are summed if they contribute equally to the production. The relevant BRs can be found in Table 2.3. Suffix „+j" in the names of LO processes indicates that the extra light quark and gluon jets are included in the ME.

Simulated $t\bar{t}W$ sample was centrally produced up to NLO in pQCD, which covered diagrams of order $(\alpha_S^2\alpha_{EW})^{1/2}$ and $(\alpha_S^3\alpha_{EW})^{1/2}$. In order to improve the modeling of the $t\bar{t}W$ process in the $t\bar{t}H$ multilepton analysis, a second MC sample was produced up to NLO in EW, thus including diagrams of order $(\alpha_{EW}^3)^{1/2}$ and $(\alpha_S\alpha_{EW}^3)^{1/2}$. The EW corrections

of order $(\alpha_S \alpha_{EW}^3)^{1/2}$ were found to increase $t\bar{t}W$ production cross section by $\sim 10\%$ with respect to the recommended value of $601\,\text{fb}$ in Ref. [50], which is consistent with the results of Ref. [343]. Although the change in the normalization improved the agreement with the SM expectation significantly, the corresponding impact on the shape of the final distributions that entered the signal extraction was rather mild. After the publication of $t\bar{t}H$ multilepton analysis [1] it was found that additional corrections in the order of $(\alpha_S^4 \alpha_{EW})^{1/2}$ and $(\alpha_S^5 \alpha_{EW})^{1/2}$ increase the estimated cross section by another 5% [355].

Since all analysis channels considered in this work require the presence of genuine e, μ or τ_h in the final state, only those background processes are considered that produce the said particles. Such contributions can either be prompt if all selected e, μ and τ_h are originating from H, W, Z or τ decays, or so-called conversions, if the selected electrons are due to a photon converting into an electron-positron pair in the detector material. Thus, the background processes include the production of vector bosons and top quarks with extra jets: W and Z/γ^* (DY) production; single (t or $\bar{t}$) and pair ($t\bar{t}$) production of top quarks, including its associated production with vector bosons ($t\bar{t}V$); diboson (VV) and triboson (VVV) production; processes with an extra on-shell photon at the ME level, which are used in estimating the γ conversion background; and other „rare" backgrounds that have a comparable cross section to the signal processes.

The designation of selected MC events to different types of contributions in a given analysis region is based on matching of the reconstructed μ, e and τ_h, in this order, to generator-level objects. The matching procedure has to be run explicitly, because the origin of reconstructed objects is lost after the detector simulation step. First, reconstructed muons are matched to generator-level prompt muons if their angular separation is less than 0.3, and if generator-level and reconstruction-level objects have transverse momentum p_T^{gen} and p_T^{reco} such that $p_T^{gen}/2 < p_T^{reco} < 3p_T^{gen}/2$. The same conditions apply to reconstructed electrons when they are matched to generator-level prompt electrons, but also in the subsequent step of matching reconstructed electrons to generator-level on-shell photons. It has been verified that these conditions are sufficient in identifying $\gamma \to e^- e^+$ conversions, where one of the leptons carries most of the energy from its parent photon, since the leading lepton would be more likely to pass the reconstruction and identification criteria. Reconstructed τ_h are matched to generator-level prompt muons and prompt electrons under the same criteria, but when eventually matching them to generator-level prompt τ leptons, the condition on transverse momentum is relaxed to $p_T^{reco} < 2p_T^{gen}$, in order to account for the energy loss due to neutrinos. If there are multiple generator-level objects that satisfy the matching criteria, then the generator-level object that has the highest transverse momentum is chosen as the match. This is because every particle collection in this procedure is sorted in descending order of transverse momentum, thus ensuring that the particles with higher transverse momentum also have a higher priority. The same generator-level particle cannot be matched to two different reconstruction-level objects. Generator-level electrons and muons that are considered in the matching need to be stable.

MC events are identified as prompt if all μ, e and τ_h in the final state are matched to prompt μ or e or, in the case of τ_h, also to a prompt τ lepton at the generator level. These events would be considered as genuine signal events if they are from the signal MC samples, or as „irreducible" background if they are from the background MC samples. One can also consider charge flip background, which is quantified by selecting those events where all reconstructed objects have been successfully matched to generator-level objects, but one of the reconstructed objects has an opposite sign compared to its generator-level match. If it turns out that the reconstructed electron does not have a prompt match at

the generator-level, but is matched to an on-shell photon at the generator level, then such MC events would be considered as „conversions". Finally, if any of the reconstructed objects fail to be matched to a generator-level object as described thus far, then this event would be considered as „fake". In these events, the reconstructed μ, e or τ_{h} that passed the event selection cuts are actually jets that have been misidentified as such. The decision process of how the MC events are distinguished based on generator-level matching is shown in Fig. 5.1. The actual share of fake and charge flip backgrounds in the SR is considered „reducible" and is estimated with data-driven techniques, which are discussed in Sections 5.3 and 5.4, respectively. The fake and charge flip backgrounds that are estimated from the MC simulation serve as a cross check or are employed in deriving systematic uncertainties for the equivalent data-driven backgrounds.

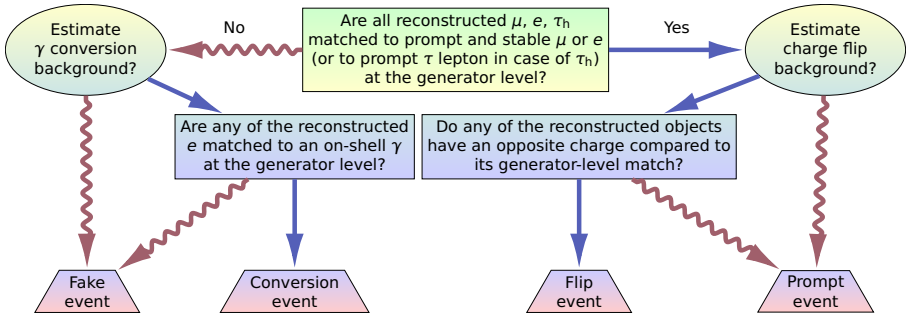


Figure 5.1: The decision process for categorizing the MC events based on generator-level matching.

The MC samples are generally used to estimate signal and background contributions in a given analysis region, while systematic shape uncertainties are estimated by appropriately reweighting the same selected events. For instance, there are dedicated event weights for evaluating the effects of shifting QCD scale in the ME or in the PS. However, in some cases special MC samples are needed in order to assess the effects of shifting other parameters in the MC simulation. One such parameter is the recoiling scheme implemented in Pythia, which is especially relevant to VBF production processes [356]. In particular, an incoming parton is directly color-connected to an outgoing parton in VBF processes, but Pythia does not take this into consideration by default when showering the events. This causes harder and more central radiation than expected in the simulation of VBF processes [357]. The corresponding effects on dijet variables can be mitigated by switching to a different recoiling scheme in Pythia. In order to quantify the effect of the recoiling scheme, two VBF HH samples are generated and analyzed for 2017 and 2018 data-taking period with this option enabled, one for the SM coupling scenario and the other for the scenario where $\kappa_{2\mathrm{V}} = 2$ instead. The effect of the recoiling scheme on the signal normalization is quantified based on the comparison of nominal event yields in individual HH analysis channels.

There can be a sizable overlap between the phase spaces of processes that feature an on-shell photon at the ME level (X+γ) and the equivalent processes without such photon (X+jets). The overlap arises from ISR and FSR photons that appear in both processes. It is resolved by keeping (rejecting) events from X+γ (X+jets) MC samples if they contain a generator-level photon with $p_T > 20\,\mathrm{GeV}$ and $|\eta| < 2.5$ that is isolated from partonic leptons up to radial distance of 0.06 and does not originate from hadronic decays. These requirements are slightly tighter than the fiducial cuts applied to the photons at the partonic level when X+γ events are generated, in order to account for the additional smearing in the showering step. The events from X+γ MC samples contribute primarily to the γ conversion

background.

Theoretical uncertainties on the cross section are attributed to the following processes that contribute to irreducible backgrounds:

- $\pm 4.2\%(\text{PDF} \oplus \alpha_\text{S})^{+2.4\%}_{-3.5\%}(\text{QCD scale})^{+2.8\%}_{-2.7\%}(m_\text{t})$ on $\text{t}\bar{\text{t}}$+jets [353, 354];
- $\pm 2.0\%(\text{PDF}) \pm 2.7\%(\alpha_\text{S})^{+12.9\%}_{-11.5\%}(\text{QCD scale})^{+0.0}_{-3.2\%}(\text{EW})$ on $\text{t}\bar{\text{t}}\text{W}$ [50];
- $\pm 3.0\%(\text{PDF})^{+8.1\%}_{-10.9\%}(\text{QCD scale})$ on $\text{t}\bar{\text{t}}\text{WW}$ [50];
- $\pm 2.8\%(\text{PDF}) \pm 2.8\%(\alpha_\text{S})^{+9.6\%}_{-11.3\%}(\text{QCD scale})^{+0.0}_{-0.2\%}(\text{EW})$ on $\text{t}\bar{\text{t}}\text{Z}$ [50];
- $\pm 7\%$ on WZ to account for the differences between multiple MC generators, and for choice of QCD scale as well as PDFs [358];
- $\pm 3\%$ on quark-initiated and $\pm 20\%$ on gluon-initiated ZZ production to account for the differences between multiple MC generators, and for choice of QCD scale as well as PDFs [359].
- $\pm 0.2\%(\text{PDF}) \pm 2\%(\text{QCD scale})$ on DY [351].

Background yields estimated from γ conversion are assigned a generous 30% normalization uncertainty. Other rare background processes that contribute to irreducible yields are given a conservative 50% normalization uncertainty. Uncertainties of the same origin are correlated between the analysis channels, data-taking years and processes that belong to the same background category.

5.2 Data-to-Monte Carlo corrections

As evidenced by Tables 5.1 and 5.2, each MC sample is normalized to the most accurate estimate of its corresponding cross section that is known at the time, even if the MC sample itself was not generated at that accuracy. In order to actually normalize the MC samples to desired cross section and branching ratio, every simulated event is given a weight of

$$w_i = \frac{\sigma \times \text{BR} \times L}{\sum_{j=1}^{N} w_j^{\text{gen}}} \times w_i^{\text{gen}}, \tag{5.1}$$

where w_i^{gen} corresponds to the weight that is assigned to each event by the MC generator. As a rule of thumb, the generator-level weights are usually positive integers if they were produced at LO. However, they can also be floating point numbers or negative numbers if the MC events were generated at NLO either with POWHEG or with MG5@NLO, respectively. Negative generator-level weights compensate for the excess of events with extra jets that arise from the PS simulation. The sum of event weights w_i across all N simulated events corresponds to the total number of events of the process that are expected to be found from data if the data amounts to integrated luminosity of L. Shifts in QCD or PS scale as described in Section 2.2.1 are automatically propagated through w_i^{gen} by the MC generator. Variations of those scales intend to affect only the shape of kinematic distributions and not the normalization of the MC samples. In general this does not hold true if analysis cuts are applied, because the variation of energy scales through the event weights would induce an effective migration of events in and out of acceptance, which is reflected by residual changes in the event yields that appear on top of the shape modulation.

Although MC generation, showering and subsequent simulation of the detector response all do a great job of creating a fairly accurate representation of the data, the simulated processes do not always model the data perfectly. This can happen for a variety

of reasons, such as imprecise or partial understanding of the phenomenology that underlies the simulated processes, as well as unexpected changes in the detector during the data-taking, which affect the recorded data but are not accounted for by the simulation. Assuming that each of those factors that cause a discrepancy between the data and MC are independent from each other, every gap that appears in distributions of certain observables can be closed with a unique data-to-MC SF, which is applied to every simulated event prior to any event selection. In practice this amounts to multiplying the generator-level weights with SFs in both the numerator and denominator of Eq. (5.1), such that the overall normalization of the generated samples remains the same.

Even if the data and MC events agree inclusively, analysis cuts may still induce sizable differences in event yields and shapes of kinematic distributions. This can happen because the efficiency for selecting data events can be different from the efficiency for selecting MC events. Every object- or event-level requirement should be treated as a potential source of such discrepancy, which should be corrected with the corresponding ratio of efficiencies in data relative to MC. Otherwise it would lead to residual disagreement between the data and simulation, which eventually would bias the signal extraction. It follows from the same argument that the SFs should be extracted from special CRs that are depleted of signal events. It is assumed that the selection efficiency of one cut does not correlate with the selection efficiency of the other cut, meaning that the corresponding SFs can be applied to the selected events independently from each other in order to close the data-to-MC discrepancy induced by both cuts.

A few known standard ways are known for extracting the SFs. One approach is to directly compare data to simulation in bins of some variable that parametrizes the SF, and choose this ratio of event yields to be the SF. The comparison could be performed at inclusive level or in a CR enriched with a background process, for which the corrections are derived. In case the extracted bin-by-bin ratios display a certain trend, it is justified to just fit these ratios against a carefully chosen analytic function to suppress statistical fluctuations.

Another common approach is the tag & probe (TnP) method [360], which is especially fitting for extracting reconstruction and ID efficiencies of individual physics objects. The core idea behind the TnP method is to reconstruct the Z boson mass peak (or J/ψ mass peak for low-p_T objects) in DY CR from the invariant masses of muon, electron or τ_{h} pairs. One object from the pair is called a „tag" and the other object a „probe". The tag object is required to satisfy very tight cuts, which guarantee that it is of high quality, while the probe object is selected based on very loose selection criteria so as to not bias the efficiency measurement. Events that are selected to the DY CR are then divided to „pass" and „fail" regions depending on whether the selected probes satisfy the criterion for which the efficiencies are measured. Additional event selection cuts may be employed to enhance the purity of DY events in both regions. The true event yields under the resonant peaks are extracted from the normalization of a Voigt[17] that is simultaneously fitted to invariant mass distributions found in both regions. The falling rate of background events is modeled with a custom exponential decay function in the fit. Event yields could be obtained by directly counting the events passing some mass window cuts without running any fits if the purity of DY events is high, which can be the case if the requirements on the probe object are sufficiently tight. The selection efficiency that is induced by the cut on the probe object is calculated from the number of events obtained in the pass region relative to the total event yields in pass and fail regions. These efficiencies are extracted from data and MC

[17] It is a probability distribution that is obtained from the convolution of Gaussian and Lorentzian profiles. Alternatively, one could also use the Crystal Ball function to model the resonant peak [361].

simulation separately. The efficiency ratio in data to MC simulation would correspond to the sought-after data-to-MC SF. The pass and fail regions can be subdivided into multiple bins based on kinematic properties of the probe if the goal is to parametrize the SFs by those variables. The TnP method can be modified for the purpose of measuring b tagging efficiencies by simply cutting and counting events in $\mathrm{t\bar{t}}$ or DY CR with $\mathrm{e}\mu$ or SFOS lepton pairs in final state, and requiring the presence of two jets, one of which is a tag that passes or fails a b tagging requirement and the other is a probe that is used for the efficiency measurement.

The rest of this section is dedicated to the description of data-to-MC SFs that are utilized in the presented analyses. They are all summarized in Table 5.3, which lists the reason for applying the SFs, when they are applied, how they are extracted and parametrized. The following paragraphs cover each SF in detail.

Source	Cut-induced	Extraction method	Parametrization
PU	No	Bin-by-bin ratio	True $\langle\mu_{\mathrm{PU}}\rangle$
Trigger	Yes	Tag & probe, orthogonal triggers	Flavor, multiplicity, (cone-)p_T, $\lvert\eta\rvert$
ℓ/τ_{h} ID	Yes	Tag & probe, bin-by-bin ratio	Flavor, (cone-)p_T, $\lvert\eta\rvert$
b tagging	Yes	Tag & probe	p_T, $\lvert\eta\rvert$, true flavor
L1 ECAL prefiring	No	Bin-by-bin ratio	Jet and photon p_T, η
MET modulation	No	Linear fit	Number of PVs
DY normalization	No	Bin-by-bin ratio	Jet and b jet multiplicity
Top quark p_T	No	Analytic fit	Generator-level top quark p_T

Table 5.3: List of data-to-MC SFs that are applied in the presented analyses. Although not explicitly mentioned, the SFs are also extracted for each data-taking year separately.

The average number of PU interactions, $\langle\mu_{\mathrm{PU}}\rangle$, that is added to simulated HS events does not quite match with the amount of PU that is present in data. This is because the PU profile that is chosen prior to the production of MC samples does not account for the actual day-to-day detector conditions, which eventually affect the luminosity measurement. The gap with respect to data is closed by reweighting the MC events as a function of the true mean of the Poisson distribution from which the number of PVs are sampled for a given BX during the PU simulation. PU profiles in data are determined from Eq. (3.2) for every BX and luminosity section after all data has been recorded, certified and properly calibrated. They can be found in Fig. 3.2. Imprecise knowledge of σ_{MB} constitutes a dominant source of uncertainty in the PU reweighting procedure. Its effects are propagated to the SFs by varying σ_{MB} up and down within its uncertainty, which shifts $\langle\mu_{\mathrm{PU}}\rangle$ in data towards higher or lower values, respectively. Uncertainties that are associated with luminosity calibration are ignored, since those are already propagated through the normalization of MC samples.

Differences in trigger efficiencies between data and MC simulation are compensated with dedicated SFs. They are measured separately for single lepton triggers, and for individual legs of lepton-plus-τ_{h} cross-triggers and double-τ_{h} triggers with the TnP technique as a function of lepton or τ_{h} p_T and $\lvert\eta\rvert$. The same method could be utilized to determine the SFs for double and triple lepton triggers, but it becomes considerably complicated because the efficiencies would have to be extracted for every trigger path separately. For this reason an alternative approach called orthogonal trigger method is employed, which defines an unbiased sample of events from those that fired a MET-based trigger. Lepton trigger efficiencies correspond to the fraction of events from the unbiased event sample that also

fired the lepton triggers. MET-based trigger was chosen to define the unbiased sample of events since the correlations between MET-based triggers and lepton triggers have been found to be negligible, on the level of less than 1%. Orthogonal trigger method is used to determine SFs for a combination of single and double lepton triggers in ee, eμ and $\mu\mu$ final states with OS charges to enhance the event statistics, and for a combination of single, double and triple lepton triggers in triple lepton final states. The SFs are parametrized as a function of leading or subleading lepton cone-p_T depending on whichever lepton exhibits stronger correlations. Uncertainties on the SFs are determined by comparing the event yields in the SRs of 2ℓSS and 3ℓ channels in the $\mathrm{t\bar{t}H}$ analysis with and without the trigger SFs applied, which yielded a difference of just 1-2%.

Trigger SFs measured in dilepton (trilepton) final states are applied in channels that require the events to fire single or double (or triple) lepton trigger paths. Event-level trigger SF in the $0\ell + 2\tau_{\mathrm{h}}$ channel of the $\mathrm{t\bar{t}H}$ analysis is estimated as the product of efficiencies found in data for both τ_{h} candidates to fire the trigger divided by the same product of efficiencies found in MC simulation. Complications arise when selecting events using lepton-plus-τ_{h} cross-trigger („X"), which are always used in conjunction with single lepton triggers („L"). As seen from Table 3.2, p_T cut of the lepton leg in lepton-plus-τ_{h} cross-triggers is lower than the p_T cut in single lepton triggers, which means that the probability for a lepton to fire the lepton leg of the cross-trigger, ε_X, is consistently higher than the probability that the lepton also fires the single lepton trigger, ε_L. The probability that an i-th τ_{h} candidate fired the τ_{h} leg of the cross-trigger is given by efficiency ε_τ^i, and so the probability that the candidate did not fire the trigger is simply equal to $(1-\varepsilon_\tau^i)$. The probability that any of the n candidates fired the cross-trigger, ε_τ, corresponds to the complementary probability that none of them fired:

$$\varepsilon_\tau = 1 - \prod_{i=1}^{n} (1-\varepsilon_\tau^i)\,.$$

Because of the correlations between lepton leg of the cross-trigger and single lepton trigger, one needs to consider three possible scenarios when estimating their combined trigger efficiencies:

$$\varepsilon = \begin{cases} \varepsilon_L(1-\varepsilon_\tau) & \text{if fired L but not X}\,, \\ (\varepsilon_X - \varepsilon_L)\varepsilon_\tau & \text{if fired X but not L}\,, \\ \varepsilon_X \varepsilon_\tau & \text{if fired both X and L}\,. \end{cases} \tag{5.2}$$

Although in principle $\varepsilon_X \geqslant \varepsilon_L$, both of those efficiencies are extracted from separate CRs, which might create a situation where this condition does not hold true anymore because of statistical fluctuations in the measurement. To account for this, the products $\varepsilon_L\varepsilon_\tau$ and $\varepsilon_X\varepsilon_\tau$ are replaced by $\varepsilon_\tau \min(\varepsilon_L, \varepsilon_X)$ in the first and third line of Eq. (5.2). The event-level trigger SF is given by the ratio of combined efficiencies in data and MC simulation, which are required to be strictly positive. Another issue arises when imposing double-τ_{h} trigger („D") conditions in a channel that requests more than two τ_{h} candidates in the final state, since any pair of the n candidates could fire the trigger. The probability for this to happen amounts to

$$\varepsilon_\tau{}' = \sum_D \prod_{i=1}^{n} \begin{cases} \varepsilon_\tau^{i\prime} & \text{if fired D}\,, \\ 1-\varepsilon_\tau^{i\prime} & \text{if did not fire D}\,, \end{cases}$$

where $\varepsilon_\tau^{i\prime}$ is the efficiency for the i-th τ_{h} candidate to fire the double-τ_{h} trigger. The sum runs over all possible $\sum_{k=2}^{n} \binom{n}{k} = (2^n - n - 1)$ combinations one can arrange the τ_{h}

candidates such that they fire the double-τ_{h} trigger. The aforementioned issues become amplified in the $1\ell+3\tau_{\mathrm{h}}$ channel of the HH analysis, since the event selection requirements impose that at least one of the single lepton triggers, lepton-plus-τ_{h} cross-triggers or double-τ_{h} must have fired, or the event would be rejected. There are no ambiguities when estimating the probability that the sole lepton fired any of those triggers:

$$\varepsilon_{LX} = \begin{cases} \min(\varepsilon_L, \varepsilon_X) & \text{if fired both X and L}, \\ \varepsilon_L - \varepsilon_X & \text{if fired L but not X}, \\ \varepsilon_X - \varepsilon_L & \text{if fired X but not L}, \\ 1 - \min(\varepsilon_L, \varepsilon_X) & \text{if fired neither X nor L}. \end{cases}$$

One can similarly define ε^i_{DX}, which represents the probability that i-th leading τ_{h} is responsible for the realized states of double-τ_{h} trigger and lepton-plus-τ_{h} cross-trigger. Event-level trigger efficiency is obtained by summing over all 7 (4) unique configurations that the three τ_{h} candidates could have fired the lepton-plus-τ_{h} (double-τ_{h}) trigger, or just one possible configuration if none of the τ_{h} triggers fired:

$$\varepsilon' = \sum_{L,X,D} \varepsilon_{LX} \prod_{i=1}^{3} \varepsilon^i_{DX} \,.$$

As per usual, event-level trigger SF are derived from the ratio of combined efficiencies between data and MC simulation.

Reconstruction and identification efficiencies of muons, electrons and τ_{h} have also been found to differ between data and MC simulation. Lepton ID efficiencies are obtained with the TnP technique, while τ_{h} ID efficiencies are determined with an analogous method as explained in Ref. [301]. The efficiencies for electrons and muons are factorized into two components: efficiency for the lepton to pass loose selection criteria, and efficiency for the loose lepton to pass the tight selection criteria. The former is assigned to leptons passing the loose requirements, whereas the latter is applied only to tight leptons. The uncertainties on loose-to-tight lepton ID SFs are extracted from the TnP fit. Final event-level SF is obtained from the product of SFs that were assigned to all leptons that were chosen to the final state of a given analysis channel. Lepton efficiencies are parametrized by lepton p_T and $|\eta|$, while τ_{h} ID efficiencies are parametrized by p_T of the τ_{h} candidate and DeepTau ID WP that the τ_{h} was required to satisfy. Separate corrections are measured for electrons and muons that satisfy the tight charge requirement. The lepton and τ_{h} ID SFs are assigned to every prompt lepton or τ_{h} that are selected to the final state of a given analysis channel. The uncertainties on tight lepton ID SFs are derived from nominal data-to-MC differences in $\mathrm{t\bar{t}} \to \mathrm{e}\mu$ CR as a function of lepton flavor, p_T and $|\eta|$ to account for potential differences in event topology between the DY events, which are used as reference for the measurement, and $\mathrm{t\bar{t}H}$ signal events, which are enriched with top quark pairs. Total uncertainties on the lepton and τ_{h} ID amount to 1–5% and 5–10%, respectively. An additional corrective SF is applied to tight leptons in the HH analysis to account for the fact that the tight lepton definition was relaxed with respect to the $\mathrm{t\bar{t}H}$ analysis. No dedicated measurement was performed for the relaxed definition of tight leptons. Instead, the corrections were extracted from data-to-MC ratios that were found for relaxed and original lepton definition in WZ CR with 3ℓ in final states. The correction is applied with 100% relative uncertainty, meaning that the „up" variation corresponds to double application of the SF, while the „down" variation means that no corrections are applied.

The τ_{h} reconstruction and ID efficiencies has been found to disagree between the data and simulation. This discrepancy is quantified with DY event in bins of p_T and $|\eta|$ of the τ_{h}

candidate, and in bins of DeepTau ID WP that is employed in τ_h selection. Uncertainties on the extracted SFs are statistically dominated and typically amount to 5–10%. Instead of dismissing those τ_h that originate from the misidentification of electrons and muons, and thereby lose sensitivity to the signal in the process, they are still considered as signal τ_h in the presented analyses. The fact that some of the selected τ_h can be lepton fakes is compensated with additional lepton-to-τ_h fake rates, which are extracted from DY events just like the τ_h ID SFs.

The probability for jets to pass the b tagging WP of DeepJet ID can be different between the data and simulation depending on the p_T, $|\eta|$ and the actual flavor of the jet. These differences are amended with dedicated SFs, which are extracted with the TnP method from a CR enriched with DL $t\bar{t}$ events or with DY events depending on whether the SFs are measured for heavy or light jets, as described in Ref. [295]. Contamination from light jets to $t\bar{t}$ CR, from b jets to DY CR, and from c jets to both regions, as well as uncorrelated linear and quadratic trends of statistical uncertainties from light and heavy contributions are taken as sources of systematic uncertainties. They typically amount to less than 5%, except for the uncertainties that are associated with the presence of c jets, which can be as high as 20%. The b tagging SFs are also fully correlated with the JES and JER uncertainties. In offline analysis, the b tagging SFs are applied to every central jet that is available after the cleaning based on their reconstructed p_T and $|\eta|$, and on the flavor of the generator-level jet that is matched to the reconstructed jet. The event-level SF is obtained from the product of those b tagging SFs. The purpose of this method is to correct the shape of b jet discriminant in MC events but not the yields. To make sure that this really is the case, a normalization factor is obtained for each MC sample prior to any event selection as a function of jet multiplicity. The normalization factor is derived from the ratio of inclusive event yields without any b tagging SFs applied to inclusive event yields with the b tagging SFs applied.

In 2016 and 2017 data-taking years, a gradual time shift in ECAL readout was observed, which caused the L1 TPs in $2 < |\eta| < 3$ to be associated with the previous BX [362]. The CMS trigger rules forbid selecting two consecutive BXs in a row after accepting the event, meaning that the event from the previous BX would be kept because it was accepted by the L1 trigger, but the event from current BX that actually produced the trigger signature would be completely lost. The so-called „prefiring" phenomenon affected about 1–2% of data events but not the MC simulation. The simulated samples had to be corrected, which is accomplished by assigning a prefiring probability to every isolated jet and photon in the event based on their p_T and η. The final event weight corresponds to the probability for the event to not prefire, which in terms of prefiring probabilities $p^i_{\text{pre}}(p_T, \eta)$ amounts to

$$\prod_i (1 - p^i_{\text{pre}}(p_T, \eta)),$$

where the product extends over all isolated jets and photons that were reconstructed within $2 < |\eta| < 3$. A 20% uncertainty is attributed to individual probabilities, which primarily reflects the nonclosure between different PDs from which the prefiring probabilities were extracted. The said uncertainty is propagated to the SFs by shifting the probabilities simultaneously up or down by 20%, and reevaluating the probability for the event to not prefire. The problem with gradual time shifts in the ECAL was spotted and promptly fixed in the earliest stages of data-taking in 2018.

Inhomogeneities in detector response have lead to apparent modulation of ϕ_T^{miss}, the distribution of which resembles a sinusoidal curve that has a period of 2π. The amplitude of these modulations scale approximately linearly with the number of reconstructed PVs, but the exact linear coefficients vary depending on the data acquisition era. Given that these artifacts do not show up in the simulation, a set of corrections were derived from

the linear relationship that helped to reduce the modulation amplitude in data events. In practice, this is accomplished by recalculating MET by shifting its x and y components as a linear function of PV multiplicity.

The DY process producing a τ lepton pair has considerable irreducible contributions to the SRs of $0\ell + 2\tau_{\mathrm{h}}$ and $1\ell + 1\tau_{\mathrm{h}}$ channels in the $\mathrm{t\bar{t}H}$ analysis. The modeling of extra b jets in simulated DY events has been found to significantly deviate from the data, causing differences of up to 40% in some sparsely populated phase space regions. In order to correct for this discrepancy, a dedicated DY CR was devised orthogonal to the SRs by considering only dielectron and dimuon final states, from which the data-to-MC SRs were extracted. The SFs were estimated in the following bins of b tagged jet multiplicity. The measurement was performed in dielectron and dimuon final states separately. The difference in SFs between the two measurements is propagated as uncertainty to the SFs measured in dimuon final states, which range from a few percent at low b jet multiplicity to 15% at high b jet multiplicity. The SFs that were extracted from dimuon final states are applied because of its superior event statistics compared to the measurement in dielectron final states. The results are given in Table 5.4.

Another irreducible background that contributes to the SRs of $0\ell + 2\tau_{\mathrm{h}}$ and $1\ell + 1\tau_{\mathrm{h}}$ channels in the $\mathrm{t\bar{t}H}$ analysis are the $\mathrm{t\bar{t}}$ events. The issue with this particular background is that the p_T spectrum of a top quark has been observed to be harder in simulation than in data. This discrepancy is corrected with an exponential decay function, which takes the p_T of the generator-level top quark as input. The function is fitted to the ratio of differential $\mathrm{t\bar{t}}$ cross section computed at NNLO in pQCD and at NLO in EW [363] to the p_T spectra found in the simulated MC samples for top quark p_T of up to 3 TeV. The SFs are evaluated in $\mathrm{t\bar{t}}$ events by taking the geometric average of the SFs obtained for top and anti-top quarks separately. They correct only for the shape in the simulated events, meaning that the inclusive $\mathrm{t\bar{t}}$ event yields remain unaffected by these corrections. However, irreducible $\mathrm{t\bar{t}}$ yields are expected to decrease because pushing the $\mathrm{t\bar{t}}$ events towards a softer spectrum means that fewer events would pass the event selection cuts compared to the case where no such reweighting is performed. The SF is applied with 100% relative uncertainty.

		# b tagged jets			
	Medium WP	$\geqslant 2$	$= 1$	$= 1$	$= 0$
	Loose WP	$\geqslant 2$	$\geqslant 2$	$= 1$	$\geqslant 2$
Year	2016	0.87 ± 0.14	1.06 ± 0.06	1.10 ± 0.05	1.03 ± 0.02
	2017	1.45 ± 0.08	1.36 ± 0.04	1.43 ± 0.03	1.30 ± 0.03
	2018	1.33 ± 0.14	1.44 ± 0.04	1.50 ± 0.05	1.42 ± 0.02

Table 5.4: Multiplicative corrections to DY normalization in bins of b tagged jet multiplicity of jets passing the DeepJet ID WPs in each data-taking year separately. The corrections were extracted from DY CR in dimuon final states. The total uncertainty on each SF has two components: the statistical uncertainty on the nominal corrections, and the absolute difference with respect to the nominal corrections that are extracted from the same CR but for dielectron final states. The two uncertainties are added in quadrature.

5.3 Fake background estimation

The present section is dedicated to fake background estimation, which was first discussed in the context of lepton selection in Section 4.2.3. More specifically, Section 5.3.1 explains how the fake factor method is derived and reiterates how exactly the extrapolation of the

fake background to the SR is performed. This is followed by Sections 5.3.2 and 5.3.3, which describe how the fake rates of prompt leptons and τ_{h} are determined. The discussion concludes with Section 5.3.4, which details the derivation and application of nonclosure uncertainties on the fake background.

5.3.1 Fake factor method

The main issue with estimating backgrounds that arise from misidentifying nonprompt leptons (or jets) as prompt leptons or τ_{h} is that the only processes that could possibly create such contributions to the SR in substantial amounts all have huge cross sections. It is impractical to model these contributions with MC simulation, because it would take an enormous amount of computing power to generate enough events that could possibly populate the SR in sufficient numbers. A common technique to get around this problem is to create sidebands depleted of signal around the SR by inverting cuts in object or event selection, collect data events to the sidebands, and extrapolate these data events to the SR by assigning some weights to them. This is the main premise of many data-driven techniques, including the FF method discussed here.

To see how the FF method works, it is practical to first focus on just single lepton final states in the following. Thus, in this case events are accepted to the SR only if they feature exactly one lepton that passes the tight cuts. A total of N_p events would be selected by this condition, of which $N_{p|1}$ events would come from genuine prompt leptons and the rest, $N_{p|0}$ events, from nonprompt leptons that are misidentified as prompt leptons. The SR can be expanded by requiring the singular lepton to instead pass fakeable cuts, which are looser than those imposed in the SR. These conditions now accept a total of N_1 events with a prompt lepton in final state and another N_0 events, where the selected lepton is actually a nonprompt lepton. A sideband, also known as fake AR, is formed from events, where the selected lepton passes the fakeable cuts but not the tight criteria. There are a total of N_f events in that sideband, from which $N_{f|1}$ events are from prompt leptons and the remaining $N_{f|0}$ events from nonprompt leptons. In the context of Fig. 4.5, the hatched area represents N_0, dotted area N_1, red area N_p and green area N_f.

With this setup it is now possible to introduce the concepts of prompt ID efficiency and FR. An ID efficiency corresponds to the probability for fakeable prompt leptons to pass the tight cuts ($\varepsilon = N_{p|1}/N_1$), whereas a FR refers to the probability for nonprompt leptons that pass the fakeable cuts to also pass the tight cuts ($f = N_{p|0}/N_0$). Reciprocals of these, $\overline{\varepsilon} = 1 - \varepsilon$ and $\overline{f} = 1 - f$, would then correspond to respective probabilities of prompt and nonprompt leptons that pass the fakeable selection to eventually fail the tight requirements. The event yields in the SR and in the fake AR can be related to the event yields that arise from prompt and nonprompt leptons as follows:

$$\begin{pmatrix} N_p \\ N_f \end{pmatrix} = \begin{pmatrix} \varepsilon & f \\ \overline{\varepsilon} & \overline{f} \end{pmatrix} \begin{pmatrix} N_1 \\ N_0 \end{pmatrix} . \tag{5.3}$$

The fake background can be estimated from the event yields in the fake AR and in the SR if the prompt ID efficiencies and FRs are already known:

$$N_p^{\text{fake}} = N_p - \varepsilon N_1 = \frac{f}{\varepsilon\overline{f} - \overline{\varepsilon} f}(\varepsilon N_f - \overline{\varepsilon} N_p) . \tag{5.4}$$

This approach is sometimes referred to as the matrix method in literature, because it exploits the full matrix information that is available in Eq. (5.3).

Although the ID efficiencies and FRs were formally defined in terms of the yields found in fake AR and SR, these probabilities could be extracted from a dedicated MR. Differences

in flavor composition between the fake AR and the MR can be reduced by carefully fine-tuning the fakeable selection criteria as well as the event selection requirements of the MR. Alternatively, one could also extract these probabilities for individual backgrounds and combine them based on the relative contribution of each background in the fake AR, like it was done in Ref. [321].

The FF method simplifies the fake background estimation by making the following assumptions: the efficiency for prompt fakeable leptons to pass the tight cuts should exceed that of fakeable nonprompt leptons ($\varepsilon > f$), which implies that $\varepsilon\overline{f} \gg \overline{\varepsilon}f$. In addition, the probability for prompt leptons to pass the tight cuts should be much higher than the relative amount of events in the SR compared to the fake AR ($\varepsilon \gg N_p/(N_p+N_f)$), from which it follows that the fake AR should be populated mostly with events where the selected lepton is a nonprompt one. These assumptions turn Eq. (5.4) into

$$N_p^{\text{fake}} \approx N_p - N_1 \approx FN_f\,, \tag{5.5}$$

where a FF given by Eq. (4.5) was introduced. A clear advantage of the FF method is that it does not require the precise knowledge of ID efficiencies. The same result can be obtained by effectively setting ε to unity in Eq. (5.3), and working out the difference between yields in the SR and total contribution from prompt leptons. Moreover, unlike the full matrix approach, the FF method does not require any explicit knowledge of the observed data yields in the SR, but rather only the event yields that are found in the fake AR. As explained in Section 6.1.4, revealing the data yields observed in the SR would conflict with the whole concept of a blinded analysis, which has to be respected in practical implementation.

The matrix method can be extended to final states with two leptons under the premise that the probability of one fakeable lepton to pass or fail the tight cuts is independent of the other lepton. Assuming a certain order of the leptons, there are three types of events that could possibly contribute to the fake AR: the first lepton passes but the second lepton fails the tight cuts (N_{pf}), the first lepton fails but the second lepton passes the tight cuts (N_{fp}), and both leptons fail the tight cuts (N_{ff}). Only the events where both leptons pass the tight cuts (N_{pp}) are added to the SR. The selected events feature leptons that are both prompt (N_{11}), one prompt and another nonprompt (N_{10} and N_{01}), and both nonprompt (N_{00}). In analogy to Eq. (5.3), these event yields can be related to each other via a matrix that is constructed from the ID efficiencies (ε_1 and ε_2) and FRs (f_1 and f_2) of the leading and subleading lepton, respectively, in the following way:

$$\begin{pmatrix} N_{pp} \\ N_{pf} \\ N_{fp} \\ N_{ff} \end{pmatrix} = \begin{pmatrix} \varepsilon_1\varepsilon_2 & \varepsilon_1 f_2 & f_1\varepsilon_2 & f_1 f_2 \\ \varepsilon_1\overline{\varepsilon}_2 & \varepsilon_1\overline{f}_2 & f_1\overline{\varepsilon}_2 & f_1\overline{f}_2 \\ \overline{\varepsilon}_1\varepsilon_2 & \overline{\varepsilon}_1 f_2 & \overline{f}_1\varepsilon_2 & \overline{f}_1 f_2 \\ \overline{\varepsilon}_1\overline{\varepsilon}_2 & \overline{\varepsilon}_1\overline{f}_2 & \overline{f}_1\overline{\varepsilon}_2 & \overline{f}_1\overline{f}_2 \end{pmatrix} \begin{pmatrix} N_{11} \\ N_{10} \\ N_{01} \\ N_{00} \end{pmatrix}.$$

The fake background yields are estimated from the event yields in SR (N_{pp}) but excluding the contribution from events where both leptons are prompt ($\varepsilon_1\varepsilon_2 N_{11}$). The FF produces a rather concise expression for the fake background yields by assuming 100% efficiency for both prompt fakeable leptons to pass the tight cuts:

$$N_{pp}^{\text{fake}} \approx N_{pp} - N_{11} \approx F_1 N_{fp} + F_2 N_{pf} - F_1 F_2 N_{ff}\,.$$

In general, if the event selection requires exactly n leptons in the final state, then the fake background can be estimated as

$$N^{\text{fake}}_{\underbrace{pp\ldots p}_{=p^n}} \approx N_{p^n} - \prod_{i=1}^{n}(N_{p_i} - F_i N_{f_i})\,, \tag{5.6}$$

which follows directly from the exponentiation of Eq. (5.5). Subindex i in Eq. (5.6) enumerates the leptons. The product of event yields in this expression corresponds to a particular final state. For example, $N_{pfp} \equiv N_{p_1} N_{f_2} N_{p_3}$ stands for the number of events where the first and third lepton pass the tight cuts but the second lepton does not. It is evident from Eq. (5.6) that the FFs are associated only with the leptons that fail the tight cuts. Furthermore, the product of FFs carries an extra minus sign in events that feature an even number of leptons failing the tight requirements. The presence of negative terms in Eq. (5.6) is one of the major drawbacks of the FF method compared to the full matrix approach because those terms are responsible for increasing relative statistical uncertainties on the estimated fake background. Furthermore, in a very low statistics regime the estimated fake yields might become negative, which either needs to be corrected to zero by hand or by rebinning the final distributions that are exploited in the signal extraction.

In summary, the FF method works by first collecting data events to the fake AR. These events are extrapolated to the SR as fake background by assigning a product of FFs to every event,

$$(-1)^{k+1} \prod_{i=1}^{k} F_i \,,$$

which extends over all selected k leptons and τ_{h} that fail the tight selection requirements. The FFs are evaluated for each lepton and τ_{h} separately based on their parameters. When comparing data to simulated yields in the fake AR, as shown in Fig. 5.2, it becomes evident that the reweighted data may include events where all selected leptons and τ_{h} are in fact prompt, thus resulting in slight overestimation of the fake background. This excess is removed by reweighting those MC events in the fake AR by the FF method that contain only prompt leptons and τ_{h} in the final state, and then subtracting the resulting yields from the extrapolated data. Systematic shifts in the MC prediction are not propagated to the fake background because the contamination from events with prompt final states to the fake AR generally amounts to less than 10%, the effect of which is further diminished by the fake background yield relative to total background.

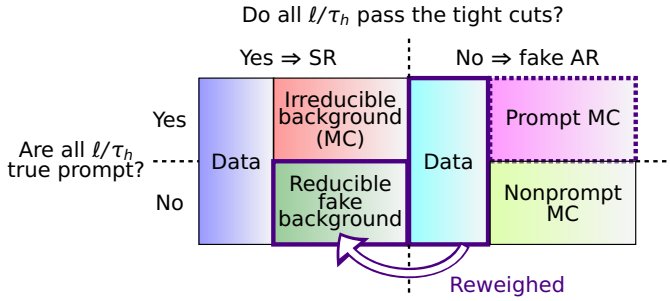


Figure 5.2: Distribution of data and MC events in the SR and fake AR based on the status of final state objects. Reducible fake background approximates the contribution from nonprompt final states to the SR. Data-driven fake background is obtained by reweighting data events and prompt MC events in the fake AR by the FF method, and subtracting the latter from the former in order to not overestimate prompt contributions to the SR.

5.3.2 Lepton fake rate measurement

The goal of lepton FR measurement is to quantify the probability for a singular nonprompt lepton or a jet that passes the fakeable lepton requirements to also satisfy the tight cuts as

a function of its cone-p_T, $|\eta|$ and flavor. The FRs are extracted from a MR that is specifically designed to capture QCD dijet events, where the two jets recoil each other at an angle that shrinks with increasing momentum imbalance of incoming partons. One of those jets is expected to produce a nonprompt lepton or to be misidentified as a jet, while the other jet is supposed to be reconstructed as intended. Therefore, the cuts that are chosen for selecting events in the MR require the presence of exactly one fakeable lepton and at least one jet in the event, whereby the jet must be separated from the lepton by $\Delta R > 0.7$ and satisfy the requirements presented in Section 4.2.5.

The FR measurement is performed for electrons and muons separately in two pseudorapidity bins. These are the barrel region, which goes up to $|\eta| < 1.2$ for muons and $|\eta| < 1.479$ for electrons, and its complementary endcap region, which covers the phase space up to $|\eta| < 2.4$ for muons and $|\eta| < 2.5$ for electrons. The MRs are further segmented by cone-p_T into multiple bins between 10 (15) and 100 GeV for muons (electrons). FRs measured in the highest cone-p_T bin are assumed for leptons that have cone-$p_T > 100$ GeV. Similarly, electron FRs measured in the lowest cone-p_T bin are applied to those electrons that have cone-$p_T < 15$ GeV. The binning in cone-p_T was chosen to closely follow the lowest p_T thresholds that are imposed on reconstructed lepton p_T at the trigger level. Events are selected to exclusive „pass" or „fail" regions in the measurement depending on whether the fakeable lepton meets the tight requirements.

The FR are measured separately for $\mathrm{t\bar{t}H}$ and HH multilepton analyses since they employ different lepton selection criteria. Likewise, the FRs measurement is repeated for each data-taking year individually to account for the changing detector conditions. Dedicated FRs are extracted for leptons that are required to satisfy the tight charge conditions, which are enforced on both fakeable and tight leptons in the $2\ell\mathrm{SS}(+1\tau_\mathrm{h})$ channels of both analyses. These FRs are only used to estimate the fake background in those channels. Electron FRs tend to be a few percent smaller under tight charge conditions, especially at low cone-p_T, but are otherwise compatible within the uncertainties with the FRs derived for the nominal selection. The effects of tight charge condition on muon FRs was found to be negligible.

In order for the selected fakeable lepton to be able to fire an HLT path, its reconstructed p_T must exceed the corresponding p_T threshold of the trigger. It is not possible to use single lepton triggers that are applied at the analysis level for three reasons: the p_T thresholds of single lepton triggers are too high compared to the p_T thresholds imposed in fakeable lepton selection; the triggers enforce implicit cuts on lepton isolation, which would inflate the FRs and thus spoil the measurement; the FRs should be extracted for every combined status of single, double and triple lepton triggers, but there are just too many to consider. The solution to all of these problems is simple in principle — just use those triggers for the measurement that do not enforce any isolation conditions and have p_T thresholds low enough to not bias the fakeable selection towards more isolated leptons. However, relaxing the trigger requirements to such a high degree raises the data rates to unmanageable levels, which necessitates the application of prescales. One would ideally use triggers with the lowest prescale factors to maximize the statistical uncertainties on data. Hence, instead of using just one trigger for this task, a mixture of triggers with increasingly higher p_T thresholds are employed, which allows a reduction of prescale factors at high cone-p_T bins. Mapping of prescaled HLT paths to cone-p_T ranges in the measurement is provided in Table 5.5. In addition to a loosely isolated lepton, some prescaled triggers used here also require the presence of a jet that has p_T above a certain threshold. To replicate this condition in the measurement, the selected recoil jet must also pass the same p_T threshold of the trigger. If no such jets are requested at the trigger level, then a minimum p_T cut of 30 GeV is implied instead.

Events can contribute to a certain cone-p_T bin only if they have fired at least one of the triggers that is associated with the bin. Prescaling is not applied to the MC simulation, meaning that simulated events are never rejected if they fire a prescaled trigger. This is obviously not the case for data, because only one collision event out of every f^{pre} that fired the prescaled trigger is actually recorded. When comparing MC samples to prescaled data recorded by the same prescaled trigger, it follows that the simulation needs to be scaled down by the prescale factor f^{pre} in order to match the yields of the data. This example can be extended to the case where the data was recorded by two triggers with distinct prescale factors of f_1^{pre} and f_2^{pre}. Assuming that both triggers are independent from each other, there is also the possibility that the same event is accepted by both triggers. The probability for this to happen amounts to $1/f_1^{\text{pre}} + 1/f_2^{\text{pre}} - 1/(f_1^{\text{pre}} f_2^{\text{pre}})$. This expression can be generalized to any number of triggers by recognizing that the probability for at least one trigger to keep an event is equivalent to the complementary probability of not keeping the event by any of the triggers. Given that the probability for an event passing the requirements of trigger i to then be discarded by prescaling at a rate of f_i^{pre} equals to $(1 - 1/f_i^{\text{pre}})$, which is independent of any other trigger, it follows that the probability for keeping the event amounts to

$$1 - \prod_i (1 - 1/f_i^{\text{pre}}) \,. \tag{5.7}$$

MC samples are normalized to match the data yields recorded with prescaled triggers by reweighting them according to Eq. (5.7), where the product extends over the triggers that fired in a given event. It is assumed here that the residual data-to-MC SFs average to unity.

HLT paths [GeV]	$f^{\text{pre}}/10^3$	Cone-p_T [GeV]	Minimum jet p_T [GeV]
$p_T(\mu) > 3$	4.8–22	10–32	40
$p_T(\mu) > 8$	7–16	15–45	✗
$p_T(\mu) > 17, 20$	0.07–1.3	32–100	✗
$p_T(\mu) > 27$	0.22–0.48	45–100	✗
$p_T(\text{e}) > 8$	5.1–11	15–45	30
$p_T(\text{e}) > 17, 23$	0.57–1.5	25–100	30

Table 5.5: List of prescaled HLT paths employed in the FR measurement. First column details the minimum reconstructed p_T that is imposed to a lepton of particular flavor at the trigger level. The second column shows corresponding prescale factors f^{pre} in multiples of thousand that were typically applied over the three-year data-taking period. The third column provides a range in cone-p_T that events firing the trigger can contribute to. The last column is reserved for specifying the minimum p_T threshold of an extra jet. A cross mark (✗) is shown instead in case no jets are requested at the trigger level.

FRs f_i in some cone-p_T, $|\eta|$ and flavor bin i are computed as a ratio of events in the pass region to the total number of events in pass and fail regions of that bin:

$$f_i = \frac{N_{\text{pass}}}{N_{\text{pass}} + N_{\text{fail}}} \,. \tag{5.8}$$

MC-driven FRs are extracted for specific background by counting the yields in pass and fail regions, in which the selected fakeable lepton is either matched to a generator-level nonprompt lepton or a jet, or does not have any generator-level matches whatsoever. FRs estimated specifically for the QCD background are obtained from simulated dijet QCD

samples that were generated with Pythia at LO in pQCD. The samples are generated for $\hat{p}_T > 15\,\text{GeV}$, where $\hat{p}_T$ refers to the transverse momentum of outgoing partons in the rest frame of the HS process. Special event selection requirements are enforced during the production of QCD samples, right before the detector simulation step, with the intention to enrich the samples with nonprompt muons (that have $p_T > 5\,\text{GeV}$) and electrons (with $p_T > 10\,\text{GeV}$), including those from heavy quark decays. The generator-level filters do not only help in cutting down on the size of QCD samples as well as saving time that would otherwise be spent on the detector simulation, but to also reducing the statistical uncertainties on the prediction by orders of magnitude. QCD-driven FRs are used in the estimation of closure uncertainties by following the procedure described in Section 5.3.4. $t\bar{t}$-driven FRs are extracted from the same MC samples listed in Table 5.2, which are also used for the purpose of estimating irreducible backgrounds in some $t\bar{t}H$ multilepton analysis channels.

FRs that are actually used for the purpose of estimating the fake background are extracted from data as follows. First, distributions in the observable

$$m_T^{\text{fix}}(\mathbf{E}_T^{\text{miss}}) = \sqrt{2 p_T^{\text{fix}} E_T^{\text{miss}} (1 - \cos\Delta\phi)} \tag{5.9}$$

are extracted from data and prompt MC in pass and fail regions. Contamination from processes featuring genuine prompt leptons, mostly from W+jets and SL $t\bar{t}$+jets, are subtracted from the data in both regions. The remaining event yields of „data fakes" in the fail region correspond to N_{fail} in Eq. (5.8), whereas N_{pass} in the same expression is obtained from the normalization of data fakes in the pass region, which together with the prompt MC yields is inferred from a maximum likelihood (ML) fit[18] to the totality of data in the pass region. However, the input shape of data fakes that enters the fit is actually taken from the fail region, which is then scaled to the fake yields in the pass region before the fit. This procedure gets around the problem that the shape as well as the pre-fit yields of data fakes can be unreliable in the pass region, especially after the removal of prompt MC events in that region. W+jets, DY and $t\bar{t}$+jets processes are assigned a 30% normalization uncertainty in the fit, and the remaining rare processes contributing to prompt MC are given a 100% normalization uncertainty. Total variations of JES, JER and unclustered MET are also propagated to the prompt backgrounds as shape uncertainties. On top of that, statistical bin-by-bin uncertainties on the prompt backgrounds enter as separate nuisance parameters in the fit. Examples of the m_T^{fix} distributions in pass and fail regions can be found in Fig. 5.3.

Other subtraction schemes have also been tried to extract the FRs. In one of those methods the normalization of QCD and prompt MC are fitted to data in both pass and fail regions simultaneously, while also correlating the systematic uncertainties on MC prediction between the two regions. Data-driven FRs are computed from data fake yields by subtracting the post-fit yields of prompt MC from the data in pass and fail regions. The FRs that are extracted with the alternative methods typically agree with nominal FRs within the uncertainties.

The m_T^{fix} variable that was chosen for extracting N_{pass} has its origins in the classic transverse mass definition given by Eq. (4.1). Because MET approximates the p_T of an unmeasured neutrino from a leptonic W boson decays rather well, the transverse mass tends to peak broadly at around W boson mass for W+jets events. This is not the case for QCD events, in which MET arises mostly from resolution effects due to lack of neutrinos. It follows that MET and, by extension, m_T are both small, and their corresponding

[18] Details of the ML fitting procedure are provided in Section 6.1.

distributions fall steeply in QCD events at far lower values than the W boson mass. Such discrimination against QCD background is desired because it allows to constrain N_{pass} and its uncertainties much better compared to the case where every bin in the fit is populated by data fakes and prompt MC in constant proportions. Evidently, m_T correlates directly with lepton p_T, but indirectly with the FR. In order to not cause any potential biases in the shape templates when extrapolating them from the fail region to the pass region, the transverse mass definition is modified by fixing the lepton p_T to a constant like it was done in Eq. (5.9). The numerical value of p_T^{fix} is set to $35\,\text{GeV}$ so that the peak would still occur at around W mass for W+jets events, therefore still providing a good discrimination against QCD events. Results of this measurement are summarized in Fig. 5.4.

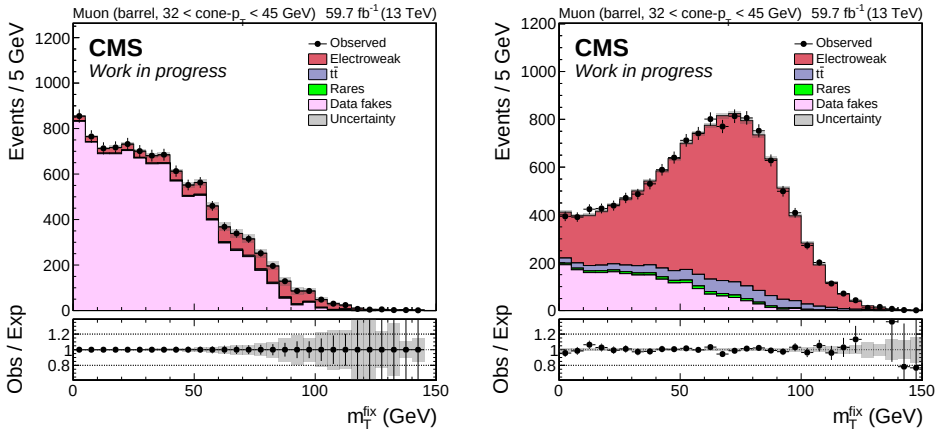


Figure 5.3: Distributions in m_T^{fix} for barrel muons with cone-p_T between 32 and $45\,\text{GeV}$ in the fail region (a) and pass region (b), both based on data recorded in 2018. Distributions shown in the pass region are obtained from ML fit to data. The label „electroweak" refers to the sum of W+jets and DY events, which are scaled by a common factor in the fit.

Contamination from conversions to the MR is compensated with an additional factor that is assigned to the measured electron FRs. The multiplicative factor is obtained from a ratio of QCD-driven FRs, where the numerator is inferred from nonprompt contributions, and the denominator from an aggregated sum of nonprompt contributions and conversions. This approach was chosen because the shape information of QCD conversions turned out to be unreliable due to its poor event statistics, which is why the total yields in pass and fail regions are used instead to scale down the electron FRs. Excluding conversions has an effect of reducing the electron FRs by 10–20% compared to nominal FRs. These additional corrections on electron FRs would not be needed, unless the conversion background had not been estimated explicitly, since otherwise it would lead to an overestimation of the fake background in the SR.

A closure test was performed in the 2ℓSS channel of the $\text{t}\bar{\text{t}}\text{H}$ multilepton analysis by comparing $\text{t}\bar{\text{t}}$- and QCD-driven FRs of the leading fakeable nonprompt lepton that did not pass the tight cuts. The $\text{t}\bar{\text{t}}$-driven FRs turned out to be 30% higher for electrons and 10% higher for muons compared to QCD-driven FRs. This discrepancy was corrected with 100% relative uncertainty in data- and QCD-driven FRs to match $\text{t}\bar{\text{t}}$-driven FRs in the $\text{t}\bar{\text{t}}\text{H}$ analysis since the latter were shown to close well with $\text{t}\bar{\text{t}}$ fakes in the SR. A similar test was performed in the 3ℓ channel of the HH multilepton analysis, showing a mild 7%

discrepancy for muons and -5% for electron in QCD-driven FRs compared to $t\bar{t}$-driven FRs. Because the discrepancy was not as severe in the HH analysis as it was in the $t\bar{t}H$ analysis, no extra corrections were applied to the FRs in the former case.

Statistical uncertainties on N_{fail} and post-fit uncertainties on N_{pass} are propagated to the FRs as shown in Fig. 5.4. A systematic uncertainty is assigned to the fake background by simultaneously varying the FRs up or down within their uncertainties. Two additional uncertainties on the FRs are considered for the fake background, which are implemented by varying the FRs up or down within their uncertainties at high or low cone-p_T and $|\eta|$ bins separately in a seesaw-like manner, similarly to how closure uncertainties are propagated to the data-driven fake background as shown in Fig. 5.8(b). These variations intend to model relative increase or decrease of fakes over the full range of input parameters, without changing the overall normalization of the fake background in the 2ℓSS channel of $t\bar{t}H$ multilepton analysis.

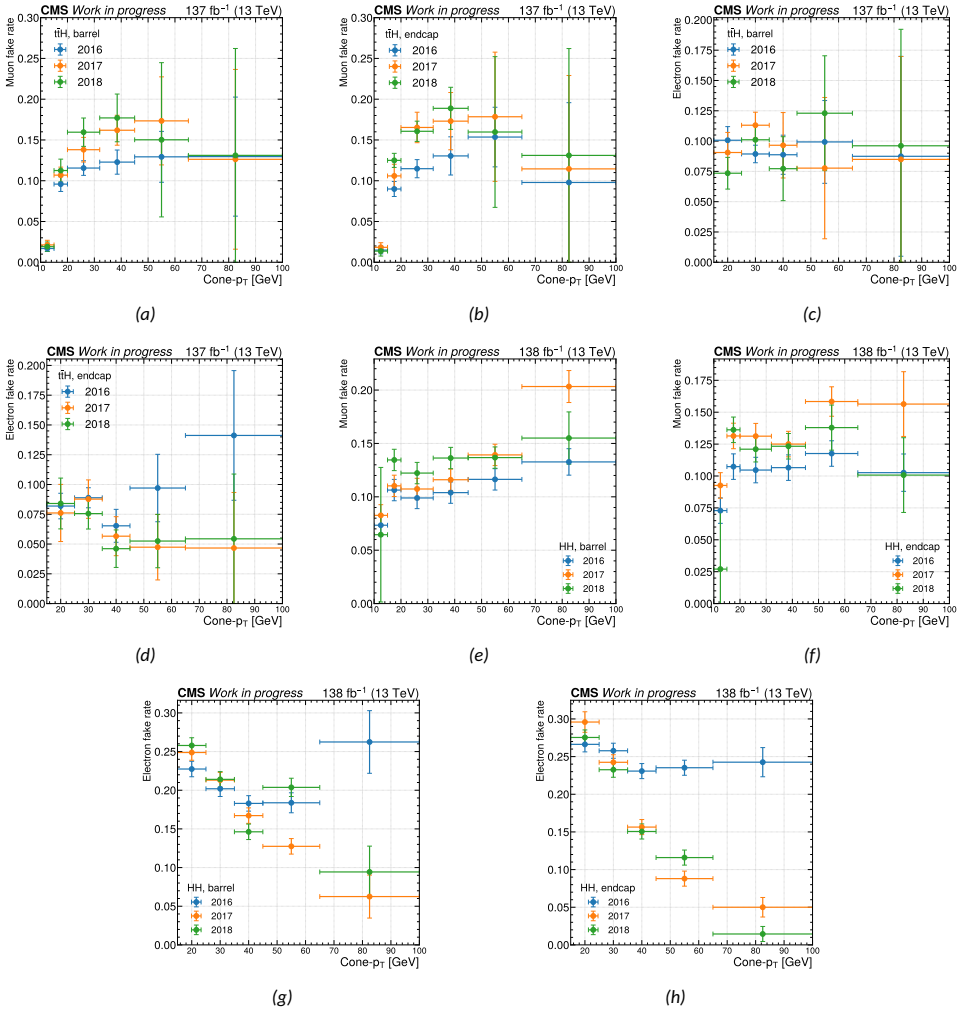


Figure 5.4: Data-driven muon and electron FRs in barrel and endcap regions for the $t\bar{t}H$ and HH multilepton analyses in each of the three data-taking years as a function of cone-p_T.

5.3.3 τ_h fake rate measurement

A jet-to-τ_h FR is defined as the probability for a jet faking as fakeable τ_h to also pass a tighter WP of $D_{\text{jet}}^{\tau_h}$, which ranges from VLoose to VTight in the $t\bar{t}H$ analysis or is set to Medium as in the HH analysis. Events where the selected fakeable τ_h passes the tight WP of $D_{\text{jet}}^{\tau_h}$ would contribute to the „pass" region, while those events that fail this condition are categorized to the „fail" region. Just like lepton FRs given by Eq. (5.8), the fake τ_h rates are determined from the number of events in the pass region to the sum of events in pass and fail regions. Those regions are further segmented by p_T and η of the τ_h candidate into barrel ($|\eta| < 1.479$) and endcap ($|\eta| > 1.479$), and into p_T bins spanning 20–$200\,\text{GeV}$. Separate measurements are performed for each data-taking year. Given that the fake background is mostly dominated by heavy flavors in the $t\bar{t}H$ analysis and light flavors in the HH analysis, dedicated CRs are used to extract the FRs for both cases. These CRs are populated mostly with one particular type of background events based on the multiplicity and flavor of tight leptons in the final state. Any extra reconstructed τ_h that may appear in the final state are assumed to originate from genuine jets that are misidentified as τ_h.

FRs used for the $t\bar{t}H$ analysis are extracted from a CR enriched with DL $t\bar{t}$+jets events, in which one of the leptons is a tight electron and the other a tight muon with opposite electric charge. The leading and subleading lepton p_T is required to exceed 25 and $15\,\text{GeV}$, respectively. These p_T thresholds are just high enough that electron-plus-muon cross-triggers imposed in the event selection reach their maximum efficiency. In addition to the cross-triggers, events are also selected to the CR if they fire any of those unprescaled single lepton triggers that are listed in Table 3.2. The purity of $t\bar{t}$+jets events in the CR is further improved by requiring no less than two central jets in final state, of which at least one jet passes the medium WP or at least two jets pass the loose WP of the DeepJet b tagging discriminant. The selected events must feature at least one fakeable τ_h that is closer than $\Delta R = 0.3$ to a central jet, whereby both the τ_h and the jet are cleaned with respect to fakeable electrons and muons before the pairing. The matching jet is required to originate from a quark or a gluon jet in MC simulation. The same event contributes to the measurement as many times as there are τ_h candidates fulfilling this condition. This workaround helps to reduce statistical uncertainties, which dominate the measurement. Events featuring low mass meson resonances are rejected because they are poorly modeled in the MC simulation.

The FRs that are measured for the HH analysis are extracted from a CR targeting DY events in dimuon final state. The event selection requirements are identical to those of $t\bar{t}$+jets CR, except that the two selected leptons must be muons, the events must fire a single or a double muon trigger, and the b jet selection criteria is inverted into a b jet veto. Furthermore, the selected muon pair must have an invariant mass closer than $30\,\text{GeV}$ from the Z boson mass, or otherwise the event would be rejected.

Jets passing the τ_h leg of a lepton-plus-τ_h cross-trigger or either leg of a double-τ_h trigger listed in Table 3.2 are also more likely to pass the tighter WP of $D_{\text{jet}}^{\tau_h}$. Such jets would therefore have higher FRs compared to those that either fail the trigger conditions or are not required to satisfy any trigger conditions whatsoever. This sort of bias, if left unaddressed, would cause the fake background to be underestimated in channels where events are selected based on the status of aforementioned triggers. For this reason, the measurement is repeated another four times to account for the cases where the selected τ_h either fires or does not fire a lepton-plus-τ_h cross-trigger or a double-τ_h trigger. This is realized by searching for the trigger-level object of the corresponding HLT path that is closer than $\Delta R = 0.05$ to the reconstructed τ_h. If no such match is found, then the selected τ_h is said to not fire the trigger.

Different jet-to-τ_h FRs are used depending on which triggers are enforced in the event selection and whether or not the selected τ_h fired those triggers. In particular, if the event selection requirements demand the presence of τ_h in final state but do not employ lepton-plus-τ_h cross-triggers nor double-τ_h triggers in the event selection, then those FRs are used in fake background estimation that were measured without any trigger requirements on the selected τ_h. The same is also true for channels that employ these triggers in combination with single lepton triggers that fired. However, if the single lepton triggers did not fire in a given event, then it is checked whether or not the selected τ_h fired a lepton-plus-τ_h cross-trigger. If none of the cross-trigger fired, then it is checked whether or not the selected τ_h fired a double-τ_h trigger. This also applies to channels that use only double-τ_h triggers in the event selection. The case where the selected τ_h failed to fire a given trigger is irrelevant in the application of FRs if the multiplicity of the final state τ_h matches to the number of τ_h legs of the requested triggers. These principles provide an algorithm for applying the jet-to-τ_h FRs as detailed in Table 5.6.

	Channel	Without any requirements on the τ_h triggers	Lepton-plus-τ_h cross-trigger		Double-τ_h trigger	
			Pass	Fail	Pass	Fail
$t\bar{t}H$	$0\ell+2\tau_h$	✗	✗	✗	✓	✗
	$1\ell+1\tau_h$	✓	✓	✗	✗	✗
	$1\ell+2\tau_h$	✓	✓	✓	✗	✗
HH	$0\ell+4\tau_h$	✗	✗	✗	✓	✓
	$1\ell+3\tau_h$	✓	✓	✓	✓	✓

Table 5.6: Application of jet-to-τ_h FRs based on the triggering conditions of the selected τ_h in $t\bar{t}H$ (top section) and HH (bottom section) analysis channels. A tick mark (✓) indicates that the designated FRs could be used in the analysis, whereas a cross mark (✗) implies otherwise. All other analysis channels that are not listed in the table but still require the presence of τ_h in the final state apply the FRs that were measured for τ_h without the imposition of any trigger conditions. Highest priority is given to the FRs that are measured without any requirements on the τ_h triggers, followed by those imposed by the lepton-plus-τ_h cross-triggers and the double-τ_h triggers.

MC-driven FRs are derived from the event yields of simulated $t\bar{t}$+jets and DY processes in their respective CRs, whereby the selected τ_h are required to not have any matches to prompt muons, electrons or τ_h at the generator level. Residual contributions from events featuring a genuine prompt τ_h are estimated from the simulation and removed from the data based on the generator-level matching status of the reconstructed τ_h. Data-driven FRs are not directly used to estimate the fake background because the extracted FRs fluctuate a lot. Instead, a linear fit to the ratio of data-driven and MC-driven FRs is performed as a function of p_T of the τ_h candidate, which intends to average out these fluctuations. SFs predicted by the linear function are then applied on top of the MC-driven FRs to yield a regressed version of data-driven FRs. Results of this measurement are displayed in Figs. 5.5 and 5.6.

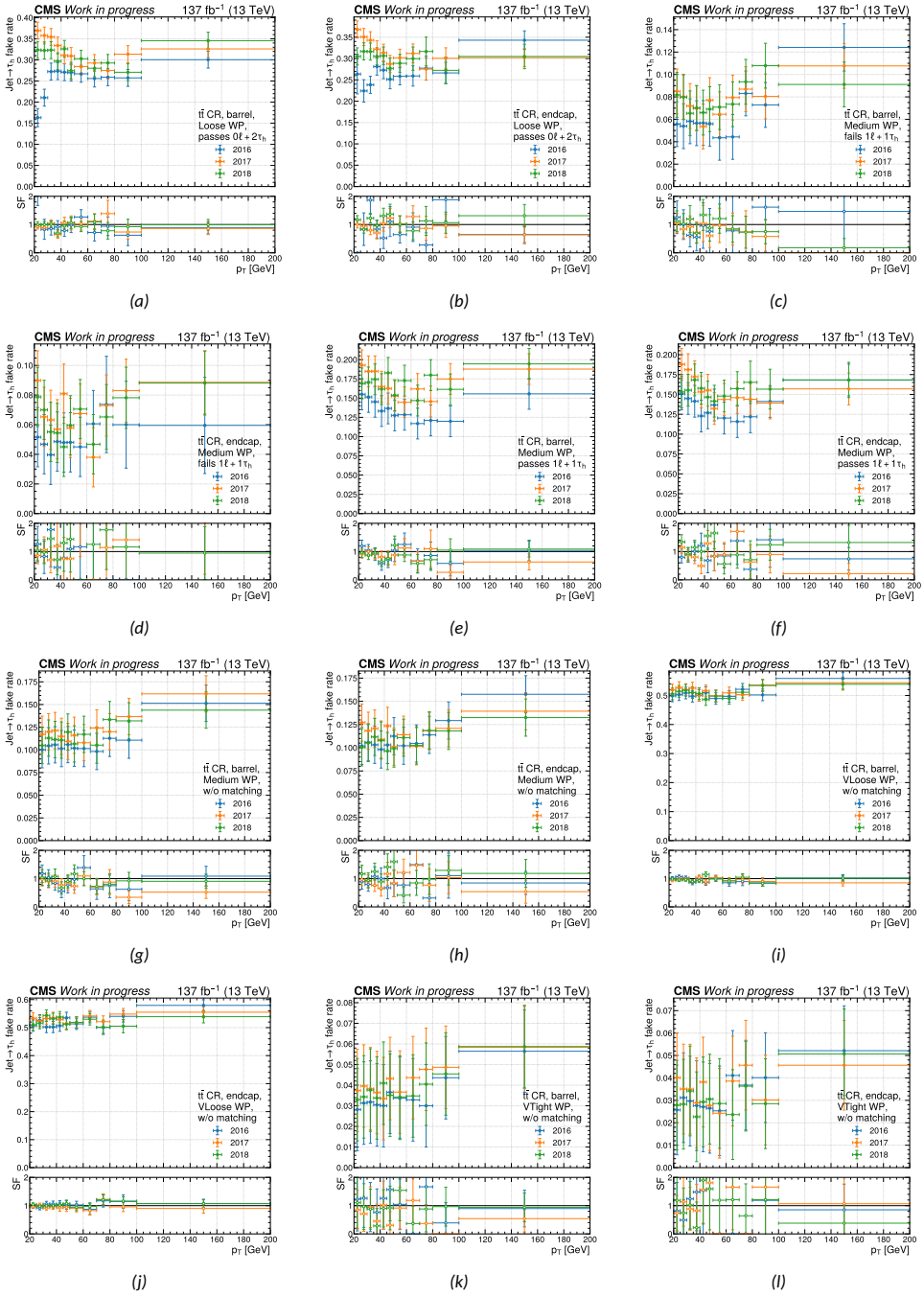


Figure 5.5: Jet-to-τ_h FRs measured in $t\bar{t}$ CR for the $t\bar{t}H$ analysis in barrel and endcap regions: for τ_h passing the Loose WP of $D_{jet}^{\tau_h}$ and double-τ_h trigger (a)–(b); for τ_h passing the Medium WP of $D_{jet}^{\tau_h}$, failing (c)–(d) or passing (e)–(f) lepton-plus-τ_h cross-trigger, and without any trigger requirements (g)–(h); for τ_h passing the VLoose WP of $D_{jet}^{\tau_h}$ and without any trigger requirements (i)–(j); for τ_h passing the VTight WP of $D_{jet}^{\tau_h}$ and without any trigger requirements (k)–(l). Top section in each plot displays the MC-driven FRs, while the bottom section shows the respective data-to-MC SFs.

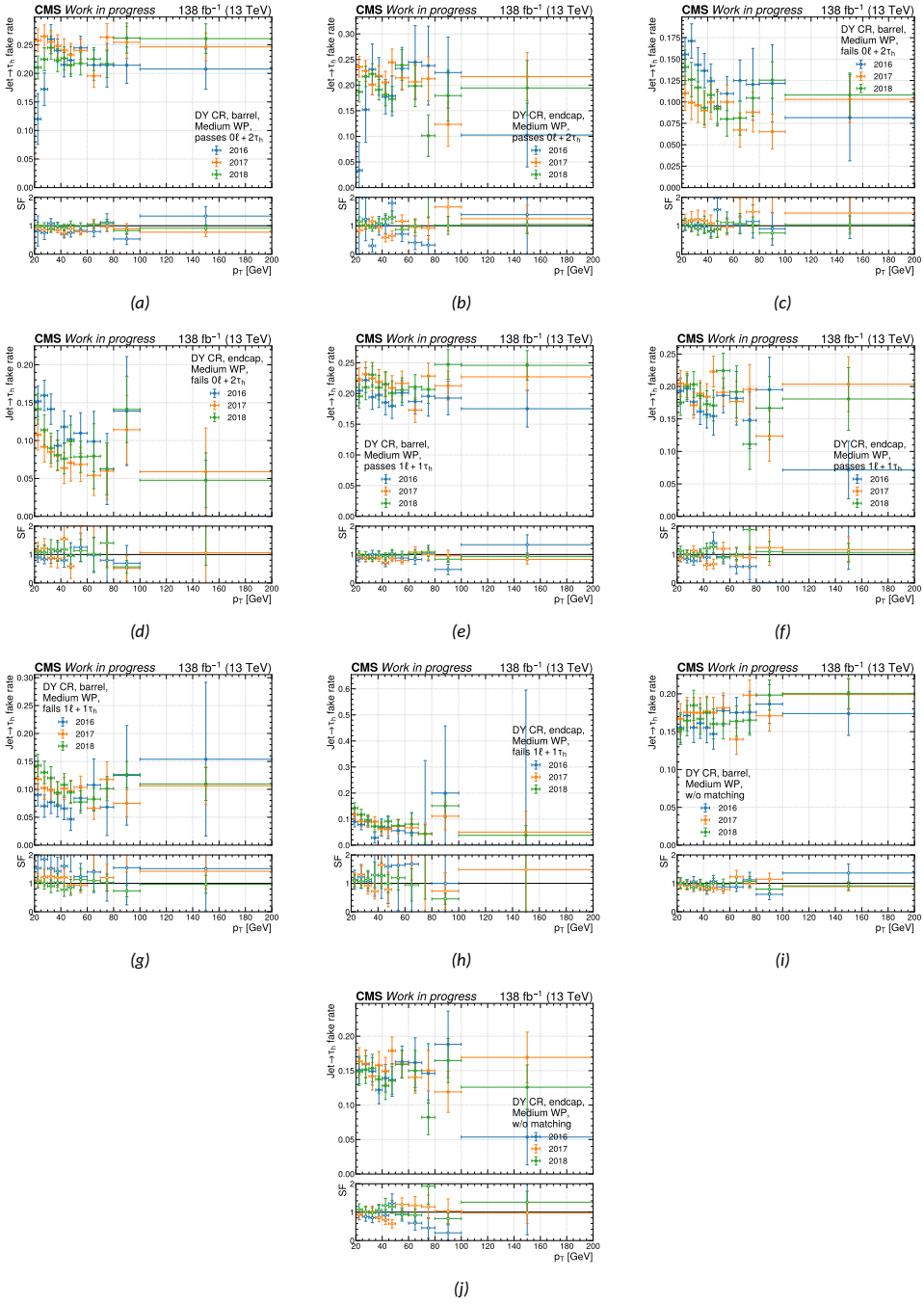


Figure 5.6: Jet-to-τ_h FRs measured in DY CR for the HH analysis in barrel and endcap regions split by year for τ_h passing the Medium WP of $D^{\tau_h}_{jet}$, passing or failing double-τ_h trigger (a)–(d) and lepton-plus-τ_h cross-trigger (e)–(h), and without any trigger requirements (i)–(j). Top section of each plot displays the MC-driven FRs, while the bottom section shows the respective data-to-MC SFs.

Coefficients $\mathbf{c} = (c_0, c_1)^T$ of linear fit function $c_0 + c_1 \cdot p_T$ are assumed to follow a two-dimensional normal distribution:

$$\mathcal{N}(\mathbf{c}|\hat{\mathbf{c}}, \Sigma) = \frac{\exp[-D_M^2(\mathbf{c}|\hat{\mathbf{c}}, \Sigma)/2]}{2\pi\sqrt{\det\Sigma}}\,, \tag{5.10}$$

where $D_M(\mathbf{c}) = \sqrt{(\mathbf{c}-\hat{\mathbf{c}})^T\Sigma^{-1}(\mathbf{c}-\hat{\mathbf{c}})}$ denotes the Mahalanobis distance [364] and $\hat{\mathbf{c}} = (\hat{c}_0, \hat{c}_1)^T$ stands for the best fit values that maximize $\mathcal{N}(\mathbf{c})$. Covariance matrix Σ returned by the fit may feature off-diagonal elements, which means that the uncertainties on slope c_1 and intercept c_0 correlate with each other. These correlations could be propagated to the final ML fit that extracts the signal rate, but a more robust approach would be to just decorrelate the uncertainties right from the beginning by diagonalizing the covariance matrix: $\Sigma = V\Lambda V^{-1}$. Here Λ refers to a diagonal matrix that has the eigenvalues of Σ as its elements, while matrix V has the eigenvectors of Σ in its columns. As illustrated by Fig. 5.7(a), the eigenvectors $\mathbf{v}_i = (v_{i0}, v_{i1})^T$ (with $i = 0, 1$) point to the direction in parameter space where the variations are independent from each other, while the corresponding eigenvalues λ_i indicate the size of these variations at which $D_M(\mathbf{c}) = 1$. Provided that the data-to-MC SFs are estimated from evaluating $\hat{c}_0 + \hat{c}_1 \cdot p_T$, the two uncorrelated variations of the fit parameters enumerated by index i are propagated to the fake background via the SFs as follows:

$$(\hat{c}_0 \pm \sqrt{\lambda}_i v_{i0}) + (\hat{c}_1 \pm \sqrt{\lambda}_i v_{i1}) \cdot p_T\,.$$

An example of a linear fit with uncorrelated systematic shifts of the fit parameters can be found in Fig. 5.7(b). The linear fit was performed using weighted least squares methods, where the residual errors are weighted by squares of reciprocal error on the data points. Residual flavor dependency in the FRs is quantified with a dedicated closure uncertainty, which is described in the next section.

In normal circumstances, all leptons and τ_h that are selected to some SR are required to be prompt in MC simulation, and any contributions from events featuring nonprompt leptons or τ_h in the final state are estimated from the data with the FF method as explained before. However, it was found that about a third of $\mathrm{t\bar{t}H}$ signal would be lost in the SRs of the $2\ell\mathrm{SS} + 1\tau_\mathrm{h}$ and $3\ell + 1\tau_\mathrm{h}$ channels in the $\mathrm{t\bar{t}H}$ analysis if the selected τ_h is required to be prompt in the simulation. This is because nearly half of the selected $\mathrm{t\bar{t}H}$ events in those two channels originate from $\mathrm{H} \to \mathrm{WW}^*$ decays. The issue is that half of those events feature hadronic W boson decays, where one of the jets is erroneously misidentified as τ_h at a rate that is proportional to the FR. To recover the events that would otherwise be lost by requiring all final state τ_h to be matched to genuine τ_h at the generator level, a modified version of the FF method was devised for the $2\ell\mathrm{SS} + 1\tau_\mathrm{h}$ and $3\ell + 1\tau_\mathrm{h}$ channels of the $\mathrm{t\bar{t}H}$ analysis, and for the $2\ell\mathrm{SS}{+}\leqslant 1\tau_\mathrm{h}$ channel of the HH analysis, in which the τ_h is required to be tight in both the SR as well as the fake AR, but no generator-level matching conditions are imposed to the selected τ_h in the simulation. Data-to-MC SF of the jet-to-τ_h FRs are instead applied to fake τ_h in both analysis regions. The FF method still applies to final state leptons as usual. This strategy recovered 30% of signal sensitivity in both channels.

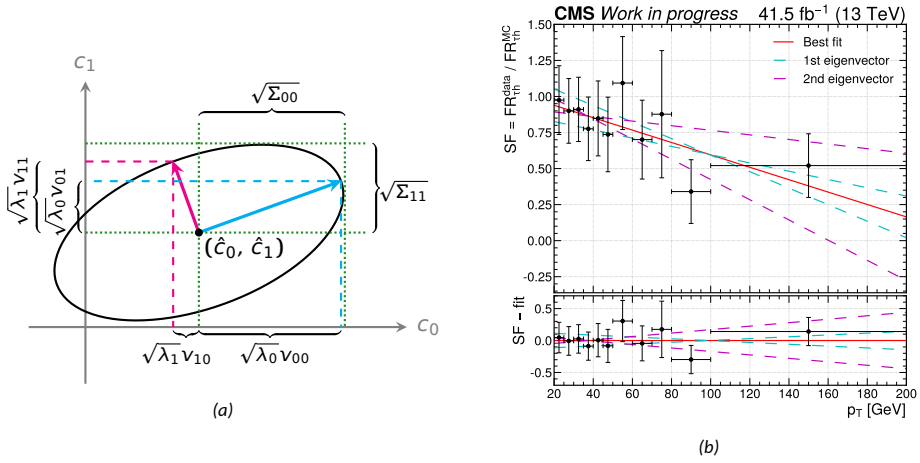


Figure 5.7: (a): Visualization of covariance matrix Σ that is estimated for parameters $\mathbf{c} = (c_0, c_1)^T$ of the fit. The ellipsoidal contour corresponds to the parameter values where $D_M(\mathbf{c}) = 1$. Projections of the ellipse in parameter space coincide with their uncertainties, which can also be expressed as square root of the diagonal elements of Σ. Decorrelated variations of the best fit parameters are obtained by projecting out either axis of the ellipse, or equivalently the components of either eigenvector of the covariance matrix times the square root of the respective eigenvalue. (b): Data-to-MC SFs of jet-to-τ_{h} FRs for the Medium WP of $D_{\mathrm{jet}}^{\tau_{\mathrm{h}}}$ extracted from $\mathrm{t\bar{t}}$ CR and parametrized by p_T of the fake τ_{h} candidate based on data collected in 2017. The SFs (points) are regressed with a linear function, which is plotted for the optimal choice of parameter values returned by the fit (red line), as well as for decorrelated variations of said parameters (dashed lines). Vertical error bars represent statistical uncertainties in data and MC added in quadrature.

5.3.4 Closure uncertainty

Uncertainties on the extracted FRs mostly reflect the fact that the event statistics was rather limited in the measurement. These uncertainties are eventually propagated to the fake background estimation via the FFs like discussed before. However, there may be other nuances in the FR measurement and application that could potentially skew the fake background estimation. One way this could happen is if the flavor composition and kinematic profile of fakes between the fake AR and MR are different, since it would break the universality property of FRs. Even if corrected for, residual differences could still arise in the FRs depending on how partons color-connect with the rest of the event. For example, b jets produced in ISR or FSR via gluon splitting tend to be more collinear and hence less isolated than those originating from a HS event. It follows that the FRs could be influenced by other factors not included in their parametrization, which would lead to larger errors in fake background estimate and cause possibly stronger tension in the ML fit where the signal rate is extracted.

It is impractical to identify and correct for every possible source of discrepancy in the fake background estimate from the measurement side. Instead, it is assumed that the presented approach offers the best description of the fake background, and any kind of bias that could influence this prediction is modeled with a nuisance parameter that allows minor adjustments in the shape and yield of the fake background during the signal extraction. These potential biases are modeled from the FR application side with a nonclosure uncertainty, which is obtained from MC simulation as follows: Dedicated „MC closure" regions are constructed for some target lepton flavor by enforcing the same object and event selection criteria as in the SR, but allowing the selected leptons or τ_{h} with the target

flavor to fail the tight cuts. For instance, in MC closure for electrons, the electrons that are selected to the final state must pass the fakeable selection criteria but can fail the tight selection, whereas the muons and τ_{h} that are also selected to the final state must satisfy the tight selection requirements. There can be up to three MC closure regions for every target flavor: one for muons, another for electrons and a third one for τ_{h}. Overlap with the SR is avoided by vetoing those events that feature only tight objects in the final state, except if all leptons or τ_{h} with the target flavor are in fact prompt[19]. At least one of the final state objects must be a fake for the event to be accepted to the MC closure region. Table 5.7 demonstrates how simulated events contribute to analysis regions of a dilepton channel based on the above description. The events that are selected to the MC closure region are then reweighted according to the FF method, whereby QCD-driven FRs are used for electrons and muons, and MC-driven FRs without the data-to-MC SFs for τ_{h}. The output of signal extraction discriminant in MC closure is then compared to that of MC fakes in the SR.

ee	FF	FT	TF	TT
NN	MCe	MCe	MCe	MCf, MCμ
NP	MCe	MCe	MCe	MCf, MCμ
PN	MCe	MCe	MCe	MCf, MCμ
PP	pMC	pMC	pMC	SR

eμ	FF	FT	TF	TT
NN	—	MCe	MCμ	MCf
NP	—	MCe	MCμ	MCf, MCμ
PN	—	MCe	MCμ	MCf, MCe
PP	pMC	pMC	pMC	SR

Table 5.7: Categorization of simulated events with an electron pair (left) and electron-muon pair (right) in final state to the SR, MC closure region for muons (MCμ) or electrons (MCe), as prompt MC (pMC) in the fake AR, or as MC fakes (MCf) in the SR of $2\ell SS(+1\tau_{\mathrm{h}})$ analysis channel based on whether the selected lepton is prompt (P) or nonprompt (N), and whether the selected lepton passes the tight cuts (T) or fails them (F). For example, events with a prompt tight electron and a nonprompt fakeable muon that fails the tight cuts contribute to MC closure region for muons. A dash (—) is used if a given combination of leptons does not contribute to any of the aforementioned analysis regions.

Two uncertainties on data-driven fake background are derived from this comparison. First is the normalization uncertainty, which is obtained from the ratio of yields in MC fakes to MC closure. This ratio is then used to uniformly scale the data-driven background yields but not by more than 100%. The second uncertainty is obtained from a linear fit to bin-by-bin ratio of distributions in MC fakes to MC closure after they have been normalized to the same integral. Average output score of the signal extraction discriminant is chosen as inflection point in the fit. The slope returned by the fit is then used to modulate the data-driven shape template by raising or lowering the tails of the distribution on either side of the inflection point as shown in Fig. 5.8[20]. These two uncertainties are extracted

[19] This special clause is necessary because the rate for prompt leptons or τ_{h} to fail the tight cuts is much lower than for them to pass those cuts. In other words, events that feature some prompt leptons or τ_{h} passing the tight cuts have higher yields compared to events where those leptons or τ_{h} fail the tight cuts, which is why the former case is not vetoed from the MC closure region, thus allowing a more fair comparison of event yields to MC fakes in the SR.

[20] The shape modulations should technically be orthogonal over the full range of the signal extraction discriminant to avoid spurious correlations between underlying parameters in the signal extraction. It would leave shifted Legendre polynomials ($\tilde{P}_0(x) = 1$, $\tilde{P}_1(x) = 2x - 1$) as the only option for decomposing the shape modulations. However, rather than being distributed uniformly, the fake background events tend to skew towards low values of the signal extraction discriminant, which is why the intercept term of $1/2$ in $\tilde{P}_1(x)$ is replaced by the average output score of MC fakes.

for muons, electrons and τ_h in each analysis channel and data-taking period separately, and are thus treated fully uncorrelated.

Additional normalization uncertainty is assigned to the fake background that is fully correlated across all analysis channels and data-taking years. The uncertainty amounts to 50% in the $t\bar{t}H$ analysis channels that are dominated by τ_h fakes ($0\ell + 2\tau_h$, $1\ell + 1\tau_h$, $1\ell + 2\tau_h$, $2\ell OS + 1\tau_h$, $2\ell + 2\tau_h$), and 30% is given to the rest of the channels. In the HH analysis, this uncertainty is split into two parts of 20%, with the first part being fully correlated as before and the second part taken as fully uncorrelated.

In the fake AR of the $1\ell + 3\tau_h$ channel in the HH analysis it was found that about two-thirds of τ_h fakes originate from DY events in dielectron final states, in which one of the electrons was misidentified as τ_h and the remaining τ_h were faked by jets. Those fakes are suppressed by introducing a Z boson veto that rejects those electron and τ_h pairs with OS charges, in which the τ_h either fails VLoose WP of $D_e^{\tau_h}$ or it falls into the ECAL crack between EB and EE ($1.460 < |\eta| < 1.588$). The τ_h track is extrapolated from the LV to account for its longitudinal shift with respect to the origin of the coordinate system. Lower threshold in Z boson mass window cut was also extended from $10\,\text{GeV}$ to $20\,\text{GeV}$ to accept more electrons since their energy tends to be underestimated when faking a τ_h. For similar reasons, the singular τ_h in final states of the $3\ell + 1\tau_h$ channel in the HH analysis is required to satisfy VVLoose WP of $D_e^{\tau_h}$, and not fall into the ECAL crack between EB and EE. Since these extra conditions in τ_h selection were not considered in the FR measurement, an additional 30% normalization uncertainty is assigned to the data-driven fake background in those two channels. The uncertainty is taken as fully correlated across the channels and data-taking years.

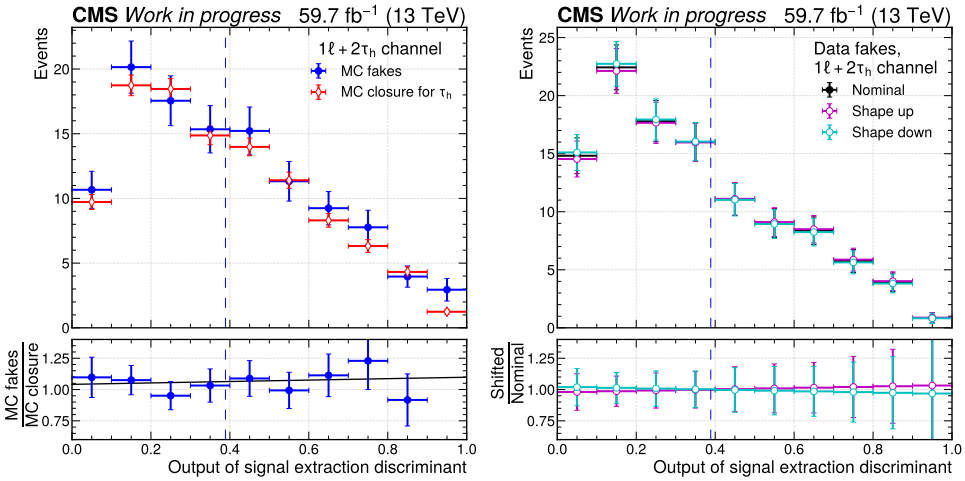


Figure 5.8: Distribution in the output of signal extraction discriminant for the $1\ell + 2\tau_h$ channel in the $t\bar{t}H$ analysis based on 2018 data comparing MC fakes to MC closure for τ_h (a), and data fakes to its linear shape modulation (b). Vertical blue dashed line denotes the average output score of MC fakes in both plots. Solid black line in the ratio plot of (a) was obtained from a linear regression to the ratio of bin-by-bin yields in MC fakes to MC closure. The corresponding slope is then used to linearly modulate the output distribution of data fakes as shown in (b). Normalization uncertainty is extracted from the intercept of the solid black line in the ratio plot of (a) at a point where it crosses the blue vertical dashed line. Statistical uncertainties on MC yields are incorporated to the linear fit with weighted least squares method.

5.4 Charge flip background estimation

The SS charge requirement that is imposed on the two selected prompt leptons in the 2ℓSS and $2\ell\text{SS}+1\tau_\text{h}$ channels intends to reject primarily DL $\text{t}\bar{\text{t}}$ events. Yet, some of those background events may still seep into the SR if the charge of either prompt lepton is mismeasured despite the tight charge condition, which is specifically utilized to counter this very problem. Contributions from such „charge flips" to the SR could be estimated directly from the MC simulation, but similarly to fake background estimation the generated samples do not contain enough events to reliably model this kind of background. Instead, a data-driven method analogous to fake background estimation is used to predict the charge flip background as detailed in the following.

The charge flip background is estimated from data events that are selected to flip AR, which is an analysis region identical to the SR but instead of demanding the selected leptons to have SS charges they are required to have OS charges. The chosen data events are then extrapolated to the SR by reweighting them using charge flip probabilities. In the 2ℓSS channel, this amounts to the probability for one lepton to flip its charge plus the probability for the other lepton to flip its charge. In the $2\ell\text{SS}+1\tau_\text{h}$ channel, however, there is another requirement in the event selection by which the charge sum of the selected two leptons and τ_h must equal to ±1. Only events that could still satisfy this cut yet feature a lepton that has its charge incorrectly measured are those events where this lepton happens to have the same charge as the selected τ_h. For this reason the charge flip probability is evaluated on leptons that have the same charge as the τ_h. Contributions from nonprompt leptons and conversions are subtracted from the extrapolated data after the reweighting, which then yields the final estimate for charge flip background in the SR. Contamination from nonprompt leptons to the flip AR are estimated from data with the FF method by treating the flip AR as the SR in the extrapolation. Charge misidentification probabilities are evaluated on electrons because they are found to be negligible for muons, in the order of 10^{-6}. Likewise, there is no practical need for subtracting genuine SS events from the data in flip AR because they are doubly-suppressed by the electron charge misidentification probabilities. The OS charge requirement in Z boson veto is dropped if the two selected leptons happen to be electrons. This is to avoid biases that arise between the SR and corresponding flip AR, since otherwise the Z boson veto would not be as effective in the former as it is in the latter.

Charge misidentification rates are measured for electrons and muons separately in three bins of p_T (10–25, 25–50 and $>50\,\text{GeV}$) and in two bins of $|\eta|$ (EB and EE), totalling six bins per lepton flavor. The following focuses only on the electron flip rate measurement, however, because the same measurement was repeated for muons based on 2016 data, which revealed that the muon flip rate is effectively negligible, in the order of 10^{-6} [365]. Electron charge misidentification rates are extracted from data by measuring the ratio of DY event yields with two SS electrons in final states to the total number of DY events that are selected in the same CR. The event selection criteria demand the presence of exactly two tight electrons satisfying the tight charge condition. Events with tight muons passing the tight charge requirement are vetoed. The measurement is performed for the $\text{t}\bar{\text{t}}\text{H}$ and HH multilepton analyses separately because both employ different requirements for selecting tight leptons. The purity of DY events in the CR is further improved by imposing single or double electron trigger conditions, as well as a cut on the invariant mass of the electron pair, which is required to be closer than $30\,\text{GeV}$ to Z boson mass. In MC simulation, the selected electrons also need to be matched to generator-level electrons, but their charges do not necessarily have to agree with each other. This is obviously not the case for electrons and muons that are selected to the SR of the 2ℓSS and $2\ell\text{SS}+1\tau_\text{h}$ channels.

Events in DY CR are further split into SS or OS category based on the reconstructed charges of the two electrons. The peak in dilepton invariant mass that is characteristic to Z boson decay should appear in both categories if sufficient number of events make the event selection cuts.

Since the goal is to extract charge flip rates for six kinematically distinct electrons, there can be 36 different combinations of electron pairs that could be selected to the DY CR. By making a fair assumption that it does not matter if it is leading or subleading electron that has its charge flipped, the number of combinations is brought down to 21. The ratio of event yields with SS electron pairs in final state to the total number of events, $r = N_{\text{SS}}/(N_{\text{SS}} + N_{\text{OS}})$, is directly proportional to the sum of probabilities for either electron to have its charge mismeasured. The case where both electrons might have their charges mismeasured is expected to be very small and therefore ignored. The resulting system of equations that relates event yield ratios to charge flip probabilities is overconstrained, because there are 21 known variables (the event yield ratios) but only six unknowns (the charge flip probabilities). The set of linear equations is solved for charge misidentification rates using the method of weighted least squares.

Event yields N_{SS} and N_{OS} correspond to the normalization of DY events in SS and OS category, respectively. They are extracted from a maximum likelihood fit of the MC prediction, including backgrounds, to data in SS and OS categories simultaneously, thus allowing to correlate systematic uncertainties between the two. Three nuisance parameters enter the fit in addition to statistical bin-by-bin uncertainties and rate uncertainties on the prediction, with two parameters modeling 1% and 2.5% uncertainty on electron energy scale in EB and EE, respectively, and a third one varying electron energy resolution by 25% from its nominal value, which is determined from absolute p_T difference between the reconstructed electron and its generator-level match. Illustrative post-fit plots obtained for one particular combination of electron pairs out of 21 possible combinations can be found in Fig. 5.9. Final results of these measurements are summarized in Table 5.8. The measurement is repeated for every data-taking year to account for changes in detector conditions. Charge flip rates tend to be higher in 2016 compared to following years, which is expected because of superior performance of the new pixel detector that was installed as part of Phase 1 upgrades. The same goes for charge flip rates in the HH analysis, because leptons selected there need to pass a looser prompt lepton MVA WP than what is used in the $\text{t}\bar{\text{t}}\text{H}$ analysis. The measured flip rates are compatible with the rates determined by the CMS e/γ POG [280].

Charge flip measurement and application was validated with the following closure test: Simulated events with genuine OS lepton pairs are selected to the flip AR of the 2ℓSS channel and subsequently extrapolated to the SR the same way as data-driven flip background is estimated. The resulting yields are compared to nominal yields of simulated flip events in the SR, where at least one of the selected electrons is required to have a charge opposite to its prompt generator-level match. Comparison of the two showed a difference of up to 30%, which is taken as rate uncertainty on the data-driven flip background.

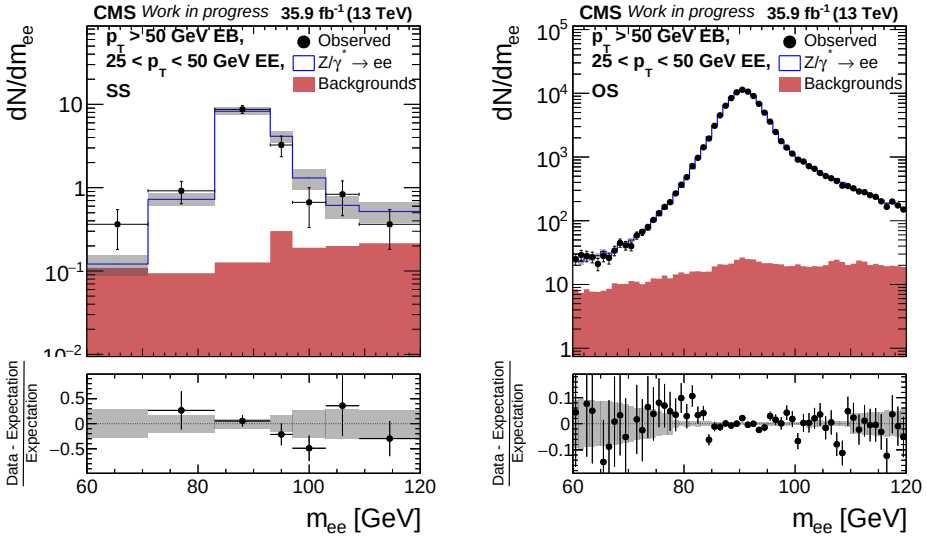


Figure 5.9: Post-fit distributions in invariant dielectron mass reconstructed from measured SS (a) and OS (b) pairs of electrons in DY CR based on data recorded in 2016. One of the electrons is reconstructed within the acceptance of EB and has a $p_T > 50\,\text{GeV}$, while the other electron is reconstructed outside of this acceptance and has a p_T between 25 and 50 GeV. The shaded band in both plots represents statistical uncertainties on the MC prediction.

		$10 \leqslant p_T < 25\,\text{GeV}$		$25 \leqslant p_T < 50\,\text{GeV}$		$p_T \geqslant 50\,\text{GeV}$	
		$t\bar{t}H$	HH	$t\bar{t}H$	HH	$t\bar{t}H$	HH
2016	$\lvert\eta\rvert < 1.479$	0.56	1.27	0.09	0.25	0.15	0.26
	$1.479 \leqslant \lvert\eta\rvert < 2.5$	0.61	1.88	1.02	3.22	1.62	3.45
2017	$\lvert\eta\rvert < 1.479$	0.12	0.31	0.05	0.04	0.10	0.11
	$1.479 \leqslant \lvert\eta\rvert < 2.5$	0.43	1.35	0.50	1.63	0.88	1.76
2018	$\lvert\eta\rvert < 1.479$	0.04	0.28	0.06	0.12	0.11	0.09
	$1.479 \leqslant \lvert\eta\rvert < 2.5$	0.36	0.90	0.51	1.30	0.97	1.58

Table 5.8: Measured electron charge flip rates (in units of per mille) as a function of p_T and $|\eta|$ of the electron, data-taking year and tight lepton definition.

6 Signal extraction

Based on the predicted contributions of data in the SR, the events that pass the selection cuts are expected to contain a mixture of signal and background events. In order to tell the two apart, one would need to construct an observable that is able to discriminate background in favor of signal, and compare its distribution in data events to the prediction, while also accounting for the statistical and systematic uncertainties in this comparison. Since this needs to be done in a well-defined and unbiased way so to be able to later compare or combine the analysis results, the ATLAS and CMS collaborations had jointly developed common statistical procedures for quantifying the presence or absence of a signal, placing constraints on the parameters characterizing the signal, and validating the modeling of signal and background processes [366]. Overview of those methods is provided in Section 6.1, while Section 6.2 summarizes the techniques that were used to develop discriminants for signal extraction in the present work.

6.1 Inference

The goal of statistical inference is to interpret empirical data by devising a model, juxtaposing it with the data, and extracting quantitative information from this comparison. The present section will touch on the following ingredients of statistical inference that are relevant in the searches of $t\bar{t}H$ and HH signal: Section 6.1.1 introduces the basic concepts of statistical analysis; Section 6.1.2 focuses on the likelihood model; Section 6.1.3 describes the limit setting procedure; and Section 6.1.4 explains, what steps are taken to validate the model without directly looking at the data. A more elaborate and comprehensive exposition of this material can be found in Refs. [24, 366, 367], which the following text attempts to summarize.

6.1.1 Basics

A statistical model is characterized by a set of variables, also known as parameters of interest (POIs), which parameterize the signal process that an analyst wishes to measure. The main objective of statistical inference is to make quantitative claims about the POIs, given the data. A variable that suits this task is signal strength modifier μ, which tells how many times the production and decay rates of the signal process deviate from the expectation. As seen from Eq. (5.1), both of these rates fully correlate with the expected yields of the signal. Since the expected yields can be directly compared to those of the data, it is natural to give signal strength modifiers the role of POIs. If the data perfectly matches the expected yields as predicted by the model, then all POIs would equal unity, which amounts to saying that nominal signal contribution appears in the data exactly as anticipated.

In order to access nonobservable parameters that are featured in underlying Lagrangian densities, one could attempt to reparametrize the signal strength modifiers in terms of those more fundamental variables and treat them as the POIs. For instance, the signal strength modifier of HH signal process scales with a self-coupling modifier as prescribed by Eq. (2.27), which makes it possible to use coupling modifiers as POIs. However, one also needs to keep in mind that the same self-coupling modifier induces changes to the rates of other single Higgs production and decay processes through loop corrections, as explained in the context of Fig. 2.22. Such scaling behavior must be accounted for to not bias the coupling measurement.

A signal process could also depend on other parameters such as spin or mass. If successful parametrization of signal strength modifiers in terms of those parameters is not

possible, then they cannot serve as the POIs. In that case the only way of probing them is to formulate a range of inference models for a number of spin and mass combinations, and extract the signal rate modifiers for each of those combinations. This strategy was chosen to study the resonant HH production, for example.

Point estimates of the POIs have no value of their own if there are no auxiliary statements about the credibility of the measurement. From a Bayesian point of view this implies prior beliefs about the POIs and the data, but these are difficult to model in practice. For this reason a frequentist approach due to Neyman is followed [368]. The idea is to consider a series of experiments that each try to extract the same POI μ. If the experiments are performed in identical conditions, then any spread in the results should arise purely from statistical fluctuations of the data. The results of each experiment x can be distilled to a single number $t_\mu(x)$ known as test statistic. It is designed to summarize the data in a way that is sensitive to the choice of μ, and would therefore follow a different probability distribution function (pdf) $f(t_\mu|\mu)$ for every μ. The probability that an experiment produces a test statistic in some continuous acceptance region $I(\mu)$ amounts to

$$\int_{t_\mu \in I(\mu)} f(t_\mu|\mu) dt_\mu = \alpha\,. \tag{6.1}$$

This statement can be inverted into a condition for finding the acceptance region at a fixed probability α. Depending on the choice of the test statistic, the acceptance region may correspond to a one-sided interval that is bound from above or from below, or a two-sided interval that is bound from both sides. All test statistics that are introduced in the following produce an acceptance interval that is bound from below.

One could envisage another set of experiments but assuming a different true value of the POI. As depicted in Fig. 6.1, for every such value μ there exists a unique interval $I(\mu)$, which the corresponding experiments are able to cover with probability α known as the confidence level (CL). Although the true POI is not known, one can still find the set of all POI candidates, the acceptance region of which includes the observed test statistic with probability α, given the outcome x_{obs} of a single experiment:

$$C(\mu) = \{\mu | t_\mu(x_{\text{obs}}) \in I(\mu)\}\,.$$

The set $C(\mu)$ defines the confidence interval (CI) for parameter μ. The convention in HEP is to report two-sided unconstrained CIs of point estimates, where „two-sided" refers to those CIs that have both an upper and lower limit, whereas „unconstrained" means that no additional requirements are assumed about the POI in the definition of the test statistic. This is in contrast to upper limits of the POIs, which are just one-sided CIs derived from a test statistic that assumes nonnegative signal rate. It is important to recognize that a CI does not represent a range that contains the true estimate with probability α, since this is a Bayesian statement. Instead, it stands for a range of plausible parameter values that are compatible with the experimental observation, in which the level of compatibility is regulated by the CL. These concepts can be generalized for a pair of POIs by constructing an acceptance area analogous to $I(\mu)$ at a given CL, and intersecting it with a plane that is compatible with the observed value of the test statistic. The resulting intersection yields a two-dimensional contour of the POIs known as the confidence region.

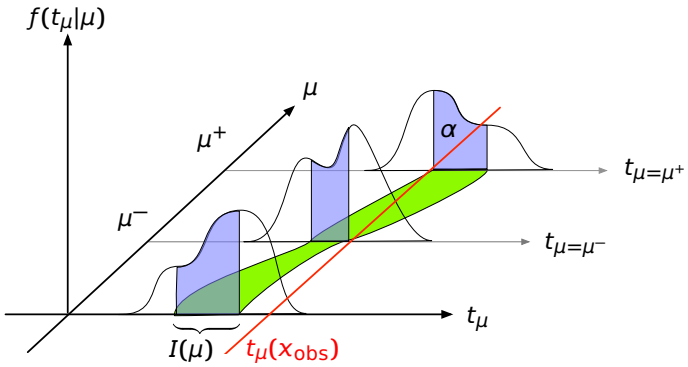


Figure 6.1: Illustration of Neyman construction. For each POI μ there exists a pdf $f(t_\mu|\mu)$ of test statistic $t_\mu(x)$, which is drawn for a number of experiments x. By specifying α as the CL, one can work out interval $I(\mu)$ for every μ, which is supposed to capture the test statistic with probability α in repeated experiments. The true value of the POI should lie inside the confidence belt at probability α, which is formed by evaluating $I(\mu)$ over some range of μ values. CI is defined from the sections of the confidence belt that feature the realized experimental value $t_\mu(x_{obs})$, which is given by interval $[\mu^-, \mu^+]$ in the picture. A version of this image can be found in Ref. [367].

Besides the best estimates of POIs and their CIs, one would also wish to know how well a certain realization of the model performs in light of data. This is accomplished with hypothesis testing, in which a hypothesis H_μ is formulated by „freezing" the POIs, that is fixing them to specific values in the model. A background-only hypothesis, H_0, is obtained by setting all POIs to zero, effectively removing all signal from the prediction, while a signal-plus-background hypothesis, H_1, is constructed by setting all POIs to unity, which adds signal in nominal amounts to the prediction. The hypothesis that one wishes to put to test or refute is chosen as the null hypotheses, while other hypotheses serve as the alternative. Based on how likely it is for the data to arise as predicted by the model, one could either incorrectly reject the null hypothesis with probability α, or incorrectly accept it with probability β. The probability that a null hypothesis H_μ would be rejected even if it were true is given by p-value

$$p_\mu = \int_{t_\mu(x_{\text{obs}})}^{\infty} f(t_\mu|\mu) dt_\mu \,, \tag{6.2}$$

where it is implied that smaller values of t_μ indicate better compatibility with the data as dictated by the so-called ordering rule. Another way of interpreting p-value is to consider it as the probability for the data to produce a test statistic value at least as extreme as $t_\mu(x_{\text{obs}})$ under hypothesis H_μ. The p-value corresponds to false positive or type-I error rate when computed against null hypothesis, and to false negative or type-II error rate when computed against the alternative hypothesis.

It is common to express a p-value in terms of significance Z_μ, which stands for the number units from zero at which point the tail area of a standard Gaussian distribution equals the p-value. If Φ denotes the cumulative distribution function of standard Gaussian distribution, then the p-value can be converted into significance with $Z_\mu = \Phi^{-1}(1 - p_\mu)$. As per convention in high energy physics, evidence or discovery of a signal can be claimed by ruling out background-only null hypothesis if its p-value falls below an equivalent significance of 3σ or 5σ, respectively. If neither possibility materializes, then one can instead invert this threshold into a condition for extracting upper limits on the POI at a given CL, as explained in Section 6.1.3. Depending on the context, one can use the

term „sensitivity" to refer either to the significance level, or to (expected) upper limits on the POI compared to its nominal or theoretical value. Figure 6.2 visualizes how type-I and type-II errors relate to each other and how the significance is determined, given the p-value. Significances $\mathbf{Z}$ obtained from multiple independent inference models under the same background-only null hypothesis can be combined into a single estimate $\overline{Z}$ with the Stouffer's method [369]: $\overline{Z} = \mathbf{Z} \cdot \mathbf{w} / \|\mathbf{w}\|_2$, where $\mathbf{w}$ stands for a vector of weights that are assigned to the models. Although it is just an approximation, the method provides a crucial insight, in that superior sensitivity can be achieved by simply combining multiple analyses that each have inferior sensitivity.

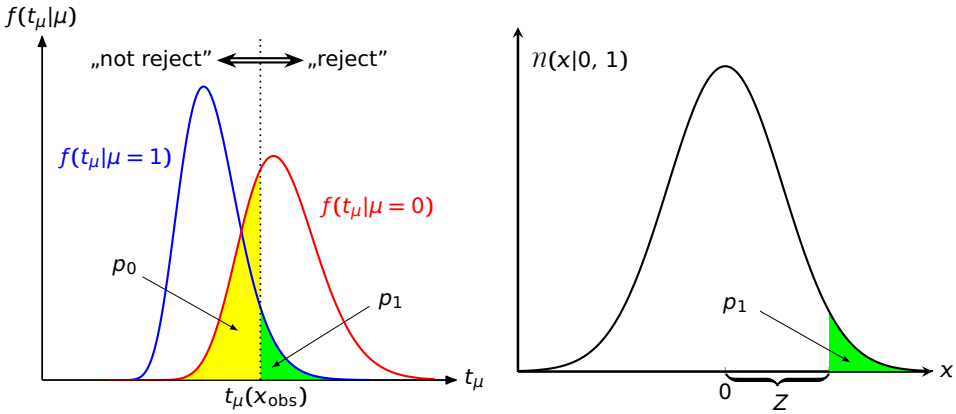


Figure 6.2: Distributions of test statistic t_μ for signal-plus-background hypothesis H_1 (blue curve) and for background-only hypothesis H_0 (red curve) on the left hand side, and how a p-value, such as p_1, can be translated to equivalent significance level Z based on single tail probability of standard Gaussian distribution as shown on the right hand side. In this example H_1 is chosen as the null hypothesis and H_0 as the alternative hypothesis, which means that p_1 and p_0 are respectively identified as type-I and type-II errors in the plot.

It is clear from Fig. 6.2 that optimal sensitivity hinges on the choice of the test statistic. According to Neyman-Pearson lemma, the test statistic that has the highest discriminatory power in rejecting the null hypothesis H_0 over the alternative hypothesis H_1 has the form of a likelihood ratio,

$$\lambda(\text{data}) = \frac{\mathcal{L}(\text{data}|H_1)}{\mathcal{L}(\text{data}|H_0)}, \tag{6.3}$$

where $\mathcal{L}(\text{data}|H_\mu)$ stands for the likelihood function that assumes the model parameters of hypothesis H_μ [370]. A likelihood function maps model parameters to a single representative number that tells how well the model matches with the data. The likelihood function that is chosen for the current analysis is introduced in Section 6.1.2.

Sensitivity to upper limits is oftentimes used as a benchmark when optimizing the analysis. However, basing the decisions on empirical data would lead to severe biases that could ultimately result in false discoveries or false rejections depending on how the model parameters are fine-tuned. Such malpractice can be avoided if one uses pseudodata instead. It can be Asimov data, which is constructed by setting the observed yields precisely equal to the predicted yields [371], or MC toys, which are obtained by randomly sampling the predicted yields. The results are deemed as „expected" if they are derived from pseudodata, or as „observed" if they are extracted directly from the data. In the initial stage of the analysis, the data is considered as „blinded" and all results are based on

pseudodata. Section 6.1.4 details the steps that are taken to validate the inference model before „unblinding" the data and extracting the final results from it. Both the expected and observed results deserve publication, since the former quantifies the sensitivity level for excluding large signals, while the latter represents the real outcome of the measurement.

To summarize, the deliverables of statistical inference are: point estimates of the POIs, their CIs, significance of background-only hypothesis, and — in case the analysis does not reach a sufficient level of significance for claiming evidence or discovery — upper limits of the POIs at some previously agreed upon CL. Each of these topics are explained in more detail in the following sections.

Statistical analysis of the data is performed using a software called `combine` [372], which was initially created by CMS experts for Higgs boson searches in the lead-up to its discovery, but was later adapted to handle a wide range of inference models. The program is based on RooStats [373] and RooFit [374] libraries, which are accessible through ROOT software [332]. Due to increased interest in HH analyses by the CMS collaborators in recent times, the efforts of running the inference with `combine`, interpreting the results and presenting them in a consistent manner were coordinated, which lead to the development of a framework that specifically addresses these points [375]. The results of HH analyses that are based on full LHC Run 2 data and published by the CMS collaboration, including the HH multilepton analysis results presented here, are all extracted with the said framework[21].

6.1.2 Likelihood model

In order to choose a suitable likelihood function for the inference model, it is imperative to first understand how the data events would be approximately distributed. Given the average probability p for an event to occur, one can estimate that the chances for n such events to occur out of N collisions amount to

$$\mathrm{Binom}(n|p,N) = \binom{N}{n} p^n (1-p)^{N-n},$$

where the combinatorial factor counts all possible arrangements of indistinguishable events that can appear in those collisions. Under these circumstances one can expect to find $\nu = Np$ events on average. However, if the number of selected events is very low compared to the number of collisions, effectively implying that $N \to \infty$, then the production of events can be modeled with Poisson distribution function:

$$\mathrm{Pois}(n|\nu) = e^{-\nu}\frac{\nu^n}{n!}, \tag{6.4}$$

where $\nu \geqslant 0$ denotes the mean as well as the variance of expected event counts.

If the current experiment actually realized n_{obs} events, then other experiments might find a different number of events purely by chance. In order to quantify the possible range for this estimate, one can construct a CI in the sense of Neyman for parameter ν at some designated CL α, which represents the probability for the CI to include the true value of ν in subsequent experiments:

$$P(n_{\text{obs}}|\nu_{\min} < \nu < \nu_{\max}) = \alpha\,.$$

This condition can be solved for the central case where the probability for the true value to be lower than $\nu_{\min}$ or higher than $\nu_{\min}$ are equal, which yields the following conditions:

$$P(n > n_{\text{obs}}|\nu_{\min}) = \frac{1-\alpha}{2}, \qquad P(n \leqslant n_{\text{obs}}|\nu_{\max}) = \frac{1-\alpha}{2}.$$

[21] This claim does not apply to HH $\to b\bar{b}\gamma\gamma$ analysis [235], the results of which were published right before the HH inference framework gained foothold.

Interestingly, the convention, presumably due to Ref. [376], is in fact to include $n = n_{\text{obs}}$ in the series sum when computing $\nu_{\min}$, since it provides more conservative coverage of the parameter value than the alternative methods. With this convention both endpoints of the CI can be simply determined from χ^2 values that match for $2n_{\text{obs}}$ degrees of freedom at tail probabilities of $(1 \pm \alpha)/2$. An exception arises if $n_{\text{obs}} = 0$, for which the upper edge of the CI can be analytically calculated as $\ln \frac{2}{1-\alpha}$, but the lower edge is cut off at zero. At large values of n_{obs} the corresponding Poisson CI can be approximated by narrower intervals of $[n_{\text{obs}} - \sqrt{n_{\text{obs}}}, n_{\text{obs}} + \sqrt{n_{\text{obs}}}]$. The CIs are usually displayed at 68% CL as error bars on binned data points, therefore implying that the event counts in each bin are expected to follow a different Poisson distribution. For this reason the CIs are interchangeably called standard deviations or errors, which actually quantify the variance of model parameters. A Poisson variable with mean ν can be thought of as a sum of ν independent Poisson variables that each have a unit mean. According to the central limit theorem, the aggregated distribution of random variables approaches to a Gaussian as the number of those variables grows indefinitely, which means that the Poisson distribution with mean ν can be further approximated by a Gaussian with identical mean and variance if ν is sufficiently large.

Individual MC events can also be thought of as Poisson processes with unit mean, except that each MC event i would be assigned a unique weight w_i by the MC generator, which is then subsequently corrected to improve agreement with data. Their combined mean and variance is estimated from the sum of weights and from the sum of squared weights, respectively [377]. In other words, the expected yields of N simulated MC events directly correspond to the sum of their weights, $\nu = \sum_{i=1}^{N} w_i$, which has a variance equal to the same weights summed in quadrature, $\sigma^2 = \sum_{i=1}^{N} w_i^2$. Whenever MC yields are plotted as data points, like in Fig. 5.8, then they would be shown with symmetric vertical error bars of length σ. Assuming for the moment that all weights are approximately distributed around some positive value k, it follows that $\nu \approx kN$ and $\sigma \approx k\sqrt{N}$, from which one can recover the unweighted number of events by squaring their ratio: $N \approx \nu^2/\sigma^2$. If $f < 0.5$ represents the fraction of events with negative weights, but all weights have approximately similar magnitudes, then the relative uncertainty on the MC yields can be estimated as $\sigma/\nu = ((1-2f)\sqrt{N})^{-1}$, which tracks Poisson error exactly in the absence of negative weights.

The likelihood of observing exactly n events, while expecting ν events is given by Eq. (6.4). A higher value returned by the likelihood function indicates better compatibility of data and prediction compared to alternative models. The expected event yields represent the sum of event yields as predicted for various signal and background processes under the assumptions of some hypothesis $H_{\boldsymbol{\mu}}$. By assigning a dedicated signal strength modifier μ_i to every signal process S_i, one would thus expect

$$\nu(\boldsymbol{\mu}, \boldsymbol{\theta}) = \sum_i \mu_i \nu^{S_i}(\boldsymbol{\theta}) + \nu^B(\boldsymbol{\theta}) \tag{6.5}$$

events in total. The predicted yields may be influenced by a multitude of factors $\boldsymbol{\theta} = \{\theta_k\}$, which are fixed by theory or extracted from ancillary measurements. They come with (systematic) uncertainties $\Delta\hat{\boldsymbol{\theta}}$, which quantify the level of ignorance that is associated with these factors. Under the background-only hypothesis, the data is conjectured to contain no signal, which is equivalent to setting all relevant signal strength parameters to zero. The alternative is to set the signal strength parameters equal to unity in signal-plus-background hypothesis, whereby it is postulated that the data contains exactly the amount of signal as proclaimed. As argued before, it is therefore reasonable to assume that signal strength parameters serve the role of POIs.

Assuming that ν is very large, one can estimate the significance of observing at least $n_{\text{obs}} \geqslant \nu$ events under the background-only hypothesis with $(n_{\text{obs}} - \nu^B)/\sqrt{\nu^B}$. However, if the data is distributed as predicted by hypothesis $H_{\boldsymbol{\mu}}$, then one would expect a (median) significance of $(\sum_i \mu_i \nu^{S_i})/\sqrt{\nu^B}$. This approximation has two important implications: First, it tells that the significance can be improved N times if the amount of data is increased by a factor of N^2. It is also the reason why conservative projections of the expected sensitivity for discovery are scaled with the inverse square root of the relative increase in integrated luminosity. Second, partitioning the data in a way that maximizes signal contribution relative to the background will also lead to a higher significance. Therefore, rather than doing a simple cut-and-count analysis, which considers only the integral of signal and background events, it is more beneficial to perform a shape analysis by splitting the data among different channels into bins of a discriminant that is specifically designed to favor signal over the background in that channel, provided that there is enough event statistics available after the selection cuts. Since every such bin can be interpreted as a statistically independent counting experiment, the overall likelihood that encompasses all bins of the discriminant can be expressed as:

$$\mathcal{L}(\text{data}|\boldsymbol{\mu}, \boldsymbol{\theta}) = \prod_i e^{-\nu_i(\boldsymbol{\mu}, \boldsymbol{\theta})} \frac{(\nu_i(\boldsymbol{\mu}, \boldsymbol{\theta}))^{d_i}}{d_i!} \prod_k g_k(\tilde{\theta}_k|\theta_k)\,. \tag{6.6}$$

To fully utilize the available data, the first product can be extended over all data-taking years, analysis channels and bins of discriminating distributions that each feature d_i data events and $\nu_i(\boldsymbol{\mu}, \boldsymbol{\theta})$ expected events in the SR. Expected yields from individual processes can be negative in some bins, which can happen if those processes were simulated at NLO accuracy, or if the background was estimated with a reweighting and subtraction procedure that involves negative event weights, like it is the case with the data-driven fake background. However, this is usually fine as long as the total sum of predicted event yields, which is what ν_i in Eq. (6.6) stands for, remains positive, since otherwise the likelihood function becomes ill-defined.

The second product in Eq. (6.6) runs over all nuisance parameters (NPs) that adjust the predicted signal and background yields via multiplicative factors. These adjustments are constrained by auxiliary pdfs g_k, which prevent the NPs θ_k from deviating too much from their initially designated values of $\tilde{\theta}_k$ [378]. Systematic uncertainties on the prediction are encoded into the auxiliary pdfs, so that shifts in the NPs would be penalized in proportions relative to their intrinsic uncertainty $\Delta\tilde{\theta}_k$. Some NPs affect only the normalization of individual processes regardless of how they are binned, in which case the event yields in each bin are scaled by the same amount for a given process — just like how POIs regulate the signal normalization. Other NPs have the capability of modulating the shape of the discriminant, which induces changes to the event yields that are correlated between adjacent bins of the discriminant. These correlations may be extended over multiple processes or data-taking years depending on how the corresponding systematic uncertainties are supposed to be treated in the analysis. The correlation of uncertainties, as well as their effects on the measured POIs in the $\text{t}\bar{\text{t}}\text{H}$ and HH multilepton analyses are all summarized in Table 6.1. The uncertainty model in each analysis follows the recommendations that have been put forth by theorists, POGs and other analysis groups in the CMS collaboration. The uncertainties that are unique to the presented analyses primarily concern the FR measurement and application. A sizable fraction of experimental uncertainties have been decorrelated by data-taking years due to changes in the detector conditions and because of the limited event statistics that was available for the ancillary measurements.

Source	Scope	Effect	Decorrelated by	Reduction relative to full CI [%]				
				$\delta\hat{\mu}_{t\bar{t}H}$	$\delta\hat{\mu}_{tH}$	$\delta\hat{\mu}_{t\bar{t}W}$	$\delta\hat{\mu}_{t\bar{t}Z}$	$\delta\hat{\mu}_{HH}$
Higgs boson BR	Higgs processes	N	Decay mode	5	2	< 1	< 1	3
PDF	Irreducible	N	Process*, production mode	15	4	26	28	4
μ_R, μ_F	Irreducible	N, S	Process*	35	15	82	74	10
PS	$t\bar{t}$	S	ISR/FSR	3	1	< 1	< 1	✗
α_{EW}	$t\bar{t}V$	N	Process			✗		1
α_S	Higgs processes	N	—			✗		2
m_t	$t\bar{t}$, HH	N	Process	6	1	2	< 1	16
Top p_T	$t\bar{t}$	S	—	3	1	< 1	< 1	✗
Recoil scheme	VBF HH	N	Channel, decay mode			✗		< 1
Luminosity	Irreducible	N	Year*	4	3	12	11	4
PU	Irreducible	S	—	10	< 1	7	10	5
L1 ECAL prefiring	Irreducible	S	Year	2	4	1	1	< 1
Trigger	Irreducible	S	Year, channel	8	8	5	8	6
Lepton ID	Irreducible	S	Flavor, tight condition	11	7	8	21	2
τ_h ID	Irreducible	S	Year	16	8	7	2	19
b tagging	Irreducible	S†	Year*	16	6	13	22	6
τ_h energy scale	Irreducible	S	Year	3	1	1	1	3
JES	Irreducible	S†	Year*	14	10	5	15	6
JER	Irreducible	S†	Year	13	16	6	15	5
Unclustered MET	Irreducible	S	Year	< 1	3	2	< 1	5
Lepton FRs	Fakes	S†	Flavor	13	47	14	7	8
τ_h FR SFs	Irreducible, fakes	S†	Year	15	10	2	4	26
MC closure	Fakes	N, S	Year, flavor, channel	13	13	5	8	23
Yield	All but data	N†	Process, (channel, flavor)*‡	8	25	4	15	35
Jet multiplicity	DY	S	b tagging condition	7	1	3	10	✗
CR extrapolation	WZ, ZZ	N§	Process	7	6	5	12	✗
Bin-by-bin	All but data	S	Year, channel, process¶	26	37	12	19	58
Statistical	Data	S	Year, channel, bin	78	67	40	41	67

* Partially decorrelated.
† Incorporates multiple systematic variations.
‡ Applies only to the fake background in the HH analysis.
§ Log-uniform pdf.
¶ Only if unweighted backgrounds total $\leqslant 10$ events.

Table 6.1: Systematic uncertainties of theoretical (top section) and experimental (middle section) origin, as well as statistical uncertainties (last row), all broken down by their scope, effect on normalization (N) or shape (S), correlation status, and relative contribution to full CI of the POIs in $t\bar{t}H$ ($\hat{\mu}_{t\bar{t}H}$, $\hat{\mu}_{tH}$, $\hat{\mu}_{t\bar{t}W}$, $\hat{\mu}_{t\bar{t}Z}$) and HH ($\hat{\mu}_{HH}$) analysis with all extracted from the real data under the SM hypothesis. The relative contributions to total uncertainty ($\delta\hat{\mu}$) are obtained by fixing the NPs to their post-fit values, profiling the rest, and subtracting in quadrature the resulting post-fit uncertainty ($\Delta\hat{\mu}'$) from the total post-fit uncertainty ($\Delta\hat{\mu}$) that was obtained for the standard case where all parameters in the fit were allowed to float: $\delta\hat{\mu} = \sqrt{1 - (\Delta\hat{\mu}'/\Delta\hat{\mu})^2}$. When summed in quadrature, the relative contributions do not necessarily add up to 100% because of correlations between the NPs induced by the ML fit. Unless specified otherwise, the corresponding NPs are correlated between individual bins, signal and background processes, channels and data-taking years. The shape effects also entail changes in accepted event yields. Cross mark (✗) indicates that the NP was not used in that particular analysis.

Log-normal or Gaussian constraints are imposed on NPs depending on whether the underlying systematic uncertainty affects only the overall normalization of individual processes, or if it also induces changes in the shape of the discriminant [366]. The former choice is justified by the argument that processes are normalized to a product of positive factors — cross section, integrated luminosity, data-to-MC SFs —, each of which can be viewed as an independent source of randomness. Since the product of random variables is expected to follow a log-normal distribution, it is appropriate to constrain the normaliza-

tion uncertainties using the same pdf. Unlike Gaussian constraints, log-normal constraints are guaranteed to keep the event yields positive and physical. Statistical uncertainties on the prediction are also included in the likelihood function by following a modified Barlow-Beeston prescription, which imposes a dedicated Gaussian-constrained NP on the sum of backgrounds in every bin, or a Poisson constraint on every process in that bin if it the total background yield remains below a certain threshold [379]. Poisson constraints on NP θ_k could be implemented with an auxiliary pdf that has the form $\mathrm{Pois}(\nu_i(\tilde{\theta}_k)|\nu_i(\theta_k))$, but given the floating-point nature of MC event yields ν_i and the NP itself, the auxiliary pdf is swapped for Gamma distribution as described in Ref. [367].

A log-normal constraint on a NP θ_k would modulate nominal event yields by a factor of $(1+\delta)^{\theta_k-\tilde{\theta}_k}$, where δ denotes normalization uncertainty at unit standard deviation and θ_k is a NP subject to auxiliary pdf $\mathcal{N}(\theta_k|\tilde{\theta}_k, \Delta\tilde{\theta}_k)$. Gaussian constraints employ the same auxiliary pdf, but their effects are propagated to nominal event yields in a different way. More specifically, given a relative statistical uncertainty δ, which is parametrized by θ_k, modifies the MC yields by a factor of $[1+\delta(\theta_k-\tilde{\theta}_k)]$ under the Gaussian constraints. In order to incorporate the shape uncertainties to the likelihood model, one would have to first determine the event yields for every shape-changing NP twice by varying the underlying quantity, which is either an energy scale or a SF, up and down by the amount that corresponds to its unit standard deviation. This procedure creates three sets of shape templates: one for the nominal case, $\nu_i(\tilde{\theta}_k)$, and another two for the shifted NPs, $\nu_i(\tilde{\theta}_k \pm \Delta\tilde{\theta}_k)$. The event yields are interpolated smoothly with a sixth order polynomial and extrapolated linearly by using the NP itself as the variable that parametrizes the spline connecting the three event yields [378]. This strategy of estimating the shape effects is also known as vertical template morphing, because it does not require access to the shape information from adjacent bins. Those NPs that induce a relative change of less than 0.1% across all bins,

$$\sum_i \frac{|\nu_i(\tilde{\theta}_k \pm \Delta\tilde{\theta}_k) - \nu_i(\tilde{\theta}_k)|}{(|\nu_i(\tilde{\theta}_k \pm \Delta\tilde{\theta}_k)| + |\nu_i(\tilde{\theta}_k)|)/2}, \tag{6.7}$$

are ignored because their effects on the shape of distributions and therefore on the likelihood itself can be considered as negligible. Energy scale variations may prompt migration of events from one bin to another, which could potentially create a scenario where the nominal event yields in a given bin are either larger or smaller compared to the event yields of both up and down shape templates. In other words, by varying the energy scale up or down, the event yields in a given bin might change in the same direction with respect to nominal yields, especially if the overall event yield in that bin is very low. If it causes a problem in the inference, then one could either rebin the distributions such that the pathology goes away, or simply ignore the NP altogether based on the argument that systematic uncertainties are surpassed by the statistical uncertainties on the prediction. This generally does not happen if the shape templates are obtained by reweighting the events unless the weights can be negative, which is the case for the FFs, for example.

To enhance the sensitivity of an analysis, rather than constraining the normalization of dominant irreducible backgrounds with a log-normal pdf, it may be more reasonable to constrain them from a CR, which is orthogonal to all SRs yet similar enough to the analysis phase space so that the extrapolation of the background normalization from the CR to the SRs has more validity to it. The event selection requirements of a CR can be based on those of a SR but with some cuts inverted. The inversion of those cuts should have the effect of depleting the CR of the signal and populating the CR with backgrounds that one wishes to constrain. The CRs can be incorporated into the likelihood function in one of the following ways: First, one has the option to just let the CR to constrain those NPs that are common

to all backgrounds in the SR. This strategy was employed in the HH analysis, where the modeling of NPs was improved with the inclusion of WZ and ZZ CRs. The second option would be to explicitly constrain those backgrounds with a log-uniform pdf, which allows the background rates to float freely within a specific range. This approach was chosen to constrain the normalization of WZ and ZZ backgrounds in the $t\bar{t}H$ analysis. If there is enough sensitivity one could also promote the aforementioned NPs to fully-fledged POI and treat the backgrounds on the same footing as signal. This is also implemented in the $t\bar{t}H$ analysis, where the rates of $t\bar{t}W$ and $t\bar{t}Z$ backgrounds are modeled with dedicated POIs.

Those POIs and NPs that maximize the likelihood function globally,

$$\hat{\boldsymbol{\mu}}, \hat{\boldsymbol{\theta}} = \underset{\boldsymbol{\mu}, \boldsymbol{\theta}}{\arg\max}\, \mathcal{L}(\text{data}|\boldsymbol{\mu}, \boldsymbol{\theta}), \tag{6.8}$$

are referred to as ML estimates (MLEs) of the model. An „estimator" is a function of the data, whereas an „estimate" refers to a particular realization of the estimator, which could either be data or pseudodata. The MLEs are deemed to provide the best description of the data. Signal rates that best fit the data are thus identified as $\hat{\boldsymbol{\mu}}$ in Eq. (6.8). Obviously, the best fit signal are rates all equal to unity by construction when extracted from the Asimov dataset that assumes signal in nominal amounts. If the ML fit returns a negative signal rate, then this could mean that some backgrounds were inadequately modeled or just not accounted for, but it could also happen if the data yields simply fluctuate downwards.

The best fit values of POIs are found by first scanning over some range of possible values and picking a trial value for one or multiple POIs, while freezing the rest. Since the likelihood function becomes dependent only on the NPs thereafter, the process of maximizing the likelihood boils down to „profiling" the NPs. The resulting NPs, $\hat{\boldsymbol{\theta}}_{\boldsymbol{\mu}}$, are deemed as conditional MLEs that maximize the likelihood function for a given trial value of the POIs. The pair of POIs and profiled NPs that globally maximize the likelihood function precisely correspond to the (technically unconditional) MLEs given by Eq. (6.8). Not only do the signal yields change through the scaling of POIs as a result of this, but the background yields might also change after the ML fit if the NPs deviate from their initially attributed values. For this reason one distinguishes between „pre-fit" and „post-fit" yields, with the former corresponding to nominal yields that enter the ML fit and the latter representing the yields that were scaled by MLEs obtained from the fit.

The MLEs are determined numerically by minimizing the negative log-likelihood function, $l(\text{data}|\boldsymbol{\mu}, \boldsymbol{\theta}) = -\ln \mathcal{L}(\text{data}|\boldsymbol{\mu}, \boldsymbol{\theta})$. This is done with Migrad minimizer in `combine`. The minimization routine is available as part of Minuit2 software library in ROOT [332, 380]. It also provides a Hessian matrix for the negative log-likelihood function [378, 381],

$$H_{ij}(\text{data}) = \left. \frac{\partial^2 l(\text{data}|\boldsymbol{\mu}, \boldsymbol{\theta})}{\partial \theta_i \partial \theta_j} \right|_{\boldsymbol{\mu}, \boldsymbol{\theta} = \hat{\boldsymbol{\mu}}, \hat{\boldsymbol{\theta}}},$$

which incidentally can be identified as a negative observed Fisher information matrix. Given this correspondence in the context of Cramér-Rao bound [382, 383], the inverse of this matrix can be interpreted as (minimal) covariance matrix of the NPs, as long as the Hessian matrix itself is positive definite or, equivalently, as long as all of its eigenvalues are positive. Square roots of the diagonal elements in the covariance matrix are then taken as post-fit uncertainties $\Delta\hat{\boldsymbol{\theta}}$ of unit standard deviation. This interpretation is somewhat simplistic because it ignores correlations with other NPs induced by the fit. Post-fit uncertainties may differ from pre-fit uncertainties $\Delta\tilde{\boldsymbol{\theta}}$, which could indicate problems with the uncertainty model if the discrepancy is large. When displaying post-fit yields in a plot or as tabulated

data, the corresponding post-fit uncertainties are generated by sampling the covariance matrix, therefore taking pairwise correlations between NPs into account [372]. However, this method ignores (anti-)correlations between individual bins (when shown in plots) or among processes (when the uncertainty is quoted for individual processes), which is why quadrature sum of estimated uncertainties would normally exceed the total uncertainty that is estimated for the aggregated sum of bins or processes.

6.1.3 Limit setting

The MLE of the POI μ, $\hat{\mu}$, constitutes a major result of the measurement. Its value is conventionally reported with the corresponding two-sided unconstrained CI, $[\hat{\mu} - \hat{\delta}^{-}, \hat{\mu} + \hat{\delta}^{+}]$, at 68% CL, which is numerically equivalent to a one-tailed Gaussian probability at one σ. It is common to express the results as $\hat{\mu}^{+\hat{\delta}^{+}}_{-\hat{\delta}^{-}}$ in the text. CIs are often interpreted as uncertainties on $\hat{\mu}$, because they represent a plausible range of values for the true POIs.

Profile likelihood ratio given by

$$q_{\mu}(\text{data}) = -2\ln\frac{\mathcal{L}(\text{data}|\mu, \hat{\theta}_{\mu})}{\mathcal{L}(\text{data}|\hat{\mu}, \hat{\theta})} \tag{6.9}$$

is chosen as the test statistic for constructing the CI. It discriminates the hypothesis that provides the best description of the data (as given by the denominator) against all other alternative formulations of the signal hypothesis. It is clear from Eq. (6.9) that $q_{\mu} \geqslant 0$ for any μ, with the equality satisfied only for the MLE itself. Given that the CI is supposed to include the point estimate, it makes sense to limit the acceptance region of q_{μ} to an interval that is bound by some upper threshold $q_{\mu,c}$. As seen from Eq. (6.1), this also requires access to its underlying pdf, $f(q_{\mu}|\mu')$. The pdf can be constructed by generating a large number of MC toys, evaluating the test statistic for each toy and aggregating them. A toy represents pseudodata that is obtained by randomly sampling the predicted yields while assuming a fixed μ' for the signal rate. For each such pdf, the threshold $q_{\mu,c}$ is found by setting its tail probability equal to the CL. The CI therefore corresponds to a range of μ values for which the observed profile likelihood ratio is less than the upper threshold: $[\hat{\mu} - \hat{\delta}^{-}, \hat{\mu} + \hat{\delta}^{+}] = \{\mu | q_{\mu}(x_{\text{obs}}) < q_{\mu,c}\}$.

Finding the CIs with this method requires a substantial amount of computing resources, since new toys would need to be generated for every trial value of μ to find $q_{\mu,c}$. Fortunately, there is a theorem due to Wilks [384], which states that a log-likelihood ratio like q_{μ} follows asymptotically — that is with increasing amount of data — χ^2 distribution at K degrees of freedom, χ^2_K, where K refers to the difference in the number of fixed parameters between the two likelihoods in the log-likelihood ratio. In the current context K denotes the number of POIs for which the confidence intervals or regions are determined. The threshold conveniently equals to m^2 at a CL equivalent of $m\sigma$ Gaussian tail probability in one-dimensional POI scans, hence the factor two in Eq. (6.9). Any CIs that are quoted for single POIs in the following are thus obtained by finding the intervals of μ where $q_{\mu}(x_{\text{obs}}) \leqslant 1$. As for the scans of POI pairs, the convention that is also followed here is to provide contours of confidence regions at CLs of 68 and 95%. In this case, the numerical thresholds that are imposed on the profile likelihood ratio must be raised from 1 to 2.3 for 68% CL, and from 4 to 6.2 for 95% CL.

The width of the CIs, $\Delta\hat{\mu} = \hat{\delta}^{+} - \hat{\delta}^{-}$, can be reduced by adding more data or by improving the modeling of systematic uncertainties. The latter can be tested by fixing one or multiple NPs in the profile likelihood ratio to their post-fit value at global minimum and profiling the rest. Since the frozen NPs do not contribute to the likelihood in any capacity, freezing them would effectively amount to removing them from the measurement. After

scanning for μ, the resulting CI, $\Delta\mu'$, becomes somewhat narrower because the ML fit has now less flexibility to decrease the likelihood for a given trial value of the POI. The difference with respect to the initial CI is estimated for upper and lower intervals separately by subtracting them in quadrature as follows: $\pm\sqrt{(\hat{\delta}^{\pm})^2 - (\hat{\delta}^{\pm\prime})^2}$. The importance of a NP or a group thereof can be assessed by comparing how much the CI shrinks after freezing the NP and profiling the rest. This is what was precisely done in Table 6.1, where the last columns quote the size reduction in CI relative to the full CI, which was obtained without freezing any NPs. Another common way of decomposing the CI into its systematic components is by progressively freezing the NPs in likelihood scans and comparing the decrease in the CIs at every step. This method guarantees that the relative reduction in CIs that is induced by gradually freezing the NPs all sum up to 100% when added in quadrature. One drawback of this approach is that the relative reduction in CIs depends on the order in which the NPs are frozen. Even when freezing all NPs there is still a residual CI left due to the limited number of data events that are available in the measurement, which is why it is deemed as the statistical component of the full CI. The only way to decrease the statistical component would be to add more data to the likelihood function.

As discussed before, experimental sensitivity of the measurement for excluding a signal is quantified by significance, which corresponds to the probability for the data to appear at least as extreme as observed while assuming a background-only hypothesis. It is evaluated as a p-value of test statistic

$$q_0(\text{data}) = -2\mathcal{H}(\hat{\mu}) \ln \frac{\mathcal{L}(\text{data}|0,\, \hat{\theta}_0)}{\mathcal{L}(\text{data}|\hat{\mu},\, \hat{\theta})}\,, \tag{6.10}$$

where the Heaviside function $\mathcal{H}$ makes sure that negative signal rate caused by sudden deficit in the data would not be interpreted as an equivalent excess. The pdf of the test statistic in Eq. (6.2) is obtained from MC toys that have been generated for background-only hypothesis. As with the profile likelihood ratio, the test statistic defined by Eq. (6.10) asymptotically follows χ^2_1 distribution thanks to Wilks' theorem, which makes it possible to express the observed significance concisely as: $Z_{0,\text{obs}} = \sqrt{q_0(x_{\text{obs}})}$. Expected (median) significance can be calculated with the same asymptotic formula on Asimov data that assumes signal in nominal amounts [371].

Another way to gauge the sensitivity of an analysis is to extract upper limits on the POIs. In simple terms, upper limits correspond to the largest possible signal that still remains compatible with the data. The test statistic that is chosen for this task is defined by

$$\tilde{q}_\mu(\text{data}) = -2\mathcal{H}(\mu - \hat{\mu}) \ln \frac{\mathcal{L}(\text{data}|\mu,\, \hat{\theta}_\mu)}{\mathcal{L}(\text{data}|\hat{\mu}',\, \hat{\theta}_{\hat{\mu}'})}\bigg|_{\hat{\mu}'=\max(0,\hat{\mu})}\,. \tag{6.11}$$

Similarly to the test statistic given by Eq. (6.10), the Heaviside function in the definition of $\tilde{q}_\mu$ is there to prevent excess in data such that $\hat{\mu} > \mu$ to be interpreted as evidence against signal hypothesis μ, which makes the corresponding CI as one-sided. The condition that is imposed in the denominator of Eq. (6.11) constrains the best fit value to be physical. Evaluating the p-value of $\tilde{q}_\mu$ on pseudo-experiments that assume no signal yields expected upper limits for the background-only hypothesis [366]. However, since this is a rather time-consuming process, it is more common nowadays to instead use an analytic expression to approximate the p-value [371]. All results presented here have been obtained with asymptotic formulae, with the exception of a few cross-checks to validate the approximation[22].

[22] In the present work, MC toys were only used to compute upper limits for SM HH signal and spin 2

One way to compute observed upper limits is by setting the p-value for signal-plus-background hypothesis equal to $1 - \mathrm{CL}$ and solving it for μ. However, in this particular definition they would no longer remain trustworthy if the backgrounds in data underfluctuate. This is because the pdfs of the test statistic for signal-plus-background and background-only hypotheses can no longer be separated, and the analysis loses credibility for claiming an upper limit as such. To keep the estimated upper limits more on the conservative side, the condition for extracting them is modified *ad hoc* to the $\mathrm{CL_s}$ criterion [385, 386],

$$\mathrm{CL_s}(\mu) = \frac{p_\mu}{1 - p_0} = 1 - \alpha\,, \tag{6.12}$$

which is solved for μ at a fixed CL α. The p-value for background-only hypothesis, that is p_0 in Eq. (6.12), represents the probability for obtaining results more compatible with the hypothesis under the test than what has been observed from the data. The plot on left-hand side of Fig. 6.2 shows the p-values as they appear in the $\mathrm{CL_s}$ criterion but assuming $\mu = 1$ for p_μ. An expected upper limit is the median of upper limits that are obtained by solving Eq. (6.12) for a number of MC toys that have been generated for background-only hypothesis. It is typically accompanied by one and two σ bands, which respectively represent 16–84% and 2.5–97.5% quantiles in the cumulative distribution of upper limits computed from the toys. Sufficient experimental sensitivity is achieved if the expected upper limits are at least as low as the nominal (theoretical) signal rate. If the an upper limit also falls below the nominal signal rate, then it is interpreted as an exclusion limit. If the observed upper limit is much greater than the expected upper limit, then this could either indicate that the backgrounds were mismodeled or that the excess in data arose due to presence of a signal. One can perform signal injection study to establish whether the expected upper limits are sensitive to the presence of the anticipated signal by evaluating the upper limits on pseudodata that features the signal. High sensitivity is reached if the upper limits increase proportionally to the amount of signal added. Signal injection tests in $\mathrm{t\bar{t}H}$ multilepton analysis demonstrated this on 2017 data alone [5], which is why no upper limits were published for the Run 2 combination of the analysis.

The current section introduced three test statistics and the next section a fourth one. Each test statistic has a unique definition and serves a different role or purpose. This information is summarized in Table 6.2 to make it more clear.

resonant HH signal at $750\,\mathrm{GeV}$ as a cross-check. Both scenarios show a reasonable disagreement of up to 10%, hence validating the asymptotic approximation.

Test statistic	Definition	Needed for
Profile likelihood ratio	$q_\mu = -2\ln \dfrac{\mathcal{L}(\text{data}\|\mu, \hat{\theta}_\mu)}{\mathcal{L}(\text{data}\|\hat{\mu}, \hat{\theta})}$	CI of the POIs
CL_s likelihood ratio	$\tilde{q}_\mu = -2\ln \begin{cases} \dfrac{\mathcal{L}(\text{data}\|\mu, \hat{\theta}_\mu)}{\mathcal{L}(\text{data}\|\hat{\mu}, \hat{\theta})} & \text{if } 0 \leqslant \hat{\mu} \leqslant \mu\,, \\ \dfrac{\mathcal{L}(\text{data}\|\mu, \hat{\theta}_\mu)}{\mathcal{L}(\text{data}\|0, \hat{\theta}_0)} & \text{if } \hat{\mu} < 0\,, \\ 1 & \text{if } \hat{\mu} > \mu \end{cases}$	Upper limits on the POI
Background-only likelihood ratio	$q_0 = -2\ln \begin{cases} \dfrac{\mathcal{L}(\text{data}\|0, \hat{\theta}_0)}{\mathcal{L}(\text{data}\|\hat{\mu}, \hat{\theta})} & \text{if } \hat{\mu} \geqslant 0\,, \\ 1 & \text{if } \hat{\mu} < 0 \end{cases}$	Significance of background-only hypothesis
Saturated likelihood ratio	$\overline{\lambda} = \dfrac{\mathcal{L}(\text{data}\|\hat{\mu}, \hat{\theta})}{\mathcal{L}(\text{Asimov data}^*\|\hat{\mu}, \hat{\theta})}$	Goodness-of-fit testing

* Fixed to post-fit yields obtained from the ML fit to data.

Table 6.2: The relevant test statistics that are used for deriving the final results.

6.1.4 Unblinding procedure

Optimizing an analysis based on real data introduces subjective biases, which essentially render the results invalid. For this reason, the effectiveness of the event selection criteria and discriminants that separate the signal from backgrounds is evaluated purely based on expected results. Observed results are never looked at while making changes to the analysis. The process of switching from expected results to observed results is called unblinding. It is executed in three stages: first by validating the modeling of yields and uncertainties, followed by fully unblinding the post-fit distributions of the final discriminants that are used for the signal extraction, and finally computing the observed limits, point estimates, intervals and significances. All CMS analyses that search for Higgs boson or related processes, including the analyses presented here, are required to follow these unblinding steps as prescribed.

The compatibility of predicted yields with the data is validated with the saturated goodness-of-fit (GoF) test [387]. It generalizes χ^2 test for data that is not normally distributed, just like the binned data that is recorded in collision experiments. The GoF test is performed by evaluating the following test statistic on MC toys and on real data:

$$\overline{\lambda}(\text{data}) = \frac{\mathcal{L}(\text{data}|\hat{\mu}, \hat{\theta})}{\mathcal{L}(\text{Asimov data}|\hat{\mu}, \hat{\theta})}\,. \tag{6.13}$$

The Asimov data in Eq. (6.13) corresponds to post-fit yields returned by the ML fit. The MC toys are produced by randomly sampling the Asimov data. The GoF test boils down to checking if the observed GoF test statistic, $\overline{\lambda}(x_\text{obs})$, remains in the bulk of the distribution generated by the MC toys. This is decided based on p-value: if the probability for observing the GoF test statistic as large as suggested by the data is less than 5%, then the realized experiment performs much worse than one would expect from pseudo-experiments. A p-value smaller than 5% is therefore indicative of poorly modeled backgrounds, but it is not as conclusive about the modeling of signal processes because of low signal yields relative to backgrounds. One has to just assume that the signal processes are modeled correctly by the MC simulation. The GoF test results of the $\text{t}\bar{\text{t}}\text{H}$ and HH multilepton analyses are shown in Fig. 6.3. The plots demonstrate that the background models of both analyses fit the data adequately.

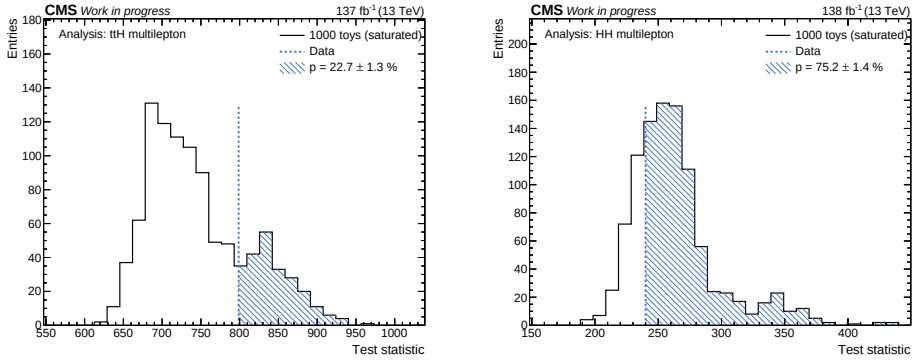


Figure 6.3: Distribution of goodness-of-fit test statistic in $t\bar{t}H$ (a) and SM HH (b) analysis.

Uncertainties are validated by studying the pulls, constraints and impacts of individual NPs. A pull quantifies how much a NP θ_i changes after the ML fit relative to its pre-fit uncertainty: $(\hat{\theta}_i - \tilde{\theta}_i)/\Delta\tilde{\theta}_i$. NPs may be pulled away from their nominal value if the ML fit is not able to compensate for the discrepancies between data and prediction by simply adding or removing signal. Another way of validating the uncertainty model is to assess how much the uncertainty of a NP changes after the ML fit: $\Delta\hat{\theta}_i/\Delta\tilde{\theta}_i$. A NP is said to be constrained if its post-fit uncertainty is much smaller compared to its pre-fit uncertainty, which could be interpreted as if the analysis is able to extract the NP with lower uncertainties than the ancillary measurements, which were specifically designed for this task. A significant pull or constraint tells that there is tension in the ML fit due to insufficient modeling of systematic uncertainties. Further insight is gained by checking the impacts of a NP, that is the change in the best fit value of a POI relative to its MLE after freezing a NP to its $\pm 1\sigma$ post-fit value, $\hat{\theta}_i \pm \Delta\hat{\theta}_i$, and profiling the remaining parameters as usual. Impacts are two-sided if the POI increases after shifting the NP in one direction and decreases after shifting the NP in the opposite direction. However, if a shape uncertainty induces marginal migration of events among different bins, then the resulting shape templates as well as impacts may end up as one-sided. ML fit prefers to pull and constrain those NPs that rank the highest in terms of impact, which is why those NPs receive the most scrutiny. Figures 6.4 and 6.5 show the pulls, constraints and impacts of the leading NPs in the $t\bar{t}H$ and HH multilepton analysis, respectively, with one plot per POI. No significant pulls or constraints are present, therefore establishing that the prepared uncertainty models are appropriate for signal extraction.

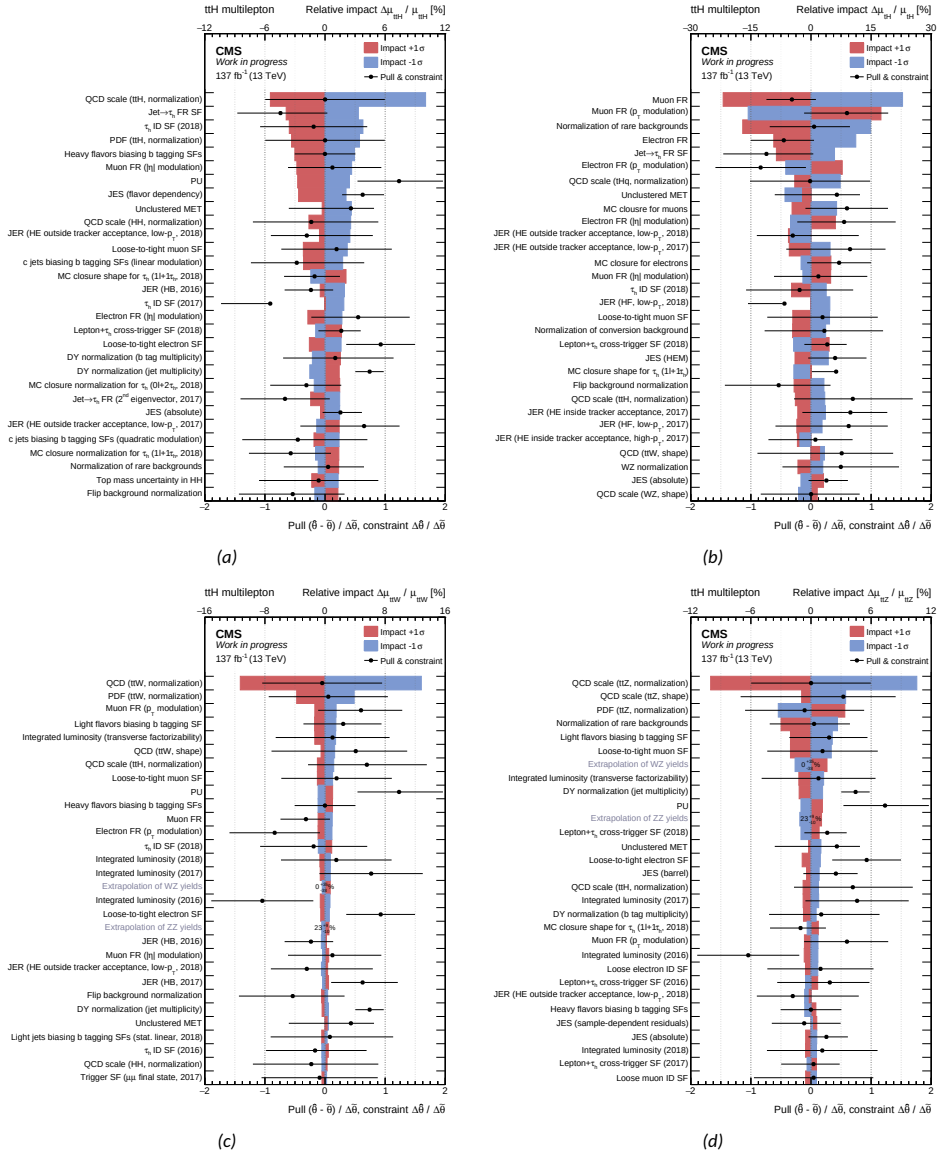


Figure 6.4: Leading pulls and impacts of NPs obtained for every POI that is extracted from the $t\bar{t}H$ analysis. Statistical bin-by-bin uncertainties are omitted for the sake of clarity.

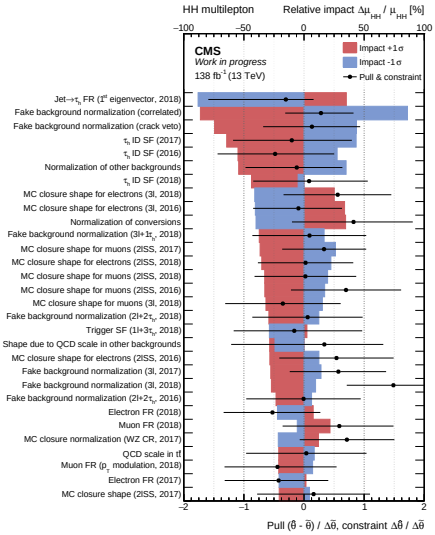


Figure 6.5: Leading pulls and impacts of NPs obtained for the signal rate in the HH analysis. Statistical bin-by-bin uncertainties are omitted for the sake of clarity.

6.2 Shape discriminant

As argued in Section 6.1.2, shape analysis yields higher sensitivity than the standard cut-and-count approach, as long as there are enough events left in the SR that can form a meaningful shape. The sensitivity is driven by the capability for the underlying shape variable to discriminate between signal and background events. Developing such a discriminant is exactly the kind of classification task that can be solved with modern machine learning and multivariate analysis techniques. The remainder of this section is precisely devoted to these topics. The discussion opens with Section 6.2.1, which introduces some basic concepts of machine learning that are particularly relevant in the context of chosen classification methods: boosted decision trees (BDTs) and deep neural networks (DNNs). Details of both models are provided separately in Sections 6.2.2 and 6.2.3, respectively. The topic concludes with Section 6.2.4, which is dedicated to the description of a likelihood-based approach known as the matrix element method (MEM). Many of the ideas presented here can be found in classic textbooks on the subject, such as in Ref. [388]

6.2.1 Machine learning

A predictive model is a function that maps a vector of input features $\mathbf{x}_i \in \mathcal{X}$ to some specific outcome $y_i \in \mathcal{Y}$, which could be represented by an interval of continuous values or by a finite set of discrete possibilities. The former class of predictive models are referred to as regression models, while the latter class of models are called classification models or simply classifiers. In HEP applications, regression models are commonly used to improve the energy resolution of reconstructed particles by approximating their p_T spectrum with a function that exploits their kinematic properties, whereas classification models are typically utilized for creating signal extraction variables. While it is true that classifiers consider inherently a discrete set of possible outcomes, the decision of which class a given set of features belongs to is usually expressed as a probability or a score. Thus, for every class of possible outcomes, the classifier is tasked to return a floating point number, which quantifies the likelihood for an event to originate from a certain class of processes. A binary classifier has to separate signal events from background, whereas a multiclass classifier

has to recognize events from more than two distinct categories of processes.

A predictive model comes with a set of tunable parameters or weights, which can be adjusted to improve the prediction accuracy. The optimal set of weights is determined through an iterative process called training, during which the weights are calculated such that the errors made by the model become progressively smaller. This is accomplished by exposing the predictive model to a training dataset $\mathcal{D} \subset \mathcal{X} \times \mathcal{Y}$, which contains correct pairings of input features $\mathbf{x}_i$ and labels y_i. The accuracy of a model is measured with an objective or loss function, which compares predicted values $\{\hat{y}_i\}$ to training examples $\{y_i\}$. Optimization method defines the rules for updating the weights in a way that leads to a lower prediction error as evaluated by the cost function. A classic example of this would be gradient descent, which moves the model parameters in the direction that is proportional to the gradient of the objective function. The relative magnitude of the incremental improvement that the classifier receives at every training cycle is controlled by learning rate (or shrinkage in BDTs). Other defining parameters of the model that remain constant throughout the training process are referred to as hyperparameters. They dictate the complexity and structure of the predictive model.

Input features are properties and attributes that can be leveraged for labeling the data correctly. They can be a heterogeneous mixture of real values (such as momentum coordinates or ID scores of individual particles or MET-related variables), integers (like charge sums or object multiplicities), and categorical data (which includes boolean flags that summarize the event in a certain way, such as one indicating the presence of SFOS lepton pairs in the event). The necessary condition is that the features remain consistent and maintain their meaning regardless of which data or MC sample they are extracted from. Because the predictive model is evaluated on both data and prediction on equal footing, the input features have to be engineered only from reconstructed information. It means that features cannot be extracted from generator-level information, unless this information is somehow used to directly parametrize signal processes [389]. Modeling of input features is validated by checking their data-to-MC agreement. However, since this has to be done before unblinding, overlaying data in the pre-fit distributions of input features is not possible, at least not in the bins that feature most of the signal. Alternatively, one could assess the data-to-MC agreement in a CR orthogonal to the SR. Another option would be to compare the shapes between data and prediction with a two-sample nonparametric test like Kolmogorov-Smirnov test [390, 391] or Anderson-Darling test [392, 393]. These tests quantify the probability that the two distributions — one from the data and the other as predicted — come from the same underlying pdf.

The dataset that the predictor is trained on must include examples of both signal and background events. These examples are extracted from MC samples, because only simulated events can be definitively labeled as signal or background. As a general rule of thumb, more training statistics allows to increase the complexity of prediction models, which in turn leads to higher prediction accuracy and improved sensitivity. It is therefore of utmost importance to supply the training algorithm with as many examples as possible. Unfortunately, the training statistics is rather limited in both $\mathrm{t\bar{t}H}$ and HH multilepton analyses, because only a few thousand events would pass the SR cuts. Two mitigation strategies have been put in place to address this problem. First, instead of training a predictor for every data-taking year separately, the training is performed once per channel on a joint dataset that has been aggregated over all data-taking years. The second trick is to relax lepton selection criteria from tight to loose and τ_{h} selection criteria from tight to fakeable to increase the selection efficiency of SRs. The data-to-MC SFs that are applied to fake τ_{h} in the $2\ell\mathrm{SS}+1\tau_{\mathrm{h}}$ and $3\ell+1\tau_{\mathrm{h}}$ channels of the $\mathrm{t\bar{t}H}$ analysis are remeasured with

the loosest DeepTau ID WP as the selection criterion for the τ_{h} candidates that define the denominator of those SFs. Both methods of data augmentation are justified as long as the reconstructed variables in the extended data have similar shapes to those in the original data. A separate issue is that all leptons and τ_{h} that pass the selection requirements of a SR must be matched to generator-level prompt leptons and τ_{h}. These matching conditions are waived when constructing the training dataset, with the purpose of exposing the training algorithm to all kinds of fakes other than QCD multijet events.

Training algorithms generally assume that the training dataset contains an equal number of signal and background events. Severe imbalances in the proportion of signal and background events in the training dataset can cause the predictor to perform poorly [394]. Straightforward remedy to this is to uniformly scale the event weights in training examples such that the sum of weights over the signal events equals that of the background events. This of course implies that the training algorithm knows how to assign weights to individual training examples.

The error produced by the predictor can be decomposed into three components: bias, variance and noise. Bias quantifies the systematic error that arises due to insufficient complexity of the predictor, for example by fitting quadratically distributed data with a linear function. Variance measures how susceptible a model can be to random fluctuations in the data. Noise refers to statistical fluctuations in the data itself, which unlike the other two the predictor has no control over. A predictor underfits in initial stages of the training, since it has not yet been fully optimized and therefore not complex enough. In that case the errors with respect to the training dataset are high and dominated by the bias term. With every training cycle, the training error is reduced alongside with its systematic component. As the training process continues, the training error still decreases even though the bias term has already plateaued. At this point the model has started to learn statistical fluctuations as representative of genuine features of the data, in which case the model is said to overfit (or overtrain, like it is commonly called in HEP). An overfit model has lost its robustness since it has learned to recognize the associations between input features and output labels in the training data very well, but it would perform relatively poorly on data that it has not yet seen. This sort of conflict between bias and variance is depicted in Fig. 6.6, which can be summarized as follows: too simple models fail to recognize genuine features from the data, whereas too complicated models fail to generalize . The bias-variance tradeoff has several implications in how machine learning models are trained.

First, one cannot infer results with a model from the same data that the model was trained on because this would lead to severe biases in the results. In the $\mathrm{t\bar{t}H}$ analysis, the issue was resolved by reserving $70–80\%$ of the MC events selected in the SR for the training, and the rest for extracting shape templates from which signal rates are inferred. The smaller dataset is referred to as the test dataset in the literature. Partitioning of the simulated data can be avoided if there are other MC samples available for the same processes. This happened to be the case for $\mathrm{t\bar{t}H}$, $\mathrm{t\bar{t}V}$ and $\mathrm{t\bar{t}}$+jets samples, which were simulated at both LO and NLO in pQCD. The former set of samples were allocated for the training, so that phenomenologically more accurate simulation is then used for signal extraction. Inspired by Ref. [395], a different strategy was chosen in the HH analysis to maximize the event yields that are passed to inference. In particular, the strategy is to divide all events that pass the SR cuts into two approximately even parts, then use one half of the dataset to train a model that can be evaluated on the other half, and vice versa, namely use the other half of the dataset to train a second model that is evaluated on the first half. There is no foul play here because both models are evaluated on events that they have never seen before. This method allows to perform inference on double the amount

of events than before at the cost of losing about a third of event statistics per model. The only piece of information that is uncorrelated with event kinematics yet available in every recorded as well as simulated event is the event number, which is why its parity is used to split the selected events into two halves, with the first half containing events with odd event numbers and the second half featuring events with even event numbers.

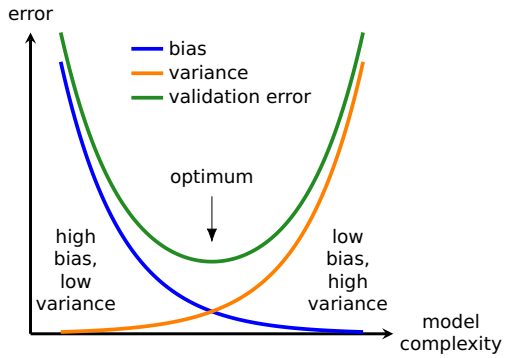


Figure 6.6: Demonstration of bias-variance tradeoff. With every training cycle, the model becomes more complex, bias decreases alongside with the training error, but variance increases. The training has reached optimal state once the sum of bias and variance has plateaued. This is gauged with validation error, which loosely tracks this sum.

The second implication of bias-variance tradeoff is that one would need to somehow track the variance while training the model to detect overfitting. This can be done by splitting the dataset that was initially reserved for the training into two: $\sim 20\%$ for assessing if the model has overfitted, and the remaining $\sim 80\%$ for the actual training. The smaller fraction of the original dataset, also known as validation dataset, is used only for evaluating the objective function. Figure 6.7 illustrates exactly how the simulated data is partitioned between training, validation and inference (or testing, like it is usually referred to as in machine learning literature) in the $t\bar{t}H$ and HH multilepton analyses. It is fairly straightforward in the $t\bar{t}H$ analysis: about 60% of the event statistics is allocated for the training, 15% to test against overfitting and the remaining 25% is reserved for inference. In the HH analysis, however, the selected events are divided into odd and even parts based on the parity of the event numbers. Both halves are further split between training and validation in the same proportions as in the $t\bar{t}H$ analysis. Shape discriminant in odd events is extracted from the output of the model that was trained on even events, and the other way round.

A model is considered overfitted if its training error has stabilized but its validation error has started to increase as the training continues. The number of training iterations can be controlled explicitly through hyperparameters, such as the number of trees in BDTs or the number of epochs in DNNs, but it could also be limited by a early stopping condition, which halts the training process once it detects that relative decrease in the validation error over a certain number of training iterations is not significant enough for justifying the continuation of the training process. Another way to detecting overfitting is to compare the distributions of the classifier score between training and validation datasets with a two sample nonparametric test. If the resulting test statistics suggest that the distributions do not come from the same pdf, then this would be indicative of overfitting.

Models typically overfit if the have too many trainable parameters relative to the number of training examples. Overfitting can be reduced with various techniques, which

aim to make the models less complicated, or at least more expensive (in terms of the cost function) to train a complicated model, or introduce randomness into the training process. One of the viable methods is to add regularizing terms to the objective function, which penalize increase in model complexity as the training continues. The DNNs that are trained for the signal extraction in the $t\bar{t}H$ analysis employ Tikhonov regularization, which suppresses the occurrence of large weights in the model [396], and dropout layers [397], which further improves overall robustness of the model by not having to rely on individual neurons.

Complexity of a model increases with the number of parameters it has to learn, which itself correlates with the number input features or is otherwise influenced by the chosen hyperparameters. Therefore, by adding more and more input features to the model without adding any training examples will ultimately cause the model to overfit. This phenomenon, also known as „peaking" [398], can be avoided if the model is instead trained on a smaller subset of input features. It makes sense to use only those feature in the training that have the most predictive power. In practice this list of features is determined iteratively for each model. At first, the model is trained on all features that might have some relevance to the classification problem at hand. After the training has concluded, the features are ranked by their importance, which measures how much a feature can influence the predicted values. Features that rank low are eliminated and the model is retrained with the remaining high ranking variables. The process of training and eliminating features continues until one is left with the desired number of features.

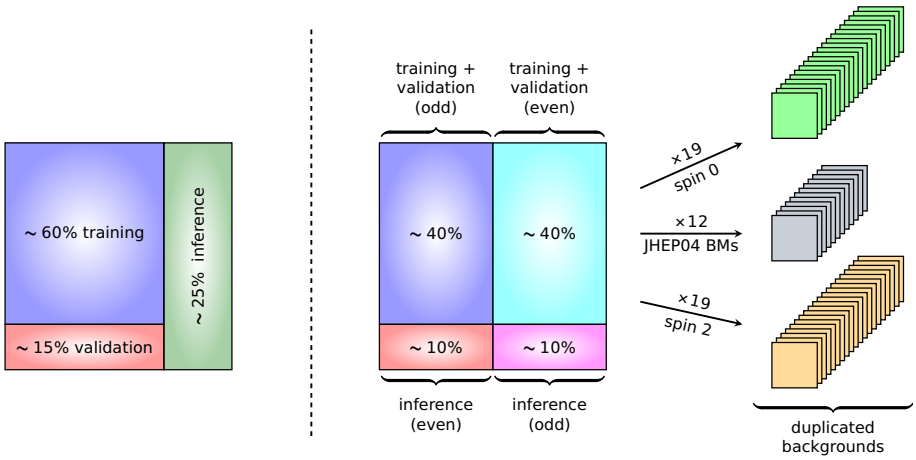


Figure 6.7: Schematic of how datasets are partitioned for training, validation and inference applications in the $t\bar{t}H$ analysis (to the left of vertical dashed line) and in the HH analysis (to the right of the dashed vertical line). In the $t\bar{t}H$ analysis there is just one trained model per channel, whereas in the HH analysis there are six trained models per channel. This is because there are three models trained on odd events, with one to distinguish nonresonant signal and the other two to recognize resonant spin-0 and spin-2 signal, and another three models, which were trained for the same purpose but on even events. As explained later, it hence implies that the models are not targeting one particular signal hypothesis but instead trying to learn all of them at once. Sensitivity to particular signal hypothesis is restored by passing the parameter that tells the different signal hypotheses apart as input to the training. These parameters are one-hot encoded JHEP04 BMs in the nonresonant case, and mass of the unknown resonance in the resonant case. To boost the performance, background events are duplicated for every parameter value for which there are signal samples present in the training.

The definition of feature importance varies with the type of classifier. In BDTs, for instance, the importance of a feature is determined by counting the total number of splits that are performed on the variable, whereas in DNNs it can be found by replacing the feature with random noise in the training data and then evaluating how much worse the model performs because of this change [399]. Features that have higher split counts or induce larger errors when replaced with random noise are interpreted as having higher importance than other features.

To maintain low complexity of the model, but to also not bias the ranking of features by their importance, features that correlate with some other feature more than 80% are also eliminated. When training a BDT, those highly correlated features would rank lower compared to the case where the BDT was trained only on uncorrelated or poorly correlated variables. This is because the training algorithm could split on any of the highly correlated variables with equal probability. In other words, the total number of splits per feature is smaller and importance lower compared to the scenario where only one of those variables is kept for the training. On the other hand, using correlated features may help with overfitting because statistical fluctuation in those features become less important.

Hyperparameters help to tailor model complexity and thereby adjust its proneness to overfitting. For instance, too large of a learning rate might cause the optimizer to overshoot global minimum of the objective function and instead leave it stuck to a local minimum, whereas if the learning rate is too small, then the optimizer may need more training iterations to converge than it would in an ideal case. Therefore, one can simply improve the performance by trying out a different combination of hyperparameters.

A metric is needed that can evaluate the performance of models with different hyperparameters. Comparing the output of objective functions does not work because they themselves depend on the choice of hyperparameters. The standard way of ranking binary classifiers is to compare their receiver operating characteristic (ROC) curves. The ROC curve is found by first imposing a cut on the classifier output. Events that pass the cut are classified as signal, while the events that fail the cut are classified as background. Given this criterion one can determine the fraction of signal events that have been identified correctly, also known as true positive rate (TPR). One can similarly obtain false positive rate (FPR), which corresponds to the fraction of background events that have been identified incorrectly. The ROC curve is formed by sliding the threshold on the classifier output and computing TPR as a function of FPR. A classifier performs better if its area under the ROC curve (AUC) is higher than other models. Random classifiers have an AUC of 0.5, whereas perfect classifiers have an AUC of 0 or 1. Any classifier with an AUC of $a < 0.5$ can be converted into a classifier with an AUC of $1 - a$ by simply inverting its decision. The performance of a multiclass classifier is assessed with a confusion matrix, which tabulates the classification rates per output category for every class of events that the model is trained to distinguish, such that the classification rates add up to 100% per output category. Confusion matrix of a perfect classifier would be an identity matrix, whereas the confusion matrix of a random classifier would contain elements that are all equal to each other.

The optimal set of hyperparameters in the $\mathrm{t\bar{t}H}$ analysis were found with grid search. The method works by iterating through a list of parameter values, retraining the model for every hyperparameter combination, and choosing the set of parameters as the winner that produces the highest AUC. In the HH analysis, it was acknowledged that grid search is not the fastest way of determining the hyperparameters, because the number of hyperparameter combinations increases exponentially with the number of values or hyperparameters one wishes to test. Alternative option would be to optimize one hyperparameter at a time,

but it might miss the best combination. Surprisingly, instead of searching the best set of parameters from a predefined list, one could simply pick them randomly and it would still produce a model that performs just as good as (if not better than) the model that was found through grid search under the same time constraints [400].

Further efforts in finding better methods for determining the optimal set of hyperparameters culminated with the adoption of particle swarm optimization algorithm [400, 401], which is an evolutionary algorithm for optimizing continuous nonlinear functions. The continuous function under question would have to quantify the performance of a model. A viable candidate that fits for this task would be the AUC that was evaluated on validation dataset. The metric is improved by giving higher preference to those models that do not overfit as much:

$$d\text{AUC} = \text{AUC}_{\text{val}} - \kappa \cdot \frac{|\text{AUC}_{\text{val}} - \text{AUC}_{\text{train}}|}{1 - \text{AUC}_{\text{val}}} . \tag{6.14}$$

The second term that is controlled by parameter κ penalizes overfitted models by attributing lower ranking to those models that show higher discrepancy in AUC between training and validation datasets. The cost of overfitting is higher in those models that are closer to a perfect classifier, hence the denominator in Eq. (6.14). Parameter κ was set to 0.3 when searching for optimal hyperparameters in the HH analysis. Particle swarm optimization algorithm showed about 10% improvement in expected upper limits over the previously chosen methods of hyperparameter optimization.

6.2.2 Boosted decision trees

Assuming that signal events are more likely to populate certain parts of feature space than background events, one can construct a classifier that carves out those regions of feature space by imposing a series of cuts on the features. For example, if signal is expected to dominate over background in feature space where $x_i > c_i$ and $x_j < c_j$, with c_i and c_j denoting constant thresholds on features x_i and x_j, then one could construct a simple classifier that accepts only those events as signal that satisfy this condition. Instead of disregarding all events with $x_i < c_i$ as background there might exist some other condition on feature x_k that rejects most of the background but keeps the signal.

The sequence of conditional cuts on the features can be represented with a binary tree, also known as decision tree [402]. It starts out from a root node, which is an internal node that implements a cut on a feature and, depending on the outcome of this cut, proceeds to branch out to two child nodes, with one going left and the other going right. The right branch is chosen whenever the cut is satisfied, and the left branch is chosen otherwise. A child node can be either an internal node or a leaf. Unlike internal nodes, leaf nodes do not implement any cuts on any of the features nor have any child nodes. Instead, they correspond to a state in the decision process where the final verdict is reached. Leaf nodes that are to the right of their parent node classify the input data as signal, while those leaf nodes that are to the left of their parent node categorize the data as background. Thus, a decision is always reached after a certain number of cuts, which is equal to the height of the tree. An example of one such decision tree can be found in Fig. 6.8.

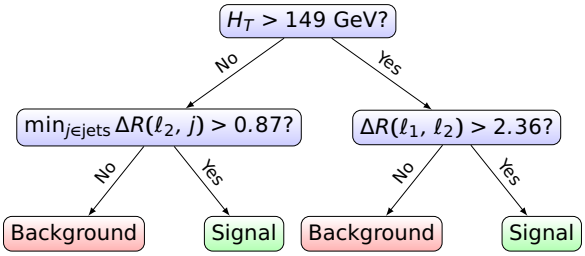


Figure 6.8: One of the 496 decision trees in the BDT that was trained to distinguish nonresonant HH signal from other processes in $2\ell SS+\leqslant 1\tau_{\text{h}}$ channel. The BDT was trained on events with even event numbers. Symbols ℓ_1 and ℓ_2 refer to leading and subleading leptons, respectively.

Decision trees do not always classify the data correctly, as some of the signal may end up in background nodes, and vice versa. One can measure this cross-contamination with (Shannon's) entropy, $H = -\sum_{i,j} p_{i,j} \log p_{i,j}$, where $p_{i,j}$ refers to the fraction of signal ($i = 1$) or background ($i = 0$) events in leaf node j. Entropy is maximized if even amounts of signal and background end up in the leaf, and minimized if the leaf has only one or the other kind of data. However, when assessing how well the decision tree classifies the data correctly, it is useful to not only know the categorical makeup of leaves, but also how it all aligns with the expectation. This argument motivates another measure called cross-entropy, which is given by

$$\hat{H} = -\sum_{i,j} q_{i,j} \log p_{i,j}\,, \tag{6.15}$$

where $q_{i,j}$ stands for the expected occurrence probability of class i in leaf j. In binary decision trees, this probability equals i in signal leaves and $1 - i$ in background leaves. Decision trees with lower cross-entropy are expectedly more accurate at classifying the data, which is why it is commonly used as an objective function. This can be done by progressively adding more and more cuts to the features to maximize the homogeinity of data in every leaf. However, growing the tree by splitting more and more features until all nodes contain only signal or only background will lead to overfitting. It is possible to suppress overfitting by adding regularization terms to the objective function, which penalize the increasing complexity of the tree, such as by imposing a condition that prevents an internal node from splitting if the entropy of the node is already low.

Bagging is a popular machine learning method that helps to combat overfitting. It works by subsampling the training data with repetitions, building a slightly weaker classifier from this data, aggregating them into an ensemble, and averaging over their outputs to retrieve the final decision. Applying this concept to decision trees produces a new type of classifier known as random forest [399]. Bagging has shown to improve resilience towards statistical fluctuations that appear in input data, and thereby reduce variance in prediction error, which is why random forests can outperform individual decision trees of the same size.

Boosting is yet another technique that helps to reduce bias in the prediction error. Instead of training individual classifiers of an ensemble on what effectively constitutes the same data, the novel idea behind boosting is to train new classifiers of the ensemble only on residual data that is currently misclassified by the existing members of the ensemble. In other words, every weak classifier that is added to the ensemble learns just about the subset of data that the previously built classifiers failed to identify correctly. This is essentially how BDTs are trained, except for the added detail that new trees are constructed to further minimize the objective function [403]. The decision of every new tree that is added to the ensemble is weighted by a factor referred to as shrinkage. The final score is

obtained by averaging over the decisions of individual trees.

BDTs are empirically known to outperform random forests in HEP applications, which is why they are still the preferred method of solving binary classification problems in the field. BDTs have several advantages over alternative classification methods. For example, there is no need to standardize the input features or preprocess in some other way; the training process runs fast, which leaves plenty of opportunities to find the optimal set of hyperparameters; the algorithm is more transparent compared to more advanced models like DNNs.

BDTs have found extensive application in this work. In particular, they are used to build shape discriminants for the majority of channels in the $t\bar{t}H$ analysis channels and for all channels in the HH analysis. BDTs were also trained to solve more generic tasks, such as identifying SL $H \to WW^*$ processes, or detecting processes where a top quark decays hadronically. All BDTs employed here are trained with XGBoost software, which was developed by the original creators of the algorithm [403]. The software is accessed from scikit-learn library [404].

Higgs-jet tagger (HJT) is a BDT that identifies processes where a Higgs boson decays into two W bosons, with one decaying leptonically and the other hadronically, but one of the hadronic jets fails the reconstruction. The BDT has been an integral part of $t\bar{t}H$ multilepton analysis since 2016 [365]. It computes a score for a jet based on its p_T, b tagging score, quark-gluon discriminant, and its minimum and maximum angular distance to fakeable leptons in the final state. The jet with the highest score returned by HJT in the event would be interpreted as the sole jet from the SL $H \to WW^*$ process that was successfully reconstructed. High score correlates with the likelihood that such process even happened, which is why it is exploited in the 2ℓSS channel where this particular decay mode is expected to dominate. The classifier was retrained with LHC Run 2 data-taking conditions by treating $t\bar{t}H$ events that fit the process description as signal and $t\bar{t}W$ events as background.

Hadronically decaying top quarks are identified with hadronic top quark tagger (HTT). The BDT has found much wider usage in the $t\bar{t}H$ analysis, because in seven analysis channels out of ten at least one of the top quarks from the signal process is expected to decay hadronically. HTT requires exactly three jets as input, with one representing the b jet from the top quark decay and the other two representing the jets from the W boson decay. The algorithm exploits their b tagging scores, quark-gluon discriminant, p_T and mass variables. HTT score is evaluated for every combination of three central jets, and for every permutation thereof. The combination and permutation of the jet triplet that produced the highest HTT score is considered as the hadronic top candidate. HTT has been around since 2016 $t\bar{t}H$ multilepton analysis [365], but unlike HJT it has undergone several upgrades over the years. The version of the algorithm that was used in this work was retrained on a mixture of $t\bar{t}H$, $t\bar{t}V$ and $t\bar{t}$+jets events, while assuming LHC Run 2 data-taking conditions.

As elaborated in Section 2.5, the event kinematics of HH processes greatly changes in response to different coupling choices in nonresonant production, or is otherwise influenced by the physical properties of the unknown resonance in resonant production. In order to extract the best possible limits for every hypothetical scenario, the obvious solution would be to train a dedicated BDT that learns to distinguish just one type of HH signal. The MC samples that were available at the time of developing the shape discriminants are the LO ggF samples that are listed in Table 5.1: 12 samples of nonresonant signal, with one sample for every JHEP04 BM that is produced per HH decay mode; and 19 samples of resonant signal, with one sample for every resonant mass point that is produced for a given spin of the resonance and its subsequent HH decay mode.

Different signals may share features that could be leveraged to reject common backgrounds, but the classifiers may not be able to learn these intricate relationships due to limited training statistics of the signal samples when training one classifier per signal hypothesis. This problem inspired the idea of parametrized learning [389]: instead of developing independent classifiers for every signal hypothesis that fundamentally change with parameter θ, one could just create a single classifier that is parametrized by θ to enhance the effects of shared features. With this approach all signal samples are labeled accordingly with θ_i and bundled into a single dataset, which is considered as signal by the BDT. Here θ_i refers to a particular realization of θ, which could either be a specific JHEP04 BM or a resonant mass point for which there is MC prediction available. The BMs are represented by one-hot encoded states, that is by integers in powers of two, since unlike resonant masses the BMs serve as category labels rather than physical observables. When training nonresonant BDTs, the same signal event enters the training as many times as there are BMs but with a different event weight obtained from the signal reweighting procedure described in Section 2.5.2. Labels θ_i enter as input to the BDT on the same footing as any other training variable. The proposed training strategy is visualized in Fig. 6.9.

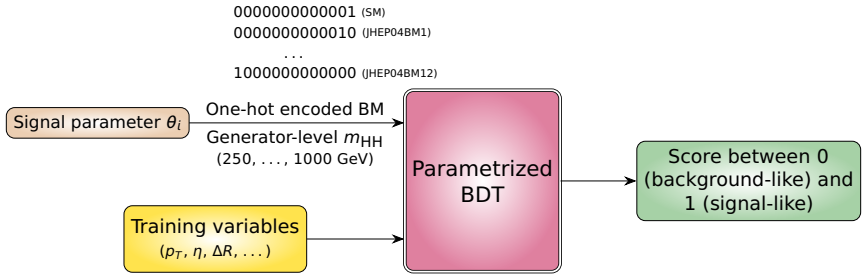


Figure 6.9: Schematic for the strategy of parametrized BDT training, which was followed in nonresonant as well as in the resonant HH analysis. All events used for the training must be labeled by signal parameter θ_i, which could either be a JHEP04 BM if the training is performed for nonresonant analysis, or m_{HH} if the training is performed for resonant analysis. In practice, the BMs in nonresonant BDT are encoded by 13 exclusive boolean flags of which one is set to true, whereas m_{HH} of resonant training is represented by a single floating point variable. They are always supplied regardless of how they would rank among other training variables in terms of feature importance. The BDT output tells on a scale from 0 to 1 how likely it is that a given event came from the HH signal process.

All events, including the background events, have to be labeled with θ_i in the parametrized BDT training. To accomplish this, one has the option to either randomly pair the background events to or duplicate them for every signal scenario θ_i as illustrated in Fig. 6.7. The former choice reduces the training statistics of backgrounds by a factor that is equal to the number of different signal hypotheses considered, which would be a factor of 12 in the nonresonant case or a factor of 19 in the resonant case. It is therefore expected that such severe reduction in background yields will cause the classifier to underperform compared to the case where the backgrounds are oversampled instead. Dedicated studies of this comparison confirm that the oversampling method yields a few percent higher AUC than the randomization method, which is why it was chosen as the default way of handling backgrounds in the parametrized BDT training. As a result of this approach, the number of background events far exceeds the number of signal events in the training. In order to make the BDT more sensitive to the features that are present in the signal, the features are transferred from signal to background by interpolating them with a high-degree polynomial as a function of generator-level m_{HH} in the training signal sample. The resulting fit function

is evaluated at a given m_{HH} value in every event, which is then factorized out in signal events and applied to background events during the training process and when building shape templates for the signal extraction. The decorrelation of BDT inputs by m_{HH} improved ROC AUC by about 1%.

To validate it all, two parametrized BDT were trained for the resonant HH analysis, where one of the models was trained on all mass points except for one, and another model that was trained on the mass point that was left out. The goal here is to see whether the latter BDT is able to interpolate between adjacent mass points by comparing it to the model that was specifically trained for that mass point. The test was performed three times, each time with a different mass point, which revealed that the interpolation works at the expense of mild degradation in the performance. Input variables to the BDTs trained for HH resonant analysis exhibit strong correlations in high BDT output region for mass points that are separated by less than $200\,\text{GeV}$ from each other. This happens due to limited experimental resolution on m_{HH}, which is caused by energy loss from neutrinos that originate from leptonic W boson decays.

6.2.3 Deep neural networks

As with solving many technical problems, a great place to draw inspiration from is to study real life biological systems, since evolutionary pressures of nature often converge to a design that is the most efficient in given circumstances. For example, it is probably not a coincidence that birds are morphologically similar to airplanes, or that honeycomb-like patterns appear in all kinds of structures that have to sustain high loads while not weighing much. Perceptron is one such mathematical model, which was first invented for the purpose of recognizing patterns from images by mimicking neural activity of human brains to accomplish the task [405, 406]. A perceptron is supposed to act like a neuron by accepting signals with varying degrees of importance, and then „firing", that is sending out a new signal if the combined inputs exceed a certain threshold. As shown in Fig. 6.10(a), a perceptron is just a function that takes a fixed set of features $\mathbf{x}$ as input, weighs them by $\mathbf{w}$ depending on whichever feature has the greatest chances of firing the neuron, sums the weighted inputs together, adds its own bias b, and runs the result through an activation function A:

$$\hat{y}(\mathbf{x}|\mathbf{w}, b) = A(\underbrace{\mathbf{w}\cdot\mathbf{x}+b}_{\equiv z}). \tag{6.16}$$

Those weights (and biases) can be adjusted such that the predicted output $\hat{y}$ replicates the expected response y as closely as possible, which allows to transform the perceptron into a machine learning model. Although perceptrons can be configured to regress linear functions, a more relevant application in the present context is its ability to distinguish binary classes of data. It does so by returning a probability that the provided features belong to one of the target classes. Activation function that is commonly chosen for this purpose is the sigmoid function, $\sigma(z) = 1/(1+e^{-z})$. The objective of the learning algorithm is then to compare the returned probabilities to the expectation by evaluating cross-entropy loss with Eq. (6.15), which runs over all classes i and examples j. As with BDTs, the model parameters should be updated such that cross-entropy decreases.

While perceptrons excel at figuring out logical conjunction, disjunction and negation operations from 2-bit data, they demonstrably fail at learning exclusive-OR gates [407], which was one of the primary reasons why research in machine learning stalled for more than a decade after these findings were published. However, just like multiple logic gates can be linked together to create more complicated circuits, perceptrons can be chained together to create more sophisticated structures that are able to learn highly nonlinear patterns like

exclusive-OR. These structures are known as multilayer perceptrons or, nowadays more commonly, as neural networks.

A neural network is a sequence of layers that each has a certain number of neurons. A neuron acts like a perceptron, except it can have a variable number of inputs and outputs[23] depending on the network architecture. In a fully connected neural network, each neuron has the same number of inputs as there are neurons in the previous layer and the same number of outputs as there are neurons in the next layer. The first (input) layer contains one neuron per input feature, while the last (output) layer has just one neuron when performing binary classification or regression, or as many neurons as there are output classes. Activation function in the output layers is generalized to softmax function [408], $\sigma_i(\mathbf{z}) = e^{z_i} / \sum_j e^{z_j}$. The layers that are sandwiched between the input and output layers are called hidden layers. Neural networks that feature more than one hidden layer are colloquially known as DNNs. A DNN can be visualized as a directed acyclic graph as shown in Fig. 6.10(b). While adding more hidden layers increases the complexity of the model and therefore reduces bias in prediction error, adding too many layers may give the model too much flexibility to the point that it starts to interpret statistical fluctuations of the data as genuine features. In other words, one has to experiment with different topologies of the network to figure out the configuration that gives the best results.

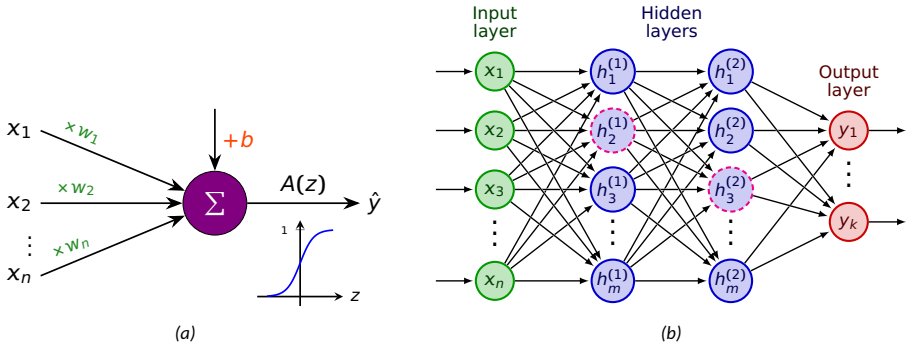


Figure 6.10: (a): Visual representation of perceptron given by Eq. (6.16). It serves as a prototype for neurons in neural networks. (b): DNN with n input features, two hidden layers containing m neurons each, and a final output layer returning probabilities for each of the k output classes. Arrows point in the direction of feedforward propagation. Overfitting is mitigated with dropout, which randomly turns off neurons in the hidden layers at every feedforward pass. In this particular instance the dead neurons are indicated by a pink dashed border. Image courtesy of I. Neutelings.

A DNN is trained in two stages: first by injecting the training data into the network to compute predictions, and then translating the prediction error into difference by which the weights are adjusted. Due to linear nature of how neurons process their inputs, the training data could be fed into the network as a column vector of features with one example at a time like how it is done in stochastic gradient descent; as a series of matrices that each represent a batch of, say, few hundred to few thousand examples; or as a single matrix that contains all examples in its columns. At every layer, the input data is multiplied by the weight matrix, each row of which corresponds to a different neuron in the layer, then shifted by biases and sent through an activation function to the next layer until a

[23] Technically, it has one output just like perceptron does, but the output is propagated to the next neuron with a different weight, hence creating the illusion that the neuron has multiple outputs.

prediction is reached. Because basic arithmetic operations in matrix multiplications are easily parallelized on commodity graphical processing units, it may seem like sending all data through the network in one go might be the best option here, but as it turns out, this is really not the case for two reasons: Firstly, the full training dataset may not fit into memory; secondly, exposing the network to all data that is available for the training may create very narrow valleys in the objective function, which are difficult for the optimizer to find and converge on [409]. On the other hand, feeding the network with too few examples at a time can slow down the training process by a significant margin, which is why the intermediate option of sending sizable batches to the network is usually the safest.

Once the network has made its prediction for the training sample, the next step is for the objective function to quantify the error between prediction and expected outcome, which in case of multiclass classifiers comes down to calculating cross-entropy loss. By taking derivatives of the objective function with respect to tunable parameters of the model, one can estimate the amount by which these parameters should be shifted in order to minimize the objective function. However, because of the chain rule the derivatives must be first taken with respect to the weights starting from the outermost layer, then with respect to the weights in the preceding layer, and so on until reaching the first layer. The weights are for this reason updated in the exact same backwards order [410]. One cycle of feedforward plus backpropagation of all training examples constitutes an epoch. The number of epochs must be specified manually since it determines the length of the training process.

Learning rate directly dictates the proportion of the gradient by which the weights are updated. As described before, too small learning rates increase the time it would take for the optimizer to converge, whereas too large learning rates cause the optimizer to excessively oscillate around the minima or even shoot over them. These oscillations can be suppressed by estimating average over more recent updates and applying it as a correction to the weights in the current iteration. Adam optimizer is one of the best algorithms currently known that adapts the learning rate of every weight based on the averages of the gradient and its square [411]. A slight variation of the algorithm, Nadam [412], improves convergence with Nesterov method [413], which shifts the weights in the direction of previous updates before taking gradient of the objective function and subtracting it from the weights.

Because sigmoid and softmax functions always map to $[0, 1]$ and hence serve their purpose of returning probabilities very well in the perceptron model, keeping them as activation functions in hidden layers might cause some problems. In particular, the issue is that the derivative of sigmoid function peaks at less than one, and since the total gradient of the current layer depends on the product of gradients from previous layer, the gradient simply vanishes in the innermost layers of the network and the weights there do not receive enough updates. These issues are overcome by using the rectifier linear unit (ReLU) as the activation function in the hidden layers [414], which makes sure that the gradients remain roughly in the same order throughout backpropagation. The ReLU function is defined as $\max(0, z)$ for some response z, where the lower bound effectively instructs the optimizer to not update the weights of those neurons that are not activated at this particular iteration. Even though ReLU is not differentiable at zero, the problem is typically ignored by setting the derivative to zero, although a more elegant approach would be to randomly sample its value from or between zero and one.

Optimizers might have to take a higher or lower number of steps to find the global minimum depending on where on the hypersurface of the objective function the searches begin. In other words, convergence somewhat depends on how the weights (and biases)

are initialized prior to the training. Setting them initially to too small values might lead to vanishing gradients, while assigning too large values might induce exploding gradients. To maintain similar variance of the gradient from layer to layer, two popular initialization methods have been proposed, with one by Glorot [415] and the other by He [416]. Both recommend randomly drawing the weights from Gaussian or uniform pdfs that have zero mean but different variances depending on the method. While He initialization conceptually suits best for networks that activate neurons with ReLU, the gain over Glorot's method is sometimes marginal at best.

To avoid excessive saturation of neurons and to promote learning, inputs to the first layer should be collectively shifted such that they would be distributed at around the threshold of the activation function. Faster convergence is also achieved if the inputs are scaled to the same (typically unit) variance [417]. Centering the features to zero and scaling them to unit variance is carried out in a single operation known as standardization. Batch normalization is a well known technique that applies the aforementioned transformations not only to the inputs of the first layer but to all hidden layers, but with the added flexibility that the scale and offset parameters themselves become learnable [418]. The method helps to smooth out kinks in the objective function, which in turn allows to increase the learning rate and thereby accelerate convergence [419]. It also improves the overall robustness of the network with respect to chosen hyperparameters and initial conditions. However, recent literature suggests that combining batch normalization with dropout layers could actually lead to performance loss compared to the case where only one or the other method is employed [420].

While the popularity of BDTs in HEP research has somewhat historical origins, not to mention their general appeal for having straightforward interpretation, there are a few practical reasons as to why BDT has remained the preferred machine learning model for developing shape discriminants in physics analysis to this day. First, DNNs are highly configurable, which obviously adds to their benefit, but since there are no universal settings that are guaranteed to yield the best performance, figuring out the best architecture requires way more effort than optimizing BDTs since they have fewer hyperparameters. It also takes anecdotally more time to train a DNN than a BDT of equivalent performance. Not only that, DNNs perform horribly when trained on limited data or on suboptimal set of features, whereas BDTs can deliver decent performance even when trained on a few thousand events. Given enough training examples, however, DNNs are definitely capable of outperforming BDTs.

DNNs are directly used in the present work to derive shape discriminants for 2ℓSS, 3ℓ and $2\ell\text{SS}+1\tau_\text{h}$ channels in the $\text{t}\bar{\text{t}}\text{H}$ analysis. Unlike BDTs, which in the current analysis are configured to perform binary classification and hence output just one score, which is the likelihood for signal process, multiclass DNNs return one score per output node, which corresponds to the probability that a given event belongs to the group of processes represented by that node. There are as many shape discriminants as there are output nodes in multiclass classifiers. An event can contribute to the shape template of just one discriminant because every bin in the likelihood function must remain statistically independent from all other bins. The shape template that a given event can contribute to is chosen based on whichever node returned the highest probability. The DNNs are implemented with TensorFlow [421], which is accessed through Keras interface [422].

6.2.4 Matrix element method

Neyman-Pearson lemma postulates that likelihood ratio (LR) or a function thereof has the highest discriminatory power in rejecting one hypothesis over another [370]. When formulated this way, it sort of implies that the „data" in the LR given by Eq. (6.3) refers to some collection of events one wishes to infer new information from. However, with a suitably chosen likelihood function, one can apply this principle to single events and convert the LR into a shape discriminant. This is exactly the idea behind the MEM [423–425], which proposes that the likelihood function Λ_i under question quantifies the compatibility of measurement p with the ME of process i as follows:

$$\Lambda_i(p) = \frac{1}{\sigma_i} \int d\sigma_i(\hat{p}) W(p|\hat{p}) \,. \tag{6.17}$$

The above integral convolves differential cross section of the process given by Eq. (2.20) with transfer functions (TFs) $W(p|\hat{p})$, which returns the probability density for reconstructing parton-level 4-momenta $\hat{p}$ as p. All TFs are normalized to unity for every process and for every possible configuration of partons. Total cross section appears in the denominator of Eq. (6.17) to ensure that Λ_i itself is also normalized to unity as one would conventionally expect.

TFs intend to emulate the smearing of physical observables that is caused by limited resolution of the detector. This is accomplished through a series of approximations, which simplify the evaluation of Eq. (6.17) immensely. For example, it is common in MEM to assert that 3-momenta of leptons as well as direction of jets and τ_h candidates are all perfectly measured. This is justified simply by the fact that none of these reconstructed observables have systematic uncertainties assigned to them. Additionally, all final state leptons and quarks as well as initial state protons are assumed to have negligible mass compared to their momenta. This does not apply to much heavier top and bottom quarks, which are instead put on their mass shells. All of these conditions are accomplished by inserting appropriate Dirac's δ functions into the integrand in Eq. (6.17). Each such insertion would constrain the integration space by one degree of freedom. Flavors of reconstructed leptons are usually ignored when pairing them to parton-level leptons. In some hypotheses, like the ones that feature $\mathrm{Z}/\gamma^* \to \ell^+\ell^-$ decays, the lepton flavors need to match at construction level, though.

Energy response of quarks (and gluons) can be modeled with a Gaussian pdf that is centered around quark energy as shown in Fig. 4.2. The approximation works well for light quarks, but not as much for b quarks. This is because heavy flavor quarks produce neutrinos in weak decays, which would then escape the jet reconstruction completely and would thus cause a sizable deficit in the jet energy compared to the initial quark energy. A more realistic response model for b quark energy would have to account for these effects and skew the energy response towards lower values such that the median response is greater than the mean. This behavior is accurately captured by two superimposed Gaussian pdfs that each have a different mean and variance [426]:

$$\begin{aligned} W(E_\mathrm{jet}|\hat{E}_q, \hat{\eta}_q) = \quad & f \cdot \mathcal{N}(E_\mathrm{jet}|\mu_q(\hat{E}_q, \hat{\eta}_q), \sigma_q(\hat{E}_q, \hat{\eta}_q)) + \\ & (1-f) \cdot \mathcal{N}(E_\mathrm{jet}|\mu'_q(\hat{E}_q, \hat{\eta}_q), \sigma'_q(\hat{E}_q, \hat{\eta}_q)) \,. \end{aligned} \tag{6.18}$$

Mean energy response (μ_q and μ'_q) is modeled after a linear function of the quark energy, while the energy resolution (σ_q and σ'_q) is decomposed into noise, stochastic and constant terms like in Eq. (3.6), with coefficients in both parametrizations depending on η for added flexibility. The coefficients are extracted from MC simulation in multiple bins of generator-level quark energy separately for barrel and endcap regions [427].

It is not always possible to assign a unique jet to every quark at parton level if the reconstructed event features fewer jets than would be expected from a given process. This can happen either because the quark goes outside of the acceptance region and would thus fail reconstruction, or because there is a second quark within the jet radius. In the latter case both quarks would be merged into a single jet by the jet reconstruction algorithm. To account for this subtlety, the TFs of the two quarks are replaced with a single TF that compares jet energy to the energy sum of both quarks. The third option would be that the quark remains below the energy threshold and would thus fail the offline selection criteria. Probability for this to happen amounts to: $\int_0^{E_c} W(E|\hat{E}_q, \hat{\eta}_q)dE$. Energy threshold in the integration limits, E_c, can be approximated by $p_T^c/\sin\hat{\theta}_q$, which ignores quark masses and energy resolution effects. Here p_T^c refers to the p_T threshold applied in offline selection and $\hat{\theta}_q$ is the polar angle of the quark. These cases where a quark happens to be closer to a charged lepton than the intrinsic radius of the lepton should be vetoed by offline selection cuts. However, it is certainly possible that a b quark decays into a lepton, which then fakes the jet that it is part of. Such fake leptons tend to maintain the same direction as its parent quark, but retain only about 60% of its energy on average [427]. The energy response of fake leptons is modeled after a Gaussian distribution, the width of which increases linearly with quark energy.

Energy response of τ_{h} candidates varies with their decay mode. The simplest decay mode, which is just 1-prong with no extra neutral pions, can be studied as a two-body decay process. Assuming unpolarized τ lepton, the energy TF for the charged pions happens to be a constant of parton-level information [427]. This translates to a flat distribution in the variable $z = E_{\mathrm{vis}}/\hat{E}_\tau$, which stands for the fraction of energy that is carried away by visible hadronic decay products of the τ lepton. The charged pion can inherit any fraction of energy from its parent τ lepton with equal probability, thereby leaving the remaining energy to the neutrino also produced in the decay, but only as long as the process is kinematically viable, which in ultrarelativistic regime boils down to the following constraint:

$$m_{\mathrm{vis}}^2/m_\tau^2 \leqslant z \leqslant 1\,. \tag{6.19}$$

It turns out that other decay modes, which all feature multiple charged and neutral pions, can still be studied as two-body decay processes $\tau \to \tau_{\mathrm{h}}\nu$, where the τ_{h} represents cascade of decays starting from the primary meson resonance and ending with fully reconstructed objects. The only caveat is that the reconstructed visible mass in the kinematic constraint given by Eq. (6.19) is no longer a constant at pion mass like it was in 1-prong decay mode, but follows a multimodal distribution, where the different peaks arise due to multiple meson resonances and neutral pions. The distribution of the z variable would no longer remain flat but is instead biased towards larger fractions, which is to say that τ_{h} tends to retain most of the energy from its parent if the parent τ lepton decays into multiple pions. The situation is the opposite for leptons that originate from τ lepton decays, because the corresponding TF was analytically found to fall monotonously with the fraction of energy that the leptons inherit from their parents [427]. The energy response of leptons that fake a τ_{h} can be approximated with a Lorentzian function in case of electrons or with a Crystal Ball function [361] in case of muons [427].

Protons that initiate the HS process can be taken as parallel to the collision axis. Some of their energy — as dictated by PDFs — is transferred to partons that initiate the HS process. Since those initial partons continue in the direction of their parent protons, it follows that those partons would have no transverse momentum either. However, this is not quite the reality at the LHC, since those partons would undergo a series of radiation before actually initiating the process. As a result, the ISR effectively shifts the partons away

from the collision axis by an amount known as hadronic recoil [428]. In order to work this phenomenon explicitly into Eq. (2.20) where the ME does not model the ISR, the integral in Eq. (6.17) is marginalized by hadronic recoil as follows [429]:

$$\Lambda_i(p) \to \Lambda_i'(p) = \int d^2\hat{\mathbf{p}}_T^\rho \Lambda_i(\hat{p}, \hat{\mathbf{p}}_T^\rho) W(\mathbf{p}_T^\rho | \hat{\mathbf{p}}_T^\rho)\,. \tag{6.20}$$

Longitudinal boosts by ISR are ignored here because there is no way to constrain them from experimental data. The total momentum of particles in the initial state must equal to that of the final state because of conservation laws. From this statement one can work out that the hadronic recoil is equal to the negative transverse momentum sum of all final state particles at the parton level:

$$\hat{\mathbf{p}}_T^\rho = -\sum_{i=1}^{n} \hat{\mathbf{p}}_T^i\,. \tag{6.21}$$

Defining hadronic recoil from reconstructed momenta is complicated by the fact that no neutrinos are reconstructed, yet the sum in Eq. (6.21) extends over all final state particles that are part of the HS, including neutrinos. Fortunately, there is MET, which serves as a proxy to total transverse momentum induced by the neutrinos. This allows to express reconstructed hadronic recoil as:

$$\mathbf{p}_T^\rho = -\left(\mathbf{E}_T^{\text{miss}} + \sum_{i=1}^{n'} \mathbf{p}_T^i\right),$$

where the second term on the right-hand side runs over all $n' \leqslant n$ reconstructed particles that are associated with the HS process. The event also features $n - n'$ neutrinos in the final state, but none of them are reconstructed. Hadronic recoil at parton level is compared to its reconstructed equivalent in Eq. (6.20) via a two-dimensional Gaussian TF, $W(\mathbf{p}_T^\rho | \hat{\mathbf{p}}_T^\rho) = \mathcal{N}(\mathbf{p}_T^\rho | \hat{\mathbf{p}}_T^\rho, V_\rho)$, where the MET covariance matrix V_ρ is estimated on a per-event basis using the MET significance algorithm [302].

Besides the aforementioned approximations, the integral in Eq. (6.20) can be further simplified by marginalizing it over the momenta of intermediate particles [24]. This is accomplished through recursive partitioning of the phase space as shown in Fig. 6.11. If justified, some of those intermediate particles can be forced to their on-shell masses using the NWA. Every on-shell condition reduces the integration space by one dimension. These simplifications eventually limit the integration to variables that describe the direction of neutrinos and τ_h energy fractions. Although it is reasonable to keep the number integration variables to a minimum, in some instances it is justified to marginalize over measured variables. For example, as argued in Ref. [4], a wrong hadronic jet is picked as the b jet in $1\text{–}10\%$ of the cases [168], which can create significant pulls in the TF given by Eq. (6.18). This sort of tension can be relieved if the b jet energy is not taken from the measurement but instead marginalized over.

Various ambiguities may arise when mapping reconstructed particles to parton-level final states. In particular, this can happen if the final state features leptons of the same charge, multiple b jets, or multiple light jets. Additional ambiguities may come about if it is not clear which of the two leptons in DL H $\to$ WW* decay should be associated with the off-shell W boson. The aforementioned ambiguities are resolved by computing Eq. (6.20) for every permutation of the reconstructed particles that have the same type, and either taking their average [4], sum [427] or maximum [430] as the likelihood score. In implementations that target hadronic W boson decays, the jet permutations can be

skipped if the invariant mass of the jet pair is more than $20\,\text{GeV}$ away from the W boson mass.

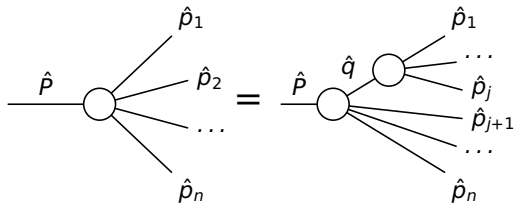


Figure 6.11: Demonstration of how an n-particle LIPS element with incoming 4-momentum $\hat{P}$ and outgoing 4-momenta $\{\hat{p}_i\}_{i=1}^n$ can be partitioned into a j-particle and an $(n-j+1)$-particle LIPS element by marginalizing over the 4-momentum $\hat{q}$ of some intermediate particle: $d\Pi_n(\hat{P};\hat{p}_1,\ldots,\hat{p}_n) = d\Pi_j(\hat{q};\hat{p}_1,\ldots,\hat{p}_j)\times d\Pi_{n-j+1}(\hat{P};\hat{q},\hat{p}_{j+1},\ldots,\hat{p}_n)\times(2\pi)^3 d\hat{q}^2$. The intermediate 4-momentum can be integrated out with Breit-Wigner trick, whereby Breit-Wigner propagator given by Eq. (2.22) and its inverse, $\frac{\pi}{m_X\Gamma_X}\delta^2(\hat{q}^2-m_X^2)$, are inserted under the integral, effectively forcing the particle to its on-shell mass m_X: $\int d\hat{q}^2 = \pi m_X\Gamma_X$.

The likelihood function in Eq. (6.20) is evaluated numerically using MC techniques. In a nutshell, MC integration is based on the idea that integral F of function $f(x)$ over some interval $[a,b]$ can be approximated by the average value of $f(x_i)$, where the samples x_i are drawn from a uniform pdf $\mathcal{U}(a,b)$ over that interval:

$$F = \int_a^b f(x)dx = \lim_{N\to\infty} \underbrace{\frac{b-a}{N}\sum_{i=1}^{N} f(x_i)}_{\equiv F_N} . \tag{6.22}$$

Each term under the sum of Eq. (6.22) could be interpreted as a very crude estimate of the integral, which is approximated by a rectangular area with sides $(b-a)$ and $f(x_i)$, and so the final estimate for the integral is simply the average over the naïve estimates. After retaining only a finite yet large number of samples N, Eq. (6.22) turns into MC estimator, which according to the central limit theorem follows asymptotically a Gaussian pdf with mean F_N and standard deviation

$$\sigma_N = \sqrt{\frac{\text{Var}[f(x)]}{N}} = (b-a)\sqrt{\sum_{i=1}^{N}\frac{\left(f(x_i)-F_N\right)^2}{N(N-1)}} . \tag{6.23}$$

It is clear from Eq. (6.23) that error on the MC estimate can be lowered by considering more samples N or by reducing the sample variance $\text{Var}[f(x)]$. Although this conclusion was derived for a one-dimensional case, it holds true for integration domains of arbitrary dimensions.

Importance sampling is a MC integration technique that seeks to minimize the variance in results [65]. It is accomplished with change of integration variables in Eq. (6.22): assuming a sampling function G that maps from $[a,b]$ to $[0,1]$ and has a Jacobian $g(x) = G'(x)$ that normalizes to unity, then Eq. (6.22) can be rewritten as follows:

$$F = \int_a^b \frac{f(x)}{g(x)}dG(x) \overset{y\equiv G(x)}{=} \int_0^1 \underbrace{\frac{f(G^{-1}(y))}{g(G^{-1}(y))}}_{\equiv w(y)} dy = \int_0^1 w(x)dx = \lim_{N\to\infty} \overbrace{\frac{1}{N}\sum_{i=1}^{N}\underbrace{w(x_i)}_{\equiv w_i}}^{\equiv F_N} . \tag{6.24}$$

Importance weight function $w(y)$ is evaluated on samples that are drawn from distribution $G(x)$ instead of $\mathcal{U}(a,b)$ like before. The transformation in Eq. (6.24) does not change the MC estimate, but it does have the potential to reduce variance considerably, especially if $g(x)$ follows very closely $f(x)$. In the extreme case where $g(x)$ is proportional to $f(x)$ by some constant, all importance weights w_i would be equal to F and the variance would thus be zero by construction.

It is worth noting that MC events are generated in very much the same way [67]: for every random event configuration $\mathbf{x}_i$, the event generator computes event weight w_i by sampling $d\sigma(\mathbf{x}_i)$. Events are unweighted with rejection sampling, whereby an event is accepted only if its weight $w_i/w_{\max}$, with $w_{\max}$ denoting the largest possible weight, is smaller than a random number between 0 and 1 that is drawn from a uniform pdf. Instead of generating a whole new event for a slightly different coupling scenario, the MC generators assign a different weights w_i' to it based on the ratio of squared MEs.

Figuring out the correct form of $G(x)$ can be challenging, though, especially if $f(x)$ has a complex structure, just like the integrand in Eq. (6.20). VEGAS is a popular integration method, which attempts to solve this issue by evaluating F_N in Eq. (6.24) multiple times and adjusting $G(x)$ every iteration such that it keeps the estimated variance minimal [431]. The sampling function is initially set to a uniform pdf, but with every integration step j its Jacobian progressively approaches the target distribution $f(x)$. The final estimate of the integral $\overline{F}_M$ and its standard error $\overline{\sigma}_M$ are aggregated over M integration steps such that higher weight is attributed to those estimates F_N^j that have lower standard error σ_N^j:

$$\overline{F}_M = \overline{\sigma}_M^2 \sum_{j=1}^{M} \frac{F_N^j}{(\sigma_N^j)^2}\,, \qquad \overline{\sigma}_M = \frac{1}{\sqrt{\sum_{j=1}^{M} 1/(\sigma_N^j)^2}}\,.$$

The VEGAS algorithm supports integration over multiple dimensions. It makes the assumption that the variable transformations factorize into unary components, which allows independent optimization of the sampling functions in every dimension. However, the issue with this approach is that it will create samples in regions of integration domain where the target function does not have any peaks whatsoever. For example, if the target function has p number of peaks in one dimension and q in another, then the algorithm would concentrate samples in pq locations of the integration domain, even though the actual number of peaks can be as low as $\max(p,q)$. Since this wastes a considerable number of sampling iterations on phantom peaks, the VEGAS algorithm implements adaptive stratified sampling to overcome this problem. It does so by dividing the multidimensional sampling volume into K subvolumes, and increasing the number of samples N_k in those subvolumes k that have higher variance, while also maintaining that $\sum_{k=1}^{K} N_k = N$ at every integration step. Integral over the full volume is estimated by simply summing over the estimates of individual subvolumes.

VEGAS does not sample the integrand efficiently if there are nontrivial correlations among integration variables, which ultimately invalidates the assumption that the sampling function can be factorized into independent unary components. This can very much be the case in MEM, because the integrand of Eq. (6.20) receives contributions from multiple MEs. Yet every ME handles the kinematic variables slightly differently, thereby making it impossible to find a universal transformation law that decouples the MEs. The issue is mitigated with adaptive multichannel techniques like VAMP [432], which attempts to identify individual peaks of the integrand dynamically and sample only those.

At every integration step, the integrator assigns a new set of values to the integration variables. These values are combined with reconstructed information in order to fully build

the 4-momenta of all particles that appear in the final state at parton level. From this one can directly estimate the Bjorken scaling variables, $x_{a,b} = \sum_{i=1}^{n}(\hat{E}_i \pm \hat{p}_z^i)/\sqrt{s}$, and the true hadronic recoil using Eq. (6.21). This is followed by the evaluation of TFs for jet and τ_h energies, and for hadronic recoil. Acceptance probabilities are evaluated for quarks that have no matching jets at the reconstruction level. PDFs are evaluated with LHAPDF [82] at an energy scale that is equal to the half invariant mass of the final state particles at parton level: $Q = \sum_{i=1}^{n} \hat{m}_i/2$.

The integration step concludes with the evaluation of squared ME of the process. The squared MEs are obtained with MadGraph5_aMCatNLO [87], which can be configured to generate a piece of C++ code for the MEs at LO. There are no tools currently available that support generating code for MEs defined at NLO, not to mention the complications one would have to face when trying to integrate out the added real emissions [433]. Profiling the MC event generation software reveals that evaluating the MEs at NLO instead of LO for the same final state, that is only adding virtual corrections to the Born-level process would increase the computing time by 1–2 orders of magnitude [4], yet the apparent gain in terms of discriminatory power is arguably marginal [433]. These arguments make a strong case for keeping the ME at LO in MEM implementation. Unless the analysis specifically targets polarized final states, the generated MEs are unpolarized, meaning that it sums over initial polarization states and averages over final spin states. Different initial states can be considered in a single iteration of the integration if the over initial partons in Eq. (2.20) is moved into the integrand and the MEs is paired with appropriate PDFs under the sum. Given that the ME is defined at LO and both partons in the initial state carry zero transverse momentum, it follows that the final state particles at parton level must be boosted into frame of reference where $\hat{\mathbf{p}}_T^\rho$ is also zero, or otherwise it would violate the conservation of momentum.

Likelihood function given by Eq. (6.20) is computed for N signal and M background hypotheses. The results are combined into a LR of the form

$$\tilde{\lambda} = \frac{\sum_{i=1}^{N} \alpha_i \Lambda_i}{\sum_{i=1}^{N} \alpha_i \Lambda_i + \sum_{j=1}^{M} \alpha_j \Lambda_j} \tag{6.25}$$

where α_i are appropriately chosen positive coefficients accompanying likelihood Λ_i. The coefficients effectively stretch or squeeze LR distribution, but they do not affect the ROC curve nor the performance as long as the distributions remain continuous. However, the coefficients do matter in binned distributions because they help to balance between two extremes, where in one case all events end up in a single bin, while in the other case they are completely spread out across all bins. The advantage of Eq. (6.25) where signal likelihoods appear in both numerator and denominator over Eq. (6.3) where the signal likelihoods appear only in the numerator is that the former always maps to $[0, 1]$, while the latter is unbounded from above, which is not ideal when trying to plot its distribution or, more importantly, place cuts on. The LR tends to be close to one for those events that are more compatible with signal hypotheses than with background hypotheses, while for backgrounds it should be the opposite. MEM LR can therefore serve as shape discriminant in signal extraction.

Discriminatory power of MEM LR has been directly utilized in a number of analyses, such as in spin correlation measurements in SL $\mathrm{t\bar{t}}$ events [434], cross section measurements of s-channel single top quark production in leptonic final states [435], in top quark mass measurements [436], and in $\mathrm{t\bar{t}H}$ production cross section measurements in $\mathrm{H} \to \mathrm{b\bar{b}}$ decay channel [426]. MEM made its first debut in $\mathrm{t\bar{t}H}$ multilepton analyses in CMS back in 2016 [365]. At the time, the MEM discriminant was developed for $2\ell\mathrm{SS} + 1\tau_\mathrm{h}$ and 3ℓ

channels to separate $t\bar{t}H$ signal from other backgrounds. The MEM discriminant was directly used as a signal extraction variable in the $2\ell SS + 1\tau_h$ channel. In 3ℓ channel a different strategy was followed, in which the MEM log-likelihoods entered as input to two BDTs, with one distinguishing $t\bar{t}H$ signal from irreducible $t\bar{t}V$ background, and the other separating $t\bar{t}H$ signal from $t\bar{t}$ fakes. Including MEM log-likelihoods as input to the BDTs improved the signal efficiency by 10–15% for the same background efficiency. A similar method was previously employed in the searches of $t\bar{t}H$ signal in $H \to b\bar{b}$ channel, where MEM LR entered as input to the DNN, the output of which was then used as a signal extraction variable [437].

The MEM discriminant in $2\ell SS + 1\tau_h$ channel aims to distinguish $t\bar{t}H$ signal where both $H \to \tau\tau$ as well as the top quark pair decay semileptonically from the following backgrounds: irreducible $t\bar{t}Z$ where both $Z/\gamma^* \to \tau\tau$ and the top quark pair decay semileptonically; reducible $t\bar{t}Z$ where $Z/\gamma^* \to \ell^+\ell^-$ but one of the leptons is misidentified as τ_h; reducible $t\bar{t} \to b\bar{b}\ell\tau_h + \nu$'s, but either of the b quarks is misidentified as a lepton that has the same charge as the real one. Even though both $H \to WW^*$ and $H \to \tau\tau$ contribute in equal amounts to the SR of $2\ell SS + 1\tau_h$ channel, the former decay mode was not considered in MEM implementation because its contributions are fragmented across multiple mechanisms. As explained in Section 5.3.3, in about half of the selected events the reconstructed τ_h in the final state is actually a jet from W boson decay that fakes it. The other half is divided between two decay modes, where in one case $H \to WW^*$ decays into $\ell + \tau_h$ and the top quark pair decays semileptonically, while in the other case it is the other way round. Given the multitude of ways how $t\bar{t}H(\to WW^*)$ events can contribute to the SR of $2\ell SS + 1\tau_h$ channel, not to mention the diluting effects caused by the fact that one of the W bosons has to be virtual, one can see why this particular signal hypothesis was not implemented in the MEM. The implementation also supports the scenario where one of the quarks has no matching jets at reconstruction level. In this „missing jet" regime, integration is performed over the energy and direction of the affected quark to evaluate its acceptance probability, which is then factorized into the MEM likelihoods. The MEM likelihoods are evaluated four times for different permutations of leptons and b jets. Permutations of light jets are reduced by imposing a W boson mass window cut on a pair of jets.

In the next iteration of the $t\bar{t}H$ multilepton analysis in 2017 [5], the event-level BDTs of 3ℓ channel were trained on MEM LRs instead of log-likelihood scores like before. The switch led to a slight improvement in the performance of the BDTs. However, including the MEM LR as input to the BDTs was found to improve the signal efficiency by just 5% compared to the case where the BDTs were not trained on the said variable. Likely reason for such a mild boost in performance can be traced back to the fact that the BDTs in the previous version of the analysis were trained with the TMVA framework [438], whereas the BDTs in 2017 iteration of the analysis were trained with the XGBoost software [403]. Combining this with improved modeling of lepton, τ_h and jet variables compared to previous year probably explains why some of the gains from MEM were rendered redundant. MEM LR was replaced by dedicated BDT in the $2\ell SS + 1\tau_h$ channel. There were plans to include MEM LRs as input to the BDT, but they were not followed through because of time constraints.

In the final iteration of the $t\bar{t}H$ multilepton analysis on full LHC Run 2 data, the MEM LRs were completely dropped from the main analysis. Instead, the MEM LR of $2\ell SS + 1\tau_h$ channel was used as a shape discriminant in control analysis (CA), which imposes the same object and event selection criteria as the main analysis, but uses different shape variables for signal extraction. The CA serves a cross check for the main analysis to highlight the improvements from using advanced machine learning algorithms compared to much

simpler shape variables. While in all previous iterations of the analysis the MEM was run on commodity central processing units (CPUs), then this time around the MEM calculations were delegated to GPUs [439], which sped up the calculations by two orders of magnitude.

The formalism of MEM inspired SVfit algorithm [429, 440], which aims to reconstruct invariant mass of the τ lepton pair from their anticipated decay products, which can be either a pair of τ_{h} candidates, a pair of leptons, or a lepton-plus-τ_{h} pair. In short, the algorithm computes the MEM likelihood for a single Higgs process, where the boson is produced via ggF and subsequently decayed to a τ lepton pair. Instead of assuming SM Higgs boson mass, however, it tries alternative mass hypotheses in the likelihood to find the one that produces the highest MEM likelihood. The mass hypothesis that maximizes the MEM likelihood is then chosen as the SVfit mass. The SVfit algorithm improved the sensitivity of SM $\mathrm{H} \to \tau\tau$ analysis by a significant margin [440], which eventually led to the discovery of the process [135]. It can also be useful in analyses that search for BSM resonances in $\tau\tau$ final states, since the MEM likelihood would peak at the mass hypothesis that corresponds to the mass of unknown resonance. The SVfit mass variable was used as input to the BDTs of $0\ell + 2\tau_{\mathrm{h}}$ and $1\ell + 1\tau_{\mathrm{h}}$ channels in the $\mathrm{t\bar{t}H}$ analysis, and in the BDTs of $0\ell + 4\tau_{\mathrm{h}}$ and $2\ell + 2\tau_{\mathrm{h}}$ channels in the HH analysis. In the latter two channels the SVfit mass was extracted from the leading τ_{h} pair. Unlike dedicated $\mathrm{H} \to \tau\tau$ searches, the SVfit algorithm does not excel at reconstructing the Higgs boson mass here because the algorithm implies that MET receives contributions only from neutrinos that result from $\mathrm{H} \to \tau\tau$ decay, which is obviously not true for $\mathrm{t\bar{t}H}$ nor HH signal.

To address these concerns explicitly in the HH analysis, the SVfit algorithm was extended to ggF $\mathrm{HH} \to \tau\tau\tau\tau$ hypothesis, where each of the four τ leptons is allowed to decay leptonically or hadronically [430]. The algorithm works in very much the same way as before, namely by trying out a range of m_{HH} hypotheses in the signal likelihood to find out the one that is most compatible with the reconstructed leptons, τ_{h} candidates and MET. The SVfit mass is used as input to the BDTs of those HH analysis channels that demand at least two τ_{h} candidates in final state. This was not attempted in other channels because of practical reasons, as every lepton that is exchanged for a τ_{h} in the signal hypothesis adds one more integration variable to the likelihood, which would not only increase the computing efforts but would also degrade the resolution on the estimated SVfit mass. In terms of feature importance, the SVfit m_{HH} ranked first in the BDTs of $0\ell + 4\tau_{\mathrm{h}}$ and $1\ell + 3\tau_{\mathrm{h}}$ channels, and placed among the leading input variables of the BDTs that were trained for the $2\ell + 2\tau_{\mathrm{h}}$ channel.

MEM has slowly fallen out of favor for several reasons. First, it takes a considerable amount of human effort to implement the integrands, plus sharing the work with other groups can be challenging since it is all custom code. This is in contrast to machine learning algorithms, for which there are dozens of software packages available that all have user-friendly interfaces one can access to build a model, train it and package it into a single file that can be easily shared with colleagues. There is a software package called MoMEMta [441], which attempts to address this problem by providing modular components that one can piece together to build a custom MEM likelihood integrand. However, it does not mean that the implementation comes for free, because one would still have to learn the framework and fill in missing pieces such as quark acceptance probabilities or energy TFs for the τ leptons.

Second, MEM requires a significant amount of computing resources and time. The issue becomes especially apparent considering that in order to propagate systematic variations of energy scales to the final shape discriminant, one would have to evaluate MEM LR for every such variation. To give some perspective, computing a single MEM LR in $2\ell\mathrm{SS} + 1\tau_{\mathrm{h}}$

channel on a CPU might take anywhere between a few seconds up to a few minutes in most cases, but some pathological events may need multiple hours to finish. Factoring in the systematic variations, it might take tens of minutes up to multiple days to process a single event, which is obviously prohibitive considering the fact that these calculations would have to be performed on all $\mathcal{O}(10^5)$ MC and data events that are selected in the SR and adjacent ARs. Of course, as mentioned earlier, these calculations can be significantly sped up with GPUs, but it implies that one has access to said hardware, which is not always the case.

Alternatively, one could train a machine learning model that regresses the MEM log-likelihoods [10]. Only those processes would have to be considered in the training for which the MEM log-likelihoods are defined, since including other processes to the training would work against the objective. Clear advantage of this approach is that the regression model returns an output in a matter of milliseconds, and does so consistently without letting spurious events create bottlenecks that otherwise occur in full-blown MEM calculations. Furthermore, importing a regression model to an analysis framework is arguably easier than writing matching interfaces to MEM code.

These ideas can be taken a step further by recognizing that the experimental smearing caused by the detector factorizes out the same way for competing hypotheses, which reduces the LR to a ratio of squared MEs [442]. Thus, by regressing the ratio of squared MEs directly with reconstructed data, one can skip the expensive MEM integration completely. This is because the experimental resolution effects are already embedded in the training dataset, so there is no need to spend time on simulating experimental noise on top of the parton-level content for it to be compared to actual reconstruction, which is what MEM integration ultimately does. The alternative approach is ideal for EFT analysis, where the different BSM scenarios arise depending on Wilson coefficients. Those coefficients can be used as inputs to a machine learning model that is trained to regress the corresponding event-level weights. The resulting model can be used to place optimal constraints on the couplings that it was trained on.

Third and perhaps the most important reason why MEM has fallen out of favor is that it does not boost the analysis sensitivity as much compared to BDTs or DNNs, at least not in the proportions to the resources that are invested into making it all work. Despite these shortcomings, MEM definitely has its place in analysis channels that are very low on (trainable) event statistics, as evidenced by the ranking of SVfit mass in terms of feature importance in the HH analysis. Additionally, MEM has a rather straightforward interpretation, whereas algorithms like DNN are somewhat less transparent in how they acquire their discriminating powers.

7 Measurement of $t\bar{t}H$ production in multilepton final states

The present discussion is fully dedicated to $t\bar{t}H$ multilepton analysis [1]. Section 7.1 touches on topics that have not yet been covered, namely the event selection criteria, the description of BDTs and DNNs that are directly utilized for signal extraction, and the different choices for binning the likelihood function. The final results are presented in Section 7.2, which concludes with the discussion of future prospects of this analysis.

7.1 Analysis

The ultimate goal of measuring inclusive $t\bar{t}H$ and tH production rates is to determine plausible values of the Yukawa coupling between Higgs bosons and top quarks. There are a few BSM models proposed that foresee potential deviations in the coupling value with respect to the SM expectation, as already argued in Section 2.4. The first experimental search of $t\bar{t}H$ production was conducted by the CDF collaboration at Tevatron right after the discovery of the Higgs boson was announced. Their results set a first upper limit of 20 times the SM cross section on $t\bar{t}H$ production [443]. All subsequent experimental searches of the process continued at the LHC.

Figure 7.1 summarizes the history of published analyses that looked for $t\bar{t}H$ or tH signal at the LHC. First evidence of $t\bar{t}H$ production was claimed by ATLAS [171] and CMS [365] collaborations in 2018 based on LHC data that was recorded in 2016. The ATLAS collaboration obtained their result by combining multiple $t\bar{t}H$ searches in Higgs boson decay modes to $b\bar{b}$, $\gamma\gamma$, $ZZ^* \to 4\ell$ and multilepton final states, while the CMS collaboration analyzed just the multilepton final states to arrive at the same qualitative conclusion. The initial searches of $t\bar{t}H$ process in multilepton final states covered six channels, which are 2ℓSS, $2\ell\text{SS} + 1\tau_\text{h}$, 3ℓ, 4ℓ, $1\ell + 2\tau_\text{h}$ and $3\ell + 1\tau_\text{h}$. Shortly thereafter an observation of $t\bar{t}H$ production was announced by both collaborations [17, 18]. The discovery was only possible after analyzing the data from both LHC Run 1 and Run 2 periods.

Sensitivity level equivalent to evidence was reclaimed by the CMS collaboration in the next iteration of the multilepton analysis that was performed on the data recorded in 2017 [5], which implemented numerous changes with respect to the previous version of the analysis. In particular, the second version of the analysis introduced the $2\ell + 2\tau_\text{h}$ channel as well as CRs for the 3ℓ and 4ℓ channels to further constrain irreducible $t\bar{t}Z + WZ$ and ZZ backgrounds, respectively. The results on 2017 data were combined with previously published results on 2016 data, which did not improve the observed significance, but reduced the uncertainties on the signal rates by 50%.

The $t\bar{t}H$ multilepton analysis presented here is the final iteration in the series of inclusive $t\bar{t}H$ cross section measurements that are published by the CMS collaboration on LHC Run 2 data. The scope of the analysis is extended further to also determine the tH production rate, which provides access to the sign of top Yukawa coupling. The production of tH process had only been studied twice in previous analyses, which targeted Higgs boson decay modes to $b\bar{b}$ and $\gamma\gamma$ decay modes as well as dilepton and trilepton final states [172, 444]. Acceptance of tH signal is enhanced by relaxing the jet multiplicity cuts in the most sensitive 2ℓSS, $2\ell\text{SS} + 1\tau_\text{h}$ and 3ℓ channels to accommodate the fact that the tH signal features fewer jets than the equivalent $t\bar{t}H$ process. Purity of tH signal in each of those channels is improved with DNN multiclass classifiers, which are trained to simultaneously distinguish $t\bar{t}H$, tHq and background processes. The DNN of the 2ℓSS channel also has a fourth output node for $t\bar{t}W$ process, which helps to further constrain the said background. On top of that, three more analysis channels were introduced, which cover $0\ell + 2\tau_\text{h}$, $1\ell + 1\tau_\text{h}$ and $2\ell\text{OS} + 1\tau_\text{h}$ final states. Finally, two more POIs are introduced that parametrize the rates of $t\bar{t}W(W)$

and $t\bar{t}Z$ processes (in addition to the other two POIs, with one for $t\bar{t}H$ signal and the other for the sum of tHq and tHW signals). This strategy was already implemented in the 2016 version of $t\bar{t}H$ multilepton analysis by the ATLAS collaborations [171]. It is done so to address the mild excess that is seen in dedicated measurements of $t\bar{t}W$ and $t\bar{t}Z$ production rates when compared to the SM expectation [445]. The excess seems to persist even after analyzing the full LHC Run 2 data [314, 446, 447], but is less pronounced for $t\bar{t}Z$ than for $t\bar{t}W$. If the rates of $t\bar{t}W$ and $t\bar{t}Z$ were not determined from the ML fit directly but instead assumed to occur at rates as predicted by the SM, then this could result in much higher rates of $t\bar{t}H$ and tH than currently measured, since the ML fit has the freedom to compensate the discrepancy between data and MC prediction by adding more signal.

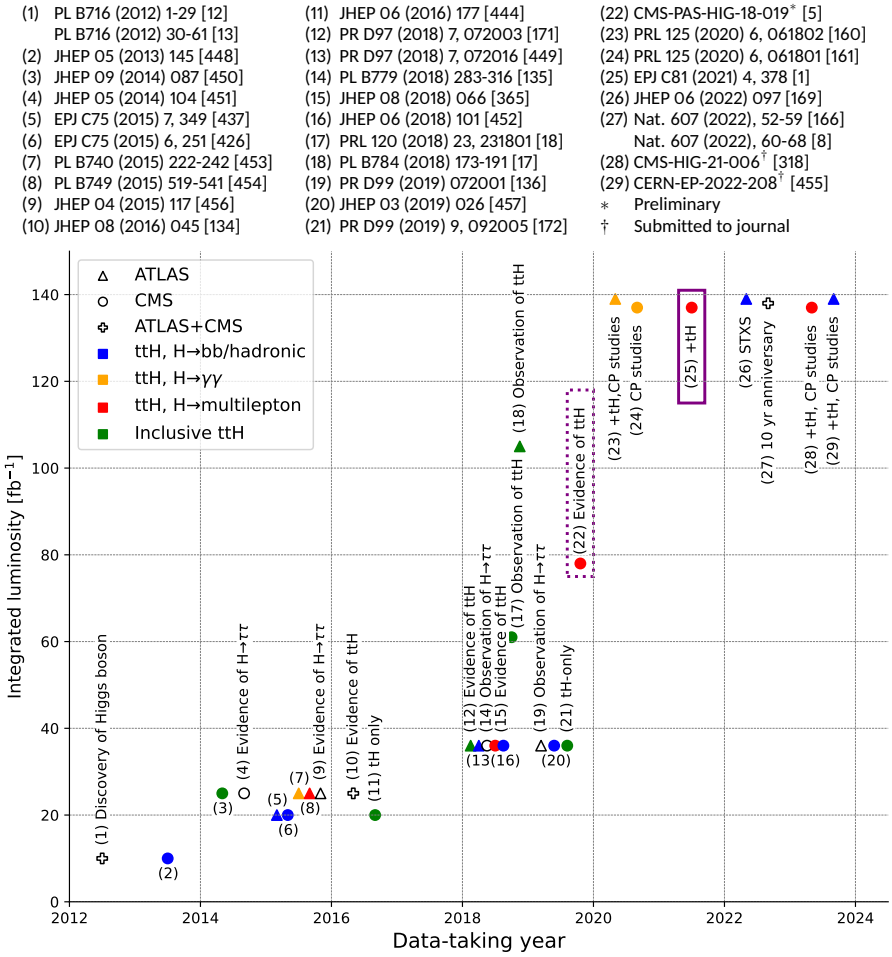


Figure 7.1: History of searches of $t\bar{t}H$ production at the LHC. The graphic also depicts milestones in the measurement of $H \to \tau\tau$ decay, as this process is particularly relevant to $t\bar{t}H$ multilepton analysis presented here. The analysis presented here is highlighted with a purple box that has a solid edge. Previous iteration of the same analysis is enclosed by a dotted line in the plot. Contributions from Higgs boson decay modes other than those indicated in the plot are found to be negligible.

The ten mutually exclusive channels of this analysis are all defined based on the multiplicity and charge of leptons and τ_h candidates in the final state. The exclusivity condition

of SRs is ensured by vetoing those events that feature more tight leptons or τ_{h} candidates than required in a given channel. However, when counting tight τ_{h} candidates it is important to keep in mind that the DeepTau ID WP, which the tight τ_{h} would have to pass, should not be the WP that is applied in the channel where the veto is implemented, but rather the loosest WP of tight τ_{h} in channels that request the same number of leptons and τ_{h} plus at least one additional τ_{h}. For example, the 2ℓSS channel can potentially overlap with the $2\ell\mathrm{SS}+1\tau_{\mathrm{h}}$, $2\ell\mathrm{OS}+1\tau_{\mathrm{h}}$ and $2\ell+2\tau_{\mathrm{h}}$ channels if no vetoes based on τ_{h} multiplicity are enforced. The tight τ_{h} candidates in each of those channels are required to pass VLoose, VTight and Medium WPs, respectively. If the tight τ_{h} veto in the 2ℓSS channel would be based on, say, Medium WP, then it would reject those events that are selected to the SRs of the $2\ell\mathrm{OS}+1\tau_{\mathrm{h}}$ and $2\ell+2\tau_{\mathrm{h}}$ channels, but would retain the events that are selected to the SR of the $2\ell\mathrm{SS}+1\tau_{\mathrm{h}}$ channel. Therefore, to avoid overlap also with the SR of the $2\ell\mathrm{SS}+1\tau_{\mathrm{h}}$ channel, the WP must be relaxed to VLoose when vetoing events with tight τ_{h} in the 2ℓSS channel. Similarly, overlap between the SR of the $2\ell\mathrm{SS}+1\tau_{\mathrm{h}}$ and $2\ell+2\tau_{\mathrm{h}}$ channels is removed when rejecting those events in the former that have more than one τ_{h} candidate passing the Medium WP. The exclusivity vetoes are enforced in the fake and flip ARs in very much the same way as in the SRs, to keep them as similar as possible and to avoid potential biases that would otherwise arise from it when estimating reducible backgrounds from the data. No limits are set on the maximum number of tight τ_{h} in channels that already request two τ_{h} or a total of four leptons plus τ_{h} candidates in the final state, since there are no channels that demand more of those objects. For the very same reason, no events are rejected from the 4ℓ channel even if they happen to feature five or more tight leptons.

The remaining event selection requirements are all documented in Table 7.1. Motivation for the implemented cuts is given in previous sections of this document. Each channel targets a particular topology of $\mathrm{t\bar{t}H}$ (and tH) signal as indicated by the first row of the table. To give an example based on the 2ℓSS channel, requiring just two leptons in final state without the SS charge requirement would populate the SR with DY events (if the leptons have the same flavor) and with $\mathrm{t\bar{t}}$ events (if the leptons have a different flavor). Thus, by demanding the selected leptons to have identical charges, it is possible to eliminate most of those huge backgrounds and keep half of the signal. The two SS lepton can arise from $\mathrm{t\bar{t}H}$ signal if the top quark pair decay semileptonically and the Higgs boson decays into a W boson pair, of which one decays leptonically and the other hadronically such that the lepton from the W boson has the same charge as the lepton that descended from the top quark pair. In this particular channel, one would expect at least six jets in total, of which two are b jets (from both top quarks) and the rest light jets (with two coming from hadronic top quark decay and another two from the Higgs boson via hadronic W boson decay). However, requiring this many jets would cut into signal acceptance and thereby reduce the overall sensitivity because some of these jets might be lost due to cleaning, acceptance cuts or reconstruction inefficiencies. To account for these possibilities, only half of the number of jets are requested in the 2ℓSS channel that would otherwise be expected from the $\mathrm{t\bar{t}H}$ signal. The same signal topology is expected from the $2\ell\mathrm{SS}+1\tau_{\mathrm{h}}$ channel, except that the hadronically decaying W boson from Higgs boson decays should instead decay into a τ lepton, which then decays hadronically. Alternatively, the same signature could arise from $\mathrm{t\bar{t}H}$ signal if the Higgs boson decays into a pair of τ leptons, which — like the top quark pair — decays semileptonically such that the resulting leptons have the same charges. Similar principles were followed when designing the event selection criteria of other channels.

	$0\ell+2\tau_h$	$1\ell+1\tau_h$	$1\ell+2\tau_h$	$2\ell+2\tau_h$	2ℓOS$+1\tau_h$	2ℓSS	2ℓSS$+1\tau_h$	3ℓ	$3\ell+1\tau_h$	4ℓ
Target $t\bar{t}$/H decay mode	FH/$\tau\tau$(FH)	FH/$\tau\tau$(SL)	SL/$\tau\tau$(FH)	DL/$\tau\tau$(FH)	SL/$\tau\tau$(SL)	SL/WW(SL)	SL/$\tau\tau$(SL)	SL/VV(DL)	DL/$\tau\tau$(SL)	DL/VV(DL)
Maximum # tight ℓ/τ_h	$0/$✗	$1/1$	$1/$✗	$2/$✗	$2/1$	$2/0$	$2/1$	$3/0$	$3/$✗	✗/✗
Charge sum (of ℓ/τ_h)	0	0	±1 ($\pm1/0$)	0 (0/0)	±1 ($0/\pm1$)	±2	±1 ($\pm2/\mp1$)	±1	0	0
Tight lepton charge	✗	✗	✗	✗	✗	✓	✓	✗	✗	✗
Tight τ_h WP selection	Loose	Medium	Medium	Medium	VTight	✗	VLoose	✗	VLoose	✗
veto	✗	Medium	✗	✗	Medium	VLoose	Medium	VLoose	✗	✗
Trigger	$2\tau_h$	1ℓ, $1\ell+1\tau_h$	1ℓ, $1\ell+1\tau_h$	1ℓ, 2ℓ	1ℓ, 2ℓ	1ℓ, 2ℓ	1ℓ, 2ℓ	1ℓ, 2ℓ, 3ℓ	1ℓ, 2ℓ, 3ℓ	1ℓ, 2ℓ, 3ℓ
Minimum cone-$p_T(\ell)$	✗	25, 30	25, 30	25/10, 15	25/10, 15	25/15	25/10, 15	25/15/10	25/15/10	25/15/15/10
Minimum $p_T(\tau_h)$	40/40	30	30/20	—	—	✗	—	✗	—	✗
Maximum $\lvert\eta\rvert$ (ℓ/τ_h)	2.1	2.1/2.3	2.1/2.3	—	—	—	—	—	—	—
Minimum # central jets	4	4	3	2	3	3*	3*	2*	2	2
Minimum E_T^{miss}LD	0	0	0	0/30/45†	30‡	30§	30§	0/30/45†‖	0/30/45†	0/30/45†
Z boson veto	✗	✗	✗	✓	✓	✓¶	✓¶	✓	✓	✓
H $\to$ ZZ* $\to 4\ell$ veto	✗	✗	✗	✗	✗	✗	✗	✓	✗	✓

* Alternatively, require at least one light jet and at least one central jet passing the medium WP of DeepJet b tagging discriminant to capture tH signal.

† Applied if $\geqslant 4$ central jets / if the selected leptons are not SFOS / if the selected leptons are SFOS.

‡ Applied only if the selected leptons have the same flavor.

§ Applied only if both leptons are electrons.

¶ OS charge requirement dropped if the two selected leptons happen to be electrons.

‖ Not applied if there is just one central jet passing the medium WP of DeepJet b tagging discriminant as expected from tH signal

Table 7.1: Target decay modes of the $t\dot{t}H$ signal (top section) and the event selection criteria (bottom section) of the $t\dot{t}H$ analysis channels. The same Higgs boson decay modes that are assumed for $t\dot{t}H$ signal in 2ℓSS$(+1\tau_h)$ and 3ℓ channels also apply to tH signal, where it is implied that the singular top quark decays leptonically. Requested number of fakeable leptons and τ_h is encoded in the channel name. In addition to the listed selection criteria, all selected events must also pass MET filters, loose dilepton mass veto and b jet selection requirement. A tick mark (✓) indicates that the selection criterion is enforced or applicable, whereas a cross mark (✗) implies the opposite. A dash (—) is used to denote that the cut is not tightened with respect to fakeable object definition as detailed in Section 4.2. Thresholds on the (cone-)p_T of leading, subleading, third and fourth physics objects are delimited by a forward slash. If there is a pair of thresholds separated by a comma, then the first value applies to muons and the second to electrons. Lower bounds on (cone-)p_T and E_T^{miss}LD are given in units of GeV. *The same cuts are applied in the SRs, fake ARs and charge flip ARs, except for the charge sum requirement of leptons in the 2ℓSS and 2ℓSS$+1\tau_h$ channels, which is inverted into OS charge requirement in their respective charge flip ARs.*

The resulting signal composition of each channel is shown in Fig. 7.2. The plot demonstrates that the 2ℓSS, 3ℓ and $2\ell\text{SS}+1\tau_\text{h}$ channels offer the most sensitivity based on the expected yields of the signal and background processes. Although the $1\ell+1\tau_\text{h}$ channel captures almost a third of the signal, it is succumbed to an enormous fake background just like in the $0\ell+2\tau_\text{h}$ channel. Both channels are also susceptible to irreducible $\text{t}\bar{\text{t}}$+jets and DY backgrounds, which have huge cross sections compared to the signal. Channels like $2\ell\text{OS}+1\tau_\text{h}$ and $1\ell+2\tau_\text{h}$ are also dominated by fakes, but they manage to capture a relatively high amount of signal events, which pushes their sensitivity to moderate levels. Due to their high multiplicity of leptons and τ_h in the final state, the remaining three channels — $3\ell+1\tau_\text{h}$, 4ℓ and $2\ell+2\tau_\text{h}$ — are characterized by very low event yields of just less than 10 events per channel per year.

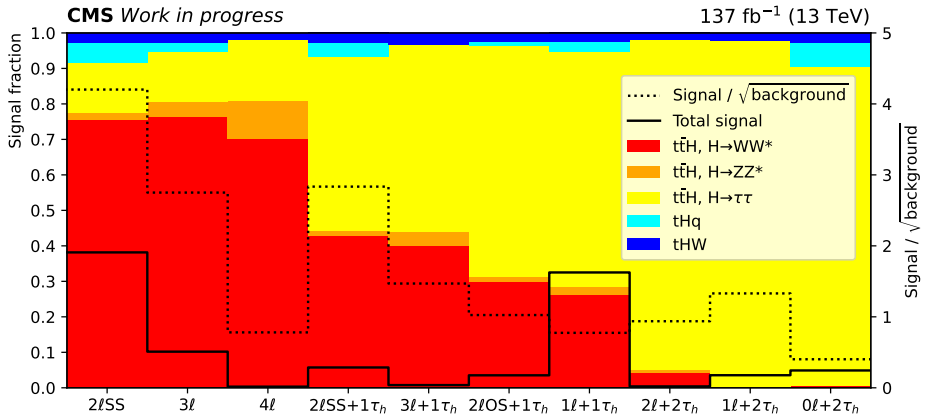


Figure 7.2: Signal composition in each of the ten channels in the $\text{t}\bar{\text{t}}H$ analysis. Contributions from $\text{t}\bar{\text{t}}H(\to b\bar{b})$ process are found to make up less than 5% of total signal in the $0\ell+2\tau_\text{h}$ and $1\ell+1\tau_\text{h}$ channels. The signal fractions are determined from simulated pre-fit yields after the event selection. The solid black line represents the signal contribution of that channel relative to total signal yield of the analysis, while the dotted line displays the ratio of total signal yield relative to the square root of total background yield as an approximate measure of sensitivity of that channel.

As discussed before, SRs of the ten analysis channels are complemented by additional two CRs, which are based on the event selection requirements of 3ℓ and 4ℓ channels. The former, 3ℓ CR, aims to constrain the rates of $\text{t}\bar{\text{t}}\text{Z}$ and WZ production, while the latter, 4ℓ CR, intends to constrain ZZ background. To achieve this, the ML fit not only considers the data that is selected to the SRs of ten analysis channels, but also the data that is selected to two CRs. Therefore, the CRs need to not only maximize the purity of anticipated backgrounds, but also remain orthogonal to the SRs. This is easily accomplished with a simple inversion of the Z boson veto, which is imposed in all SRs by default. Requirements on b jet multiplicity are dropped in the CRs since the diboson backgrounds are not expected to generate any b jets. On top of that, the cut on E_T^missLD is always enforced regardless of how many b jets there are that pass the medium WP of the b tagging discriminant, since it is expected that the dominant processes contributing to 3ℓ CR produce neutrinos. Few other CRs were devised for the purpose of validating the modeling of input variables to DNNs, but also the modeling of irreducible $\text{t}\bar{\text{t}}$ background in the $0\ell+2\tau_\text{h}$ and $1\ell+1\tau_\text{h}$ channels, as well as the modeling of fake backgrounds in the $1\ell+2\tau_\text{h}$ channel based on data-to-MC agreement. No extreme outliers nor systematic trends were spotted in this comparison. Event selection requirements of the aforementioned CRs are detailed in Table 7.2.

Control region	Baseline selection	Changes with respect to the baseline selection	Purpose
3ℓ CR	3ℓ SR	Inverted Z boson veto, at least one central jet, any number of b jets, E_T^{miss} LD cut always applied	Constrain $t\bar{t}Z$ and WZ backgrounds in signal extraction
4ℓ CR	4ℓ SR	Inverted Z boson veto, any number of jets and b jets	Constrain ZZ background in signal extraction
$t\bar{t}W$ CR	2ℓSS SR	Exactly three central jets	Validate data-to-MC agreement based on DNN input variables and output scores
$t\bar{t}Z$ CR	3ℓ SR	Inverted Z boson veto, at least two central jets	
WZ CR	$t\bar{t}Z$ CR	Inverted b jet veto	
$t\bar{t}$ CR	τ_{h} FR MR	Any number of τ_{h}	Validate the modeling of irreducible $t\bar{t}$ background in $0\ell + 2\tau_{\text{h}}$ and $1\ell + 1\tau_{\text{h}}$
Fake CR	$1\ell + 2\tau_{\text{h}}$ SR	τ_{h} must have SS charges	Validate the modeling of reducible backgrounds

Table 7.2: Event selection criteria for the CRs of the $t\bar{t}H$ analysis. Data-driven fake and flip backgrounds are estimated the same way in the CRs as they were in the SRs. Only the 3ℓ and 4ℓ CRs contribute to the ML fit from where the signal rates are extracted.

The input variables and hyperparameters that were eventually chosen for the DNNs and BDTs are summarized in Tables 7.3 and 7.4, respectively. One DNN or BDT was trained per analysis channel. Initially, the machine learning models were trained on a superset of variables listed in the tables, which is then progressively trimmed down based on feature importance as described in Section 6.2.1. The preliminary set of input variables was curated by hand. It includes angular differences and pseudorapidity observables, which remain invariant under certain rotations or boosts, but also variables that inform the machine learning model about the energy scale of considered processes, such as invariant and transverse mass as well as (cone-)p_T of final state objects. Some input variables represent a simple aggregation of low-level quantities like jet multiplicities and charge sums, while others are defined at a much higher level, such as the output of HJT or HTT algorithms, SVfit masses and b tagging scores to name a few.

The DNNs in the $2\ell\text{SS} + 1\tau_{\text{h}}$ and 3ℓ channels are trained to simultaneously identify $t\bar{t}H$ and tHq signal from the sum of $t\bar{t}V$ and $t\bar{t}$+jets backgrounds, which respectively contaminate the SRs in irreducible and reducible capacity. The DNN in the 2ℓSS channel is additionally tasked to recognize $t\bar{t}W$ events. The goal of the DNNs is to maximize the purity of processes in their respective output nodes. The reason for considering just tHq and not the sum of tHq and tHW as the objective is because tHW tends to have a jet topology that resembles more $t\bar{t}H$ than tHq. More specifically, the tHq signal produces a higher number of forward jets than tHW due to contributions received from s-channel in the latter case, which similarly to $t\bar{t}H$ production skews the multiplicity of forward jets towards lower values. After all, the tHW and $t\bar{t}H$ processes have identical final states at LO if the former process is defined in 4FS. The justification for using DNNs instead of BDTs was based on comparing their performance in the most sensitive 2ℓSS channel. It revealed that switching from the BDT of the previous iteration to the DNN in the latest iteration of the analysis showed a 10% improvement in expected median upper limits.

Variable	2ℓSS	$2\ell\text{SS}+1\tau_\text{h}$	3ℓ
Average ΔR(jets)	8$^{\text{th}}$	3$^{\text{rd}}$	1$^{\text{st}}$
Invariant mass of b jets[*]	5$^{\text{th}}$	21$^{\text{st}}$	17$^{\text{th}}$
Highest HTT score	1$^{\text{st}}$	24$^{\text{th}}$	24$^{\text{th}}$
E_T^{miss}LD	22$^{\text{nd}}$	9$^{\text{th}}$	9$^{\text{th}}$
p_T, $\lvert\eta\rvert$ of leading forward jet	2$^{\text{nd}}$, 3$^{\text{rd}}$	15$^{\text{th}}$, 35$^{\text{th}}$	5$^{\text{th}}$, 26$^{\text{th}}$
3-momenta of leading central jets[†]	4$^{\text{th}}$–35$^{\text{th}}$	12$^{\text{th}}$–41$^{\text{st}}$	3$^{\text{rd}}$–37$^{\text{th}}$
Minimum ΔR(jets, ℓ/τ_h)	25$^{\text{th}}$, 27$^{\text{th}}$	11$^{\text{th}}$, 18$^{\text{th}}$, 22$^{\text{nd}}$	4$^{\text{th}}$, 11$^{\text{th}}$, 16$^{\text{th}}$
3-momenta of ℓ/τ_h	23$^{\text{rd}}$–32$^{\text{nd}}$	5$^{\text{th}}$–36$^{\text{th}}$	6$^{\text{th}}$–33$^{\text{rd}}$
# b jets[‡]	15$^{\text{th}}$, 19$^{\text{th}}$	40$^{\text{th}}$, 25$^{\text{th}}$	36$^{\text{th}}$, 23$^{\text{rd}}$
# central jets	9$^{\text{th}}$	36$^{\text{th}}$	27$^{\text{th}}$
# forward jets	36$^{\text{th}}$	26$^{\text{th}}$	25$^{\text{th}}$
# electrons	30$^{\text{th}}$	28$^{\text{th}}$	29$^{\text{th}}$
Transverse mass of $E_T^{\text{miss}}+\ell/\tau_\text{h}$	13$^{\text{th}}$, 21$^{\text{st}}$	2$^{\text{nd}}$, 7$^{\text{th}}$, 10$^{\text{th}}$[§]	✗
Minimum ΔR between ℓ/τ_h	✗	6$^{\text{th}}$	12$^{\text{th}}$
Hadronic top p_T	✗	17$^{\text{th}}$	14$^{\text{th}}$
Minimum $\Delta\eta$ between ↪ central and forward jets	✗	19$^{\text{th}}$	18$^{\text{th}}$
Charge sum of ℓ/τ_h	✗	20$^{\text{th}}$	15$^{\text{th}}$
Invariant mass of ℓ/τ_h	✗	1$^{\text{st}}$, 4$^{\text{th}}$[¶]	✗
Highest HJT score	11$^{\text{th}}$	✗	✗
Lepton charge	16$^{\text{th}}$	✗	✗
Maximum $\lvert\eta(\ell/\tau_\text{h})\rvert$	20$^{\text{th}}$	✗	✗
Presence of a SFOS ℓ pair	✗	✗	22$^{\text{nd}}$
# input variables	36	41	37
# hidden layers	11	4	5
Nodes / hidden layer ($\times$ layers)	$32, 16\times5, 8\times5$	$16\times3, 8$	$32\times3, 16\times2$
Initializer	Glorot (normal)	He (uniform)	He (uniform)
Optimizer	Adam	Nadam	Nadam
Learning rate	0.1%	0.2%	0.1%
Dropout rate	1%	10%	10%
# epochs	300	45	45
Batch size	1500	246	246

[*] Computed from leading two jets passing the loose WP of DeepJet b tagging discriminant.
[†] Up to four jets in 2ℓSS, up to three jets in $2\ell\text{SS}+1\tau_\text{h}$ and 3ℓ.
[‡] Computed from jets passing loose and medium WPs of DeepJet ID, respectively.
[§] Computed for each individual lepton and for the 4-momentum sum of leptons and τ_h.
[¶] Computed for pairs of ℓ and τ_h.

Table 7.3: List of variables with corresponding ranking in terms of feature importance (top section) and hyperparameters (bottom section), which were used to train the DNNs for the $t\bar{t}H$ analysis. A range between highest and lowest ranking variable is provided features that include more than three variables. Unless specified otherwise, the jet-related variables are derived from the central AK4 jet collection. All lepton-related variables are computed using their cone-p_T as input. Symbol ℓ/τ_h stands for all muons, electrons and τ_h that are available in the final state. Cross mark (✗) means that the variable was not used in that particular training.

Variable	$0\ell+2\tau_h$	$1\ell+1\tau_h$	$1\ell+2\tau_h$	$2\ell+2\tau_h$	$2\ell\text{OS}+1\tau_h$	$3\ell+1\tau_h$	4ℓ
Invariant mass of ℓ/τ_h	2nd	12th	1st, 4th*	1st†	1st‡	1st, 2nd‡, 3rd§	1st§
(Cone-)p_T of ℓ/τ_h	10th, 13th	3rd, 13th	5th, 6th, 11th	2nd, 7th†	2nd, 6th, 15th	4th, 6th, 8th, 9th	3rd–6th
E_T^{miss}LD	7th	4th	3rd	8th	16th	5th	2nd
Pairwise ΔR between ℓ/τ_h	3rd	9th	8th, 12th, 14th¶	5th‖	3rd, 5th, 12th¶	✗	✗
Minimum ΔR(jets, ℓ/τ_h)	4th, 9th	2nd**	9th**	3rd‖	8th, 10th, 14th	✗	✗
Average ΔR(jets)	8th	15th	16th	4th	13th	✗	✗
Invariant mass of b jets††	6th	12th	10th	9th	17th	✗	✗
Highest HTT score	1st	1st, 9th‡‡	2nd	✗	7th	✗	✗
Transverse mass of $E_T^{\text{miss}}+\ell/\tau_h$	11th, 12th	8th, 11th	7th**	✗	4th, 11th**	✗	✗
$\cos\theta^*$ between ℓ/τ_h	15th	16th	17th†	6th†	✗	✗	✗
Maximum $\lvert\eta(\ell/\tau_h)\rvert$	14th	14th**	15th**	✗	18th	✗	✗
SVfit mass of ℓ/τ_h	5th	7th	✗	✗	✗	✗	✗
Presence of SFOS ℓ pairs	✗	✗	✗	✗	✗	7th	7th
Hadronic top p_T	✗	✗	13th	✗	9th	✗	✗
Charge sum of ℓ/τ_h	✗	6th◇	✗	✗	✗	✗	✗
# input variables	15	16	17	9	18	9	7
# trees	1500	1000	300	600	1400	300	1000
Tree depth	3	3	3	3	3	4	3
Learning rate [%]	1	4	10	10	3	2	1.5

* Considering the τ_h pair as well as all final state particles.
† Considering only the τ_h candidate(s).
‡ Computed for lepton-plus-τ_h pair(s) with OS charges.
§ Computed for a lepton pair with the smallest invariant mass.
¶ Distinguishing between OS and SS pairs.
‖ Minimum aggregated over all ℓ and τ_h.
** Considering only the lepton(s).
†† Computed from leading two jets passing the loose WP of DeepJet b tagging discriminant.
‡‡ Computed twice, with the second iteration excluding those jets that returned the highest HTT score.
◇ The training was performed on a sample of events that were selected without the OS charge condition.

Table 7.4: List of variables with corresponding ranking in terms of feature importance (top section) and hyperparameters (bottom section), which were used to train the BDTs for the $t\bar{t}H$ analysis. Unless specified otherwise, the jet-related variables are derived from central AK4 jet collection. All lepton-related variables are computed using their cone-p_T as input. Symbol ℓ/τ_h stands for all muons, electrons and τ_h that are available in final state. Cross mark (✗) means that the variable was not used in that particular training.

Each DNN output node of the 2ℓSS channel is further divided into three subcategories based on lepton flavor (ee, eμ and $\mu\mu$) to enhance experimental sensitivity by exploiting differences in ID efficiencies and charge flip rates of electrons and muons. The same is also done for the background node of the DNN in the 3ℓ channel. All DNN output nodes and lepton subcategories of the 3ℓ channel are split into two subcategories based on whether the event features two jets passing the medium b tagging WP, except for the eee subcategory in the background node because it has relatively low event yields. Partitioning the phase space in this manner helps to separate irreducible $t\bar{t}V$ background, which always produces some b jets, from reducible backgrounds, which not only covers $t\bar{t}$ but also multijet production. No extra subcategories are created in the DNN output nodes of $2\ell\text{SS}+1\tau_h$ channel due to lack of events, nor in any other SR for that matter due to lower sensitivity of the remaining channels. Unlike the SRs, no special shape variables were developed for the CRs that are directly utilized by the ML fit. Instead, events in the CRs are partitioned into bins based on the multiplicity regular (central) jets and b jets, lepton flavor and charge as indicated by Table 7.5. Due to the presence of b jets in the final state of the $t\bar{t}Z$ process, the b jet multiplicity variable is particularly effective at separating this background from diboson events.

Sensitivity of an analysis clearly relies on how the shape discriminants are binned in

the likelihood function. Two binning schemes were attempted, with one scheme assuming equidistant bin edges while the other bins the discriminant in quantiles of background yields, so that the resulting bins contain approximately the same amount of background. The test involved comparing expected upper limits as a function of number of bins, which was found to plateau after a certain number of bins had been reached. Whichever binning scheme produced the lowest expected upper limits is chosen as the binning scheme for that channel or subcategory. The lowest number of bins required for reaching the plateau in expected upper limits is chosen as the number of bins for that channel. The results of these tests are also documented in Table 7.5, which tells that the DNN output scores are binned in quantiles of background, as are the BDT scores of the $2\ell + 2\tau_\mathrm{h}$, $3\ell + 1\tau_\mathrm{h}$ and 4ℓ channels to avoid bins with empty event yields. The BDT scores of the remaining four channels are binned uniformly. The bin edges are fine-tuned separately in each subcategory of the 2ℓSS, $2\ell\mathrm{SS} + 1\tau_\mathrm{h}$ and 3ℓ channels.

Signal extraction variable	Channel	Subcategories #	Subcategories Details	Binning #	Binning Criterion
DNN score	2ℓSS	12	DNN node ($\mathrm{t\bar{t}H}$, $\mathrm{t\bar{t}W}$, $\mathrm{tH}q$, other), lepton flavor ($\mu\mu$, $\mathrm{e}\mu$, ee)	Varies by subcategory	Quantiles in background
	3ℓ	11	DNN node ($\mathrm{t\bar{t}H}$, tH, background), lepton flavor ($\mu\mu\mu$, $\mathrm{e}\mu\mu$, $\mathrm{ee}\mu$, eee) in the background node, multiplicity of b jets passing the medium WP of DeepJet ID (< 2, $\geqslant 2$) in all nodes but eee in the background node		
	$2\ell\mathrm{SS} + 1\tau_\mathrm{h}$	3	DNN node ($\mathrm{t\bar{t}H}$, tH, other)		
BDT score	$0\ell + 2\tau_\mathrm{h}$	0		10	Equidistant
	$1\ell + 1\tau_\mathrm{h}$				
	$1\ell + 2\tau_\mathrm{h}$				
	$2\ell\mathrm{OS} + 1\tau_\mathrm{h}$				
	$2\ell + 2\tau_\mathrm{h}$			2	Quantiles in background
	$3\ell + 1\tau_\mathrm{h}$			4	
	4ℓ			2	
Event counts	3ℓ CR	48	Multiplicity of b jets passing the medium WP of DeepJet ID ($N_\mathrm{b} = 0, 1, > 1$), multiplicity of central jets ($N_j + 1, N_j + 2, N_j + 3$, $> N_j + 3$ with $N_j = \min(N_\mathrm{b}, 2)$), lepton flavor ($\mu\mu\mu$, $\mathrm{e}\mu\mu$, $\mathrm{ee}\mu$, eee)		
	4ℓ CR	4	Multiplicity of SFOS lepton pairs satisfying inverted Z boson veto (1, 2), multiplicity of b jets passing the medium WP of DeepJet ID (0, 1, > 1) but only if there is just one SFOS lepton pair compatible with Z boson		

Table 7.5: Subcategorization of analysis channels and binning scheme of discriminating distributions in the $\mathrm{t\bar{t}}H$ analysis.

A control analysis (CA) was devised in addition to the main analysis, with the intention to test how much sensitivity can be gained with sophisticated machine learning methods compared to a single variable analysis. The CA aims to measure $\mathrm{t\bar{t}H}$, $\mathrm{t\bar{t}W}$ and $\mathrm{t\bar{t}Z}$ production rates. The tH process is normalized to the SM expectation and treated as a background. The CA includes 2ℓSS, 3ℓ, 4ℓ and $2\ell\mathrm{SS} + 1\tau_\mathrm{h}$ channels as well as both CRs of the main analysis. The event selection criteria are identical to the main analysis, except for the 2ℓSS channel, where the event selection requirements are modified to accept only those events that have at least four central jets. Subcategorization strategy is also completely revised, as the 2ℓSS and 3ℓ channels are instead split based on whether the selected events

feature at least six and four jets, respectively, to induce more clear distinction between reducible backgrounds and $t\bar{t}V$ processes, though the partitioning by lepton flavors still applies to the 2ℓSS channel. In addition to the above, the 2ℓSS and 3ℓ channels are further divided into two subcategories each based on the charge sum of final state leptons to exploit differences in production rates of $t\bar{t}W^+$ and $t\bar{t}W^-$ processes [314]. Just like in the main analysis, the 4ℓ channel is not subcategorized in the CA either due to lack of events. All channels aside from $2\ell\text{SS}+1\tau_\text{h}$ use invariant mass of final state leptons as the signal extraction variable. As discussed in Section 6.2.4, the shape variable that is chosen in the $2\ell\text{SS}+1\tau_\text{h}$ channel for signal extraction is the MEM LR.

7.2 Results

The unblinding procedure concludes with the inspection of post-fit yields and distributions of discriminating observables in each analysis channel to ascertain if the data and prediction are in good agreement with each other. The results are obtained by scaling $t\bar{t}H$ signal contribution by $\hat{\mu}_{t\bar{t}H}$, tHq and tHW by $\hat{\mu}_{tH}$, $t\bar{t}W$ and $t\bar{t}WW$ by $\mu_{t\bar{t}W}$ and $t\bar{t}Z$ by $\mu_{t\bar{t}Z}$. All POIs are concurrently extracted from the same ML fit to the data. The resulting post-fit yields are tabulated in Table 7.6. Post-fit distributions in the output of the DNN in each subcategory of the 2ℓSS channel are displayed in Fig. 7.3, and of the 3ℓ and $2\ell\text{SS}+1\tau_\text{h}$ channels in Fig. 7.4. Post-fit distributions in the BDTs output of the $1\ell+2\tau_\text{h}$, $2\ell\text{OS}+1\tau_\text{h}$ and $3\ell+1\tau_\text{h}$ channels are given in Fig. 7.5, and of the $0\ell+2\tau_\text{h}$, $1\ell+1\tau_\text{h}$ and $2\ell+2\tau_\text{h}$ channels in Fig. 7.6. Post-fit distributions in 3ℓ and 4ℓ CRs are shown in Fig. 7.7. The results demonstrate good compatibility between the data and the predicted yields. The only notable feature of these results is that the data in the $2\ell+2\tau_\text{h}$ channel appears to under-fluctuate, since about seven events were expected across all three years, or about two-to-three events per year, but only three were delivered, with only one event per year. The under-fluctuation corresponds to a significance of 1.9σ if assuming that the $t\bar{t}H$ signal appears in nominal amounts as predicted by the SM. Similar under-fluctuation was also observed in the previous iteration of the analysis, where the channel was first introduced [5].

The best fit signal rates of $t\bar{t}H$ and tH production are extracted from the ML fit and amount to $\hat{\mu}_{t\bar{t}H} = 0.92^{+0.26}_{-0.23}$ ($1.00^{+0.26}_{-0.22}$ expected) and $\hat{\mu}_{tH} = 5.7^{+4.1}_{-4.0}$ ($1.00^{+3.8}_{-3.7}$ expected), respectively. This is equivalent to $t\bar{t}H$ production cross section of $\sigma_{t\bar{t}H} = 466^{+132}_{-112}$ fb and tH production cross section of $\sigma_{tHq+tHW} = 510^{+360}_{-370}$ fb. The significance of the $t\bar{t}H$ measurement under the background-only hypothesis was observed at 4.2σ while expecting 5.0σ, thus showing clear improvement with respect to the observed significance of 3.2σ (4.0σ expected) attained in the previous iteration of the same analysis [5]. The observed (expected) significance is increased by 0.5σ (0.2σ) when fixing the tH production to SM instead of letting it float. The significance of the tH measurement under the background-only hypothesis was found to be just 1.4σ while the expectation is 0.3σ. These results show a clear evidence of $t\bar{t}H$ production, almost up to the level that would be required for claiming an observation. These are the most sensitive results of any $t\bar{t}H$ analysis covering multilepton final states that have been published thus far. As seen from Table 2.7, this analysis has similar sensitivity compared to other analyses that search for the $t\bar{t}H$ signal in $H \to b\bar{b}$ decay channel [169, 170] and in $H \to \gamma\gamma$ channel [160, 161].

	$0\ell+2\tau_h$	$1\ell+1\tau_h$	$1\ell+2\tau_h$	$2\ell+2\tau_h$	$2\ell\text{OS}+1\tau_h$	$2\ell\text{SS}$	$2\ell\text{SS}+1\tau_h$	3ℓ	$3\ell+1\tau_h$	4ℓ	3ℓ CR	4ℓ CR
$t\bar{t}H$	24.4 ± 6.0	183 ± 41	19.3 ± 4.2	2.2 ± 0.5	19.1 ± 4.3	222 ± 51	28.9 ± 6.4	61 ± 15	4.0 ± 0.9	2.0 ± 0.5	15.9 ± 4.4	1.4 ± 0.4
tH	16 ± 12	65 ± 46	2.6 ± 1.9	0.3 ± 0.2	4.8 ± 3.4	119 ± 85	12.7 ± 9.0	20 ± 14	0.8 ± 0.6	0.2 ± 0.2	4.4 ± 3.0	—
$t\bar{t}Z$	27.1 ± 3.8	203 ± 24	20.3 ± 2.1	2.5 ± 0.3	25.5 ± 2.9	322 ± 25	29.6 ± 3.3	145 ± 11	6.6 ± 0.7	5.9 ± 0.4	550 ± 43	41.5 ± 3.0
$t\bar{t}W(W)$	3.8 ± 0.5	254 ± 34	2.6 ± 0.4	—	17.4 ± 2.4	1153 ± 64	47.4 ± 6.5	171.1 ± 9.5	1.1 ± 0.2	0.2 ± 0.0	26.8 ± 1.7	—
WZ	42.5 ± 8.7	198 ± 37	11.8 ± 2.2	—	8.4 ± 1.6	296 ± 31	19.4 ± 2.9	89.7 ± 9.7	—	—	4320 ± 120	—
ZZ	34.2 ± 4.8	98 ± 13	1.8 ± 0.3	0.2 ± 0.0	1.9 ± 0.3	31.2 ± 3.3	1.6 ± 0.3	16.2 ± 1.6	0.3 ± 0.1	0.6 ± 0.2	298 ± 18	1030 ± 32
DY	1430 ± 220	4480 ± 460	—	—	—	—	—	—	—	—	—	—
$t\bar{t}$+jets	861 ± 98	41900 ± 1900	—	—	—	—	—	—	—	—	—	—
Single Higgs boson	26.7 ± 3.6	38.5 ± 3.6	—		0.8 ± 0.1	35.3 ± 4.0	1.8 ± 0.3	3.4 ± 0.3	—	—	42.8 ± 3.1	5.8 ± 0.4
Rare processes	60 ± 14	1930 ± 420	5.6 ± 1.3	0.3 ± 0.1	5.9 ± 1.3	222 ± 48	13.3 ± 3.1	41.0 ± 8.9	1.0 ± 0.3	0.6 ± 0.1	311 ± 61	17.0 ± 3.4
Fakes	3790 ± 220	25300 ± 1900	250 ± 16	3.4 ± 0.9	519 ± 28	1217 ± 91	52.0 ± 9.6	140 ± 11	1.5 ± 0.9	—	210 ± 20	—
Flips	—	—	—	—	—	121 ± 19	—	—	—	—	—	—
Conversions	—	—	0.5 ± 0.2	—	—	42 ± 12	—	5.6 ± 1.6	—	—	1.0 ± 0.3	0.1 ± 0.1
Total background	6290 ± 130	73550 ± 610	295 ± 16	6.8 ± 1.0	584 ± 27	3517 ± 85	179 ± 13	627 ± 20	11.5 ± 1.3	7.4 ± 0.5	5761 ± 99	1094 ± 33
Data	6310	73736	307	3	603	3738	201	744	18	12	5778	1089

Table 7.6: Post-fit yields with corresponding statistical and systematical uncertainties in each of the ten analysis channels and in the two auxiliary CRs that help to constrain irreducible $t\bar{t}Z$ and diboson backgrounds. Symbol „—" is used if the process contributes by less than 0.1 events.

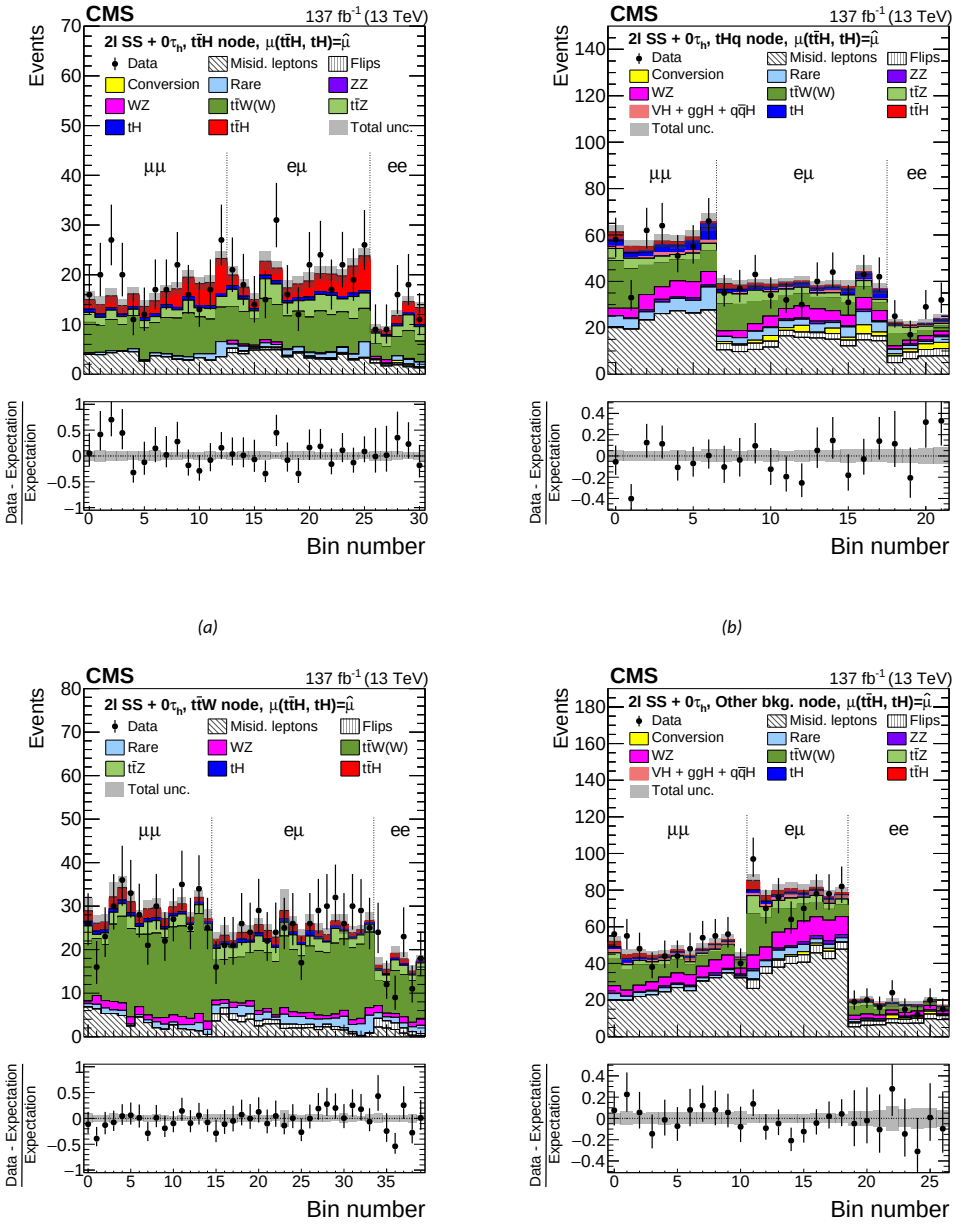
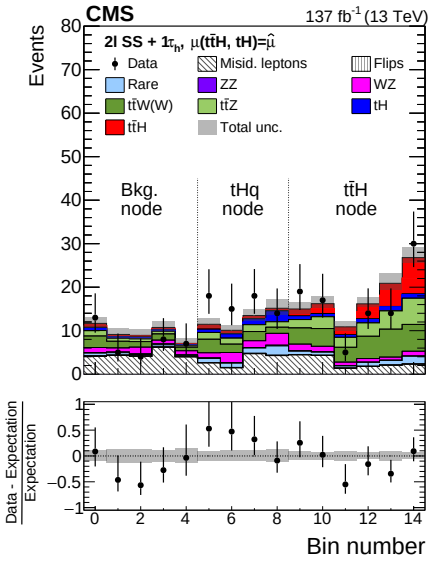
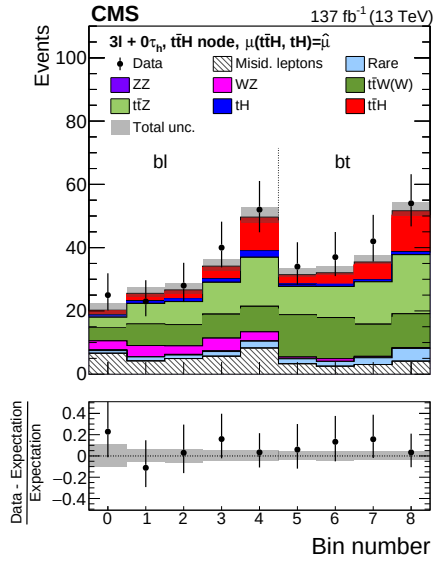


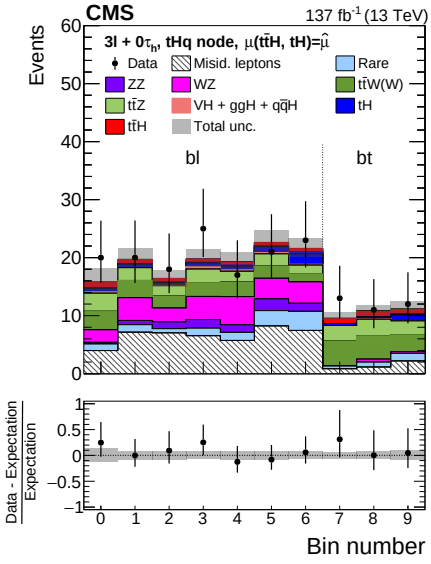
Figure 7.3: Post-fit distributions in the output of the DNN that was trained for the 2ℓSS channel. Events selected in the SR of the 2ℓSS channel are subsequently classified as $t\bar{t}H$ (a), tHq (b), $t\bar{t}W$ (c), or as other background (d) based on whichever output node had the highest DNN score. They are further categorized as ee, $e\mu$ or $\mu\mu$ based on the flavor of the selected two leptons. The bins are sorted by the DNN output score in ascending order per DNN output node. The same plots are also published in Ref. [1].



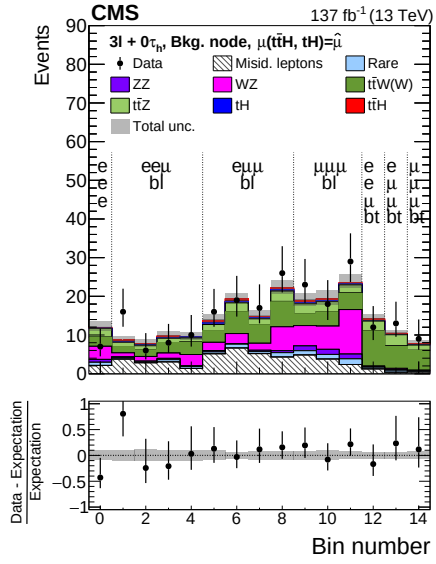
(a)



(b)

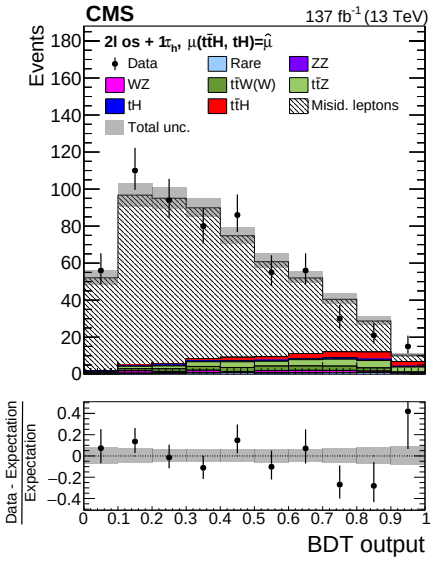


(c)

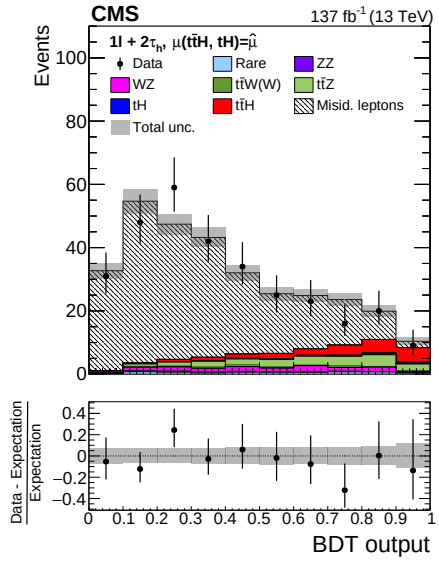


(d)

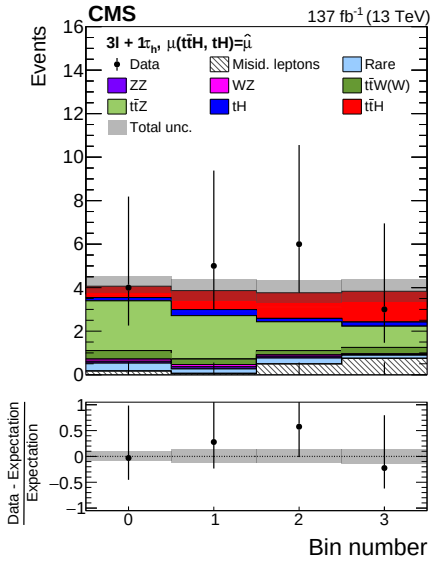
Figure 7.4: Post-fit distributions in the output of DNN that was trained for the $2\ell SS + 1\tau_h$ channel (a), and for the 3ℓ channel, with events selected in the SR of the 3ℓ channel further classified as $t\bar{t}H$ (b), tH (c) or as background (d) based on whichever output node had the highest DNN score. Events selected in 3ℓ SR are further categorized depending on whether they feature at least two b jets passing the medium WP of DeepJet ID („bt") or not („bl"). Events in the background node of the 3ℓ channel are additionally distinguished based on the flavor of the three leptons that are selected to the final state. The bins in each DNN output node are sorted by the DNN output score in ascending order. The same plots are also published in Ref. [1].



(a)

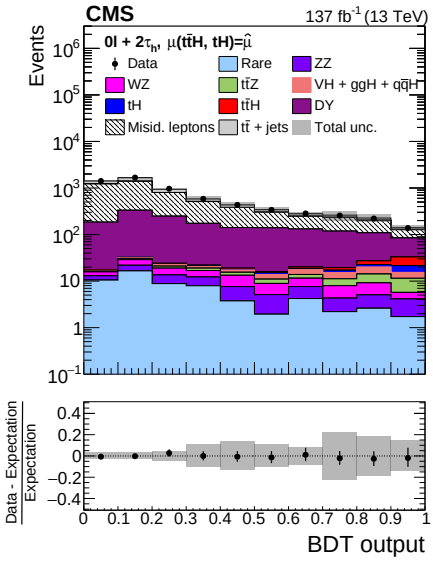


(b)

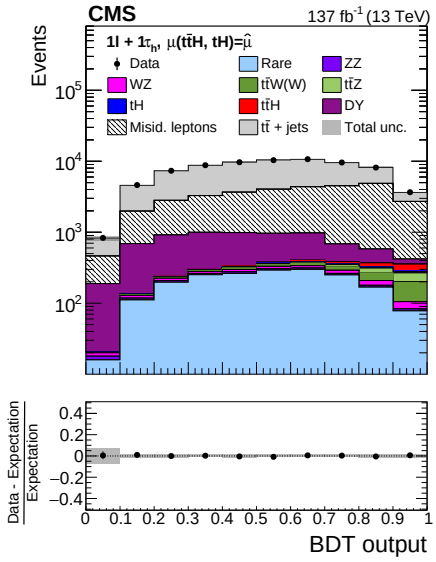


(c)

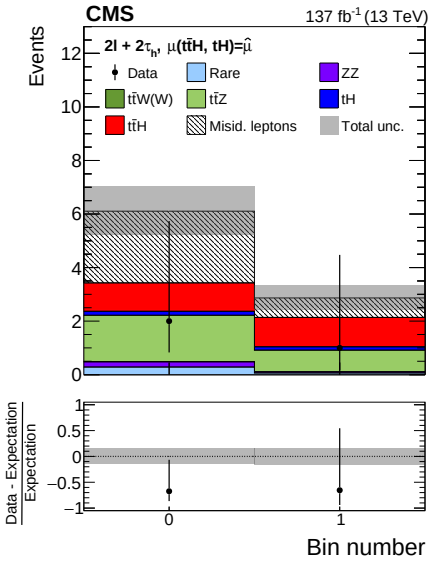
Figure 7.5: Post-fit distributions in the BDT output of the most sensitive channels featuring at least on τ_h in the final state: $2\ell OS + 1\tau_h$ (a), $1\ell + 2\tau_h$ (b), and $3\ell + 1\tau_h$ (c). Bins in the distribution of $3\ell + 1\tau_h$ BDT are sorted by the respective output score in increasing order. The same plots are also published in Ref. [1].



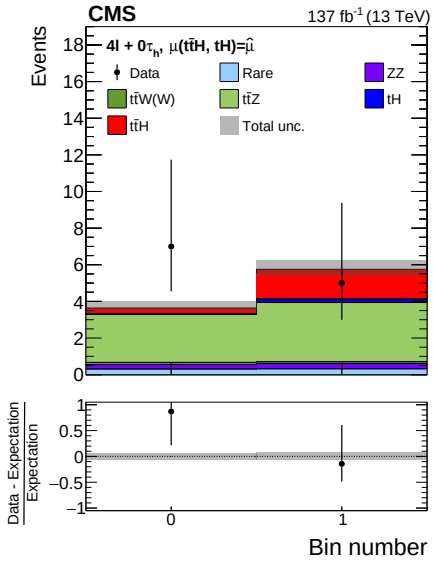
(a)



(b)

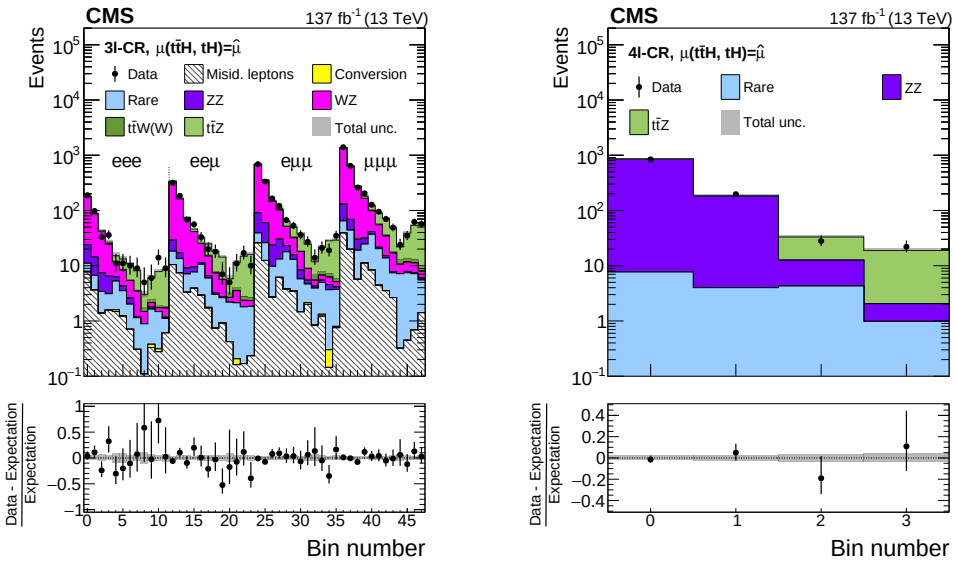


(c)



(d)

Figure 7.6: Post-fit distributions in the BDT output of least sensitive channels: $0\ell + 2\tau_{\mathrm{h}}$ (a), $1\ell + 1\tau_{\mathrm{h}}$ (b),$2\ell + 2\tau_{\mathrm{h}}$ (c), and 4ℓ (d). The bins in the distributions of $2\ell + 2\tau_{\mathrm{h}}$ and 4ℓ BDTs are sorted by the respective BDT output score in increasing order. The same plots are also published in Ref. [1].



(a) *(b)*

Figure 7.7: Post-fit distributions in 3ℓ CR (a) and 4ℓ CR (b). The distribution in 3ℓ CR consists of four categories by lepton flavor that each is made of 12 bins, each of which is grouped into three subcategories of four bins based on the multiplicity of b jets. In each group of four bins, a higher bin index is assigned to those events that feature a higher number of central jets. The leftmost bin of the distribution in 4ℓ CR corresponds to the case where the two SFOS lepton pairs are both compatible with the Z boson mass; the remaining bins correspond to the case where the final state features only one SFOS lepton pair and either 0, 1 or > 1 b jets passing the medium WP of DeepJet ID. The same plots are also published in Ref. [1].

The production rates of $\mathrm{t\bar{t}W(W)}$ and $\mathrm{t\bar{t}Z}$ processes are extracted from the very same ML fit as $\mathrm{t\bar{t}H}$ and tH production rates. They amount to $\hat{\mu}_{\mathrm{t\bar{t}W}} = 1.43^{+0.23}_{-0.20}$ ($1.00^{+0.17}_{-0.15}$ expected) and $\hat{\mu}_{\mathrm{t\bar{t}Z}} = 1.03^{+0.17}_{-0.15}$ ($1.00^{+0.15}_{-0.13}$ expected), respectively. Even though there is a slight excess in $\mathrm{t\bar{t}W}$, which is driven by the corresponding DNN node in the 2ℓSS channel, it still remains compatible with the SM at 2σ CL. Similar excess in $\mathrm{t\bar{t}W}$ production rate has surfaced in previous iteration of this analysis [5], in another $\mathrm{t\bar{t}H}$ multilepton analysis by the ATLAS collaboration [458], in $\mathrm{t\bar{t}t\bar{t}}$ measurements [459], and in dedicated $\mathrm{t\bar{t}W}$ measurements [314, 445]. Approximately 5% of this excess can be attributed to an inferior cross section estimate caused by missing EW corrections [355]. Figure 7.8 compares the $\mathrm{t\bar{t}H}$ and tH production rates that are extracted from individual analysis channels. As expected, the most sensitive channels are the 2ℓSS and 3ℓ channels, followed by the $2\ell\mathrm{SS} + 1\tau_\mathrm{h}$ and $1\ell + 2\tau_\mathrm{h}$ channels. Channels like $2\ell\mathrm{OS} + 1\tau_\mathrm{h}$ and $3\ell + 1\tau_\mathrm{h}$ offer moderate sensitivity in comparison, while all other channels suffer from limited event statistics ($2\ell + 2\tau_\mathrm{h}$ and 4ℓ) or are contaminated by huge fake backgrounds ($0\ell + 2\tau_\mathrm{h}$ and $1\ell + 1\tau_\mathrm{h}$), which decimate their sensitivity. The CI of $\mathrm{t\bar{t}H}$ production rate is significantly overconstrained in the $2\ell + 2\tau_\mathrm{h}$ channel, because the assumptions of asymptotic approximation in the limit setting procedure break down if there are no data events available. As a result, the log-likelihood function becomes linearly dependent on the $\mathrm{t\bar{t}H}$ production rate. Since such likelihood functions cannot be maximized, the $\mathrm{t\bar{t}H}$ production rate is constrained to be nonnegative when extracted from

the $2\ell + 2\tau_h$ channel. This artifact does not have any meaningful effects on the overall results due to very low event yields in that channel.

As evidenced by Table 7.7, the statistical and systematic uncertainties on $\hat{\mu}_{t\bar{t}H}$ and $\hat{\mu}_{tH}$ are in the same ballpark for both POIs, but clearly dominated by systematic uncertainties in the measurement of $\hat{\mu}_{t\bar{t}W}$ and $\hat{\mu}_{t\bar{t}Z}$. A more detailed breakdown of the uncertainties in Table 6.1 reveals that the leading systematic uncertainties on $\hat{\mu}_{t\bar{t}W}$ and $\hat{\mu}_{t\bar{t}Z}$ are primarily concerned with b tagging and lepton ID or driven by relatively poor event statistics of the generated MC samples. Pairwise correlations between the four POIs are presented in Fig. 7.9. The plot shows that $t\bar{t}W$ and $t\bar{t}Z$ rates are positively correlated with each other, while the $t\bar{t}H$ production rate is negatively correlated with all other rates. The anti-correlations between $\hat{\mu}_{t\bar{t}H}$ and $\hat{\mu}_{tH}$ persist when combined with other CMS analyses [8]. Figure 7.10 presents the two-dimensional likelihood scans between $t\bar{t}H$ signal rate and the remaining three rates, and between the rates of $t\bar{t}W$ and $t\bar{t}Z$ production. The plots show contours of confidence regions at 68 and 95% CL. All measured production rates, regardless of whether they are extracted from one- or two-dimensional likelihood scans, demonstrate good compatibility with the SM expectation at 95% CL.

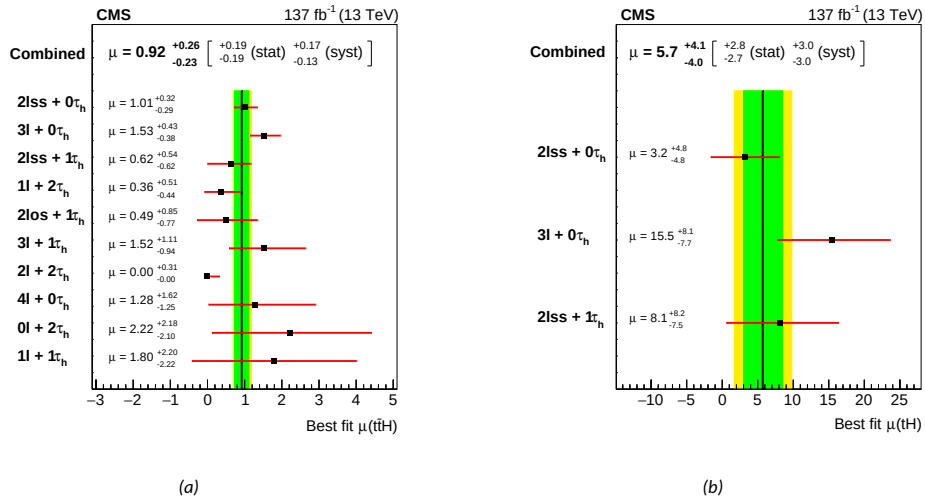


Figure 7.8: Production rates and corresponding CIs of $t\bar{t}H$ (a) and tH (b) processes in individual analysis channels and for their combination at 68% CL. Black vertical lines with green and yellow bands represent the SM expected value with its 68 and 95% CLs error bands as estimated from the Asimov dataset. The signal rate in the $2\ell + 2\tau_h$ channel has been restricted to be nonnegative values to avoid numerical issues in the ML fit that arise from the lack of data events in that channel. Only three channels are presented in (b) due to lack of sensitivity for tH production in other channels. The same plots are also published in Ref. [1].

POI	Best fit value in the main analysis	Uncertainty	
		Statistical	Systematical
$\hat{\mu}_{t\bar{t}H}$	$0.92^{+0.26}_{-0.23}\left(1.00^{+0.26}_{-0.22}\right)$	$\pm0.19\ (\pm0.18)$	$^{+0.17}_{-0.13}\left(^{+0.18}_{-0.12}\right)$
$\hat{\mu}_{tH}$	$5.7^{+4.1}_{-4.0}\left(1.0^{+3.8}_{-3.7}\right)$	$^{+2.8}_{-2.7}\left(^{+2.7}_{-2.6}\right)$	$\pm3.0\left(^{+2.7}_{-2.6}\right)$
$\hat{\mu}_{t\bar{t}W}$	$1.43^{+0.23}_{-0.20}\left(1.0^{+0.17}_{-0.15}\right)$	$^{+0.09}_{-0.08}\ (\pm0.08)$	$^{+0.21}_{-0.18}\left(^{+0.15}_{-0.12}\right)$
$\hat{\mu}_{t\bar{t}Z}$	$1.03^{+0.15}_{-0.14}\left(1.0^{+0.15}_{-0.13}\right)$	$\pm0.06\ (\pm0.06)$	$^{+0.14}_{-0.12}\left(^{+0.14}_{-0.12}\right)$

Table 7.7: Observed (expected) signal rates of $t\bar{t}H$, tH, $t\bar{t}W(W)$ and $t\bar{t}Z$ processes in units of SM production cross section, and corresponding CIs at 68% CL broken down into statistical and systematical components. All POIs are extracted simultaneously from the ML fit of the main analysis.

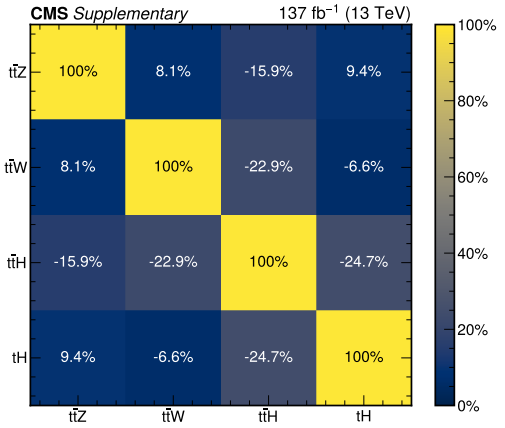


Figure 7.9: Correlation matrix of POIs obtained from the ML fit.

In addition to signal rates, the main analysis also places constraints on κ_t, while assuming fixed or floating κ_V. This is accomplished with reparametrization of the likelihood function in terms of said coupling modifiers. Higgs boson coupling to W bosons is scaled by the same amount as its coupling to Z bosons in the scan. In this regime, the $t\bar{t}H$ signal and ggF background yields are scaled by κ_t^2 in the likelihood function, while the yields of tHq and tHW processes are scaled by Eqs. (2.25) and (2.26), respectively. Similarly, the yields of VBF and VH production, and $H \to VV^*$ decays are all scaled by κ_V^2. The effects of Higgs boson self-coupling are ignored, since the HH event yields, even when taking into account the scaling by κ_λ and κ_t, do not contribute to this analysis in any significant capacity. One-dimensional likelihood scan of κ_t with profiled κ_V is shown in Fig. 7.11(a). From this one can ascertain that κ_t is constrained to $[-0.9, -0.7] \cup [0.7, 1.1]$ ($[-1.0, -0.9] \cup [0.8, 1.2]$ expected) at 95% CL, with slight preference for SM-like signal over the ITC scenario. Scanning κ_t with κ_V fixed to SM still does not rule out ITC scenario, as it constrains κ_t to $[-1.0, -0.7] \cup [0.8, 1.1]$ ($[0.8, 1.2]$ expected) instead. Two-dimensional likelihood scan between κ_t and κ_V is available in Fig. 7.11(b). The confidence regions still include the ITC scenario at 95% CL but exclude at 68% CL. ITC is firmly disfavored by more sensitive $H \to \gamma\gamma$ analysis [160, 161].

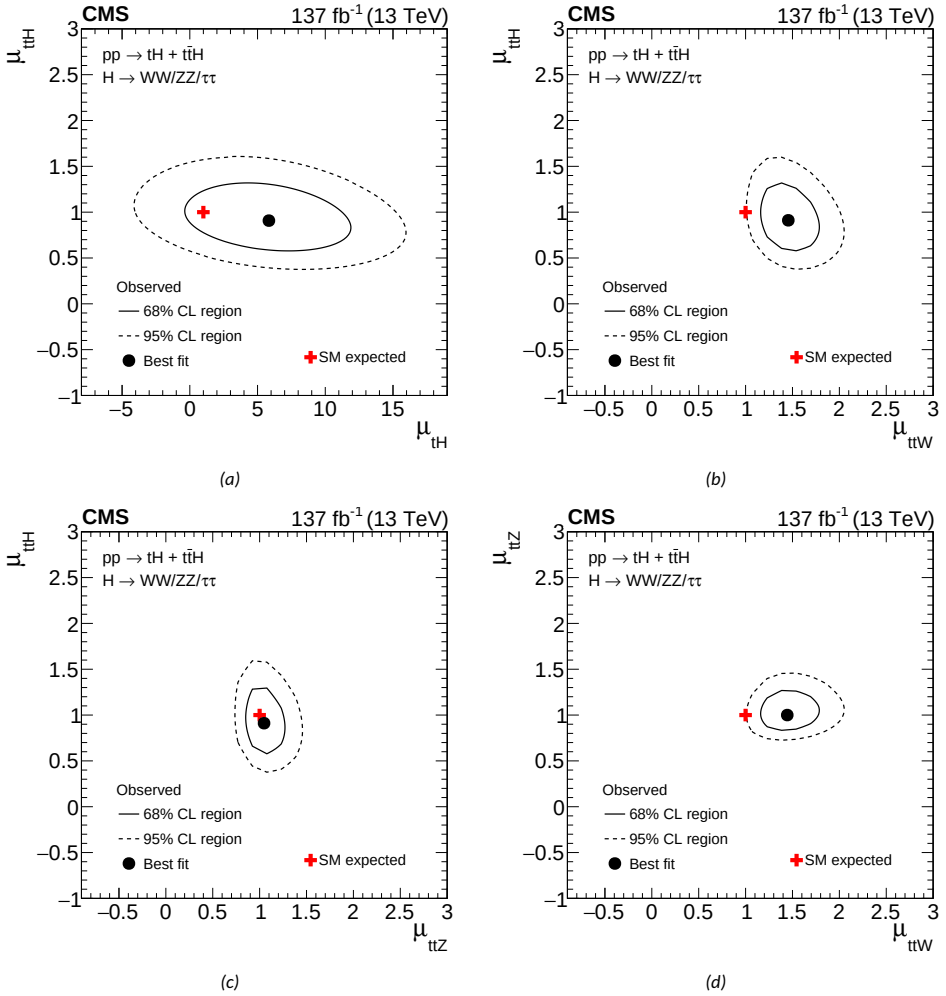
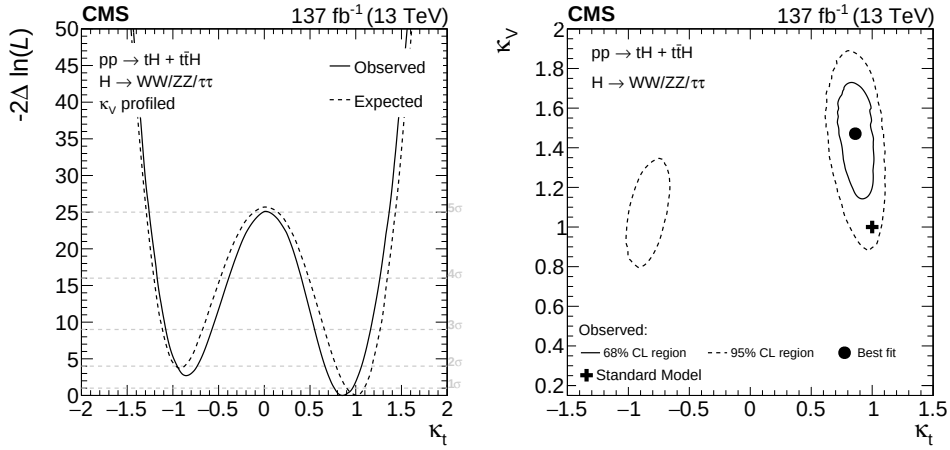


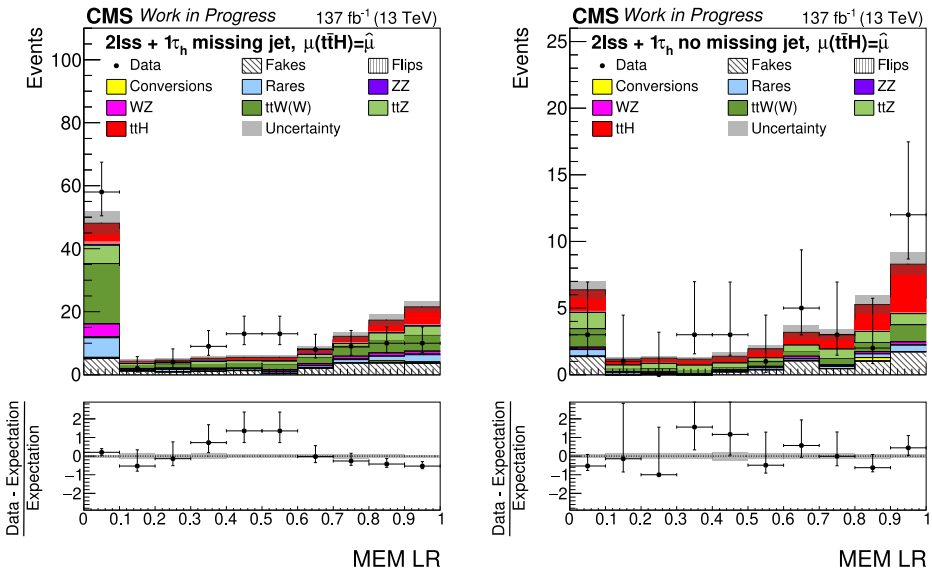
Figure 7.10: Simultaneous likelihood scans of two POIs: $\mu_{t\bar{t}H}$–μ_{tH} (a), $\mu_{t\bar{t}H}$–$\mu_{t\bar{t}W}$ (b), $\mu_{t\bar{t}H}$–$\mu_{t\bar{t}Z}$ (c), and $\mu_{t\bar{t}Z}$–$\mu_{t\bar{t}W}$ (d). Each plots shows the best fit value (black dot) with all other POIs profiled and their confidence contours at 68 and 95% CL (solid and dashed line), all extracted from the real data. Values predicted by the SM are marked with a red cross. The same plots are also published in Ref. [1].



(a) *(b)*

Figure 7.11: Likelihood scan of κ_t with κ_V profiled (a) and two-dimensional scan of κ_V and κ_t (a). In one-dimensional κ_t scan, both the observed and expected negative log-likelihoods are shown, whereas the two-dimensional plot provides contours for 68 and 95% CL (solid and dashed line), including the best fit value extracted from the real data (dot) and the SM prediction (cross). The same plots are also published in Ref. [1].

The remaining results are delivered by the CA, which simultaneously extracts the production rates of $t\bar{t}H$, $t\bar{t}W$ and $t\bar{t}Z$ processes while keeping tH production at SM in the ML fit. The resulting post-fit distributions in the MEM LR of the $2\ell SS + 1\tau_h$ channel are provided in Fig. 7.12. The corresponding production rates that scale the $t\bar{t}H$, $t\bar{t}W$ and $t\bar{t}Z$ contributions accordingly are summarized in Table 7.8. They are very similar to the results of the main analysis, although no excess in $t\bar{t}W$ was found. This may be caused by poor separation of $t\bar{t}W$ from other processes, since it was not considered as potential background candidate in the MEM, whereas the main analysis utilizes DNN for capturing the said background. The significance of measured $t\bar{t}H$ production rate under background-only hypothesis amounts to 3.8σ (4.0σ expected). Unsurprisingly, the main analysis offers more sensitivity than the CA, as seen from their direct comparison in Table 7.9.



(a) *(b)*

Figure 7.12: Post-fit distribution in MEM LR of the $2\ell SS + 1\tau_h$ channel that was developed for the CA. The MEM LR is derived for the „missing jet" regime (a) and for the case where each parton-level quark in final state could be assigned a reconstructed jet (b).

POI	Best fit value in the CA
$\hat{\mu}_{t\bar{t}H}$	$0.91^{+0.30}_{-0.26}\left(1.00^{+0.32}_{-0.28}\right)$
$\hat{\mu}_{t\bar{t}W}$	$1.08^{+0.21}_{-0.18}\left(1.00^{+0.20}_{-0.17}\right)$
$\hat{\mu}_{t\bar{t}Z}$	$0.89^{+0.15}_{-0.13}\left(1.00^{+0.16}_{-0.14}\right)$

Table 7.8: Observed (expected) signal rates of $t\bar{t}H$, $t\bar{t}W(W)$ and $t\bar{t}Z$ processes in units of SM production cross section with corresponding CIs at 68% CL. All POIs are extracted simultaneously from the ML fit of the CA.

Analysis	POI	Observed	Expected
Main	$\hat{\mu}_{t\bar{t}H}$	4.2σ	5.0σ
	$\hat{\mu}_{tH}$	1.4σ	0.3σ
Control	$\hat{\mu}_{t\bar{t}H}$	3.8σ	4.0σ

Table 7.9: Observed and expected significances of $t\bar{t}H$ and tH production under background-only hypothesis in the main analysis as well as in the CA. The production rate of tH is fixed to SM in the CA.

Although the analysis techniques have been refined with every iteration, there is definitely some room for improvement, especially when it comes to signal extraction. For example, instead of producing shape templates for every grid point in κ_t–κ_V scan explicitly, it is computationally more efficient to generate MC samples for three coupling scenarios unique in κ_t/κ_V and extrapolate to any other coupling scenario with matrix-based reweighting, exactly like it was done with κ_λ scans in the HH analysis as described in Section 2.5.2. By continuing with the analogy, the $t\bar{t}H$ analysis could definitely benefit from enhancing the event statistics that is reserved for inference by training separate machine learning models for events with odd and even event numbers. Sensitivity to BSM coupling scenarios could be enhanced with parametrized training, in which the relevant couplings of the signal become input variables to the training. Hyperparameter optimization can also be improved by switching from inferior grid-based search to more advanced methods that are based on evolutionary algorithms [400], Bayesian techniques [460] or successive halving approaches [461].

As reducible backgrounds constitute a major source of uncertainty in most of the SRs, it may be worth exploring alternative options that help to further constrain them. One possibility is to drop the FF method in favor of the full matrix method when estimating fake backgrounds, as it allows the introduction of additional NPs that model the uncertainties on fakeable-to-tight SFs. The change could benefit channels that expect just two leptons or τ_h candidates in the final state, since the full matrix method may run into stability issues when applied to other channels with higher final state multiplicity. More fine-grained control over the backgrounds caused by jets faking τ_h candidates can be assumed if the FRs are extracted for individual processes and combined based on the fake background composition that is expected in the SR by following the procedure described in Ref. [321]. The charge flip background estimation could be extended to τ_h, given that their charge is incorrectly measured at a rate of up to 1% [462], which considerably exceeds the charge flip rates of electrons. One could also replace the DY sample with embedded $Z \to \tau\tau$ samples, which are constructed from $Z \to \mu\mu$ data events but with muon pairs swapped for τ lepton pair, which are taken from simulated $Z \to \tau\tau$ events [463]. The benefit of using embedded samples over MC samples to model the DY process is that the former does not require as many corrections since most of the event contents are already identical to the data. Impact of other systematic uncertainties, in particular the JES and b tagging uncertainties on the DNN output can be reduced by incorporating the corresponding NPs as inputs to the training [464].

There are at least four possible directions that the $t\bar{t}H$ multilepton analysis may follow in future iterations. The most obvious one would be to just continue with the inclusive cross section measurements of $t\bar{t}H$ and tH production as more data pours in, but put more emphasis on exploring more advanced machine learning techniques in prompt lepton ID and signal extraction. The latest HL-LHC projections foresee a significant reduction in the statistical uncertainties on the top Yukawa coupling modifier, which bring the total uncertainty down to 3% level [8]. The projections are based on results by the ATLAS collaboration on data recorded in 2016, but with theoretical uncertainties cut in half, statistical uncertainties scaled down by the square root of the integrated luminosity (so approximately an order of magnitude), and systematical uncertainties are either kept constant or scaled the same way as the statistical uncertainties depending on their type [156]. The same projections also predict a reduction in the relative uncertainty on inclusive $t\bar{t}H$ rate to a level of less than 10%, which the current analysis results exceed by a factor of 2–3. Upper limits on tH production cross section are expected to reach the SM sensitivity by the end of the HL-LHC program. To attain or even surpass the prognosed sensitivity, more

work is needed to reduce systematical uncertainties of the measurement. Judging from Table 6.1, the leading systematic uncertainties are mostly caused by limited statistics of the MC samples, or concern lepton and τ_{h} FR measurement.

The other three possible avenues that could be explored in the context of $\mathrm{t\bar{t}H}$ multilepton analysis all extend the scope of the analysis. More specifically, these are the differential measurement of Higgs boson p_T (in STXS bins), the measurement of CP-mixing phase in top Yukawa coupling, and the measurement of Wilson coefficients that the $\mathrm{t\bar{t}H}$ and tH processes are sensitive to. Studying the Higgs boson p_T distribution in multilepton final states is challenged by the fact that the Higgs boson leaves some of its energy to neutrinos when it decays, which deteriorates the resolution on reconstructed Higgs boson p_T. This is not the case with the other two Higgs boson decay modes ($\mathrm{H} \to \mathrm{b\bar{b}}$ and $\mathrm{H} \to \gamma\gamma$) in which the $\mathrm{t\bar{t}H}$ process is commonly studied. The CP-mixing angles were measured in a follow-up study [318], which directly benefited from the refined analysis techniques presented in this thesis, but with more focus placed on discriminating between CP-odd and CP-even coupling scenarios. For the record, the study strongly disfavors CP-odd top Yukawa interactions, which is in alignment with the results of more sensitive $\mathrm{H} \to \gamma\gamma$ analyses. Finally, the $\mathrm{t\bar{t}H}$ and tH processes could be studied together with $\mathrm{t\bar{t}V}$ production in an EFT framework to place constraints on the relevant Wilson coefficients. Previous studies have thus far considered only fully leptonic final states [465], so the natural way to extend its scope is to incorporate those multilepton channels to the analysis that feature one or multiple τ_{h} in the final state.

8 Measurement of HH production in multilepton final states

The present section focuses entirely on HH multilepton analysis [2]. Section 8.1 covers the remaining details of the analysis that have not yet been discussed: the event selection criteria, the description of BDTs that are used to extract the signal, and the different binning strategies of the likelihood function. The final results as well as potential outlook of this analysis are provided in Section 8.2.

8.1 Analysis

The analysis presented here searches for HH signal in WW^*WW^*, $WW^*\tau\tau$ and $\tau\tau\tau\tau$ decay modes with multiple electrons, muons and τ_h candidates in final state. Both ggF and VBF mechanisms of nonresonant HH production are considered here. Due to low cross section of the VBF HH process, which is further diminished by the BRs of leptonic vector boson decays, the analysis requirements are optimized only for the ggF HH production. The analysis has two complementary objectives, with one focusing on nonresonant production of HH process while the other is looking for possible signs of its resonant production. Even though the two targets are conceptually independent from each other, the same analysis methods are utilized in both, including background estimation, object definitions, event selection requirements, and binning schemes.

The HH process has been previously studied in multilepton final states once by the ATLAS collaboration in 2016, but considering only those 2ℓSS, 3ℓ and 4ℓ final states that arise from HH $\rightarrow WW^*WW^*$ decays. The analysis established an upper limit of 160 (expecting 120) times the SM prediction on nonresonant HH production cross section and an upper limit of 3–10 pb on HH production via massive resonances between 260 and 500 GeV [246].

The primary objective in both nonresonant and resonant analyses is to extract upper limits on the HH production rate, since no evidence of HH signal has been found yet. The limits are set on inclusive HH production cross section out of necessity, as the analysis here considers multiple decay modes of the Higgs boson pair, providing limits on inclusive HH production rate makes it easier to directly compare the results of different HH analyses who do the same without having to divide the reported limits on production and subsequent decay of the Higgs boson pair by the corresponding BR to obtain limits on just the HH production. For this reason, the inclusive production cross section of the assumed HH signal is normalized to 1 pb prior to the ML fit when studying the EFT BM scenarios and the resonant HH production, so that the extracted POI automatically represents the HH production cross section in the correct physical units. In all other cases, the HH signal is normalized to the proper theoretical cross section as predicted by the SM, which is then appropriately scaled by the κ-framework when constraining individual couplings or coupling pairs.

There are two major goals in the nonresonant HH analysis. The first one concerns upper limits, which are placed on SM HH production rate, and on HH production cross section for the SM scenario as well as for the twenty EFT shape BMs. In the former case, the POI does not represent an effective cross section but a constant factor $\hat{\mu}_{HH}$, which uniformly scales the shape templates of SM ggF and VBF HH signal. Theoretical uncertainties on SM HH production cross sections in Table 2.9 are incorporated into the ML fit when setting limits on production rates, but not when setting them on production cross section itself. It also explains why the effective limits on production cross section are slightly lower than the equivalent limits on production rate (when multiplying them with the theoretical cross section of the SM), because the ML has more flexibility to scale the signal in the latter case. In addition to upper limits, HH signal rates that result in optimal compatibility with the

data are extracted directly from the ML fit. The VBF HH process is ignored when setting limits on the EFT BMs because the EFT formalism was developed only for the ggF HH process. The omission of the VBF HH in this limit setting procedure is justified because (as later confirmed by the result presented in Section 8.2) the upper limits on this process exceed the SM VBF HH production cross section by two orders of magnitude, plus there is no real sensitivity to the VBF HH signal.

The second objective of nonresonant HH searches is to ascertain plausible ranges of relevant SM coupling modifiers κ_λ and $\kappa_{2\mathrm{V}}$, and on EFT coupling c_2. These ranges can be determined from likelihood scans and from upper limits. In both approaches the POI becomes a function of the relevant couplings for which the ranges are determined. The points in coupling space at which the negative log-likelihood exceeds a certain threshold or where the upper limit becomes smaller than the theoretical cross section are then chosen to represent the boundaries which the coupling or couplings are confined to. The production and decay rates of single SM Higgs boson processes (and theoretical uncertainties on HH production cross section) are appropriately scaled as a function of the coupling modifiers (if their constraints are derived from likelihood scans). All other processes not affected by the coupling modifiers are configured to their SM expectation.

The analysis phase space is divided into seven mutually exclusive channels based on the multiplicity and charge of the leptons and τ_h candidates in the final state that pass the tight selection requirements. Each analysis channel intends to target particular HH decay modes: The $0\ell + 4\tau_\mathrm{h}$ and $1\ell + 3\tau_\mathrm{h}$ channels aim to capture HH $\to \tau\tau\tau\tau$ events where either all τ leptons decay hadronically (as in the former channel), or all but one τ leptons decay hadronically and the remaining τ lepton decays leptonically (as in the latter channel); the $2\ell + 2\tau_\mathrm{h}$ and $3\ell + 1\tau_\mathrm{h}$ channels target the HH $\to \mathrm{WW}^*\tau\tau$ decay mode where both or just one of the τ leptons decay hadronically while the W bosons decay leptonically; and the $2\ell\mathrm{SS}+\leqslant 1\tau_\mathrm{h}$, 3ℓ and 4ℓ channels target HH $\to \mathrm{WW}^*\mathrm{WW}^*$ decay mode, but assuming that either both, one or none of the W bosons decay hadronically while the rest of the W bosons decay leptonically. Due to high multiplicity of τ_h in the final states of $0\ell + 4\tau_\mathrm{h}$ and $1\ell + 3\tau_\mathrm{h}$ channels, the corresponding event yields are extremely low relative to other channels, totaling to less than 10 events across all data-taking years. The other three channels that require exactly four objects in the final state — $2\ell + 2\tau_\mathrm{h}$, $3\ell + 1\tau_\mathrm{h}$ and 4ℓ — all have similar event yields, averaging to about 20 events per channel per year. The remaining two channels accept the largest fraction of signal events, with the $2\ell\mathrm{SS}+\leqslant 1\tau_\mathrm{h}$ channel accepting a total of $\mathcal{O}(10^4)$ events while the 3ℓ channel having just about a quarter of that. Since every final state lepton and τ_h candidate is expected to originate from Higgs boson decays, the channels that require exactly four of those also demand that the sum of their charges must equal to zero. The analysis receive contributions from other decay modes like HH $\to \mathrm{ZZ}^*\tau\tau$ and HH $\to \mathrm{ZZ}^*\mathrm{WW}^*$, but in much lower quantities due to three times smaller leptonic BR of Z bosons compared to W bosons, not to mention the Z boson vetoes that are implemented in all channels but $0\ell + 4\tau_\mathrm{h}$. Figure 8.1 shows the actual signal composition by channel as well as the fraction of total signal in each channel before any ML fit.

The largest fraction of signal goes to the $2\ell\mathrm{SS}+\leqslant 1\tau_\mathrm{h}$ channel[24], which as the name already implies accepts $2\ell\mathrm{SS}$ events with or without the extra τ_h. Real origin of the additional τ_h is ignored because it could arise from genuine hadronic decays of prompt τ leptons as well as from hadronic W boson decays, which produce a jet that is incorrectly identified as τ_h. For this reason the τ_h is omitted from the FF method when estimating fake background in that channel. Compared to the case where $2\ell\mathrm{SS}$ events with any τ_h

[24] The channel is labeled as „2ℓSS" in the published plots.

are vetoed, the consideration of an additional τ_h doubled the signal yields and tripled the background yields. This translated to an improvement in expected upper limits of up to 30–40% in the resonant analysis across the whole mass range, and to an improvement of more than 80% in the expected limits of some EFT BMs.

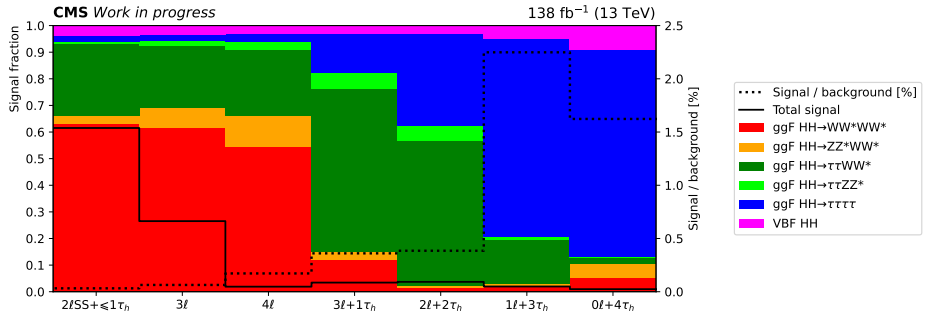


Figure 8.1: Composition of SM signal in each of the seven channels in the HH analysis. The signal fractions are extracted from simulated SM pre-fit yields after the event selection. The solid black line represents the signal contribution of that channel relative to the total signal yield of the analysis. The dotted black line indicates S/B of that channel in percentages.

Just like in the $t\bar{t}H$ analysis, the exclusivity of SRs in this analysis is fulfilled by vetoing those events that include more tight leptons or τ_h candidates than what is nominally expected in a given channel. For example, the SR of the 3ℓ channel rejects those events that have more than three leptons or at least one τ_h passing the tight cuts, since it would otherwise overlap with the SR of the 4ℓ or $3\ell + 1\tau_h$ channel, respectively. Implementation of the veto based on multiplicity of τ_h is rather straightforward, since all analysis channels assume the same definition for tight τ_h candidates. No vetoes are applied based on the multiplicity of tight τ_h in channels that already request four objects in the final state. Orthogonality[25] with $t\bar{t}H$ analysis is ensured by inverting the b jet selection requirement imposed in the $t\bar{t}H$ analysis, which means rejecting those events that feature at least two b jets passing the loose WP of DeepJet ID or just one b jet satisfies the medium WP. Consequently, the background composition in the HH multilepton analysis is geared more towards single, double and triple vector boson production since they lack b jets. The channels with low lepton multiplicity are especially susceptible to irreducible WZ process and to conversions of on-shell photons, which accompany massive vector boson production. Channels that allow at least one τ_h in the final state receive contributions predominantly from fakes.

Sensitivity to boosted HH signal is enhanced in the $2\ell\text{SS}+\leqslant 1\tau_h$ and 3ℓ channels by considering the cases in which one of the two jets from hadronic W boson decays cannot be resolved by the reconstruction algorithm. To identify those events, the event selection requirements first check the presence of any AK8 jets that satisfy the criteria described in Section 4.2.5. The AK8 jets represent boosted decays of hadronic W boson, which do not include any loose leptons that may arise from the second W boson in $H \to WW^*$ decays. If no such AK8 jets are found in the 3ℓ channel, the requirement is replaced with the condition that demands the presence of at least one central AK4 jet, thus accepting the

[25] Orthogonality between the SRs of $t\bar{t}H$ and HH multilepton analyses would only be needed when performing signal extraction on their combined results. As standalone analyses, the orthogonality condition would not be necessary.

possibility that the second resolved jet might be lost due to acceptance cuts or removed through cleaning against leptons and τ_{h}. In the $2\ell\mathrm{SS}{+}\leqslant 1\tau_{\mathrm{h}}$ channel, however, one might expect to find one or two hadronically decaying W boson, depending on whether or not the event also features an extra prompt τ_{h}. Three possible signal topologies are considered in $2\ell\mathrm{SS}{+}\leqslant 1\tau_{\mathrm{h}}$, with the highest priority given to the case where both hadronically decaying W bosons are boosted, followed by the possibility that just one of those W bosons is boosted („semiboosted"), and finally considering the option that neither of those W bosons are in fact boosted („resolved"). The event selection requirements of the $2\ell\mathrm{SS}{+}\leqslant 1\tau_{\mathrm{h}}$ channel demand the presence of at least two AK8 jets in boosted category, exactly one AK8 jet in semiboosted category, or at least two central AK4 jets in the resolved category. Only those additional AK4 jets are considered in semiboosted case that are not enclosed by the selected AK8 jet. The relaxed requirement on jet multiplicities in semiboosted and resolved categories help to recover signals that would otherwise be lost due to jets occasionally failing the acceptance cuts or removed by cleaning. All other event selection requirements imposed in each of the seven channels are summarized Table 8.1.

The parametrized BDTs that were trained for nonresonant analysis simultaneously targeted the SM HH process and the twelve JHEP04 BMs (excluding the 8a BM). The only signal samples that were available for the training at the time were generated precisely for those thirteen coupling scenarios but at LO. Individual MC samples are aggregated and reweighted to the desired coupling scenario with Eq. (2.28) in bins of m_{HH} and $|\cos\theta^*|$ as described in Section 2.5.2. Each aggregated sample carries a one-hot encoded label in the parametrized BDT training. The BDTs of the $2\ell\mathrm{SS}{+}\leqslant 1\tau_{\mathrm{h}}$ and 3ℓ channels were retrained to include additional NLO corrections to the HH signal. However, since the additional corrections had virtually no impact on the performance of the BDTs, this recipe was not followed in other channels.

JHEP03 BMs were initially omitted from the training for historical reasons, since the additional eight BMs had not been considered by any other HH analysis prior to this one. Setting those BMs as additional targets in the parametrized BDT would not improve the overall distinction of individual BMs because both sets of EFT BMs are somewhat redundant: the JHEP04 BMs are supposed to represent all possible kinematic configurations that could potentially arise from nonresonant ggF HH production, while the JHEP03 BMs also take the constraints on individual couplings into consideration. To figure out which one-hot encoded label to use when evaluating the BDT scores for JHEP03 BMs, a mapping from JHEP03 to JHEP04 BMs is determined based on the similarities in m_{HH} distribution. The similarities were quantified with Eq. (6.7), where i runs over individual bins of m_{HH} distribution. Results of this comparison are documented in Table 8.2. This idea could be turned around by inferring constraints on individual BM scenarios from the limits on certain ranges of couplings that share similar kinematic features with those BMs.

	$0\ell+4\tau_{\mathrm{h}}$	$1\ell+3\tau_{\mathrm{h}}$	$2\ell+2\tau_{\mathrm{h}}$	2ℓSS$+\leqslant 1\tau_{\mathrm{h}}$	3ℓ	$3\ell+1\tau_{\mathrm{h}}$	4ℓ
Target HH decay mode	$\tau\tau$(FH)$\tau\tau$(FH)	$\tau\tau$(FH)$\tau\tau$(SL)	$\tau\tau$(FH)$\tau\tau$/WW(DL)	WW(SL)WW(SL)	WW(SL)WW(DL)	WW(DL)$\tau\tau$(SL)	WW(DL)WW(DL)
Maximum # tight ℓ/τ_{h}	$0/$✗	$1/$✗	$2/$✗	$2/1$	$3/0$	$3/$✗	✗/✗
Charge sum (of ℓ/τ_{h})	0	0	0	$(\pm 2/\mp 1)$	± 1	0	0
Tight lepton charge	✗	✗	✗	✓	✗	✗	✗
Trigger	$2\tau_{\mathrm{h}}$	$1\ell, 1\ell+1\tau_{\mathrm{h}}, 2\tau_{\mathrm{h}}$	$1\ell, 2\ell$	$1\ell, 2\ell$	$1\ell, 2\ell, 3\ell$	$1\ell, 2\ell, 3\ell$	$1\ell, 2\ell, 3\ell$
Minimum cone-$p_T(\ell)$	✗	15, 20	25/15	25/15	25/15/10	25/15/10	25/15/15/10
Minimum $p_T(\tau_{\mathrm{h}})$	40/40/20/20	40/30/20	—	—	✗	—	✗
Maximum $\lvert\eta\rvert$ (ℓ/τ_{h})	—	2.1/2.3	—	—	—	—	—
Minimum # central jets	0	0	0	2*	1*	0	0
Minimum E_T^{miss}LD	0	0	0	30†	30/45‡	0	0
ECAL crack veto§	✗	✗	✗	✗	✗	✓	✗
Z boson veto	✗	✓¶	✓	✓‖	✓	✓	✓
H $\to$ ZZ* $\to 4\ell$ veto	✗	✗	✗	✓	✓	✗	✓

* Includes AK8 jets.

† Applied only if both leptons are electrons.

‡ Applied if the selected leptons are not SFOS / if the selected leptons are SFOS.

§ Reject the event if the selected τ_{h} falls into the gap between EB and EE ($1.460 < |\eta| < 1.588$), or if it fails VVLoose WP of $D_{\mathrm{e}}^{\tau_{\mathrm{h}}}$.

¶ Applies to events where the selected lepton happens to be an electron that together with an OS τ_{h} have invariant mass closer than $^{+10}_{-20}$ GeV to Z boson mass, and if the τ_{h} falls into the ECAL crack ($1.460 < |\eta| < 1.588$) or if the τ_{h} fails VLoose WP of $D_{\mathrm{e}}^{\tau_{\mathrm{h}}}$.

‖ OS charge requirement dropped if the two selected leptons happen to be electrons.

Table 8.1: Target decay modes of the HH signal (top section) and event selection criteria (bottom section) of the HH analysis channels. Requested number of fakeable leptons and τ_{h} is encoded in the channel name. All selected and vetoed tight τ_{h} are required to pass the Medium WP of DeepTau ID. In addition to the listed selection criteria, all selected events must also pass MET filters, loose dilepton mass veto and b jet veto requirements. A tick mark (✓) indicates that the selection criterion is enforced or applicable, whereas a cross mark (✗) implies the opposite. A dash (—) is used to denote that the cut is not tightened with respect to fakeable object definition as detailed in Section 4.2. Thresholds on the (cone-)p_T of leading, subleading, third and fourth physics objects are delimited by a forward slash. If there is a pair of thresholds separated by a comma, then the first value applies to muons and the second to electrons. Lower bounds on (cone-)p_T and E_T^{miss}LD are given in units of GeV. *The same cuts are applied in the SRs, fake ARs and charge flip ARs, except for the charge sum requirement of leptons in the $2\ell SS+\leqslant 1\tau_{\mathrm{h}}$ channel, which is inverted into OS charge requirement in the respective charge flip ARs.*

Coupling scenario or use case	BDT output
JHEP03BM1	JHEP04BM11
JHEP03BM2	JHEP04BM11
JHEP03BM3	JHEP04BM5
JHEP03BM4	JHEP04BM3
JHEP03BM5	JHEP04BM9
JHEP03BM6	JHEP04BM3
JHEP03BM7	JHEP04BM9
JHEP04BM8a	JHEP03BM9
Coupling scans	JHEP04BM7

Table 8.2: BDT outputs that were chosen to extract limits for a given BM scenario or for a range of coupling values that were not considered in the BDT training. Limits for SM and JHEP03 BMs are extracted from the corresponding BDT output.

By following the same logic in coupling scans, every coupling scenario that is probed by the scan should likewise map to one of the twelve JHEP04 BMs or to the SM. For example, the event kinematics that is induced by large positive values of κ_λ with its sharply falling tail in m_{HH} is most similar to JHEP04BM7 scenario, while the large negative values of κ_λ give rise to m_{HH} spectrum that is more compatible with JHEP04BM12, which has much more pronounced tail compared to other BMs [182]. In principle it should be possible to use a different BDT output for every coupling scenario that is tried during the scan, but it is a very resource-intensive procedure, plus it might create discontinuities in upper limits. Instead, all coupling scans are performed based on the BDT output of a single EFT BM, so that the presented results always remain compatible with each other regardless of whichever coupling (modifier) was frozen or floating in the scan. The default BDT output for the coupling scan was determined based on whichever produced the lowest expected upper limits across the whole scan range. Given this condition, the optimal limits are produced from the BDT output of JHEP04BM7 in c_2 scans, but the dependency of upper limits on the coupling scenarios is rather weak, as the limits vary by just 1%. This is certainly not the case with upper limits on κ_λ, which were found to vary by as much as 10% at high negative values of κ_λ and change constraints by 2%. All BSM coupling scans presented in this document are derived from the BDT output that corresponds to JHEP04BM7, since it was found to produce optimal limits at all values of κ_λ. Upper limits on SM production cross section as well as upper limits on individual JHEP04 BMs are extracted from the corresponding BDT output.

A parametrized BDT was trained to target nonresonant HH signal, spin-0 resonant signal and spin-2 resonant signal in each of the seven analysis channels and for both halves of the training dataset split by parity of event numbers. Common hyperparameters are used for odd and even halves, but the training variables were optimized for each of the 42 BDTs separately. Table 8.3 documents the final list of variables that were chosen to train the BDTs.

Although not explicitly indicated in the table, many of the variables were specifically engineered to exploit certain features of relevant processes. For example, the invariant mass variable used in the training of BDTs in the $0\ell + 4\tau_{\text{h}}$ channel is built from the OS τ_{h} pair that have the smallest angular distance, which is motivated by the fact that the τ lepton pair from Higgs boson decays tend move in similar direction. On the other hand, invariant mass of the second SFOS τ_{h} pair that is most compatible with the Z boson mass has also shown to provide decent discriminatory power against reducible DY and irreducible ZZ backgrounds in the same channel.

Variable	$0\ell+4\tau_h$	$1\ell+3\tau_h$	$2\ell+2\tau_h$	$2\ell\text{SS}+\leqslant 1\tau_h$	3ℓ	$3\ell+1\tau_h$	4ℓ
(Cone-)$\mathbf{p}(\ell/\tau_h)$	✓/✓/✓	✓/✗/✗	✗/✗/✗	✓/✗/✗	✗/✗/✗	✗/✗/✗	✗/✗/✗
ΔR(jets)	✗/✗/✗	✗/✗/✗	✗/✗/✗	✗/✓/✓	✗/✗/✗	✗/✗/✗	✗/✗/✗
$\Delta R(\ell/\tau_h$, jets)	✗/✗/✗	✗/✗/✗	✗/✗/✗	✓/✓/✓	✓/✓/✓	✗/✗/✗	✗/✗/✗
ΔR between ℓ/τ_h	✓/✓/✓	✓/✓/✓	✓/✓/✓	✓/✓/✓	✓/✓/✓	✓/✓/✓	✗/✗/✗
$\Delta\eta$ between ℓ/τ_h	✗/✓/✗	✗/✗/✗	✗/✗/✗	✗/✗/✗	✗/✗/✗	✗/✗/✗	✗/✓/✓
$\Delta\phi$ between ℓ/τ_h	✗/✗/✗	✗/✗/✗	✗/✗/✗	✗/✗/✗	✗/✗/✗	✗/✗/✗	✗/✓/✓
$m(\sum$ jets)	✗/✗/✗	✗/✗/✗	✗/✗/✗	✓/✗/✗	✗/✗/✗	✗/✗/✗	✗/✗/✗
$m(\sum\ell/\tau_h+$jets)	✗/✗/✗	✗/✗/✗	✗/✗/✗	✗/✓/✓	✓/✓/✓	✗/✗/✗	✗/✗/✗
$m(\sum\ell/\tau_h)$	✓/✓/✓	✓/✓/✓	✓/✓/✓	✓/✓/✓	✓/✓/✓	✓/✓/✓	✓/✓/✓
$p_T(\sum\ell/\tau_h)$	✗/✗/✗	✓/✗/✗	✓/✗/✗	✗/✗/✗	✗/✗/✗	✗/✗/✗	✗/✗/✗
$m_T(E_T^{\text{miss}},\ell/\tau_h)$	✗/✗/✗	✓/✓/✓	✗/✗/✗	✗/✓/✓	✗/✗/✗	✗/✗/✗	✗/✗/✗
$\Delta\phi(E_T^{\text{miss}},\ell/\tau_h)$	✗/✗/✗	✗/✗/✗	✗/✗/✗	✗/✗/✗	✗/✗/✗	✗/✗/✗	✓/✓/✓
SVfit (m_H or m_{HH})	✓/✓/✓	✓/✓/✓	✓/✓/✓	✗/✗/✗	✗/✗/✗	✗/✗/✗	✗/✗/✗
$\mathbf{E}_T^{\text{miss}}$	✓/✗/✓	✓/✗/✗	✓/✗/✗	✗/✗/✗	✗/✗/✗	✗/✗/✗	✓/✓/✓
E_T^{miss}LD	✓/✓/✗	✗/✗/✗	✗/✗/✗	✗/✓/✓	✓/✓/✓	✓/✓/✓	✗/✗/✗
H_T^{miss}	✗/✗/✗	✓/✗/✗	✗/✗/✗	✓/✗/✗	✗/✗/✗	✗/✗/✗	✓/✓/✓
H_T	✗/✗/✗	✗/✗/✗	✓/✗/✗	✓/✗/✗	✗/✗/✗	✓/✗/✗	✓/✗/✗
S_T^{MET}	✓/✗/✗	✗/✗/✗	✗/✗/✗	✗/✗/✗	✗/✗/✗	✗/✗/✗	✗/✗/✗
$\sqrt{s}_{\text{min}}$	✗/✗/✗	✗/✗/✗	✓/✓/✓	✗/✗/✗	✗/✗/✗	✗/✗/✗	✗/✗/✗
# SFOS ℓ pairs	✗/✗/✗	✗/✗/✗	✗/✗/✗	✗/✗/✗	✓/✓/✓	✗/✗/✗	✗/✗/✗
# variables	15/9/9	15/9/9	10/10/10	10/10/10	9/9/9	8/7/7	9/9/9
# trees	204/22/22	160/166/166	73/343/232	496/500/186	96/252/189	115/129/71	65/106/106
Tree depth	1/4/4	4/4/4	3/3/3	2/2/3	2/2/2	2/2/3	3/2/2
Learning rate [%]	25/41/41	6/15/15	16/7/8	17/25/21	37/34/55	16/50/29	10/31/31

Table 8.3: Condensed summary of training variables (top section) and hyperparameters (bottom section) of the BDTs that were trained for nonresonant/resonant spin-0/resonant spin-2 HH signal for each analysis channel. Generator-level m_{HH} (used in resonant training) as well as the one-hot encoded twelve JHEP04 BMs plus the SM BM (in nonresonant training) are excluded from the variable listing and count. A check mark (✓) tells that the variable was used in that particular training, whereas a cross mark (✗) indicates the opposite. The sum symbol represents pairwise combinations as well as combination of all visible objects in the final state.

The angular differences that enter as input to the BDTs in the $3\ell+1\tau_h$ channel are constructed from lepton and τ_h pairs that are carefully chosen to match the event kinematics typically expected from the HH signal in that channel. There the HH signal mostly decays via $WW^*\tau\tau$, where one of the τ leptons decays leptonically and the other hadronically. Both Higgs bosons lose their energy to neutrinos, which would mean that the mass of each Higgs boson reconstructed from their visible decay products tends to be lower than the invariant mass of the boson itself. Thus, the three leptons and the τ_h are correctly paired together if they have OS charges and their combined mass is less than $125\,\text{GeV}$. If this is not possible, then the leading lepton is paired together with the only lepton that has OS charge. The fallback solution is inspired by the observation that leptons descending from off-shell W bosons or from τ leptons tend to be soft because of their light parents, while the leptons from on-shell W boson decays tend to be harder. Similar arguments apply to $HH\to WW^*WW^*$ signal in the same channel as well as in the 4ℓ channel.

All channels profit mostly from the invariant mass variables or analogous observables that are built from all leptons and τ_h that are selected to the final state. In terms of feature importance, the variables with most discriminatory power are the SVfit HH masses in the $0\ell+4\tau_h$ and $1\ell+3\tau_h$ channels; $\sqrt{s}_{\text{min}}$ computed with Eq. (4.2) from all four leptons and τ_h in the $2\ell+2\tau_h$ channel; invariant mass of the three leptons (and τ_h) in the $3\ell(+1\tau_h)$ channel; and invariant mass of the lepton pair(s) in the $2\ell\text{SS}+\leqslant 1\tau_h$ (4ℓ) channel.

Similarly to the $t\bar{t}H$ analysis, two CRs are defined for the 3ℓ and 4ℓ channels to let the ML fit to validate the modeling of irreducible WZ and ZZ backgrounds, which dominate most channels despite the imposed Z boson veto, but to also constrain shape uncertainties

that are assigned to the MC prediction by taking advantage of high event yields in those CRs. The event selection requirements of 3ℓ (WZ) and 4ℓ (ZZ) CRs are based on the requirements of the corresponding SRs, except for the Z boson veto, which is inverted in the CRs. Because of this requirement, the events that are selected to 3ℓ and 4ℓ CRs must feature at least one pair of SFOS leptons. The lower limit on jet multiplicities implemented in the 3ℓ channel is removed from 3ℓ CR since no jets are expected from WZ events if both bosons decay leptonically. In case there are two SFOS pairs of leptons in 3ℓ CR, then the lepton pair that is closest to Z boson mass is chosen to represent the Z boson, and the remaining third lepton would be associated with the W boson. Transverse mass of that lepton provides a proxy to W boson mass, which can be used to discriminate against other processes as explained in the context of lepton FR measurement in Section 5.3.2. Events that are selected to 3ℓ CR enter the ML fit in $10\,\text{GeV}$ bins of the transverse mass variable. Invariant mass of the four leptons is chosen to constrain the ZZ background in 4ℓ CR since it provides discrimination against other processes as it approximates the invariant mass of the Z boson pair. No significant deviations are found between data and MC simulation in other observables not directly utilized by the ML fit. Constraining the normalization of WZ and ZZ processes with dedicated NPs was tried, but it did not improve the expected sensitivity.

Another CR is devised for the purpose of validating the modeling of conversion background, which makes up roughly 10% of the backgrounds in the SR of the $2\ell\text{SS}+\leqslant 1\tau_{\text{h}}$ channel. The CR targets $\text{Z}+\gamma$ events, where the Z boson decays into a pair of muons while the on-shell photon converts into a pair of electrons inside the detector, of which only one electron survives the reconstruction and identification cuts while the other electron fails them. To increase the likelihood that the selected electron is indeed originating from photon conversions, the selected electron must have at least one missing hit in the tracker or it must fail the conversion veto condition. Otherwise, the event selection criteria are identical to that of 3ℓ CR, except no conditions are imposed on the number of τ_{h} candidates and $E_T^{\text{miss}}\text{LD} < 45\,\text{GeV}$ must hold true at all times since no neutrinos are expected from the target process. Other CRs are constructed to study the modeling of BDT input variables in sidebands that are adjacent to the SRs of the $2\ell\text{SS}+\leqslant 1\tau_{\text{h}}$, $2\ell+2\tau_{\text{h}}$ and $3\ell+1\tau_{\text{h}}$ channels. As seen from Table 8.4, the CRs are defined by simply inverting the Z boson veto, b jet veto or charge sum requirements of the SRs, which makes the CRs automatically orthogonal to the respective SRs. Data-to-MC agreement of BDT input variables in the other four channels was verified with post-fit plots, where the data was blinded in high BDT bins.

BDT output scores are binned in quantiles of signal[26] in the $2\ell\text{SS}+\leqslant 1\tau_{\text{h}}$ and 3ℓ channels, since those two channels have the highest background yields, which allows for rather fine binning compared to some other channels. The same binning strategy is also employed in the 4ℓ channel. Even though the background yields appear quite small in that channel, it is dominated by the ZZ background, which itself is in fact modeled with hundreds of thousands of MC events. The resulting distributions of HH signal become approximately flat, yet the background yields fall with increasing bin number, so that

[26] All BDT distributions are initially divided into 100 equidistant bins, which are then later merged according to the intended binning scheme. However, it turns out that even this many bins may not be enough to ensure that the signal distribution stays flat at all times over the whole range of BDT output. The reason for it is that most of the signal events receive very high BDT scores, which puts them in the last few rightmost bins of the BDT distribution. Those last few bins may contain more signal than would be expected from quantile binning. The effects of it can be seen from Figs. 8.11(c) and 8.11(d), where the HH signal tends to increase alongside with the bin index despite the requirement that each bin should hold approximately the same number of signal events.

the sensitivity to signal is maximized in bins of high BDT output, while the backgrounds are mostly concentrated in bins of low BDT output, which in turn help to constrain their normalization. For these reasons, the binning strategy mostly benefits those channels that have relatively high (effective) event yields. In the other four channels that have rather low background yields, the BDT output scores are binned in quantiles of fake background, which causes the HH signal to visibly peak at high BDT output. This binning scheme helps to constrain dominant (mostly reducible) background rates in bins that are depleted of signal.

Control region	Baseline selection	Changes with respect to the baseline selection	Purpose
WZ CR	3ℓ SR	Inverted Z boson veto based on the selected three leptons, any number of jets allowed	Constrain WZ background in signal extraction based on transverse mass distribution of MET and the lepton not associated with the Z boson
ZZ CR	4ℓ SR	Inverted Z boson veto	Constrain ZZ background in signal extraction based on invariant mass distribution of the four leptons in final state
$Z+\gamma$ CR	WZ CR	$\mu^-\mu^+$e final state, with the muon pair satisfying inverted Z boson veto, and the electron having at least one lost hit in the tracker or failing the conversion veto, any number of τ_h in the event, E_T^{miss}LD < 45 GeV	Validate the conversion background
Fake CRs	$3\ell+1\tau_h$ SR, $2\ell+2\tau_h$ SR	No Z boson veto, nonzero charge sum	Validate data-to-MC agreement of BDT input variables in a given analysis channel
b enriched CRs	$3\ell+1\tau_h$ SR 2ℓSS$+\leqslant 1\tau_h$ SR	Inverted b jet veto	
Secondary ZZ CR	$3\ell+1\tau_h$ SR	Inverted Z boson veto	

Table 8.4: Event selection criteria for the CRs of the HH analysis. Data-driven fake background is estimated the same way in the CRs as in the SRs.

While the binning strategy itself is fixed in every channel, the bin edges are reevaluated for every EFT BM and resonant mass point for which upper limits are extracted. Regardless of the binning scheme, the number of bins is determined from the condition that relative statistical uncertainties in each bin should not exceed 15% when summed over all three data-taking years to ensure that every bin in the likelihood function is sufficiently populated. This condition was modified in the $0\ell+4\tau_h$, $1\ell+3\tau_h$, $2\ell+2\tau_h$ and $3\ell+1\tau_h$ channels to counter the fact that some of the bins occasionally feature fake background events with negative weights, which inflate relative statistical uncertainties on the fake backgrounds. The modification entails applying the 15% condition only to irreducible backgrounds, and additionally enforcing that relative statistical uncertainties on the fake background should not exceed 50% in any of the bins. Due to extremely low yields in the $0\ell+4\tau_h$ and $1\ell+3\tau_h$ channels, none of these conditions could be fulfilled, and so the BDT distributions there are instead split by quantiles of total background into five bins.

The different signal hypotheses probed in coupling scans are obtained by reweighting the HH signal samples. In particular, the same set of NLO ggF HH events are used to build three (or six in case of κ_λ–c_2 scan) shape templates that each correspond to a different coupling scenario. The three or six shape templates are obtained by pooling the signal

events together and reweight them to desired coupling scenario using Eq. (2.29) after flattening their distributions in m_{HH}–$|\cos\theta^*|$ space. No such reweighting is needed in $\kappa_{2\mathrm{V}}$ scans, because MC samples with the intended coupling scenarios are already available. The shape templates can be combined with Eq. (2.32) to extract shape templates for any other point in the coupling space that is being scanned. Table 8.5 details exactly, which coupling scenarios are utilized in each type of coupling scan. BRs of Higgs boson decays and production cross sections of single Higgs boson processes are adjusted as a function of κ_λ during the scans as depicted in Fig. 2.22. The production cross section of single Higgs boson processes (ggF, gg $\to$ ZH, $\mathrm{t\bar{t}H}$ and tH) are scaled as a function of κ_t in the coupling scans as described in [164]. Likewise, the decays of the Higgs boson to the vector boson pair as well as VBF, VH and tH production processes are scaled as a function of κ_V. No production or decay processes other than the VBF HH process are affected by $\kappa_{2\mathrm{V}}$, though.

Type of coupling scan						Coupling scenario				Interpretation
κ_λ	c_2	κ_t–κ_λ	κ_t–c_2	κ_λ-c_2	$\kappa_{2\mathrm{V}}$	κ_λ	κ_t	c_2	$\kappa_{2\mathrm{V}}$	
✓	✓	✓	✓	✓	✓	1	1	0	1	SM
✓	✗	✓	✗	✓	✗	2.45	1	0	1	Maximum destructive interference
✓	✗	✗	✗	✗	✗	5	1	0	1	Asymptotic high-κ_λ regime
✗	✗	✓	✗	✓	✗	0	1	0	1	Box-only ggF
✗	✓	✗	✓	✓	✗	1	1	0.35	1	Maximum destructive interference
✗	✓	✗	✓	✓	✗	1	1	3	1	Asymptotic high-c_2 regime
✗	✗	✗	✗	✓	✗	0	1	1	1	—
✗	✗	✗	✗	✗	✓	1	1	0	0	No $g_{2\mathrm{V}}$ coupling
✗	✗	✗	✗	✗	✓	1	1	0	2	—

Table 8.5: List of coupling scenarios used for performing matrix-based reweighting in coupling scans. Like with the EFT BMs, shape templates for the chosen couplings are obtained through reweighting with Eq. (2.29) *in bins of m_{HH} and $|\cos\theta^*|$.*

8.2 Results

No indication of background mismodeling is found based on GoF statistic shown in Fig. 6.3(b), nor do the pulls and impacts of NPs in Fig. 6.5 show any symptoms of poorly modeled systematic uncertainties. Both the GoF as well as the pulls and impacts, like any other plot that is shown in the context of nonresonant analysis, are all extracted from the BDT output that corresponds to JHEP04 BM7. The same diagnostic plots were obtained for other HH signal hypotheses at different EFT BMs and at selected mass points of resonant HH signal. None of them suggests that there could be any problems with the modeling of backgrounds and systematic uncertainties.

The unblinding procedure thus proceeded with the extraction of post-fit event yields, which are tabulated in Table 8.6. The presented yields demonstrate good agreement between data and post-fit prediction. Breakdown of post-fit event yields into bins of BDT output are shown for the $2\ell\mathrm{SS}{+}\leqslant 1\tau_\mathrm{h}$, 3ℓ and 4ℓ channels in Fig. 8.2; for the remaining four analysis channels in Fig. 8.3(d); and for the two CRs in Fig. 8.4. No significant excess (larger than two standard deviations) with respect to SM prediction is found in these plots, although there is a slight excess in the rightmost bin of the BDT output in the 3ℓ channel, which drives most of the sensitivity of that channel because S/B is lowest in that bin by construction.

	$0\ell+4\tau_h$	$1\ell+3\tau_h$	$2\ell+2\tau_h$	2ℓSS$+\leqslant 1\tau_h$	3ℓ	$3\ell+1\tau_h$	4ℓ	WZ CR	ZZ CR
SM HH $\to$ WW*WW* ($\times 30$)	0.3 ± 0.0	0.2 ± 0.0	0.2 ± 0.0	73 ± 6	33 ± 3	0.9 ± 0.1	2.2 ± 0.2	—	—
SM HH $\to$ WW$^*\tau\tau$ ($\times 30$)	0.1 ± 0.0	0.6 ± 0.1	3.9 ± 0.4	31 ± 3	12 ± 1	4.1 ± 0.3	0.9 ± 0.1	—	—
SM HH $\to \tau\tau\tau\tau$ ($\times 30$)	1.3 ± 0.2	2.6 ± 0.4	2.3 ± 0.3	3 ± 0	1 ± 0	0.9 ± 0.1	0.1 ± 0.0	—	—
WZ	—	—	—	2003 ± 58	1321 ± 27	0.2 ± 0.0	0.4 ± 0.1	$12\,546 \pm 148$	—
ZZ	0.7 ± 0.1	1.9 ± 0.2	18.5 ± 1.0	121 ± 2	109 ± 2	24.3 ± 0.8	54.7 ± 1.8	799 ± 24	2032 ± 60
Single Higgs boson	0.4 ± 0.1	0.8 ± 0.4	2.9 ± 0.5	216 ± 4	62 ± 1	3.8 ± 0.2	2.4 ± 0.3	—	—
Other processes	—	—	2.1 ± 0.4	2690 ± 224	293 ± 20	2.7 ± 0.3	4.1 ± 0.4	620 ± 54	59 ± 6
Fakes	1.5 ± 0.9	2.1 ± 1.7	33.5 ± 4.6	3939 ± 267	670 ± 55	25.1 ± 4.4	2.3 ± 1.0	908 ± 122	13 ± 4
Flips	—	—	—	366 ± 52	—	—	—	—	—
Conversions	—	—	0.1 ± 0.1	1009 ± 170	146 ± 24	0.1 ± 0.0	0.9 ± 0.4	134 ± 22	3 ± 0
Total background	2.6 ± 0.9	4.9 ± 1.7	57.0 ± 4.8	$10\,346 \pm 396$	2601 ± 68	56.2 ± 4.5	64.8 ± 2.1	$15\,006 \pm 202$	2108 ± 60
Data	1	6	55	10 344	2621	55	62	14 994	2096

Table 8.6: Post-fit yields with corresponding statistical and systematical uncertainties in each of the seven analysis channels and in the two auxiliary CRs that help to constrain irreducible diboson backgrounds. The SM HH yields are normalized to an inclusive production cross section of about 1 pb *in the table. Symbol „—" is used if the process contributes by less than* 0.1 *events.*

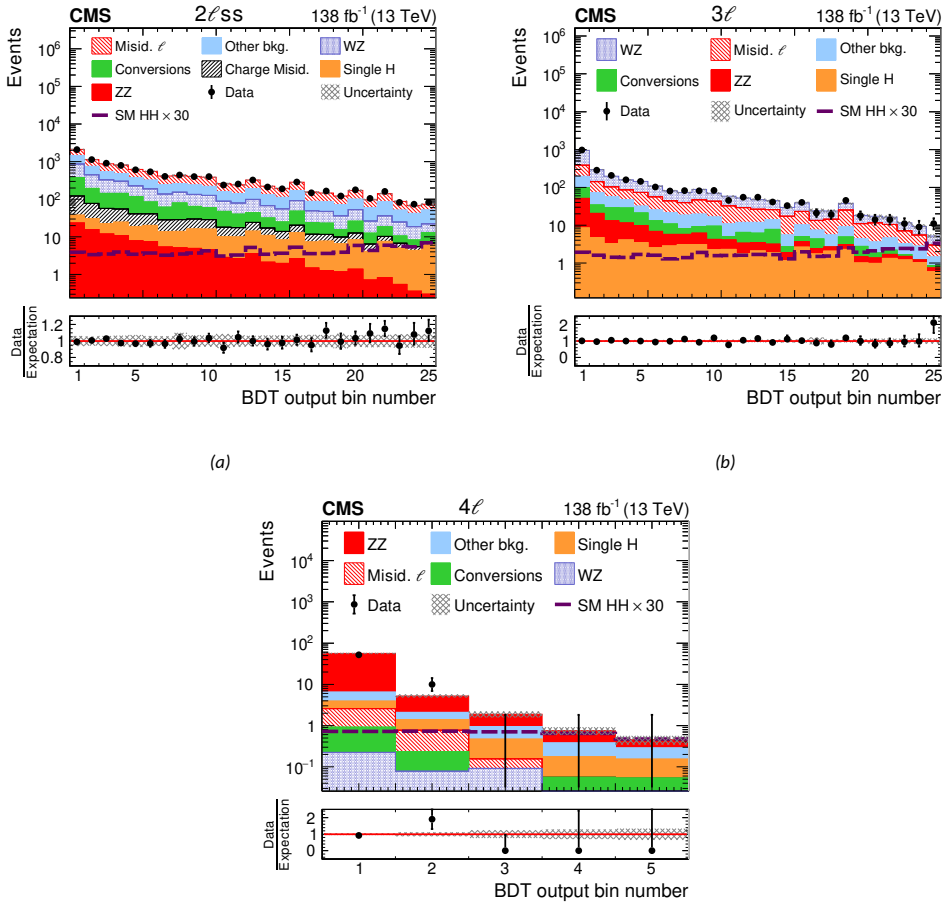


Figure 8.2: Post-fit distributions in the output of BDTs that were trained to recognize nonresonant HH signal in JHEP04BM7 coupling configuration in $2\ell SS+\leqslant 1\tau_h$ (a), 3ℓ (b) and 4ℓ (c) final states. The distributions are presented such that more signal-like events are more likely to occupy rightmost bins. The SM HH signal displayed in the plot is scaled by a factor of 30 for better visibility, effectively normalizing HH production cross section to 1 pb. The uncertainty is obtained from ML fit, and it includes both systematic and statistical components. No data was found in the three rightmost bins of the BDT distribution in the 4ℓ channel. The same plots are also published in Ref. [2].

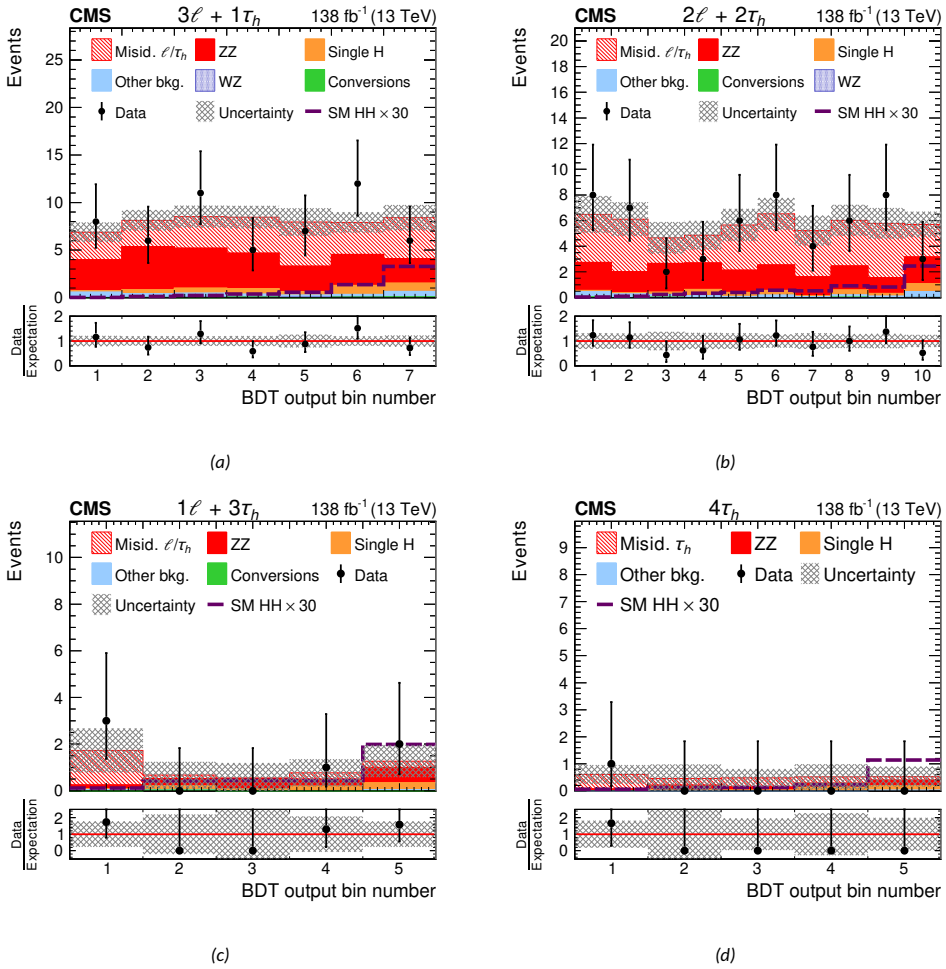
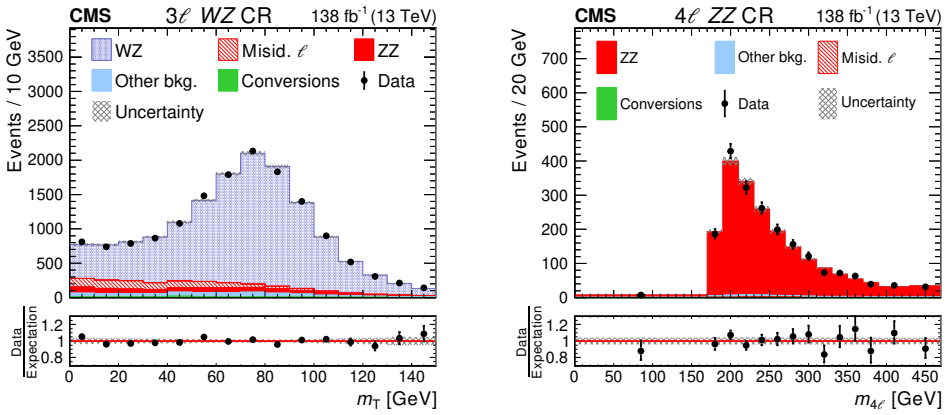


Figure 8.3: Post-fit distributions in the output of BDTs that were trained to recognize nonresonant HH signal in JHEP04BM7 coupling configuration in $3\ell+1\tau_{\mathrm{h}}$ (a), $2\ell+2\tau_{\mathrm{h}}$ (b), $1\ell+3\tau_{\mathrm{h}}$ (c) and $0\ell+4\tau_{\mathrm{h}}$ (d) final states. The distributions are presented such that more signal-like events are more likely to occupy rightmost bins. The SM HH signal displayed in the plot is scaled by a factor of 30 for better visibility, effectively normalizing HH production cross section to 1 pb. The uncertainty is obtained from ML fit, and it includes both systematic and statistical components. No data was found in the two middle bins of the BDT distribution in the $1\ell+3\tau_{\mathrm{h}}$ channel, and in all bins but the first bin of the BDT distribution in the $0\ell+4\tau_{\mathrm{h}}$ channel. The same plots are also published in Ref. [2].



(a) *(b)*

Figure 8.4: Post-fit distributions in the kinematic observables that were utilized as signal extraction variables in 3ℓ CR (a) and in 4ℓ CR (b). The variable plotted for 3ℓ CR is the transverse mass given by Eq. (4.1) of the lepton that is not associated with the resonant peak in Z boson mass. The shape variable chosen for signal extraction in 4ℓ CR is computed as the invariant mass of the four leading leptons in the final state. No HH signal is displayed here due to lack thereof. The uncertainty is obtained from ML fit, and it includes both systematic and statistical components. The same plots are also published in Ref. [2].

The MLE of the production rate that corresponds to the sum of ggF and VBF HH signals amounts to $\hat{\mu}_{\text{HH}} = 2 \pm 10$ times the SM expectation. The result is compatible with both the background-only hypothesis as well as with the SM scenario. Upper limits are set on HH production rate since no indication of HH signal has been found thus far. Asymptotic 95% CL upper limits on SM HH production cross section in each channel and for their combination are displayed in Fig. 8.5. The upper limit on HH production rate is set to 21.3 (for an expectation of 19.4) times the SM production cross section, which translates to an upper limit of 661 (602) fb. This result is compatible with the observed (expected) upper limit of 651 (592) fb on HH production cross section. The results are not exactly identical to each other because of theoretical uncertainties on SM HH production cross section that are considered in the extraction of the former limits.

Compared to ATLAS results on 2016 data [246], this analysis delivers four (three) times lower observed (expected) limits at an equivalent luminosity. Most of the gain in sensitivity of this analysis can be attributed to looser event selection criteria, which boosts the acceptance of events by two orders of magnitude in the $2\ell\text{SS}+\leqslant 1\tau_{\text{h}}$ and 3ℓ channels, and to the addition of another four analysis channels, which all feature at least a τ_{h} in final state. On top of that the limits in Ref. [246] are extracted from cut-and-count analysis, whereas the upper limits of this analysis are extracted by exploiting the shape information of BDT output distributions.

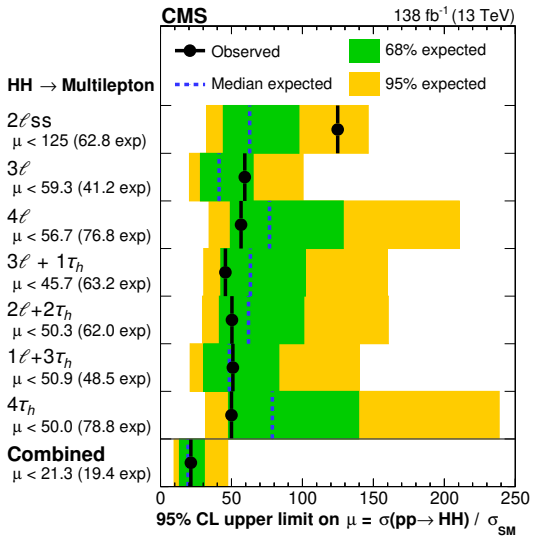
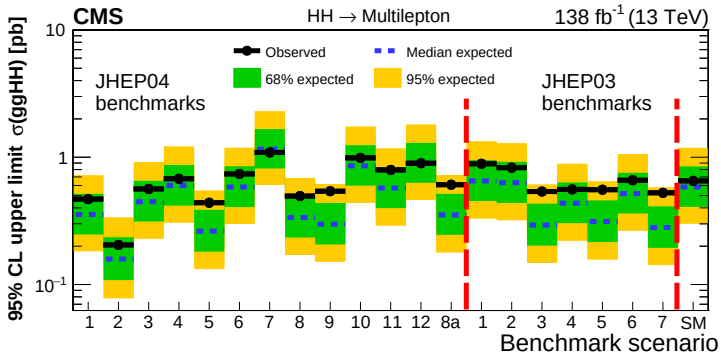
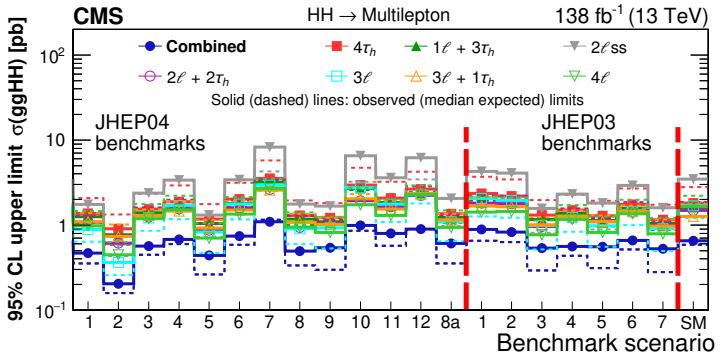


Figure 8.5: Asymptotic observed and expected upper limits on inclusive SM HH production cross section rate at 95% CL, obtained for each of the seven analysis channels and for their combination. The upper limits were extracted from the BDT output that corresponds to the SM scenario. The same plot is also published in Ref. [2].

It is the first analysis that published upper limits for both JHEP03 and JHEP04 shape BMs. The corresponding upper limits on each of the twenty coupling scenarios are shown in Fig. 8.6 for individual analysis channels as well as for their combination. Theoretical cross sections are omitted from these plots, because each EFT BM is supposed to represent a class of coupling scenarios that share similar features in m_{HH}–$\cos\theta^*$ space. The BSM signal would be recognized as such if it produces a significant excess in the observed limits relative to the expectation. The m_{HH} spectrum for JHEP04 BMs 10–12, but especially for JHEP04 BM7 as well as for JHEP03 BMs 1 and 2 is rather soft, which explains their relatively high upper limits compared to some other BMs. The results presented here are in the same ballpark as the results obtained from the previous combination of HH analyses by the CMS collaboration in 2016 [250]. Limits on EFT BMs of more recent HH analyses on full LHC Run 2 data are about four times lower in $\mathrm{b\bar{b}b\bar{b}}$ [227], three times lower in $\mathrm{b\bar{b}}\gamma\gamma$ [235], and marginally lower in $\mathrm{b\bar{b}WW}^*$ [7] analysis, but about an order of magnitude higher in $\mathrm{WW}^*\gamma\gamma$ [241] analysis. These findings are consistent with the results presented here if they are scaled to the same sensitivity that is expected from SM HH signal in this analysis. However, compared to other analyses, the limits in this analysis are slightly more stringent on those shape BMs that are characterized by soft m_{HH} spectrum relative to the limits on other BMs.



(a)



(b)

Figure 8.6: Asymptotic observed and expected upper limits on inclusive nonresonant HH production cross section via ggF for the twelve (plus one) JHEP03 EFT BMs, for the seven JHEP04 EFT BMs and for the SM at 95% CL, shown for the combination of all analysis channels (a) and for individual channels (b). The same plots are also published in Ref. [2].

Constraints on κ_λ are derived by computing upper limits for a number of coupling values and comparing the results to the theoretical cross section as shown in Fig. 8.7. The comparison to observed limits constrains κ_λ to $[-6.9, +11.1]$, while the same comparison based on expected limits constrain it to $[-6.9, +11.7]$. The upper limits tend to be lower for coupling scenarios for which the corresponding m_{HH} spectrum is softer. The reason for it is that a soft Higgs boson pair would eventually produce soft decay products, which are more likely to fail the imposed trigger and analysis cuts or otherwise considered as background by the BDTs. The same arguments apply to resonant limits discussed later where the distinction of soft and hard m_{HH} spectrum is much more explicit. Sensitivity to large positive (negative) values of the Higgs boson self-coupling modifier is driven by the 3ℓ and 4ℓ ($2\ell+2\tau_{\mathrm{h}}$) channels. Therefore, the multilepton channels provide relatively stringent limits especially at high positive κ_λ compared to other HH decay modes. However, it also means that the relevance of this analysis diminishes as the coupling modifier becomes more constrained around the SM point in future iterations of HH searches.

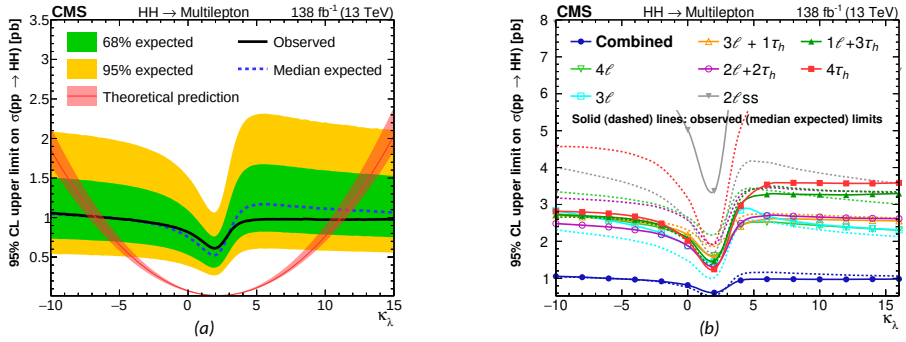


Figure 8.7: Asymptotic observed and expected upper limits on inclusive nonresonant HH production cross section as a function κ_λ at 95% CL, obtained for the combination of all analysis channels (a) and for each channel separately (b). All other couplings remain at their designated SM values in the scan. The red curve in (a) directly follows the sum of ggF and VBF HH curves of Figure 2.24(b). The upper limit on κ_λ constrain it to $[-6.9, +11.1]$, while expecting $[-6.9, +11.7]$. The same plots are also published in Ref. [2].

There is no real sensitivity to VBF HH production in this analysis, primarily because none of the channels were specifically optimized for it, but also because the event yields from the VBF process are extremely low, constituting less than 10% of total HH signal as attested by Fig. 8.1. Nevertheless, to establish some sort of baseline for future iterations of the analysis, observed (expected) upper limits on VBF HH production cross section are established at 95% CL, which amount to 357 (491) times the SM prediction. Figure 8.8(a) illustrates the observed (and expected) bounds on κ_{2V}, which constrain it to $[-3.4, +5.5]$ (for an expectation of $[-2.6, 4.7]$) at 95% CL. Sensitivity to κ_{2V} is mostly driven by the $2\ell\text{SS}+\leqslant 1\tau_\text{h}$ and 3ℓ channels, which deliver most of the events.

The same type of scan was performed for c_2 coupling, which represents effective contact interaction between pairs of Higgs bosons and gluons. As shown in Fig. 8.8(b), the coupling is constrained to $[-1.05, +1.48]$ for an expectation of $[-0.96, +1.37]$. Two-dimensional κ_t-c_2, κ_t-κ_λ and κ_λ-c_2 coupling scans are presented in Fig. 8.9. The one- and two-dimensional constraints on SM and EFT couplings are consistent with the SM expectation at 95% CL.

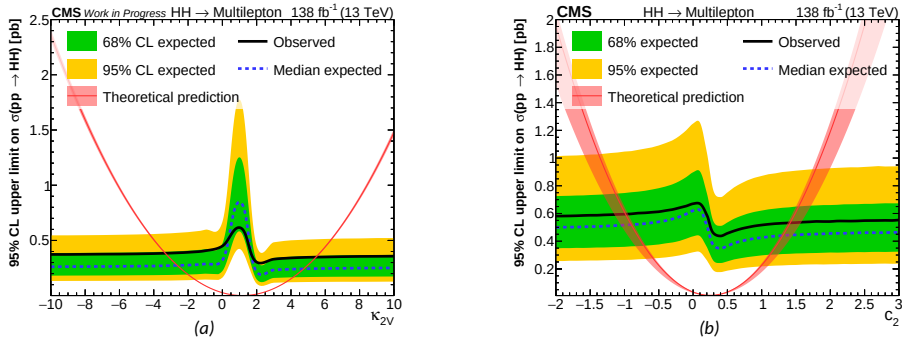


Figure 8.8: Asymptotic observed and expected upper limits on inclusive nonresonant HH production cross section as a function κ_{2V} (a) and c_2 (b) at 95% CL. The red curve in (a) directly follows the VBF HH curve of Figure 2.24(b). Based on the upper limits, κ_{2V} is constrained to $[-3.4, +5.5]$ (while expecting $[-2.6, +4.7]$), whereas c_2 is confined to $[-1.05, +1.48]$ (while expecting $[-0.96, +1.37]$). The same plots are also published in Ref. [2].

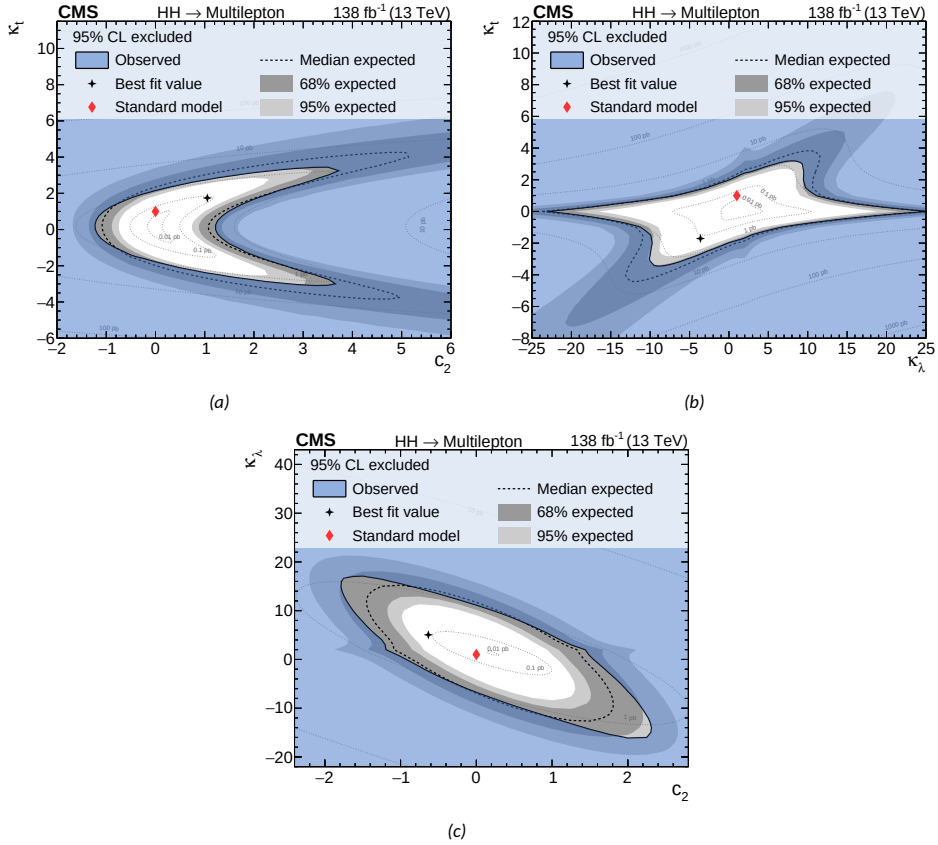
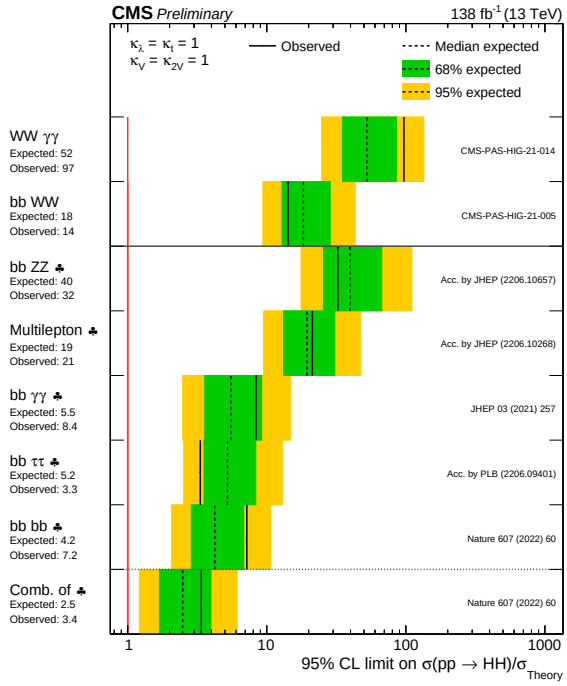
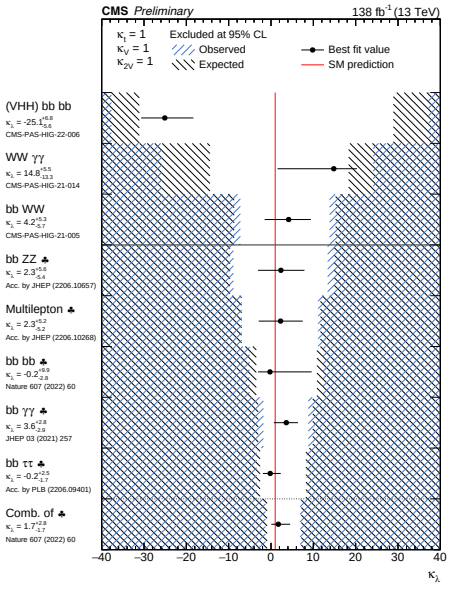


Figure 8.9: Two-dimensional asymptotic observed and expected exclusion limits on inclusive nonresonant HH production cross section in κ_t–c_2 (a), κ_t–κ_λ (b) and κ_λ–c_2 (c) planes. The fain dotted lines represent isocontours of theoretical cross section. The same plots are also published in Ref. [2].

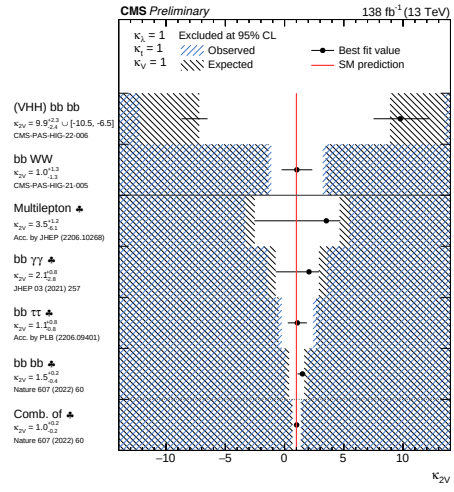
In terms of sensitivity to SM HH signal, the multilepton and $b\bar{b}WW^*$ [7] decay modes are right behind $b\bar{b}b\bar{b}$ [227, 228], $b\bar{b}\tau\tau$ [232, 233] and $b\bar{b}\gamma\gamma$ [234, 235] channels, as seen from the ranking of CMS analyses in Fig. 8.10(a). Latest combinations of HH analyses by ATLAS [249] and CMS [8] collaborations have placed observed (expected) upper limits on HH production cross section at 95% CL, which respectively amount to 2.4 (2.9) and 3.4 (2.5) times the SM production rate. The combination of CMS analyses published in Ref. [8] includes the results presented in this document. Upper limits as a function of coupling modifiers constrain κ_λ to $[-0.4, +6.3]$ and $[-1.2, +6.5]$ for an expectation of $[-1.9, +7.5]$ and $[-1.0, +6.3]$, and κ_{2V} to $[0.1, 2.0]$ and $[0.7, 1.4]$ for an expectation of $[0.0, 2.1]$ and $[0.7, 1.4]$. As evidenced by Figure 8.10(b), the constraints on κ_λ set by the HH multilepton analysis are fairly competitive compared to other CMS analyses, especially at high κ_λ, thus putting the HH multilepton analysis right behind the most sensitive $b\bar{b}\tau\tau$ [233], $b\bar{b}\gamma\gamma$ [235] and $b\bar{b}b\bar{b}$ [228] analyses. However, the constraints on κ_{2V} are not as stringent compared to other CMS analyses, as seen from Figure 8.10(c). Based on the combination of HH analyses performed by the CMS collaboration, the hypothetical scenario where κ_{2V} is zero while all other couplings are at their designated SM values is excluded at significance of 6.6σ [8], therefore confirming that coupling indeed exists in one way or another. The combination of HH results provide the most stringent limits on nonresonant HH production as well as on κ_λ and κ_{2V} to date.



(a)



(b)



(c)

Figure 8.10: Asymptotic observed (blue hatch) and expected (black hatch) upper limits on inclusive SM HH production cross section at 95% CL (a), and best fit value (black point) with corresponding CIs at 68% CL (solid line) for κ_λ (b) and κ_{2V} (c), all extracted from the ML fits of the latest HH analyses published by the CMS collaboration [466].

The final set of results concerns resonant production of HH events. Four representative post-fit distributions in the BDT output out of 266 (or 342 when counting the CRs) possible post-fit plots are shown in Fig. 8.11. The plots are compiled for the 3ℓ channel to demonstrate the trends since it has second largest event yields and decent sensitivity. As such, it appears that at high masses of spin-0 and spin-2 resonances (beyond $600\,\text{GeV}$) a slight excess in data events arises in the rightmost bins of the corresponding distributions, while no such trends are observed at lower masses of the resonance. The same trends are also present in the $2\ell\text{SS}+\leqslant 1\tau_\text{h}$ channel. The excess appears in bins of the BDT distributions that are most sensitive to the resonant HH signal, and thus carries over to upper limits as illustrated by Fig. 8.12. However, the perceived excess is not particularly significant, as its significance in spin-2 resonances at $750\,\text{GeV}$ mass point under background-only hypothesis where the excess is most pronounced amounts to 1.9σ, which persists at 1.5–2σ level even beyond the $1\,\text{TeV}$ scale. This estimate is „local" in the sense that it does not account for the look-elsewhere effect [467], which would further dilute the ascertained significance by considering the possibility that an excess could appear at any other mass point, not specifically at the point that was tested. The sentiment that the mild excess at high mass ranges has no real significance is further supported by the fact that more sensitive HH analyses in $\text{b}\bar{\text{b}}\text{b}\bar{\text{b}}$ [226], $\text{b}\bar{\text{b}}\tau\tau$ [232] and $\text{b}\bar{\text{b}}\gamma\gamma$ [234, 245] decay modes at equivalent luminosity place up to an order of magnitude lower limits at high mass regions. The reduced sensitivity to the resonant signal at higher masses is expected in this analysis because no efforts were made to tailor the analysis for boosted topologies. In particular, it has been shown that the ID efficiency of individual τ_h candidates drops by a factor of three in $\text{HH} \to \text{b}\bar{\text{b}}\tau\tau$ events if the scalar resonance producing the Higgs boson pair becomes highly boosted [300]. Besides, none of the BDTs here were trained to include boosted signal, which further degrades the sensitivity at high mass regions.

Figure 8.12 concludes that resonant HH signals stronger than $1\,\text{pb}$ are excluded at 95% CL across the whole mass range. The limits are lower for high mass resonances, in the order of 200–$300\,\text{fb}$ at the tail end of 900–$1000\,\text{GeV}$, while expecting 80–$100\,\text{fb}$. The obtained limits are equivalent to excluding energy scales of new physics lower than 2–$6\,\text{TeV}$ depending on the mass of the hypothetical radions. Bulk gravitons of any mass produced at $\tilde{k} > 0.25$ are also excluded at 95% CL. These results are comparable to the limits extracted from the combination of most sensitive HH analyses performed on 2016 data [248, 250]. Compared to the most recent CMS analyses, the HH multilepton analysis ranks right behind the $\text{b}\bar{\text{b}}\gamma\gamma$ [245] and $\text{b}\bar{\text{b}}\tau\tau$ [244] (not displayed in Figure 8.13) analyses for resonances below $500\,\text{GeV}$. However, as the $\text{HH} \to \text{b}\bar{\text{b}}\text{WW}^*$ analysis [7] becomes more sensitive to resonances with masses higher than $500\,\text{GeV}$, the HH multilepton analysis takes fourth place in this ranking. The limits on spin-2 resonances are a bit lower overall compared to spin-0 resonances. The phenomenon could be explained by Fig. 2.31, which demonstrates that the Higgs boson pairs stemming from graviton decays are more likely to fly apart in the transverse plane than the Higgs boson pairs that originate from radion decays. This in turn gives a higher chance for the decay products of gravitons to pass the analysis cuts and thereby boost the corresponding signal acceptance over radions, as seen from their limits.

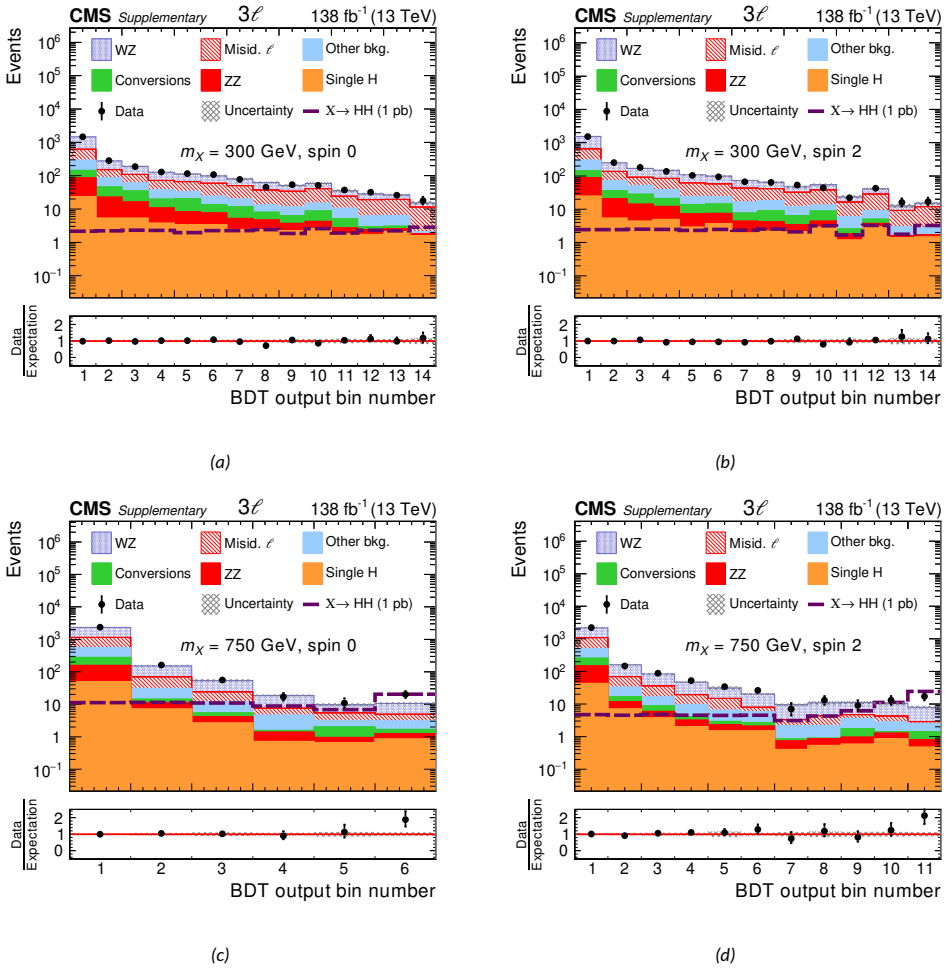


Figure 8.11: Post-fit distributions in the output of BDTs in the 3ℓ channel that were trained to recognize HH resonances from spin-0 ((a) and (c)) and spin-2 ((b) and (d)) particles with invariant masses of 300 GeV ((a) and (b)) and 750 GeV ((c) and (d)) each. Cross section of HH production via the intermediate resonance is normalized to 1 pb. The same plots are also published in Ref. [2] as supplementary material.

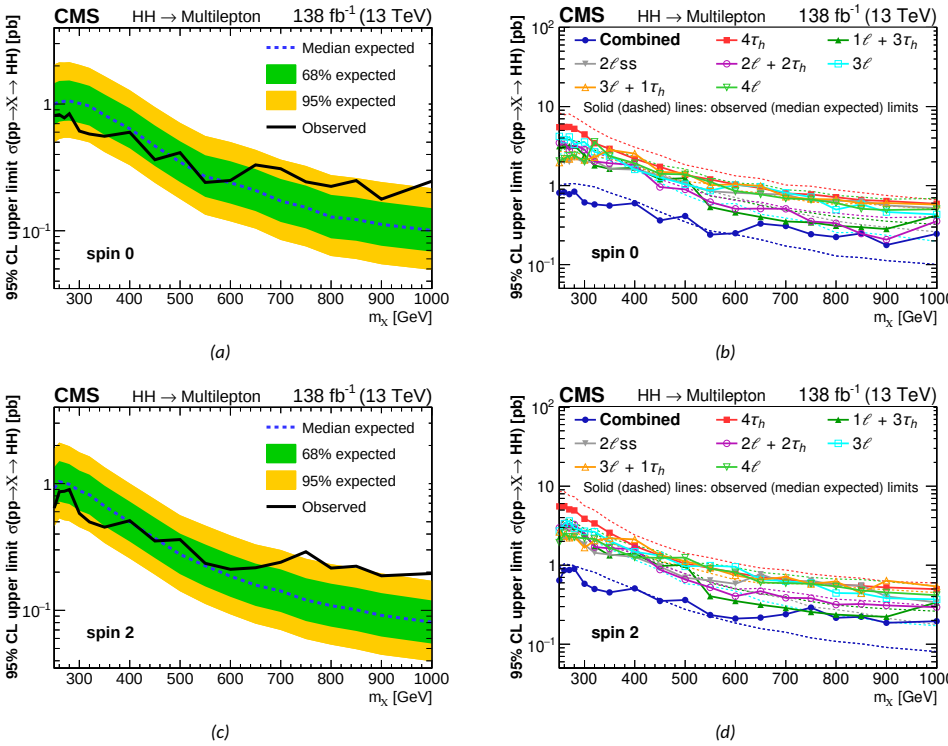


Figure 8.12: Asymptotic observed and expected upper limits on resonant HH production cross section at 95% CL via the decay of spin-0 and spin-2 resonances for a range of resonant mass points between 250 GeV and 1 TeV, obtained for the combination of all analysis channels in (a) and (c), and for per individual analysis channel in (b) and (d). The same plots are also published in Ref. [2].

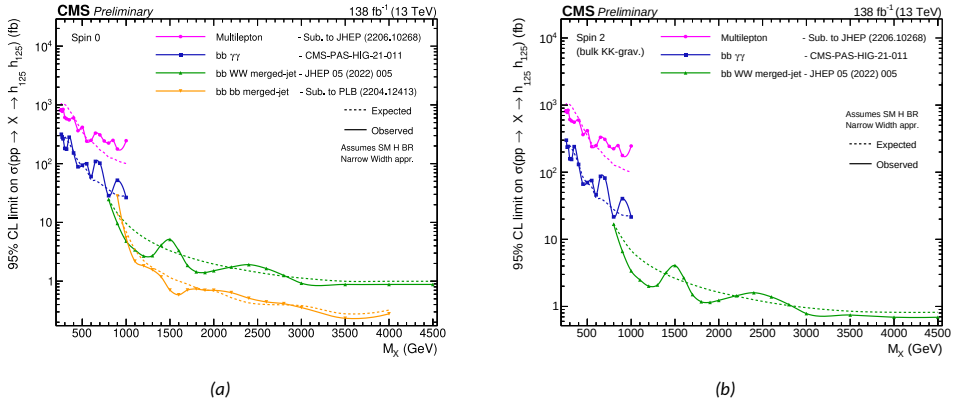


Figure 8.13: Comparison of observed and expected upper limits on resonant HH production cross section via spin-0 (a) and spin-2 (b) resonances at 95% CL between various HH analyses published by the CMS collaboration. The results of this analysis are shown in magenta. Both plots were published by Higgs Physics Analysis Group of CMS collaboration on their web site [466].

Relative impact of NPs on the best fit signal rate in Table 6.1 and in Fig. 6.5 indicates that the most restricting factor of this analysis by far is the limited amount of recorded data and simulated MC events, which is followed by the rather sizable uncertainties that are associated with the fake background and the τ_{h} ID. The lack of data events becomes less important in the era of HL-LHC, as the ultimate goal of $3\,\mathrm{ab}^{-1}$ of integrated luminosity should reduce the statistical uncertainties by a factor of five. The increase in integrated luminosity should also directly benefit the fake background estimation, since the large uncertainties on the extracted FRs arise mostly because of poor event yields in the MRs, especially at high p_T.

However, more work is needed to address other limitations. For instance, it is not sufficient to generate additional MC samples to only match the current levels of effective event statistics, but instead it is necessary to improve upon it. This would not only reduce the bin-by-bin uncertainties in the final results, but would also improve the performance of the BDTs by having more samples to train on. Another way of augmenting the training data would be to create new training samples by making new copies of the existing data and manipulating them in some manner, such as by adding noise to continuous observables [468], or by randomly boosting and rotating the events in accordance with Lorentz symmetries. The said transformations could be exploited to automatically generate novel input features for the BDTs. This strategy has already been tried in the context of $\mathrm{HH} \to \mathrm{b\bar{b}WW}^*$ analysis [7], in which the process of feature engineering was delegated to a special DNN [469]. The production of MC samples for dominant irreducible backgrounds can be sped up by simplifying the detector simulation [470], but not necessarily to the level of Delphes [471]. Downside of this approach, though, is that one would then need to measure and apply custom data-to-MC SFs to these samples, which unnecessarily complicates the analysis. Alternatively, one could employ generative deep learning techniques to regress energy scale and resolution effects of the full-fledged simulation, given the generator-level observables as input [472]. It would speed up the MC sample production immensely, because the most time-consuming step of the whole process — simulation of the detector response — would be replaced with the regression model, analogously to how regressing the MEM LRs with a DNN eliminates the resource-intensive task of numerical integration [10]. As for the systematic uncertainties on the fake background, one viable option to reduce them would be to use a likelihood-based method to estimate the fake background [473, 474], which was found to especially benefit analyses that are severely limited due to lack of events [475]. This method has been successfully utilized once by the ATLAS collaboration in $\mathrm{t\bar{t}Z}$ production measurement in multilepton final states [447].

While the HH multilepton analysis presented here is already quite comprehensive in its scope, there are a few ways to broaden it. One possibility would be to improve the sensitivity to the VBF HH signal. Steps in that direction have already been taken, as preliminary attempts to separate it from the ggF HH signal in the $2\ell\mathrm{SS}{+}\leqslant 1\tau_{\mathrm{h}}$ channel improved the expected upper limits by a factor of four [476]. Constraints on $\kappa_{2\mathrm{V}}$ could be improved by choosing a different set of coupling scenarios for the matrix-based reweighting to reduce statistical uncertainties at extrapolated points in the coupling space, since the current basis has mostly historic origins [201] and not optimized like how it was done in c_2 scans. Another option would be to complement the BSM coupling measurement by an analogous measurement of the Wilson coefficients that have a particular relevance to the HH production. The most recent $\mathrm{HH} \to \mathrm{b\bar{b}b\bar{b}}$ analysis by the ATLAS collaboration already provided first constraints on the SMEFT coefficients by studying the production rate of ggF HH process [227]. The idea that all possible EFT coupling scenarios give rise to a finite number of signal topologies could be explored to specifically study the VBF HH signal or

a BSM signal induced by nonrenormalizable operators. Resonant HH measurements in multilepton final states could be extended beyond $1\,\mathrm{TeV}$, but there are no good arguments to believe that it will improve the sensitivity to respective signals relative to other HH analyses involving $\mathrm{H} \to \mathrm{b\bar{b}}$ decays. It might be worthwhile to explore resonant $\mathrm{X} \to \mathrm{YH}$ production, though, especially if the second Higgs-like particle Y decays more often into a pair of vector bosons or τ leptons as one would expect from a SM-like Higgs boson heavier than $200\,\mathrm{GeV}$ [143]

9 Summary

The CMS experiment has delivered unprecedented amounts of proton-proton collision data at $13\,\text{TeV}$ c.o.m energy over the last three years of the LHC Run 2 data-taking period, which allows to probe rare processes and compare the results to SM expectations. In this work, signs of new physics are searched for in interactions involving the production of a Higgs boson in association with a pair of top quarks ($\text{t}\bar{\text{t}}\text{H}$) or with a single top quark (tH), and in interactions involving the production of Higgs boson pairs (HH). The analyses are independently performed in multilepton final states, in which multiple electrons, muons, and hadronically decaying τ leptons (τ_h) result from Higgs boson decays into either vector bosons (W, Z) or to τ leptons. The electrons and muons are commonly referred to as „leptons" (ℓ). The two analyses use common techniques to identify leptons, τ_h and jets, estimate backgrounds and impose event selection requirements, but diverge in how the signals are inferred and results interpreted. The phase spaces of either analysis are kept separate with b tagging requirements, which are imposed in the $\text{t}\bar{\text{t}}\text{H}$ analysis, but inverted in the HH analysis. The analyses detailed in this document are combined with other Higgs boson analyses performed by the CMS collaboration, the results of which are published in Ref. [8].

The primary objective of the $\text{t}\bar{\text{t}}\text{H}$ analysis is to ascertain plausible ranges of the top Yukawa coupling, which quantifies the interaction strength between top quarks and Higgs bosons, and to measure the inclusive $\text{t}\bar{\text{t}}\text{H}$ production cross section, which provides direct access to this coupling. Deviations from the SM are expressed in terms of the coupling modifier κ_t, which is a multiplicative factor to the SM expectation for this coupling.

The analysis is performed in ten mutually exclusive channels based on the multiplicity and charges of the final state leptons and τ_h. The event selection requirements are designed to maximize the sensitivity to the $\text{t}\bar{\text{t}}\text{H}$ and tH signal. Dominant irreducible contributions to the most sensitive $2\ell\text{SS}$, 3ℓ, and $2\ell\text{SS}+1\tau_\text{h}$ channels are due to the $\text{t}\bar{\text{t}}\text{W}(\text{W})$ and $\text{t}\bar{\text{t}}\text{Z}$ processes, whereas in all other subleading channels the signal is buried under enormous reducible backgrounds, apart from $3\ell+1\tau_\text{h}$ and 4ℓ channels, which have very low event yields. Another two CRs are implemented to constrain the modeling of the irreducible diboson and $\text{t}\bar{\text{t}}\text{Z}$ backgrounds, which appear in most of the analysis channels. Reducible backgrounds that arise from an incorrectly measured electron charge (in the $2\ell\text{SS}$ and $2\ell\text{SS}+1\tau_\text{h}$ channels), or from jets that are misidentified as leptons or τ_h are estimated using data-driven techniques, while the irreducible backgrounds are estimated from MC simulation. The latter is corrected with SFs to improve the modeling of the data. Signal rates are extracted from an ML fit by analyzing the shape of distributions in the output of BDTs and DNNs, which have been optimized to discriminate the $\text{t}\bar{\text{t}}\text{H}$ and tH signal from background processes by exploiting differences in event kinematics. A simplified control analysis based on the MEM LR and single invariant mass variables was performed as a cross-check to demonstrate that the machine learning methods utilized in the main analysis indeed provide ultimate sensitivity to the signal at hand.

The $\text{t}\bar{\text{t}}\text{H}$ production cross section is measured to be $466^{+132}_{-112}\,\text{fb}$. The measurement is compatible with the theoretical SM cross section of $507.1\,\text{fb}$ computed at NLO accuracy in pQCD. The observed statistical significance of this result under the background-only hypothesis amounts to 4.2σ for an expectation of 5.0σ. The measured tH production cross section is compatible with the SM expectation, amounting to $5.7^{+4.1}_{-4.0}$ times the SM expectation, but the result has much lower significance of 1.4σ (for an expectation of 0.3σ) under the background-only hypothesis. The top Yukawa coupling is constrained to be within $-0.9 < \kappa_\text{t} < -0.7$ or $0.7 < \kappa_\text{t} < 1.1$ times the SM prediction at 95% CL. Similar constraints are derived for a combination of κ_t and κ_V values, where κ_V refers to the

multiplicative factor that parametrizes the deviations of the Higgs boson coupling to vector bosons from the SM expectation. These results establish multilepton channels as one of the three major analyses that provide excellent sensitivity to the $t\bar{t}H$ and tH processes, and to the top Yukawa coupling. Future versions of the analysis can be broadened in scope to accommodate differential cross section measurements, to study the CP phase of the top Yukawa coupling, and to measure the Wilson coefficients arising from EFT extensions of the SM.

The second part of this work covered the HH multilepton analysis. One of the main aims in this analysis is to set upper limits on the HH production cross section and, based on that, place constraints on Higgs boson self-coupling λ. The deviations of λ from the SM prediction are parametrized through the coupling modifier κ_λ. EFT extensions of HH production via ggF encompass variations in κ_λ and κ_t, as well as the addition of another three nonrenormalizable couplings, including the c_2 coupling, which represents the contact interaction strength between Higgs boson pairs and top quark pairs. All possible combinations of those five couplings can generate up to twenty kinematic configurations of the Higgs boson pair that are unique in terms of their invariant masses and angles. The Higgs boson pair could also arise from the decays of heavy even-spin resonances like radions and gravitons.

The HH signal is searched in seven mutually exclusive multilepton channels, which are defined based on the multiplicity and charges of the final state leptons and τ_h. Each such lepton and τ_h is expected to originate from the HH decay modes to WW^*WW^*, $WW^*\tau\tau$ or $\tau\tau\tau\tau$. The analysis channels are complemented by two CRs enriched with diboson backgrounds, in order to constrain systematic uncertainties. The HH multilepton analysis relies heavily on particle ID and background estimation methods that were developed or optimized in the context of the $t\bar{t}H$ multilepton analysis. Much of the effort is invested into training the BDTs to efficiently differentiate HH events from backgrounds. Three kinds of BDTs are trained: one for the case where the Higgs boson pair is created through SM-like processes, and another two for the case where the Higgs boson pair is produced via spin-0 and spin-2 resonances. The BDTs are parametrized by properties of the HH signal to enhance the number of events that is reserved for the training and thereby improve sensitivity to the said signal. Furthermore, a data augmentation strategy is implemented to maximize the event statistics available for the statistical inference. Both of these techniques help to combat the main limiting factor of the HH analysis, which is the lack of simulated and recorded events.

As no HH signal was observed, an upper limit of 21.3 times the SM prediction was placed on HH production cross section at 95% CL, which is in agreement with an expected limit of 19.4 times the SM rate. Based on these results, the Higgs boson self-coupling is constrained to be within the range $-6.9 < \kappa_\lambda < 11.1$ times the SM expectation. Likewise, c_2 is confined to the interval $[-1.05, +1.48]$. The cross sections for HH production in different EFT scenarios range from 0.2 to 1.1 pb at 95% CL. In case of resonant HH production, the upper limits extend from 1 pb near the kinematic threshold of HH production to 0.2–0.3 pb for heavy resonances with invariant mass of about 1 TeV. No noteworthy excesses over the SM expectation are observed in the data. With the adoption of more advanced machine learning methods and data augmentation techniques, the substantial increase in the amount of recorded data that is expected in upcoming years, it is certainly possible that the sensitivity to SM HH production can be reached by the end of LHC Run 3 operation in case the results of all ATLAS and CMS analyses of the different HH decay modes are combined.

Unfortunately, no clear signs of new physics have been found from the LHC data since

the discovery of the Higgs boson a decade ago. All results thus far indicate good compatibility with the SM. Nevertheless, incredible progress has been made in the development of analysis techniques during the LHC Run 2 data-taking period, primarily thanks to the increased adoption of advanced machine learning techniques, but also because of a stronger emphasis on automating and streamlining the analysis efforts, which have made it possible to deliver the results presented in this thesis. Hopefully, this effort will be continually improved upon in the years to come.

List of Figures

2.1 Feynman diagrams for QCD interactions: quark-gluon coupling (a), trilinear gluon self-coupling (b) and quartic gluon self-coupling (c). Diagram (a) explicates the color flow from a pair of a quark and its anti-quark $q\overline{q}$ (shown with arrows) in initial state to the gluon g (curly line) with extra lines colored as blue (B) and „anti-green" ($\overline{G}$, *i.e.*, magenta), while in self-interaction diagrams (b)–(c) the color states have already been summed over and the extra colored lines are hence omitted. Probability amplitude of diagrams (a) and (b) scale with g_S, while the amplitude of (c) scales with g_S^2. 9

2.2 Feynman diagrams generated by EW Lagrangian density defined by Eq. (2.8) after rearrangement of gauge fields into physical fields: three-point (a) and four-point (b) interactions between the EW bosons (shown with wavy lines); decay of electrically neutral γ and Z bosons into a pair of a lepton and its anti-lepton ($\ell^-\ell^+$), into a pair of a quark and its anti-quark ($q\overline{q}$), or into a pair of a neutrino and its anti-neutrino ($\nu_\ell\bar{\nu}_\ell$), all shown with solid arrows (c); decay of W^- boson into a pair of a lepton and an anti-neutrino of the same lepton flavor ($\ell^-\bar{\nu}_\ell$), or into a pair of a down-type quark and an up-type anti-quark ($q_d\overline{q}_u$) (d). The decay of W^+ boson (not shown) would proceed into a pair of an anti-lepton and lepton neutrino of the same lepton flavor ($\ell^-\nu_\ell$), or into a pair of down-type anti-quark and up-type quark ($q_u\overline{q}_d$). Probability amplitudes of all Feynman diagrams scale with e, except for (b), which scales with e^2. 12

2.3 Feynman diagrams for processes involving Higgs boson: three-point (a) and four-point (b) interaction of Higgs boson (shown with a dashed line) with vector massive bosons ($W^\pm$, Z); Higgs boson interaction with a pair of a charged lepton and its anti-lepton ($\ell^-\ell^+$), or with a pair of a quark and its anti-quark ($q\overline{q}$) (c); trilinear (d) and quartic (e) self-couplings. Probability amplitudes of (a) and (b) are respectively proportional to g_V and g_{2V}, which are given by Eq. (2.14); the probability amplitude for the fermion vertex (c) is linearly proportional to the corresponding Yukawa coupling or, equivalently, to the mass of the involved fermion; the probability amplitude for self-coupling diagrams (d) and quartic (e) are directly proportional to the self-coupling λ. 15

2.4 (a): Feynman diagrams of β decay for the cases when the W boson could be resolved at high energies Q, as shown on the left-hand side, and when the description becomes effective at significantly lower energies than the mass of the boson m_W, which is depicted on the right-hand side. (b): Illustration of the EFT formalism. Yet unknown UV-completing theories (shown with blue lines) beyond some scale Λ can lead to the same effective description below that scale (demarcated by a green vertical line), thus altering the production rate of known particles with respect to the SM prediction (the latter of which is highlighted with a dashed pink line). Discrepancy between the SM and the effective description (yellow shaded area) can be measured if Λ is reachable by experiments. 18

2.5 Proton PDFs with uncertainty bands from NNPDF 3.1 NNLO set for various partons as a function of the Bjorken scaling variable. Labels u_v and d_v stand for valence u and d quarks. All remaining quarks and gluons are deemed as sea partons. The plot is created with LHAPDF [82]. 22

2.6 Illustration of a proton-proton collision [95]. 24

2.7 Dimuon invariant mass spectrum reconstructed from CMS data collected in 2018 [96]. 26
2.8 Feynman diagram illustrating a τ lepton decay. 27
2.9 Anatomy of a b jet. The B meson is significantly displaced from the HS collision point (★) before it decays weakly into a D meson. The D meson itself may convert into a kaon K through weak interaction. A charged lepton (ℓ^-) may be created as a byproduct of weak decays. Hadron constituents may emit extra QCD or EM radiation. Other hadrons produced in the b quark hadronization may enter the b jet cone, but they are not displayed here. 29
2.10 Loop-induced Higgs boson decays: into a pair of gluons via fermion loop dominated by top quarks (a); into $\gamma\gamma$ or $Z\gamma$ via the same fermion loop (b), or via cubic (c) or quartic (d) W fusion. 31
2.11 LO Feynman diagrams for the dominant production modes of a single Higgs boson: ggF dominated by virtual top quarks (a), VBF (b), VH initiated by quarks (c), and associated production with a pair of top quarks initiated by gluons (d)–(e) and by light quarks (f). 33
2.12 LO Feynman diagrams for the subdominant production modes of a single Higgs boson: gluon-induced ZH via triangle (a) and box (b) loop dominated by top quarks, and one of the many possibilities for $t\bar{t}VH$ production (c). In the latter case, the Higgs boson may be radiated from the V leg also. 33
2.13 Cross sections for various Higgs boson production mechanisms parametrized by c.o.m energy at the LHC [50]. 34
2.14 Coupling modifiers of Higgs boson to fermions and massive vector bosons as function of their mass measured in CMS data recorded in LHC Run 2 [8]. The results published in Ref. [1] are included in this measurement. Higgs boson mass is quoted from dedicated measurement performed by the CMS collaboration on data collected in 2016 [121]. 37
2.15 STXS stage 1.2 binning of the following Higgs boson production modes: ggF (blue, 16 bins); VBF and VH with hadronically decaying vector boson (orange, 10 bins); VH with leptonically decaying vector boson (green, 15 bins) and $t\bar{t}H$ (purple, 5 bins). The variables featured in the binning scheme are: multiplicity of jets; transverse momentum of the Higgs boson (p_T^{H}) and massive vector boson (p_T^{V}); dijet mass (m_{jj}); magnitude of the transverse momentum sum of the Higgs boson and a single jet ($p_T^{\mathrm{H}j}$), or Higgs boson and two jets ($p_T^{\mathrm{H}jj}$). Only those signal events are considered for the binning, where absolute pseudorapidity of the Higgs boson is less than 2.5. All thresholds on momentum and mass variables are given in units of GeV. The plots are created by the LHC Higgs Working Group [50]. 38
2.16 Stability regions of SM vacuum as a function of Higgs boson and top quark masses spanning over a wide range of values (a) and zoomed into experimentally relevant range (b) [148]. In unstable regions, the effective vacuum potential $V(\phi)$ becomes unbounded from below; in meta-stable regions, the current minimum of $V(\phi)$ is not global; in stable regions, the current minimum of $V(\phi)$ coincides with the global minimum. The red dotted lines correspond to the energy scale given in GeV, at which the vacuum becomes unstable. The shaded contour regions that are centered around Higgs boson and top quark mass indicate the associated uncertainties. 39

2.17 Feynman diagrams at LO for the production of a Higgs boson in association with a single top quark in the s-channel. ... 42
2.18 Feynman diagrams at LO for the production of a Higgs boson in association with a single top quark and a W boson in the s-channel (a)–(b) and t-channel (c)–(d), all in 5FS. ... 42
2.19 Feynman diagrams at LO for the production of a Higgs boson in association with a single top quark in the t-channel in 5FS (a)–(b) and in 4FS (c)–(d). ... 42
2.20 Contour plots showing expected BSM cross section in units of SM cross section as a function of κ_t and κ_W values for the tHq process (a) and for the tHW process (b), computed at $\sqrt{s} = 13\,\text{TeV}$ in 5FS. Only the pairs of κ_t and κ_W coupling modifiers that are marked with orange crosses in the plot are considered in the BSM coupling scan. Each of these points define a unique ratio of κ_t/κ_W. The SM and ITC scenarios are marked with a star (★) and a diamond (♦) symbol, respectively. ... 43
2.21 Feynman diagrams of some single Higgs boson processes that are sensitive to Higgs boson self-coupling λ at the loop level: ggF (a) and $t\bar{t}H$ (b) production, and $H \to ZZ^*$ decay (c). ... 47
2.22 Approximate scaling of production cross section of single Higgs boson processes at $\sqrt{s} = 13\,\text{TeV}$ (a) and branching ratios of Higgs boson decay modes (b) as a function of trilinear self-coupling modifier κ_λ computed to NLO in EW. The scaling behavior in both cases is perturbatively valid only for $|\kappa_\lambda| \lesssim 20$. Symbol $f\bar{f}$ in (b) stands for any pair of massive fermions. The plots are recreated from the information available in Refs. [146, 178]. ... 47
2.23 Feynman diagrams at LO for the SM production of two Higgs bosons via ggF (a)–(b) and via VBF (c)–(e). ... 48
2.24 (a): density plot for invariant mass of the Higgs boson pair, m_{HH}, for selected values of κ_λ in ggF HH production process. The distributions are scaled to match the expected signal yield N delivered by the LHC in Run 2 data-taking period. The plot is obtained from MC samples simulated at NLO in pQCD; (b): cross sections of ggF (blue) and VBF (red) HH production as a function of κ_λ, and VBF HH production as a function of κ_{2V} (green). The uncertainty band covers the effects of choosing QCD scale and top mass scheme in ggF HH cross section estimate. ... 49
2.25 Feynman diagrams at LO for the ggF production of two Higgs bosons with effective BSM couplings. ... 50
2.26 Density plots of m_{HH} for all EFT BM scenarios that are listed in Table 2.10. The distributions are obtained by reweighting MC samples that are simulated at LO or at NLO in pQCD. No NLO corrections are applied to distributions extracted from the LO samples. Grid lines are spaced by the same amount in all plots. ... 53
2.27 Density plots of m_{HH} for the intended 56 scan points of c_2 (solid lines) between -2 (yellow, for reference) and $+3$, plus another scenario for κ_t–c_2 scan (dashed line). All other couplings not explicated in the legend are set to their SM values. Colored lines highlight the chosen points used in the c_2 scan. The corresponding BSM cross sections are quoted in parentheses as multiple of the SM cross section, both computed at NLO accuracy in pQCD using Eq. (2.29). The distributions are obtained by reweighting SM MC samples that are simulated at NLO in pQCD. ... 57

2.28 Density plots of m_{HH} (a) and $|\cos\theta^*|$ (b) for various coupling values in VBF HH production. SM values are assumed for all couplings not explicitly shown in the legend. The distributions are extracted from corresponding MC samples that are simulated at LO. The corresponding BSM cross sections are quoted in parentheses as multiple of the SM cross section, both estimated from the MC samples. 58
2.29 Feynman diagram for ggF production of an intermediate resonance X and its subsequent decay into two SM-like Higgs bosons. 59
2.30 Schematic of the original RS model. 60
2.31 Theoretical HH production cross section at $13\,\mathrm{TeV}$ via radions (blue line) and gravitons (orange line) as a function of mass m_X of the resonance as they appear in the bulk RS model [221]. Symbol $\tilde{k}$ stands for $k/\overline{\Lambda}_{\mathrm{Planck}}$, where $\overline{\Lambda}_{\mathrm{Planck}} = \Lambda_{\mathrm{Planck}}/\sqrt{8\pi} \approx 2.4 \times 10^{18}$ GeV denotes the reduced Planck scale. The shaded bands cover QCD scale and PDF uncertainties, which are added in quadrature. HH production cross section increases with $1/\Lambda_{\mathrm{IR}}^2$ in case of radions and with $\tilde{k}^2$ in case of gravitons. 61
2.32 Angular distribution of spin-0 (blue) and spin-2 (orange) resonances produced via ggF that subsequently decay into a pair of Higgs bosons at polar angle θ^* in the rest frame of the resonance. The distributions extracted from LO MC samples (solid histogram) are compared to shapes as predicted by theory (dashed curve). 62
2.33 Branching ratios of Higgs boson pair decays. Inputs are taken from [50]. Cells marked with a green tick symbol (✓) indicate the decay modes for which there are published analysis results based on LHC Run 2 data. Multilepton decay modes are highlighted with blue cell borders. Dashed cell borders indicate that the decay mode is technically included in the signal hypothesis but the analysis was not optimized for those events. 63
3.1 Schematic of the CERN accelerator complex at the tail end of the LHC Run 2 operations in 2018 [253]. Each accelerator system in the plot is labeled by its name, date of commission and, in case circular accelerators, its circumference. Injection paths from one system to another are shown with arrows, the color of which tells the type of particle that is transferred, as indicated by the legend. 67
3.2 PU profile in LHC Run 2 data broken down by data-taking years [256]. 69
3.3 Long-term schedule of the LHC program. The plot shows c.o.m energy $\sqrt{s}$ (blue line), peak instantaneous luminosity $\mathcal{L}_{\mathrm{inst}}$ (red circles) and accumulated integrated luminosity L (solid green areas) of pp collisions delivered by the LHC in each data-taking year or projected period. The projections are based on Refs. [177, 257]. 70
3.4 Cutaway view of the CMS detector [19]. 71
3.5 Transverse view of one of the twelve azimuthal sectors of the CMS detector at its center point facing in the direction of Beam 2. The sketch demonstrates how different particles interact with various parts of the detector [259]. 72
3.6 (a): Coordinate systems parametrizing three-momentum (shown in red), viewed from the ground surface inside the LHC ring. The Cartesian projections are shown in orange, while the default CMS coordinates are shown in green. (b): A selection of values for pseudorapidity η and corresponding polar angle θ. 73

3.7 Longitudinal view of a quadrant of the CMS detector that highlights the following subdetectors and structural elements [260]: tracker (green); ECAL (white) split between barrel (EB) and endcap (EE) regions; HCAL (yellow) in barrel (HB), endcap (HE) and forward (HE) regions; muon detectors (blue) in barrel (MB) and endcap (ME) regions, interleaved with the steel yoke (YB and YE, in gray). Muon detectors are segmented into five „wheels" in the barrel region or into two „rings" in the endcap region (both enumerated by the first number), and into four „stations" in both MB and ME (indicated by the second number). Magnetic field generated by the solenoid (CB) points from left to right. 74

3.8 Layout of one quadrant of the pixel detector before the Phase 1 upgrade (below) and after the upgrade (above) in longitudinal view [262]. 75

3.9 Longitudinal view of the CMS tracker, including its pixel detector before the Phase 1 upgrade [263]. Silicon strips shown by thin black (thick blue) lines provide measurement in two (three) coordinates, which is achieved with a single (double) layer of silicon strip modules. The pixel detector, which is indicated by thick red lines, also measures coordinates in three dimensions in each layer. 76

3.10 Layout of the CMS ECAL [19]: the EB (green) consisting of two sets of 18 supermodules, two „Dees" on either side of the EE (blue) and the ES (red) in front of them. 77

3.11 Segmentation of the CMS HCAL [19]. The outer numbers (1–29) enumerate the η towers, while the inner numbers (0–16 in HB, 0–17 in HE) count the layers in a calorimeter tower. The different colors represent a group of scintillator units that can be read out and calibrated separately (before the Phase 1 upgrade). 79

3.12 Elements of the muon system. (a): Layout of DT chambers in the muon barrel system. (b): A DT cell with its anode wire and surrounding electrode strips on each side of the cell that shape the electric field inside of it. (c): Cutaway sketch of a CSC sector. Figures (a) and (b) were taken from Ref. [260], while (c) was obtained from Ref. [19]. 81

4.1 Schematic for factorized application of JECs to jets that are reconstructed in data and simulated MC events. RC (random cone) and MJB (multijet balance) refer to specific jet energy calibration methods. Image is adapted from Ref. [265]. 93

4.2 Illustrative density plot for jet energy response $\mathcal{R}$, which is defined as a ratio of reconstructed jet p_T over generator-level jet p_T. JES (dotted lines) determines the mean response, whereas JER (dashed lines) tells how the responses are spread around the mean. Either of those can be shifted up (blue lines) or down (red lines) within their designated uncertainties. Black line shows the nominal jet energy response after all JECs and smearing steps have been applied. 94

4.3 Visualization of lepton (red) and its associated jet (black) momenta. The relative lepton-to-jet p_T variable (green) is constructed by projecting lepton momentum onto a plane that is perpendicular to the lepton-subtracted jet momentum (blue). 103

4.4 Mechanics of the FF method demonstrated on single lepton (left), dilepton (middle) and triple lepton (right) final states. All fakeable leptons that pass the tight cuts („T") contribute to the SR (highlighted with a blue hatched pattern). However, if any of the fakeable leptons fail the tight cuts („F"), then they enter the fake AR (shaded in solid yellow) instead. Extrapolation of an event from the fake AR to the SR is indicated with a curved arrow, which is accompanied by a corresponding FF of the form $F_i \equiv f_i/(1-f_i)$, where f_i refers to the FR of some lepton i that failed the tight cuts. If more than one lepton fails the tight cuts, then the final event weight is given by the product of the corresponding FFs. An extra minus sign is assigned to the event weight if an even number of fakeable leptons fail the tight cuts, which prevents the fake background to be overestimated in the SR. 105

4.5 Venn diagram showing how events with prompt (dots) and nonprompt (hatched area) in single lepton final states could populate the fake AR (pink) and the SR (green), and how the corresponding prompt ID efficiencies (ε) and FRs (f) are inferred from those event counts. 105

5.1 The decision process for categorizing the MC events based on generator-level matching. 116

5.2 Distribution of data and MC events in the SR and fake AR based on the status of final state objects. Reducible fake background approximates the contribution from nonprompt final states to the SR. Data-driven fake background is obtained by reweighting data events and prompt MC events in the fake AR by the FF method, and subtracting the latter from the former in order to not overestimate prompt contributions to the SR. 126

5.3 Distributions in m_T^{fix} for barrel muons with cone-p_T between 32 and 45 GeV in the fail region (a) and pass region (b), both based on data recorded in 2018. Distributions shown in the pass region are obtained from ML fit to data. The label „electroweak" refers to the sum of W+jets and DY events, which are scaled by a common factor in the fit. 130

5.4 Data-driven muon and electron FRs in barrel and endcap regions for the $\mathrm{t\bar{t}H}$ and HH multilepton analyses in each of the three data-taking years as a function of cone-p_T. 131

5.5 Jet-to-τ_{h} FRs measured in $\mathrm{t\bar{t}}$ CR for the $\mathrm{t\bar{t}H}$ analysis in barrel and endcap regions: for τ_{h} passing the Loose WP of $D_{\text{jet}}^{\tau_{\mathrm{h}}}$ and double-τ_{h} trigger (a)–(b); for τ_{h} passing the Medium WP of $D_{\text{jet}}^{\tau_{\mathrm{h}}}$, failing (c)–(d) or passing (e)–(f) lepton-plus-τ_{h} cross-trigger, and without any trigger requirements (g)–(h); for τ_{h} passing the VLoose WP of $D_{\text{jet}}^{\tau_{\mathrm{h}}}$ and without any trigger requirements (i)–(j); for τ_{h} passing the VTight WP of $D_{\text{jet}}^{\tau_{\mathrm{h}}}$ and without any trigger requirements (k)–(l). Top section in each plot displays the MC-driven FRs, while the bottom section shows the respective data-to-MC SFs. 134

5.6 Jet-to-τ_{h} FRs measured in DY CR for the HH analysis in barrel and endcap regions split by year for τ_{h} passing the Medium WP of $D_{\text{jet}}^{\tau_{\mathrm{h}}}$, passing or failing double-τ_{h} trigger (a)–(d) and lepton-plus-τ_{h} cross-trigger (e)–(h), and without any trigger requirements (i)–(j). Top section of each plot displays the MC-driven FRs, while the bottom section shows the respective data-to-MC SFs. 135

5.7 (a): Visualization of covariance matrix Σ that is estimated for parameters $\mathbf{c} = (c_0, c_1)^T$ of the fit. The ellipsoidal contour corresponds to the parameter values where $D_M(\mathbf{c}) = 1$. Projections of the ellipse in parameter space coincide with their uncertainties, which can also be expressed as square root of the diagonal elements of Σ. Decorrelated variations of the best fit parameters are obtained by projecting out either axis of the ellipse, or equivalently the components of either eigenvector of the covariance matrix times the square root of the respective eigenvalue. (b): Data-to-MC SFs of jet-to-τ_{h} FRs for the Medium WP of $D_{\mathrm{jet}}^{\tau_{\mathrm{h}}}$ extracted from $\mathrm{t\bar{t}}$ CR and parametrized by p_T of the fake τ_{h} candidate based on data collected in 2017. The SFs (points) are regressed with a linear function, which is plotted for the optimal choice of parameter values returned by the fit (red line), as well as for decorrelated variations of said parameters (dashed lines). Vertical error bars represent statistical uncertainties in data and MC added in quadrature. 137

5.8 Distribution in the output of signal extraction discriminant for the $1\ell + 2\tau_{\mathrm{h}}$ channel in the $\mathrm{t\bar{t}H}$ analysis based on 2018 data comparing MC fakes to MC closure for τ_{h} (a), and data fakes to its linear shape modulation (b). Vertical blue dashed line denotes the average output score of MC fakes in both plots. Solid black line in the ratio plot of (a) was obtained from a linear regression to the ratio of bin-by-bin yields in MC fakes to MC closure. The corresponding slope is then used to linearly modulate the output distribution of data fakes as shown in (b). Normalization uncertainty is extracted from the intercept of the solid black line in the ratio plot of (a) at a point where it crosses the blue vertical dashed line. Statistical uncertainties on MC yields are incorporated to the linear fit with weighted least squares method. 139

5.9 Post-fit distributions in invariant dielectron mass reconstructed from measured SS (a) and OS (b) pairs of electrons in DY CR based on data recorded in 2016. One of the electrons is reconstructed within the acceptance of EB and has a $p_T > 50\,\mathrm{GeV}$, while the other electron is reconstructed outside of this acceptance and has a p_T between 25 and $50\,\mathrm{GeV}$. The shaded band in both plots represents statistical uncertainties on the MC prediction. 142

6.1 Illustration of Neyman construction. For each POI μ there exists a pdf $f(t_\mu|\mu)$ of test statistic $t_\mu(x)$, which is drawn for a number of experiments x. By specifying α as the CL, one can work out interval $I(\mu)$ for every μ, which is supposed to capture the test statistic with probability α in repeated experiments. The true value of the POI should lie inside the confidence belt at probability α, which is formed by evaluating $I(\mu)$ over some range of μ values. CI is defined from the sections of the confidence belt that feature the realized experimental value $t_\mu(x_{\mathrm{obs}})$, which is given by interval $[\mu^-, \mu^+]$ in the picture. A version of this image can be found in Ref. [367]. 145

6.2 Distributions of test statistic t_μ for signal-plus-background hypothesis H_1 (blue curve) and for background-only hypothesis H_0 (red curve) on the left hand side, and how a p-value, such as p_1, can be translated to equivalent significance level Z based on single tail probability of standard Gaussian distribution as shown on the right hand side. In this example H_1 is chosen as the null hypothesis and H_0 as the alternative hypothesis, which means that p_1 and p_0 are respectively identified as type-I and type-II errors in the plot. 146

6.3 Distribution of goodness-of-fit test statistic in $t\bar{t}H$ (a) and SM HH (b) analysis. 157

6.4 Leading pulls and impacts of NPs obtained for every POI that is extracted from the $t\bar{t}H$ analysis. Statistical bin-by-bin uncertainties are omitted for the sake of clarity. 158

6.5 Leading pulls and impacts of NPs obtained for the signal rate in the HH analysis. Statistical bin-by-bin uncertainties are omitted for the sake of clarity. 159

6.6 Demonstration of bias-variance tradeoff. With every training cycle, the model becomes more complex, bias decreases alongside with the training error, but variance increases. The training has reached optimal state once the sum of bias and variance has plateaued. This is gauged with validation error, which loosely tracks this sum. 162

6.7 Schematic of how datasets are partitioned for training, validation and inference applications in the $t\bar{t}H$ analysis (to the left of vertical dashed line) and in the HH analysis (to the right of the dashed vertical line). In the $t\bar{t}H$ analysis there is just one trained model per channel, whereas in the HH analysis there are six trained models per channel. This is because there are three models trained on odd events, with one to distinguish nonresonant signal and the other two to recognize resonant spin-0 and spin-2 signal, and another three models, which were trained for the same purpose but on even events. As explained later, it hence implies that the models are not targeting one particular signal hypothesis but instead trying to learn all of them at once. Sensitivity to particular signal hypothesis is restored by passing the parameter that tells the different signal hypotheses apart as input to the training. These parameters are one-hot encoded JHEP04 BMs in the nonresonant case, and mass of the unknown resonance in the resonant case. To boost the performance, background events are duplicated for every parameter value for which there are signal samples present in the training. 163

6.8 One of the 496 decision trees in the BDT that was trained to distinguish nonresonant HH signal from other processes in $2\ell\text{SS}+\leqslant 1\tau_\text{h}$ channel. The BDT was trained on events with even event numbers. Symbols ℓ_1 and ℓ_2 refer to leading and subleading leptons, respectively. 166

6.9 Schematic for the strategy of parametrized BDT training, which was followed in nonresonant as well as in the resonant HH analysis. All events used for the training must be labeled by signal parameter θ_i, which could either be a JHEP04 BM if the training is performed for nonresonant analysis, or m_{HH} if the training is performed for resonant analysis. In practice, the BMs in nonresonant BDT are encoded by 13 exclusive boolean flags of which one is set to true, whereas m_{HH} of resonant training is represented by a single floating point variable. They are always supplied regardless of how they would rank among other training variables in terms of feature importance. The BDT output tells on a scale from 0 to 1 how likely it is that a given event came from the HH signal process. 168

6.10 (a): Visual representation of perceptron given by Eq. (6.16). It serves as a prototype for neurons in neural networks. (b): DNN with n input features, two hidden layers containing m neurons each, and a final output layer returning probabilities for each of the k output classes. Arrows point in the direction of feedforward propagation. Overfitting is mitigated with dropout, which randomly turns off neurons in the hidden layers at every feedforward pass. In this particular instance the dead neurons are indicated by a pink dashed border. Image courtesy of I. Neutelings. 170

6.11 Demonstration of how an n-particle LIPS element with incoming 4-momentum $\hat{P}$ and outgoing 4-momenta $\{\hat{p}_i\}_{i=1}^n$ can be partitioned into a j-particle and an $(n-j+1)$-particle LIPS element by marginalizing over the 4-momentum $\hat{q}$ of some intermediate particle: $d\Pi_n(\hat{P};\hat{p}_1,\ldots,\hat{p}_n) = d\Pi_j(\hat{q};\hat{p}_1,\ldots,\hat{p}_j)\times d\Pi_{n-j+1}(\hat{P};\hat{q},\hat{p}_{j+1},\ldots,\hat{p}_n)\times(2\pi)^3 d\hat{q}^2$. The intermediate 4-momentum can be integrated out with Breit-Wigner trick, whereby Breit-Wigner propagator given by Eq. (2.22) and its inverse, $\frac{\pi}{m_X\Gamma_X}\delta^2(\hat{q}^2-m_X^2)$, are inserted under the integral, effectively forcing the particle to its on-shell mass m_X: $\int d\hat{q}^2 = \pi m_X\Gamma_X$. 176

7.1 History of searches of $\text{t}\bar{\text{t}}\text{H}$ production at the LHC. The graphic also depicts milestones in the measurement of $\text{H}\to\tau\tau$ decay, as this process is particularly relevant to $\text{t}\bar{\text{t}}\text{H}$ multilepton analysis presented here. The analysis presented here is highlighted with a purple box that has a solid edge. Previous iteration of the same analysis is enclosed by a dotted line in the plot. Contributions from Higgs boson decay modes other than those indicated in the plot are found to be negligible. 183

7.2 Signal composition in each of the ten channels in the $\text{t}\bar{\text{t}}\text{H}$ analysis. Contributions from $\text{t}\bar{\text{t}}\text{H}(\to \text{b}\bar{\text{b}})$ process are found to make up less than 5% of total signal in the $0\ell+2\tau_{\text{h}}$ and $1\ell+1\tau_{\text{h}}$ channels. The signal fractions are determined from simulated pre-fit yields after the event selection. The solid black line represents the signal contribution of that channel relative to total signal yield of the analysis, while the dotted line displays the ratio of total signal yield relative to the square root of total background yield as an approximate measure of sensitivity of that channel. 186

7.3 Post-fit distributions in the output of the DNN that was trained for the 2ℓSS channel. Events selected in the SR of the 2ℓSS channel are subsequently classified as $t\bar{t}H$ (a), tHq (b), $t\bar{t}W$ (c), or as other background (d) based on whichever output node had the highest DNN score. They are further categorized as ee, eμ or $\mu\mu$ based on the flavor of the selected two leptons. The bins are sorted by the DNN output score in ascending order per DNN output node. The same plots are also published in Ref. [1]. 193

7.4 Post-fit distributions in the output of DNN that was trained for the $2\ell\text{SS} + 1\tau_\text{h}$ channel (a), and for the 3ℓ channel, with events selected in the SR of the 3ℓ channel further classified as $t\bar{t}H$ (b), tH (c) or as background (d) based on whichever output node had the highest DNN score. Events selected in 3ℓ SR are further categorized depending on whether they feature at least two b jets passing the medium WP of DeepJet ID („bt") or not („bl"). Events in the background node of the 3ℓ channel are additionally distinguished based on the flavor of the three leptons that are selected to the final state. The bins in each DNN output node are sorted by the DNN output score in ascending order. The same plots are also published in Ref. [1]. 194

7.5 Post-fit distributions in the BDT output of the most sensitive channels featuring at least on τ_h in the final state: $2\ell\text{OS} + 1\tau_\text{h}$ (a), $1\ell + 2\tau_\text{h}$ (b), and $3\ell + 1\tau_\text{h}$ (c). Bins in the distribution of $3\ell + 1\tau_\text{h}$ BDT are sorted by the respective output score in increasing order. The same plots are also published in Ref. [1]. 195

7.6 Post-fit distributions in the BDT output of least sensitive channels: $0\ell + 2\tau_\text{h}$ (a), $1\ell + 1\tau_\text{h}$ (b),$2\ell + 2\tau_\text{h}$ (c), and 4ℓ (d). The bins in the distributions of $2\ell + 2\tau_\text{h}$ and 4ℓ BDTs are sorted by the respective BDT output score in increasing order. The same plots are also published in Ref. [1]. 196

7.7 Post-fit distributions in 3ℓ CR (a) and 4ℓ CR (b). The distribution in 3ℓ CR consists of four categories by lepton flavor that each is made of 12 bins, each of which is grouped into three subcategories of four bins based on the multiplicity of b jets. In each group of four bins, a higher bin index is assigned to those events that feature a higher number of central jets. The leftmost bin of the distribution in 4ℓ CR corresponds to the case where the two SFOS lepton pairs are both compatible with the Z boson mass; the remaining bins correspond to the case where the final state features only one SFOS lepton pair and either 0, 1 or > 1 b jets passing the medium WP of DeepJet ID. The same plots are also published in Ref. [1]. 197

7.8 Production rates and corresponding CIs of $t\bar{t}H$ (a) and tH (b) processes in individual analysis channels and for their combination at 68% CL. Black vertical lines with green and yellow bands represent the SM expected value with its 68 and 95% CLs error bands as estimated from the Asimov dataset. The signal rate in the $2\ell + 2\tau_\text{h}$ channel has been restricted to be nonnegative values to avoid numerical issues in the ML fit that arise from the lack of data events in that channel. Only three channels are presented in (b) due to lack of sensitivity for tH production in other channels. The same plots are also published in Ref. [1]. 198

7.9 Correlation matrix of POIs obtained from the ML fit. 199

7.10 Simultaneous likelihood scans of two POIs: $\mu_{t\bar{t}H}$–μ_{tH} (a), $\mu_{t\bar{t}H}$–$\mu_{t\bar{t}W}$ (b), $\mu_{t\bar{t}H}$–$\mu_{t\bar{t}Z}$ (c), and $\mu_{t\bar{t}Z}$–$\mu_{t\bar{t}W}$ (d). Each plots shows the best fit value (black dot) with all other POIs profiled and their confidence contours at 68 and 95% CL (solid and dashed line), all extracted from the real data. Values predicted by the SM are marked with a red cross. The same plots are also published in Ref. [1]. 200

7.11 Likelihood scan of κ_t with κ_V profiled (a) and two-dimensional scan of κ_V and κ_t (a). In one-dimensional κ_t scan, both the observed and expected negative log-likelihoods are shown, whereas the two-dimensional plot provides contours for 68 and 95% CL (solid and dashed line), including the best fit value extracted from the real data (dot) and the SM prediction (cross). The same plots are also published in Ref. [1]. 201

7.12 Post-fit distribution in MEM LR of the $2\ell\text{SS} + 1\tau_h$ channel that was developed for the CA. The MEM LR is derived for the „missing jet" regime (a) and for the case where each parton-level quark in final state could be assigned a reconstructed jet (b). 202

8.1 Composition of SM signal in each of the seven channels in the HH analysis. The signal fractions are extracted from simulated SM pre-fit yields after the event selection. The solid black line represents the signal contribution of that channel relative to the total signal yield of the analysis. The dotted black line indicates S/B of that channel in percentages. 207

8.2 Post-fit distributions in the output of BDTs that were trained to recognize nonresonant HH signal in JHEP04BM7 coupling configuration in $2\ell\text{SS}+\leqslant 1\tau_h$ (a), 3ℓ (b) and 4ℓ (c) final states. The distributions are presented such that more signal-like events are more likely to occupy rightmost bins. The SM HH signal displayed in the plot is scaled by a factor of 30 for better visibility, effectively normalizing HH production cross section to $1\,\text{pb}$. The uncertainty is obtained from ML fit, and it includes both systematic and statistical components. No data was found in the three rightmost bins of the BDT distribution in the 4ℓ channel. The same plots are also published in Ref. [2]. 216

8.3 Post-fit distributions in the output of BDTs that were trained to recognize nonresonant HH signal in JHEP04BM7 coupling configuration in $3\ell + 1\tau_h$ (a), $2\ell + 2\tau_h$ (b), $1\ell + 3\tau_h$ (c) and $0\ell + 4\tau_h$ (d) final states. The distributions are presented such that more signal-like events are more likely to occupy rightmost bins. The SM HH signal displayed in the plot is scaled by a factor of 30 for better visibility, effectively normalizing HH production cross section to $1\,\text{pb}$. The uncertainty is obtained from ML fit, and it includes both systematic and statistical components. No data was found in the two middle bins of the BDT distribution in the $1\ell + 3\tau_h$ channel, and in all bins but the first bin of the BDT distribution in the $0\ell + 4\tau_h$ channel. The same plots are also published in Ref. [2]. 217

8.4 Post-fit distributions in the kinematic observables that were utilized as signal extraction variables in 3ℓ CR (a) and in 4ℓ CR (b). The variable plotted for 3ℓ CR is the transverse mass given by Eq. (4.1) of the lepton that is not associated with the resonant peak in Z boson mass. The shape variable chosen for signal extraction in 4ℓ CR is computed as the invariant mass of the four leading leptons in the final state. No HH signal is displayed here due to lack thereof. The uncertainty is obtained from ML fit, and it includes both systematic and statistical components. The same plots are also published in Ref. [2]. 218

8.5 Asymptotic observed and expected upper limits on inclusive SM HH production cross section rate at 95% CL, obtained for each of the seven analysis channels and for their combination. The upper limits were extracted from the BDT output that corresponds to the SM scenario. The same plot is also published in Ref. [2]. 219

8.6 Asymptotic observed and expected upper limits on inclusive nonresonant HH production cross section via ggF for the twelve (plus one) JHEP03 EFT BMs, for the seven JHEP04 EFT BMs and for the SM at 95% CL, shown for the combination of all analysis channels (a) and for individual channels (b). The same plots are also published in Ref. [2]. 220

8.7 Asymptotic observed and expected upper limits on inclusive nonresonant HH production cross section as a function κ_λ at 95% CL, obtained for the combination of all analysis channels (a) and for each channel separately (b). All other couplings remain at their designated SM values in the scan. The red curve in (a) directly follows the sum of ggF and VBF HH curves of Figure 2.24(b). The upper limit on κ_λ constrain it to $[-6.9, +11.1]$, while expecting $[-6.9, +11.7]$. The same plots are also published in Ref. [2]. 221

8.8 Asymptotic observed and expected upper limits on inclusive nonresonant HH production cross section as a function κ_{2V} (a) and c_2 (b) at 95% CL. The red curve in (a) directly follows the VBF HH curve of Figure 2.24(b). Based on the upper limits, κ_{2V} is constrained to $[-3.4, +5.5]$ (while expecting $[-2.6, +4.7]$), whereas c_2 is confined to $[-1.05, +1.48]$ (while expecting $[-0.96, +1.37]$). The same plots are also published in Ref. [2]. 221

8.9 Two-dimensional asymptotic observed and expected exclusion limits on inclusive nonresonant HH production cross section in κ_t-c_2 (a), κ_t-κ_λ (b) and κ_λ-c_2 (c) planes. The fain dotted lines represent isocontours of theoretical cross section. The same plots are also published in Ref. [2]. 222

8.10 Asymptotic observed (blue hatch) and expected (black hatch) upper limits on inclusive SM HH production cross section at 95% CL (a), and best fit value (black point) with corresponding CIs at 68% CL (solid line) for κ_λ (b) and κ_{2V} (c), all extracted from the ML fits of the latest HH analyses published by the CMS collaboration [466]. 223

8.11 Post-fit distributions in the output of BDTs in the 3ℓ channel that were trained to recognize HH resonances from spin-0 ((a) and (c)) and spin-2 ((b) and (d)) particles with invariant masses of $300\,\text{GeV}$ ((a) and (b)) and $750\,\text{GeV}$ ((c) and (d)) each. Cross section of HH production via the intermediate resonance is normalized to $1\,\text{pb}$. The same plots are also published in Ref. [2] as supplementary material. 225

8.12 Asymptotic observed and expected upper limits on resonant HH production cross section at 95% CL via the decay of spin-0 and spin-2 resonances for a range of resonant mass points between $250\,\text{GeV}$ and $1\,\text{TeV}$, obtained for the combination of all analysis channels in (a) and (c), and for per individual analysis channel in (b) and (d). The same plots are also published in Ref. [2]. 226
8.13 Comparison of observed and expected upper limits on resonant HH production cross section via spin-0 (a) and spin-2 (b) resonances at 95% CL between various HH analyses published by the CMS collaboration. The results of this analysis are shown in magenta. Both plots were published by Higgs Physics Analysis Group of CMS collaboration on their web site [466]. 226

List of Tables

2.1 List of SM bosons, their spin, eigenvalues of weak isospin T_3, weak hypercharge Y and electric charge Q, and mass m with 1σ experimental uncertainty. The masses are taken from Particle Data Group (PDG) [24]..... 16

2.2 List of SM up- and down-type leptons (first two rows) and quarks (last two rows), their eigenvalues of weak isospin T_3, weak hypercharge Y and electric charge Q, and mass m. The weak isospin and hypercharge values are listed for left (L) and right (R) chirality separately. The masses are quoted from Ref. [24] (PDG) for each of the three generations. All quark masses are given in $\overline{\text{MS}}$ scheme, except for the top quark mass that is directly measured from data. The cross mark (✗) indicates that the particles (right-handed neutrinos in this case) do not exist in given representation. The signs of all charges are flipped for anti-fermions..... 16

2.3 Measured leptonic and hadronic branching ratios (BRs) of W, Z and τ lepton [24]. 27

2.4 Common τ_{h} decay modes and corresponding BRs [24]. The BRs are quoted with respect to the decay width of τ_{h}. Dominant final state of each exclusive decay mode, primary resonance and the full BR of the final state are shown separately on indented lines. 28

2.5 Branching ratios of the Higgs boson at mass $m_{\text{H}} = 125\,\text{GeV}$ as predicted by the SM [50]. Uncertainties on the BRs are obtained by adding theoretical uncertainties and parametric uncertainties resulting from heavy quark masses and strong coupling α_{S} in quadrature. Theoretical uncertainties reflect the omission of higher order corrections in the corresponding MEs. 31

2.6 Cross sections of processes that produce a single Higgs boson with mass $m_{\text{H}} = 125\,\text{GeV}$ at c.o.m energy of $13\,\text{TeV}$ at the LHC [50, 142]. The PDF and α_{S} uncertainties are computed as recommended by the PDF4LHC working group [79]. The QCD scale uncertainties are due to missing higher orders in perturbation theory. All cross sections are computed in 5FS, except for the cross section of $\text{b}\bar{\text{b}}\text{H}$ that is obtained from matching 4FS (NLO in pQCD) and 5FS (NNLO in pQCD) calculations. Cross sections of $\text{t}\bar{\text{t}}\text{H}$, tH and $\text{t}\bar{\text{t}}\text{VH}$ are computed to NLO in pQCD; VBF and VH to NNLO in pQCD; ggF to N^3LO in pQCD. Cross sections of all processes but tH and $\text{b}\bar{\text{b}}\text{H}$ include additional NLO EW corrections. The uncertainties on $\text{b}\bar{\text{b}}\text{H}$ cross section are added in quadrature. Symbol ✗ means that the uncertainty is not available. 34

2.7 Observed 1σ constraints on κ_{t} and κ_{W} coupling modifiers, while assuming no BSM interactions with the Higgs boson. 44

2.8 Summary of the latest dedicated $\text{t}\bar{\text{t}}\text{H}$ analyses performed by the ATLAS and CMS collaborations on LHC Run 2 data. Signal strength μ of $\text{t}\bar{\text{t}}\text{H}$ production rate is quoted with the corresponding observed (expected) significance. .. 45

2.9 Cross section of dominant processes that produce two on-shell Higgs bosons with mass $m_{\text{H}} = 125\,\text{GeV}$ at $\sqrt{s} = 13\,\text{TeV}$ at the LHC. Cross section of the ggF process is computed to NNLO in pQCD using heavy top limit approximation [175]. The last column indicates the uncertainty that captures the effects of the top mass scheme, which is the leading source of uncertainty in this estimate. Cross section of the VBF HH process is calculated to the full N^3LO accuracy in pQCD and hence does not feature the uncertainty that is associated with the top mass approximation [181]. . 48

2.10 EFT shape BMs in terms of five couplings (κ_λ, κ_t, c_2, c_g, c_{2g}) that were developed to study BSM effects in ggF HH signal. Second middle horizontal line separates older BMs derived in LO theory, which were subsequently published in JHEP 04 journal [182], from those later found in NLO pQCD theory and then released in JHEP 03 publication [189]. The only exception is JHEP04BM8a, which was proposed in Ref. [187]. The second-to-last column quotes the ratio of the corresponding cross section to the SM cross section, both computed at NLO in pQCD. The last column lists NLO-to-LO k-factors computed with Eqs. (2.28) and (2.29), where the LO cross section coefficients are taken from [182] and the NLO coefficients from Table 2.11, while assuming $\sigma_{\text{ggF}}^{\text{SM,LO}} = 19.85\,\text{fb}$ [187]. 52

2.11 Cross section coefficients in Eq. (2.29) that parametrize inclusive ggF HH cross section at NLO in pQCD. 56

2.12 Summary of the latest HH analyses performed by the ATLAS and CMS collaborations on LHC Run 2 data. Mass ranges of the unknown resonance are given in the units of GeV. Last two columns quote observed and expected upper limits on HH production cross section in the units of SM cross section and constraints on various couplings based upper limits at 95% CL. Expected limits are given in parentheses. The combination of ATLAS results considers single Higgs boson channels plus three HH channels (which are marked with a black triangle, ▲), while the combination of CMS results includes only five HH channels (which are marked with a black bullet, ●). 65

3.1 A selection of parameters characterizing the LHC machine during its Run 2 operations. Parameters marked with a dagger (†) indicate their peak values. If the parameter changed between the data-taking years, a range is shown instead. 69

3.2 List of the HLT paths used in the current work. Only the p_T thresholds applied to the trigger objects are shown (in units of GeV). A combination of multiple HLT paths with different p_T thresholds was employed, either to combat higher instantaneous luminosity conditions or to take advantage of other looser selection criteria of the trigger (not shown in the table). These are also the main reasons for prescaling the triggers, since the trigger rates would otherwise be too high for data recording. Prescaled triggers are marked with a dagger (†) in the table. Different p_T thresholds on the leading, subleading and third objects are delimited by a comma. This nomenclature refers to the ranking of objects after they have been sorted by their p_T in descending order. 83

3.3 Amount of pp collision data recorded by the CMS detector in 2016 [274], 2017 [275] and 2018 [276] data-taking years when the detector was fully operational. Integrated luminosities and corresponding uncertainties that are given in parentheses refer to a preliminary recommendation that was based on the initial luminosity measurement on data collected in 2016 [277] and was later revised in Ref. [274]. Breakdown of correlated uncertainties between individual years and by systematic sources is not shown. 85

4.1 WPs of the DeepTau ID discriminant, corresponding τ_{h} identification efficiencies and approximate misidentification rates for low-p_T τ_{h} candidates, both expressed in terms of percentages [301]. Identification efficiencies are extracted from simulated H $\to \tau\tau$ events. The misidentification rates for $D_{\mathrm{jet}}^{\tau_{\mathrm{h}}}$ are obtained from simulated W+jets and $\mathrm{t\bar{t}}$ events, and from simulated DY events for $D_{\mathrm{e}}^{\tau_{\mathrm{h}}}$ and $D_{\mu}^{\tau_{\mathrm{h}}}$. Jets from W+jets sample tend to pass as genuine τ_{h} more frequently than jets from $\mathrm{t\bar{t}}$ sample for the same WP. The WPs are referred to by labels given in columns. The letter „V" in WP names stands for „very", *e.g.*, VVLoose reads as „very very loose". A cross mark (✗) means that the WP is not defined for a given label. 96

4.2 Tiered selection criteria for muons (top section) and electrons (bottom section). Tick (cross) mark indicates that the cut is (not) applied. Left arrow (←) means that the cut from the previous tier is imposed. The sliding cut on DeepJet score of the nearby jet that is associated with a fakeable muon is defined as linear interpolation from medium WP at cone-p_T of $20\,\mathrm{GeV}$ to loose WP at cone-p_T of $45\,\mathrm{GeV}$. 108

5.1 List of MC samples for single and double Higgs boson production processes that are generated for estimating signal and background contributions. The corresponding cross sections with appropriate uncertainties are detailed in Tables 2.6 and 2.9 and relevant BRs in Tables 2.3 and 2.5. The abbreviation „MG5@NLO" stands for MadGraph5_aMCatNLO. Processes that have (not) been marked with the „§" sign are produced in 4FS (5FS). Suffix „+j" in the names of LO processes indicates that the extra light quark and gluon jets are included in the ME. 113

5.2 List of MC samples that are generated for the purpose of estimating contributions from background processes and for developing systematic uncertainties on data-driven background yields. Cross sections σ correspond to $\sqrt{s} = 13\,\mathrm{TeV}$ at the LHC. If the cross section value is accompanied by asterisk (*), then the inclusive production cross section is quoted instead. The symbol ℓ stands for e, μ or τ in the above. MC generator MadGraph5_aMCatNLO is abbreviated as „MG5@NLO" in the table. Processes that have (not) been marked with the „§" sign are produced in 4FS (5FS). The cross section of processes with single top quark or anti-quark are summed if they contribute equally to the production. The relevant BRs can be found in Table 2.3. Suffix „+j" in the names of LO processes indicates that the extra light quark and gluon jets are included in the ME. 114

5.3 List of data-to-MC SFs that are applied in the presented analyses. Although not explicitly mentioned, the SFs are also extracted for each data-taking year separately. 119

5.4 Multiplicative corrections to DY normalization in bins of b tagged jet multiplicity of jets passing the DeepJet ID WPs in each data-taking year separately. The corrections were extracted from DY CR in dimuon final states. The total uncertainty on each SF has two components: the statistical uncertainty on the nominal corrections, and the absolute difference with respect to the nominal corrections that are extracted from the same CR but for dielectron final states. The two uncertainties are added in quadrature. 123

5.5 List of prescaled HLT paths employed in the FR measurement. First column details the minimum reconstructed p_T that is imposed to a lepton of particular flavor at the trigger level. The second column shows corresponding prescale factors f^{pre} in multiples of thousand that were typically applied over the three-year data-taking period. The third column provides a range in cone-p_T that events firing the trigger can contribute to. The last column is reserved for specifying the minimum p_T threshold of an extra jet. A cross mark (✗) is shown instead in case no jets are requested at the trigger level. 128

5.6 Application of jet-to-τ_{h} FRs based on the triggering conditions of the selected τ_{h} in $\text{t}\bar{\text{t}}\text{H}$ (top section) and HH (bottom section) analysis channels. A tick mark (✓) indicates that the designated FRs could be used in the analysis, whereas a cross mark (✗) implies otherwise. All other analysis channels that are not listed in the table but still require the presence of τ_{h} in the final state apply the FRs that were measured for τ_{h} without the imposition of any trigger conditions. Highest priority is given to the FRs that are measured without any requirements on the τ_{h} triggers, followed by those imposed by the lepton-plus-τ_{h} cross-triggers and the double-τ_{h} triggers. 133

5.7 Categorization of simulated events with an electron pair (left) and electron-muon pair (right) in final state to the SR, MC closure region for muons (MCμ) or electrons (MCe), as prompt MC (pMC) in the fake AR, or as MC fakes (MCf) in the SR of $2\ell\text{SS}(+1\tau_{\text{h}})$ analysis channel based on whether the selected lepton is prompt (P) or nonprompt (N), and whether the selected lepton passes the tight cuts (T) or fails them (F). For example, events with a prompt tight electron and a nonprompt fakeable muon that fails the tight cuts contribute to MC closure region for muons. A dash (—) is used if a given combination of leptons does not contribute to any of the aforementioned analysis regions. 138

5.8 Measured electron charge flip rates (in units of per mille) as a function of p_T and $|\eta|$ of the electron, data-taking year and tight lepton definition. ... 142

6.1 Systematic uncertainties of theoretical (top section) and experimental (middle section) origin, as well as statistical uncertainties (last row), all broken down by their scope, effect on normalization (N) or shape (S), correlation status, and relative contribution to full CI of the POIs in $\text{t}\bar{\text{t}}\text{H}$ ($\hat{\mu}_{\text{t}\bar{\text{t}}\text{H}}$, $\hat{\mu}_{\text{tH}}$, $\hat{\mu}_{\text{t}\bar{\text{t}}\text{W}}$, $\hat{\mu}_{\text{t}\bar{\text{t}}\text{Z}}$) and HH ($\hat{\mu}_{\text{HH}}$) analysis with all extracted from the real data under the SM hypothesis. The relative contributions to total uncertainty ($\delta\hat{\mu}$) are obtained by fixing the NPs to their post-fit values, profiling the rest, and subtracting in quadrature the resulting post-fit uncertainty ($\Delta\hat{\mu}'$) from the total post-fit uncertainty ($\Delta\hat{\mu}$) that was obtained for the standard case where all parameters in the fit were allowed to float: $\delta\hat{\mu} = \sqrt{1-(\Delta\hat{\mu}'/\Delta\hat{\mu})^2}$. When summed in quadrature, the relative contributions do not necessarily add up to 100% because of correlations between the NPs induced by the ML fit. Unless specified otherwise, the corresponding NPs are correlated between individual bins, signal and background processes, channels and data-taking years. The shape effects also entail changes in accepted event yields. Cross mark (✗) indicates that the NP was not used in that particular analysis. 150

6.2 The relevant test statistics that are used for deriving the final results. 156

7.1 Target decay modes of the $t\bar{t}H$ signal (top section) and the event selection criteria (bottom section) of the $t\bar{t}H$ analysis channels. The same Higgs boson decay modes that are assumed for $t\bar{t}H$ signal in $2\ell SS(+1\tau_h)$ and 3ℓ channels also apply to tH signal, where it is implied that the singular top quark decays leptonically. Requested number of fakeable leptons and τ_h is encoded in the channel name. In addition to the listed selection criteria, all selected events must also pass MET filters, loose dilepton mass veto and b jet selection requirement. A tick mark (✓) indicates that the selection criterion is enforced or applicable, whereas a cross mark (✗) implies the opposite. A dash (—) is used to denote that the cut is not tightened with respect to fakeable object definition as detailed in Section 4.2. Thresholds on the (cone-)p_T of leading, subleading, third and fourth physics objects are delimited by a forward slash. If there is a pair of thresholds separated by a comma, then the first value applies to muons and the second to electrons. Lower bounds on (cone-)p_T and E_T^{miss}LD are given in units of GeV. The same cuts are applied in the SRs, fake ARs and charge flip ARs, except for the charge sum requirement of leptons in the $2\ell SS$ and $2\ell SS + 1\tau_h$ channels, which is inverted into OS charge requirement in their respective charge flip ARs. 185

7.2 Event selection criteria for the CRs of the $t\bar{t}H$ analysis. Data-driven fake and flip backgrounds are estimated the same way in the CRs as they were in the SRs. Only the 3ℓ and 4ℓ CRs contribute to the ML fit from where the signal rates are extracted. 187

7.3 List of variables with corresponding ranking in terms of feature importance (top section) and hyperparameters (bottom section), which were used to train the DNNs for the $t\bar{t}H$ analysis. A range between highest and lowest ranking variable is provided features that include more than three variables. Unless specified otherwise, the jet-related variables are derived from the central AK4 jet collection. All lepton-related variables are computed using their cone-p_T as input. Symbol ℓ/τ_h stands for all muons, electrons and τ_h that are available in the final state. Cross mark (✗) means that the variable was not used in that particular training. 188

7.4 List of variables with corresponding ranking in terms of feature importance (top section) and hyperparameters (bottom section), which were used to train the BDTs for the $t\bar{t}H$ analysis. Unless specified otherwise, the jet-related variables are derived from central AK4 jet collection. All lepton-related variables are computed using their cone-p_T as input. Symbol ℓ/τ_h stands for all muons, electrons and τ_h that are available in final state. Cross mark (✗) means that the variable was not used in that particular training. . 189

7.5 Subcategorization of analysis channels and binning scheme of discriminating distributions in the $t\bar{t}H$ analysis. 190

7.6 Post-fit yields with corresponding statistical and systematical uncertainties in each of the ten analysis channels and in the two auxiliary CRs that help to constrain irreducible $t\bar{t}Z$ and diboson backgrounds. Symbol „—" is used if the process contributes by less than 0.1 events. 192

7.7 Observed (expected) signal rates of $t\bar{t}H$, tH, $t\bar{t}W(W)$ and $t\bar{t}Z$ processes in units of SM production cross section, and corresponding CIs at 68% CL broken down into statistical and systematical components. All POIs are extracted simultaneously from the ML fit of the main analysis. 199

7.8 Observed (expected) signal rates of $t\bar{t}H$, $t\bar{t}W(W)$ and $t\bar{t}Z$ processes in units of SM production cross section with corresponding CIs at 68% CL. All POIs are extracted simultaneously from the ML fit of the CA. 202
7.9 Observed and expected significances of $t\bar{t}H$ and tH production under background-only hypothesis in the main analysis as well as in the CA. The production rate of tH is fixed to SM in the CA. 202
8.1 Target decay modes of the HH signal (top section) and event selection criteria (bottom section) of the HH analysis channels. Requested number of fakeable leptons and τ_h is encoded in the channel name. All selected and vetoed tight τ_h are required to pass the Medium WP of DeepTau ID. In addition to the listed selection criteria, all selected events must also pass MET filters, loose dilepton mass veto and b jet veto requirements. A tick mark (✓) indicates that the selection criterion is enforced or applicable, whereas a cross mark (✗) implies the opposite. A dash (—) is used to denote that the cut is not tightened with respect to fakeable object definition as detailed in Section 4.2. Thresholds on the (cone-)p_T of leading, subleading, third and fourth physics objects are delimited by a forward slash. If there is a pair of thresholds separated by a comma, then the first value applies to muons and the second to electrons. Lower bounds on (cone-)p_T and E_T^{miss}LD are given in units of GeV. The same cuts are applied in the SRs, fake ARs and charge flip ARs, except for the charge sum requirement of leptons in the $2\ell\text{SS}+\leqslant 1\tau_h$ channel, which is inverted into OS charge requirement in the respective charge flip ARs. 209
8.2 BDT outputs that were chosen to extract limits for a given BM scenario or for a range of coupling values that were not considered in the BDT training. Limits for SM and JHEP03 BMs are extracted from the corresponding BDT output. 210
8.3 Condensed summary of training variables (top section) and hyperparameters (bottom section) of the BDTs that were trained for nonresonant/resonant spin-0/resonant spin-2 HH signal for each analysis channel. Generator-level m_{HH} (used in resonant training) as well as the one-hot encoded twelve JHEP04 BMs plus the SM BM (in nonresonant training) are excluded from the variable listing and count. A check mark (✓) tells that the variable was used in that particular training, whereas a cross mark (✗) indicates the opposite. The sum symbol represents pairwise combinations as well as combination of all visible objects in the final state. 211
8.4 Event selection criteria for the CRs of the HH analysis. Data-driven fake background is estimated the same way in the CRs as in the SRs. 213
8.5 List of coupling scenarios used for performing matrix-based reweighting in coupling scans. Like with the EFT BMs, shape templates for the chosen couplings are obtained through reweighting with Eq. (2.29) in bins of m_{HH} and $|\cos\theta^*|$. 214
8.6 Post-fit yields with corresponding statistical and systematical uncertainties in each of the seven analysis channels and in the two auxiliary CRs that help to constrain irreducible diboson backgrounds. The SM HH yields are normalized to an inclusive production cross section of about $1\,\text{pb}$ in the table. Symbol „—" is used if the process contributes by less than 0.1 events. 215

References

[1] CMS Collaboration, "Measurement of the Higgs boson production rate in association with top quarks in final states with electrons, muons, and hadronically decaying tau leptons at $\sqrt{s} = 13$ TeV," *Eur. Phys. J. C*, vol. 81, no. 4, p. 378, 2021. doi: 10.1140/epjc/s10052-021-09014-x. arXiv: 2011.03652 [hep-ex] [Cited on pages iv, 1, 37, 44, 45, 115, 182, 183, 193–198, 200, 201, 291, B].

[2] CMS Collaboration, "Search for Higgs boson pairs decaying to WW^*WW^*, $WW^*\tau\tau$, and $\tau\tau\tau\tau$ in proton-proton collisions at $\sqrt{s} = 13$ TeV," *JHEP*, vol. 07, p. 095, 2023. doi: 10.1007/JHEP07(2023)095. arXiv: 2206.10268 [hep-ex] [Cited on pages iv, v, 1, 65, 205, 216–222, 225, 226, 345, B].

[3] K. Ehatäht and C. Veelken, "Stitching Monte Carlo samples," *Eur. Phys. J. C*, vol. 82, no. 5, p. 484, 2022. doi: 10.1140/epjc/s10052-022-10407-9. arXiv: 2106.04360 [physics.data-an] [Cited on pages iv, 113, 413, B].

[4] K. Ehatäht and C. Veelken, "Application of the matrix element method to Higgs boson pair production in the channel $HH \to b\bar{b}WW^*$ at the LHC," *Nucl. Instrum. Meth. A*, vol. 1028, p. 166 373, 2022. doi: 10.1016/j.nima.2022.166373. arXiv: 2108.05267 [hep-ph] [Cited on pages iv, 175, 178, 431, B].

[5] CMS Collaboration, "Measurement of the associated production of a Higgs boson with a top quark pair in final states with electrons, muons and hadronically decaying τ leptons in data recorded in 2017 at $\sqrt{s} = 13$ TeV," 2018, [Available on CDS: CMS-PAS-HIG-18-019] [Cited on pages v, 155, 179, 182, 183, 191, 197].

[6] K. Ehatäht, CMS collaboration, "NANOAOD: a new compact event data format in CMS," *EPJ Web Conf.*, vol. 245, ed. by C. Doglioni, D. Kim, *et al.*, p. 06 002, 2020. doi: 10.1051/epjconf/202024506002 [Cited on pages v, 112, B].

[7] CMS Collaboration, "Search for HH production in the bbWW decay mode," 2023, [Available on CDS: CMS-PAS-HIG-21-005] [Cited on pages v, vi, 63, 65, 103, 219, 222, 224, 227].

[8] CMS Collaboration, "A portrait of the Higgs boson by the CMS experiment ten years after the discovery," *Nature*, vol. 607, no. 7917, pp. 60–68, 2022. doi: 10.1038/s41586-022-04892-x. arXiv: 2207.00043 [hep-ex] [Cited on pages v, vi, 37, 44–46, 58, 65, 183, 198, 203, 222, 229].

[9] K. Ehatäht, "Search for Higgs boson pair production in WWWW, WW$\tau\tau$, and $\tau\tau\tau\tau$ decay modes based on proton-proton collision data recorded by the CMS detector in LHC Run 2," 2nd CERN Baltic Conference, 2022 [Cited on page vi].

[10] F. Bury and C. Delaere, "Matrix element regression with deep neural networks — Breaking the CPU barrier," *JHEP*, vol. 04, p. 020, 2021. doi: 10.1007/JHEP04(2021)020. arXiv: 2008.10949 [hep-ex] [Cited on pages vi, 181, 227].

[11] CERN, "LHC machine," *JINST*, vol. 3, ed. by L. Evans and P. Bryant, S08001, 2008. doi: 10.1088/1748-0221/3/08/S08001 [Cited on pages 1, 66].

[12] ATLAS Collaboration, "Observation of a new particle in the search for the standard model Higgs boson with the ATLAS detector at the LHC," *Phys. Lett. B*, vol. 716, pp. 1–29, 2012. doi: 10.1016/j.physletb.2012.08.020. arXiv: 1207.7214 [hep-ex] [Cited on pages 1, 30, 32, 183].

[13] CMS Collaboration, "Observation of a new boson at a mass of 125 GeV with the CMS experiment at the LHC," *Phys. Lett. B*, vol. 716, pp. 30–61, 2012. doi: 10.1016/j.physletb.2012.08.021. arXiv: 1207.7235 [hep-ex] [Cited on pages 1, 30, 32, 183].

[14] F. Englert and R. Brout, "Broken symmetry and the mass of gauge vector mesons," *Phys. Rev. Lett.*, vol. 13, pp. 321–323, 9 Aug. 1964. doi: 10.1103/PhysRevLett.13.321 [Cited on pages 1, 12, 29].

[15] P. W. Higgs, "Broken symmetries and the masses of gauge bosons," *Phys. Rev. Lett.*, vol. 13, pp. 508–509, 16 Oct. 1964. doi: 10.1103/PhysRevLett.13.508 [Cited on pages 1, 12, 29].

[16] G. S. Guralnik, C. R. Hagen, and T. W. B. Kibble, "Global conservation laws and massless particles," *Phys. Rev. Lett.*, vol. 13, pp. 585–587, 20 Nov. 1964. doi: 10.1103/PhysRevLett.13.585 [Cited on pages 1, 12, 29].

[17] ATLAS Collaboration, "Observation of Higgs boson production in association with a top quark pair at the LHC with the ATLAS detector," *Phys. Lett. B*, vol. 784, pp. 173–191, 2018. doi: 10.1016/j.physletb.2018.07.035. arXiv: 1806.00425 [hep-ex] [Cited on pages 1, 45, 182, 183].

[18] CMS Collaboration, "Observation of $t\bar{t}H$ production," *Phys. Rev. Lett.*, vol. 120, no. 23, p. 231 801, 2018. doi: 10.1103/PhysRevLett.120.231801. arXiv: 1804.02610 [hep-ex] [Cited on pages 1, 45, 182, 183].

[19] CMS Collaboration, "The CMS experiment at the CERN LHC," *JINST*, vol. 3, S08004, 2008. doi: 10.1088/1748-0221/3/08/S08004 [Cited on pages 1, 66, 71, 77, 79, 81].

[20] M. D. Schwartz, *Quantum field theory and the standard model*. Cambridge University Press, 2013. doi: 10.1017/9781139540940 [Cited on page 3].

[21] M. Robinson, *Symmetry and the standard model*. Springer New York, 2011. doi: 10.1007/978-1-4419-8267-4 [Cited on page 3].

[22] M. E. Peskin and D. V. Schroeder, *An introduction to quantum field theory*. Reading, USA: Addison-Wesley, 1995, isbn: 978-0-201-50397-5 [Cited on page 3].

[23] A. Buckley, M. White, and C. White, *Practical hadron collider physics*. Institute of Physics Publishing, 2021, isbn: 978-0-750-32442-7 [Cited on page 3].

[24] Particle Data Group, "Review of particle physics," *Progress of Theoretical and Experimental Physics*, vol. 2020, no. 8, Aug. 2020, 083C01, issn: 2050-3911. doi: 10.1093/ptep/ptaa104 [Cited on pages 3, 9, 11, 14, 16, 25–28, 30, 78, 98, 143, 175].

[25] E. Noether, "Invariante Variationsprobleme," *Gott. Nachr.*, vol. 1918, pp. 235–257, 1918, [English translation: Transp. Theory Statist. Phys. 1:186-207 (1971); arXiv: physics/0503066] [Cited on page 4].

[26] C.-N. Yang and R. L. Mills, "Conservation of isotopic spin and isotopic gauge invariance," *Phys. Rev.*, vol. 96, ed. by J.-P. Hsu and D. Fine, pp. 191–195, 1954. doi: 10.1103/PhysRev.96.191 [Cited on page 5].

[27] W. Pauli, "The connection between spin and statistics," *Phys. Rev.*, vol. 58, pp. 716–722, 1940. doi: 10.1103/PhysRev.58.716 [Cited on page 6].

[28] A. Deur, S. J. Brodsky, and G. F. de Teramond, "The QCD running coupling," *Nucl. Phys.*, vol. 90, p. 1, 2016. doi: 10.1016/j.ppnp.2016.04.003. arXiv: 1604.08082 [hep-ph] [Cited on page 9].

[29] B. Andersson, G. Gustafson, G. Ingelman, and T. Sjostrand, "Parton fragmentation and string dynamics," *Phys. Rept.*, vol. 97, pp. 31–145, 1983. doi: 10.1016/0370-1573(83)90080-7 [Cited on page 9].

[30] G. Marchesini and B. R. Webber, "Simulation of QCD jets including soft gluon interference," *Nucl. Phys. B*, vol. 238, pp. 1–29, 1984. doi: 10.1016/0550-3213(84)90463-2 [Cited on page 10].

[31] B. R. Webber, "A QCD model for jet fragmentation including soft gluon interference," *Nucl. Phys. B*, vol. 238, pp. 492–528, 1984. doi: 10.1016/0550-3213(84)90333-X [Cited on page 10].

[32] S. L. Glashow, "The renormalizability of vector meson interactions," *Nucl. Phys.*, vol. 10, pp. 107–117, 1959. doi: 10.1016/0029-5582(59)90196-8 [Cited on pages 10, 29].

[33] A. Salam and J. C. Ward, "Weak and electromagnetic interactions," *Nuovo Cim.*, vol. 11, pp. 568–577, 1959. doi: 10.1007/BF02726525 [Cited on pages 10, 29].

[34] S. Weinberg, "A Model of Leptons," *Phys. Rev. Lett.*, vol. 19, pp. 1264–1266, 1967. doi: 10.1103/PhysRevLett.19.1264 [Cited on pages 10, 29].

[35] C. S. Wu *et al.*, "Experimental test of parity conservation in β decay," *Phys. Rev.*, vol. 105, pp. 1413–1414, 1957. doi: 10.1103/PhysRev.105.1413 [Cited on page 10].

[36] I. Dunietz, O. W. Greenberg, and D.-d. Wu, "*A priori* definition of maximal cp violation," *Phys. Rev. Lett.*, vol. 55, p. 2935, 1985. doi: 10.1103/PhysRevLett.55.2935 [Cited on page 10].

[37] T. Nakano and K. Nishijima, "Charge independence for V-particles," *Prog. Theor. Phys.*, vol. 10, pp. 581–582, 1953. doi: 10.1143/PTP.10.581 [Cited on page 11].

[38] K. Nishijima, "Charge independence theory of V particles," *Prog. Theor. Phys.*, vol. 13, no. 3, pp. 285–304, 1955. doi: 10.1143/PTP.13.285 [Cited on page 11].

[39] M. Gell-Mann, "The interpretation of the new particles as displaced charge multiplets," *Nuovo Cim.*, vol. 4, no. S2, pp. 848–866, 1956. doi: 10.1007/BF02748000 [Cited on page 11].

[40] W. Pauli, W. Heisenberg, L. Landau, and L. Rosenfeld, *Niels Bohr and the development of physics: Essays dedicated to Niels Bohr on the occasion of his seventieth birthday*. London: Pergamon Press, 1955 [Cited on page 11].

[41] N. Cabibbo, "Unitary symmetry and leptonic decays," *Phys. Rev. Lett.*, vol. 10, pp. 531–533, 1963. doi: 10.1103/PhysRevLett.10.531 [Cited on page 14].

[42] M. Kobayashi and T. Maskawa, "CP violation in the renormalizable theory of weak interaction," *Prog. Theor. Phys.*, vol. 49, pp. 652–657, 1973. doi: 10.1143/PTP.49.652 [Cited on page 14].

[43] LHCb Collaboration, "Measurement of the flavour-specific CP-violating asymmetry a^s_{sl} in B^0_s decays," *Phys. Lett. B*, vol. 728, pp. 607–615, 2014. doi: 10.1016/j.physletb.2013.12.030. arXiv: 1308.1048 [hep-ex] [Cited on page 14].

[44] Super-Kamiokande Collaboration, "Measurement of the flux and zenith angle distribution of upward through going muons by Super-Kamiokande," *Phys. Rev. Lett.*, vol. 82, pp. 2644–2648, 1999. doi: 10.1103/PhysRevLett.82.2644. arXiv: hep-ex/9812014 [Cited on page 16].

[45] SNO Collaboration, "Direct evidence for neutrino flavor transformation from neutral current interactions in the Sudbury Neutrino Observatory," *Phys. Rev. Lett.*, vol. 89, p. 011 301, 2002. doi: 10.1103/PhysRevLett.89.011301. arXiv: nucl-ex/0204008 [Cited on page 16].

[46] Planck Collaboration, "Planck 2018 results. VI. Cosmological parameters," *Astron. Astrophys.*, vol. 641, A6, 2020, [Erratum: Astron.Astrophys. 652, C4 (2021)]. doi: 10.1051/0004-6361/201833910. arXiv: 1807.06209 [astro-ph.CO] [Cited on page 16].

[47] C. N. Leung, S. T. Love, and S. Rao, "Low-energy manifestations of a new interaction scale: Operator analysis," *Z. Phys. C*, vol. 31, p. 433, 1986. doi: 10.1007/BF01588041 [Cited on page 17].

[48] W. Buchmüller and D. Wyler, "Effective Lagrangian analysis of new interactions and flavor conservation," *Nucl. Phys. B*, vol. 268, pp. 621–653, 1986. doi: 10.1016/0550-3213(86)90262-2 [Cited on page 17].

[49] A. de Gouvea, J. Herrero-Garcia, and A. Kobach, "Neutrino masses, grand unification, and baryon number violation," *Phys. Rev. D*, vol. 90, no. 1, p. 016 011, 2014. doi: 10.1103/PhysRevD.90.016011. arXiv: 1404.4057 [hep-ph] [Cited on page 17].

[50] LHC Higgs Cross Section Working Group, "Handbook of LHC Higgs cross sections: 4. Deciphering the nature of the Higgs sector," vol. 2/2017, Oct. 2016, [Revised recommendations: https://twiki.cern.ch/twiki/bin/view/LHCPhysics/LHCHWG]. doi: 10.23731/CYRM-2017-002. arXiv: 1610.07922 [hep-ph] [Cited on pages 17, 21, 30, 31, 34, 37, 38, 47, 63, 114, 115, 117].

[51] J. Alison *et al.*, "Higgs boson potential at colliders: Status and perspectives," *Rev. Phys.*, vol. 5, ed. by B. Di Micco, M. Gouzevitch, *et al.*, p. 100 045, 2020. doi: 10.1016/j.revip.2020.100045. arXiv: 1910.00012 [hep-ph] [Cited on pages 18, 46, 48, 59].

[52] B. Grzadkowski, M. Iskrzynski, M. Misiak, and J. Rosiek, "Dimension-six terms in the standard model Lagrangian," *JHEP*, vol. 10, p. 085, 2010. doi: 10.1007/JHEP10(2010)085. arXiv: 1008.4884 [hep-ph] [Cited on page 18].

[53] G. F. Giudice, C. Grojean, A. Pomarol, and R. Rattazzi, "The strongly-interacting light Higgs," *JHEP*, vol. 06, p. 045, 2007. doi: 10.1088/1126-6708/2007/06/045. arXiv: hep-ph/0703164 [Cited on page 18].

[54] R. Contino *et al.*, "Effective Lagrangian for a light Higgs-like scalar," *JHEP*, vol. 07, p. 035, 2013. doi: 10.1007/JHEP07(2013)035. arXiv: 1303.3876 [hep-ph] [Cited on page 18].

[55] J. Elias-Miró, C. Grojean, R. S. Gupta, and D. Marzocca, "Scaling and tuning of EW and Higgs observables," *JHEP*, vol. 05, p. 019, 2014. doi: 10.1007/JHEP05(2014)019. arXiv: 1312.2928 [hep-ph] [Cited on page 18].

[56] G. Buchalla, O. Cata, and C. Krause, "A systematic approach to the SILH Lagrangian," *Nucl. Phys. B*, vol. 894, pp. 602–620, 2015. doi: 10.1016/j.nuclphysb.2015.03.024. arXiv: 1412.6356 [hep-ph] [Cited on page 18].

[57] R. S. Gupta, A. Pomarol, and F. Riva, "Leading effects beyond the standard model," *Phys. Rev. D*, vol. 91, no. 3, p. 035 001, 2015. doi: 10.1103/PhysRevD.91.035001. arXiv: 1405.0181 [hep-ph] [Cited on page 18].

[58] R. Alonso *et al.*, "The effective chiral Lagrangian for a light dynamical "Higgs particle"," *Phys. Lett. B*, vol. 722, pp. 330–335, 2013, [Erratum: Phys.Lett.B 726, 926 (2013)]. doi: 10.1016/j.physletb.2013.04.037. arXiv: 1212.3305 [hep-ph] [Cited on page 18].

[59] G. Buchalla, O. Catà, and C. Krause, "Complete electroweak chiral Lagrangian with a light Higgs at NLO," *Nucl. Phys. B*, vol. 880, pp. 552–573, 2014, [Erratum: Nucl.Phys.B 913, 475–478 (2016)]. doi: 10.1016/j.nuclphysb.2014.01.018. arXiv: 1307.5017 [hep-ph] [Cited on page 18].

[60] A. Falkowski and R. Rattazzi, "Which EFT," *JHEP*, vol. 10, p. 255, 2019. doi: 10.1007/JHEP10(2019)255. arXiv: 1902.05936 [hep-ph] [Cited on page 18].

[61] R. Gröber *et al.*, "Effective Field Theory descriptions of Higgs boson pair production," Apr. 2023, [Available on CDS: LHCHWG-2022-004]. arXiv: 2304.01968 [hep-ph] [Cited on pages 18, 50].

[62] R. P. Feynman and M. Gell-Mann, "Theory of Fermi interaction," *Phys. Rev.*, vol. 109, ed. by L. M. Brown, pp. 193–198, 1958. doi: 10.1103/PhysRev.109.193 [Cited on pages 18, 29].

[63] E. C. G. Sudarshan and R. e. Marshak, "Chirality invariance and the universal Fermi interaction," *Phys. Rev.*, vol. 109, pp. 1860–1860, 1958. doi: 10.1103/PhysRev.109.1860.2 [Cited on pages 18, 29].

[64] F. James, "Monte-Carlo phase space," May 1968. doi: 10.5170/CERN-1968-015 [Cited on page 19].

[65] T. Kloek and H. K. van Dijk, "Bayesian estimates of equation system parameters: An application of integration by Monte Carlo," *Econometrica*, vol. 46, no. 1, pp. 1–19, 1978, issn: 00129682, 14680262. doi: 10.2307/1913641 [Cited on pages 19, 176].

[66] R. Kleiss and R. Pittau, "Weight optimization in multichannel Monte Carlo," *Comput. Phys. Commun.*, vol. 83, pp. 141–146, 1994. doi: 10.1016/0010-4655(94)90043-4. arXiv: hep-ph/9405257 [Cited on page 19].

[67] HSF Physics Event Generator WG, "Challenges in Monte Carlo Event Generator Software for High-Luminosity LHC," *Comput. Softw. Big Sci.*, vol. 5, no. 1, ed. by A. Valassi, E. Yazgan, *et al.*, p. 12, 2021. doi: 10.1007/s41781-021-00055-1. arXiv: 2004.13687 [hep-ph] [Cited on pages 20, 177].

[68] J. D. Bjorken, "Asymptotic sum rules at infinite momentum," *Phys. Rev.*, vol. 179, pp. 1547–1553, 1969. doi: 10.1103/PhysRev.179.1547 [Cited on page 20].

[69] T. Kinoshita, "Mass singularities of Feynman amplitudes," *Journal of Mathematical Physics*, vol. 3, no. 4, pp. 650–677, 1962. doi: 10.1063/1.1724268 [Cited on page 21].

[70] T. D. Lee and M. Nauenberg, "Degenerate systems and mass singularities," *Phys. Rev.*, vol. 133, B1549–B1562, 6B Mar. 1964. doi: 10.1103/PhysRev.133.B1549 [Cited on page 21].

[71] G. Altarelli and G. Parisi, "Asymptotic freedom in parton language," *Nucl. Phys. B*, vol. 126, pp. 298–318, 1977. doi: 10.1016/0550-3213(77)90384-4 [Cited on page 21].

[72] Y. L. Dokshitzer, "Calculation of the structure functions for deep inelastic scattering and $e^+ e^-$ annihilation by perturbation theory in quantum chromodynamics," *Sov. Phys. JETP*, vol. 46, pp. 641–653, 1977 [Cited on page 21].

[73] V. N. Gribov and L. N. Lipatov, "Deep inelastic ep scattering in perturbation theory," *Sov. J. Nucl. Phys.*, vol. 15, pp. 438–450, 1972 [Cited on page 21].

[74] M. Cacciari *et al.*, "The $t\bar{t}$ cross-section at 1.8 and 1.96 TeV: a study of the systematics due to parton densities and scale dependence," *JHEP*, vol. 04, p. 068, 2004. doi: 10.1088/1126-6708/2004/04/068. arXiv: hep-ph/0303085 [Cited on page 21].

[75] S. Catani, D. de Florian, M. Grazzini, and P. Nason, "Soft gluon resummation for Higgs boson production at hadron colliders," *JHEP*, vol. 07, p. 028, 2003. doi: 10.1088/1126-6708/2003/07/028. arXiv: hep-ph/0306211 [Cited on page 21].

[76] NNPDF Collaboration, "Parton distributions for the LHC Run II," *JHEP*, vol. 04, p. 040, 2015. doi: 10.1007/JHEP04(2015)040. arXiv: 1410.8849 [hep-ph] [Cited on page 21].

[77] NNPDF Collaboration, "Parton distributions from high-precision collider data," *Eur. Phys. J. C*, vol. 77, no. 10, p. 663, 2017. doi: 10.1140/epjc/s10052-017-5199-5. arXiv: 1706.00428 [hep-ph] [Cited on page 21].

[78] A. Accardi *et al.*, "A critical appraisal and evaluation of modern PDFs," *Eur. Phys. J. C*, vol. 76, no. 8, p. 471, 2016. doi: 10.1140/epjc/s10052-016-4285-4. arXiv: 1603.08906 [hep-ph] [Cited on page 21].

[79] J. Butterworth *et al.*, "PDF4LHC recommendations for LHC Run II," *J. Phys. G*, vol. 43, p. 023 001, 2016. doi: 10.1088/0954-3899/43/2/023001. arXiv: 1510.03865 [hep-ph] [Cited on pages 21, 34].

[80] J. Rojo *et al.*, "The PDF4LHC report on PDFs and LHC data: Results from Run I and preparation for Run II," *J. Phys. G*, vol. 42, p. 103 103, 2015. doi: 10.1088/0954-3899/42/10/103103. arXiv: 1507.00556 [hep-ph] [Cited on page 21].

[81] A. Manohar, P. Nason, G. P. Salam, and G. Zanderighi, "How bright is the proton? A precise determination of the photon parton distribution function," *Phys. Rev. Lett.*, vol. 117, no. 24, p. 242 002, 2016. doi: 10.1103/PhysRevLett.117.242002. arXiv: 1607.04266 [hep-ph] [Cited on page 22].

[82] A. Buckley *et al.*, "LHAPDF6: Parton density access in the LHC precision era," *Eur. Phys. J. C*, vol. 75, p. 132, 2015. doi: 10.1140/epjc/s10052-015-3318-8. arXiv: 1412.7420 [hep-ph] [Cited on pages 22, 178].

[83] F. Maltoni, G. Ridolfi, and M. Ubiali, "b-initiated processes at the LHC: A reappraisal," *JHEP*, vol. 07, p. 022, 2012, [Erratum: JHEP 04, 095 (2013)]. doi: 10.1007/JHEP07(2012)022. arXiv: 1203.6393 [hep-ph] [Cited on page 22].

[84] T. Sjöstrand *et al.*, "An introduction to PYTHIA 8.2," *Comput. Phys. Commun.*, vol. 191, pp. 159–177, 2015. doi: 10.1016/j.cpc.2015.01.024. arXiv: 1410.3012 [hep-ph] [Cited on pages 23, 112].

[85] J. Alwall *et al.*, "Comparative study of various algorithms for the merging of parton showers and matrix elements in hadronic collisions," *Eur. Phys. J. C*, vol. 53, pp. 473–500, 2008. doi: 10.1140/epjc/s10052-007-0490-5. arXiv: 0706.2569 [hep-ph] [Cited on page 23].

[86] R. Frederix and S. Frixione, "Merging meets matching in MC@NLO," *JHEP*, vol. 12, p. 061, 2012. doi: 10.1007/JHEP12(2012)061. arXiv: 1209.6215 [hep-ph] [Cited on page 23].

[87] J. Alwall *et al.*, "The automated computation of tree-level and next-to-leading order differential cross sections, and their matching to parton shower simulations," *JHEP*, vol. 07, p. 079, 2014. doi: 10.1007/JHEP07(2014)079. arXiv: 1405.0301 [hep-ph] [Cited on pages 23, 55, 112, 178].

[88] A. Kalogeropoulos and J. Alwall, "The SysCalc code: A tool to derive theoretical systematic uncertainties," Jan. 2018. doi: 10.48550/arXiv.1801.08401. arXiv: 1801.08401 [hep-ph] [Cited on pages 23, 112].

[89] P. Nason, "A New method for combining NLO QCD with shower Monte Carlo algorithms," *JHEP*, vol. 11, p. 040, 2004. doi: 10.1088/1126-6708/2004/11/040. arXiv: hep-ph/0409146 [Cited on pages 23, 112].

[90] S. Frixione, P. Nason, and C. Oleari, "Matching NLO QCD computations with parton shower simulations: The POWHEG method," *JHEP*, vol. 11, p. 070, 2007. doi: 10.1088/1126-6708/2007/11/070. arXiv: 0709.2092 [hep-ph] [Cited on pages 23, 112].

[91] S. Alioli, P. Nason, C. Oleari, and E. Re, "A general framework for implementing NLO calculations in shower Monte Carlo programs: The POWHEG BOX," *JHEP*, vol. 06, p. 043, 2010. doi: 10.1007/JHEP06(2010)043. arXiv: 1002.2581 [hep-ph] [Cited on pages 23, 112].

[92] CMS Collaboration, "CMS PYTHIA 8 colour reconnection tunes based on underlying-event data," May 2022. arXiv: 2205.02905 [hep-ex] [Cited on page 23].

[93] CMS Collaboration, "Extraction and validation of a new set of CMS PYTHIA8 tunes from underlying-event measurements," *Eur. Phys. J. C*, vol. 80, no. 1, p. 4, 2020. doi: 10.1140/epjc/s10052-019-7499-4. arXiv: 1903.12179 [hep-ex] [Cited on page 23].

[94] CMS Collaboration, "Event generator tunes obtained from underlying event and multiparton scattering measurements," *Eur. Phys. J. C*, vol. 76, no. 3, p. 155, 2016. doi: 10.1140/epjc/s10052-016-3988-x. arXiv: 1512.00815 [hep-ex] [Cited on page 23].

[95] T. Gleisberg *et al.*, "Event generation with SHERPA 1.1," *JHEP*, vol. 02, p. 007, 2009. doi: 10.1088/1126-6708/2009/02/007. arXiv: 0811.4622 [hep-ph] [Cited on page 24].

[96] CMS Collaboration, "HLT dimuon invariant mass distributions in 2017 and 2018," 2018, [Available on CDS: CMS-DP-2018-055] [Cited on page 26].

[97] M. L. Perl, "The tau lepton," *Ann. Rev. Nucl. Part. Sci.*, vol. 30, pp. 299–335, 1980. doi: 10.1146/annurev.ns.30.120180.001503 [Cited on page 27].

[98] F. Nichitiu, "An introduction to the vector meson," in *Nato Advanced Study Institute: Hadron Spectroscopy and the Confinement Problem*, Nov. 1995, pp. 0219–240 [Cited on page 27].

[99] M. Gell-Mann, "The eightfold way: A theory of strong interaction symmetry," Mar. 1961. doi: 10.2172/4008239 [Cited on page 28].

[100] Y. Ne'eman, "Derivation of strong interactions from a gauge invariance," *Nucl. Phys.*, vol. 26, ed. by R. Ruffini and Y. Verbin, pp. 222–229, 1961. doi: 10.1016/0029-5582(61)90134-1 [Cited on page 28].

[101] J. H. Kuhn and E. Mirkes, "Structure functions in tau decays," *Z. Phys. C*, vol. 56, pp. 661–672, 1992, [Erratum: Z.Phys.C 67, 364 (1995)]. doi: 10.1007/BF01474741 [Cited on page 28].

[102] CLEO Collaboration, "Resonant structure of $\tau \to 3\pi\pi^0\nu_\tau$ and $\tau \to \omega\pi\nu_\tau$ decays," *Phys. Rev. D*, vol. 61, p. 072 003, 2000. doi: 10.1103/PhysRevD.61.072003. arXiv: hep-ex/9908024 [Cited on page 28].

[103] ATLAS Collaboration, "Comparison of Monte Carlo generator predictions for bottom and charm hadrons in the decays of top quarks and the fragmentation of high pT jets," 2014, [Available on CDS: ATL-PHYS-PUB-2014-008] [Cited on page 29].

[104] CMS Collaboration, "Identification of b-quark jets with the CMS experiment," *JINST*, vol. 8, P04013, 2013. doi: 10.1088/1748-0221/8/04/P04013. arXiv: 1211.4462 [hep-ex] [Cited on pages 29, 91].

[105] G. 't Hooft, "Renormalizable Lagrangians for massive Yang-Mills fields," *Nucl. Phys. B*, vol. 35, ed. by J. C. Taylor, pp. 167–188, 1971. doi: 10.1016/0550-3213(71)90139-8 [Cited on page 29].

[106] B. W. Lee and J. Zinn-Justin, "Spontaneously broken gauge symmetries part 1: Preliminaries," *Phys. Rev. D*, vol. 5, pp. 3121–3137, 1972. doi: 10.1103/PhysRevD.5.3121 [Cited on page 29].

[107] B. W. Lee and J. Zinn-Justin, "Spontaneously broken gauge symmetries part 2: Perturbation theory and renormalization," *Phys. Rev. D*, vol. 5, pp. 3137–3155, 1972, [Erratum: Phys.Rev.D 8, 4654 (1973)]. doi: 10.1103/PhysRevD.5.3137 [Cited on page 29].

[108] B. W. Lee and J. Zinn-Justin, "Spontaneously broken gauge symmetries part 3: Equivalence," *Phys. Rev. D*, vol. 5, pp. 3155–3160, 1972. doi: 10.1103/PhysRevD.5.3155 [Cited on page 29].

[109] B. W. Lee and J. Zinn-Justin, "Spontaneously broken gauge symmetries part 4: General gauge formulation," *Phys. Rev. D*, vol. 7, pp. 1049–1056, 1973. doi: 10.1103/PhysRevD.7.1049 [Cited on page 29].

[110] J. Ellis, M. K. Gaillard, and D. V. Nanopoulos, "A historical profile of the Higgs boson," Jan. 2012. arXiv: 1201.6045 [hep-ph] [Cited on page 29].

[111] F. J. Hasert *et al.*, "Search for elastic ν_μ electron scattering," *Phys. Lett. B*, vol. 46, pp. 121–124, 1973. doi: 10.1016/0370-2693(73)90494-2 [Cited on page 30].

[112] Gargamelle Neutrino Collaboration, "Observation of neutrino like interactions without muon or electron in the Gargamelle neutrino experiment," *Phys. Lett. B*, vol. 46, pp. 138–140, 1973. doi: 10.1016/0370-2693(73)90499-1 [Cited on page 30].

[113] UA1 Collaboration, "Experimental observation of isolated large transverse energy electrons with associated missing energy at $\sqrt{s} = 540$ GeV," *Phys. Lett. B*, vol. 122, pp. 103–116, 1983. doi: 10.1016/0370-2693(83)91177-2 [Cited on page 30].

[114] UA2 Collaboration, "Observation of single isolated electrons of high transverse momentum in events with missing transverse energy at the CERN $\bar{p}p$ collider," *Phys. Lett. B*, vol. 122, pp. 476–485, 1983. doi: 10.1016/0370-2693(83)91605-2 [Cited on page 30].

[115] UA1 Collaboration, "Experimental observation of lepton pairs of invariant mass around 95 GeV/c^2 at the CERN SPS collider," *Phys. Lett. B*, vol. 126, pp. 398–410, 1983. doi: 10.1016/0370-2693(83)90188-0 [Cited on page 30].

[116] UA2 Collaboration, "Evidence for $Z^0 \to e^+e^-$ at the CERN $\bar{p}p$ Collider," *Phys. Lett. B*, vol. 129, pp. 130–140, 1983. doi: 10.1016/0370-2693(83)90744-X [Cited on page 30].

[117] CDF Collaboration, "Observation of top quark production in $\bar{p}p$ collisions," *Phys. Rev. Lett.*, vol. 74, pp. 2626–2631, 1995. doi: 10.1103/PhysRevLett.74.2626. arXiv: hep-ex/9503002 [Cited on page 30].

[118] D0 Collaboration, "Observation of the top quark," *Phys. Rev. Lett.*, vol. 74, pp. 2632–2637, 1995. doi: 10.1103/PhysRevLett.74.2632. arXiv: hep-ex/9503003 [Cited on page 30].

[119] DONUT Collaboration, "Observation of tau neutrino interactions," *Phys. Lett. B*, vol. 504, pp. 218–224, 2001. doi: 10.1016/S0370-2693(01)00307-0. arXiv: hep-ex/0012035 [Cited on page 30].

[120] ATLAS and CMS Collaborations, "Combined measurement of the Higgs boson mass in pp collisions at $\sqrt{s} = 7$ and 8 TeV with the ATLAS and CMS experiments," *Phys. Rev. Lett.*, vol. 114, p. 191 803, 2015. doi: 10.1103/PhysRevLett.114.191803. arXiv: 1503.07589 [hep-ex] [Cited on page 30].

[121] CMS Collaboration, "A measurement of the Higgs boson mass in the diphoton decay channel," *Phys. Lett. B*, vol. 805, p. 135 425, 2020. doi: 10.1016/j.physletb.2020.135425. arXiv: 2002.06398 [hep-ex] [Cited on pages 30, 37].

[122] CMS Collaboration, "Measurements of properties of the Higgs boson decaying into the four-lepton final state in pp collisions at $\sqrt{s} = 13$ TeV," *JHEP*, vol. 11, p. 047, 2017. doi: 10.1007/JHEP11(2017)047. arXiv: 1706.09936 [hep-ex] [Cited on pages 30, 100].

[123] F. Caola and K. Melnikov, "Constraining the Higgs boson width with ZZ production at the LHC," *Phys. Rev. D*, vol. 88, p. 054 024, 2013. doi: 10.1103/PhysRevD.88.054024. arXiv: 1307.4935 [hep-ph] [Cited on page 30].

[124] CMS Collaboration, "Measurement of the Higgs boson width and evidence of its off-shell contributions to ZZ production," *Nature Phys.*, vol. 18, no. 11, pp. 1329–1334, 2022. doi: 10.1038/s41567-022-01682-0. arXiv: 2202.06923 [hep-ex] [Cited on page 30].

[125] T. G. Rizzo, "Decays of heavy Higgs bosons," *Phys. Rev. D*, vol. 22, p. 722, 1980. doi: 10.1103/PhysRevD.22.722 [Cited on page 30].

[126] L. D. Landau, "On the angular momentum of a system of two photons," *Dokl. Akad. Nauk SSSR*, vol. 60, no. 2, pp. 207–209, 1948. doi: 10.1016/B978-0-08-010586-4.50070-5 [Cited on page 32].

[127] C.-N. Yang, "Selection rules for the dematerialization of a particle into two photons," *Phys. Rev.*, vol. 77, pp. 242–245, 1950. doi: 10.1103/PhysRev.77.242 [Cited on page 32].

[128] ATLAS Collaboration, "Study of the spin and parity of the Higgs boson in diboson decays with the ATLAS detector," *Eur. Phys. J. C*, vol. 75, no. 10, p. 476, 2015, [Erratum: Eur.Phys.J.C 76, 152 (2016)]. doi: 10.1140/epjc/s10052-015-3685-1. arXiv: 1506.05669 [hep-ex] [Cited on page 32].

[129] CMS Collaboration, "Constraints on the spin-parity and anomalous HVV couplings of the Higgs boson in proton collisions at 7 and 8 TeV," *Phys. Rev. D*, vol. 92, no. 1, p. 012 004, 2015. doi: 10.1103/PhysRevD.92.012004. arXiv: 1411.3441 [hep-ex] [Cited on page 32].

[130] ATLAS Collaboration, "Observation of $H \to b\bar{b}$ decays and VH production with the ATLAS detector," *Phys. Lett. B*, vol. 786, pp. 59–86, 2018. doi: 10.1016/j.physletb.2018.09.013. arXiv: 1808.08238 [hep-ex] [Cited on pages 32, 35].

[131] CMS Collaboration, "Observation of Higgs boson decay to bottom quarks," *Phys. Rev. Lett.*, vol. 121, no. 12, p. 121 801, 2018. doi: 10.1103/PhysRevLett.121.121801. arXiv: 1808.08242 [hep-ex] [Cited on pages 32, 35].

[132] ATLAS Collaboration, "Observation and measurement of Higgs boson decays to WW* with the ATLAS detector," *Phys. Rev. D*, vol. 92, no. 1, p. 012 006, 2015. doi: 10.1103/PhysRevD.92.012006. arXiv: 1412.2641 [hep-ex] [Cited on page 32].

[133] CMS Collaboration, "Measurements of properties of the Higgs boson decaying to a W boson pair in pp collisions at $\sqrt{s} = 13$ TeV," *Phys. Lett. B*, vol. 791, p. 96, 2019. doi: 10.1016/j.physletb.2018.12.073. arXiv: 1806.05246 [hep-ex] [Cited on page 32].

[134] ATLAS and CMS Collaborations, "Measurements of the Higgs boson production and decay rates and constraints on its couplings from a combined ATLAS and CMS analysis of the LHC pp collision data at $\sqrt{s} = 7$ and 8 TeV," *JHEP*, vol. 08, p. 045, 2016. doi: 10.1007/JHEP08(2016)045. arXiv: 1606.02266 [hep-ex] [Cited on pages 32, 44, 183].

[135] CMS Collaboration, "Observation of the Higgs boson decay to a pair of τ leptons with the CMS detector," *Phys. Lett. B*, vol. 779, pp. 283–316, 2018. doi: 10.1016/j.physletb.2018.02.004. arXiv: 1708.00373 [hep-ex] [Cited on pages 32, 180, 183].

[136] ATLAS Collaboration, "Cross-section measurements of the Higgs boson decaying into a pair of τ-leptons in proton-proton collisions at $\sqrt{s} = 13$ TeV with the ATLAS detector," *Phys. Rev. D*, vol. 99, p. 072 001, 2019. doi: 10.1103/PhysRevD.99.072001. arXiv: 1811.08856 [hep-ex] [Cited on pages 32, 183].

[137] ATLAS Collaboration, "A search for the dimuon decay of the standard model Higgs boson with the ATLAS detector," *Phys. Lett. B*, vol. 812, p. 135 980, 2021. doi: 10.1016/j.physletb.2020.135980. arXiv: 2007.07830 [hep-ex] [Cited on page 32].

[138] CMS Collaboration, "Evidence for Higgs boson decay to a pair of muons," *JHEP*, vol. 01, p. 148, 2021. doi: 10.1007/JHEP01(2021)148. arXiv: 2009.04363 [hep-ex] [Cited on page 32].

[139] The ATLAS and CMS Collaborations, "Evidence for the Higgs boson decay to a Z boson and a photon at the LHC," 2023, [Available on CDS: CMS-PAS-HIG-23-002] [Cited on page 32].

[140] ATLAS Collaboration, "Direct constraint on the Higgs-charm coupling from a search for Higgs boson decays into charm quarks with the ATLAS detector," *Eur. Phys. J. C*, vol. 82, p. 717, 2022. doi: 10.1140/epjc/s10052-022-10588-3. arXiv: 2201.11428 [hep-ex] [Cited on page 32].

[141] CMS Collaboration, "Search for Higgs boson decay to a charm quark-antiquark pair in proton-proton collisions at $\sqrt{s} = 13$ TeV," May 2022. arXiv: 2205.05550 [hep-ex] [Cited on page 32].

[142] F. Demartin *et al.*, "tWH associated production at the LHC," *Eur. Phys. J. C*, vol. 77, no. 1, p. 34, 2017. doi: 10.1140/epjc/s10052-017-4601-7. arXiv: 1607.05862 [hep-ph] [Cited on page 34].

[143] LHC Higgs Cross Section Working Group, "Handbook of LHC Higgs cross sections: 3. Higgs properties," ed. by S. Heinemeyer, C. Mariotti, *et al.*, Jul. 2013. doi: 10.5170/CERN-2013-004. arXiv: 1307.1347 [hep-ph] [Cited on pages 36, 228].

[144] J. R. Andersen *et al.*, "Les Houches 2015: Physics at TeV Colliders Standard Model Working Group Report," in *9th Les Houches Workshop on Physics at TeV Colliders*, May 2016. arXiv: 1605.04692 [hep-ph] [Cited on page 37].

[145] ATLAS Collaboration, "Combined measurements of Higgs boson production and decay using up to $139\,\text{fb}^{-1}$ of proton-proton collision data at $\sqrt{s} = 13$ TeV collected with the ATLAS experiment," 2021, Available on CDS: ATLAS-CONF-2021-053 [Cited on page 37].

[146] F. Maltoni, D. Pagani, A. Shivaji, and X. Zhao, "Trilinear Higgs coupling determination via single-Higgs differential measurements at the LHC," *Eur. Phys. J. C*, vol. 77, no. 12, p. 887, 2017. doi: 10.1140/epjc/s10052-017-5410-8. arXiv: 1709.08649 [hep-ph] [Cited on pages 38, 46, 47].

[147] I. W. Stewart and F. J. Tackmann, "Theory uncertainties for Higgs and other searches using jet bins," *Phys. Rev. D*, vol. 85, p. 034 011, 2012. doi: 10.1103/PhysRevD.85.034011. arXiv: 1107.2117 [hep-ph] [Cited on page 38].

[148] G. Degrassi *et al.*, "Higgs mass and vacuum stability in the standard model at NNLO," *JHEP*, vol. 08, p. 098, 2012. doi: 10.1007/JHEP08(2012)098. arXiv: 1205.6497 [hep-ph] [Cited on page 39].

[149] F. Bezrukov and M. Shaposhnikov, "Why should we care about the top quark Yukawa coupling?" *J. Exp. Theor. Phys.*, vol. 120, pp. 335–343, 2015. doi: 10.1134/S1063776115030152. arXiv: 1411.1923 [hep-ph] [Cited on page 39].

[150] S. Biswas, E. Gabrielli, F. Margaroli, and B. Mele, "Direct constraints on the top-Higgs coupling from the 8 TeV LHC data," *JHEP*, vol. 07, p. 073, 2013. doi: 10.1007/JHEP07(2013)073. arXiv: 1304.1822 [hep-ph] [Cited on pages 39, 40].

[151] T. Appelquist and M. S. Chanowitz, "Unitarity bound on the scale of fermion mass generation," *Phys. Rev. Lett.*, vol. 59, p. 2405, 1987, [Erratum: Phys.Rev.Lett. 60, 1589 (1988)]. doi: 10.1103/PhysRevLett.59.2405 [Cited on page 39].

[152] G. C. Branco *et al.*, "Theory and phenomenology of two-Higgs-doublet models," *Phys. Rept.*, vol. 516, pp. 1–102, 2012. doi: 10.1016/j.physrep.2012.02.002. arXiv: 1106.0034 [hep-ph] [Cited on page 40].

[153] A. Djouadi, "The anatomy of electro-weak symmetry breaking. II. The Higgs bosons in the minimal supersymmetric model," *Phys. Rept.*, vol. 459, pp. 1–241, 2008. doi: 10.1016/j.physrep.2007.10.005. arXiv: hep-ph/0503173 [Cited on page 40].

[154] Z. Chacko, Y. Nomura, M. Papucci, and G. Perez, "Natural little hierarchy from a partially goldstone twin Higgs," *JHEP*, vol. 01, p. 126, 2006. doi: 10.1088/1126-6708/2006/01/126. arXiv: hep-ph/0510273 [Cited on page 40].

[155] J. Mrazek *et al.*, "The other natural two Higgs doublet model," *Nucl. Phys. B*, vol. 853, pp. 1–48, 2011. doi: 10.1016/j.nuclphysb.2011.07.008. arXiv: 1105.5403 [hep-ph] [Cited on page 40].

[156] M. Cepeda *et al.*, "Report from Working Group 2: Higgs physics at the HL-LHC and HE-LHC," *CERN Yellow Rep. Monogr.*, vol. 7, ed. by A. Dainese, M. Mangano, *et al.*, pp. 221–584, 2019. doi: 10.23731/CYRM-2019-007.221. arXiv: 1902.00134 [hep-ph] [Cited on pages 40, 203].

[157] P. Artoisenet *et al.*, "A framework for Higgs characterisation," *JHEP*, vol. 11, p. 043, 2013. doi: 10.1007/JHEP11(2013)043. arXiv: 1306.6464 [hep-ph] [Cited on page 40].

[158] F. Demartin, F. Maltoni, K. Mawatari, and M. Zaro, "Higgs production in association with a single top quark at the LHC," *Eur. Phys. J. C*, vol. 75, no. 6, p. 267, 2015. doi: 10.1140/epjc/s10052-015-3475-9. arXiv: 1504.00611 [hep-ph] [Cited on pages 40, 41, 43].

[159] J. A. Aguilar-Saavedra, "A Minimal set of top-Higgs anomalous couplings," *Nucl. Phys. B*, vol. 821, pp. 215–227, 2009. doi: 10.1016/j.nuclphysb.2009.06.022. arXiv: 0904.2387 [hep-ph] [Cited on page 40].

[160] ATLAS Collaboration, "CP properties of Higgs boson interactions with top quarks in the $t\bar{t}H$ and tH processes using $H \to \gamma\gamma$ with the ATLAS detector," *Phys. Rev. Lett.*, vol. 125, no. 6, p. 061 802, 2020. doi: 10.1103/PhysRevLett.125.061802. arXiv: 2004.04545 [hep-ex] [Cited on pages 40, 44, 45, 183, 191, 199].

[161] CMS Collaboration, "Measurements of $\mathrm{t\bar{t}H}$ production and the CP structure of the Yukawa interaction between the Higgs boson and top quark in the diphoton decay channel," *Phys. Rev. Lett.*, vol. 125, no. 6, p. 061 801, 2020. doi: 10.1103/PhysRevLett.125.061801. arXiv: 2003.10866 [hep-ex] [Cited on pages 40, 44, 45, 183, 191, 199].

[162] B. Hespel, F. Maltoni, and E. Vryonidou, "Higgs and Z boson associated production via gluon fusion in the SM and the 2HDM," *JHEP*, vol. 06, p. 065, 2015. doi: 10.1007/JHEP06(2015)065. arXiv: 1503.01656 [hep-ph] [Cited on page 40].

[163] G. Bordes and B. van Eijk, "On the associate production of a neutral intermediate mass Higgs boson with a single top quark at the LHC and SSC," *Phys. Lett. B*, vol. 299, pp. 315–320, 1993. doi: 10.1016/0370-2693(93)90266-K [Cited on page 41].

[164] CMS Collaboration, "Combined measurements of Higgs boson couplings in proton-proton collisions at $\sqrt{s} = 13$ TeV," *Eur. Phys. J. C*, vol. 79, no. 5, p. 421, 2019. doi: 10.1140/epjc/s10052-019-6909-y. arXiv: 1809.10733 [hep-ex] [Cited on pages 41, 44, 214].

[165] ATLAS Collaboration, "Combined measurements of Higgs boson production and decay using up to 80 fb^{-1} of proton-proton collision data at $\sqrt{s} = 13$ TeV collected with the ATLAS experiment," *Phys. Rev. D*, vol. 101, no. 1, p. 012 002, 2020. doi: 10.1103/PhysRevD.101.012002. arXiv: 1909.02845 [hep-ex] [Cited on page 44].

[166] ATLAS Collaboration, "A detailed map of Higgs boson interactions by the ATLAS experiment ten years after the discovery," *Nature*, vol. 607, no. 7917, pp. 52–59, 2022, [Erratum: Nature 612, E24 (2022)]. doi: 10.1038/s41586-022-04893-w. arXiv: 2207.00092 [hep-ex] [Cited on pages 44, 45, 183].

[167] ATLAS Collaboration, "ATLAS b-jet identification performance and efficiency measurement with $t\bar{t}$ events in pp collisions at $\sqrt{s} = 13$ TeV," *Eur. Phys. J. C*, vol. 79, no. 11, p. 970, 2019. doi: 10.1140/epjc/s10052-019-7450-8. arXiv: 1907.05120 [hep-ex] [Cited on pages 44, 64].

[168] E. Bols *et al.*, "Jet flavour classification using DeepJet," *JINST*, vol. 15, no. 12, P12012, 2020. doi: 10.1088/1748-0221/15/12/P12012. arXiv: 2008.10519 [hep-ex] [Cited on pages 44, 64, 92, 175].

[169] ATLAS Collaboration, "Measurement of Higgs boson decay into b-quarks in associated production with a top-quark pair in pp collisions at $\sqrt{s} = 13$ TeV with the ATLAS detector," *JHEP*, vol. 06, p. 097, 2022. doi: 10.1007/JHEP06(2022)097. arXiv: 2111.06712 [hep-ex] [Cited on pages 44, 45, 183, 191].

[170] CMS Collaboration, "Measurement of $\mathrm{t\bar{t}H}$ production in the $\mathrm{H} \to \mathrm{b\bar{b}}$ decay channel in 41.5 fb^{-1} of proton-proton collision data at $\sqrt{s} = 13$ TeV," 2019, [Available on CDS: CMS-PAS-HIG-18-030] [Cited on pages 44, 45, 191].

[171] ATLAS Collaboration, "Evidence for the associated production of the Higgs boson and a top quark pair with the ATLAS detector," *Phys. Rev. D*, vol. 97, no. 7, p. 072 003, 2018. doi: 10.1103/PhysRevD.97.072003. arXiv: 1712.08891 [hep-ex] [Cited on pages 45, 182, 183].

[172] CMS Collaboration, "Search for associated production of a Higgs boson and a single top quark in proton-proton collisions at $\sqrt{s} = 13$ TeV," *Phys. Rev. D*, vol. 99, no. 9, p. 092 005, 2019. doi: 10.1103/PhysRevD.99.092005. arXiv: 1811.09696 [hep-ex] [Cited on pages 45, 182, 183].

[173] D. E. Morrissey and M. J. Ramsey-Musolf, "Electroweak baryogenesis," *New J. Phys.*, vol. 14, p. 125 003, 2012. doi: 10.1088/1367-2630/14/12/125003. arXiv: 1206.2942 [hep-ph] [Cited on page 46].

[174] A. Noble and M. Perelstein, "Higgs self-coupling as a probe of electroweak phase transition," *Phys. Rev. D*, vol. 78, p. 063 518, 2008. doi: 10.1103/PhysRevD.78.063518. arXiv: 0711.3018 [hep-ph] [Cited on page 46].

[175] M. Grazzini *et al.*, "Higgs boson pair production at NNLO with top quark mass effects," *JHEP*, vol. 05, p. 059, 2018. doi: 10.1007/JHEP05(2018)059. arXiv: 1803.02463 [hep-ph] [Cited on pages 46, 48, 49].

[176] D. de Florian, I. Fabre, and J. Mazzitelli, "Triple Higgs production at hadron colliders at NNLO in QCD," *JHEP*, vol. 03, p. 155, 2020. doi: 10.1007/JHEP03(2020)155. arXiv: 1912.02760 [hep-ph] [Cited on page 46].

[177] I. Zurbano Fernandez *et al.*, "High-Luminosity Large Hadron Collider (HL-LHC): Technical design report," vol. 10/2020, ed. by I. Béjar Alonso, O. Brüning, *et al.*, Dec. 2020. doi: 10.23731/CYRM-2020-0010 [Cited on pages 46, 70].

[178] G. Degrassi, P. P. Giardino, F. Maltoni, and D. Pagani, "Probing the Higgs self coupling via single Higgs production at the LHC," *JHEP*, vol. 12, p. 080, 2016. doi: 10.1007/JHEP12(2016)080. arXiv: 1607.04251 [hep-ph] [Cited on pages 46, 47].

[179] ATLAS Collaboration, "Constraint of the Higgs boson self-coupling from Higgs boson differential production and decay measurements," 2019 [Cited on page 47].

[180] CMS Collaboration, "Combined Higgs boson production and decay measurements with up to 137 fb^{-1} of proton-proton collision data at $\sqrt{s} = 13$ TeV," 2020 [Cited on page 47].

[181] F. A. Dreyer and A. Karlberg, "Vector-boson fusion Higgs pair production at N^{3}LO," *Phys. Rev. D*, vol. 98, no. 11, p. 114 016, 2018. doi: 10.1103/PhysRevD.98.114016. arXiv: 1811.07906 [hep-ph] [Cited on pages 48, 50].

[182] A. Carvalho *et al.*, "Higgs pair production: Choosing benchmarks with cluster analysis," *JHEP*, vol. 04, p. 126, 2016. doi: 10.1007/JHEP04(2016)126. arXiv: 1507.02245 [hep-ph] [Cited on pages 49–52, 54, 210].

[183] J. Baglio *et al.*, "$gg \to HH$: Combined uncertainties," *Phys. Rev. D*, vol. 103, no. 5, p. 056 002, 2021. doi: 10.1103/PhysRevD.103.056002. arXiv: 2008.11626 [hep-ph] [Cited on page 49].

[184] F. Bishara, R. Contino, and J. Rojo, "Higgs pair production in vector-boson fusion at the LHC and beyond," *Eur. Phys. J. C*, vol. 77, no. 7, p. 481, 2017. doi: 10.1140/epjc/s10052-017-5037-9. arXiv: 1611.03860 [hep-ph] [Cited on pages 50, 58].

[185] A. Carvalho *et al.*, "On the reinterpretation of non-resonant searches for Higgs boson pairs," *JHEP*, vol. 02, p. 049, 2021. doi: 10.1007/JHEP02(2021)049. arXiv: 1710.08261 [hep-ph] [Cited on pages 50, 55, 57].

[186] A. Carvalho *et al.*, "Analytical parametrization and shape classification of anomalous HH production in the EFT approach," Jul. 2016, [Available on CDS: LHCHXSWG-INT-2016-001]. arXiv: 1608.06578 [hep-ph] [Cited on page 51].

[187] G. Buchalla *et al.*, "Higgs boson pair production in non-linear Effective Field Theory with full m_t-dependence at NLO QCD," *JHEP*, vol. 09, p. 057, 2018. doi: 10.1007/JHEP09(2018)057. arXiv: 1806.05162 [hep-ph] [Cited on pages 51–53, 55, 57].

[188] D. de Florian *et al.*, "Anomalous couplings in Higgs-boson pair production at approximate NNLO QCD," *JHEP*, vol. 09, p. 161, 2021. doi: 10.1007/JHEP09(2021)161. arXiv: 2106.14050 [hep-ph] [Cited on page 51].

[189] M. Capozi and G. Heinrich, "Exploring anomalous couplings in Higgs boson pair production through shape analysis," *JHEP*, vol. 03, p. 091, 2020. doi: 10.1007/JHEP03(2020)091. arXiv: 1908.08923 [hep-ph] [Cited on pages 52–54].

[190] D. E. Rumelhart, G. E. Hinton, and R. J. Williams, "Learning internal representations by error propagation," 1986 [Cited on page 53].

[191] H. Steinhaus, "Sur la division des corps matériels en parties," French, *Bull. Acad. Pol. Sci., Cl. III*, vol. 4, pp. 801–804, 1957, issn: 0001-4095 [Cited on page 53].

[192] J. MacQueen, "Some methods for classification and analysis of multivariate observations," English, in *5th Berkeley Symposium on Mathematical Statistics and Probability*, vol. 1, University of California, 1967, pp. 281–297 [Cited on page 53].

[193] L. Cadamuro, "Search for Higgs boson pair production in the $b\bar{b}\tau^+\tau^-$ decay channel with the CMS detector at the LHC," Ph.D. dissertation, U. Paris-Saclay, 2017. doi: 10.1007/978-3-030-04055-0 [Cited on page 54].

[194] B. N. Datta, *Numerical Linear Algebra and Applications*, 2nd. Society for Industrial and Applied Mathematics, 2010, isbn: 978-0-898-71685-6 [Cited on pages 54, 55].

[195] A. Dresden, "The fourteenth western meeting of the American Mathematical Society," *Bulletin of the American Mathematical Society*, vol. 26, no. 9, pp. 385–397, Jun. 1920. doi: 10.1090/s0002-9904-1920-03322-7 [Cited on page 54].

[196] R. Penrose, "A generalized inverse for matrices," *Mathematical Proceedings of the Cambridge Philosophical Society*, vol. 51, no. 3, pp. 406–413, Jul. 1955. doi: 10.1017/s0305004100030401 [Cited on page 54].

[197] G. Heinrich *et al.*, "NLO predictions for Higgs boson pair production with full top quark mass dependence matched to parton showers," *JHEP*, vol. 08, p. 088, 2017. doi: 10.1007/JHEP08(2017)088. arXiv: 1703.09252 [hep-ph] [Cited on pages 55, 56, 113].

[198] G. Heinrich *et al.*, "Probing the trilinear Higgs boson coupling in di-Higgs production at NLO QCD including parton shower effects," *JHEP*, vol. 06, p. 066, 2019. doi: 10.1007/JHEP06(2019)066. arXiv: 1903.08137 [hep-ph] [Cited on pages 55, 56, 113].

[199] G. Heinrich, S. P. Jones, M. Kerner, and L. Scyboz, "A non-linear EFT description of $gg \to HH$ at NLO interfaced to POWHEG," *JHEP*, vol. 10, p. 021, 2020. doi: 10.1007/JHEP10(2020)021. arXiv: 2006.16877 [hep-ph] [Cited on pages 55, 56, 113].

[200] T. Lange, "Search for rare Higgs boson decays at a center of mass energy of $\sqrt{s} = 13$ TeV with the CMS Experiment at the LHC," [Available on: https://ediss.sub.uni-hamburg.de/handle/ediss/9632], Ph.D. dissertation, Universität Hamburg, U. Hamburg, Dept. Phys., 2022 [Cited on page 56].

[201] G. Brooijmans *et al.*, "Les Houches 2013: Physics at TeV Colliders: New Physics Working Group Report," May 2014. arXiv: 1405.1617 [hep-ph] [Cited on pages 58, 227].

[202] H. Davoudiasl, R. Kitano, T. Li, and H. Murayama, "The new minimal standard model," *Phys. Lett. B*, vol. 609, pp. 117–123, 2005. doi: 10.1016/j.physletb.2005.01.026. arXiv: hep-ph/0405097 [Cited on page 58].

[203] R. M. Schabinger and J. D. Wells, "A Minimal spontaneously broken hidden sector and its impact on Higgs boson physics at the large hadron collider," *Phys. Rev. D*, vol. 72, p. 093 007, 2005. doi: 10.1103/PhysRevD.72.093007. arXiv: hep-ph/0509209 [Cited on page 58].

[204] C. Englert, T. Plehn, D. Zerwas, and P. M. Zerwas, "Exploring the Higgs portal," *Phys. Lett. B*, vol. 703, pp. 298–305, 2011. doi: 10.1016/j.physletb.2011.08.002. arXiv: 1106.3097 [hep-ph] [Cited on page 59].

[205] J. M. No and M. Ramsey-Musolf, "Probing the Higgs portal at the LHC through resonant di-Higgs production," *Phys. Rev. D*, vol. 89, no. 9, p. 095 031, 2014. doi: 10.1103/PhysRevD.89.095031. arXiv: 1310.6035 [hep-ph] [Cited on page 59].

[206] V. Barger *et al.*, "CERN LHC phenomenology of an extended standard model with a real scalar singlet," *Phys. Rev. D*, vol. 77, p. 035 005, 2008. doi: 10.1103/PhysRevD.77.035005. arXiv: 0706.4311 [hep-ph] [Cited on page 59].

[207] M. Carena and H. E. Haber, "Higgs boson theory and phenomenology," *Prog. Part. Nucl. Phys.*, vol. 50, pp. 63–152, 2003. doi: 10.1016/S0146-6410(02)00177-1. arXiv: hep-ph/0208209 [Cited on page 59].

[208] N. Craig, J. Galloway, and S. Thomas, "Searching for signs of the second Higgs doublet," May 2013. arXiv: 1305.2424 [hep-ph] [Cited on page 59].

[209] B. Hespel, D. Lopez-Val, and E. Vryonidou, "Higgs pair production via gluon fusion in the Two-Higgs-Doublet Model," *JHEP*, vol. 09, p. 124, 2014. doi: 10.1007/JHEP09(2014)124. arXiv: 1407.0281 [hep-ph] [Cited on page 59].

[210] I. F. Ginzburg, M. Krawczyk, and P. Osland, "Two Higgs doublet models with CP violation," in *International Workshop on Linear Colliders (LCWS 2002)*, Nov. 2002, pp. 703–706. arXiv: hep-ph/0211371 [Cited on page 59].

[211] M. Carena *et al.*, "Alignment limit of the NMSSM Higgs sector," *Phys. Rev. D*, vol. 93, no. 3, p. 035 013, 2016. doi: 10.1103/PhysRevD.93.035013. arXiv: 1510.09137 [hep-ph] [Cited on page 59].

[212] T. Robens, T. Stefaniak, and J. Wittbrodt, "Two-real-scalar-singlet extension of the SM: LHC phenomenology and benchmark scenarios," *Eur. Phys. J. C*, vol. 80, no. 2, p. 151, 2020. doi: 10.1140/epjc/s10052-020-7655-x. arXiv: 1908.08554 [hep-ph] [Cited on page 59].

[213] S. F. King, M. Mühlleitner, R. Nevzorov, and K. Walz, "Discovery prospects for NMSSM Higgs bosons at the high-energy Large Hadron Collider," *Phys. Rev. D*, vol. 90, no. 9, p. 095 014, 2014. doi: 10.1103/PhysRevD.90.095014. arXiv: 1408.1120 [hep-ph] [Cited on page 59].

[214] T. Kaluza, "Zum Unitätsproblem der Physik," *Sitzungsber. Preuss. Akad. Wiss. Berlin (Math. Phys.)*, vol. 1921, pp. 966–972, 1921. doi: 10.1142/S0218271818700017. arXiv: 1803.08616 [physics.hist-ph] [Cited on page 59].

[215] O. Klein, "Quantum theory and five-dimensional theory of relativity. (In German and English)," *Z. Phys.*, vol. 37, ed. by J. C. Taylor, pp. 895–906, 1926. doi: 10.1007/BF01397481 [Cited on page 59].

[216] L. Randall and R. Sundrum, "A Large mass hierarchy from a small extra dimension," *Phys. Rev. Lett.*, vol. 83, pp. 3370–3373, 1999. doi: 10.1103/PhysRevLett.83.3370. arXiv: hep-ph/9905221 [Cited on page 60].

[217] W. D. Goldberger and M. B. Wise, "Bulk fields in the Randall-Sundrum compactification scenario," *Phys. Rev. D*, vol. 60, p. 107 505, 1999. doi: 10.1103/PhysRevD.60.107505. arXiv: hep-ph/9907218 [Cited on page 60].

[218] W. D. Goldberger and M. B. Wise, "Modulus stabilization with bulk fields," *Phys. Rev. Lett.*, vol. 83, pp. 4922–4925, 1999. doi: 10.1103/PhysRevLett.83.4922. arXiv: hep-ph/9907447 [Cited on page 61].

[219] C. Csaki, M. L. Graesser, and G. D. Kribs, "Radion dynamics and electroweak physics," *Phys. Rev. D*, vol. 63, p. 065 002, 2001. doi: 10.1103/PhysRevD.63.065002. arXiv: hep-th/0008151 [Cited on page 61].

[220] A. L. Fitzpatrick, J. Kaplan, L. Randall, and L.-T. Wang, "Searching for the Kaluza-Klein graviton in bulk RS models," *JHEP*, vol. 09, p. 013, 2007. doi: 10.1088/1126-6708/2007/09/013. arXiv: hep-ph/0701150 [Cited on page 61].

[221] A. Carvalho, "Gravity particles from Warped Extra Dimensions, predictions for LHC," Mar. 2014. arXiv: 1404.0102 [hep-ph] [Cited on page 61].

[222] B. C. Allanach *et al.*, "Exploring small extra dimensions at the large hadron collider," *JHEP*, vol. 12, p. 039, 2002. doi: 10.1088/1126-6708/2002/12/039. arXiv: hep-ph/0211205 [Cited on page 61].

[223] CMS Collaboration, "Search for Higgs boson pair production in the $bb\tau\tau$ final state in proton-proton collisions at $\sqrt{s} = 8$ TeV," *Phys. Rev. D*, vol. 96, no. 7, p. 072 004, 2017. doi: 10.1103/PhysRevD.96.072004. arXiv: 1707.00350 [hep-ex] [Cited on page 62].

[224] ATLAS Collaboration, "Searches for Higgs boson pair production in the $hh \to bb\tau\tau$, $\gamma\gamma WW^*$, $\gamma\gamma bb$, $bbbb$ channels with the ATLAS detector," *Phys. Rev. D*, vol. 92, p. 092 004, 2015. doi: 10.1103/PhysRevD.92.092004. arXiv: 1509.04670 [hep-ex] [Cited on page 62].

[225] ATLAS Collaboration, "Search for the $HH \to b\bar{b}b\bar{b}$ process via vector-boson fusion production using proton-proton collisions at $\sqrt{s} = 13$ TeV with the ATLAS detector," *JHEP*, vol. 07, p. 108, 2020, [Errata: JHEP 01, 145 (2021), JHEP 05, 207 (2021)]. doi: 10.1007/JHEP07(2020)108. arXiv: 2001.05178 [hep-ex] [Cited on pages 63, 65].

[226] ATLAS Collaboration, "Search for resonant pair production of Higgs bosons in the $b\bar{b}b\bar{b}$ final state using pp collisions at $\sqrt{s} = 13$ TeV with the ATLAS detector," *Phys. Rev. D*, vol. 105, no. 9, p. 092 002, 2022. doi: 10.1103/PhysRevD.105.092002. arXiv: 2202.07288 [hep-ex] [Cited on pages 63, 65, 224].

[227] ATLAS Collaboration, "Search for nonresonant pair production of Higgs bosons in the $b\bar{b}b\bar{b}$ final state in pp collisions at $\sqrt{s} = 13$ TeV with the ATLAS detector," Jan. 2023. arXiv: 2301.03212 [hep-ex] [Cited on pages 63, 65, 219, 222, 227].

[228] CMS Collaboration, "Search for Higgs boson pair production in the four b quark final state in proton-proton collisions at $\sqrt{s} = 13$ TeV," *Phys. Rev. Lett.*, vol. 129, no. 8, p. 081 802, 2022. doi: 10.1103/PhysRevLett.129.081802. arXiv: 2202.09617 [hep-ex] [Cited on pages 63, 65, 222].

[229] CMS Collaboration, "Search for nonresonant pair production of highly energetic Higgs bosons decaying to bottom quarks," May 2022. arXiv: 2205.06667 [hep-ex] [Cited on pages 63, 65].

[230] CMS Collaboration, "Search for resonant Higgs boson pair production in four b quark final state using large-area jets in proton-proton collisions at $\sqrt{s} = 13$ TeV," 2021, [Available on CDS: CMS-PAS-B2G-20-004] [Cited on pages 63, 65].

[231] ATLAS Collaboration, "Reconstruction and identification of boosted di-τ systems in a search for Higgs boson pairs using 13 TeV proton-proton collision data in ATLAS," *JHEP*, vol. 11, p. 163, 2020. doi: 10.1007/JHEP11(2020)163. arXiv: 2007.14811 [hep-ex] [Cited on pages 63, 65].

[232] ATLAS Collaboration, "Search for resonant and non-resonant Higgs boson pair production in the $b\bar{b}\tau^+\tau^-$ decay channel using 13 TeV pp collision data from the ATLAS detector," Sep. 2022. arXiv: 2209.10910 [hep-ex] [Cited on pages 63, 65, 222, 224].

[233] CMS Collaboration, "Search for nonresonant Higgs boson pair production in final state with two bottom quarks and two tau leptons in proton-proton collisions at $\sqrt{s} = 13$ TeV," *Phys. Lett. B*, vol. 842, p. 137 531, 2023. doi: 10.1016/j.physletb.2022.137531. arXiv: 2206.09401 [hep-ex] [Cited on pages 63, 65, 222].

[234] ATLAS Collaboration, "Search for Higgs boson pair production in the two bottom quarks plus two photons final state in pp collisions at $\sqrt{s} = 13$ TeV with the ATLAS detector," *Phys. Rev. D*, vol. 106, no. 5, p. 052 001, 2022. doi: 10.1103/PhysRevD.106.052001. arXiv: 2112.11876 [hep-ex] [Cited on pages 63, 65, 222, 224].

[235] CMS Collaboration, "Search for nonresonant Higgs boson pair production in final states with two bottom quarks and two photons in proton-proton collisions at $\sqrt{s} = 13$ TeV," *JHEP*, vol. 03, p. 257, 2021. doi: 10.1007/JHEP03(2021)257. arXiv: 2011.12373 [hep-ex] [Cited on pages 63, 65, 147, 219, 222].

[236] ATLAS Collaboration, "Search for Higgs boson pair production in the $b\bar{b}WW^*$ decay mode at $\sqrt{s} = 13$ TeV with the ATLAS detector," *JHEP*, vol. 04, p. 092, 2019. doi: 10.1007/JHEP04(2019)092. arXiv: 1811.04671 [hep-ex] [Cited on pages 63, 65].

[237] CMS Collaboration, "Search for heavy resonances decaying to a pair of Lorentz-boosted Higgs bosons in final states with leptons and a bottom quark pair at $\sqrt{s} = 13$ TeV," *JHEP*, vol. 05, p. 005, 2022. doi: 10.1007/JHEP05(2022)005. arXiv: 2112.03161 [hep-ex] [Cited on pages 63, 65].

[238] ATLAS Collaboration, "Search for non-resonant Higgs boson pair production in the $bb\ell\nu\ell\nu$ final state with the ATLAS detector in pp collisions at $\sqrt{s} = 13$ TeV," *Phys. Lett. B*, vol. 801, p. 135 145, 2020. doi: 10.1016/j.physletb.2019.135145. arXiv: 1908.06765 [hep-ex] [Cited on pages 63, 65].

[239] CMS Collaboration, "Search for nonresonant Higgs boson pair production in the four leptons plus two b jets final state in proton-proton collisions at $\sqrt{s} = 13$ TeV," Jun. 2022. arXiv: 2206.10657 [hep-ex] [Cited on pages 63, 65, 100].

[240] ATLAS Collaboration, "Search for Higgs boson pair production in the $\gamma\gamma WW^*$ channel using pp collision data recorded at $\sqrt{s} = 13$ TeV with the ATLAS detector," *Eur. Phys. J. C*, vol. 78, no. 12, p. 1007, 2018. doi: 10.1140/epjc/s10052-018-6457-x. arXiv: 1807.08567 [hep-ex] [Cited on pages 63, 65].

[241] CMS Collaboration, "Search for nonresonant Higgs boson pair production in the WW$\gamma\gamma$ channel in pp collisions at $\sqrt{s} = 13$ TeV," 2022, [Available on CDS: CMS-PAS-HIG-21-014] [Cited on pages 63, 65, 219].

[242] CMS Collaboration, "Search for Higgs boson pair production with one associated vector boson in proton-proton collisions at $\sqrt{s} = 13$ TeV," 2023, [Available on CDS: CMS-PAS-HIG-22-006] [Cited on pages 63, 65].

[243] CMS Collaboration, "Search for a massive scalar resonance decaying to a light scalar and a Higgs boson in the four b quarks final state with boosted topology," Apr. 2022. doi: 10.1016/j.physletb.2022.137392. arXiv: 2204.12413 [hep-ex] [Cited on pages 64, 65].

[244] CMS Collaboration, "Search for a heavy Higgs boson decaying into two lighter Higgs bosons in the $\tau\tau bb$ final state at 13 TeV," *JHEP*, vol. 11, p. 057, 2021. doi: 10.1007/JHEP11(2021)057. arXiv: 2106.10361 [hep-ex] [Cited on pages 64, 65, 224].

[245] CMS Collaboration, "Search for a new resonance decaying to two scalars in the final state with two bottom quarks and two photons in proton-proton collisions at $\sqrt{s} = 13$ TeV," 2022, [Available on CDS: CMS-PAS-HIG-21-011] [Cited on pages 64, 65, 224].

[246] ATLAS Collaboration, "Search for Higgs boson pair production in the WW^*WW^* decay channel using ATLAS data recorded at $\sqrt{s} = 13$ TeV," *JHEP*, vol. 05, p. 124, 2019. doi: 10.1007/JHEP05(2019)124. arXiv: 1811.11028 [hep-ex] [Cited on pages 65, 205, 218].

[247] CMS Collaboration, "Search for resonances decaying to a pair of Higgs bosons in the $\mathrm{b\bar{b}q\bar{q}'}\ell\nu$ final state in proton-proton collisions at $\sqrt{s} = 13$ TeV," *JHEP*, vol. 10, p. 125, 2019. doi: 10.1007/JHEP10(2019)125. arXiv: 1904.04193 [hep-ex] [Cited on pages 65, 90].

[248] ATLAS Collaboration, "Combination of searches for Higgs boson pairs in pp collisions at $\sqrt{s} = 13$ TeV with the ATLAS detector," *Phys. Lett. B*, vol. 800, p. 135 103, 2020. doi: 10.1016/j.physletb.2019.135103. arXiv: 1906.02025 [hep-ex] [Cited on pages 65, 224].

[249] ATLAS Collaboration, "Constraining the Higgs boson self-coupling from single- and double-Higgs production with the ATLAS detector using pp collisions at $\sqrt{s} = 13$ TeV," Nov. 2022. arXiv: 2211.01216 [hep-ex] [Cited on pages 65, 222].

[250] CMS Collaboration, "Combination of searches for Higgs boson pair production in proton-proton collisions at $\sqrt{s} = 13$ TeV," *Phys. Rev. Lett.*, vol. 122, no. 12, p. 121 803, 2019. doi: 10.1103/PhysRevLett.122.121803. arXiv: 1811.09689 [hep-ex] [Cited on pages 65, 219, 224].

[251] CERN, "CERN annual report 2021," CERN, Geneva, Tech. Rep., 2022. doi: 10.17181/AnnualReport2021 [Cited on page 66].

[252] The LHC Study Group, "Design study of the Large Hadron Collider (LHC): A multiparticle collider in the LEP tunnel," May 1991. doi: 10.5170/CERN-1991-003 [Cited on page 66].

[253] E. Mobs, "The CERN accelerator complex - August 2018. Complexe des accélérateurs du CERN - Août 2018," [Available on CDS: https://cds.cern.ch/record/2636343], Aug. 2018 [Cited on page 67].

[254] W. Herr and B. Muratori, "Concept of luminosity," 2006. doi: 10.5170/CERN-2006-002.361 [Cited on page 68].

[255] W. Herr, "Luminosity limitations in the LHC due to beam-beam effects for different bunch spacings," CERN, Geneva, Tech. Rep., Sep. 1992, [Available on CDS: SL-Note-92-51-AP] [Cited on page 68].

[256] CMS Collaboration, "Pileup mitigation at CMS in 13 TeV data," *JINST*, vol. 15, no. 09, P09018, 2020. doi: 10.1088/1748-0221/15/09/P09018. arXiv: 2003.00503 [hep-ex] [Cited on pages 68, 69, 91].

[257] S. Fartoukh *et al.*, "LHC configuration and operational scenario for Run 3," CERN, Tech. Rep., Nov. 2021, [Available on CDS: CERN-ACC-2021-0007] [Cited on page 70].

[258] P. Billoir and S. Qian, "Fast vertex fitting with a local parametrization of tracks," *Nucl. Instrum. Meth. A*, vol. 311, pp. 139–150, 1992. doi: 10.1016/0168-9002(92)90859-3 [Cited on page 71].

[259] CMS Collaboration, "Particle-flow reconstruction and global event description with the CMS detector," *JINST*, vol. 12, no. 10, P10003, 2017. doi: 10.1088/1748-0221/12/10/P10003. arXiv: 1706.04965 [physics.ins-det] [Cited on pages 72, 86, 91].

[260] CMS Collaboration, "Performance of the CMS drift tube chambers with cosmic rays," *JINST*, vol. 5, T03015, 2010. doi: 10.1088/1748-0221/5/03/T03015. arXiv: 0911.4855 [physics.ins-det] [Cited on pages 74, 81].

[261] CMS Collaboration, "Strategies and performance of the CMS silicon tracker alignment during LHC Run 2," *Nucl. Instrum. Meth. A*, vol. 1037, p. 166 795, 2022. doi: 10.1016/j.nima.2022.166795. arXiv: 2111.08757 [physics.ins-det] [Cited on page 74].

[262] CMS Tracker Group, "The CMS Phase-1 pixel detector upgrade," *JINST*, vol. 16, no. 02, P02027, 2021. doi: 10.1088/1748-0221/16/02/P02027. arXiv: 2012.14304 [physics.ins-det] [Cited on pages 75, 78].

[263] CMS Collaboration, "Description and performance of track and primary-vertex reconstruction with the CMS tracker," *JINST*, vol. 9, no. 10, P10009, 2014. doi: 10.1088/1748-0221/9/10/P10009. arXiv: 1405.6569 [physics.ins-det] [Cited on pages 76, 86].

[264] CMS ECAL/HCAL Collaborations, "The CMS barrel calorimeter response to particle beams from 2 to 350 GeV/c," *Eur. Phys. J. C*, vol. 60, pp. 359–373, 2009, [Erratum: Eur.Phys.J.C 61, 353–356 (2009)]. doi: 10.1140/epjc/s10052-009-0959-5 [Cited on page 78].

[265] CMS Collaboration, "Jet energy scale and resolution in the CMS experiment in pp collisions at 8 TeV," *JINST*, vol. 12, no. 02, P02014, 2017. doi: 10.1088/1748-0221/12/02/P02014. arXiv: 1607.03663 [hep-ex] [Cited on pages 78, 92–94].

[266] CMS HCAL Collaboration, "Design, performance, and calibration of CMS hadron-barrel calorimeter wedges," *Eur. Phys. J. C*, vol. 55, no. 1, pp. 159–171, 2008. doi: 10.1140/epjc/s10052-008-0573-y [Cited on page 78].

[267] F. De Guio, CMS collaboration, "First results from the CMS SiPM-based hadronic endcap calorimeter," *J. Phys. Conf. Ser.*, vol. 1162, no. 1, p. 012 009, 2019. doi: 10.1088/1742-6596/1162/1/012009 [Cited on page 78].

[268] A. Lobanov, CMS collaboration, "The CMS outer HCAL SiPM upgrade," *J. Phys. Conf. Ser.*, vol. 587, no. 1, p. 012 005, 2015. doi: 10.1088/1742-6596/587/1/012005 [Cited on page 79].

[269] R. M. Hadjiiska, CMS collaboration, "Detector performance and stability of the CMS RPC system during Run-2," CERN, Geneva, Tech. Rep., 2019, [Available on CDS: CMS-CR-2019-252] [Cited on page 81].

[270] CMS Collaboration, "The CMS trigger system," *JINST*, vol. 12, no. 01, P01020, 2017. doi: 10.1088/1748-0221/12/01/P01020. arXiv: 1609.02366 [Cited on page 81].

[271] S. Choudhury, CMS collaboration, "Performance of the high-level trigger system at CMS in LHC Run-2," *IEEE Trans. Nucl. Sci.*, vol. 68, no. 8, pp. 2035–2042, 2021. doi: 10.1109/TNS.2021.3087618 [Cited on page 82].

[272] S. Mukherjee, CMS collaboration, "Data scouting and data parking with the CMS high level trigger," *PoS*, vol. EPS-HEP2019, p. 139, 2020. doi: 10.22323/1.364.0139 [Cited on page 82].

[273] CMS Collaboration, "Performance of electron reconstruction and selection with the CMS detector in proton-proton collisions at $\sqrt{s} = 8$ TeV," *JINST*, vol. 10, no. 06, P06005, 2015. doi: 10.1088/1748-0221/10/06/P06005. arXiv: 1502.02701 [physics.ins-det] [Cited on pages 82, 89].

[274] CMS Collaboration, "Precision luminosity measurement in proton-proton collisions at $\sqrt{s} = 13$ TeV in 2015 and 2016 at CMS," *Eur. Phys. J. C*, vol. 81, no. 9, p. 800, 2021. doi: 10.1140/epjc/s10052-021-09538-2. arXiv: 2104.01927 [hep-ex] [Cited on page 85].

[275] CMS Collaboration, "CMS luminosity measurement for the 2017 data-taking period at $\sqrt{s} = 13$ TeV," 2018 [Cited on page 85].

[276] CMS Collaboration, "CMS luminosity measurement for the 2018 data-taking period at $\sqrt{s} = 13$ TeV," 2019 [Cited on page 85].

[277] CMS Collaboration, "CMS Luminosity Measurements for the 2016 Data Taking Period," 2017 [Cited on page 85].

[278] CMS Collaboration, "Performance of the CMS muon detector and muon reconstruction with proton-proton collisions at $\sqrt{s} = 13$ TeV," *JINST*, vol. 13, no. 06, P06015, 2018. doi: 10.1088/1748-0221/13/06/P06015. arXiv: 1804.04528 [physics.ins-det] [Cited on page 87].

[279] M. Backhaus *et al.*, "Impact of radiation on electronics and opto-electronics," *CERN Yellow Rep. Monogr.*, vol. 1, ed. by M. Bindi and E. Butz, pp. 87–121, 2021. doi: 10.23731/CYRM-2021-001.87 [Cited on page 88].

[280] CMS Collaboration, "Electron and photon reconstruction and identification with the CMS experiment at the CERN LHC," *JINST*, vol. 16, no. 05, P05014, 2021. doi: 10.1088/1748-0221/16/05/P05014. arXiv: 2012.06888 [hep-ex] [Cited on pages 88, 89, 141].

[281] CMS Collaboration, "Performance of photon reconstruction and identification with the CMS Detector in proton-proton collisions at $\sqrt{s} = 8$ TeV," *JINST*, vol. 10, no. 08, P08010, 2015. doi: 10.1088/1748-0221/10/08/P08010. arXiv: 1502.02702 [physics.ins-det] [Cited on page 89].

[282] G. P. Salam and G. Soyez, "A practical seedless infrared-safe cone jet algorithm," *JHEP*, vol. 05, p. 086, 2007. doi: 10.1088/1126-6708/2007/05/086. arXiv: 0704.0292 [hep-ph] [Cited on page 89].

[283] M. Cacciari, G. P. Salam, and G. Soyez, "The anti-k_t jet clustering algorithm," *JHEP*, vol. 04, p. 063, 2008. doi: 10.1088/1126-6708/2008/04/063. arXiv: 0802.1189 [hep-ph] [Cited on pages 89, 90].

[284] M. Cacciari, G. P. Salam, and G. Soyez, "FastJet user manual," *Eur. Phys. J. C*, vol. 72, p. 1896, 2012. doi: 10.1140/epjc/s10052-012-1896-2. arXiv: 1111.6097 [hep-ph] [Cited on pages 89, 92].

[285] S. D. Ellis and D. E. Soper, "Successive combination jet algorithm for hadron collisions," *Phys. Rev. D*, vol. 48, pp. 3160–3166, 1993. doi: 10.1103/PhysRevD.48.3160. arXiv: hep-ph/9305266 [Cited on page 90].

[286] Y. L. Dokshitzer, G. D. Leder, S. Moretti, and B. R. Webber, "Better jet clustering algorithms," *JHEP*, vol. 08, p. 001, 1997. doi: 10.1088/1126-6708/1997/08/001. arXiv: hep-ph/9707323 [Cited on page 90].

[287] M. Wobisch and T. Wengler, "Hadronization corrections to jet cross-sections in deep inelastic scattering," in *Workshop on Monte Carlo Generators for HERA Physics (Plenary Starting Meeting)*, Apr. 1998, pp. 270–279. arXiv: hep-ph/9907280 [Cited on page 90].

[288] M. Cacciari and G. P. Salam, "Pileup subtraction using jet areas," *Phys. Lett. B*, vol. 659, pp. 119–126, 2008. doi: 10.1016/j.physletb.2007.09.077. arXiv: 0707.1378 [hep-ph] [Cited on page 90].

[289] M. Cacciari, G. P. Salam, and G. Soyez, "The catchment area of jets," *JHEP*, vol. 04, p. 005, 2008. doi: 10.1088/1126-6708/2008/04/005. arXiv: 0802.1188 [hep-ph] [Cited on page 90].

[290] CMS Collaboration, "Determination of jet energy calibration and transverse momentum resolution in CMS," *JINST*, vol. 6, P11002, 2011. doi: 10.1088/1748-0221/6/11/P11002. arXiv: 1107.4277 [physics.ins-det] [Cited on pages 90, 92].

[291] C. Brust *et al.*, "Identifying boosted new physics with non-isolated leptons," *JHEP*, vol. 04, p. 079, 2015. doi: 10.1007/JHEP04(2015)079. arXiv: 1410.0362 [hep-ph] [Cited on page 90].

[292] D. Bertolini, P. Harris, M. Low, and N. Tran, "Pileup per particle identification," *JHEP*, vol. 10, p. 059, 2014. doi: 10.1007/JHEP10(2014)059. arXiv: 1407.6013 [hep-ph] [Cited on page 91].

[293] CMS Collaboration, "Jet algorithms performance in 13 TeV data," 2017, [Available on CDS: CMS-PAS-JME-16-003] [Cited on pages 91, 111].

[294] J. Thaler and K. Van Tilburg, "Identifying boosted objects with N-subjettiness," *JHEP*, vol. 03, p. 015, 2011. doi: 10.1007/JHEP03(2011)015. arXiv: 1011.2268 [hep-ph] [Cited on page 91].

[295] CMS Collaboration, "Identification of heavy-flavour jets with the CMS detector in pp collisions at 13 TeV," *JINST*, vol. 13, no. 05, P05011, 2018. doi: 10.1088/1748-0221/13/05/P05011. arXiv: 1712.07158 [physics.ins-det] [Cited on pages 91, 122].

[296] CMS Collaboration, "A deep neural network for simultaneous estimation of b jet energy and resolution," *Comput. Softw. Big Sci.*, vol. 4, no. 1, p. 10, 2020. doi: 10.1007/s41781-020-00041-z. arXiv: 1912.06046 [physics.data-an] [Cited on page 91].

[297] S. Gong *et al.*, "An efficient Lorentz equivariant graph neural network for jet tagging," *JHEP*, vol. 07, p. 030, 2022. doi: 10.1007/JHEP07(2022)030. arXiv: 2201.08187 [hep-ph] [Cited on page 92].

[298] H. Qu, C. Li, and S. Qian, "Particle transformer for jet tagging," Feb. 2022. arXiv: 2202.03772 [hep-ph] [Cited on page 92].

[299] CMS Collaboration, "Identification of heavy, energetic, hadronically decaying particles using machine-learning techniques," *JINST*, vol. 15, no. 06, P06005, 2020. doi: 10.1088/1748-0221/15/06/P06005. arXiv: 2004.08262 [hep-ex] [Cited on page 92].

[300] CMS Collaboration, "Performance of reconstruction and identification of τ leptons decaying to hadrons and ν_τ in pp collisions at $\sqrt{s} = 13$ TeV," *JINST*, vol. 13, no. 10, P10005, 2018. doi: 10.1088/1748-0221/13/10/P10005. arXiv: 1809.02816 [hep-ex] [Cited on pages 95, 224].

[301] CMS Collaboration, "Identification of hadronic tau lepton decays using a deep neural network," *JINST*, vol. 17, P07023, 2022. doi: 10.1088/1748-0221/17/07/P07023. arXiv: 2201.08458 [hep-ex] [Cited on pages 96, 121].

[302] CMS Collaboration, "Performance of missing transverse momentum reconstruction in proton-proton collisions at $\sqrt{s} = 13$ TeV using the CMS detector," *JINST*, vol. 14, no. 07, P07004, 2019. doi: 10.1088/1748-0221/14/07/P07004. arXiv: 1903.06078 [hep-ex] [Cited on pages 97, 99, 175].

[303] CMS Collaboration, "Search for the standard model Higgs boson produced in association with top quarks in multilepton final states," 2013, [Available on CDS: CMS-PAS-HIG-13-020] [Cited on page 97].

[304] P. Konar, K. Kong, and K. T. Matchev, "$\sqrt{\hat{s}}_{min}$: A global inclusive variable for determining the mass scale of new physics in events with missing energy at hadron colliders," *JHEP*, vol. 03, p. 085, 2009. doi: 10.1088/1126-6708/2009/03/085. arXiv: 0812.1042 [hep-ph] [Cited on page 98].

[305] J. H. Kim, K. Kong, K. T. Matchev, and M. Park, "Probing the triple Higgs self-interaction at the Large Hadron Collider," *Phys. Rev. Lett.*, vol. 122, no. 9, p. 091801, 2019. doi: 10.1103/PhysRevLett.122.091801. arXiv: 1807.11498 [hep-ph] [Cited on page 98].

[306] ATLAS Collaboration, "Higgsness and Topness plots for non-resonant HH production in the single lepton $bbWW$ decay channel," 2019, [Available on CDS: ATL-PHYS-PUB-2019-040] [Cited on page 98].

[307] M. Burns, K. Kong, K. T. Matchev, and M. Park, "Using subsystem M_{T2} for complete mass determinations in decay chains with missing energy at hadron colliders," *JHEP*, vol. 03, p. 143, 2009. doi: 10.1088/1126-6708/2009/03/143. arXiv: 0810.5576 [hep-ph] [Cited on page 98].

[308] A. J. Barr, M. J. Dolan, C. Englert, and M. Spannowsky, "Di-Higgs final states augMT2ed – selecting hh events at the high luminosity LHC," *Phys. Lett. B*, vol. 728, pp. 308–313, 2014. doi: 10.1016/j.physletb.2013.12.011. arXiv: 1309.6318 [hep-ph] [Cited on page 98].

[309] CMS Collaboration, "Search for heavy neutrinos and third-generation leptoquarks in hadronic states of two τ leptons and two jets in proton-proton collisions at $\sqrt{s} = 13$ TeV," *JHEP*, vol. 03, p. 170, 2019. doi: 10.1007/JHEP03(2019)170. arXiv: 1811.00806 [hep-ex] [Cited on page 98].

[310] K. Rehermann and B. Tweedie, "Efficient identification of boosted semileptonic top quarks at the LHC," *JHEP*, vol. 03, p. 059, 2011. doi: 10.1007/JHEP03(2011)059. arXiv: 1007.2221 [hep-ph] [Cited on page 102].

[311] S. Sánchez Cruz, "Search for new physics in events with high transverse momentum leptons with the CMS detector at the LHC," [Available on: https://hdl.handle.net/10651/57892], Ph.D. dissertation, Oviedo U., 2020 [Cited on page 102].

[312] CMS Collaboration, "Identification of prompt and isolated muons using multivariate techniques at the CMS experiment in proton-proton collisions at $\sqrt{s} = 13$ TeV," 2023, [Available on CDS: CMS-PAS-MUO-22-001] [Cited on page 102].

[313] CMS Collaboration, "Observation of four top quark production in proton-proton collisions at $\sqrt{s} = 13$ TeV," May 2023. arXiv: 2305.13439 [hep-ex] [Cited on page 103].

[314] CMS Collaboration, "Measurement of the cross section of top quark-antiquark pair production in association with a W boson in proton-proton collisions at $\sqrt{s} = 13$ TeV," Aug. 2022. arXiv: 2208.06485 [hep-ex] [Cited on pages 103, 183, 191, 197].

[315] CMS Collaboration, "Measurements of the Higgs boson production cross section and couplings in the W boson pair decay channel in proton-proton collisions at $\sqrt{s} = 13$ TeV," Jun. 2022. arXiv: 2206.09466 [hep-ex] [Cited on page 103].

[316] CMS Collaboration, "Observation of same-sign WW production from double parton scattering in proton-proton collisions at $\sqrt{s} = 13$ TeV," Jun. 2022. arXiv: 2206.02681 [hep-ex] [Cited on page 103].

[317] CMS Collaboration, "Search for electroweak production of charginos and neutralinos in proton-proton collisions at $\sqrt{s} = 13$ TeV," *JHEP*, vol. 04, p. 147, 2022. doi: 10.1007/JHEP04(2022)147. arXiv: 2106.14246 [hep-ex] [Cited on page 103].

[318] CMS Collaboration, "Search for CP violation in ttH and tH production in multilepton channels in proton-proton collisions at $\sqrt{s} = 13$ TeV," Aug. 2022. arXiv: 2208.02686 [hep-ex] [Cited on pages 103, 183, 204].

[319] CMS Collaboration, "Search for new physics in top quark production with additional leptons in the context of effective field theory using 138fb^{-1} of proton-proton collisions at $\sqrt{s} = 13$ TeV," 2023, Available on CDS: CMS-PAS-TOP-22-006 [Cited on page 103].

[320] CMS Collaboration, "Search for new physics in same-sign dilepton events in proton-proton collisions at $\sqrt{s} = 13$ TeV," *Eur. Phys. J. C*, vol. 76, no. 8, p. 439, 2016. doi: 10.1140/epjc/s10052-016-4261-z. arXiv: 1605.03171 [hep-ex] [Cited on page 106].

[321] CMS Collaboration, "Measurement of the $Z\gamma^* \to \tau\tau$ cross section in pp collisions at $\sqrt{s} = 13$ TeV and validation of τ lepton analysis techniques," *Eur. Phys. J. C*, vol. 78, no. 9, p. 708, 2018. doi: 10.1140/epjc/s10052-018-6146-9. arXiv: 1801.03535 [hep-ex] [Cited on pages 107, 110, 125, 203].

[322] J. M. Campbell and R. K. Ellis, "Update on vector boson pair production at hadron colliders," *Phys. Rev. D*, vol. 60, p. 113 006, 1999. doi: 10.1103/PhysRevD.60.113006. arXiv: hep-ph/9905386 [Cited on page 112].

[323] J. M. Campbell, R. K. Ellis, and C. Williams, "Vector boson pair production at the LHC," *JHEP*, vol. 07, p. 018, 2011. doi: 10.1007/JHEP07(2011)018. arXiv: 1105.0020 [hep-ph] [Cited on page 112].

[324] J. M. Campbell, R. K. Ellis, and W. T. Giele, "A Multi-Threaded Version of MCFM," *Eur. Phys. J. C*, vol. 75, no. 6, p. 246, 2015. doi: 10.1140/epjc/s10052-015-3461-2. arXiv: 1503.06182 [physics.comp-ph] [Cited on page 112].

[325] P. Artoisenet, R. Frederix, O. Mattelaer, and R. Rietkerk, "Automatic spin-entangled decays of heavy resonances in Monte Carlo simulations," *JHEP*, vol. 03, p. 015, 2013. doi: 10.1007/JHEP03(2013)015. arXiv: 1212.3460 [hep-ph] [Cited on page 112].

[326] Y. Gao *et al.*, "Spin determination of single-produced resonances at hadron colliders," *Phys. Rev. D*, vol. 81, p. 075 022, 2010. doi: 10.1103/PhysRevD.81.075022. arXiv: 1001.3396 [hep-ph] [Cited on page 112].

[327] S. Bolognesi *et al.*, "On the spin and parity of a single-produced resonance at the LHC," *Phys. Rev. D*, vol. 86, p. 095 031, 2012. doi: 10.1103/PhysRevD.86.095031. arXiv: 1208.4018 [hep-ph] [Cited on page 112].

[328] I. Anderson *et al.*, "Constraining anomalous HVV interactions at proton and lepton colliders," *Phys. Rev. D*, vol. 89, no. 3, ed. by N. A. Graf, M. E. Peskin, *et al.*, p. 035 007, 2014. doi: 10.1103/PhysRevD.89.035007. arXiv: 1309.4819 [hep-ph] [Cited on page 112].

[329] A. V. Gritsan, R. Röntsch, M. Schulze, and M. Xiao, "Constraining anomalous Higgs boson couplings to the heavy flavor fermions using matrix element techniques," *Phys. Rev. D*, vol. 94, no. 5, p. 055 023, 2016. doi: 10.1103/PhysRevD.94.055023. arXiv: 1606.03107 [hep-ph] [Cited on page 112].

[330] GEANT4 Collaboration, "GEANT4–a simulation toolkit," *Nucl. Instrum. Meth. A*, vol. 506, pp. 250–303, 2003. doi: 10.1016/S0168-9002(03)01368-8 [Cited on page 112].

[331] D. J. Lange, M. Hildreth, V. N. Ivantchenko, and I. Osborne, CMS collaboration, "Upgrades for the CMS simulation," *J. Phys. Conf. Ser.*, vol. 608, no. 1, ed. by L. Fiala, M. Lokajicek, *et al.*, p. 012 056, 2015. doi: 10.1088/1742-6596/608/1/012056 [Cited on page 112].

[332] R. Brun and F. Rademakers, "ROOT: An object oriented data analysis framework," *Nucl. Instrum. Meth. A*, vol. 389, ed. by M. Werlen and D. Perret-Gallix, pp. 81–86, 1997. doi: 10.1016/S0168-9002(97)00048-X [Cited on pages 112, 147, 152].

[333] G. Petrucciani, A. Rizzi, and C. Vuosalo, CMS collaboration, "Mini-AOD: A new analysis data format for CMS," *J. Phys. Conf. Ser.*, vol. 664, no. 7, p. 7, 2015. doi: 10.1088/1742-6596/664/7/072052. arXiv: 1702.04685 [physics.ins-det] [Cited on page 112].

[334] M. Peruzzi, G. Petrucciani, and A. Rizzi, CMS collaboration, "The NanoAOD event data format in CMS," *J. Phys. Conf. Ser.*, vol. 1525, no. 1, p. 012 038, 2020. doi: 10.1088/1742-6596/1525/1/012038 [Cited on page 112].

[335] I. Bird *et al.*, "Update of the computing models of the WLCG and the LHC experiments," Tech. Rep., Apr. 2014, [Available on CDS: LCG-TDR-002] [Cited on page 113].

[336] D. Spiga *et al.*, "The CMS Remote Analysis Builder (CRAB)," *Lect. Notes Comput. Sci.*, vol. 4873, pp. 580–586, 2007. doi: 10.1007/978-3-540-77220-0_52 [Cited on page 113].

[337] E. Bagnaschi, G. Degrassi, P. Slavich, and A. Vicini, "Higgs production via gluon fusion in the POWHEG approach in the SM and in the MSSM," *JHEP*, vol. 02, p. 088, 2012. doi: 10.1007/JHEP02(2012)088. arXiv: 1111.2854 [hep-ph] [Cited on page 113].

[338] P. Nason and C. Oleari, "NLO Higgs boson production via vector-boson fusion matched with shower in POWHEG," *JHEP*, vol. 02, p. 037, 2010. doi: 10.1007/JHEP02(2010)037. arXiv: 0911.5299 [hep-ph] [Cited on page 113].

[339] G. Luisoni, P. Nason, C. Oleari, and F. Tramontano, "$HW^{\pm}/HZ$ + 0 and 1 jet at NLO with the POWHEG BOX interfaced to GoSam and their merging within MiNLO," *JHEP*, vol. 10, p. 083, 2013. doi: 10.1007/JHEP10(2013)083. arXiv: 1306.2542 [hep-ph] [Cited on page 113].

[340] S. Frixione, P. Nason, and G. Ridolfi, "A positive-weight next-to-leading-order Monte Carlo for heavy flavour hadroproduction," *JHEP*, vol. 09, p. 126, 2007. doi: 10.1088/1126-6708/2007/09/126. arXiv: 0707.3088 [hep-ph] [Cited on page 114].

[341] E. Re, "Single-top Wt-channel production matched with parton showers using the POWHEG method," *Eur. Phys. J. C*, vol. 71, p. 1547, 2011. doi: 10.1140/epjc/s10052-011-1547-z. arXiv: 1009.2450 [hep-ph] [Cited on page 114].

[342] R. Frederix, E. Re, and P. Torrielli, "Single-top t-channel hadroproduction in the four-flavour scheme with POWHEG and aMC@NLO," *JHEP*, vol. 09, p. 130, 2012. doi: 10.1007/JHEP09(2012)130. arXiv: 1207.5391 [hep-ph] [Cited on page 114].

[343] R. Frederix, D. Pagani, and M. Zaro, "Large NLO corrections in $t\bar{t}W^{\pm}$ and $t\bar{t}t\bar{t}$ hadroproduction from supposedly subleading EW contributions," *JHEP*, vol. 02, p. 031, 2018. doi: 10.1007/JHEP02(2018)031. arXiv: 1711.02116 [hep-ph] [Cited on pages 114, 115].

[344] T. Melia, P. Nason, R. Rontsch, and G. Zanderighi, "W^+W^-, WZ and ZZ production in the POWHEG BOX," *JHEP*, vol. 11, p. 078, 2011. doi: 10.1007/JHEP11(2011)078. arXiv: 1107.5051 [hep-ph] [Cited on page 114].

[345] P. Nason and G. Zanderighi, "W^+W^-, WZ and ZZ production in the POWHEG-BOX-V2," *Eur. Phys. J. C*, vol. 74, no. 1, p. 2702, 2014. doi: 10.1140/epjc/s10052-013-2702-5. arXiv: 1311.1365 [hep-ph] [Cited on page 114].

[346] T. Gehrmann *et al.*, "W^+W^- production at hadron colliders in next to next to leading order QCD," *Phys. Rev. Lett.*, vol. 113, no. 21, p. 212 001, 2014. doi: 10.1103/PhysRevLett.113.212001. arXiv: 1408.5243 [hep-ph] [Cited on page 114].

[347] M. Grazzini, S. Kallweit, and M. Wiesemann, "Fully differential NNLO computations with MATRIX," *Eur. Phys. J. C*, vol. 78, no. 7, p. 537, 2018. doi: 10.1140/epjc/s10052-018-5771-7. arXiv: 1711.06631 [hep-ph] [Cited on page 114].

[348] F. Cascioli *et al.*, "ZZ production at hadron colliders in NNLO QCD," *Phys. Lett. B*, vol. 735, pp. 311–313, 2014. doi: 10.1016/j.physletb.2014.06.056. arXiv: 1405.2219 [hep-ph] [Cited on page 114].

[349] J. M. Campbell, R. K. Ellis, and C. Williams, "Bounding the Higgs width at the LHC using full analytic results for $gg \to e^- e^+ \mu^- \mu^+$," *JHEP*, vol. 04, p. 060, 2014. doi: 10.1007/JHEP04(2014)060. arXiv: 1311.3589 [hep-ph] [Cited on page 114].

[350] F. Caola, K. Melnikov, R. Röntsch, and L. Tancredi, "QCD corrections to ZZ production in gluon fusion at the LHC," *Phys. Rev. D*, vol. 92, no. 9, p. 094 028, 2015. doi: 10.1103/PhysRevD.92.094028. arXiv: 1509.06734 [hep-ph] [Cited on page 114].

[351] R. Gavin, Y. Li, F. Petriello, and S. Quackenbush, "W physics at the LHC with FEWZ 2.1," *Comput. Phys. Commun.*, vol. 184, pp. 208–214, 2013. doi: 10.1016/j.cpc.2012.09.005. arXiv: 1201.5896 [hep-ph] [Cited on pages 114, 117].

[352] M. Czakon and A. Mitov, "Top++: A program for the calculation of the top-pair cross-section at hadron colliders," *Comput. Phys. Commun.*, vol. 185, p. 2930, 2014. doi: 10.1016/j.cpc.2014.06.021. arXiv: 1112.5675 [hep-ph] [Cited on page 114].

[353] M. Aliev *et al.*, "HATHOR: HAdronic Top and Heavy quarks crOss section calculatoR," *Comput. Phys. Commun.*, vol. 182, pp. 1034–1046, 2011. doi: 10.1016/j.cpc.2010.12.040. arXiv: 1007.1327 [hep-ph] [Cited on pages 114, 117].

[354] P. Kant *et al.*, "HatHor for single top-quark production: Updated predictions and uncertainty estimates for single top-quark production in hadronic collisions," *Comput. Phys. Commun.*, vol. 191, pp. 74–89, 2015. doi: 10.1016/j.cpc.2015.02.001. arXiv: 1406.4403 [hep-ph] [Cited on pages 114, 117].

[355] R. Frederix and I. Tsinikos, "On improving NLO merging for $t\bar{t}W$ production," *JHEP*, vol. 11, p. 029, 2021. doi: 10.1007/JHEP11(2021)029. arXiv: 2108.07826 [hep-ph] [Cited on pages 115, 197].

[356] B. Cabouat and T. Sjöstrand, "Some dipole shower studies," *Eur. Phys. J. C*, vol. 78, no. 3, p. 226, 2018. doi: 10.1140/epjc/s10052-018-5645-z. arXiv: 1710.00391 [hep-ph] [Cited on page 116].

[357] A. Ballestrero *et al.*, "Precise predictions for same-sign W-boson scattering at the LHC," *Eur. Phys. J. C*, vol. 78, no. 8, p. 671, 2018. doi: 10.1140/epjc/s10052-018-6136-y. arXiv: 1803.07943 [hep-ph] [Cited on page 116].

[358] CMS Collaboration, "Measurements of the pp $\to$ WZ inclusive and differential production cross section and constraints on charged anomalous triple gauge couplings at $\sqrt{s} = 13$ TeV," *JHEP*, vol. 04, p. 122, 2019. doi: 10.1007/JHEP04(2019)122. arXiv: 1901.03428 [hep-ex] [Cited on page 117].

[359] CMS Collaboration, "Measurements of pp$\to$ZZ production cross sections and constraints on anomalous triple gauge couplings at $\sqrt{s} = 13$ TeV," *Eur. Phys. J. C*, vol. 81, no. 3, p. 200, 2021. doi: 10.1140/epjc/s10052-020-08817-8. arXiv: 2009.01186 [hep-ex] [Cited on page 117].

[360] CMS Collaboration, "Measurement of the inclusive W and Z production cross sections in pp collisions at $\sqrt{s} = 7$ TeV," *JHEP*, vol. 10, p. 132, 2011. doi: 10.1007/JHEP10(2011)132. arXiv: 1107.4789 [hep-ex] [Cited on page 118].

[361] M. Oreglia, "A study of the reactions $\psi' \to \gamma\gamma\psi$," Ph.D. dissertation, Dec. 1980 [Cited on pages 118, 174].

[362] CMS Collaboration, "Performance of the CMS Level-1 trigger in proton-proton collisions at $\sqrt{s} = 13$ TeV," *JINST*, vol. 15, no. 10, P10017, 2020. doi: 10.1088/1748-0221/15/10/P10017. arXiv: 2006.10165 [hep-ex] [Cited on page 122].

[363] M. Czakon *et al.*, "Top-pair production at the LHC through NNLO QCD and NLO EW," *JHEP*, vol. 10, p. 186, 2017. doi: 10.1007/JHEP10(2017)186. arXiv: 1705.04105 [hep-ph] [Cited on page 123].

[364] P. C. Mahalanobis, "On the generalized distance in statistics," *Proceedings of the National Institute of Sciences*, vol. 2, pp. 49–55, 1936 [Cited on page 136].

[365] CMS Collaboration, "Evidence for associated production of a Higgs boson with a top quark pair in final states with electrons, muons, and hadronically decaying τ leptons at $\sqrt{s} = 13$ TeV," *JHEP*, vol. 08, p. 066, 2018. doi: 10.1007/JHEP08(2018)066. arXiv: 1803.05485 [hep-ex] [Cited on pages 140, 167, 178, 182, 183].

[366] ATLAS, CMS, LHC Higgs Combination Group, "Procedure for the LHC Higgs boson search combination in Summer 2011," Aug. 2011, [Available on CDS: CMS-NOTE-2011-005; ATL-PHYS-PUB-2011-11] [Cited on pages 143, 150, 154].

[367] K. Cranmer, "Practical statistics for the LHC," in *2011 European School of High-Energy Physics*, 2014, pp. 267–308. doi: 10.5170/CERN-2014-003.267. arXiv: 1503.07622 [physics.data-an] [Cited on pages 143, 145, 151].

[368] J. Neyman, "Outline of a theory of statistical estimation based on the classical theory of probability," *Philosophical Transactions of the Royal Society of London. Series A, Mathematical and Physical Sciences*, vol. 236, no. 767, pp. 333–380, Aug. 1937. doi: 10.1098/rsta.1937.0005 [Cited on page 144].

[369] S. A. Stouffer *et al.*, "The American soldier: Volume I, Adjustment during army life," *Social Forces*, vol. 28, no. 1, pp. 87–90, Oct. 1949 [Cited on page 146].

[370] J. Neyman and E. S. Pearson, "On the problem of the most efficient tests of statistical hypotheses," *Phil. Trans. Roy. Soc. Lond. A*, vol. 231, no. 694-706, pp. 289–337, 1933. doi: 10.1098/rsta.1933.0009 [Cited on pages 146, 173].

[371] G. Cowan, K. Cranmer, E. Gross, and O. Vitells, "Asymptotic formulae for likelihood-based tests of new physics," *Eur. Phys. J. C*, vol. 71, p. 1554, 2011, [Erratum: Eur.Phys.J.C 73, 2501 (2013)]. doi: 10.1140/epjc/s10052-011-1554-0. arXiv: 1007.1727 [physics.data-an] [Cited on pages 146, 154].

[372] CMS Higgs Physics Analysis Group, *combine*, https://github.com/cms-analysis/HiggsAnalysis-CombinedLimit, Release v8.2.0, 2023 [Cited on pages 147, 153].

[373] L. Moneta *et al.*, "The RooStats project," *PoS*, vol. ACAT2010, ed. by T. Speer, F. Boudjema, *et al.*, p. 057, 2010. doi: 10.22323/1.093.0057. arXiv: 1009.1003 [physics.data-an] [Cited on page 147].

[374] W. Verkerke and D. P. Kirkby, "The RooFit toolkit for data modeling," in *Statistical Problems in Particle Physics, Astrophysics and Cosmology*, ed. by L. Lyons and M. Karagoz, May 2006, pp. 186–189. doi: 10.1142/9781860948985_0039. arXiv: physics/0306116 [Cited on page 147].

[375] CMS Higgs Physics Analysis Group, *HH inference*, https://gitlab.cern.ch/hh/tools/inference, 2023 [Cited on page 147].

[376] F. Garwood, "Fiducial limits for the Poisson distribution," *Biometrika*, vol. 28, no. 3/4, p. 437, Dec. 1936. doi: 10.2307/2333958 [Cited on page 148].

[377] G. Bohm and G. Zech, "Statistics of weighted Poisson events and its applications," *Nucl. Instrum. Meth. A*, vol. 748, pp. 1–6, 2014. doi: 10.1016/j.nima.2014.02.021. arXiv: 1309.1287 [physics.data-an] [Cited on page 148].

[378] J. S. Conway, "Incorporating nuisance parameters in likelihoods for multisource spectra," in *PHYSTAT 2011*, 2011, pp. 115–120. doi: 10.5170/CERN-2011-006.115. arXiv: 1103.0354 [physics.data-an] [Cited on pages 149, 151, 152].

[379] R. J. Barlow and C. Beeston, "Fitting using finite Monte Carlo samples," *Comput. Phys. Commun.*, vol. 77, pp. 219–228, 1993. doi: 10.1016/0010-4655(93)90005-W [Cited on page 151].

[380] F. James and M. Roos, "Minuit: A system for function minimization and analysis of the parameter errors and correlations," *Comput. Phys. Commun.*, vol. 10, pp. 343–367, 1975. doi: 10.1016/0010-4655(75)90039-9 [Cited on page 152].

[381] F. James, "Interpretation of the shape of the likelihood function around its minimum," *Comput. Phys. Commun.*, vol. 20, pp. 29–35, 1980. doi: 10.1016/0010-4655(80)90103-4 [Cited on page 152].

[382] H. Cramér, *Mathematical methods Of statistics*. Princeton, USA: Princeton University Press, 1946, isbn: 978-0-691-08004-6 [Cited on page 152].

[383] C. R. Rao, "Information and the accuracy attainable in the estimation of statistical parameters," *Bull. Calcutta Math. Soc.*, vol. 37, pp. 81–91, 1945 [Cited on page 152].

[384] S. S. Wilks, "The large-sample distribution of the likelihood ratio for testing composite hypotheses," *The Annals of Mathematical Statistics*, vol. 9, no. 1, pp. 60–62, Mar. 1938. doi: 10.1214/aoms/1177732360 [Cited on page 153].

[385] T. Junk, "Confidence level computation for combining searches with small statistics," *Nucl. Instrum. Meth. A*, vol. 434, pp. 435–443, 1999. doi: 10.1016/S0168-9002(99)00498-2. arXiv: hep-ex/9902006 [Cited on page 155].

[386] A. L. Read, "Presentation of search results: The CL_s technique," *J. Phys. G*, vol. 28, ed. by M. R. Whalley and L. Lyons, pp. 2693–2704, 2002. doi: 10.1088/0954-3899/28/10/313 [Cited on page 155].

[387] R. D. Cousins, "Generalization of chisquare goodness-of-fit test for binned data using saturated models, with application to histograms," 2013 [Cited on page 156].

[388] T. Hastie, R. Tibshirani, and J. Friedman, *The Elements of Statistical Learning*, 2nd. Springer New York, Aug. 2009, isbn: 978-0-387-84858-7. doi: 10.1007/978-0-387-84858-7 [Cited on page 159].

[389] P. Baldi *et al.*, "Parameterized neural networks for high-energy physics," *Eur. Phys. J. C*, vol. 76, no. 5, p. 235, 2016. doi: 10.1140/epjc/s10052-016-4099-4. arXiv: 1601.07913 [hep-ex] [Cited on pages 160, 168].

[390] A. N. Kolmogorov, "Sulla determinazione empirica di una legge didistribuzione," *Giorn Dell'inst Ital Degli Att*, vol. 4, pp. 89–91, 1933 [Cited on page 160].

[391] N. Smirnov, "Table for estimating the goodness of fit of empirical distributions," *The Annals of Mathematical Statistics*, vol. 19, no. 2, pp. 279–281, Jun. 1948. doi: 10.1214/aoms/1177730256 [Cited on page 160].

[392] T. W. Anderson and D. A. Darling, “Asymptotic theory of certain "goodness of fit" criteria based on stochastic processes,” *The Annals of Mathematical Statistics*, vol. 23, no. 2, pp. 193–212, Jun. 1952. doi: 10.1214/aoms/1177729437 [Cited on page 160].

[393] T. W. Anderson and D. A. Darling, “A test of goodness of fit,” *Journal of the American Statistical Association*, vol. 49, no. 268, pp. 765–769, Dec. 1954. doi: 10.1080/01621459.1954.10501232 [Cited on page 160].

[394] G. King and L. Zeng, “Logistic regression in rare events data,” *Political Analysis*, vol. 9, pp. 137–163, 2001. doi: 10.1093/oxfordjournals.pan.a004868 [Cited on page 161].

[395] CMS Collaboration, “Prospects for HH measurements at the HL-LHC,” 2018, [Available on CDS: CMS-PAS-FTR-18-019] [Cited on page 161].

[396] A. N. Tikhonov, “Solution of incorrectly formulated problems and the regularization method,” *Soviet Math. Dokl.*, vol. 4, pp. 1035–1038, 1963 [Cited on page 163].

[397] N. Srivastava *et al.*, “Dropout: A simple way to prevent neural networks from overfitting,” *Journal of Machine Learning Research*, vol. 15, no. 56, pp. 1929–1958, 2014 [Cited on page 163].

[398] C. Sima and E. R. Dougherty, “The peaking phenomenon in the presence of feature-selection,” *Pattern Recognition Letters*, vol. 29, no. 11, pp. 1667–1674, Aug. 2008. doi: 10.1016/j.patrec.2008.04.010 [Cited on page 163].

[399] L. Breiman, “Random forests,” *Machine Learning*, vol. 45, no. 1, pp. 5–32, 2001. doi: 10.1023/a:1010933404324 [Cited on pages 164, 166].

[400] L. Tani, D. Rand, C. Veelken, and M. Kadastik, “Evolutionary algorithms for hyperparameter optimization in machine learning for application in high energy physics,” *Eur. Phys. J. C*, vol. 81, no. 2, p. 170, 2021. doi: 10.1140/epjc/s10052-021-08950-y. arXiv: 2011.04434 [hep-ex] [Cited on pages 165, 203].

[401] J. Kennedy and R. Eberhart, “Particle swarm optimization,” in *Proceedings of ICNN’95 - International Conference on Neural Networks*, vol. 4, IEEE, 1995, pp. 1942–1948. doi: 10.1109/ICNN.1995.488968 [Cited on page 165].

[402] L. Breiman, J. Friedman, C. Stone, and R. Olshen, *Classification and Regression Trees*. Taylor & Francis, 1984, isbn: 978-0-412-04841-8 [Cited on page 165].

[403] T. Chen and C. Guestrin, “XGBoost,” in *Proceedings of the 22nd ACM SIGKDD International Conference on Knowledge Discovery and Data Mining*, ACM, Aug. 2016. doi: 10.1145/2939672.2939785 [Cited on pages 166, 167, 179].

[404] F. Pedregosa *et al.*, “Scikit-learn: Machine learning in Python,” *Journal of Machine Learning Research*, vol. 12, pp. 2825–2830, 2011. arXiv: 1201.0490 [Cited on page 167].

[405] W. S. McCulloch and W. Pitts, “A logical calculus of the ideas immanent in nervous activity,” *The Bulletin of Mathematical Biophysics*, vol. 5, no. 4, pp. 115–133, Dec. 1943. doi: 10.1007/bf02478259 [Cited on page 169].

[406] F. Rosenblatt, “The perceptron — A perceiving and recognizing automaton,” Cornell Aeronautical Laboratory, Ithaca, New York, Tech. Rep. 85-460-1, Jan. 1957 [Cited on page 169].

[407] M. Minsky and S. Papert, *Perceptrons: an Introduction to Computational Geometry*. MIT Press, 1969, isbn: 978-0-262-63022-1 [Cited on page 169].

[408] J. Bridle, "Training stochastic model recognition algorithms as networks can lead to maximum mutual information estimation of parameters," in *Advances in Neural Information Processing Systems*, ed. by D. Touretzky, vol. 2, Morgan-Kaufmann, 1989, pp. 211–217 [Cited on page 170].

[409] N. S. Keskar *et al.*, "On large-batch training for deep learning: Generalization gap and sharp minima," 2016. arXiv: 1609.04836 [Cited on page 171].

[410] D. E. Rumelhart, G. E. Hinton, and R. J. Williams, "Learning representations by back-propagating errors," *Nature*, vol. 323, no. 6088, pp. 533–536, Oct. 1986. doi: 10.1038/323533a0 [Cited on page 171].

[411] D. P. Kingma and J. Ba, "Adam: A method for stochastic optimization," in *3rd International Conference on Learning Representations, ICLR 2015, San Diego, CA, USA, May 7-9, 2015, Conference Track Proceedings*, ed. by Y. Bengio and Y. LeCun, 2015. arXiv: 1412.6980 [Cited on page 171].

[412] I. Sutskever, J. Martens, G. Dahl, and G. Hinton, "On the importance of initialization and momentum in deep learning," in *Proceedings of the 30th International Conference on Machine Learning*, ed. by S. Dasgupta and D. McAllester, ser. Proceedings of Machine Learning Research, vol. 28, PMLR, Jun. 2013, pp. 1139–1147 [Cited on page 171].

[413] Y. E. Nesterov, "A method of solving a convex programming problem with convergence rate $O\left(\frac{1}{k^2}\right)$," *Sov. Math., Dokl.*, vol. 269, pp. 543–547, 3 1983 [Cited on page 171].

[414] X. Glorot, A. Bordes, and Y. Bengio, "Deep sparse rectifier neural networks," in *International Conference on Artificial Intelligence and Statistics*, 2011 [Cited on page 171].

[415] X. Glorot and Y. Bengio, "Understanding the difficulty of training deep feedforward neural networks," in *Proceedings of the Thirteenth International Conference on Artificial Intelligence and Statistics*, ed. by Y. W. Teh and M. Titterington, ser. Proceedings of Machine Learning Research, vol. 9, PMLR, May 2010, pp. 249–256 [Cited on page 172].

[416] K. He, X. Zhang, S. Ren, and J. Sun, "Delving deep into rectifiers: Surpassing human-level performance on ImageNet classification," in *Proceedings of the IEEE international conference on computer vision*, 2015, pp. 1026–1034. doi: 10.1109/ICCV.2015.123. arXiv: 1502.01852 [Cited on page 172].

[417] Y. A. LeCun, L. Bottou, G. B. Orr, and K.-R. Müller, "Efficient BackProp," in *Lecture Notes in Computer Science*. Springer Berlin Heidelberg, 2012, pp. 9–48, isbn: 978-3-642-35289-8. doi: 10.1007/978-3-642-35289-8_3 [Cited on page 172].

[418] S. Ioffe and C. Szegedy, "Batch normalization: Accelerating deep network training by reducing internal covariate shift," *CoRR*, 2015. arXiv: 1502.03167 [Cited on page 172].

[419] S. Santurkar, D. Tsipras, A. Ilyas, and A. Madry, "How does batch normalization help optimization?" In *Neural Information Processing Systems*, 2018. arXiv: 1805.11604 [Cited on page 172].

[420] X. Li, S. Chen, X. Hu, and J. Yang, "Understanding the disharmony between dropout and batch normalization by variance shift," *IEEE*, pp. 2677–2685, Jun. 2018. doi: 10.1109/CVPR.2019.00279. arXiv: 1801.05134 [Cited on page 172].

[421] M. Abadi *et al.*, *TensorFlow: Large-scale machine learning on heterogeneous systems*, Software available from https://tensorflow.org, 2015. doi: 10.5281/zenodo.4724125 [Cited on page 172].

[422] F. Chollet *et al.*, *Keras*, Software available from https://github.com/fchollet/keras, 2015 [Cited on page 172].

[423] K. Kondo, "Dynamical likelihood method for reconstruction of events with missing momentum. I. Method and toy models," *Journal of the Physical Society of Japan*, vol. 57, no. 12, pp. 4126–4140, Dec. 1988. doi: 10.1143/jpsj.57.4126 [Cited on page 173].

[424] K. Kondo, "Dynamical likelihood method for reconstruction of events with missing momentum. II. Mass spectra for 2→2 processes," *Journal of the Physical Society of Japan*, vol. 60, no. 3, pp. 836–844, Mar. 1991. doi: 10.1143/jpsj.60.836 [Cited on page 173].

[425] I. Volobouev, "Matrix element method in HEP: Transfer functions, efficiencies, and likelihood normalization," Jan. 2011. arXiv: 1101.2259 [physics.data-an] [Cited on page 173].

[426] CMS Collaboration, "Search for a standard model Higgs boson produced in association with a top-quark pair and decaying to bottom quarks using a matrix element method," *Eur. Phys. J. C*, vol. 75, no. 6, p. 251, 2015. doi: 10.1140/epjc/s10052-015-3454-1. arXiv: 1502.02485 [hep-ex] [Cited on pages 173, 178, 183].

[427] T. Strebler, "Probing the Higgs coupling to the top quark at the LHC in the CMS experiment," Ph.D. dissertation, Ecole Polytechnique, 2017 [Cited on pages 173–175].

[428] J. Alwall, A. Freitas, and O. Mattelaer, "The matrix element method and QCD radiation," *Phys. Rev. D*, vol. 83, p. 074 010, 2011. doi: 10.1103/PhysRevD.83.074010. arXiv: 1010.2263 [hep-ph] [Cited on page 175].

[429] L. Bianchini *et al.*, "Reconstruction of the Higgs mass in events with Higgs bosons decaying into a pair of τ leptons using matrix element techniques," *Nucl. Instrum. Meth. A*, vol. 862, pp. 54–84, 2017. doi: 10.1016/j.nima.2017.05.001. arXiv: 1603.05910 [hep-ex] [Cited on pages 175, 180].

[430] K. Ehatäht, L. Marzola, and C. Veelken, "Reconstruction of the mass of Higgs boson pairs in events with Higgs boson pairs decaying into four τ leptons," Sep. 2018. arXiv: 1809.06140 [hep-ex] [Cited on pages 175, 180].

[431] G. P. Lepage, "A new algorithm for adaptive multidimensional integration," *Journal of Computational Physics*, vol. 27, no. 2, pp. 192–203, May 1978. doi: 10.1016/0021-9991(78)90004-9 [Cited on page 177].

[432] T. Ohl, "Vegas revisited: Adaptive Monte Carlo integration beyond factorization," *Comput. Phys. Commun.*, vol. 120, pp. 13–19, 1999. doi: 10.1016/S0010-4655(99)00209-X. arXiv: hep-ph/9806432 [Cited on page 177].

[433] J. M. Campbell, W. T. Giele, and C. Williams, "The matrix element method at next-to-leading order," *JHEP*, vol. 11, p. 043, 2012. doi: 10.1007/JHEP11(2012)043. arXiv: 1204.4424 [hep-ph] [Cited on page 178].

[434] CMS Collaboration, "Measurement of spin correlations in $t\bar{t}$ production using the matrix element method in the muon+jets final state in pp collisions at $\sqrt{s} = 8$ TeV," *Phys. Lett. B*, vol. 758, pp. 321–346, 2016. doi: 10.1016/j.physletb.2016.05.005. arXiv: 1511.06170 [hep-ex] [Cited on page 178].

[435] ATLAS Collaboration, "Evidence for single top-quark production in the s-channel in proton-proton collisions at $\sqrt{s} = 8$ TeV with the ATLAS detector using the Matrix Element Method," *Phys. Lett. B*, vol. 756, pp. 228–246, 2016. doi: 10.1016/j.physletb.2016.03.017. arXiv: 1511.05980 [hep-ex] [Cited on page 178].

[436] DØ Collaboration, "Measurement of the top quark mass using the matrix element technique in dilepton final states," *Phys. Rev. D*, vol. 94, no. 3, p. 032 004, 2016. doi: 10.1103/PhysRevD.94.032004. arXiv: 1606.02814 [hep-ex] [Cited on page 178].

[437] ATLAS Collaboration, "Search for the standard model Higgs boson produced in association with top quarks and decaying into $b\bar{b}$ in pp collisions at $\sqrt{s} = 8$ TeV with the ATLAS detector," *Eur. Phys. J. C*, vol. 75, no. 7, p. 349, 2015. doi: 10.1140/epjc/s10052-015-3543-1. arXiv: 1503.05066 [hep-ex] [Cited on pages 179, 183].

[438] A. Hoecker *et al.*, "TMVA - Toolkit for multivariate data analysis," 1, vol. 1504, 2012, pp. 1013–1016. doi: 10.1063/1.4771869. arXiv: physics/0703039 [Cited on page 179].

[439] G. Grasseau *et al.*, "Deployment of a Matrix Element Method code for the ttH channel analysis on GPU's platform," *EPJ Web Conf.*, vol. 214, ed. by A. Forti, L. Betev, *et al.*, p. 06 028, 2019. doi: 10.1051/epjconf/201921406028 [Cited on page 180].

[440] L. Bianchini, J. Conway, E. K. Friis, and C. Veelken, "Reconstruction of the Higgs mass in $H \to \tau\tau$ events by dynamical likelihood techniques," *J. Phys. Conf. Ser.*, vol. 513, ed. by D. L. Groep and D. Bonacorsi, p. 022 035, 2014. doi: 10.1088/1742-6596/513/2/022035 [Cited on page 180].

[441] S. Brochet *et al.*, "MoMEMta, a modular toolkit for the Matrix Element Method at the LHC," *Eur. Phys. J. C*, vol. 79, no. 2, p. 126, 2019. doi: 10.1140/epjc/s10052-019-6635-5. arXiv: 1805.08555 [hep-ph] [Cited on page 180].

[442] J. Brehmer, F. Kling, I. Espejo, and K. Cranmer, "MadMiner: Machine learning-based inference for particle physics," *Comput. Softw. Big Sci.*, vol. 4, no. 1, p. 3, 2020. doi: 10.1007/s41781-020-0035-2. arXiv: 1907.10621 [hep-ph] [Cited on page 181].

[443] CDF Collaboration, "Search for the standard model Higgs boson produced in association with top quarks using the full CDF data set," *Phys. Rev. Lett.*, vol. 109, p. 181 802, 2012. doi: 10.1103/PhysRevLett.109.181802. arXiv: 1208.2662 [hep-ex] [Cited on page 182].

[444] CMS Collaboration, "Search for the associated production of a Higgs boson with a single top quark in proton-proton collisions at $\sqrt{s} = 8$ TeV," *JHEP*, vol. 06, p. 177, 2016. doi: 10.1007/JHEP06(2016)177. arXiv: 1509.08159 [hep-ex] [Cited on pages 182, 183].

[445] CMS Collaboration, "Measurement of the cross section for top quark pair production in association with a W or Z boson in proton-proton collisions at $\sqrt{s} = 13$ TeV," *JHEP*, vol. 08, p. 011, 2018. doi: 10.1007/JHEP08(2018)011. arXiv: 1711.02547 [hep-ex] [Cited on pages 183, 197].

[446] CMS Collaboration, "Measurement of top quark pair production in association with a Z boson in proton-proton collisions at $\sqrt{s} = 13$ TeV," *JHEP*, vol. 03, p. 056, 2020. doi: 10.1007/JHEP03(2020)056. arXiv: 1907.11270 [hep-ex] [Cited on page 183].

[447] ATLAS Collaboration, "Measurements of the inclusive and differential production cross sections of a top-quark–antiquark pair in association with a Z boson at $\sqrt{s} = 13$ TeV with the ATLAS detector," *Eur. Phys. J. C*, vol. 81, no. 8, p. 737, 2021. doi: 10.1140/epjc/s10052-021-09439-4. arXiv: 2103.12603 [hep-ex] [Cited on pages 183, 227].

[448] CMS Collaboration, "Search for the standard model Higgs boson produced in association with a top-quark pair in pp collisions at the LHC," *JHEP*, vol. 05, p. 145, 2013. doi: 10.1007/JHEP05(2013)145. arXiv: 1303.0763 [hep-ex] [Cited on page 183].

[449] ATLAS Collaboration, "Search for the standard model Higgs boson produced in association with top quarks and decaying into a $b\bar{b}$ pair in pp collisions at $\sqrt{s} = 13$ TeV with the ATLAS detector," *Phys. Rev. D*, vol. 97, no. 7, p. 072 016, 2018. doi: 10.1103/PhysRevD.97.072016. arXiv: 1712.08895 [hep-ex] [Cited on page 183].

[450] CMS Collaboration, "Search for the associated production of the Higgs boson with a top-quark pair," *JHEP*, vol. 09, p. 087, 2014, [Erratum: JHEP 10, 106 (2014)]. doi: 10.1007/JHEP09(2014)087. arXiv: 1408.1682 [hep-ex] [Cited on page 183].

[451] CMS Collaboration, "Evidence for the 125 GeV Higgs boson decaying to a pair of τ leptons," *JHEP*, vol. 05, p. 104, 2014. doi: 10.1007/JHEP05(2014)104. arXiv: 1401.5041 [hep-ex] [Cited on page 183].

[452] CMS Collaboration, "Search for $\mathrm{t\bar{t}H}$ production in the all-jet final state in proton-proton collisions at $\sqrt{s} = 13$ TeV," *JHEP*, vol. 06, p. 101, 2018. doi: 10.1007/JHEP06(2018)101. arXiv: 1803.06986 [hep-ex] [Cited on page 183].

[453] ATLAS Collaboration, "Search for $H \to \gamma\gamma$ produced in association with top quarks and constraints on the Yukawa coupling between the top quark and the Higgs boson using data taken at 7 TeV and 8 TeV with the ATLAS detector," *Phys. Lett. B*, vol. 740, pp. 222–242, 2015. doi: 10.1016/j.physletb.2014.11.049. arXiv: 1409.3122 [hep-ex] [Cited on page 183].

[454] ATLAS Collaboration, "Search for the associated production of the Higgs boson with a top quark pair in multilepton final states with the ATLAS detector," *Phys. Lett. B*, vol. 749, pp. 519–541, 2015. doi: 10.1016/j.physletb.2015.07.079. arXiv: 1506.05988 [hep-ex] [Cited on page 183].

[455] ATLAS Collaboration, "Probing the CP nature of the top-Higgs Yukawa coupling in $t\bar{t}H$ and tH events with $H \to b\bar{b}$ decays using the ATLAS detector at the LHC," Mar. 2023. arXiv: 2303.05974 [hep-ex] [Cited on page 183].

[456] ATLAS Collaboration, "Evidence for the Higgs-boson Yukawa coupling to tau leptons with the ATLAS detector," *JHEP*, vol. 04, p. 117, 2015. doi: 10.1007/JHEP04(2015)117. arXiv: 1501.04943 [hep-ex] [Cited on page 183].

[457] CMS Collaboration, "Search for $\mathrm{t\bar{t}H}$ production in the $\mathrm{H} \to \mathrm{b\bar{b}}$ decay channel with leptonic $\mathrm{t\bar{t}}$ decays in proton-proton collisions at $\sqrt{s} = 13$ TeV," *JHEP*, vol. 03, p. 026, 2019. doi: 10.1007/JHEP03(2019)026. arXiv: 1804.03682 [hep-ex] [Cited on page 183].

[458] ATLAS Collaboration, "Analysis of $t\bar{t}H$ and $t\bar{t}W$ production in multilepton final states with the ATLAS detector," Oct. 2019, [Available on CDS: ATLAS-CONF-2019-045] [Cited on page 197].

[459] ATLAS Collaboration, "Evidence for $t\bar{t}t\bar{t}$ production in the multilepton final state in proton-proton collisions at $\sqrt{s} = 13$ TeV with the ATLAS detector," *Eur. Phys. J. C*, vol. 80, no. 11, p. 1085, 2020. doi: 10.1140/epjc/s10052-020-08509-3. arXiv: 2007.14858 [hep-ex] [Cited on page 197].

[460] L. Tani and C. Veelken, "Comparison of Bayesian and particle swarm algorithms for hyperparameter optimisation in machine learning applications in high energy physics," Jan. 2022. arXiv: 2201.06809 [physics.data-an] [Cited on page 203].

[461] L. Li *et al.*, "A system for massively parallel hyperparameter tuning," *Proceedings of Machine Learning and Systems*, vol. 2, pp. 230–246, 2020. arXiv: 1810.05934 [Cited on page 203].

[462] CMS Collaboration, "Performance of reconstruction and identification of tau leptons in their decays to hadrons and tau neutrino in LHC Run-2," 2016, [Available on CDS: CMS-PAS-TAU-16-002] [Cited on page 203].

[463] CMS Collaboration, "An embedding technique to determine $\tau\tau$ backgrounds in proton-proton collision data," *JINST*, vol. 14, no. 06, P06032, 2019. doi: 10.1088/1748-0221/14/06/P06032. arXiv: 1903.01216 [hep-ex] [Cited on page 203].

[464] A. Ghosh, B. Nachman, and D. Whiteson, "Uncertainty-aware machine learning for high energy physics," *Phys. Rev. D*, vol. 104, no. 5, p. 056 026, 2021. doi: 10.1103/PhysRevD.104.056026. arXiv: 2105.08742 [physics.data-an] [Cited on page 203].

[465] CMS Collaboration, "Search for new physics in top quark production with additional leptons in proton-proton collisions at $\sqrt{s} = 13$ TeV using effective field theory," *JHEP*, vol. 03, p. 095, 2021. doi: 10.1007/JHEP03(2021)095. arXiv: 2012.04120 [hep-ex] [Cited on page 204].

[466] CMS Higgs Physics Analysis Group, *Summary plots*, https://twiki.cern.ch/twiki/bin/view/CMSPublic/SummaryResultsHIG, 32nd revision, 2023 [Cited on pages 223, 226].

[467] E. Gross and O. Vitells, "Trial factors for the look elsewhere effect in high energy physics," *Eur. Phys. J. C*, vol. 70, pp. 525–530, 2010. doi: 10.1140/epjc/s10052-010-1470-8. arXiv: 1005.1891 [physics.data-an] [Cited on page 224].

[468] D. Freer and G.-Z. Yang, "Data augmentation for self-paced motor imagery classification with C-LSTM," *Journal of Neural Engineering*, vol. 17, no. 1, p. 016 041, Jan. 2020. doi: 10.1088/1741-2552/ab57c0 [Cited on page 227].

[469] M. Erdmann, E. Geiser, Y. Rath, and M. Rieger, "Lorentz Boost Networks: Autonomous physics-inspired feature engineering," *JINST*, vol. 14, no. 06, P06006, 2019. doi: 10.1088/1748-0221/14/06/P06006. arXiv: 1812.09722 [hep-ex] [Cited on page 227].

[470] S. Sekmen, CMS collaboration, "Recent developments in CMS fast simulation," *PoS*, vol. ICHEP2016, p. 181, 2016. doi: 10.22323/1.282.0181. arXiv: 1701.03850 [physics.ins-det] [Cited on page 227].

[471] J. de Favereau *et al.*, DELPHES 3 collaboration, "DELPHES 3: A modular framework for fast simulation of a generic collider experiment," *JHEP*, vol. 02, p. 057, 2014. doi: 10.1007/JHEP02(2014)057. arXiv: 1307.6346 [hep-ex] [Cited on page 227].

[472] C. Chen *et al.*, "Data augmentation at the LHC through analysis-specific fast simulation with deep learning," Oct. 2020. arXiv: 2010.01835 [physics.comp-ph] [Cited on page 227].

[473] T. P. S. Gillam and C. G. Lester, "Improving estimates of the number of 'fake' leptons and other mis-reconstructed objects in hadron collider events: BoB's your UNCLE," *JHEP*, vol. 11, p. 031, 2014. doi: 10.1007/JHEP11(2014)031. arXiv: 1407.5624 [hep-ph] [Cited on page 227].

[474] J. Erdmann *et al.*, "Reformulation of a likelihood approach to fake-lepton estimation in the framework of Bayesian inference," *Nucl. Instrum. Meth. A*, vol. 1021, p. 165 939, 2022. doi: 10.1016/j.nima.2021.165939. arXiv: 2106.13628 [hep-ph] [Cited on page 227].

[475] ATLAS Collaboration, "Tools for estimating fake/non-prompt lepton backgrounds with the ATLAS detector at the LHC," Nov. 2022. arXiv: 2211.16178 [hep-ex] [Cited on page 227].

[476] N. Seeba, "Prospects for Di-Higgs boson searches with multilepton final states in the qqHH production mode," 2nd CERN Baltic Conference, 2022 [Cited on page 227].

Acknowledgements

I want to express my utmost gratitude to both of my supervisors, Mario Kadastik and Christian Veelken. I commend Mario for his ability in creating a pleasant environment for physicists to thrive in, and for making this whole journey as smooth as possible. Christian has supervised me since the start of my master's program and has provided me much of the guidance throughout my Ph.D. studies.

Many thanks to Xandra, Sergio, Marco and Cristina, as working with them on the $t\bar{t}H$ multilepton analysis was really efficient, which — thinking back — I should not have taken for granted. I thank Torben, Laurits, Andrew, Tobias and Siddhesh for their contributions to the HH multilepton analysis. I definitely look forward to team up with them again if such an opportunity presents itself. I also thank Benjamin, Dennis and Peter, as well as Agni and Florian for having me in the $HH \rightarrow b\bar{b}WW^{*}$ analysis. I would like to shout-out my former and current colleagues at KBFI, including Ram and Saswati, and especially Lauri for keeping our computing cluster alive and well.

Special thanks again to Christian, Torben, Laurits and Mario for agreeing to review parts of this thesis and for providing constructive feedback.

I extend my gratitude to Oxana Smirnova and Thomas Strebler for kindly agreeing to fulfill the opposing role in my PhD defense on such a short notice.

I also thank the administrative people at TalTech for their patience and for keeping me enrolled.

I am very grateful to my parents and friends for their support and understanding.

This work was financed by the Estonian Research Council, grants IUT23-4, MOBTT86 and PRG445.

There are no solutions. There are only trade-offs.

—Thomas Sowell

Abstract

Measurement of Higgs Boson Couplings in Final States Featuring Multiple Leptons and Hadronic τ Decay Products

The discovery of the Higgs boson in 2012 completed the experimental unification of the standard model (SM) as it was formulated many decades prior. Although the SM provides an excellent description of the elementary building blocks of the universe, it still remains incompatible with a modern theory of gravity and fails to explain the presence of additional „dark" matter inferred from astronomical observations. To make progress on these matters, the SM must be thoroughly tested and repeatedly verified in the hopes that someday a discrepancy is found between the SM predictions and the experimental data. Given that the SM is expected to fall apart in conditions similar to the earliest stages of the universe, signs of new physics are searched for in particle collision experiments at very high energies to replicate the environment of the early universe as closely as possible.

This thesis presents the searches for two types of scattering processes, which are expected to occur in these high energy particle collisions: Higgs boson production in association with a single top quark (tH) or with a pair pair of top quarks ($\mathrm{t\bar{t}H}$), and the production of Higgs boson pairs (HH). The $\mathrm{t\bar{t}H}$ and tH processes provide direct access to the top Yukawa coupling, which quantifies the interaction strength between Higgs bosons and top quarks, whereas HH production allows to probe Higgs boson self-coupling. Plausible numerical values of those couplings are inferred from the measured production rates of the corresponding signal processes. The measurement is based on analyzing data that has been recorded by the CMS experiment at a center-of-momentum energy of $13\,\mathrm{TeV}$ during the Run 2 data-taking period of the LHC in the years of 2016 to 2018.

The $\mathrm{t\bar{t}H}$ and HH production is analyzed in final states that feature multiple electrons (e), muons (μ) and hadronically decaying τ leptons (τ_h), to complement analogous measurements in other final states. The e, μ and τ_h are expected to arise from Higgs boson decays into pairs of vector bosons and pairs of τ leptons. Although multilepton final states offer a relatively clean experimental environment for studying $\mathrm{t\bar{t}H}$ and HH production compared to other decay modes, they considerably limit the amount of data that would be available for the measurements. To overcome these challenges, the signals are searched for in multiple analysis channels, which are defined based on the multiplicity and charges of final state particles. The sensitivity for the signal is improved with multivariate analysis techniques and machine learning methods.

The $\mathrm{t\bar{t}H}$ and tH production rates are measured to be $0.92^{+0.17}_{-0.13}(\mathrm{syst}) \pm 0.19(\mathrm{stat})$ and $5.7 \pm 3.0(\mathrm{syst})^{+2.8}_{-2.7}(\mathrm{stat})$ times the SM prediction, respectively. The statistical significance of the $\mathrm{t\bar{t}H}$ signal over the background-only hypothesis amounts to 4.2σ. The top Yukawa coupling is constrained to the range $[-0.9, -0.7] \cup [0.7, 1.1]$ times the SM prediction, with a slight preference towards positive values of the coupling. These results represent the most stringent constraints on the top Yukawa coupling set by any individual $\mathrm{t\bar{t}H}$ analysis to date and establish multilepton channels as among the leading decay modes in terms of sensitivity.

As no HH signal has been observed yet, an upper limit of 21.3 times the SM prediction is placed on the HH production rate. Upper limits are also set on a range of physics scenarios that arise from effective field theory extensions of the SM, as well as on physics models where the two Higgs bosons result from the decays of a yet unknown spin-0 or spin-2 particle with a mass anywhere between 250 and $1000\,\mathrm{GeV}$. The Higgs boson self-coupling is constrained to $[-6.9, 11.1]$ times the SM prediction. All results are compatible with the SM expectation. No significant excesses of the data over the SM expectation are observed.

While the results on HH production are not the most stringent compared to other HH decay modes, every analysis channel that improves the overall sensitivity to the HH signal will help when the results of different HH analyses are interpreted in combination.

Kokkuvõte

Higgsi bosoni seoseparameetrite mõõtmine mitmeid leptoneid ja hadronilisi τ laguprodukte sisaldavates lõppolekutes

Higgsi bosoni avastus 2012. aastal kuulutas ühtlasi ka standardmudeli valmimist, mille esmased sugemed ulatuvad poole sajandi tagusesse aega. Olgugi et tegu on seni parima teooriaga, mis kirjeldab Universumi kõige fundamentaalsemaid osakesi, jääb sellest siiski väheks, kuna ta ei ühildu täielikult üldrelatiivsusteooriaga ega suuda selgitada tumeaine olemust, mille kohta on leitud kaudseid tõendeid mitmetest sõltumatutest astronoomilistest vaatlustest. Et tagada mingigi progress nende probleemide lahendamise suunas, peab standardmudelit põhjalikult ja korduvalt testima lootuses, et leitakse ebakõla standardmudel ennustuse ja empiiriliste andmete vahel. Kuna kõigi eelduste kohaselt peaks standardmudel oma kehtivuse kaotama tingimustes, mis on väga sarnased varajasele Universumile, siis üritatakse uue füüsika jälgi leida eksperimentides, kus osakesi põrgatatakse kokku väga kõrgetel energiatel, et esile kutsuda hajuvusprotsesse sarnaselt varajasele Universumile.

Käesolev doktoritöö uurib kahte sellist hajuvusprotsessi: Higgsi bosoni tekkimine ühe tipukvargiga (tH) või tipukvargi paariga ($\mathrm{t\bar{t}H}$) ning Higgsi bosoni paaride teke (HH). Protsessid $\mathrm{t\bar{t}H}$ ja tH võimaldavad otseselt mõõta Yukawa seoseparameetrit, mis määratleb interaktsiooni tugevust Higgsi bosoni ja tipukvarkide vahel, samas kui HH annab ligipääsu Higgsi bosoni eneseinteraktsiooni seoseparameetrile. Seoseparameetrite võimalikud väärtused ekstraheeritakse vastavate tekkeprotsesside ristlõigetest. Nende mõõtmised teostati seni kõige suuremahulisema andmestiku peal, mida CMS-i detektor kogus aastatel 2016–2018. Analüüsitavad andmed on toodetud Suur Hadronite Põrgutiga (LHC), mis kiirendab prootonid energiale $6.5\,\mathrm{TeV}$ ning seejärel põrgatab nad iga $25\,\mathrm{ns}$ tagant detektori keskmes.

Kõnealuseid protsesse otsitakse lõppolekutes, milles esineb mitu müüonit, elektroni ja hadronilist τ leptoni laguprodukti. Nimetatud osakesed pärinevad eeldatavasti Higgsi bosoni lagunemisest vektor-bosonite või τ leptonite kaudu. Antud uuringud on komplementaarsed analoogsetele otsingutele muudes signaali lagunemiskanalites. Kuigi multileptonilised lõppolekud on võrdlemisi kergesti tuvastatavad, jääb andmetes paraku signaali väga väheks. Et üle saada nendest takistustest, uuritakse multileptonilisi lõppolekuid spetsiifilistes kanalites, mida defineeritakse nende arvukuse ja elektrilise laengu põhjal. Tundlikkust signaali suhtes võimendatakse erinevate mitmemõõtmelise analüüsi ja masinõppe meetoditega.

Protsesside $\mathrm{t\bar{t}H}$ ja tH tekkeristlõikeks standardmudeli suhtes mõõdeti vastavalt $0.92^{+0.17}_{-0.13}\,(\text{süst}) \pm 0.19(\text{stat})$ ja $5.7 \pm 3.0(\text{süst})^{+2.8}_{-2.7}(\text{stat})$. Esimesele mõõtetulemusele leiti statiliseks olulisuseks 4.2σ. Tipukvarkide ja Higgsi bosoni vaheline seoseparameeter standardmudeli suhtes piiritleti vahemikku $[-0.9,\, -0.7] \cup [0.7,\, 1.1]$, ent kerge eelistus on pigem positiivsete väärtuste poolel. Tegu on seni kõige täpsema mõõtetulemusega multileptonilistes lõppolekutes, mis ühtlasi demonstreerib antud analüüsi tähtsust $\mathrm{t\bar{t}H}$ protsessi mõõtmises.

Kuna HH signaali pole seni tuvastatud, siis seati selle tekkeristlõikele ülempiir, mis on võrdne 21.3-kordse standardmudeli poolt ennustatav tekkeristlõikega. Ristlõike ülempiire seati lisaks veel hüpoteetilistele stsenaariumitele, mis laiendavad standardmudelit efektiivse väljateooriaga või ennustavad uusi spinn-0 ja spinn-2 osakesi massiga 250–$1000\,\mathrm{GeV}$, mis Higgsi bosoni paariks laguneb. Higgsi bosoni eneseinteraktsiooni parameeter standardmudeli suhtes piiritleti vahemikku $[-6.9,\, 11.1]$. Kõik seninähtud tulemused on kooskõlas standardmudeli ennustusega 95-protsendilisel usaldusnivool ning statiliselt olulisi ülejääke andmetest ei leitud. Ehkki tegu pole just kõige tundlikuma analüüsiga võrreldes mõne teise lagunemiskanaliga, omab HH uurimine igas võimalikus kanalis mõtet vähemalt seni, kuni see protsess on jätkuvalt avastamata.

Appendix 1

I

CMS Collaboration, “Measurement of the Higgs boson production rate in association with top quarks in final states with electrons, muons, and hadronically decaying tau leptons at $\sqrt{s} = 13$ TeV”, *Eur. Phys. J. C*, vol. 81, no. 4, p. 378, 2021. doi: 10.1140/epjc/s10052-021-09014-x. arXiv: 2011.03652 [hep-ex]

Eur. Phys. J. C (2021) 81:378
https://doi.org/10.1140/epjc/s10052-021-09014-x

THE EUROPEAN PHYSICAL JOURNAL C

Regular Article - Experimental Physics

Measurement of the Higgs boson production rate in association with top quarks in final states with electrons, muons, and hadronically decaying tau leptons at $\sqrt{s} = 13$ TeV

CMS Collaboration*

CERN, 1211 Geneva 23, Switzerland

Received: 6 November 2020 / Accepted: 1 March 2021 / Published online: 30 April 2021
© CERN for the benefit of the CMS Collaboration 2021, corrected publication 2021

Abstract The rate for Higgs (H) bosons production in association with either one (tH) or two ($\mathrm{t\bar{t}H}$) top quarks is measured in final states containing multiple electrons, muons, or tau leptons decaying to hadrons and a neutrino, using proton–proton collisions recorded at a center-of-mass energy of 13 TeV by the CMS experiment. The analyzed data correspond to an integrated luminosity of 137 fb^{-1}. The analysis is aimed at events that contain $\mathrm{H} \to \mathrm{WW}$, $\mathrm{H} \to \tau\tau$, or $\mathrm{H} \to \mathrm{ZZ}$ decays and each of the top quark(s) decays either to lepton+jets or all-jet channels. Sensitivity to signal is maximized by including ten signatures in the analysis, depending on the lepton multiplicity. The separation among tH, $\mathrm{t\bar{t}H}$, and the backgrounds is enhanced through machine-learning techniques and matrix-element methods. The measured production rates for the $\mathrm{t\bar{t}H}$ and tH signals correspond to $0.92 \pm 0.19\,(\mathrm{stat})^{+0.17}_{-0.13}\,(\mathrm{syst})$ and $5.7 \pm 2.7\,(\mathrm{stat}) \pm 3.0\,(\mathrm{syst})$ of their respective standard model (SM) expectations. The corresponding observed (expected) significance amounts to 4.7 (5.2) standard deviations for $\mathrm{t\bar{t}H}$, and to 1.4 (0.3) for tH production. Assuming that the Higgs boson coupling to the tau lepton is equal in strength to its expectation in the SM, the coupling y_t of the Higgs boson to the top quark divided by its SM expectation, $\kappa_\mathrm{t} = y_\mathrm{t}/y_\mathrm{t}^{\mathrm{SM}}$, is constrained to be within $-0.9 < \kappa_\mathrm{t} < -0.7$ or $0.7 < \kappa_\mathrm{t} < 1.1$, at 95% confidence level. This result is the most sensitive measurement of the $\mathrm{t\bar{t}H}$ production rate to date.

1 Introduction

The discovery of a Higgs (H) boson by the ATLAS and CMS experiments at the CERN LHC [1–3] opened a new field for exploration in the realm of particle physics. Detailed measurements of the properties of this new particle are important to ascertain if the discovered resonance is indeed the Higgs boson predicted by the standard model (SM) [4–7]. In the SM, the Yukawa coupling y_f of the Higgs boson to fermions is proportional to the mass m_f of the fermion, namely $y_\mathrm{f} = m_\mathrm{f}/v$, where $v = 246$ GeV denotes the vacuum expectation value of the Higgs field. With a mass of $m_\mathrm{t} = 172.76 \pm 0.30$ GeV [8], the top quark is by far the heaviest fermion known to date, and its Yukawa coupling is of order unity. The large mass of the top quark may indicate that it plays a special role in the mechanism of electroweak symmetry breaking [9–11]. Deviations of y_t from the SM prediction of m_t/v would indicate the presence of physics beyond the SM.

The measurement of the Higgs boson production rate in association with a top quark pair ($\mathrm{t\bar{t}H}$) provides a model-independent determination of the magnitude of y_t, but not of its sign. The sign of y_t is determined from the associated production of a Higgs boson with a single top quark (tH). Leading-order (LO) Feynman diagrams for $\mathrm{t\bar{t}H}$ and tH production are shown in Figs. 1 and 2, respectively. The diagrams for tH production are separated into three contributions: the t-channel (tHq) and the s-channel, that proceed via the exchange of a virtual W boson, and the associated production of a Higgs boson with a single top quark and a W boson (tHW). The interference between the diagrams where the Higgs boson couples to the top quark (Fig. 2 upper and lower left), and those where the Higgs boson couples to the W boson (Fig. 2 upper and lower right) is destructive when y_t and g_W have the same sign, where the latter denotes the coupling of the Higgs boson to the W boson. This reduces the tH cross section and influences the kinematical properties of the event as a function of y_t and g_W. The interference becomes constructive when the coupling of the g_W and y_t have opposite signs, causing an increase in the cross section of up to one order of magnitude. This is referred to as inverted top quark coupling.

Indirect constraints on the magnitude of y_t are obtained from the rate of Higgs boson production via gluon fusion and from the decay rate of Higgs bosons to photon pairs [12], where in both cases, y_t enters through top quark loops. The

* e-mail: cms-publication-committee-chair@cern.ch

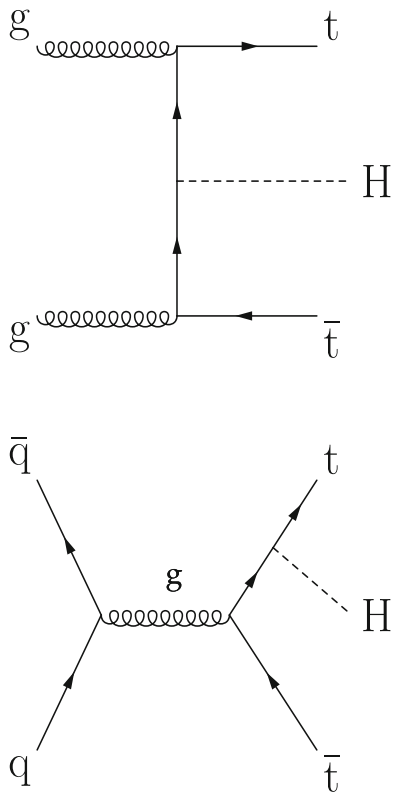


Fig. 1 Feynman diagrams at LO for $\mathrm{t\bar{t}H}$ production

$\mathrm{H} \to \gamma\gamma$ decay rate also provides sensitivity to the sign of y_t [13], as does the rate for associated production of a Higgs boson with a Z boson [14]. The measured rates of these processes suggest that the Higgs boson coupling to top quarks is SM-like. However, contributions from non-SM particles to these loops can compensate, and therefore mask, deviations of y_t from its SM value. A model-independent direct measurement of the top quark Yukawa coupling in $\mathrm{t\bar{t}H}$ and tH production is therefore very important. The comparison of the magnitude and sign of y_t obtained from the measurement of the $\mathrm{t\bar{t}H}$ and tH production rates, where y_t enters at lowest "tree" level, with the value of y_t obtained from processes where y_t enters via loop contributions can provide evidence about such contributions.

This manuscript presents the measurement of the $\mathrm{t\bar{t}H}$ and tH production rates in final states containing multiple electrons, muons, or τ leptons that decay to hadrons and a neutrino (τ_h). In the following, we refer to τ_h as "hadronically decaying τ". We also refer to electrons and muons collectively as "leptons" (ℓ). The measurement is based on data recorded by the CMS experiment in pp collisions at $\sqrt{s} = 13\,\mathrm{TeV}$ during Run 2 of the LHC, that corresponds to an integrated luminosity of $137\,\mathrm{fb}^{-1}$.

The associated production of Higgs bosons with top quark pairs was previously studied by the ATLAS and CMS experiments, with up to $24.8\,\mathrm{fb}^{-1}$ of data recorded at $\sqrt{s} = 7$ and 8 TeV during LHC Run 1 [15–19], and up to $79.8\,\mathrm{fb}^{-1}$ of data recorded at $\sqrt{s} = 13\,\mathrm{TeV}$ during LHC Run 2 [20–26]. The combined analysis of data recorded at $\sqrt{s} = 7$, 8, and 13 TeV resulted in the observation of $\mathrm{t\bar{t}H}$ production by CMS and ATLAS [27,28]. The production of Higgs bosons in association with a single top quark was also studied using the data recorded during LHC Run 1 [29] and Run 2 [30,31]. These analyses covered Higgs boson decays to $\mathrm{b\bar{b}}$, $\gamma\gamma$, WW, ZZ, and $\tau\tau$.

The measurement of the $\mathrm{t\bar{t}H}$ and tH production rates presented in this manuscript constitutes their first simultaneous analysis in this channel. This approach is motivated by the high degree of overlap between the experimental signatures of both production processes and takes into account the dependence of the $\mathrm{t\bar{t}H}$ and tH production rates as a function of y_t. Compared to previous work [23], the sensitivity of the present analysis is enhanced by improvements in the identification of τ_h decays and of jets originating from the hadronization of bottom quarks, as well as by performing the analysis in four additional experimental signatures, also referred to as analysis channels, that add up to a total of ten. The signatures involve Higgs boson decays to WW, $\tau\tau$, and ZZ, and are defined according to the lepton and τ_h multiplicities in the events. Some of them require leptons to have the same (opposite) sign of electrical charge and are therefore referred to as SS (OS). The signatures $2\ell\mathrm{SS}+0\tau_\mathrm{h}$, $3\ell+0\tau_\mathrm{h}$, $2\ell\mathrm{SS}+1\tau_\mathrm{h}$, $2\ell\mathrm{OS}+1\tau_\mathrm{h}$, $1\ell+2\tau_\mathrm{h}$, $4\ell+0\tau_\mathrm{h}$, $3\ell+1\tau_\mathrm{h}$, and $2\ell+2\tau_\mathrm{h}$ target events where at least one top quark decays via $\mathrm{t} \to \mathrm{bW}^+ \to \mathrm{b}\ell^+\nu_\ell$, whereas the signatures $1\ell+1\tau_\mathrm{h}$ and $0\ell+2\tau_\mathrm{h}$ target events where all top quarks decay via $\mathrm{t} \to \mathrm{bW}^+ \to \mathrm{bq\bar{q}}'$. We refer to the first and latter top quark decay signatures as semi-leptonically and hadronically decaying top quarks, respectively. Here and in the following, the term top quark includes the corresponding charge-conjugate decays of top antiquarks. As in previous analyses, the separation of the $\mathrm{t\bar{t}H}$ and tH signals from backgrounds is improved through machine-learning techniques, specifically boosted decision trees (BDTs) and artificial neural networks (ANNs) [32–34], and through the matrix-element method [35,36]. Machine-learning techniques are also employed to improve the separation between the $\mathrm{t\bar{t}H}$ and tH signals. We use the measured $\mathrm{t\bar{t}H}$ and tH production rates to set limits on the magnitude and sign of y_t.

This paper is organized as follows. After briefly describing the CMS detector in Sect. 2, we proceed to discuss the data and simulated events used in the measurement in Sect. 3. Section 4 covers the object reconstruction and selection from signals recorded in the detector, while Sect. 5 describes the

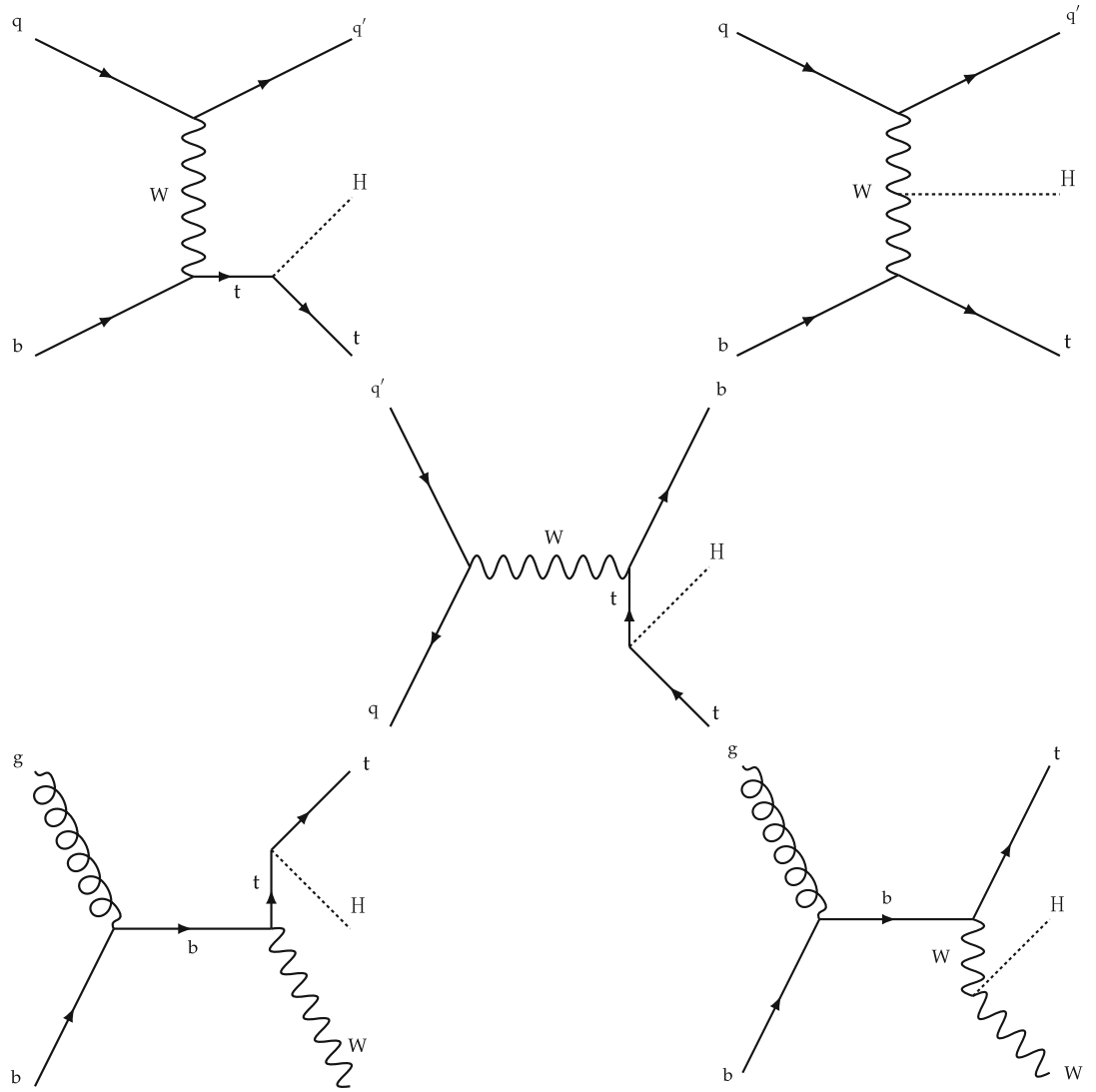


Fig. 2 Feynman diagrams at LO for tH production via the t-channel (tHq in upper left and upper right) and s-channel (middle) processes, and for associated production of a Higgs boson with a single top quark and a W boson (tHW in lower left and lower right). The tHq and tHW production processes are shown for the five-flavor scheme

selection criteria applied to events in the analysis. These events are grouped in categories, defined in Sect. 6, while the estimation of background contributions in these categories is described in Sect. 7. The systematic uncertainties affecting the measurements are given in Sect. 8, and the statistical analysis and the results of the measurements in Sect. 9. We end the paper with a brief summary in Sect. 10.

2 The CMS detector

The central feature of the CMS apparatus is a superconducting solenoid of 6 m internal diameter, providing a magnetic field of 3.8 T. A silicon pixel and strip tracker, a lead tungstate crystal electromagnetic calorimeter (ECAL), and a brass and scintillator hadron calorimeter (HCAL), each composed of a barrel and two endcap sections, are positioned

within the solenoid volume. The silicon tracker measures charged particles within the pseudorapidity range $|\eta| < 2.5$. The ECAL is a fine-grained hermetic calorimeter with quasi-projective geometry, and is segmented into the barrel region of $|\eta| < 1.48$ and in two endcaps that extend up to $|\eta| < 3.0$. The HCAL barrel and endcaps similarly cover the region $|\eta| < 3.0$. Forward calorimeters extend the coverage up to $|\eta| < 5.0$. Muons are measured and identified in the range $|\eta| < 2.4$ by gas-ionization detectors embedded in the steel flux-return yoke outside the solenoid. A two-level trigger system [37] is used to reduce the rate of recorded events to a level suitable for data acquisition and storage. The first level of the CMS trigger system, composed of custom hardware processors, uses information from the calorimeters and muon detectors to select the most interesting events with a latency of 4 μs. The high-level trigger processor farm further decreases the event rate from around 100 kHz to about 1 kHz. Details of the CMS detector and its performance, together with a definition of the coordinate system and the kinematic variables used in the analysis, are reported in Ref. [38].

3 Data samples and Monte Carlo simulation

The analysis uses pp collision data recorded at $\sqrt{s} = 13$ TeV at the LHC during 2016-2018. Only the data-taking periods during which the CMS detector was fully operational are included in the analysis. The total integrated luminosity of the analyzed data set amounts to 137 fb^{-1}, of which 35.9 [39], 41.5 [40], and 59.7 [41] fb^{-1} have been recorded in 2016, 2017, and 2018, respectively.

The event samples produced via Monte Carlo (MC) simulation are used for the purpose of calculating selection efficiencies for the $\mathrm{t\bar{t}H}$ and tH signals, estimating background contributions, and training machine-learning algorithms. The contribution from $\mathrm{t\bar{t}H}$ signal and the backgrounds arising from $\mathrm{t\bar{t}}$ production in association with W and Z bosons ($\mathrm{t\bar{t}W}$, $\mathrm{t\bar{t}Z}$), from triboson (WWW, WWZ, WZZ, ZZZ, WZγ) production, as well as from the production of four top quarks ($\mathrm{t\bar{t}t\bar{t}}$) are generated at next-to-LO (NLO) accuracy in perturbative quantum chromodynamics (pQCD) making use of the program MadGraph5_aMC@NLO 2.2.2 or 2.3.3 [42–45], whereas the tH signal and the $\mathrm{t\bar{t}}\gamma$, $\mathrm{t\bar{t}}\gamma^*$, tZ, $\mathrm{t\bar{t}WW}$, W+jets, Drell–Yan (DY), Wγ, and Zγ backgrounds are generated at LO accuracy using the same program. The symbols γ^* and γ are employed to distinguish virtual photons from the real ones. The event samples with virtual photons also include contributions from virtual Z bosons. The DY production of electron, muon, and τ lepton pairs are referred to as $\mathrm{Z}/\gamma^* \to \mathrm{ee}$, $\mathrm{Z}/\gamma^* \to \mu\mu$, and $\mathrm{Z}/\gamma^* \to \tau\tau$, respectively. The modeling of the $\mathrm{t\bar{t}W}$ background includes additional $\alpha_S\alpha^3$ electroweak corrections [46,47], simulated using MadGraph5_aMC@NLO. The NLO program powheg v2.0 [48–50] is used to simulate the backgrounds arising from $\mathrm{t\bar{t}}$+jets, tW, and diboson ($\mathrm{W^{\pm}W^{\mp}}$, WZ, ZZ) production, and from the production of single top quarks, and from SM Higgs boson production via gluon fusion (ggH) and vector boson fusion (qqH) processes, and from the production of SM Higgs bosons in association with W and Z bosons (WH, ZH) and with W and Z bosons along with a pair of top quarks ($\mathrm{t\bar{t}WH}$, $\mathrm{t\bar{t}ZH}$). The modeling of the top quark transverse momentum (p_{T}) distribution of $\mathrm{t\bar{t}}$+jets events simulated with the program powheg is improved by reweighting the events to the differential cross section computed at next-to-NLO (NNLO) accuracy in pQCD, including electroweak corrections computed at NLO accuracy [51]. We refer to the sum of WH plus ZH contributions by using the symbol VH and to the sum of $\mathrm{t\bar{t}WH}$ plus $\mathrm{t\bar{t}ZH}$ contributions by using the symbol $\mathrm{t\bar{t}VH}$. The SM production of Higgs boson pairs or a Higgs boson in association with a pair of b quarks is not considered as a background to this analysis, because its impact on the event yields in all categories is found to be negligible. The production of same-sign W pairs (SSW) is simulated using the program MadGraph5_aMC@NLO in LO accuracy, except for the contribution from double-parton interactions, which is simulated with pythia v8.2 [52] (referred to as pythia hereafter). The NNPDF3.0LO (NNPDF3.0NLO) [53–55] set of parton distribution functions (PDF) is used for the simulation of LO (NLO) 2016 samples, while NNPDF3.1 NNLO [56] is used for 2017 and 2018 LO and NLO samples.

Different flavor schemes are chosen to simulate the tHq and tHW processes. In the five-flavor scheme (5 FS), bottom quarks are considered as sea quarks of the proton and may appear in the initial state of proton–proton (pp) scattering processes, as opposed to the four-flavor scheme (4 FS), where only up, down, strange, and charm quarks are considered as valence or sea quarks of the proton, whereas bottom quarks are produced by gluon splitting at the matrix-element level, and therefore appear only in the final state [57]. In the 5 FS the distinction of tHq, s-channel, and tHW contributions to tH production is well-defined up to NLO, whereas at higher orders in perturbation theory the tHq and s-channel production processes start to interfere and can no longer be uniquely separated [58]. Similarly, in the same regime the tHW process starts to interfere with $\mathrm{t\bar{t}H}$ production at NLO. In the 4 FS, the separation among the tHq, s-channel, and tHW (if the W boson decays hadronically) processes holds only up to LO, and the tHW process starts to interfere with $\mathrm{t\bar{t}H}$ production already at tree level [58].

The tHq process is simulated at LO in the 4 FS and the tHW process in the 5 FS, so that interference contributions of latter with $\mathrm{t\bar{t}H}$ production are not present in the simulation. The contribution from s-channel tH production is negligible and is not considered in this analysis.

Parton showering, hadronization, and the underlying event are modeled using pythia with the tune CP5, CUETP8M1,

CUETP8M2, or CUETP8M2T4 [59–61], depending on the dataset, as are the decays of τ leptons, including polarization effects. The matching of matrix elements to parton showers is done using the MLM scheme [42] for the LO samples and the FxFx scheme [44] for the samples simulated at NLO accuracy.

The modeling of the $t\bar{t}H$ and tH signals, as well as of the backgrounds, is improved by normalizing the simulated event samples to cross sections computed at higher order in pQCD. The cross section for tH production is computed in the 5 FS. The SM cross section for tHq production has been computed at NLO accuracy in pQCD as 74.3 fb [62], and the SM cross section for $t\bar{t}H$ production has been computed at NLO accuracy in pQCD as 506.5 fb with electroweak corrections calculated at the same order in perturbation theory [62]. Both cross sections are computed for pp collisions at $\sqrt{s} = 13$ TeV. The tHW cross section is computed to be 15.2 fb at NLO in the 5 FS, using the DR2 scheme [63] to remove overlapping contributions between the tHW process and $t\bar{t}H$ production. The cross sections for $t\bar{t}$+jets, W+jets, DY, and diboson production are computed at NNLO accuracy [64–66].

Event samples containing Higgs bosons are normalized using the SM cross sections published in Ref. [62]. Event samples of $t\bar{t}Z$ production are normalized to the cross sections published in Ref. [62], while $t\bar{t}W$ simulated samples are normalized to the cross section published in the same reference increased by the contribution from the $\alpha_S\alpha^3$ electroweak corrections [46,47]. The SM cross sections for the $t\bar{t}H$ and tH signals and for the most relevant background processes are given in Table 1.

The $t\bar{t}H$ and tH samples are produced assuming all couplings of the Higgs boson have the values expected in the SM. The variation in kinematical properties of tH signal events, which stem from the interference of the diagrams in Fig. 2 described in Sect. 1, for values of y_t and g_W that differ from the SM expectation, is accounted for by applying weights calculated for each tH signal event with MADGRAPH5_aMC@NLO, following the approach suggested in [67,68]. No such reweighting is necessary for the $t\bar{t}H$ signal, because any variation of y_t would only affect the inclusive cross section for $t\bar{t}H$ production, which increases proportional to y_t^2, leaving the kinematical properties of $t\bar{t}H$ signal events unaltered.

The presence of simultaneous pp collisions in the same or nearby bunch crossings, referred to as pileup (PU), is modeled by superimposing inelastic pp interactions, simulated using PYTHIA, to all MC events. Simulated events are weighed so the PU distribution of simulated samples matches the one observed in the data.

All MC events are passed through a detailed simulation of the CMS apparatus, based on GEANT4 [69,70], and are processed using the same version of the CMS event reconstruction software used for the data.

Simulated events are corrected by means of weights or by varying the relevant quantities to account for residual differences between data and simulation. These differences arise in: trigger efficiencies; reconstruction and identification efficiencies for electrons, muons, and τ_h; the energy scale of τ_h and jets; the efficiency to identify jets originating from the hadronization of bottom quarks and the corresponding misidentification rates for light-quark and gluon jets; and the resolution in missing transverse momentum. The corrections are typically at the level of a few percent [71–75]. They are measured using a variety of SM processes, such as $Z/\gamma^* \to ee$, $Z/\gamma^* \to \mu\mu$, $Z/\gamma^* \to \tau\tau$, $t\bar{t}$+jets, and γ+jets production.

4 Event reconstruction

The CMS particle-flow (PF) algorithm [76] provides a global event description that optimally combines the information from all subdetectors, to reconstruct and identify all individual particles in the event. The particles are subsequently classified into five mutually exclusive categories: electrons, muons, photons, and charged and neutral hadrons.

Electrons are reconstructed combining the information from tracker and ECAL [77] and are required to satisfy $p_T > 7$ GeV and $|\eta| < 2.5$. Their identification is based on a multivariate (MVA) algorithm that combines observables sensitive to: the matching of measurements of the electron energy and direction obtained from the tracker and the calorimeter; the compactness of the electron cluster; and the bremsstrahlung emitted along the electron trajectory. Electron candidates resulting from photon conversions are removed by requiring that the track has no missing hits in the innermost layers of the silicon tracker and by vetoing candidates that are matched to a reconstructed conversion vertex. In the $2\ell SS + 0\tau_h$ and $2\ell SS + 1\tau_h$ channels (see Sect. 5 for channel definitions), we apply further electron selection criteria that demand the consistency among three independent measurements of the electron charge, described as "selective algorithm" in Ref. [77].

The reconstruction of muons is based on linking track segments reconstructed in the silicon tracker to hits in the muon detectors that are embedded in the steel flux-return yoke [78]. The quality of the spatial matching between the individual measurements in the tracker and in the muon detectors is used to discriminate genuine muons from hadrons punching through the calorimeters and from muons produced by in-flight decays of kaons and pions. Muons selected in the analysis are required to have $p_T > 5$ GeV and $|\eta| < 2.4$. For events selected in the $2\ell SS + 0\tau_h$ and $2\ell SS + 1\tau_h$ channels, the relative uncertainty in the curvature of the muon track is

Table 1 Standard model cross sections for the $t\bar{t}H$ and tH signals as well as for the most relevant background processes. The cross sections are quoted for pp collisions at $\sqrt{s} = 13$ TeV. The quoted value for DY production includes a generator-level requirement of $m_{Z/\gamma^*} > 50$ GeV

Process	Cross section (fb)	Process	Cross section (fb)
$t\bar{t}H$	507 [62]	$t\bar{t}Z$	839 [62]
tHq	74.3 [62]	$t\bar{t}W$	650 [46,47,62]
tHW	15.2 [63]	$t\bar{t}WW$	6.98 [45]
ggH	4.86×10^4 [62]	$t\bar{t}$+jets	8.33×10^5 [65]
qqH	3.78×10^3 [62]	DY	6.11×10^7 [64]
WH	1.37×10^3 [62]	WW	1.19×10^5 [64]
ZH	884 [62]	WZ	4.50×10^4 [64]
		ZZ	1.69×10^4 [64]

required to be less than 20% to ensure a high-quality charge measurement.

The electrons and muons satisfying the aforementioned selection criteria are referred to as "loose leptons" in the following. Additional selection criteria are applied to discriminate electrons and muons produced in decays of W and Z bosons and leptonic τ decays ("prompt") from electrons and muons produced in decays of b hadrons ("nonprompt"). The removal of nonprompt leptons reduces, in particular, the background arising from $t\bar{t}$+jets production. To maximally exploit the information available in each event, we use MVA discriminants that take as input the charged and neutral particles reconstructed in a cone around the lepton direction besides the observables related to the lepton itself. The jet reconstruction and b tagging algorithms are applied, and the resulting reconstructed jets are used as additional inputs to the MVA. In particular, the ratio of the lepton p_T to the reconstructed jet p_T and the component of the lepton momentum in a direction perpendicular to the jet direction are found to enhance the separation of prompt leptons from leptons originating from b hadron decays, complementing more conventional observables such as the relative isolation of the lepton, calculated in a variable cone size depending on the lepton p_T [79,80], and the longitudinal and transverse impact parameters of the lepton trajectory with respect to the primary pp interaction vertex. Electrons and muons passing a selection on the MVA discriminants are referred to as "tight leptons".

Because of the presence of PU, the primary pp interaction vertex typically needs to be chosen among the several vertex candidates that are reconstructed in each pp collision event. The candidate vertex with the largest value of summed physics-object p_T^2 is taken to be the primary pp interaction vertex. The physics objects are the jets, clustered using the jet finding algorithm [81,82] with the tracks assigned to candidate vertices as inputs, and the associated missing transverse momentum, taken as the negative vector sum of the p_T of those jets.

While leptonic decay products of τ leptons are selected by the algorithms described above, hadronic decays are reconstructed and identified by the "hadrons-plus-strips" (HPS) algorithm [74]. The algorithm is based on reconstructing individual hadronic decay modes of the τ lepton: $\tau^- \to h^-\nu_\tau$, $\tau^- \to h^-\pi^0\nu_\tau$, $\tau^- \to h^-\pi^0\pi^0\nu_\tau$, $\tau^- \to h^-h^+h^-\nu_\tau$, $\tau^- \to h^-h^+h^-\pi^0\nu_\tau$, and all the charge-conjugate decays, where the symbols h^- and h^+ denotes either a charged pion or a charged kaon. The photons resulting from the decay of neutral pions that are produced in the τ decay have a sizeable probability to convert into an electron-positron pair when traversing the silicon tracker. The conversions cause a broadening of energy deposits in the ECAL, since the electrons and positrons produced in these conversions are bent in opposite azimuthal directions by the magnetic field and may also emit bremsstrahlung photons. The HPS algorithm accounts for this broadening when it reconstructs the neutral pions, by means of clustering photons and electrons in rectangular strips that are narrow in η but wide in ϕ. The subsequent identification of τ_h candidates is performed by the "DeepTau" algorithm [83]. The algorithm is based on a convolutional ANN [84], using as input a set of 42 high-level observables in combination with low-level information obtained from the silicon tracker, the electromagnetic and hadronic calorimeters, and the muon detectors. The high-level observables comprise the p_T, η, ϕ, and mass of the τ_h candidate; the reconstructed τ_h decay mode; observables that quantify the isolation of the τ_h with respect to charged and neutral particles; as well as observables that provide sensitivity to the small distance that a τ lepton typically traverses between its production and decay. The low-level information quantifies the particle activity within two $\eta \times \phi$ grids, an "inner" grid of size 0.2×0.2, filled with cells of size 0.02×0.02, and an "outer" grid of size 0.5×0.5 (partially overlapping with the inner grid) and cells of size 0.05×0.05. Both grids are centered on the direction of the τ_h candidate. The τ_h considered in the analysis are required to have $p_T > 20$ GeV and $|\eta| < 2.3$ and to pass a selection on

the output of the convolutional ANN. The selection differs by analysis channel, targeting different efficiency and purity levels. We refer to these as the very loose, loose, medium, and tight τ_h selections, depending on the requirement imposed on the ANN output.

Jets are reconstructed using the anti-k_T algorithm [81,82] with a distance parameter of 0.4 and with the particles reconstructed by the PF algorithm as inputs. Charged hadrons associated with PU vertices are excluded from the clustering. The energy of the reconstructed jets is corrected for residual PU effects using the method described in Refs. [85,86] and calibrated as a function of jet p_T and η [72]. The jets considered in the analysis are required to: satisfy $p_T > 25$ GeV and $|\eta| < 5.0$; pass identification criteria that reject spurious jets arising from calorimeter noise [87]; and not overlap with any identified electron, muon or hadronic τ within $\Delta R = \sqrt{(\Delta\eta)^2 + (\Delta\phi)^2} < 0.4$. We tighten the requirement on the transverse momentum to the condition $p_T > 60$ GeV for jets reconstructed within the range $2.7 < |\eta| < 3.0$, to further reduce the effect of calorimeter noise, which is sizeable in this detector region. Jets passing these selection criteria are then categorized into central and forward jets, the former satisfying the condition $|\eta| < 2.4$ and the latter $2.4 < |\eta| < 5.0$. The presence of a high-p_T forward jet in the event is a characteristic signature of tH production in the t-channel and is used to separate the $\mathrm{t\bar{t}H}$ from the tH process in the signal extraction stage of the analysis.

Jets reconstructed within the region $|\eta| < 2.4$ and originating from the hadronization of bottom quarks are denoted as b jets and identified by the DeepJet algorithm [88]. The algorithm exploits observables related to the long lifetime of b hadrons as well as to the higher particle multiplicity and mass of b jets compared to light-quark and gluon jets. The properties of charged and neutral particle constituents of the jet, as well as of secondary vertices reconstructed within the jet, are used as inputs to a convolutional ANN. Two different selections on the output of the algorithm are employed in the analysis, corresponding to b jet selection efficiencies of 84 ("loose") and 70% ("tight"). The respective mistag rates for light-quark and gluon jets (c jet) are 11 and 1.1% (50% and 15%).

The missing transverse momentum vector, denoted by the symbol $\vec{p}_T^{\,\mathrm{miss}}$, is computed as the negative of the vector p_T sum of all particles reconstructed by the PF algorithm. The magnitude of this vector is denoted by the symbol p_T^{miss}. The analysis employs a linear discriminant, denoted by the symbol L_D, to remove backgrounds in which the reconstructed p_T^{miss} arises from resolution effects. The discriminant also reduces PU effects and is defined by the relation $L_D = 0.6p_T^{\mathrm{miss}} + 0.4H_T^{\mathrm{miss}}$, where the observable H_T^{miss} corresponds to the magnitude of the vector p_T sum of electrons, muons, τ_h, and jets [23]. The discriminant is constructed to combine the higher resolution of p_T^{miss} with the robustness to PU of H_T^{miss}.

5 Event selection

The analysis targets $\mathrm{t\bar{t}H}$ and tH production in events where the Higgs boson decays via $H \to WW$, $H \to \tau\tau$, or $H \to ZZ$, with subsequent decays $WW \to \ell^+\nu_\ell q q'$ or $\ell^+\nu_\ell\ell^-\bar{\nu}_\ell$; $\tau\tau \to \ell^+\nu_\ell\bar{\nu}_\tau\ell^-\bar{\nu}_\ell\nu_\tau$, $\ell^+\nu_\ell\bar{\nu}_\tau\tau_h\nu_\tau$, or $\tau_h\bar{\nu}_\tau\tau_h\nu_\tau$; $ZZ \to \ell^+\ell^- q q'$ or $\ell^+\ell^-\nu\bar{\nu}$; and the corresponding charge-conjugate decays. The decays $H \to ZZ \to \ell^+\ell^-\ell^+\ell^-$ are covered by the analysis published in Ref. [20]. The top quark may decay either semi-leptonically via $t \to bW^+ \to b\ell^+\nu_\ell$ or hadronically via $t \to bW^+ \to bqq'$, and analogously for the top antiquarks. The experimental signature of $\mathrm{t\bar{t}H}$ and tH signal events consists of: multiple electrons, muons, and τ_h; p_T^{miss} caused by the neutrinos produced in the W and Z bosons, and tau lepton decays; one (tH) or two ($\mathrm{t\bar{t}H}$) b jets from top quark decays; and further light-quark jets, produced in the decays of either the Higgs boson or of the top quark(s).

The events considered in the analysis are selected in ten nonoverlapping channels, targeting the signatures $2\ell\mathrm{SS} + 0\tau_h$, $3\ell + 0\tau_h$, $2\ell\mathrm{SS} + 1\tau_h$, $1\ell + 1\tau_h$, $0\ell + 2\tau_h$, $2\ell\mathrm{OS} + 1\tau_h$, $1\ell + 2\tau_h$, $4\ell + 0\tau_h$, $3\ell + 1\tau_h$, and $2\ell + 2\tau_h$, as stated earlier. The channels $1\ell + 1\tau_h$ and $0\ell + 2\tau_h$ specifically target events in which the Higgs boson decays via $H \to \tau\tau$ and the top quarks decay hadronically, the other channels target a mixture of $H \to WW$, $H \to \tau\tau$, and $H \to ZZ$ decays in events with either one or two semi-leptonically decaying top quarks.

Events are selected at the trigger level using a combination of single-, double-, and triple-lepton triggers, lepton+τ_h triggers, and double-τ_h triggers. Spurious triggers are discarded by demanding that electrons, muons, and τ_h reconstructed at the trigger level match electrons, muons, and τ_h reconstructed offline. The p_T thresholds of the triggers typically vary by a few GeV during different data-taking periods, depending on the instantaneous luminosity. For example, the threshold of the single-electron trigger ranges between 25 and 35 GeV in the analyzed data set, and that of the single-muon trigger varies between 22 and 27 GeV. The double-lepton (triple-lepton) triggers reduce the p_T threshold that is applied to the lepton of highest p_T to 23 (16) GeV in case this lepton is an electron and to 17 (8) GeV in case it is an muon. The electron+τ_h (muon+τ_h) trigger requires the presence of an electron of $p_T > 24$ GeV (muon of $p_T > 19$ or 20 GeV) in combination with a τ_h of $p_T > 20$ or 30 GeV ($p_T > 20$ or 27 GeV), where the lower p_T thresholds were used in 2016 and the higher ones in 2017 and 2018. The threshold of the double-τ_h trigger ranges between 35 and 40 GeV and is applied to both τ_h. In order to attain these p_T thresholds, the geometric acceptance of the lepton+τ_h and double-τ_h triggers is restricted to the range $|\eta| < 2.1$ for electrons, muons,

and τ_h. The p_T thresholds applied to electrons, muons, and τ_h in the offline event selection are chosen above the trigger thresholds.

The charge of leptons and τ_h is required to match the signature expected for the $t\bar{t}H$ and tH signals. The $0\ell + 2\tau_h$ and $1\ell + 2\tau_h$ channels target events where the Higgs boson decays to a τ lepton pair and both τ leptons decay hadronically. Consequently, the two τ_h are required to have OS charges in these channels. In events selected in the channels $4\ell + 0\tau_h$, $3\ell + 1\tau_h$, and $2\ell + 2\tau_h$, the leptons and τ_h are expected to originate from either the Higgs boson decay or from the decay of the top quark–antiquark pair and the sum of their charges is required to be zero. In the $3\ell + 0\tau_h$, $2\ell\text{SS} + 1\tau_h$, $2\ell\text{OS} + 1\tau_h$, and $1\ell + 2\tau_h$ channels the charge-sum of leptons plus τ_h is required to be either $+1$ or -1. No requirement on the charge of the lepton and of the τ_h is applied in the $1\ell + 1\tau_h$ channel, because studies performed with simulated samples of signal and background events indicate that the sensitivity of this channel is higher when no charge requirement is applied. The $2\ell\text{SS} + 0\tau_h$ channel targets events in which one lepton originates from the decay of the Higgs boson and the other lepton from a top quark decay. Requiring SS leptons reduces the signal yield by about half, but increases the signal-to-background ratio by a large factor by removing in particular the large background arising from $t\bar{t}$+jets production with dileptonic decays of the top quarks. The more favorable signal-to-background ratio for events with SS, rather than OS, lepton pairs motivates the choice of analyzing the events containing two leptons and one τ_h separately, in the two channels $2\ell\text{SS} + 1\tau_h$ and $2\ell\text{OS} + 1\tau_h$.

The selection criteria on b jets are designed to maintain a high efficiency for the $t\bar{t}H$ signal: one b jet can be outside of the p_T and η acceptance of the jet selection or can fail the b tagging criteria, provided that the other b jet passes the tight b tagging criteria. This choice is motivated by the observation that the main background contributions, arising from the associated production of single top quarks or top quark pairs with W and Z bosons, photons, and jets, feature genuine b jets with a multiplicity resembling that of the $t\bar{t}H$ and tH signals.

The requirements on the overall multiplicity of jets, including b jets, take advantage of the fact that the multiplicity of jets is typically higher in signal events compared to the background. The total number of jets expected in $t\bar{t}H$ (tH) signal events with the H boson decaying into WW, ZZ, and $\tau\tau$ amounts to $N_j = 10 - 2N_\ell - 2N_\tau$ ($N_j = 7 - 2N_\ell - 2N_\tau$), where N_j, N_ℓ and N_τ denote the total number of jets, electrons or muons, and hadronic τ decays, respectively. The requirements on N_j applied in each channel permit up to two jets to be outside of the p_T and η acceptance of the jet selection. In the $2\ell\text{SS} + 0\tau_h$ channel, the requirement on N_j is relaxed further, to increase the signal efficiency in particular for the tH process.

Background contributions arising from $t\bar{t}Z$, tZ, WZ, and DY production are suppressed by vetoing events containing OS pairs of leptons of the same flavor, referred to as SFOS lepton pairs, passing the loose lepton selection criteria and having an invariant mass $m_{\ell\ell}$ within 10 GeV of the Z boson mass, $m_Z = 91.19$ GeV [8]. We refer to this selection criterion as "Z boson veto". In the $2\ell\text{SS} + 0\tau_h$ and $2\ell\text{SS} + 1\tau_h$ channels, the Z boson veto is also applied to SS electron pairs, because the probability to mismeasure the charge of electrons is significantly higher than the corresponding probability for muons.

Background contributions arising from DY production in the $2\ell\text{SS} + 0\tau_h$, $3\ell + 0\tau_h$, $2\ell\text{SS} + 1\tau_h$, $4\ell + 0\tau_h$, $3\ell + 1\tau_h$, and $2\ell + 2\tau_h$ channels are further reduced by imposing a requirement on the linear discriminant, $L_D > 30$ GeV. The requirement on L_D is relaxed or tightened, depending on whether or not the event meets certain conditions, in order to either increase the efficiency to select $t\bar{t}H$ and tH signal events or to reject more background. In the $2\ell\text{SS} + 0\tau_h$ and $2\ell\text{SS}+1\tau_h$ channels, the requirement on L_D is only applied to events where both reconstructed leptons are electrons, to suppress the contribution of DY production entering the selection through a mismeasurement of the electron charge. In the $3\ell + 0\tau_h$, $4\ell + 0\tau_h$, $3\ell + 1\tau_h$, and $2\ell + 2\tau_h$ channels, the distribution of N_j is steeply falling for the DY background, thus rendering the expected contribution of this background small if the event contains a high number of jets; we take advantage of this fact by applying the requirement on L_D only to events with three or fewer jets. If events with $N_j \leq 3$ contain an SFOS lepton pair, the requirement on L_D is tightened to the condition $L_D > 45$ GeV. Events considered in the $3\ell + 0\tau_h$, $4\ell + 0\tau_h$, $3\ell + 1\tau_h$, and $2\ell + 2\tau_h$ channels containing three or fewer jets and no SFOS lepton pair are required to satisfy the nominal condition $L_D > 30$ GeV.

Events containing a pair of leptons passing the loose selection criteria and having an invariant mass $m_{\ell\ell}$ of less than 12 GeV are vetoed, to remove events in which the leptons originate from quarkonium decays, cascade decays of heavy-flavor hadrons, and low-mass DY production, because such events are not well modeled by the MC simulation.

In the $3\ell + 0\tau_h$ and $4\ell + 0\tau_h$ channels, events containing four leptons passing the loose selection criteria and having an invariant mass of $m_{4\ell}$ of the four-lepton system of less than 140 GeV are vetoed, to remove $t\bar{t}H$ and tH signal events in which the Higgs boson decays via $H \to ZZ \to \ell^+\ell^-\ell^+\ell^-$, thereby avoiding overlap with the analysis published in Ref. [20].

A summary of the event selection criteria applied in the different channels is given in Tables 2, 3 and 4.

Table 2 Event selections applied in the $2\ell\mathrm{SS}+0\tau_\mathrm{h}$, $2\ell\mathrm{SS}+1\tau_\mathrm{h}$, $3\ell+0\tau_\mathrm{h}$, and $3\ell+1\tau_\mathrm{h}$ channels. The p_T thresholds applied to the lepton of highest, second-highest, and third-highest p_T are separated by slashes. The symbol "–" indicates that no requirement is applied

Selection step	$2\ell\mathrm{SS}+0\tau_\mathrm{h}$	$2\ell\mathrm{SS}+1\tau_\mathrm{h}$
Targeted $\mathrm{t\bar{t}H}$ decay	$\mathrm{t}\to\mathrm{b}\ell\nu$, $\mathrm{t}\to\mathrm{bqq}'$ with $\mathrm{H}\to\mathrm{WW}\to\ell\nu\mathrm{qq}'$	$\mathrm{t}\to\mathrm{b}\ell\nu$, $\mathrm{t}\to\mathrm{bqq}'$ with $\mathrm{H}\to\tau\tau\to\ell\nu\nu\tau_\mathrm{h}\nu$
Targeted tH decays	$\mathrm{t}\to\mathrm{b}\ell\nu$, $\mathrm{H}\to\mathrm{WW}\to\ell\nu\mathrm{qq}'$	$\mathrm{t}\to\mathrm{b}\ell\nu$, $\mathrm{H}\to\tau\tau\to\ell\tau_\mathrm{h}+\nu$'s
Trigger	Single- and double-lepton triggers	Single- and double-lepton triggers
Lepton p_T	$p_\mathrm{T}>25$ / 15 GeV	$p_\mathrm{T}>25$ / 15 GeV (e) or 10 GeV (μ)
Lepton η	$\lvert\eta\rvert<2.5$ (e) or 2.4 (μ)	$\lvert\eta\rvert<2.5$ (e) or 2.4 (μ)
τ_h p_T	–	$p_\mathrm{T}>20$ GeV
τ_h η	–	$\lvert\eta\rvert<2.3$
τ_h identification	–	Very loose
Charge requirements	2 SS leptons and charge quality requirements	2 SS leptons and charge quality requirements $\sum_{\ell,\tau_\mathrm{h}} q=\pm1$
Multiplicity of central jets	$\geq$3 jets	$\geq$3 jets
b tagging requirements	$\geq$1 tight b-tagged jet or $\geq$2 loose b-tagged jets	$\geq$1 tight b-tagged jet or $\geq$2 loose b-tagged jets
Missing transverse momentum	$L_\mathrm{D}>30$ GeV†	$L_\mathrm{D}>30$ GeV†
Dilepton invariant mass	$\lvert m_{\ell\ell}-m_\mathrm{Z}\rvert>10$ GeV‡ and $m_{\ell\ell}>12$ GeV	
Selection step	$3\ell+0\tau_\mathrm{h}$	$3\ell+1\tau_\mathrm{h}$
Targeted $\mathrm{t\bar{t}H}$ decays	$\mathrm{t}\to\mathrm{b}\ell\nu$, $\mathrm{t}\to\mathrm{b}\ell\nu$ with $\mathrm{H}\to\mathrm{WW}\to\ell\nu\mathrm{qq}'$; $\mathrm{t}\to\mathrm{b}\ell\nu$, $\mathrm{t}\to\mathrm{bqq}'$ with $\mathrm{H}\to\mathrm{WW}\to\ell\nu\ell\nu$; $\mathrm{t}\to\mathrm{b}\ell\nu$, $\mathrm{t}\to\mathrm{bqq}'$ with $\mathrm{H}\to\mathrm{ZZ}\to\ell\ell\mathrm{qq}'$ or $\ell\ell\nu\nu$	$\mathrm{t}\to\mathrm{b}\ell\nu$, $\mathrm{t}\to\mathrm{b}\ell\nu$ with $\mathrm{H}\to\tau\tau\to\ell\nu\nu\tau_\mathrm{h}\nu$
Targeted tH decays	$\mathrm{t}\to\mathrm{b}\ell\nu$, $\mathrm{H}\to\mathrm{WW}\to\ell\nu\ell\nu$	–
Trigger	Single-, double- and triple-lepton triggers	Single-, double- and triple-lepton triggers
Lepton p_T	$p_\mathrm{T}>25$ / 15 / 10 GeV	$p_\mathrm{T}>25$ / 15 / 10 GeV
Lepton η	$\lvert\eta\rvert<2.5$ (e) or 2.4 (μ)	$\lvert\eta\rvert<2.5$ (e) or 2.4 (μ)
τ_h p_T	–	$p_\mathrm{T}>20$ GeV
τ_h η	–	$\lvert\eta\rvert<2.3$
τ_h identification	–	Very loose
Charge requirements	$\sum_\ell q=\pm1$	$\sum_{\ell,\tau_\mathrm{h}} q=0$
Multiplicity of central jets	$\geq$2 jets	$\geq$2 jets
b tagging requirements	$\geq$1 tight b-tagged jet or $\geq$2 loose b-tagged jets	$\geq$1 tight b-tagged jet or $\geq$2 loose b-tagged jets
Missing transverse momentum	$L_\mathrm{D}>0$/30/45 GeV‡	$L_\mathrm{D}>0$/30/45 GeV‡
Dilepton invariant mass	$m_{\ell\ell}>12$ GeV and $\lvert m_{\ell\ell}-m_\mathrm{Z}\rvert>10$ GeV§	$m_{\ell\ell}>12$ GeV and $\lvert m_{\ell\ell}-m_\mathrm{Z}\rvert>10$ GeV§
Four-lepton invariant mass	$m_{4\ell}>140$ GeV¶	–

† A complete description of this requirement can be found in the main text
‡ Applied to all SFOS lepton pairs and to pairs of electrons of SS charge
§ Applied to all SFOS lepton pairs
¶ If the event contains two SFOS pairs of leptons that pass the loose lepton selection criteria

Table 3 Event selections applied in the $0\ell + 2\tau_h$, $1\ell + 1\tau_h$, $1\ell + 2\tau_h$, and $2\ell + 2\tau_h$ channels. The p_T thresholds applied to the lepton and to the τ_h of highest and second-highest p_T are separated by slashes. The symbol "–" indicates that no requirement is applied

Selection step	$0\ell + 2\tau_h$	$1\ell + 1\tau_h$
Targeted $t\bar{t}H$ decays	$t \to bqq'$, $t \to bqq'$ with $H \to \tau\tau \to \tau_h\nu\tau_h\nu$	$t \to bqq'$, $t \to bqq'$ with $H \to \tau\tau \to \ell\nu\nu\tau_h\nu$
Trigger	Double-τ_h trigger	Single-lepton and lepton+τ_h triggers
Lepton p_T	–	$p_T > 30$ (e) or 25 GeV (μ)
Lepton η	–	$\lvert\eta\rvert < 2.1$
τ_h p_T	$p_T > 40$ GeV	$p_T > 30$ GeV
τ_h η	$\lvert\eta\rvert < 2.1$	$\lvert\eta\rvert < 2.1$
τ_h identification	Loose	Medium
Charge requirements	$\sum_{\tau_h} q = 0$	$\sum_{\ell,\tau_h} q = 0$
Multiplicity of central jets	$\geq$4 jets	$\geq$4 jets
b tagging requirements	$\geq$1 tight b-tagged jet or $\geq$2 loose b-tagged jets	$\geq$1 tight b-tagged jet or $\geq$2 loose b-tagged jets
Dilepton invariant mass	$m_{\ell\ell} > 12$ GeV	$m_{\ell\ell} > 12$ GeV
Selection step	$1\ell + 2\tau_h$	$2\ell + 2\tau_h$
Targeted $t\bar{t}H$ decays	$t \to b\ell\nu$, $t \to bqq'$ with $H \to \tau^+\tau^- \to \tau_h\nu\tau_h\nu$	$t \to b\ell\nu$, $t \to b\ell\nu$ with $H \to \tau^+\tau^- \to \tau_h\nu\tau_h\nu$
Trigger	Single-lepton and lepton+τ_h triggers	Single- and double-lepton triggers
Lepton p_T	$p_T > 30$ (e) or 25 GeV (μ)	$p_T > 25$ / 10 (15) GeV (e)
Lepton η	$\lvert\eta\rvert < 2.1$	$\lvert\eta\rvert < 2.5$ (e) or 2.4 (μ)
τ_h p_T	$p_T > 30$ / 20 GeV	$p_T > 20$ GeV
τ_h η	$\lvert\eta\rvert < 2.1$	$\lvert\eta\rvert < 2.3$
τ_h identification	medium	medium
Charge requirements	$\sum_{\ell,\tau_h} q = \pm 1$	$\sum_{\ell,\tau_h} q = 0$
Multiplicity of central jets	$\geq$3 jets	$\geq$2 jets
b tagging requirements	$\geq$1 tight b-tagged jet or $\geq$2 loose b-tagged jets	$\geq$1 tight b-tagged jet or $\geq$2 loose b-tagged jets
Missing transverse momentum	–	$L_D > 0$ / 30 / 45 GeV†
Dilepton invariant mass	$m_{\ell\ell} > 12$ GeV	$m_{\ell\ell} > 12$ GeV

† A complete description of this requirement can be found in the main text

6 Event classification, signal extraction, and analysis strategy

Contributions from background processes that pass the event selection criteria detailed in Sect. 5, significantly exceed the expected $t\bar{t}H$ and tH signal rates. The ratio of expected signal to background yields is particularly unfavorable in channels with a low multiplicity of leptons and τ_h, notwithstanding that these channels also provide the highest acceptance for the $t\bar{t}H$ and tH signals. In order to separate the $t\bar{t}H$ and tH signals from the background contributions, we employ a maximum-likelihood (ML) fit to the distributions of a number of discriminating observables. The choice of these observables is based on studies, performed with simulated samples of signal and background events, that aim at maximizing the expected sensitivity of the analysis. Compared to the alternative of reducing the background by applying more stringent event selection criteria, the chosen strategy has the advantage of retaining events reconstructed in kinematic regions of low signal-to-background ratio for analysis. Even though these events enter the ML fit with a lower "weight" compared to the signal events reconstructed in kinematic regions where the signal-to-background ratio is high, the retained events increase the overall sensitivity of the statistical analysis, firstly by increasing the overall $t\bar{t}H$ and tH signal yield and secondly by simultaneously constraining the background contributions. The likelihood function used in the ML fit is described in Sect. 9. The diagram displayed in Fig. 3 describes the classification employed in each of the categories, which defines the regions that are fitted in the signal extraction fit.

The chosen discriminating observables are the outputs of machine-learning algorithms that are trained using simulated samples of $t\bar{t}H$ and tH signal events as well as $t\bar{t}W$, $t\bar{t}Z$,

Table 4 Event selections applied in the $2\ell\mathrm{OS}+1\tau_\mathrm{h}$ and $4\ell+0\tau_\mathrm{h}$ channels. The symbol "–" indicates that no requirement is applied

Selection step	$2\ell\mathrm{OS}+1\tau_\mathrm{h}$	$4\ell+0\tau_\mathrm{h}$
Targeted $\mathrm{t\bar{t}H}$ decays	$\mathrm{t}\to\mathrm{b}\ell\nu$, $\mathrm{t}\to\mathrm{bqq}'$ with $\mathrm{H}\to\tau^+\tau^-\to\ell\nu\nu\tau_\mathrm{h}\nu$	$\mathrm{t}\to\mathrm{b}\ell\nu$, $\mathrm{t}\to\mathrm{b}\ell\nu$ with $\mathrm{H}\to\mathrm{WW}\to\ell\nu\ell\nu$ $\mathrm{t}\to\mathrm{b}\ell\nu$, $\mathrm{t}\to\mathrm{b}\ell\nu$ with $\mathrm{H}\to\mathrm{ZZ}\to\ell\ell\mathrm{qq}'$ or $\ell\ell\nu\nu$
Trigger	Single- and double-lepton triggers	Single-, double- and triple-lepton triggers
Lepton p_T	$p_\mathrm{T}>25$ / 15 GeV (e) or 10 GeV (μ)	$p_\mathrm{T}>25$ / 15 / 15 / 10 GeV
Lepton η	$\lvert\eta\rvert<2.5$ (e) or 2.4 (μ)	$\lvert\eta\rvert<2.5$ (e) or 2.4 (μ)
τ_h p_T	$p_\mathrm{T}>20$ GeV	–
τ_h η	$\lvert\eta\rvert<2.3$	–
τ_h identification	Tight	–
Charge requirements	$\sum_\ell q=0$ and $\sum_{\ell,\tau_\mathrm{h}} q=\pm1$	$\sum_\ell q=0$
Multiplicity of central jets	$\geq$3 jets	$\geq$2 jets
b tagging requirements	$\geq$1 tight b-tagged jet or $\geq$2 loose b-tagged jets	$\geq$1 tight b-tagged jet or $\geq$2 loose b-tagged jets
Missing transverse momentum	$L_\mathrm{D}>30$ GeV†	$L_\mathrm{D}>0$ / 30 / 45 GeV‡
Dilepton invariant mass	$m_{\ell\ell}>12$ GeV	$\lvert m_{\ell\ell}-m_Z\rvert>10$ GeV§ and $m_{\ell\ell}>12$ GeV
Four-lepton invariant mass	–	$m_{4\ell}>140$ GeV¶

† Only applied to events containing two electrons
‡ A complete description of this requirement can be found in the main text
§ Applied to all SFOS lepton pairs
¶ If the event contains two SFOS pairs of leptons passing the loose lepton selection criteria

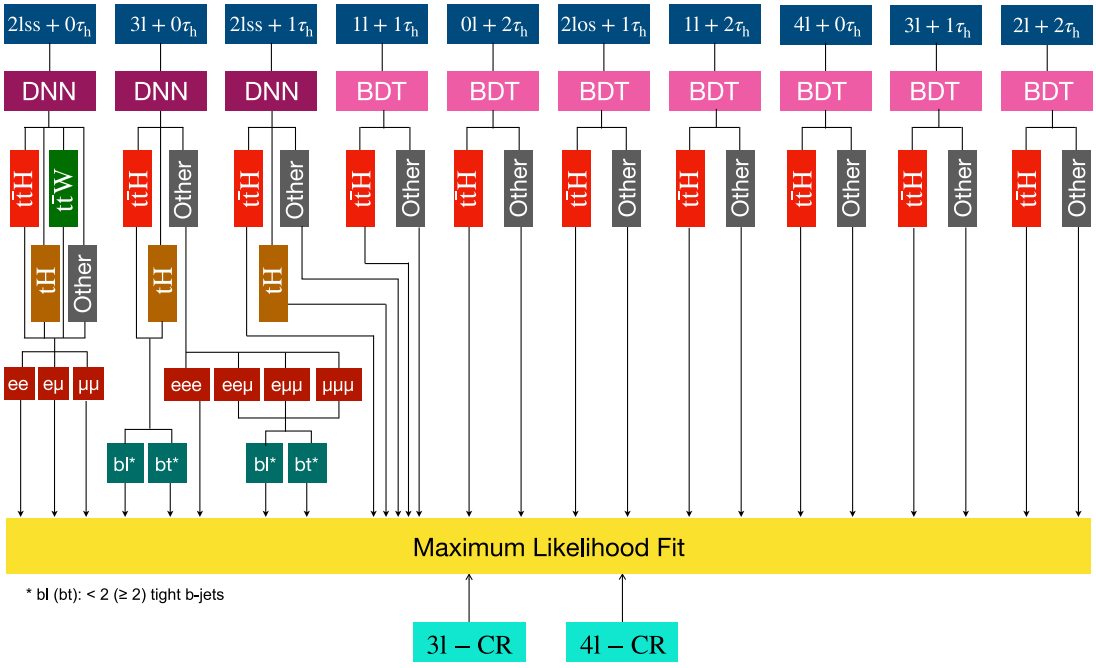


Fig. 3 Diagram showing the categorization strategy used for the signal extraction, making use of MVA-based algorithms and topological variables. In addition to the ten channels, the ML fit receives input from two control regions (CRs) defined in Sect. 7.3

$\mathrm{t\bar{t}}$+jets, and diboson background samples. For the purpose of separating the $\mathrm{t\bar{t}H}$ and tH signals from backgrounds, the $2\ell\mathrm{SS} + 0\tau_\mathrm{h}$, $3\ell + 0\tau_\mathrm{h}$, and $2\ell\mathrm{SS} + 1\tau_\mathrm{h}$ channels employ ANNs, which allows to discriminate among the two signals and background simultaneously, while the other channels use BDTs.

The observables used as input to the ANNs and BDTs are outlined in Table 5. These are chosen to maximize the discrimination power of the discriminators, with the objective of maximizing the expected sensitivity of the analysis. The optimization is performed separately for each of the ten analysis channels. Typical observables used are: the number of leptons, τ_h, and jets that are reconstructed in the event, where electrons and muons, as well as forward jets, central jets, and jets passing the loose and the tight b tagging criteria are counted separately; the 3-momentum of leptons, τ_h, and jets; the magnitude of the missing transverse momentum, quantified by the linear discriminant L_D; the angular separation between leptons, τ_h, and jets; the average ΔR separation between pairs of jets; the sum of charges for different combinations of leptons and τ_h; observables related to the reconstruction of specific top quark and Higgs boson decay modes; as well as a few other observables that provide discrimination between the $\mathrm{t\bar{t}H}$ and tH signals. A boolean variable that indicates whether the event has an SFOS lepton pair passing looser isolation criteria is included in regions with at least three leptons in the final state.

Input variables are included related to the reconstruction of specific top quark and Higgs boson decay modes comprise the transverse mass of a given lepton, $m_\mathrm{T} = \sqrt{2 p_\mathrm{T}^{\ell} p_\mathrm{T}^{\mathrm{miss}} (1 - \cos\Delta\phi)}$, where $\Delta\phi$ refers to the angle in the transverse plane between the lepton momentum and the $\vec{p}_\mathrm{T}^{\,\mathrm{miss}}$ vector; the invariant masses of different combinations of leptons and τ_h; and the invariant mass of the pair of jets with the highest and second-highest values of the b tagging discriminant. These observables are complemented by the outputs of MVA-based algorithms, documented in Ref. [23], that reconstruct hadronic top quark decays and identify the jets originating from $\mathrm{H} \to \mathrm{WW} \to \ell^+\nu_\ell \mathrm{q\bar{q}}'$ decays.

In the $0\ell + 2\tau_\mathrm{h}$ channel, we use as additional inputs the invariant mass of the τ lepton pair, which is expected to be close to the Higgs boson mass in signal events and is reconstructed using the algorithm documented in Ref. [89] (SVFit), in conjunction with the decay angle, denoted by $\cos\theta^*$, of the two tau leptons in the Higgs boson rest frame.

In the $2\ell\mathrm{SS} + 0\tau_\mathrm{h}$, $3\ell + 0\tau_\mathrm{h}$, and $2\ell\mathrm{SS} + 1\tau_\mathrm{h}$ channels, the p_T and η of the forward jet of highest p_T, as well as the distance $\Delta\eta$ of this jet to the jet nearest in pseudorapidity, are used as additional inputs to the ANN, in order to improve the separation of the tH from the $\mathrm{t\bar{t}H}$ signal. The presence of such a jet is a characteristic signature of tH production in the t-channel. The forward jet in such tH signal events is expected to be separated from other jets in the event by a pseudorapidity gap, since there is no color flow at tree level between this jet and the jets originating from the top quark and Higgs boson decays.

The number of simulated signal and background events that pass the event selection criteria described in Sect. 5 and are available for training the BDTs and ANNs typically amount to a few thousand. In order to increase the number of events in the training samples, in particular for the channels with a high multiplicity of leptons and τ_h where the amount of available events is most limited, we relax the identification criteria for electrons, muons, and hadronically decaying tau leptons. The resulting increase in the ratio of misidentified to genuine leptons and τ_h is corrected. We have checked that the distributions of the observables used for the BDT and ANN training are compatible, within statistical uncertainties, between events selected with relaxed and with nominal lepton and τ_h selection criteria, provided that these corrections are applied.

The ANNs used in the $2\ell\mathrm{SS} + 0\tau_\mathrm{h}$, $3\ell + 0\tau_\mathrm{h}$, and $2\ell\mathrm{SS} + 1\tau_\mathrm{h}$ channels are of the multiclass type. Such ANNs have multiple output nodes that, besides discriminating the $\mathrm{t\bar{t}H}$ and tH signals from backgrounds, accomplish both the separation of the tH from the $\mathrm{t\bar{t}H}$ signal and the distinction between individual types of backgrounds. In the $2\ell\mathrm{SS} + 0\tau_\mathrm{h}$ channel, we use four output nodes, to distinguish between $\mathrm{t\bar{t}H}$ signal, tH signal, $\mathrm{t\bar{t}W}$ background, and other backgrounds. No attempt is made to distinguish between individual types of backgrounds in the $3\ell + 0\tau_\mathrm{h}$ and $2\ell\mathrm{SS} + 1\tau_\mathrm{h}$ channels, which therefore use three output nodes. The ANNs in the $2\ell\mathrm{SS} + 0\tau_\mathrm{h}$, $3\ell + 0\tau_\mathrm{h}$, and $2\ell\mathrm{SS} + 1\tau_\mathrm{h}$ channels implement 16, 5 and 3 hidden layers, respectively, each one of them containing 8 to 32 neurons. The softmax [90] function is chosen as an activation function for all output nodes, permitting the interpretation of their activation values as probability for a given event to be either $\mathrm{t\bar{t}H}$ signal, tH signal, $\mathrm{t\bar{t}W}$ background, or other background ($\mathrm{t\bar{t}H}$ signal, tH signal, or background) in the $2\ell\mathrm{SS} + 0\tau_\mathrm{h}$ channel (in the $3\ell + 0\tau_\mathrm{h}$ and $2\ell\mathrm{SS} + 1\tau_\mathrm{h}$ channels). The events selected in the $2\ell\mathrm{SS} + 0\tau_\mathrm{h}$ channel ($3\ell + 0\tau_\mathrm{h}$ and $2\ell\mathrm{SS} + 1\tau_\mathrm{h}$ channels) are classified into four (three) categories, corresponding to the $\mathrm{t\bar{t}H}$ signal, tH signal, $\mathrm{t\bar{t}W}$ background, or other background ($\mathrm{t\bar{t}H}$ signal, tH signal, or background), according to the output node that has the highest such probability value. We refer to these categories as ANN output node categories. The four (three) distributions of the probability values of the output nodes in the $2\ell\mathrm{SS} + 0\tau_\mathrm{h}$ channel (in the $3\ell + 0\tau_\mathrm{h}$ and $2\ell\mathrm{SS} + 1\tau_\mathrm{h}$ channels) are used as input to the ML fit. Events are prevented from entering more than one of these distributions by assigning each event only to the distribution corresponding to the output node that has the highest activation value. The rectified linear activation function [91] is used for the hidden layers. The training is performed using the TensorFlow

Table 5 Input variables to the multivariate discriminants in each of the ten analysis channels. The symbol "–" indicates that the variable is not used. For all objects, the three-momentum is constituted by the p_T, η, and ϕ components of the object momentum

	$2\ell SS + 0\tau_h$	$2\ell SS + 1\tau_h$	$3\ell + 0\tau_h$	$1\ell + 1\tau_h$	$0\ell + 2\tau_h$	$2\ell OS + 1\tau_h$	$1\ell + 2\tau_h$	$4\ell + 0\tau_h$	$3\ell + 1\tau_h$	$2\ell + 2\tau_h$
Electron multiplicity	✓	✓	✓	–	–	–	–	–	–	–
Three-momenta of leptons and/or τ_hs	✓	✓	✓	✓	✓	✓	✓	–	✓	✓
p_T of leptons and/or τ_hs	–	–	–	–	–	–	–	✓	–	–
Transverse mass of leptons and/or τ_hs	✓	✓	–	✓	✓	✓	✓	–	–	–
Invariant mass of leptons and/or τ_hs	✓	–	–	✓	✓	✓	✓	✓	✓	✓
SVFit mass of leptons and/or τ_hs	–	–	–	✓	✓	–	–	–	–	–
ΔR between leptons and/or τ_hs	✓	✓	✓	✓	✓	✓	✓	–	–	✓
$\cos\theta^*$ of leptons and τ_hs	–	–	–	✓	✓	–	✓	–	–	✓
Charge of leptons and/or τ_hs	✓	✓	✓	✓	–	–	–	–	–	–
Has SFOS lepton pairs	–	–	✓	–	–	–	–	✓	✓	–
Jet multiplicity	✓	✓	✓	–	–	–	–	–	–	–
Jets three-momenta	✓	✓	✓	–	–	–	–	–	–	–
Average ΔR between jets	✓	✓	✓	✓	✓	✓	✓	–	–	✓
Forward jet multiplicity	✓	✓	✓	–	–	–	–	–	–	–
Leading forward jet three-momenta	✓	✓	✓	–	–	–	–	–	–	–
Minimum $\lvert\Delta\eta\rvert$ between leading forward jet and jets	–	✓	✓	–	–	–	–	–	–	–
b jet multiplicity	✓	✓	✓	–	–	–	–	–	–	–
Invariant mass of b jets	✓	✓	✓	✓	✓	✓	✓	–	–	✓
Linear discriminant L_D	✓	✓	✓	✓	✓	✓	✓	✓	✓	✓
Hadronic top quark tagger	✓	✓	✓	✓	✓	✓	✓	–	–	–
Hadronic top p_T	–	✓	✓	–	–	✓	✓	–	–	–
Higgs boson jet tagger	✓	–	–	–	–	–	–	–	–	–
Number of variables	36	41	37	16	15	18	17	7	9	9

[92] package with the KERAS [93] interface. The objective of the training is to minimize the cross-entropy loss function [94]. Batch gradient descent is used to update the weights of the ANN during the training. Overtraining is minimized by using Tikhonov regularization [95] and dropout [96].

The sensitivity of the $2\ell SS + 0\tau_h$ and $3\ell + 0\tau_h$ channels, which are the channels with the largest event yields out of the three using multiclass ANN, is further improved by analyzing selected events in subcategories based on the flavor (electron or muon) of the leptons and on the number of jets passing the tight b tagging criteria. The motivation for distinguishing events by lepton flavor is that the rate for misidentifying nonprompt leptons as prompt ones and, in the $2\ell SS + 0\tau_h$ channel, also the probability for mismeasuring the lepton charge is significantly higher for electrons compared to muons. Distinguishing events by the multiplicity of b jets improves in particular the separation of the $t\bar{t}H$ signal from the $t\bar{t}$+jets background. This occurs because if a nonprompt lepton produced in the decay of a b hadron gets misidentified as a prompt lepton, the remaining particles resulting from the hadronization of the bottom quark are less likely to pass the b jet identification criteria, thereby reducing the number of b jets in such $t\bar{t}$+jets background events. The distribution of the multiplicity of b jets in $t\bar{t}$+jets background events in which a nonprompt lepton is misidentified as prompt lepton ("nonprompt") and in $t\bar{t}$+jets background events in which this is not the case ("prompt") is shown in Fig. 4. The figure also shows the distributions of p_T and η of bottom quarks produced in top quark decays in $t\bar{t}H$ signal events compared to in $t\bar{t}$+jets background events. The $t\bar{t}H$ signal features more bottom quarks of high p_T, whereas the distribution of η is similar for the $t\bar{t}H$ signal and for the $t\bar{t}$+jets background.

The number of subcategories is optimized for each of the four (three) ANN output categories of the $2\ell SS + 0\tau_h$ ($3\ell + 0\tau_h$) channel individually. In the $2\ell SS + 0\tau_h$ channel, each of the 4 ANN output node categories is subdivided into three subcategories, based on the flavor of the two leptons (ee, $e\mu$, $\mu\mu$). In the $3\ell + 0\tau_h$ channel, the ANN output node categories corresponding to the $t\bar{t}H$ signal and to the tH signal are

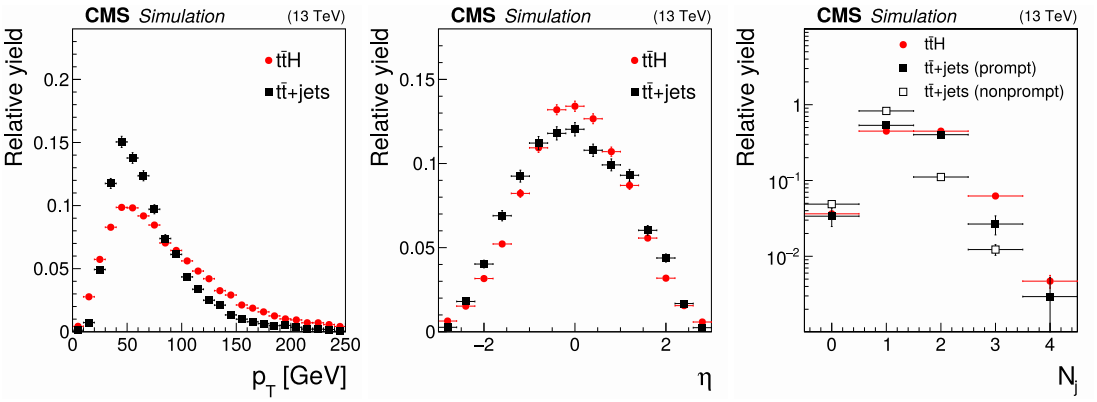


Fig. 4 Transverse momentum (left) and pseudorapidity (middle) distributions of bottom quarks produced in top quark decays in $t\bar{t}H$ signal events compared to $t\bar{t}$+jets background events, and multiplicity of jets passing tight b jet identification criteria (right). The latter distribution is shown separately for $t\bar{t}$+jets background events in which a nonprompt lepton is misidentified as a prompt lepton and for those background events in which all reconstructed leptons are prompt leptons. The events are selected in the $2\ell SS + 0\tau_h$ channel

subdivided into two subcategories, based on the multiplicity of jets passing tight b tagging criteria (bl: <2 tight b-tagged jets, bt: ≥2 tight b-tagged jets), while the output node category corresponding to the backgrounds is subdivided into seven subcategories, based on the flavor of the three leptons and on the multiplicity of jets passing tight b tagging criteria (eee; eeμ bl, eeμ bt; eμμ bl, eμμ bt; μμμ bl, μμμ bt), where bl (bt) again corresponds to the condition of <2 (≥2) tight b-tagged jets. The eee subcategory is not further subdivided by the number of b-tagged jets, because of the lower number of events containing three electrons compared to events in other categories. The aforementioned event categories are constructed based on the output of the BDTs and ANNs with the goal of enhancing the analysis sensitivity, while keeping a sufficiently high rate of background events for a precise estimation.

The BDTs used in the $1\ell + 1\tau_h$, $0\ell + 2\tau_h$, $2\ell OS + 1\tau_h$, $1\ell + 2\tau_h$, $4\ell + 0\tau_h$, $3\ell + 1\tau_h$, and $2\ell + 2\tau_h$ channels address the binary classification problem of separating the sum of $t\bar{t}H$ and tH signals from the aggregate of all backgrounds. The training is performed using the SCIKIT- LEARN [34] package with the XGBOOST [33] algorithm. The training parameters are chosen to maximize the integral, or area-under-the-curve, of the receiver-operating-characteristic curve of the BDT output.

7 Background estimation

The dominant background in most channels comes from the production of top quarks in association with W and Z bosons. We collectively refer to the sum of $t\bar{t}W$ and $t\bar{t}WW$ backgrounds using the notation $t\bar{t}W(W)$. In $t\bar{t}W(W)$ and $t\bar{t}Z$ background events selected in the signal regions (SRs), reconstructed leptons typically originate from genuine prompt leptons or reconstructed b jets arising from the hadronization of bottom quarks, whereas reconstructed τ_h are a mixture of genuine hadronic τ decays and misidentified quark or gluon jets. Background events from $t\bar{t}Z$ production may pass the Z boson veto applied in the $2\ell SS + 0\tau_h$, $3\ell + 0\tau_h$, $2\ell SS + 1\tau_h$, $2\ell OS + 1\tau_h$, $4\ell + 0\tau_h$, and $3\ell + 1\tau_h$ channels in the case that the Z boson either decays to leptons and one of the leptons fails to get selected, or the Z boson decays to τ leptons and the τ leptons subsequently decay to electrons or muons. In the latter case, the invariant mass $m_{\ell\ell}$ of the lepton pair is shifted to lower values because of the neutrinos produced in the τ decays. Additional background contributions arise from off-shell $t\bar{t}\gamma^*$ and $t\gamma^*$ production: we include them in the $t\bar{t}Z$ background. The $t\bar{t}$+jets production cross section is about three orders of magnitude larger than the cross section for associated production of top quarks with W and Z bosons, but in most channels the $t\bar{t}$+jets background is strongly reduced by the lepton and τ_h identification criteria. Except for the channels $1\ell + 1\tau_h$ and $0\ell + 2\tau_h$, the $t\bar{t}$+jets background contributes solely in the cases that a nonprompt lepton (or a jet) is misidentified as a prompt lepton, a quark or gluon jet is misidentified as τ_h, or the charge of a genuine prompt lepton is mismeasured. Photon conversions are a relevant background in the event categories with one or more reconstructed electrons in the $2\ell SS + 0\tau_h$ and $3\ell + 0\tau_h$ channels. The production of WZ and ZZ pairs in events with two or more jets constitutes another relevant background in most channels. In the $1\ell + 1\tau_h$ and $0\ell + 2\tau_h$ channels, an

additional background arises from DY production of τ lepton pairs.

We categorize the contributions of background processes into reducible and irreducible ones. A background is considered irreducible if all reconstructed electrons and muons are genuine prompt leptons and all reconstructed τ_h are genuine hadronic τ decays; in the $2\ell SS + 0\tau_h$ and $2\ell SS + 1\tau_h$ channels, we further require that the measured charge of reconstructed electrons and muons matches their true charge. The irreducible background contributions are modeled using simulated events fulfilling the above criteria to avoid double-counting of all the other background contributions, which are considered to be reducible and are mostly determined from data.

Throughout the analysis, we distinguish three sources of reducible background contributions: misidentified leptons and τ_h ("misidentified leptons"), asymmetric conversions of a photon into electrons ("conversions"), and mismeasurement of the lepton charge ("flips").

The background from misidentified leptons and τ_h refers to events in which at least one reconstructed electron or muon is caused by the misidentification of a nonprompt lepton or hadron, or at least one reconstructed τ_h arises from the misidentification of a quark or gluon jet. The main contribution to this background stems from $t\bar{t}$+jets production, reflecting the large cross section for this background process.

The conversions background consists of events in which one or more reconstructed electrons are due to the conversion of a photon. The conversions background is typically caused by $t\bar{t}\gamma$ events in which one electron or positron produced in the photon conversion carries most of the energy of the converted photon, whereas the other electron or positron is of low energy and fails to get reconstructed. We refer to such photon conversions as asymmetric conversions.

The flips background is specific to the $2\ell SS + 0\tau_h$ and $2\ell SS + 1\tau_h$ channels and consists in events where the charge of a reconstructed lepton is mismeasured. The main contribution to the flips background stems from $t\bar{t}$+jets events in which both top quarks decay semi-leptonically. In case of the $2\ell SS + 1\tau_h$ channel, a quark or gluon jet is additionally misidentified as τ_h. The mismeasurement of the electron charge typically results from the emission of a hard bremsstrahlung photon, followed by an asymmetric conversion of this photon. The reconstructed electron is typically the electron or positron that carries most of the energy of the converted photon, resulting in an equal probability for the reconstructed electron to have either the same or opposite charge compared to the charge of the electron or positron that emitted the bremsstrahlung photon [77]. The probability of mismeasuring the charge of muons is negligible in this analysis.

The three types of reducible background are made mutually exclusive by giving preference to the misidentified leptons type over the flips and conversions types and by giving preference to the flips type over the conversions type when an event qualifies for more than one type of reducible background. The misidentified leptons and flips backgrounds are determined from data, whereas the conversions background is modeled using the MC simulation. The procedures for estimating the misidentified leptons and flips backgrounds are described in Sects. 7.1 and 7.2, respectively. We performed dedicated studies in the data to ascertain that photon conversions are adequately modeled by the MC simulation similar to the ones performed in Ref. [97]. To avoid potential double-counting of the background estimates obtained from data with background contributions modeled using the MC simulation, we match reconstructed electrons, muons, and τ_h to their generator-level equivalents and veto simulated signal and background events selected in the SR that qualify as misidentified leptons or flips backgrounds.

Concerning the irreducible backgrounds, we refer to the aggregate of background contributions other than those arising from $t\bar{t}W(W)$, $t\bar{t}Z$, $t\bar{t}$+jets, DY, and diboson backgrounds, or from SM Higgs boson production via the processes ggH, qqH, WH, ZH, $t\bar{t}WH$, and $t\bar{t}ZH$ as "rare" backgrounds. The rare backgrounds typically yield a minor background contribution to each of the ten analysis channels and include such processes as tW and tZ production, the production of SSW boson pairs, triboson, and $t\bar{t}t\bar{t}$ production.

We validate the modeling of the $t\bar{t}W(W)$, $t\bar{t}Z$, WZ, and ZZ backgrounds in dedicated control regions (CRs) whose definitions are detailed in Sect. 7.3.

7.1 Estimation of the "misidentified leptons" background

The background from misidentified leptons and τ_h is estimated using the misidentification probability (MP) method [23]. The method is based on selecting a sample of events satisfying all selection criteria of the SR, detailed in Sect. 5, except that the electrons, muons, and τ_h used to construct the signal regions are required to pass relaxed selections instead of the nominal ones. We refer to this sample of events as the application region (AR) of the MP method. Events in which all leptons and τ_h satisfy the nominal selections are vetoed, to avoid overlap with the SR.

An estimate of the background from misidentified leptons and τ_h in the SR is obtained by applying suitably chosen weights to the events selected in the AR. The weights, denoted by the symbol w, are given by the expression:

$$w = (-1)^{n+1} \prod_{i=1}^{n} \frac{f_i}{1 - f_i} \tag{1}$$

where the product extends over all electrons, muons, and τ_h that pass the relaxed, but fail the nominal selection criteria,

and n refers to the total number of such leptons and τ_h. The symbol f_i denotes the probability for an electron, muon, or τ_h passing the relaxed selection to also satisfy the nominal one. The contributions of irreducible backgrounds to the AR are subtracted based on the MC expectation of such contributions. The $t\bar{t}H$ and tH signal yields in the AR are found to be negligible.

The probabilities f_i for leptons are measured in multijet events, separately for electrons and muons, and are binned in p_T and η of the lepton candidate. The measurement is based on selecting events containing exactly one electron or muon that passes the relaxed selection and at least one jet separated from the lepton by $\Delta R > 0.7$. Selected events are then subdivided into "pass" and "fail" samples, depending on whether the lepton candidate passes the nominal selection or not. The fail sample is dominated by the contribution of multijet events. The contributions of other processes, predominantly arising from W+jets, DY, diboson, and $t\bar{t}$+jets production, are subtracted based on MC estimates of these contributions. The number of multijet events in the pass sample is obtained by an ML fit to the distribution of the observable:

$$m_T^{\text{fix}} = \sqrt{2\, p_T^{\text{fix}}\, p_T^{\text{miss}}\, (1 - \cos\Delta\phi)}, \tag{2}$$

where p_T^{fix} is a constant value set to 35 GeV, and the symbol $\Delta\phi$ refers to the angle in the transverse plane between the lepton momentum and the $\vec{p}_T^{\,\text{miss}}$ vector. p_T^{fix} is used instead of the lepton p_T to reduce the correlation between m_T^{fix} and the lepton p_T. The ML fit is similar to the one used in the measurement of the $t\bar{t}H$ and tH signal rates, described in Sect. 9. The distribution of W+jets, DY, diboson, $t\bar{t}$+jets, and rare backgrounds in the observable m_T^{fix} is modeled using the MC simulation, whereas the distribution of multijet events in the pass sample is obtained from data in the fail region, from which the W+jets, DY, diboson, and $t\bar{t}$+jets contributions are subtracted based on their MC estimate. The observable m_T^{fix} exploits the fact that the p_T^{miss} reconstructed in multijet events is mainly caused by resolution effects and is typically small, resulting in a falling distribution of m_T^{fix}, whereas W+jets and $t\bar{t}$+jets events exhibit a broad maximum around $m_W \approx 80$ GeV. Compared to the usual transverse mass, the observable m_T^{fix} has the advantage of not depending on the p_T of the lepton, and is therefore better suited for the purpose of measuring the probabilities f_i in bins of lepton p_T. For illustration, the distributions of m_T^{fix} in the pass and fail samples are shown in Fig. 5 for events containing an electron of $25 < p_T < 35$ GeV in the ECAL barrel. The contributions from W+jets, DY, and diboson production are assumed to scale by a common factor with respect to their MC expectation in the fit; we refer to their sum as "electroweak" (EWK) background. Finally, denoting the number of multijet events in the pass and fail samples by the symbols N_{pass} and N_{fail}, the probabilities f_i are given by $f_i = N_{\text{pass}}/(N_{\text{pass}} + N_{\text{fail}})$.

The f_i for τ_h are determined as a function of p_T and η of the τ_h candidate in a region enriched in $t\bar{t}$+jets events containing a reconstructed opposite-sign electron-muon pair and at least two loose b-tagged jets in addition to the τ_h candidate. Contributions of genuine τ_h are modeled using the MC simulation and subtracted.

The event samples used to measure the f_i are referred to as measurement regions (MRs) of the MP method. Potential biases in the estimate of the background from misidentified leptons and τ_h, arising from differences between AR and MR in the p_T spectrum of the lepton and τ_h candidates and in the mixture of nonprompt leptons and hadrons that are misidentified as prompt leptons, are mitigated as detailed in Ref. [80]. A closure test performed using simulated $t\bar{t}$+jets and multijet events reveals a residual difference between the probabilities f_i for electrons in $t\bar{t}$+jets and those in multijet events. The test is illustrated in Fig. 6, which compares the distributions of p_T of nonprompt electrons in simulated $t\bar{t}$+jets events for three cases: nonprompt electrons passing the nominal selection criteria ("nominal"); nonprompt electrons passing the relaxed, but failing the nominal selection criteria, weighted by probabilities f_i determined in simulated $t\bar{t}$+jets events ("relaxed, f_i from $t\bar{t}$+jets"); and nonprompt electrons passing the relaxed, but failing the nominal selection criteria, weighted by probabilities f_i determined in simulated multijet events ("relaxed, f_i from multijet"). The electron and muon p_T distributions obtained in the first and second cases are in agreement, demonstrating the performance of the MP method. The ratio of the distributions obtained in the second and third cases is fitted by a linear function in p_T of the lepton and is applied as a multiplicative correction to the f_i measured in data, that accounts for the different flavor composition of jets between AR and MR. For the lepton and τ_h selections used in this analysis, the probabilities f_i range from 0.04 to 0.13, 0.02 to 0.20, and 0.10 to 0.50 for electrons, muons, and τ_h, respectively.

The probabilities f_i for electrons and muons obtained as described above are validated in a CR dominated by semileptonic $t\bar{t}$+jets events. The events are selected by requiring the presence of two SS leptons and exactly three jets, one of which exactly passes the tight b tagging criteria. The three jets are interpreted as originating from the hadronic decay of one of the top quarks, while the other top quark decays semileptonically. One of the two reconstructed leptons is assumed to arise from the misidentification of a b hadron originating from the semi-leptonically decaying top quark. A kinematic fit using the constraints from kinematic relations between the top quark decay products is employed to increase the purity of semileptonic $t\bar{t}$+jets events that are correctly reconstructed in this CR. The level of compatibility of selected events with the aforementioned experimental signature is quantified using a

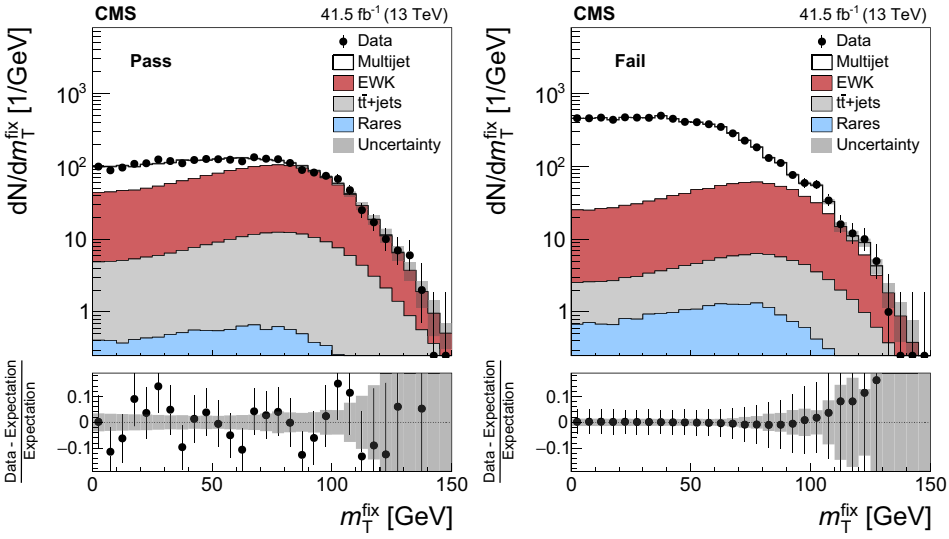


Fig. 5 Distributions of $m_{\mathrm{T}}^{\mathrm{fix}}$ for events containing an electron candidate of $25 < p_{\mathrm{T}} < 35$ GeV in the ECAL barrel, which (left) passes the nominal selection and (right) passes the relaxed, but fails the nominal selection. The "electroweak" (EWK) background refers to the sum of W+jets, DY, and diboson production. The "rare" backgrounds are defined in the text. The data in the fail sample agrees with the sum of multijet, EWK, $\mathrm{t\bar{t}}$+jets, and rare backgrounds by construction, as the number of multijet events in the fail sample is computed by subtracting the sum of EWK, $\mathrm{t\bar{t}}$+jets, and rare background contributions from the data. The misidentification probabilities are derived separately for each era: this figure shows, as an example, the results obtained with the 2017 data set. The uncertainty band represents the total uncertainty after the fit has been performed

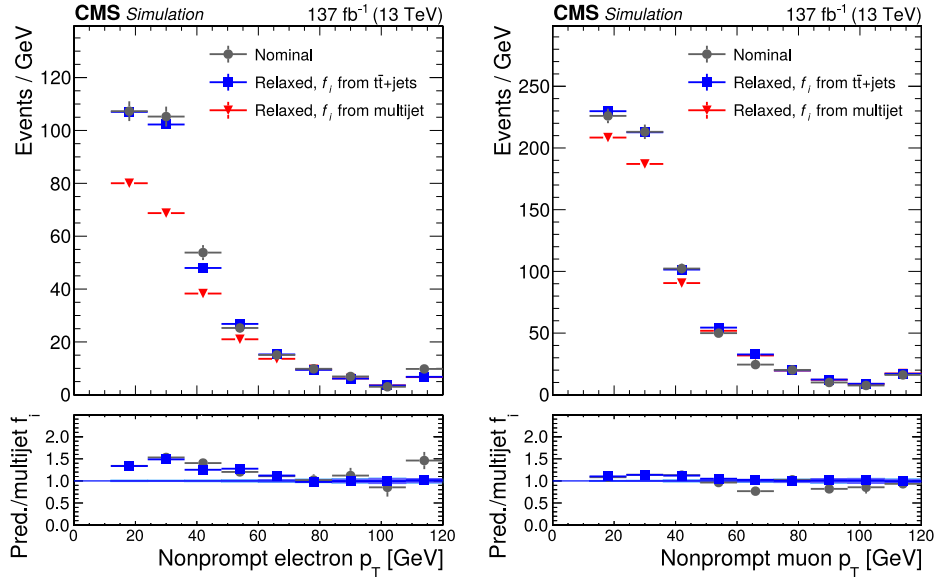


Fig. 6 Transverse momentum distributions of nonprompt (left) electrons and (right) muons in simulated $\mathrm{t\bar{t}}$+jets events, for the three cases "nominal", "relaxed, f_i from $\mathrm{t\bar{t}}$+jets", and "relaxed, f_i from multijet" discussed in text. The figure illustrates that a nonclosure correction needs to be applied to the probabilities f_i measured for electrons in data, while no such correction is needed for muons

χ^2 criterion; events with a high value of χ^2, corresponding to a poor-quality fit, are discarded. Good agreement is observed between semileptonic $\mathrm{t\bar{t}}$+jets events where both leptons pass the nominal selection and semileptonic $\mathrm{t\bar{t}}$+jets events where both leptons pass the relaxed selection, but one or both leptons fail the nominal selection, provided that the weights given by Eq. (1) are applied to the latter events by using the probabilities f_i measured in multijet events and corrected (for electrons) as described in the previous paragraph.

The MP method is applied in all channels except for $2\ell\mathrm{SS}+1\tau_\mathrm{h}$ and $3\ell+1\tau_\mathrm{h}$, where a modified version of the method is used, in which only the selections for the leptons are relaxed in the AR, while the τ_h is required to satisfy the nominal selection. Correspondingly, only the leptons are considered when computing the weights w, given by Eq. (1), that are applied to events in the AR of the $2\ell\mathrm{SS}+1\tau_\mathrm{h}$ and $3\ell+1\tau_\mathrm{h}$ channels. Background contributions where the reconstructed leptons are genuine prompt leptons and the reconstructed τ_h is due to the misidentification of a quark or gluon jet are modeled using the MC simulation. Weights are applied to these simulated events to correct for differences in the τ_h misidentification rates between data and simulation. Using a modified version of the MP method in the $2\ell\mathrm{SS}+1\tau_\mathrm{h}$ and $3\ell+1\tau_\mathrm{h}$ channels permits the retention as signal of those $\mathrm{t\bar{t}H}$ and tH signal events in which the reconstructed τ_h is not a genuine hadronic τ decay, but arises instead from the misidentification of a quark or gluon jet. The fraction of $\mathrm{t\bar{t}H}$ and tH signal events retained as signal amounts to approximately 30% of the total $\mathrm{t\bar{t}H}$ and tH signal yield in the $2\ell\mathrm{SS}+1\tau_\mathrm{h}$ and $3\ell+1\tau_\mathrm{h}$ channels.

7.2 Estimation of the "flips" background

The flips background, relevant for events containing either one or two reconstructed electrons in the $2\ell\mathrm{SS}+0\tau_\mathrm{h}$ and $2\ell\mathrm{SS}+1\tau_\mathrm{h}$ channels, is estimated using a procedure similar to the MP method. A sample of events passing all selection criteria of the SR, except that both leptons are required to be of OS instead of SS, are selected and assigned appropriately chosen weights. In the $2\ell\mathrm{SS}+0\tau_\mathrm{h}$ channel, the weight is given by the sum of the probabilities for the charge of either lepton to be mismeasured, whereas in the $2\ell\mathrm{SS}+1\tau_\mathrm{h}$ channel, only the lepton that has the same charge as the τ_h is considered, since only those events in which the charge of this lepton is mismeasured satisfy the condition $\sum_{\ell,\tau_\mathrm{h}} q = \pm 1$ that is applied in the SR of this channel.

The probability for the charge of electrons to be mismeasured, referred to as the electron charge misidentification rate, is determined using $\mathrm{Z}/\gamma^* \rightarrow \mathrm{ee}$ events. The events are selected by requiring the presence of an electron pair of invariant mass m_ee within the range $60 < m_\mathrm{ee} < 120\,\mathrm{GeV}$. No requirement is imposed on the charge of the electron pair. Contributions to the selected event sample arising from processes other than DY production of electron pairs are determined by performing an ML fit to the m_ee distribution. Referring to the number of $\mathrm{Z}/\gamma^* \rightarrow \mathrm{ee}$ events containing reconstructed SS and OS electron pairs, respectively, by the symbols N_SS and N_OS, the electron charge misidentification rate is given by the ratio $N_\mathrm{SS}/(N_\mathrm{OS}+N_\mathrm{SS})$. The ratio is measured as a function of electron p_T and η and varies between 5.1×10^{-5} for electrons of low p_T in the ECAL barrel and 1.6×10^{-3} for electrons of high p_T in the ECAL endcap. For illustration, the m_ee distributions for SS and OS electron pairs are shown in Fig. 7 for events in which both electrons are reconstructed in the ECAL barrel and have p_T within the range $25 < p_\mathrm{T} < 50\,\mathrm{GeV}$.

7.3 Control regions for irreducible backgrounds

The accuracy of the simulation-based modeling of the main irreducible backgrounds, arising from $\mathrm{t\bar{t}W(W)}$, $\mathrm{t\bar{t}Z}$, WZ, and ZZ production, is validated in three CRs. The first CR is based on the SR for the $3\ell+0\tau_\mathrm{h}$ channel and targets the $\mathrm{t\bar{t}Z}$ and WZ backgrounds. We refer to this CR as the 3ℓ-CR. The selection criteria applied in the 3ℓ-CR differ from those applied in the SR of the $3\ell+0\tau_\mathrm{h}$ channel in that: no Z boson veto is applied in the 3ℓ-CR; the presence of at least one SFOS lepton pair of invariant mass $m_{\ell\ell}$ with $|m_{\ell\ell}-m_\mathrm{Z}|<10\,\mathrm{GeV}$ is demanded instead; the requirement on the multiplicity of jets is relaxed to demanding the presence of at least one jet; and no requirement on the presence of b-tagged jets is applied. The contributions arising from $\mathrm{t\bar{t}Z}$ and from WZ production are separated by binning the events selected in the 3ℓ-CR in the flavor of the three leptons (eee, eeμ, e$\mu\mu$, $\mu\mu\mu$) and in the multiplicity of jets and of b-tagged jets. The second CR targets the ZZ background. We refer to it as the 4ℓ-CR, since it is based on the SR for the $4\ell+0\tau_\mathrm{h}$ channel. Compared to the latter, the event selection criteria applied in the 4ℓ-CR are modified by applying no Z veto, instead requiring the presence of at least one SFOS lepton pair of invariant mass $m_{\ell\ell}$ with $|m_{\ell\ell}-m_\mathrm{Z}|<10\,\mathrm{GeV}$, and applying no requirements on the multiplicity of jets and of b-tagged jets. To separate the ZZ background from other backgrounds, predominantly arising from $\mathrm{t\bar{t}Z}$ production, the events selected in the 4ℓ-CR are binned in the multiplicity of SFOS lepton pairs of invariant mass $|m_{\ell\ell}-m_\mathrm{Z}|<10\,\mathrm{GeV}$ and in the number of jets passing tight b tagging criteria. The third CR targets the $\mathrm{t\bar{t}W(W)}$ background and is identical to the SR of the $2\ell\mathrm{SS}+0\tau_\mathrm{h}$ channel, except that the output node of the ANN that has the highest activation value is required to be the output node corresponding to the $\mathrm{t\bar{t}W}$ background.

The numbers of events observed in the 3ℓ- and 4ℓ-CRs and in the CR for the $\mathrm{t\bar{t}W(W)}$ background are given in Table 6. The contributions arising from the misidentified leptons and flips backgrounds are estimated using the methods described in Sects. 7.1 and 7.2, respectively. The uncertainties include

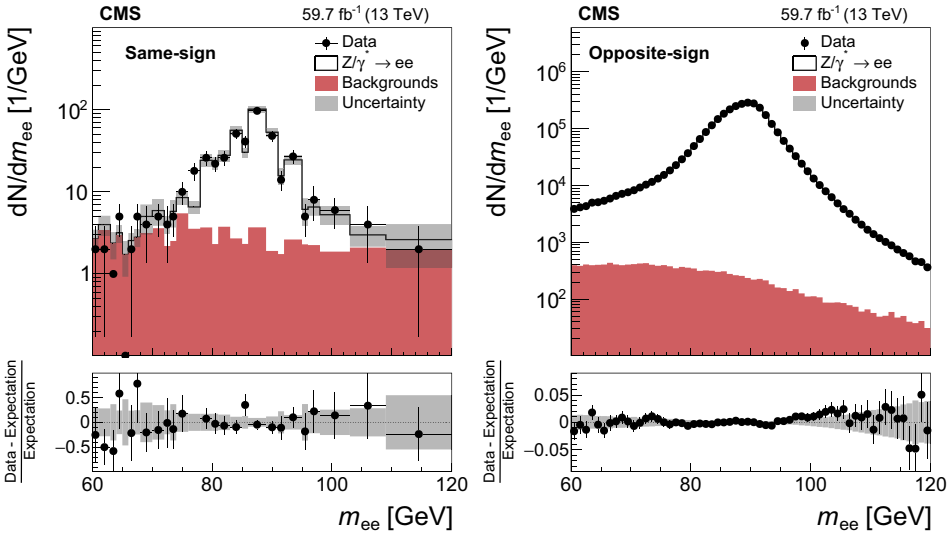


Fig. 7 Distributions of m_{ee} for (left) SS and (right) OS electron pairs in $Z/\gamma^* \rightarrow ee$ candidate events in which both electrons are in the ECAL barrel and have transverse momenta within the range $25 < p_T < 50$ GeV, for data recorded in 2018, compared to the expectation. Uncertainties shown are statistical only. A similar level of agreement is present in all the other momentum ranges and data-taking periods

both statistical and systematic sources, added in quadrature. The systematic uncertainties that are relevant for the CRs are similar to the ones applied to the SR. The latter are detailed in Sect. 8.

Figure 12, discussed in Sect. 9, shows the distributions of events selected in the 3ℓ- and 4ℓ-CRs in the binning scheme employed to separate the WZ and ZZ backgrounds from the $t\bar{t}Z$ backgrounds. The events selected in the 3ℓ-CR are first subdivided by lepton flavor and then by the multiplicity of jets and b-tagged jets. For each lepton flavor, 12 bins are used, defined as follows (in order of increasing bin number): 0 jets passing the tight b tagging criteria with 1, 2, 3, or $\geq$4 jets in total; 1 jet passing the tight b tagging criteria with 2, 3, 4, or $\geq$5 jets in total; $\geq$2 jets passing the tight b tagging criteria with 2, 3, 4, or $\geq$5 jets in total. In the 4ℓ-CR, 4 bins are used in total, defined as (again in order of increasing bin number): 2 SFOS lepton pairs of invariant mass $|m_{\ell\ell} - m_Z| < 10$ GeV; 1 such SFOS lepton pair with 0, 1, or $\geq$2 jets passing the tight b tagging criteria.

The data in the 3ℓ- and 4ℓ-CRs and in the CR for the $t\bar{t}W(W)$ background are in agreement with the background estimates within the quoted uncertainties.

8 Systematic uncertainties

The event rates and the distributions of the discriminating observables used for signal extraction may be altered by several experiment- or theory-related effects, referred to as systematic uncertainties. Experimental sources comprise the uncertainties in auxiliary measurements, performed to validate and, if necessary, correct the modeling of the data by the MC simulation, and the uncertainties in the data-driven estimates of the misidentified leptons and flips backgrounds. The latter are largely unaffected by potential inaccuracies of the MC simulation. Theoretical uncertainties mainly arise from missing higher-order corrections to the perturbative expansions employed for the computation of cross sections and from uncertainties in the PDFs.

The efficiencies of triggers based on the presence of one, two, or three electrons or muons are measured as a function of the lepton multiplicity with an uncertainty ranging from 1 to 2%, using samples of $t\bar{t}$+jets and diboson events that have been recorded using triggers based on p_T^{miss}.

The efficiencies for electrons and muons to pass the offline reconstruction and identification criteria are measured as a function of the lepton p_T and η by applying the "tag-and-probe" method detailed in Ref. [71] to $Z/\gamma^* \rightarrow ee$ and $Z/\gamma^* \rightarrow \mu\mu$ events. Additionally, we cross-check these efficiencies in a CR enriched in $t\bar{t}$+jets events to account for differences in event topology between DY events and the events in the SR of this analysis, which may cause a change in the efficiencies for electrons and muons to pass isolation requirements. Events in the $t\bar{t}$+jets CR are selected by requiring the presence of an OS e+μ pair and at least two jets. Nonprompt-

Table 6 Number of events selected in the 3ℓ- and 4ℓ-CRs and in the CR for the $t\bar{t}W(W)$ background, compared to the event yields expected from different types of background and from the $t\bar{t}H$ and tH signals, after the fit to data is performed as described in Sect. 9. Uncertainties shown include all systematic components. The symbol "–" indicates that the corresponding background does not apply

Process	3ℓ-CR	4ℓ-CR	$t\bar{t}W(W)$ CR
$t\bar{t}H$	15.9 ± 4.4	1.4 ± 0.4	62 ± 14
tH	4.4 ± 3.0	–	22 ± 18
$t\bar{t}Z + t\bar{t}\gamma^*$	550 ± 43	41.5 ± 3.0	100.3 ± 8.1
$t\bar{t}W + t\bar{t}WW$	26.8 ± 1.7	–	588 ± 35
WZ	4320 ± 120	–	51.6 ± 7.5
ZZ	298 ± 18	1030 ± 32	0.2 ± 0.1
Nonprompt leptons	210 ± 20	–	102 ± 14
Flips	–	–	24.9 ± 4.0
Rare backgrounds	311 ± 61	17.0 ± 3.4	58 ± 13
Conversions	1.0 ± 0.3	0.1 ± 0.1	1.4 ± 0.6
$ggH + qqH + VH + t\bar{t}VH$	42.8 ± 3.1	5.8 ± 0.4	1.6 ± 0.3
Total expected background	5761 ± 99	1094 ± 33	949 ± 33
Data	5778	1089	986

lepton backgrounds in the CR are subtracted using a sideband region SS e+μ events. The difference between the efficiency measured in the $t\bar{t}$+jets CR and the one measured in DY events is included as a systematic uncertainty, amounting to 1–2%. The τ_h identification efficiency and energy scale are measured with respective uncertainties of 5 and 1.2% using $Z/\gamma^* \to \tau\tau$ events [74].

The energy scale of jets is measured with an uncertainty amounting to a few percent, depending on the jet p_T and η, using the p_T-balance method, which is applied to $Z/\gamma^* \to ee$, $Z/\gamma^* \to \mu\mu$, γ+jets, dijet, and multijet events [72]. The resulting effect on signal and background expectations is evaluated by varying the energies of jets in simulated events within their uncertainties, recalculating all kinematic observables, and reapplying the event selection criteria. The effect of uncertainties in the jet energy resolution is evaluated in a similar way, but is smaller than the effect of the uncertainties in the jet energy scale.

The b tagging efficiency is measured with an uncertainty of a few per cent in $t\bar{t}$+jets and multijet events as a function of jet p_T and η. The heavy-flavor content of the multijet events is enriched by requiring the presence of a muon in the event. The mistag rates for light-quark and gluon jets are measured in multijet events yielding an uncertainty of 5–10% for the loose and 20–30% for the tight b tagging criteria, depending on p_T and η [73].

The integrated luminosities of the 2016, 2017, and 2018 data-taking periods are individually known with uncertainties in the 2.3–2.5% range [39–41], while the total Run 2 (2016–2018) integrated luminosity has an uncertainty of 1.8%, the improvement in precision reflecting the (uncorrelated) time evolution of some systematic effects.

The uncertainties related to the number of PU interactions are evaluated by varying the number of inelastic pp interactions that are superimposed on simulated events by 4.6% [98]. The resulting effect on the $t\bar{t}H$ and tH signal yields and on the yields of background contributions modeled using the MC simulation amounts to less than 1%.

The effect of theory-related uncertainties on the event yields and on the distributions of the BDTs and ANNs classifier outputs that are used for the signal extraction is assessed for the $t\bar{t}H$ and tH signals, as well as for the main irreducible backgrounds that arise from $t\bar{t}W$, $t\bar{t}WW$, and $t\bar{t}Z$ production. The uncertainties in the production cross sections amount to $^{+6.8}_{-9.9}$ and $^{+5.1}_{-7.3}$% for the $t\bar{t}H$ and tH signals, and to $^{+13.5}_{-12.2}$, $^{+8.6}_{-11.3}$, and $^{+11.7}_{-10.2}$% for the $t\bar{t}W$, $t\bar{t}WW$, and $t\bar{t}Z$ backgrounds, respectively. These uncertainties are taken from Ref. [62] and consist of the sum in quadrature of three sources: missing higher-order corrections in the perturbative expansion, different choices of PDFs, and uncertainties in the value of the strong coupling constant α_S. The uncertainties in the cross sections are relevant for the purpose of quoting the measured production rates with respect to their SM expectations for these rates. In addition, the uncertainty in the $t\bar{t}H$ and tH production cross sections is relevant for setting limits on the coupling of the Higgs boson to the top quark. The effect of missing higher-order corrections on the distributions of the discriminating observables is estimated by varying the renormalization and factorization scales up and down by a factor of two with respect to their nominal value, following the recommendations of Refs. [99–101], avoiding cases in which the two variations are done in opposite directions. The effect of uncertainties in the PDFs on these distributions is evaluated following the recommendations given in Ref. [102]. The

uncertainties in the branching fractions of the Higgs boson decay modes $H \to WW$, $H \to \tau\tau$, and $H \to ZZ$ are taken from Ref. [62] and amount to 1.5, 1.7, and 1.5%, respectively.

In the $1\ell + 1\tau_h$ and $0\ell + 2\tau_h$ channels, the $t\bar{t}$+jets and DY production may contribute as irreducible backgrounds and are modeled using the MC simulation. The $t\bar{t}$+jets and DY production cross sections are known to an uncertainty of 5 [65] and 4% [103], respectively. An additional uncertainty on the modeling of top quark p_T distribution of $t\bar{t}$+jets events is considered, defined as the difference between the nominal POWHEG sample and that sample reweighed to improve the quality of the top quark p_T modeling, as described in Sect. 3. The modeling of the multiplicity of jets and of b-tagged jets in simulated DY events is improved by comparing these multiplicities between MC simulation and data using $Z/\gamma^* \to ee$ and $Z/\gamma^* \to \mu\mu$ events. The average ratio of data and MC simulation in the $Z/\gamma^* \to ee$ and $Z/\gamma^* \to \mu\mu$ event samples is taken as a correction, while the difference between the ratios measured in $Z/\gamma^* \to ee$ and $Z/\gamma^* \to \mu\mu$ events is taken as the systematic uncertainty and added in quadrature to the statistical uncertainties in these ratios. The $Z/\gamma^* \to ee$ and $Z/\gamma^* \to \mu\mu$ event samples used to determine this correction have little overlap with the SRs of the $1\ell + 1\tau_h$ and $0\ell + 2\tau_h$ channels, since most of the DY background in these channels arises from $Z/\gamma^* \to \tau\tau$ events.

Other background processes, notably the conversions and rare backgrounds, are modeled using the MC simulation; the uncertainty in their event yields is conservatively taken to be 50%. This choice accounts for the extrapolation from the inclusive phase space to the phase space relevant for this analysis, in particular to events with a high multiplicity of jets and b-tagged jets, as required to pass the event selection criteria detailed in Sect. 5. The inclusive cross sections for most of these background processes have been measured with uncertainties amounting to significantly less than 50% by previous analyses of the LHC data.

The extrapolation of the WZ and ZZ background rates from the 3ℓ- and 4ℓ-CRs to the SR depends on the heavy-flavor content of WZ and ZZ background events. According to the MC simulation, most of the b jets reconstructed in WZ and ZZ background events arise from the misidentification of light-quark or gluon jets rather than from charm or bottom quarks. We assign an uncertainty of 40% to the modeling of the heavy-flavor content in WZ and ZZ background events, accounting for the differences in the jet multiplicity distribution between data and simulation in the 3ℓ CR. The misidentification of light quark or gluon jets as b jets is covered by a separate systematic uncertainty.

The uncertainties in the rate and in the distribution of the discriminating observables for the background from misidentified leptons and τ_h stem from statistical uncertainties in the events selected in the MR and AR as well as from systematic uncertainties related to the subtraction of the prompt-lepton contributions from the data selected in the MR and AR of the MP method. The effect of these uncertainties on the analysis is evaluated by applying independent variations of the probabilities f_i for electrons and muons in different bins of lepton-candidate p_T and η and determining the resulting change in the yield and distribution of the misidentified leptons background estimate. We introduce an additional uncertainty in the nonclosure correction to the f_i for electrons and muons, accounting for differences between the probabilities f_i in $t\bar{t}$+jets and multijet events shown in Fig. 6. The size of this uncertainty is equal to the magnitude of the correction. In case of τ_h, the misidentification rates f_i measured in each bin in η and reconstructed τ_h decay mode are fitted by a linear function in p_T of the τ_h candidate and the uncertainty in the slope and offset of this fit is propagated to the final result. The uncertainty in the rate of the misidentified leptons background is, in general, higher for channels with τ_h. The uncertainty varies between 10% in the $2\ell SS + 0\tau_h$ channel and 60% in the $2\ell + 2\tau_h$ channel. The resulting uncertainty in the distribution of the discriminating observables is of moderate size. Additional nonclosure uncertainties account for small differences between the misidentified leptons background estimate obtained by computing the probabilities f_i for simulated events and applying the weights w given by Eq. (1) to simulated events selected in the AR, and the background estimates obtained by modeling the background from misidentified leptons and τ_h in the SR using the MC simulation directly.

The uncertainty in the flips background in the $2\ell SS + 0\tau_h$ and $2\ell SS + 1\tau_h$ channels is evaluated in a similar way: it amounts to 30% in each channel.

The effects of systematic uncertainties representing the same source are treated as fully correlated between all ten analysis channels. Theoretical uncertainties are furthermore treated as fully correlated among all data-taking periods, whereas the uncertainties arising from experimental sources are treated as uncorrelated between the data recorded in each of the years 2016, 2017, and 2018. The latter treatment is justified by the fact that the uncertainties related to the auxiliary measurements that are performed to validate, and if necessary correct, the modeling of the data by the MC simulation, are mainly of statistical origin and hence independent for measurements that are performed independently for each of the three data-taking periods because of the changes in the detector conditions from one period to another.

The impact of the systematic and statistical uncertainties on the measurement of the $t\bar{t}H$ and tH signal rates is summarized in Table 7. The largest impacts are due to: the statistical uncertainty of observed data; the uncertainty in the efficiency to reconstruct and identify τ_h; the uncertainties related to the estimation of the misidentified leptons and flips backgrounds; and the theoretical uncertainties, which affect the yield and the distribution of the discriminating observables

Table 7 Summary of the sources of systematic and statistical uncertainties and their impact on the measurement of the $t\bar{t}H$ and tH signal rates, and the measured value of the unconstrained nuisance parameters. The quantity $\Delta\mu_x/\mu_x$ corresponds to the change in uncertainty when fixing the nuisance parameters associated with that uncertainty in the fit. Under the label "MC and sideband statistical uncertainty" are the uncertainties associated with the limited number of simulated MC events and the amount of data events in the application region of the MP method

Source	$\Delta\mu_{t\bar{t}H}/\mu_{t\bar{t}H}$ (%)	$\Delta\mu_{tH}/\mu_{tH}$ (%)	$\Delta\mu_{t\bar{t}W}/\mu_{t\bar{t}W}$ (%)	$\Delta\mu_{t\bar{t}Z}/\mu_{t\bar{t}Z}$ (%)
Trigger efficiency	2.3	8.1	1.2	1.9
e, μ reconstruction and identification efficiency	2.9	7.1	1.7	3.2
τ_h identification efficiency	4.6	9.1	1.7	1.3
b tagging efficiency and mistag rate	3.6	13.6	1.3	2.9
Misidentified leptons and flips	6.0	36.8	2.6	1.4
Jet energy scale and resolution	3.4	8.3	1.1	1.2
MC sample and sideband statistical uncertainty	7.1	27.2	2.4	2.3
Theory-related sources affecting acceptance and shape of distributions	4.6	18.2	2.0	4.2
Normalization of MC-estimated processes	13.3	12.3	13.9	11.3
Integrated luminosity	2.2	4.6	1.8	3.1
Statistical uncertainty	20.9	48.0	5.9	5.8

for the $t\bar{t}H$ and tH signals as well as for the main irreducible backgrounds, arising from $t\bar{t}W$, $t\bar{t}WW$, tW, $t\bar{t}Z$, and tZ production.

8.1 Additional checks

As a cross-check, and to highlight the enhancement in sensitivity provided by machine-learning techniques, a complementary measurement of the $t\bar{t}H$ signal rate is performed using a set of alternative observables in the ML fit. We refer to this cross-check as the control analysis, as distinguished from the analysis previously discussed, which we refer to as the main analysis. The control analysis (CA) is restricted to the $2\ell SS + 0\tau_h$, $3\ell + 0\tau_h$, $2\ell SS + 1\tau_h$, and $4\ell + 0\tau_h$ channels. The production rate of the tH signal is fixed to its SM expectation in the CA. In the $2\ell SS + 0\tau_h$ channel, the invariant mass of the lepton pair is used as the discriminating observable. The event selection criteria applied in the CA in this channel are modified to the condition $N_j \geq 4$ and the events are analyzed in subcategories based on lepton flavor, the charge-sum of the leptons (+2 or −2), and the multiplicity of jets. In the $3\ell + 0\tau_h$ channel, the invariant mass of the three-lepton system is used as discriminating observable and the events are analyzed in subcategories based on the multiplicity of jets and on the charge-sum of the leptons (+1 or −1). A discriminant based on the matrix-element method [35,36] is used as discriminating observable in the $2\ell SS+1\tau_h$ channel and the events are analyzed in two subcategories based on the multiplicity of jets, defined by the conditions $N_j = 3$ and $N_j \geq 4$, and referred to as the "missing-jet" and "no-missing-jet" subcategories. The computation of the discriminant exploits the fact that the differential cross sections for the $t\bar{t}H$ signal, as well as for the dominant background processes in the $2\ell SS + 1\tau_h$ channel, are well known; this permits the computation of the probabilities for a given event to be either signal or background, given the measured values of kinematic observables in the event and taking into account the experimental resolution of the detector. The probabilities are computed for the $t\bar{t}H$ signal hypothesis and for three types of background hypotheses: $t\bar{t}Z$ events in which the Z boson decays into a pair of τ leptons; $t\bar{t}Z$ events in which the Z boson decays into a pair of electrons or muons and one lepton is misidentified as τ_h; and $t\bar{t} \to b\ell\nu\,\bar{b}\tau\nu$ events with one additional nonprompt lepton originating from a b hadron decay. Details on the computation of these probabilities are given in Ref. [23]. The ratio of the probability for a given event to be $t\bar{t}H$ signal to the sum of the probabilities for the event to be one of the three backgrounds constitutes, according to the Neyman-Pearson lemma [104], an optimal observable for the purpose of separating the $t\bar{t}H$ signal from backgrounds and is taken as the discriminant used for the signal extraction. In the $4\ell + 0\tau_h$ channel, the invariant mass of the four-lepton system, $m_{4\ell}$, is used as the discriminating observable.

9 Statistical analysis and results

The production rates of the $t\bar{t}H$ and tH signals are determined through a binned simultaneous ML fit to the total of 105 distributions: the outputs of the BDTs in each of the seven channels $1\ell + 1\tau_h$, $0\ell + 2\tau_h$, $2\ell OS + 1\tau_h$, $1\ell + 2\tau_h$, $4\ell + 0\tau_h$, $3\ell + 1\tau_h$, and $2\ell + 2\tau_h$; the distributions of the 10 output nodes of the ANNs in the $2\ell SS + 0\tau_h$, $3\ell + 0\tau_h$, and $2\ell SS+1\tau_h$ channels in the categories described in Fig. 3; and the distributions of the observables that discriminate the $t\bar{t}Z$ background from each of the WZ and ZZ backgrounds in the

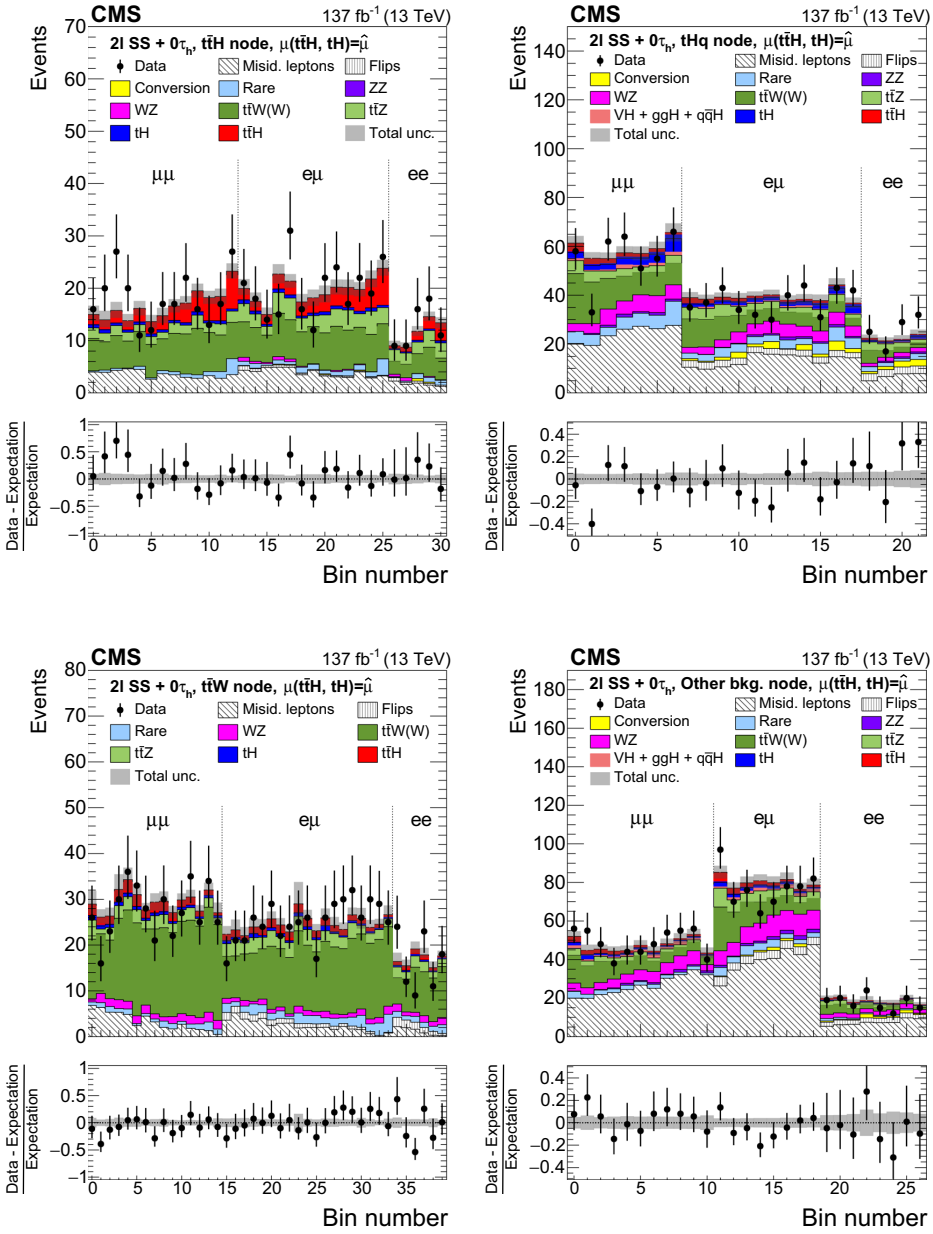


Fig. 8 Distributions of the activation value of the ANN output node with the highest activation value for events selected in the $2\ell SS + 0\tau_h$ channel and classified as $t\bar{t}H$ signal (upper left), tH signal (upper right), $t\bar{t}W$ background (lower left), and other backgrounds (lower right). The distributions expected for the $t\bar{t}H$ and tH signals and for background processes are shown for the values of the parameters of interest and of the nuisance parameters obtained from the ML fit. The best fit value of the $t\bar{t}H$ and tH production rates amounts to $\hat{\mu}_{t\bar{t}H} = 0.92$ and $\hat{\mu}_{tH} = 5.7$ times the rates expected in the SM

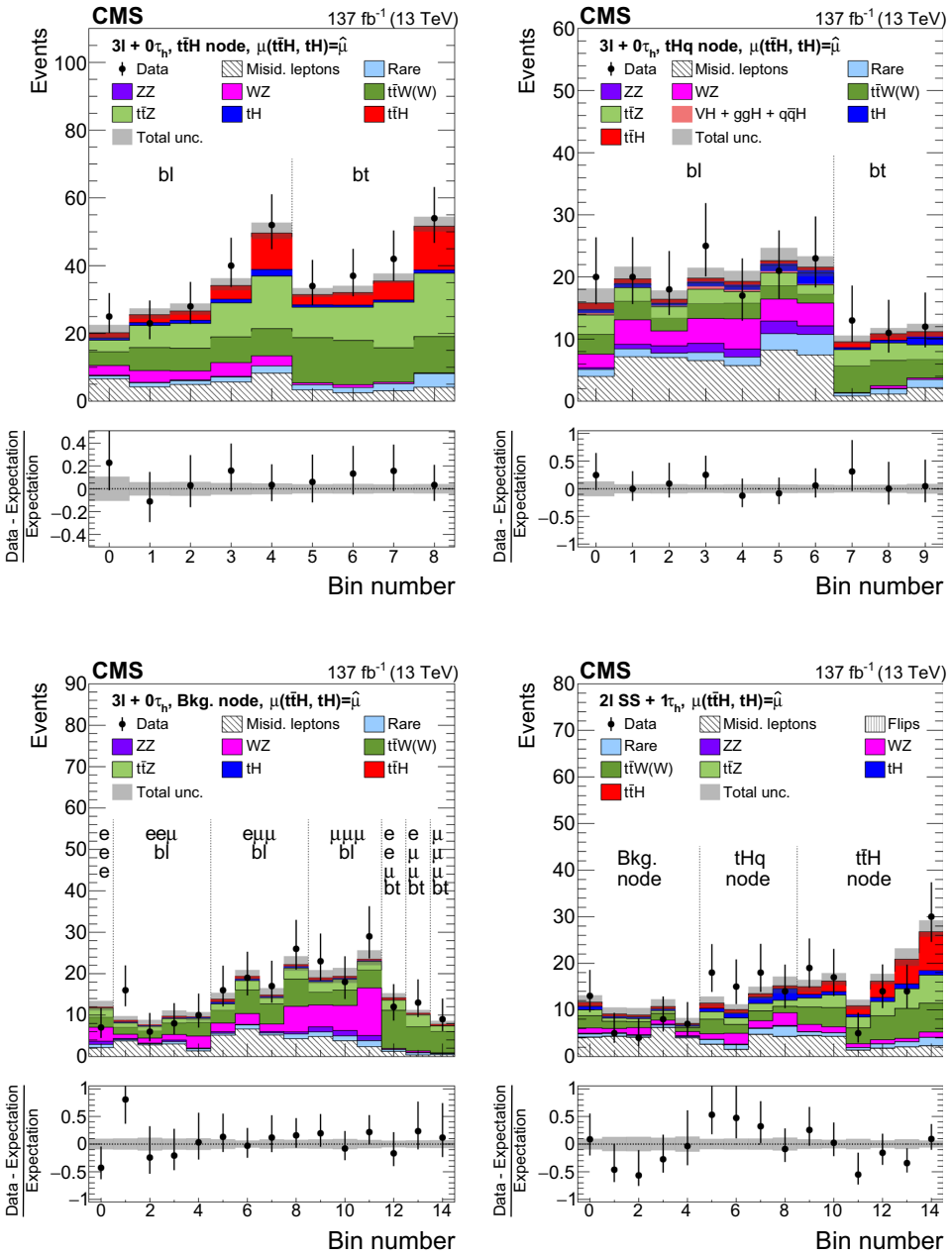


Fig. 9 Distributions of the activation value of the ANN output node with the highest activation value for events selected in the $3\ell + 0\tau_h$ channel and classified as $t\bar{t}H$ signal (upper left), tH signal (upper right), and background (lower left), and for events selected in the $2\ell SS + 1\tau_h$ channel (lower right). In case of the $2\ell SS + 1\tau_h$ channel, the activation value of the ANN output nodes for $t\bar{t}H$ signal, tH signal, and background are shown together in a single histogram, concatenating histogram bins as appropriate and enumerating the bins by a monotonously increasing number. The distributions expected for the $t\bar{t}H$ and tH signals and for background processes are shown for the values of the parameters of interest and of the nuisance parameters obtained from the ML fit. The best fit value of the $t\bar{t}H$ and tH production rates amounts to $\hat{\mu}_{t\bar{t}H} = 0.92$ and $\hat{\mu}_{tH} = 5.7$ times the rates expected in the SM

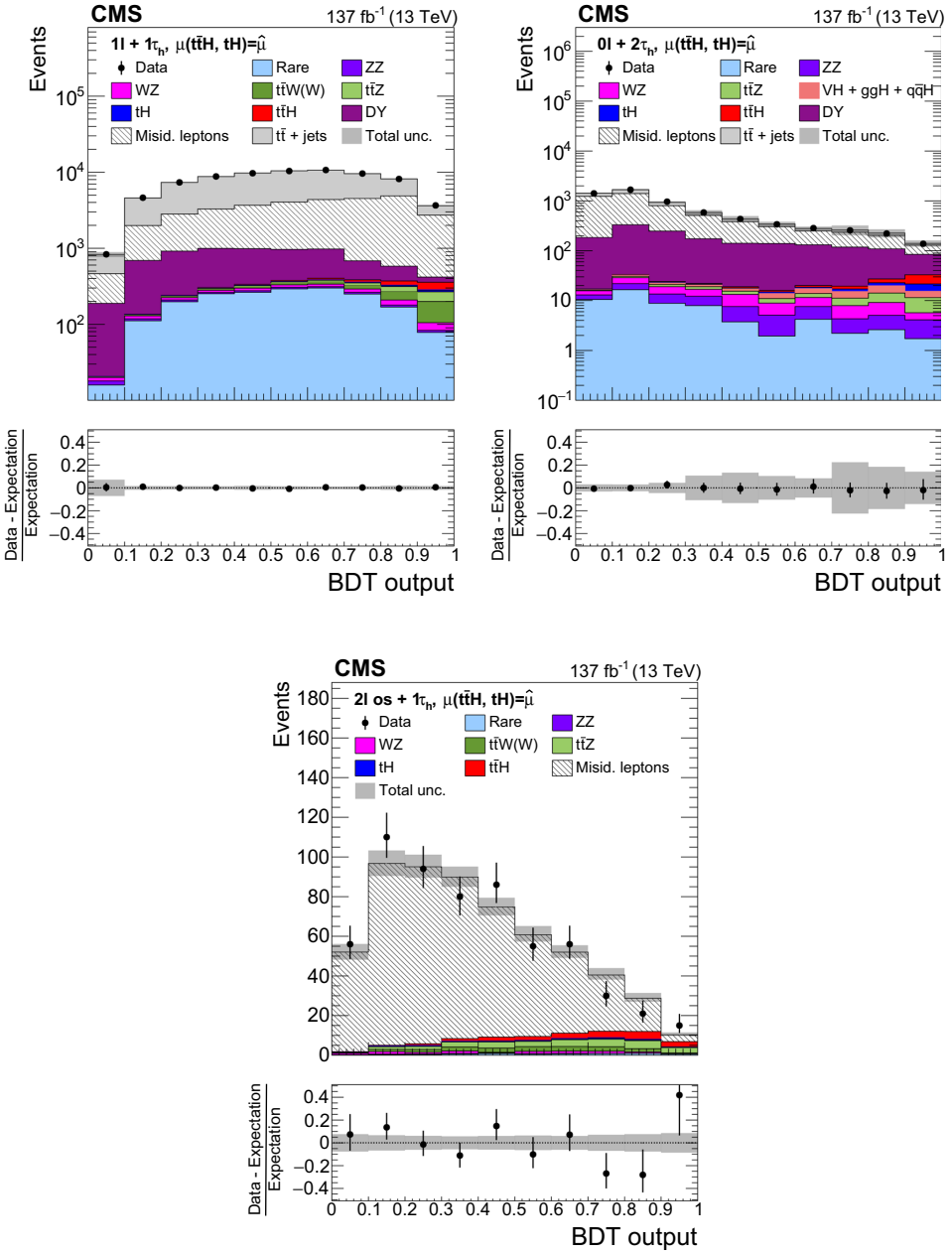


Fig. 10 Distributions of the BDT output for events selected in the $1\ell + 1\tau_h$ (upper left), $0\ell + 2\tau_h$ (upper right), and $2\ell\text{OS} + 1\tau_h$ (lower) channels. The distributions expected for the $t\bar{t}H$ and tH signals and for background processes are shown for the values of the parameters of interest and of the nuisance parameters obtained from the ML fit. The best fit value of the $t\bar{t}H$ and tH production rates amounts to $\hat{\mu}_{t\bar{t}H} = 0.92$ and $\hat{\mu}_{tH} = 5.7$ times the rates expected in the SM

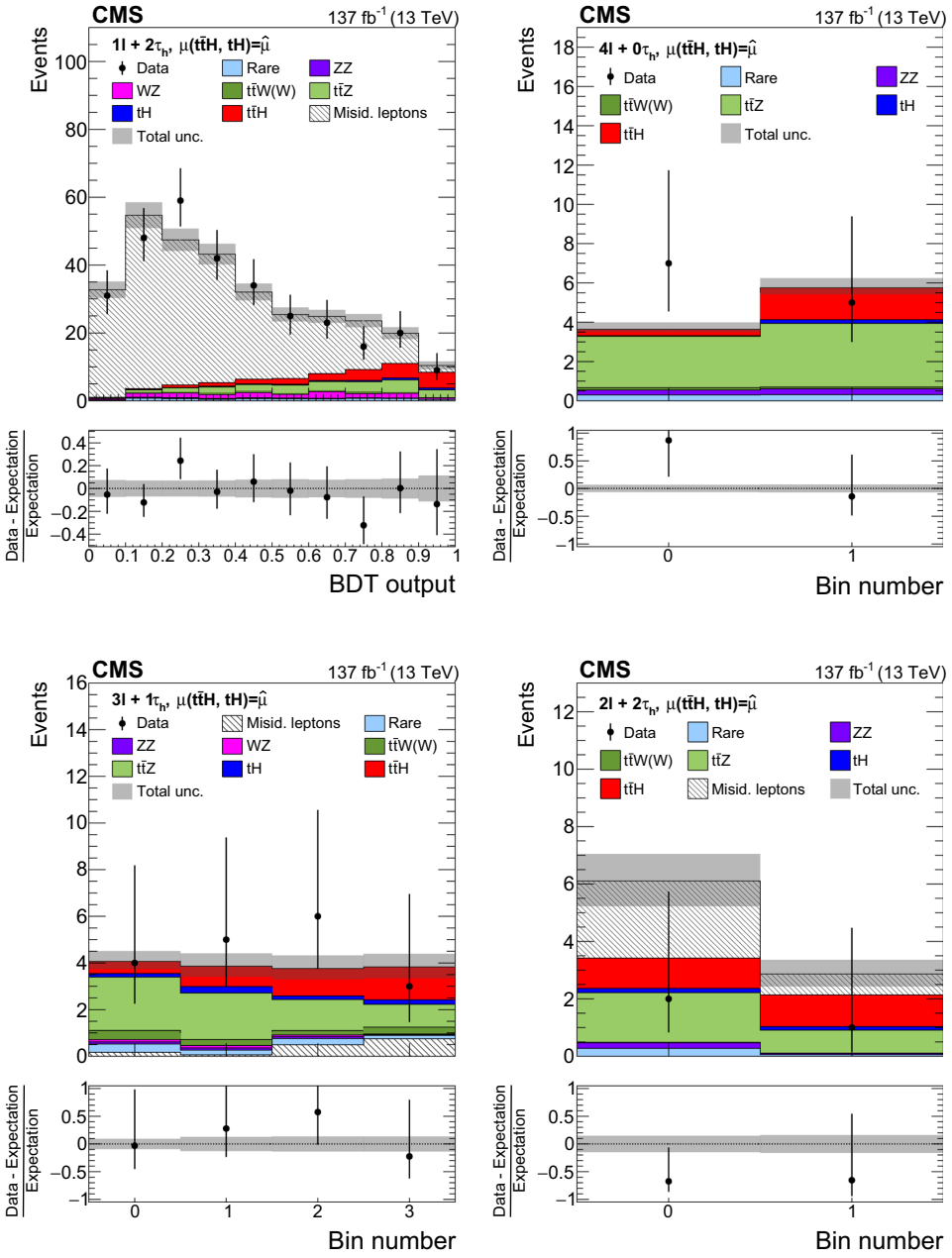


Fig. 11 Distributions of the BDT output used for the signal extraction in the $1\ell + 2\tau_h$ (upper left), $4\ell + 0\tau_h$ (upper right), $3\ell + 1\tau_h$ (lower left), and $2\ell + 2\tau_h$ (lower right) channels. The distributions expected for the $t\bar{t}H$ and tH signals and for background processes are shown for the values of the parameters of interest and of the nuisance parameters obtained from the ML fit. The best fit value of the $t\bar{t}H$ and tH production rates amounts to $\hat{\mu}_{t\bar{t}H} = 0.92$ and $\hat{\mu}_{tH} = 5.7$ times the rates expected in the SM

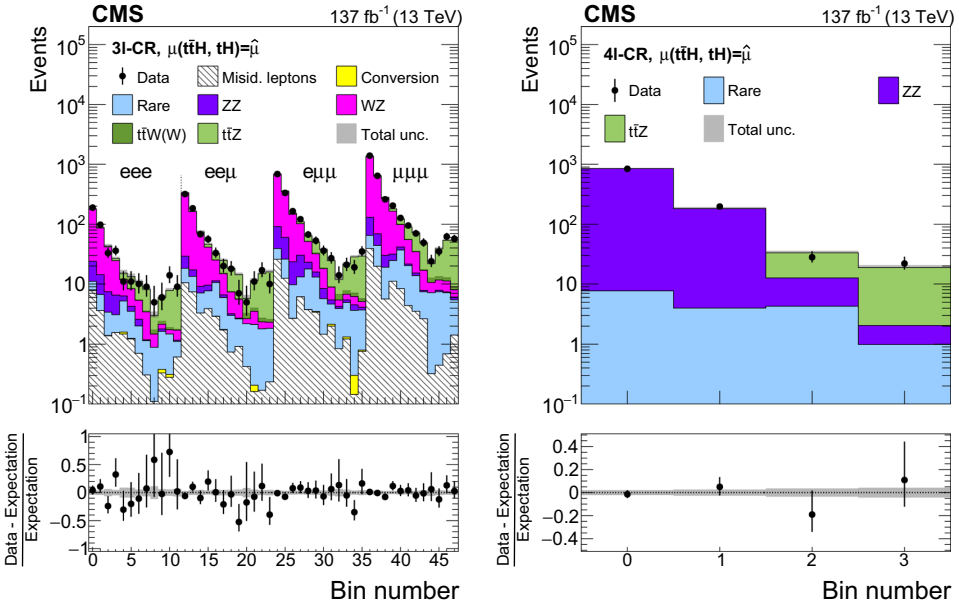


Fig. 12 Distributions of discriminating observables in the $3\ell + 0\tau_h$ (left) and $4\ell + 0\tau_h$ (right) control region. The distributions expected for the $t\bar{t}H$ and tH signals and for background processes are shown for the values of the parameters of interest and of the nuisance parameters obtained from the ML fit. The best fit value of the $t\bar{t}H$ and tH production rates amounts to $\hat{\mu}_{t\bar{t}H} = 0.92$ and $\hat{\mu}_{tH} = 5.7$ times the rates expected in the SM

3ℓ- and 4ℓ-CRs, respectively; separately for the three data-taking periods considered in the analysis. The $2\ell SS + 0\tau_h$ ($3\ell + 0\tau_h$) channel contributes a total of 12 (11) distributions per data-taking period to the ML fit, reflecting the subdivision of these channels into event categories based on lepton flavor and on the multiplicity of b-tagged jets.

The production rates of the $t\bar{t}H$ and tH signals constitute the parameters of interest (POI) in the fit. We denote by the symbols $\mu_{t\bar{t}H}$ and μ_{tH} the ratio of these production rates to their SM expectation and use the notation $\boldsymbol{\mu}$ to refer to the set of both POIs.

The likelihood function is denoted by the symbol $\mathcal{L}$ and is given by the expression:

$$\mathcal{L}\left(\text{data} \,|\, \boldsymbol{\mu}, \boldsymbol{\theta}\right) = \prod_i \mathcal{P}\left(n_i \,|\, \boldsymbol{\mu}, \boldsymbol{\theta}\right) \prod_k \mathrm{p}\left(\tilde{\theta}_k | \theta_k\right), \tag{3}$$

where the index i refers to individual bins of the 105 distributions of the discriminating observables that are included in the fit, and the factor $\mathcal{P}\left(n_i \,|\, \boldsymbol{\mu}, \boldsymbol{\theta}\right)$ represents the probability to observe n_i events in a given bin i, where $\nu_i(\boldsymbol{\mu}, \boldsymbol{\theta})$ events are expected from the sum of signal and background contributions in that bin. The number of expected events is a linear function of the two POIs indicated by $\mu_{t\bar{t}H}$ and μ_{tH}

$$\nu_i(\boldsymbol{\mu}, \boldsymbol{\theta}) = \mu_{t\bar{t}H} \nu_i^{t\bar{t}H}(\boldsymbol{\theta}) + \mu_{tH} \nu_i^{tH}(\boldsymbol{\theta}) + \nu_i^{B}(\boldsymbol{\theta}), \tag{4}$$

where the symbols $\nu_i^{t\bar{t}H}$, ν_i^{tH}, and ν_i^{B} denote, respectively, the SM expectation for the $t\bar{t}H$ and tH signal contributions and the aggregate of contributions expected from background processes in bin i. We use the notation $\nu_i(\boldsymbol{\mu}, \boldsymbol{\theta})$ to indicate that the number of events expected from signal and background processes in each bin i depends on a set of parameters, denoted by the symbol $\boldsymbol{\theta}$, that represent the systematic uncertainties detailed in Sect. 8 and are referred to as nuisance parameters. Via the dependency of the $\nu_i(\boldsymbol{\mu}, \boldsymbol{\theta})$ on $\boldsymbol{\theta}$, the nuisance parameters accommodate for variations of the event yields as well as of the distributions of the discriminating observables during the fit. The probability $\mathcal{P}\left(n_i \,|\, \boldsymbol{\mu}, \boldsymbol{\theta}\right)$ is given by the Poisson distribution:

$$\mathcal{P}\left(n_i \,|\, \boldsymbol{\mu}, \boldsymbol{\theta}\right) = \frac{\left(\nu_i(\boldsymbol{\mu}, \boldsymbol{\theta})\right)^{n_i}}{n_i!} \exp\left(-\nu_i(\boldsymbol{\mu}, \boldsymbol{\theta})\right). \tag{5}$$

Individual elements of the set of nuisance parameters $\boldsymbol{\theta}$ are denoted by the symbol θ_k, where each θ_k represents a specific source of systematic uncertainty. The function $\mathrm{p}(\tilde{\theta}_k|\theta_k)$ represents the probability to observe a value $\tilde{\theta}_k$ in an auxiliary measurement of the nuisance parameter, given that its true value is θ_k. Systematic uncertainties that affect only the

Table 8 Number of events selected in each of the ten analysis channels compared to the event yields expected from the $t\bar{t}H$ and tH signals and from background processes. The expected event yields are computed for the values of nuisance parameters and of the POI obtained from the ML fit. The best fit values of the POI amount to $\hat{\mu}_{t\bar{t}H} = 0.92$ and $\hat{\mu}_{tH} = 5.7$. Quoted uncertainties represent the sum of statistical and systematic components. The symbol "–" indicates that the corresponding expected contribution is smaller than 0.1 events

Process	$2\ell SS + 0\tau_h$	$3\ell + 0\tau_h$	$2\ell SS + 1\tau_h$
$t\bar{t}H$	222 ± 51	61 ± 15	28.9 ± 6.4
tH	119 ± 85	20 ± 14	12.7 ± 9.0
$t\bar{t}Z + t\bar{t}\gamma^*$	322 ± 25	145 ± 11	29.6 ± 3.3
$t\bar{t}W + t\bar{t}WW$	1153 ± 64	171.1 ± 9.5	47.4 ± 6.5
WZ	296 ± 31	89.7 ± 9.7	19.4 ± 2.9
ZZ	31.2 ± 3.3	16.2 ± 1.6	1.6 ± 0.3
Misidentified leptons	1217 ± 91	140 ± 11	52.0 ± 9.6
Flips	121 ± 19	–	–
Rare backgrounds	222 ± 48	41.0 ± 8.9	13.3 ± 3.1
Conversion	42 ± 12	5.6 ± 1.6	–
$ggH + qqH + VH + t\bar{t}VH$	35.3 ± 4.0	3.4 ± 0.3	1.8 ± 0.3
Total expected background	3517 ± 85	627 ± 20	179 ± 13
Data	3738	744	201

Process	$1\ell + 1\tau_h$	$0\ell + 2\tau_h$	$2\ell OS + 1\tau_h$	$1\ell + 2\tau_h$
$t\bar{t}H$	183 ± 41	24.4 ± 6.0	19.1 ± 4.3	19.3 ± 4.2
tH	65 ± 46	16 ± 12	4.8 ± 3.4	2.6 ± 1.9
$t\bar{t}Z + t\bar{t}\gamma^*$	203 ± 24	27.1 ± 3.8	25.5 ± 2.9	20.3 ± 2.1
$t\bar{t}W + t\bar{t}WW$	254 ± 34	3.8 ± 0.5	17.4 ± 2.4	2.6 ± 0.4
WZ	198 ± 37	42.5 ± 8.7	8.4 ± 1.6	11.8 ± 2.2
ZZ	98 ± 13	34.2 ± 4.8	1.9 ± 0.3	1.8 ± 0.3
DY	4480 ± 460	1430.0 ± 220	519 ± 28	250 ± 16
$t\bar{t}$+jets	41900 ± 1900	861 ± 98	–	–
Misidentified leptons	25300 ± 1900	3790 ± 220	–	–
Rare backgrounds	1930 ± 420	60 ± 14	5.9 ± 1.3	5.6 ± 1.3
Conversion	–	–	0.5 ± 0.2	–
$ggH + qqH + VH + t\bar{t}VH$	38.5 ± 3.6	26.7 ± 3.6	0.8 ± 0.1	–
Total expected background	73550 ± 610	6290 ± 130	584 ± 27	295 ± 16
Data	73736	6310	603	307

Process	$4\ell + 0\tau_h$	$3\ell + 1\tau_h$	$2\ell + 2\tau_h$
$t\bar{t}H$	2.0 ± 0.5	4.0 ± 0.9	2.2 ± 0.5
tH	0.2 ± 0.2	0.8 ± 0.6	0.3 ± 0.2
$t\bar{t}Z + t\bar{t}\gamma^*$	5.9 ± 0.4	6.6 ± 0.7	2.5 ± 0.3
$t\bar{t}W + t\bar{t}WW$	0.2 ± 0.0	1.1 ± 0.2	–
ZZ	0.6 ± 0.2	0.3 ± 0.1	0.2 ± 0.0
Misidentified leptons	–	1.5 ± 0.9	3.4 ± 0.9
Rare backgrounds	0.6 ± 0.1	1.0 ± 0.3	0.3 ± 0.1
Conversion	–	–	–
Total expected background	7.4 ± 0.5	11.5 ± 1.3	6.8 ± 1.0
Data	12	18	3

normalization, but not the shape of the distribution of the discriminating observables, are represented by a Gamma probability density function if they are statistical in origin, e.g. if they correspond to the number of events observed in a CR, and otherwise by a log-normal probability density function; systematic uncertainties that also affect the shape of distributions of the discriminating observables are incorporated into the ML fit via the technique detailed in Ref. [105] and represented by a Gaussian probability density function.

The rates of the $t\bar{t}W$ and $t\bar{t}Z$ backgrounds are separately left unconstrained in the fit. The rate of the small $t\bar{t}WW$ background is constrained to scale by the same factor with respect to its SM expectation as the rate of the $t\bar{t}W$ background.

Statistical fluctuations in the background predictions arise because of a limited number of events in the MC simulation as well as in the ARs that are used to estimate the misidentified leptons and flips backgrounds from data. These fluctuations are incorporated into the likelihood function via the approach described in Ref. [106].

Further details concerning the treatment of systematic uncertainties and concerning the choice of the functions $p(\tilde{\theta}_k|\theta_k)$ are given in Refs. [105,107,108].

A complication in the signal extraction arises from the fact that a deviation in the top quark Yukawa coupling y_t with respect to the SM expectation m_t/v would change the distribution of kinematic observables for the tH signal and alter the proportion between the tH and $t\bar{t}H$ signal rates. We address this complication by first determining the production rates for the tH and $t\bar{t}H$ signals, assuming that the distributions of kinematic observables for the tH signal conform to the distributions expected in the SM; we then determine the Yukawa coupling y_t of the Higgs boson to the top quark, accounting for modifications in the interference effects for the tH signal. These studies assume a Higgs boson mass of 125 GeV.

Assuming the distributions of the discriminating observables for the tH and $t\bar{t}H$ signals agree with their SM expectation, the production rate for the $t\bar{t}H$ signal is measured to be $\mu_{t\bar{t}H} = 0.92 \pm 0.19\,(\text{stat})^{+0.17}_{-0.13}\,(\text{syst})$ times the SM expectation, equivalent to a $t\bar{t}H$ production cross section for $t\bar{t}H$ production of $466 \pm 96\,(\text{stat})^{+70}_{-56}\,(\text{syst})$ fb, and that of the tH signal is measured to be $\mu_{tH} = 5.7 \pm 2.7\,(\text{stat}) \pm 3.0\,(\text{syst})$ times the SM expectation for this production rate, equivalent to a cross section for tH production of $510 \pm 200\,(\text{stat}) \pm 220\,(\text{syst})$ fb. The corresponding observed (expected) significance of the $t\bar{t}H$ signal amounts to 4.7 (5.2) standard deviations, assuming the tH process to have the SM production rate, and that of the tH signal to 1.4 (0.3) standard deviations, also assuming the $t\bar{t}H$ process to have the SM production rate. We have estimated the agreement between the data and our statistical model by using a goodness-of-fit test to the saturated model, obtaining a p-value of 0.097, showing no indication of a significant difference between data and the assumed model.

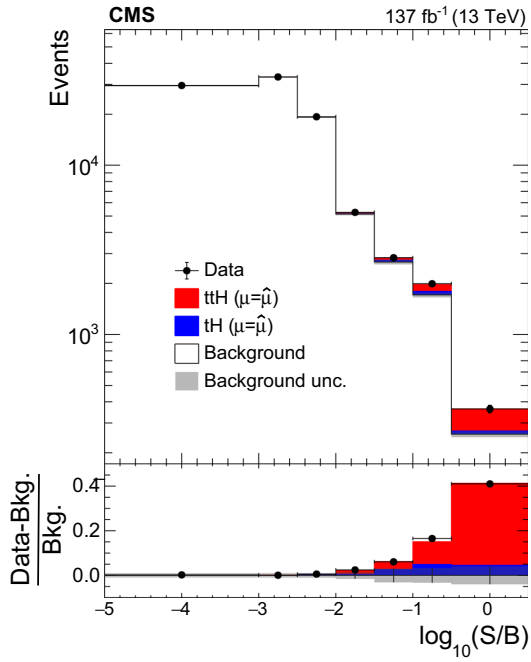
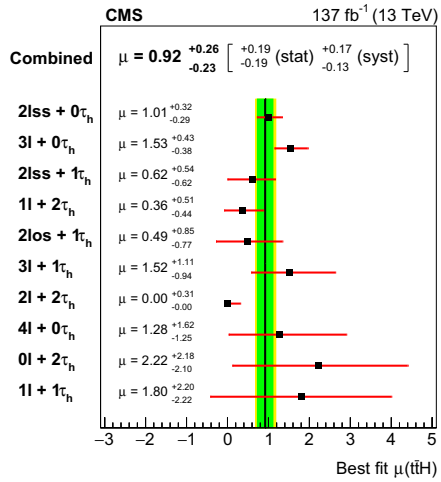


Fig. 13 Distribution of the decimal logarithm of the ratio between the expected $t\bar{t}H + tH$ signal and the expected sum of background contributions in each bin of the 105 distributions that are included in the ML fit used for the signal extraction. The distributions expected for signal and background processes are computed for $\hat{\mu}_{t\bar{t}H} = 0.92$, $\hat{\mu}_{tH} = 5.7$, and the values of nuisance parameters obtained from the ML fit

The distributions that are included in the ML fit are shown in Figs. 8, 9, 10, 11 and 12. In the $2\ell\text{SS} + 0\tau_h$ and $3\ell + 0\tau_h$ channels, we show the distributions of the activation values of ANN output nodes in the different subcategories based on lepton flavor and on the multiplicity of b-tagged jets in a single histogram, concatenating histogram bins as appropriate, and enumerate the bins by a monotonically increasing number. The distributions expected for the $t\bar{t}H$ and tH signals, as well as the expected background contributions, are shown for the value of the POI and of nuisance parameters obtained from the ML fit. The uncertainty bands shown in the figures represent the total uncertainty in the sum of signal and background contributions that remains after having determined the value of the nuisance parameters through the ML fit. These bands are computed by randomly sampling from the covariance matrix of the nuisance parameters as determined by the ML fit and adding the statistical uncertainties in the background predictions in quadrature. The data are in agreement with the sum of contributions estimated by the ML fit for the $t\bar{t}H$ and tH signals and for the background processes. The corresponding event yields are given in Table 8. In the $2\ell\text{SS} + 0\tau_h$, $3\ell + 0\tau_h$, and $2\ell\text{SS} + 1\tau_h$ channels, the sums



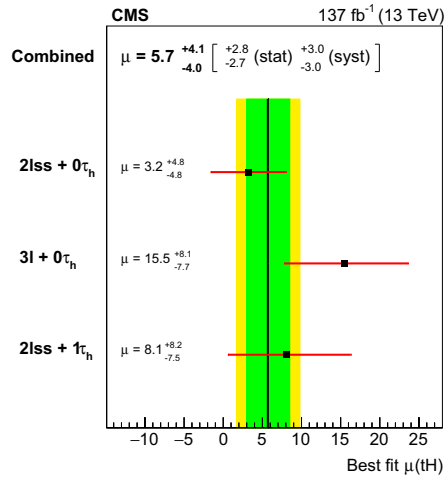


Fig. 14 Production rate $\hat{\mu}_{t\bar{t}H}$ of the $t\bar{t}H$ signal (left) and $\hat{\mu}_{tH}$ of tH signal (right), in units of their rate of production expected in the SM, measured in each of the ten channels individually and for the combination of all channels. The central value of the signal strength in the $2\ell + 2\tau_h$is constrained to be greater than zero

of events yields in all ANN output node categories are given in the table.

The event yields of background processes obtained from the ML fit agree reasonably well with their expected production rate, given the uncertainties. In particular, the production rates of the $t\bar{t}Z$ and $t\bar{t}W$ backgrounds are determined to be $\mu_{t\bar{t}Z} = 1.03 \pm 0.14$ (stat+syst) and $\mu_{t\bar{t}W} = 1.43 \pm 0.21$ (stat+syst) times their SM expectation, as obtained from the MC simulation.

The evidence for the presence of the $t\bar{t}H$ and tH signals in the data is illustrated in Fig. 13, in which each bin of the distributions that are included in the ML fit is classified according to the expected ratio of the number of $t\bar{t}H + tH$ signal (S) over background (B) events in that bin. A significant excess of events with respect to the background expectation is visible in the bins with the highest expected S/B ratio.

The $t\bar{t}H$ signal rates measured in the ten individual channels are shown in Fig. 14, obtained by performing a likelihood fit in which signal rates are parametrized with independent parameters, one for each channel. The measurement of the tH production rate is only shown in the $2\ell SS + 0\tau_h$, $3\ell + 0\tau_h$, and $2\ell SS + 1\tau_h$ channels, which employ a multiclass ANN to separate the tH from the $t\bar{t}H$ signal. The sensitivity of the other channels to the tH signal is small. The $t\bar{t}H$ and tH production rates obtained from the simultaneous fit of all channels are also shown in the figure. The signal rates measured in individual channels are compatible with each other and with the $t\bar{t}H$ and tH production rates obtained from the simultaneous fit of all channels. The largest deviation from the SM expectation is observed in the $t\bar{t}H$ production rate in the $2\ell + 2\tau_h$ channel, where the best fit value of the $t\bar{t}H$ signal rate is negative, reflecting the deficit of observed events compared to the background expectation in this channel, as shown in Fig. 11. The value and uncertainty shown in Fig. 14 are obtained after requiring the $t\bar{t}H$ production rates in this channel to be positive. The value measured in the $2\ell + 2\tau_h$ channel is compatible with the SM expectation at the level of 1.94 standard deviations when constraining the signal strength in that channel to be larger than zero. The sensitivity of individual channels can be inferred from the size of the uncertainty band in the measured signal strengths. The channel providing the highest sensitivity is the $2\ell SS + 0\tau_h$ channel, which is the channel providing the largest signal yield, followed by the $3\ell + 0\tau_h$ and $2\ell SS + 1\tau_h$ channels.

Figure 15 shows the correlations between the measured $t\bar{t}H$ and tH signal rates and those between the signal rates and the production rates of the $t\bar{t}Z$ and $t\bar{t}W$ backgrounds. All correlations are of moderate size, demonstrating the performance achieved by the multiclass ANN in distinguishing between the tH and $t\bar{t}H$ signals as well as in separating the $t\bar{t}H$ and tH signals from the $t\bar{t}Z$ and $t\bar{t}W$ backgrounds.

In the CA described in Sect. 8.1, the measured production rate for the $t\bar{t}H$ signal is $\hat{\mu}_{t\bar{t}H} = 0.5 \pm 0.3$ (stat+syst), $\hat{\mu}_{t\bar{t}H} = 1.3 \pm 0.5$ (stat+syst), $\hat{\mu}_{t\bar{t}H} = 0.9 \pm 0.4$ (stat+syst), and $\hat{\mu}_{t\bar{t}H} = 1.5 \pm 1.5$ (stat+syst) times the SM expectation, in the $2\ell SS + 0\tau_h$, $3\ell + 0\tau_h$, $2\ell SS + 1\tau_h$, and $4\ell + 0\tau_h$ channels, respectively, while $\hat{\mu}_{t\bar{t}H} = 0.91 \pm 0.21$ (stat) ± 0.18 (syst) is obtained for the simultaneous ML fit of all four channels. The 3ℓ- and 4ℓ-CRs are included in each of these ML fits. The corresponding

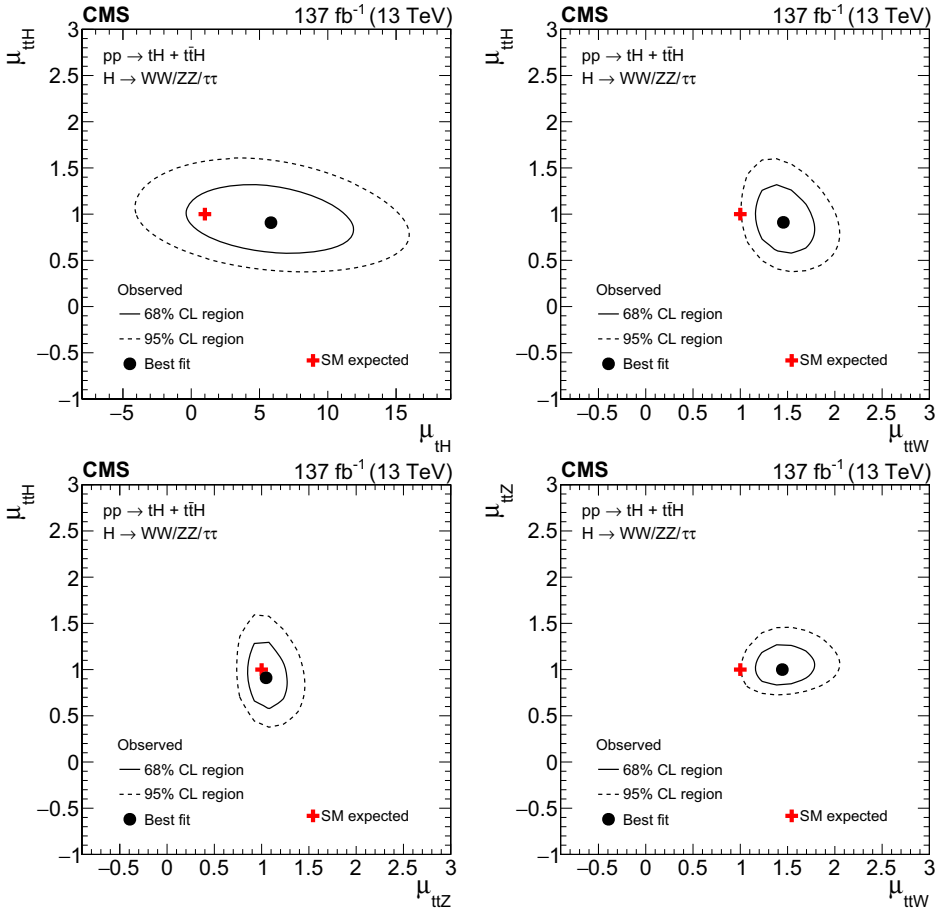


Fig. 15 Two-dimensional contours of the likelihood function $\mathcal{L}$, given by Eq. (3), as a function of the production rates of the $\mathrm{t\bar{t}H}$ and tH signals ($\mu_{\mathrm{t\bar{t}H}}$ and μ_{tH}) and of the $\mathrm{t\bar{t}Z}$ and $\mathrm{t\bar{t}W}$ backgrounds ($\mu_{\mathrm{t\bar{t}Z}}$ and $\mu_{\mathrm{t\bar{t}W}}$). The two production rates that are not shown on either the x or the y axis are profiled such that the function $\mathcal{L}$ attains its minimum at each point in the x-y plane

observed (expected) significance of the $\mathrm{t\bar{t}H}$ signal in the CA amounts to 3.8 (4.0) standard deviations.

We now drop the assumption that the distributions of kinematic observables for the tH signal conform to the distributions expected in the SM and determine the Yukawa coupling y_{t} of the Higgs boson to the top quark. We parametrize the production rates $\hat{\mu}_{\mathrm{t\bar{t}H}}$ and $\hat{\mu}_{\mathrm{tH}}$ of the $\mathrm{t\bar{t}H}$ and tH signals as a function of the ratio of the top quark Yukawa coupling y_{t} to its SM expectation m_{t}/v. We refer to this ratio as the coupling modifier and denote it by the symbol κ_{t}. The effect of the interference, described in Sect. 1, between the diagrams in Fig. 2 on the distributions of kinematic observables is parametrized as a function of κ_{t} and fully taken into account, adjusting the event yield for the tH signal as well as the distributions of the outputs of the BDTs and ANNs for each value of κ_{t}. The changes in the kinematical properties of the event affect the probability for tH signal events to pass the event selection criteria. The effect is illustrated in Fig. 16, which shows the variation of the product of acceptance and efficiency for the tHq and tHW signal contributions in each decay mode of the Higgs boson as a function of the ratio $\kappa_{\mathrm{t}}/\kappa_{\mathrm{V}}$, where κ_{V} denotes the coupling of the Higgs boson to the W boson with respect to the SM expectation for this coupling. The coupling of the Higgs boson to the Z boson with respect to its SM expectation is assumed to scale by the same value κ_{V}. Variations of the coupling modifier κ_{V} from the SM expectation $\kappa_{\mathrm{V}} = 1$ affect the interference between the diagrams in Fig. 2 as well as the branching fractions of

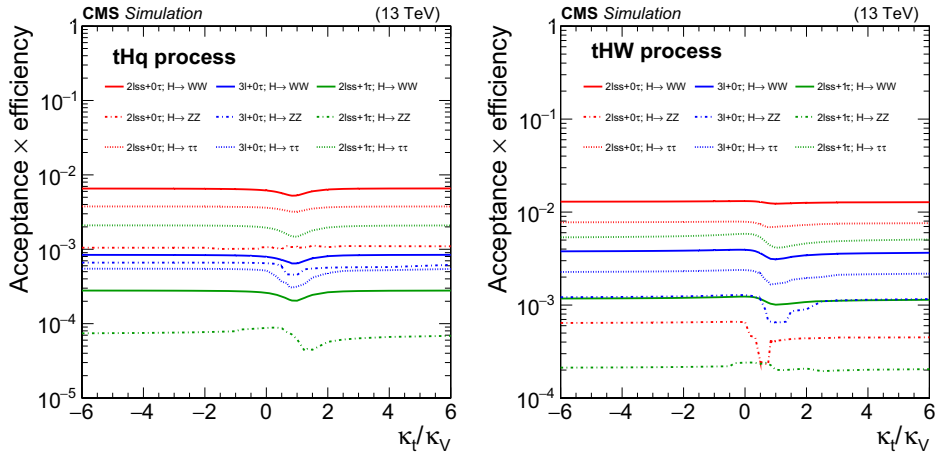


Fig. 16 Probability for tH signal events produced by the tHq (left) and tHW (right) production process to pass the event selection criteria for the $2\ell\mathrm{SS}+0\tau_\mathrm{h}$, $3\ell+0\tau_\mathrm{h}$, and $2\ell\mathrm{SS}+1\tau_\mathrm{h}$ channels in each of the Higgs boson decay modes as a function of the ratio $\kappa_\mathrm{t}/\kappa_\mathrm{V}$ of the Higgs boson couplings to the top quark and to the W boson

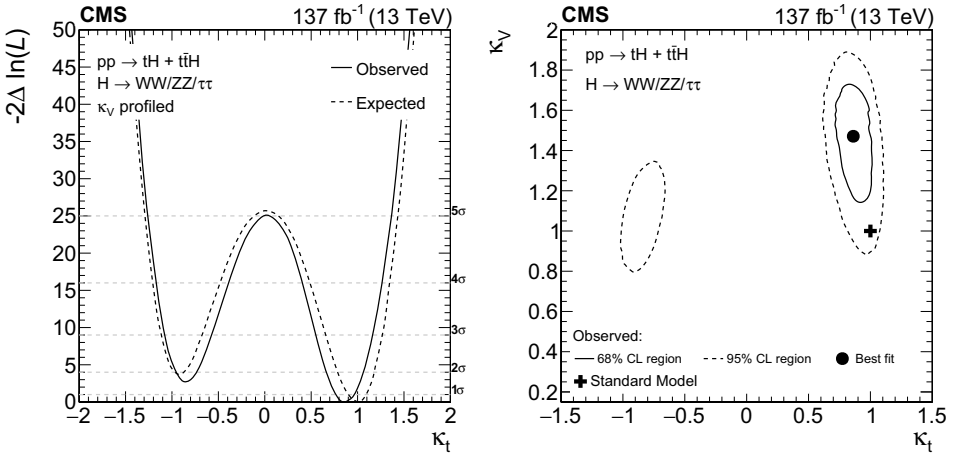


Fig. 17 Dependence of the likelihood function $\mathcal{L}$ in Eq. (3), as a function of κ_t, profiling over κ_V (left), and as a function of κ_t and κ_V (right)

the Higgs boson decay modes $\mathrm{H} \to \mathrm{WW}$ and $\mathrm{H} \to \mathrm{ZZ}$. We compute the compatibility of the data with different values of κ_t and κ_V, as is shown in Fig. 17. We obtain a 95% confidence level (CL) region on κ_t consisting of the union of the two intervals $-0.9 < \kappa_\mathrm{t} < -0.7$ and $0.7 < \kappa_\mathrm{t} < 1.1$ at 95% confidence level (CL). At 95% CL, both the inverted top coupling scenario and the SM expectation $\kappa_\mathrm{t} = 1$ are in agreement with the data.

10 Summary

The rate for Higgs boson production in association with either one or two top quarks has been measured in events containing multiple electrons, muons, and hadronically decaying tau leptons, using data recorded by the CMS experiment in pp collisions at $\sqrt{s} = 13\,\mathrm{TeV}$ in 2016, 2017, and 2018. The analyzed data corresponds to an integrated luminosity of $137\,\mathrm{fb}^{-1}$. Ten different experimental signatures are considered in the analysis, differing by the multiplicity of electrons, muons, and hadronically decaying tau leptons, and targeting events in which the Higgs boson decays

via $H \to WW$, $H \to \tau\tau$, or $H \to ZZ$, whereas the top quark(s) decay either semi-leptonically or hadronically. The measured production rates for the $t\bar{t}H$ and tH signals amount to $0.92 \pm 0.19\,(\text{stat})^{+0.17}_{-0.13}\,(\text{syst})$ and $5.7 \pm 2.7\,(\text{stat}) \pm 3.0\,(\text{syst})$ times their respective standard model (SM) expectations. The corresponding observed (expected) significance amounts to 4.7 (5.2) standard deviations for $t\bar{t}H$, and to 1.4 (0.3) for tH production. Assuming that the Higgs boson coupling to the tau lepton is equal in strength to the values expected in the SM, the coupling y_t of the Higgs boson to the top quark divided by its SM expectation, $\kappa_t = y_t/y_t^{SM}$, is constrained to be within $-0.9 < \kappa_t < -0.7$ or $0.7 < \kappa_t < 1.1$, at 95% confidence level. This result is the most sensitive measurement of the $t\bar{t}H$ production rate to date.

Acknowledgements We congratulate our colleagues in the CERN accelerator departments for the excellent performance of the LHC and thank the technical and administrative staffs at CERN and at other CMS institutes for their contributions to the success of the CMS effort. In addition, we gratefully acknowledge the computing centers and personnel of the Worldwide LHC Computing Grid for delivering so effectively the computing infrastructure essential to our analyses. Finally, we acknowledge the enduring support for the construction and operation of the LHC and the CMS detector provided by the following funding agencies: BMBWF and FWF (Austria); FNRS and FWO (Belgium); CNPq, CAPES, FAPERJ, FAPERGS, and FAPESP (Brazil); MES (Bulgaria); CERN; CAS, MoST, and NSFC (China); COLCIENCIAS (Colombia); MSES and CSF (Croatia); RIF (Cyprus); SENESCYT (Ecuador); MoER, ERC PUT and ERDF (Estonia); Academy of Finland, MEC, and HIP (Finland); CEA and CNRS/IN2P3 (France); BMBF, DFG, and HGF (Germany); GSRT (Greece); NKFIA (Hungary); DAE and DST (India); IPM (Iran); SFI (Ireland); INFN (Italy); MSIP and NRF (Republic of Korea); MES (Latvia); LAS (Lithuania); MOE and UM (Malaysia); BUAP, CINVESTAV, CONACYT, LNS, SEP, and UASLP-FAI (Mexico); MOS (Montenegro); MBIE (New Zealand); PAEC (Pakistan); MSHE and NSC (Poland); FCT (Portugal); JINR (Dubna); MON, RosAtom, RAS, RFBR, and NRC KI (Russia); MESTD (Serbia); SEIDI, CPAN, PCTI, and FEDER (Spain); MOSTR (Sri Lanka); Swiss Funding Agencies (Switzerland); MST (Taipei); ThEPCenter, IPST, STAR, and NSTDA (Thailand); TUBITAK and TAEK (Turkey); NASU (Ukraine); STFC (United Kingdom); DOE and NSF (USA).
Individuals have received support from the Marie-Curie program and the European Research Council and Horizon 2020 Grant, contract Nos. 675440, 724704, 752730, and 765710 (European Union); the Leventis Foundation; the A.P. Sloan Foundation; the Alexander von Humboldt Foundation; the Belgian Federal Science Policy Office; the Fonds pour la Formation à la Recherche dans l'Industrie et dans l'Agriculture (FRIA-Belgium); the Agentschap voor Innovatie door Wetenschap en Technologie (IWT-Belgium); the F.R.S.-FNRS and FWO (Belgium) under the "Excellence of Science – EOS" – be.h project n. 30820817; the Beijing Municipal Science and Technology Commission, No. Z191100007219010; the Ministry of Education, Youth and Sports (MEYS) of the Czech Republic; the Deutsche Forschungsgemeinschaft (DFG) under Germany's Excellence Strategy – EXC 2121 "Quantum Universe" – 390833306; the Lendület ("Momentum") Program and the János Bolyai Research Scholarship of the Hungarian Academy of Sciences, the New National Excellence Program ÚNKP, the NKFIA research grants 123842, 123959, 124845, 124850, 125105, 128713, 128786, and 129058 (Hungary); the Council of Science and Industrial Research, India; the HOMING PLUS program of the Foundation for Polish Science, cofinanced from European Union, Regional Development Fund, the Mobility Plus program of the Ministry of Science and Higher Education, the National Science Center (Poland), contracts Harmonia 2014/14/M/ST2/00428, Opus 2014/13/B/ST2/02543, 2014/15/B/ST2/03998, and 2015/19/B/ST2/02861, Sonata-bis 2012/07/E/ST2/01406; the National Priorities Research Program by Qatar National Research Fund; the Ministry of Science and Higher Education, project no. 02.a03.21.0005 (Russia); the Tomsk Polytechnic University Competitiveness Enhancement Program; the Programa Estatal de Fomento de la Investigación Científica y Técnica de Excelencia María de Maeztu, grant MDM-2015-0509 and the Programa Severo Ochoa del Principado de Asturias; the Thalis and Aristeia programs cofinanced by EU-ESF and the Greek NSRF; the Rachadapisek Sompot Fund for Postdoctoral Fellowship, Chulalongkorn University and the Chulalongkorn Academic into Its 2nd Century Project Advancement Project (Thailand); the Kavli Foundation; the Nvidia Corporation; the SuperMicro Corporation; the Welch Foundation, contract C-1845; and the Weston Havens Foundation (USA).

Data Availability Statement This manuscript has no associated data or the data will not be deposited. [Authors' comment: Release and preservation of data used by the CMS Collaboration as the basis for publications is guided by the CMS policy as written in its document "CMS data preservation, re-use and open access policy" (https://cms-docdb.cern.ch/cgi-bin/PublicDocDB/RetrieveFile?docid=6032&filename=CMSDataPolicyV1.2.pdf&version=2).]

Declarations

Conflict of interest The authors declare that they have no conflict of interest.

Open Access This article is licensed under a Creative Commons Attribution 4.0 International License, which permits use, sharing, adaptation, distribution and reproduction in any medium or format, as long as you give appropriate credit to the original author(s) and the source, provide a link to the Creative Commons licence, and indicate if changes were made. The images or other third party material in this article are included in the article's Creative Commons licence, unless indicated otherwise in a credit line to the material. If material is not included in the article's Creative Commons licence and your intended use is not permitted by statutory regulation or exceeds the permitted use, you will need to obtain permission directly from the copyright holder. To view a copy of this licence, visit http://creativecommons.org/licenses/by/4.0/.
Funded by SCOAP[3].

References

1. ATLAS Collaboration, Observation of a new particle in the search for the standard model Higgs boson with the ATLAS detector at the LHC. Phys. Lett. B **716**, 1 (2012). https://doi.org/10.1016/j.physletb.2012.08.020. arXiv:1207.7214
2. CMS Collaboration, Observation of a new boson at a mass of 125 GeV with the CMS experiment at the LHC. Phys. Lett. B **716**, 30 (2012). https://doi.org/10.1016/j.physletb.2012.08.021. arXiv:1207.7235
3. CMS Collaboration, Observation of a new boson with mass near 125 GeV in pp collisions at $\sqrt{s} = 7$ and 8 TeV. JHEP **06**, 081 (2013). https://doi.org/10.1007/JHEP06(2013)081. arXiv:1303.4571
4. F. Englert, R. Brout, Broken symmetry and the mass of gauge vector mesons. Phys. Rev. Lett. **13**, 321 (1964). https://doi.org/10.1103/PhysRevLett.13.321

5. P.W. Higgs, Broken symmetries, massless particles and gauge fields. Phys. Lett. **12**, 132 (1964). https://doi.org/10.1016/0031-9163(64)91136-9
6. P.W. Higgs, Broken symmetries and the masses of gauge bosons. Phys. Rev. Lett. **13**, 508 (1964). https://doi.org/10.1103/PhysRevLett.13.508
7. G.S. Guralnik, C.R. Hagen, T.W.B. Kibble, Global conservation laws and massless particles. Phys. Rev. Lett. **13**, 585 (1964). https://doi.org/10.1103/PhysRevLett.13.585
8. Particle Data Group, P.A. Zyla et al., Review of particle physics. Prog. Theor. Exp. Phys. **2020**, 083C01 (2020). https://doi.org/10.1093/ptep/ptaa104
9. B.A. Dobrescu, C.T. Hill, Electroweak symmetry breaking via top condensation seesaw. Phys. Rev. Lett. **81**, 2634 (1998). https://doi.org/10.1103/PhysRevLett.81.2634. arXiv:hep-ph/9712319
10. R.S. Chivukula, B.A. Dobrescu, H. Georgi, C.T. Hill, Top quark seesaw theory of electroweak symmetry breaking. Phys. Rev. D **59**, 075003 (1999). https://doi.org/10.1103/PhysRevD.59.075003. arXiv:hep-ph/9809470
11. D. Delepine, J.M. Gerard, R Gonzalez Felipe, Is the standard Higgs scalar elementary? Phys. Lett. B **372**, 271 (1996). https://doi.org/10.1016/0370-2693(96)00048-2. arXiv:hep-ph/9512339
12. ATLAS and C. Collaborations, Measurements of the Higgs boson production and decay rates and constraints on its couplings from a combined ATLAS and CMS analysis of the LHC pp collision data at $\sqrt{s} = 7$ and 8 TeV. JHEP **08**, 045 (2016). https://doi.org/10.1007/JHEP08(2016)045. arXiv:1606.02266
13. S. Biswas, E. Gabrielli, F. Margaroli, B. Mele, Direct constraints on the top-Higgs coupling from the 8 TeV LHC data. JHEP **07**, 073 (2013). https://doi.org/10.1007/JHEP07(2013)073. arXiv:1304.1822
14. B. Hespel, F. Maltoni, E. Vryonidou, Higgs and Z boson associated production via gluon fusion in the SM and the 2HDM. JHEP **06**, 065 (2015). https://doi.org/10.1007/JHEP06(2015)065. arXiv:1503.01656
15. CMS Collaboration, Search for the associated production of the Higgs boson with a top quark pair. JHEP **09**, 087 (2014). https://doi.org/10.1007/JHEP09(2014)087. arXiv:1408.1682 [Erratum: https://doi.org/10.1007/JHEP10(2014)106]
16. ATLAS Collaboration, Search for $H \to \gamma\gamma$ produced in association with top quarks and constraints on the Yukawa coupling between the top quark and the Higgs boson using data taken at 7 TeV and 8 TeV with the ATLAS detector. Phys. Lett. B **740**, 222 (2015). https://doi.org/10.1016/j.physletb.2014.11.049. arXiv:1409.3122
17. ATLAS Collaboration, Search for the standard model Higgs boson produced in association with top quarks and decaying into $b\bar{b}$ in pp collisions at $\sqrt{s} = 8$ TeV with the ATLAS detector. Eur. Phys. J. C **75**, 349 (2015). https://doi.org/10.1140/epjc/s10052-015-3543-1. arXiv:1503.05066
18. ATLAS Collaboration, Search for the associated production of the Higgs boson with a top quark pair in multilepton final states with the ATLAS detector. Phys. Lett. B **749**, 519 (2015). https://doi.org/10.1016/j.physletb.2015.07.079. arXiv:1506.05988
19. ATLAS Collaboration, Search for the standard model Higgs boson decaying into $b\bar{b}$ produced in association with top quarks decaying hadronically in pp collisions at $\sqrt{s} = 8$ TeV with the ATLAS detector. JHEP **05** 160 (2016). https://doi.org/10.1007/JHEP05(2016)160. arXiv:1604.03812
20. CMS Collaboration, Measurements of properties of the Higgs boson decaying into the four-lepton final state in pp collisions at $\sqrt{s} = 13$ TeV. JHEP **11**, 047 (2017). https://doi.org/10.1007/JHEP11(2017)047. arXiv:1706.09936
21. ATLAS Collaboration, Evidence for the associated production of the Higgs boson and a top quark pair with the ATLAS detector. Phys. Rev. D **97**, (2018). https://doi.org/10.1103/PhysRevD.97.072003. arXiv:1712.08891
22. ATLAS Collaboration, Search for the standard model Higgs boson produced in association with top quarks and decaying into a $b\bar{b}$ pair in pp collisions at $\sqrt{s} = 13$ TeV with the ATLAS detector. Phys. Rev. D **97**, (2018). https://doi.org/10.1103/PhysRevD.97.072016. arXiv:1712.08895
23. CMS Collaboration, Evidence for associated production of a Higgs boson with a top quark pair in final states with electrons, muons, and hadronically decaying τ leptons at $\sqrt{s} = 13$ TeV. JHEP **08**, 066 (2018). https://doi.org/10.1007/JHEP08(2018)066. arXiv:1803.05485
24. CMS Collaboration, Search for $t\bar{t}H$ production in the all-jet final state in proton-proton collisions at $\sqrt{s} = 13$ TeV. JHEP **06**, 101 (2018). https://doi.org/10.1007/JHEP06(2018)101. arXiv:1803.06986
25. CMS Collaboration, Measurements of Higgs boson properties in the diphoton decay channel in proton-proton collisions at $\sqrt{s} = 13$ TeV. JHEP **11**, 185 (2018). https://doi.org/10.1007/JHEP11(2018)185. arXiv:1804.02716
26. CMS Collaboration, Search for $t\bar{t}H$ production in the $H \to b\bar{b}$ decay channel with leptonic $t\bar{t}$ decays in proton-proton collisions at $\sqrt{s} = 13$ TeV. JHEP **03**, 026 (2019). https://doi.org/10.1007/JHEP03(2019)026. arXiv:1804.03682
27. CMS Collaboration, Observation of $t\bar{t}H$ production. Phys. Rev. Lett. **120**, 231801 (2018). https://doi.org/10.1103/PhysRevLett.120.231801. arXiv:1804.02610
28. ATLAS Collaboration, Observation of Higgs boson production in association with a top quark pair at the LHC with the ATLAS detector. Phys. Lett. B **784**, 173 (2018). https://doi.org/10.1016/j.physletb.2018.07.035. arXiv:1806.00425
29. CMS Collaboration, Search for the associated production of a Higgs boson with a single top quark in proton-proton collisions at $\sqrt{s} = 8$ TeV. JHEP **06**, 177 (2016). https://doi.org/10.1007/JHEP06(2016)177. arXiv:1509.08159
30. CMS Collaboration, Search for associated production of a Higgs boson and a single top quark in proton-proton collisions at $\sqrt{s} = 13$ TeV. Phys. Rev. D **99**, 092005 (2019). https://doi.org/10.1103/PhysRevD.99.092005. arXiv:1811.09696
31. ATLAS Collaboration, *CP* properties of Higgs boson interactions with top quarks in the $t\bar{t}H$ and tH processes using $H \to \gamma\gamma$ with the ATLAS detector. Phys. Rev. Lett. **125** 061802 (2020). https://doi.org/10.1103/PhysRevLett.125.061802. arXiv:2004.04545
32. H. Voss, A. Höcker, J. Stelzer, F. Tegenfeldt, TMVA, the toolkit for multivariate data analysis with ROOT. in *XIth International Workshop on Advanced Computing and Analysis Techniques in Physics Research (ACAT)*, p. 40. (2007). arXiv:physics/0703039 [PoS(ACAT)040]. https://doi.org/10.22323/1.050.0040
33. T. Chen, C. Guestrin, XGBoost: a scalable tree boosting system. in *Proceedings of the 22nd ACM SIGKDD International Conference on Knowledge Discovery and Data Mining* (2016). https://doi.org/10.1145/2939672.2939785
34. F. Pedregosa et al., Scikit-learn: machine learning in python. JMLR **12**, 2825 (2011). https://doi.org/10.5555/1953048.2078195
35. K. Kondo, Dynamical likelihood method for reconstruction of events with missing momentum. 1: method and toy models. J. Phys. Soc. Jpn. **57**, 4126 (1988). https://doi.org/10.1143/JPSJ.57.4126
36. K. Kondo, Dynamical likelihood method for reconstruction of events with missing momentum. 2: mass spectra for $2 \to 2$ processes. J. Phys. Soc. Jpn. **60**, 836 (1991). https://doi.org/10.1143/JPSJ.60.836
37. CMS Collaboration, The CMS trigger system. JINST **12**, P01020 (2017). https://doi.org/10.1088/1748-0221/12/01/P01020. arXiv:1609.02366

38. CMS Collaboration, The CMS experiment at the CERN LHC. JINST **3**, S08004 (2008). https://doi.org/10.1088/1748-0221/3/08/S08004
39. CMS Collaboration, CMS luminosity measurements for the 2016 data-taking period. CMS Physics Analysis Summary CMS-PAS-LUM-17-001 (2017)
40. CMS Collaboration, CMS luminosity measurement for the 2017 data-taking period at $\sqrt{s} = 13$ TeV. CMS Physics Analysis Summary CMS-PAS-LUM-17-004 (2017)
41. CMS Collaboration, CMS luminosity measurement for the 2018 data-taking period at $\sqrt{s} = 13$ TeV. CMS Physics Analysis Summary CMS-PAS-LUM-18-002 (2018)
42. J. Alwall et al., Comparative study of various algorithms for the merging of parton showers and matrix elements in hadronic collisions. Eur. Phys. J. C **53**, 473 (2008). https://doi.org/10.1140/epjc/s10052-007-0490-5. arXiv:0706.2569
43. P. Artoisenet, R. Frederix, O. Mattelaer, R. Rietkerk, Automatic spin-entangled decays of heavy resonances in Monte Carlo simulations. JHEP **03**, 015 (2013). https://doi.org/10.1007/JHEP03(2013)015. arXiv:1212.3460
44. R. Frederix, S. Frixione, Merging meets matching in MC@NLO. JHEP **12**, 061 (2012). https://doi.org/10.1007/JHEP12(2012)061. arXiv:1209.6215
45. J. Alwall et al., The automated computation of tree-level and next-to-leading order differential cross sections, and their matching to parton shower simulations. JHEP **07**, 079 (2014). https://doi.org/10.1007/JHEP07(2014)079. arXiv:1405.0301
46. R. Frederix, I. Tsinikos, Subleading EW corrections and spin-correlation effects in $t\bar{t}W$ multi-lepton signatures. Eur. Phys. J. C **80**, 803 (2020). https://doi.org/10.1140/epjc/s10052-020-8388-6. arXiv:2004.09552
47. J.A. Dror, M. Farina, E. Salvioni, J. Serra, Strong tW scattering at the LHC. JHEP **01**, 071 (2016). https://doi.org/10.1007/JHEP01(2016)071. arXiv:1511.03674
48. P. Nason, A new method for combining NLO QCD with shower Monte Carlo algorithms. JHEP **11**, 040 (2004). https://doi.org/10.1088/1126-6708/2004/11/040. arXiv:hep-ph/0409146
49. S. Frixione, P. Nason, C. Oleari, Matching NLO QCD computations with parton shower simulations: the powheg method. JHEP **11**, 070 (2007). https://doi.org/10.1088/1126-6708/2007/11/070. arXiv:0709.2092
50. S. Alioli, P. Nason, C. Oleari, E. Re, A general framework for implementing NLO calculations in shower Monte Carlo programs: the powheg box. JHEP **06**, 043 (2010). https://doi.org/10.1007/JHEP06(2010)043. arXiv:1002.2581
51. M. Czakon et al., Top-pair production at the LHC through NNLO QCD and NLO EW. JHEP **10**, 186 (2017). https://doi.org/10.1007/JHEP10(2017)186. arXiv:1705.04105
52. T. Sjöstrand et al., An introduction to pythia 8.2. Comput. Phys. Commun. **191**, 159 (2015). https://doi.org/10.1016/j.cpc.2015.01.024. arXiv:1410.3012
53. NNPDF Collaboration, Unbiased global determination of parton distributions and their uncertainties at NNLO and at LO. Nucl. Phys. B **855**, 153 (2012). https://doi.org/10.1016/j.nuclphysb.2011.09.024. arXiv:1107.2652
54. NNPDF Collaboration, Parton distributions with QED corrections. Nucl. Phys. B **877**, 290 (2013). https://doi.org/10.1016/j.nuclphysb.2013.10.010. arXiv:1308.0598
55. NNPDF Collaboration, Parton distributions for the LHC Run 2. JHEP **04**, 040 (2015). https://doi.org/10.1007/JHEP04(2015)040. arXiv:1410.8849
56. NNPDF Collaboration, Parton distributions from high-precision collider data. Eur. Phys. J. C **77**, 663 (2017). https://doi.org/10.1140/epjc/s10052-017-5199-5. arXiv:1706.00428
57. F. Maltoni, G. Ridolfi, M. Ubiali, b-initiated processes at the LHC: a reappraisal. JHEP **07**, 022 (2012). https://doi.org/10.1007/JHEP07(2012)022. arXiv:1203.6393 [Erratum: https://doi.org/10.1007/JHEP04(2013)095]
58. F. Demartin, F. Maltoni, K. Mawatari, M. Zaro, Higgs production in association with a single top quark at the LHC. Eur. Phys. J. C **75**, 267 (2015). https://doi.org/10.1140/epjc/s10052-015-3475-9. arXiv:1504.00611
59. CMS Collaboration, Extraction and validation of a new set of CMS pythia 8 tunes from underlying-event measurements. Eur. Phys. J. C **80**, 4 (2020). https://doi.org/10.1140/epjc/s10052-019-7499-4. arXiv:1903.12179
60. CMS Collaboration, Investigations of the impact of the parton shower tuning in PYTHIA 8 in the modelling of $t\bar{t}$ at $\sqrt{s} = 8$ and 13 TeV. Technical Report CMS-PAS-TOP-16-021, CERN (2016)
61. CMS Collaboration, Event generator tunes obtained from underlying event and multiparton scattering measurements. Eur. Phys. J. C **76**, 155 (2016). https://doi.org/10.1140/epjc/s10052-016-3988-x. arXiv:1512.00815
62. LHC Higgs Cross Section Working Group, Handbook of LHC Higgs cross sections: 4. deciphering the nature of the Higgs sector. CERN (2016) https://doi.org/10.23731/CYRM-2017-002. arXiv:1610.07922
63. F. Demartin et al., tWH associated production at the LHC. Eur. Phys. J. C **77**, 34 (2017). https://doi.org/10.1140/epjc/s10052-017-4601-7. arXiv:1607.05862
64. J.M. Campbell, R.K. Ellis, C. Williams, Vector boson pair production at the LHC. JHEP **07**, 018 (2011). https://doi.org/10.1007/JHEP07(2011)018. arXiv:1105.0020
65. M. Czakon, A. Mitov, Top++: a program for the calculation of the top-pair cross section at hadron colliders. Comput. Phys. Commun. **185**, 2930 (2014). https://doi.org/10.1016/j.cpc.2014.06.021. arXiv:1112.5675
66. Y. Li, F. Petriello, Combining QCD and electroweak corrections to dilepton production in fewz. Phys. Rev. D **86**, 094034 (2012). https://doi.org/10.1103/PhysRevD.86.094034. arXiv:1208.5967
67. J.S. Gainer et al., Exploring theory space with Monte Carlo reweighting. JHEP **10**, 078 (2014). https://doi.org/10.1007/JHEP10(2014)078. arXiv:1404.7129
68. O. Mattelaer, On the maximal use of Monte Carlo samples: re-weighting events at NLO accuracy. Eur. Phys. J. C **76**, 674 (2016). https://doi.org/10.1140/epjc/s10052-016-4533-7. arXiv:1607.00763
69. GEANT4 Collaboration, Geant4—a simulation toolkit. Nucl. Instrum. Methods A **506**, 250 (2003). https://doi.org/10.1016/S0168-9002(03)01368-8
70. J. Allison et al., Recent developments in Geant4. Nucl. Instrum. Methods A **835**, 186 (2016). https://doi.org/10.1016/j.nima.2016.06.125
71. CMS Collaboration, Measurements of inclusive W and Z cross sections in pp collisions at $\sqrt{s} = 7$ TeV. JHEP **01**, 080 (2011). https://doi.org/10.1007/JHEP01(2011)080. arXiv:1012.2466
72. CMS Collaboration, Jet energy scale and resolution in the CMS experiment in pp collisions at 8 TeV. JINST **12**, P02014 (2017). https://doi.org/10.1088/1748-0221/12/02/P02014. arXiv:1607.03663
73. CMS Collaboration, Identification of heavy-flavour jets with the CMS detector in pp collisions at 13 TeV. JINST **13**, P05011 (2018). https://doi.org/10.1088/1748-0221/13/05/P05011. arXiv:1712.07158
74. CMS Collaboration, Performance of reconstruction and identification of τ leptons decaying to hadrons and ν_τ in pp collisions at $\sqrt{s} = 13$ TeV. JINST **13**, P10005 (2018). https://doi.org/10.1088/1748-0221/13/10/P10005. arXiv:1809.02816
75. CMS Collaboration, Performance of missing transverse momentum reconstruction in proton-proton collisions at $\sqrt{s} = 13$ TeV using the CMS detector. JINST **14**, P07004 (2019). https://doi.org/10.1088/1748-0221/14/07/P07004. arXiv:1903.06078

76. CMS Collaboration, Particle-flow reconstruction and global event description with the CMS detector. JINST **12**, P10003 (2017). https://doi.org/10.1088/1748-0221/12/10/P10003. arXiv:1706.04965
77. CMS Collaboration, Performance of electron reconstruction and selection with the CMS detector in proton-proton collisions at $\sqrt{s} = 8$ TeV. JINST **10**, P06005 (2015). https://doi.org/10.1088/1748-0221/10/06/P06005. arXiv:1502.02701
78. CMS Collaboration, Performance of the CMS muon detector and muon reconstruction with proton-proton collisions at $\sqrt{s} =$ 13 TeV. JINST **13**(06), P06015 (2018). https://doi.org/10.1088/1748-0221/13/06/P06015. arXiv:1804.04528
79. K. Rehermann, B. Tweedie, Efficient identification of boosted semileptonic top quarks at the LHC. JHEP **03**, 059 (2011). https://doi.org/10.1007/JHEP03(2011)059. arXiv:1007.2221
80. CMS Collaboration, Search for new physics in same-sign dilepton events in proton-proton collisions at $\sqrt{s} = 13$ TeV. Eur. Phys. J. C **76**, 439 (2016). https://doi.org/10.1140/epjc/s10052-016-4261-z. arXiv:1605.03171
81. M. Cacciari, G.P. Salam, G. Soyez, The anti-k_T jet clustering algorithm. JHEP **04**, 063 (2008). https://doi.org/10.1088/1126-6708/2008/04/063. arXiv:0802.1189
82. M. Cacciari, G.P. Salam, G. Soyez, FastJet user manual. Eur. Phys. J. C **72**, 1896 (2012). https://doi.org/10.1140/epjc/s10052-012-1896-2. arXiv:1111.6097
83. CMS Collaboration, Performance of the DeepTau algorithm for the discrimination of taus against jets, electrons, and muons. CMS Detector Performance Summary CMS-DP-2019-033 (2019)
84. Y. Lecun, Generalization and network design strategies. Technical Report of the University of Toronto, CRG-TR-89-4
85. M. Cacciari, G.P. Salam, G. Soyez, The catchment area of jets. JHEP **04**, 005 (2008). https://doi.org/10.1088/1126-6708/2008/04/005. arXiv:0802.1188
86. M. Cacciari, G.P. Salam, Pileup subtraction using jet areas. Phys. Lett. B **659**, 119 (2008). https://doi.org/10.1016/j.physletb.2007.09.077. arXiv:0707.1378
87. CMS Collaboration, Jet algorithms performance in 13 TeV data. CMS Physics Analysis Summary CMS-PAS-JME-16-003 (2016)
88. CMS Collaboration, CMS Phase 1 heavy flavour identification performance and developments. CMS Detector Performance Summary CMS-DP-2017-013 (2017)
89. L. Bianchini et al., Reconstruction of the Higgs mass in events with Higgs bosons decaying into a pair of τ leptons using matrix element techniques. Nucl. Instrum. Methods A **862**, 54 (2017). https://doi.org/10.1016/j.nima.2017.05.001. arXiv:1603.05910
90. J.S. Bridle, Training stochastic model recognition algorithms as networks can lead to maximum mutual information estimation of parameters. in *Proceedings, conference on advances in neural information processing systems 2 (NIPS 1989)*, p. 211 (1990)
91. X. Glorot, A. Bordes, Y. Bengio, Deep sparse rectifier neural networks. in *Proceedings, 14th international conference on artificial intelligence and statistics (AISTATS 2011)*, vol. 15, p. 315. (2011)
92. M. Abadi et al., TensorFlow: large-scale machine learning on heterogeneous distributed systems (2016). arXiv:1603.04467
93. F. Chollet et al., Keras. GitHub (2015). https://github.com/fchollet/keras
94. I. Goodfellow, Y. Bengio, A. Courville, *Deep learning* (MIT Press, 2016). http://www.deeplearningbook.org
95. A.N. Tikhonov, Solution of incorrectly formulated problems and the regularization method. Sov. Math. Dokl. **4**, 1035 (1963)
96. N. Srivastava et al., Dropout: a simple way to prevent neural networks from overfitting. JMLR **15**, 1929 (2014)
97. CMS Collaboration, Search for electroweak production of charginos and neutralinos in multilepton final states in proton-proton collisions at $\sqrt{s} = 13$ TeV. JHEP **03**, 166 (2018). https://doi.org/10.1007/JHEP03(2018)166. arXiv:1709.05406
98. CMS Collaboration, Measurement of the inelastic proton-proton cross section at $\sqrt{s} = 13$ TeV. JHEP **07**, 161 (2018). https://doi.org/10.1007/JHEP07(2018)161. arXiv:1802.02613
99. M. Cacciari et al., The $t\bar{t}$ cross-section at 1.8 TeV and 1.96 TeV: a study of the systematics due to parton densities and scale dependence. JHEP **04**, 068 (2004). https://doi.org/10.1088/1126-6708/2004/04/068. arXiv:hep-ph/0303085
100. S. Catani, D. de Florian, M. Grazzini, P. Nason, Soft gluon resummation for Higgs boson production at hadron colliders. JHEP **07**, 028 (2003). https://doi.org/10.1088/1126-6708/2003/07/028. arXiv:hep-ph/0306211
101. R. Frederix et al., Four-lepton production at hadron colliders: MadGraph5_a mc@nlo predictions with theoretical uncertainties. JHEP **02**, 099 (2012). https://doi.org/10.1007/JHEP02(2012)099. arXiv:1110.4738
102. J. Butterworth et al., PDF4LHC recommendations for LHC Run 2. J. Phys. G **43**, 023001 (2016). https://doi.org/10.1088/0954-3899/43/2/023001. arXiv:1510.03865
103. R. Gavin, Y. Li, F. Petriello, S. Quackenbush, FEWZ 2.0: a code for hadronic Z production at next-to-next-to-leading order. Comput. Phys. Commun. **182**, 2388 (2011). https://doi.org/10.1016/j.cpc.2011.06.008. arXiv:1011.3540
104. J. Neyman, Outline of a theory of statistical estimation based on the classical theory of probability. Philos. Trans. R. Soc. Lond. A **236**, 333 (1937). https://doi.org/10.1098/rsta.1937.0005
105. J.S. Conway, Incorporating nuisance parameters in likelihoods for multisource spectra. in *Proceedings, workshop on statistical issues related to discovery claims in search experiments and unfolding (PHYSTAT 2011)*, p. 115. (2011). arXiv:1103.0354. https://doi.org/10.5170/CERN-2011-006.115
106. R.J. Barlow, C. Beeston, Fitting using finite Monte Carlo samples. Comput. Phys. Commun. **77**, 219 (1993). https://doi.org/10.1016/0010-4655(93)90005-W
107. The ATLAS Collaboration, The CMS Collaboration, The LHC Higgs Combination Group, Procedure for the LHC Higgs boson search combination in Summer 2011. Technical Report CMS-NOTE-2011-005, ATL-PHYS-PUB-2011-11 (2011)
108. CMS Collaboration, Combined results of searches for the standard model Higgs boson in pp collisions at $\sqrt{s} = 7$ TeV. Phys. Lett. B **710**, 26 (2012). https://doi.org/10.1016/j.physletb.2012.02.064. arXiv:1202.1488

CMS Collaboration

Yerevan Physics Institute, Yerevan, Armenia
A. M. Sirunyan[†], A. Tumasyan

Institut für Hochenergiephysik, Vienna, Austria
W. Adam, T. Bergauer, M. Dragicevic, J. Erö, A. Escalante Del Valle, R. Frühwirth[1], M. Jeitler[1], N. Krammer, L. Lechner, D. Liko, I. Mikulec, F. M. Pitters, N. Rad, J. Schieck[1], R. Schöfbeck, M. Spanring, S. Templ, W. Waltenberger, C. -E. Wulz[1], M. Zarucki

Institute for Nuclear Problems, Minsk, Belarus
V. Chekhovsky, A. Litomin, V. Makarenko, J. Suarez Gonzalez

Universiteit Antwerpen, Antwerp, Belgium
M. R. Darwish[2], E. A. De Wolf, D. Di Croce, X. Janssen, T. Kello[3], A. Lelek, M. Pieters, H. Rejeb Sfar, H. Van Haevermaet, P. Van Mechelen, S. Van Putte, N. Van Remortel

Vrije Universiteit Brussel, Brussels, Belgium
F. Blekman, E. S. Bols, S. S. Chhibra, J. D'Hondt, J. De Clercq, D. Lontkovskyi, S. Lowette, I. Marchesini, S. Moortgat, A. Morton, D. Müller, Q. Python, S. Tavernier, W. Van Doninck, P. Van Mulders

Université Libre de Bruxelles, Brussels, Belgium
D. Beghin, B. Bilin, B. Clerbaux, G. De Lentdecker, B. Dorney, L. Favart, A. Grebenyuk, A. K. Kalsi, I. Makarenko, L. Moureaux, L. Pétré, A. Popov, N. Postiau, E. Starling, L. Thomas, C. Vander Velde, P. Vanlaer, D. Vannerom, L. Wezenbeek

Ghent University, Ghent, Belgium
T. Cornelis, D. Dobur, M. Gruchala, I. Khvastunov[4], M. Niedziela, C. Roskas, K. Skovpen, M. Tytgat, W. Verbeke, B. Vermassen, M. Vit

Université Catholique de Louvain, Louvain-la-Neuve, Belgium
G. Bruno, F. Bury, C. Caputo, P. David, C. Delaere, M. Delcourt, I. S. Donertas, H. El Faham, A. Giammanco, V. Lemaitre, K. Mondal, J. Prisciandaro, A. Taliercio, M. Teklishyn, P. Vischia, S. Wertz, S. Wuyckens

Centro Brasileiro de Pesquisas Fisicas, Rio de Janeiro, Brazil
G. A. Alves, C. Hensel, A. Moraes

Universidade do Estado do Rio de Janeiro, Rio de Janeiro, Brazil
W. L. Aldá Júnior, E. Belchior Batista Das Chagas, H. Brandao Malbouisson, W. Carvalho, J. Chinellato[5], E. Coelho, E. M. Da Costa, G. G. Da Silveira[6], D. De Jesus Damiao, S. Fonseca De Souza, J. Martins[7], D. Matos Figueiredo, M. Medina Jaime[8], C. Mora Herrera, L. Mundim, H. Nogima, P. Rebello Teles, L. J. Sanchez Rosas, A. Santoro, S. M. Silva Do Amaral, A. Sznajder, M. Thiel, F. Torres Da Silva De Araujo, A. Vilela Pereira

Universidade Estadual Paulista[a], Universidade Federal do ABC[b], São Paulo, Brazil
C. A. Bernardes[a,a], L. Calligaris[a], T. R. Fernandez Perez Tomei[a], E. M. Gregores[a,b], D. S. Lemos[a], P. G. Mercadante[a,b], S. F. Novaes[a], Sandra S. Padula[a]

Institute for Nuclear Research and Nuclear Energy, Bulgarian Academy of Sciences, Sofia, Bulgaria
A. Aleksandrov, G. Antchev, I. Atanasov, R. Hadjiiska, P. Iaydjiev, M. Misheva, M. Rodozov, M. Shopova, G. Sultanov

University of Sofia, Sofia, Bulgaria
A. Dimitrov, T. Ivanov, L. Litov, B. Pavlov, P. Petkov, A. Petrov

Beihang University, Beijing, China
T. Cheng, W. Fang[3], Q. Guo, H. Wang, L. Yuan

Department of Physics, Tsinghua University, Beijing, China
M. Ahmad, G. Bauer, Z. Hu, Y. Wang, K. Yi[9,10]

Institute of High Energy Physics, Beijing, China
E. Chapon, G. M. Chen[11], H. S. Chen[11], M. Chen, T. Javaid[11], A. Kapoor, D. Leggat, B. Li[11], H. Liao, Z. -A. LIU[11], R. Sharma, A. Spiezia, J. Tao, J. Thomas-wilsker, J. Wang, H. Zhang, S. Zhang[11], J. Zhao

State Key Laboratory of Nuclear Physics and Technology, Peking University, Beijing, China
A. Agapitos, Y. Ban, C. Chen, Q. Huang, A. Levin, Q. Li, M. Lu, X. Lyu, Y. Mao, S. J. Qian, D. Wang, Q. Wang, J. Xiao

Sun Yat-Sen University, Guangzhou, China
Z. You

Institute of Modern Physics and Key Laboratory of Nuclear Physics and Ion-beam Application (MOE), Fudan University, Shanghai, China
X. Gao[3]

Zhejiang University, Hangzhou, China
M. Xiao

Universidad de Los Andes, Bogota, Colombia
C. Avila, A. Cabrera, C. Florez, J. Fraga, A. Sarkar, M. A. Segura Delgado

Universidad de Antioquia, Medellin, Colombia
J. Jaramillo, J. Mejia Guisao, F. Ramirez, J. D. Ruiz Alvarez, C. A. Salazar González, N. Vanegas Arbelaez

University of Split, Faculty of Electrical Engineering, Mechanical Engineering and Naval Architecture, Split, Croatia
D. Giljanovic, N. Godinovic, D. Lelas, I. Puljak

University of Split, Faculty of Science, Split, Croatia
Z. Antunovic, M. Kovac, T. Sculac

Institute Rudjer Boskovic, Zagreb, Croatia
V. Brigljevic, D. Ferencek, D. Majumder, M. Roguljic, A. Starodumov[12], T. Susa

University of Cyprus, Nicosia, Cyprus
M. W. Ather, A. Attikis, E. Erodotou, A. Ioannou, G. Kole, M. Kolosova, S. Konstantinou, J. Mousa, C. Nicolaou, F. Ptochos, P. A. Razis, H. Rykaczewski, H. Saka, D. Tsiakkouri

Charles University, Prague, Czech Republic
M. Finger[13], M. Finger Jr.[13], A. Kveton, J. Tomsa

Escuela Politecnica Nacional, Quito, Ecuador
E. Ayala

Universidad San Francisco de Quito, Quito, Ecuador
E. Carrera Jarrin

Academy of Scientific Research and Technology of the Arab Republic of Egypt, Egyptian Network of High Energy Physics, Cairo, Egypt
H. Abdalla[14], Y. Assran[15,16], S. Khalil[17]

Center for High Energy Physics (CHEP-FU), Fayoum University, El-Fayoum, Egypt
M. A. Mahmoud, Y. Mohammed[18]

National Institute of Chemical Physics and Biophysics, Tallinn, Estonia
S. Bhowmik, A. Carvalho Antunes De Oliveira, R. K. Dewanjee, K. Ehataht, M. Kadastik, M. Raidal, C. Veelken

Department of Physics, University of Helsinki, Helsinki, Finland
P. Eerola, L. Forthomme, H. Kirschenmann, K. Osterberg, M. Voutilainen

Helsinki Institute of Physics, Helsinki, Finland
E. Brücken, F. Garcia, J. Havukainen, V. Karimäki, M. S. Kim, R. Kinnunen, T. Lampén, K. Lassila-Perini, S. Lehti, T. Lindén, H. Siikonen, E. Tuominen, J. Tuominiemi

Lappeenranta University of Technology, Lappeenranta, Finland
P. Luukka, T. Tuuva

IRFU, CEA, Université Paris-Saclay, Gif-sur-Yvette, France
C. Amendola, M. Besancon, F. Couderc, M. Dejardin, D. Denegri, J. L. Faure, F. Ferri, S. Ganjour, A. Givernaud, P. Gras, G. Hamel de Monchenault, P. Jarry, B. Lenzi, E. Locci, J. Malcles, J. Rander, A. Rosowsky, M.Ö. Sahin, A. Savoy-Navarro[19], M. Titov, G. B. Yu

Laboratoire Leprince-Ringuet, CNRS/IN2P3, Ecole Polytechnique, Institut Polytechnique de Paris, Palaiseau, France
S. Ahuja, F. Beaudette, M. Bonanomi, A. Buchot Perraguin, P. Busson, C. Charlot, O. Davignon, B. Diab, G. Falmagne, R. Granier de Cassagnac, A. Hakimi, I. Kucher, A. Lobanov, C. Martin Perez, M. Nguyen, C. Ochando, P. Paganini, J. Rembser, R. Salerno, J. B. Sauvan, Y. Sirois, A. Zabi, A. Zghiche

Université de Strasbourg, CNRS, IPHC UMR 7178, Strasbourg, France
J. -L. Agram[20], J. Andrea, D. Bloch, G. Bourgatte, J. -M. Brom, E. C. Chabert, C. Collard, J. -C. Fontaine[20], D. Gelé, U. Goerlach, C. Grimault, A. -C. Le Bihan, P. Van Hove

Université de Lyon, Université Claude Bernard Lyon 1, CNRS-IN2P3, Institut de Physique Nucléaire de Lyon, Villeurbanne, France
E. Asilar, S. Beauceron, C. Bernet, G. Boudoul, C. Camen, A. Carle, N. Chanon, D. Contardo, P. Depasse, H. El Mamouni, J. Fay, S. Gascon, M. Gouzevitch, B. Ille, Sa. Jain, I. B. Laktineh, H. Lattaud, A. Lesauvage, M. Lethuillier, L. Mirabito, L. Torterotot, G. Touquet, M. Vander Donckt, S. Viret

Georgian Technical University, Tbilisi, Georgia
A. Khvedelidze[13], Z. Tsamalaidze[13]

RWTH Aachen University, I. Physikalisches Institut, Aachen, Germany
L. Feld, K. Klein, M. Lipinski, D. Meuser, A. Pauls, M. Preuten, M. P. Rauch, J. Schulz, M. Teroerde

RWTH Aachen University, III. Physikalisches Institut A, Aachen, Germany
D. Eliseev, M. Erdmann, P. Fackeldey, B. Fischer, S. Ghosh, T. Hebbeker, K. Hoepfner, H. Keller, L. Mastrolorenzo, M. Merschmeyer, A. Meyer, G. Mocellin, S. Mondal, S. Mukherjee, D. Noll, A. Novak, T. Pook, A. Pozdnyakov, Y. Rath, H. Reithler, J. Roemer, A. Schmidt, S. C. Schuler, A. Sharma, S. Wiedenbeck, S. Zaleski

RWTH Aachen University, III. Physikalisches Institut B, Aachen, Germany
C. Dziwok, G. Flügge, W. Haj Ahmad[21], O. Hlushchenko, T. Kress, A. Nowack, C. Pistone, O. Pooth, D. Roy, H. Sert, A. Stahl[22], T. Ziemons

Deutsches Elektronen-Synchrotron, Hamburg, Germany
H. Aarup Petersen, M. Aldaya Martin, P. Asmuss, I. Babounikau, S. Baxter, O. Behnke, A. Bermúdez Martínez, A. A. Bin Anuar, K. Borras[23], V. Botta, D. Brunner, A. Campbell, A. Cardini, P. Connor, S. Consuegra Rodríguez, V. Danilov, A. De Wit, M. M. Defranchis, L. Didukh, D. Domínguez Damiani, G. Eckerlin, D. Eckstein, T. Eichhorn, L. I. Estevez Banos, E. Gallo[24], A. Geiser, A. Giraldi, A. Grohsjean, M. Guthoff, A. Harb, A. Jafari[25], N. Z. Jomhari, H. Jung, A. Kasem[23], M. Kasemann, H. Kaveh, C. Kleinwort, J. Knolle, D. Krücker, W. Lange, T. Lenz, J. Lidrych, K. Lipka, W. Lohmann[26], T. Madlener, R. Mankel, I. -A. Melzer-Pellmann, J. Metwally, A. B. Meyer, M. Meyer, M. Missiroli, J. Mnich, A. Mussgiller, V. Myronenko, Y. Otarid, D. Pérez Adán, S. K. Pflitsch, D. Pitzl, A. Raspereza, A. Saggio, A. Saibel, M. Savitskyi, V. Scheurer, C. Schwanenberger, A. Singh, R. E. Sosa Ricardo, N. Tonon, O. Turkot, A. Vagnerini, M. Van De Klundert, R. Walsh, D. Walter, Y. Wen, K. Wichmann, C. Wissing, S. Wuchterl, O. Zenaiev, R. Zlebcik

University of Hamburg, Hamburg, Germany
R. Aggleton, S. Bein, L. Benato, A. Benecke, K. De Leo, T. Dreyer, A. Ebrahimi, M. Eich, F. Feindt, A. Fröhlich, C. Garbers, E. Garutti, P. Gunnellini, J. Haller, A. Hinzmann, A. Karavdina, G. Kasieczka, R. Klanner,

R. Kogler, V. Kutzner, J. Lange, T. Lange, A. Malara, C. E. N. Niemeyer, A. Nigamova, K. J. Pena Rodriguez, O. Rieger, P. Schleper, S. Schumann, J. Schwandt, D. Schwarz, J. Sonneveld, H. Stadie, G. Steinbrück, B. Vormwald, I. Zoi

Karlsruher Institut fuer Technologie, Karlsruhe, Germany
J. Bechtel, T. Berger, E. Butz, R. Caspart, T. Chwalek, W. De Boer, A. Dierlamm, A. Droll, K. El Morabit, N. Faltermann, K. Flöh, M. Giffels, A. Gottmann, F. Hartmann[22], C. Heidecker, U. Husemann, I. Katkov[27], P. Keicher, R. Koppenhöfer, S. Maier, M. Metzler, S. Mitra, Th. Müller, M. Musich, G. Quast, K. Rabbertz, J. Rauser, D. Savoiu, D. Schäfer, M. Schnepf, M. Schröder, D. Seith, I. Shvetsov, H. J. Simonis, R. Ulrich, M. Wassmer, M. Weber, R. Wolf, S. Wozniewski

Institute of Nuclear and Particle Physics (INPP), NCSR Demokritos, Aghia Paraskevi, Greece
G. Anagnostou, P. Asenov, G. Daskalakis, T. Geralis, A. Kyriakis, D. Loukas, G. Paspalaki, A. Stakia

National and Kapodistrian University of Athens, Athens, Greece
M. Diamantopoulou, D. Karasavvas, G. Karathanasis, P. Kontaxakis, C. K. Koraka, A. Manousakis-katsikakis, A. Panagiotou, I. Papavergou, N. Saoulidou, K. Theofilatos, E. Tziaferi, K. Vellidis, E. Vourliotis

National Technical University of Athens, Athens, Greece
G. Bakas, K. Kousouris, I. Papakrivopoulos, G. Tsipolitis, A. Zacharopoulou

University of Ioánnina, Ioánnina, Greece
I. Evangelou, C. Foudas, P. Gianneios, P. Katsoulis, P. Kokkas, K. Manitara, N. Manthos, I. Papadopoulos, J. Strologas

MTA-ELTE Lendület CMS Particle and Nuclear Physics Group, Eötvös Loránd University, Budapest, Hungary
M. Bartók[28], M. Csanad, M. M. A. Gadallah[29], S. Lökös[30], P. Major, K. Mandal, A. Mehta, G. Pasztor, O. Surányi, G. I. Veres

Wigner Research Centre for Physics, Budapest, Hungary
G. Bencze, C. Hajdu, D. Horvath[31], F. Sikler, V. Veszpremi, G. Vesztergombi[†]

Institute of Nuclear Research ATOMKI, Debrecen, Hungary
S. Czellar, J. Karancsi[28], J. Molnar, Z. Szillasi, D. Teyssier

Institute of Physics, University of Debrecen, Debrecen, Hungary
P. Raics, Z. L. Trocsanyi, G. Zilizi

Eszterhazy Karoly University, Karoly Robert Campus, Gyongyos, Hungary
T. Csorgo[32], F. Nemes[32], T. Novak

Indian Institute of Science (IISc), Bangalore, India
S. Choudhury, J. R. Komaragiri, D. Kumar, L. Panwar, P. C. Tiwari

National Institute of Science Education and Research, HBNI, Bhubaneswar, India
S. Bahinipati[33], D. Dash, C. Kar, P. Mal, T. Mishra, V. K. Muraleedharan Nair Bindhu, A. Nayak[34], D. K. Sahoo[33], N. Sur, S. K. Swain

Panjab University, Chandigarh, India
S. Bansal, S. B. Beri, V. Bhatnagar, G. Chaudhary, S. Chauhan, N. Dhingra[35], R. Gupta, A. Kaur, S. Kaur, P. Kumari, M. Meena, K. Sandeep, S. Sharma, J. B. Singh, A. K. Virdi

University of Delhi, Delhi, India
A. Ahmed, A. Bhardwaj, B. C. Choudhary, R. B. Garg, M. Gola, S. Keshri, A. Kumar, M. Naimuddin, P. Priyanka, K. Ranjan, A. Shah

Saha Institute of Nuclear Physics, HBNI, Kolkata, India
M. Bharti[37], R. Bhattacharya, S. Bhattacharya, D. Bhowmik, S. Dutta, S. Ghosh, B. Gomber[37], M. Maity[38], S. Nandan, P. Palit, P. K. Rout, G. Saha, B. Sahu, S. Sarkar, M. Sharan, B. Singh[36], S. Thakur[36]

Indian Institute of Technology Madras, Madras, India
P. K. Behera, S. C. Behera, P. Kalbhor, A. Muhammad, R. Pradhan, P. R. Pujahari, A. Sharma, A. K. Sikdar

Bhabha Atomic Research Centre, Mumbai, India
D. Dutta, V. Kumar, K. Naskar[39], P. K. Netrakanti, L. M. Pant, P. Shukla

Tata Institute of Fundamental Research-A, Mumbai, India
T. Aziz, M. A. Bhat, S. Dugad, R. Kumar Verma, G. B. Mohanty, U. Sarkar

Tata Institute of Fundamental Research-B, Mumbai, India
S. Banerjee, S. Bhattacharya, S. Chatterjee, R. Chudasama, M. Guchait, S. Karmakar, S. Kumar, G. Majumder, K. Mazumdar, S. Mukherjee, D. Roy

Indian Institute of Science Education and Research (IISER), Pune, India
S. Dube, B. Kansal, M. K. Maurya[40], S. Pandey, A. Rane, A. Rastogi, S. Sharma

Department of Physics, Isfahan University of Technology, Isfahan, Iran
H. Bakhshiansohi[41], M. Zeinali[42]

Institute for Research in Fundamental Sciences (IPM), Tehran, Iran
S. Chenarani[43], S. M. Etesami, M. Khakzad, M. Mohammadi Najafabadi

University College Dublin, Dublin, Ireland
M. Felcini, M. Grunewald

INFN Sezione di Bari[a], Università di Bari[b], Politecnico di Bari[c], Bari, Italy
M. Abbrescia[a,b], R. Aly[a,b,44], C. Aruta[a,b], A. Colaleo[a], D. Creanza[a,c], N. De Filippis[a,c], M. De Palma[a,b], A. Di Florio[a,b], A. Di Pilato[a,b], W. Elmetenawee[a,b], L. Fiore[a], A. Gelmi[a,b], M. Gul[a], G. Iaselli[a,c], M. Ince[a,b], S. Lezki[a,b], G. Maggi[a,c], M. Maggi[a], I. Margjeka[a,b], V. Mastrapasqua[a,b], J. A. Merlin[a], S. My[a,b], S. Nuzzo[a,b], A. Pompili[a,b], G. Pugliese[a,c], A. Ranieri[a], G. Selvaggi[a,b], L. Silvestris[a], F. M. Simone[a,b], R. Venditti[a], P. Verwilligen[a]

INFN Sezione di Bologna[a], Università di Bologna[b], Bologna, Italy
G. Abbiendi[a], C. Battilana[a,b], D. Bonacorsi[a,b], L. Borgonovi[a], S. Braibant-Giacomelli[a,b], R. Campanini[a,b], P. Capiluppi[a,b], A. Castro[a,b], F. R. Cavallo[a], C. Ciocca[a], M. Cuffiani[a,b], G. M. Dallavalle[a], T. Diotalevi[a,b], F. Fabbri[a], A. Fanfani[a,b], E. Fontanesi[a,b], P. Giacomelli[a], L. Giommi[a,b], C. Grandi[a], L. Guiducci[a,b], F. Iemmi[a,b], S. Lo Meo[a,45], S. Marcellini[a], G. Masetti[a], F. L. Navarria[a,b], A. Perrotta[a], F. Primavera[a,b], A. M. Rossi[a,b], T. Rovelli[a,b], G. P. Siroli[a,b], N. Tosi[a]

INFN Sezione di Catania[a], Università di Catania[b], Catania, Italy
S. Albergo[a,b,46], S. Costa[a,b], A. Di Mattia[a], R. Potenza[a,b], A. Tricomi[a,b,47], C. Tuve[a,b]

INFN Sezione di Firenze[a], Università di Firenze[b], Florence, Italy
G. Barbagli[a], A. Cassese[a], R. Ceccarelli[a,b], V. Ciulli[a,b], C. Civinini[a], R. D'Alessandro[a,b], F. Fiori[a], E. Focardi[a,b], G. Latino[a,b], P. Lenzi[a,b], M. Lizzo[a,b], M. Meschini[a], S. Paoletti[a], R. Seidita[a,b], G. Sguazzoni[a], L. Viliani[a]

INFN Laboratori Nazionali di Frascati, Frascati, Italy
L. Benussi, S. Bianco, D. Piccolo

INFN Sezione di Genova[a], Università di Genova[b], Genoa, Italy
M. Bozzo[a,b], F. Ferro[a], R. Mulargia[a,b], E. Robutti[a], S. Tosi[a,b]

INFN Sezione di Milano-Bicocca[a], Università di Milano-Bicocca[b], Milan, Italy
A. Benaglia[a], A. Beschi[a,b], F. Brivio[a,b], F. Cetorelli[a,b], V. Ciriolo[a,b,22], F. De Guio[a,b], M. E. Dinardo[a,b], P. Dini[a], S. Gennai[a], A. Ghezzi[a,b], P. Govoni[a,b], L. Guzzi[a,b], M. Malberti[a], S. Malvezzi[a], A. Massironi[a], D. Menasce[a], F. Monti[a,b], L. Moroni[a], M. Paganoni[a,b], D. Pedrini[a], S. Ragazzi[a,b], T. Tabarelli de Fatis[a,b], D. Valsecchi[a,b,22], D. Zuolo[a,b]

INFN Sezione di Napoli[a], Università di Napoli 'Federico II'[b], Naples, Italy, Università della Basilicata[c], Potenza, Italy, Università G. Marconi[d], Rome, Italy
S. Buontempo[a], N. Cavallo[a,c], A. De Iorio[a,b], F. Fabozzi[a,c], F. Fienga[a], A. O. M. Iorio[a,b], L. Lista[a,b], S. Meola[a,d,22], P. Paolucci[a,22], B. Rossi[a], C. Sciacca[a,b], E. Voevodina[a,b]

INFN Sezione di Padova[a], Università di Padova[b], Padua, Italy, Università di Trento[c], Trento, Italy
P. Azzi[a], N. Bacchetta[a], D. Bisello[a,b], P. Bortignon[a], A. Bragagnolo[a,b], R. Carlin[a,b], P. Checchia[a], P. De Castro Manzano[a], T. Dorigo[a], F. Gasparini[a,b], U. Gasparini[a,b], S. Y. Hoh[a,b], L. Layer[a,47], M. Margoni[a,b], A. T. Meneguzzo[a,b], M. Presilla[a,b], P. Ronchese[a,b], R. Rossin[a,b], F. Simonetto[a,b], G. Strong[a], M. Tosi[a,b], H. YARAR[a,b], M. Zanetti[a,b], P. Zotto[a,b], A. Zucchetta[a,b], G. Zumerle[a,b]

INFN Sezione di Pavia[a], Università di Pavia[b], Pavia, Italy
C. Aime'[a,b], A. Braghieri[a], S. Calzaferri[a,b], D. Fiorina[a,b], P. Montagna[a,b], S. P. Ratti[a,b], V. Re[a], M. Ressegotti[a,b], C. Riccardi[a,b], P. Salvini[a], I. Vai[a], P. Vitulo[a,b]

INFN Sezione di Perugia[a], Università di Perugia[b], Perugia, Italy
M. Biasini[a,b], G. M. Bilei[a], D. Ciangottini[a,b], L. Fanò[a,b], P. Lariccia[a,b], G. Mantovani[a,b], V. Mariani[a,b], M. Menichelli[a], F. Moscatelli[a], A. Piccinelli[a,b], A. Rossi[a,b], A. Santocchia[a,b], D. Spiga[a], T. Tedeschi[a,b]

INFN Sezione di Pisa[a], Università di Pisa[b], Scuola Normale Superiore di Pisa[c], Pisa, Italy
K. Androsov[a], P. Azzurri[a], G. Bagliesi[a], V. Bertacchi[a,c], L. Bianchini[a], T. Boccali[a], R. Castaldi[a], M. A. Ciocci[a,b], R. Dell'Orso[a], M. R. Di Domenico[a,b], S. Donato[a], L. Giannini[a,c], A. Giassi[a], M. T. Grippo[a], F. Ligabue[a,c], E. Manca[a,c], G. Mandorli[a,c], A. Messineo[a,b], F. Palla[a], G. Ramirez-Sanchez[a,c], A. Rizzi[a,b], G. Rolandi[a,c], S. Roy Chowdhury[a,c], A. Scribano[a], N. Shafiei[a,b], P. Spagnolo[a], R. Tenchini[a], G. Tonelli[a,b], N. Turini[a], A. Venturi[a], P. G. Verdini[a]

INFN Sezione di Roma[a], Sapienza Università di Roma[b], Rome, Italy
F. Cavallari[a], M. Cipriani[a,b], D. Del Re[a,b], E. Di Marco[a], M. Diemoz[a], E. Longo[a,b], P. Meridiani[a], G. Organtini[a,b], F. Pandolfi[a], R. Paramatti[a,b], C. Quaranta[a,b], S. Rahatlou[a,b], C. Rovelli[a], F. Santanastasio[a,b], L. Soffi[a,b], R. Tramontano[a,b]

INFN Sezione di Torino[a], Università di Torino[b], Turin, Italy, Università del Piemonte Orientale[c], Novara, Italy
N. Amapane[a,b], R. Arcidiacono[a,c], S. Argiro[a,b], M. Arneodo[a,c], N. Bartosik[a], R. Bellan[a,b], A. Bellora[a,b], J. Berenguer Antequera[a,b], C. Biino[a], A. Cappati[a,b], N. Cartiglia[a], S. Cometti[a], M. Costa[a,b], R. Covarelli[a,b], N. Demaria[a], B. Kiani[a,b], F. Legger[a], C. Mariotti[a], S. Maselli[a], E. Migliore[a,b], V. Monaco[a,b], E. Monteil[a,b], M. Monteno[a], M. M. Obertino[a,b], G. Ortona[a], L. Pacher[a,b], N. Pastrone[a], M. Pelliccioni[a], G. L. Pinna Angioni[a,b], M. Ruspa[a,c], R. Salvatico[a,b], F. Siviero[a,b], V. Sola[a], A. Solano[a,b], D. Soldi[a,b], A. Staiano[a], M. Tornago[a,b], D. Trocino[a,b]

INFN Sezione di Trieste[a], Università di Trieste[b], Trieste, Italy
S. Belforte[a], V. Candelise[a,b], M. Casarsa[a], F. Cossutti[a], A. Da Rold[a,b], G. Della Ricca[a,b], F. Vazzoler[a,b]

Kyungpook National University, Daegu, Korea
S. Dogra, C. Huh, B. Kim, D. H. Kim, G. N. Kim, J. Lee, S. W. Lee, C. S. Moon, Y. D. Oh, S. I. Pak, B. C. Radburn-Smith, S. Sekmen, Y. C. Yang

Chonnam National University, Institute for Universe and Elementary Particles, Kwangju, Korea
H. Kim, D. H. Moon

Hanyang University, Seoul, Korea
B. Francois, T. J. Kim, J. Park

Korea University, Seoul, Korea
S. Cho, S. Choi, Y. Go, S. Ha, B. Hong, K. Lee, K. S. Lee, J. Lim, J. Park, S. K. Park, J. Yoo

Department of Physics, Kyung Hee University, Seoul, Republic of Korea
J. Goh, A. Gurtu

Sejong University, Seoul, Korea
H. S. Kim, Y. Kim

Seoul National University, Seoul, Korea
J. Almond, J. H. Bhyun, J. Choi, S. Jeon, J. Kim, J. S. Kim, S. Ko, H. Kwon, H. Lee, K. Lee, S. Lee, K. Nam, B. H. Oh, M. Oh, S. B. Oh, H. Seo, U. K. Yang, I. Yoon

University of Seoul, Seoul, Korea
D. Jeon, J. H. Kim, B. Ko, J. S. H. Lee, I. C. Park, Y. Roh, D. Song, I. J. Watson

Yonsei University, Department of Physics, Seoul, Korea
H. D. Yoo

Sungkyunkwan University, Suwon, Korea
Y. Choi, C. Hwang, Y. Jeong, H. Lee, Y. Lee, I. Yu

Riga Technical University, Riga, Latvia
V. Veckalns[48]

Vilnius University, Vilnius, Lithuania
A. Juodagalvis, A. Rinkevicius, G. Tamulaitis, A. Vaitkevicius

National Centre for Particle Physics, Universiti Malaya, Kuala Lumpur, Malaysia
W. A. T. Wan Abdullah, M. N. Yusli, Z. Zolkapli

Universidad de Sonora (UNISON), Hermosillo, Mexico
J. F. Benitez, A. Castaneda Hernandez, J. A. Murillo Quijada, L. Valencia Palomo

Centro de Investigacion y de Estudios Avanzados del IPN, Mexico City, Mexico
G. Ayala, H. Castilla-Valdez, E. De La Cruz-Burelo, I. Heredia-De La Cruz[49], R. Lopez-Fernandez, C. A. Mondragon Herrera, D. A. Perez Navarro, A. Sanchez-Hernandez

Universidad Iberoamericana, Mexico City, Mexico
S. Carrillo Moreno, C. Oropeza Barrera, M. Ramirez-Garcia, F. Vazquez Valencia

Benemerita Universidad Autonoma de Puebla, Puebla, Mexico
J. Eysermans, I. Pedraza, H. A. Salazar Ibarguen, C. Uribe Estrada

Universidad Autónoma de San Luis Potosí, San Luis Potosí, Mexico
A. Morelos Pineda

University of Montenegro, Podgorica, Montenegro
J. Mijuskovic[4], N. Raicevic

University of Auckland, Auckland, New Zealand
D. Krofcheck

University of Canterbury, Christchurch, New Zealand
S. Bheesette, P. H. Butler

National Centre for Physics, Quaid-I-Azam University, Islamabad, Pakistan
A. Ahmad, M. I. Asghar, A. Awais, M. I. M. Awan, H. R. Hoorani, W. A. Khan, M. A. Shah, M. Shoaib, M. Waqas

AGH University of Science and Technology, Faculty of Computer Science, Electronics and Telecommunications, Krakow, Poland
V. Avati, L. Grzanka, M. Malawski

National Centre for Nuclear Research, Swierk, Poland
H. Bialkowska, M. Bluj, B. Boimska, T. Frueboes, M. Górski, M. Kazana, M. Szleper, P. Traczyk, P. Zalewski

Institute of Experimental Physics, Faculty of Physics, University of Warsaw, Warsaw, Poland
K. Bunkowski, K. Doroba, A. Kalinowski, M. Konecki, J. Krolikowski, M. Walczak

Laboratório de Instrumentação e Física Experimental de Partículas, Lisbon, Portugal
M. Araujo, P. Bargassa, D. Bastos, A. Boletti, P. Faccioli, M. Gallinaro, J. Hollar, N. Leonardo, T. Niknejad, J. Seixas, K. Shchelina, O. Toldaiev, J. Varela

Joint Institute for Nuclear Research, Dubna, Russia
S. Afanasiev, M. Gavrilenko, A. Golunov, I. Golutvin, I. Gorbunov, A. Kamenev, V. Karjavine, I. Kashunin, V. Korenkov, A. Lanev, A. Malakhov, V. Matveev[50,51], V. V. Mitsyn, V. Palichik, V. Perelygin, M. Savina, S. Shmatov, S. Shulha, V. Smirnov, O. Teryaev, B. S. Yuldashev[52], A. Zarubin

Petersburg Nuclear Physics Institute, Gatchina (St. Petersburg), Russia
G. Gavrilov, V. Golovtcov, Y. Ivanov, V. Kim[53], E. Kuznetsova[54], V. Murzin, V. Oreshkin, I. Smirnov, D. Sosnov, V. Sulimov, L. Uvarov, S. Volkov, A. Vorobyev

Institute for Nuclear Research, Moscow, Russia
Yu. Andreev, A. Dermenev, S. Gninenko, N. Golubev, A. Karneyeu, M. Kirsanov, N. Krasnikov, A. Pashenkov, G. Pivovarov, D. Tlisov†, A. Toropin

Institute for Theoretical and Experimental Physics named by A.I. Alikhanov of NRC 'Kurchatov Institute', Moscow, Russia
V. Epshteyn, V. Gavrilov, N. Lychkovskaya, A. Nikitenko[55], V. Popov, G. Safronov, A. Spiridonov, A. Stepennov, M. Toms, E. Vlasov, A. Zhokin

Moscow Institute of Physics and Technology, Moscow, Russia
T. Aushev

National Research Nuclear University 'Moscow Engineering Physics Institute' (MEPhI), Moscow, Russia
O. Bychkova, M. Chadeeva[56], D. Philippov, E. Popova, V. Rusinov

P.N. Lebedev Physical Institute, Moscow, Russia
V. Andreev, M. Azarkin, I. Dremin, M. Kirakosyan, A. Terkulov

Skobeltsyn Institute of Nuclear Physics, Lomonosov Moscow State University, Moscow, Russia
A. Belyaev, E. Boos, V. Bunichev, M. Dubinin[57], L. Dudko, V. Klyukhin, O. Kodolova, N. Korneeva, I. Lokhtin, S. Obraztsov, M. Perfilov, S. Petrushanko, V. Savrin

Novosibirsk State University (NSU), Novosibirsk, Russia
V. Blinov[58], T. Dimova[58], L. Kardapoltsev[58], I. Ovtin[58], Y. Skovpen[58]

Institute for High Energy Physics of National Research Centre 'Kurchatov Institute', Protvino, Russia
I. Azhgirey, I. Bayshev, V. Kachanov, A. Kalinin, D. Konstantinov, V. Petrov, R. Ryutin, A. Sobol, S. Troshin, N. Tyurin, A. Uzunian, A. Volkov

National Research Tomsk Polytechnic University, Tomsk, Russia
A. Babaev, A. Iuzhakov, V. Okhotnikov, L. Sukhikh

Tomsk State University, Tomsk, Russia
V. Borchsh, V. Ivanchenko, E. Tcherniaev

University of Belgrade, Faculty of Physics and VINCA Institute of Nuclear Sciences, Belgrade, Serbia
P. Adzic[59], P. Cirkovic, M. Dordevic, P. Milenovic, J. Milosevic

Centro de Investigaciones Energéticas Medioambientales y Tecnológicas (CIEMAT), Madrid, Spain
M. Aguilar-Benitez, J. Alcaraz Maestre, A. Álvarez Fernández, I. Bachiller, M. Barrio Luna, Cristina F. Bedoya, C. A. Carrillo Montoya, M. Cepeda, M. Cerrada, N. Colino, B. De La Cruz, A. Delgado Peris, J. P. Fernández Ramos, J. Flix, M. C. Fouz, A. García Alonso, O. Gonzalez Lopez, S. Goy Lopez, J. M. Hernandez, M. I. Josa, J. León Holgado, D. Moran, Á. Navarro Tobar, A. Pérez-Calero Yzquierdo, J. Puerta Pelayo, I. Redondo, L. Romero, S. Sánchez Navas, M. S. Soares, A. Triossi, L. Urda Gómez, C. Willmott

Universidad Autónoma de Madrid, Madrid, Spain
C. Albajar, J. F. de Trocóniz, R. Reyes-Almanza

Universidad de Oviedo, Instituto Universitario de Ciencias y Tecnologías Espaciales de Asturias (ICTEA), Oviedo, Spain
B. Alvarez Gonzalez, J. Cuevas, C. Erice, J. Fernandez Menendez, S. Folgueras, I. Gonzalez Caballero, E. Palencia Cortezon, C. Ramón Álvarez, J. Ripoll Sau, V. Rodríguez Bouza, S. Sanchez Cruz, A. Soto Rodríguez, A. Trapote

Instituto de Física de Cantabria (IFCA), CSIC-Universidad de Cantabria, Santander, Spain
J. A. Brochero Cifuentes, I. J. Cabrillo, A. Calderon, B. Chazin Quero, J. Duarte Campderros, M. Fernandez, P. J. Fernández Manteca, G. Gomez, C. Martinez Rivero, P. Martinez Ruiz del Arbol, F. Matorras, J. Piedra Gomez, C. Prieels, F. Ricci-Tam, T. Rodrigo, A. Ruiz-Jimeno, L. Scodellaro, I. Vila, J. M. Vizan Garcia

University of Colombo, Colombo, Sri Lanka
MK Jayananda, B. Kailasapathy[60], D. U. J. Sonnadara, DDC Wickramarathna

Department of Physics, University of Ruhuna, Matara, Sri Lanka
W. G. D. Dharmaratna, K. Liyanage, N. Perera, N. Wickramage

CERN, European Organization for Nuclear Research, Geneva, Switzerland
T. K. Aarrestad, D. Abbaneo, E. Auffray, G. Auzinger, J. Baechler, P. Baillon, A. H. Ball, D. Barney, J. Bendavid, N. Beni, M. Bianco, A. Bocci, E. Bossini, E. Brondolin, T. Camporesi, G. Cerminara, L. Cristella, D. d'Enterria, A. Dabrowski, N. Daci, V. Daponte, A. David, A. De Roeck, M. Deile, R. Di Maria, M. Dobson, M. Dünser, N. Dupont, A. Elliott-Peisert, N. Emriskova, F. Fallavollita[61], D. Fasanella, S. Fiorendi, A. Florent, G. Franzoni, J. Fulcher, W. Funk, S. Giani, D. Gigi, K. Gill, F. Glege, L. Gouskos, M. Guilbaud, D. Gulhan, M. Haranko, J. Hegeman, Y. Iiyama, V. Innocente, T. James, P. Janot, J. Kaspar, J. Kieseler, M. Komm, N. Kratochwil, C. Lange, S. Laurila, P. Lecoq, K. Long, C. Lourenço, L. Malgeri, S. Mallios, M. Mannelli, F. Meijers, S. Mersi, E. Meschi, F. Moortgat, M. Mulders, S. Orfanelli, L. Orsini, F. Pantaleo[22], L. Pape, E. Perez, M. Peruzzi, A. Petrilli, G. Petrucciani, A. Pfeiffer, M. Pierini, T. Quast, D. Rabady, A. Racz, M. Rieger, M. Rovere, H. Sakulin, J. Salfeld-Nebgen, S. Scarfi, C. Schäfer, C. Schwick, M. Selvaggi, A. Sharma, P. Silva, W. Snoeys, P. Sphicas[62], S. Summers, V. R. Tavolaro, D. Treille, A. Tsirou, G. P. Van Onsem, A. Vartak, M. Verzetti, K. A. Wozniak, W. D. Zeuner

Paul Scherrer Institut, Villigen, Switzerland
L. Caminada[63], W. Erdmann, R. Horisberger, Q. Ingram, H. C. Kaestli, D. Kotlinski, U. Langenegger, T. Rohe

ETH Zurich-Institute for Particle Physics and Astrophysics (IPA), Zurich, Switzerland
M. Backhaus, P. Berger, A. Calandri, N. Chernyavskaya, A. De Cosa, G. Dissertori, M. Dittmar, M. Donegà, C. Dorfer, T. Gadek, T. A. Gómez Espinosa, C. Grab, D. Hits, W. Lustermann, A. -M. Lyon, R. A. Manzoni, M. T. Meinhard, F. Micheli, F. Nessi-Tedaldi, J. Niedziela, F. Pauss, V. Perovic, G. Perrin, S. Pigazzini, M. G. Ratti, M. Reichmann, C. Reissel, T. Reitenspiess, B. Ristic, D. Ruini, D. A. Sanz Becerra, M. Schönenberger, V. Stampf, J. Steggemann[64], M. L. Vesterbacka Olsson, R. Wallny, D. H. Zhu

Universität Zürich, Zurich, Switzerland
C. Amsler[65], C. Botta, D. Brzhechko, M. F. Canelli, R. Del Burgo, J. K. Heikkilä, M. Huwiler, A. Jofrehei, B. Kilminster, S. Leontsinis, A. Macchiolo, P. Meiring, V. M. Mikuni, U. Molinatti, I. Neutelings, G. Rauco, A. Reimers, P. Robmann, K. Schweiger, Y. Takahashi

National Central University, Chung-Li, Taiwan
C. Adloff[66], C. M. Kuo, W. Lin, A. Roy, T. Sarkar[38], S. S. Yu

National Taiwan University (NTU), Taipei, Taiwan
L. Ceard, P. Chang, Y. Chao, K. F. Chen, P. H. Chen, W. -S. Hou, Y.y. Li, R. -S. Lu, E. Paganis, A. Psallidas, A. Steen, E. Yazgan

Department of Physics, Faculty of Science, Chulalongkorn University, Bangkok, Thailand
B. Asavapibhop, C. Asawatangtrakuldee, N. Srimanobhas

Physics Department, Science and Art Faculty, Çukurova University, Adana, Turkey
F. Boran, S. Damarseckin[67], Z. S. Demiroglu, F. Dolek, C. Dozen[68], I. Dumanoglu[69], E. Eskut, G. Gokbulut, Y. Guler,

E. Gurpinar Guler[71], I. Hos[71], C. Isik, E. E. Kangal[73], O. Kara, A. Kayis Topaksu, U. Kiminsu, G. Onengut, K. Ozdemir[73], A. Polatoz, A. E. Simsek, B. Tali[74], U. G. Tok, S. Turkcapar, I. S. Zorbakir, C. Zorbilmez

Physics Department, Middle East Technical University, Ankara, Turkey
B. Isildak[75], G. Karapinar[76], K. Ocalan[77], M. Yalvac[78]

Bogazici University, Istanbul, Turkey
B. Akgun, I. O. Atakisi, E. Gülmez, M. Kaya[79], O. Kaya[80], Ö. Özçelik, S. Tekten[81], E. A. Yetkin[82]

Istanbul Technical University, Istanbul, Turkey
A. Cakir, K. Cankocak[69], Y. Komurcu, S. Sen[83]

Istanbul University, Istanbul, Turkey
F. Aydogmus Sen, S. Cerci[74], B. Kaynak, S. Ozkorucuklu, D. Sunar Cerci[74]

Institute for Scintillation Materials of National Academy of Science of Ukraine, Kharkov, Ukraine
B. Grynyov

National Scientific Center, Kharkov Institute of Physics and Technology, Kharkov, Ukraine
L. Levchuk

University of Bristol, Bristol, UK
E. Bhal, S. Bologna, J. J. Brooke, E. Clement, D. Cussans, H. Flacher, J. Goldstein, G. P. Heath, H. F. Heath, L. Kreczko, B. Krikler, S. Paramesvaran, T. Sakuma, S. Seif El Nasr-Storey, V. J. Smith, N. Stylianou[84], J. Taylor, A. Titterton

Rutherford Appleton Laboratory, Didcot, UK
K. W. Bell, A. Belyaev[85], C. Brew, R. M. Brown, D. J. A. Cockerill, K. V. Ellis, K. Harder, S. Harper, J. Linacre, K. Manolopoulos, D. M. Newbold, E. Olaiya, D. Petyt, T. Reis, T. Schuh, C. H. Shepherd-Themistocleous, A. Thea, I. R. Tomalin, T. Williams

Imperial College, London, UK
R. Bainbridge, P. Bloch, S. Bonomally, J. Borg, S. Breeze, O. Buchmuller, A. Bundock, V. Cepaitis, G. S. Chahal[86], D. Colling, P. Dauncey, G. Davies, M. Della Negra, G. Fedi, G. Hall, G. Iles, J. Langford, L. Lyons, A. -M. Magnan, S. Malik, A. Martelli, V. Milosevic, J. Nash[87], V. Palladino, M. Pesaresi, D. M. Raymond, A. Richards, A. Rose, E. Scott, C. Seez, A. Shtipliyski, M. Stoye, A. Tapper, K. Uchida, T. Virdee[22], N. Wardle, S. N. Webb, D. Winterbottom, A. G. Zecchinelli

Brunel University, Uxbridge, UK
J. E. Cole, P. R. Hobson, A. Khan, P. Kyberd, C. K. Mackay, I. D. Reid, L. Teodorescu, S. Zahid

Baylor University, Waco, USA
S. Abdullin, A. Brinkerhoff, K. Call, B. Caraway, J. Dittmann, K. Hatakeyama, A. R. Kanuganti, C. Madrid, B. McMaster, N. Pastika, S. Sawant, C. Smith, J. Wilson

Catholic University of America, Washington, DC, USA
R. Bartek, A. Dominguez, R. Uniyal, A. M. Vargas Hernandez

The University of Alabama, Tuscaloosa, USA
A. Buccilli, O. Charaf, S. I. Cooper, S. V. Gleyzer, C. Henderson, C. U. Perez, P. Rumerio, C. West

Boston University, Boston, USA
A. Akpinar, A. Albert, D. Arcaro, C. Cosby, Z. Demiragli, D. Gastler, J. Rohlf, K. Salyer, D. Sperka, D. Spitzbart, I. Suarez, S. Yuan, D. Zou

Brown University, Providence, USA
G. Benelli, B. Burkle, X. Coubez[23], D. Cutts, Y.t. Duh, M. Hadley, U. Heintz, J. M. Hogan[88], K. H. M. Kwok, E. Laird, G. Landsberg, K. T. Lau, J. Lee, M. Narain, S. Sagir[89], R. Syarif, E. Usai, W. Y. Wong, D. Yu, W. Zhang

University of California, Davis, Davis, USA
R. Band, C. Brainerd, R. Breedon, M. Calderon De La Barca Sanchez, M. Chertok, J. Conway, R. Conway, P. T. Cox, R. Erbacher, C. Flores, G. Funk, F. Jensen, W. Ko†, O. Kukral, R. Lander, M. Mulhearn, D. Pellett, J. Pilot, M. Shi, D. Taylor, K. Tos, M. Tripathi, Y. Yao, F. Zhang

University of California, Los Angeles, USA
M. Bachtis, R. Cousins, A. Dasgupta, D. Hamilton, J. Hauser, M. Ignatenko, M. A. Iqbal, T. Lam, N. Mccoll, W. A. Nash, S. Regnard, D. Saltzberg, C. Schnaible, B. Stone, V. Valuev

University of California, Riverside, Riverside, USA
K. Burt, Y. Chen, R. Clare, J. W. Gary, G. Hanson, G. Karapostoli, O. R. Long, N. Manganelli, M. Olmedo Negrete, M. I. Paneva, W. Si, S. Wimpenny, Y. Zhang

University of California, San Diego, La Jolla, USA
J. G. Branson, P. Chang, S. Cittolin, S. Cooperstein, N. Deelen, J. Duarte, R. Gerosa, D. Gilbert, V. Krutelyov, J. Letts, M. Masciovecchio, S. May, S. Padhi, M. Pieri, V. Sharma, M. Tadel, F. Würthwein, A. Yagil

Department of Physics, University of California, Santa Barbara, Santa Barbara, USA
N. Amin, C. Campagnari, M. Citron, A. Dorsett, V. Dutta, J. Incandela, B. Marsh, H. Mei, A. Ovcharova, H. Qu, M. Quinnan, J. Richman, U. Sarica, D. Stuart, S. Wang

California Institute of Technology, Pasadena, USA
A. Bornheim, O. Cerri, I. Dutta, J. M. Lawhorn, N. Lu, J. Mao, H. B. Newman, J. Ngadiuba, T. Q. Nguyen, J. Pata, M. Spiropulu, J. R. Vlimant, C. Wang, S. Xie, Z. Zhang, R. Y. Zhu

Carnegie Mellon University, Pittsburgh, USA
J. Alison, M. B. Andrews, T. Ferguson, T. Mudholkar, M. Paulini, M. Sun, I. Vorobiev

University of Colorado, Boulder, Boulder, USA
J. P. Cumalat, W. T. Ford, E. MacDonald, T. Mulholland, R. Patel, A. Perloff, K. Stenson, K. A. Ulmer, S. R. Wagner

Cornell University, Ithaca, USA
J. Alexander, Y. Cheng, J. Chu, D. J. Cranshaw, A. Datta, A. Frankenthal, K. Mcdermott, J. Monroy, J. R. Patterson, D. Quach, A. Ryd, W. Sun, S. M. Tan, Z. Tao, J. Thom, P. Wittich, M. Zientek

Fermi National Accelerator Laboratory, Batavia, USA
M. Albrow, M. Alyari, G. Apollinari, A. Apresyan, A. Apyan, S. Banerjee, L. A. T. Bauerdick, A. Beretvas, D. Berry, J. Berryhill, P. C. Bhat, K. Burkett, J. N. Butler, A. Canepa, G. B. Cerati, H. W. K. Cheung, F. Chlebana, M. Cremonesi, V. D. Elvira, J. Freeman, Z. Gecse, E. Gottschalk, L. Gray, D. Green, S. Grünendahl, O. Gutsche, R. M. Harris, S. Hasegawa, R. Heller, T. C. Herwig, J. Hirschauer, B. Jayatilaka, S. Jindariani, M. Johnson, U. Joshi, P. Klabbers, T. Klijnsma, B. Klima, M. J. Kortelainen, S. Lammel, D. Lincoln, R. Lipton, M. Liu, T. Liu, J. Lykken, K. Maeshima, D. Mason, P. McBride, P. Merkel, S. Mrenna, S. Nahn, V. O'Dell, V. Papadimitriou, K. Pedro, C. Pena[57], O. Prokofyev, F. Ravera, A. Reinsvold Hall, L. Ristori, B. Schneider, E. Sexton-Kennedy, N. Smith, A. Soha, W. J. Spalding, L. Spiegel, S. Stoynev, J. Strait, L. Taylor, S. Tkaczyk, N. V. Tran, L. Uplegger, E. W. Vaandering, H. A. Weber, A. Woodard

University of Florida, Gainesville, USA
D. Acosta, P. Avery, D. Bourilkov, L. Cadamuro, V. Cherepanov, F. Errico, R. D. Field, D. Guerrero, B. M. Joshi, M. Kim, J. Konigsberg, A. Korytov, K. H. Lo, K. Matchev, N. Menendez, G. Mitselmakher, D. Rosenzweig, K. Shi, J. Sturdy, J. Wang, S. Wang, X. Zuo

Florida State University, Tallahassee, USA
T. Adams, A. Askew, D. Diaz, R. Habibullah, S. Hagopian, V. Hagopian, K. F. Johnson, R. Khurana, T. Kolberg, G. Martinez, H. Prosper, C. Schiber, R. Yohay, J. Zhang

Florida Institute of Technology, Melbourne, USA
M. M. Baarmand, S. Butalla, T. Elkafrawy[90], M. Hohlmann, D. Noonan, M. Rahmani, M. Saunders, F. Yumiceva

University of Illinois at Chicago (UIC), Chicago, USA
M. R. Adams, L. Apanasevich, H. Becerril Gonzalez, R. Cavanaugh, X. Chen, S. Dittmer, O. Evdokimov, C. E. Gerber, D. A. Hangal, D. J. Hofman, C. Mills, G. Oh, T. Roy, M. B. Tonjes, N. Varelas, J. Viinikainen, X. Wang, Z. Wu, Z. Ye

The University of Iowa, Iowa City, USA
M. Alhusseini, K. Dilsiz[91], S. Durgut, R. P. Gandrajula, M. Haytmyradov, V. Khristenko, O. K. Köseyan, J. -P. Merlo, A. Mestvirishvili[92], A. Moeller, J. Nachtman, H. Ogul[93], Y. Onel, F. Ozok[94], A. Penzo, C. Snyder, E. Tiras, J. Wetzel

Johns Hopkins University, Baltimore, USA
O. Amram, B. Blumenfeld, L. Corcodilos, M. Eminizer, A. V. Gritsan, S. Kyriacou, P. Maksimovic, C. Mantilla, J. Roskes, M. Swartz, T.Á. Vámi

The University of Kansas, Lawrence, USA
C. Baldenegro Barrera, P. Baringer, A. Bean, A. Bylinkin, T. Isidori, S. Khalil, J. King, G. Krintiras, A. Kropivnitskaya, C. Lindsey, N. Minafra, M. Murray, C. Rogan, C. Royon, S. Sanders, E. Schmitz, J. D. Tapia Takaki, Q. Wang, J. Williams, G. Wilson

Kansas State University, Manhattan, USA
S. Duric, A. Ivanov, K. Kaadze, D. Kim, Y. Maravin, T. Mitchell, A. Modak, A. Mohammadi

Lawrence Livermore National Laboratory, Livermore, USA
F. Rebassoo, D. Wright

University of Maryland, College Park, USA
E. Adams, A. Baden, O. Baron, A. Belloni, S. C. Eno, Y. Feng, N. J. Hadley, S. Jabeen, G. Y. Jeng, R. G. Kellogg, T. Koeth, A. C. Mignerey, S. Nabili, M. Seidel, A. Skuja, S. C. Tonwar, L. Wang, K. Wong

Massachusetts Institute of Technology, Cambridge, USA
D. Abercrombie, B. Allen, R. Bi, S. Brandt, W. Busza, I. A. Cali, Y. Chen, M. D'Alfonso, G. Gomez Ceballos, M. Goncharov, P. Harris, D. Hsu, M. Hu, M. Klute, D. Kovalskyi, J. Krupa, Y. -J. Lee, P. D. Luckey, B. Maier, A. C. Marini, C. Mcginn, C. Mironov, S. Narayanan, X. Niu, C. Paus, D. Rankin, C. Roland, G. Roland, Z. Shi, G. S. F. Stephans, K. Sumorok, K. Tatar, D. Velicanu, J. Wang, T. W. Wang, Z. Wang, B. Wyslouch

University of Minnesota, Minneapolis, USA
R. M. Chatterjee, A. Evans, P. Hansen, J. Hiltbrand, Sh. Jain, M. Krohn, Y. Kubota, Z. Lesko, J. Mans, M. Revering, R. Rusack, R. Saradhy, N. Schroeder, N. Strobbe, M. A. Wadud

University of Mississippi, Oxford, USA
J. G. Acosta, S. Oliveros

University of Nebraska-Lincoln, Lincoln, USA
K. Bloom, S. Chauhan, D. R. Claes, C. Fangmeier, L. Finco, F. Golf, J. R. González Fernández, C. Joo, I. Kravchenko, J. E. Siado, G. R. Snow[†], W. Tabb, F. Yan

State University of New York at Buffalo, Buffalo, USA
G. Agarwal, H. Bandyopadhyay, C. Harrington, L. Hay, I. Iashvili, A. Kharchilava, C. McLean, D. Nguyen, J. Pekkanen, S. Rappoccio, B. Roozbahani

Northeastern University, Boston, USA
G. Alverson, E. Barberis, C. Freer, Y. Haddad, A. Hortiangtham, J. Li, G. Madigan, B. Marzocchi, D. M. Morse, V. Nguyen, T. Orimoto, A. Parker, L. Skinnari, A. Tishelman-Charny, T. Wamorkar, B. Wang, A. Wisecarver, D. Wood

Northwestern University, Evanston, USA
S. Bhattacharya, J. Bueghly, Z. Chen, A. Gilbert, T. Gunter, K. A. Hahn, N. Odell, M. H. Schmitt, K. Sung, M. Velasco

University of Notre Dame, Notre Dame, USA
R. Bucci, N. Dev, R. Goldouzian, M. Hildreth, K. Hurtado Anampa, C. Jessop, D. J. Karmgard, K. Lannon, N. Loukas, N. Marinelli, I. Mcalister, F. Meng, K. Mohrman, Y. Musienko[50], R. Ruchti, P. Siddireddy, S. Taroni, M. Wayne, A. Wightman, M. Wolf, L. Zygala

The Ohio State University, Columbus, USA
J. Alimena, B. Bylsma, B. Cardwell, L. S. Durkin, B. Francis, C. Hill, A. Lefeld, B. L. Winer, B. R. Yates

Princeton University, Princeton, USA
B. Bonham, P. Das, G. Dezoort, A. Dropulic, P. Elmer, B. Greenberg, N. Haubrich, S. Higginbotham, A. Kalogeropoulos, G. Kopp, S. Kwan, D. Lange, M. T. Lucchini, J. Luo, D. Marlow, K. Mei, I. Ojalvo, J. Olsen, C. Palmer, P. Piroué, D. Stickland, C. Tully

University of Puerto Rico, Mayaguez, USA
S. Malik, S. Norberg

Purdue University, West Lafayette, USA
V. E. Barnes, R. Chawla, S. Das, L. Gutay, M. Jones, A. W. Jung, G. Negro, N. Neumeister, C. C. Peng, S. Piperov, A. Purohit, H. Qiu, J. F. Schulte, M. Stojanovic[19], N. Trevisani, F. Wang, A. Wildridge, R. Xiao, W. Xie

Purdue University Northwest, Hammond, USA
J. Dolen, N. Parashar

Rice University, Houston, USA
A. Baty, S. Dildick, K. M. Ecklund, S. Freed, F. J. M. Geurts, M. Kilpatrick, A. Kumar, W. Li, B. P. Padley, R. Redjimi, J. Roberts†, J. Rorie, W. Shi, A. G. Stahl Leiton

University of Rochester, Rochester, USA
A. Bodek, P. de Barbaro, R. Demina, J. L. Dulemba, C. Fallon, T. Ferbel, M. Galanti, A. Garcia-Bellido, O. Hindrichs, A. Khukhunaishvili, E. Ranken, R. Taus

Rutgers, The State University of New Jersey, Piscataway, USA
B. Chiarito, J. P. Chou, A. Gandrakota, Y. Gershtein, E. Halkiadakis, A. Hart, M. Heindl, E. Hughes, S. Kaplan, O. Karacheban[26], I. Laflotte, A. Lath, R. Montalvo, K. Nash, M. Osherson, S. Salur, S. Schnetzer, S. Somalwar, R. Stone, S. A. Thayil, S. Thomas, H. Wang

University of Tennessee, Knoxville, USA
H. Acharya, A. G. Delannoy, S. Spanier

Texas A&M University, College Station, USA
O. Bouhali[95], M. Dalchenko, A. Delgado, R. Eusebi, J. Gilmore, T. Huang, T. Kamon[96], H. Kim, S. Luo, S. Malhotra, R. Mueller, D. Overton, L. Perniè, D. Rathjens, A. Safonov

Texas Tech University, Lubbock, USA
N. Akchurin, J. Damgov, V. Hegde, S. Kunori, K. Lamichhane, S. W. Lee, T. Mengke, S. Muthumuni, T. Peltola, S. Undleeb, I. Volobouev, Z. Wang, A. Whitbeck

Vanderbilt University, Nashville, USA
E. Appelt, S. Greene, A. Gurrola, R. Janjam, W. Johns, C. Maguire, A. Melo, H. Ni, K. Padeken, F. Romeo, P. Sheldon, S. Tuo, J. Velkovska

University of Virginia, Charlottesville, USA
M. W. Arenton, B. Cox, G. Cummings, J. Hakala, R. Hirosky, M. Joyce, A. Ledovskoy, A. Li, C. Neu, B. Tannenwald, Y. Wang, E. Wolfe, F. Xia

Wayne State University, Detroit, USA
P. E. Karchin, N. Poudyal, P. Thapa

University of Wisconsin-Madison, Madison, WI, USA
K. Black, T. Bose, J. Buchanan, C. Caillol, S. Dasu, I. De Bruyn, P. Everaerts, C. Galloni, H. He, M. Herndon, A. Hervé, U. Hussain, A. Lanaro, A. Loeliger, R. Loveless, J. Madhusudanan Sreekala, A. Mallampalli, D. Pinna, A. Savin, V. Shang, V. Sharma, W. H. Smith, D. Teague, S. Trembath-reichert, W. Vetens

† **Deceased**

1: Also at Vienna University of Technology, Vienna, Austria
2: Also at Institute of Basic and Applied Sciences, Faculty of Engineering, Arab Academy for Science, Technology and Maritime Transport, Alexandria, Egypt, Alexandria, Egypt
3: Also at Université Libre de Bruxelles, Brussels, Belgium
4: Also at IRFU, CEA, Université Paris-Saclay, Gif-sur-Yvette, France
5: Also at Universidade Estadual de Campinas, Campinas, Brazil
6: Also at Federal University of Rio Grande do Sul, Porto Alegre, Brazil
7: Also at UFMS, Nova Andradina, Brazil
8: Also at Universidade Federal de Pelotas, Pelotas, Brazil
9: Also at Nanjing Normal University Department of Physics, Nanjing, China
10: Now at The University of Iowa, Iowa City, USA
11: Also at University of Chinese Academy of Sciences, Beijing, China
12: Also at Institute for Theoretical and Experimental Physics named by A.I. Alikhanov of NRC 'Kurchatov Institute', Moscow, Russia
13: Also at Joint Institute for Nuclear Research, Dubna, Russia
14: Also at Cairo University, Cairo, Egypt
15: Also at Suez University, Suez, Egypt
16: Now at British University in Egypt, Cairo, Egypt
17: Also at Zewail City of Science and Technology, Zewail, Egypt
18: Now at Fayoum University, El-Fayoum, Egypt
19: Also at Purdue University, West Lafayette, USA
20: Also at Université de Haute Alsace, Mulhouse, France
21: Also at Erzincan Binali Yildirim University, Erzincan, Turkey
22: Also at CERN, European Organization for Nuclear Research, Geneva, Switzerland
23: Also at RWTH Aachen University, III. Physikalisches Institut A, Aachen, Germany
24: Also at University of Hamburg, Hamburg, Germany
25: Also at Department of Physics, Isfahan University of Technology, Isfahan, Iran
26: Also at Brandenburg University of Technology, Cottbus, Germany
27: Also at Skobeltsyn Institute of Nuclear Physics, Lomonosov Moscow State University, Moscow, Russia
28: Also at Institute of Physics, University of Debrecen, Debrecen, Hungary
29: Also at Physics Department, Faculty of Science, Assiut University, Assiut, Egypt
30: Also at Eszterhazy Karoly UniversityKaroly Robert Campus, Gyongyos, Hungary
31: Also at Institute of Nuclear Research ATOMKI, Debrecen, Hungary
32: Also at Wigner Research Centre for Physics, Budapest, Hungary
33: Also at IIT Bhubaneswar, Bhubaneswar, India
34: Also at Institute of Physics, Bhubaneswar, India
35: Also at G.H.G. Khalsa College, Punjab, India
36: Also at Shoolini University, Solan, India
37: Also at University of Hyderabad, Hyderabad, India
38: Also at University of Visva-Bharati, Santiniketan, India
39: Also at Indian Institute of Technology (IIT), Mumbai, India
40: Also at Tata Institute of Fundamental Research-B, Mumbai, India
41: Also at Deutsches Elektronen-Synchrotron, Hamburg, Germany
42: Also at Sharif University of Technology, Tehran, Iran
43: Also at Department of Physics, University of Science and Technology of Mazandaran, Behshahr, Iran
44: Now at INFN Sezione di Bari[a], Università di Bari[b], Politecnico di Bari[c], Bari, Italy
45: Also at Italian National Agency for New Technologies, Energy and Sustainable Economic Development, Bologna, Italy
46: Also at Centro Siciliano di Fisica Nucleare e di Struttura Della Materia, Catania, Italy
47: Also at Università di Napoli 'Federico II', Naples, Italy
48: Also at Riga Technical University, Riga, Latvia
49: Also at Consejo Nacional de Ciencia y Tecnología, Mexico City, Mexico
50: Also at Institute for Nuclear Research, Moscow, Russia
51: Now at National Research Nuclear University 'Moscow Engineering Physics Institute' (MEPhI), Moscow, Russia

52: Also at Institute of Nuclear Physics of the Uzbekistan Academy of Sciences, Tashkent, Uzbekistan
53: Also at St. Petersburg State Polytechnical University, St. Petersburg, Russia
54: Also at University of Florida, Gainesville, USA
55: Also at Imperial College, London, UK
56: Also at Moscow Institute of Physics and Technology, Moscow, Russia
57: Also at California Institute of Technology, Pasadena, USA
58: Also at Budker Institute of Nuclear Physics, Novosibirsk, Russia
59: Also at Faculty of Physics, University of Belgrade, Belgrade, Serbia
60: Also at Trincomalee Campus, Eastern University, Nilaveli, Sri Lanka
61: Also at INFN Sezione di Pavia[a], Università di Pavia[b], Pavia, Italy
62: Also at National and Kapodistrian University of Athens, Athens, Greece
63: Also at Universität Zürich, Zurich, Switzerland
64: Also at Ecole Polytechnique Fédérale Lausanne, Lausanne, Switzerland
65: Also at Stefan Meyer Institute for Subatomic Physics, Vienna, Austria
66: Also at Laboratoire d'Annecy-le-Vieux de Physique des Particules, IN2P3-CNRS, Annecy-le-Vieux, France
67: Also at Şırnak University, Sirnak, Turkey
68: Also at Department of Physics, Tsinghua University, Beijing, China
69: Also at Near East University, Research Center of Experimental Health Science, Nicosia, Turkey
70: Also at Beykent University, Istanbul, Turkey
71: Also at Istanbul Aydin University, Application and Research Center for Advanced Studies (App. & Res. Cent. for Advanced Studies), Istanbul, Turkey
72: Also at Mersin University, Mersin, Turkey
73: Also at Piri Reis University, Istanbul, Turkey
74: Also at Adiyaman University, Adiyaman, Turkey
75: Also at Ozyegin University, Istanbul, Turkey
76: Also at Izmir Institute of Technology, Izmir, Turkey
77: Also at Necmettin Erbakan University, Konya, Turkey
78: Also at Bozok Universitetesi Rektörlügü, Yozgat, Turkey, Yozgat, Turkey
79: Also at Marmara University, Istanbul, Turkey
80: Also at Milli Savunma University, Istanbul, Turkey
81: Also at Kafkas University, Kars, Turkey
82: Also at Istanbul Bilgi University, Istanbul, Turkey
83: Also at Hacettepe University, Ankara, Turkey
84: Also at Vrije Universiteit Brussel, Brussels, Belgium
85: Also at School of Physics and Astronomy, University of Southampton, Southampton, UK
86: Also at IPPP Durham University, Durham, UK
87: Also at Monash University, Faculty of Science, Clayton, Australia
88: Also at Bethel University, St. Paul, Minneapolis, USA
89: Also at Karamanoğlu Mehmetbey University, Karaman, Turkey
90: Also at Ain Shams University, Cairo, Egypt
91: Also at Bingol University, Bingol, Turkey
92: Also at Georgian Technical University, Tbilisi, Georgia
93: Also at Sinop University, Sinop, Turkey
94: Also at Mimar Sinan University, Istanbul, Istanbul, Turkey
95: Also at Texas A&M University at Qatar, Doha, Qatar
96: Also at Kyungpook National University, Daegu, Korea

Appendix 2

II

CMS Collaboration, "Search for Higgs boson pairs decaying to WW*WW*, WW*$\tau\tau$, and $\tau\tau\tau\tau$ in proton-proton collisions at $\sqrt{s} = 13$ TeV", *JHEP*, vol. 07, p. 095, 2023. doi: 10.1007/JHEP07(2023)095. arXiv: 2206.10268 [hep-ex]

Published for SISSA by Springer

Received: *June 21, 2022*
Accepted: *November 27, 2022*
Published: *July 12, 2023*

Search for Higgs boson pairs decaying to WW^*WW^*, $WW^*\tau\tau$, and $\tau\tau\tau\tau$ in proton-proton collisions at $\sqrt{s} = 13$ TeV



The CMS collaboration

E-mail: cms-publication-committee-chair@cern.ch

Abstract: The results of a search for Higgs boson pair (HH) production in the WW^*WW^*, $WW^*\tau\tau$, and $\tau\tau\tau\tau$ decay modes are presented. The search uses 138 fb^{-1} of proton-proton collision data recorded by the CMS experiment at the LHC at a center-of-mass energy of 13 TeV from 2016 to 2018. Analyzed events contain two, three, or four reconstructed leptons, including electrons, muons, and hadronically decaying tau leptons. No evidence for a signal is found in the data. Upper limits are set on the cross section for nonresonant HH production, as well as resonant production in which a new heavy particle decays to a pair of Higgs bosons. For nonresonant production, the observed (expected) upper limit on the cross section at 95% confidence level (CL) is 21.3 (19.4) times the standard model (SM) prediction. The observed (expected) ratio of the trilinear Higgs boson self-coupling to its value in the SM is constrained to be within the interval −6.9 to 11.1 (−6.9 to 11.7) at 95% CL, and limits are set on a variety of new-physics models using an effective field theory approach. The observed (expected) limits on the cross section for resonant HH production range from 0.18 to 0.90 (0.08 to 1.06) pb at 95% CL for new heavy-particle masses in the range 250–1000 GeV.

Keywords: Hadron-Hadron Scattering, Higgs Physics

ArXiv ePrint: 2206.10268

Open Access, Copyright CERN,
for the benefit of the CMS Collaboration.
Article funded by SCOAP[3].

https://doi.org/10.1007/JHEP07(2023)095

Contents

1 Introduction 1

2 The CMS detector 5

3 Data samples and Monte Carlo simulation 5

4 Event reconstruction 8

5 Event selection 11

6 Analysis strategy 13

7 Background estimation 18
- 7.1 Lepton and τ_h misidentification background 19
- 7.2 Charge misidentification background 21

8 Systematic uncertainties 21

9 Results 24

10 Summary 33

The CMS collaboration 44

JHEP07(2023)095

1 Introduction

Since the discovery of the Higgs (H) boson [1–3], many of its properties have already been measured with high precision [4–6]. One important property that remains largely unknown is the H boson self-coupling. A precise measurement of this coupling is necessary to determine the shape of the Higgs potential, and thus verify that the mechanism breaking the electroweak gauge symmetry is indeed the Higgs mechanism [7–12] of the standard model (SM) [13–15]. The SM predicts the existence of both trilinear and quartic H boson self-couplings. Due to the very low predicted cross section for triple H boson production, the SM quartic self-coupling will not be experimentally accessible at the CERN LHC, even with the full integrated luminosity of 3000 fb^{-1} scheduled to be delivered after the high-luminosity LHC upgrade [16, 17]. The strength of the trilinear self-coupling, however, can be determined using measurements of H boson pair (HH) production.

In the SM, most HH pairs are produced in two types of processes. The Feynman diagrams for the dominant "gluon fusion" (ggHH) process at leading order (LO) in perturbative quantum chromodynamics (QCD) are shown in figure 1. The left "triangle" diagram

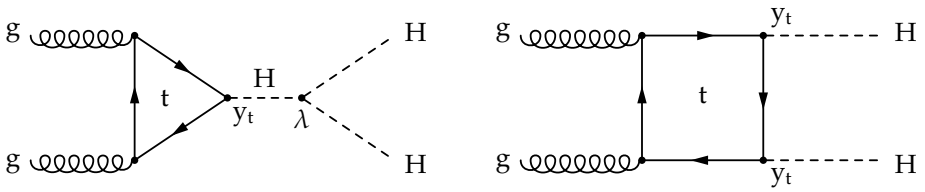


Figure 1. Leading order Feynman diagrams for SM nonresonant HH production via gluon fusion, including the "triangle" diagram (left) and the "box" diagram (right).

JHEP07(2023)095

amplitude varies proportionally to the H boson self-coupling (λ) and the Yukawa coupling of the top quark (y_t), while the right "box" diagram amplitude is insensitive to λ and varies as y_t^2. The triangle and box diagrams interfere destructively, so the ggHH cross section exhibits a strong dependence on both λ and y_t. The ggHH cross section in the SM has been computed to be $31.1^{+2.1}_{-7.2}$ fb at next-to-next-to-LO (NNLO) accuracy in QCD using the FT_{approx} scheme, in which the true top quark mass is used for the real radiation matrix elements, while the virtual part is computed using an infinite top quark mass [18]. The predicted SM cross section for the subdominant "vector boson fusion" (qqHH) process is 1.73 ± 0.04 fb at next-to-NNLO accuracy in QCD [19].

Deviations of the coupling strength modifiers $\kappa_\lambda = \lambda/\lambda^{SM}$ and $\kappa_t = y_t/y_t^{SM}$ from unity would affect both the rate of HH production and kinematic distributions of the HH signal. The HH invariant mass (m_{HH}) is particularly sensitive to changes in κ_λ and κ_t, as these couplings affect the triangle and box diagram amplitudes differently. Because SM ggHH and qqHH production do not include a heavy resonant particle, and typically result in a broad m_{HH} distribution, they are referred to as "nonresonant". Changes in κ_λ and κ_t also influence the rate of single Higgs boson production and the Higgs boson decay branching fractions [20, 21].

The presence of undiscovered particles or interactions, predicted by a variety of theoretical models beyond the SM, may alter the HH production rate as well as observable kinematic distributions. Such particles could give rise to loop diagrams similar to the one shown on the left of figure 1. These diagrams may significantly enhance the HH production rate, as they occur at the same loop level as HH production in the SM. Since no particles beyond those predicted by the SM have been observed so far, their mass may be at the TeV scale or higher, well above the scale of electroweak symmetry breaking. Loop contributions of such heavy particles can be approximated as contact interactions with the H boson using an effective field theory (EFT) approach [22, 23]. Following ref. [24], the contact interactions relevant for HH production are parametrized by the couplings c_g, c_{2g}, and c_2, referring to the interactions between two gluons and one H boson, two gluons and two H bosons, and two top quarks and two H bosons, respectively. The corresponding Feynman diagrams for ggHH production are shown in figure 2. The LO diagrams for qqHH production contain no gluons or top quarks, so the impacts of c_g, c_{2g}, and c_2 are only considered in the ggHH signal in this publication.

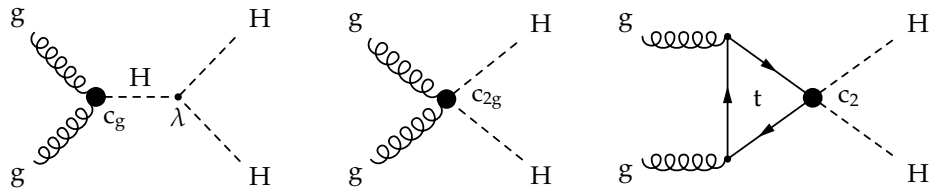


Figure 2. Leading order Feynman diagrams for nonresonant HH production via gluon fusion in an EFT approach, where loop-mediated contact interactions between (left) two gluons and one H boson, (middle) two gluons and two H bosons, and (right) two top quarks and two H bosons are parametrized by three effective couplings: c_g, c_{2g}, and c_2.

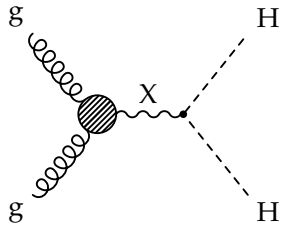


Figure 3. Leading order Feynman diagram for resonant HH production.

An excess of HH signal events may also result from decays of new heavy particles, denoted as X, into pairs of H bosons. Various theoretical models of new physics postulate such decays, in particular two-Higgs-doublet models [25, 26], composite-Higgs models [27, 28], Higgs portal models [29, 30], and models inspired by warped extra dimensions [31]. In the last class of models, the new heavy particles may have spin 0 ("radions") or spin 2 ("gravitons") [32]. In this paper, the resulting "resonant" HH production is sought for mass values of X from 250 to 1000 GeV, and the width of X is assumed to be negligible compared to the experimental resolution in m_{HH}. This would create a peak in the reconstructed m_{HH} distribution around the mass m_{X} of the resonance. The Feynman diagram for this process is shown in figure 3. For resonance masses above 1 TeV the strongest constraints are given by searches for HH production targeting H boson decays to bottom quarks [33–35], as the selection and reconstruction efficiency for hadronic decays increases, in particular in the trigger, and relevant backgrounds decrease with energy. For leptonic decay modes, the selection and reconstruction efficiency in general is high and as such do not increase notably for high masses above 1 TeV.

Phenomenological studies of the prospects for discovering HH signal in the $\mathrm{WW^*WW^*}$ decay mode are documented in refs. [36–40], where the symbol $*$ denotes virtual particles. The ATLAS Collaboration published results of a search for nonresonant and resonant HH pairs decaying to $\mathrm{WW^*WW^*}$ based on 36 fb^{-1} of proton-proton (pp) collision data recorded at $\sqrt{s} = 13$ TeV [41], placing an upper limit of 160 times the SM predicted cross section for nonresonant HH production at 95% confidence level (CL). Searches for HH production in pp collisions at $\sqrt{s} = 7$, 8, and 13 TeV have previously been performed by

JHEP07(2023)095

the CMS and ATLAS Collaborations in the decay modes $\mathrm{bb}\gamma\gamma$ [42, 43], bbbb [33, 44–47], $\mathrm{bb}\tau\tau$ [35, 48, 49], bbWW^* [34, 50–52], and $\mathrm{WW}^*\gamma\gamma$ [53]. Limits on HH production obtained from a combination of some of these analyses have been published by the CMS and ATLAS Collaborations [54, 55].

Searches targeting the $\mathrm{bb}\tau\tau$ [48], bbbb [45, 46], and $\mathrm{bb}\gamma\gamma$ [42] final states in CMS, and $\mathrm{bb}\tau\tau$ [35] and $\mathrm{bb}\gamma\gamma$ [43] in ATLAS, provide the strongest constraints on nonresonant HH production to date, with observed (expected) 95% CL upper limits ranging from 3.3 to 9.9 (3.9 to 7.8) times the SM predicted cross section. The corresponding lower bounds on κ_λ vary from -1.5 to -3.3 (-2.4 to -5.0 expected), with upper bounds between 6.7 and 9.4 (7.7 to 12.0 expected). The ATLAS $\mathrm{bb}\gamma\gamma$ analysis places a 95% CL upper limit of 0.64 pb on resonant HH production with a mass around 250 GeV (where 0.39 pb was expected) [43], while the ATLAS resonant bbbb search constrains higher mass hypotheses most strongly, with observed and expected limits around 0.01 pb at 1 TeV [33]. The ATLAS $\mathrm{bb}\tau\tau$ performs best for many mass points in between [35]. The only published HH search using an EFT approach comes from CMS in the $\mathrm{bb}\gamma\gamma$ final state, with 95% CL upper limits on the HH production cross section ranging from 0.1 to 0.6 pb, depending on the EFT scenario [42].

This paper presents the first search for H boson pairs decaying to $\mathrm{WW}^*\mathrm{WW}^*$, $\mathrm{WW}^*\tau\tau$, and $\tau\tau\tau\tau$. Both nonresonant and resonant HH production in final states with multiple reconstructed leptons, i.e., electrons (e), muons (μ), or hadronically decaying tau leptons (τ_h) are covered. The search is based on LHC pp collision data recorded by the CMS experiment at a center-of-mass energy of 13 TeV, corresponding to an integrated luminosity of 138 fb^{-1}. Signal candidate events are subdivided into seven mutually exclusive "search categories" based on ℓ (e, μ) and τ_h multiplicity: two same-sign ℓ with fewer than two τ_h ($2\ell\mathrm{ss}$), three ℓ with no τ_h (3ℓ), four ℓ (4ℓ), three ℓ with one additional τ_h ($3\ell+1\tau_\mathrm{h}$), two ℓ with two τ_h ($2\ell+2\tau_\mathrm{h}$), one ℓ with three τ_h ($1\ell+3\tau_\mathrm{h}$), or four τ_h with no ℓ ($4\tau_\mathrm{h}$). In final states with a total of four ℓ and τ_h, the charge sum of all ℓ and τ_h candidates is required to be zero. The seven search categories target HH signal events in which the H boson pair decays into $\mathrm{WW}^*\mathrm{WW}^*$, $\mathrm{WW}^*\tau\tau$, or $\tau\tau\tau\tau$. Multivariate analysis (MVA) methods are used to distinguish the HH signal from backgrounds.

The paper is structured as follows. A brief overview of the CMS detector is given in section 2. Section 3 lists the data sets and simulation samples used. The reconstruction of e, μ, τ_h, and jets, along with various kinematic observables, is detailed in section 4. This is followed by a description, in section 5, of the event selection criteria defining the seven search categories. The multivariate methods used to distinguish the HH signal from backgrounds are detailed in section 6. The estimation of these backgrounds is described in section 7, followed by an outline of the relevant systematic uncertainties in section 8. The statistical procedure used to extract limits on the HH production rate in the SM, as well as constraints on SM coupling strengths, EFT benchmark scenarios, and resonant HH production rates are presented in section 9. The paper concludes with a summary in section 10.

JHEP07(2023)095

2 The CMS detector

The central feature of the CMS apparatus is a superconducting solenoid of 6 m internal diameter, providing a magnetic field of 3.8 T. Within the solenoid volume are a silicon pixel and strip tracker, a lead tungstate crystal electromagnetic calorimeter (ECAL), and a brass and scintillator hadron calorimeter (HCAL), each composed of one barrel and two endcap sections. The silicon tracker measures charged particles within the pseudorapidity range $|\eta| < 2.5$ for data recorded in 2016, and within the range $|\eta| < 3.0$ for data recorded in 2017 and 2018. The ECAL is a fine-grained hermetic calorimeter with quasi-projective geometry, and is divided into a barrel region covering $|\eta| < 1.5$, and two endcaps that extend to $|\eta| = 3.0$. The HCAL barrel and endcaps similarly cover the region $|\eta| < 3.0$. Forward calorimeters extend beyond these endcaps to $|\eta| = 5.0$. Muons are detected within the range $|\eta| < 2.4$ by gas-ionization detectors embedded in the steel flux-return yoke outside the solenoid. Collision events of interest are selected using a two-tiered trigger system. The level-1 trigger, composed of custom hardware processors, uses information from the calorimeters and muon detectors to select less than 100 kHz of events from a 40 MHz base event rate, within a fixed latency of 4 μs [56]. The second tier, known as the high-level trigger, is a processor farm which runs a version of the full event reconstruction software optimized for fast processing, and reduces the event rate to around 1 kHz before data storage [57]. A more detailed description of the CMS detector, together with a definition of the coordinate system used and the most relevant kinematic variables, can be found in ref. [58].

3 Data samples and Monte Carlo simulation

The analyzed pp collision data correspond to an integrated luminosity of 138 fb^{-1}, collected by the CMS detector over three years: 36 fb^{-1} in 2016, 42 fb^{-1} in 2017, and 60 fb^{-1} in 2018 [59–61]. This analysis uses triggers requiring one or more reconstructed e, μ, or τ_h candidates to be associated with the same collision vertex. The exact triggers and their thresholds varied slightly from year to year because of changes in luminosity and detector conditions, as well as improvements to the trigger algorithms. The transverse momentum (p_T) thresholds imposed by the trigger on the "leading" (highest p_T), "subleading" (second-highest p_T), and third e, μ, or τ_h, and the corresponding η requirements for each year are shown in table 1. All triggers include identification and isolation requirements on the e, μ, and τ_h candidates [57]. When combined, the triggers achieve an efficiency of 95–100% for simulated SM HH signal events in each of the seven search categories.

Monte Carlo (MC) simulated samples are used to model HH signal events and a wide range of SM background processes that produce final states with e, μ, or τ_h. Background MC samples include processes producing a single W or Z boson, two bosons (WW, WZ, ZZ, Wγ, and Zγ), three bosons (WWW, WWZ, WZZ, ZZZ, and WZγ), a single H boson (via gluon fusion, vector boson fusion, or associated production with a W or Z boson), a single top quark, a top quark-antiquark pair ($t\bar{t}$), and top quarks associated with one or more bosons ($t\bar{t}W$, $t\bar{t}Z$, $t\bar{t}H$, tHq, and tHW). All MC samples were generated using either

JHEP07(2023)095

Trigger	Selection requirements for reconstructed e, μ, and τ_h objects
Single e	$p_T(e) > 27$–35 GeV
Single μ	$p_T(\mu) > 22$–27 GeV
Double e	$p_T(e) > 23, 12$ GeV
e + μ	$p_T(e) > 23$ GeV, $p_T(\mu) > 8$ GeV
μ + e	$p_T(\mu) > 23$ GeV, $p_T(e) > 8$–12 GeV
Double μ	$p_T(\mu) > 17, 8$ GeV
e + τ_h	$p_T(e) > 24$ GeV, $p_T(\tau_h) > 20$–30 GeV, $\lvert\eta(e, \tau_h)\rvert < 2.1$
μ + τ_h	$p_T(\mu) > 19$–20 GeV, $p_T(\tau_h) > 20$–27 GeV, $\lvert\eta(\mu, \tau_h)\rvert < 2.1$
Double τ_h	$p_T(\tau_h) > 35$–40 GeV, $\lvert\eta(\tau_h)\rvert < 2.1$
Triple e	$p_T(e) > 16, 12, 8$ GeV
Two e + μ	$p_T(e) > 12, 12$ GeV, $p_T(\mu) > 8$ GeV
Two μ + e	$p_T(\mu) > 9, 9$ GeV, $p_T(e) > 9$ GeV
Triple μ	$p_T(\mu) > 12, 10, 5$ GeV

Table 1. Selection requirements on p_T and η of reconstructed electrons (e), muons (μ), and hadronically decaying tau leptons (τ_h) applied by the triggers used in this analysis. The trigger p_T thresholds for leading, subleading, and third e, μ, or τ_h are separated by commas. For trigger thresholds that varied over time, the range of variation is indicated.

MadGraph5_aMC@NLO v2 [62, 63], POWHEG v2 [64–66], MCFM v7 [67–69], or PYTHIA v8.2 [70]. All samples that include a H boson were produced for a H boson mass of 125 GeV. Specific details of the simulated processes are summarized in table 2.

The parton distribution functions (PDFs) of the proton are modeled using the NNPDF3.0 and NNPDF3.1 PDF sets [85–89]. Parton shower, hadronization processes, and τ decays are modeled by PYTHIA, using the tunes CP5, CUETP8M1, CUETP8M2, or CUETP8M2T4 [90–92], depending on the process and the data-taking period that is being modeled. The matching of matrix elements to parton showers is performed using the MLM scheme [93] for the LO samples and the FxFx scheme [94] for the NLO samples. The interactions of particles with the CMS detector material was simulated in detail using Geant4 [95]. Simulated events were reconstructed using the same procedure as in data. The response of the trigger is included in the simulation. Additional pp interactions (pileup) were generated with PYTHIA and overlaid on all MC events, with event weights used to match the collision multiplicity to the distribution inferred from data. Residual differences between data and simulation are rectified by applying corrections to simulated events.

A variety of HH signal samples were generated at LO and NLO accuracy in QCD to simulate nonresonant HH production, covering the ggHH and qqHH production processes, with the H bosons decaying to either WW^*, ZZ^*, or ττ. The NLO samples are used to extract the rate of the HH signal from the data, while LO samples with a larger number of simulated events are used to train machine learning algorithms. Separate ggHH samples are produced for SM HH production and for a total of twelve EFT benchmark (BM) scenarios in the Higgs Effective Field Theory (HEFT) approach [24]. These benchmarks, along with

JHEP07(2023)095

Process	MC generator (order)	Cross section order
ggHH	MadGraph5_aMC@NLO v2 (LO) [71, 72]	NNLO $\mathrm{FT}_{\mathrm{approx}}$
	POWHEG v2 (NLO) [73–75]	
qqHH	MadGraph5_aMC@NLO v2 (LO)	N3LO
Single H boson production		
(via gluon fusion)	POWHEG v2 (NLO) [76]	N3LO QCD, NLO EW
(via vector boson fusion)	POWHEG v2 (NLO) [77]	NNLO QCD, NLO EW
(with a W or a Z boson)	POWHEG v2 (NLO) [78]	NNLO QCD, NLO EW
(with a pair of top quarks)	MadGraph5_aMC@NLO v2 (NLO)	NLO QCD, NLO EW
(with a single top quark)	MadGraph5_aMC@NLO v2 (LO)	NLO
W	MadGraph5_aMC@NLO v2 (LO)	NNLO
Z	MadGraph5_aMC@NLO v2 (LO)	NNLO QCD, NLO EW
WW (double-parton interaction)	PYTHIA v8.2 (LO)	LO
(same-sign pair)	MadGraph5_aMC@NLO v2 (LO)	LO
(opposite-sign pair)	POWHEG v2 (NLO) [79, 80]	NNLO
WZ	MadGraph5_aMC@NLO v2 (NLO)	NNLO
ZZ (quark-initiated)	POWHEG v2 (NLO) [79, 80]	NNLO
(gluon-initiated)	MCFM v7 (LO) [81]	NLO
$\mathrm{W}\gamma$, $\mathrm{Z}\gamma$, $\mathrm{WZ}\gamma$, $\mathrm{t}\gamma$, $\mathrm{t\bar{t}}\gamma$	MadGraph5_aMC@NLO v2 (NLO)	NLO
WWW, WWZ, WZZ, ZZZ	MadGraph5_aMC@NLO v2 (NLO)	NLO
Single top	POWHEG v2 (NLO) [82]	NLO
(with a W boson)	POWHEG v2 (NLO) [83]	NLO
(with a Z boson)	MadGraph5_aMC@NLO v2 (NLO)	NLO
$\mathrm{t\bar{t}}$	POWHEG v2 (NLO) [84]	NNLO
$\mathrm{t\bar{t}t\bar{t}}$	MadGraph5_aMC@NLO v2 (NLO)	NLO
$\mathrm{t\bar{t}W}$	MadGraph5_aMC@NLO v2 (NLO QCD, NLO EW)	NLO QCD, NLO EW
$\mathrm{t\bar{t}Z}$	MadGraph5_aMC@NLO v2 (NLO)	NLO QCD, NLO EW
$\mathrm{t\bar{t}WW}$, $\mathrm{t\bar{t}WZ}$, $\mathrm{t\bar{t}ZZ}$	MadGraph5_aMC@NLO v2 (LO)	LO

Table 2. The MC generators that are used to simulate HH signal and background processes. The order of MC simulation and cross section calculation both refer to the perturbative expansion in QCD. Additional higher order electroweak (EW) corrections, if present, are indicated separately.

the seven benchmarks from ref. [96], represent different combinations of κ_λ, κ_t, $\mathrm{c_g}$, $\mathrm{c_{2g}}$, and $\mathrm{c_2}$ HEFT parameter values, and are chosen to probe distinct classes of HH kinematic configurations. These benchmarks are referred to as JHEP04 BM1-12, and JHEP03 BM1-7, respectively. The benchmark JHEP04 BM8 is complemented by a modified version of this benchmark, published in ref. [97], denoted as JHEP04 BM8a. The parameter values of these twenty BM scenarios are shown in table 3. The values of the $\mathrm{c_g}$ and $\mathrm{c_{2g}}$ couplings published in ref. [96] have been scaled by factors of 1.5 and -3, respectively, to convert them to the convention introduced for these couplings in ref. [24]. In order to increase the number of simulated events and to model kinematic configurations not explicitly generated, such as JHEP03 BM1-7, the ggHH samples are merged and the events in the merged samples are reweighted, using the procedure documented in ref. [98], to match the distributions in m_{HH} and $|\cos\theta^*|$ computed at NLO accuracy and published in ref. [97]. This procedure is applied to the LO and NLO ggHH samples separately. The symbol $\cos\theta^*$ denotes the cosine of the polar angle of one H with respect to the beam axis in the HH rest frame. The qqHH samples are produced only for SM HH production.

JHEP07(2023)095

Benchmark	κ_λ	κ_t	c_2	c_g	c_{2g}
JHEP04 BM1	7.5	1.0	−1.0	0.0	0.0
JHEP04 BM2	1.0	1.0	0.5	−0.8	0.6
JHEP04 BM3	1.0	1.0	−1.5	0.0	−0.8
JHEP04 BM4	−3.5	1.5	−3.0	0.0	0.0
JHEP04 BM5	1.0	1.0	0.0	0.8	−1.0
JHEP04 BM6	2.4	1.0	0.0	0.2	−0.2
JHEP04 BM7	5.0	1.0	0.0	0.2	−0.2
JHEP04 BM8	15.0	1.0	0.0	−1.0	1.0
JHEP04 BM8a	1.0	1.0	0.5	4/15	0.0
JHEP04 BM9	1.0	1.0	1.0	−0.6	0.6
JHEP04 BM10	10.0	1.5	−1.0	0.0	0.0
JHEP04 BM11	2.4	1.0	0.0	1.0	−1.0
JHEP04 BM12	15.0	1.0	1.0	0.0	0.0
JHEP03 BM1	3.94	0.94	−1/3	0.75	−1
JHEP03 BM2	6.84	0.61	1/3	0	1
JHEP03 BM3	2.21	1.05	−1/3	0.75	−1.5
JHEP03 BM4	2.79	0.61	1/3	−0.75	−0.5
JHEP03 BM5	3.95	1.17	−1/3	0.25	1.5
JHEP03 BM6	5.68	0.83	1/3	−0.75	−1
JHEP03 BM7	−0.10	0.94	1	0.25	0.5
SM	1.0	1.0	0.0	0.0	0.0

Table 3. Parameter values for κ_λ, κ_t, c_2, c_g, and c_{2g} in MC samples modeling twenty benchmark scenarios in the EFT approach, plus SM HH production.

Resonant HH production was simulated at LO for both spin-0 (radion) and spin-2 (graviton) scenarios with m_X values of 250, 260, 270, 280, 300, 320, 350, 400, 450, 500, 550, 600, 650, 700, 750, 800, 850, 900, and 1000 GeV.

4 Event reconstruction

The CMS particle-flow (PF) algorithm [99] aims to reconstruct and identify each individual particle in an event, using an optimized combination of information from the various elements of the CMS detector. The particles are subsequently classified into five mutually exclusive types: electrons, muons, photons, and charged and neutral hadrons. These particles are then combined to reconstruct hadronic τ decays, jets, and the missing transverse momentum in the event.

The candidate vertex with the largest value of summed physics-object p_T^2 is taken to be the primary pp interaction vertex. The physics objects used for this determination are the jets, clustered using the infrared and collinear safe anti-k_T algorithm [100, 101], with the tracks assigned to candidate vertices as inputs, and the associated missing transverse momentum, taken as the negative vector sum of the p_T of those jets.

Electrons are reconstructed within the geometric acceptance of the tracking detectors ($|\eta| < 2.5$) by combining information from the tracker and the ECAL [102]. They are

JHEP07(2023)095

initially identified using an MVA classifier which distinguishes real electrons from hadrons, along with requirements that the track be associated with the collision vertex, and limits on hadronic energy deposits separated by $\Delta R < 0.4$ from the electrons (their "isolation"). The angular separation between two particles is defined as $\Delta R = \sqrt{(\eta_1 - \eta_2)^2 + (\phi_1 - \phi_2)^2}$, where the symbol ϕ refers to the azimuthal angle of the particle. Electrons passing this initial selection are referred to as "loose". In this analysis, events with electrons originating from hadron decays ("nonprompt"), or with hadrons misidentified as electrons, constitute the largest source of background. This motivates the use of an additional MVA classifier, which is trained to select "prompt" electrons from W, Z, and τ lepton decays, and to reject nonprompt or misidentified electrons. This MVA classifier was previously used for measurements of $\mathrm{t\bar{t}H}$ production in events with multiple leptons [103]. It combines observables comparing measurements of the electron energy and direction in the tracker and the ECAL, the compactness of the electron cluster, the bremsstrahlung emitted along the electron trajectory, and the electron isolation. Two levels of thresholds on the output of this MVA classifier are used in the analysis, referred to as the "tight" and "medium" electron selections for the more and less restrictive thresholds, respectively. The tight selection has an average efficiency of 60% for electrons from SM HH decays. Only the electrons passing the tight selections are used to reconstruct signal candidate events, while data events with electrons passing the medium selections and failing the tight selections are used to estimate the contribution of misidentified- and nonprompt-electron backgrounds in each search category. Compared to ref. [103], this analysis uses lower thresholds on the MVA classifier output for the medium and tight electron selections, in order to increase the efficiency in particular for low-p_{T} electrons, which frequently appear in the HH signal events studied in this analysis. Electrons from photon conversions in the tracker are suppressed by requiring that the track is missing no hits in the innermost layers of the silicon tracker, and is not matched to a reconstructed conversion vertex. In the 2ℓss category, further electron selection criteria are applied, which require agreement among three independent measurements of the electron charge, including the Gaussian sum filter and Kalman filter track curvatures, as well as the ECAL supercluster position [104]. The remaining charge misidentification rate is measured to be less than 0.1% for $|\eta| < 1.479$, and under 0.4% for $|\eta| > 1.479$. The charge quality requirement reduces the electron identification efficiency by about 4%.

Muons are reconstructed by extrapolating tracks in the silicon tracker to hits in the gas-ionization muon detectors embedded in the steel flux-return yoke outside the solenoid [105]. To pass the initial loose identification requirement for this analysis, muons must satisfy criteria related to isolation and track proximity to the primary interaction vertex, as well as track quality observables and matching between the tracker and muon chambers. Additional requirements on the prompt vs. nonprompt muon identification MVA classifier from ref. [103] serve to select muons passing a tight selection for signal candidate events, and a medium selection for nonprompt background estimation. Inputs to this MVA classifier include energy deposits close to the muon in the ECAL and HCAL, the hits and track segments reconstructed in the muon detectors located outside the solenoid, the quality of

JHEP07(2023)095

the spatial matching between the track segments reconstructed in the silicon tracker and in the muon detectors, and the isolation of the muon with respect to other particles. Again, lower selection thresholds on the MVA classifier output compared to ref. [103] bring higher efficiency for the HH signal, amounting to 80% per muon in simulated SM HH events for the tight selection. In the 2ℓss channel, the uncertainty in the curvature of the muon track is required to be less than 20% to ensure a high-quality charge measurement [103]. This requirement reduces the muon identification efficiency by about 2%.

Hadronic decays of tau leptons are identified using the "hadrons-plus-strips" algorithm [106]. This algorithm classifies individual hadronic decay modes of the τ by combining charged hadrons from the PF reconstruction with neutral pions. The latter are reconstructed by clustering electrons and photons into rectangular strips, which are narrow in η but wide in the ϕ direction. The spread in ϕ accounts for photons originating from neutral pion decays that convert into electron-positron (e^-e^+) pairs while traversing the silicon tracker. The e^- and e^+ are bent in opposite directions in ϕ by the magnetic field, and may further emit bremsstrahlung photons before reaching the ECAL. The decay modes considered in this analysis produce one charged pion or kaon plus up to two neutral pions (collectively referred to as "one-prong" τ_h), or three charged pions or kaons plus zero or one neutral pion (referred to as "three-prong" τ_h). The DeepTau algorithm [107] distinguishes true τ_h objects from quark and gluon jets, electrons, and muons using a convolutional artificial neural network (NN) [108] with 42 high-level observables as input, together with low-level information obtained from the silicon tracker, ECAL, HCAL, and the muon detectors. The former include the p_T, η, ϕ, and mass of the τ_h candidate, the reconstructed τ_h decay mode, its isolation with respect to charged and neutral particles, and the estimated distance that the τ lepton traverses between its production and decay. For three-prong τ_h candidates, this distance is determined by reconstructing the decay vertex, while for one-prong τ_h candidates, the transverse impact parameter of the charged pion track with respect to the primary pp interaction vertex is used as an estimate of the distance. The low-level information quantifies the particle activity within two $\eta \times \phi$ grids, centered on the direction of the τ_h candidate: an inner grid of size 0.2×0.2, filled with 0.02×0.02 cells, and an outer grid of size 0.5×0.5 (partially overlapping with the inner grid), with 0.05×0.05 cells. Selected τ_h candidates in this analysis must have $p_T > 20\,\text{GeV}$ and $|\eta| < 2.3$, and are subjected to two levels of thresholds on the NN output that separates τ_h from quark and gluon jets, referred to as the tight and medium τ_h selections, respectively.

Hadronic jets (j) are reconstructed with the anti-k_T algorithm using the particles reconstructed with the PF algorithm as input, and serve to identify $H \to WW^* \to jj\ell\nu$ decays in this analysis. Jets reconstructed with size parameters of 0.4 ("small-radius jets") and 0.8 ("large-radius jets") are both used: two small-radius jets to reconstruct the two quarks from low-p_T W boson decays, or a single large-radius jet to reconstruct high-p_T W boson decays, where the quarks are collimated. Overlap between small-radius jets and electrons, muons, and τ_h is resolved by discarding those small-radius jets that contain one or more PF particles matched to an electron, a muon, or a constituent of a τ_h passing the medium selection criteria. In case of large-radius jets, electrons and muons passing

JHEP07(2023)095

the loose selection are removed from the collection of PF particles used as input to the jet reconstruction, so that leptons produced in $H \to WW^* \to jj\ell\nu$ decays of Lorentz-boosted H bosons are not clustered into those jets.

The effect of pileup on the reconstruction of large-radius jets is mitigated by applying the pileup per particle identification algorithm (PUPPI) [109, 110] to the collection of particles used as input to the jet reconstruction. For small-radius jets, the effect of pileup is reduced by removing charged particles identified with pileup vertices from the jet reconstruction, and applying corrections to the jet energy to account for neutral particles from pileup.

After calibration, the jet energy resolution at the central rapidities amounts to 15–20% at 30 GeV, 10% at 100 GeV, and 5% at 1 TeV [111]. This analysis only considers jets reconstructed in the region $|\eta| < 2.4$. Small-radius jets must have $p_T > 25$ GeV, while large-radius jets must have $p_T > 170$ GeV. Additional criteria requiring that each large-radius jet contain exactly two identifiable, energetic subjets are applied to specifically select those from boosted hadronic W boson decays [112].

Events containing small-radius jets identified with the hadronization of bottom quarks (b jets) are vetoed in this analysis. The DeepJet algorithm [113] exploits observables related to the long lifetime of b hadrons and the higher particle multiplicity and mass of b jets compared to light quark and gluon jets. Both "loose" and "medium" b jet selections on the DeepJet output are employed in this analysis, corresponding to b jet selection efficiencies of 84 and 70%, while the misidentification rates for light-quark or gluon jets are 11 and 1.1%, respectively.

The missing transverse momentum vector $\vec{p}_T^{\,miss}$ is computed as the negative vector p_T sum of all the particles reconstructed by the PF algorithm in an event, and its magnitude is denoted as p_T^{miss} [114]. The $\vec{p}_T^{\,miss}$ is modified to account for corrections to the energy scale of the reconstructed jets in the event. A linear discriminant, denoted as $p_T^{miss,LD}$, is employed to remove background events in which the reconstructed p_T^{miss} arises from resolution effects. The discriminant is defined by the relation $p_T^{miss,LD} = 0.6 p_T^{miss} + 0.4 H_T^{miss}$, where H_T^{miss} corresponds to the magnitude of the vector p_T sum of e, μ, and τ_h passing the medium selection criteria, and small-radius jets satisfying the criteria detailed above [115].

5 Event selection

Events are selected with the aim of maximizing the acceptance for HH decays to WW^*WW^*, $WW^*\tau\tau$, and $\tau\tau\tau\tau$, while simultaneously rejecting the large backgrounds from multijet production, single and pair production of W and Z bosons, and $t\bar{t}$ production. To achieve this, each event must contain multiple reconstructed ℓ or τ_h associated with the primary interaction vertex. The ℓ and τ_h may originate from the decay of a W boson or a τ lepton. Seven mutually exclusive search categories, distinguished by the number of reconstructed ℓ and τ_h candidates, are included in the analysis: 2ℓss, 3ℓ, 4ℓ, $3\ell + 1\tau_h$, $2\ell + 2\tau_h$, $1\ell + 3\tau_h$, and $4\tau_h$. Here "ss" indicates a same-sign $\ell\ell$ pair, with two leptons of identical electric charge. The ℓ and τ_h candidates selected in any of the seven search categories must pass the tight selection criteria described in section 4. In addition,

JHEP07(2023)095

they are required to pass category-specific p_T thresholds motivated by the trigger selection. Further requirements are placed on the sum of ℓ and τ_h charges, and, in two categories, on the discriminant $p_T^{miss,LD}$ and the multiplicity of jets.

The leading and subleading leptons in the 2ℓss category must pass p_T selection thresholds of 25 and 15 GeV, respectively. Events in this category are required to contain two or more small-radius jets, or at least one large-radius jet, targeting hadronic W boson decays. Dielectron events must have $p_T^{miss,LD} > 30$ GeV and $m(\ell\ell) < 81$ GeV or $m(\ell\ell) > 101$ GeV, in order to suppress charge-misidentified $Z \to ee$ background. If the event contains a τ_h, the charge of the τ_h must be opposite to the charge of the leptons. After this selection, the main backgrounds in the 2ℓss category arise from WZ production, from $W\gamma$ events in which the photon converts into an e^-e^+ pair and either the e^- or the e^+ is not reconstructed, and from events in which one or both reconstructed leptons are due to a nonprompt ℓ or a misidentified hadron, as shown in table 6. The "other" background given in the table is dominated by same-sign W boson pairs and WWW production. The WW^*WW^* decay mode accounts for roughly 70% of SM HH signal events selected in the 2ℓss category, with $WW^*\tau\tau$ events accounting for the other 30%.

In the 3ℓ category, the leading, subleading, and third ℓ are required to have p_T values greater than 25, 15, and 10 GeV, respectively, and the sum of their charges must be either $+1$ or -1. At least one small- or large-radius jet must be present, and the $p_T^{miss,LD}$ quantity must be greater than 30 GeV, or 45 GeV if there is at least one same-flavor opposite-sign (SFOS) $\ell\ell$ pair in the event. Again, backgrounds are dominated by WZ production and events with misidentified ℓ. Notable contributions to the "other" background arise from WWW and WWZ production. The signal composition is similar to the 2ℓss category.

The 4ℓ category has identical lepton selection criteria to the 3ℓ category, except that the third ℓ must have $p_T > 15$ GeV, and a fourth ℓ with $p_T > 10$ GeV is required, and the sum of the four lepton charges is required to be equal to zero. In this category and all the remaining categories, there are no selection requirements on jets or $p_T^{miss,LD}$. Almost 70% of signal events come from the WW^*WW^* decay mode, and about 30% from $WW^*\tau\tau$, while ZZ production accounts for 85% of the background.

Events in the $3\ell + 1\tau_h$ category are required to satisfy the 3ℓ criteria on the ℓ objects, except that an additional τ_h with $p_T > 20$ GeV and charge opposite to the sum of the ℓ charges is required. Background events in which the reconstructed τ_h fails a loose selection on the NN output of the DeepTau algorithm that separates τ_h from electrons, or falls near the ECAL barrel-endcap transition region in $1.460 < |\eta| < 1.558$ are removed. About 70% of signal events come from the $WW^*\tau\tau$ decay mode, while ZZ production and events with at least one misidentified ℓ or τ_h dominate the background.

In the $2\ell+2\tau_h$ category, the leading and subleading ℓ are required to pass p_T thresholds of 25 and 15 GeV, while the two τ_h must have $p_T > 20$ GeV. The sum of ℓ plus τ_h charges is required to be zero. Signal contributions are mostly from the $WW^*\tau\tau$ (60%) and $\tau\tau\tau\tau$ (40%) decay modes, while background contributions arise from ZZ production and events with a misidentified ℓ or τ_h candidate.

In the $1\ell + 3\tau_h$ category, the ℓ is required to satisfy the conditions $|\eta| < 2.1$ and $p_T > 20$ (15) GeV if it is an electron (muon). The leading, subleading, and third τ_h must

JHEP07(2023)095

have $p_T > 40$, 30, and 20 GeV, respectively, and the sum of τ_h and ℓ charges is required to be zero. Background events containing a $Z \to ee$ decay where one electron is misidentified as a τ_h are vetoed by discarding events containing an e-τ_h pair of opposite charge and mass $71 < m(e\tau_h) < 101$ GeV, and in which the τ_h either fails a loose selection on the discriminant that separates τ_h from electrons, or falls into the region $1.460 < |\eta| < 1.558$. Around 80% of HH signal events selected in the $1\ell + 3\tau_h$ category are from $\tau\tau\tau\tau$ and 20% from the $WW^*\tau\tau$ decay mode, while the majority of background events stem from ZZ production or contain a misidentified ℓ or τ_h.

The $4\tau_h$ category requires the leading and subleading τ_h to pass p_T thresholds of 40 and 30 GeV, respectively, and the third and fourth τ_h to have $p_T > 20$ GeV. Given the extremely low backgrounds in this category, no charge sum criterion or $Z \to ee$ veto is applied. Almost all signal events come from the $\tau\tau\tau\tau$ decay mode, while 55% of the background events contain at least one misidentified τ_h candidate, and the remainder arises from ZZ (30%) and single Higgs boson (15%) production.

In all seven search categories, the background contamination from processes with top quarks is reduced by discarding events with at least one selected small-radius jet passing the medium b jet identification, or at least two passing the loose b jet identification. Leptons originating from low-mass Drell–Yan production, decays of J/ψ and Υ mesons, cascade decays of bottom quarks, and photon conversions are removed by vetoing events containing any pair of loose ℓ with mass $m(\ell\ell) < 12$ GeV. To eliminate overlap with events selected in the ongoing search for HH production in the $b\bar{b}ZZ$, $ZZ \to 4\ell$ decay mode, no event in the 2ℓss, 3ℓ, and 4ℓ categories may contain two SFOS loose $\ell\ell$ pairs with a mass of the four-ℓ system of less than 140 GeV. In addition, to reduce the $Z \to \ell\ell$ background, these three categories along with $2\ell + 2\tau_h$ and $3\ell + 1\tau_h$ exclude events where any SFOS loose $\ell\ell$ pair has an invariant mass of 81–101 GeV (Z boson veto).

A summary of the event selection criteria applied in the different categories is given in table 4. Criteria that are common to all seven search categories are given in table 5.

Two control regions (CRs) are used to validate the modeling of the WZ and ZZ backgrounds. These CRs match the signal regions of the 3ℓ and 4ℓ categories, but with the Z boson veto inverted, and are referred to as the "3ℓ WZ" CR and "4ℓ ZZ" CR, respectively.

The number of events selected in the signal regions of each of the seven search categories and in the 3ℓ WZ and 4ℓ ZZ CRs are given in table 6. The contribution expected from nonresonant HH production with event kinematics as predicted by the SM, but 30 times the SM cross section, is given separately for HH decays into WW^*WW^*, $WW^*\tau\tau$, and $\tau\tau\tau\tau$ in the upper three rows of each table. The event yields given in the rows labeled WW^*WW^* include a small contribution from HH decays into WW^*ZZ^* and ZZ^*ZZ^*, and, similarly, the numbers quoted in the rows labeled $WW^*\tau\tau$ include a small contribution from HH decays into $ZZ^*\tau\tau$.

6 Analysis strategy

The rate of the HH signal is extracted through a binned maximum likelihood (ML) fit to the distributions in the output of boosted decision tree (BDT) classifiers [116], which are

JHEP07(2023)095

Category	2ℓss	3ℓ	4ℓ
Targeted HH decays	WW^*WW^*	WW^*WW^*	WW^*WW^*
Trigger	Single- and double-lepton	Single-, double- and triple-lepton	Single-, double- and triple-lepton
Lepton p_T	>25 / 15 GeV	>25 / 15 / 10 GeV	>25 / 15 / 15 / 10 GeV
Lepton charge sum	±2, with charge quality requirements applied	±1	0
Dilepton invariant mass	$\lvert m_{\ell\ell} - m_Z \rvert > 10$ GeV [†]	$\lvert m_{\ell\ell} - m_Z \rvert > 10$ GeV [‡]	$\lvert m_{\ell\ell} - m_Z \rvert > 10$ GeV [‡]
Jets	$\geq$2 small-radius jets or $\geq$1 large-radius jet	$\geq$1 small-radius jet or $\geq$1 large-radius jet	—
Missing p_T	$p_T^{miss,LD} > 30$ GeV [§]	$p_T^{miss,LD} > 30$ GeV [‖]	—

Category	$3\ell + 1\tau_h$	$2\ell + 2\tau_h$
Targeted HH decays	$WW^*\tau\tau$	$WW^*\tau\tau$, $\tau\tau\tau\tau$
Trigger	Single-, double-, and triple-lepton	Single- and double-lepton
Lepton p_T	>25 / 15 / 10 GeV	>25 / 15 GeV
τ_h p_T	>20 GeV	>20 GeV
Lepton and τ_h charge	ℓ and τ_h charges sum to 0	ℓ and τ_h charges sum to 0
Dilepton invariant mass	$\lvert m_{\ell\ell} - m_Z \rvert > 10$ GeV [‡]	$\lvert m_{\ell\ell} - m_Z \rvert > 10$ GeV [‡]

Category	$1\ell + 3\tau_h$	$4\tau_h$
Targeted HH decays	$\tau\tau\tau\tau$	$\tau\tau\tau\tau$
Trigger	Single-lepton, lepton+τ_h and double-τ_h	Double-τ_h
Lepton η	$\lvert\eta\rvert < 2.1$	—
Lepton p_T	>20 GeV (e) or >15 GeV (μ)	—
τ_h p_T	>40 / 30 / 20 GeV	>40 / 30 / 20 / 20 GeV
Lepton and τ_h charge	ℓ and τ_h charges sum to 0	τ_h charges sum to 0
$Z \to ee$ veto	$\lvert m_{e\tau_h} - 86\,\text{GeV} \rvert > 15$ GeV [¶]	—

[†] Applied to all SFOS $\ell\ell$ pairs and electron pairs with the same charge.
[‡] Applied to all SFOS $\ell\ell$ pairs.
[§] Only applied to events containing two electrons.
[‖] Tightened to $p_T^{miss,LD} > 45$ GeV if event contains a SFOS $\ell\ell$ pair.
[¶] For τ_h classified as electrons by the DeepTau algorithm or with $1.460 < \lvert\eta\rvert < 1.558$.

Table 4. Event selection criteria applied in the seven search categories. The p_T thresholds for ℓ and τ_h with the highest, second-, third-, and fourth-highest p_T are separated by slashes. The symbol "—" indicates that no requirement is applied.

Object and event properties	Selection criteria
Lepton and τ_h pseudorapidity	$\lvert\eta\rvert < 2.5$ for e, $\lvert\eta\rvert < 2.4$ for μ, $\lvert\eta\rvert < 2.3$ for τ_h
Dilepton invariant mass	$m_{\ell\ell} > 12$ GeV (all $\ell\ell$ pairs)
Four-lepton invariant mass	$m_{4\ell} > 140$ GeV (any two SFOS $\ell\ell$ pairs)
b jet veto	0 medium and ≤ 1 loose b-tagged small-radius jet

Table 5. Reconstructed object and event selection requirements in all seven search categories. Electrons or muons in the $\ell\ell$ pairs include any leptons passing the loose selection criteria.

trained to discriminate the HH signal from backgrounds, along with kinematic distributions from the two CRs above. The data from each of the three years are fit separately. Three classifiers are trained for each of the seven search categories using a mix of MC simulation

JHEP07(2023)095

Process	2ℓss	3ℓ	4ℓ
SM HH $\to$ WW^*WW^* ($\times$ 30)	73 $\pm$ 6	33 $\pm$ 3	2.2 $\pm$ 0.2
SM HH $\to$ $WW^*\tau\tau$ ($\times$ 30)	31 $\pm$ 3	12 $\pm$ 1	0.9 $\pm$ 0.1
SM HH $\to$ $\tau\tau\tau\tau$ ($\times$ 30)	3 $\pm$ 0	1 $\pm$ 0	0.1 $\pm$ 0.0
WZ	1999 $\pm$ 122	1318 $\pm$ 78	0.4 $\pm$ 0.1
ZZ	121 $\pm$ 3	109 $\pm$ 3	53.9 $\pm$ 3.1
Misidentified ℓ	4842 $\pm$ 1327	510 $\pm$ 94	2.2 $\pm$ 1.1
Conversion electrons	804 $\pm$ 174	117 $\pm$ 24	0.7 $\pm$ 0.3
Electron charge misid.	394 $\pm$ 61	—	—
Single Higgs boson	214 $\pm$ 6	61 $\pm$ 1	2.4 $\pm$ 0.3
Other backgrounds	2740 $\pm$ 338	289 $\pm$ 29	4.0 $\pm$ 0.5
Total expected background	11 114 $\pm$ 1387	2404 $\pm$ 128	63.7 $\pm$ 3.3
Data	10 344	2621	62

Process	$3\ell + 1\tau_h$	$2\ell + 2\tau_h$	$1\ell + 3\tau_h$	$4\tau_h$
SM HH $\to$ WW^*WW^* ($\times$ 30)	0.9 $\pm$ 0.1	0.2 $\pm$ 0.0	0.2 $\pm$ 0.0	0.3 $\pm$ 0.0
SM HH $\to$ $WW^*\tau\tau$ ($\times$ 30)	4.1 $\pm$ 0.3	3.9 $\pm$ 0.4	0.6 $\pm$ 0.1	0.1 $\pm$ 0.0
SM HH $\to$ $\tau\tau\tau\tau$ ($\times$ 30)	0.9 $\pm$ 0.1	2.3 $\pm$ 0.3	2.6 $\pm$ 0.4	1.3 $\pm$ 0.2
WZ	0.2 $\pm$ 0.0	<0.1	<0.1	<0.1
ZZ	24.1 $\pm$ 1.4	18.4 $\pm$ 1.3	1.9 $\pm$ 0.2	0.7 $\pm$ 0.1
Misidentified ℓ and τ_h	23.9 $\pm$ 6.6	31.9 $\pm$ 10.1	2.2 $\pm$ 2.1	2.2 $\pm$ 1.6
Conversion electrons	0.1 $\pm$ 0.0	0.1 $\pm$ 0.1	<0.1	<0.1
Single Higgs boson	3.8 $\pm$ 0.4	2.8 $\pm$ 0.7	0.8 $\pm$ 0.4	0.4 $\pm$ 0.3
Other backgrounds	2.8 $\pm$ 0.4	2.2 $\pm$ 0.8	0.1 $\pm$ 0.1	<0.1
Total expected background	54.9 $\pm$ 6.8	55.4 $\pm$ 10.3	5.0 $\pm$ 2.2	3.4 $\pm$ 1.6
Data	55	55	6	1

Process	3ℓ WZ CR	4ℓ ZZ CR
WZ	12 565 $\pm$ 705	<1
ZZ	765 $\pm$ 47	2000 $\pm$ 108
Misidentified ℓ	804 $\pm$ 211	13 $\pm$ 4
Conversion electrons	106 $\pm$ 21	2 $\pm$ 0
Other backgrounds	625 $\pm$ 76	60 $\pm$ 8
Total expected background	14 866 $\pm$ 742	2074 $\pm$ 108
Data	14 994	2096

Table 6. The number of expected and observed events in each of the seven search categories, and in two CRs, which validate the modeling of the WZ and ZZ backgrounds. The symbol "—" indicates that the background is not relevant for the category. The HH signal represents the sum of the ggHH and qqHH production processes and is normalized to 30 times the event yield expected in the SM, corresponding to a cross section of about 1 pb. The event yields are obtained by performing the event selection and applying appropriate corrections to the simulated events. Quoted uncertainties represent the sum of statistical and systematic components. Uncertainties that are smaller than half the value of the least significant digit have been rounded to zero.

JHEP07(2023)095

from all three years, targeting nonresonant HH production and resonant HH production from the decay of heavy particles of spin 0 and of spin 2. The binning is chosen with the objective of maximizing the sensitivity for the HH signal, while maintaining sufficient background events in each bin to keep the statistical uncertainty in the background prediction under control. In the two categories with high event yields (2ℓss and 3ℓ) the BDT output binning is chosen such that each bin contains a similar number of expected HH signal events. The four categories containing events with τ_h ($3\ell + 1\tau_h$, $2\ell + 2\tau_h$, $1\ell + 3\tau_h$, and $4\tau_h$) have low event yields and sizable background contributions arising from the misidentification of ℓ and τ_h candidates, which are determined from data and statistically limited. For these categories, we choose the binning for each BDT output distribution such that a similar number of expected background events is contained in each bin. In the 4ℓ category, the fact that the background is dominated by ZZ production, which is modeled by the MC simulation with low statistical uncertainties, allows one to choose the binning in the same way as for the 2ℓss and 3ℓ categories. The number of bins is determined by the condition that the relative statistical uncertainty in the background prediction in each bin does not exceed 15%. Higher bin numbers correspond to a higher BDT output value, and feature a higher signal-to-background ratio. For the SM HH signal, the bins with the highest BDT output values feature a signal-to-background ratio up to 10 times higher than the inclusive ratio in each category.

The inputs to the BDT classifiers differ by search category and include the p_T and η of reconstructed ℓ and τ_h; the angular separation ΔR and invariant mass of $\ell\ell$, $\ell\tau_h$, and $\tau_h\tau_h$ pairs; the ΔR and invariant mass between an ℓ or τ_h candidate and the nearest jet(s); the number of jets in the event; the discriminant $p_T^{\text{miss,LD}}$; the scalar p_T sum of all reconstructed e, μ, τ_h, and jets; the "visible" mass of the Higgs boson pair, given by the mass of the system of reconstructed e, μ, τ_h, and jets; and where applicable, the "full" mass of the HH system, including neutrinos, reconstructed using the algorithm from ref. [117] designed for reconstructing Higgs pair decays into τ leptons. This algorithm targets HH signal events decaying to $\tau\tau\tau\tau$ and thus works best in the $4\tau_h$ and $1\ell + 3\tau_h$ search categories. Distributions in some of the observables used as inputs to the BDT classifiers in the 2ℓss and 3ℓ categories are shown in figure 4.

These observables are complemented by further inputs, which parametrize the BDT as a function of the model parameters: the Higgs boson couplings λ, y_t, c_g, c_{2g}, and c_2 for nonresonant HH production, and the mass of the heavy particle X in resonant HH production. When training the BDT that targets nonresonant HH production, the values for the couplings are chosen according to the twelve EFT benchmark scenarios given in ref. [24] and the SM, indicated by thirteen binary inputs to the BDT. The BDT classifiers used for the analysis of resonant HH production are trained separately for spin-0 and spin-2 on the full set of resonance masses listed in section 3, and the resonance mass is used as an input to the BDT. Each simulated background event is replicated multiple times in the training sample, with different values assigned to the Higgs boson couplings and the mass of the heavy particle X.

The training is performed using simulated samples of signal and background events. The signal events used in the training consist of ggHH events in the HH decay modes

JHEP07(2023)095

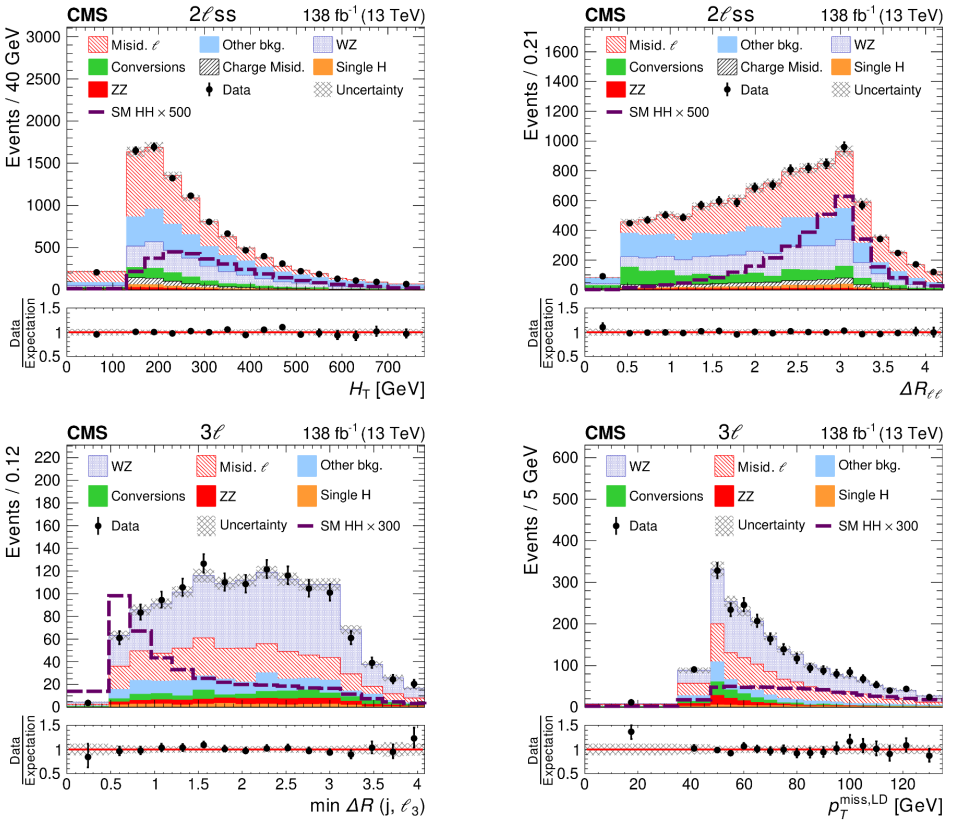


Figure 4. Distributions in a few observables used as inputs to the BDT classifiers in the 2ℓss and 3ℓ categories: the scalar p_{T} sum, denoted as H_{T}, of the two reconstructed ℓ and all small-radius jets in the 2ℓss category (upper left); the angular separation ΔR between the two ℓ in the 2ℓss category (upper right); the angular separation between ℓ_3 and the nearest small-radius jet in the 3ℓ category (lower left); and $p_{\mathrm{T}}^{\mathrm{miss,LD}}$ in the 3ℓ category (lower right). The ℓ_3 in the 3ℓ category is defined as the ℓ that is not part of the opposite-sign $\ell\ell$ pair of lowest mass. The normalization and shape of the distributions expected for the different background processes are shown for the values of nuisance parameters obtained from an ML fit in which the HH signal is constrained to be zero. The gray shaded area indicates the sum of statistical and systematic uncertainties on the background prediction obtained from this ML fit.

$\mathrm{WW^*WW^*}$, $\mathrm{WW^*}\tau\tau$, and $\tau\tau\tau\tau$. Background contributions arising from the misidentification of ℓ and τ_{h} candidates and from the mismeasurement of the electron charge are included in the simulation. The signal and background events used in the training are required to pass the event selection criteria for the respective search category, described in section 5. The number of training events is increased by applying the medium ℓ and τ_{h} identification criteria instead of the tight ones. Weights are applied to background events arising from different sources, such that the relative fractions of different types of back-

JHEP07(2023)095

grounds in the training match the fractions expected in the signal region of the analysis, i.e. when the tight ℓ and τ_h identification criteria are applied. The MC samples used for the BDT training overlap with the samples used to model signal and background contributions in the analysis. To avoid potential biases, the training samples are split into two samples of equal size, based on even and odd event numbers. The BDTs trained on even events are evaluated on odd events, and vice versa, thereby ensuring that BDTs are not trained and evaluated on the same events. The training is performed using the XGBoost algorithm [118], interfaced to the Scikit-learn machine learning library [119]. The parameters of the BDT training (so-called "hyperparameters") are optimized using the particle swarm optimization algorithm described in ref. [120].

7 Background estimation

Background contributions are classified as either "reducible" or "irreducible". In this analysis, three types of reducible backgrounds are considered, arising from misidentified ℓ or τ_h, electron charge misidentification, and electrons from photon conversions. Background events in which all selected ℓ and τ_h come from W, Z, or H boson decays, and are reconstructed with the correct charge, are considered "irreducible". The ℓ/τ_h misidentification and electron charge misidentification backgrounds are both determined from data, while electron conversions and irreducible backgrounds are modeled using MC simulation.

The ℓ/τ_h misidentification background (which includes nonprompt leptons) is the largest reducible background in all search categories. Nonprompt ℓ are either electrons or muons produced in bottom and charm quark decays, or muons that originate from pion and kaon decays. Hadronic jets may also be misidentified as electrons or τ_h. The ℓ/τ_h misidentification background estimate is detailed in section 7.1. The electron charge misidentification background is only relevant for the 2ℓss search category, and is described in section 7.2. The modeling of photon conversion events by the MC simulation has been validated in data as described in refs. [103, 121].

The main contribution to the irreducible background arises from WZ production in the 2ℓss and 3ℓ categories, and ZZ production in the remaining five categories. The production of pairs of bosons (γ, W, Z, or H) other than WZ, ZZ and HH, and production of bosons with top quarks, including Wγ, Zγ, WH, ZH, tH, t$\bar{\text{t}}$H, tW, t$\bar{\text{t}}$W, tZ, t$\bar{\text{t}}$Z, tγ, and t$\bar{\text{t}}\gamma$, constitute subdominant additional backgrounds. The tZ and t$\bar{\text{t}}$Z backgrounds also include contributions from off-shell t$\bar{\text{t}}\gamma^*$ and tγ^* production. Background processes which include at least one top quark are suppressed by the b jet veto described in section 5, but are still sizable compared to the expected HH signal. All irreducible backgrounds are modeled using the MC simulation.

The modeling of the dominant irreducible WZ and ZZ backgrounds is validated using the "3ℓ WZ" and "4ℓ ZZ" CRs introduced in section 5. Distributions in kinematic observables from these CRs (shown in figure 5) are included in the ML fit that is used to extract the HH signal, described in section 9. This provides in-situ constraints on the WZ and ZZ backgrounds and on systematic uncertainties related to lepton identification and trigger efficiency. The transverse mass, $m_T = \sqrt{2\, p_T^{\ell}\, p_T^{\text{miss}}\, (1 - \cos\Delta\phi)}$, in the 3ℓ WZ CR is computed using the ℓ that is not identified as originating from the Z boson decay. The

JHEP07(2023)095

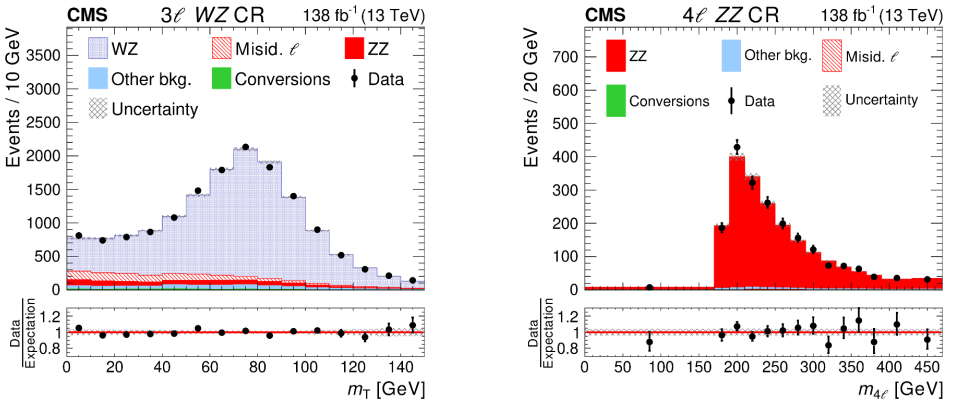


Figure 5. Distributions in m_{T} in the 3ℓ WZ CR (left) and in $m_{4\ell}$ in the 4ℓ ZZ CR (right). The normalization and shape of the distributions expected for WZ, ZZ, and other background processes are shown for the values of nuisance parameters obtained from the ML fit described in section 9. The gray shaded area indicates the sum of statistical and systematic uncertainties on the background prediction obtained from the ML fit.

symbol $\Delta\phi$ refers to the angle in the transverse plane between the ℓ momentum and the $\vec{p}_{\mathrm{T}}^{\,\mathrm{miss}}$. The observable $m_{4\ell}$ refers to the mass of the 4ℓ system in the 4ℓ ZZ CR.

The modeling of the reducible ℓ/τ_{h} misidentification background is validated in two further CRs, the "2ℓss CR" and the "$2\ell + 2\tau_{\mathrm{h}}$ CR". They are based on the signal regions (SRs) of the 2ℓss and $2\ell + 2\tau_{\mathrm{h}}$ categories. In the 2ℓss CR, no b jet veto is applied, and at least one small-radius jet passing the medium b jet identification is required. The $2\ell + 2\tau_{\mathrm{h}}$ CR differs from the SR of the $2\ell + 2\tau_{\mathrm{h}}$ category in that the sum of ℓ plus τ_{h} charges is required to be non-zero, and no Z boson veto is applied. The 2ℓss CR is dominated by events with misidentified ℓ, while the $2\ell + 2\tau_{\mathrm{h}}$ CR is dominated by events with misidentified τ_{h}. Distributions in the transverse mass m_{T} in the 2ℓss CR and in the mass of the HH candidate in the $2\ell + 2\tau_{\mathrm{h}}$ CR, reconstructed by the algorithm described in ref. [117], are shown in figure 6. The transverse mass in the 2ℓss CR is computed using the leading ℓ. The data agree well with the background prediction in both CRs.

Simulated events are only considered as irreducible background if every selected e, μ, and τ_{h} candidate matches a prompt MC generator-level counterpart. Events with at least one selected electron from a photon conversion, and the remaining ℓ and τ_{h} candidates matched to prompt leptons in MC simulation, are classified as conversion background. Electrons that are misidentified as τ_{h}, and τ_{h} that are misidentified as e are also modeled using the MC simulation. All other simulated events are discarded, as the ℓ/τ_{h} misidentification and charge misidentification backgrounds are estimated from data, as described below.

7.1 Lepton and τ_{h} misidentification background

The background from events with misidentified ℓ and τ_{h} candidates is estimated using the "fake factor" or "FF" method from ref. [115]. An estimate of this background's contribution

JHEP07(2023)095

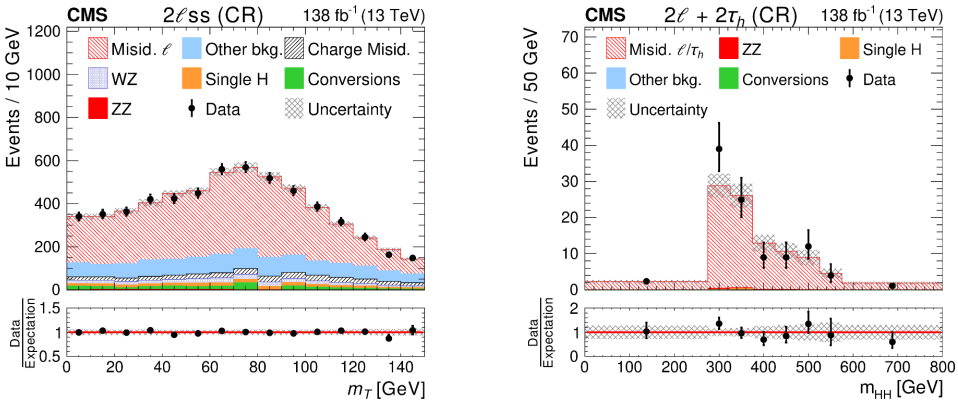


Figure 6. Distributions in m_{T} in the 2ℓss CR (left) and in the mass of the HH candidate in the $2\ell+2\tau_{\mathrm{h}}$ CR (right). The normalization and shape of the distributions expected for the misidentified ℓ/τ_{h} background and other background processes are shown for the values of nuisance parameters obtained from an ML fit in which the HH signal is constrained to be zero. The gray shaded area indicates the sum of statistical and systematic uncertainties on the background prediction obtained from this ML fit.

to the SR of each search category is obtained by selecting a sample of events that satisfy all selection criteria of the SR for the respective search category, except that the e, μ, and τ_{h} are required to pass the medium selections instead of the tight ones. The sample of events thus obtained is referred to as the application region (AR) of the FF method. Events in which every ℓ and τ_{h} satisfies the tight selections are excluded from the AR.

The prediction for misidentification backgrounds in the SR is obtained by applying suitably chosen weights w to the events selected in the AR, where w is given by the expression

$$w = (-1)^{n+1} \prod_{i=1}^{n} \frac{f_i(p_{\mathrm{T}}, \eta)}{1 - f_i(p_{\mathrm{T}}, \eta)}. \tag{7.1}$$

The product extends over all e, μ, and τ_{h} that pass the medium, but fail the tight selection criteria, and n refers to the total number of such ℓ and τ_{h}. The symbol $f_i(p_{\mathrm{T}}, \eta)$ corresponds to the probability for a single e, μ, or τ_{h} that passes the medium selection to also pass the tight selection. These probabilities are measured separately for e, μ, and τ_{h} candidates, parametrized as a function of p_{T} and η, and vary between 5 and 30%. The contributions of irreducible backgrounds to the AR are subtracted based on the MC expectation of such processes. The alternating sign in eq. (7.1) is necessary to avoid double-counting arising from events with more than one misidentified ℓ or τ_{h} [115].

The probabilities $f_i(p_{\mathrm{T}}, \eta)$ for electrons and muons are measured in multijet events, as described in ref. [103]. The $f_i(p_{\mathrm{T}}, \eta)$ for τ_{h} are measured using $\mathrm{Z} \to \mu\mu$+jets events, where the misidentified τ_{h} candidates arise from quark or gluon jets. These events are selected by requiring a muon pair passing the tight selection, with opposite charge and invariant mass

JHEP07(2023)095

$60 < m_{\mu\mu} < 120\,\text{GeV}$, plus at least one τ_h candidate that passes the medium τ_h selection. The leading and subleading muons must have $p_T > 25$ and 15 GeV, respectively. Events must also pass the b jet veto described in section 5 to remove $t\bar{t}$ background.

7.2 Charge misidentification background

The electron charge misidentification background in the 2ℓss category is estimated using the method described in ref. [103]. A sample of dielectron events passing all selection criteria of the SR of the 2ℓss category, except that both electrons are required to have opposite- instead of same-sign charge, is selected and assigned appropriately chosen weights. The weights are computed by summing the probabilities for the charge of either electron to be mismeasured. The probability for the mismeasurement of the electron charge is determined using $Z \to ee$ events, and ranges from under 0.1% in the barrel up to 0.4% in the endcap. The probability for mismeasuring the charge of muons is negligible [103].

8 Systematic uncertainties

Multiple sources of systematic uncertainty affect the predicted event yields, the distributions in the output of the BDT classifiers, or both. These uncertainties may be theoretical, affecting the predicted cross section or decay kinematics of the collision process, or experimental, accounting for differences in object reconstruction and calibration between data and the MC simulation, or for uncertainties on the estimates of the ℓ/τ_h misidentification and electron charge misidentification background obtained from data. The systematic uncertainties may be correlated or uncorrelated across the three data-taking years, and among the various signal and background processes considered in the analysis.

The SM prediction for the ggHH production cross section at $\sqrt{s} = 13\,\text{TeV}$ has a relative uncertainty of $+6.7\%/-23.2\%$ [122], while the qqHH cross section uncertainty is $\pm 2.1\%$ [19]. The predicted H boson decay branching fractions to WW^*, $\tau\tau$, and ZZ^* have relative uncertainties of 1.54%, 1.65%, and 1.54%, respectively [123]. Correlations between these uncertainties have a negligible effect. Alternate HH predictions are generated with the renormalization and factorization scales varied up and down by a factor of 2. Variations that increase the factorization scale and decrease the renormalization scale (and vice versa) are excluded, following the recommendation of ref. [123]. All theoretical uncertainties in the HH signal model are correlated across all three data-taking years and among the seven search categories. The uncertainties in the H boson decay branching fractions and the effect of renormalization and factorization scale uncertainties in the signal acceptance impact the measurement of cross sections for both nonresonant and resonant HH production. Conversely, the uncertainties in the SM prediction for the ggHH and qqHH cross sections only affect the measurement of the HH production rate as a ratio to the SM prediction.

Theoretical uncertainties also affect the irreducible background prediction. The relative uncertainties in the cross sections of the dominant WZ and ZZ backgrounds are 2.1 and 6.3%, respectively [124–126]. The uncertainties in the cross sections for the subdominant single H boson backgrounds range from 2 to 9% for ggHH, qqHH, WH, and ZH. The cross sections for the production of W, Z, or H bosons with one or two top quarks are known with uncertainties of 8–15%. The event yields of extremely rare backgrounds not

JHEP07(2023)095

mentioned above (e.g., triple boson or four top quark production) are given a conservative uncertainty of 50%, since the analysis has little sensitivity to these processes. Following ref. [103], background contributions arising from photon conversions are assigned a 30% yield uncertainty. The theoretical uncertainties affecting background cross sections are partially correlated among different processes. Here, contributions arising from uncertainties in the proton PDFs are correlated among processes with a similar initial state. Processes involving single H boson production are an exception. These uncertainties are uncorrelated from other background processes but correlated among each other depending on the initial state. Uncertainties arising from the choice of the renormalization and factorization scales are correlated for processes with similar production modes, for example among all processes involving diboson production (WW, WZ, ZZ, Wγ, and Zγ). Uncertainties in α_s are correlated among all background processes. The theoretical cross section uncertainties for signal processes are uncorrelated with those of background processes, but otherwise follow the same uncertainty scheme for proton PDF, scale, and α_s contributions. All theoretical cross section uncertainties are treated as correlated across the different data-taking years and among all seven search categories.

The rate of the misidentified ℓ/τ_h background is assigned a 30% uncertainty in all search categories, to account for variations in the misidentification rates between the ARs of the FF method and the multijet ($Z \to \mu\mu$+jets) event samples used to measure the $f_i(p_T, \eta)$ for e and μ (τ_h). In the $3\ell + 1\tau_h$ and $1\ell + 3\tau_h$ categories, an additional uncertainty of 30% (uncorrelated with the other 30% uncertainty) is assigned to the rate of the misidentified ℓ/τ_h background, to account for the extra uncertainty arising from the modified τ_h selection criteria that suppress the misidentification of electrons as τ_h. The effect of statistical uncertainties in the probabilities $f_i(p_T, \eta)$ for electrons and muons is evaluated by varying these probabilities in bins of p_T and η and determining the resulting change in the shape of the BDT classifier output distribution obtained for the misidentified ℓ/τ_h background. For τ_h, the effect of statistical uncertainties in $f_i(p_T, \eta)$ is evaluated by fitting the probabilities in bins of η with functions that are linear in p_T, varying the slope of these functions up and down within the uncertainties obtained from the fit, and determining the resulting change in the shape of the BDT classifier output distribution.

An additional uncertainty in the BDT output shape in each category is evaluated for events with a nonprompt or misidentified ℓ or τ_h as follows: Simulated events passing all signal selection criteria are compared to those with at least one ℓ or τ_h candidate failing the tight identification criteria, scaled according to the FF method described in section 7, but with the probabilities $f_i(p_T, \eta)$ taken from the MC simulation instead of from the data. The ratio of these two shapes is fitted with a linear function, which is convoluted with the misidentified ℓ/τ_h background prediction from the data to serve as an uncertainty in the BDT output shape for these events in the SR. The systematic uncertainties associated with the misidentified ℓ/τ_h background prediction and the uncertainty associated with the electron charge misidentification rate are treated as uncorrelated among the different data-taking years.

The rate of the electron charge misidentification background in the 2ℓss category is assigned a 30% uncertainty. It covers the uncertainty on the electron charge misidentification

JHEP07(2023)095

rates measured in $Z \to ee$ events, including the effect of background contamination in these samples, and accounts for differences observed in the following "closure" test: Simulated events are required to pass all signal selection criteria of the 2ℓss category, except that the two leptons are required to have opposite-sign electric charges. The selected events are scaled according to the electron charge misidentification probability in simulated events, determined by applying the procedure detailed in section 7.2 to MC simulation. The resulting background estimate is compared to the one obtained by applying the nominal signal selection criteria of the 2ℓss category to simulated events.

Uncertainties in the modeling of the trigger and object reconstruction efficiency affect all signal and background processes that are estimated using MC simulation. Trigger efficiencies for events with at least two ℓ are compared between data and MC simulation in control regions enriched in the $t\bar{t}$, WZ, and ZZ background processes, as a function of lepton flavor, p_T, and η. This results in a small p_T-dependent uncertainty correlated between the 2ℓss and $2\ell + 2\tau_h$ categories, and a 1% normalization uncertainty, which is correlated among the 3ℓ, $3\ell + 1\tau_h$, and 4ℓ categories. The data-to-simulation agreement in trigger efficiency for the $4\tau_h$ and $1\ell + 3\tau_h$ categories is computed using an independent set of data, as a function of the p_T and η of the ℓ and all τ_h, and the reconstructed decay modes of all τ_h. The trigger uncertainties for these two categories are treated as uncorrelated. All systematic uncertainties related to trigger modeling are correlated across different physics processes, but uncorrelated among the three data-taking years.

The uncertainties in the reconstruction and identification efficiencies for e, μ, and τ_h candidates have been measured in Z boson enriched regions in data for each level of identification criteria (tight, medium, and loose), and are applied to each event as a function of p_T and η for leptons and of p_T and the reconstructed hadronic decay mode for τ_h. The reconstructed τ_h energy has an uncertainty of around 1%, depending on the data-taking year and reconstructed τ_h decay mode. These uncertainties affect the predicted rate and BDT output shape for signal and background, and are correlated among the different physics processes, but uncorrelated across different data-taking years.

The jet energy scale and resolution are determined using dijet control regions [111, 127]. The jet energy scale is evaluated using 11 separate components, accounting for partial correlations between the data recorded in different years. The jet energy resolution uncertainty is uncorrelated among the three data-taking years. Jet energy uncertainties are also propagated to the p_T^{miss} calculation. An additional uncertainty in $\vec{p}_T^{miss}$ comes from uncertainty in the energy of "unclustered" PF hadrons (PF hadrons not clustered into either small- or large-radius jets), which is uncorrelated across different years. The probability for true b jets to fail the multivariate b jet identification criteria, or for jets from gluons or light flavored quarks to be misidentified as b jets, is compared in data and MC simulation in event regions that are enriched in light-flavor quark or gluon, or heavy-flavor jets. The resulting uncertainty in the data-to-simulation agreement affects the yields and BDT output shapes of multiple physics processes. The statistical component of this uncertainty is treated as uncorrelated across different data-taking years, while other experimental sources are correlated.

The integrated luminosities for data collected in 2016, 2017, and 2018 have 1.2–2.5% individual uncertainties [59–61], while the overall uncertainty for the 2016–2018 period is

JHEP07(2023)095

1.6%. The uncertainty in the measured cross section for inelastic pp collisions, amounting to 5% [128], is taken into account by varying the number of pileup interactions in MC simulation, which impacts the jet reconstruction and the isolation of ℓ and τ_h.

The sources of systematic uncertainty which create the largest uncertainties in the measured ratio of the HH production cross section to its SM prediction are the theoretical uncertainties in the HH production cross section and decay branching fractions (25%), the uncertainties in the rate and shape of backgrounds from misidentified ℓ or τ_h (22%), and in the rates of backgrounds modeled using MC simulation (13%). These uncertainties in the signal measurement are determined by removing uncertainties that correspond to a given systematic source from an ML fit to pseudodata, as described in section 9, and subtracting the obtained uncertainty in the signal measurement in quadrature from the total uncertainty. The impacts of systematic uncertainties are small compared to the effect of the statistical uncertainty in the data (79%), and are comparable to the statistical uncertainties in the distributions in the BDT classifier output for background processes (33%). The latter includes the effect of statistical uncertainties in the MC simulation and in the ℓ/τ_h misidentification and electron charge misidentification backgrounds obtained from data. All other sources of uncertainty have an impact of 5% or less.

9 Results

The data selected in the seven search categories are tested against multiple HH production hypotheses: the SM prediction; variations of the SM coupling strength modifiers κ_λ, κ_t, κ_V, and κ_{2V}; the effective couplings c_g, c_{2g}, and c_2 in the EFT approach; and resonant production of H boson pairs originating from the decay of heavy particles with spins of 0 or 2 and masses m_X ranging from 250 to 1000 GeV. In each case, the data observed in the seven search categories is fit simultaneously to a model composed of the background prediction (with uncertainties) and the HH signal hypothesis under consideration. The distributions in m_T in the 3ℓ WZ CR and in $m_{4\ell}$ in the 4ℓ ZZ CR shown in figure 5 are included in these fits, in order to obtain in-situ constraints on the systematic uncertainties described in section 8. This in turn reduces the uncertainties in the signal and background predictions.

The SM "signal strength" parameter μ is defined as the ratio of the measured HH production cross section to its predicted value in the SM. This parameter modifies the expected signal yield by the same proportion in each category. By contrast, variations in the κ modifiers may affect the signal yields in each category differently, and also change the BDT classifier output shape for HH events. The twenty benchmark scenarios spanning combinations of κ_λ, κ_t, c_g, c_{2g}, and c_2 values in the coupling parameter space each correspond to different kinematic distributions, so the HH production cross section for each point is measured separately. Similarly, signal efficiency and BDT classifier output shapes vary dramatically for different resonant masses, and thus a separate measurement is performed for each mass and spin hypothesis. The SM signal strength measurement is performed using the output of the BDT classifier that has been trained for SM nonresonant HH production, while the κ_λ measurement uses the BDT trained for benchmark scenario

JHEP07(2023)095

JHEP04 BM7. In the scenario JHEP04 BM7, the m_{HH} value tends to be close to the lower limit of 250 GeV, which matches the event kinematics for nonresonant HH production in the κ_λ range of the expected limit. When setting limits on the twenty different benchmark scenarios, the binary BDT inputs correspond to the given scenario, or in case of the benchmarks from ref. [96] the kinematically closest scenario. In case of resonant HH production, the BDT input for the resonance mass is set to the m_{X} value for which the limit is computed.

The SM signal strength is measured using a profile likelihood test statistic [129], with systematic uncertainties treated as nuisance parameters θ in a frequentist approach [130]. The effect of variations in θ on the shape of the BDT classifier output distribution for the HH signal and for background processes is incorporated into the ML fit using the technique described in ref. [131]. Statistical uncertainties in these distributions are also taken into account using the approach detailed in ref. [131]. The likelihood ratio q_μ for a fixed "test" signal strength value μ is

$$q_\mu = -2\Delta \ln \mathcal{L} = -2 \ln \frac{\mathcal{L}(\mathrm{data}|\mu, \hat{\theta}_\mu)}{\mathcal{L}(\mathrm{data}|\hat{\mu}, \hat{\theta})},$$

where $\hat{\mu}$ and $\hat{\theta}$ are the signal strength and nuisance parameter values that give the maximum value of the likelihood function $\mathcal{L}$ for the given set of data (requiring $\hat{\mu} \geq 0$), and $\hat{\theta}_\mu$ is the set of θ values which maximize $\mathcal{L}$ for the fixed μ. The 95% confidence level (CL) upper limit for μ is obtained using the $\mathrm{CL_s}$ criterion [132, 133], with q_μ set to 0 when $\mu < \hat{\mu}$. The probabilities to observe a given value of the likelihood ratio q_μ under the signal-plus-background and background-only hypotheses are computed using the asymptotic approximation from ref. [129]. The limits on μ obtained using the asymptotic approximation, match the limits obtained with toy MC experiments [130] within 10%. The SM coupling strength modifiers and the cross sections for the various HH production hypotheses are measured by scanning the likelihood ratio q_μ as a function of μ. Theoretical and experimental uncertainties affecting the signal and background yields or the shape of the BDT classifier output distributions may be correlated or uncorrelated across different years, search categories, and BDT output bins, as described in section 8.

For the case of nonresonant HH production with event kinematics as predicted by the SM, the best-fit value of the HH production rate, obtained from the simultaneous fit of all seven search categories, amounts to $\hat{\mu} = 2 \pm 8\,(\mathrm{stat.}) \pm 6\,(\mathrm{syst.})$ times the SM expectation. The measured value of the signal strength refers to the sum of ggHH and qqHH production and is compatible with both the SM and background-only hypotheses, within statistical and systematic uncertainties. Distributions in the output of the BDT classifier for SM nonresonant HH production in the seven search categories are shown in figures 7 and 8, and the corresponding expected event yields are given in table 7. The data excess in the rightmost bin of the BDT classifier output distribution for the 3ℓ category is not statistically significant: 11 events are observed in this bin, while $5.2 \pm 0.7\,(\mathrm{stat.}) \pm 0.2\,(\mathrm{syst.})$ are expected from background processes, amounting to a local significance of about 1.7 standard deviations. The observed (expected) 95% CL upper limit on the cross section for

JHEP07(2023)095

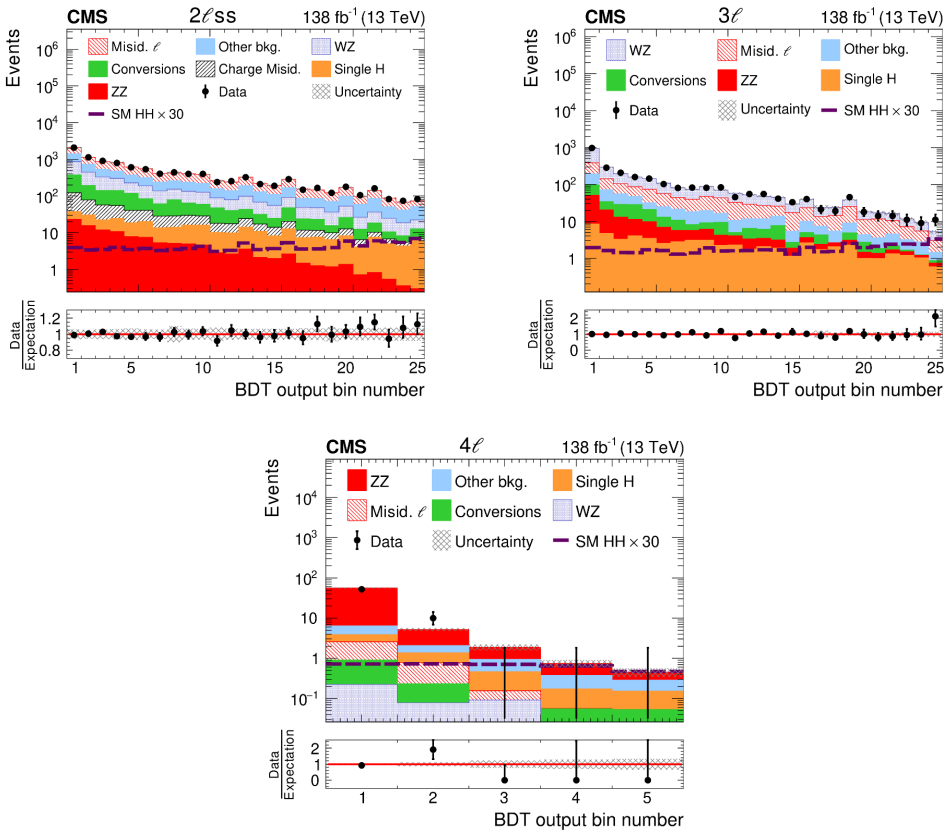


Figure 7. Distribution in the output of the BDT trained for nonresonant HH production and evaluated for the benchmark scenario JHEP04 BM7 for the 2ℓss (upper left), 3ℓ (upper right), and 4ℓ (lower) categories. The SM HH signal is shown for a cross section amounting to 30 times the value predicted in the SM. The normalization and shape of the distributions expected for the background processes are shown for the values of nuisance parameters obtained from the ML fit of the signal+background hypothesis to the data. The gray shaded area indicates the sum of statistical and systematic uncertainties on the background prediction obtained from the ML fit. No data events are observed in the three rightmost bins of the BDT output distribution in the 4ℓ category.

nonresonant HH production is 651 (592) fb. Taking into account the theoretical uncertainties in the SM HH production cross section, this corresponds to an observed (expected) limit on the nonresonant HH production rate of 21.3 (19.4) times the SM expectation. These limits are shown in figure 9 for individual categories and for the combination of all seven search categories, which is referred to as the "HH → multilepton" result. The 3ℓ and $1\ell + 3\tau_h$ categories are the most sensitive to SM HH production, followed closely by the other categories.

JHEP07(2023)095

Process	2ℓss	3ℓ	4ℓ
SM HH $\to$ WW*WW* ($\times$ 30)	73 $\pm$ 6	33 $\pm$ 3	2.2 $\pm$ 0.2
SM HH $\to$ WW$^*\tau\tau$ ($\times$ 30)	31 $\pm$ 3	12 $\pm$ 1	0.9 $\pm$ 0.1
SM HH $\to \tau\tau\tau\tau$ ($\times$ 30)	3 $\pm$ 0	1 $\pm$ 0	0.1 $\pm$ 0.0
WZ	2003 $\pm$ 58	1321 $\pm$ 27	0.4 $\pm$ 0.1
ZZ	121 $\pm$ 2	109 $\pm$ 2	54.7 $\pm$ 1.8
Misidentified ℓ	3939 $\pm$ 267	670 $\pm$ 55	2.3 $\pm$ 1.0
Conversion electrons	1009 $\pm$ 170	146 $\pm$ 24	0.9 $\pm$ 0.4
Electron charge misid.	366 $\pm$ 52	—	—
Single Higgs boson	216 $\pm$ 4	62 $\pm$ 1	2.4 $\pm$ 0.3
Other backgrounds	2690 $\pm$ 224	293 $\pm$ 20	4.1 $\pm$ 0.4
Total expected background	10 346 $\pm$ 396	2601 $\pm$ 68	64.8 $\pm$ 2.1
Data	10 344	2621	62

Process	$3\ell + 1\tau_h$	$2\ell + 2\tau_h$	$1\ell + 3\tau_h$	$4\tau_h$
SM HH $\to$ WW*WW* ($\times$ 30)	0.9 $\pm$ 0.1	0.2 $\pm$ 0.0	0.2 $\pm$ 0.0	0.3 $\pm$ 0.0
SM HH $\to$ WW$^*\tau\tau$ ($\times$ 30)	4.1 $\pm$ 0.3	3.9 $\pm$ 0.4	0.6 $\pm$ 0.1	0.1 $\pm$ 0.0
SM HH $\to \tau\tau\tau\tau$ ($\times$ 30)	0.9 $\pm$ 0.1	2.3 $\pm$ 0.3	2.6 $\pm$ 0.4	1.3 $\pm$ 0.2
WZ	0.2 $\pm$ 0.0	<0.1	<0.1	<0.1
ZZ	24.3 $\pm$ 0.8	18.5 $\pm$ 1.0	1.9 $\pm$ 0.2	0.7 $\pm$ 0.1
Misidentified ℓ and τ_h	25.1 $\pm$ 4.4	33.5 $\pm$ 4.6	2.1 $\pm$ 1.7	1.5 $\pm$ 0.9
Conversion electrons	0.1 $\pm$ 0.0	0.1 $\pm$ 0.1	<0.1	<0.1
Single Higgs boson	3.8 $\pm$ 0.2	2.9 $\pm$ 0.5	0.8 $\pm$ 0.4	0.4 $\pm$ 0.1
Other backgrounds	2.7 $\pm$ 0.3	2.1 $\pm$ 0.4	0.1 $\pm$ 0.0	<0.1
Total expected background	56.2 $\pm$ 4.5	57.0 $\pm$ 4.8	4.9 $\pm$ 1.7	2.6 $\pm$ 0.9
Data	55	55	6	1

Process	3ℓ WZ CR	4ℓ ZZ CR
WZ	12 546 $\pm$ 148	<1
ZZ	799 $\pm$ 24	2032 $\pm$ 60
Misidentified ℓ	908 $\pm$ 122	13 $\pm$ 4
Conversion electrons	134 $\pm$ 22	3 $\pm$ 0
Other backgrounds	620 $\pm$ 54	59 $\pm$ 6
Total expected background	15 006 $\pm$ 202	2108 $\pm$ 60
Data	14 994	2096

Table 7. The number of expected and observed events in each of the seven search categories, and in two CRs, which validate the modeling of the WZ and ZZ backgrounds. The ℓ/τ_h misidentification and electron charge misidentification backgrounds are determined from data, as described in section 7, while the HH signal and all other backgrounds are modeled using MC simulation. The symbol "—" indicates that the background is not relevant for the category. The HH signal represents the sum of the ggHH and qqHH production processes and is normalized to 30 times the event yield expected in the SM, corresponding to a cross section of about 1 pb. The expected event yields are computed for the values of nuisance parameters obtained from the ML fit described in section 9. Quoted uncertainties represent the sum of statistical and systematic components. Uncertainties that are smaller than half the value of the least significant digit have been rounded to zero.

JHEP07(2023)095

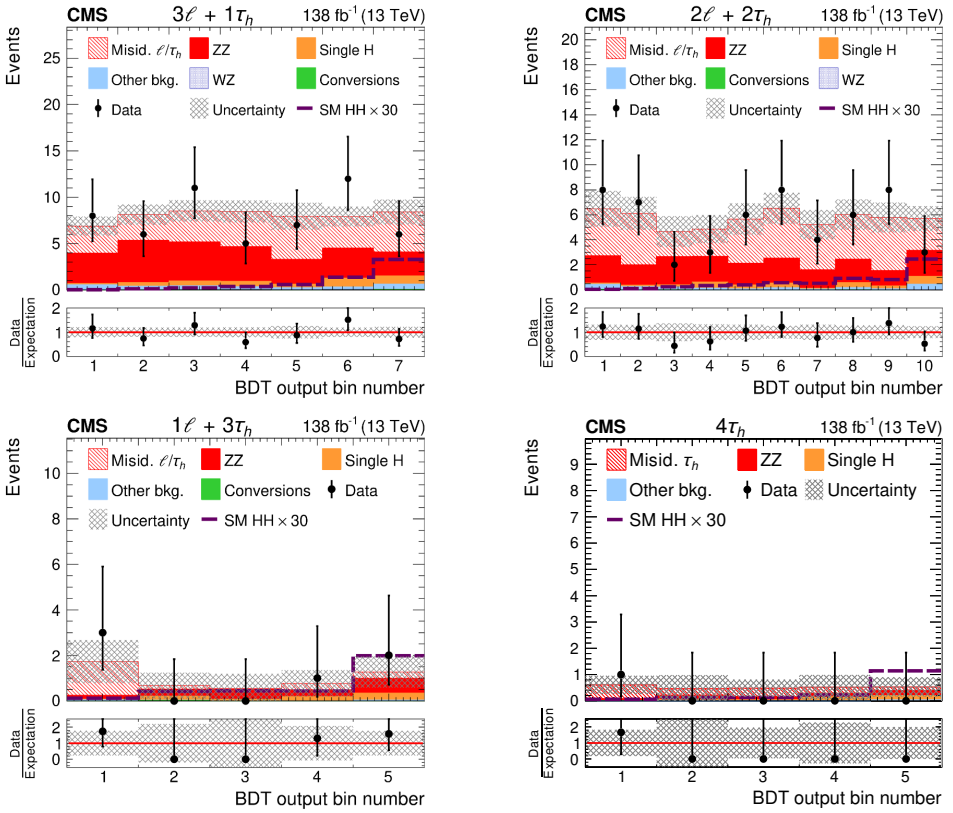


Figure 8. Distribution in the output of the BDT trained for nonresonant HH production and evaluated for the benchmark scenario JHEP04 BM7 for the $3\ell + 1\tau_h$ (upper left), $2\ell + 2\tau_h$ (upper right), $1\ell + 3\tau_h$ (lower left), and $4\tau_h$ (lower right) categories. The SM HH signal is shown for a cross section amounting to 30 times the value predicted in the SM. The normalization and shape of the distributions expected for the background processes are shown for the values of nuisance parameters obtained from the ML fit of the signal+background hypothesis to the data. The gray shaded area indicates the sum of statistical and systematic uncertainties on the background prediction obtained from the ML fit.

The observed (expected) 95% CL interval for the H boson trilinear self-coupling strength modifier is measured to be $-6.9 < \kappa_\lambda < 11.1$ ($-6.9 < \kappa_\lambda < 11.7$). The upper limit on κ_λ is one of the strongest constraints on this fundamental SM parameter to date, with only HH searches in the bb$\gamma\gamma$ [42, 43] and bbbb [45] decay modes providing tighter bounds. The observed and expected upper limits on the HH production cross section as a function of κ_λ, obtained from the simultaneous fit of all seven search categories, are shown in figure 10, along with the limits obtained for each category individually.

The observed and expected limits on the ggHH production cross section for the twenty benchmark scenarios are shown in figure 11 and summarized in table 8. Signal contribu-

JHEP07(2023)095

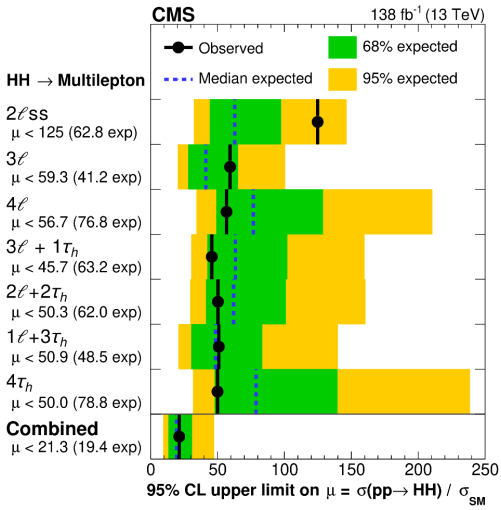


Figure 9. Observed and expected 95% CL upper limits on the SM HH production cross section, obtained for both individual search categories and from a simultaneous fit of all seven categories combined.

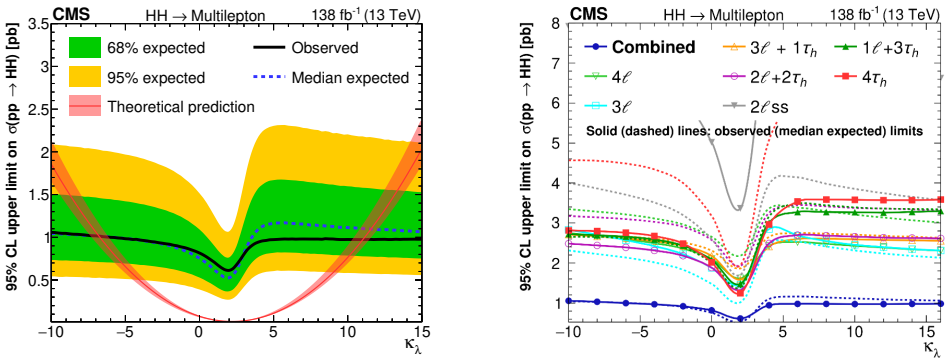


Figure 10. Observed and expected 95% CL upper limits on the HH production cross section as a function of the H boson self-coupling strength modifier κ_λ. All H boson couplings other than λ are assumed to have the values predicted in the SM. The left plot shows the result obtained by combining all seven search categories, while the right plot shows the limits obtained for each category separately. The red curve in the left plot represents the SM prediction for the HH production cross section as a function of κ_λ, and the red shaded band the theoretical uncertainty in this prediction.

JHEP07(2023)095

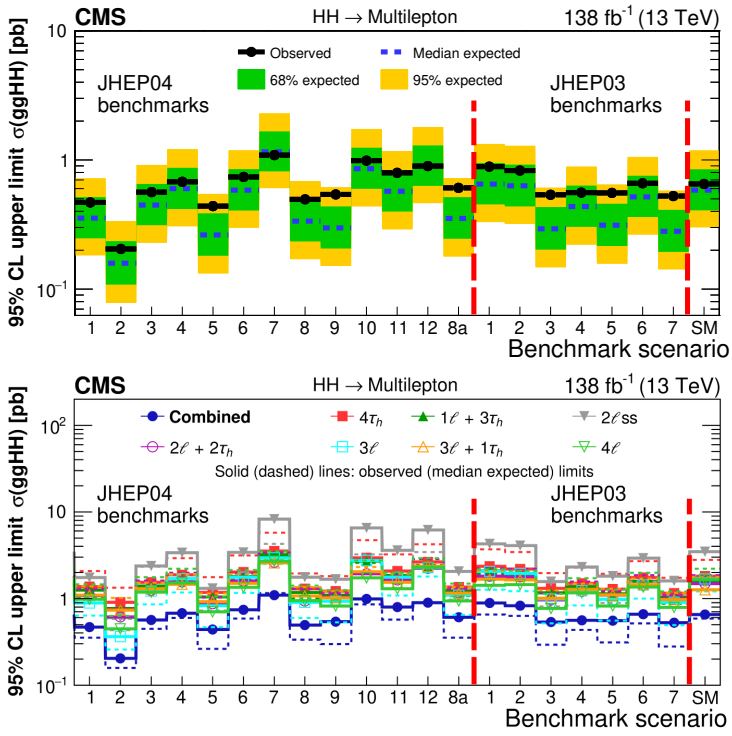


Figure 11. Observed and expected 95% CL upper limits on the HH production cross section for the twelve benchmark scenarios from ref. [24], the additional benchmark scenario 8a from ref. [97], the seven benchmark scenarios from ref. [96], and for the SM. The upper plot shows the result obtained by combining all seven search categories, while the lower plot shows the limits obtained for each category separately, and the combined limit.

tions from the qqHH process, at the rate expected in the SM, are about two orders of magnitude lower than the limits that we set on the rate of the ggHH signal in these measurements and are therefore neglected. The observed (expected) limits on nonresonant HH production in the different benchmark scenarios range from 0.21 to 1.09 (0.16 to 1.16) pb, depending on the scenario. These limits are a factor of 2–3 higher than those obtained by the CMS measurement in the bb$\gamma\gamma$ final state [42]. The variation in expected limits reflects differences in the m_{HH} distribution among the benchmark scenarios, which in turn affect the p_{T} and angles between the particles produced in the H boson decays. As a consequence, the signal acceptance can change, along with the separation of the HH signal from backgrounds through the BDT classifiers described in section 6. The most and least stringent limits on the cross section are expected for the benchmark scenarios JHEP04 BM2 and BM7, respectively. The former has a pronounced tail of the m_{HH} distribution extending to high values, while the latter is characterized by low m_{HH} values, as seen in figure 5 of ref. [24].

JHEP07(2023)095

JHEP04 benchmark	Observed (expected) limit [fb]
BM1	469 (354)
BM2	205 (159)
BM3	563 (447)
BM4	677 (600)
BM5	439 (263)
BM6	739 (584)
BM7	1090 (1156)
BM8	495 (336)
BM9	541 (298)
BM10	988 (855)
BM11	795 (572)
BM12	897 (898)
BM8a	608 (353)
JHEP03 benchmark	**Observed (expected) limit [fb]**
BM1	888 (650)
BM2	828 (632)
BM3	538 (293)
BM4	559 (436)
BM5	556 (313)
BM6	660 (518)
BM7	525 (280)

Table 8. Observed (expected) 95% CL upper limits on the ggHH production cross section for the twelve benchmark scenarios from ref. [24], the additional benchmark scenario 8a from ref. [97] and the seven benchmark scenarios from ref. [96]. The corresponding observed (expected) upper limit for the SM is 652 (583) fb. The limits correspond to the combination of all seven search categories.

Figure 12 shows the observed and expected upper limits on the HH production cross section as a function of the coupling c_2, and the region excluded in the κ_t–c_2 plane. The effects of variations in κ_λ and κ_t on the rate of the SM single H boson background [21] and on the H boson decay branching fractions [20] are taken into account when computing these limits and those shown in figure 10. The magnitude of these effects is typically 5 to 10% within the scanned range of κ_λ and κ_t. Assuming κ_t and κ_λ are both equal to 1, the coupling c_2 is observed (expected) to be constrained to the interval $-1.05 < c_2 < 1.48$ ($-0.96 < c_2 < 1.37$) at 95% CL.

Similar to the right part of figure 12, Figure 13 shows the observed and expected regions excluded in the κ_t–κ_λ and κ_λ–c_2 planes.

Figure 14 shows the observed and expected limits on the resonant HH production cross section as a function of m_X for a spin-0 or spin-2 particle X decaying to HH. The mass points probed are listed in the fourth paragraph of section 3. The limits are expected to become more stringent as m_X increases, as the acceptance for the HH signal increases and the signal can be more easily distinguished from backgrounds. The observed (expected) 95% CL upper limits on the resonant HH production cross section range from 0.18 to 0.90 (0.08 to 1.06) pb, depending on the mass and spin. Tabulated results are provided

JHEP07(2023)095

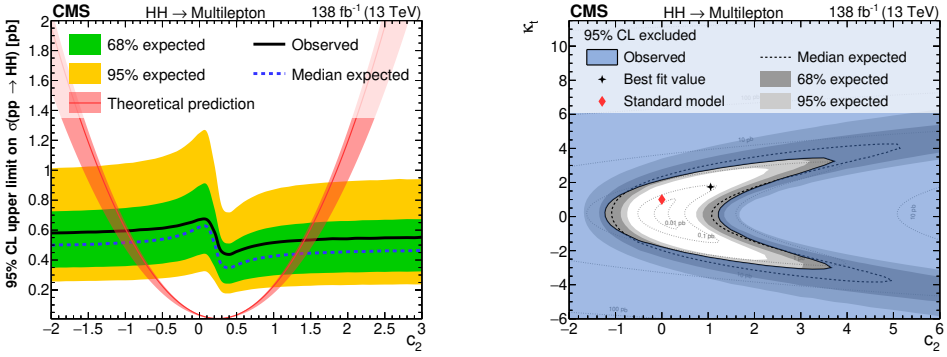


Figure 12. Observed and expected limits on the HH production cross section as a function of the effective coupling c_2 (left), and the region excluded in the κ_t–c_2 plane (right). All limits are computed at 95% CL. H boson couplings other than the ones shown in the plots (c_2 in the left plot and c_2 and κ_t in the right plot) are assumed to have the values predicted by the SM.

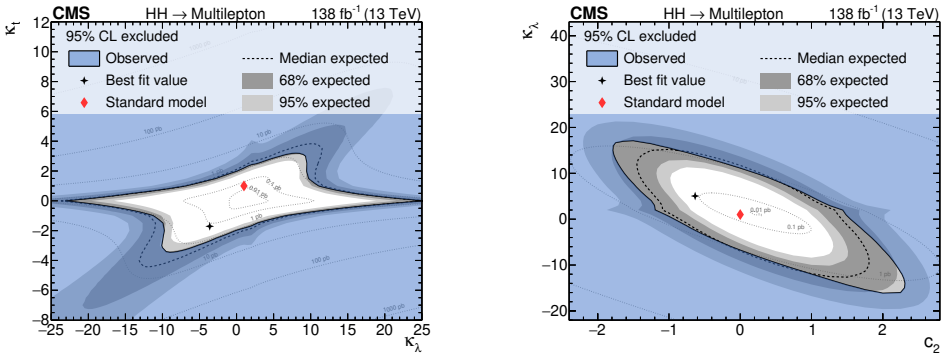


Figure 13. Observed and expected regions excluded in the κ_t–κ_λ (left) and κ_λ–c_2 (right) planes. H boson couplings other than the ones shown in the plots (κ_λ and κ_t in the left plot, and c_2 and κ_λ in the right plot) are assumed to have the values predicted by the SM.

in the HEPData record for this analysis [134]. Only the ATLAS search in the bbγγ final state achieves more stringent limits at low masses (close to 250 GeV) [43], while the low-mass limits from ATLAS in the bbττ decay mode are roughly the same [35]. Both these analyses, along with the ATLAS search for bbbb decays [33], set much more stringent limits at higher masses.

For $m_X \gtrsim 600$ GeV, the observed limit is less stringent than the expected limit, due to a small excess of events in the data that is concentrated near $m_X = 750$ GeV in the 2ℓss and 3ℓ categories. The distributions in the output of the BDT classifier targeting resonances with spin 2 and mass 750 GeV in the 2ℓss and 3ℓ categories are shown in figure 15. A small excess of events can be seen in the rightmost bin of both distributions. In the 2ℓss (3ℓ) category, 42 (17) events are observed in this bin in the data, while $27.3 \pm 2.8\,(\text{stat.}) \pm 0.7\,(\text{syst.})$ $(8.0 \pm 0.8\,(\text{stat.}) \pm 0.5\,(\text{syst.}))$ are expected from background processes, amounting to a

JHEP07(2023)095

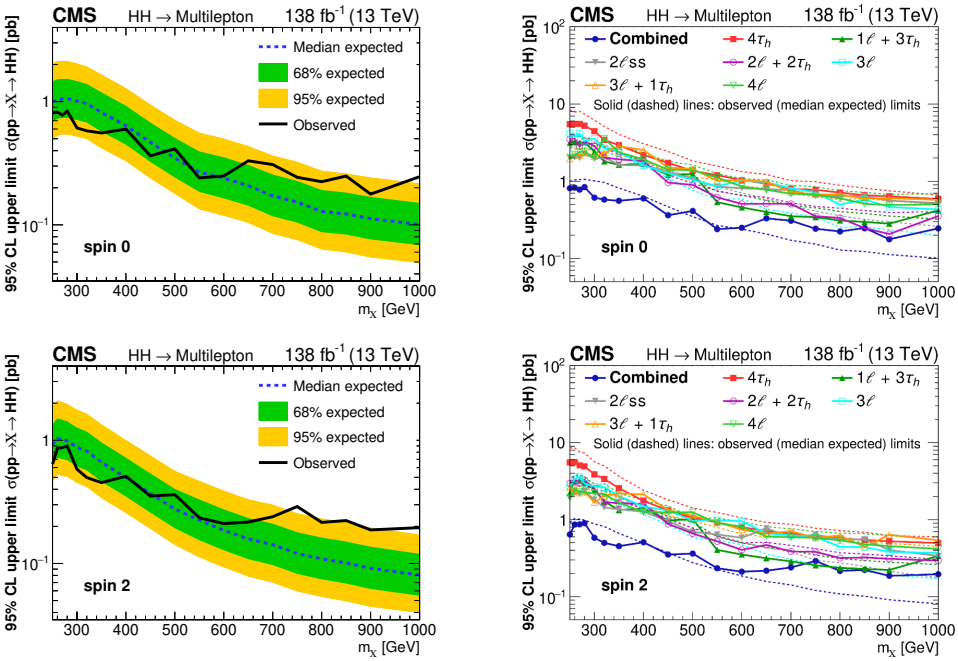


Figure 14. Observed and expected 95% CL upper limits on the production of new particles X of spin 0 (upper) and spin 2 (lower) and mass m_X in the range 250–1000 GeV, which decay to H boson pairs. The plot on the left shows the result obtained by combining all seven search categories, while the plot on the right shows the limits obtained for each category separately, and the combined limit.

local significance of about 2.1 (2.1) standard deviations. The excess affects the observed limits in a broad mass range from 600 to 1000 GeV. No measurement is made for masses above 1000 GeV, as limits on HH decays producing at least one bottom quark pair are much more stringent in this phase space [33, 34]. The presence of multiple neutrinos in HH signal events in these categories, coming from W boson or τ lepton decays, limits the experimental resolution on m_X and causes the BDT classifier output distributions to be highly correlated for resonances of similar mass. No significant excess is observed in any of the other five search categories. The significance for the combination of all seven search categories at 750 GeV amounts to 1.9 standard deviations, without accounting for the "look elsewhere effect" [135].

10 Summary

The results of a search for nonresonant and resonant Higgs boson pair (HH) production in final states with multiple reconstructed leptons, including electrons and muons (ℓ) and hadronically decaying tau leptons (τ_h), has been presented. The search targets the HH decay modes WW^*WW^*, $WW^*\tau\tau$, and $\tau\tau\tau\tau$, using proton-proton collision data recorded by the CMS experiment at a center-of-mass energy of 13 TeV and corresponding to an

JHEP07(2023)095

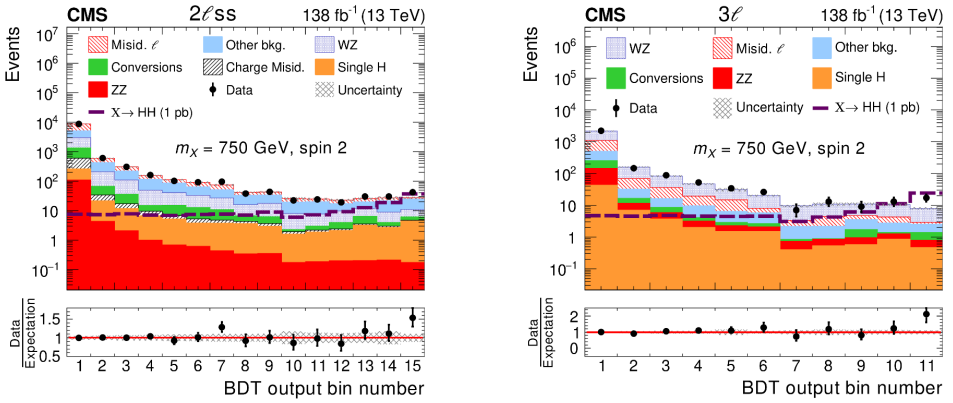


Figure 15. Distribution in BDT classifier output for resonances of spin 2 and mass 750 GeV in the 2ℓss (left) and 3ℓ (right) categories. The resonant HH signal is shown for a cross section amounting to 1 pb. The distributions expected for the background processes are shown for the values of nuisance parameters obtained from the ML fit of the signal+background hypothesis to the data.

integrated luminosity of 138 fb^{-1}. Seven search categories, distinguished by ℓ and τ_h multiplicity, are included in the analysis: 2ℓss, 3ℓ, 4ℓ, $3\ell + 1\tau_\text{h}$, $2\ell + 2\tau_\text{h}$, $1\ell + 3\tau_\text{h}$, and $4\tau_\text{h}$, where "ss" indicates an $\ell\ell$ pair with the same charge. No evidence for a signal is found in the data. Upper limits on the cross sections for both nonresonant and resonant HH production are set. The observed (expected) limits on the nonresonant HH production cross section in twenty EFT benchmark scenarios range from 0.21 to 1.09 (0.16 to 1.16) pb at 95% confidence level (CL), depending on the scenario. For nonresonant HH production with event kinematics as predicted by the standard model (SM), the observed (expected) 95% CL upper limit on the HH production rate is 21.3 (19.4) times the rate expected in the SM. The results of the search for nonresonant HH production are used to exclude regions in the plane of the H boson coupling to the top quark, y_t, and of the trilinear Higgs boson self-coupling, λ. Assuming y_t has the value expected in the SM, the observed (expected) 95% CL interval for λ is between -6.9 and 11.1 (-6.9 and 11.7) times the value expected in the SM. The resonant production of H boson pairs, resulting from decays of new heavy particles X with mass m_X, is probed within the mass range 250–1000 GeV. The corresponding observed (expected) 95% CL upper limits on the cross section for resonant HH production range from 0.18 to 0.90 (0.08 to 1.06) pb, depending on the mass and spin of the resonance.

Acknowledgments

We congratulate our colleagues in the CERN accelerator departments for the excellent performance of the LHC and thank the technical and administrative staffs at CERN and at other CMS institutes for their contributions to the success of the CMS effort. In addition, we gratefully acknowledge the computing centers and personnel of the Worldwide

JHEP07(2023)095

LHC Computing Grid and other centers for delivering so effectively the computing infrastructure essential to our analyses. Finally, we acknowledge the enduring support for the construction and operation of the LHC, the CMS detector, and the supporting computing infrastructure provided by the following funding agencies: BMBWF and FWF (Austria); FNRS and FWO (Belgium); CNPq, CAPES, FAPERJ, FAPERGS, and FAPESP (Brazil); MES and BNSF (Bulgaria); CERN; CAS, MoST, and NSFC (China); MINCIENCIAS (Colombia); MSES and CSF (Croatia); RIF (Cyprus); SENESCYT (Ecuador); MoER, ERC PUT and ERDF (Estonia); Academy of Finland, MEC, and HIP (Finland); CEA and CNRS/IN2P3 (France); BMBF, DFG, and HGF (Germany); GSRI (Greece); NKFIH (Hungary); DAE and DST (India); IPM (Iran); SFI (Ireland); INFN (Italy); MSIP and NRF (Republic of Korea); MES (Latvia); LAS (Lithuania); MOE and UM (Malaysia); BUAP, CINVESTAV, CONACYT, LNS, SEP, and UASLP-FAI (Mexico); MOS (Montenegro); MBIE (New Zealand); PAEC (Pakistan); MES and NSC (Poland); FCT (Portugal); MESTD (Serbia); MCIN/AEI and PCTI (Spain); MOSTR (Sri Lanka); Swiss Funding Agencies (Switzerland); MST (Taipei); MHESI and NSTDA (Thailand); TUBITAK and TENMAK (Turkey); NASU (Ukraine); STFC (United Kingdom); DOE and NSF (USA).

Individuals have received support from the Marie-Curie program and the European Research Council and Horizon 2020 Grant, contract Nos. 675440, 724704, 752730, 758316, 765710, 824093, 884104, and COST Action CA16108 (European Union); the Leventis Foundation; the Alfred P. Sloan Foundation; the Alexander von Humboldt Foundation; the Belgian Federal Science Policy Office; the Fonds pour la Formation à la Recherche dans l'Industrie et dans l'Agriculture (FRIA-Belgium); the Agentschap voor Innovatie door Wetenschap en Technologie (IWT-Belgium); the F.R.S.-FNRS and FWO (Belgium) under the "Excellence of Science — EOS" — be.h project n. 30820817; the Beijing Municipal Science & Technology Commission, No. Z191100007219010; the Ministry of Education, Youth and Sports (MEYS) of the Czech Republic; the Hellenic Foundation for Research and Innovation (HFRI), Project Number 2288 (Greece); the Deutsche Forschungsgemeinschaft (DFG), under Germany's Excellence Strategy — EXC 2121 "Quantum Universe" — 390833306, and under project number 400140256 — GRK2497; the Hungarian Academy of Sciences, the New National Excellence Program — ÚNKP, the NKFIH research grants K 124845, K 124850, K 128713, K 128786, K 129058, K 131991, K 133046, K 138136, K 143460, K 143477, 2020-2.2.1-ED-2021-00181, and TKP2021-NKTA-64 (Hungary); the Council of Science and Industrial Research, India; the Latvian Council of Science; the Ministry of Education and Science, project no. 2022/WK/14, and the National Science Center, contracts Opus 2021/41/B/ST2/01369 and 2021/43/B/ST2/01552 (Poland); the Fundação para a Ciência e a Tecnologia, grant CEECIND/01334/2018 (Portugal); the National Priorities Research Program by Qatar National Research Fund; MCIN/AEI/10.13039/501100011033, ERDF "a way of making Europe", and the Programa Estatal de Fomento de la Investigación Científica y Técnica de Excelencia María de Maeztu, grant MDM-2017-0765 and Programa Severo Ochoa del Principado de Asturias (Spain); the Chulalongkorn Academic into Its 2nd Century Project Advancement Project, and the National Science, Research and Innovation Fund via the Program Management Unit for Human Resources & Institutional Development, Research and Innovation, grant B05F650021

JHEP07(2023)095

(Thailand); the Kavli Foundation; the Nvidia Corporation; the SuperMicro Corporation; the Welch Foundation, contract C-1845; and the Weston Havens Foundation (USA).

Open Access. This article is distributed under the terms of the Creative Commons Attribution License (CC-BY 4.0), which permits any use, distribution and reproduction in any medium, provided the original author(s) and source are credited.

References

[1] ATLAS collaboration, *Observation of a new particle in the search for the Standard Model Higgs boson with the ATLAS detector at the LHC*, *Phys. Lett. B* **716** (2012) 1 [arXiv:1207.7214] [INSPIRE].

[2] CMS collaboration, *Observation of a new boson at a mass of* 125 *GeV with the CMS experiment at the LHC*, *Phys. Lett. B* **716** (2012) 30 [arXiv:1207.7235] [INSPIRE].

[3] CMS collaboration, *Observation of a new boson with mass near* 125 *GeV in pp collisions at* $\sqrt{s} = 7$ *and* 8 *TeV*, *JHEP* **06** (2013) 081 [arXiv:1303.4571] [INSPIRE].

[4] CMS collaboration, *Combined measurements of Higgs boson couplings in proton–proton collisions at* $\sqrt{s} = 13$ *TeV*, *Eur. Phys. J. C* **79** (2019) 421 [arXiv:1809.10733] [INSPIRE].

[5] ATLAS collaboration, *Combined measurements of Higgs boson production and decay using up to* 80 fb^{-1} *of proton-proton collision data at* $\sqrt{s} = 13$ *TeV collected with the ATLAS experiment*, *Phys. Rev. D* **101** (2020) 012002 [arXiv:1909.02845] [INSPIRE].

[6] CMS collaboration, *Measurement of the Higgs boson width and evidence of its off-shell contributions to ZZ production*, *Nature Phys.* **18** (2022) 1329 [arXiv:2202.06923] [INSPIRE].

[7] F. Englert and R. Brout, *Broken symmetry and the mass of gauge vector mesons*, *Phys. Rev. Lett.* **13** (1964) 321 [INSPIRE].

[8] P.W. Higgs, *Broken symmetries, massless particles and gauge fields*, *Phys. Lett.* **12** (1964) 132 [INSPIRE].

[9] P.W. Higgs, *Broken symmetries and the masses of gauge bosons*, *Phys. Rev. Lett.* **13** (1964) 508 [INSPIRE].

[10] G.S. Guralnik, C.R. Hagen and T.W.B. Kibble, *Global conservation laws and massless particles*, *Phys. Rev. Lett.* **13** (1964) 585 [INSPIRE].

[11] P.W. Higgs, *Spontaneous symmetry breakdown without massless bosons*, *Phys. Rev.* **145** (1966) 1156 [INSPIRE].

[12] T.W.B. Kibble, *Symmetry breaking in non-Abelian gauge theories*, *Phys. Rev.* **155** (1967) 1554 [INSPIRE].

[13] S.L. Glashow, *Partial symmetries of weak interactions*, *Nucl. Phys.* **22** (1961) 579 [INSPIRE].

[14] S. Weinberg, *A model of leptons*, *Phys. Rev. Lett.* **19** (1967) 1264 [INSPIRE].

[15] A. Salam, *Weak and electromagnetic interactions*, *Conf. Proc. C* **680519** (1968) 367 [INSPIRE].

[16] D. de Florian, I. Fabre and J. Mazzitelli, *Triple Higgs production at hadron colliders at NNLO in QCD*, *JHEP* **03** (2020) 155 [arXiv:1912.02760] [INSPIRE].

JHEP07(2023)095

[17] O. Aberle et al., *High-Luminosity Large Hadron Collider (HL-LHC): Technical Design Report V. 0.1*, CERN-2017-007-M (2017) [DOI:10.23731/CYRM-2017-004] [INSPIRE].

[18] M. Grazzini et al., *Higgs boson pair production at NNLO with top quark mass effects*, *JHEP* **05** (2018) 059 [arXiv:1803.02463] [INSPIRE].

[19] F.A. Dreyer and A. Karlberg, *Vector-boson fusion Higgs pair production at N^3LO*, *Phys. Rev. D* **98** (2018) 114016 [arXiv:1811.07906] [INSPIRE].

[20] G. Degrassi, P.P. Giardino, F. Maltoni and D. Pagani, *Probing the Higgs self coupling via single Higgs production at the LHC*, *JHEP* **12** (2016) 080 [arXiv:1607.04251] [INSPIRE].

[21] F. Maltoni, D. Pagani, A. Shivaji and X. Zhao, *Trilinear Higgs coupling determination via single-Higgs differential measurements at the LHC*, *Eur. Phys. J. C* **77** (2017) 887 [arXiv:1709.08649] [INSPIRE].

[22] W. Buchmuller and D. Wyler, *Effective Lagrangian analysis of new interactions and flavor conservation*, *Nucl. Phys. B* **268** (1986) 621 [INSPIRE].

[23] B. Grzadkowski, M. Iskrzynski, M. Misiak and J. Rosiek, *Dimension-six terms in the Standard Model Lagrangian*, *JHEP* **10** (2010) 085 [arXiv:1008.4884] [INSPIRE].

[24] A. Carvalho et al., *Higgs pair production: choosing benchmarks with cluster analysis*, *JHEP* **04** (2016) 126 [arXiv:1507.02245] [INSPIRE].

[25] N. Craig, J. Galloway and S. Thomas, *Searching for signs of the second Higgs doublet*, arXiv:1305.2424 [INSPIRE].

[26] D.T. Nhung, M. Mühlleitner, J. Streicher and K. Walz, *Higher order corrections to the trilinear Higgs self-couplings in the real NMSSM*, *JHEP* **11** (2013) 181 [arXiv:1306.3926] [INSPIRE].

[27] R. Grober and M. Mühlleitner, *Composite Higgs boson pair production at the LHC*, *JHEP* **06** (2011) 020 [arXiv:1012.1562] [INSPIRE].

[28] R. Contino et al., *Strong double Higgs production at the LHC*, *JHEP* **05** (2010) 089 [arXiv:1002.1011] [INSPIRE].

[29] C. Englert, T. Plehn, D. Zerwas and P.M. Zerwas, *Exploring the Higgs portal*, *Phys. Lett. B* **703** (2011) 298 [arXiv:1106.3097] [INSPIRE].

[30] J.M. No and M. Ramsey-Musolf, *Probing the Higgs portal at the LHC through resonant di-Higgs production*, *Phys. Rev. D* **89** (2014) 095031 [arXiv:1310.6035] [INSPIRE].

[31] L. Randall and R. Sundrum, *A large mass hierarchy from a small extra dimension*, *Phys. Rev. Lett.* **83** (1999) 3370 [hep-ph/9905221] [INSPIRE].

[32] K.-M. Cheung, *Phenomenology of radion in Randall-Sundrum scenario*, *Phys. Rev. D* **63** (2001) 056007 [hep-ph/0009232] [INSPIRE].

[33] ATLAS collaboration, *Search for resonant pair production of Higgs bosons in the $b\bar{b}b\bar{b}$ final state using pp collisions at $\sqrt{s} = 13$ TeV with the ATLAS detector*, *Phys. Rev. D* **105** (2022) 092002 [arXiv:2202.07288] [INSPIRE].

[34] CMS collaboration, *Search for heavy resonances decaying to a pair of Lorentz-boosted Higgs bosons in final states with leptons and a bottom quark pair at $\sqrt{s} = 13$ TeV*, *JHEP* **05** (2022) 005 [arXiv:2112.03161] [INSPIRE].

JHEP07(2023)095

[35] ATLAS collaboration, *Search for resonant and non-resonant Higgs boson pair production in the $b\bar{b}\tau^+\tau^-$ decay channel using 13 TeV pp collision data from the ATLAS detector*, arXiv:2209.10910 [INSPIRE].

[36] U. Baur, T. Plehn and D.L. Rainwater, *Measuring the Higgs boson self coupling at the LHC and finite top mass matrix elements*, *Phys. Rev. Lett.* **89** (2002) 151801 [hep-ph/0206024] [INSPIRE].

[37] U. Baur, T. Plehn and D.L. Rainwater, *Determining the Higgs boson selfcoupling at hadron colliders*, *Phys. Rev. D* **67** (2003) 033003 [hep-ph/0211224] [INSPIRE].

[38] Q. Li, Z. Li, Q.-S. Yan and X. Zhao, *Probe Higgs boson pair production via the $3\ell 2j+\not{E}$ mode*, *Phys. Rev. D* **92** (2015) 014015 [arXiv:1503.07611] [INSPIRE].

[39] A. Adhikary et al., *Revisiting the non-resonant Higgs pair production at the HL-LHC*, *JHEP* **07** (2018) 116 [arXiv:1712.05346] [INSPIRE].

[40] J. Ren et al., *LHC search of new Higgs boson via resonant di-Higgs production with decays into 4W*, *JHEP* **06** (2018) 090 [arXiv:1706.05980] [INSPIRE].

[41] ATLAS collaboration, *Search for Higgs boson pair production in the $WW^{(*)}WW^{(*)}$ decay channel using ATLAS data recorded at $\sqrt{s} = 13$ TeV*, *JHEP* **05** (2019) 124 [arXiv:1811.11028] [INSPIRE].

[42] CMS collaboration, *Search for nonresonant Higgs boson pair production in final states with two bottom quarks and two photons in proton-proton collisions at $\sqrt{s} = 13$ TeV*, *JHEP* **03** (2021) 257 [arXiv:2011.12373] [INSPIRE].

[43] ATLAS collaboration, *Search for Higgs boson pair production in the two bottom quarks plus two photons final state in pp collisions at $\sqrt{s} = 13$ TeV with the ATLAS detector*, *Phys. Rev. D* **106** (2022) 052001 [arXiv:2112.11876] [INSPIRE].

[44] ATLAS collaboration, *Search for the $HH \to b\bar{b}b\bar{b}$ process via vector-boson fusion production using proton-proton collisions at $\sqrt{s} = 13$ TeV with the ATLAS detector*, *JHEP* **07** (2020) 108 [*Erratum ibid.* **01** (2021) 145] [arXiv:2001.05178] [INSPIRE].

[45] CMS collaboration, *Search for Higgs boson pair production in the four b quark final state in proton-proton collisions at $\sqrt{s} = 13$ TeV*, *Phys. Rev. Lett.* **129** (2022) 081802 [arXiv:2202.09617] [INSPIRE].

[46] CMS collaboration, *Search for nonresonant pair production of highly energetic Higgs bosons decaying to bottom quarks*, arXiv:2205.06667 [INSPIRE].

[47] CMS collaboration, *Search for resonant pair production of Higgs bosons decaying to bottom quark-antiquark pairs in proton-proton collisions at 13 TeV*, *JHEP* **08** (2018) 152 [arXiv:1806.03548] [INSPIRE].

[48] CMS collaboration, *Search for nonresonant Higgs boson pair production in final state with two bottom quarks and two tau leptons in proton-proton collisions at $\sqrt{s} = 13$ TeV*, *Phys. Lett. B* **842** (2023) 137531 [arXiv:2206.09401] [INSPIRE].

[49] ATLAS collaboration, *Reconstruction and identification of boosted di-τ systems in a search for Higgs boson pairs using 13 TeV proton-proton collision data in ATLAS*, *JHEP* **11** (2020) 163 [arXiv:2007.14811] [INSPIRE].

[50] CMS collaboration, *Search for resonant and nonresonant Higgs boson pair production in the $b\bar{b}\ell\nu\ell\nu$ final state in proton-proton collisions at $\sqrt{s} = 13$ TeV*, *JHEP* **01** (2018) 054 [arXiv:1708.04188] [INSPIRE].

JHEP07(2023)095

[51] ATLAS collaboration, *Search for non-resonant Higgs boson pair production in the $bb\ell\nu\ell\nu$ final state with the ATLAS detector in pp collisions at $\sqrt{s} = 13$ TeV*, *Phys. Lett. B* **801** (2020) 135145 [arXiv:1908.06765] [INSPIRE].

[52] ATLAS collaboration, *Search for Higgs boson pair production in the $b\bar{b}WW^*$ decay mode at $\sqrt{s} = 13$ TeV with the ATLAS detector*, *JHEP* **04** (2019) 092 [arXiv:1811.04671] [INSPIRE].

[53] ATLAS collaboration, *Search for Higgs boson pair production in the $\gamma\gamma WW^*$ channel using pp collision data recorded at $\sqrt{s} = 13$ TeV with the ATLAS detector*, *Eur. Phys. J. C* **78** (2018) 1007 [arXiv:1807.08567] [INSPIRE].

[54] CMS collaboration, *Combination of searches for Higgs boson pair production in proton-proton collisions at $\sqrt{s} = 13$ TeV*, *Phys. Rev. Lett.* **122** (2019) 121803 [arXiv:1811.09689] [INSPIRE].

[55] ATLAS collaboration, *Combination of searches for Higgs boson pairs in pp collisions at $\sqrt{s} = 13$ TeV with the ATLAS detector*, *Phys. Lett. B* **800** (2020) 135103 [arXiv:1906.02025] [INSPIRE].

[56] CMS collaboration, *Performance of the CMS Level-1 trigger in proton-proton collisions at $\sqrt{s} = 13$ TeV*, 2020 *JINST* **15** P10017 [arXiv:2006.10165] [INSPIRE].

[57] CMS collaboration, *The CMS trigger system*, 2017 *JINST* **12** P01020 [arXiv:1609.02366] [INSPIRE].

[58] CMS collaboration, *The CMS Experiment at the CERN LHC*, 2008 *JINST* **3** S08004 [INSPIRE].

[59] CMS collaboration, *Precision luminosity measurement in proton-proton collisions at $\sqrt{s} = 13$ TeV in 2015 and 2016 at CMS*, *Eur. Phys. J. C* **81** (2021) 800 [arXiv:2104.01927] [INSPIRE].

[60] CMS collaboration, *CMS luminosity measurement for the 2017 data-taking period at $\sqrt{s} = 13$ TeV*, CMS-PAS-LUM-17-004, CERN, Geneva (2018).

[61] CMS collaboration, *CMS luminosity measurement for the 2018 data-taking period at $\sqrt{s} = 13$ TeV*, CMS-PAS-LUM-18-002, CERN, Geneva (2019).

[62] J. Alwall et al., *The automated computation of tree-level and next-to-leading order differential cross sections, and their matching to parton shower simulations*, *JHEP* **07** (2014) 079 [arXiv:1405.0301] [INSPIRE].

[63] A. Kalogeropoulos and J. Alwall, *The SysCalc code: a tool to derive theoretical systematic uncertainties*, arXiv:1801.08401 [INSPIRE].

[64] P. Nason, *A New method for combining NLO QCD with shower Monte Carlo algorithms*, *JHEP* **11** (2004) 040 [hep-ph/0409146] [INSPIRE].

[65] S. Frixione, P. Nason and C. Oleari, *Matching NLO QCD computations with Parton Shower simulations: the POWHEG method*, *JHEP* **11** (2007) 070 [arXiv:0709.2092] [INSPIRE].

[66] S. Alioli, P. Nason, C. Oleari and E. Re, *A general framework for implementing NLO calculations in shower Monte Carlo programs: the POWHEG BOX*, *JHEP* **06** (2010) 043 [arXiv:1002.2581] [INSPIRE].

[67] J.M. Campbell and R.K. Ellis, *An Update on vector boson pair production at hadron colliders*, *Phys. Rev. D* **60** (1999) 113006 [hep-ph/9905386] [INSPIRE].

JHEP07(2023)095

[68] J.M. Campbell, R.K. Ellis and C. Williams, *Vector boson pair production at the LHC*, *JHEP* **07** (2011) 018 [arXiv:1105.0020] [INSPIRE].

[69] J.M. Campbell, R.K. Ellis and W.T. Giele, *A multi-threaded version of MCFM*, *Eur. Phys. J. C* **75** (2015) 246 [arXiv:1503.06182] [INSPIRE].

[70] T. Sjöstrand et al., *An introduction to PYTHIA 8.2*, *Comput. Phys. Commun.* **191** (2015) 159 [arXiv:1410.3012] [INSPIRE].

[71] B. Hespel, D. Lopez-Val and E. Vryonidou, *Higgs pair production via gluon fusion in the Two-Higgs-Doublet Model*, *JHEP* **09** (2014) 124 [arXiv:1407.0281] [INSPIRE].

[72] A. Carvalho, *Gravity particles from warped extra dimensions, predictions for LHC*, arXiv:1404.0102 [INSPIRE].

[73] G. Heinrich et al., *NLO predictions for Higgs boson pair production with full top quark mass dependence matched to parton showers*, *JHEP* **08** (2017) 088 [arXiv:1703.09252] [INSPIRE].

[74] G. Heinrich et al., *Probing the trilinear Higgs boson coupling in di-Higgs production at NLO QCD including parton shower effects*, *JHEP* **06** (2019) 066 [arXiv:1903.08137] [INSPIRE].

[75] G. Heinrich, S.P. Jones, M. Kerner and L. Scyboz, *A non-linear EFT description of $gg \to HH$ at NLO interfaced to POWHEG*, *JHEP* **10** (2020) 021 [arXiv:2006.16877] [INSPIRE].

[76] E. Bagnaschi, G. Degrassi, P. Slavich and A. Vicini, *Higgs production via gluon fusion in the POWHEG approach in the SM and in the MSSM*, *JHEP* **02** (2012) 088 [arXiv:1111.2854] [INSPIRE].

[77] P. Nason and C. Oleari, *NLO Higgs boson production via vector-boson fusion matched with shower in POWHEG*, *JHEP* **02** (2010) 037 [arXiv:0911.5299] [INSPIRE].

[78] G. Luisoni, P. Nason, C. Oleari and F. Tramontano, *$HW^{\pm}/HZ + 0$ and 1 jet at NLO with the POWHEG BOX interfaced to GoSam and their merging within MiNLO*, *JHEP* **10** (2013) 083 [arXiv:1306.2542] [INSPIRE].

[79] T. Melia, P. Nason, R. Rontsch and G. Zanderighi, *W^+W^-, WZ and ZZ production in the POWHEG BOX*, *JHEP* **11** (2011) 078 [arXiv:1107.5051] [INSPIRE].

[80] P. Nason and G. Zanderighi, *W^+W^- , WZ and ZZ production in the POWHEG-BOX-V2*, *Eur. Phys. J. C* **74** (2014) 2702 [arXiv:1311.1365] [INSPIRE].

[81] J.M. Campbell, R.K. Ellis and C. Williams, *Bounding the Higgs width at the LHC using full analytic results for $gg \to e^-e^+\mu^-\mu^+$*, *JHEP* **04** (2014) 060 [arXiv:1311.3589] [INSPIRE].

[82] R. Frederix, E. Re and P. Torrielli, *Single-top t-channel hadroproduction in the four-flavour scheme with POWHEG and aMC@NLO*, *JHEP* **09** (2012) 130 [arXiv:1207.5391] [INSPIRE].

[83] E. Re, *Single-top Wt-channel production matched with parton showers using the POWHEG method*, *Eur. Phys. J. C* **71** (2011) 1547 [arXiv:1009.2450] [INSPIRE].

[84] S. Frixione, P. Nason and G. Ridolfi, *A positive-weight next-to-leading-order Monte Carlo for heavy flavour hadroproduction*, *JHEP* **09** (2007) 126 [arXiv:0707.3088] [INSPIRE].

[85] NNPDF collaboration, *Parton distributions for the LHC Run II*, *JHEP* **04** (2015) 040 [arXiv:1410.8849] [INSPIRE].

JHEP07(2023)095

[86] NNPDF collaboration, *Parton distributions from high-precision collider data*, *Eur. Phys. J. C* **77** (2017) 663 [arXiv:1706.00428] [INSPIRE].

[87] J. Butterworth et al., *PDF4LHC recommendations for LHC Run II*, *J. Phys. G* **43** (2016) 023001 [arXiv:1510.03865] [INSPIRE].

[88] J. Rojo et al., *The PDF4LHC report on PDFs and LHC data: Results from Run I and preparation for Run II*, *J. Phys. G* **42** (2015) 103103 [arXiv:1507.00556] [INSPIRE].

[89] A. Accardi et al., *A critical appraisal and evaluation of modern PDFs*, *Eur. Phys. J. C* **76** (2016) 471 [arXiv:1603.08906] [INSPIRE].

[90] CMS collaboration, *Event generator tunes obtained from underlying event and multiparton scattering measurements*, *Eur. Phys. J. C* **76** (2016) 155 [arXiv:1512.00815] [INSPIRE].

[91] CMS collaboration, *Extraction and validation of a new set of CMS PYTHIA8 tunes from underlying-event measurements*, *Eur. Phys. J. C* **80** (2020) 4 [arXiv:1903.12179] [INSPIRE].

[92] P. Skands, S. Carrazza and J. Rojo, *Tuning PYTHIA 8.1: the Monash 2013 tune*, *Eur. Phys. J. C* **74** (2014) 3024 [arXiv:1404.5630] [INSPIRE].

[93] J. Alwall et al., *Comparative study of various algorithms for the merging of parton showers and matrix elements in hadronic collisions*, *Eur. Phys. J. C* **53** (2008) 473 [arXiv:0706.2569] [INSPIRE].

[94] R. Frederix and S. Frixione, *Merging meets matching in MC@NLO*, *JHEP* **12** (2012) 061 [arXiv:1209.6215] [INSPIRE].

[95] GEANT4 collaboration, *GEANT4 — a simulation toolkit*, *Nucl. Instrum. Meth. A* **506** (2003) 250 [INSPIRE].

[96] M. Capozi and G. Heinrich, *Exploring anomalous couplings in Higgs boson pair production through shape analysis*, *JHEP* **03** (2020) 091 [arXiv:1908.08923] [INSPIRE].

[97] G. Buchalla et al., *Higgs boson pair production in non-linear Effective Field Theory with full m_t-dependence at NLO QCD*, *JHEP* **09** (2018) 057 [arXiv:1806.05162] [INSPIRE].

[98] A. Carvalho et al., *On the reinterpretation of non-resonant searches for Higgs boson pairs*, *JHEP* **02** (2021) 049 [arXiv:1710.08261] [INSPIRE].

[99] CMS collaboration, *Particle-flow reconstruction and global event description with the CMS detector*, 2017 *JINST* **12** P10003 [arXiv:1706.04965] [INSPIRE].

[100] M. Cacciari, G.P. Salam and G. Soyez, *The anti-k_t jet clustering algorithm*, *JHEP* **04** (2008) 063 [arXiv:0802.1189] [INSPIRE].

[101] M. Cacciari, G.P. Salam and G. Soyez, *FastJet user manual*, *Eur. Phys. J. C* **72** (2012) 1896 [arXiv:1111.6097] [INSPIRE].

[102] CMS collaboration, *Electron and photon reconstruction and identification with the CMS experiment at the CERN LHC*, 2021 *JINST* **16** P05014 [arXiv:2012.06888] [INSPIRE].

[103] CMS collaboration, *Measurement of the Higgs boson production rate in association with top quarks in final states with electrons, muons, and hadronically decaying tau leptons at $\sqrt{s} = 13$ TeV*, *Eur. Phys. J. C* **81** (2021) 378 [arXiv:2011.03652] [INSPIRE].

[104] CMS collaboration, *Performance of electron reconstruction and selection with the CMS detector in proton-proton collisions at $\sqrt{s} = 8$ TeV*, 2015 *JINST* **10** P06005 [arXiv:1502.02701] [INSPIRE].

JHEP07(2023)095

[105] CMS collaboration, *Performance of the CMS muon detector and muon reconstruction with proton-proton collisions at $\sqrt{s} = 13$ TeV*, 2018 *JINST* **13** P06015 [arXiv:1804.04528] [INSPIRE].

[106] CMS collaboration, *Performance of reconstruction and identification of τ leptons decaying to hadrons and ν_τ in pp collisions at $\sqrt{s} = 13$ TeV*, 2018 *JINST* **13** P10005 [arXiv:1809.02816] [INSPIRE].

[107] CMS collaboration, *Identification of hadronic tau lepton decays using a deep neural network*, 2022 *JINST* **17** P07023 [arXiv:2201.08458] [INSPIRE].

[108] Y. LeCun, *Generalization and network design strategies*, in *Connectionism in perspective*, R. Pfeife et al. eds., Zurich, Switzerland (1989).

[109] CMS collaboration, *Pileup mitigation at CMS in 13 TeV data*, 2020 *JINST* **15** P09018 [arXiv:2003.00503] [INSPIRE].

[110] D. Bertolini, P. Harris, M. Low and N. Tran, *Pileup per particle identification*, *JHEP* **10** (2014) 059 [arXiv:1407.6013] [INSPIRE].

[111] CMS collaboration, *Jet energy scale and resolution in the CMS experiment in pp collisions at 8 TeV*, 2017 *JINST* **12** P02014 [arXiv:1607.03663] [INSPIRE].

[112] CMS collaboration, *Search for resonances decaying to a pair of Higgs bosons in the $b\bar{b}q\bar{q}'\ell\nu$ final state in proton-proton collisions at $\sqrt{s} = 13$ TeV*, *JHEP* **10** (2019) 125 [arXiv:1904.04193] [INSPIRE].

[113] E. Bols et al., *Jet flavour classification using DeepJet*, 2020 *JINST* **15** P12012 [arXiv:2008.10519] [INSPIRE].

[114] CMS collaboration, *Performance of missing transverse momentum reconstruction in proton-proton collisions at $\sqrt{s} = 13$ TeV using the CMS detector*, 2019 *JINST* **14** P07004 [arXiv:1903.06078] [INSPIRE].

[115] CMS collaboration, *Evidence for associated production of a Higgs boson with a top quark pair in final states with electrons, muons, and hadronically decaying τ leptons at $\sqrt{s} = 13$ TeV*, *JHEP* **08** (2018) 066 [arXiv:1803.05485] [INSPIRE].

[116] L. Breiman, J. Friedman, R.A. Olshen and C.J. Stone, *Classification and regression trees*, Chapman and Hall/CRC (1984) [INSPIRE].

[117] K. Ehatäht, L. Marzola and C. Veelken, *Reconstruction of the mass of Higgs boson pairs in events with Higgs boson pairs decaying into four τ leptons*, arXiv:1809.06140 [INSPIRE].

[118] T. Chen and C. Guestrin, *XGBoost: a scalable tree boosting system*, arXiv:1603.02754 [DOI:10.1145/2939672.2939785] [INSPIRE].

[119] F. Pedregosa et al., *Scikit-learn: machine learning in Python*, *J. Machine Learning Res.* **12** (2011) 2825 [arXiv:1201.0490] [INSPIRE].

[120] L. Tani, D. Rand, C. Veelken and M. Kadastik, *Evolutionary algorithms for hyperparameter optimization in machine learning for application in high energy physics*, *Eur. Phys. J. C* **81** (2021) 170 [arXiv:2011.04434] [INSPIRE].

[121] CMS collaboration, *Search for electroweak production of charginos and neutralinos in multilepton final states in proton-proton collisions at $\sqrt{s} = 13$ TeV*, *JHEP* **03** (2018) 166 [arXiv:1709.05406] [INSPIRE].

JHEP07(2023)095

[122] J. Baglio et al., *$gg \to HH$: combined uncertainties*, *Phys. Rev. D* **103** (2021) 056002 [arXiv:2008.11626] [INSPIRE].

[123] LHC Higgs Cross Section Working Group collaboration, *Handbook of LHC Higgs Cross Sections: 4. Deciphering the nature of the Higgs sector*, arXiv:1610.07922 [DOI:10.23731/CYRM-2017-002] [INSPIRE].

[124] M. Grazzini, S. Kallweit, D. Rathlev and M. Wiesemann, *$W^{\pm}Z$ production at hadron colliders in NNLO QCD*, *Phys. Lett. B* **761** (2016) 179 [arXiv:1604.08576] [INSPIRE].

[125] F. Cascioli et al., *ZZ production at hadron colliders in NNLO QCD*, *Phys. Lett. B* **735** (2014) 311 [arXiv:1405.2219] [INSPIRE].

[126] F. Caola, K. Melnikov, R. Röntsch and L. Tancredi, *QCD corrections to ZZ production in gluon fusion at the LHC*, *Phys. Rev. D* **92** (2015) 094028 [arXiv:1509.06734] [INSPIRE].

[127] CMS collaboration, *Jet algorithms performance in 13 TeV data*, CMS-PAS-JME-16-003, CERN, Geneva (2017).

[128] CMS collaboration, *Measurement of the inelastic proton-proton cross section at $\sqrt{s} = 13$ TeV*, *JHEP* **07** (2018) 161 [arXiv:1802.02613] [INSPIRE].

[129] G. Cowan, K. Cranmer, E. Gross and O. Vitells, *Asymptotic formulae for likelihood-based tests of new physics*, *Eur. Phys. J. C* **71** (2011) 1554 [*Erratum ibid.* **73** (2013) 2501] [arXiv:1007.1727] [INSPIRE].

[130] ATLAS, CMS collaboration and L.H.C.H.C. Group, *Procedure for the LHC Higgs boson search combination in summer 2011*, ATL-PHYS-PUB-2011-011 (2011).

[131] J.S. Conway, *Incorporating Nuisance Parameters in Likelihoods for Multisource Spectra*, in the proceedings of the *PHYSTAT 2011*, (2011), p. 115–120 [DOI:10.5170/CERN-2011-006.115] [arXiv:1103.0354] [INSPIRE].

[132] T. Junk, *Confidence level computation for combining searches with small statistics*, *Nucl. Instrum. Meth. A* **434** (1999) 435 [hep-ex/9902006] [INSPIRE].

[133] A.L. Read, *Presentation of search results: The CL_s technique*, *J. Phys. G* **28** (2002) 2693 [INSPIRE].

[134] CMS collaboration, *Search for Higgs boson pairs decaying to WWWW, $WW\tau\tau$, and $\tau\tau\tau\tau$ in proton-proton collisions at $\sqrt{s} = 13$ TeV*, https://www.hepdata.net/record/ins2098277 [DOI:10.17182/HEPDATA.130795].

[135] E. Gross and O. Vitells, *Trial factors for the look elsewhere effect in high energy physics*, *Eur. Phys. J. C* **70** (2010) 525 [arXiv:1005.1891] [INSPIRE].

JHEP07(2023)095

The CMS collaboration

Yerevan Physics Institute, Yerevan, Armenia

A. Tumasyan[1]

Institut für Hochenergiephysik, Vienna, Austria

W. Adam, J.W. Andrejkovic, T. Bergauer, S. Chatterjee, K. Damanakis, M. Dragicevic, A. Escalante Del Valle, M. Jeitler[2], N. Krammer, L. Lechner, D. Liko, I. Mikulec, P. Paulitsch, F.M. Pitters, J. Schieck[2], R. Schöfbeck, D. Schwarz, S. Templ, W. Waltenberger, C.-E. Wulz[2]

Universiteit Antwerpen, Antwerpen, Belgium

M.R. Darwish[3], E.A. De Wolf, T. Janssen, T. Kello[4], A. Lelek, H. Rejeb Sfar, P. Van Mechelen, N. Van Remortel

Vrije Universiteit Brussel, Brussel, Belgium

E.S. Bols, J. D'Hondt, A. De Moor, M. Delcourt, H. El Faham, S. Lowette, S. Moortgat, A. Morton, D. Müller, A.R. Sahasransu, S. Tavernier, W. Van Doninck, D. Vannerom

Université Libre de Bruxelles, Bruxelles, Belgium

D. Beghin, B. Clerbaux, G. De Lentdecker, L. Favart, J. Jaramillo, K. Lee, M. Mahdavikhorrami, I. Makarenko, A. Malara, S. Paredes, L. Pétré, A. Popov, N. Postiau, E. Starling, L. Thomas, M. Vanden Bemden, C. Vander Velde, P. Vanlaer

Ghent University, Ghent, Belgium

D. Dobur, J. Knolle, L. Lambrecht, G. Mestdach, M. Niedziela, C. Rendón, C. Roskas, A. Samalan, K. Skovpen, M. Tytgat, N. Van Den Bossche, B. Vermassen, L. Wezenbeek

Université Catholique de Louvain, Louvain-la-Neuve, Belgium

A. Benecke, A. Bethani, G. Bruno, F. Bury, C. Caputo, P. David, C. Delaere, I.S. Donertas, A. Giammanco, K. Jaffel, Sa. Jain, V. Lemaitre, K. Mondal, J. Prisciandaro, A. Taliercio, T.T. Tran, P. Vischia, S. Wertz

Centro Brasileiro de Pesquisas Fisicas, Rio de Janeiro, Brazil

G.A. Alves, E. Coelho, C. Hensel, A. Moraes, P. Rebello Teles

Universidade do Estado do Rio de Janeiro, Rio de Janeiro, Brazil

W.L. Aldá Júnior, M. Alves Gallo Pereira, M. Barroso Ferreira Filho, H. Brandao Malbouisson, W. Carvalho, J. Chinellato[5], E.M. Da Costa, G.G. Da Silveira[6], D. De Jesus Damiao, V. Dos Santos Sousa, S. Fonseca De Souza, J. Martins[7], C. Mora Herrera, K. Mota Amarilo, L. Mundim, H. Nogima, A. Santoro, S.M. Silva Do Amaral, A. Sznajder, M. Thiel, F. Torres Da Silva De Araujo[8], A. Vilela Pereira

JHEP07(2023)095

Universidade Estadual Paulista, Universidade Federal do ABC, São Paulo, Brazil

C.A. Bernardes[6], L. Calligaris, T.R. Fernandez Perez Tomei, E.M. Gregores, P.G. Mercadante, S.F. Novaes, Sandra S. Padula

Institute for Nuclear Research and Nuclear Energy, Bulgarian Academy of Sciences, Sofia, Bulgaria

A. Aleksandrov, G. Antchev, R. Hadjiiska, P. Iaydjiev, M. Misheva, M. Rodozov, M. Shopova, G. Sultanov

University of Sofia, Sofia, Bulgaria

A. Dimitrov, T. Ivanov, L. Litov, B. Pavlov, P. Petkov, A. Petrov

Beihang University, Beijing, China

T. Cheng, T. Javaid[9], M. Mittal, L. Yuan

Department of Physics, Tsinghua University, Beijing, China

M. Ahmad, G. Bauer[10], Z. Hu, K. Yi[10,11]

Institute of High Energy Physics, Beijing, China

G.M. Chen[9], H.S. Chen[9], M. Chen[9], F. Iemmi, C.H. Jiang, A. Kapoor, H. Liao, Z.-A. Liu[12], V. Milosevic, F. Monti, R. Sharma, J. Tao, J. Thomas-Wilsker, J. Wang, H. Zhang, J. Zhao

State Key Laboratory of Nuclear Physics and Technology, Peking University, Beijing, China

A. Agapitos, Y. An, Y. Ban, C. Chen, A. Levin, Q. Li, X. Lyu, Y. Mao, S.J. Qian, X. Sun, D. Wang, J. Xiao, H. Yang

Sun Yat-Sen University, Guangzhou, China

M. Lu, Z. You

Institute of Modern Physics and Key Laboratory of Nuclear Physics and Ion-beam Application (MOE) — Fudan University, Shanghai, China

X. Gao[4], D. Leggat, H. Okawa, Y. Zhang

Zhejiang University, Hangzhou, Zhejiang, China

Z. Lin, M. Xiao

Universidad de Los Andes, Bogota, Colombia

C. Avila, A. Cabrera, C. Florez, J. Fraga

Universidad de Antioquia, Medellin, Colombia

J. Mejia Guisao, F. Ramirez, J.D. Ruiz Alvarez

University of Split, Faculty of Electrical Engineering, Mechanical Engineering and Naval Architecture, Split, Croatia

D. Giljanovic, N. Godinovic, D. Lelas, I. Puljak

JHEP07(2023)095

University of Split, Faculty of Science, Split, Croatia
Z. Antunovic, M. Kovac, T. Sculac

Institute Rudjer Boskovic, Zagreb, Croatia
V. Brigljevic, B.K. Chitroda, D. Ferencek, D. Majumder, M. Roguljic, A. Starodumov[13], T. Susa

University of Cyprus, Nicosia, Cyprus
A. Attikis, K. Christoforou, G. Kole, M. Kolosova, S. Konstantinou, J. Mousa, C. Nicolaou, F. Ptochos, P.A. Razis, H. Rykaczewski, H. Saka

Charles University, Prague, Czech Republic
M. Finger[13], M. Finger Jr.[13], A. Kveton

Escuela Politecnica Nacional, Quito, Ecuador
E. Ayala

Universidad San Francisco de Quito, Quito, Ecuador
E. Carrera Jarrin

Academy of Scientific Research and Technology of the Arab Republic of Egypt, Egyptian Network of High Energy Physics, Cairo, Egypt
H. Abdalla[14], Y. Assran[15,16]

Center for High Energy Physics (CHEP-FU), Fayoum University, El-Fayoum, Egypt
M.A. Mahmoud, Y. Mohammed

National Institute of Chemical Physics and Biophysics, Tallinn, Estonia
S. Bhowmik, R.K. Dewanjee, K. Ehataht, M. Kadastik, S. Nandan, C. Nielsen, J. Pata, M. Raidal, L. Tani, C. Veelken

Department of Physics, University of Helsinki, Helsinki, Finland
P. Eerola, H. Kirschenmann, K. Osterberg, M. Voutilainen

Helsinki Institute of Physics, Helsinki, Finland
S. Bharthuar, E. Brücken, F. Garcia, J. Havukainen, M.S. Kim, R. Kinnunen, T. Lampén, K. Lassila-Perini, S. Lehti, T. Lindén, M. Lotti, L. Martikainen, M. Myllymäki, J. Ott, M.m. Rantanen, H. Siikonen, E. Tuominen, J. Tuominiemi

Lappeenranta-Lahti University of Technology, Lappeenranta, Finland
P. Luukka, H. Petrow, T. Tuuva

IRFU, CEA, Université Paris-Saclay, Gif-sur-Yvette, France
C. Amendola, M. Besancon, F. Couderc, M. Dejardin, D. Denegri, J.L. Faure, F. Ferri, S. Ganjour, P. Gras, G. Hamel de Monchenault, P. Jarry, V. Lohezic, J. Malcles, J. Rander, A. Rosowsky, M.Ö. Sahin, A. Savoy-Navarro[17], P. Simkina, M. Titov

JHEP07(2023)095

Laboratoire Leprince-Ringuet, CNRS/IN2P3, Ecole Polytechnique, Institut Polytechnique de Paris, Palaiseau, France

S. Ahuja, C. Baldenegro Barrera, F. Beaudette, M. Bonanomi, A. Buchot Perraguin, P. Busson, A. Cappati, C. Charlot, O. Davignon, B. Diab, G. Falmagne, B.A. Fontana Santos Alves, S. Ghosh, R. Granier de Cassagnac, A. Hakimi, B. Harikrishnan, J. Motta, M. Nguyen, C. Ochando, L. Portales, J. Rembser, R. Salerno, U. Sarkar, J.B. Sauvan, Y. Sirois, A. Tarabini, E. Vernazza, A. Zabi, A. Zghiche

Université de Strasbourg, CNRS, IPHC UMR 7178, Strasbourg, France

J.-L. Agram[18], J. Andrea, D. Apparu, D. Bloch, G. Bourgatte, J.-M. Brom, E.C. Chabert, C. Collard, D. Darej, U. Goerlach, C. Grimault, A.-C. Le Bihan, E. Nibigira, P. Van Hove

Institut de Physique des 2 Infinis de Lyon (IP2I), Villeurbanne, France

S. Beauceron, C. Bernet, G. Boudoul, C. Camen, A. Carle, N. Chanon, D. Contardo, P. Depasse, H. El Mamouni, J. Fay, S. Gascon, M. Gouzevitch, G. Grenier, B. Ille, I.B. Laktineh, M. Lethuillier, L. Mirabito, S. Perries, K. Shchablo, V. Sordini, L. Torterotot, M. Vander Donckt, S. Viret

Georgian Technical University, Tbilisi, Georgia

I. Bagaturia[19], I. Lomidze, Z. Tsamalaidze[13]

RWTH Aachen University, I. Physikalisches Institut, Aachen, Germany

V. Botta, L. Feld, K. Klein, M. Lipinski, D. Meuser, A. Pauls, N. Röwert, M. Teroerde

RWTH Aachen University, III. Physikalisches Institut A, Aachen, Germany

A. Dodonova, N. Eich, D. Eliseev, M. Erdmann, P. Fackeldey, B. Fischer, T. Hebbeker, K. Hoepfner, F. Ivone, M.y. Lee, L. Mastrolorenzo, M. Merschmeyer, A. Meyer, S. Mondal, S. Mukherjee, D. Noll, A. Novak, A. Pozdnyakov, Y. Rath, H. Reithler, A. Schmidt, S.C. Schuler, A. Sharma, L. Vigilante, S. Wiedenbeck, S. Zaleski

RWTH Aachen University, III. Physikalisches Institut B, Aachen, Germany

C. Dziwok, G. Flügge, W. Haj Ahmad[20], O. Hlushchenko, T. Kress, A. Nowack, O. Pooth, A. Stahl[21], T. Ziemons, A. Zotz

Deutsches Elektronen-Synchrotron, Hamburg, Germany

H. Aarup Petersen, M. Aldaya Martin, P. Asmuss, S. Baxter, M. Bayatmakou, O. Behnke, A. Bermúdez Martínez, S. Bhattacharya, A.A. Bin Anuar, F. Blekman[22], K. Borras[23], D. Brunner, A. Campbell, A. Cardini, C. Cheng, F. Colombina, S. Consuegra Rodríguez, G. Correia Silva, M. De Silva, L. Didukh, G. Eckerlin, D. Eckstein, L.I. Estevez Banos, O. Filatov, E. Gallo[22], A. Geiser, A. Giraldi, G. Greau, A. Grohsjean, V. Guglielmi, M. Guthoff, A. Jafari[24], N.Z. Jomhari, B. Kaech, A. Kasem[23], M. Kasemann, H. Kaveh, C. Kleinwort, R. Kogler,

JHEP07(2023)095

D. Krücker, W. Lange, K. Lipka, W. Lohmann[25], R. Mankel, I.-A. Melzer-Pellmann, M. Mendizabal Morentin, J. Metwally, A.B. Meyer, G. Milella, M. Mormile, A. Mussgiller, A. Nürnberg, Y. Otarid, D. Pérez Adán, A. Raspereza, B. Ribeiro Lopes, J. Rübenach, A. Saggio, A. Saibel, M. Savitskyi, M. Scham[26,23], V. Scheurer, S. Schnake[23], P. Schütze, C. Schwanenberger[22], M. Shchedrolosiev, R.E. Sosa Ricardo, D. Stafford, N. Tonon[†], M. Van De Klundert, F. Vazzoler, R. Walsh, D. Walter, Q. Wang, Y. Wen, K. Wichmann, L. Wiens[23], C. Wissing, S. Wuchterl, A. Zimermmane Castro Santos

University of Hamburg, Hamburg, Germany

R. Aggleton, S. Albrecht, S. Bein, L. Benato, P. Connor, K. De Leo, M. Eich, K. El Morabit, F. Feindt, A. Fröhlich, C. Garbers, E. Garutti, M. Hajheidari, J. Haller, A. Hinzmann, G. Kasieczka, R. Klanner, W. Korcari, T. Kramer, V. Kutzner, J. Lange, T. Lange, A. Lobanov, C. Matthies, A. Mehta, L. Moureaux, M. Mrowietz, A. Nigamova, K.J. Pena Rodriguez, M. Rieger, O. Rieger, P. Schleper, M. Schröder, J. Schwandt, H. Stadie, G. Steinbrück, A. Tews, M. Wolf

Karlsruher Institut fuer Technologie, Karlsruhe, Germany

J. Bechtel, S. Brommer, M. Burkart, E. Butz, R. Caspart, T. Chwalek, A. Dierlamm, A. Droll, N. Faltermann, M. Giffels, J.O. Gosewisch, A. Gottmann, F. Hartmann[21], C. Heidecker, M. Horzela, U. Husemann, P. Keicher, R. Koppenhöfer, S. Maier, S. Mitra, Th. Müller, M. Neukum, G. Quast, K. Rabbertz, J. Rauser, D. Savoiu, M. Schnepf, D. Seith, I. Shvetsov, H.J. Simonis, R. Ulrich, J. van der Linden, R.F. Von Cube, M. Wassmer, M. Weber, S. Wieland, R. Wolf, S. Wozniewski, S. Wunsch

Institute of Nuclear and Particle Physics (INPP), NCSR Demokritos, Aghia Paraskevi, Greece

G. Anagnostou, P. Assiouras, G. Daskalakis, A. Kyriakis, A. Stakia

National and Kapodistrian University of Athens, Athens, Greece

M. Diamantopoulou, D. Karasavvas, P. Kontaxakis, A. Manousakis-Katsikakis, A. Panagiotou, I. Papavergou, N. Saoulidou, K. Theofilatos, E. Tziaferi, K. Vellidis, E. Vourliotis

National Technical University of Athens, Athens, Greece

G. Bakas, K. Kousouris, I. Papakrivopoulos, G. Tsipolitis, A. Zacharopoulou

University of Ioánnina, Ioánnina, Greece

K. Adamidis, I. Bestintzanos, I. Evangelou, C. Foudas, P. Gianneios, P. Katsoulis, P. Kokkas, N. Manthos, I. Papadopoulos, J. Strologas

MTA-ELTE Lendület CMS Particle and Nuclear Physics Group, Eötvös Loránd University, Budapest, Hungary

M. Csanád, K. Farkas, M.M.A. Gadallah[27], S. Lökös[28], P. Major, K. Mandal, G. Pásztor, A.J. Rádl, O. Surányi, G.I. Veres

JHEP07(2023)095

Wigner Research Centre for Physics, Budapest, Hungary
M. Bartók[29], G. Bencze, C. Hajdu, D. Horvath[30,31], F. Sikler, V. Veszpremi

Institute of Nuclear Research ATOMKI, Debrecen, Hungary
N. Beni, S. Czellar, D. Fasanella, J. Karancsi[29], J. Molnar, Z. Szillasi, D. Teyssier

Institute of Physics, University of Debrecen, Debrecen, Hungary
P. Raics, B. Ujvari[32], G. Zilizi

Karoly Robert Campus, MATE Institute of Technology, Gyongyos, Hungary
T. Csorgo[33], F. Nemes[33], T. Novak

Panjab University, Chandigarh, India
J. Babbar, S. Bansal, S.B. Beri, V. Bhatnagar, G. Chaudhary, S. Chauhan, N. Dhingra[34], R. Gupta, A. Kaur, H. Kaur, M. Kaur, P. Kumari, M. Meena, K. Sandeep, J.B. Singh[35], A. K. Virdi

University of Delhi, Delhi, India
A. Ahmed, A. Bhardwaj, B.C. Choudhary, M. Gola, S. Keshri, A. Kumar, M. Naimuddin, P. Priyanka, K. Ranjan, S. Saumya, A. Shah

Saha Institute of Nuclear Physics, HBNI, Kolkata, India
R. Bhattacharya, S. Bhattacharya, D. Bhowmik, S. Dutta, S. Dutta, B. Gomber[36], M. Maity[37], P. Palit, P.K. Rout, G. Saha, B. Sahu, S. Sarkar

Indian Institute of Technology Madras, Madras, India
P.K. Behera, S.C. Behera, P. Kalbhor, J.R. Komaragiri[38], D. Kumar[38], A. Muhammad, L. Panwar[38], R. Pradhan, P.R. Pujahari, A. Sharma, A.K. Sikdar, P.C. Tiwari[38]

Bhabha Atomic Research Centre, Mumbai, India
K. Naskar[39]

Tata Institute of Fundamental Research-A, Mumbai, India
T. Aziz, S. Dugad, M. Kumar, G.B. Mohanty, P. Suryadevara

Tata Institute of Fundamental Research-B, Mumbai, India
S. Banerjee, R. Chudasama, M. Guchait, S. Karmakar, S. Kumar, G. Majumder, K. Mazumdar, S. Mukherjee

National Institute of Science Education and Research, An OCC of Homi Bhabha National Institute, Bhubaneswar, Odisha, India
S. Bahinipati[40], C. Kar, P. Mal, T. Mishra, V.K. Muraleedharan Nair Bindhu[41], A. Nayak[41], P. Saha, N. Sur, S.K. Swain, D. Vats[41]

Indian Institute of Science Education and Research (IISER), Pune, India
A. Alpana, S. Dube, B. Kansal, A. Laha, S. Pandey, A. Rastogi, S. Sharma

JHEP07(2023)095

Isfahan University of Technology, Isfahan, Iran
H. Bakhshiansohi[42], E. Khazaie, M. Zeinali[43]

Institute for Research in Fundamental Sciences (IPM), Tehran, Iran
S. Chenarani[44], S.M. Etesami, M. Khakzad, M. Mohammadi Najafabadi

University College Dublin, Dublin, Ireland
M. Grunewald

INFN Sezione di Bari[a], Università di Bari[b], Politecnico di Bari[c], Bari, Italy
M. Abbrescia[a,b], R. Aly[a,c,45], C. Aruta[a,b], A. Colaleo[a], D. Creanza[a,c], N. De Filippis[a,c], M. De Palma[a,b], A. Di Florio[a,b], W. Elmetenawee[a,b], F. Errico[a,b], L. Fiore[a], G. Iaselli[a,c], M. Ince[a,b], S. Lezki[a,b], G. Maggi[a,c], M. Maggi[a], I. Margjeka[a,b], V. Mastrapasqua[a,b], S. My[a,b], S. Nuzzo[a,b], A. Pellecchia[a,b], A. Pompili[a,b], G. Pugliese[a,c], R. Radogna[a], D. Ramos[a], A. Ranieri[a], G. Selvaggi[a,b], L. Silvestris[a], F.M. Simone[a,b], Ü. Sözbilir[a], R. Venditti[a], P. Verwilligen[a]

INFN Sezione di Bologna[a], Università di Bologna[b], Bologna, Italy
G. Abbiendi[a], C. Battilana[a,b], D. Bonacorsi[a,b], L. Borgonovi[a], L. Brigliadori[a], R. Campanini[a,b], P. Capiluppi[a,b], A. Castro[a,b], F.R. Cavallo[a], M. Cuffiani[a,b], G.M. Dallavalle[a], T. Diotalevi[a,b], F. Fabbri[a], A. Fanfani[a,b], P. Giacomelli[a], L. Giommi[a,b], C. Grandi[a], L. Guiducci[a,b], S. Lo Meo[a,46], L. Lunerti[a,b], S. Marcellini[a], G. Masetti[a], F.L. Navarria[a,b], A. Perrotta[a], F. Primavera[a,b], A.M. Rossi[a,b], T. Rovelli[a,b], G.P. Siroli[a,b]

INFN Sezione di Catania[a], Università di Catania[b], Catania, Italy
S. Costa[a,b,47], A. Di Mattia[a], R. Potenza[a,b], A. Tricomi[a,b,47], C. Tuve[a,b]

INFN Sezione di Firenze[a], Università di Firenze[b], Firenze, Italy
G. Barbagli[a], B. Camaiani[a,b], A. Cassese[a], R. Ceccarelli[a,b], V. Ciulli[a,b], C. Civinini[a], R. D'Alessandro[a,b], E. Focardi[a,b], G. Latino[a,b], P. Lenzi[a,b], M. Lizzo[a,b], M. Meschini[a], S. Paoletti[a], R. Seidita[a,b], G. Sguazzoni[a], L. Viliani[a]

INFN Laboratori Nazionali di Frascati, Frascati, Italy
L. Benussi, S. Bianco, D. Piccolo

INFN Sezione di Genova[a], Università di Genova[b], Genova, Italy
M. Bozzo[a,b], F. Ferro[a], R. Mulargia[a], E. Robutti[a], S. Tosi[a,b]

INFN Sezione di Milano-Bicocca[a], Università di Milano-Bicocca[b], Milano, Italy
A. Benaglia[a], G. Boldrini[a], F. Brivio[a,b], F. Cetorelli[a,b], F. De Guio[a,b], M.E. Dinardo[a,b], P. Dini[a], S. Gennai[a], A. Ghezzi[a,b], P. Govoni[a,b], L. Guzzi[a,b], M.T. Lucchini[a,b], M. Malberti[a], S. Malvezzi[a], A. Massironi[a], D. Menasce[a],

L. Moroni[a], M. Paganoni[a,b], D. Pedrini[a], B.S. Pinolini[a], S. Ragazzi[a,b], N. Redaelli[a], T. Tabarelli de Fatis[a,b], D. Zuolo[a,b]

INFN Sezione di Napoli[a], Università di Napoli 'Federico II'[b], Napoli, Italy; Università della Basilicata[c], Potenza, Italy; Università G. Marconi[d], Roma, Italy

S. Buontempo[a], F. Carnevali[a,b], N. Cavallo[a,c], A. De Iorio[a,b], F. Fabozzi[a,c], A.O.M. Iorio[a,b], L. Lista[a,b,48], S. Meola[a,d,21], P. Paolucci[a,21], B. Rossi[a], C. Sciacca[a,b]

INFN Sezione di Padova[a], Università di Padova[b], Padova, Italy; Università di Trento[c], Trento, Italy

P. Azzi[a], N. Bacchetta[a], D. Bisello[a,b], P. Bortignon[a], A. Bragagnolo[a,b], R. Carlin[a,b], P. Checchia[a], T. Dorigo[a], F. Gasparini[a,b], U. Gasparini[a,b], G. Grosso[a], L. Layer[a,49], E. Lusiani[a], M. Margoni[a,b], F. Marini[a], A.T. Meneguzzo[a,b], J. Pazzini[a,b], P. Ronchese[a,b], R. Rossin[a,b], F. Simonetto[a,b], G. Strong[a], M. Tosi[a,b], H. Yarar[a,b], M. Zanetti[a,b], P. Zotto[a,b], A. Zucchetta[a,b], G. Zumerle[a,b]

INFN Sezione di Pavia[a], Università di Pavia[b], Pavia, Italy

C. Aimè[a,b], A. Braghieri[a], S. Calzaferri[a,b], D. Fiorina[a,b], P. Montagna[a,b], V. Re[a], C. Riccardi[a,b], P. Salvini[a], I. Vai[a], P. Vitulo[a,b]

INFN Sezione di Perugia[a], Università di Perugia[b], Perugia, Italy

P. Asenov[a,50], G.M. Bilei[a], D. Ciangottini[a,b], L. Fanò[a,b], M. Magherini[a,b], G. Mantovani[a,b], V. Mariani[a,b], M. Menichelli[a], F. Moscatelli[a,50], A. Piccinelli[a,b], M. Presilla[a,b], A. Rossi[a,b], A. Santocchia[a,b], D. Spiga[a], T. Tedeschi[a,b]

INFN Sezione di Pisa[a], Università di Pisa[b], Scuola Normale Superiore di Pisa[c], Pisa, Italy; Università di Siena[d], Siena, Italy

P. Azzurri[a], G. Bagliesi[a], V. Bertacchi[a,c], L. Bianchini[a,b], T. Boccali[a], E. Bossini[a,b], D. Bruschini[a,c], R. Castaldi[a], M.A. Ciocci[a,b], V. D'Amante[a,d], R. Dell'Orso[a], M.R. Di Domenico[a,d], S. Donato[a], A. Giassi[a], F. Ligabue[a,c], E. Manca[a,c], G. Mandorli[a,c], D. Matos Figueiredo[a], A. Messineo[a,b], M. Musich[a,b], F. Palla[a], S. Parolia[a,b], G. Ramirez-Sanchez[a,c], A. Rizzi[a,b], G. Rolandi[a,c], S. Roy Chowdhury[a,c], A. Scribano[a], N. Shafiei[a,b], P. Spagnolo[a], R. Tenchini[a], G. Tonelli[a,b], N. Turini[a,d], A. Venturi[a], P.G. Verdini[a]

INFN Sezione di Roma[a], Sapienza Università di Roma[b], Roma, Italy

P. Barria[a], M. Campana[a,b], F. Cavallari[a], D. Del Re[a,b], E. Di Marco[a], M. Diemoz[a], E. Longo[a,b], P. Meridiani[a], G. Organtini[a,b], F. Pandolfi[a], R. Paramatti[a,b], C. Quaranta[a,b], S. Rahatlou[a,b], C. Rovelli[a], F. Santanastasio[a,b], L. Soffi[a], R. Tramontano[a,b]

INFN Sezione di Torino[a], Università di Torino[b], Torino, Italy; Università del Piemonte Orientale[c], Novara, Italy

N. Amapane[a,b], R. Arcidiacono[a,c], S. Argiro[a,b], M. Arneodo[a,c], N. Bartosik[a], R. Bellan[a,b], A. Bellora[a,b], J. Berenguer Antequera[a,b], C. Biino[a], N. Cartiglia[a],

M. Costa[a,b], R. Covarelli[a,b], N. Demaria[a], M. Grippo[a,b], B. Kiani[a,b], F. Legger[a], C. Mariotti[a], S. Maselli[a], A. Mecca[a,b], E. Migliore[a,b], E. Monteil[a,b], M. Monteno[a], M.M. Obertino[a,b], G. Ortona[a], L. Pacher[a,b], N. Pastrone[a], M. Pelliccioni[a], M. Ruspa[a,c], K. Shchelina[a], F. Siviero[a,b], V. Sola[a], A. Solano[a,b], D. Soldi[a,b], A. Staiano[a], M. Tornago[a,b], D. Trocino[a], G. Umoret[a,b], A. Vagnerini[a,b]

INFN Sezione di Trieste[a], Università di Trieste[b], Trieste, Italy

S. Belforte[a], V. Candelise[a,b], M. Casarsa[a], F. Cossutti[a], A. Da Rold[a,b], G. Della Ricca[a,b], G. Sorrentino[a,b]

Kyungpook National University, Daegu, Korea

S. Dogra, C. Huh, B. Kim, D.H. Kim, G.N. Kim, J. Kim, J. Lee, S.W. Lee, C.S. Moon, Y.D. Oh, S.I. Pak, S. Sekmen, Y.C. Yang

Chonnam National University, Institute for Universe and Elementary Particles, Kwangju, Korea

H. Kim, D.H. Moon

Hanyang University, Seoul, Korea

E. Asilar, J. Choi, T.J. Kim, J. Park

Korea University, Seoul, Korea

S. Cho, S. Choi, B. Hong, K. Lee, K.S. Lee, J. Lim, J. Park, S.K. Park, J. Yoo

Kyung Hee University, Department of Physics, Seoul, Korea

J. Goh

Sejong University, Seoul, Korea

H. S. Kim, Y. Kim

Seoul National University, Seoul, Korea

J. Almond, J.H. Bhyun, J. Choi, S. Jeon, J. Kim, J. Kim, J.S. Kim, S. Ko, H. Kwon, H. Lee, S. Lee, B.H. Oh, M. Oh, S.B. Oh, H. Seo, U.K. Yang, I. Yoon

University of Seoul, Seoul, Korea

W. Jang, D.Y. Kang, Y. Kang, D. Kim, S. Kim, B. Ko, J.S.H. Lee, Y. Lee, J.A. Merlin, I.C. Park, Y. Roh, M.S. Ryu, D. Song, Watson, I.J., S. Yang

Yonsei University, Department of Physics, Seoul, Korea

S. Ha, H.D. Yoo

Sungkyunkwan University, Suwon, Korea

M. Choi, H. Lee, Y. Lee, I. Yu

College of Engineering and Technology, American University of the Middle East (AUM), Dasman, Kuwait

T. Beyrouthy, Y. Maghrbi

JHEP07(2023)095

Riga Technical University, Riga, Latvia
K. Dreimanis, V. Veckalns

Vilnius University, Vilnius, Lithuania
M. Ambrozas, A. Carvalho Antunes De Oliveira, A. Juodagalvis, A. Rinkevicius, G. Tamulaitis

National Centre for Particle Physics, Universiti Malaya, Kuala Lumpur, Malaysia
N. Bin Norjoharuddeen, S.Y. Hoh[51], I. Yusuff[51], Z. Zolkapli

Universidad de Sonora (UNISON), Hermosillo, Mexico
J.F. Benitez, A. Castaneda Hernandez, H.A. Encinas Acosta, L.G. Gallegos Maríñez, M. León Coello, J.A. Murillo Quijada, A. Sehrawat, L. Valencia Palomo

Centro de Investigacion y de Estudios Avanzados del IPN, Mexico City, Mexico
G. Ayala, H. Castilla-Valdez, E. De La Cruz-Burelo, I. Heredia-De La Cruz[52], R. Lopez-Fernandez, C.A. Mondragon Herrera, D.A. Perez Navarro, A. Sánchez Hernández

Universidad Iberoamericana, Mexico City, Mexico
C. Oropeza Barrera, F. Vazquez Valencia

Benemerita Universidad Autonoma de Puebla, Puebla, Mexico
I. Pedraza, H.A. Salazar Ibarguen, C. Uribe Estrada

University of Montenegro, Podgorica, Montenegro
I. Bubanja, J. Mijuskovic[53], N. Raicevic

National Centre for Physics, Quaid-I-Azam University, Islamabad, Pakistan
A. Ahmad, M.I. Asghar, A. Awais, M.I.M. Awan, H.R. Hoorani, W.A. Khan, M. Shoaib, M. Waqas

AGH University of Science and Technology Faculty of Computer Science, Electronics and Telecommunications, Krakow, Poland
V. Avati, L. Grzanka, M. Malawski

National Centre for Nuclear Research, Swierk, Poland
H. Bialkowska, M. Bluj, B. Boimska, M. Górski, M. Kazana, M. Szleper, P. Zalewski

Institute of Experimental Physics, Faculty of Physics, University of Warsaw, Warsaw, Poland
K. Bunkowski, K. Doroba, A. Kalinowski, M. Konecki, J. Krolikowski

JHEP07(2023)095

Laboratório de Instrumentação e Física Experimental de Partículas, Lisboa, Portugal

M. Araujo, P. Bargassa, D. Bastos, A. Boletti, P. Faccioli, M. Gallinaro, J. Hollar, N. Leonardo, T. Niknejad, M. Pisano, J. Seixas, O. Toldaiev, J. Varela

VINCA Institute of Nuclear Sciences, University of Belgrade, Belgrade, Serbia

P. Adzic[54], M. Dordevic, P. Milenovic, J. Milosevic

Centro de Investigaciones Energéticas Medioambientales y Tecnológicas (CIEMAT), Madrid, Spain

M. Aguilar-Benitez, J. Alcaraz Maestre, A. Álvarez Fernández, M. Barrio Luna, Cristina F. Bedoya, C.A. Carrillo Montoya, M. Cepeda, M. Cerrada, N. Colino, B. De La Cruz, A. Delgado Peris, J.P. Fernández Ramos, J. Flix, M.C. Fouz, O. Gonzalez Lopez, S. Goy Lopez, J.M. Hernandez, M.I. Josa, J. León Holgado, D. Moran, C. Perez Dengra, A. Pérez-Calero Yzquierdo, J. Puerta Pelayo, I. Redondo, D.D. Redondo Ferrero, L. Romero, S. Sánchez Navas, J. Sastre, L. Urda Gómez, J. Vazquez Escobar, C. Willmott

Universidad Autónoma de Madrid, Madrid, Spain

J.F. de Trocóniz

Universidad de Oviedo, Instituto Universitario de Ciencias y Tecnologías Espaciales de Asturias (ICTEA), Oviedo, Spain

B. Alvarez Gonzalez, J. Cuevas, J. Fernandez Menendez, S. Folgueras, I. Gonzalez Caballero, J.R. González Fernández, E. Palencia Cortezon, C. Ramón Álvarez, V. Rodríguez Bouza, A. Soto Rodríguez, A. Trapote, N. Trevisani, C. Vico Villalba

Instituto de Física de Cantabria (IFCA), CSIC-Universidad de Cantabria, Santander, Spain

J.A. Brochero Cifuentes, I.J. Cabrillo, A. Calderon, J. Duarte Campderros, M. Fernandez, C. Fernandez Madrazo, P.J. Fernández Manteca, A. García Alonso, G. Gomez, C. Lasaosa García, C. Martinez Rivero, P. Martinez Ruiz del Arbol, F. Matorras, P. Matorras Cuevas, J. Piedra Gomez, C. Prieels, A. Ruiz-Jimeno, L. Scodellaro, I. Vila, J.M. Vizan Garcia

University of Colombo, Colombo, Sri Lanka

M.K. Jayananda, B. Kailasapathy[55], D.U.J. Sonnadara, D.D.C. Wickramarathna

University of Ruhuna, Department of Physics, Matara, Sri Lanka

W.G.D. Dharmaratna, K. Liyanage, N. Perera, N. Wickramage

JHEP07(2023)095

CERN, European Organization for Nuclear Research, Geneva, Switzerland

T.K. Aarrestad, D. Abbaneo, J. Alimena, E. Auffray, G. Auzinger, J. Baechler, P. Baillon[†], D. Barney, J. Bendavid, M. Bianco, B. Bilin, A. Bocci, E. Brondolin, C. Caillol, T. Camporesi, G. Cerminara, N. Chernyavskaya, S.S. Chhibra, S. Choudhury, M. Cipriani, L. Cristella, D. d'Enterria, A. Dabrowski, A. David, A. De Roeck, M.M. Defranchis, M. Deile, M. Dobson, M. Dünser, A. Elliott-Peisert, F. Fallavollita[56], A. Florent, L. Forthomme, W. Funk, S. Ghosh, S. Giani, D. Gigi, K. Gill, F. Glege, L. Gouskos, E. Govorkova, M. Haranko, J. Hegeman, V. Innocente, T. James, P. Janot, J. Kaspar, J. Kieseler, M. Komm, N. Kratochwil, S. Laurila, P. Lecoq, A. Lintuluoto, C. Lourenço, B. Maier, L. Malgeri, M. Mannelli, A.C. Marini, F. Meijers, S. Mersi, E. Meschi, F. Moortgat, M. Mulders, S. Orfanelli, L. Orsini, F. Pantaleo, E. Perez, M. Peruzzi, A. Petrilli, G. Petrucciani, A. Pfeiffer, M. Pierini, D. Piparo, M. Pitt, H. Qu, T. Quast, D. Rabady, A. Racz, G. Reales Gutiérrez, M. Rovere, H. Sakulin, S. Scarfi, M. Selvaggi, A. Sharma, P. Silva, W. Snoeys, P. Sphicas[57], A.G. Stahl Leiton, S. Summers, K. Tatar, V.R. Tavolaro, D. Treille, P. Tropea, A. Tsirou, J. Wanczyk[58], K.A. Wozniak, W.D. Zeuner

Paul Scherrer Institut, Villigen, Switzerland

L. Caminada[59], A. Ebrahimi, W. Erdmann, R. Horisberger, Q. Ingram, H.C. Kaestli, D. Kotlinski, C. Lange, M. Missiroli[59], L. Noehte[59], T. Rohe

ETH Zurich — Institute for Particle Physics and Astrophysics (IPA), Zurich, Switzerland

K. Androsov[58], M. Backhaus, P. Berger, A. Calandri, A. De Cosa, G. Dissertori, M. Dittmar, M. Donegà, C. Dorfer, F. Eble, K. Gedia, F. Glessgen, T.A. Gómez Espinosa, C. Grab, D. Hits, W. Lustermann, A.-M. Lyon, R.A. Manzoni, L. Marchese, C. Martin Perez, A. Mascellani[58], M.T. Meinhard, F. Nessi-Tedaldi, J. Niedziela, F. Pauss, V. Perovic, S. Pigazzini, M.G. Ratti, M. Reichmann, C. Reissel, T. Reitenspiess, B. Ristic, D. Ruini, D.A. Sanz Becerra, J. Steggemann[58], D. Valsecchi[21], R. Wallny

Universität Zürich, Zurich, Switzerland

C. Amsler[60], P. Bärtschi, C. Botta, D. Brzhechko, M.F. Canelli, K. Cormier, A. De Wit, R. Del Burgo, J.K. Heikkilä, M. Huwiler, W. Jin, A. Jofrehei, B. Kilminster, S. Leontsinis, S.P. Liechti, A. Macchiolo, P. Meiring, V.M. Mikuni, U. Molinatti, I. Neutelings, A. Reimers, P. Robmann, S. Sanchez Cruz, K. Schweiger, M. Senger, Y. Takahashi

National Central University, Chung-Li, Taiwan

C. Adloff[61], C.M. Kuo, W. Lin, S.S. Yu

National Taiwan University (NTU), Taipei, Taiwan

L. Ceard, Y. Chao, K.F. Chen, P.H. Chen, P.s. Chen, H. Cheng, W.-S. Hou, Y.y. Li, R.-S. Lu, E. Paganis, A. Psallidas, A. Steen, H.y. Wu, E. Yazgan, P.r. Yu

JHEP07(2023)095

Chulalongkorn University, Faculty of Science, Department of Physics, Bangkok, Thailand

C. Asawatangtrakuldee, N. Srimanobhas

Çukurova University, Physics Department, Science and Art Faculty, Adana, Turkey

D. Agyel, F. Boran, Z.S. Demiroglu, F. Dolek, I. Dumanoglu[62], E. Eskut, Y. Guler[63], E. Gurpinar Guler[63], C. Isik, O. Kara, A. Kayis Topaksu, U. Kiminsu, G. Onengut, K. Ozdemir[64], A. Polatoz, A.E. Simsek, B. Tali[65], U.G. Tok, S. Turkcapar, E. Uslan, I.S. Zorbakir

Middle East Technical University, Physics Department, Ankara, Turkey

G. Karapinar, K. Ocalan[66], M. Yalvac[67]

Bogazici University, Istanbul, Turkey

B. Akgun, I.O. Atakisi, E. Gülmez, M. Kaya[68], O. Kaya[69], Ö. Özçelik, S. Tekten[70]

Istanbul Technical University, Istanbul, Turkey

A. Cakir, K. Cankocak[62], Y. Komurcu, S. Sen[71]

Istanbul University, Istanbul, Turkey

O. Aydilek, S. Cerci[65], B. Hacisahinoglu, I. Hos[72], B. Isildak[73], B. Kaynak, S. Ozkorucuklu, C. Simsek, D. Sunar Cerci[65]

Institute for Scintillation Materials of National Academy of Science of Ukraine, Kharkiv, Ukraine

B. Grynyov

National Science Centre, Kharkiv Institute of Physics and Technology, Kharkiv, Ukraine

L. Levchuk

University of Bristol, Bristol, United Kingdom

D. Anthony, E. Bhal, J.J. Brooke, A. Bundock, E. Clement, D. Cussans, H. Flacher, M. Glowacki, J. Goldstein, G.P. Heath, H.F. Heath, L. Kreczko, B. Krikler, S. Paramesvaran, S. Seif El Nasr-Storey, V.J. Smith, N. Stylianou[74], K. Walkingshaw Pass, R. White

Rutherford Appleton Laboratory, Didcot, United Kingdom

A.H. Ball, K.W. Bell, A. Belyaev[75], C. Brew, R.M. Brown, D.J.A. Cockerill, C. Cooke, K.V. Ellis, K. Harder, S. Harper, M.-L. Holmberg[76], J. Linacre, K. Manolopoulos, D.M. Newbold, E. Olaiya, D. Petyt, T. Reis, T. Schuh, C.H. Shepherd-Themistocleous, I.R. Tomalin, T. Williams

JHEP07(2023)095

Imperial College, London, United Kingdom

R. Bainbridge, P. Bloch, S. Bonomally, J. Borg, S. Breeze, O. Buchmuller, V. Cepaitis, G.S. Chahal[77], D. Colling, P. Dauncey, G. Davies, M. Della Negra, S. Fayer, G. Fedi, G. Hall, M.H. Hassanshahi, G. Iles, J. Langford, L. Lyons, A.-M. Magnan, S. Malik, D.G. Monk, J. Nash[78], M. Pesaresi, B.C. Radburn-Smith, D.M. Raymond, A. Richards, A. Rose, E. Scott, C. Seez, A. Shtipliyski, R. Shukla, A. Tapper, K. Uchida, T. Virdee[21], M. Vojinovic, N. Wardle, D. Winterbottom

Brunel University, Uxbridge, United Kingdom

K. Coldham, J.E. Cole, A. Khan, P. Kyberd, I.D. Reid, L. Teodorescu, S. Zahid

Baylor University, Waco, Texas, USA

S. Abdullin, A. Brinkerhoff, B. Caraway, J. Dittmann, K. Hatakeyama, A.R. Kanuganti, B. McMaster, M. Saunders, S. Sawant, C. Sutantawibul, J. Wilson

Catholic University of America, Washington, DC, USA

R. Bartek, A. Dominguez, R. Uniyal, A.M. Vargas Hernandez

The University of Alabama, Tuscaloosa, Alabama, USA

A. Buccilli, S.I. Cooper, D. Di Croce, S.V. Gleyzer, C. Henderson, C.U. Perez, P. Rumerio[79], C. West

Boston University, Boston, Massachusetts, USA

A. Akpinar, A. Albert, D. Arcaro, C. Cosby, Z. Demiragli, C. Erice, E. Fontanesi, D. Gastler, S. May, J. Rohlf, K. Salyer, D. Sperka, D. Spitzbart, I. Suarez, A. Tsatsos, S. Yuan

Brown University, Providence, Rhode Island, USA

G. Benelli, B. Burkle, X. Coubez[23], D. Cutts, M. Hadley, U. Heintz, J.M. Hogan[80], T. Kwon, G. Landsberg, K.T. Lau, D. Li, M. Lukasik, J. Luo, M. Narain, N. Pervan, S. Sagir[81], F. Simpson, E. Usai, W.Y. Wong, X. Yan, D. Yu, W. Zhang

University of California, Davis, Davis, California, USA

J. Bonilla, C. Brainerd, R. Breedon, M. Calderon De La Barca Sanchez, M. Chertok, J. Conway, P.T. Cox, R. Erbacher, G. Haza, F. Jensen, O. Kukral, G. Mocellin, M. Mulhearn, D. Pellett, B. Regnery, D. Taylor, Y. Yao, F. Zhang

University of California, Los Angeles, California, USA

M. Bachtis, R. Cousins, A. Datta, D. Hamilton, J. Hauser, M. Ignatenko, M.A. Iqbal, T. Lam, W.A. Nash, S. Regnard, D. Saltzberg, B. Stone, V. Valuev

University of California, Riverside, Riverside, California, USA

Y. Chen, R. Clare, J.W. Gary, M. Gordon, G. Hanson, G. Karapostoli, O.R. Long, N. Manganelli, W. Si, S. Wimpenny, Y. Zhang

JHEP07(2023)095

University of California, San Diego, La Jolla, California, USA

J.G. Branson, P. Chang, S. Cittolin, S. Cooperstein, D. Diaz, J. Duarte, R. Gerosa, L. Giannini, J. Guiang, R. Kansal, V. Krutelyov, R. Lee, J. Letts, M. Masciovecchio, F. Mokhtar, M. Pieri, B.V. Sathia Narayanan, V. Sharma, M. Tadel, F. Würthwein, Y. Xiang, A. Yagil

University of California, Santa Barbara — Department of Physics, Santa Barbara, California, USA

N. Amin, C. Campagnari, M. Citron, G. Collura, A. Dorsett, V. Dutta, J. Incandela, M. Kilpatrick, J. Kim, B. Marsh, P. Masterson, H. Mei, M. Oshiro, M. Quinnan, J. Richman, U. Sarica, F. Setti, J. Sheplock, P. Siddireddy, D. Stuart, S. Wang

California Institute of Technology, Pasadena, California, USA

A. Bornheim, O. Cerri, I. Dutta, J.M. Lawhorn, N. Lu, J. Mao, H.B. Newman, T. Q. Nguyen, M. Spiropulu, J.R. Vlimant, C. Wang, S. Xie, Z. Zhang, R.Y. Zhu

Carnegie Mellon University, Pittsburgh, Pennsylvania, USA

J. Alison, S. An, M.B. Andrews, P. Bryant, T. Ferguson, A. Harilal, C. Liu, T. Mudholkar, S. Murthy, M. Paulini, A. Roberts, A. Sanchez, W. Terrill

University of Colorado Boulder, Boulder, Colorado, USA

J.P. Cumalat, W.T. Ford, A. Hassani, G. Karathanasis, E. MacDonald, R. Patel, A. Perloff, C. Savard, N. Schonbeck, K. Stenson, K.A. Ulmer, S.R. Wagner, N. Zipper

Cornell University, Ithaca, New York, USA

J. Alexander, S. Bright-Thonney, X. Chen, Y. Cheng, D.J. Cranshaw, J. Fan, X. Fan, D. Gadkari, S. Hogan, J. Monroy, J.R. Patterson, D. Quach, J. Reichert, M. Reid, A. Ryd, J. Thom, P. Wittich, R. Zou

Fermi National Accelerator Laboratory, Batavia, Illinois, USA

M. Albrow, M. Alyari, G. Apollinari, A. Apresyan, L.A.T. Bauerdick, D. Berry, J. Berryhill, P.C. Bhat, K. Burkett, J.N. Butler, A. Canepa, G.B. Cerati, H.W.K. Cheung, F. Chlebana, K.F. Di Petrillo, J. Dickinson, V.D. Elvira, Y. Feng, J. Freeman, A. Gandrakota, Z. Gecse, L. Gray, D. Green, S. Grünendahl, O. Gutsche, R.M. Harris, R. Heller, T.C. Herwig, J. Hirschauer, L. Horyn, B. Jayatilaka, S. Jindariani, M. Johnson, U. Joshi, T. Klijnsma, B. Klima, K.H.M. Kwok, S. Lammel, D. Lincoln, R. Lipton, T. Liu, C. Madrid, K. Maeshima, C. Mantilla, D. Mason, P. McBride, P. Merkel, S. Mrenna, S. Nahn, J. Ngadiuba, V. Papadimitriou, K. Pedro, C. Pena[82], F. Ravera, A. Reinsvold Hall[83], L. Ristori, E. Sexton-Kennedy, N. Smith, A. Soha, L. Spiegel, J. Strait, L. Taylor, S. Tkaczyk, N.V. Tran, L. Uplegger, E.W. Vaandering, H.A. Weber, I. Zoi

JHEP07(2023)095

University of Florida, Gainesville, Florida, USA

P. Avery, D. Bourilkov, L. Cadamuro, V. Cherepanov, R.D. Field, D. Guerrero, M. Kim, E. Koenig, J. Konigsberg, A. Korytov, K.H. Lo, K. Matchev, N. Menendez, G. Mitselmakher, A. Muthirakalayil Madhu, N. Rawal, D. Rosenzweig, S. Rosenzweig, K. Shi, J. Wang, Z. Wu

Florida State University, Tallahassee, Florida, USA

T. Adams, A. Askew, R. Habibullah, V. Hagopian, R. Khurana, T. Kolberg, G. Martinez, H. Prosper, C. Schiber, O. Viazlo, R. Yohay, J. Zhang

Florida Institute of Technology, Melbourne, Florida, USA

M.M. Baarmand, S. Butalla, T. Elkafrawy[84], M. Hohlmann, R. Kumar Verma, D. Noonan, M. Rahmani, F. Yumiceva

University of Illinois at Chicago (UIC), Chicago, Illinois, USA

M.R. Adams, H. Becerril Gonzalez, R. Cavanaugh, S. Dittmer, O. Evdokimov, C.E. Gerber, D.J. Hofman, D. S. Lemos, A.H. Merrit, C. Mills, G. Oh, T. Roy, S. Rudrabhatla, M.B. Tonjes, N. Varelas, J. Viinikainen, X. Wang, Z. Ye

The University of Iowa, Iowa City, Iowa, USA

M. Alhusseini, K. Dilsiz[85], L. Emediato, R.P. Gandrajula, O.K. Köseyan, J.-P. Merlo, A. Mestvirishvili[86], J. Nachtman, H. Ogul[87], Y. Onel, A. Penzo, C. Snyder, E. Tiras[88]

Johns Hopkins University, Baltimore, Maryland, USA

O. Amram, B. Blumenfeld, L. Corcodilos, J. Davis, A.V. Gritsan, S. Kyriacou, P. Maksimovic, J. Roskes, M. Swartz, T.Á. Vámi

The University of Kansas, Lawrence, Kansas, USA

A. Abreu, J. Anguiano, P. Baringer, A. Bean, Z. Flowers, T. Isidori, S. Khalil, J. King, G. Krintiras, M. Lazarovits, C. Le Mahieu, C. Lindsey, J. Marquez, N. Minafra, M. Murray, M. Nickel, C. Rogan, C. Royon, R. Salvatico, S. Sanders, E. Schmitz, C. Smith, Q. Wang, Z. Warner, J. Williams, G. Wilson

Kansas State University, Manhattan, Kansas, USA

S. Duric, A. Ivanov, K. Kaadze, D. Kim, Y. Maravin, T. Mitchell, A. Modak, D. Roy

Lawrence Livermore National Laboratory, Livermore, California, USA

F. Rebassoo, D. Wright

University of Maryland, College Park, Maryland, USA

E. Adams, A. Baden, O. Baron, A. Belloni, S.C. Eno, N.J. Hadley, S. Jabeen, R.G. Kellogg, T. Koeth, Y. Lai, S. Lascio, A.C. Mignerey, S. Nabili, C. Palmer, C. Papageorgakis, M. Seidel, L. Wang, K. Wong

JHEP07(2023)095

Massachusetts Institute of Technology, Cambridge, Massachusetts, USA

D. Abercrombie, G. Andreassi, R. Bi, W. Busza, I.A. Cali, Y. Chen, M. D'Alfonso, G. Gomez-Ceballos, M. Goncharov, P. Harris, M. Hu, M. Klute, D. Kovalskyi, J. Krupa, Y.-J. Lee, C. Mironov, C. Paus, D. Rankin, C. Roland, G. Roland, Z. Shi, G.S.F. Stephans, J. Wang, B. Wyslouch

University of Minnesota, Minneapolis, Minnesota, USA

R.M. Chatterjee, A. Evans, J. Hiltbrand, Sh. Jain, B.M. Joshi, M. Krohn, Y. Kubota, J. Mans, M. Revering, R. Rusack, R. Saradhy, N. Schroeder, N. Strobbe, M.A. Wadud

University of Mississippi, Oxford, Mississippi, USA

L.M. Cremaldi

University of Nebraska-Lincoln, Lincoln, Nebraska, USA

K. Bloom, M. Bryson, S. Chauhan, D.R. Claes, C. Fangmeier, L. Finco, F. Golf, C. Joo, I. Kravchenko, I. Reed, J.E. Siado, G.R. Snow[†], W. Tabb, A. Wightman, F. Yan, A.G. Zecchinelli

State University of New York at Buffalo, Buffalo, New York, USA

G. Agarwal, H. Bandyopadhyay, L. Hay, I. Iashvili, A. Kharchilava, C. McLean, D. Nguyen, J. Pekkanen, S. Rappoccio, A. Williams

Northeastern University, Boston, Massachusetts, USA

G. Alverson, E. Barberis, Y. Haddad, Y. Han, A. Hortiangtham, A. Krishna, J. Li, J. Lidrych, G. Madigan, B. Marzocchi, D.M. Morse, V. Nguyen, T. Orimoto, A. Parker, L. Skinnari, A. Tishelman-Charny, T. Wamorkar, B. Wang, A. Wisecarver, D. Wood

Northwestern University, Evanston, Illinois, USA

S. Bhattacharya, J. Bueghly, Z. Chen, A. Gilbert, T. Gunter, K.A. Hahn, Y. Liu, N. Odell, M.H. Schmitt, M. Velasco

University of Notre Dame, Notre Dame, Indiana, USA

R. Band, R. Bucci, M. Cremonesi, A. Das, R. Goldouzian, M. Hildreth, K. Hurtado Anampa, C. Jessop, K. Lannon, J. Lawrence, N. Loukas, L. Lutton, J. Mariano, N. Marinelli, I. Mcalister, T. McCauley, C. Mcgrady, K. Mohrman, C. Moore, Y. Musienko[13], R. Ruchti, A. Townsend, M. Wayne, H. Yockey, M. Zarucki, L. Zygala

The Ohio State University, Columbus, Ohio, USA

B. Bylsma, L.S. Durkin, B. Francis, C. Hill, A. Lesauvage, M. Nunez Ornelas, K. Wei, B.L. Winer, B.R. Yates

JHEP07(2023)095

Princeton University, Princeton, New Jersey, USA
F.M. Addesa, B. Bonham, G. Dezoort, P. Elmer, A. Frankenthal, B. Greenberg, N. Haubrich, S. Higginbotham, A. Kalogeropoulos, G. Kopp, S. Kwan, D. Lange, D. Marlow, K. Mei, I. Ojalvo, J. Olsen, D. Stickland, C. Tully

University of Puerto Rico, Mayaguez, Puerto Rico, USA
S. Malik, S. Norberg

Purdue University, West Lafayette, Indiana, USA
A.S. Bakshi, V.E. Barnes, R. Chawla, S. Das, L. Gutay, M. Jones, A.W. Jung, D. Kondratyev, A.M. Koshy, M. Liu, G. Negro, N. Neumeister, G. Paspalaki, S. Piperov, A. Purohit, J.F. Schulte, M. Stojanovic, J. Thieman, F. Wang, R. Xiao, W. Xie

Purdue University Northwest, Hammond, Indiana, USA
J. Dolen, N. Parashar

Rice University, Houston, Texas, USA
D. Acosta, A. Baty, T. Carnahan, M. Decaro, S. Dildick, K.M. Ecklund, S. Freed, P. Gardner, F.J.M. Geurts, A. Kumar, W. Li, B.P. Padley, R. Redjimi, J. Rotter, W. Shi, S. Yang, E. Yigitbasi, L. Zhang[89], Y. Zhang, X. Zuo

University of Rochester, Rochester, New York, USA
A. Bodek, P. de Barbaro, R. Demina, J.L. Dulemba, C. Fallon, T. Ferbel, M. Galanti, A. Garcia-Bellido, O. Hindrichs, A. Khukhunaishvili, E. Ranken, R. Taus, G.P. Van Onsem

The Rockefeller University, New York, New York, USA
K. Goulianos

Rutgers, The State University of New Jersey, Piscataway, New Jersey, USA
B. Chiarito, J.P. Chou, Y. Gershtein, E. Halkiadakis, A. Hart, M. Heindl, O. Karacheban[25], I. Laflotte, A. Lath, R. Montalvo, K. Nash, M. Osherson, S. Salur, S. Schnetzer, S. Somalwar, R. Stone, S.A. Thayil, S. Thomas, H. Wang

University of Tennessee, Knoxville, Tennessee, USA
H. Acharya, A.G. Delannoy, S. Fiorendi, T. Holmes, S. Spanier

Texas A&M University, College Station, Texas, USA
O. Bouhali[90], M. Dalchenko, A. Delgado, R. Eusebi, J. Gilmore, T. Huang, T. Kamon[91], H. Kim, S. Luo, S. Malhotra, R. Mueller, D. Overton, D. Rathjens, A. Safonov

Texas Tech University, Lubbock, Texas, USA
N. Akchurin, J. Damgov, V. Hegde, K. Lamichhane, S.W. Lee, T. Mengke, S. Muthumuni, T. Peltola, I. Volobouev, Z. Wang, A. Whitbeck

JHEP07(2023)095

Vanderbilt University, Nashville, Tennessee, USA

E. Appelt, S. Greene, A. Gurrola, W. Johns, A. Melo, F. Romeo, P. Sheldon, S. Tuo, J. Velkovska

University of Virginia, Charlottesville, Virginia, USA

B. Cardwell, B. Cox, G. Cummings, J. Hakala, R. Hirosky, M. Joyce, A. Ledovskoy, A. Li, C. Neu, C.E. Perez Lara, B. Tannenwald

Wayne State University, Detroit, Michigan, USA

P.E. Karchin, N. Poudyal

University of Wisconsin — Madison, Madison, Wisconsin, USA

S. Banerjee, K. Black, T. Bose, S. Dasu, I. De Bruyn, P. Everaerts, C. Galloni, H. He, M. Herndon, A. Herve, C.K. Koraka, A. Lanaro, A. Loeliger, R. Loveless, J. Madhusudanan Sreekala, A. Mallampalli, A. Mohammadi, D. Pinna, A. Savin, V. Shang, V. Sharma, W.H. Smith, D. Teague, S. Trembath-Reichert, W. Vetens

Authors affiliated with an institute or an international laboratory covered by a cooperation agreement with CERN

S. Afanasiev, V. Andreev, Yu. Andreev, T. Aushev, M. Azarkin, A. Babaev, A. Belyaev, V. Blinov[92], E. Boos, V. Borshch, D. Budkouski, V. Bunichev, M. Chadeeva[92], V. Chekhovsky, A. Dermenev, T. Dimova[92], I. Dremin, M. Dubinin[82], L. Dudko, V. Epshteyn, A. Ershov, G. Gavrilov, V. Gavrilov, S. Gninenko, V. Golovtcov, N. Golubev, I. Golutvin, I. Gorbunov, V. Ivanchenko, Y. Ivanov, V. Kachanov, L. Kardapoltsev[92], V. Karjavine, A. Karneyeu, V. Kim[92], M. Kirakosyan, D. Kirpichnikov, M. Kirsanov, V. Klyukhin, O. Kodolova[93], D. Konstantinov, V. Korenkov, A. Kozyrev[92], N. Krasnikov, E. Kuznetsova[94], A. Lanev, P. Levchenko, A. Litomin, N. Lychkovskaya, V. Makarenko, A. Malakhov, V. Matveev[92], V. Murzin, A. Nikitenko[95], S. Obraztsov, V. Okhotnikov, A. Oskin, I. Ovtin[92], V. Palichik, P. Parygin, V. Perelygin, M. Perfilov, S. Petrushanko, G. Pivovarov, V. Popov, E. Popova, O. Radchenko[92], V. Rusinov, M. Savina, V. Savrin, D. Selivanova, V. Shalaev, S. Shmatov, S. Shulha, Y. Skovpen[92], S. Slabospitskii, V. Smirnov, D. Sosnov, A. Stepennov, V. Sulimov, E. Tcherniaev, A. Terkulov, O. Teryaev, I. Tlisova, M. Toms, A. Toropin, L. Uvarov, A. Uzunian, E. Vlasov, A. Vorobyev, N. Voytishin, B.S. Yuldashev[96], A. Zarubin, I. Zhizhin, A. Zhokin

† *Deceased*

[1] *Also at Yerevan State University, Yerevan, Armenia*

[2] *Also at TU Wien, Vienna, Austria*

[3] *Also at Institute of Basic and Applied Sciences, Faculty of Engineering, Arab Academy for Science, Technology and Maritime Transport, Alexandria, Egypt*

[4] *Also at Université Libre de Bruxelles, Bruxelles, Belgium*

[5] *Also at Universidade Estadual de Campinas, Campinas, Brazil*

[6] *Also at Federal University of Rio Grande do Sul, Porto Alegre, Brazil*

[7] *Also at UFMS, Nova Andradina, Brazil*

JHEP07(2023)095

[8] Also at The University of the State of Amazonas, Manaus, Brazil
[9] Also at University of Chinese Academy of Sciences, Beijing, China
[10] Also at Nanjing Normal University Department of Physics, Nanjing, China
[11] Now at The University of Iowa, Iowa City, Iowa, USA
[12] Also at University of Chinese Academy of Sciences, Beijing, China
[13] Also at an institute or an international laboratory covered by a cooperation agreement with CERN
[14] Also at Cairo University, Cairo, Egypt
[15] Also at Suez University, Suez, Egypt
[16] Now at British University in Egypt, Cairo, Egypt
[17] Also at Purdue University, West Lafayette, Indiana, USA
[18] Also at Université de Haute Alsace, Mulhouse, France
[19] Also at Ilia State University, Tbilisi, Georgia
[20] Also at Erzincan Binali Yildirim University, Erzincan, Turkey
[21] Also at CERN, European Organization for Nuclear Research, Geneva, Switzerland
[22] Also at University of Hamburg, Hamburg, Germany
[23] Also at RWTH Aachen University, III. Physikalisches Institut A, Aachen, Germany
[24] Also at Isfahan University of Technology, Isfahan, Iran
[25] Also at Brandenburg University of Technology, Cottbus, Germany
[26] Also at Forschungszentrum Jülich, Juelich, Germany
[27] Also at Physics Department, Faculty of Science, Assiut University, Assiut, Egypt
[28] Also at Karoly Robert Campus, MATE Institute of Technology, Gyongyos, Hungary
[29] Also at Institute of Physics, University of Debrecen, Debrecen, Hungary
[30] Also at Institute of Nuclear Research ATOMKI, Debrecen, Hungary
[31] Now at Universitatea Babes-Bolyai — Facultatea de Fizica, Cluj-Napoca, Romania
[32] Also at Faculty of Informatics, University of Debrecen, Debrecen, Hungary
[33] Also at Wigner Research Centre for Physics, Budapest, Hungary
[34] Also at Punjab Agricultural University, Ludhiana, India
[35] Also at UPES — University of Petroleum and Energy Studies, Dehradun, India
[36] Also at University of Hyderabad, Hyderabad, India
[37] Also at University of Visva-Bharati, Santiniketan, India
[38] Also at Indian Institute of Science (IISc), Bangalore, India
[39] Also at Indian Institute of Technology (IIT), Mumbai, India
[40] Also at IIT Bhubaneswar, Bhubaneswar, India
[41] Also at Institute of Physics, Bhubaneswar, India
[42] Also at Deutsches Elektronen-Synchrotron, Hamburg, Germany
[43] Also at Sharif University of Technology, Tehran, Iran
[44] Also at Department of Physics, University of Science and Technology of Mazandaran, Behshahr, Iran
[45] Also at Helwan University, Cairo, Egypt
[46] Also at Italian National Agency for New Technologies, Energy and Sustainable Economic Development, Bologna, Italy
[47] Also at Centro Siciliano di Fisica Nucleare e di Struttura Della Materia, Catania, Italy
[48] Also at Scuola Superiore Meridionale, Università di Napoli 'Federico II', Napoli, Italy
[49] Also at Università di Napoli 'Federico II', Napoli, Italy
[50] Also at Consiglio Nazionale delle Ricerche — Istituto Officina dei Materiali, Perugia, Italy
[51] Also at Department of Applied Physics, Faculty of Science and Technology, Universiti Kebangsaan Malaysia, Bangi, Malaysia
[52] Also at Consejo Nacional de Ciencia y Tecnología, Mexico City, Mexico
[53] Also at IRFU, CEA, Université Paris-Saclay, Gif-sur-Yvette, France
[54] Also at Faculty of Physics, University of Belgrade, Belgrade, Serbia
[55] Also at Trincomalee Campus, Eastern University, Sri Lanka, Nilaveli, Sri Lanka
[56] Also at INFN Sezione di Pavia, Università di Pavia, Pavia, Italy
[57] Also at National and Kapodistrian University of Athens, Athens, Greece

JHEP07(2023)095

[58] *Also at Ecole Polytechnique Fédérale Lausanne, Lausanne, Switzerland*
[59] *Also at Universität Zürich, Zurich, Switzerland*
[60] *Also at Stefan Meyer Institute for Subatomic Physics, Vienna, Austria*
[61] *Also at Laboratoire d'Annecy-le-Vieux de Physique des Particules, IN2P3-CNRS, Annecy-le-Vieux, France*
[62] *Also at Near East University, Research Center of Experimental Health Science, Mersin, Turkey*
[63] *Also at Konya Technical University, Konya, Turkey*
[64] *Also at Izmir Bakircay University, Izmir, Turkey*
[65] *Also at Adiyaman University, Adiyaman, Turkey*
[66] *Also at Necmettin Erbakan University, Konya, Turkey*
[67] *Also at Bozok Universitetesi Rektörlügü, Yozgat, Turkey*
[68] *Also at Marmara University, Istanbul, Turkey*
[69] *Also at Milli Savunma University, Istanbul, Turkey*
[70] *Also at Kafkas University, Kars, Turkey*
[71] *Also at Hacettepe University, Ankara, Turkey*
[72] *Also at Istanbul University — Cerrahpasa, Faculty of Engineering, Istanbul, Turkey*
[73] *Also at Yildiz Technical University, Istanbul, Turkey*
[74] *Also at Vrije Universiteit Brussel, Brussel, Belgium*
[75] *Also at School of Physics and Astronomy, University of Southampton, Southampton, United Kingdom*
[76] *Also at University of Bristol, Bristol, United Kingdom*
[77] *Also at IPPP Durham University, Durham, United Kingdom*
[78] *Also at Monash University, Faculty of Science, Clayton, Australia*
[79] *Also at Università di Torino, Torino, Italy*
[80] *Also at Bethel University, St. Paul, Minnesota, USA*
[81] *Also at Karamanoğlu Mehmetbey University, Karaman, Turkey*
[82] *Also at California Institute of Technology, Pasadena, California, USA*
[83] *Also at United States Naval Academy, Annapolis, Maryland, USA*
[84] *Also at Ain Shams University, Cairo, Egypt*
[85] *Also at Bingol University, Bingol, Turkey*
[86] *Also at Georgian Technical University, Tbilisi, Georgia*
[87] *Also at Sinop University, Sinop, Turkey*
[88] *Also at Erciyes University, Kayseri, Turkey*
[89] *Also at Institute of Modern Physics and Key Laboratory of Nuclear Physics and Ion-beam Application (MOE) — Fudan University, Shanghai, China*
[90] *Also at Texas A&M University at Qatar, Doha, Qatar*
[91] *Also at Kyungpook National University, Daegu, Korea*
[92] *Also at another institute or international laboratory covered by a cooperation agreement with CERN*
[93] *Also at Yerevan Physics Institute, Yerevan, Armenia*
[94] *Now at University of Florida, Gainesville, Florida, USA*
[95] *Also at Imperial College, London, United Kingdom*
[96] *Also at Institute of Nuclear Physics of the Uzbekistan Academy of Sciences, Tashkent, Uzbekistan*

JHEP07(2023)095

Appendix 3

III

K. Ehatäht and C. Veelken, “Stitching Monte Carlo samples”, *Eur. Phys. J. C*, vol. 82, no. 5, p. 484, 2022. doi: 10.1140/epjc/s10052-022-10407-9. arXiv: 2106.04360 [physics.data-an]

Eur. Phys. J. C (2022) 82:484
https://doi.org/10.1140/epjc/s10052-022-10407-9

THE EUROPEAN PHYSICAL JOURNAL C

Regular Article - Experimental Physics

Stitching Monte Carlo samples

Karl Ehatäht[a], **Christian Veelken**[b]

National Institute of Chemical Physics and Biophysics (NICPB), Akadeemia tee 23, 12618 Tallinn, Estonia

Received: 9 June 2021 / Accepted: 7 May 2022
© The Author(s) 2022

Abstract Monte Carlo (MC) simulations are extensively used for various purposes in modern high-energy physics (HEP) experiments. Precision measurements of established Standard Model processes or searches for new physics often require the collection of vast amounts of data. It is often difficult to produce MC samples containing an adequate number of events to allow for a meaningful comparison with the data, as substantial computing resources are required to produce and store such samples. One solution often employed when producing MC samples for HEP experiments is to partition the phase space of particle interactions into multiple regions and produce the MC samples separately for each region. This approach allows to adapt the size of the MC samples to the needs of physics analyses that are performed in these regions. In this paper we present a procedure for combining MC samples that overlap in phase space. The procedure is based on applying suitably chosen weights to the simulated events. We refer to the procedure as "stitching". The paper includes different examples for applying the procedure to simulated proton-proton collisions at the CERN Large Hadron Collider.

1 Introduction

Monte Carlo (MC) simulations [1,2] are used for a plethora of different purposes in contemporary high-energy physics (HEP) experiments. Applications for experiments currently in operation include detector calibration; optimization of analysis techniques, including the training of machine learning algorithms; the modelling of backgrounds, as well as the modelling of signal acceptance and efficiency. Besides, MC simulations are extensively used for detector development and for estimating the physics reach of experiments that are presently in construction or planned in the future.

The production of MC samples containing a sufficient number of events often poses a material challenge in terms of the computing resources required to produce and store such samples [3]. This is especially true for experiments at the CERN Large Hadron Collider (LHC) [4–6], firstly due to the large cross section for proton-proton (pp) scattering and secondly due to the large luminosity delivered by the LHC.

The number of pp scattering interactions, N_{data}, that occur within a given interval of time is given by the product of the pp scattering cross section, σ, and of the integrated luminosity, L, that the LHC has delivered during this time: $N_{\text{data}} = \sigma L$. We refer to the ensemble of pp scattering interactions that occur within the same crossing of the proton bunches as an "event". The interaction with the highest momentum exchange between the protons is referred to as the "hard-scatter" interaction, and the remaining interactions are referred to as "pileup". The inelastic pp scattering cross section at the center-of-mass energy of $\sqrt{s} = 13$ TeV, the energy achieved during the recently completed Run 2 of the LHC (in the period 2015–2018), amounts to ≈ 75 mb [7,8]. The pp scattering data recorded by the ATLAS and CMS experiments during LHC Run 2 amounts to an integrated luminosity of ≈ 140 fb^{-1} per experiment [9–12]. Thus, $N_{\text{data}} \approx 10^{16}$ inelastic pp scattering interactions occurred in each of the two experiments during this time. Ideally, one would want the number of simulated events to be higher than the number of events in the data, such that the statistical uncertainties on the MC simulation are small compared to the statistical uncertainties on the data. The production of such large MC samples is clearly prohibitive, however.

Even if one restricts the production of MC samples to processes with a cross section that is significantly smaller than the inelastic pp scattering cross section, such as Drell–Yan (DY) production, the production of W bosons (W+jets), and the production of top quark pairs ($t\bar{t}$+jets), the production of MC samples containing a sufficient number of events to allow for a meaningful comparison with the data represents a formidable challenge. The DY, W+jets, and $t\bar{t}$+jets produc-

[a] e-mail: karl.ehataht@cern.ch
[b] e-mail: christian.veelken@cern.ch (corresponding author)

Published online: 26 May 2022

tion processes are used for detector calibration and Standard Model (SM) precision measurements. They also constitute relevant backgrounds to searches for physics beyond the SM. Their cross sections amount to 6.08 nb for DY production, 61.5 nb for W+jets production, and 832 pb for $t\bar{t}$+jets production [13–15].[1] The ATLAS and CMS experiments would each need to produce MC samples containing 840 million DY, 8.61 billion W+jets, and 116 million $t\bar{t}$+jets events in order to reduce the statistical uncertainties on the MC simulation to the same level as the uncertainties on the LHC Run 2 data.

In order to mitigate the effect of limited computing resources, both experiments employ sophisticated strategies for the production of MC samples. A common feature of these strategies is to vary the expenditure of computing resources across phase space (PS), depending on the needs of physics analyses. When searching for new physics, for example, it is important to produce sufficiently many events in the tails of distributions, as otherwise potential signals may be obscured by the statistical uncertainties on the SM background.

Different mechanisms for adapting the expenditure of computing resources to the needs of physics analyses have been proposed in the literature. Modern MC programs ("generators") such as POWHEG [16–18], MADGRAPH5_aMC@NLO [19], SHERPA [20], PYTHIA [21], and HERWIG [22] provide functionality that allows to adjust the number of events sampled in different regions of PS through user-defined weighting functions. This approach has been used in Ref. [23]. An alternative approach is to partition the PS into distinct regions ("slices") and to produce separate independent MC samples covering each slice. Following Ref. [3], we refer to the first approach as "biasing" and to the second one as "slicing".

In this paper, we focus on the case that MC samples have already been produced and present a method that makes optimal use of these samples, where "optimal" refers to yielding the lowest statistical uncertainty on the signal or background estimate that is obtained from these samples. The samples in general overlap in PS. For example, one set of MC samples may partition the PS based on the number of jets, whereas another set of samples may partition the PS based on H_{T}, the scalar sum in p_{T} of these jets. Our method is general enough to handle arbitrary overlaps between these samples. The overlap is accounted for by applying appropriately chosen weights to the simulated events. We refer to the procedure as "stitching". One useful feature of the stitching method is that it allows to increase the number of simulated events incrementally in certain regions of PS in case these regions are not yet sufficiently populated by the existing MC samples.

In the following, we will assume that all MC samples that are subject to the stitching procedure have been produced with the same version of the MC program and consistent (i.e. identical) settings for parton distribution functions, scale choices, parton-shower and underlying-event tunes, etc. In case a given set of MC samples was produced with inconsistent settings, the effect of the inconsistencies either need to be small (compared to e.g. the systematic uncertainties) or the events need to be reweighted to make all MC samples consistent prior to applying the stitching procedure.

Variants of the stitching procedure described in the first part of this manuscript have been used by the ATLAS and CMS experiments since LHC Run 1, but, to the best of our knowledge, have not been described in detail in a public document yet. The formalism for the computation of stitching weights is detailed in Sect. 2. Concrete examples for using the formalism in physics analyses are given in Sects. 3.1.1 and 3.1.2. The examples characterize the use of the stitching procedure by the CMS experiment during LHC Runs 1 and 2. They are chosen with the intention to provide a reference. In Sect. 3.2 we extend the stitching procedure to the case of estimating trigger rates at the High-Luminosity LHC (HL-LHC) [24], scheduled to start operation in 2027. The distinguishing feature between the applications of the stitching procedure described in Sects. 3.1 and 3.2 is that in the former (but not in the latter) the cross section of the process that is modeled by the MC simulation is orders of magnitude smaller compared to the inelastic pp scattering cross section. In the former case one can make the simplifying assumption that the process of interest (the process modeled by the MC simulation) solely occurs in the hard-scatter interaction and not in pileup interactions. For the purpose of estimating trigger rates, a relevant use case is that the hard-scatter interaction as well as the pileup interactions are inelastic pp scattering interactions, and the hard-scatter interaction is in fact indistinguishable from the pileup. As described in detail in Sect. 3.2, we account for this indistinguishability by making suitable modifications to the formalism for the computation of stitching weights. The modified stitching procedure detailed in Sect. 3.2 has been used to estimate trigger rates for the HL-LHC upgrade technical design report of the CMS experiment [25]. We conclude the paper with a summary in Sect. 4.

2 Computation of stitching weights

As explained in the introduction, contemporary HEP experiments often employ MC production schemes that first partition the PS into multiple regions and then produce separate MC samples covering each region. We use the term "MC pro-

[1] The quoted cross sections refer to, respectively, DY production of lepton (electron, muon, and τ) pairs of mass > 50 GeV, W+jets production with subsequent leptonic decay of the W boson, and to the pair production of top quarks of mass 172.5 GeV.

duction scheme" to refer to the strategy for choosing which MC samples to produce and how to produce these samples (which MC generator programs to use, how to partition the PS into regions, which settings to use when executing the MC generator programs, etc) and the term "MC sample" to refer to the set of all output files produced by one execution of a MC generator program. When using these MC samples in physics analyses, the overlap of the samples in PS needs to be accounted for by applying weights to the simulated events. The weights need to be chosen such that the weighted sum of simulated events in each region i of PS matches the SM prediction in that region:

$$\sum_j P_j^i \, s_j^i \sum_{k=1}^{N_j} w_j^k = L \, \sigma^i , \tag{1}$$

where the symbol L corresponds to the integrated luminosity of the analyzed dataset and σ^i denotes the fiducial cross section for the process under study in the PS region i. The first (second) sum on the left-hand side extends over the MC samples j (over the events k in the jth MC sample, where N_j denotes the total number of simulated events in the sample j). The symbol w_j^k denotes the weight assigned to event k by the MC generator program, while s_j^i denotes the "stitching" weight that is applied to events from the sample j falling into the PS region i. The symbol P_j^i corresponds to the probability for an event in MC sample j to fall into PS region i. Equation (1) holds separately for each signal or background process under study.

One can show that the statistical uncertainty on the signal or background estimate gets reduced when all simulated events that fall into PS region i have the same weight, regardless of which MC sample j contains the event. We hence choose the stitching weight to depend only on the PS region i (and not on the MC sample j) and refer to these weights using the symbol s^i from now on.

We define the symbol P_{incl}^i as the ratio of the fiducial cross section σ^i to the "inclusive" cross section σ_{incl}, which refers to the whole PS:

$$P_{\text{incl}}^i = \frac{\sigma^i}{\sigma_{\text{incl}}} \quad \Longleftrightarrow \quad \sigma^i = \sigma_{\text{incl}} \, P_{\text{incl}}^i .$$

Upon inserting this relation into Eq. (1) and solving for the weight s^i, we obtain:

$$s^i = \frac{L \, \sigma_{\text{incl}} \, P_{\text{incl}}^i}{P_j^i \sum_{k=1}^{N_j} w_j^k} . \tag{2}$$

A special case, which is frequently encountered in practice, is that one MC sample covers the whole PS, while additional MC samples are used to reduce the statistical uncertainties in the tails of distributions. We refer to the MC sample that covers the whole PS as the "inclusive" sample and the corresponding PS as the "inclusive" PS. In this case, Eq. (2) can be rewritten in the form:

$$s^i = \frac{L \, \sigma_{\text{incl}}}{\sum_{k=1}^{N_{\text{incl}}} w_{\text{incl}}^k} \frac{P_{\text{incl}}^i \sum_{k=1}^{N_{\text{incl}}} w_{\text{incl}}^k}{P_{\text{incl}}^i \sum_{k=1}^{N_{\text{incl}}} w_{\text{incl}}^k + \sum_j P_j^i \sum_{k=1}^{N_j} w_j^k} , \tag{3}$$

where w_{incl}^k refers to the weights assigned to events in the inclusive sample by the MC generator program and N_{incl} denotes the total number of events in the inclusive sample. The sum over j in Eq. (3) extends over the additional MC samples, which each cover a different region in PS. We will refer to these samples as the "exclusive" samples. We assume that the weights w_{incl}^k and w_j^k are normalized such that the average of these weights, $\bar{w}_{\text{incl}} = \frac{1}{N_{\text{incl}}} \sum_{k=1}^{N_{\text{incl}}} w_{\text{incl}}^k$ and $\bar{w}_j = \frac{1}{N_j} \sum_{k=1}^{N_j} w_j^k$, equals unity for the inclusive sample and for each exclusive sample j [2]. The two factors in Eq. (3) may be interpreted in the following way: The product of w_{incl}^k and the first factor, $w_{\text{incl}}^k \frac{L \, \sigma_{\text{incl}}}{\sum_{k=1}^{N_{\text{incl}}} w_{\text{incl}}^k}$, corresponds to the weight that one would apply to an event in PS region i in case no exclusive samples are available and the signal or background estimate in PS region i is based solely on the inclusive sample. The availability of the additional exclusive samples increases the number of simulated events in the PS region i, from $N_{\text{incl}} \, P_{\text{incl}}^i$ to $N_{\text{incl}} \, P_{\text{incl}}^i + \sum_j N_j \, P_j^i$, and reduces the weights that are applied to simulated events falling into the region i. The reduction in the event weight is given by the second factor in Eq. (3). It has the effect of reducing the statistical uncertainty on the signal or background estimate in PS region i by the square-root of this factor, i.e. by $\sqrt{\frac{P_{\text{incl}}^i \sum_{k=1}^{N_{\text{incl}}} w_{\text{incl}}^k}{P_{\text{incl}}^i \sum_{k=1}^{N_{\text{incl}}} w_{\text{incl}}^k + \sum_j P_j^i \sum_{k=1}^{N_j} w_j^k}}$.

3 Examples

In this section, we illustrate the formalism developed in Sect. 2 with concrete examples, drawn from two different applications: the modelling of W+jets production in physics analyses at the LHC and the estimation of trigger rates at the HL-LHC.

[2] If this is not the case for a given set of MC samples, it can be achieved by a simple multiplication of the weights w_{incl}^k and w_j^k by the factors $1/\bar{w}_{\text{incl}}$ and $1/\bar{w}_j$.

3.1 Modelling of W+jets production in physics analyses at the LHC

The production of W bosons is interesting to study at the LHC for several reasons. The measurement of the mass of the W boson is an important input to global fits to SM parameters [26]. The fits allow to test the overall consistency of the SM and to set constraints on physics beyond the SM. The sensitivity of these fits is currently limited by the precision of the W boson mass measurement [26]. Differential measurements of the cross section for W+jets production are used to constrain parton distribution functions [27–30]. In particular, the measurement of the associated production of a W boson with a charm quark provides sensitivity to the strange quark content of the proton [31–33] and allows to tune MC generators to improve the modelling of heavy flavour production at hadron colliders. The production of W bosons also constitutes a relevant background to measurements of other SM processes and to searches for new physics, see for example Refs. [34–37]. In this section, we focus on W+jets production with subsequent leptonic decay of the W boson.

Simulated samples of W+jets events have been produced for pp collisions at $\sqrt{s} = 13$ TeV center-of-mass energy using matrix elements computed at leading order (LO) accuracy in perturbative quantum chromodynamics (pQCD) with the program MadGraph5_aMC@NLO 2.6.5 [19]. The parton distribution functions of the proton are modeled using the NNPDF3.1 set [38]. Parton showering, hadronization, and the underlying event are modeled using the program Pythia v8.240 [21] with the tune CP5 [39]. The matching of matrix elements to parton showers is done using the MLM scheme [40]. We restrict the analysis of these samples to particles originating from the hard-scatter interaction and do not add any pileup to these samples. Samples containing either 1, 2, 3, or 4 jets at matrix-element level are complemented by an "inclusive" sample and by samples binned in the scalar sum in p_{T} of these jets. We denote the multiplicity of jets at the matrix-element level by the symbol N_{jet} and the scalar sum in p_{T} of these jets by the symbol H_{T}. The inclusive and H_{T}-binned samples contain events with between 0 and 4 jets at the matrix-element level.

The weights w_j^k and w_{incl}^k are equal to one for all events in these samples. Thus, $\sum_{k=1}^{N_j} w_j^k = N_j$ and $\sum_{k=1}^{N_{\mathrm{incl}}} w_{\mathrm{incl}}^k = N_{\mathrm{incl}}$ for this example, which allows us to simplify Eq. (3) to:

$$s^i = \frac{L\,\sigma_{\mathrm{incl}}}{N_{\mathrm{incl}}} \frac{P^i_{\mathrm{incl}}\,N_{\mathrm{incl}}}{P^i_{\mathrm{incl}}\,N_{\mathrm{incl}} + P^i_j\,N_j}. \tag{4}$$

All samples are normalized using a k-factor of 1.14, given by the ratio of the inclusive cross section computed at next-to-next-to leading order (NNLO) accuracy in pQCD, with electroweak corrections taken into account up to NLO accuracy [14], and the inclusive cross section computed at LO accuracy by the program MadGraph5_aMC@NLO. The product of the inclusive W+jets production cross section times the branching fraction for the decay to a charged lepton and a neutrino amounts to 61.5 nb.

We will demonstrate the stitching of these samples based on the two observables N_{jet} and H_{T}. The PS region in which we perform the stitching will be either one- or two-dimensional. We will show that for our formalism it makes little difference whether the stitching is performed in one dimension or in two. The stitching of W+jets samples based on the observable N_{jet} will be discussed first and then we will discuss the stitching of W+jets samples based on the two observables N_{jet} and H_{T}.

3.1.1 Stitching of W+jets samples by N_{jet}

In this example, an inclusive W+jets sample simulated at LO accuracy in pQCD is stitched with exclusive samples containing events with N_{jet} equal to either 1, 2, 3, or 4. The inclusive sample contains events with N_{jet} between 0 and 4. We partition the PS into slices based on the multiplicity of jets at the matrix-element level and set the index i equal to N_{jet}. The number of events in each MC sample is chosen such that the stitching weights decrease by about a factor of two for each increase in jet multiplicity. The decrease in the cross section as function of N_{jet} allows to reduce the statistical uncertainties in the tail of the N_{jet} distribution without significantly increasing the expenditure of computing resources required to produce and store these samples. The number of events contained in each sample and the values of the probabilities P^i_{incl} and P^i_j are given in Tables 1 and 2. The probabilities P^1_{incl}, P^2_{incl}, P^3_{incl}, and P^4_{incl} are computed by taking the ratio of cross sections, computed at LO accuracy by the program MadGraph5_aMC@NLO, for the exclusive samples with respect to the cross section σ_{incl} of the inclusive sample. The probability P^0_{incl} is obtained using the relation $P^0_{\mathrm{incl}} = 1 - \sum_{i=1}^{4} P^i_{\mathrm{incl}}$. The probabilities P^i_j for the exclusive samples are 1 if $i = j$ and 0 otherwise, as each of the exclusive samples j covers exactly one PS region i. The corresponding stitching weights s^i, computed according to Eq. (4), are given in Table 3.

In order to demonstrate that the stitching procedure is unbiased, we compare the normalization and shape of distributions obtained using the stitching procedure with the normalization and shape of distributions obtained from the inclusive sample. Distributions in p_{T} of the "leading" and "subleading" jet (the jets of, respectively, highest and second-highest p_{T} in the event), in the multiplicity of jets and in the observable H_{T} are shown in Fig. 1. The distributions obtained from the inclusive sample are represented by black

Table 1 Number of events in the inclusive W+jets sample and in the W+jets samples produced in bins of N_{jet}, and corresponding cross sections

Sample	Index j	Number of events	Cross section [nb][a]
Inclusive	–	3×10^6	61.5
$N_{\text{jet}} = 1$	1	5×10^6	10.1
$N_{\text{jet}} = 2$	2	4.7×10^6	3.21
$N_{\text{jet}} = 3$	3	3.2×10^5	0.938
$N_{\text{jet}} = 4$	4	3.3×10^5	0.443

[a]Computed at LO accuracy in pQCD, then scaled to NNLO

Table 2 Probabilities P^i for the events in the inclusive and exclusive samples to populate the different PS regions i. The PS regions i are defined by the multiplicity of jets at the matrix-element level

Sample	Probabilities				
	P^0	P^1	P^2	P^3	P^4
Inclusive	0.758	0.167	0.052	0.015	0.007
$N_{\text{jet}} = 1$	0	1	0	0	0
$N_{\text{jet}} = 2$	0	0	1	0	0
$N_{\text{jet}} = 3$	0	0	0	1	0
$N_{\text{jet}} = 4$	0	0	0	0	1

Table 3 Stitching weights s^i for the case that the inclusive and exclusive W+jets samples given in Table 1 are stitched based on N_{jet}. The weights are computed for an integrated luminosity of 140 fb^{-1}

	Multiplicity of jets				
	0	1	2	3	4
Stitching weight	2870	1440	714	362	180

markers ("inclusive only"), while those obtained by applying the stitching procedure to the combination of the inclusive sample and the samples binned in N_{jet} are represented by pink lines ("stitched"). The contributions of individual exclusive samples j to the stitched distribution are indicated by shaded areas of different color in the upper part of each figure. The white area ("inclusive stitched") represents the contribution of the inclusive sample to the stitched distribution. The shaded areas of different color and the white area add up to the pink line. We remark that the "inclusive only" and "inclusive stitched" distributions contain the exact same events. The sole difference between these two distributions is that the stitching weights, given in Table 3, are applied to the "inclusive stitched", but not to the "inclusive only" distribution. In the lower part of each figure, we show the difference in normalization and shape between the distribution obtained using the stitching procedure and the distribution obtained when using solely the inclusive sample. The differences are given relative to the distribution obtained from our stitching procedure. The size of statistical uncertainties on the "inclusive only" and "stitched" distributions is visualized in the lower part of each figure and is represented by the length of the error bars and by the height of the dark shaded area, respectively. The jets shown in the figure are reconstructed using the anti-k_t algorithm [41,42] with a distance parameter of 0.4, using all stable generator-level particles (after hadron shower and hadronization) except neutrinos as input, and are required to satisfy the selection criteria $p_T > 25$ GeV and $|\eta| < 5.0$. The observable H_T is computed as the scalar sum in p_T of these jets. Note that the multiplicity of jets and the observable H_T shown in Fig. 1 differ from the observables N_{jet} and H_T that are used in the stitching procedure: The former refer to jets at the generator (detector) level, while the latter refer to jets at the matrix-element level. The distributions are normalized to an integrated luminosity of 140 fb^{-1}.

The distributions for the inclusive sample and for the sum of inclusive plus exclusive samples, with the stitching weights applied, are in agreement within the statistical uncertainties. The exclusive samples reduce the statistical uncertainties in particular in the tails of the distributions.

3.1.2 Stitching of W+jets samples by N_{jet} and H_T

This example extends the previous example. It demonstrates the stitching procedure based on two observables, N_{jet} and H_T. The exclusive samples are simulated for jet multiplicities of $N_{\text{jet}} = 1, 2, 3,$ and 4 and for H_T in the ranges 70–100, 100–200, 200–400, 400–600, 600–800, 800–1200, 1200–2500, and > 2500 GeV (up to the kinematic limit). We refer to the exclusive samples produced in slices of N_{jet} as the "N_{jet}-

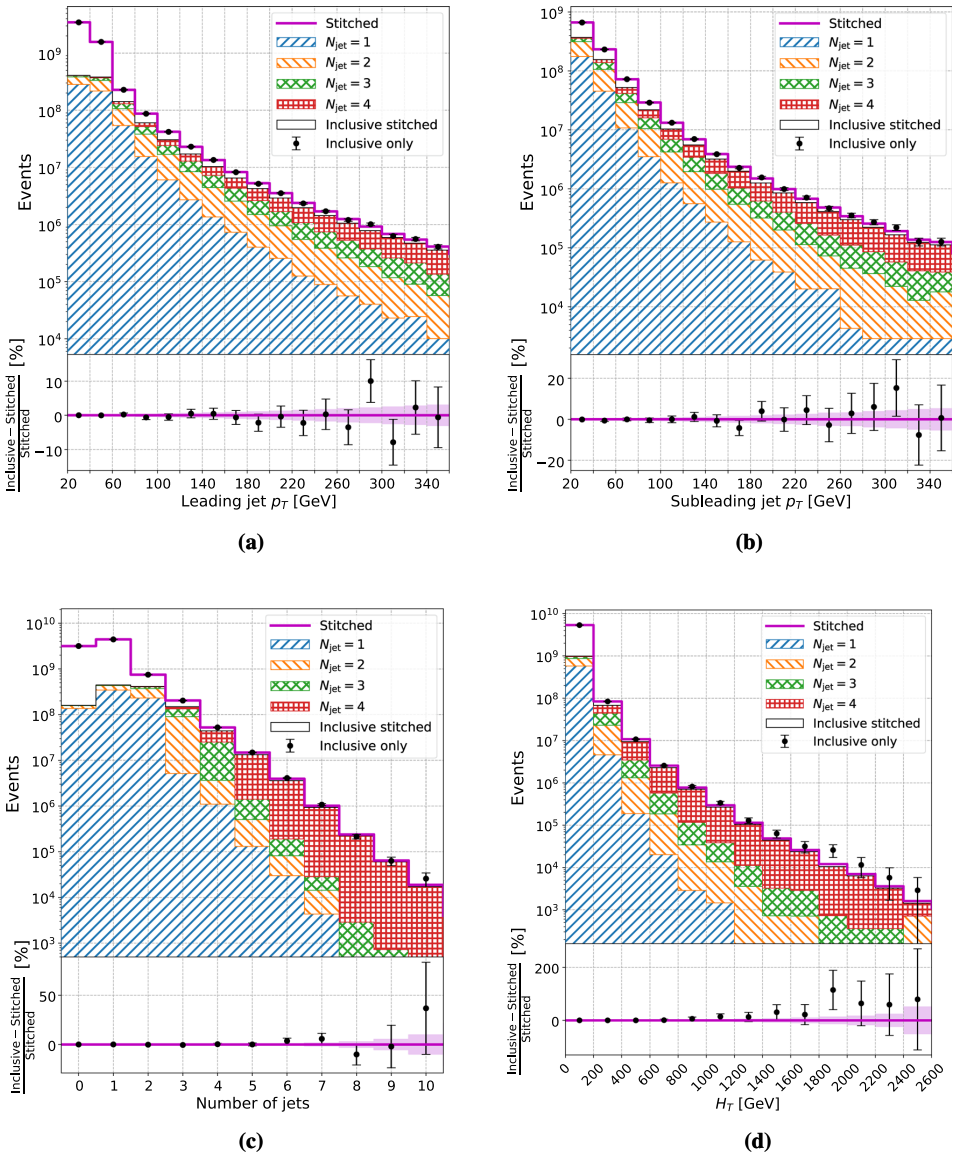


Fig. 1 Distributions in p_T of the **a** leading and **b** subleading jet, in **c** the multiplicity of generator-level jets and in **d** the observable H_T, the scalar sum in p_T of these jets, for the case of W+jets samples that are stitched based on the observable N_{jet} at the matrix-element level. The W bosons are required to decay leptonically. The event yields are computed for an integrated luminosity of 140 fb^{-1}

samples" and to the samples simulated in ranges in H_T as the "H_T-samples". The inclusive sample contains events with jet multiplicities between 0 and 4 and covers the full range in H_T. The number of events in the H_T-samples are given in Table 4. The information for the inclusive sample and for the N_{jet}-samples is the same as for the previous example and is given in Table 1.

The corresponding PS regions i, defined in the plane of N_{jet} versus H_T, are shown in Fig. 2. In total, the probabilities P^i_{incl} and P^i_j and the corresponding stitching weights s^i are computed for 45 separate PS regions.

Table 4 Number of events in the W+jets samples produced in ranges in H_T and corresponding cross sections

Sample	Index j	Number of events	Cross section [pb][a]
$70 \leqslant H_T < 100$ GeV	5	1.4×10^5	1430
$100 \leqslant H_T < 200$ GeV	6	2.8×10^5	1410
$200 \leqslant H_T < 400$ GeV	7	1.5×10^5	379
$400 \leqslant H_T < 600$ GeV	8	4×10^4	51.3
$600 \leqslant H_T < 800$ GeV	9	2×10^4	12.6
$800 \leqslant H_T < 1200$ GeV	10	2×10^4	5.34
$1200 \leqslant H_T < 2500$ GeV	11	1.3×10^4	1.51
$H_T \geqslant 2500$ GeV	12	6.5×10^2	0.052

[a]Computed at LO accuracy in pQCD, then scaled to NNLO

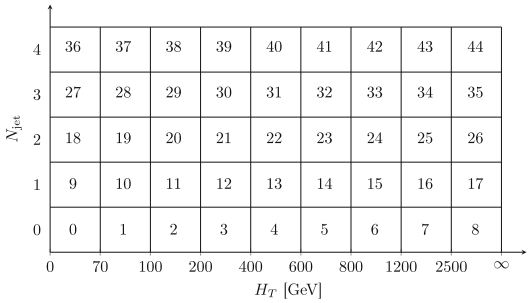


Fig. 2 Definition of the PS regions i in the plane of N_{jet} versus H_T, for the case of W+jets samples that are stitched based on the observables N_{jet} and H_T

In some of the 45 PS regions, the probabilities P^i_{incl} are rather low, on the level of 10^{-7}. In order to reduce the statistical uncertainties on the probabilities P^i_{incl} and P^i_j, we compute these probabilities using the following procedure: For all regions i of PS that are covered by the inclusive sample and by one or more N_{jet}- or H_T-samples, we determine the probabilities P^i_{incl} and P^i_j by the method of least squares [43]. Details of the computation are given in the appendix. The probability P^0_{incl} for the PS region $N_{jet} = 0$ and $H_T < 70$ GeV, which is solely covered by the inclusive sample, is computed according to the relation $P^0_{incl} = 1 - \sum_{i=1}^{44} P^i_{incl}$. The numerical values of the probabilities P^i_{incl} and P^i_j obtained by the least-square method and of the stitching weights s^i, computed according to Eq. (4), are given in Tables 7 and 8.

Distributions in p_T of the leading and subleading jet, in the multiplicity of jets, and in the observable H_T obtained from our stitching procedure are compared to the distributions obtained from the inclusive sample in Fig. 3. The distributions obtained by stitching the inclusive sample with the samples binned in N_{jet} and in H_T are represented by pink lines, while those obtained when using solely the inclusive sample are represented by black markers. The weights given in Table 8 are applied to the stitched distributions. The contribution of all N_{jet}-binned samples to the stitched distribution is represented by the blue shaded area ("sum of N_{jet} samples"), while the contribution of all samples produced in ranges in H_T is represented by the yellow shaded area ("sum of H_T samples") in the upper part of the figures. Following Fig. 1, the white area represents the contribution of the inclusive sample to the stitched distribution. The jets are reconstructed as described in Sect. 3.1.1 and are required to pass the selection criteria $p_T > 25$ GeV and $|\eta| < 5.0$. In the lower part of each figure, we again show the difference between the distributions obtained from the inclusive sample and obtained by using our stitching procedure, and also the respective statistical uncertainties. As one would expect, the addition of samples simulated in ranges in H_T to the example given in Sect. 3.1.1 reduces the statistical uncertainties in the tails of the distributions. The reduction is most pronounced in the tails of the distributions in leading and subleading jet p_T and in the observable H_T.

3.2 Estimation of trigger rates at the HL-LHC

We choose the task of estimating trigger rates for the upcoming high-luminosity data-taking period of the LHC as second example to illustrate the stitching procedure. The "rate" of a trigger corresponds to the number of pp collision events that satisfy the trigger condition per unit of time. The estimation of trigger rates constitutes an important task for demonstrating the physics potential of the HL-LHC. The HL-LHC physics program demands a large amount of integrated luminosity to be delivered by the LHC, in order to facilitate measurements of rare signal processes (such as the precise measurement of H boson couplings and the study of H boson pair production), as well as to enhance the sensitivity of searches for new physics, by the ATLAS and CMS experiments. In order to satisfy this demand, the HL-LHC is expected to operate at an instantaneous luminosity of $5–7.5 \times 10^{34}$ cm^{-2} s^{-1} at a center-of-mass energy of $\sqrt{s} = 14$ TeV [24]. The challenge of developing triggers for the HL-LHC is to design the triggers such that rare signal processes pass the triggers with a high efficiency, while the rate of background processes gets

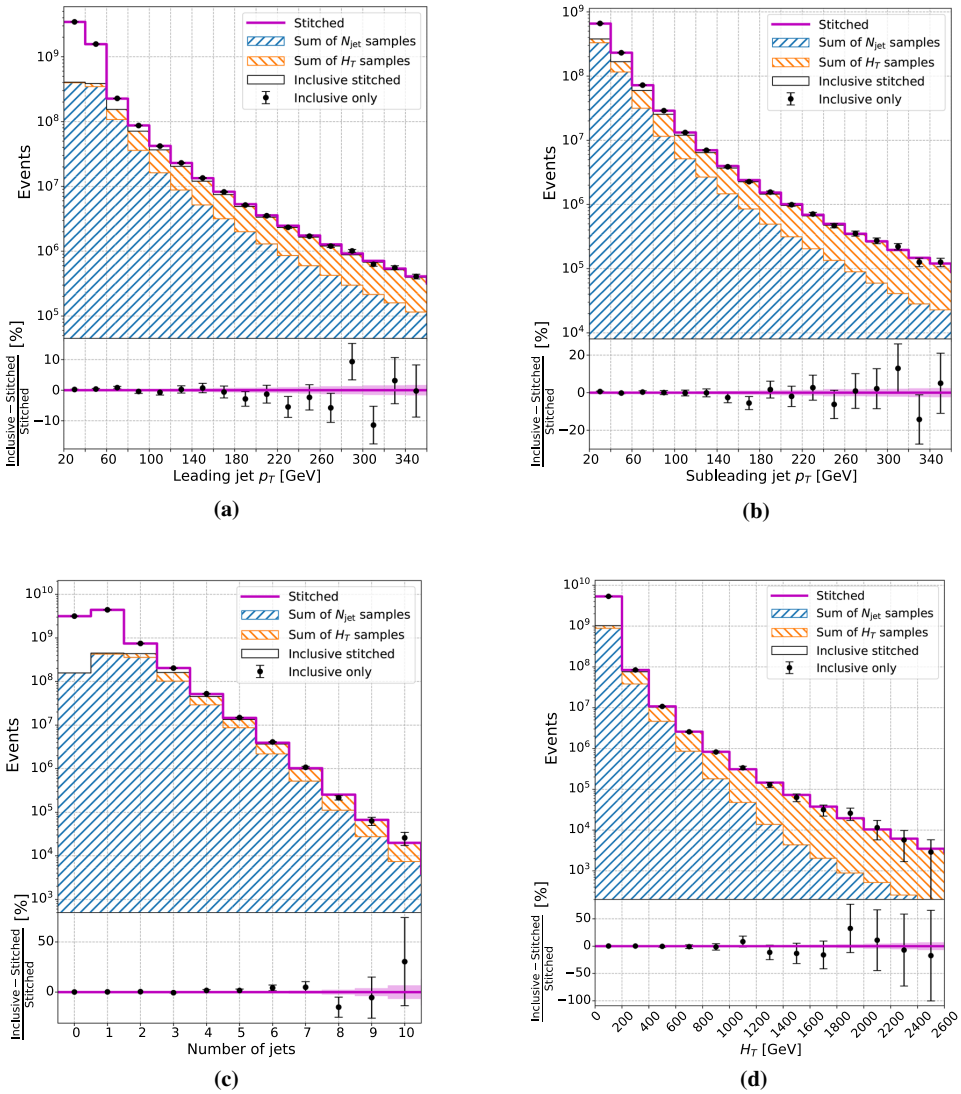


Fig. 3 Distributions in p_T of the **a** leading and **b** subleading jet, in **c** the multiplicity of generator-level jets and in **d** the observable H_T, the scalar sum in p_T of these jets, for the case of W+jets samples that are stitched based on the observables N_{jet} and H_T at the matrix-element level. The W bosons are required to decay leptonically. The event yields are computed for an integrated luminosity of 140 fb^{-1}

reduced by many orders of magnitude, in order not to exceed bandwidth limitations on the detector read-out and on the rate with which events can be written to permanent storage.

The inelastic pp scattering cross section at $\sqrt{s} = 14$ TeV amounts to ≈ 80 mb, resulting in up to 200 simultaneous pp interactions per crossing of the proton beams at the nominal HL-LHC instantaneous luminosity [24]. The vast majority of these interactions are inelastic pp scatterings with low momentum exchange, which predominantly arise from the exchange of gluons between the colliding protons. We refer to inelastic pp scattering interactions with no further selection applied as "minimum bias" events. In order to estimate the rates of triggers at the HL-LHC, MC samples of minimum bias events are produced at LO in pQCD using the program PYTHIA. The minimum bias samples are complemented by samples of inelastic pp scattering interactions in which a sig-

nificant amount of transverse momentum, denoted by the symbol $\hat{p}_{\mathrm{T}}$, is exchanged between the scattered protons. The stitching of the minimum bias samples with samples generated for different ranges in $\hat{p}_{\mathrm{T}}$ allows to estimate the trigger rates with lower statistical uncertainties.

The production of MC samples used for estimating trigger rates at the HL-LHC proceeds by first simulating one "hard-scatter" (HS) interaction within a given range in $\hat{p}_{\mathrm{T}}$ and then adding a number of additional inelastic pp scattering interactions of the minimum bias kind to the same event, in order to simulate the pileup (PU). We use the symbol N_{PU} to denote the total number of PU interactions that occur in the same crossing of the proton beams as the HS interaction. No selection on $\hat{p}_{\mathrm{T}}$ is applied when simulating the PU interactions. We remark that the distinction between the HS interaction and the PU interactions is artificial and solely made for the purpose of MC production. The HS interaction and the PU interactions will be indistinguishable in the data that will be recorded at the HL-LHC: The scattering in which the transverse momentum exchange between the protons amounts to $\hat{p}_{\mathrm{T}}$ may occur in any of the $N_{\mathrm{PU}}+1$ simultaneous pp interactions. Our formalism treats the HS interaction and the PU interactions on an equal footing.

The "inclusive" sample in this example are events containing $N_{\mathrm{PU}}+1$ minimum bias interactions, where for each event the number of PU interactions, N_{PU}, is sampled at random from the Poisson probability distribution:

$$\mathrm{Poisson}(N_{\mathrm{PU}}|\bar{N}) = \frac{\bar{N}^{N_{\mathrm{PU}}}\, e^{-\bar{N}}}{N_{\mathrm{PU}}!} \tag{5}$$

with a mean $\bar{N} = 200$. The exclusive samples contain one HS interaction of transverse momentum within a specified range in $\hat{p}_{\mathrm{T}}$ in addition to N_{PU} minimum bias interactions. The latter represent the PU. The number N_{PU} of PU interactions is again sampled at random from a Poisson distribution with a mean of $\bar{N} = 200$.

We enumerate the ranges in $\hat{p}_{\mathrm{T}}$ by the index i and denote the number of $\hat{p}_{\mathrm{T}}$ ranges used to produce the exclusive samples by the symbol m. We further introduce the symbol n_i to refer to the number of inelastic pp scattering interactions that fall into the ith interval in $\hat{p}_{\mathrm{T}}$. The inelastic pp scatterings may occur either in the HS interaction or in any of the N_{PU} PU interactions. The "phase space" corresponding to a given event is represented by a vector $I = n_1, \ldots, n_m$ of dimension m. The ith component of this vector indicates the number of inelastic pp scattering interactions that fall into the ith interval in $\hat{p}_{\mathrm{T}}$.

The probability P^I for an event in the inclusive sample that contains N_{PU} pileup interactions to feature n_1 inelastic pp scatterings that fall into the first interval in $\hat{p}_{\mathrm{T}}$, n_2 that fall into the second,..., and n_m that fall into the mth follows a multinomial distribution [44] and is given by:

$$P^I_{\mathrm{incl}} = \frac{(N_{\mathrm{PU}}+1)!}{n_1!\,\ldots\,n_m!}\, p_1^{n_1}\,\ldots\,p_m^{n_m}, \tag{6}$$

where the symbols p_i correspond to the probability for a single inelastic pp scattering interaction to feature a transverse momentum exchange that falls into the ith interval in $\hat{p}_{\mathrm{T}}$. The n_i satisfy the condition $\sum_{i=1}^{m} n_i = N_{\mathrm{PU}}+1$.

The corresponding probability P^I_j for an event in the jth exclusive sample that contains N_{PU} pileup interactions is given by:

$$P^I_j = \begin{cases} \frac{N_{\mathrm{PU}}!}{n_1!\,\ldots\,(n_j-1)!\,\ldots\,n_m!} \\ \quad p_1^{n_1}\,\ldots\,p_j^{(n_j-1)}\,\ldots\,p_m^{n_m}\,, & \text{if } n_j \geq 1 \\ 0\,, & \text{otherwise.} \end{cases} \tag{7}$$

The n_i again satisfy the condition $N_{\mathrm{PU}}+1 = \sum_{i=1}^{m} n_i$. The fact that for all events in the jth exclusive sample the transverse momentum $\hat{p}_{\mathrm{T}}$ that is exchanged in the HS interaction falls into the jth interval in $\hat{p}_{\mathrm{T}}$ implies that $N_{\mathrm{PU}}+1$ needs to be replaced by N_{PU} and n_j by n_j-1 in Eq. (7) compared to Eq. (6), as one of the inelastic pp scatterings that fall into the jth interval in $\hat{p}_{\mathrm{T}}$ is "fixed" and thus not subject to the random fluctuations, which are modeled by the multinomial distribution. The ratio of Eq. (7) to Eq. (6) is given by the expression:

$$\frac{P^I_j}{P^I_{\mathrm{incl}}} = \frac{n_j}{(N_{\mathrm{PU}}+1)\,p_j}. \tag{8}$$

The validity of Eq. (8) includes the case $n_j = 0$.

The expression for the stitching weight s^I is given by an expression similar to Eq. (3), the main difference being that the index i is replaced by the vector I, the probabilities P^i_{incl} and P^i_j are replaced by the probabilities P^I_{incl} and P^I_j and the product of luminosity times cross section, $L\,\sigma_{\mathrm{incl}}$, is replaced by the frequency F of pp collisions:

$$s^I = \frac{F}{\sum_{k=1}^{N_{\mathrm{incl}}} w^k_{\mathrm{incl}}}\, \frac{P^I_{\mathrm{incl}} \sum_{k=1}^{N_{\mathrm{incl}}} w^k_{\mathrm{incl}}}{P^I_{\mathrm{incl}} \sum_{k=1}^{N_{\mathrm{incl}}} w^k_{\mathrm{incl}} + \sum_j P^I_j \sum_{k=1}^{N_j} w^k_j}. \tag{9}$$

The probabilities P^I_{incl} and P^I_j are given by Eqs. (6) and (7). Dividing both numerator and denominator on the right-hand side of Eq. (9) by P^I_{incl} and replacing the ratio $P^I_j/P^I_{\mathrm{incl}}$ by Eq. (8) yields:

$$s^I = \frac{F}{\sum_{k=1}^{N_{\mathrm{incl}}} w^k_{\mathrm{incl}} + \sum_j \frac{n_j}{(N_{\mathrm{PU}}+1)\,p_j} \sum_{k=1}^{N_j} w^k_j}. \tag{10}$$

Table 5 Number of events in the inclusive and exclusive samples used to estimate trigger rates at the HL-LHC

Sample	Number of events
Inclusive	8×10^5
$30 \leqslant \hat{p}_\mathrm{T} < 50$ GeV	4×10^5
$50 \leqslant \hat{p}_\mathrm{T} < 80$ GeV	2×10^5
$80 \leqslant \hat{p}_\mathrm{T} < 120$ GeV	1×10^5
$120 \leqslant \hat{p}_\mathrm{T} < 170$ GeV	5×10^4
$170 \leqslant \hat{p}_\mathrm{T} < 300$ GeV	5×10^4
$300 \leqslant \hat{p}_\mathrm{T} < 470$ GeV	5×10^4
$470 \leqslant \hat{p}_\mathrm{T} < 600$ GeV	5×10^4
$\hat{p}_\mathrm{T} \geqslant 600$ GeV	5×10^4

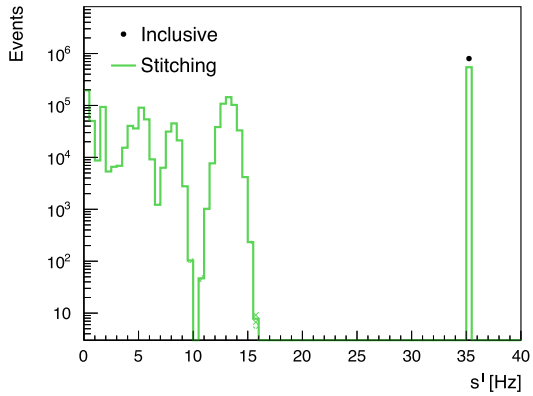


Fig. 4 Stitching weights s^I, computed according to Eq. (11), for the inclusive sample and for the samples produced in ranges of $\hat{p}_\mathrm{T}$

The sum over j refers to the exclusive samples. At the HL-LHC, the pp collision frequency F amounts to 28 MHz.[3] Eq. (10) represents the equivalent of Eq. (3), tailored to the case of estimating trigger rates instead of estimating event yields. The weights w^k_incl and w^k_j are equal to one for all events in this example, which allows to simplify Eq. (10). Using the relations $\sum_{k=1}^{N_\mathrm{incl}} w^k_\mathrm{incl} = N_\mathrm{incl}$ and $\sum_{k=1}^{N_j} w^k_j = N_j$, we obtain the expression:

$$s^I = \frac{F}{N_\mathrm{incl} + \sum_j \frac{n_j}{(N_\mathrm{PU}+1)\, p_j} N_j}. \tag{11}$$

The ranges in $\hat{p}_\mathrm{T}$ used to produce the exclusive samples and the number of events contained in each sample are given in Table 5. The association of the index i to the different ranges in $\hat{p}_\mathrm{T}$ and the corresponding values of the probabilities p_i are given in Table 6. The probabilities p_i are computed by taking the ratio of cross sections computed by the program PYTHIA for the case of single inelastic pp scattering interactions with a transverse momentum exchange that is within the ith interval in $\hat{p}_\mathrm{T}$ and for the case that no condition is imposed on $\hat{p}_\mathrm{T}$.

We cannot give numerical values of the stitching weights s^I for this example, as I is a high-dimensional vector, and also because the stitching weights vary depending on N_PU. Instead, we show in Fig. 4 the spectrum of the stitching weights that we obtain when inserting the numbers given in Tables 5 and 6 into Eq. (11). For comparison, we also show the corresponding weight, given by $s_\mathrm{incl} = F/N_\mathrm{incl}$, for the case that only the inclusive sample is used to estimate the trigger rate. The weight s_incl amounts to 35 Hz in this example. As can be seen in Fig. 4, the addition of samples produced in ranges of $\hat{p}_\mathrm{T}$ to the inclusive sample reduces the weights. Lower weights in turn reduce the statistical uncertainties on the trigger rate estimate. The different maxima in the distribution of stitching weights s^I correspond to events in which the transverse momentum exchanged between the scattered protons falls into different ranges in $\hat{p}_\mathrm{T}$. The spectrum of weights shown in Fig. 4 is plotted before any trigger selection is applied. As the probability for an event to pass the trigger increases with $\hat{p}_\mathrm{T}$, the stitching weights s^I are on average smaller for events that pass than for events that fail the trigger selection. Consequently, the reduction in statistical uncertainties that one obtains by using the exclusive samples and applying the stitching weights becomes even more pronounced after the trigger selection is applied (the weight s_incl remains fixed at 35 Hz).

The rates expected for a single jet trigger and for a dijet trigger at the HL-LHC are shown in Fig. 5. The rates are computed as function of the p_T threshold that is applied to the jets. In case of the dijet trigger, the same p_T threshold is applied to both jets. The jets are reconstructed as described in Sect. 3.1.1 and are required to be within the geometric acceptance $|\eta| < 5.0$. All stable generator-level particles

[3] The beams cross every 25 ns, but pp collisions occur only in $\approx 70\%$ of those beam crossings [24].

Table 6 Probabilities p_i for a single inelastic pp scattering interaction to feature a transverse momentum exchange between the protons that is within the ith interval in $\hat{p}_\mathrm{T}$

Range in $\hat{p}_\mathrm{T}$ [GeV]	< 30	30–50	50–80	80–120	120–170	170–300	300–470	470–600	> 600
Index i	0	1	2	3	4	5	6	7	8
Probability p_i	0.998	1.51×10^{-3}	2.25×10^{-4}	3.38×10^{-5}	6.00×10^{-6}	1.55×10^{-6}	1.05×10^{-7}	8.73×10^{-9}	3.12×10^{-9}

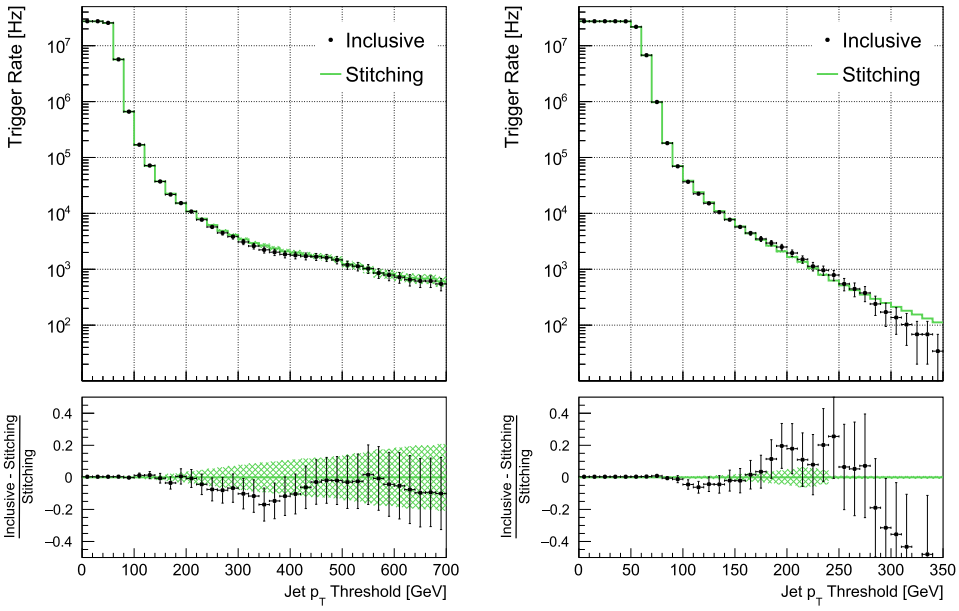


Fig. 5 Rate expected for **a** a single jet trigger and **b** a dijet trigger at the HL-LHC, as function of the p_{T} threshold that is applied to the jets

(except neutrinos) originating either from the HS interaction or from any of the PU interactions are used as input to the jet reconstruction. The statistical uncertainties on the rate estimates obtained from the inclusive sample are represented by error bars, while those obtained from the sum of inclusive plus exclusive samples are represented by the shaded area.

The rate estimate obtained for the inclusive sample and for the sum of inclusive plus exclusive samples, with the stitching weights computed according to Eq. (11), agree within statistical uncertainties, demonstrating that the estimate of the trigger rate obtained from the stitching procedure is unbiased. The modest difference between the rate estimates for the dijet trigger with jet p_{T} thresholds higher than 280 GeV is not statistically significant. It is important to keep in mind that the trigger rate estimates for adjacent bins are correlated, because all events that pass the trigger for a given jet p_{T} threshold also pass the trigger for all lower thresholds.

For both triggers and all jet p_{T} thresholds, the statistical uncertainties obtained with the stitching procedure are smaller than the uncertainties obtained in case only the inclusive sample is used. The reduction in the statistical uncertainties is significantly less pronounced for the single jet trigger than for the dijet trigger, however. For the latter, the stitching procedure reduces the statistical uncertainties in particular for jet p_{T} thresholds higher than 100 GeV. The reduction in the statistical uncertainties for the single jet trigger is limited by events with low $\hat{p}_{\mathrm{T}}$ that contain a single jet of high p_{T}. The stitching weights s^I for these low $\hat{p}_{\mathrm{T}}$ events are not much smaller than the weights for the inclusive sample. These low $\hat{p}_{\mathrm{T}}$ events also cause a "flattening" of the single jet trigger rate for jet p_{T} thresholds higher than 400 GeV. The requirement of a second high p_{T} jet removes most of these low $\hat{p}_{\mathrm{T}}$ events, with the effect that the dijet trigger rate decreases more rapidly as function of the jet p_{T} threshold and the stitching procedure becomes more effective in reducing the statistical uncertainties for the dijet trigger.

4 Summary

The production of MC samples containing a sufficient number of events to allow for a meaningful comparison with the data is often a challenge in modern HEP experiments, due to the computing resources required to produce and store such samples. This is particularly true for experiments at the CERN LHC, firstly because of the large cross sections of relevant processes (e.g. DY, W+jets, and $\mathrm{t\bar{t}}$+jets production) and secondly because of the large luminosity delivered by the LHC.

In this paper we have focused on the case that the MC samples have already been produced and we have presented a procedure that allows to reduce the statistical uncertainties by

Table 7 Probabilities P^i_{incl} and P^i_j for the events in the inclusive and exclusive W+jets samples to populate the different PS regions i. The definition of the PS regions i in the plane of N_{jet} versus H_{T} is shown in Fig. 2. A hyphen (–) indicates that PS regions i are not populated by a given sample j. The presence of a hyphen is equivalent to the probability P^i_j being zero

Sample	P^0	P^1	P^2	P^3	P^4	P^5	P^6	P^7	P^8	P^9	P^{10}	P^{11}	P^{12}	P^{13}	P^{14}
Inclusive	0.760	–	–	–	–	–	–	–	–	0.156	6.04×10^{-3}	2.51×10^{-3}	1.50×10^{-4}	4.48×10^{-6}	–
$N_{\text{jet}} = 1$	–	–	–	–	–	–	–	–	–	0.948	3.67×10^{-2}	1.52×10^{-2}	9.08×10^{-4}	2.72×10^{-5}	1.71×10^{-6}
$N_{\text{jet}} = 2$	–	–	–	–	–	–	–	–	–	–	–	–	–	–	–
$N_{\text{jet}} = 3$	–	–	–	–	–	–	–	–	–	–	–	–	–	–	–
$N_{\text{jet}} = 4$	–	–	–	–	–	–	–	–	–	–	–	–	–	–	–
$70 \leqslant H_{\text{T}} < 100$ GeV	–	–	–	–	–	–	–	–	–	–	0.261	–	–	–	–
$100 \leqslant H_{\text{T}} < 200$ GeV	–	–	–	–	–	–	–	–	–	–	–	0.109	–	–	–
$200 \leqslant H_{\text{T}} < 400$ GeV	–	–	–	–	–	–	–	–	–	–	–	–	2.43×10^{-2}	–	–
$400 \leqslant H_{\text{T}} < 600$ GeV	–	–	–	–	–	–	–	–	–	–	–	–	–	5.37×10^{-3}	–
$600 \leqslant H_{\text{T}} < 800$ GeV	–	–	–	–	–	–	–	–	–	–	–	–	–	–	1.37×10^{-3}
$800 \leqslant H_{\text{T}} < 1200$ GeV	–	–	–	–	–	–	–	–	–	–	–	–	–	–	–
$1200 \leqslant H_{\text{T}} < 2500$ GeV	–	–	–	–	–	–	–	–	–	–	–	–	–	–	–
$H_{\text{T}} \geqslant 2500$ GeV	–	–	–	–	–	–	–	–	–	–	–	–	–	–	–

Sample	P^{15}	P^{16}	P^{17}	P^{18}	P^{19}	P^{20}	P^{21}	P^{22}	P^{23}	P^{24}	P^{25}	P^{26}	P^{27}	P^{28}	P^{29}
Inclusive	9.20×10^{-8}	–	–	2.84×10^{-2}	1.29×10^{-2}	9.68×10^{-3}	1.23×10^{-3}	7.58×10^{-5}	1.22×10^{-5}	3.49×10^{-6}	6.61×10^{-7}	–	1.36×10^{-3}	4.07×10^{-3}	7.61×10^{-3}
$N_{\text{jet}} = 1$	5.40×10^{-7}	–	–	–	–	–	–	–	–	–	–	–	–	–	–
$N_{\text{jet}} = 2$	–	–	–	0.543	0.247	0.185	2.36×10^{-2}	1.45×10^{-3}	2.33×10^{-4}	6.68×10^{-5}	1.26×10^{-5}	–	–	–	–
$N_{\text{jet}} = 3$	–	–	–	–	–	–	–	–	–	–	–	–	8.93×10^{-2}	0.267	0.499
$N_{\text{jet}} = 4$	–	–	–	–	–	–	–	–	–	–	–	–	–	–	–

Table 7 continued

Sample	P^{15}	P^{16}	P^{17}	P^{18}	P^{19}	P^{20}	P^{21}	P^{22}	P^{23}	P^{24}	P^{25}	P^{26}	P^{27}	P^{28}	P^{29}
$70 \leqslant H_T < 100$ GeV	–	–	–	–	0.557	–	–	–	–	–	–	–	–	0.176	–
$100 \leqslant H_T < 200$ GeV	–	–	–	–	–	0.422	–	–	–	–	–	–	–	–	0.331
$200 \leqslant H_T < 400$ GeV	–	–	–	–	–	–	0.200	–	–	–	–	–	–	–	–
$400 \leqslant H_T < 600$ GeV	–	–	–	–	–	–	–	9.09×10^{-2}	–	–	–	–	–	–	–
$600 \leqslant H_T < 800$ GeV	–	–	–	–	–	–	–	–	5.94×10^{-2}	–	–	–	–	–	–
$800 \leqslant H_T < 1200$ GeV	1.06×10^{-4}	–	–	–	–	–	–	–	–	4.02×10^{-2}	–	–	–	–	–
$1200 \leqslant H_T < 2500$ GeV	–	3.07×10^{-4}	–	–	–	–	–	–	–	–	2.69×10^{-2}	–	–	–	–
$H_T \geqslant 2500$ GeV	–	–	–	–	–	–	–	–	–	–	–	2.15×10^{-2}	–	–	–

Sample	P^{30}	P^{31}	P^{32}	P^{33}	P^{34}	P^{35}	P^{36}	P^{37}	P^{38}	P^{39}	P^{40}	P^{41}	P^{42}	P^{43}	P^{44}
Inclusive	1.94×10^{-3}	1.70×10^{-4}	3.06×10^{-5}	1.00×10^{-5}	1.99×10^{-6}	–	1.39×10^{-5}	3.01×10^{-4}	3.25×10^{-3}	2.83×10^{-3}	5.76×10^{-4}	1.61×10^{-4}	7.27×10^{-5}	2.17×10^{-5}	–
$N_{jet} = 1$	–	–	–	–	–	–	–	–	–	–	–	–	–	–	–
$N_{jet} = 2$	–	–	–	–	–	–	–	–	–	–	–	–	–	–	–
$N_{jet} = 3$	0.127	1.12×10^{-2}	2.00×10^{-3}	6.57×10^{-4}	1.30×10^{-4}	–	–	–	–	–	–	–	–	–	–
$N_{jet} = 4$	–	–	–	–	–	–	1.93×10^{-3}	4.17×10^{-2}	0.452	0.394	8.00×10^{-2}	2.23×10^{-2}	1.01×10^{-2}	3.02×10^{-3}	1.09×10^{-4}
$70 \leqslant H_T < 100$ GeV	–	–	–	–	–	–	–	1.30×10^{-2}	–	–	–	–	–	–	–
$100 \leqslant H_T < 200$ GeV	–	–	–	–	–	–	–	–	0.142	–	–	–	–	–	–
$200 \leqslant H_T < 400$ GeV	0.315	–	–	–	–	–	–	–	–	0.460	–	–	–	–	–
$400 \leqslant H_T < 600$ GeV	–	0.204	–	–	–	–	–	–	–	–	0.691	–	–	–	–
$600 \leqslant H_T < 800$ GeV	–	–	0.149	–	–	–	–	–	–	–	–	0.783	–	–	–
$800 \leqslant H_T < 1200$ GeV	–	–	–	0.116	–	–	–	–	–	–	–	–	0.838	–	–
$1200 \leqslant H_T < 2500$ GeV	–	–	–	–	8.09×10^{-2}	–	–	–	–	–	–	–	–	0.884	–
$H_T \geqslant 2500$ GeV	–	–	–	–	–	4.77×10^{-2}	–	–	–	–	–	–	–	–	0.926

Table 8 Stitching weights s^i for the case that the inclusive and exclusive W+jets samples given in Tables 1 and 4 are stitched based on the observables N_{jet} and H_{T}. The weights are computed for an integrated luminosity of 140 fb^{-1}. Events with $N_{\text{jet}} = 0$ all have $H_{\text{T}} < 70$ GeV, and, similarly, events with $N_{\text{jet}} = 1$ all have $H_{\text{T}} < 2500$ GeV. Hence, the stitching weights cannot be computed for the eight PS regions with $N_{\text{jet}} = 0$ and $H_{\text{T}} \geqslant 70$ GeV and for the single PS region with $N_{\text{jet}} = 1$ and $H_{\text{T}} \geqslant 2500$ GeV. These stitching weights are not needed, since there are no events in these regions. The corresponding PS regions are indicated by a hyphen (–) in the table

	$N_{\text{jet}} = 0$	$N_{\text{jet}} = 1$	$N_{\text{jet}} = 2$	$N_{\text{jet}} = 3$	$N_{\text{jet}} = 4$
$H_{\text{T}} < 70$ GeV	2870	1420	718	359	176
$70 \leqslant H_{\text{T}} < 100$ GeV	–	714	478	287	157
$100 \leqslant H_{\text{T}} < 200$ GeV	–	472	357	238	141
$200 \leqslant H_{\text{T}} < 400$ GeV	–	283	237	178	118
$400 \leqslant H_{\text{T}} < 600$ GeV	–	158	144	120	89.6
$600 \leqslant H_{\text{T}} < 800$ GeV	–	83.8	78.6	71.0	60.0
$800 \leqslant H_{\text{T}} < 1200$ GeV	–	36.0	35.1	33.7	31.2
$1200 \leqslant H_{\text{T}} < 2500$ GeV	–	16.3	15.9	15.4	15.3
$H_{\text{T}} \geqslant 2500$ GeV	–	–	11.2	11.2	10.9

combining MC samples which overlap in PS. The procedure is based on applying suitably chosen weights to the simulated events. We refer to the procedure as "stitching".

The formalism for computing the stitching weights is general enough to be applied to a variety of use-cases. When used in physics analyses, the stitching procedure allows to reduce the statistical uncertainties in particular in the tails of distributions. Examples that document the typical use of the stitching procedure in physics analyses performed by the CMS experiment during LHC Runs 1 and 2 have been presented. The formalism has been extended to the case of estimating trigger rates at the HL-LHC. Up to 200 simultaneous pp collisions are expected per crossing of the proton beams at the HL-LHC. The distinguishing feature of this application of the stitching procedure is that the same physics process, inelastic pp scattering interactions in which a transverse momentum $\hat{p}_{\text{T}}$ is exchanged between the protons, may occur in the "hard-scatter" (HS) interaction and in "pileup" (PU) interactions. Our formalism for computing the stitching weight treats the HS and PU interactions on equal footing.

The examples demonstrate that the stitching procedure provides unbiased estimates of event yields and rates as well as of the shapes of distributions. The reduction in the statistical uncertainties achieved by the stitching method depends on the number of events contained in the MC samples that are subject to the stitching procedure and ranges from moderate to significant.

Acknowledgements This work was supported by the Estonian Research Council Grant PRG445.

Data Availability Statement This manuscript has no associated data or the data will not be deposited. [Authors' comment: There is no data to be submitted with this publication, because all the results of the paper are based on Monte Carlo simulation.]

Open Access This article is licensed under a Creative Commons Attribution 4.0 International License, which permits use, sharing, adaptation, distribution and reproduction in any medium or format, as long as you give appropriate credit to the original author(s) and the source, provide a link to the Creative Commons licence, and indicate if changes were made. The images or other third party material in this article are included in the article's Creative Commons licence, unless indicated otherwise in a credit line to the material. If material is not included in the article's Creative Commons licence and your intended use is not permitted by statutory regulation or exceeds the permitted use, you will need to obtain permission directly from the copyright holder. To view a copy of this licence, visit http://creativecommons.org/licenses/by/4.0/.
Funded by SCOAP^3.

Appendix

In this section, we detail the application of the least-squares method [43] to the computation of the probabilities P^i_{incl} and P^i_j in the example given in Sect. 3.1.2. The aim is to make the computation of these probabilities less prone to statistical fluctuations in the MC samples.

Our use of the least-squares method is based on assuming the following relation to hold:

$$\sigma_{\text{incl}}\, P^i_{\text{incl}} = \sigma_j\, P^i_j \quad \forall\, j, \tag{12}$$

except for statistical fluctuations on the P^i_{incl} and P^i_j. The P^i_{incl} and P^i_j are obtained by determining the fraction of events in the inclusive and exclusive MC samples that fall into PS region i. The symbol j in Eq. (12) refers to those N_{jet}- and H_{T}-samples that cover the PS region i. The symbol σ_j refers to the fiducial cross section corresponding to the sample j. We denote the unknown true value of the left-hand side (and equivalently of the right-hand side) of Eq. (12) by the symbol λ_i and use the symbols r^i_{incl} and r^i_j to refer to the

deviations ("residuals"), caused by statistical fluctuations, between the true values of the probabilities P^i_{incl} and P^i_j and the values obtained using the MC samples. We further use the symbols e^i_{incl} and e^i_j to denote the expected statistical fluctuations ("errors") of these probabilities. According to the least-squares method, the best estimate for the value of λ_i is given by the solution to the following system of equations:

$$\sigma_{\text{incl}} \left(P^i_{\text{incl}} + r^i_{\text{incl}} \right) - \lambda_i = 0 \quad \text{and}$$
$$\sigma_j \left(P^i_j + r^i_j \right) - \lambda_i = 0 \quad \forall\, j,$$

subject to the condition that the sum of residuals:

$$\left(\frac{r^i_{\text{incl}}}{e^i_{\text{incl}}} \right)^2 + \sum_j \left(\frac{r^i_j}{e^i_j} \right)^2$$

attains its minimal value. The expected statistical fluctuations e^i_{incl} and e^i_j of the probabilities P^i_{incl} and P^i_j are given by the standard errors of the Binomial distribution [43]:

$$e^i_{\text{incl}} = \sqrt{\frac{P^i_{\text{incl}} \left(1 - P^i_{\text{incl}}\right)}{N_{\text{incl}}}} \quad \text{and} \quad e^i_j = \sqrt{\frac{P^i_j \left(1 - P^i_j\right)}{N_j}}.$$

The fluctuations decrease proportional to the inverse of the square-root of the number of events in the MC samples. The solution for λ_i is given by the expression:

$$\lambda_i = \frac{\alpha^i_{\text{incl}}\, \sigma_{\text{incl}}\, P^i_{\text{incl}} + \sum_j \alpha^i_j\, \sigma_j\, P^i_j}{\alpha^i_{\text{incl}} + \sum_j \alpha^i_j}, \tag{13}$$

from which the probabilities $P^i_{\text{incl}} = \lambda_i / \sigma_{\text{incl}}$ and $P^i_j = \lambda_i / \sigma_j$ follow. The symbols α^i_{incl} and α^i_j are defined as:

$$\alpha^i_{\text{incl}} = \frac{1}{\left(\sigma_{\text{incl}}\, e^i_{\text{incl}}\right)^2} \quad \text{and} \quad \alpha^i_j = \frac{1}{\left(\sigma_j\, e^i_j\right)^2}$$

and act as "weights" in the expression on the right-hand side of Eq. (13), which has the form of a weighted average. We use the symbols α^i_{incl} and α^i_j to refer to these weights, in order to distinguish them from the weights w^k_{incl} and w^k_j computed by the MC generator program and from the stitching weights s^i.

References

1. W.L. Dunn, J.K. Shultis, *Exploring Monte Carlo methods* (Elsevier Science, Amsterdam, 2011)
2. D.P. Kroese, T. Brereton, T. Taimre, Z. Botev, Why the Monte Carlo method is so important today. Wiley Interdiscip. Rev. Comput. Stat. **6**, 386 (2014)
3. S. Amoroso et al., Challenges in Monte Carlo event generator software for High-Luminosity LHC. Comput. Softw. Big Sci. **5**(1), 12 (2021). https://doi.org/10.1007/s41781-021-00055-1
4. LHC Design Report Vol. 1: The LHC main ring (2004). https://doi.org/10.5170/CERN-2004-003-V-1
5. LHC Design Report Vol. 2: The LHC infrastructure and general services (2004). https://doi.org/10.5170/CERN-2004-003-V-2
6. LHC Design Report Vol. 3: The LHC injector chain (2004). https://doi.org/10.5170/CERN-2004-003-V-3
7. ATLAS Collaboration, Measurement of the inelastic proton-proton cross section at $\sqrt{s} = 13$ TeV with the ATLAS Detector at the LHC. Phys. Rev. Lett. **117**(18), 182,002 (2016). https://doi.org/10.1103/PhysRevLett.117.182002
8. CMS Collaboration, Measurement of the inelastic proton-proton cross section at $\sqrt{s} = 13$ TeV. JHEP **07**, 161 (2018). https://doi.org/10.1007/JHEP07(2018)161
9. ATLAS Collaboration, Luminosity determination in pp collisions at $\sqrt{s} = 13$ TeV using the ATLAS detector at the LHC. ATLAS CONF Note (ATLAS-CONF-2019-021). https://cds.cern.ch/record/2677054
10. CMS Collaboration, CMS luminosity measurements for the 2016 data-taking period. CMS Physics Analysis Summary (CMS-PAS-LUM-17-001). http://cds.cern.ch/record/2257069
11. CMS Collaboration, CMS luminosity measurement for the 2017 data-taking period at $\sqrt{s} = 13$TeV. CMS Physics Analysis Summary (CMS-PAS-LUM-17-004). http://cds.cern.ch/record/2621960
12. CMS Collaboration, CMS luminosity measurement for the 2018 data-taking period at $\sqrt{s} = 13$TeV. CMS Physics Analysis Summary (CMS-PAS-LUM-18-002). http://cds.cern.ch/record/2676164
13. M. Czakon, A. Mitov, Top++: a program for the calculation of the top-pair cross section at hadron colliders. Comput. Phys. Commun. **185**, 2930 (2014). https://doi.org/10.1016/j.cpc.2014.06.021
14. Y. Li, F. Petriello, Combining QCD and electroweak corrections to dilepton production in FEWZ. Phys. Rev. D **86**, 094,034 (2012). https://doi.org/10.1103/PhysRevD.86.094034
15. K. Melnikov, F. Petriello, Electroweak gauge boson production at hadron colliders through $O(\alpha_s^2)$. Phys. Rev. D **74**, 114,017 (2006). https://doi.org/10.1103/PhysRevD.74.114017
16. S. Alioli, P. Nason, C. Oleari, E. Re, A general framework for implementing NLO calculations in shower Monte Carlo programs: the Powheg box. JHEP **06**, 043 (2010). https://doi.org/10.1007/JHEP06(2010)043
17. S. Frixione, P. Nason, C. Oleari, Matching NLO QCD computations with parton shower simulations: the Powheg method. JHEP **11**, 070 (2007). https://doi.org/10.1088/1126-6708/2007/11/070
18. P. Nason, A new method for combining NLO QCD with shower Monte Carlo algorithms. JHEP **11**, 040 (2004). https://doi.org/10.1088/1126-6708/2004/11/040
19. J. Alwall, R. Frederix, S. Frixione, V. Hirschi, F. Maltoni, O. Mattelaer, H.S. Shao, T. Stelzer, P. Torrielli, M. Zaro, The automated computation of tree-level and next-to-leading order differential cross sections, and their matching to parton shower simulations. JHEP **07**, 079 (2014). https://doi.org/10.1007/JHEP07(2014)079
20. T. Gleisberg, S. Höche, F. Krauss, M. Schönherr, S. Schumann, F. Siegert, J. Winter, Event generation with SHERPA 1.1. JHEP **02**, 007 (2009). https://doi.org/10.1088/1126-6708/2009/02/007
21. T. Sjöstrand, S. Ask, J.R. Christiansen, R. Corke, N. Desai, P. Ilten, S. Mrenna, S. Prestel, C.O. Rasmussen, P.Z. Skands, An introduction to PYTHIA 8.2. Comput. Phys. Commun. **191**, 159 (2015). https://doi.org/10.1016/j.cpc.2015.01.024
22. M. Bahr et al., Herwig++ physics and manual. Eur. Phys. J. C **58**, 639 (2008). https://doi.org/10.1140/epjc/s10052-008-0798-9

23. ATLAS Collaboration, Modelling and computational improvements to the simulation of single vector-boson plus jet processes for the ATLAS experiment (2021) arXiv:2112.09588 [hep-ex]
24. G. Apollinari, I. Béjar Alonso, O. Brüning, P. Fessia, M. Lamont, L. Rossi, L. Tavian, High-Luminosity Large Hadron Collider (HL-LHC). CERN Yellow Rep. Monogr. **4**, 1 (2017). https://doi.org/10.23731/CYRM-2017-004
25. CMS Collaboration, The Phase-2 upgrade of the CMS data acquisition and high-level trigger. Technical Design Report **(in preparation)**
26. M. Baak, J. Cúth, J. Haller, A. Hoecker, R. Kogler, K. Mönig, M. Schott, J. Stelzer, The global electroweak fit at NNLO and prospects for the LHC and ILC. Eur. Phys. J. C **74**, 3046 (2014). https://doi.org/10.1140/epjc/s10052-014-3046-5
27. ATLAS Collaboration, Precision measurement and interpretation of inclusive W^+, W^- and Z/γ^* production cross sections with the ATLAS detector. Eur. Phys. J. C **77**(6), 367 (2017). https://doi.org/10.1140/epjc/s10052-017-4911-9
28. ATLAS Collaboration, Measurement of the cross section and charge asymmetry of W bosons produced in pp collisions at $\sqrt{s} = 8$ TeV with the ATLAS detector. Eur. Phys. J. C **79**(9), 760 (2019). https://doi.org/10.1140/epjc/s10052-019-7199-0
29. CMS Collaboration, Measurement of the differential cross section and charge asymmetry for inclusive $pp \to W^{\pm} + X$ production at $\sqrt{s} = 8$ TeV. Eur. Phys. J. C **76**(8), 469 (2016). https://doi.org/10.1140/epjc/s10052-016-4293-4
30. CMS Collaboration, Measurements of the W boson rapidity, helicity, double-differential cross sections, and charge asymmetry in pp collisions at $\sqrt{s} = 13$ TeV. Phys. Rev. D **102**(9), 092,012 (2020). https://doi.org/10.1103/PhysRevD.102.092012
31. ATLAS Collaboration, Measurement of the production of a W boson in association with a charm quark in pp collisions at $\sqrt{s} = 7$ TeV with the ATLAS detector. JHEP **05**, 068 (2014). https://doi.org/10.1007/JHEP05(2014)068
32. CMS Collaboration, Measurement of associated W + charm production in pp collisions at $\sqrt{s} = 7$ TeV. JHEP **02**, 013 (2014). https://doi.org/10.1007/JHEP02(2014)013
33. CMS Collaboration, Measurement of associated production of a W boson and a charm quark in proton-proton collisions at $\sqrt{s} = 13$ TeV. Eur. Phys. J. C **79**(3), 269 (2019). https://doi.org/10.1140/epjc/s10052-019-6752-1
34. ATLAS Collaboration, Observation and measurement of Higgs boson decays to WW* with the ATLAS detector. Phys. Rev. D **92**(1), 012,006 (2015). https://doi.org/10.1103/PhysRevD.92.012006
35. ATLAS Collaboration, Search for non-resonant Higgs boson pair production in the bb$l\nu l\nu$ final state with the ATLAS detector in pp collisions at $\sqrt{s} = 13$ TeV. Phys. Lett. B **801**, 135,145 (2020). https://doi.org/10.1016/j.physletb.2019.135145
36. CMS Collaboration, Search for the Standard Model Higgs boson in the H $\to$ WW $\to$ $l\nu$jj decay channel in pp collisions at the LHC. CMS Physics Analysis Summary (CMS-PAS-HIG-13-027). http://cds.cern.ch/record/1743804
37. CMS Collaboration, Search for resonant and non-resonant Higgs boson pair production in the $b\bar{b}l\nu l\nu$ final state in proton-proton collisions at $\sqrt{s} = 13$ TeV. JHEP **01**, 054 (2018). https://doi.org/10.1007/JHEP01(2018)054
38. R.D. Ball et al., Parton distributions from high-precision collider data. Eur. Phys. J. C **77**, 663 (2017). https://doi.org/10.1140/epjc/s10052-017-5199-5
39. CMS Collaboration, Extraction and validation of a new set of CMS Pythia 8 tunes from underlying-event measurements. Eur. Phys. J. C **80**(1), 4 (2020). https://doi.org/10.1140/epjc/s10052-019-7499-4
40. J. Alwall et al., Comparative study of various algorithms for the merging of parton showers and matrix elements in hadronic collisions. Eur. Phys. J. C **53**, 473 (2008). https://doi.org/10.1140/epjc/s10052-007-0490-5
41. M. Cacciari, G.P. Salam, G. Soyez, The anti-k_t jet clustering algorithm. JHEP **04**, 063 (2008). https://doi.org/10.1088/1126-6708/2008/04/063
42. M. Cacciari, G.P. Salam, G. Soyez, FastJet user manual. Eur. Phys. J. C **72**, 1896 (2012). https://doi.org/10.1140/epjc/s10052-012-1896-2
43. G. Cowan, *Statistical data analysis* (Oxford University Press, Oxford, 1998)
44. M. Evans, N. Hastings, B. Peacock, C. Forbes, *Statistical distributions* (Wiley, New York, 2011)

Appendix 4

IV

K. Ehatäht and C. Veelken, “Application of the matrix element method to Higgs boson pair production in the channel $\mathrm{HH} \to \mathrm{b\bar{b}WW}^{*}$ at the LHC”, *Nucl. Instrum. Meth. A*, vol. 1028, p. 166 373, 2022. doi: 10.1016/j.nima.2022.166373. arXiv: 2108.05267 [hep-ph]

Nuclear Inst. and Methods in Physics Research, A 1028 (2022) 166373

Contents lists available at ScienceDirect

Nuclear Inst. and Methods in Physics Research, A

journal homepage: www.elsevier.com/locate/nima

Application of the matrix element method to Higgs boson pair production in the channel HH → bb̄WW* at the LHC

Karl Ehatäht, Christian Veelken *

National Institute for Chemical Physics and Biophysics, 10143 Tallinn, Estonia

ARTICLE INFO

Keywords:
Matrix element method
Higgs boson
Higgs boson pair production
LHC

ABSTRACT

We apply the matrix element method (MEM) to the search for non-resonant Higgs boson pair (HH) production in the channel HH → bb̄WW* at the LHC and study the separation between the HH signal and the large irreducible background, which arises from the production of top quark pairs (tt̄). Our study focuses on events containing two leptons (electrons or muons) in the final state. The separation between signal and background is studied for experimental conditions characteristic for the ATLAS and CMS experiments during LHC Run 2, using the DELPHES fast-simulation package. We find that the tt̄ background can be reduced to a level of 0.26% for a signal efficiency of 35%.

1. Introduction

The discovery of a Higgs (H) boson by the ATLAS and CMS experiments [1,2] represents a major step towards our understanding of electroweak symmetry breaking (EWSB), as well as of the mechanism that generates the masses of quarks and leptons, the particles that constitute the " ordinary" matter in our universe. In a combined analysis of the data recorded by ATLAS and CMS during LHC Run 1, the mass of the H boson has been measured to be 125.09±0.24 GeV [3]. Recent analyses of data collected during LHC Run 2 corroborate this value [4,5]. The Standard Model (SM) of particle physics makes precise predictions for all properties of the H boson, given its mass. The predictions have been probed by measurements of its spin and CP quantum numbers [6–9], of its couplings to gauge bosons and to down-type fermions [10], and of its total decay width, including decays to invisible particles [11–14]. So far, all measured properties of the discovered particle are consistent with the expectation for a SM H boson within the uncertainties of these measurements. Evidence for its coupling to up-type fermions, at a strength compatible with the SM expectation, has been observed recently [15,16].

The SM predicts H boson self-interactions via trilinear and quartic couplings. Measurements of the H boson self-interactions will allow to determine the potential of the Higgs field, thereby ultimately either confirming or falsifying that the Brout–Englert–Higgs mechanism of the SM is responsible for EWSB. The measurement of the quartic coupling is not possible at the LHC [17], even with the 3000 fb^{-1} of data foreseen to be recorded at $\sqrt{s}$ = 14 TeV center-of-mass energy during the upcoming HL-LHC data-taking period [18], as the cross section of the corresponding process, triple H boson production, is much too small, on the level of $5 \cdot 10^{-2}$ fb [19,20].

The trilinear coupling (λ) can be determined at the LHC, by measuring the rate for H boson pair production (HH). In analogy to the production of single H bosons, four different processes are relevant for HH production at the LHC: gluon fusion (ggHH), vector boson fusion (qqHH), the associated production with a W or Z boson (VHH), and associated production of the H boson pair with a pair of top quarks (tt̄HH). The total HH production rate is dominated by the ggHH process. Its cross section has been computed at next-to-next-to-leading order (NNLO) in perturbative quantum chromodynamics (pQCD), with resummation of soft gluon contributions at next-to-next-to-leading logarithmic accuracy. Including corrections for finite top quark mass effects, computed at next-to-leading order (NLO), the SM cross section for the ggHH process amounts to $31.05^{+1.40}_{-1.98}$ fb at $\sqrt{s}$ = 13 TeV center-of-mass energy [21]. The cross section is rather small, as the production of H boson pairs through gluon fusion is a loop induced process, and is further reduced by the negative interference of two competing production mechanisms. The leading order (LO) Feynman diagrams for the two competing production mechanisms are shown in Fig. 1. The right diagram, referred to as the "box" diagram, does actually not depend on the trilinear H boson self-coupling λ. The diagram that provides the sensitivity to λ is the "triangle" diagram shown on the left. Both diagrams depend on the coupling of the H boson to the top quark, denoted by the symbol y_t, which is measured with an uncertainty of order 10% at present [15,16]. The cross sections for the qqHH, VHH, and tt̄HH process are more than one order of magnitude smaller [22]. As the sensitivity of experimental analyses at the LHC is limited by the small signal rate at present, we will focus on the ggHH production process in this paper.

* Corresponding author.
E-mail addresses: karl.ehataht@cern.ch (K. Ehatäht), christian.veelken@cern.ch (C. Veelken).

https://doi.org/10.1016/j.nima.2022.166373
Received 17 August 2021; Received in revised form 22 December 2021; Accepted 15 January 2022
Available online 22 January 2022
0168-9002/© 2022 Elsevier B.V. All rights reserved.

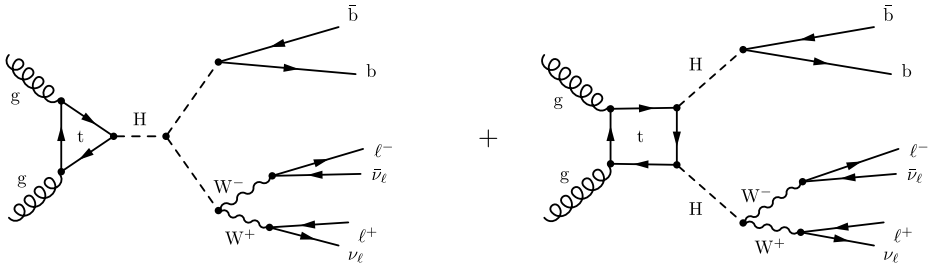


Fig. 1. Leading order (LO) Feynman diagrams for the ggHH production process in pp collisions at the LHC, with subsequent decay of the H boson pair via HH → $b\bar{b}WW^*$ → $b\bar{b}\ell^+\nu\ell^-\bar{\nu}$. The asterisk (*) denotes an off-shell W boson.

The HH production rate may be enhanced significantly in case an as yet unknown resonance decays to pairs of H bosons. Such resonances are predicted in models with two Higgs doublets [23,24], composite H boson models [25,26], Higgs portal models [27,28], and models involving extra dimensions [29]. In the absence of new resonances decaying into H boson pairs, the HH production rate may be enhanced by deviations of the couplings λ and y_t from the SM expectation for these couplings and by the contribution of new particles to the loops that are present in the triangle and box diagrams shown in Fig. 1. The effect of contributions from new particles to these loops can adequately be described by anomalous H boson couplings in an effective field theory (EFT) approach [30,31]. The production of H boson pairs in the absence of new resonances is referred to as non-resonant HH production, the case that we focus on in this paper.

The ATLAS and CMS collaborations have searched for non-resonant HH production in the decay channels HH → $b\bar{b}b\bar{b}$, $b\bar{b}\tau\tau$, $b\bar{b}WW^*$, $b\bar{b}\gamma\gamma$ using the data recorded during LHC Runs 1 and 2 [32–41]. ATLAS has further performed searches in the decay channels HH → $\gamma\gamma WW^*$ and WW^*WW^* [37,42,43]. The asterisk (*) denotes W bosons that are off-shell. Phenomenological studies of non-resonant HH production are presented in Refs. [22,44–54]. No evidence for a signal has been found in the LHC data so far. The present analyses are able to probe the existence of a SM-like HH signal produced with a cross section of order 10 times the SM production rate.

The decay channel providing the highest sensitivity for an SM-like HH signal is the $b\bar{b}\tau\tau$ channel in case of ATLAS [40] and the $b\bar{b}\gamma\gamma$ channel in case of CMS [36]. Both channels provide a favorable signal-to-background ratio and are limited mainly by statistical uncertainties at present, resulting from the limited amount of data that has been recorded so far, compared to the small SM ggHH production cross section. The channels $b\bar{b}b\bar{b}$ and $b\bar{b}WW^*$ provide a significantly larger signal rate, but suffer from sizeable backgrounds, arising from QCD multijet production in case of the $b\bar{b}b\bar{b}$ channel and from top quark pair ($t\bar{t}$) production in case of the $b\bar{b}WW^*$ channel. In this paper, we focus on the $b\bar{b}WW^*$ channel, and in particular on events in which both W bosons decay to leptons (electrons or muons). The latter are denoted by the symbol ℓ.

The separation of the HH signal from the large $t\bar{t}$ background constitutes the main experimental challenge in the $b\bar{b}WW^*$ channel. For a top quark mass of m_t = 172.8 GeV [55], the cross section for $t\bar{t}$ production amounts to $825.9^{+46.1}_{-50.5}$ pb at $\sqrt{s}$ = 13 TeV center-of-mass energy [56]. The $t\bar{t}$ background is irreducible in this channel, as it produces the exact same multiplicity of charged leptons, neutrinos, and b-jets as the HH signal. The LO Feynman diagrams for $t\bar{t}$ production are shown in Fig. 2. The main handle to separate the HH signal from the $t\bar{t}$ background is the difference in event kinematics, that is, the differences in the distributions of the energies and angles of the charged leptons, of the b-jets, and of the missing transverse momentum reconstructed in the event.

The present CMS analysis [34] utilizes machine-learning methods, based on a Deep Neural Network [57,58], to separate the HH signal from the $t\bar{t}$ background, while the current ATLAS analysis [41] employs a sequence of hard cuts for this purpose. In this paper, we propose an alternative multivariate method for the separation of the HH signal from the $t\bar{t}$ background, the matrix element method (MEM) [59,60].

The paper is structured as follows: In Section 2 we describe the MEM and its application to the $b\bar{b}WW^*$ channel. The application of the MEM requires the computation of multi-dimensional integrals. The evaluation of the integrals is performed numerically and demands a significant amount of computing time, in the order of a few seconds per event. In order to make the integrals suitable for numeric integration, analytic transformations need to be performed. The most relevant of these transformations will be described in Section 2 and further details will be given in the appendix. The performance of the MEM in separating the HH signal from the $t\bar{t}$ background is studied in Section 3. The performance is studied on Monte-Carlo truth and on detector level, for experimental conditions that are characteristic for the ATLAS and CMS experiments during LHC Run 2. The latter are simulated using the DELPHES fast-simulation framework [61]. Section 3 also presents a study of the effect of using matrix elements of leading order when applying the MEM to the $b\bar{b}WW^*$ channel and discusses the computing-time requirements of the MEM. We conclude the paper with a summary in Section 4.

2. The matrix element method

The MEM computes probability densities (PDs) $w_i(\boldsymbol{p})$ for obtaining the measured observables $\boldsymbol{p}$, assuming that the event has been produced by the process i. The PDs $w_i(\boldsymbol{p})$ are interpreted as quantifying the compatibility of the measured observables $\boldsymbol{p}$ with the signal (i = 0) and background (i = 1) hypothesis. In the analysis of HH production in the decay channel HH → $b\bar{b}WW^*$ → $b\bar{b}\ell^+\nu\ell^-\bar{\nu}$ the observables $\boldsymbol{p}$ refer to the measured momenta of the two b-jets, of the two charged leptons, and of the measured missing transverse momentum ($\boldsymbol{p}_T^{\text{miss}}$) in the event. The vector $\boldsymbol{p}_T^{\text{miss}}$ represents the measured value of the vectorial sum of the two neutrino momenta in the plane transverse to the beam axis. We use symbols with a hat to denote the true values of energies and momenta. Bold letters denote vector quantities. The vector $\hat{\boldsymbol{p}}$ denotes the true values of the b-jet and charged lepton momenta and the true values of the momenta of the two neutrinos produced in the W boson decays.

As already mentioned, HH → $b\bar{b}WW^*$ → $b\bar{b}\ell^+\nu\ell^-\bar{\nu}$ signal events contain the same number of b-jets, charged leptons, and neutrinos as the dominant background, arising from $t\bar{t}$ → $bW\bar{b}W$ → $b\ell^+\nu\,\bar{b}\ell^-\bar{\nu}$. The separation of the HH signal from the irreducible $t\bar{t}$ background is based on the difference in event kinematics, causing the PD $w_0(\boldsymbol{p})$ to be in general higher when evaluated on signal events and lower when evaluated on background events, and vice versa for the PD $w_1(\boldsymbol{p})$. Given the PDs $w_0(\boldsymbol{p})$ and $w_1(\boldsymbol{p})$ for the signal and background hypotheses, the Neyman–Pearson lemma [62] postulates that the likelihood ratio (LR):

$$P(\boldsymbol{p}) = \frac{w_0(\boldsymbol{p})}{w_0(\boldsymbol{p}) + w_1(\boldsymbol{p})} \tag{1}$$

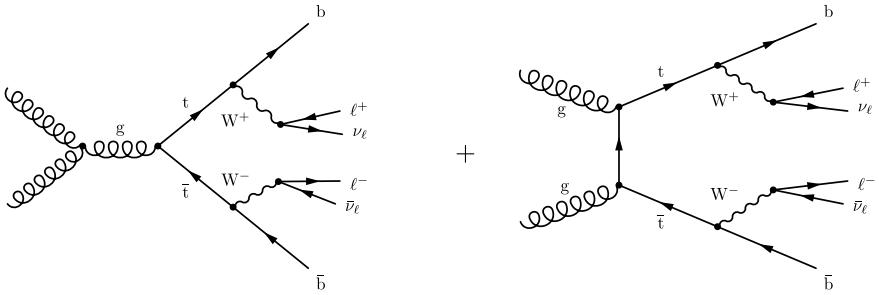


Fig. 2. LO Feynman diagrams for $t\bar{t}$ production in pp collisions at the LHC, with subsequent decay of the top quark pair via $t\bar{t} \to bW\bar{b}W \to b\ell^+\nu\,\bar{b}\ell^-\bar{\nu}$.

provides the optimal separation of the HH signal from the irreducible $t\bar{t}$ background.

Different nomenclatures and conventions for the MEM exist in the literature. In this note, we follow the nomenclature and conventions introduced in Ref. [63]. The PDs $w_i(\boldsymbol{p})$ are given by the integral:

$$w_i(\boldsymbol{p}) = \frac{\Omega(\boldsymbol{p})}{\sigma_i \cdot \mathcal{A}_i} \int d\hat{x}_a\, d\hat{x}_b\, d\boldsymbol{\Phi}_n\, \frac{f(\hat{x}_a, Q)\, f(\hat{x}_b, Q)}{2\,\hat{x}_a\,\hat{x}_b\,s}\, (2\pi)^4\, \delta \times \left(\hat{x}_a\,\hat{E}_a + \hat{x}_b\,\hat{E}_b - \sum_k^n \hat{E}_{(k)}\right) \cdot\, \delta^3\left(\hat{x}_a\,\hat{\boldsymbol{p}}^a + \hat{x}_b\,\hat{\boldsymbol{p}}^b - \sum_k^n \hat{\boldsymbol{p}}^{(k)}\right) |\mathcal{M}_i(\hat{\boldsymbol{p}})|^2\, W(\boldsymbol{p}|\hat{\boldsymbol{p}})\, \epsilon_i(\hat{\boldsymbol{p}})\,. \tag{2}$$

The symbol $|\mathcal{M}_i(\hat{\boldsymbol{p}})|^2$ denotes the squared modulus of the matrix element (ME), averaged over helicity states, for either the signal ($i = 0$) or for the background ($i = 1$) hypothesis. We use ME generated at LO accuracy with the program MadGraph_aMCatNLO 2.3.3 [64] for the signal as well as for the background hypothesis. The ME for the signal hypothesis is generated using the infinite top quark mass approximation [65]. In this approximation, the top quark degrees of freedom are integrated out, replacing the top quark loops in the triangle and box diagrams shown in Fig. 1 by point-like effective couplings of, respectively, two gluons to one H boson and two gluons to two H bosons. The point-like effective couplings are specified via a Universal FeynRules Output (UFO) model file [66,67] given to MadGraph_aMCatNLO. The usage of the infinite top quark mass approximation is necessary, because at present the program MadGraph_aMCatNLO does not support the generation of ME code for processes involving loops.

The symbols $\hat{E}_a$ and $\hat{E}_b$ ($\hat{\boldsymbol{p}}^a$ and $\hat{\boldsymbol{p}}^b$) denote the energies (momenta) of the two colliding protons, $\sqrt{s}$ their center-of-mass energy, $\hat{x}_a$ and $\hat{x}_b$ the Bjorken scaling variables [68], and $f(\hat{x}_a, Q)$ and $f(\hat{x}_b, Q)$ the corresponding parton distribution functions (PDFs) [69]. Besides their dependence on the Bjorken scaling variables, the PDFs depend on a scale parameter Q. We use the MSTW 2008 LO PDF set [70] to evaluate $f(\hat{x}_a, Q)$ and $f(\hat{x}_b, Q)$ and set the scale Q to half the mass of the HH system and to twice the value of the top quark mass when computing the PD $w_0(\boldsymbol{p})$ and $w_1(\boldsymbol{p})$ for the signal and background hypothesis, respectively. We denote by n the number of particles in the final state, and by $\boldsymbol{p}^{(k)}$ ($\hat{\boldsymbol{p}}^{(k)}$) the measured (true) momentum of the kth final state particle. The δ-functions $\delta(\hat{x}_a\,\hat{E}_a + \hat{x}_b\,\hat{E}_b - \sum_k^n \hat{E}_{(k)})$ and $\delta^3(\hat{x}_a\,\hat{\boldsymbol{p}}^a + \hat{x}_b\,\hat{\boldsymbol{p}}^b - \sum_k^n \hat{\boldsymbol{p}}^{(k)})$ impose conservation of energy and momentum.

The functions $W(\boldsymbol{p}|\hat{\boldsymbol{p}})$ are referred to as "transfer functions" (TF) in the literature. They represent the PD to observe the measured values $\boldsymbol{p}$, given the true values $\hat{\boldsymbol{p}}$. The function $\Omega(\boldsymbol{p})$ is referred to as "indicator function" in the literature [63,71]. It attains the value 1 in case the event represented by the measured observables $\boldsymbol{p}$ passes the event selection criteria and otherwise attains the value 0. The efficiency for an event originating at the phase-space (PS) point $\hat{\boldsymbol{p}}$ to pass the event selection, i.e. to end up with measured observables $\boldsymbol{p}$ for which $\Omega(\boldsymbol{p}) = 1$, is denoted by $\epsilon_i(\hat{\boldsymbol{p}})$. Finally, the symbol $\mathcal{A}_i$ denotes the acceptance of the event selection, that is, the percentage of events which pass the event selection criteria, while σ_i denotes the cross section of process i. The subscript i of the symbols σ_i, $\mathcal{A}_i$, and ϵ_i emphasize that the cross section, acceptance, and efficiency differ between the signal and the background hypothesis. Division of the right-hand-side (RHS) of Eq. (2) by the product $\sigma_i \cdot \mathcal{A}_i$ ensures that $w_i(\boldsymbol{p})$ has the correct normalization required for a probability density, i.e. $\int d\boldsymbol{p}\, w_i(\boldsymbol{p}) = 1$, provided that the TF satisfy the normalization condition $\int d\boldsymbol{p}\, \Omega(\boldsymbol{p})\, W(\boldsymbol{p}|\hat{\boldsymbol{p}}) = 1$ for every $\hat{\boldsymbol{p}}$.

The symbol $d\boldsymbol{\Phi}_n = \prod_k^n \frac{d^3\hat{\boldsymbol{p}}^{(k)}}{(2\pi)^3\, 2\hat{E}_{(k)}}$ represents the differential n-particle PS element. For the HH signal as well as for the $t\bar{t}$ background hypothesis, $n = 6$. We express the PS element $d\boldsymbol{\Phi}_6$ in terms of the energies $\hat{E}_{(k)}$, the polar angles $\hat{\theta}_{(k)}$, and the azimuthal angles $\hat{\phi}_{(k)}$ of the two b quarks, of the two charged leptons, and of the two neutrinos:

$$\begin{aligned} d\boldsymbol{\Phi}_6 &= \prod_k^6 \frac{d^3\hat{\boldsymbol{p}}^{(k)}}{(2\pi)^3\, 2\,\hat{E}_{(k)}} = \frac{1}{2^{24}\,\pi^{18}} \prod_k^6 \frac{d^3\hat{\boldsymbol{p}}^{(k)}}{\hat{E}_{(k)}} \\ &= \frac{1}{2^{24}\,\pi^{18}} \prod_k^6 \frac{d\hat{E}_{(k)}\, d\hat{\theta}_{(k)}\, d\hat{\phi}_{(k)}\, |\hat{\boldsymbol{p}}^{(k)}|\, \hat{E}_{(k)}\, \sin\hat{\theta}_{(k)}}{\hat{E}_{(k)}} \\ &= \frac{1}{2^{24}\,\pi^{18}} \prod_k^6 d\hat{E}_{(k)}\, d\hat{\theta}_{(k)}\, d\hat{\phi}_{(k)}\, \hat{\beta}_{(k)}\, \hat{E}_{(k)}\, \sin\hat{\theta}_{(k)}\,. \end{aligned} \tag{3}$$

All energies $\hat{E}_{(k)}$ as well as the angles $\hat{\theta}_{(k)}$ and $\hat{\phi}_{(k)}$ refer to the laboratory (detector) frame. The velocity $\hat{\beta}_{(k)}$ of particle k, given by $\hat{\beta}_{(k)} \equiv \frac{|\hat{\boldsymbol{p}}^{(k)}|}{\hat{E}_{(k)}}$, has been used to simplify the expression for $d\boldsymbol{\Phi}_6$ in the last step. Note that the velocity $\hat{\beta}_{(k)}$ is a function of energy $\hat{E}_{(k)}$ and hence cannot be treated as constant when evaluating the integral over $d\hat{E}_{(k)}$. Similarly, the magnitude of the momentum $|\hat{\boldsymbol{p}}^{(k)}|$ is a function of the energy $\hat{E}_{(k)}$. In the following, we use the identities $|\hat{\boldsymbol{p}}^{(k)}| = \sqrt{\hat{E}_{(k)}^2 - m_{(k)}^2}$ and $\hat{\beta}_{(k)} = \frac{\sqrt{\hat{E}_{(k)}^2 - m_{(k)}^2}}{\hat{E}_{(k)}}$ to make the dependency on the energy $\hat{E}_{(k)}$ explicit.

The form of Eq. (3) is useful, as it allows to trivially perform the integration over the angles $\hat{\theta}_{(k)}$ and $\hat{\phi}_{(k)}$ for the two b quarks and for the two charged leptons, taking advantage of the fact that the directions of quarks (jets) and charged leptons can be measured with negligible experimental resolution. With the further assumption that also the energy of charged leptons can be measured with negligible experimental resolution, the integration over $d\hat{E}_{\ell^+}$ and $d\hat{E}_{\ell^-}$ can be carried out trivially too. We shall only consider events that pass the event selection criteria, i.e. for which the indicator function $\Omega(\boldsymbol{p})$ is equal to 1. For simplicity, we neglect the effect of the efficiency $\epsilon_i(\hat{\boldsymbol{p}})$ and of the acceptance $\mathcal{A}_i$. With these assumptions and upon inserting the expressions for the TF given by Eqs. (18), (19), and (20) in the

appendix into Eq. (3), we obtain:

$$w_i(\boldsymbol{p}) = \frac{1}{2^{21}\,\pi^{14}\,\sigma_i\,E_{\ell^+}\,E_{\ell^-}\,E_{\mathrm{b}}\,E_{\bar{\mathrm{b}}}} \int d\hat{x}_a\,d\hat{x}_b\,d\hat{E}_{\bar{\mathrm{b}}}\,\frac{d^3\hat{\boldsymbol{p}}_\nu}{\hat{E}_\nu}\,\frac{d^3\hat{\boldsymbol{p}}_{\bar{\nu}}}{\hat{E}_{\bar{\nu}}}\,\frac{f(\hat{x}_a,Q)\,f(\hat{x}_b,Q)}{\hat{x}_a\,\hat{x}_b\,s}$$
$$\cdot\,\delta\left(\hat{x}_a\,\hat{E}_a + \hat{x}_b\,\hat{E}_b - \sum_k^6 \hat{E}_{(k)}\right)\delta^3\left(\hat{x}_a\,\hat{\boldsymbol{p}}^a + \hat{x}_b\,\hat{\boldsymbol{p}}^b - \sum_k^6 \hat{\boldsymbol{p}}^{(k)}\right)$$
$$\cdot\,|\mathcal{M}_i(\hat{\boldsymbol{p}})|^2\,\frac{\hat{\beta}_{\mathrm{b}}\,\hat{E}_{\mathrm{b}}}{\beta_{\mathrm{b}}\,E_{\mathrm{b}}}\,W(E_{\mathrm{b}}|\hat{E}_{\mathrm{b}})\,\frac{\hat{\beta}_{\bar{\mathrm{b}}}\,\hat{E}_{\bar{\mathrm{b}}}}{\beta_{\bar{\mathrm{b}}}\,E_{\bar{\mathrm{b}}}}\,W(E_{\bar{\mathrm{b}}}|\hat{E}_{\bar{\mathrm{b}}})\,. \tag{4}$$

The terms $\frac{\hat{\beta}_{\mathrm{b}}\,\hat{E}_{\mathrm{b}}}{\beta_{\mathrm{b}}\,E_{\mathrm{b}}}$ and $\frac{\hat{\beta}_{\bar{\mathrm{b}}}\,\hat{E}_{\bar{\mathrm{b}}}}{\beta_{\bar{\mathrm{b}}}\,E_{\bar{\mathrm{b}}}}$ arise because the integration over the PS elements $d^3\hat{\boldsymbol{p}}$ of the b and $\bar{\mathrm{b}}$ quarks yields a factor $\hat{\beta}\,\hat{E}^2\,\sin\hat{\theta}$, while the normalization of the TF yields a factor $\frac{1}{\beta\,E^2\,\sin\theta}$, cf. Eq. (20). The terms $\sin\hat{\theta}$ and $\frac{1}{\sin\theta}$ cancel, due to the presence of the δ-function $\delta(\theta-\hat{\theta})$ in the integrand, cf. Eq. (19). No similar terms arise for the charged leptons, as the TF for charged leptons demand $\hat{\beta}=\beta$, $\hat{E}=E$, and $\hat{\theta}=\theta$, cf. Eq. (18).

We simplify the four-dimensional δ-function $\delta(\hat{x}_a\,\hat{E}_a+\hat{x}_b\,\hat{E}_b-\sum_k^6\hat{E}_{(k)})\cdot\delta^3(\hat{x}_a\,\hat{\boldsymbol{p}}^a+\hat{x}_b\,\hat{\boldsymbol{p}}^b-\sum_k^6\hat{\boldsymbol{p}}^{(k)})$ by assuming the momentum vectors of the colliding protons to be aligned in direction parallel and anti-parallel to the beam axis and neglecting the small transverse momenta of the partons within the protons as well as parton masses. With this assumption, we can eliminate the energy and longitudinal momentum components of the δ-function and solve for the Bjorken scaling variables $\hat{x}_a$ and $\hat{x}_b$ as function of the energies and longitudinal momenta of the particles in the final state. This yields:

$$\hat{x}_a = \frac{1}{\sqrt{s}}\sum_k^6\left(\hat{E}_{(k)} + \hat{p}_{\mathrm{z}}^{(k)}\right) \quad \text{and} \quad \hat{x}_b = \frac{1}{\sqrt{s}}\sum_k^6\left(\hat{E}_{(k)} - \hat{p}_{\mathrm{z}}^{(k)}\right). \tag{5}$$

For the purpose of eliminating the transverse momentum components of the four-dimensional δ-function, we follow the approach of Ref. [72]. The approach is based on introducing the "hadronic recoil", denoted by the symbol ρ, as a means to account for QCD radiation, which causes additional jets to be produced besides the two b-jets that originate from the decay of the H boson (in signal events) or from the decay of the two top quarks (in background events). As detailed in Ref. [73], significant amounts of QCD radiation, in particular initial-state radiation (ISR), are a typical feature of most signal and background processes at the LHC. The longitudinal momentum of the additional jets produced by QCD radiation alters the relations for $\hat{x}_a$ and $\hat{x}_b$ somewhat, compared to the values given by Eq. (5). We expect the effect of QCD radiation on the energy and longitudinal momentum components to be small and thus neglect it. The effect on the transverse momentum balance is important, however, as QCD radiation distorts the kinematic relations that would be expected to hold in the absence of such radiation. As a consequence, the δ-functions that ensure the conservation of momentum in the transverse plane need to be modified. Their modified form reads: $\delta(\hat{p}_{\mathrm{x}}^{\rho}+\sum_k^6\hat{p}_{\mathrm{x}}^{(k)})$ and $\delta(\hat{p}_{\mathrm{y}}^{\rho}+\sum_k^6\hat{p}_{\mathrm{y}}^{(k)})$, where $\hat{p}_{\mathrm{x}}^{\rho}$ and $\hat{p}_{\mathrm{y}}^{\rho}$ denote the true value of the momentum of the hadronic recoil ρ in x and y direction, respectively. They imply the relations:

$$\begin{aligned}\hat{p}_{\mathrm{x}}^{\rho} &= -\left(\hat{p}_{\mathrm{x}}^{\mathrm{b}} + \hat{p}_{\mathrm{x}}^{\bar{\mathrm{b}}} + \hat{p}_{\mathrm{x}}^{\ell^+} + \hat{p}_{\mathrm{x}}^{\nu} + \hat{p}_{\mathrm{x}}^{\ell^-} + \hat{p}_{\mathrm{x}}^{\bar{\nu}}\right) \text{ and} \\ \hat{p}_{\mathrm{y}}^{\rho} &= -\left(\hat{p}_{\mathrm{y}}^{\mathrm{b}} + \hat{p}_{\mathrm{y}}^{\bar{\mathrm{b}}} + \hat{p}_{\mathrm{y}}^{\ell^+} + \hat{p}_{\mathrm{y}}^{\nu} + \hat{p}_{\mathrm{y}}^{\ell^-} + \hat{p}_{\mathrm{y}}^{\bar{\nu}}\right).\end{aligned} \tag{6}$$

The corresponding relations for the measured momenta read:

$$\begin{aligned}p_{\mathrm{x}}{}^{\rho} &= -\left(p_{\mathrm{x}}{}^{\mathrm{b}} + p_{\mathrm{x}}{}^{\bar{\mathrm{b}}} + p_{\mathrm{x}}{}^{\ell^+} + p_{\mathrm{x}}{}^{\ell^-} + p_{\mathrm{x}}^{\mathrm{miss}}\right) \text{ and} \\ p_{\mathrm{y}}{}^{\rho} &= -\left(p_{\mathrm{y}}{}^{\mathrm{b}} + p_{\mathrm{y}}{}^{\bar{\mathrm{b}}} + p_{\mathrm{y}}{}^{\ell^+} + p_{\mathrm{y}}{}^{\ell^-} + p_{\mathrm{y}}^{\mathrm{miss}}\right).\end{aligned} \tag{7}$$

We use Eq. (7) to compute the measured values of $p_{\mathrm{x}}{}^{\rho}$ and $p_{\mathrm{y}}{}^{\rho}$, given the measured momenta of the two b-jets, of the two charged leptons, and of the measured $\boldsymbol{p}_{\mathrm{T}}^{\mathrm{miss}}$. The experimental resolution on $p_{\mathrm{x}}{}^{\rho}$ and $p_{\mathrm{y}}{}^{\rho}$ is accounted for by introducing a TF for the hadronic recoil into the integrand of Eq. (4). We assume that the resolution on the transverse momentum components of ρ follows a two-dimensional normal distribution:

$$W_\rho(p_{\mathrm{x}}{}^{\rho}, p_{\mathrm{y}}{}^{\rho}|\hat{p}_{\mathrm{x}}^{\rho}, \hat{p}_{\mathrm{y}}^{\rho}) = \frac{1}{2\pi\sqrt{|V|}}\exp\left(-\frac{1}{2}\begin{pmatrix} p_{\mathrm{x}}{}^{\rho}-\hat{p}_{\mathrm{x}}^{\rho} \\ p_{\mathrm{y}}{}^{\rho}-\hat{p}_{\mathrm{y}}^{\rho}\end{pmatrix}^T\cdot V^{-1}\cdot\begin{pmatrix} p_{\mathrm{x}}{}^{\rho}-\hat{p}_{\mathrm{x}}^{\rho} \\ p_{\mathrm{y}}{}^{\rho}-\hat{p}_{\mathrm{y}}^{\rho}\end{pmatrix}\right), \tag{8}$$

where the matrix V quantifies the resolution on the hadronic recoil in the transverse plane.

The CMS collaboration computes the matrix V on an event-by-event basis, using an algorithm referred to as the "$p_{\mathrm{T}}^{\mathrm{miss}}$-significance" algorithm [74]. Alternatively, one could determine an average resolution σ_ρ for a sample of HH signal and $\mathrm{t\bar{t}}$ background events using the Monte Carlo simulation and take the matrix V to be $V=\sigma_\rho^2\cdot I_2$, where I_2 denotes the identity matrix of size 2. We follow the procedure detailed in Ref. [72] and replace the δ-functions $\delta(\hat{p}_{\mathrm{x}}^{\rho}+\sum_k^6\hat{p}_{\mathrm{x}}^{(k)})$ and $\delta(\hat{p}_{\mathrm{y}}^{\rho}+\sum_k^6\hat{p}_{\mathrm{y}}^{(k)})$, which ensure the momentum conservation in the transverse plane, with the TF for the hadronic recoil, given by Eq. (8).

A remaining issue is that we use LO ME $\mathcal{M}_i(\hat{\boldsymbol{p}})$ for the HH signal and for the $\mathrm{t\bar{t}}$ background in Eq. (4). The LO ME for the signal (background) requires that the HH ($\mathrm{t\bar{t}}$) system has zero p_{T}, a condition that only holds in case the hadronic recoil has zero p_{T}. As previously discussed, the case that the hadronic recoil has negligible p_{T} is rare at the LHC, due to the abundance of QCD radiation. The issue that the LO ME is only well-defined for events with zero ISR is resolved by evaluating the ME $\mathcal{M}_i(\hat{\boldsymbol{p}})$ in a frame in which the HH ($\mathrm{t\bar{t}}$) system has zero p_{T}, to which we refer as the zero-transverse-momentum (ZTM) frame. The Lorentz transformation of the energy $\hat{E}_{(k)}$ and momenta $\hat{\boldsymbol{p}}^{(k)}$ in Eq. (4) from the laboratory to the ZTM frame is performed using the vector $\left(-\frac{\hat{p}_{\mathrm{x}}^{\rho}}{\hat{p}_{\mathrm{T}}^{\rho}}, -\frac{\hat{p}_{\mathrm{y}}^{\rho}}{\hat{p}_{\mathrm{T}}^{\rho}}, 0\right)$ as the boost vector. The values of $\hat{p}_{\mathrm{x}}^{\rho}$, $\hat{p}_{\mathrm{y}}^{\rho}$, and $\hat{p}_{\mathrm{T}}^{\rho}$ are computed using Eq. (6). The momentum components $\hat{p}_{\mathrm{x}}^{\ell^+}$, $\hat{p}_{\mathrm{x}}^{\ell^-}$, $\hat{p}_{\mathrm{y}}^{\ell^+}$, and $\hat{p}_{\mathrm{y}}^{\ell^-}$ are set to their measured values, while the components $\hat{p}_{\mathrm{x}}^{\mathrm{b}}$, $\hat{p}_{\mathrm{x}}^{\bar{\mathrm{b}}}$, $\hat{p}_{\mathrm{x}}^{\nu}$, $\hat{p}_{\mathrm{x}}^{\bar{\nu}}$, $\hat{p}_{\mathrm{y}}^{\mathrm{b}}$, $\hat{p}_{\mathrm{y}}^{\bar{\mathrm{b}}}$, $\hat{p}_{\mathrm{y}}^{\nu}$, and $\hat{p}_{\mathrm{y}}^{\bar{\nu}}$ are recomputed as function of the integration variables $\hat{E}_{\mathrm{b}}$, $\hat{E}_{\bar{\mathrm{b}}}$, $\hat{\boldsymbol{p}}_\nu$, and $\hat{\boldsymbol{p}}_{\bar{\nu}}$ when evaluating Eq. (6).

Eliminating the energy and longitudinal momentum components of the four-dimensional δ-function $\delta(\hat{x}_a\,\hat{E}_a+\hat{x}_b\,\hat{E}_b-\sum_k^6\hat{E}_{(k)})\cdot\delta(\hat{x}_a\,\hat{p}_{\mathrm{z}}^{a}+\hat{x}_b\,\hat{p}_{\mathrm{z}}^{b}-\sum_k^6\hat{p}_{\mathrm{z}}^{(k)})\cdot\delta(\hat{p}_{\mathrm{x}}^{\rho}+\sum_k^6\hat{p}_{\mathrm{x}}^{(k)})\cdot\delta(\hat{p}_{\mathrm{y}}^{\rho}+\sum_k^6\hat{p}_{\mathrm{y}}^{(k)})$ by means of Eq. (5) and replacing its transverse momentum components by the TF $W_\rho(p_{\mathrm{x}}{}^{\rho}, p_{\mathrm{y}}{}^{\rho}|\hat{p}_{\mathrm{x}}^{\rho}, \hat{p}_{\mathrm{y}}^{\rho})$ for the hadronic recoil ρ, the expression for the PD $w_i(\boldsymbol{p})$ in Eq. (4) becomes:

$$w_i(\boldsymbol{p}) = \frac{1}{2^{21}\,\pi^{14}\,\sigma_i\,E_{\ell^+}\,E_{\ell^-}\,E_{\mathrm{b}}\,E_{\bar{\mathrm{b}}}} \int d\hat{E}_{\mathrm{b}}\,d\hat{E}_{\bar{\mathrm{b}}}\,d\hat{E}_\nu\,d\hat{\theta}_\nu\,d\hat{\phi}_\nu\,d\hat{E}_{\bar{\nu}}\,d\hat{\theta}_{\bar{\nu}}\,d\hat{\phi}_{\bar{\nu}}$$
$$\cdot\,\hat{\beta}_\nu\,\hat{E}_\nu\,\sin\hat{\theta}_\nu\,\hat{\beta}_{\bar{\nu}}\,\hat{E}_{\bar{\nu}}\,\sin\hat{\theta}_{\bar{\nu}}\,\frac{f(\hat{x}_a,Q)\,f(\hat{x}_b,Q)}{\hat{x}_a\,\hat{x}_b\,s}$$
$$\cdot\,|\mathcal{M}_i(\hat{\boldsymbol{p}})|^2\,\frac{\hat{\beta}_{\mathrm{b}}\,\hat{E}_{\mathrm{b}}}{\beta_{\mathrm{b}}\,E_{\mathrm{b}}}\,W(E_{\mathrm{b}}|\hat{E}_{\mathrm{b}})\,\frac{\hat{\beta}_{\bar{\mathrm{b}}}\,\hat{E}_{\bar{\mathrm{b}}}}{\beta_{\bar{\mathrm{b}}}\,E_{\bar{\mathrm{b}}}}\,W(E_{\bar{\mathrm{b}}}|\hat{E}_{\bar{\mathrm{b}}})\,W_\rho(p_{\mathrm{x}}{}^{\rho}, p_{\mathrm{y}}{}^{\rho}|\hat{p}_{\mathrm{x}}^{\rho}, \hat{p}_{\mathrm{y}}^{\rho}). \tag{9}$$

The expression in Eq. (9) concludes our discussion of analytic transformations of the expressions for the PD $w_i(\boldsymbol{p})$ that are common to the signal as well as to the background hypothesis.

A few more analytic transformations need to be performed to handle the presence of Breit–Wigner (BW) propagators in the ME $\mathcal{M}_i(\hat{\boldsymbol{p}})$, as the presence of these propagators represent an obstacle for the numeric integration of Eq. (9). The effect of the BW propagators is that only narrow slices in the 6-particle PS yield sizeable contributions to the integral, namely the regions where the 6 final state particles satisfy certain mass constraints. The mass constraints arise from the presence of on-shell H bosons, W bosons, and top quarks in the decay chains $\mathrm{HH}\to\mathrm{b\bar{b}WW^*}\to\mathrm{b\bar{b}}\,\ell^+\nu\ell^-\bar{\nu}$ and $\mathrm{t\bar{t}}\to\mathrm{bW\bar{b}W}\to\mathrm{b}\ell^+\nu\,\bar{\mathrm{b}}\ell^-\bar{\nu}$. Their presence renders the numeric integration inefficient, unless the mass constraints are treated analytically. We use the narrow-width approximation (NWA) [75] to handle the mass constraints and replace the BW propagators by δ-functions. The NWA has the effect of restricting the numerical integration to the narrow slices in the 6-particle PS where the mass constraints are satisfied and the ME $\mathcal{M}_i(\hat{\boldsymbol{p}})$ yields a sizeable contribution to the integral. The analytic transformations

that are needed to handle the BW propagators differ for the signal and for the background hypothesis, reflecting the presence of different resonances in the respective decay chains. The transformations that are specific to the signal hypothesis are detailed in Section 2.1, while those specific to the background hypothesis are presented in Section 2.2.

Finally, the numeric integration is performed using the VAMP algorithm [76], a variant of the popular VEGAS algorithm [77], which has been optimized for the case of integrating multimodal functions that typically appear in the integration of ME over regions in PS. We use 2500 evaluations of the integrand when computing the PD $w_0(\boldsymbol{p})$ for the signal hypothesis and 25000 evaluations of the integrand for the computation of the PD $w_1(\boldsymbol{p})$ for the background hypothesis. The number of evaluations has been chosen such that the computation of $w_0(\boldsymbol{p})$ and $w_1(\boldsymbol{p})$ take approximately the same time and the computation of the likelihood ratio $P(\boldsymbol{p})$ takes about one minute per event, using a single core of a 2.30 GHz Intel® Xeon® E5-2695V3 processor.

2.1. Analytic transformations specific to the signal hypothesis

When evaluating the integrand in Eq. (9) for the signal hypothesis, only those points in the 6-particle PS provide a sizeable contribution to the value of the integral $w_0(\boldsymbol{p})$ which satisfy the following conditions:

- The mass of the 2-particle system comprised of the two b quarks equals $m_{\mathrm{H}} = 125.1$ GeV [3].
- The mass of the 2-particle system comprised of the charged lepton and of the neutrino, which originate from the decay of the on-shell W boson, equals $m_{\mathrm{W}} = 80.4$ GeV [55].
- The mass of the 4-particle system comprised of the two charged leptons and of the two neutrinos equals m_{H}.

We formally introduce these mass constraints by inserting three δ-functions $\delta(g(x))$ into the integrand of Eq. (9). The procedure is explained in Section A.2 of the appendix. More specifically, we insert one δ-function of the type $g(\hat{E}_{\bar{\mathrm{b}}})$ given by Eq. (23), one of the type $g(\hat{E}_{\nu})$ given by Eq. (26), and one of the type $g(\hat{E}_{\nu^*})$ given by Eq. (29) into the integrand of Eq. (9). We denote the charged lepton and the neutrino originating from the decay of the off-shell W boson, which can be either the W^+ or the W^-, by an asterisk. The charged lepton and the neutrino that are referred to without asterisks are subject to the W mass constraint.

After solving for the δ-functions analytically, as detailed in Sections A.2.1, A.2.2, and A.2.3 of the appendix, the resulting expression for the PD $w_0(\boldsymbol{p})$ of the signal hypothesis reads:

$$
\begin{aligned}
w_0(\boldsymbol{p}) = & \frac{(m_{\mathrm{H}}\,\Gamma_{\mathrm{H}})^2\, m_{\mathrm{W}}\,\Gamma_{\mathrm{W}}}{2^{23}\,\pi^{14}\,\sigma_0\,s\,E_{\ell}^2\,E_{\ell^*}\,\beta_{\mathrm{b}}\,E_{\mathrm{b}}^2\,\beta_{\bar{\mathrm{b}}}\,E_{\bar{\mathrm{b}}}^2} \int d\hat{E}_{\mathrm{b}}\,d\hat{\theta}_{\nu}\,d\hat{\phi}_{\nu}\,d\hat{\theta}_{\nu^*}\,d\hat{\phi}_{\nu^*} \\
& \cdot\, \hat{p}_{\mathrm{T}}^{\nu}\,\hat{p}_{\mathrm{T}}^{\nu^*}\,\frac{f(\hat{x}_a,Q)\,f(\hat{x}_b,Q)}{\hat{x}_a\,\hat{x}_b} \\
& \cdot\, |\mathcal{M}_0(\hat{\boldsymbol{p}})|^2\,\hat{\beta}_{\mathrm{b}}\,W(E_{\mathrm{b}}|\hat{E}_{\mathrm{b}})\,\hat{\beta}_{\bar{\mathrm{b}}}\,\hat{E}_{\bar{\mathrm{b}}}\,W(E_{\bar{\mathrm{b}}}|\hat{E}_{\bar{\mathrm{b}}})\,W_{\rho}(p_{\mathrm{x}}{}^{\rho},p_{\mathrm{y}}{}^{\rho}|\hat{p}_{\mathrm{x}}^{\rho},\hat{p}_{\mathrm{y}}^{\rho}) \\
& \cdot\, \left[\left|1-\frac{\hat{\beta}_{\mathrm{b}}}{\hat{\beta}_{\bar{\mathrm{b}}}}\,\cos\sphericalangle(\boldsymbol{e}_{\mathrm{b}},\boldsymbol{e}_{\bar{\mathrm{b}}})\right|\right. \\
& \left.\cdot\, \sin^2\left(\frac{\sphericalangle(\boldsymbol{e}_{\ell},\hat{\boldsymbol{e}}_{\nu})}{2}\right)\,\hat{E}_{\ell\nu\ell^*}\left(1-\hat{\beta}_{\ell\nu\ell^*}\,\cos\sphericalangle(\hat{\boldsymbol{e}}_{\ell\nu\ell^*},\hat{\boldsymbol{e}}_{\nu^*})\right)\right]^{-1},
\end{aligned}
\tag{10}
$$

with:

$$
\begin{aligned}
\hat{E}_{\bar{\mathrm{b}}} &= \frac{a\,\Delta_{m_{\mathrm{H}}} + |b|\,\sqrt{\Delta_{m_{\mathrm{H}}}^2 - (a^2-b^2)\,m_{\mathrm{b}}^2}}{a^2-b^2} \\
\hat{E}_{\nu} &= \frac{m_{\mathrm{W}}^2}{4\,\hat{E}_{\ell}\,\sin^2\left(\frac{\sphericalangle(\boldsymbol{e}_{\ell},\hat{\boldsymbol{e}}_{\nu})}{2}\right)} \\
\hat{E}_{\nu^*} &= \frac{m_{\mathrm{H}}^2 - m_{\ell\nu\ell^*}^2}{2\,\hat{E}_{\ell\nu\ell^*}\,\left(1-\hat{\beta}_{\ell\nu\ell^*}\,\cos\sphericalangle(\hat{\boldsymbol{e}}_{\ell\nu\ell^*},\hat{\boldsymbol{e}}_{\nu^*})\right)},
\end{aligned}
\tag{11}
$$

where:

$$
\begin{aligned}
\Delta_{m_{\mathrm{H}}} &= \frac{m_{\mathrm{H}}^2}{2} - m_{\mathrm{b}}^2 \\
a &= \hat{E}_{\mathrm{b}} \\
b &= \hat{\beta}_{\mathrm{b}}\,\hat{E}_{\mathrm{b}}\,\cos\sphericalangle(\boldsymbol{e}_{\mathrm{b}},\boldsymbol{e}_{\bar{\mathrm{b}}}).
\end{aligned}
\tag{12}
$$

The integral on the RHS of Eq. (10) is ready to be evaluated by numeric integration. The integral extends over the 5 variables $\hat{E}_{\mathrm{b}}$, $\hat{\theta}_{\nu}$, $\hat{\phi}_{\nu}$, $\hat{\theta}_{\nu^*}$, and $\hat{\phi}_{\nu^*}$. The symbol $\boldsymbol{e}_k$ refers to a unit vector in direction of particle k, and the symbol $\sphericalangle(\hat{\boldsymbol{e}}_k,\hat{\boldsymbol{e}}_{k'})$ denotes the angle between the directions of particles k and k'. This notation includes the case that the "particles" k and k' are systems of multiple particles, e.g. $\hat{\boldsymbol{e}}_{\ell\nu\ell^*}$ denotes the direction of the momentum vector of the 3-particle system composed of the charged lepton and the neutrino produced in the decay of the on-shell W boson and of the charged lepton produced in the decay of the off-shell W boson. The hat in the symbol $\hat{\boldsymbol{e}}_{\ell\nu\ell^*}$ indicates that this direction refers to the true momenta of the neutrinos, which are computed as function of the integration variables $\hat{\theta}_{\nu}$, $\hat{\phi}_{\nu}$, $\hat{\theta}_{\nu^*}$, $\hat{\phi}_{\nu^*}$ and Eq. (11). For the charged leptons and the b-jets, the true direction is equal to the measured direction, as the direction of charged leptons and jets is measured with negligible experimental resolution.

There is one further aspect, which needs to be taken into account when computing the compatibility of a given event with the signal hypothesis, and that is that there exists a fourfold ambiguity in associating the two measured b-jets to the b and $\bar{\mathrm{b}}$ quarks and in associating the two measured charged leptons to the on-shell and off-shell W bosons. We deal with the fourfold ambiguity by evaluating the integral $w_0(\boldsymbol{p})$ given by Eq. (10) four times, once for each of the four possible associations of measured b-jets to the b and $\bar{\mathrm{b}}$ quarks and of the measured charged leptons to the on-shell and off-shell W bosons, and using the average of these four values when evaluating the LR in Eq. (1).

2.2. Analytic transformations specific to the background hypothesis

In $\mathrm{t\bar{t}} \to \mathrm{bW\bar{b}W} \to \mathrm{b}\ell^+\nu\,\bar{\mathrm{b}}\ell^-\bar{\nu}$ background events, both W bosons are on-shell. Sizeable contributions to the value of the integral $w_1(\boldsymbol{p})$ are obtained only for those points $\hat{\boldsymbol{p}}$ in the 6-particle PS for which:

- The masses of the $\ell^+\nu$ as well as of the $\ell^-\bar{\nu}$ system are equal to $m_{\mathrm{W}} = 80.4$ GeV [55].
- The masses of the $\mathrm{b}\ell^+\nu$ and $\bar{\mathrm{b}}\ell^-\bar{\nu}$ systems are equal to the top quark mass of $m_{\mathrm{t}} = 172.8$ GeV [55].

We account for these mass constraints by inserting four δ-functions $\delta(g(x))$ into the integrand of Eq. (9): two δ-functions of the type $g(\hat{E}_{\nu})$, given by Eq. (26), and two δ-functions of the type $g(\hat{E}_{\mathrm{b}})$, given by Eq. (32). We denote the second δ-function of the type given by Eq. (26) by the symbol $g(\hat{E}_{\bar{\nu}})$ and the second δ-function of the type given by Eq. (32) by the symbol $g(\hat{E}_{\bar{\mathrm{b}}})$ to indicate that they refer to the anti-neutrino and to the anti-bottom quark, which both are produced in the decay of the anti-top quark.

After solving for the δ-functions analytically, following Sections A.2.2 and A.2.4 of the appendix, we obtain the following expression for the integral $w_1(\boldsymbol{p})$ for the background hypothesis:

$$
\begin{aligned}
w_1(\boldsymbol{p}) = & \frac{(m_{\mathrm{t}}\,\Gamma_{\mathrm{t}})^2\,(m_{\mathrm{W}}\,\Gamma_{\mathrm{W}})^2}{2^{25}\,\pi^{14}\,\sigma_1\,s\,E_{\ell^+}^2\,E_{\ell^-}^2\,\beta_{\mathrm{b}}\,E_{\bar{\mathrm{b}}}^2\,\beta_{\bar{\mathrm{b}}}\,E_{\bar{\mathrm{b}}}^2} \int d\hat{\theta}_{\nu}\,d\hat{\phi}_{\nu}\,d\hat{\theta}_{\bar{\nu}}\,d\hat{\phi}_{\bar{\nu}} \\
& \cdot\, \hat{p}_{\mathrm{T}}^{\nu}\,\hat{p}_{\mathrm{T}}^{\bar{\nu}}\,\frac{f(\hat{x}_a,Q)\,f(\hat{x}_b,Q)}{\hat{x}_a\,\hat{x}_b} \\
& \cdot\, |\mathcal{M}_1(\hat{\boldsymbol{p}})|^2\,\hat{\beta}_{\mathrm{b}}\,\hat{E}_{\mathrm{b}}\,W(E_{\mathrm{b}}|\hat{E}_{\mathrm{b}})\,\hat{\beta}_{\bar{\mathrm{b}}}\,\hat{E}_{\bar{\mathrm{b}}}\,W(E_{\bar{\mathrm{b}}}|\hat{E}_{\bar{\mathrm{b}}})\,W_{\rho}(p_{\mathrm{x}}{}^{\rho},p_{\mathrm{y}}{}^{\rho}|\hat{p}_{\mathrm{x}}^{\rho},\hat{p}_{\mathrm{y}}^{\rho}) \\
& \cdot\, \left[\sin^2\left(\frac{\sphericalangle(\boldsymbol{e}_{\ell^+},\hat{\boldsymbol{e}}_{\nu})}{2}\right)\,\sin^2\left(\frac{\sphericalangle(\boldsymbol{e}_{\ell^-},\hat{\boldsymbol{e}}_{\bar{\nu}})}{2}\right)\right. \\
& \left.\cdot\, \hat{E}_{\ell^+\nu}\left|1-\frac{\hat{\beta}_{\ell^+\nu}}{\hat{\beta}_{\mathrm{b}}}\,\cos\sphericalangle(\hat{\boldsymbol{e}}_{\ell^+\nu},\boldsymbol{e}_{\mathrm{b}})\right|\,\hat{E}_{\ell^-\bar{\nu}}\left|1-\frac{\hat{\beta}_{\ell^-\bar{\nu}}}{\hat{\beta}_{\bar{\mathrm{b}}}}\,\cos\sphericalangle(\hat{\boldsymbol{e}}_{\ell^-\bar{\nu}},\boldsymbol{e}_{\bar{\mathrm{b}}})\right|\right]^{-1},
\end{aligned}
\tag{13}
$$

with:

$$\hat{E}_{\mathrm{b}} = \frac{a_{\mathrm{t}}\,\Delta_{m_{\mathrm{t}}} + |b_{\mathrm{t}}|\sqrt{\Delta_{m_{\mathrm{t}}}^2 - (a_{\mathrm{t}}^2 - b_{\mathrm{t}}^2)\,m_{\mathrm{b}}^2}}{a_{\mathrm{t}}^2 - b_{\mathrm{t}}^2}$$

$$\hat{E}_{\bar{\mathrm{b}}} = \frac{a_{\bar{\mathrm{t}}}\,\Delta_{m_{\mathrm{t}}} + |b_{\bar{\mathrm{t}}}|\sqrt{\Delta_{m_{\mathrm{t}}}^2 - (a_{\bar{\mathrm{t}}}^2 - b_{\bar{\mathrm{t}}}^2)\,m_{\mathrm{b}}^2}}{a_{\bar{\mathrm{t}}}^2 - b_{\bar{\mathrm{t}}}^2}$$

$$\hat{E}_{\nu} = \frac{m_{\mathrm{W}}^2}{4\,\hat{E}_{\ell^+}\,\sin^2\left(\frac{\sphericalangle(e_{\ell^+},\hat{e}_{\nu})}{2}\right)}$$

$$\hat{E}_{\bar{\nu}} = \frac{m_{\mathrm{W}}^2}{4\,\hat{E}_{\ell^-}\,\sin^2\left(\frac{\sphericalangle(e_{\ell^-},\hat{e}_{\bar{\nu}})}{2}\right)}, \tag{14}$$

where:

$$\begin{aligned}
\Delta_{m_{\mathrm{t}}} &= \frac{m_{\mathrm{t}}^2 - m_{\mathrm{b}}^2 - m_{\mathrm{W}}^2}{2} \\
a_{\mathrm{t}} &= \hat{E}_{\ell^+\nu} \\
b_{\mathrm{t}} &= \sqrt{\hat{E}_{\ell^+\nu}^2 - m_{\mathrm{W}}^2}\,\cos\sphericalangle(\hat{e}_{\ell^+\nu}, e_{\mathrm{b}}) \\
a_{\bar{\mathrm{t}}} &= \hat{E}_{\ell^-\bar{\nu}} \\
b_{\bar{\mathrm{t}}} &= \sqrt{\hat{E}_{\ell^-\bar{\nu}}^2 - m_{\mathrm{W}}^2}\,\cos\sphericalangle(\hat{e}_{\ell^-\bar{\nu}}, e_{\bar{\mathrm{b}}}).
\end{aligned} \tag{15}$$

The integral given by Eq. (13) extends over 4 remaining variables, which are integrated numerically: $\hat{\theta}_{\nu}$, $\hat{\phi}_{\nu}$, $\hat{\theta}_{\bar{\nu}}$, and $\hat{\phi}_{\bar{\nu}}$. The symbol $\ell^+\nu$ ($\ell^-\bar{\nu}$) refers to the true direction of the W^+ (W^-) boson, which are computed by summing the momenta of the lepton of positive (negative) charge and of the neutrino (anti-neutrino). The neutrino and anti-neutrino momenta are computed as function of the integration variables $\hat{\theta}_{\nu}$, $\hat{\phi}_{\nu}$, $\hat{\theta}_{\bar{\nu}}$, $\hat{\phi}_{\bar{\nu}}$ and Eq. (14).

When evaluating the compatibility of a given event with the background hypothesis, there exists a twofold ambiguity in associating the two measured b-jets to the b and $\bar{\mathrm{b}}$ quarks. We deal with this ambiguity by evaluating the integral $w_1(\boldsymbol{p})$ given by Eq. (10) two times, corresponding to the two possible associations of the measured b-jets to the b and $\bar{\mathrm{b}}$ quarks. In contrast to the signal hypothesis, there is no ambiguity in associating the two measured leptons to the two W bosons, as in $\mathrm{t\bar{t}}$ background events both W bosons are on-shell, and the measurement of the lepton charge allows for a unique association of each charged lepton to either the W^+ or the W^- boson.

3. Performance

We study the separation of the HH signal from the $\mathrm{t\bar{t}}$ background, achieved by the LR $P(\boldsymbol{p})$ given by Eq. (1), using samples of signal and background events produced by Monte Carlo (MC) simulation. The samples are simulated at LO and at NLO accuracy in pQCD and are analyzed at MC-truth as well as at detector level. The former corresponds to the case of an ideal experimental resolution, while the latter aims to simulate the experimental conditions characteristic for the ATLAS and CMS experiments during LHC Run 2. The LO and NLO HH signal samples each contain about three hundred thousand events and the LO and NLO $\mathrm{t\bar{t}}$ background samples each contain about five million events. All samples simulated at LO accuracy in pQCD are produced with the program MadGraph_aMCatNLO 2.2.2, while the samples simulated at NLO accuracy in pQCD are produced using the program POWHEG $v2$ [78–84]. The NNPDF3.0 LO set of PDF is used for the simulation of the LO samples and the NNPDF3.0 NLO set for the NLO samples [85–87]. Parton shower and hadronization processes are modeled using the program PYTHIA $v8.2$ [88] with the tune CP5 [89]. All events are generated for proton–proton collisions at $\sqrt{s} = 13$ TeV center-of-mass energy. Events in which the electrons or muons originate from τ lepton decays, i.e. from the decay chains $\mathrm{W}^+ \to \tau^+\nu_{\tau} \to \ell^+\nu_{\ell}\bar{\nu}_{\tau}\nu_{\tau}$ or $\mathrm{W}^- \to \tau^-\bar{\nu}_{\tau} \to \ell^-\bar{\nu}_{\ell}\nu_{\tau}\bar{\nu}_{\tau}$, are discarded. Detector effects are simulated using the program DELPHES $v3.5.0$ [61] with the card for the CMS detector. On average forty inelastic proton–proton interactions (pileup) are added to each simulated event in order to simulate the data-taking conditions during Run 2 of the LHC.

Jets are reconstructed using the anti-k_{T} algorithm [90,91] with a distance parameter of 0.4, using the detector-level particle-flow objects created by DELPHES as input. We refer to these jets as detector-level jets. Their energy is corrected for pileup effects using the method described in Refs. [92,93] and is calibrated as function of jet p_{T} and η, where $\eta = -\ln\tan(\theta/2)$ denotes the pseudorapidity of the jet. The calibration is performed such that the energy of the jets that are tagged, at detector level, as originating from the hadronization of a bottom quark on average matches the energy of the bottom quarks that result from H boson or top quark decays at the parton level. We refer to detector-level jets that pass the b-tagging criteria as b-jets. By calibrating detector-level jets to the energy of the bottom quarks at the parton level, the calibration procedure corrects the jet energy for out-of-cone effects and for the energy carried away, on average, by the neutrinos produced in heavy-flavor decays.

The simulated HH signal and $\mathrm{t\bar{t}}$ background events considered in this section are required to pass event selection criteria similar to the analysis of HH production performed, in the channel $\mathrm{HH} \to \mathrm{b\bar{b}WW}^*$, by the CMS collaboration during LHC Run 2 [34]. The events are required to contain two electrons or muons and two b-jets. The leptons must be within the region $|\eta| < 2.5$ if they are electrons and $|\eta| < 2.4$ if they are muons, and are required to be isolated. Their isolation is computed by summing the p_{T} of detector-level particle-flow objects that are within a cone of size $\delta R = \sqrt{(\delta\eta)^2 + (\delta\phi)^2} = 0.5$ around the lepton direction, excluding the lepton itself. The sum is corrected for the contribution of particles from pileup using the method described in Refs. [92,93]. Electrons and muons are considered isolated if the pileup-corrected sum amounts to less than 0.10 times the p_{T} of the lepton. The lepton of higher p_{T} is required to have $p_{\mathrm{T}} > 25$ GeV and the lepton of lower p_{T} must have $p_{\mathrm{T}} > 15$ GeV. These p_{T} thresholds are motivated by trigger requirements. The b-jets are required to satisfy the conditions $p_{\mathrm{T}} > 25$ GeV and $|\eta| < 2.4$ and to be both tagged as b-jets at detector level. The b-tagging criteria implemented in the DELPHES card for the CMS detector corresponds to the medium working-point of the "combined secondary vertex" b-tagging algorithm published in Ref. [94]. The algorithm identifies jets originating from the hadronization of a bottom quark with an efficiency of approximately 70%, for a misidentification rate for light-quark and gluon jets of about 1.5% [94]. Events containing more than two b-tagged jets of $p_{\mathrm{T}} > 25$ GeV and $|\eta| < 2.4$ are vetoed. The latter condition rejects a small fraction of events, amounting to 7.7% of the HH signal and 5.1% of the $\mathrm{t\bar{t}}$ background, and avoids ambiguities in choosing the correct pair of b-jets when computing the PDs $w_0(\boldsymbol{p})$ and $w_1(\boldsymbol{p})$ according to Eqs. (10) and (13). The selection criteria are applied to generator-level leptons and jets when analyzing simulated events at MC-truth level and to detector-level leptons and jets when analyzing simulated events at the detector level. In case the selection criteria are applied at MC-truth level, no isolation requirements are applied to the leptons, the conditions $p_{\mathrm{T}} > 25$ GeV and $|\eta| < 2.4$ of the jet selection are applied at the parton level, to the bottom quarks that are produced in the H boson or top quark decays, and no detector-level b-tagging criteria are applied.

Fig. 3 shows the distribution in m_{bb}, the mass of the two b-tagged jets at detector level, in HH signal and $\mathrm{t\bar{t}}$ background events that pass the selection criteria described in the previous paragraph. Only events in which both detector-level jets are matched, within a cone of size $\delta R = 0.3$, to bottom quarks that originate from either a H boson or from top quark decays, are shown in the figure. According to the DELPHES simulation, 95.0% of HH and 96.4% of $\mathrm{t\bar{t}}$ events that pass the selection criteria described in the previous paragraph fulfill this matching condition, i.e. in 5.0% of selected HH and 3.6% of selected $\mathrm{t\bar{t}}$ events one of the bottom quarks is not reconstructed as b-jet at detector level and a light quark or gluon jet is misidentified as b-jet instead. The figure shows that the jet calibration shifts the peak of the m_{bb} distribution by about 20%. After calibration, the m_{bb} distribution in HH

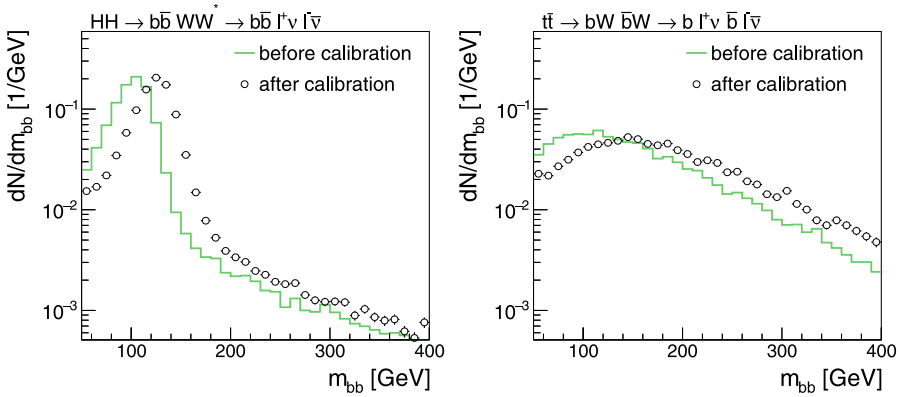


Fig. 3. Distribution in m_{bb}, the mass of the two detector-level jets that are tagged as b-jets, in HH signal (left) and $\mathrm{t\bar{t}}$ background (right) events before and after the jet energy calibration is applied.

signal events peaks close to 125 GeV. The calibration also reduces the relative width, defined as the root mean square divided by the mean, of the m_{bb} distribution in HH signal events by about 20%.

In order to compute the PDs $w_0(\boldsymbol{p})$ and $w_1(\boldsymbol{p})$ according to Eqs. (10) and (13), we need to determine the TFs for the energy of b-jets and for the transverse momentum components of the hadronic recoil such that the TFs match the experimental resolution in the DELPHES simulation. We model the experimental resolution on the energy of b-jets using a normal distribution:

$$W(E|\hat{E}) = \frac{1}{\sqrt{2\pi\sigma_{\mathrm{b}}^2}}\, e^{-\frac{(p_{\mathrm{T}}-\hat{p}_{\mathrm{T}})^2}{2\,\sigma_{\mathrm{b}}^2}}, \tag{16}$$

where $p_{\mathrm{T}} = E \cdot \sin\theta$, $\hat{p}_{\mathrm{T}} = \hat{E} \cdot \sin\theta$, and θ refers to the polar angle of the jet. The standard deviation σ_{b} depends on the jet energy and θ. We make the ansatz $\sigma_{\mathrm{b}} = k \cdot \sqrt{\hat{E} \cdot \sin\theta}$ and determine the constant of proportionality k such that it fits the resolution on the energy of b-jets in the DELPHES simulation, yielding $k = 100\%$. Our model for the jet energy resolution agrees with the resolution measured by the CMS collaboration during LHC Run 2, shown in Fig. 3 of Ref. [95].[1] The hadronic recoil ρ is not directly available in the DELPHES simulation. To determine the resolution on ρ, we compute the transverse momentum components of the hadronic recoil as function of the transverse momenta of the two leptons, the two b-jets, and $\boldsymbol{p}_{\mathrm{T}}^{\mathrm{miss}}$, using Eq. (6), with the substitutions $\hat{p}_{\mathrm{x}}^{\nu} + \hat{p}_{\mathrm{x}}^{\bar{\nu}} = \hat{p}_{\mathrm{x}}^{\mathrm{miss}}$ and $\hat{p}_{\mathrm{y}}^{\nu} + \hat{p}_{\mathrm{y}}^{\bar{\nu}} = \hat{p}_{\mathrm{y}}^{\mathrm{miss}}$, for the computation at MC-truth level and Eq. (7) for the computation at detector level. The resolution on $p_{\mathrm{x}}{}^{\rho}$ and $p_{\mathrm{y}}{}^{\rho}$ in the DELPHES simulation amounts to 32 GeV for the HH signal and to 30 GeV for the $\mathrm{t\bar{t}}$ background. The resolution on the energy of b-jets is small compared to the resolution on the hadronic recoil. The resolution on the latter is thus similar to the resolution on $\boldsymbol{p}_{\mathrm{T}}^{\mathrm{miss}}$. This similarity allows us to compare the resolutions on $p_{\mathrm{x}}{}^{\rho}$ and $p_{\mathrm{y}}{}^{\rho}$ in the DELPHES simulation to the resolution on $\boldsymbol{p}_{\mathrm{T}}^{\mathrm{miss}}$ published by the ATLAS collaboration for simulated $\mathrm{t\bar{t}}$ events during LHC Run 2,[2] which is shown in Fig. 9 of Ref. [96] and amounts to 25 – 30 GeV. We assume that the resolutions on $p_{\mathrm{x}}{}^{\rho}$ and $p_{\mathrm{y}}{}^{\rho}$ are uncorrelated and amount to the same for signal and background events. Rounding the numbers for the resolution on $p_{\mathrm{x}}{}^{\rho}$ and $p_{\mathrm{y}}{}^{\rho}$ to one significant digit, we use:

$$V = \sigma_{\rho}^2 \cdot I_2 \tag{17}$$

with $\sigma_{\rho} = 30$ GeV for when computing the PDs $w_0(\boldsymbol{p})$ and $w_1(\boldsymbol{p})$ for HH signal and $\mathrm{t\bar{t}}$ background events.

We can now proceed to compute the PDs $w_0(\boldsymbol{p})$ and $w_1(\boldsymbol{p})$. Distributions in $w_0(\boldsymbol{p})$ and $w_1(\boldsymbol{p})$ for HH signal and $\mathrm{t\bar{t}}$ background events are shown in Fig. 4. The horizontal axis is drawn in logarithmic scale to better visualize small values of the PDs. The PDs are computed at MC-truth and at detector level. When computing the PDs at MC-truth level, we set the "measured" momenta of electrons and muons to their generator-level values, the "measured" momenta of the b-jets to the momenta of the corresponding parton-level bottom quarks, and the "measured" transverse momentum components of the hadronic recoil to their true values $\hat{p}_{\mathrm{x}}^{\rho}$ and $\hat{p}_{\mathrm{y}}^{\rho}$. The latter are computed according to Eq. (6). We also demand that both b-jets are matched, within a cone of size $\delta R = 0.3$, to bottom quarks that originate from either a H boson or from top quark decays when we compute the PDs at MC-truth level. The same TFs, described in the previous paragraph, are used when computing the PDs $w_0(\boldsymbol{p})$ and $w_1(\boldsymbol{p})$ at MC-truth and at detector level. The distributions in the PDs for the "correct" hypothesis ($w_0(\boldsymbol{p})$ for signal and $w_1(\boldsymbol{p})$ for background events) peak close to one and fall rapidly towards smaller values, while the distributions in the PDs for the "wrong" hypothesis ($w_1(\boldsymbol{p})$ for signal and $w_0(\boldsymbol{p})$ for background events) exhibit more pronounced tails towards small values. Interestingly, the distributions in the PDs for the wrong hypothesis change only by a small amount between MC-truth and detector level. The main effect of the experimental resolutions on the energy of b-jets and on the transverse momentum of the hadronic recoil as well as of the misidentification of light quark or gluon jets as b-jets is to increase the tail towards small values for the distributions in the PDs for the correct hypothesis.

The corresponding distributions in the LR $P(\boldsymbol{p})$, computed according to Eq. (1), are shown in Fig. 5. Signal events are characterized by high values of $P(\boldsymbol{p})$, while background events typically have low values. The secondary peaks in the leftmost (rightmost) bin of the distribution for the HH signal ($\mathrm{t\bar{t}}$ background) are due to events in which the event kinematics are atypical for signal (background) events, resulting in the PD for the wrong hypothesis $w_1(\boldsymbol{p})$ ($w_0(\boldsymbol{p})$) to be higher than the PD for the correct hypothesis $w_0(\boldsymbol{p})$ ($w_1(\boldsymbol{p})$). About 4% of signal (10% of background) events populate the leftmost (rightmost) bin of the distribution in case the LR $P(\boldsymbol{p})$ is computed at MC-truth level. In case the LR is computed at detector level, the fraction of HH signal ($\mathrm{t\bar{t}}$ background) events that populate the leftmost (rightmost) bin increases to 14% (decreases to 7%). The "receiver-operating-characteristic" (ROC)

[1] Our assumption that the polar angle θ of the jet is measured with negligible experimental resolution (cf. Section A.1 of the appendix) is justified by Fig. 5 of Ref. [95], which shows that the resolution on θ amounts to about 0.02 radians for jets of $p_{\mathrm{T}} = 25$ GeV and decreases for jets of higher p_{T}.

[2] The CMS collaboration has not published the $p_{\mathrm{T}}^{\mathrm{miss}}$ resolution during LHC Run 2 specifically for $\mathrm{t\bar{t}}$ events.

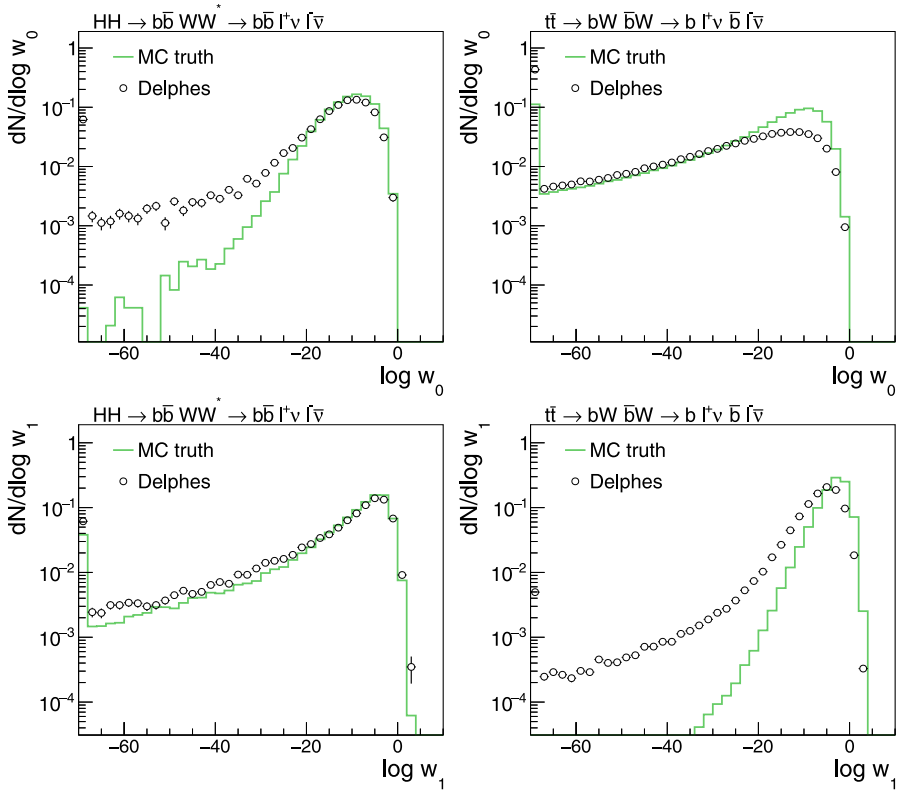


Fig. 4. Distributions in the PDs $w_0(\boldsymbol{p})$ (upper) and $w_1(\boldsymbol{p})$ (lower), computed according to Eqs. (10) and (13), for HH signal (left) and $t\bar{t}$ background (right) events. The PDs are computed at MC-truth and at detector level.

curves [97] that correspond to these distributions are shown in Fig. 6. The ROC curve quantifies the separation between the HH signal and the $t\bar{t}$ background and is obtained by varying the threshold of a cut on the LR $P(\boldsymbol{p})$ and plotting the fractions of signal and background events passing the cut. For a signal efficiency of 35%, the $t\bar{t}$ background is reduced by about three orders of magnitude, to a level of 0.09%, in case the LR is computed at MC-truth level. In case the LR is computed at detector level, the $t\bar{t}$ background is reduced to a level of 0.26%. The degradation in separation power that occurs at detector level is mainly due to signal events in which one of the bottom quarks originating from the H boson decay is not reconstructed as b-jet at detector level and a light quark or gluon jet is misidentified as b-jet instead. If this happens, the mass of the two detector-level jets that are reconstructed as b-jets are often incompatible with m_{H}. The presence of a BW propagator in the ME $\mathcal{M}_0(\hat{\boldsymbol{p}})$ for the signal hypothesis, which enforces that the mass of the pair of b-jets equals m_{H}, then introduces large "pulls" in the TF $W(E|\hat{E})$ for the b-jet energy, which diminish the value of the integrand.

To better gauge the level of separation of the HH signal from the $t\bar{t}$ background presented in Fig. 6, we compute signal efficiencies and background rates that one would obtain by cutting on the mass, m_{bb}, of the b-jet pair, shown in Fig. 3, for comparison. The observable m_{bb} is presumably one of the most powerful single observables to separate the HH signal from the $t\bar{t}$ background. Fitting the peak of the distribution in the mass of the b-jet pair in HH signal events, obtained after the jet energy calibration is applied, with a normal distribution yields a mean of 123 GeV and a standard deviation of 20 GeV. Requiring events to have a value of m_{bb} within 1 (2) standard deviations around the mean selects 78% (89%) of the HH signal and 27% (43%) of the $t\bar{t}$ background. Compared to the cut on m_{bb}, the LR $P(\boldsymbol{p})$ allows for a significantly higher reduction in the rate of $t\bar{t}$ background by exploiting the full difference in event kinematics between the HH signal and the $t\bar{t}$ background.

We remark that the misidentification of hadrons as leptons is not simulated in DELPHES and hence not accounted for in the detector-level ROC curve shown in Fig. 6. Based on the analysis of HH production performed in the decay channel $b\bar{b}WW^*$ by the CMS collaboration during LHC Run 2 [34], which found the background arising from the misidentification of hadrons as leptons to be negligible, we expect the misidentification of hadrons as leptons to have at most a small effect on the ROC curve.

We conclude this section on the performance of the MEM with a study of the effect of using ME of LO when computing the weights $w_0(\boldsymbol{p})$ and $w_1(\boldsymbol{p})$ by means of Eqs. (10) and (13) and with a discussion of the computing-time requirements of the MEM.

Unfortunately, we cannot compare the performance of the MEM for the case of using ME generated at LO versus ME generated at NLO in Eqs. (10) and (13) directly, because the program MadGraph_aMCatNLO does not support the generation of code for NLO ME at present and also because the usage of NLO ME in the MEM would increase the computing-time requirements by 1 – 2 orders of magnitude. Instead, we use ME generated at LO accuracy in Eqs. (10) and (13) and compare the resulting performance in separating the HH signal from the $t\bar{t}$ background for MC samples simulated at LO and at NLO accuracy in pQCD. The NLO samples are expected to provide the more accurate modeling of real data and the LO samples are taken as a (more or less precise) approximation. We take the difference in performance

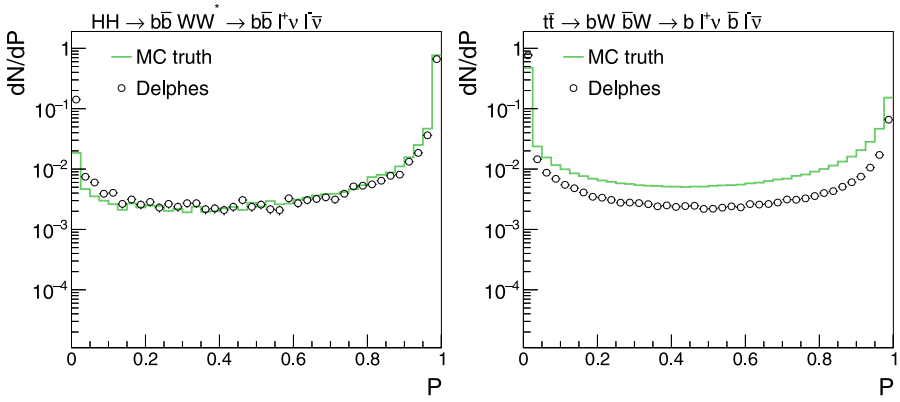


Fig. 5. Distributions in the LR $P(\boldsymbol{p})$, computed according to Eq. (1), for HH signal (left) and $t\bar{t}$ background (right) events. The LR $P(\boldsymbol{p})$ is computed using the PDs $w_0(\boldsymbol{p})$ and $w_1(\boldsymbol{p})$ shown in Fig. 4 as input and is computed at MC-truth and at detector level.

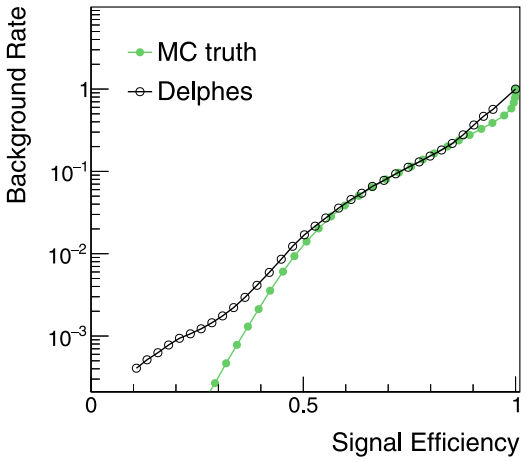


Fig. 6. Graphs of background rate versus signal efficiency ("ROC curve"), at MC-truth and at detector level, obtained by varying the threshold of a cut applied on the distributions in the LR $P(\boldsymbol{p})$ shown in Fig. 5.

achieved by the MEM on the MC samples simulated at LO and at NLO accuracy as an estimate for the loss in discrimination power that results from our choice of using LO ME and ignoring the effects of higher orders in the MEM. Distributions in the LR $P(\boldsymbol{p})$ computed for HH signal and $t\bar{t}$ background events simulated at LO and at NLO accuracy in pQCD are shown in Fig. 7. The events are analyzed at MC-truth level. The corresponding ROC curve is presented in Fig. 8. The usage of LO ME causes a moderate loss in the separation of the HH signal from the $t\bar{t}$ background, amounting to a few percent loss in signal efficiency (for the same background rate). We conclude from these figures that the usage of LO ME represents a viable approximation.

The computing time required to evaluate the integrals given by Eqs. (10) and (13) may represent a challenge in practical applications of the MEM. Experimental analyses will usually need to evaluate these integrals multiple times for each event in order to assess the effect of systematic uncertainties. Taken together with the large cross section for $t\bar{t}$ production at the LHC, the integrals in Eqs. (10) and (13) may need to be computed in the order of 100 million times. Even with several thousands of computing jobs running in parallel, as it is nowadays commonplace for experimental data analyses performed at the LHC, the computation still requires a few weeks of nonstop computing time. Several possibilities to speed up the numeric integrations, which take most of the computing time in practical applications of the MEM, have been explored in the literature. One alternative is to use vector integrands to evaluate the likelihood ratio for all systematic uncertainties simultaneously [98], taking advantage of the fact that the systematic uncertainties typically constitute small changes with respect to the nominal value. Another alternative is to take advantage of the parallelizability of multidimensional integration and perform the integration on graphics processing units (GPUs). Speedup factors of order 100, compared to using a single core of a general-purpose central processing unit (CPU) such as the 2.30 GHz Intel® Xeon® E5-2695V3 processor that we used for the studies presented in this paper, are reported in the literature for performing numeric integrations on GPUs [99–104].

4. Summary

We presented an application of the matrix element method to the search for non-resonant HH production in the channel HH → bb̄WW* at LHC, focusing on events in which the two W bosons decay to a pair of electrons or muons. According to the Neyman–Pearson lemma, the likelihood ratio $P(\boldsymbol{p})$ given by Eq. (1) provides the optimal separation of the HH signal from the dominant irreducible $t\bar{t}$ background. We have studied the separation of the HH signal from the $t\bar{t}$ background at Monte-Carlo truth and at detector level. The latter has been simulated using the DELPHES fast-simulation framework. For experimental conditions characteristic for the ATLAS and CMS experiments during LHC Run 2, we find that the $t\bar{t}$ background can be reduced to a level of 0.26% for a signal efficiency of 35%. We regard the potential of the matrix element method for enhancing the sensitivity of the analysis of HH production in the channel HH → bb̄WW* as promising and we hope this paper will motivate the ATLAS and CMS collaborations to employ the method in a full analysis.

CRediT authorship contribution statement

Karl Ehatäht: Methodology, Software, Formal analysis, Writing – review & editing. **Christian Veelken:** Conceptualization, Methodology, Software, Validation, Formal analysis, Investigation, Writing – original draft, Writing – review & editing, Visualization, Supervision, Project administration, Funding acquisition.

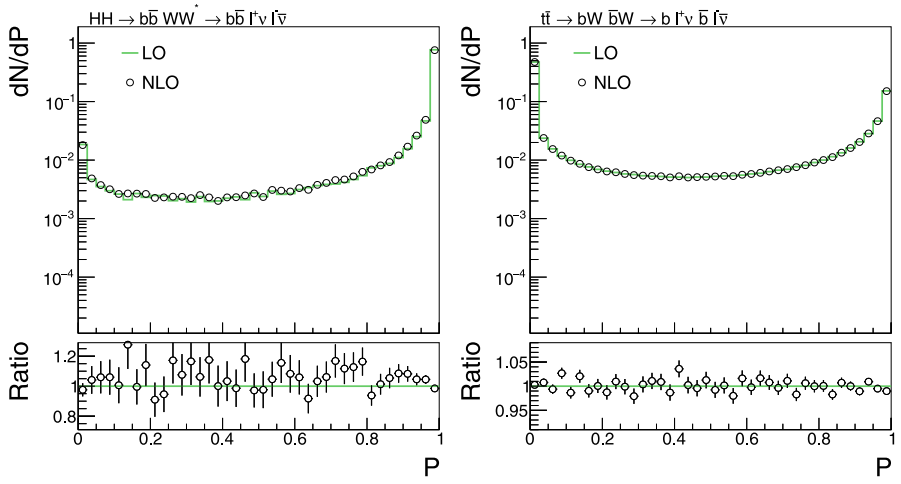


Fig. 7. Distribution in the LR $P(\boldsymbol{p})$ for HH signal (left) and $t\bar{t}$ background (right) events simulated at LO and at NLO accuracy in pQCD. The likelihood ratios are computed at MC-truth level.

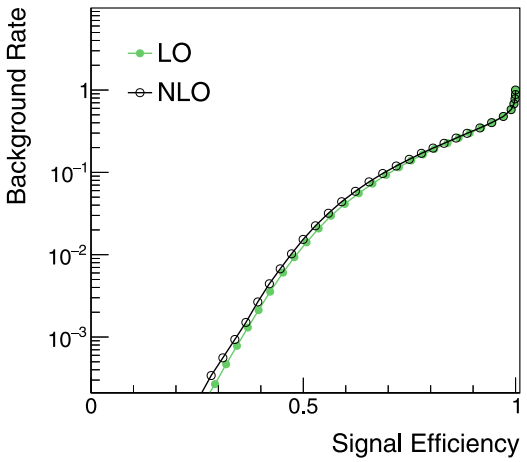


Fig. 8. Separation between the HH signal and the $t\bar{t}$ background for events simulated at LO and at NLO accuracy in pQCD. The graphs of background rate versus signal efficiency shown in the figure are obtained by applying a cut on the distributions in the likelihood ratios $P(\boldsymbol{p})$ shown in Fig. 7.

Declaration of competing interest

The authors declare that they have no known competing financial interests or personal relationships that could have appeared to influence the work reported in this paper.

Acknowledgment

This work has been supported by the Estonian Research Council, Estonia grant PRG445.

Appendix

In this section, we derive a few useful relations that allow us to simplify the expression for the probability density $w_i(\boldsymbol{p})$ starting from Eq. (2). We begin by deriving relations for the TF of charged leptons and of b-jets, which we present in Appendix A.1. In Appendix A.2, we will derive relations corresponding to various mass constraints. The constraints arise from the presence of BW propagators in the ME $\mathcal{M}_i(\hat{\boldsymbol{p}})$ for the signal ($i = 0$) and for the background ($i = 1$) hypothesis. The effect of the BW propagators is that only those points $\hat{\boldsymbol{p}}$ in the 6-particle phase space contribute to the value of the integral in Eq. (2) for which certain systems of final state particles satisfy certain mass conditions. The relations derived in Appendices A.1 and A.2 are used to transform Eq. (2) into Eq. (10) for the HH signal hypothesis and into Eq. (13) for the $t\bar{t}$ background hypothesis, respectively.

A.1. Relations for transfer functions

We assume that the directions of electrons, muons, and b-jets as well as the energies of electrons and muons are measured with negligible experimental resolution. Our assumption implies that the TF for electrons and muons is given by:

$$W_{\ell}(\boldsymbol{p}|\hat{\boldsymbol{p}}) = f(E,\theta,\phi)\,\delta(E-\hat{E})\cdot\delta(\theta-\hat{\theta})\cdot\delta(\phi-\hat{\phi})\,, \tag{18}$$

while the TF for b-jets is given by:

$$W(\boldsymbol{p}|\hat{\boldsymbol{p}}) = f(E,\theta,\phi)\,W(E|\hat{E})\cdot\delta(\theta-\hat{\theta})\cdot\delta(\phi-\hat{\phi})\,, \tag{19}$$

where E denotes the energy, θ the polar angle, and ϕ the azimuthal angle of the electron, muon, or b-jet. The function $W(E|\hat{E})$ quantifies the experimental resolution with which the energy of b-jets is measured. We choose the function $W(E|\hat{E})$ such that it satisfies the following normalization condition:

$$\int dE\, W(E|\hat{E}) \equiv 1.$$

The function $f(E,\theta,\phi)$ ensures that the TF satisfy the normalization condition

$$\int d^3\boldsymbol{p}\,\Omega(\boldsymbol{p})\,W(\boldsymbol{p}|\hat{\boldsymbol{p}}) = 1\,.$$

We only consider those events, which pass the event selection criteria, i.e. for which $\Omega(\boldsymbol{p})$ is equal to one. With $d^3\boldsymbol{p} = \beta\,E^2\,\sin\theta\,dE\,d\theta\,d\phi$, it follows that:

$$1 \equiv \int dE\,d\theta\,d\phi\,\beta\,E^2\,\sin\theta\,f(E,\theta,\phi)\,W(E|\hat{E})\,\delta(\theta-\hat{\theta})\cdot\delta(\phi-\hat{\phi})\,,$$

which implies:

$$f(E,\theta,\phi) = \frac{1}{\beta\, E^2\, \sin\theta}\,. \tag{20}$$

Eq. (20) holds for electrons and muons as well as for b-jets.

A.2. Relations for mass constraints

As explained in Section 2, the presence of BW propagators in the ME $\mathcal{M}_i(\hat{p})$ renders the numeric integration inefficient, unless the numeric integration is restricted to those narrow slices in the 6-particle PS where the mass constraints are satisfied. We achieve the desired restriction by inserting suitable δ-functions into the integrand on the RHS of Eq. (9). In order to avoid that the insertion of the δ-functions changes the value of the integral, we formally insert a factor of 1, which we write as:

$$\begin{aligned} 1 \equiv \mathrm{BW}\cdot\mathrm{BW}^{-1} &= \frac{\pi}{m_\mathrm{X}\,\Gamma_\mathrm{X}}\,\delta(E_\mathrm{X}^2 - |\boldsymbol{p}_\mathrm{X}|^2 - m_\mathrm{X}^2) \\ &\quad\cdot\left((E_\mathrm{X}^2 - |\boldsymbol{p}_\mathrm{X}|^2 - m_\mathrm{X}^2)^2 + (m_\mathrm{X}\,\Gamma_\mathrm{X})^2\right) \\ &= \pi\, m_\mathrm{X}\,\Gamma_\mathrm{X}\,\delta(E_\mathrm{X}^2 - |\boldsymbol{p}_\mathrm{X}|^2 - m_\mathrm{X}^2)\,, \end{aligned} \tag{21}$$

where we have used the narrow-width approximation to replace the first BW propagator by a δ-function. The symbol X in Eq. (21) refers to the on-shell particle, of mass m_X and width Γ_X, which imposes the mass constraint.

We insert Eq. (21) into the integrand on the RHS of Eq. (9) and then use the δ-function $\delta(E_\mathrm{X}^2 - |\boldsymbol{p}_\mathrm{X}|^2 - m_\mathrm{X}^2)$ to eliminate the integration over $\hat{E}$ for one of the daughter particles that the particle X decays into. The δ-function rule:

$$\delta\left(g(x)\right) = \frac{1}{|g'(x_0)|}\,\delta(x - x_0) \tag{22}$$

yields a factor of $|g'(x_0)|^{-1} \equiv \left|\frac{\partial g}{\partial x}\right|_{x=x_0}$, which we account for when eliminating the integration over $\hat{E}$. The symbol x_0 denotes the root of $g(x)$.

A.2.1. Energy of $\bar{\mathrm{b}}$ produced in $\mathrm{H}\to\mathrm{b}\bar{\mathrm{b}}$ decay

The condition that the mass of the 2-particle system of b plus $\bar{\mathrm{b}}$ quark equals m_H implies that:

$$\begin{aligned} m_\mathrm{H}^2 \equiv m_{\mathrm{b}\bar{\mathrm{b}}}^2 &= (\hat{E}_\mathrm{b} + \hat{E}_{\bar{\mathrm{b}}})^2 - (\hat{\boldsymbol{p}}_\mathrm{b} + \hat{\boldsymbol{p}}_{\bar{\mathrm{b}}})^2 \\ &= \hat{E}_\mathrm{b}^2 + \hat{E}_{\bar{\mathrm{b}}}^2 + 2\,\hat{E}_\mathrm{b}\,\hat{E}_{\bar{\mathrm{b}}} - |\hat{\boldsymbol{p}}_\mathrm{b}|^2 - |\hat{\boldsymbol{p}}_{\bar{\mathrm{b}}}|^2 - 2\,\hat{\boldsymbol{p}}_\mathrm{b}\cdot\hat{\boldsymbol{p}}_{\bar{\mathrm{b}}} \\ &= \underbrace{\hat{E}_\mathrm{b}^2 - |\hat{\boldsymbol{p}}_\mathrm{b}|^2}_{=m_\mathrm{b}^2} + \underbrace{\hat{E}_{\bar{\mathrm{b}}}^2 - |\hat{\boldsymbol{p}}_{\bar{\mathrm{b}}}|^2}_{=m_{\bar{\mathrm{b}}}^2} + 2\,\underbrace{\hat{E}_\mathrm{b}}_{\equiv a}\,\hat{E}_{\bar{\mathrm{b}}} \\ &\quad - 2\,\underbrace{\sqrt{\hat{E}_\mathrm{b}^2 - m_\mathrm{b}^2}\,\hat{\boldsymbol{e}}_\mathrm{b}\cdot\hat{\boldsymbol{e}}_{\bar{\mathrm{b}}}}_{\equiv b}\,\sqrt{\hat{E}_{\bar{\mathrm{b}}}^2 - m_{\bar{\mathrm{b}}}^2} \\ \Longrightarrow 0 &= \underbrace{\frac{m_\mathrm{H}^2}{2} - m_\mathrm{b}^2}_{\equiv\Delta_{m_\mathrm{H}}} - a\,\hat{E}_{\bar{\mathrm{b}}} + b\,\sqrt{\hat{E}_{\bar{\mathrm{b}}}^2 - m_{\bar{\mathrm{b}}}^2} \equiv g(\hat{E}_{\bar{\mathrm{b}}})\,, \end{aligned} \tag{23}$$

where the symbol $\hat{\boldsymbol{e}}_\mathrm{b}$ denotes a unit vector in direction of the b quark and the symbol $\bar{\mathrm{b}}$ a unit vector in direction of the $\bar{\mathrm{b}}$ quark. Eq. (23) has two solutions:

$$\hat{E}_{\bar{\mathrm{b}}} = \frac{a\,\Delta_{m_\mathrm{H}} \pm |b|\,\sqrt{\Delta_{m_\mathrm{H}}^2 - (a^2 - b^2)\,m_\mathrm{b}^2}}{a^2 - b^2}\,. \tag{24}$$

We discard the solution of lower energy and consider the solution of higher energy only, i.e. we take the solution corresponding to the + sign in Eq. (24).

The derivative of the RHS of Eq. (23) with respect to $\hat{E}_{\bar{\mathrm{b}}}$ amounts to:

$$\begin{aligned} \frac{1}{|g'(\hat{E}_{\bar{\mathrm{b}}})|} &= \frac{1}{\left|a - \underbrace{\frac{b\,\hat{E}_{\bar{\mathrm{b}}}}{\sqrt{\hat{E}_{\bar{\mathrm{b}}}^2 - m_{\bar{\mathrm{b}}}^2}}}_{=\hat{\beta}_{\bar{\mathrm{b}}}\,\hat{E}_{\bar{\mathrm{b}}}}\right|} = \frac{1}{\left|a - \frac{1}{\hat{\beta}_{\bar{\mathrm{b}}}}\,b\right|} \\ &= \frac{1}{\left|\hat{E}_\mathrm{b} - \frac{1}{\hat{\beta}_{\bar{\mathrm{b}}}}\,\underbrace{\sqrt{\hat{E}_{\bar{\mathrm{b}}}^2 - m_{\bar{\mathrm{b}}}^2}}_{=\hat{\beta}_\mathrm{b}\,\hat{E}_\mathrm{b}}\,\underbrace{\hat{\boldsymbol{e}}_\mathrm{b}\cdot\hat{\boldsymbol{e}}_{\bar{\mathrm{b}}}}_{\equiv\cos\sphericalangle(\hat{\boldsymbol{e}}_\mathrm{b},\hat{\boldsymbol{e}}_{\bar{\mathrm{b}}})}\right|} \\ &= \frac{1}{\left|\hat{E}_\mathrm{b}\left(1 - \frac{\hat{\beta}_\mathrm{b}}{\hat{\beta}_{\bar{\mathrm{b}}}}\,\cos\sphericalangle(\hat{\boldsymbol{e}}_\mathrm{b},\hat{\boldsymbol{e}}_{\bar{\mathrm{b}}})\right)\right|}\,. \end{aligned} \tag{25}$$

A.2.2. Energy of ν produced in $\mathrm{W}\to\ell\nu$ decay

The condition that the mass of the 2-particle system of ℓ plus ν equals m_W implies that:

$$\begin{aligned} m_\mathrm{W}^2 \equiv m_{\ell\nu}^2 &= (\hat{E}_\ell + \hat{E}_\nu)^2 - (\hat{\boldsymbol{p}}_\ell + \hat{\boldsymbol{p}}_\nu)^2 \\ &= \hat{E}_\ell^2 + \hat{E}_\nu^2 + 2\,\hat{E}_\ell\,\hat{E}_\nu - |\hat{\boldsymbol{p}}_\ell|^2 - |\hat{\boldsymbol{p}}_\nu|^2 - 2\,\hat{\boldsymbol{p}}_\ell\cdot\hat{\boldsymbol{p}}_\nu \\ &= \underbrace{\hat{E}_\ell^2 - |\hat{\boldsymbol{p}}_\ell|^2}_{=m_\ell^2\approx 0} + \underbrace{\hat{E}_\nu^2 - |\hat{\boldsymbol{p}}_\nu|^2}_{=m_\nu^2\approx 0} + 2\,\hat{E}_\ell\,\hat{E}_\nu \\ &\quad - 2\,\underbrace{|\hat{\boldsymbol{p}}_\ell|}_{\approx\hat{E}_\ell}\,\underbrace{|\hat{\boldsymbol{p}}_\nu|}_{\approx\hat{E}_\nu}\,\underbrace{\hat{\boldsymbol{e}}_\ell\cdot\hat{\boldsymbol{e}}_\nu}_{\equiv\cos\sphericalangle(\hat{\boldsymbol{e}}_\ell,\hat{\boldsymbol{e}}_\nu)} \\ &= 2\,\hat{E}_\ell\,\hat{E}_\nu\,\underbrace{\left(1 - \cos\sphericalangle(\hat{\boldsymbol{e}}_\ell,\hat{\boldsymbol{e}}_\nu)\right)}_{=2\,\sin^2\left(\frac{\sphericalangle(\hat{\boldsymbol{e}}_\ell,\hat{\boldsymbol{e}}_\nu)}{2}\right)} = 4\,\hat{E}_\ell\,\hat{E}_\nu\,\sin^2\left(\frac{\sphericalangle(\hat{\boldsymbol{e}}_\ell,\hat{\boldsymbol{e}}_\nu)}{2}\right) \\ \Longrightarrow 0 &= m_\mathrm{W}^2 - 4\,\hat{E}_\ell\,\hat{E}_\nu\,\sin^2\left(\frac{\sphericalangle(\hat{\boldsymbol{e}}_\ell,\hat{\boldsymbol{e}}_\nu)}{2}\right) \equiv g(\hat{E}_\nu)\,, \end{aligned} \tag{26}$$

which has the solution:

$$\hat{E}_\nu = \frac{m_\mathrm{W}^2}{4\,\hat{E}_\ell\,\sin^2\left(\frac{\sphericalangle(\hat{\boldsymbol{e}}_\ell,\hat{\boldsymbol{e}}_\nu)}{2}\right)}\,. \tag{27}$$

The symbol $\sphericalangle(\hat{\boldsymbol{e}}_\ell,\hat{\boldsymbol{e}}_\nu)$ refers to the angle between the directions of the charged lepton and of the neutrino.

The derivative of the RHS of Eq. (26) with respect to $\hat{E}_\nu$ yields:

$$\frac{1}{|g'(\hat{E}_\nu)|} = \frac{1}{4\,\hat{E}_\ell\,\sin^2\left(\frac{\sphericalangle(\hat{\boldsymbol{e}}_\ell,\hat{\boldsymbol{e}}_\nu)}{2}\right)}\,. \tag{28}$$

A.2.3. Energy of ν^* produced in $\mathrm{H}\to\mathrm{WW}^*\to\ell\nu\,\ell^*\nu^*$ decay

As mentioned previously, we denote by ℓ^* and ν^* the charged lepton and the neutrino that originate from the decay of the off-shell W boson. The condition that the mass of the 4-particle system of ℓ, ν, ℓ^*, and ν^* equals m_H implies that:

$$\begin{aligned} m_\mathrm{H}^2 \equiv m_{\ell\nu\ell^*\nu^*}^2 &= (\underbrace{\hat{E}_\ell + \hat{E}_\nu + \hat{E}_{\ell^*}}_{\equiv\hat{E}_{\ell\nu\ell^*}} + \hat{E}_{\nu^*})^2 - (\underbrace{\hat{\boldsymbol{p}}_\ell + \hat{\boldsymbol{p}}_\nu + \hat{\boldsymbol{p}}_{\ell^*}}_{\equiv\hat{\boldsymbol{p}}_{\ell\nu\ell^*}} + \hat{\boldsymbol{p}}_{\nu^*})^2 \\ &= \hat{E}_{\ell\nu\ell^*}^2 + \hat{E}_{\nu^*}^2 + 2\,\hat{E}_{\ell\nu\ell^*}\,\hat{E}_{\nu^*} - |\hat{\boldsymbol{p}}_{\ell\nu\ell^*}|^2 \\ &\quad - |\hat{\boldsymbol{p}}_{\nu^*}|^2 - 2\,\hat{\boldsymbol{p}}_{\ell\nu\ell^*}\cdot\hat{\boldsymbol{p}}_{\nu^*} \\ &= \underbrace{\hat{E}_{\ell\nu\ell^*}^2 - |\hat{\boldsymbol{p}}_{\ell\nu\ell^*}|^2}_{\equiv m_{\ell\nu\ell^*}^2} + \underbrace{\hat{E}_{\nu^*}^2 - |\hat{\boldsymbol{p}}_{\nu^*}|^2}_{=m_\nu^2\approx 0} + 2\,\underbrace{\hat{E}_{\ell\nu\ell^*}}_{\equiv a}\,\hat{E}_{\nu^*} \end{aligned}$$

$$
\begin{aligned}
&\underbrace{-2\,\sqrt{\hat{E}^2_{\ell\nu\ell^*} - m^2_{\ell\nu\ell^*}}\,\hat{\boldsymbol{e}}_{\ell\nu\ell^*}\cdot\hat{\boldsymbol{e}}_{\nu^*}}_{\equiv b}\;\underbrace{|\hat{\boldsymbol{p}}_{\nu^*}|}_{\approx\hat{E}_{\nu^*}} \\
&= m^2_{\ell\nu\ell^*} + 2\,a\,\hat{E}_{\nu^*} - 2\,b\,\hat{E}_{\nu^*} \\
\Longrightarrow 0 &= \underbrace{\frac{m^2_{\mathrm{H}} - m^2_{\ell\nu\ell^*}}{2}}_{\equiv\Delta_{m_{\mathrm{H}}}} - a\,\hat{E}_{\nu^*} + b\,\hat{E}_{\nu^*} \equiv g(\hat{E}_{\nu^*}),
\end{aligned}
\tag{29}
$$

which has the solution:

$$
\begin{aligned}
\hat{E}_{\nu^*} &= \frac{\Delta_{m_{\mathrm{H}}}}{a-b} = \frac{m^2_{\mathrm{H}} - m^2_{\ell\nu\ell^*}}{2\left(\hat{E}_{\ell\nu\ell^*} - \underbrace{\sqrt{\hat{E}^2_{\ell\nu\ell^*} - m^2_{\ell\nu\ell^*}}}_{=\hat{\beta}_{\ell\nu\ell^*}\,\hat{E}_{\ell\nu\ell^*}}\;\underbrace{\hat{\boldsymbol{e}}_{\ell\nu\ell^*}\cdot\hat{\boldsymbol{e}}_{\nu^*}}_{\equiv\cos\sphericalangle(\hat{\boldsymbol{e}}_{\ell\nu\ell^*},\hat{\boldsymbol{e}}_{\nu^*})}\right)} \\
&= \frac{m^2_{\mathrm{H}} - m^2_{\ell\nu\ell^*}}{2\,\hat{E}_{\ell\nu\ell^*}\,\left(1 - \hat{\beta}_{\ell\nu\ell^*}\,\cos\sphericalangle(\hat{\boldsymbol{e}}_{\ell\nu\ell^*},\hat{\boldsymbol{e}}_{\nu^*})\right)},
\end{aligned}
\tag{30}
$$

where, for the purpose of shortening the nomenclature, we denote by the symbols $\hat{E}_{\ell\nu\ell^*}$ and $\hat{\boldsymbol{p}}_{\ell\nu\ell^*}$ the energy and the momentum of the 3-particle system comprised of the neutrino originating from the decay of the on-shell W boson and of the two charged leptons, by $\hat{\boldsymbol{e}}_{\ell\nu\ell^*}$ a unit vector in direction of $\hat{\boldsymbol{p}}_{\ell\nu\ell^*}$, and by $m_{\ell\nu\ell^*}$ the mass of this 3-particle system.

The derivative of the RHS of Eq. (29) with respect to $\hat{E}_{\nu^*}$ amounts to:

$$
\begin{aligned}
\frac{1}{|g'(\hat{E}_{\nu^*})|} &= \frac{1}{|a-b|} = \frac{1}{\left|\hat{E}_{\ell\nu\ell^*} - \underbrace{\sqrt{\hat{E}^2_{\ell\nu\ell^*} - m^2_{\ell\nu\ell^*}}}_{=\hat{\beta}_{\ell\nu\ell^*}\,\hat{E}_{\ell\nu\ell^*}}\,\cos\sphericalangle(\hat{\boldsymbol{e}}_{\ell\nu\ell^*},\hat{\boldsymbol{e}}_{\nu^*})\right|} \\
&= \frac{1}{\hat{E}_{\ell\nu\ell^*}\left|1 - \hat{\beta}_{\ell\nu\ell^*}\,\cos\sphericalangle(\hat{\boldsymbol{e}}_{\ell\nu\ell^*},\hat{\boldsymbol{e}}_{\nu^*})\right|}.
\end{aligned}
\tag{31}
$$

When inserting Eq. (31) into Eq. (9) to obtain the expression for the PD $w_0(\boldsymbol{p})$ of the signal hypothesis in Eq. (10), we will omit the modulus in the denominator. The modulus is redundant, because the argument $1 - \hat{\beta}_{\ell\nu\ell^*}\,\cos\sphericalangle(\hat{\boldsymbol{e}}_{\ell\nu\ell^*},\hat{\boldsymbol{e}}_{\nu^*})$ is never negative.

A.2.4. Energy of b ($\bar{\mathrm{b}}$) *produced in* $\mathrm{t}\to\mathrm{bW}^+\to\mathrm{b}\ell^+\nu$ ($\bar{\mathrm{t}}\to\bar{\mathrm{b}}\mathrm{W}^-\to\bar{\mathrm{b}}\ell^-\bar{\nu}$) *decay*

The condition that the mass of the 3-particle system comprised of the b quark, the charged anti-lepton, and the neutrino equals m_{t} implies that:

$$
\begin{aligned}
m^2_{\mathrm{t}} \equiv m^2_{\mathrm{b}\ell^+\nu} &= (\hat{E}_{\mathrm{b}} + \underbrace{\hat{E}_{\ell^+} + \hat{E}_{\nu}}_{\equiv\hat{E}_{\ell^+\nu}})^2 - (\hat{\boldsymbol{p}}_{\mathrm{b}} + \underbrace{\hat{\boldsymbol{p}}_{\ell^+} + \hat{\boldsymbol{p}}_{\nu}}_{\equiv\hat{\boldsymbol{p}}_{\ell^+\nu}})^2 \\
&= \hat{E}^2_{\mathrm{b}} + \hat{E}^2_{\ell^+\nu} + 2\,\hat{E}_{\mathrm{b}}\,\hat{E}_{\ell^+\nu} - |\hat{\boldsymbol{p}}_{\mathrm{b}}|^2 - |\hat{\boldsymbol{p}}_{\ell^+\nu}|^2 - 2\,\hat{\boldsymbol{p}}_{\mathrm{b}}\cdot\hat{\boldsymbol{p}}_{\ell^+\nu} \\
&= \underbrace{\hat{E}^2_{\mathrm{b}} - |\hat{\boldsymbol{p}}_{\mathrm{b}}|^2}_{=m^2_{\mathrm{b}}} + \underbrace{\hat{E}^2_{\ell^+\nu} - |\hat{\boldsymbol{p}}_{\ell^+\nu}|^2}_{=m^2_{\mathrm{W}}} + 2\,\underbrace{\hat{E}_{\ell^+\nu}}_{\equiv a}\,\hat{E}_{\mathrm{b}} \\
&\quad\underbrace{-2\,\sqrt{\hat{E}^2_{\ell^+\nu} - m^2_{\mathrm{W}}}\,\hat{\boldsymbol{e}}_{\ell^+\nu}\cdot\hat{\boldsymbol{e}}_{\mathrm{b}}}_{\equiv b}\,\sqrt{\hat{E}^2_{\mathrm{b}} - m^2_{\mathrm{b}}} \\
\Longrightarrow 0 &= \underbrace{\frac{m^2_{\mathrm{t}} - m^2_{\mathrm{b}} - m^2_{\mathrm{W}}}{2}}_{\equiv\Delta_{m_{\mathrm{t}}}} - a\,\hat{E}_{\mathrm{b}} + b\,\sqrt{\hat{E}^2_{\mathrm{b}} - m^2_{\mathrm{b}}} \equiv g(\hat{E}_{\mathrm{b}}),
\end{aligned}
\tag{32}
$$

where we denote the energy of the system of the charged anti-lepton and of the neutrino by the symbol $\hat{E}_{\ell^+\nu}$ and the momentum of this system by the symbol $\hat{\boldsymbol{p}}_{\ell^+\nu}$. The symbol $\hat{\boldsymbol{e}}_{\ell^+\nu}$ denotes a unit vector in direction of $\hat{\boldsymbol{p}}_{\ell^+\nu}$. The mass of this system equals m_{W}, as the W boson produced in the decay $\mathrm{t}\to\mathrm{bW}^+$ is on-shell. Eq. (32) has two solutions:

$$
\hat{E}_{\mathrm{b}} = \frac{a\,\Delta_{m_{\mathrm{t}}} \pm |b|\,\sqrt{\Delta^2_{m_{\mathrm{t}}} - (a^2-b^2)\,m^2_{\mathrm{b}}}}{a^2-b^2}.
\tag{33}
$$

We discard the solution of lower energy and consider the solution of higher energy only, i.e. we take the solution corresponding to the + sign in Eq. (33).

The derivative of the RHS of Eq. (32) with respect to $\hat{E}_{\mathrm{b}}$ yields:

$$
\begin{aligned}
\frac{1}{|g'(\hat{E}_{\mathrm{b}})|} &= \frac{1}{\left|a - \underbrace{\frac{b\,\hat{E}_{\mathrm{b}}}{\sqrt{\hat{E}^2_{\mathrm{b}} - m^2_{\mathrm{b}}}}}_{=\hat{\beta}_{\mathrm{b}}\,\hat{E}_{\mathrm{b}}}\right|} = \frac{1}{\left|a - \frac{1}{\hat{\beta}_{\mathrm{b}}}\,b\right|} \\
&= \frac{1}{\left|\hat{E}_{\ell^+\nu} - \frac{1}{\hat{\beta}_{\mathrm{b}}}\,\underbrace{\sqrt{\hat{E}^2_{\ell^+\nu} - m^2_{\mathrm{W}}}}_{=\hat{\beta}_{\ell^+\nu}\,\hat{E}_{\ell^+\nu}}\;\underbrace{\hat{\boldsymbol{e}}_{\ell^+\nu}\cdot\hat{\boldsymbol{e}}_{\mathrm{b}}}_{\equiv\cos\sphericalangle(\hat{\boldsymbol{e}}_{\ell^+\nu},\hat{\boldsymbol{e}}_{\mathrm{b}})}\right|} \\
&= \frac{1}{\left|\hat{E}_{\ell^+\nu}\left(1 - \frac{\hat{\beta}_{\ell^+\nu}}{\hat{\beta}_{\mathrm{b}}}\,\cos\sphericalangle(\hat{\boldsymbol{e}}_{\ell^+\nu},\hat{\boldsymbol{e}}_{\mathrm{b}})\right)\right|}.
\end{aligned}
\tag{34}
$$

The corresponding expressions for the case of $\bar{\mathrm{b}}$ quark, charged lepton, and anti-neutrino are identical to Eqs. (33) and (34), except that the symbol b is replaced by $\bar{\mathrm{b}}$ and the symbols ℓ^+ and ν are replaced by ℓ^- and $\bar{\nu}$.

References

[1] G. Aad, et al., ATLAS Collaboration, Observation of a new particle in the search for the Standard Model Higgs boson with the ATLAS detector at the LHC, Phys. Lett. B 716 (2012) 1, http://dx.doi.org/10.1016/j.physletb.2012.08.020, arXiv:1207.7214.

[2] S. Chatrchyan, et al., CMS Collaboration, Observation of a new boson at a mass of 125 GeV with the CMS experiment at the LHC, Phys. Lett. B 716 (2012) 30, http://dx.doi.org/10.1016/j.physletb.2012.08.021, arXiv:1207.7235.

[3] G. Aad, et al., ATLAS and CMS Collaborations, Combined measurement of the Higgs boson mass in pp collisions at $\sqrt{s} = 7$ and 8 TeV with the ATLAS and CMS experiments, Phys. Rev. Lett. 114 (2015) 191803, http://dx.doi.org/10.1103/PhysRevLett.114.191803, arXiv:1503.07589.

[4] ATLAS Collaboration, Measurement of the Higgs boson mass in the $\mathrm{H}\to\mathrm{ZZ}^*\to 4\ell$ decay channel with $\sqrt{s} = 13$ TeV pp collisions using the ATLAS detector at the LHC, Tech. rep., 2020, URL https://cdsweb.cern.ch/record/2714883.

[5] A.M. Sirunyan, et al., CMS Collaboration, A measurement of the Higgs boson mass in the diphoton decay channel, Phys. Lett. B 805 (2020) 135425, http://dx.doi.org/10.1016/j.physletb.2020.135425, arXiv:2002.06398.

[6] V. Khachatryan, et al., CMS Collaboration, Constraints on the spin-parity and anomalous HVV couplings of the Higgs boson in proton collisions at 7 and 8 TeV, Phys. Rev. D 92 (1) (2015) 012004, http://dx.doi.org/10.1103/PhysRevD.92.012004, arXiv:1411.3441.

[7] G. Aad, et al., ATLAS Collaboration, Study of the spin and parity of the Higgs boson in diboson decays with the ATLAS detector, Eur. Phys. J. C 75 (10) (2015) 476, http://dx.doi.org/10.1140/epjc/s10052-015-3685-1,10.1140/epjc/s10052-016-3934-y, arXiv:1506.05669.

[8] G. Aad, et al., ATLAS Collaboration, Test of CP invariance in vector-boson fusion production of the Higgs boson in the $\mathrm{H}\to\tau\tau$ channel in proton-proton collisions at $\sqrt{s} = 13$ TeV with the ATLAS detector, Phys. Lett. B 805 (2020) 135426, http://dx.doi.org/10.1016/j.physletb.2020.135426, arXiv:2002.05315.

[9] A.M. Sirunyan, et al., CMS Collaboration, Constraints on anomalous Higgs boson couplings to vector bosons and fermions in its production and decay using the four-lepton final state, Phys. Rev. D 104 (5) (2021) 052004, http://dx.doi.org/10.1103/PhysRevD.104.052004, arXiv:2104.12152.

[10] G. Aad, et al., ATLAS and CMS Collaborations, Measurements of the Higgs boson production and decay rates and constraints on its couplings from a combined ATLAS and CMS analysis of the LHC pp collision data at $\sqrt{s} = 7$ and 8 TeV, J. High Energy Phys. 08 (2016) 045, http://dx.doi.org/10.1007/JHEP08(2016)045, arXiv:1606.02266.

[11] A.M. Sirunyan, et al., CMS Collaboration, Search for invisible decays of a Higgs boson produced through vector boson fusion in proton-proton collisions at $\sqrt{s} = 13$ TeV, Phys. Lett. B 793 (2019) 520, http://dx.doi.org/10.1016/j.physletb.2019.04.025, arXiv:1809.05937.

[12] A.M. Sirunyan, et al., CMS Collaboration, Measurements of the Higgs boson width and anomalous HVV couplings from on-shell and off-shell production in the four-lepton final state, Phys. Rev. D 99 (11) (2019) 112003, http://dx.doi.org/10.1103/PhysRevD.99.112003, arXiv:1901.00174.

[13] G. Aad, et al., ATLAS Collaboration, Constraints on new phenomena via Higgs boson couplings and invisible decays with the ATLAS detector, J. High Energy Phys. 11 (2015) 206, http://dx.doi.org/10.1007/JHEP11(2015)206, arXiv:1509.00672.

[14] M. Aaboud, et al., ATLAS Collaboration, Constraints on off-shell Higgs boson production and the Higgs boson total width in ZZ → 4ℓ and ZZ → 2ℓ2ν final states with the ATLAS detector, Phys. Lett. B 786 (2018) 223, http://dx.doi.org/10.1016/j.physletb.2018.09.048, arXiv:1808.01191.

[15] M. Aaboud, et al., ATLAS Collaboration, Observation of Higgs boson production in association with a top quark pair at the LHC with the ATLAS detector, Phys. Lett. B 784 (2018) 173, http://dx.doi.org/10.1016/j.physletb.2018.07.035, arXiv:1806.00425.

[16] A.M. Sirunyan, et al., CMS Collaboration, Observation of $t\bar{t}H$ production, Phys. Rev. Lett. 120 (23) (2018) 231801, http://dx.doi.org/10.1103/PhysRevLett.120.231801, arXiv:1804.02610.

[17] D. de Florian, I. Fabre, J. Mazzitelli, Triple Higgs production at hadron colliders at NNLO in QCD, J. High Energy Phys. 03 (2020) 155, http://dx.doi.org/10.1007/JHEP03(2020)155, arXiv:1912.02760.

[18] I. Zurbano Fernandez, et al., in: I. Béjar Alonso, O. Brüuning, P. Fessia, L. Rossi, L. Tavian, M. Zerlauth (Eds.), High-Luminosity Large Hadron Collider (HL-LHC): Technical design report 10/2020, 2020, http://dx.doi.org/10.23731/CYRM-2020-0010.

[19] T. Plehn, M. Rauch, The quartic Higgs coupling at hadron colliders, Phys. Rev. D 72 (2005) 053008, http://dx.doi.org/10.1103/PhysRevD.72.053008, arXiv:hep-ph/0507321.

[20] T. Binoth, S. Karg, N. Kauer, R. Rückl, Multi-Higgs boson production in the Standard Model and beyond, Phys. Rev. D 74 (2006) 113008, http://dx.doi.org/10.1103/PhysRevD.74.113008, arXiv:hep-ph/0608057.

[21] M. Grazzini, et al., Higgs boson pair production at NNLO with top quark mass effects, J. High Energy Phys. 05 (2018) 059, http://dx.doi.org/10.1007/JHEP05(2018)059, arXiv:1803.02463.

[22] J. Baglio, A. Djouadi, R. Gröber, M.M. Mühlleitner, J. Quevillon, M. Spira, The measurement of the Higgs self coupling at the LHC: theoretical status, J. High Energy Phys. 04 (2013) 151, http://dx.doi.org/10.1007/JHEP04(2013)151, arXiv:1212.5581.

[23] N. Craig, J. Galloway, S. Thomas, Searching for signs of the second Higgs doublet, 2013, arXiv:1305.2424.

[24] D.T. Nhung, M. Mühlleitner, J. Streicher, K. Walz, Higher order corrections to the trilinear Higgs self-couplings in the real NMSSM, J. High Energy Phys. 1311 (2013) 181, http://dx.doi.org/10.1007/JHEP11(2013)181, arXiv:1306.3926.

[25] R. Grober, M. Mühlleitner, Composite Higgs boson pair production at the LHC, J. High Energy Phys. 1106 (2011) 020, http://dx.doi.org/10.1007/JHEP06(2011)020, arXiv:1012.1562.

[26] R. Contino, C. Grojean, M. Moretti, F. Piccinini, R. Rattazzi, Strong double Higgs production at the LHC, J. High Energy Phys. 1005 (2010) 089, http://dx.doi.org/10.1007/JHEP05(2010)089, arXiv:1002.1011.

[27] C. Englert, T. Plehn, D. Zerwas, P.M. Zerwas, Exploring the Higgs portal, Phys. Lett. B 703 (2011) 298, http://dx.doi.org/10.1016/j.physletb.2011.08.002, arXiv:1106.3097.

[28] J.M. No, M. Ramsey-Musolf, Probing the Higgs portal at the LHC through resonant di-Higgs production, Phys. Rev. D 89 (2014) 095031, http://dx.doi.org/10.1103/PhysRevD.89.095031, arXiv:1310.6035.

[29] L. Randall, R. Sundrum, A large mass hierarchy from a small extra dimension, Phys. Rev. Lett. 83 (1999) 3370, http://dx.doi.org/10.1103/PhysRevLett.83.3370, arXiv:hep-ph/9905221.

[30] G. Buchalla, O. Cata, A. Celis, C. Krause, Note on anomalous Higgs-boson couplings in effective field theory, Phys. Lett. B 750 (2015) 298, http://dx.doi.org/10.1016/j.physletb.2015.09.027, arXiv:1504.01707.

[31] F. Goertz, A. Papaefstathiou, L.L. Yang, J. Zurita, Higgs boson pair production in the D=6 extension of the SM, J. High Energy Phys. 04 (2015) 167, http://dx.doi.org/10.1007/JHEP04(2015)167, arXiv:1410.3471.

[32] V. Khachatryan, et al., CMS Collaboration, Search for two Higgs bosons in final states containing two photons and two bottom quarks in proton-proton collisions at 8 TeV, Phys. Rev. D 94 (5) (2016) 052012, http://dx.doi.org/10.1103/PhysRevD.94.052012, arXiv:1603.06896.

[33] A.M. Sirunyan, et al., CMS Collaboration, Search for Higgs boson pair production in the $b\bar{b}\tau\tau$ final state in proton-proton collisions at $\sqrt{s} = 8$ TeV, Phys. Rev. D 96 (7) (2017) 072004, http://dx.doi.org/10.1103/PhysRevD.96.072004, arXiv:1707.00350.

[34] A.M. Sirunyan, et al., CMS Collaboration, Search for resonant and nonresonant Higgs boson pair production in the $b\bar{b}\ell\nu\ell\nu$ final state in proton-proton collisions at $\sqrt{s} = 13$ TeV, J. High Energy Phys. 01 (2018) 054, http://dx.doi.org/10.1007/JHEP01(2018)054, arXiv:1708.04188.

[35] A.M. Sirunyan, et al., CMS Collaboration, Combination of searches for Higgs boson pair production in proton-proton collisions at $\sqrt{s} = 13$ TeV, Phys. Rev. Lett. 122 (12) (2019) 121803, http://dx.doi.org/10.1103/PhysRevLett.122.121803, arXiv:1811.09689.

[36] A.M. Sirunyan, et al., CMS Collaboration, Search for nonresonant Higgs boson pair production in final states with two bottom quarks and two photons in proton-proton collisions at $\sqrt{s} = 13$ TeV, J. High Energy Phys. 03 (2021) 257, http://dx.doi.org/10.1007/JHEP03(2021)257, arXiv:2011.12373.

[37] G. Aad, et al., ATLAS Collaboration, Searches for Higgs boson pair production in the HH → $b\bar{b}\tau\tau, \gamma\gamma WW^*, \gamma\gamma b\bar{b}, b\bar{b}b\bar{b}$ channels with the ATLAS detector, Phys. Rev. D 92 (2015) 092004, http://dx.doi.org/10.1103/PhysRevD.92.092004, arXiv:1509.04670.

[38] M. Aaboud, et al., ATLAS Collaboration, Search for pair production of Higgs bosons in the $b\bar{b}b\bar{b}$ final state using proton-proton collisions at $\sqrt{s} = 13$ TeV with the ATLAS detector, J. High Energy Phys. 01 (2019) 030, http://dx.doi.org/10.1007/JHEP01(2019)030, arXiv:1804.06174.

[39] M. Aaboud, et al., ATLAS Collaboration, Search for Higgs boson pair production in the $\gamma\gamma b\bar{b}$ final state with 13 TeV pp collision data collected by the ATLAS experiment, J. High Energy Phys. 11 (2018) 040, http://dx.doi.org/10.1007/JHEP11(2018)040, arXiv:1807.04873.

[40] M. Aaboud, et al., ATLAS Collaboration, Search for resonant and non-resonant Higgs boson pair production in the $b\bar{b}\tau^+\tau^-$ decay channel in pp collisions at $\sqrt{s} = 13$ TeV with the ATLAS detector, Phys. Rev. Lett. 121 (19) (2018) 191801, http://dx.doi.org/10.1103/PhysRevLett.121.191801, arXiv:1808.00336.

[41] M. Aaboud, et al., ATLAS Collaboration, Search for Higgs boson pair production in the $b\bar{b}WW^*$ decay mode at $\sqrt{s} = 13$ TeV with the ATLAS detector, J. High Energy Phys. 04 (2019) 092, http://dx.doi.org/10.1007/JHEP04(2019)092, arXiv:1811.04671.

[42] M. Aaboud, et al., ATLAS Collaboration, Search for Higgs boson pair production in the $\gamma\gamma WW^*$ channel using pp collision data recorded at $\sqrt{s} = 13$ TeV with the ATLAS detector, Eur. Phys. J. C 78 (12) (2018) 1007, http://dx.doi.org/10.1140/epjc/s10052-018-6457-x, arXiv:1807.08567.

[43] M. Aaboud, et al., ATLAS Collaboration, Search for Higgs boson pair production in the WW^*WW^* decay channel using ATLAS data recorded at $\sqrt{s} = 13$ TeV, J. High Energy Phys. 05 (2019) 124, http://dx.doi.org/10.1007/JHEP05(2019)124, arXiv:1811.11028.

[44] U. Baur, T. Plehn, D.L. Rainwater, Measuring the Higgs boson self coupling at the LHC and finite top mass matrix elements, Phys. Rev. Lett. 89 (2002) 151801, http://dx.doi.org/10.1103/PhysRevLett.89.151801, arXiv:hep-ph/0206024.

[45] U. Baur, T. Plehn, D.L. Rainwater, Determining the Higgs boson self coupling at hadron colliders, Phys. Rev. D 67 (2003) 033003, http://dx.doi.org/10.1103/PhysRevD.67.033003, arXiv:hep-ph/0211224.

[46] U. Baur, T. Plehn, D.L. Rainwater, Examining the Higgs boson potential at lepton and hadron colliders: a comparative analysis, Phys. Rev. D 68 (2003) 033001, http://dx.doi.org/10.1103/PhysRevD.68.033001, arXiv:hep-ph/0304015.

[47] U. Baur, T. Plehn, D.L. Rainwater, Probing the Higgs self coupling at hadron colliders using rare decays, Phys. Rev. D 69 (2004) 053004, http://dx.doi.org/10.1103/PhysRevD.69.053004, arXiv:hep-ph/0310056.

[48] M.J. Dolan, C. Englert, M. Spannowsky, Higgs self-coupling measurements at the LHC, J. High Energy Phys. 10 (2012) 112, http://dx.doi.org/10.1007/JHEP10(2012)112, arXiv:1206.5001.

[49] A. Papaefstathiou, L.L. Yang, J. Zurita, Higgs boson pair production at the LHC in the $b\bar{b}W^+W^-$ channel, Phys. Rev. D 87 (1) (2013) 011301, http://dx.doi.org/10.1103/PhysRevD.87.011301, arXiv:1209.1489.

[50] D.E. Ferreira de Lima, A. Papaefstathiou, M. Spannowsky, Standard model Higgs boson pair production in the $b\bar{b}b\bar{b}$ final state, J. High Energy Phys. 08 (2014) 030, http://dx.doi.org/10.1007/JHEP08(2014)030, arXiv:1404.7139.

[51] D. Wardrope, E. Jansen, N. Konstantinidis, B. Cooper, R. Falla, N. Norjoharuddeen, Non-resonant Higgs pair production in the $b\bar{b}b\bar{b}$ final state at the LHC, Eur. Phys. J. C 75 (5) (2015) 219, http://dx.doi.org/10.1140/epjc/s10052-015-3439-0, arXiv:1410.2794.

[52] J.K. Behr, D. Bortoletto, J.A. Frost, N.P. Hartland, C. Issever, J. Rojo, Boosting Higgs pair production in the $b\bar{b}b\bar{b}$ final state with multivariate techniques, Eur. Phys. J. C 76 (7) (2016) 386, http://dx.doi.org/10.1140/epjc/s10052-016-4215-5, arXiv:1512.08928.

[53] Q. Li, Z. Li, Q.-S. Yan, X. Zhao, Probe Higgs boson pair production via the $3\ell 2j + p_T^{miss}$ mode, Phys. Rev. D 92 (1) (2015) 014015, http://dx.doi.org/10.1103/PhysRevD.92.014015, arXiv:1503.07611.

[54] A. Adhikary, S. Banerjee, R.K. Barman, B. Bhattacherjee, S. Niyogi, Revisiting the non-resonant Higgs pair production at the HL-LHC, J. High Energy Phys. 07 (2018) 116, http://dx.doi.org/10.1007/JHEP07(2018)116, arXiv:1712.05346.

[55] P.A. Zyla, et al., Particle Data Group Collaboration, Review of particle physics, PTEP 2020 (8) (2020) 083C01, http://dx.doi.org/10.1093/ptep/ptaa104.

[56] M. Czakon, A. Mitov, Top++: A program for the calculation of the top-pair cross-section at hadron colliders, Comput. Phys. Comm. 185 (2014) 2930, http://dx.doi.org/10.1016/j.cpc.2014.06.021, arXiv:1112.5675.

[57] A.K. Jain, J. Mao, K.M. Mohiuddin, Artificial neural networks: a tutorial, Computer 29 (3) (1996) 31, http://dx.doi.org/10.1109/2.485891.

[58] F. Chollet, et al., Keras, GitHub, 2015, https://github.com/fchollet/keras.

[59] K. Kondo, Dynamical likelihood method for reconstruction of events with missing momentum. 1: method and toy models, J. Phys. Soc. Jap. 57 (1988) 4126, http://dx.doi.org/10.1143/JPSJ.57.4126.

[60] K. Kondo, Dynamical likelihood method for reconstruction of events with missing momentum. 2: mass spectra for 2 → 2 processes, J. Phys. Soc. Jap. 60 (1991) 836, http://dx.doi.org/10.1143/JPSJ.60.836.

[61] J. de Favereau, C. Delaere, P. Demin, A. Giammanco, V. Lemaître, A. Mertens, M. Selvaggi, DELPHES 3 Collaboration, DELPHES 3: A modular framework for fast simulation of a generic collider experiment, J. High Energy Phys. 02 (2014) 057, http://dx.doi.org/10.1007/JHEP02(2014)057, arXiv:1307.6346.

[62] J. Neyman, E.S. Pearson, On the problem of the most efficient tests of statistical hypotheses, Phil. Trans. Roy. Soc. Lond. A 231 (694–706) (1933) 289, http://dx.doi.org/10.1098/rsta.1933.0009.
[63] I. Volobouev, Matrix element method in HEP: transfer functions, efficiencies, and likelihood normalization, 2011, arXiv:1101.2259.
[64] J. Alwall, R. Frederix, S. Frixione, V. Hirschi, F. Maltoni, O. Mattelaer, H.S. Shao, T. Stelzer, P. Torrielli, M. Zaro, The automated computation of tree-level and next-to-leading order differential cross sections, and their matching to parton shower simulations, J. High Energy Phys. 07 (2014) 079, http://dx.doi.org/10.1007/JHEP07(2014)079, arXiv:1405.0301.
[65] B. Grinstein, M. Trott, A Higgs-Higgs bound state due to new physics at a TeV, Phys. Rev. D 76 (2007) 073002, http://dx.doi.org/10.1103/PhysRevD.76.073002, arXiv:0704.1505.
[66] C. Degrande, C. Duhr, B. Fuks, D. Grellscheid, O. Mattelaer, T. Reiter, UFO: The universal FeynRules output, Comput. Phys. Comm. 183 (2012) 1201, http://dx.doi.org/10.1016/j.cpc.2012.01.022, arXiv:1108.2040.
[67] B. Hespel, D. Lopez-Val, E. Vryonidou, Higgs pair production via gluon fusion in the Two-Higgs-Doublet model, J. High Energy Phys. 09 (2014) 124, http://dx.doi.org/10.1007/JHEP09(2014)124, arXiv:1407.0281.
[68] J.D. Bjorken, Asymptotic sum rules at infinite momentum, Phys. Rev. 179 (1969) 1547, http://dx.doi.org/10.1103/PhysRev.179.1547.
[69] A. Buckley, J. Ferrando, S. Lloyd, K. Nordström, B. Page, M. Rüfenacht, M. Schönherr, G. Watt, LHAPDF6: Parton density access in the LHC precision era, Eur. Phys. J. C 75 (3) (2015) 132, http://dx.doi.org/10.1140/epjc/s10052-015-3318-8.
[70] A.D. Martin, W.J. Stirling, R.S. Thorne, G. Watt, Parton distributions for the LHC, Eur. Phys. J. C 63 (2009) 189, http://dx.doi.org/10.1140/epjc/s10052-009-1072-5, arXiv:0901.0002.
[71] F. Fiedler, A. Grohsjean, P. Haefner, P. Schieferdecker, The matrix element method and its application in measurements of the top quark mass, Nucl. Instrum. Methods A 624 (2010) 203, http://dx.doi.org/10.1016/j.nima.2010.09.024, arXiv:1003.1316.
[72] L. Bianchini, B. Calpas, J. Conway, A. Fowlie, L. Marzola, C. Veelken, L. Perrini, Reconstruction of the Higgs mass in events with Higgs bosons decaying into a pair of τ leptons using matrix element techniques, Nucl. Instrum. Methods A 862 (2017) 54, http://dx.doi.org/10.1016/j.nima.2017.05.001, arXiv:1603.05910.
[73] J. Alwall, A. Freitas, O. Mattelaer, The matrix element method and QCD radiation, Phys. Rev. D 83 (2011) 074010, http://dx.doi.org/10.1103/PhysRevD.83.074010, arXiv:1010.2263.
[74] S. Chatrchyan, et al., CMS Collaboration, Missing transverse energy performance of the CMS detector, JINST 6 (2011) P09001, http://dx.doi.org/10.1088/1748-0221/6/09/P09001, arXiv:1106.5048.
[75] D. Berdine, N. Kauer, D. Rainwater, Breakdown of the narrow width approximation for new physics, Phys. Rev. Lett. 99 (2007) 111601, http://dx.doi.org/10.1103/PhysRevLett.99.111601, arXiv:hep-ph/0703058.
[76] T. Ohl, Vegas revisited: adaptive Monte Carlo integration beyond factorization, Comput. Phys. Comm. 120 (1999) 13, http://dx.doi.org/10.1016/S0010-4655(99)00209-X, arXiv:hep-ph/9806432.
[77] G.P. Lepage, A new algorithm for adaptive multidimensional integration, J. Comput. Phys. 27 (1978) 192, http://dx.doi.org/10.1016/0021-9991(78)90004-9.
[78] P. Nason, A new method for combining NLO QCD with shower Monte Carlo algorithms, J. High Energy Phys. 11 (2004) 040, http://dx.doi.org/10.1088/1126-6708/2004/11/040, arXiv:hep-ph/0409146.
[79] S. Frixione, P. Nason, C. Oleari, Matching NLO QCD computations with parton shower simulations: the POWHEG method, J. High Energy Phys. 11 (2007) 070, http://dx.doi.org/10.1088/1126-6708/2007/11/070, arXiv:0709.2092.
[80] S. Alioli, P. Nason, C. Oleari, E. Re, A general framework for implementing NLO calculations in shower Monte Carlo programs: the POWHEG BOX, J. High Energy Phys. 06 (2010) 043, http://dx.doi.org/10.1007/JHEP06(2010)043, arXiv:1002.2581.
[81] J.M. Campbell, R.K. Ellis, P. Nason, E. Re, Top-pair production and decay at NLO matched with parton showers, J. High Energy Phys. 04 (2015) 114, http://dx.doi.org/10.1007/JHEP04(2015)114, arXiv:1412.1828.
[82] S. Alioli, S.-O. Moch, P. Uwer, Hadronic top-quark pair-production with one jet and parton showering, J. High Energy Phys. 01 (2012) 137, http://dx.doi.org/10.1007/JHEP01(2012)137, arXiv:1110.5251.
[83] G. Heinrich, S.P. Jones, M. Kerner, G. Luisoni, E. Vryonidou, NLO Predictions for Higgs boson pair production with full top quark mass dependence matched to parton showers, J. High Energy Phys. 08 (2017) 088, http://dx.doi.org/10.1007/JHEP08(2017)088, arXiv:1703.09252.
[84] G. Heinrich, S.P. Jones, M. Kerner, G. Luisoni, L. Scyboz, Probing the trilinear Higgs boson coupling in di-Higgs production at NLO QCD including parton shower effects, J. High Energy Phys. 06 (2019) 066, http://dx.doi.org/10.1007/JHEP06(2019)066, arXiv:1903.08137.
[85] R.D. Ball, V. Bertone, S. Carrazza, L. Del Debbio, S. Forte, A. Guffanti, N.P. Hartland, J. Rojo, NNPDF Collaboration, Parton distributions with QED corrections, Nuclear Phys. B 877 (2013) 290, http://dx.doi.org/10.1016/j.nuclphysb.2013.10.010, arXiv:1308.0598.
[86] R.D. Ball, V. Bertone, F. Cerutti, L. Del Debbio, S. Forte, A. Guffanti, J.I. Latorre, J. Rojo, M. Ubiali, NNPDF Collaboration, Unbiased global determination of parton distributions and their uncertainties at NNLO and at LO, Nuclear Phys. B 855 (2012) 153, http://dx.doi.org/10.1016/j.nuclphysb.2011.09.024, arXiv:1107.2652.
[87] R.D. Ball, et al., NNPDF Collaboration, Parton distributions for the LHC run II, J. High Energy Phys. 04 (2015) 040, http://dx.doi.org/10.1007/JHEP04(2015)040, arXiv:1410.8849.
[88] T. Sjöstrand, S. Ask, J.R. Christiansen, R. Corke, N. Desai, P. Ilten, S. Mrenna, S. Prestel, C.O. Rasmussen, P.Z. Skands, An introduction to PYTHIA 8.2, Comput. Phys. Comm. 191 (2015) 159, http://dx.doi.org/10.1016/j.cpc.2015.01.024, arXiv:1410.3012.
[89] A.M. Sirunyan, et al., CMS Collaboration, Extraction and validation of a new set of CMS PYTHIA 8 tunes from underlying-event measurements, Eur. Phys. J. C 80 (2020) 4, http://dx.doi.org/10.1140/epjc/s10052-019-7499-4, arXiv:1903.12179.
[90] M. Cacciari, G.P. Salam, G. Soyez, The anti-k_T jet clustering algorithm, J. High Energy Phys. 04 (2008) 063, http://dx.doi.org/10.1088/1126-6708/2008/04/063, arXiv:0802.1189.
[91] M. Cacciari, G.P. Salam, G. Soyez, FastJet User manual, Eur. Phys. J. C 72 (2012) 1896, http://dx.doi.org/10.1140/epjc/s10052-012-1896-2, arXiv:1111.6097.
[92] M. Cacciari, G.P. Salam, G. Soyez, The catchment area of jets, J. High Energy Phys. 04 (2008) 005, http://dx.doi.org/10.1088/1126-6708/2008/04/005, arXiv:0802.1188.
[93] M. Cacciari, G.P. Salam, Pileup subtraction using jet areas, Phys. Lett. B 659 (2008) 119, http://dx.doi.org/10.1016/j.physletb.2007.09.077, arXiv:0707.1378.
[94] S. Chatrchyan, et al., CMS Collaboration, Identification of b-quark jets with the CMS experiment, JINST 8 (2013) P04013, http://dx.doi.org/10.1088/1748-0221/8/04/P04013, arXiv:1211.4462.
[95] A.M. Sirunyan, et al., CMS Collaboration, Pileup mitigation at CMS in 13 TeV data, JINST 15 (09) (2020) P09018, http://dx.doi.org/10.1088/1748-0221/15/09/P09018, arXiv:2003.00503.
[96] M. Aaboud, et al., ATLAS Collaboration, Performance of missing transverse momentum reconstruction with the ATLAS detector using proton-proton collisions at $\sqrt{s} = 13$ TeV, Eur. Phys. J. C 78 (11) (2018) 903, http://dx.doi.org/10.1140/epjc/s10052-018-6288-9, arXiv:1802.08168.
[97] D.M. Green, J.A. Swets, Signal detection theory and psychophysics, Wiley, New York, 1966.
[98] T. Hahn, CUBA: A library for multidimensional numerical integration, Comput. Phys. Comm. 168 (2005) 78, http://dx.doi.org/10.1016/j.cpc.2005.01.010, arXiv:hep-ph/0404043.
[99] K. Hagiwara, J. Kanzaki, N. Okamura, D. Rainwater, T. Stelzer, Fast calculation of HELAS amplitudes using graphics processing unit (GPU), Eur. Phys. J. C 66 (2010) 477, http://dx.doi.org/10.1140/epjc/s10052-010-1276-8, arXiv:0908.4403.
[100] K. Hagiwara, J. Kanzaki, N. Okamura, D. Rainwater, T. Stelzer, Calculation of HELAS amplitudes for QCD processes using graphics processing unit (GPU), Eur. Phys. J. C 70 (2010) 513, http://dx.doi.org/10.1140/epjc/s10052-010-1465-5, arXiv:0909.5257.
[101] J. Kanzaki, Monte Carlo Integration on GPU, Eur. Phys. J. C 71 (2011) 1559, http://dx.doi.org/10.1140/epjc/s10052-011-1559-8, arXiv:1010.2107.
[102] K. Hagiwara, J. Kanzaki, Q. Li, N. Okamura, T. Stelzer, Fast computation of MadGraph amplitudes on graphics processing unit (GPU), Eur. Phys. J. C 73 (2013) 2608, http://dx.doi.org/10.1140/epjc/s10052-013-2608-2, arXiv:1305.0708.
[103] D. Schouten, A. DeAbreu, B. Stelzer, Accelerated matrix element method with parallel computing, Comput. Phys. Comm. 192 (2015) 54, http://dx.doi.org/10.1016/j.cpc.2015.02.020, arXiv:1407.7595.
[104] G. Grasseau, S. Lisniak, D. Chamont, Hybrid implementation of the VEGAS Monte Carlo algorithm, in: Proceedings, GPU Computing In High Energy Physics (GPUHEP2014): Pisa, Italy, September 10-12, 2014, 2015, p. 103, http://dx.doi.org/10.3204/DESY-PROC-2014-05/19.

Curriculum Vitae

1. Personal data

Name	Karl Ehatäht
Date and place of birth	9 September 1991 in Tartu, Estonia
Nationality	Estonian

2. Contact information

Address	National Institute of Chemical Physics and Biophysics, Laboratory of High Energy and Computational Physics, Rävala pst 10, 10143 Tallinn, Estonia
E-mail	karl.ehataht[at]cern.ch

3. Education

2017–2023	Tallinn University of Technology, School of Science, Applied Physics, PhD studies
2015–2017	University of Tartu, Faculty of Science and Technology, Institute of Physics, Physics, MSc *cum laude*
2010–2015	University of Tartu, Faculty of Science and Technology, Institute of Physics, Physics, BSc

4. Language competence

Estonian	native
English	professional working proficiency
German	elementary proficiency

5. Professional employment

2020– …	National Institute of Chemical Physics and Biophysics, Junior Researcher
2014–2015	Bang & Olufsen, Software Engineer
2011–2012	Conscript in Viru Infantry Battalion

6. Training courses

2021	Machine Learning in High Energy Physics Summer School
2020	Virtual Pipelines Training
2014	CERN Summer Student Program

7. Computer skills

- Operating systems: GNU/Linux, MS Windows
- Document preparation: LaTeX, LibreOffice, MS Office, markup
- Programming languages: C/C++, Python, Bash, Java, R
- Scientific packages: Wolfram Mathematica, MathCad

8. Defended theses

- 2017, Search for $\mathrm{t\bar{t}H}$ production in $3\ell + 1\tau_{\mathrm{h}}$ in final state, MSc, supervisors PhD Christian Veelken and PhD Luca Marzola, University of Tartu, Institute of Physics
- 2015, Constraints on the mass and charge of millicharged dark matter, BSc, supervisors PhD Hardi Veermäe and PhD Luca Marzola, University of Tartu, Institute of Physics

9. Field of research

- High Energy Physics

10. Scientific work
Papers

1. CMS Collaboration, "Measurement of the Higgs boson production rate in association with top quarks in final states with electrons, muons, and hadronically decaying tau leptons at $\sqrt{s} = 13$ TeV", *Eur. Phys. J. C*, vol. 81, no. 4, p. 378, 2021. doi: 10.1140/epjc/s10052-021-09014-x. arXiv: 2011.03652 [hep-ex]
2. CMS Collaboration, "Search for Higgs boson pairs decaying to $\mathrm{WW^*WW^*}$, $\mathrm{WW^*}\tau\tau$, and $\tau\tau\tau\tau$ in proton-proton collisions at $\sqrt{s} = 13$ TeV", *JHEP*, vol. 07, p. 095, 2023. doi: 10.1007/JHEP07(2023)095. arXiv: 2206.10268 [hep-ex]
3. K. Ehatäht and C. Veelken, "Stitching Monte Carlo samples", *Eur. Phys. J. C*, vol. 82, no. 5, p. 484, 2022. doi: 10.1140/epjc/s10052-022-10407-9. arXiv: 2106.04360 [physics.data-an]
4. K. Ehatäht and C. Veelken, "Application of the matrix element method to Higgs boson pair production in the channel $\mathrm{HH} \to \mathrm{b\bar{b}WW^*}$ at the LHC", *Nucl. Instrum. Meth. A*, vol. 1028, p. 166 373, 2022. doi: 10.1016/j.nima.2022.166373. arXiv: 2108.05267 [hep-ph]

Conference presentations

1. CHEP 2019 (poster): K. Ehatäht, CMS collaboration, "NANOAOD: a new compact event data format in CMS", *EPJ Web Conf.*, vol. 245, ed. by C. Doglioni, D. Kim, *et al.*, p. 06 002, 2020. doi: 10.1051/epjconf/202024506002
2. CBC 2022 (presentation): K. Ehatäht, CMS collaboration, "Search for Higgs boson pair production in WWWW, $\mathrm{WW}\tau\tau$, and $\tau\tau\tau\tau$ decay modes based on proton-proton collision data recorded by the CMS detector in LHC Run 2"

Elulookirjeldus

1. Isikuandmed

Nimi	Karl Ehatäht
Sünniaeg ja -koht	09.09.1991, Tartu, Eesti
Kodakondsus	Eesti

2. Kontaktandmed

Aadress	Keemilise ja Bioloogilise Füüsika Instituut, Kõrge Energia ja Arvutusfüüsika Laboratoorium, Rävala pst 10, 10143 Tallinn, Estonia
E-post	karl.ehataht[at]cern.ch

3. Haridus

2017–2023	Tallinna Tehnikaülikool, Loodusteaduskond, Küberneetika Instituut, Rakendusfüüsika, doktoriõpe
2015–2017	Tartu Ülikool, Loodusteaduskond, Füüsika Instituut, Füüsika, MSc *cum laude*
2010–2015	Tartu Ülikool, Loodusteaduskond, Füüsika Instituut, Füüsika, BSc

4. Keelteoskus

eesti keel	emakeel
inglise keel	kõrgtase
saksa keel	algtase

5. Teenistuskäik

2020– …	Keemilise ja Bioloogilise Füüsika Instituut, nooremteadur
2014–2015	Bang & Olufsen, tarkvaraarendaja
2011–2012	ajateenistus Viru Pataljonis

6. Koolituskursused

2021	Machine Learning in High Energy Physics Summer School
2020	Virtual Pipelines Training
2014	CERNi suvekool

7. Arvutioskused

- Operatsioonisüsteemid: GNU/Linux, MS Windows
- Kontoritarkvara: LaTeX, LibreOffice, MS Office
- Programmeerimiskeeled: C/C++, Python, Bash, Java, R, markup
- Teadustarkvara paketid: Wolfram Mathematica, MathCad

8. Kaitstud lõputööd

- 2017, Protsessi $\mathrm{t\bar{t}H}$ uurimine $3\ell + 1\tau_{\mathrm{h}}$ lõppolekuga, MSc,
  juhendajad PhD Christian Veelken ja PhD Luca Marzola,
  Tartu Ülikool, Loodusteaduskond, Füüsika Instituut
- 2015, Piirangud millilaetud tumeaine massile ja laengule, BSc,
  juhendajad PhD Hardi Veermäe ja PhD Luca Marzola,
  Tartu Ülikool, Loodusteaduskond, Füüsika Instituut

9. Teadustöö põhisuunad

- Kõrge energia füüsika

10. Teadustegevus
Teadusartiklite, konverentsiteeside ja konverentsiettekannete loetelu on toodud inglis-keelse elulookirjelduse juures.

ISSN 2585-6901 (PDF)
ISBN 978-9916-80-058-4 (PDF)